CODEN: JASMAN

ISSN: 0001-4966

The Journal of the Acoustical Society of America

Vol. 118, No. 1 July 2005

(Continued)

THE JOURNAL OF THE ACOUSTICAL SOCIETY OF AMERICA VOL. 118, NO. 1, JULY 2005

CONTENTS—*Continued from preceding page*

(Continued)

THE JOURNAL OF THE ACOUSTICAL SOCIETY OF AMERICA VOL. 118, NO. 1, JULY 2005

CONTENTS—*Continued from preceding page*

(Continued)

THE JOURNAL OF THE ACOUSTICAL SOCIETY OF AMERICA VOL. 118, NO. 1, JULY 2005

CONTENTS—*Continued from preceding page*

ACOUSTICAL NEWS—USA

Elaine Moran
Acoustical Society of America, Suite 1NO1, 2 Huntington Quadrangle, Melville, NY 11747–4502

Editor's Note: *Readers of this journal are encouraged to submit news items on awards, appointments, and other activities about themselves or their colleagues. Deadline dates for news items and notices are 2 months prior to publication.*

New Fellows of the Acoustical Society of America

Michael Ainslie—For contributions to modeling seabed reflection and sonar performance.

Bennett M. Brooks—For contributions to noise control enginering, standards and noise policy.

Call for Business Meeting of the Society

Notice. A business meeting of the Society will be held starting at 3:30 p.m. on 19 October 2005 at the Hilton Hotel in Minneapolis, Minnesota. All ASA Fellows and Members are urged to attend for the purpose of voting on proposed amendments to **Section 6. Treasurer** of **Article V Officers**, of the Bylaws of the Society.

Rationale for the proposed Bylaw amendments. In the past several years the financial activities concerned with the Society's operations have greatly increased and become more complex. Numerous operational changes have occurred to deal with this situation, and incorporated into changes to the Rules as approved from time to time by the Executive Council of the Society. For example, an Audit Committee and a Committee on Investments have been established. In addition the Headquarters Office performs many of the daily financial transactions, and an accountant routinely reviews and updates the financial records of the Society. There have also been minor changes to the financial responsibilities of the Executive Director and the Standards Director. Gradually the duties and responsibilities of the Treasurer have been modified as the financial operations of the Society have changed. The Bylaws of the Society should be modified to insure that the Bylaws and current practice are again in harmony.

Motion to be presented at the business meeting. The motion concerns a single clause of the Bylaws, namely **Section 6 Treasurer** of **Article V Officers.** A proposed amendment may be adopted by a two-thirds vote of the Members and Fellows present and voting in person. Additions to the wording of this Section 6 are shown in bold type and deletions to the wording by means of a strike through.

Motion. To approve the following revised version of Section 6 of Article V Officers:

The Treasurer shall ~~be responsible~~ **account** for all funds, securities, and other property of the Society and shall be the chief adviser to the Executive Council on all ~~business and~~ financial matters. With the assistance of other officers of the Society designated by the President, he or she shall prepare the Society's budgets and be responsible for business transactions of the Society as **assigned and** authorized by the Executive Council. The Treasurer shall ~~also be responsible~~ **arrange** for the collection of all dues **and other amounts receivable by the Society**, and shall periodically make such financial reports to the Executive Council and to members of the Society as are requested by the Executive Council. With the approval of the Executive Council, the Treasurer may delegate some of these responsibilities to others.

CHARLES E. SCHMID
Executive Director

F.V. Hunt Postdoctoral Research Fellowship awarded to Catherine L. Berchok

The 2005–06 F. V. Hunt Postdoctoral Research Fellowship in Acoustics was awarded to Catherine L. Berchok. During her Hunt Fellowship year, Dr. Berchok will undertake a research program at the Scripps Institution of Oceanography, University of California, San Diego. The subject of her research is on the investigation of the Lombard effect for marine mammals. Dr. Berchok received a B.S. degree from the University of Pittsburgh and a Ph.D. in Acoustics from Pennsylvania State University. Her Ph.D. thesis is titled "Characterization of St. Lawrence blue whale vocalizations and their correlation with field observations."

 0001-4966/2005/118(1)/1/7/$22.50

The Hunt Fellowship is granted each year to an ASA member who has recently received his or her doctorate or will be receiving the degree in the year in which the fellowship is to be granted. The recipient of the fellowship is that individual who, through personal qualifications and a proposed research topic, is judged to exhibit the highest potential for benefiting any aspect of the science of sound and promoting its usefulness to society. Further information about the fellowship is available from the Acoustical Society of America, Suite 1NO1, 2 Huntington Quadrangle, Melville, NY 11747-4502. Phone: 516-576-2360; fax: 516-576-2377; E-mail: asa@aip.org; Web: asa.aip.org/fellowships.html

USA Meetings Calendar

Following is a summary of meetings related to acoustics to be held in the U.S. in the future. The month/year notation refers to the issue in which a complete meeting announcement appeared.

2005

18–22 July	17th International Symposium on Nonlinear Acoustics, State College, PA [Anthony Atchley, The Pennsylvania State University, 217 Applied Research Lab Building, University Park, PA 16802; Tel.: 814-865-6364; E-mail: ISNA17@outreach.psu.edu; www:http:// www.outreach.psu.edu/c&i/isna17/
17–21 October	150th Meeting joint with NOISE-CON 2005, Minneapolis, MN [Acoustical Society of America, Suite 1NO1, 2 Huntington Quadrangle, Melville, NY 11747-4502; Tel.: 516-576-2360; Fax: 516-576-2377; E-mail: asa@aip.org; WWW: http://asa.aip.org].
27–29 October	Fifth International Symposium on Therapeutic Ultrasound, Boston, MA [www.istu2005.org; Email: info@istu2005.org}.

2008

28 July–1 August	Ninth International Congress on Noise as a Public Health Problem (Quintennial meeting of ICBEN, the International Commission on Biological Effects of Noise). Foxwoods Resort, Mashantucket, CT [Jerry V. Tobias, ICBEN 9, Post Office Box 1609, Groton, CT 06340-1609, Tel. 860-572-0680; www.icben.org; Email: icben2008@att.net.

Cumulative Indexes to the Journal of the Acoustical Society of America

Ordering information: Orders must be paid by check or money order in U.S. funds drawn on a U.S. bank or by Mastercard, Visa, or American Express credit cards. Send orders to Circulation and Fulfillment Division, American Institute of Physics, Suite 1NO1, 2 Huntington Quadrangle, Melville, NY 11747-4502; Tel.: 516-576-2270. Non-U.S. orders add $11 per index.

Some indexes are out of print as noted in the following.

Volumes 1–10, 1929–1938: JASA, and Contemporary Literature, 1937–1939. Classified by subject and indexed by author. 131 pp. Price: ASA members $5; Nonmembers $10.

Volumes 11–20, 1939–1948: JASA, Contemporary Literature and Patents. Classified by subject and indexed by author and inventor. 395 pp. Out of Print.

Volumes 21–30, 1949–1958: JASA, Contemporary Literature and Patents. Classified by subject and indexed by author and inventor. 952 pp. Price: ASA members $20; Nonmembers $75.

Volumes 31–35, 1959–1963: JASA, Contemporary Literature and Patents. Classified by subject and indexed by author and inventor. 1140 pp. Price: ASA members $20; Nonmembers $90.

Volumes 36–44, 1964–1968: JASA and Patents. Classified by subject and indexed by author and inventor. 485 pp. Out of Print.

Volumes 36–44, 1964–1968: Contemporary Literature. Classified by subject and indexed by author. 1060 pp. Out of Print.

Volumes 45–54, 1969–1973: JASA and Patents. Classified by subject and indexed by author and inventor. 540 pp. Price: $20 (paperbound); ASA members $25 (clothbound); Nonmembers $60 (clothbound).

Volumes 55–64, 1974–1978: JASA and Patents. Classified by subject and indexed by author and inventor. 816 pp. Price: $20 (paperbound); ASA members $25 (clothbound); Nonmembers $60 (clothbound).

Volumes 65–74, 1979–1983: JASA and Patents. Classified by subject and indexed by author and inventor. 624 pp. Price: ASA members $25 (paperbound); Nonmembers $75 (clothbound).

Volumes 75–84, 1984–1988: JASA and Patents. Classified by subject and indexed by author and inventor. 625 pp. Price: ASA members $30 (paperbound); Nonmembers $80 (clothbound).

Volumes 85–94, 1989–1993: JASA and Patents. Classified by subject and indexed by author and inventor. 736 pp. Price: ASA members $30 (paperbound); Nonmembers $80 (clothbound).

Volumes 95–104, 1994–1998: JASA and Patents. Classified by subject and indexed by author and inventor. 632 pp. Price: ASA members $40 (paperbound); Nonmembers $90 (clothbound).

Volumes 105–114, 1999–2003: JASA and Patents. Classified by subject and indexed by author and inventor. 616 pp. Price: ASA members $50; Nonmembers $90 (paperbound).

REVISION LIST

New Associates

Aden, Eric T., Walthall & Associates, Acoustical, 2180 Creighton Rd., Pensacola, FL 32504 Ahlstrom, Jayne B., 1315 Deepwater Dr., Mt. Pleasant, SC 29464

Bateman, Craig A., Maritime Systems Eng., Texas A & M Univ. at Galveston, 200 Seawolf Park Way, Galveston, TX 77553

Bellinger, Sherri M., 6 Amy Ln., New Windsor, NY 12553

Brock-Nannestad, George, Patent Tactics, Resedavej 40, Gentofte DK-2820, Denmark

Brown, Christopher A., Arizona State Univ., Speech and Hearing Science, P.O. Box 870102, Tempe, AZ 85287-0102

Burcsak, Stephen, 603 Ctr. St., Unit 201, Herndon, VA 20170

Cass, Hugo A., 97 Knowsley Rd., Norwich NR3 4PT, UK

Chhetri, Dinesh, 22664 Ingomar St., West Hills, CA 91304

Choi, Chul–Hee, Baylor College of Medicine, Otorhinolaryngology and Communicative Science, Neurosensory Ctr. NA 500, One Baylor Plaza, Houston, TX 77030

Clements, Jessica S., Merck and Hill Consultants, Inc., 1995 North Park Pl., Ste. 200, Atlanta, GA 30339

Cole, Jennifer S., Linguistics, Univ. of Illinois at Urbana–Champaign, 707 South Mathews, 4080 FLB, Urbana, IL 61801

Cusick, Michael J., SAVI, 14 Solar Dr., Clifton Park, NY 12065

Desutter-Grandcolas, Laure, Museum National D'Histoire Naturelle, Systematique et Evolution–UMR 5202 CNRS, Case Postale 50, Paris, 75231 Cedex 05, France

Digerness, Joseph K., 22-4 Mountainview Dr., Birmingham, AL 35216

Drob, Douglas P., Naval Research Lab., Upper Atmospheric Physics Branch, 4555 Overlook Ave., Washington, DC 20375

Dyckmans, John J., 218 Tullis St., Moncks Corner, SC 29461

Fels, Sidney S., Electrical and Computer Eng., Univ. of British Columbia, 2356 Main Mall, Vancouver BC V6T 1Z4, Canada

Freeman, Alena A., Bernafon LLC, 200 Cottontail Ln., Bldg. B, Somerset, NJ 08873 Gatley, Robert W., 3 Beechwood Ave., Charlton, NY 12019

Gilmore, Richard G., Estuarine, Coastal and Ocean Science, Inc., 5920 1st St., SW, Vero Beach, FL 32962

Grainger, Martin, Grainger Communication, Unit 29b, Gortrush Industrial Estate, Omagh, co. Tyrone BT78 5EJ, UK

Gravel, Sylvain, Hydroi-Quebec, IREQ, 1800, Lionel Boulet, Varennes QC J3X 1S1, Canada Guo, Hongkai, Piezo Technologies, 1600 West Main St., Lebanon, IN 46052

Heavner, Matt, Univ. of Alaska Southeast, Natural Science, 11120 Glacier Highway, Juneau, AK 99801

Ho, Ken K., Fortis Technologies, 2249 Federal Ave., Los Angeles, CA 90064

Hofer, Daniel, SoundSense, LLC, 29 Gann Rd., East Hampton, NY 11937

Houston, Derek M., Otolaryngology, Indiana Univ. School of Medicine, 699 West Dr., RR 044, Indianapolis, IN 46202

Huang, Tsan, SUNY at Buffalo, Linguistics, 609 Baldy Hall, Buffalo, NY 14260

Hultz, Paul B., Bose Corporation, MS 15B, The Mountain, Framingham, MA 01701

Itakura, Famitada, Takabaridai 3-506, Meito-ku, Nagoya, Aichi–ken, 465-0054, Japan
Jabeen, Farkhanda, MSL, H. No. 311, Main Margala Rd., F 11/3, Islamabad 45000, Pakistan
Janik, Vincent M., Gatty Marine Lab., School of Biology, Univ. of St. Andrews, St. Andrews, Fife KY16 8LB, UK
Johnson, Paul A., BAE Systems, 1601 Research Blvd., Rockville, MD 20850
Johnson, Roland E., Dassault Falcon Jet, P.O. Box 967, Dept. 210, Little Rock, AR 72203
Joseph, John E., 15755 Alto Way, Salinas, CA 93907
Karavitaki, K. Domenica, Harvard Medical School, Neurobiology, 220 Longwood Ave., Goldenson 443, Boston, MA 02115
Kemp, Mathieu, 2211 Meade Ln., Durham, NC 27707
Kettman, Nick D., Shure Incorporated, 5800 West Touhy Ave., Niles, IL 60714
Kheong, Lim S., All Good Gifts Limited, 203 Henderson Rd., #07–09, Singapore 159547
King, Heather B., Deakin Univ., School of Communication and Creative Arts, Pigdons Rd., Waurn Ponds, Victoria 3216, Australia
Langston, Charles A., Ctr. for Earthquake Res. and Info., Univ. of Memphis, 3876 Central Ave., Ste. 1, Memphis, TN 38152-3050
Lee, Kyun Kyung, Kyungpook National Univ., School of Electrical Eng. and Computer Science, E10-827, Sankyuk-dong 1370, Buk-gu, Daegu, 702701, Republic of Korea
Lucifredi, Irena, Scientific Solutions Inc., 99 Perimeter Rd., Nashua, NH 03063
Macomber, Dwight F., P.O. Box 202, Devon, PA 19333
Maki, Katuhiro, NTT Corporation, NTT Communication Science Laboratories, 3-1 Morinosato-wakamiya, Atsugi 243-0198, Japan
Manzara, Leonard C., 43 Hunter St., Northwest, Calgary, Alberta T2K 2B8, Canada
Marasinghe, Chandrajith Ashuboda, The Univ. of Aizu, Software Eng. Lab., Tsuruga, Ikkimachi, Aizu-Wakamatsu, Fukushima 965-8580, Japan
Marlin, David H., 4925 Raevin Court, Las Cruces, NM 88007
Martinez, Francisco, Ingenieria Mecanica, Univ. de Zaragoza, Ed Betancourt Zaragoza 50018, Spain
Masuda-Katsuse, Ikuyo, School of Humanity-Oritented Sci. and Eng., Kinki Univ., Kayanomori, Iizuka-city, Fukuoka 820-8555, Japan
Mazzarella, Livio, Politecnico di Milano, Piazza Leonardo da Vinci 32, Milano 20133, Italy
McCall, Andrew M., Sercel, Inc., 17200 Park Row, Houston, TX 77084
McClure, Bob E., BioSonics, Inc., 4027 Leary Way NW, Seattle, WA 98107
McKeown, Eugene P., Biospheric Eng., Ltd., Truskey East, Bearna, Ireland
Mi, Bin, Guidant Corp., R&T, 4100 Hamline Ave., North, St. Paul, MN 55112
Miller, Douglas A., Cochlear Americas, Research, 400 Inverness Pkwy., Englewood, CO 80112
Moehring, Mark A., Spencer Technologies, 701 16th Ave., Seattle, WA 98122
Murphy, Patrick E., Veneklasen Associates, 1711 16th St., Santa Monica, CA 90034
Murphy, Peter J., Univ. of Limerick, Electronic and Computer Eng., Limerick, Ireland
Murray, Jay R., 369 El Caminito, Carmel Valley, CA 93924
Nakama, Masahiro, Univ. of Ryukyus, Faculty of Education, 1 Senbaru, Nishihara, Okinawa 903-0213, Japan
Negrescu, Cristian P.O., Blvd. Octavian Goga No. 16, Bloc M42, Sc2, Ap. 31, Sector 3, Bucharest, RO 050461, Romania
Nelson, Dan, 532 West Lynwood, Phoenix, AZ 85003
Park, Daejin, DJU Consulting, CPO Box 950, Seoul 100-609, South Korea
Preston, Renwick, 12322 Astoria Blvd., Houston, TX 77089
Qin, Yixian, Stony Brook Univ., Biomedical Eng., 350 Psych-A Bldg., Stony Brook, NY 11794
Quinlan, John A., Rutgers Univ., Inst. of Marine and Coastal Sciences, 71 Dudley Rd., New Brunswick, NJ 08901
Redford, Melissa A., Linguistics, Univ. of Oregon, 1290 Univ. of Oregon, Eugene, OR 97403
Reichmuth Kastak, Colleen, Inst. of Marine Sciences, Univ. of California, LML 100 Shaffer Rd., Santa Cruz, CA 95060
Reynolds, Paul, Weidlinger Associates, Inc., 4410 El Camino Real, Ste. 110, Los Altos, CA 94022
Rogers, Tracey L., Australian Marine Mammal Research Centre, P.O. Box 20, Mosman NSW 2048,
Australia
Rorick, Timothy P., 4710 South Webster Rd., New Haven, IN 46774
Sachwald, Benjamin H., AKRF Acoustics, 117 East 29th St., New York, NY 10016
Sai Jayram, Akula, No. 115, 11A Cross, Thimmaiah Garden, RTNagar, Bangalore, Karnataka, 560032, India
Sassaroli, Elisabetta, 31 Winslow, Apt. 4, Brookline, MA 02446
Schuster, Bill, Honeywell Engines Systems and Services, Installation Aerodynamics and Acoustics, 111 South 34th St., MS 503-428, Phoenix, AZ 85034
Sharma, Gaurav, Optima International, LLC, Acoustic, P.O. Box 115858, Dubai 9714, United Arab Emirates
Shull, Steve W., Acoustic Dimensions, 15505 Wright Brothers Dr., Addison, TX 75001
Solway, Joseph W., 300 Cathedral Pkwy., Apt. 14D, New York, NY 10026
Sridhar, Kalluri, Starkey Hearing Research Ctr., 2150 Shattuck St., Ste. 408, Berkeley, CA 94704
Stoneham, Emily T., 48399 Surfside Dr., Lexington Park, MD 20653
Teranishi, Arthur M., 805 Lochwood Pl., Escondido, CA 92026
Thomas, Rebecca E., NOAA Fisheries—NWFSC, FRAM, 2725 Montlake Blvd., E, Seattle, WA 98112
Unoki, Masashi, Japan Advanced Inst. of Sci. and Tech., School of Information Science, 1-1 Asahidai, Tatsunokuchi, Ishikawa 923-1292, Japan
Van Wijk, Kasper, Colorado School of Mines, Geophysics, 1500 Illinois St., Golden, CO 80401
Vanhuffelen, Wim M., Audiological Centre, Oosterlaan 20, Zwolle, Overijssel 8011 GC, The Netherlands
Walters, Edward P., 6494 Wildwood Rd., Holland, MI 49423
Watkins, Glen, ETS-Lindgren, Marketing, 1301 Arrow Point Dr., Cedar Park, TX 78613
Williams, Michael, 62 Bis Quai de L″artois, Le Perreux Sur Marne 94170, France
Wright, Chris, P.O. Box 275, 54 Massaoag Way, Dunstable, MA 01827

New Students

Abouzeid, Jad, 10 Bonser Rd., London, Middlesex TW1 4RG, UK
Aronoff, Justin, Neuroscience Program, Univ. of Southern California, HNB 28c, Los Angeles, CA 90089
Bahng, Junghwa, Univ. of Tennessee, Audiology and Speech Pathology, 578 South Stadium, Knoxville, TN 37996
Baker, Adam, 6538 Calle Sin Nombre, Tucson, AZ 85718
Barand, John S., 39A Paunui St., St. Heliers, Auckland, 1007, New Zealand
Barley, Raymond B., 341-TE Oakville Dr., Pittsburgh, PA 15220-4326
Beierholm, Thomas, Saven A2, 2th, Taastrup 2630, Denmark
Benson-Amram, Sarah, Michigan State Univ., Dept. of Zoology, 203 Natural Sciences, East Lansing, MI 48823
Bentil, Sarah A., 1920 Ala Moana Blvd., Apt. 1103, Honolulu, HI 96815
Berke, Gur M., Mechanical Eng., Univ. of Massachusetts, Lowell, One University Ave., Lowell, MA 01854
Berkowitz, Shari, 64-15 231st St., Oakland Gardens, NY 11364
Bidet-Caulet, Aurelie, INSERM, U280, 151 cours Albert Thomas, Lyon, Rhone-Alpes 69003, France
Black, Paul R., 569 Wmount Terrace, Provo, UT 84604
Brown, Judson M., 8208 Illinois Rte. 120, Woodstock, IL 60098
Brunner, Jana, Zentrum fur Allgemeine Sprachwissenschaft, Jagerstrabe 10/11, Berlin 10117, Germany
Burgess, Sean A., 5402 20th Ave., NE, Seattle, WA 98105
Buye, Xu, Brigham Young Univ., Dept. of Physics and Astronomy, Provo, UT 84602
Camacho-Ramirez, Cecilia, 19119 Cypress Reach Ln., Tampa, FL 33647
Cappiello, Michael, 7284 West Myrtle Ave., Chicago, IL 60631
Casper, Brandon M., Univ. of South Florida, College of Marine Science, 140 7th Ave., South, St. Petersburg, FL 33701
Chavez-Peon, Mario E., Linguistics, Univ. of British Columbia, 1866 Main Mall, Buchanan E270, Vancouver BC V6T 1Z1, Canada

Chen, Zhixin, Montana State Univ., Electrical and Computer Eng. Dept., 636 Cobleigh Hall, Bozeman, MT 59715
Chen, Yian A., 1440 Orange Grove Rd., Charleston, SC 29407
Chung, Yoojin, Boston Univ., Biomedical Eng., 44 Cummington, Boston, MA 02215
Colletti, Steven R., 41870 Pedersen Dr., Antioch, IL 60002
Cook, Mandy L. H., College of Marine Science, Univ. of South Florida, 140 Seventh Ave., South, St. Petersburg, FL 33701-5016
Datta, Saurabh, Biomedical Eng., Univ. of Cincinnati, 231 Albert Sabine Way, Cincinnati, OH 45242
Dellwo, Volker, Phonetics and Linguistics, Univ. College London, 4 Stephenson Way, London NW1 2HE, UK
Deng, Huiqun, Electrical and Computer Eng. Dept., Univ. of British Columbia, 2356 Main Mall, Vancouver BC V6T 1Z4, Canada
Derrick, Donald J., Univ. of British Columbia, Linguistics, 1866 Main Mall E273, Vancouver, BC V6T 1Z1, Canada
DeWolf, Scott J., 111 1/2 North Main St., #2, River Falls, WI 54022
Dimulescu, Bianca, LIMSI-CNRS, CHM, B.P. 133, Orsay, Essonne F-91403, France
Donabed, Ninos J., 19 Orono St., Milton, MA 02186
Dosemeciler, Ayce, IZMIR Inst. of Technology, Faculty of Architecture, Gulbahce Urla, Izmir 35430
Drummond, Jeremiah, 5715 202nd St., Southwest #3, Lynnwood, WA 98036
Dudley, Chris, Washington State Univ., Physics, Webster Physical Science Bldg., Pullman, WA 99164
Eckstein, Veronica, 2316 Santa Ana Ave., Apt. #7, Costa Mesa, CA 92627
Erdener, Vahit Dogu, Univ. of Western Sydney, Marcs Auditory Laboratories, Locked Bag 1797, Penrith South DC, NSW 1797, Australia
Espana, Aubrey L., 310 NW Larry St., Apt. B, Pullman, WA 99163
Faehndrich, Burgel R. M., 1422 Heulu St., A203, Honolulu, HI 96822
Farinella-Bocian, Kimberly, 5700 North Williams Dr., Tucson, AZ 85704
Foley, Erin L., 2981 S. Lyman St., Chicago, IL 60608
Frederic, Botte, 150 Blvd de la villette, Paris 75019, France
Galeano, Christina N., 1307 McKenzie Ave., Bellingham, WA 98225
Ganse, Andrew, Applied Physics Lab., Univ. of Washington, 1013 NE 40th St., Seattle, WA 98105
Gao, Man, Haskins Laboratories, 270 Crown St., New Haven, CT 06511-6695
Gibson, William I., 2201 North Campbell Ave., Chicago, IL 60647
Guild, Matthew, 1071 Clayton Ln. #1516, Austin, TX 78723
Ha, Ho Kyung, Virginia Inst. of Marine Science, Physical Sciences, 1208 Greate Rd., Gloucester Point, VA 23062
Harght, Pamela J., 143 Park Dr., #18, Boston, MA 02215
Harman, Pamela R., 3929 Mayfield Ave., Glendale, CA 91214
Haworth, Kevin J., Univ. of Michigan, 200 Zina Pitcher Pl., Kresge III, Rm. 3322, Ann Arbor, MI 48109-0553
Hernandez, Erica N., Univ. of Southern Mississippi, Psychology, 118 College Dr., Box 5025, Hattiesburg, MS 39406
Hodoshima, Nao, 1-7-7 Hashiba Taito-ku, Tokyo 111-0023, Japan
Holmes, Jason D., Boston Univ., Mechanical and Aerospace Eng., 110 Cummington St., Boston, MA 02215
Holmes, Jason D., Mechanical and Aerospace Eng., Boston Univ., 110 Cummington St., Boston, MA 02215
Jones, Ackland, 92 Lyman St., Apt. 1, South Hadley, MA 01075
Jones, Thomas M., 606 St. Paul St., Box #256, Baltimore, MD 21202
Khakparaghi, Mehrdad, Sharif Univ. of Technology, Electrical Eng., Azadi Ave., Tehran, 11365-9363, Iran
Kilanski, Kelley J., Univ. of Washington, Linguistics, Box 354340, Seattle, WA 98195
Kim, Minjung, 5325 18th Ave., NE, Seattle, WA 98105
Kim, Yunjung, 4817 Sheboygan Ave., #620, Madison, WI 53705
Kodavaty, Isaac S., Mechanical Eng., Univ. of Idaho, Moscow, P.O. Box 440902, Moscow, ID 83844-0902
Kruse, Roland, Oldenburg Univ., Physics/Acoustics, Carl-von-Ossietzky Str. 9-11, Oldenburg 26111, Germany
Kyong, Jeong-Sug, Univ. College London, Phonetics, 4 Stephenson Way, Wolfson House, London NW1 2HE, UK
Lalk, Samuel J., Columbia College Chicago, 33 East Congress, Ste. 601, Chicago, IL 60605
Lammers, Matt D., 118 Fowler, West Lafayette, IN 47906
Lane, Janet M., 17416 6th Ave., SW, Seattle, WA 98166
Larsen, Niels W., Technical Univ. of Denmark, Akademivej 352, Lyngby 2800, Denmark
Lee, Jungwoo, 123 South Catalina St., #205, Los Angeles, CA 90004
Lewiston, Craig, Massachusetts Inst. of Technology, Research Lab. of Electronics, 77 Massachusetts Ave., Rm. 36-766, Cambridge, MA 02139
Li, Weichang, Woods Hole Oceanographic Inst., Ocean Physics and Eng. Dept., MS16, 93 Water St., Woods Hole, MA 02543
Lipscomb, Philip A., Peabody Inst. of Johns Hopkins Univ., 606 St. Paul St., #713, Baltimore, MD 21202
Lu, Guangqing, 2711 Main Ave., Northport, AL 35476
Lunoe, Michael W., Univ. of Hartford, 200 Bloomfield Ave., Box 1717, West Hartford, CT 06117
Luo, Wenbo, Applied Physics Lab., Univ. of Washington, 1013 NE 40th St., Seattle, WA 98105
Mardin, Mursalim, Jl. Kebon Sirih III, No. 139/5b, Bandung, West Java 40117, Indonesia
Matsubara, Juri, Teachers College, Columbia Univ., 1230 Amsterdam Ave., Rm. 536, New York, NY 10027
Matsugu, Yika, East Asian Studies, Univ. of Arizona, P.O. Box 210105, Tucson, AZ 85721-0105
McMillan, Corey T., 2A/3 Albany St., Edinburgh, Scotland EH1 3QB, UK
Mefferd, Antje, 2749 Cable Ave., Lincoln, NE 68502
Midtlyng, Patrick J., Univ. of Chicago, Linguistics, 1010 East 59th St., Chicago, IL 60637
Molnar, Monika T., School of Communication Sciences and □ Disorders, McGill Univ., 1266 Pine Ave., West, Montreal, QC H3G 1A8, Canada
Mullins, Geoff, 63 Keefer Pl., Apt. #2010, Vancouver, BC V6B 6N6, Canada
Muzzy, Philip G., 2634 West Logan Blvd., Apt. #2, Chicago, IL 60647
Nahirnyak, Volodymyr M., Univ. of Cincinnati, Biomedical Eng., 231 Albert Sabin Way, MSB, ML0586, R.6152, Cincinnati, OH 45267
Nesbitt, Jonathan R., 296 Gibbs Rd., Wiscasset, ME 04578
Notestine, Lewis S., Univ. of Oregon, Linguistics Dept., 1290 Univ. of Oregon, Eugene, OR 97403-1290
Ogasawara, Naomi, Univ. of Arizona, Linguistics, Douglass 200E, P.O. Box 210028, Tucson, AZ 85721
Ong, Aven, Blk. 523 Jurong West St. 52, #13-235, Singapore 640523, Singapore
Otu-Nyarko, Ebenezer, 214 Foster Dr., Apt. E, Willimantic, CT 06226
Palahanska-Mavrov, Milena S., 1938 South 38th Ave., Apt. 115, Omaha, NE 68105
Palan, Vikrant C., Mechanical Eng., Univ. of Alabama, 290 Hardaway Hall, 7th Ave., Tuscaloosa, AL 35487
Piel, Alexander K., Anthropology, Univ. of California, San Diego, 9500 Gilman Dr., La Jolla, CA 92093
Podlipsky, Vaclav Jonas, Palacky Univ., Dept. of English and American Studies, Krizkovskeho 10, Olomouc, Czech Republic 77180
Raisamo, Jukka M.K., Univ. of Tampere, Dept. of Computer Sciences, Kanslerinrinne 1, Tampere, FIN-33014, Finland
Rasmussen, Karl L., 207 East Pleasant St., P.O. Box 688, Elk Point, SD 57025
Reynolds, Laura B., 9 Allapartus Rd., Ossining, NY 10562
Richtsmeier, Peter T., The Univ. of Arizona, Linguistics, P.O. Box 210028, Tucson, AZ 85721-0028
Roeder, Rebecca V., 428 South Clemens Ave., Lansing, MI 48912
Rozell, Christopher J., Electrical and Computer Eng., Rice University, MS 366, P.O. Box 1892, Houston, TX 77251-1892
Sakata, Yohei, 2140 10th Ave., #302A, Honolulu, HI 96816
Samuel, Yianna, Earth and Atmospheric Science, Cornell Univ., 2154 Snee Hall, Ithaca, NY 14853
Satyavarta Cognitive and Neural Systems, Boston Univ., 677 Beacon St., #110, Boston, MA 02215
Saulus, Jennifer A., P.O. Box 20056, Juneau, AK 99802
Schlezinger, Yotam, 720 West Randolph, #501, Chicago, IL 60661
Schotten, Michiel, Marine Mammal Research Program, Hawaii Inst. of Marine Biology, Univ. of Hawaii, 46-007 Lilipuna Rd., Kaneohe, HI 96744
Scott, Ryan S., 3110 SW 1st Ave., Gainesville, FL 32607
Secules, Stephen D., Dartmouth College, HB 3602 Dartmouth College, Hanover, NH 03755
Shiung, Cindy, 41 Milburn Dr., Hillsborough, NJ 08844

Shosted, Ryan K., Linguistics, Univ. of California, Berkeley, 1203 Dwinelle Hall, Berkeley, CA 94720-2650
Shravage, Paresh, 283, Plot No. 49, Vidyaprabha, Nr. Sivaji Uday Mandal, Tanaji Nagar,
Chinchwad, Pune Maharashtra 411033, India
Sikora, Joseph J., 550 Memorial Dr., 23A-3, Cambridge, MA 02139
Sloan, William N., 33 Pond Cir., Boston, MA 02130-2420
Smith, Denise A. B., Biomedical Eng., Univ. of Cincinnati, 231 Albert Sabin Way, Rm. 6159, Cincinnati, OH 45267-0586
Smith, Marc N., Speech and Hearing Science, The Ohio State Univ., 110 Pressey Hall, 1070 Carmack Rd., Columbus, OH 43210
Statzer, Nicholas L., Univ. of Hartford, Box 3330-200 Bloomfield Ave., West Hartford, CT 06117-1599
Stojanovic, Diana, 2825 South King St., #802, Honolulu, HI 96826
Strandem, Oyvind, 11 Princes Ave., Liverpool, Merseyside L8 2TA, UK
Subkey, Alan J., Wilkinson Bldg., City Rd., Darlington, NSW 2006, Australia
Suied, Clara, IRCAM, 1, Pl. Igor Stravinsky, Paris, 75004 France
Swanson, Brett A., Cochlear Ltd., 14 Mars Rd., Ln. Cove NSW 2006, Australia
Tapia, Angel D., 4150 South Fairfield Ave., Apt. #2, Chicago, IL 60632
Tobin, Stephen J., Linguistics Dept., Univ. of Southern California, 3601 Watt Way, GFS 301, Los Angeles, CA 90089-1693
Van Uffelen, Lora J., Scripps Institution of Oceanography, 9500 Gilman Dr., Mail Code 0238, La Jolla, CA 92093-0238
VanDam, Mark, Indiana Univ., Linguistics, Memorial Hall 322, 1021 East 3rd St., Bloomington, IN 47403
Vavva, Zoi, 35980 Ithaca Dr., Avon, OH 44011
Venkatesh, Lakshmi, Dept. of Speech and Hearing Sci., Univ. of Washington, 1417 NE 42nd St., Seattle, WA 98105
Vidal, Lori E., 1424 Rue Beauvais, Mandeville, LA 70471
von Lueders, Sebastian, Trangsundgard, Huddinge 14262, Sweden
Walker, Ashley Hart, Pembroke College, St. Aldates, Oxford, Oxfordshire OX1 1DW, UK
Walker, Kent G., 6735 Sherbrooke Ouest, Apt. 14, Montreal, QC H4B 1P3, Canada
Walker, Oveal J., Univ. of Miami, Music Eng. Dept., 1314 Miller Dr., Miami, FL 33146
Wang, Xin, Speech and Hearing Sciences, Indiana Univ., 200 South Jordan Ave., Bloomington, IN 47405
Ward, Chris J., 13 Langaton Ln., Pinhoe, Pinhoe, Exeter, Devon EX1 3SP, UK
Wilcox Jr., Douglas Alan, P.O. Box 232, South Montrose, PA 18843
Winkler, Ralf, Ostender strabe 2, Berlin 13353, Germany
Wirtzfeld, Michael, 30 Chapman Court, Apt. 406, London, ON N6G 4Y4, Canada
Wygonik, Benjamin J., Double Door, 1572 North Milwaukee Ave., Chicago, IL 60622
Yu, Yan H., 153-37 58th Rd., Flushing, NY 11355
Zhang, Yanhong, 228-09 Arnold Dr., West Lafayette, IN 47906
Zheng, Xiaoju, Purdue Univ., Linguistics, 302 Wood St., Young Hall, Rm. 814, West Lafayette, IN 47907-2108

New Electronic Associates

Allard, Jean F., Rte. des 4 Rte.s, Vallon sur Gee, 72540, France
Anson, Peter L., Lotek Wireless Inc., 115 Pony Dr., Newmarket, ON L3Y 7B5, Canada
Bian, Lin, Univ. of Kansas Medical Ctr., Hearing and Speech, 3901 Rainbow Blvd., Kansas City, KS 66160
Bottai, Giola, Mechanical Eng., Univ. of South Carolina, 300 Main St., Columbia, SC 29208
Bowman, J. R., SAIC, 10260 Campus Point Dr., MS-A3, San Diego, CA 92121
Brennan, Marc A., William S. Middleton Memorial Hospital, Audiology, 2500 Overlook Ter., Madison, WI 53705
Broadstone, Steven R., Teratech Corporation, 77-79 Terrace Hall Ave., Burlington, MA 1803
Cheol-An, Kim, Medison, R&D, Medison Venture Tower, 997-10, Deachi-dong, Seoul 135-280, Republic of Korea
Crosswhite, Katherine M., Rice Univ., Dept. of Linguistics, Mail Stop 23, 6100 Main St., Houston, TX 77005
Dinsmore, Michael L., 5832 Cliffside Dr., Troy, MI 48085
Dunne, James, Integrated Acoustic Solutions, 21 Bluebell Business Park, Old Naas Rd., Dublin
D12, Ireland
Frankenfield, Glenn, P.O. Box 308, East Wilton, ME 04234
Gauld, Stephen M., Day Design Pty. Ltd., Ste. 17, 808 Forest Rd., Peakhurst NSW 2210, Australia
Goldberg, Paul R., Dynaura, 744 La Para Ave., Palo Alto, CA 94306
Iwase, Ryoichi, JAMSTEC, Computer and Information Dept., 3173-25 Showa-machi, Kanazawa-ku, Yokohama, Kanagawa 236-0001, Japan
Iynde, Gerald D., Baker Oil Tools, Inc., Eng., 9100 Emmott Rd., Houston, TX 77040
Jibiki, Takao, GE Yokogawa Medical Systems, Ltd., Ultrasound Business Division, 7-127, Asahigaoka 4-chome, Hino-shi, Tokyo 191-8503, Japan
Jo, Tetsuya, Liberal Arts, Nagoya Gakuin Univ., 1350 Kamishinano, Seto, Aichi, 480-1298, Japan
Jones, Michelle A., Entech Consulting Group, 27740 Jefferson Ave., Ste. 230, Temecula, CA 92590
Jonsdottir, Valdis Ingibjorg, Thad er Malith, Furuvellir 13, Akureyri 600, Akureyri 600, Iceland
Kim-Boyle, David R., Univ. of Maryland, Baltimore County, Music, 1000 Hilltop Cir., Baltimore, MD 21250
Kunchur, Milind N., Univ. of South Carolina, Physics and Astronomy, USC Dept. of Physics, 712 Main St., Jones PSC Bldg., Rm. 404, Columbia, SC 29208
Lane, Harlan, MIT, Speech Communications, RLE, 50 Vasaar St., Cambridge, MA 02139 McCloud, James, 595 Peppertree Ln., Pensacola, FL 32506
McCluney, Robert J., Krieger Specialty Products, 4880 Gregg Rd., Pico Rivera, CA 90660
Norton, Susan J., Audiology, Children″s Hospital and Regional Medical Ctr., 4800 Sand Point Way, NE, Seattle, WA 98105
Puffenberger, Steve, Advent Media, Inc., 5629 Fraley Court, Columbus, OH 43235
Rambod, Edmond, BioQuantetics, Inc., 2675 Junipero Ave., Ste. 800, Signal Hill, CA 90755
Rickman, Benjamin, Ultra Electronics SCS, Countermeasure Systems, 419 Bridport Rd., Greenford, UB6 8UA, UK
Rosenfeld, Martin L., MLR Tech Services, 2413 Silver Fox Ln., Reston, VA 20191-2628
Sabat, Marc, Gneisenaustr. 43, HH 3OG Rechts, Berlin 10961, Germany
Sabra, Karim G., Scripps Inst. of Oceanography, Marine Physical Lab., 9500 Gilman Dr., La Jolla, CA 92093-0238
Sato, Hayato, Kobe Univ., Nadaku Rokkodaicho 1-1, Kobe, Hyogo, 657 8501, Japan
Stiles, Timothy A., Medical Physics, Univ. of Wisconsin-Madison, 1300 University Ave., Rm. 1530 MSC, Madison, WI 53706
Terrinoni, Anthony A., 161 Hickok Ave., Syracuse, NY 13206
Therrien, Ron, 1107 Bay Dr., North, Bradenton Beach, FL 34217
Toomey, Aoife C., Lawrence Berkeley Natl. Lab., Earth Science Div., 1 Cyclotron Rd., Berkeley, CA 94720
Travkin, Vladi S., HSPT, 10431 Larwin Ave., Chatsworth, CA 91311
Uther, Maria, Univ. of Portsmouth, Psychology, King Henry Bldg., King Henry 1 St., Portsmouth, Hampshire PO1 2DY, UK
Waltham, Christopher E., Univ. of British Columbia, 6224 Agricultural Rd., Vancouver, BC V6T 1Z1, Canada
Wolfe, Michael L., Fail Safe Products, LLC, 22 Old Bridge Way, Ormond Beach, FL 32174
Zagrai, Nikolai P., Dept. of Hydroacoustics and Medical Eng., Taganrog State Univ. of Radio Eng., 44 Nekrasovsky, GSP-17A, Taganrog 347928, Russian Federation
Zaleski, Laurie A., 1111 Ostrander Ave., Riverhead, NY 11901
Zipperle, Carl F., Goldman Sachs, 30 Hudson St., Jersey City, NJ 07302

New Corresponding Electronic Associates

Bekker, Ian, English Language and Linguistics, Rhodes Univ., P.O. Box 94, Grahamstown 6140, South Africa
Birsan, Ancuta, Calea Dumbravii bl. 17, sc. B ap. 18, Sibiu, 2400, Romania

Choi, Sunghoon, KRRI, Rolling Stock Research Dept., 360-1 Woulam-dong, Uiwang-city, Kyunggi 437-757, Republic of Korea
Davies, Jevon R., Peninsula Univ. of Technology, Ctr. for Instrumentation Res., Faculty of Eng., Rm. 5, 16D Tennant St., District Six, Cape Town, Western Province 8001, South Africa
Gadek, Jakub, Woskowa 32, Lodz 91-603, Poland
Gubaidullin, Amir A., Tyumen Branch, Inst. of Applied and Theor. Mech., Siberian Branch, Russian Academy of Sciences, Taymyrskaya St. 74, Tyumen 625026, Russia
Park, Jangyeon, Nayio Media Inc., C-2112 Daerim Acrotel, 467-6 Dogok-dong, Gangnam-gu, Seoul, 135-856, Republic of Korea
Peng, Zhaohui, Inst. of Acoustics, Chinese Academy of Sciences, National Lab. of Acoustics, 21 Beisihuanxilu, P.O. Box 2712, Beijing 100080, P.R. China
Predoi, Mihai Valentin, Calea Plevnei 94, Bl. 10D2, Ap. 12, Bucharest 010236, Romania

Reinstated

C. N. Corrado, D. G. Fagen, R. A. Lester, J. M. Suarez, L. M. Zurk—*Members*
N. T. Cooley, W-L. W. Ho, G. Kaduchak, J, C. Machado, M. F. McKinney—*Associates*
J. A. Busenitz—*Electronic Associate*
C. Sodsri—*Corresponding Electronic Associate*

Associates Elected Members

A. M. Adams, J. I. Arvelo, Jr., F. E. Barber, G. Brambilia, A. C. Chen, J. M. Cushner, S. F. Disner, E. C. Duncan, D. J. Fenneman, A. L. Francis, T. A. Gorne, W. M. Holliday, E. Y. Hsieh, J. Jiang, G. Kaduchak, M. S. Kinch, L. L. Koenig, T. L. Lavallee, P-C. Li, B. W. Libbey, S. McClatchie, A. M. Nakashima, Y. A. Pischalnikov, M. E. Poese, Z. Qiong, W. Rothermich, A. E. Russo, M. Snellen, D. P. Williams, D. A. York, J. A. Young, D. N. Zotkin

Member to Student

E. Larsen

Students to Associates

M. Ardila, K. J. Bastyr, J. J. Bauer, C. L. Berchok, R. B. Biziorek, J. Boes, K. T. Boike, L. V. Borruel, A. C. Carballeira, M. J. Carney, M. P. Coughlin, E. Diakoumakou, A. Di Angelo, J. Guan, M. J. Hamilton, J. M. Harte, J. P. Hoffman, M. C. Johnston, III, D. G. Kasper, J. A. Keefe, J. E. King, L. J. Leibold, E. S. Levy, C. Liu, T. M. Lorenzen, K. J. Mattock, J. A. McConnell, P. A. Mehta, R. E. Millman, P. Mokhtari, R. A. G. Murray, M. M. Narendran, M. W. L. Ng, D. M. Pierson, P. Plantevin, A. D. Puckett, S. C. Renaud, C. J. Richie, W. Rolshofen, R. A. Romond, J. W. Rouse, J.-P. Roy, S. S. Sainclair, C. R. Thomas, M. Thompson, S. L. Thomson, E. Way, Y. Zhang

Members to Electronic Associates

J. M. Huckabay, C. Kaernbach, O. Kirkeby, O. T. Lawu, J. L. Punch, P. A. Santi

Associates to Electronic Associates

C. B. Allen, S. F. Bird, M. A. Blommer, D. J. Caswell, D. Chelidze, Y. Chen, A. D′Amico, M. Deffenbaugh, F. Desharnais, A. B. Druzhinin, T. L. Eadie, N. Frazer, K. K. Govindarajan, S. Greenberg, K. R. Gustafson, M. A. Hayner, I. Hertrich, T. Hikichi, X. Jiang, H. Miyazaki, T. J. Potter, J. A. Scales, H. Takenaka, W-B. Yang

Students to Electronic Associates

T. Aoki, T. A. Bigelow, D. J. Bodony, S. Choi, P. Danilov, B. J. Doty, M. Grassi, L. J. Lee, B. Ma, D. A. Outing, I. N. Pieleanu, R. A. Scarborough, G. S. Sparks, M. Sutor, N. Weiland, L. Yang, H. Yoon, X. Zhang

Corresponding Electronic Associate to Electronic Associate

G. Hyun

Member to Corresponding Electronic Associate

B. Kostek

Associate to Corresponding Electronic Associate

A. L. Varfolomeev

Students to Corresponding Electronic Associates

L. Nieva, K. Saleh

Resigned

D. H. Eldredge, M. Harrison, J. Hawkins, J. Royster, V. Salmon, J, Shibayama—*Fellows*
C. Ahlstrom, A.J. Berkhout, C.D. Bohl, D. F. Bolka, C. F. Bove, J. Burrows, G. L. Canavet, P. A. Chinnery, S. E. Demain, M. H. Dunn, R.E. Hoffman, Jr., J. Ignaczak, S. Kowalyshyn, Jr., B. Marn, J. R. Oswin, C.E. Rosenkilde, P.R. Van Dyke—*Members*
P. Bouchilloux, J. K. Brigham, W. D. Clarke, III, B. Craig Dickson, R. Fountoulakis, S. E. Johnston, J.T. Kalb, R. Lemieux, J. R. McGlathery, M. Miyatake, J.O. Mysing, J.J. Ridings, G. J. Sotos—*Associates*
P. Barriault, K. Cox, D. Frisk, L, Jaouen, Y. Jung, S. Mokris—*Students*
A. Day, A. Spaargaren—*Electronic Associates*

Deceased

J. E. Blue, B. H. Goodfriend, J. Merhaut—*Fellows*
A. Cho, D. C. Coulter, J. W. Joiner, L. R. Moss, T. W. Parsons—*Members*

Dropped

Ansorge, Michael, Ator, Gregory A., Bae, Jong-Rim, Balant, Anne C., Blomberg, Leslie D., Bonfils, Pierre, Bowen, David L., Brandstein, Michael S., Brekken, Andreas, Bryant, Rebecca S., Candel, Sebastien M., Chen, Yian-Nian, Chong, Fan, Christoff, James T., David, Pascal M., Davis, Rickie R., Derengowski, Mary A., Dindinger, Philip M., Emerson, George F., England, Wesley B., Fabre, Josette P., Feldman, Eliot D., Feller, Allan R., Gibson, Ralph H., Guan, Dinghua, Han, Sang-Kyu, Hancock, Maurice, Haton, Jean-Paul, Herbertz, Joachim, Hill, Nicholas I., Hodgson, Philip N., Hussain, Syed S. M., Iliev, Alexander I., Inoue, Yoshinori, Ishikawa, Yasushi, Jarinko, David A., Javel, Eric, Johnson, Michael P., Joiner, David P., Kamm, Candace A., Kasputis, Stephen R., Kreamer, Elizabeth W., Lane, Samuel R., Ljunggren, Sten G., Lungstrum, Richard W., Martinez, Michael M., Mayberry, John P., Mills, David M., Moody, David B., Myrberg, Arthur A., Narang, Prem P., Nielsen, Donald W., Nielsen, Knud Skovgaard, Owen, Ann Marie, Ripper, Arthur P., Robinson, Carlos J., Roderick, William I., Rothman, Howard B., Saunders, Melvin L., Seiji, Ohshimo, Sun, Edward C., Todd, Frank J., Trout, J. D., Van Biesen, Leo P., Veillette, Randy, Vovk, Igor V., Walker, John R., Wang, Shuozhong, Waters, Timothy R., Young, A Mark, Zeng, Li Jun, Zhang, Chao Ying, Zhu, Guozhen—*Members*

Abel, Jonathan S., Agness, John R., Ahting, Peter A., Amman, Scott A., Anderson, Robert M., Auriemmo, Jane, Backman, Juha R., Ballachanda, Bopanna B., Basu, Debashis, Bates, Bradley O., Benazzato, Roberto, Benson, Robert H., Bernacki, Robert, Bishop, Diane S., Bistafa, Sylvio R., Blomgren, Michael, Boober, Walter H., Bosch, Lauren A., Boulahbal, Djamil, Brock, Daniel K., Butler, Michael J., Byrd, Matthew C., Byrnes, Gregory, Carlson, Nancy E., Chang, Enson, Chen, Cheng-Hsiung, Chen, Pei-Tai, Chen, Shaohai, Chennoukh, Samir, Cherng, John G., Choi, Myoung-Seon, Ciccozzi, Marco G., Colby, Leider, Coudron, Chad D., Council, Orin P., Crow, Daniel P., Cummings, Alan, Daniel, Peter, Dedes, Ioannis, Deyesso, Joseph P., Diaz, Jose A., Dickey, Nolan S., Distler, Mark A., Ditthardt, Alfred R., Dittmar, James H., Dorta-Luis, Josefa, Driesch, Patricia L., Early, Thomas A., Evans, Kirk E., Fajinmi, Olatunji K., Feist,

Jeffrey P., Fick, Douglas D., Flatau, Alison B., Flege, James E., Foley, Dennis L., Friedman, Adam D., Garcia, Jose M., Gatell, Francisco, Gibbons, Joel D., Giles, Peter M., Gonneau, Eric, Gonzales, Joel, Gordon, Jonathan C. D., Goye, Alain, Green, Kent C., Griffin, James A., Guo, Yuqing, Gurdak, Diane D., Halmrast, Tor, Hamm, Craig A., Harley, Heidi E., Hasse, Roger D., Hodge, Colin G., Honda, Ethan P., Hongerholt, Derrick D., Hopkins, Lawrence G., Hsu, Chaur-Jian, Hulce, Emily A., Hwang, Ho-Jin, Ishiwata, Tsuneo, Ives, Terri E., Iyer, Nandini, Jahn, Darrell D., Jain, Sushil Kumar, Jensen, Janet K., Ji, Zhenlin, Josephson, David L., Juan, Betts F., Kakita, Yuki, Kamm, Teresa M., Kim, Byoung, Kim, Mi-Ran, Kim, Tae-Gun, Kimizuka, Ikuo, King, Gregory D., Kirwan, Albert E., Kitahara, Michihiro, Klepko, John, Kook, Hyungseok, Korman, Murray S., Koshigoe, Shozo, Kujawa, Sharon G., Kurowski, Kathleen M., Lafleur, Francois, Lalime, Aimee L., Lambacher, Stephen G., Landis, Donald H., Lee, Joon-Hyun, Lee, Kelvin, Lee, Yang-Sub, Lindemann, Stephanie A., Liu, Jin-Yuan, Loftman, Rickard C., Lohrmann, Atle, Lussier, Justin R., Mann, Virginia A., Marchand, Sylvain, Marler, Jeffrey A., Marty, Pierre N., Max, Ludo, Mayer, Larry A., McGarrity, Cheryl, McKinley, Bruce L., Medina, Thomas, Mellacheruvu, Venkata S. Mellody, Maureen, Meyer, Georg F., Michael, Kevin L., Miyake, Tatsuo, Moran, Mark L., Motta, Mauricio S., Muhammad, Asim I., Munson, Albert G., Myungho, Han, Nelson, Bradley A., Nelson, John A., Neumann, John Joseph, Niedzielski, Nancy A., Noel, Benjamin E., Nyland, David L., Oeschger, John W., Olofsson, Niten B., Ono, Nobutaka, Oxley, Brylie, Padgett, Robert B., Parente, Carlos E., Park, Chong Yun, Paul, Donald W., Pehl, Gerald J., Pellicano, Anthony J., Perry, Matthew R., Pinkowski, Ben C., Porterfield, Randall L., Posey, Roger D., Pryshepa, John A., Rao, Rama V. N., Rehder, Douglas E., Reilly, Thomas G., Rhee, Huinam, Richardson, Suzanne D., Ricketts, Todd A., Rimmer, Thomas W., Roberts, Richard A., Rodriguez, Arturo Campos, Rodriguez, Rose T., Rollings, Tom D., Rozo, Juan Pablo, Ruffa, Francisco, Ruiz, Robert, Salvadores, Silvia R., Samuels, Ruth F., Samuels, Timothy O., Scandrett, Clyde, Schmidt, Val Eugene, Schreiner, Peter G., Schroder, Anna C., Schwartz, Gregory L., Scott, Dan W., Scott, David E., Scott, Kimberly R., Sennett, William F., Serridge, Mark, Seyed-Bolorforosh, Mirsaid, Shreves, Joseph W., Sketch, Michael G.M., Soltano, Emily G., Somin, Martin E., Spahn, Kevin K., Sprague, Mark W., Stevens, Alexander A., Stockmann, Elle S., Taiwo, Michael M., Tang, Hsin Min, Tanner, Dennis C., Teeple, Ryan J., Too, Gee-Pinn J., Tran, Joseph B., Tsoflias, Sarah L., Tuominen, Heikki T., Ugolotti, Emanuele, Vaitekunas, Jeffrey J., Vick, Jennell C., Vizza, Gregg J., Wang, Jack, Weisser, Olaf, White, Jeffrey R., White, Lee A., Whiteford, William D., Willt, Ben D., Wood, Michael N., Wright, James T., Yan, Hong Y., Yates, Gregory D., Yu, Man H., Zellner-Keller, Brigitte, Zeng, Qinqian, Zhou, Shuliang, Zigler, Gary R., Zuroski, Michael T., de Castro, Sandro—*Associates*

Agarwal, Mahesh C., Alencar, Adriano M., Alonso, Victor, Ban, Thomas O., Beuselinck, Michael T., Cetinkaya, Cetink, Collins, Simon W., Culbertson, Deborah S., Daigle, Marie A., Diazgranados, Maria C., Fishman, Louis, Gage, Nicole M., Garces, Milton A., Guirao, Miguelina, Hahn, Steven R., Hedges, Robert A., Herlin, Bo, Herman, Vladimir, Hnilo, Margarita S., Hunt, Dave L., Johansen, Espen S., Kaibin, Qiu, Kasam, Mallikarjuna Rao, Kimberley, Barry P., Latimer, Paul J., Lessley, Ted D., MacInnes, Craig S., Mahon, Mark P., Makepeace, Shawn L., Masta, Robert I., Mohammed, Ichchou, Moksnes, Knut, Nelson, Tobey L., Oboznenko, Igor L., Pelletier, Anik, Piliavin, Michael A., Plazaola, Carlos R., Poinsett, David, Pompei, F. Joseph, Price, Marshall, Qiang, Lin, Sanchez, Maria M., Sharma, Devdutt, Stack, Janet W., Stultz, Carlton D., Sveshnikov, Boris V., Tateno, Takashi, Torres, Eddie G., Traykovski, Peter, Ulrich, Kathleen M., Wong, Yuen Kwan—*Electronic and Corresponding Electronic Associates*

Abrams, Daniel A., Acharyya, Ranjan, Agarwal, Anurag, Alvarado-Juarez, Miguel, Amin, Samrat A., Armstrong, Peter R., Ayala, Christopher D., Bachand, Corey L., Bajwa, Manjit S., Bartsch, Guido, Beamer, Walter C., Beltran, Alicia, Berbee, Matthew W., Bier, Peter J., Billon, Alexis J., Blackwell, Ezra L., Bobba, Kumar M., Boemio, Anthony B., Bose, Arpita, Boukis, Christos G., Bowles, Benjamin G., Bravo Pinto, Ernesto M., Cederroth, Christopher R., Ceperley, Daniel P., Chia, Natasha J., Christensen, Mads G., Chupp, Aaron A., Coker, Ian C., Coudriet, Gregory A., Crave, Olivier., Culley, Tonya L., Daley, Michael J., Damljanovic, Vesna, Daniels, Michelle, Davis, Brian A., Deja, Cynthia Anne, DiStefano, Carlos A., DiTuro, William J., Doellinger, Michael, Edwards, William D., Ericsson, Johan A., Faust, Bryan K., Fedak, Larissa A., Fitzgerald, Erin C., Fonseca-Madrigal, Javier J., Ford, N., Ganapathiraju, Madhavi K., Gao, Wen, Gazagnaire, Julia, Ghosh, Satrajit S., Gifford, Rene Headrick, Gladden, Joseph R., Gonzalez, Jorge E., Gopalan, Harish, Gregory, Joseph W., Grinnan, Christopher P., Gudigundla, Sai P., Guise, Paul E., Hacopian, Narineh, Haldipur, Pranaam, Hanlon, Ellie H., Hardy, Pierre, Hirst, Jonathan M., Howarth, Eric, Howell, Carl A., Hozjan, Vladimir, Ingvalson, Erin M., Jang, Kyunga, Johnson, Wayne M., Kang, Kookjin, Karner, Christopher J., Kayan, Thomas E., Kenderian, Shant, Kennedy, Daniel J., Kim, Bumjun, Kim, Ji Eun, Kinney, Andrew W., Knight, Gary D., Knight, Troy E., Kogan, Pablo, Konepally, Niranjan R., Koperda, Eric F., Kroeff, Gia, Landis, Cody J., Langlois, Christian, Lawrence, Cecile A., Leary, Adam P., Lee, Hyun-Kook, Lee, Keum Won, Lee, Shane, Lewis, Clifford F., Linscomb, Sommer H., Low, Stephen W. K., Maehr, Michael D., Marshall, Vincent T., Masica, David L., Maul, Kristen K., Maurice, Kristin L., May-Bowers, Carie L., McCabe, Marie E., McClanahan, Richard D., McDuffee, Matthew R., Mehta, Tejas, Menezes, Caroline M., Menezes, Pedro L., Methuku, Reddy S., Mirman, Daniel, Moseley, Stephen C., Myers, Melodie M., Naidu, Manish, Nandur, Vuday, Napoletano, Brian M., Newman, Matt M., Ngan, Kwok Hung, Novascone, Stephen R., O'Connell-Rodwell, Caitlin E., Onsuwan, Chutamanee, Osgood, Jonathan H., Oyewole, Olanrewaju, Ozer, Mehmet B., Pacheco, Andres A., Padilla, Monica, Pauli, Nathan S., Pegors, Katherine, Perry, Susan R., Philips Heck, Jennifer D., Politis, Zafiris G., Reed, Allen H., Reilly, Kevin J., Ripley, Jennifer L., Ross, David A., Rout, Ayasakanta, Saad, Omar, Saire, Javier A., Sands, Kathy L., Sarwono, Joko J. S., Scales, E. Steven, Schein, David Brian, Scimone, Lisa M., Scott, James N., Seckman, Aaron M., Serafin, Stefania, Shapley, Kathy L., Shiao, Tsung-Jieh, Shunmugavelu, Sokka D., Sinha, Shiva R., Smith, Jessalyn A., Smith, Mitchell C., Smith, Steven S., Snook, Bradley M., Steenberg, Matthew, Stephens, Joseph D., Streeter, Timothy M., Suh, Sanghoon, Suzuki, Ryuji, Szamatowicz, Brandon J., Talley, Jim, Tam, Mei-Wa T., Teddy, Sintiani D., Thompson, Robert L., Thorn, Aisha, Tooley-Young, Carolyn J., Tornberg, Jarkko, Usher, John., Van Cauwelaert, Javier., Vier, Matthew S., Vodila, Benjamin J., Walker, Christopher D., Wang, Weifang, Watson, Kevin D., Whitehead, Jeff J., Woodall, Ashley R., Wullens, Frederic, Yin, Xiangtao, Yoo, Junehee, Yuan, River H., Zvonik, Elena, van Alphen, Petra M.—*Students*

Fellow	881
Members	2308
Asociates	2585
Student	905
Electronic Associates	417
	7096

ACOUSTICAL STANDARDS NEWS

Susan B. Blaeser, Standards Manager
Standards Secretariat, Acoustical Society of America, 35 Pinelawn Rd., Suite 114E, Melville, NY 11747
[Tel.: (631) 390-0215; Fax: (631) 390-0217; e-mail: asastds@aip.org]

George S. K. Wong
Acoustical Standards, Institute for National Measurement Standards, National Research Council, Ottawa, Ontario K1A 0R6, Canada [Tel.: (613) 993-6159; Fax: (613) 990-8765; e-mail: george.wong@nrc.ca]

American National Standards (ANSI Standards) developed by Accredited Standards Committees S1, S2, S3, and S12 in the areas of acoustics, mechanical vibration and shock, bioacoustics, and noise, respectively, are published by the Acoustical Society of America (ASA). In addition to these standards, ASA publishes Catalogs of Acoustical Standards, both National and International. To receive copies of the latest Standards Catalogs, please contact Susan B. Blaeser.

Comments are welcomed on all material in Acoustical Standards News.

This Acoustical Standards News section in JASA, as well as the National and International Catalogs of Acoustical Standards, and other information on the Standards Program of the Acoustical Society of America, are available via the ASA home page: http://asa.aip.org.

Standards Meetings Calendar National

At the 150th ASA Meeting joint with Noise-Con, Minneapolis, MN at the Hilton Hotel and Towers, 17–21 October 2005, the ASA Committee on Standards (ASACOS) and ASACOS STEERING Committees will meet as follows:

• ***Monday, 17 October 2005***
ASACOS Steering Committee
• ***Thusday, 20 October 2005***
ASA Committee on Standards (ASACOS). Meeting of the Committee that directs the Standards Program of the Acoustical Society.

International Standard Committee Meetings

12–16 December 2005
ISO/TC 108/SC 5 Condition monitoring and diagnostics of machines. This committee and its working groups will meet at the SeaTeach Campus of the Florida Atlantic University Graduate School of Ocean Engineering, in Dania Beach, Florida.

Accredited Standards Committee on Acoustics, S1

(J. P. Seiler, Chair; G. S. K. Wong, Vice Chair)

Scope: Standards, specifications, methods of measurement and test, and terminology in the field of physical acoustics including architectural acoustics, electroacoustics, sonics and ultrasonics, and underwater sound, but excluding those aspects that pertain to biological safety, tolerance, and comfort.

S1 Working Groups

S1/Advisory—Advisory Planning Committee to S1 (G. S. K. Wong);
S1/WG1—Standard Microphones and their Calibration (V. Nedzelnitsky);
S1/WG4—Measurement of Sound Pressure Levels in Air (M. Nobile).
S1/WG5—Band Filter Sets (A. H. Marsh);
S1/WG17—Sound Level Meters and Integrating Sound Level Meters (B. M. Brooks);
S1/WG19—Insertion Loss of Windscreens (A. J. Campanella);
S1/WG20—Ground Impedance (K. Attenborough, Chair; J. Sabatier, Vice Chair);
S1/WG22—Bubble Detection and Cavitation Monitoring (Vacant);
S1/WG25—Specification for Acoustical Calibrators (P. Battenberg);
S1/WG26—High Frequency Calibration of the Pressure Sensitivity of Microphones (A. Zuckerwar);
S1/WG27—Acoustical Terminology (J. Vipperman).
S1/WG28—Passive Acoustic Monitoring for Marine Mammal Mitigation for Seismic Surveys (A. Thode).

S1 Inactive Working Groups

S1/WG16—FFT Acoustical Analyzers (R. J. Peppin, Chair)

S1 STANDARDS ON ACOUSTICS

ANSI S1.1-1994 (R 2004) American National Standard Acoustical Terminology
ANSI S1.4-1983 (R 2001) American National Standard Specification for Sound Level Meters
ANSI S1.4A-1985 (R 2001) Amendment to ANSI S1.4-1983
ANSI S1.6-1984 (R 2001) American National Standard Preferred Frequencies, Frequency Levels, and Band Numbers for Acoustical Measurements
ANSI S1.8-1989 (R 2001) American National Standard Reference Quantities for Acoustical Levels
ANSI S1.9-1996 (R 2001) American National Standard Instruments for the Measurement of Sound Intensity
ANSI S1.11-2004 American National Standard Specification for Octave-Band and Fractional-Octave-Band Analog and Digital Filters
ANSI S1.13-1995 (R 1999) American National Standard Measurement of Sound Pressure Levels in Air
ANSI S1.14-1998 (R 2003) American National Standard Recommendations for Specifying and Testing the Susceptibility of Acoustical Instruments to Radiated Radio-Frequency Electromagnetic Fields, 25 MHz to 1 GHz
ANSI S1.15-1997/Part 1 (R 2001) American National Standard Measurement Microphones, Part 1: Specifications for Laboratory Standard Microphones
ANSI S1.15-2005/Part 2 American National Standard Measurement Microphones, Part 2: Primary Method for Pressure Calibration of Laboratory Standard Microphones by the Reciprocity Technique
ANSI S1.16-2000 (R 2005) American National Standard Method for Measuring the Performance of Noise Discriminating and Noise Canceling Microphones
ANSI S1.17/1-2000/Part 1 American National Standard Microphone Windscreens—Part 1: Measurements and Specification of Insertion Loss in Still or Slightly Moving Air
ANSI S1.18-1999 (R 2004) American National Standard Template Method for Ground Impedance
ANSI S1.20-1988 (R 2003) American National Standard Procedures for Calibration of Underwater Electroacoustic Transducers
ANSI S1.22-1992 (R 2002) American National Standard Scales and Sizes for Frequency Characteristics and Polar Diagrams in Acoustics
ANSI S1.24 TR-2002 ANSI Technical Report Bubble Detection and Cavitation Monitoring

 0001-4966/2005/118(1)/9/7/$20.00

ANSI S1.25-1991 (R 2002) American National Standard Specification for Personal Noise Dosimeters
ANSI S1.26-1995 (R 2004) American National Standard Method for Calculation of the Absorption of Sound by the Atmosphere
ANSI S1.40-1984 (R 2001) American National Standard Specification for Acoustical Calibrators
ANSI S1.42-2001 American National Standard Design Response of Weighting Networks for Acoustical Measurements
ANSI S1.43-1997 (R 2002) American National Standard Specifications for Integrating–Averaging Sound Level Meters

Accredited Standards Committee on Mechanical Vibration and Shock, S2

(R. J. Peppin, Chair; D. J. Evans, Vice Chair)

Scope: Standards, specifications, methods of measurement and test, and terminology in the field of mechanical vibration and shock, and condition monitoring and diagnostics of machines, including the affects of mechanical vibration and shock on humans, including those aspects that pertain to biological safety, tolerance, and comfort.

S2 Working Groups

S2/WG1—S2 Advisory Planning Committee (D. J. Evans);
S2/WG2—Terminology and Nomenclature in the Field of Mechanical Vibration and Shock and Condition Monitoring and Diagnostics of Machines (D. J. Evans);
S2/WG3—Signal Processing Methods (T. S. Edwards);
S2/WG4—Characterization of the Dynamic Mechanical Properties of Viscoelastic Polymers (W. M. Madigosky);
S2/WG5—Use and Calibration of Vibration and Shock Measuring Instruments (D. J. Evans, Chair; B. E. Douglas, Vice Chair);
S2/WG6—Vibration and Shock Actuators (G. Booth);
S2/WG7—Acquisition of Mechanical Vibration and Shock Measurement Data (B. E. Douglas);
S2/WG8—Analysis Methods of Structural Dynamics (B. E. Douglas);
S2/WG9—Training and Accreditation (R. Eshleman, Chair);
S2/WG10—Measurement and Evaluation of Machinery for Acceptance and Condition (R. Eshleman, Chair; H. Pusey, Vice Chair);
S2/WG10/Panel 1—Balancing (R. Eshleman);
S2/WG10/Panel 2—Operational Monitoring and Condition Evaluation—J. Niemkiewicz);
S2/WG10/Panel 3—Machinery Testing (R. Eshleman);
S2/WG10/Panel 4—Prognosis (R. Eshleman);
S2/WG10/Panel 5—Data Processing, Communication, and Presentation (K. Bever);
S2/WG11—Measurement and Evaluation of Mechanical Vibration of Vehicles (A. F. Kilcullen);
S2/WG12—Measurement and Evaluation of Structures and Structural Systems for Assessment and Condition Monitoring (B. E. Douglas, Chair; R. J. Peppin, Vice Chair);
S2/WG13—Shock Test Requirements for Commercial Electronic Systems (P. D. Loeffler);
S2/WG39 (S3)—Human Exposure to Mechanical Vibration and Shock—Parallel to ISO/TC 108/SC 4 (D. D. Reynolds, Chair; H. E. von Gierke, Vice Chair).

S2 Inactive Working Group

S2/WG54—Atmospheric Blast Effects (J. W. Reed)

S2 STANDARDS ON MECHANICAL VIBRATION AND SHOCK

ANSI S2.1-2000 ISO 2041:1990 Nationally Adopted International Standard Vibration and Shock—Vocabulary
ANSI S2.2-1959 (R 2001) American National Standard Methods for the Calibration of Shock and Vibration Pickups
ANSI S2.4-1976 (R 2004) American National Standard Method for Specifying the Characteristics of Auxiliary Analog Equipment for Shock and Vibration Measurements
ANSI S2.7-1982 (R 2004) American National Standard Balancing Terminology
ANSI S2.8-1972 (R 2001) American National Standard Guide for Describing the Characteristics of Resilient Mountings
ANSI S2.9-1976 (R 2001) American National Standard Nomenclature for Specifying Damping Properties of Materials
ANSI S2.13-1996/Part 1 (R 2001) American National Standard Mechanical Vibration of Nonreciprocating Machines—Measurements on Rotating Shafts and Evaluation Part 1: General Guidelines
ANSI S2.16-1997 (R 2001) American National Standard Vibratory Noise Measurements and Acceptance Criteria of Shipboard Equipment
ANSI S2.17-1980 (R 2004) American National Standard Techniques of Machinery Vibration Measurement
ANSI S2.19-1999 (R 2004) American National Standard Mechanical Vibration—Balance Quality Requirements of Rigid Rotors, Part 1: Determination of Permissible Residual Unbalance, Including Marine Applications
ANSI S2.20-1983 (R 2001) American National Standard Estimating Airblast Characteristics for Single Point Explosions in Air, with a Guide to Evaluation of Atmospheric Propagation and Effects
ANSI S2.21-1998 (R 2002) American National Standard Method for Preparation of a Standard Material for Dynamic Mechanical Measurements
ANSI S2.22-1998 (R 2002) American National Standard Resonance Method for Measuring the Dynamic Mechanical Properties of Viscoelastic Materials
ANSI S2.23-1998 (R 2002) American National Standard Single Cantilever Beam Method for Measuring the Dynamic Mechanical Properties of Viscoelastic Materials
ANSI S2.24-2001 American National Standard Graphical Presentation of the Complex Modulus of Viscoelastic Materials
ANSI S2.25-2004 American National Standard Guide for the Measurement, Reporting, and Evaluation of Hull and Superstructure Vibration in Ships
ANSI S2.26-2001 American National Standard Vibration Testing Requirements and Acceptance Criteria for Shipboard Equipment
ANSI S2.27-2002 American National Standard Guidelines for the Measurement and Evaluation of Vibration of Ship Propulsion Machinery
ANSI S2.28-2003 American National Standard Guidelines for the Measurement and Evaluation of Vibration of Shipboard Machinery
ANSI S2.29-2003 American National Standard Guidelines for the Measurement and Evaluation of Vibration of Marine Shafts on Shipboard Machinery
ANSI S2.31-1979 (R 2004) American National Standard Method for the Experimental Determination of Mechanical Mobility, Part 1: Basic Definitions and Transducers
ANSI S2.32-1982 (R 2004) American National Standard Methods for the Experimental Determination of Mechanical Mobility, Part 2: Measurements Using Single-Point Translational Excitation
ANSI S2.34-1984 (R 2005) American National Standard Guide to the Experimental Determination of Rotational Mobility Properties and the Complete Mobility Matrix
ANSI S2.41-1985 (R 2001) American National Standard Mechanical Vibration of Large Rotating Machines with Speed Range from 10 to 200 rev/s—Measurement and Evaluation of Vibration Severity *In Situ*
ANSI S2.42-1982 (R 2004) American National Standard Procedures for Balancing Flexible Rotors
ANSI S2.43-1984 (R 2005) American National Standard Criteria for Evaluating Flexible Rotor Balance
ANSI S2.45-1983 (R 2001) American National Standard Electrodynamic Test Equipment for Generating Vibration—Methods of Describing Equipment Characteristics
ANSI S2.46-1989 (R 2005) American National Standard Characteristics to be Specified for Seismic Transducers
ANSI S2.47-1990 (R 2001) American National Standard Vibrations of Buildings—Guidelines for the Measurements of Vibrations and Evaluation of Their Effects on Buildings
ANSI S2.48-1993 (R 2001) American National Standard Servo-Hydraulic Test Equipment for Generating Vibration—Methods of Describing Characteristics
ANSI S2.58-1983 (R 2001) American National Standard Auxiliary Tables for Vibration Generators—Methods of Describing Equipment Characteristics
ANSI S2.60-1987 (R 2005) American National Standard Balancing Machines—Enclosures and Other Safety Measures

ANSI S2.61-1989 (R 2005) American National Standard Guide to the Mechanical Mounting of Accelerometers

Accredited Standards Committee on Bioacoustics, S3

(R. F. Burkard, Chair; C. Champlin, Vice Chair)

Scope: Standards, specifications, methods of measurement and test, and terminology in the fields of psychological and physiological acoustics, including aspects of general acoustics, which pertain to biological safety, tolerance, and comfort.

S3 Working Groups

S3/Advisory—Advisory Planning Committee to S3 (R. F. Burkard);
S3/WG35—Audiometers (R. L. Grason);
S3/WG36—Speech Intelligibility (R. S. Schlauch);
S3/WG37—Coupler Calibration of Earphones (B. Kruger);
S3/WG43—Method for Calibration of Bone Conduction Vibrator (J. Durrant);
S3/WG48—Hearing Aids (D. A. Preves);
S3/WG51—Auditory Magnitudes (R. P. Hellman);
S3/WG56—Criteria for Background Noise for Audiometric Testing (J. Franks);
S3/WG59—Measurement of Speech Levels (Vacant);
S3/WG60—Measurement of Acoustic Impedance and Admittance of the Ear (Vacant);
S3/WG62—Impulse Noise with Respect to Hearing Hazard (J. H. Patterson);
S3/WG67—Manikins (M. D. Burkhard);
S3/WG72—Measurement of Auditory Evoked Potentials (R. F. Burkhard);
S3/WG76—Computerized Audiometry (A. J. Miltich);
S3/WG78—Thresholds (W. A. Yost);
S3/WG79—Methods for Calculation of the Speech Intelligibility Index (C. V. Pavlovic);
S3/WG81—Hearing Assistance Technologies (L. Thibodeau and L. A. Wilber, Co-chairs);
S3/WG82—Basic Vestibular Function Test Battery (C. Wall III);
S3/WG83—Sound Field Audiometry (T. R. Letowski);
S3/WG84—Otoacoustic Emission (G. R. Long);
S3/WG86—Audiometric Data Structures (W. A. Cole and B. Kruger, Co-Chairs);
S3/WG87—Human Response to Repetitive Mechanical Shock (N. Alem);
S3/WG88—Standard Audible Emergency Evacuation and Other Signals (I. Mande);
S3/WG89—Spatial Audiometry in Real and Virtual Environments (J. Besing);
S3/WG90—Animal Bioacoustics (A. E. Bowles);
S3/WG91—Text-to-Speech Synthesis Systems (A. K. Syrdal and C. Bickley, Co-Chairs)
S2/WG39 (S3)—Human Exposure to Mechanical Vibration and Shock—Parallel to ISO/TC 108/SC 4 (D. D. Reynolds).

S3 Liaison Group

S3/L-1 S3 U.S. TAG Liaison to IEC/TC 87 Ultrasonics (W. L. Nyborg).

S3 Inactive Working Groups

S3/WG71—Artificial Mouths (R. L. McKinley);
S3/WG80—Probe-tube Measurements of Hearing Aid Performance (W. A. Cole);
S3/WG58—Hearing Conservation Criteria.

S3 STANDARDS ON BIOACOUSTICS

ANSI S3.1-1999 (R 2003) American National Standard Maximum Permissible Ambient Noise Levels for Audiometric Test Rooms
ANSI S3.2-1989 (R 1999) American National Standard Method for Measuring the Intelligibility of Speech over Communication Systems
ANSI S3.4-1980 (2003) American National Standard Procedure for the Computation of Loudness of Noise
ANSI S3.5-1997 (R 2002) American National Standard Methods for Calculation of the Speech Intelligibility Index
ANSI S3.6-2004 American National Standard Specification for Audiometers
ANSI S3.7-1995 (R 2003) American National Standard Method for Coupler Calibration of Earphones
ANSI S3.13-1987 (R 2002) American National Standard Mechanical Coupler for Measurement of Bone Vibrators
ANSI S3.14-1977 (R 1997) American National Standard for Rating Noise with Respect to Speech Interference
ANSI S3.18-2002/Part 1 ISO 2631-1:1997 Nationally Adopted International Standard Mechanical Vibration and Shock—Evaluation of Human Exposure to Whole-Body Vibration—Part 1: General Requirements
ANSI S3.18-2003/Part 4 ISO 2631-4: 2001 Nationally Adopted International Standard Mechanical Vibration and Shock—Evaluation of Human Exposure to Whole Body Vibration—Part 4: Guidelines for the Evaluation of the Effects of Vibration and Rotational Motion on Passenger and Crew Comfort in Fixed-Guideway Transport Systems
ANSI S3.20-1995 (R 2003) American National Standard Bioacoustical Terminology
ANSI S3.21-2004 American National Standard Methods for Manual Pure-Tone Threshold Audiometry
ANSI S3.22-2003 American National Standard Specification of Hearing Aid Characteristics. (Revision of ANSI S3.22-1996)
ANSI S3.25-1989 (R 2003) American National Standard for an Occluded Ear Simulator
ANSI S3.29-1983 (R 2001) American National Standard Guide to the Evaluation of Human Exposure to Vibration in Buildings
ANSI S3.34-1986 (R 1997) American National Standard Guide for the Measurement and Evaluation of Human Exposure to Vibration Transmitted to the Hand
ANSI S3.35-2004 American National Standard Method of Measurement of Performance Characteristics of Hearing Aids under Simulated Real-Ear Working Conditions
ANSI S3.36-1985 (R 2001) American National Standard Specification for a Manikin for Simulated *In Situ* Airborne Acoustic Measurements
ANSI S3.37-1987 (R 2002) American National Standard Preferred Earhook Nozzle Thread for Postauricular Hearing Aids
ANSI S3.39-1987 (R 2002) American National Standard Specifications for Instruments to Measure Aural Acoustic Impedance and Admittance (Aural Acoustic Immittance)
ANSI S3.40-2002 ISO 10819:1996 Nationally Adopted International Standard Mechanical Vibration and Shock—Hand–arm Vibration—Method For the Measurement and Evaluation of the Vibration Transmissibility of Gloves at the Palm of the Hand
ANSI S3.41-1990 (R 2001) American National Standard Audible Emergency Evacuation Signal
ANSI S3.42-1992 (R 2002) American National Standard Testing Hearing Aids with a Broadband Noise Signal
ANSI S3.44-1996 (R 2001) American National Standard Determination of Occupational Noise Exposure and Estimation of Noise-Induced Hearing Impairment
ANSI S3.45-1999 American National Standard Procedure for Testing Basic Vestibular Function
ANSI S3.46-1997 (R 2002) American National Standard Methods of Measurement of Real-Ear Performance Characteristics of Hearing Aids

Accredited Standards Committee on Noise, S12

(R. D. Hellweg, Chair; VACANT, Vice Chair)

Scope: Standards, specifications, and terminology in the field of acoustical noise pertaining to methods of measurement, evaluation, and control; including biological safety, tolerance and comfort, and physical acoustics as related to environmental and occupational noise.

S12 Working Groups

S12/Advisory—Advisory Planning Committee to S12 (R. D. Hellweg);
S12/WG3—Measurement of Noise from Information Technology and Telecommunications Equipment (K. X. C. Man);
S12/WG11—Hearing Protector Attenuation and Performance (E. H. Berger);
S12/WG12—Evaluation of Hearing Conservation Programs (J. D. Royster, Chair; E. H. Berger, Vice Chair);

S12/WG13—Method for the Selection of Hearing Protectors that Optimize the Ability to Communicate (D. Byrne);
12/WG14—Measurement of the Noise Attenuation of Active and/or Passive Level Dependent Hearing Protective Devices (J. Kalb, Chair; W. J. Murphy, Vice Chair);
S12/WG15—Measurement and Evaluation of Outdoor Community Noise (P. D. Schomer);
S12/WG18—Criteria for Room Noise (R. J. Peppin);
S12/WG23—Determination of Sound Power (R. J. Peppin and B. M. Brooks, Co-chairs);
S12/WG31—Predicting Sound Pressure Levels Outdoors (R. J. Peppin);
S12/WG32—Revision of ANSI S12.7-1986 Methods for Measurement of Impulse Noise (A. H. Marsh);
S12/WG33—Revision of ANSI S5.1-1971 Test Code for the Measurement of Sound from Pneumatic Equipment (B. M. Brooks);
S12/WG36—Development of Methods for Using Sound Quality (G. L. Ebbit and P. Davies, Co-Chairs);
S12/WG37—Measuring Sleep Disturbance Due to Noise (K. S. Pearsons);
S12/WG38—Noise Labeling in Products (R. D. Hellweg and J. Pope, Co-Chairs);
S12/WG40—Measurement of the Noise Aboard Ships (S. Antonides, Chair; S. Fisher, Vice Chair);
S12/WG41—Model Community Noise Ordinances (L. Finegold, Chair; B. M. Brooks, Vice Chair);
S12/WG43—Rating Noise with Respect to Speech Interference (M. Alexander).

S12 Liaison Groups

S12/L-1—IEEE 85 Committee for TAG Liaison—Noise Emitted by Rotating Electrical Machines (Parallel to ISO/TC 43/SC 1/WG 13) (R. G. Bartheld);
S12/L-2—Measurement of Noise from Pneumatic Compressors Tools and Machines (Parallel to ISO/TC 43/SC 1/WG 9) (Vacant);
S12/L-3—SAE Committee for TAG Liaison on Measurement and Evaluation of Motor Vehicle Noise (parallel to ISO/TC 43/SC 1/WG 8) (R. F. Schumacher);
S12/L-4—SAE Committee A-21 for TAG Liaison on Measurement and Evaluation of Aircraft Noise (J. Brooks);
S12/L-5—ASTM E-33 on Environmental Acoustics (to include activities of ASTM E33.06 on Building Acoustics, parallel to ISO/TC 43/SC 2 and ASTM E33.09 on Community Noise) (K. P. Roy);
S12/L-6—SAE Construction—Agricultural Sound Level Committee (I. Douell);
S12/L-7—SAE Specialized Vehicle and Equipment Sound Level Committee (T. Disch);
S12/L-8—ASTM PTC 36 Measurement of Industrial Sound (R. A. Putnam, Chair; B. M. Brooks, Vice Chair).

S12 Inactive Working Groups

S12/WG27—Outdoor Measurement of Sound Pressure Level (G. Daigle)
S12/WG8—Determination of Interference of Noise with Speech Intelligibility (L. Marshall)
S12/WG9—Annoyance Response to Impulsive Noise (L. C. Sutherland)
S12/WG19—Measurement of Occupational Noise Exposure (J. P. Barry/R. Goodwin, Co-chairs)
S12/WG29—Field Measurement of the Sound Output of Audible Public-Warning Devices (Sirens) (P. Graham)
S12/WG34—Methodology for Implementing a Hearing Conservation Program (J. P. Barry)

S12 STANDARDS ON NOISE

ANSI S12.1-1983 (R 2001) American National Standard Guidelines for the Preparation of Standard Procedures to Determine the Noise Emission from Sources
ANSI S12.2-1995 (R 1999) American National Standard Criteria for Evaluating Room Noise
ANSI S12.3-1985 (R 2001) American National Standard Statistical Methods for Determining and Verifying Stated Noise Emission Values of Machinery and Equipment
ANSI S12.5-1990 (R 1997) American National Standard Requirements for the Performance and Calibration of Reference Sound Sources
ANSI S12.6-1997 (R 2002) American National Standard Methods for Measuring the Real-Ear Attenuation of Hearing Protectors
ANSI S12.7-1986 (R 1998) American National Standard Methods for Measurements of Impulse Noise
ANSI S12.8-1998 (R 2003) American National Standard Methods for Determining the Insertion Loss of Outdoor Noise Barriers
ANSI S12.9-1988 Part 1 (R 2003) American National Standard Quantities and Procedures for Description and Measurement of Environmental Sound, Part 1
ANSI S12.9-1992 Part 2 (R 2003) American National Standard Quantities and Procedures for Description and Measurement of Environmental Sound, Part 2: Measurement of Long-Term, Wide-Area Sound
ANSI S12.9-1993 Part 3 (R 2003) American National Standard Quantities and Procedures for Description and Measurement of Environmental Sound, Part 3: Short-Term Measurements With an Observer Present
ANSI S12.9-1996 Part 4 (R 2001) American National Standard Quantities and Procedures for Description and Measurement of Environmental Sound, Part 4: Noise Assessment and Prediction of Long-Term Community Response
ANSI S12.9-1998 Part 5 (R 2003) American National Standard Quantities and Procedures for Description and Measurement of Environmental Sound, Part 5: Sound Level Descriptors for Determination of Compatible Land Use
ANSI S12.9-2000 Part 6 American National Standard Quantities and Procedures for Description and Measurement of Environmental Sound Part 6: Methods for Estimation of Awakenings Associated with Aircraft Noise Events Heard in Homes
ANSI S12.10-2002 ISO 7779:1999 Nationally Adopted International Standard Acoustics—Measurement of Airborne Noise Emitted by Information Technology and Telecommunications Equipment
ANSI S12.11-2003/Part 1 ISO 10302: 1996 (MOD) American National Standard Acoustics—Measurement of Noise and Vibration of Small Air-Moving Devices—Part 1: Airborne Noise Emission
ANSI S12.11-2003/Part 2 American National Standard Acoustics—Measurement of Noise and Vibration of Small Air-Moving Devices—Part 2: Structure-Borne Vibration
ANSI S12.12-1992 (R2002) American National Standard Engineering Method for the Determination of Sound Power Levels of Noise Sources Using Sound Intensity
ANSI S12.13 TR-2002 ANSI Technical Report Evaluating the Effectiveness of Hearing Conservation Programs through Audiometric Data Base Analysis
ANSI S12.14-1992 (R 2002) American National Standard Methods for the Field Measurement of the Sound Output of Audible Public Warning Devices Installed at Fixed Locations Outdoors
ANSI S12.15-1992 (R 2002) American National Standard For Acoustics *B* Portable Electric Power Tools, Stationary and Fixed Electric Power Tools, and Gardening Appliances—Measurement of Sound Emitted
ANSI S12.16-1992 (R 2002) American National Standard Guidelines for the Specification of Noise of New Machinery
ANSI S12.17-1996 (R 2001) American National Standard Impulse Sound Propagation for Environmental Noise Assessment
ANSI S12.18-1994 (R 2001) American National Standard Procedures for Outdoor Measurement of Sound Pressure Level
ANSI S12.19-1996 (R 2001) American National Standard Measurement of Occupational Noise Exposure
ANSI S12.23-1989 (R 2001) American National Standard Method for the Designation of Sound Power Emitted by Machinery and Equipment
ANSI S12.30-1990 (R 2002) American National Standard Guidelines for the Use of Sound Power Standards and for the Preparation of Noise Test Codes
ANSI S12.35-1990 (R 2001) American National Standard Precision Methods for the Determination of Sound Power Levels of Noise Sources in Anechoic and Hemi-Anechoic Rooms
ANSI S12.42-1995 (R 2004) American National Standard Microphone-in-Real-Ear and Acoustic Test Fixture Methods for the Measurement of Insertion Loss of Circumaural Hearing Protection Devices
ANSI S12.43-1997 (R 2002) American National Standard Methods for Measurement of Sound Emitted by Machinery and Equipment at Workstations and other Specified Positions
ANSI S12.44-1997 (R 2002) American National Standard Methods for Calculation of Sound Emitted by Machinery and Equipment at Workstations

and other Specified Positions from Sound Power Level

ANSI S12.50-2002 ISO 3740:2000 Nationally Adopted International Standard Acoustics—Determination of Sound Power Levels of Noise Sources—Guidelines for the Use of Basic Standards

ANSI S12.51-2002 ISO 3741:1999 Nationally Adopted International Standard Acoustics—Determination of Sound Power Levels of Noise Sources Using Sound Pressure—Precision Method for Reverberation Rooms

ANSI S12.53/1-1999 (R 2004) ISO 3743-1:1994 Nationally Adopted International Standard Acoustics—Determination of Sound Power Levels of Noise Sources—Engineering Methods for Small, Movable Sources in Reverberant Fields—Part 1: Comparison Method for Hard-Walled Test Rooms

ANSI S12.53/2-1999 (R 2004) ISO 3743-2:1994 Nationally Adopted International Standard Acoustics—Determination of Sound Power Levels of Noise Sources Using Sound Pressure-Engineering Methods for Small, Movable Sources in Reverberant Fields—Part 2: Methods for Special Reverberation Test Rooms

ANSI S12.54-1999 (R 2004) ISO 3744:1994 Nationally Adopted International Standard Acoustics—Determination of Sound Power Levels of Noise Sources Using Sound Pressure—Engineering Method in an Essentially Free Field Over a reflecting Plane

ANSI S12.56-1999 (R 2004) ISO 3746:1995 Nationally Adopted International Standard Acoustics—Determination of Sound Power Levels of Noise Sources Using Sound Pressure—Survey Method Using an Enveloping Measurement Surface over a Reflecting Plane

ANSI S12.57-2002 ISO 3747:2000 Nationally Adopted International Standard Acoustics—Determination of Sound Power Levels of Noise Sources Using Sound Pressure—Comparison Method *In Situ*

ANSI S12.60-2002 American National Standard Acoustical Performance Criteria, Design Requirements, and Guidelines for Schools

ASA Committee on Standards (ASACOS)

ASACOS (P. D. Schomer, Chair and ASA Standards Director)

U.S. Technical Advisory Groups (TAGS) for International Standards Committees

ISO/TC 43 Acoustics, **ISO/TC 43/SC 1** Noise (P. D. Schomer, U.S. TAG Chair)

ISO/TC 108 Mechanical Vibration and Shock (D. J. Evans, U.S. TAG Chair)

ISO/TC 108/SC2 Measurement and Evaluation of Mechanical Vibration and Shock as Applied to Machines, Vehicles and Structures (A. F. Kilcullen, and R. F. Taddeo U.S. TAG Co-Chairs)

ISO/TC 108/SC3 Use and Calibration of Vibration and Shock Measuring Instruments (D. J. Evans, U.S. TAG Chair)

ISO/TC 108/SC4 Human Exposure to Mechanical Vibration and Shock (D. D. Reynolds, U.S. TAG Chair)

ISO/TC 108/SC5 Condition Monitoring and Diagnostic Machines (D. J. Vendittis, U.S. TAG Chair, R. F. Taddeo, U.S. TAG Vice Chair)

ISO/TC 108/SC6 Vibration and Shock Generating Systems (G. Booth, U.S. TAG Chair)

IEC/TC 29 Electroacoustics (V. Nedzelnitsky, U.S. Technical Advisor)

Standards News from the United States

(Partially derived from *ANSI Reporter*, and *ANSI Standards Action*, with appreciation)

American National Standards Call for Comment on Proposals Listed

This section solicits comments on proposed new American National Standards and on proposals to revise, reaffirm, or withdraw approval of existing standards. The dates listed in parenthesis are for information only.

ASA (ASC S1) (Acoustical Society of America)

ASA (ASC S2) (Acoustical Society of America)

Reaffirmations

IEEE (ASC C63) (Institute of Electrical and Electronics Engineers)

Revisions

BSR C63.19-200x, Methods of Measurement of Compatibility between Wireless Communications Devices and Hearing Aids (revision of ANSI C63.19-2001) (6 June 2005)

Sets forth uniform methods of measurement and parametric requirements for the electromagnetic and operational compatibility and accessibility of hearing aids used with wireless communications devices operating in the range of 800 MHz to 3 GHz. However, this version is focused on existing services, which are in common use.

ASA (ASC S3) (Acoustical Society of America)

Revisions

BSR S3.4-200x, Procedure for the Computation of Loudness of Steady Sounds [revision of ANSI S3.4-1980 (R2003)] (9 May 2005)

Specifies a procedure for calculating the loudness of steady sounds as perceived by a typical group of listeners with normal hearing, based on the spectra of the sounds. The possible sounds include simple and complex tones (both harmonic and inharmonic) and bands of noise. The spectra can be specified exactly, in terms of the frequencies and levels of individual spectral components, or approximately, in terms of the levels in 1/3 octave bands covering center frequencies from 50 to 16 000 Hz. Sounds can be presented in the free field with frontal incidence, in a diffuse field, or via headphones.

ASA (ASC S12) (Acoustical Society of America)

Revisions

BSR S12.9-Part 4-200x, Quantities and Procedures for Description and Measurement of Environmental Sound—Part 4: Noise Assessment and Prediction of Long-Term Community Response [revision of ANSI S12.9-Part 4-1996 (R2001)] (25 April 2005)

Specifies methods to assess environmental sounds and to predict the annoyance response of communities to long-term noise from any and all types of environmental sounds produced by one or more distinct or distributed sound sources. The sound sources may be separate or in various combinations. Application of the method of the Standard is limited to areas where people reside and related long-term land uses.

ASTM (ASTM International)

Reaffirmations

BSR/ASTM E1662-1995A (R200x), Classification for Serviceability of an Office Facility for Sound and Visual Environment [reaffirmation of ANSI/ASTM E1662-1995A (R99)]

Meeting Notices (for information only)

AMT—The Association For Manufacturing Technology

B11.TR5 Subcommittee—Noise Measurement

The B11.TR5 Subcommittee, sponsored by the Secretariat (AMT), will hold their next meeting on Thursday and Friday, April 21–22, 2005 at AMT headquarters in McLean, VA. The B11 Committee is an ANSI-Accredited Standards Committee on machine tool safety, and the B11.TR5 Subcommittee deals with noise measurement of machine tools. The purpose of this meeting is to continue revision work on an existing 30 year old industry standard as a new Technical Report and as an integral part in the B11 series of American National Standards on machine tool safety. This meeting is open to anyone with an interest in machine tool safety, particularly as it relates to noise measurement, and who wishes to participate in standards development.

Final Actions on American National Standards

The standards actions listed below have been approved by the ANSI Board of Standards Review (BSR) or by an ANSI-Audited Designator, as applicable.

ASA (ASC S1) (Acoustical Society of America)

New Standards

ANSI S1.15-2005/Part 2, Measurement Microphones—Part 2: Primary Method for Pressure Calibration of Laboratory Standard Microphones by the Reciprocity Technique (new standard): (9 March 2005)

Withdrawals

ANSI S1.10-1966 (R2001), Calibration of Microphones [withdrawal of ANSI S1.10-1966 (R2001)]: (9 March 2005)

Reaffirmations

BSR S1.16-2000 (R2005), Method for Measuring the Performance of Noise Discriminating and Noise Canceling Microphones (reaffirmation of ANSI S1.16-2000) (25 April 2005)

Describes procedures for measuring the performance of noise-discriminating and noise-canceling microphones. The signal-to-noise ratio is measured at 1/3 octave band intervals with the desired test source in a diffuse noise field.

ASA (ASC S2) (Acoustical Society of America)

Reaffirmations

ANSI S2.34-1984 (R2005), Guide to the Experimental Determination of Rotational Mobility Properties and the Complete Mobility Matrix [reaffirmation of ANSI S2.34-1984 (R2001)]

This guide delineates the methods and procedures that may be used to determine the structural mobility properties, translational and rotational, of a system of points on a structure. This publication is to be used for guidance only, since the state of the art is still in flux.

ANSI S2.43-1984 (R2005), Criteria for Evaluating Flexible Rotor Balance [reaffirmation of ANSI S2.43-1984 (R2001)]

Specifies two methods for evaluating the quality of balance of a flexible rotor in a balancing facility before machine assembly, with the aim that the rotor will run satisfactorily after machine assembly and installation on site. The criteria specified are those to be met when the rotor is tested in the balancing facility, but they are derived from those specified for the complete machine, when installed, or from values known to ensure satisfactory running of the rotor when it is installed.

ANSI S2.46-1989 (R2005), Characteristics to be Specified for Seismic Transducers [reaffirmation of ANSI S2.46-1989 (R2001)]

This standard specifies rules for the presentation of important characteristics for electro-mechanical shock and vibration transducers (seismic pickups), the electrical outputs of which are known functions of the uniaxial, multiaxial, or angular accelerations, velocities, or displacements of objects the motions of which are being measured.

ANSI S2.60-1987 (R2005), Balancing Machines—Enclosures and Other Safety Measures.

Specifies requirements for enclosures and other safety measures used to minimize hazards associated with the operation of balancing machines under a variety of rotor and balancing conditions. It defines different classes of protection that enclosures and other protective features have to provide, and describes the limits of applicability for each class of protection.

ANSI S2.61-1989 (R2005), Guide to Mechanical Mounting of Accelerometers [reaffirmation of ANSI S2.61-1989 (R2001)]

Describes the mounting characteristics of accelerometers to be specified by the manufacturer and makes recommendations to the user for mounting accelerometers. The application of this standard is limited to the mounting of electromechanical transducers of the type that are attached on the surface of the structure in motion. It does not cover other types, such as relative motion pickups. This standard is in general accordance with ISO 5348-1987.

Withdrawals

ANSI S2.38-1982 (R2001), Field Balancing Equipment—Description and Evaluation [withdrawal of ANSI S2.38-1982 (R2001)] (25 April 2005)

Concerns itself with the description and evaluation of portable equipment used for field (in-place) balancing of rotating machinery. It tells the equipment manufacturer that performance parameters need to be specified and in what terms, so that the prospective user can assess the applicability of the equipment for his purpose. At the same time, a prospective user is given guidance on how to describe his requirements to the equipment manufacturer.

ANSI S2.40-1984 (R2001), Mechanical Vibration of Rotating and Reciprocating Machinery—Requirements for Instruments for Measuring Vibration Severity [withdrawal of ANSI S2.40-1984 (R2001)] (18 April 2005)

This standard establishes the requirements of instrumentation for accurately measuring the vibration severity of machinery. Limitations for frequency, sensitivity, amplitude range, calibration, and environmental factors are presented in this standard.

Project Initiation Notification System (PINS)

ANSI Procedures require notification of ANSI by ANSI-accredited standards developers of the initiation and scope of activities expected to result in new or revised American National Standards. This information is a key element in planning and coordinating American National Standards.

The following is a list of proposed new American National Standards or revisions to existing American National Standards that have been received from ANSI-accredited standards developers that utilize the periodic maintenance option in connection with their standards. Directly and materially affected interests wishing to receive more information should contact the standards developer directly.

ASA (ASC S3) (Acoustical Society of America)

BSR S3.50-200X, Text to Speech Synthesis Systems (new standard)

To provide a standard for an evaluation of the intelligibility of synthetic speech output from text-to-speech systems. Evaluation of speech intelligibility of the synthetic speech output of text-to-speech (TTS) systems, which convert text input to audible speech output.

ASA (ASC S12) (Acoustical Society of America)

BSR S12.51-Part 2-200x, Acoustics—Determination of Sound Power Levels of Noise Sources Using Sound Pressure—Precision Method for Reverberation Rooms—Part 2: Immovable Noise Sources (New Standard)

Specifies a comparison method for determining the sound power level that would be produced by a source that may be difficult or undesirable to move within the test facilities. It applies to both broadband noise sources and sources with discrete frequency components. It specifies test room qualification requirements, source location, instrumentation and techniques for determining sound power levels of the source with a grade 1 accuracy. This standard does not provide the means to determine directivity and temporal variation of sound from a source.

When S12 nationally adopted ISO 3741:1999 as ANSI S12.51-2002, it unwittingly eliminated a precision method to be used when it is impractical to move the noise source being tested within the chamber or when the source is located outside the chamber and connected via a duct. This part will provide these procedures as a separate document.

IEEE (Institute of Electrical and Electronics Engineers)

BSR/IEEE 115-200x, Test Procedures for Synchronous Machines [revision of ANSI/IEEE 115-1995 (R2002)]

The scope of the project is to (a) new test results published in IEEE requires revision of section 7.3.6; and (b) in view of increased interest in vibration tests, a new section on vibration test procedures should be added. The standard does not include methods of measurement of vibration in synchronous machines. Vibration tests are now required for both diagnostic and acceptance testing by industrial customers and utilities. New test results reported in IEEE papers require the revision of the acceleration torque test procedure in the current document.

Newly Published ISO and IEC Standards

Listed here are new and revised standards recently approved and promulgated by ISO-the International Organization for Standardization

ISO Standards

MECHANICAL VIBRATION AND SHOCK (TC 108)

ISO 8041:2005, Human response to vibration—Measuring instrumentation

ISO 18437-2:2005"Mechanical vibration and shock—Characterization of the dynamic mechanical properties of visco-eleastic materials—Part 2: Resonance method"

ISO 18437-3:2005 "Mechanical vibration and shock—Characterization of the dynamic mechanical properties of visco-elastic materials—Part 3: Cantilever shear beam method"

IEC Standards

IEC 60704-2-6 Ed. 2.0 b: 2005, Household and similar electrical appliances—Test code for the determination of airborne acoustical noise—Part 2-6: Particular requirements for tumble dryers

ENVIRONMENTAL CONDITIONS, CLASSIFICATION AND METHODS OF TEST (TC 104)

IEC 60068-2-47 Ed. 3.0 b: 2005, Environmental testing—Part 2-47: Test—Mounting of specimens for vibration, impact, and similar dynamic tests

IEC Technical Specifications

WIND TURBINE GENERATOR SYSTEMS (TC 88)

IEC/TS 61400-14 Ed. 1.0 en:2005, Wind turbines—Part 14: Declaration of apparent sound power level and tonality values

ISO Draft Standard

MECHANICAL VIBRATION AND SHOCK (TC 108)

ISO/DIS 362-1, Acoustics—Engineering method for the measurement of noise emitted by accelerating road vehicles—Part 1: Vehicles of categories M and N (2 July 2005)

ISO/DIS 362-2, Acoustics—Engineering method for the measurement of noise emitted by accelerating road vehicles—Part 2: Vehicles of category L (2 July 2005)

ISO/DIS 18431-4, Mechanical vibration and shock—Signal processing—Part 4: Shock response spectrum analysis (25 May 2005)

ISO/DIS 18434-1, Condition monitoring and diagnostics of machines—Thermography—Part 1: General procedures (25 June 2005)

IEC Draft Standard

104/363/FDIS, IEC 60068-2-80 Ed.1.0: Environmental testing—Part 2-80: Tests—Test Fi: Vibration—Mixed mode (15 April 2005)

49/714/FDIS, IEC 61019-2 Ed.2: Surface acoustic wave (SAW) resonators—Part 2: Guide to the use (22 April 2005)

49/720/FDIS, IEC 62276 Ed.1: Single crystal wafers for surface acoustic wave (SAW) device applications—Specifications and measuring methods (13 May 2005)

59A/120/FDIS, IEC 60704-2-3-A1 Ed 2.0: Household and similar electrical appliances—Test code for the determination of airborne acoustical noise—Part 2-3: Particular requirements for dishwashers (3 June 2005)

FIG. 1. Standards Director Paul Schomer presents a plaque to George S. K. Wong, Vice Chair of S1, Acoustics, for his contributions as Project Leader in regard to two recently published American National Standards: ANSI S1.11-2004 Specification for Octave-Band and Fractional-Octave-Band Analog and Digital Filters, and ANSI S1.15-2005/Part 2 Measurement Microphones—Part 2: Primary Method for Pressure Calibration of Laboratory Standard Microphones by the Reciprocity Technique.

FIG. 2. Standards Dirctor Paul Schomer presents a plaque to Richard J. Peppin, for his contributions as Chair of S1/WG 17, in regard to the publication of ANSI S1.17-2004/Part 1 American National Standard Microphone Windscreens—Part 1: Measurements and Specification of Insertion Loss in Still or Slightly Moving Air.

FIG. 3. The ASA Committee on Standards met in Vancouver. Member and guests present include (standing) Bruce Douglas, Richard Harmening, Shri Narayanan, Kerry Commander, Victor Nedzenitsky, David Evans, George Wong, (seated) Mahlon Burkhard, Steven Lind, Robert Hellweg, Ridhard Peppin, Paul Schomer.

REVIEWS OF ACOUSTICAL PATENTS

Lloyd Rice
11222 Flatiron Drive, Lafayette, Colorado 80026

The purpose of these acoustical patent reviews is to provide enough information for a Journal reader to decide whether to seek more information from the patent itself. Any opinions expressed here are those of reviewers as individuals and are not legal opinions. Printed copies of United States Patents may be ordered at $3.00 each from the Commissioner of Patents and Trademarks, Washington, DC 20231. Patents are available via the Internet at http://www.uspto.gov.

Reviewers for this issue:

GEORGE L. AUGSPURGER, *Perception, Incorporated, Box 39536, Los Angeles, California 90039*
JOHN M. EARGLE, *JME Consulting Corporation, 7034 Macapa Drive, Los Angeles, California 90068*
SEAN A. FULOP, *California State University, Fresno, 5245 N. Backer Avenue M/S PB92, Fresno, California 93740-8001*
JEROME A. HELFFRICH, *Southwest Research Institute, San Antonio, Texas 78228*
MARK KAHRS, *Department of Electrical Engineering, University of Pittsburgh, Pittsburgh, Pennsylvania 15261*
DAVID PREVES, *Starkey Laboratories, 6600 Washington Ave. S., Eden Prarie, Minnesota 55344*
DANIEL R. RAICHEL, *2727 Moore Lane, Fort Collins, Colorado 80526*
CARL J. ROSENBERG, *Acentech Incorporated, 33 Moulton Street, Cambridge, Massachusetts 02138*
NEIL A. SHAW, *Menlo Scientific Acoustics, Inc., Post Office Box 1610, Topanga, California 90290*
WILLIAM THOMPSON, JR., *Pennsylvania State University, University Park, Pennsylvania 16802*
ERIC E. UNGAR, *Acentech Incorporated, 33 Moulton Street, Cambridge, Massachusetts 02138*
ROBERT C. WAAG, *University of Rochester, Department of Electrical and Computer Engineering, Rochester, New York 14627*

6,849,910

43.25.Nm SYSTEMS AND METHODS FOR IMPROVING THE PERFORMANCE OF SENSING DEVICES USING OSCILLATORY DEVICES

Bruce J. Oberhardt, Raleigh, North Carolina *et al.*
1 February 2005 (Class 257/414); filed 20 May 2003

This inventor claims to have been first to invent micromechanical piezoelectric fans for use as ''surface pumps'' that move a gas or liquid in a flow channel. By operating the fan (in the form of cilia), it is said that the boundary layer of the liquid is agitated and mixed, improving the performance of downstream sensors, such as a smoke alarm. The supposed benefit is increased rapidity of response of said sensor. The use of such fans is not new; they have been used to cool integrated circuits for about twenty years. It is interesting that the novelty claimed is not the mechanism but the principle of pumping the medium past the sensor.—JAH

6,837,177

43.25.Ts WHISTLE HAVING AIR FLOW CONVERTER

Masayuki Tanaka, assignor to Molten Corporation
4 January 2005 (Class 116/137 R); filed in Japan 24 July 2000

The inventor argues that the use of ''air flow converters'' **9a** and **9b** will create extra higher harmonics and increase the SPL in the resonant chambers. Experimental data is presented to back up the assertions.—MK

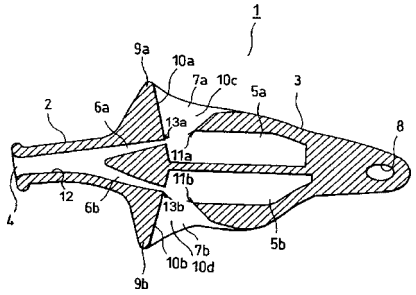

6,851,990

43.28.Ra METHOD AND DEVICE FOR LOW-NOISE UNDERWATER PROPULSION

Ahmed A. Hassan *et al.*, assignors to The Boeing Company
8 February 2005 (Class 440/38); filed 18 December 2002

A method and apparatus are described for propelling a watercraft by repetitively sucking in and expelling water from an on-board liquid chamber. This propulsion system is also said to result in low acoustic emissions.—WT

6,845,062

43.30.Sf MANATEE WARNING SYSTEM

Christopher Niezrecki *et al.*, assignors to University of Florida Reasearch Foundation, Incorporated
18 January 2005 (Class 367/131); filed 14 October 2003

While the title of this patent may suggest that this is a device to warn a manatee of an approaching boat, in fact, the system described is basically a ''big fish'' finder that warns the boat operator of the presence of a manatee. The system comprises a projector, which can be mounted on a buoy, a mooring, some other underwater structure, or the boat in question, plus a hydrophone, and a signal processor unit mounted on the boat, which can process the received echoes and make a decision about the presence of a particular type of creature and then warn the operator visually or audibly or even control some operating parameter of the boat.—WT

 0001-4966/2005/118(1)/17/15/$20.00

6,859,419

43.35.Sx LASER-BASED ACOUSTO-OPTIC UPLINK COMMUNICATIONS TECHNIQUE

Fletcher A. Blackmon *et al.*, assignors to the United States of America as represented by the Secretary of the Navy
22 February 2005 (Class 367/134); filed 18 August 2003

An apparatus is described for enabling communication between a submerged vehicle and a nearby airborne aircraft. An acoustic signal is radiated from the submerged vehicle toward the water's surface, causing small perturbations of the surface. The aircraft transmits a laser beam toward the same surface, and by appropriately processing the difference between this transmitted laser beam and its reflection from the surface, a signal representing the original acoustic signal is generated.—WT

6,850,465

43.35.Wa PULSE GENERATING DRIVE CIRCUIT FOR AN ELECTROMAGNETIC SOURCE FOR GENERATING ACOUSTIC WAVES

Arnim Rohwedder, assignor to Siemens Aktiengesellschaft
1 February 2005 (Class 367/137); filed in Germany 22 February 2002

This invention is concerned with the generation of ultrasonic shock waves for use in medical procedures—the destruction of kidney stones, for example. Using known prior art, a suitable electrical drive pulse can be generated by discharging capacitor **22** through transducer coil **23**. The new

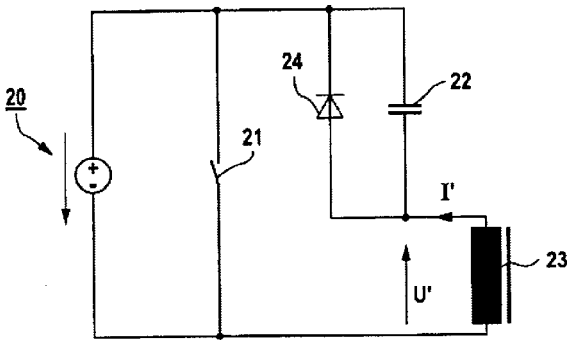

feature disclosed here is the addition of diode **24** to lengthen the initial pulse and damp subsequent ringing. Anyone who has had experience with electromechanical relays will find the technique familiar rather than novel.—GLA

6,853,315

43.35.Zc PIEZOELECTRIC RATE SENSOR SYSTEM AND METHOD

Peter J. Schiller *et al.*, assignors to Triad Sensors, Incorporated
8 February 2005 (Class 340/974); filed 23 January 2002

This patent describes an inertial guidance system for use in commercial and private aircraft comprising two gyros, three accelerometers, and a three-axis magnetometer. The proposed novelty is the combination of accelerometers and gyros into one ''single sheet of piezoelectric material.'' No data are presented nor calculations given of how well such an arrangement might work, but many assertions are made for being able to compensate the resulting outputs for temperature and acceleration. The arrangement given would not likely result in high enough sensitivity to be useful on the MEMS scale.—JAH

6,851,512

43.38.Ar MODULAR MICROPHONE ARRAY FOR SURROUND SOUND RECORDING

Charles Fox, and Wade McGregor, North Vancouver, British Columbia, both of Canada
8 February 2005 (Class 181/158); filed in Canada 1 March 2002

While the patent drawings describe an azimuthal microphone array consisting of five equally spaced pressure elements, the text further states that the quantity can be varied, suggesting possibilities for higher-order microphone synthesis. Further descriptions are given of the modular nature of the assembly and its overall geometry and utility.—JME

6,853,733

43.38.Ar TWO-WIRE INTERFACE FOR DIGITAL MICROPHONES

Wouter Groothedde *et al.*, assignors to National Semiconductor Corporation
8 February 2005 (Class 381/111); filed 18 June 2003

As the abstract states, ''A two-wire interface for a digital microphone circuit includes a power line and a ground line. The interface utilizes the ground line as a 'voltage active line' to transmit both clock and data signals between the digital microphone circuit and a receiving circuit. The digital

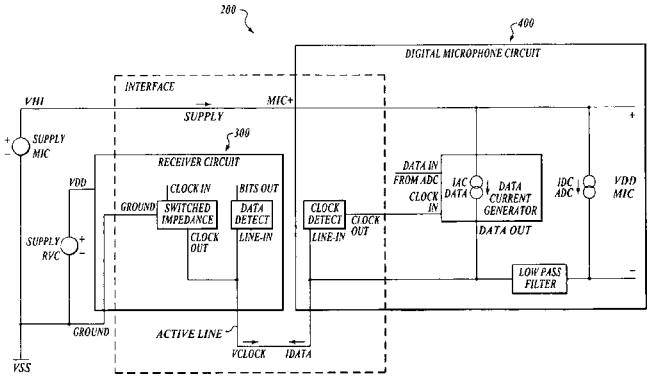

microphone circuit detects the clock signal on the voltage active line and uses the detected clock signal to operate an ADC to provide digital data.''—JME

6,854,338

43.38.Bs FLUIDIC DEVICE WITH INTEGRATED CAPACITIVE MICROMACHINED ULTRASONIC TRANSDUCERS

Butrus T. Khuri-Yakub and F. Levent Degertekin, assignors to The Board of Trustees of the Leland Stanford Junior University
15 February 2005 (Class 73/861.27); filed 12 July 2001

The authors devote much space to giving applications for their previously patented ''capacitive micromachined ultrasonic transducer'' (United States Patent 5,619,476) in the fields of fluid pumping and measurement of fluid properties. No supporting data are given on the efficacy of these devices, and the reader is advised to look to the earlier patent and the two others cited here for information on how these devices work.—JAH

6,839,302

43.38.Fx ACOUSTIC EMITTERS FOR USE IN MARINE SEISMIC SURVEYING

Peter Austad and Rolf Rustad, assignors to WesternGeco
4 January 2005 (Class 367/19); filed in the United Kingdom 4 May 2000

In a seismic survey system, rather than having the acoustic source transducer be a separately towed unit, it is proposed to make the source an insert that is connected coaxially with adjacent hydrophone streamer sections. The annular-shaped source transducer, preferably of piezoelectric material and preferably a flextensional type transducer, allows for passage of the electrical cable to the downstream hydrophones. This transducer element is encased in a housing, which protects it from the damaging effects of bending stresses during retrieval and spooling of the entire streamer, but which is also acoustically transparent. As an alternative embodiment, rather than a single flextensional transducer, a number of much smaller flextensionals is proposed, each mounted near the outer surface of the same sized cylindrical housing as before and looking radially outward.—WT

6,850,623

43.38.Fx PARAMETRIC LOUDSPEAKER WITH IMPROVED PHASE CHARACTERISTICS

Elwood G. Norris *et al.*, assignors to American Technology Corporation
1 February 2005 (Class 381/97); filed 29 October 1999

A parametric loudspeaker modulates an ultrasonic beam to produce sound from empty air. To achieve the required output level at a modulation frequency of 40 kHz or so, it is usual to employ an array of piezoelectric transducers driven at resonance. Unfortunately, it is almost impossible to acquire a large group of such transducers that are precisely matched. Because of the rapid change of phase near resonance, a slight mistuning can result in destructive interference between individual units. The patent recommends shifting the modulation frequency slightly upward into a region of relatively flat phase response. The resulting loss in maximum achievable sensitivity is more than offset by the practical gain in coherent summation.—GLA

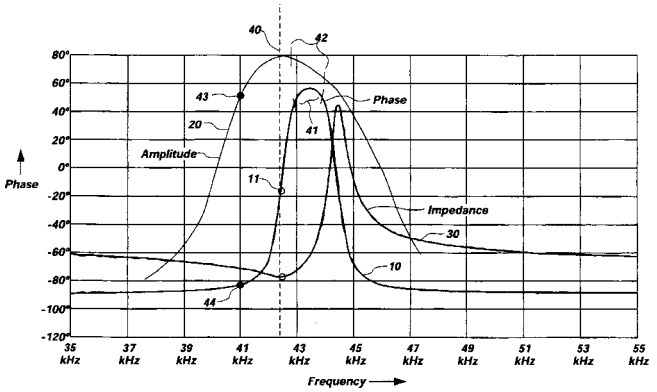

6,856,580

43.38.Fx NAVAL-HULL MOUNTED SONAR FOR NAVAL SHIP

Michel Eyries, assignor to Thales
15 February 2005 (Class 367/165); filed in France 8 December 2000

A hull-mounted sonar comprises a projector **20** surrounded by two coaxial and concentric cylindrical arrays of hydrophones **210**. The projector is formed from a stack of piezoelectric rings **201** whose diameter is chosen according to the desired transmission frequency. The projector is either gimbal mounted **202** to keep it vertical, in spite of ship pitch and roll, or the direction of transmission is electrically stabilized by individually exciting the rings of the stack. The hydrophones **210** are mounted with random positioning on the two cylindrical frames, which are acoustically transparent. The outputs of the various hydrophones are processed to achieve certain desired directivity characteristics.—WT

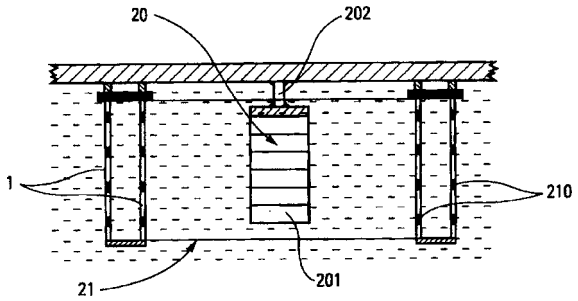

6,837,333

43.38.Ja LOUDSPEAKER SYSTEM WITH FORCED AIR CIRCULATION AND CONTROL CIRCUIT THEREFORE

Bruce Howze, assignor to Community Light and Sound, Incorporated
4 January 2005 (Class 181/148); filed 1 April 2002

Heat is a byproduct of electrodynamic acoustic transducer operations. In this patent, a fan **100** is used to blow air **102**, **92**, and **106** through the pole piece vent **58**, gaps **92** and **94**, the volume defined by the dust cap **18**, cone vent holes **35**, and airflow director **70**, and then to the exterior of the loudspeaker, thereby providing cooling in addition to that obtained by convection and radiation. The fan is energized when the applied electrical power is above a predetermined limit. The patent describes how this method is an improvement over prior art and also provides a capsule discussion of the thermodynamic considerations of concern.—NAS

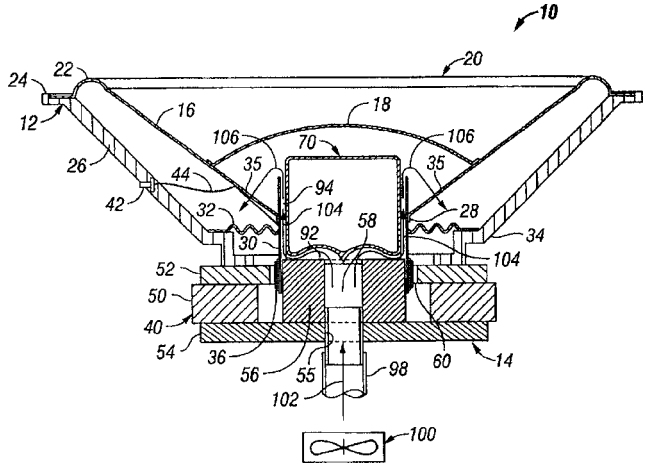

6,845,166

43.38.Ja PLANE DRIVING TYPE ELECTROACOUSTIC TRANSDUCER

Akira Hara and Kunio Kondo, assignors to Foster Electric Company, Limited
18 January 2005 (Class 381/399); filed in Japan 2 November 2000

Planar transducers are all the rage right now. This patent offers some solutions to some problems found in some models of this type. The three main areas of improvement listed in the patent are (a) better damping of the diaphragm, (b) a lessening of the difference in the flexural rigidity in the

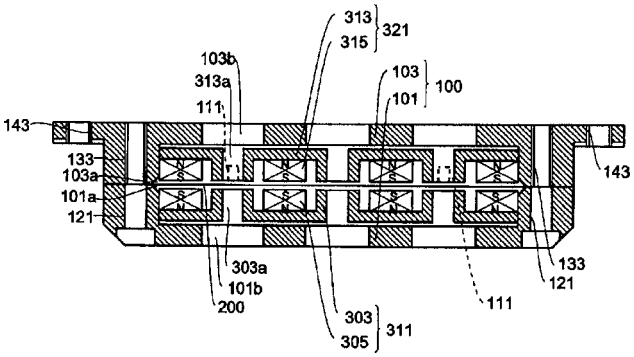

plane of the material, and (c) a means of reducing the cost of assembly. The patent is relatively easy to read.—NAS

6,853,734

43.38.Ja AUDIO SPEAKER DAMPER WITH ELECTRICALLY CONDUCTIVE PATHS THEREON TO CARRY VOICE COIL SIGNALS AND A METHOD THEREFORE

Joseph Y. Sahyoun, Redwood City, California
8 February 2005 (Class 381/404); filed 19 May 2003

The voice coil centering device of an old electrodynamic loudspeaker was called a spider because it looked like a spider. In today's designs it is shaped more like a bellows and Japanese manufacturers call it a damper.

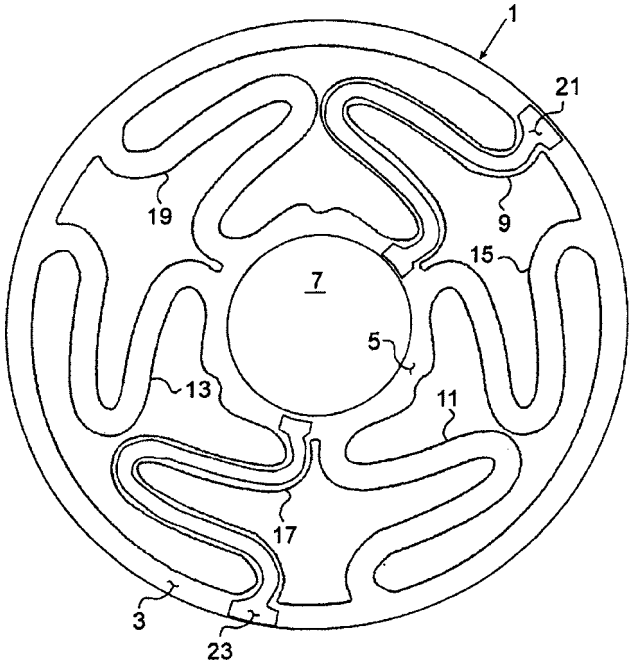

This patent suggests that a variation of the earlier design not only can supply a more linear restoring force but can also include reliable conductive traces for electrical connections.—GLA

6,859,543

43.38.Ja SPEAKER SYSTEM AND METHOD FOR MAKING THE SAME

Kenneth A. Fingleton, Byron Center, Michigan
22 February 2005 (Class 381/338); filed 25 November 2002

A vertical cylinder has an upward-firing speaker mounted on its top, a forward-facing tweeter near the top, and a vent near the bottom. As is the current fashion in audio patents, all three locations are "predetermined."—GLA

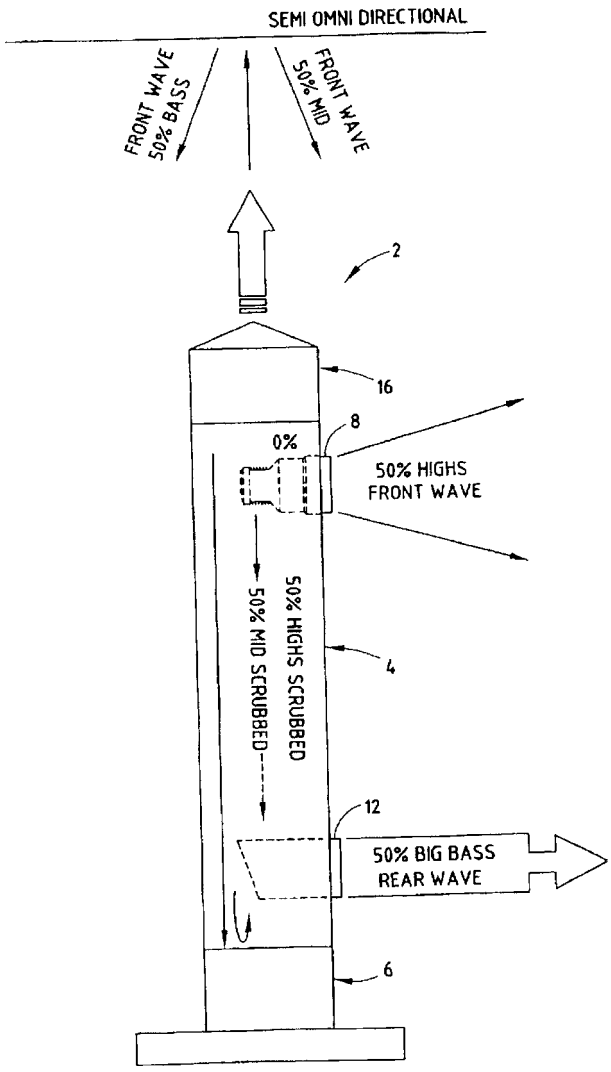

6,856,691

43.38.Ja ELECTRONIC APPARATUS INCLUDING LOUDSPEAKER SYSTEM

Shuji Saiki *et al.*, assignors to Matsushita Electric Industrial Company, Limited
15 February 2005 (Class 381/388); filed in Japan 29 August 2002

All laptop computers house one or two tiny loudspeakers. Many laptops, including those made by Matsushita, utilize a touch pad in place of a joystick or mouse. Might it be possible to combine the touchpad and loudspeaker into a single small assembly? Better yet, why not use the touchpad itself as a sound-emitting diaphragm, coupled to the speaker through a small volume of air? (Actually, since this is a computer patent, sound is outputted rather than emitted.) Moreover, by properly choosing the frequency ranges

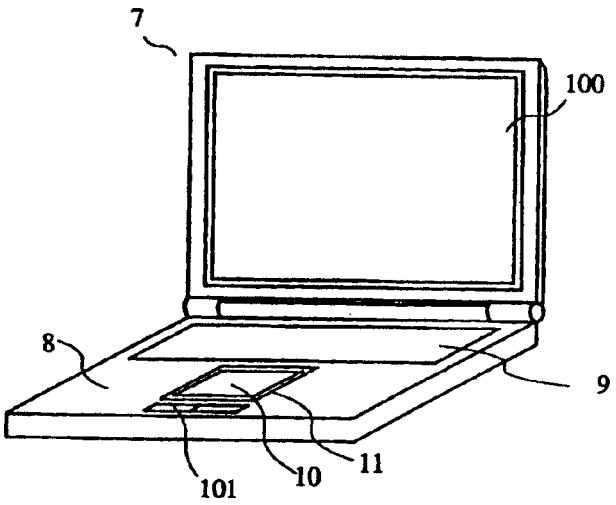

of clicks and beeps, the user can be alerted through touch as well as sound.—GLA

6,856,192

43.38.Lc CLASS-D AMPLIFIER OF BTL OUTPUT TYPE USING FILTER COIL AND LOW-PASS FILTER

Toshihiko Muramatsu, assignor to Yamaha Corporation
15 February 2005 (Class 330/10); filed in Japan 10 October 2001

The illustration shows a stereo class-D audio amplifier. Each bridge-type output includes a pair of L–C lowpass filters. Consider inductors **L1** and **L2**. If these are wound in opposite directions, they can be mounted side by side in a single package, thus suppressing radiation and reducing manufacturing cost.—GLA

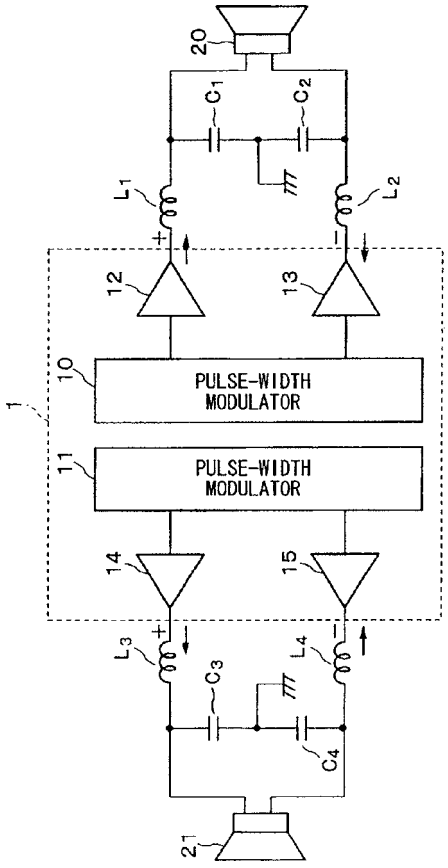

6,856,194

43.38.Lc CENTER OF GRAVITY COMPENSATION OF CLASS-D AMPLIFIER

Johan Nilsson *et al.*, assignors to Dialog Semiconductor GmbH
15 February 2005 (Class 330/10); filed in the European Patent Office 11 December 2002

The patent explains that power supply fluctations in a class-D amplifier distort the output signal. If pulse width is modified to supply the required compensation, then jitter is introduced. A method is described whereby the leading edge and trailing edge are also corrected in time so that each pulse

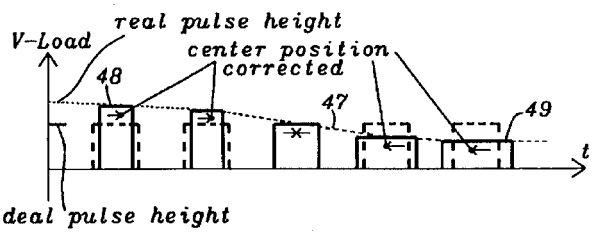

is centered at its nominal clock position. The method utilizes a ''predelay integrator'' and a ''length-of-pulse integrator'' to control start and stop times based on integration of the actual supply voltage.—GLA

6,848,996

43.38.Md GAMING DEVICE WITH SOUND RECORDING CHANGES ASSOCIATED WITH PLAYER INPUTS

William L. Hecht and Kristopher E. Landrum, assignors to IGT
1 February 2005 (Class 463/35); filed 15 October 2001

Take a slot machine. Add a simple finite state control together with fixed sound tracks. Next, add humans willing to enthusiastically engage such a machine with coins. The result? A perfect Las Vegas marriage. Complete with soundtrack.—MK

6,856,923

43.38.Md METHOD FOR ANALYZING MUSIC USING SOUNDS INSTRUMENTS

Doill Jung, assignor to AMUSETEC Company, Limited
15 February 2005 (Class 702/71); filed in the Republic of Korea 5 December 2000

The inventor presents two overly broad ideas: (1) using a recursive FFT to analyze the spectrum in more detail and (2) tracking from frame to frame. Conveniently, there is absolutely no mention of the extensive work in sinusoidal tracking over frames (like MQ coding).—MK

6,792,116

43.38.Si EARPHONE WITH CONTROL DEVICE OF TIMING CALL SETTING

Min-Yi Liu, Taoyuan, Taiwan, Province of China
14 September 2004 (Class 381/74); filed 4 March 2002

In one page of badly broken English, this patent uses the eight words of the title at least eight times in a nearly futile attempt to state the purpose

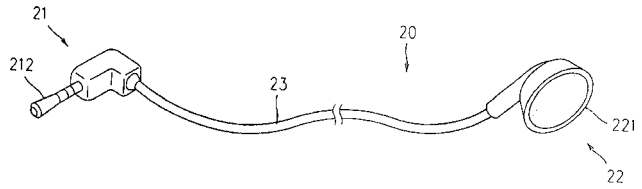

of the device. It seems to be a programmable alarm function built into an earphone. The same cryptic eight-word phrase appears again in the first claim.—DLR

6,856,690

43.38.Si COMFORTABLE EARPHONE CUSHIONS

Gerald W. Skulley, assignor to Plantronics, Incorporated
15 February 2005 (Class 381/371); filed 9 January 2002

A headset incorporates a new cushion that provides improved long-term comfort because it requires less pressure to conform to the user's ear. How is this achieved? By making the cushion from a material that is ''resiliently comformable,'' thus requiring less pressure. However, the patent

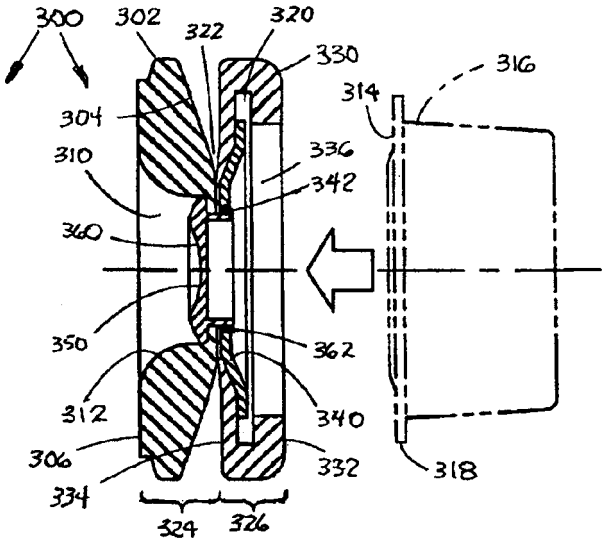

does describe one interesting feature: the use of a material ''capable of endothermic phase changes at a constant temperature such that the cushion more effectively conducts heat away from the ear.''—GLA

6,859,657

43.38.Si PERSONAL COMMUNICATIONS APPARATUS

Michael E. Barnard, assignor to Koninklijke Philips Electronics N.V.
22 February 2005 (Class 455/575.6); filed in the United Kingdom 29 August 1998

If you combine your Dick Tracy wrist radio with your Orphan Annie secret decoder ring, what do you get? Answer: a two-way communications device that transmits data and power between the two components through

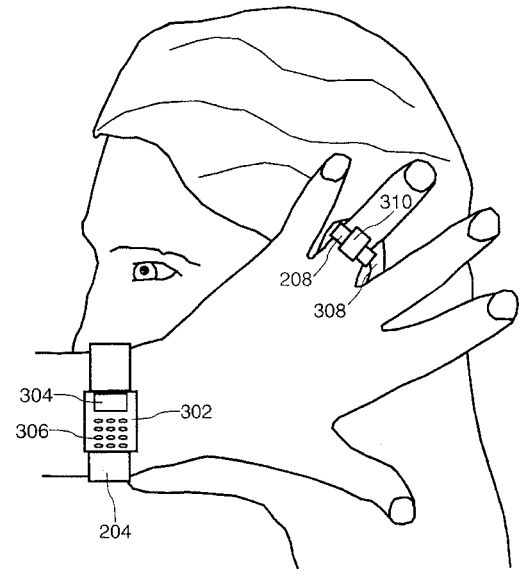

the user's skin. Philips is serious about this approach, and the patent includes published references demonstrating that it can be done.—GLA

6,839,441

43.38.Tj SOUND MIXING CONSOLE WITH MASTER CONTROL SECTION

Timothy Clay Powers and Howard Churchill Page, assignors to Showco, Incorporated
4 January 2005 (Class 381/119); filed 20 January 1998

There are many digital sound mixing consoles used in live and post-

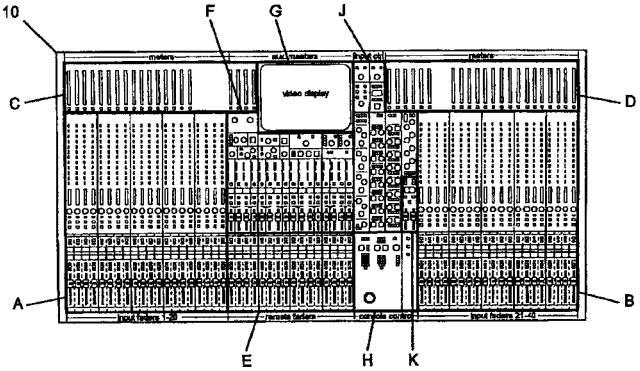

production environments. This is one of them, which now also happens to be patented, in this case, for ''live concert performances, etc.''—NAS

6,845,840

43.38.Tj SURFACE MOUNTED LOUDSPEAKER AND BRACKET FOR THE MOUNTING THEREOF

Jeffrey N. Cowan *et al.*, assignors to Boston Acoustics, Incorporated
25 January 2005 (Class 181/150); filed 9 August 2001

A means is described of attaching a loudspeaker enclosure of a certain form in many different orientations while also providing ''good aesthetics.''

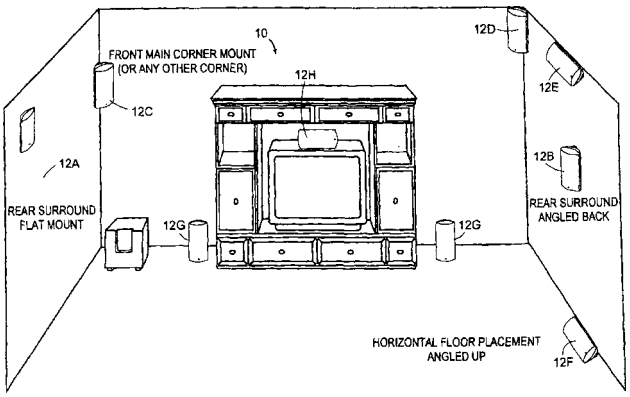

Question: how many domestic divas would concur with the adjective "good" as applied in this context?—NAS

6,847,584

43.38.Zp METHOD AND APPARATUS FOR ACOUSTIC IMAGING OF OBJECTS IN WATER

Vance A. Deason and Kenneth L. Telschow, assignors to Bechtel BWXT Idaho, LLC
25 January 2005 (Class 367/10); filed 30 June 2003

The preferred embodiment of an underwater camera **120** is described. An acoustic source **122** ensonifies target **104**. The reflected acoustic waves **126** are focused by acoustic lens **108** upon a mechanically compliant screen **12**, made of a thin polymer or plastic. A hydrostatic pressure compensating

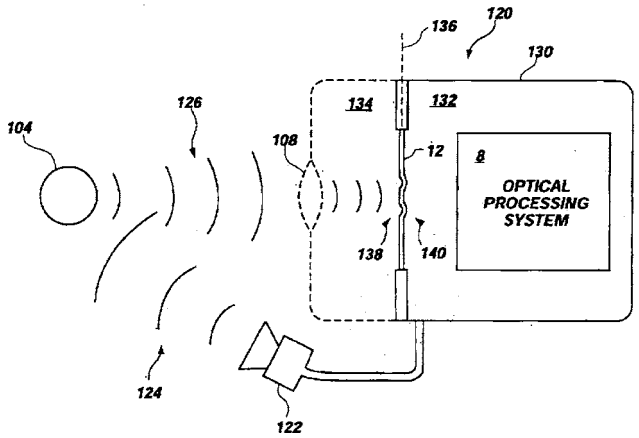

procedure must be utilized. The optical processing system **8**, described in some detail in the patent, converts the acoustically induced vibrations of the screen **12** into optical intensity images representative of the target.—WT

6,858,911

43.40.At MEMS ACTUATORS

Hirokazu Tamura *et al.*, assignors to Advanced Micriosensors; Furukawa American, Incorporated
22 February 2005 (Class 257/421); filed 4 December 2002

What could not be claimed under a title like this? The patent is actually quite specific in its scope, covering magnetically driven linear actuators for use in linearizing and otherwise altering the force-displacement curve of a cantilever beam. Despite the abundance of diagrams supplied, it is not clear what use this has, as the claims are generic and the real devices must be of millimeter dimensions, making their actuation capabilities rather limited.—JAH

6,843,044

43.40.Le DETECTION ARRANGEMENT FOR THE DETECTION OF A CROP JAM IN A HARVESTING MACHINE

Steffen Clauss, assignor to Deere & Company
18 January 2005 (Class 56/10.3); filed in Germany 6 September 2002

Crop harversting machines are expensive. Damage to them, as well as the downtime, is also expensive. This patent describes a method of determining when the torque in the driveline to the crop harvesting mechanism **20** exceeds an upper limit, which is said to be indicative of a crop jam in the harvesting mechanism. A cam controlled overload clutch **54** is inserted in

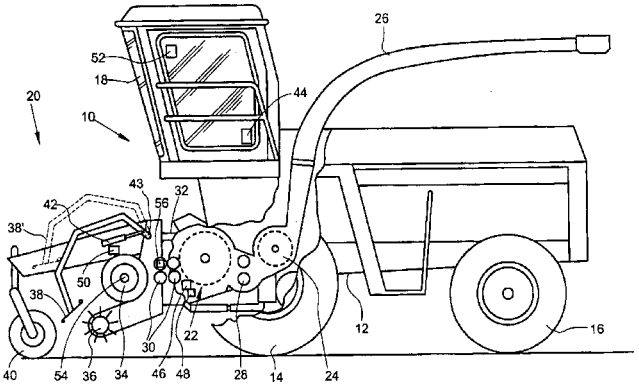

the drive line and this clutch generates a rattle when the torque limit is exceeded. This rattle is transmitted by the whole of the crop take-up arrangement **20** and the intake housing **32** to a knock sensor **48**, the signal of which is processed to determine when the driveline should be operated in a crop jam clearing manner, while also notifying the operator.—NAS

6,851,529

43.40.Tm MULTIFUNCTION VIBRATION ISOLATION STRUT

Stephen R. Jones *et al.*, assignors to Honeywell International Incorporated
8 February 2005 (Class 188/378); filed 18 April 2002

This strut is intended for applications where a rigid connection between a support and a payload is desired under normal conditions, but where a resilient connection is wanted in the event that the support vibrates violently, as, for example, due to a seismic event. In a strut according to this patent, the rod that carries the piston of a dual-chamber hydraulic system also carries a larger-diameter piston of a dual-chamber pneumatic system. The hydraulic-system chamber is rigidly connected to one end of the pneumatic chamber. Under normal conditions, flow of the fluid in the hydraulic system between its two chambers is blocked by a valve, so that the assembly is practically rigid. If severe support vibrations are detected by a sensor, the valve is opened, so that the piston can move and the pneumatic system comes into play.—EEU

6,846,385

43.40.Tm SUSPENSION ARRANGEMENT FOR A ROLL

Tord Gustavsson, assignor to Metso Paper Karlstad AB
25 January 2005 (Class 162/199); filed in Sweden 25 March 1999

Techniques for the manufacture of paper have been around for a long time. Current mass production methods for web-based products, such as paper or cardboard, typically use heavy cylinders to calender or roll the product. These rolls, **1** and **2**, can vibrate, even subtly, due to variations in

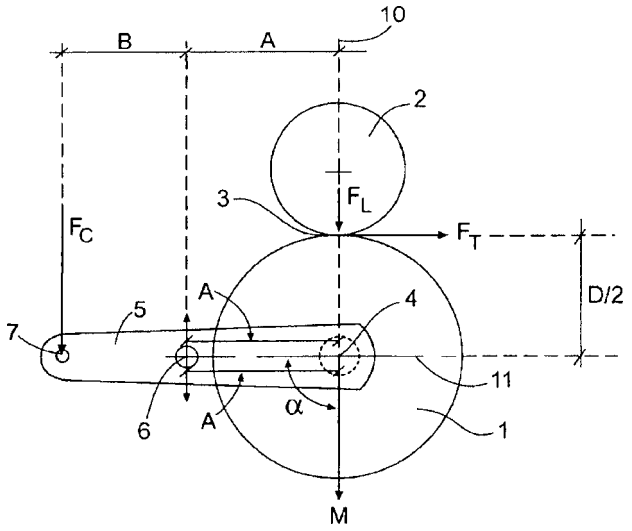

the coating of the cylinders, thickness of the product, among other things, and these vibrations can affect the quality of the finished product. Prior art uses an offset support arm, with the roll mounted between the point of application of the balancing force Fc and the pinned support of the arm. The present invention uses a pivot mounting arrangement for the roll arm **5**. The location of pivot point **6** is chosen to reduce, and even eliminate, the effect of these irregularities in the process.—NAS

6,855,039

43.40.Tm STABILIZING COLLAR FOR A CONCRETE SAW BLADE

David L. Vidmore, Anaheim, California
15 February 2005 (Class 451/342); filed 23 April 2002

In order to suppress vibrations of a rotary saw blade, the blade is clamped between two metal discs, with only the outermost portion of the blade protruding from the disks. Some of the disks' material near the axis of rotation is removed, so that these disks clamp the blade essentially only near their rims.—EEU

6,858,970

43.40.Tm MULTI-FREQUENCY PIEZOELECTRIC ENERGY HARVESTER

Matthew C. Malkin and Christopher L. Davis, assignors to The Boeing Company
22 February 2005 (Class 310/322); filed 21 October 2002

This intriguing-sounding patent discloses a piezoelectric device for harvesting vibrational energy using an array of cantilever beams. Each beam is composed of a mass on the end of a piezoelectric bimorph shaft. The design is carefully described and well thought out, but the resonant frequencies are apparently in the kHz range, making the device applicable mainly to power generation from turbines and other high-speed machinery.—JAH

6,857,231

43.40.Vn PROPELLER-CONTROLLED ACTIVE TUNED-LIQUID-COLUMN DAMPER

Yung-Hsiang Chen, Junghe, Taipei, Taiwan, Province of China
22 February 2005 (Class 52/167.2); filed 9 April 2003

The device described in this patent is intended for the suppression of low-frequency vibrations of ships, buildings, bridges, etc., due to earthquakes, wind, water waves, and the like. The device consists of a U-shaped vessel that is partially filled with a fluid, with one or more propellers installed in the horizontal section of the vessel. These propellers are driven by servomotors in response to signals generated by a controller, which receives inputs from a structural motion sensor and from fluid-surface and fluid-velocity sensors.—EEU

6,848,314

43.40.Yq DATA RECEIVING DEVICE FOR USE IN AN IMPULSE-BASED DATA TRANSMISSION SYSTEM

Ilan Goldman, Herzliya, Israel
1 February 2005 (Class 73/649); filed in Israel 10 February 2000

Although the title refers to a device only, the claims of this patent also cover "A data transmission system" and "A method for transmission of data." As a practical example, consider an electronic door lock. Instead of

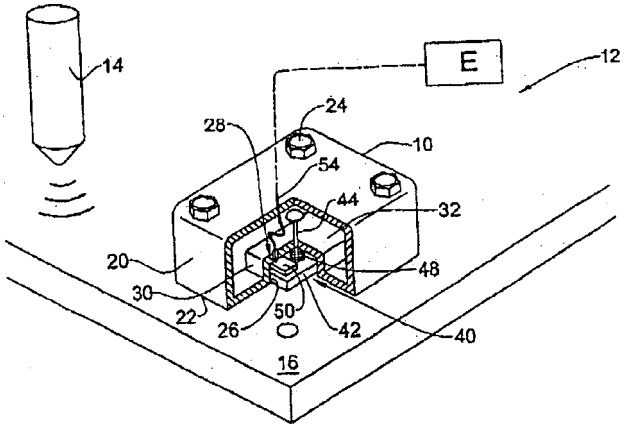

using a keypad for entry, might it not be easier to tap out a simple code on the door itself? The receiving device described and shown appears to be a generic inertia transducer, presumably optimized for this application.—GLA

6,849,053

43.40.Yq SHOCK WAVE SOURCE WITH A WAVE DAMPING COIL CARRIER

Mario Bechtold *et al.*, assignors to Siemens Aktiengesellschaft
1 February 2005 (Class 601/4); filed in Germany 10 September 2001

Electromagnetic sources of shock waves in water are used in a variety of medical applications, for example, for the disintegration of kidney stones. Such a shock wave source consists of a coil carrier, a coil, and a metallic membrane that is insulated from the coil. As waves are launched into the water when the membrane is actuated, oscillations are induced in the coil carrier, resulting in unpleasant audible noise. According to this patent, this noise is reduced by use of a coil carrier material with relatively high damping, by use of a coil carrier with an axially aligned honeycomb structure, and/or by making the coil carrier highly asymmetric.—EEU

6,855,398

43.55.Ev SOUND ABSORBING AND HEAT INSULATING MATERIAL, AND METHOD OF MANUFACTURING SAME

Fumikazu Machino *et al.*, assignors to Osaka Gas Company, Limited
15 February 2005 (Class 428/198); filed 12 February 1999

This thermal and acoustics insulation material is made using wool-like carbon fibers that are made from anisotropic pitch. The fibers have high tensile strength, durability, and compression resilience. They are light-

weight, chemically stable, incombustible, and do not generate toxic fumes. Most notably, because of the carbonizing temperature at which the carbon fibers are set, they have reduced electrical conductivity. This material is well suited for high-speed train cars and aircraft. The patent also describes the manufacturing process for the fibers.—CJR

6,792,404

43.58.Kr STI MEASURING

Kenneth Dylan Jacob, assignor to Bose Corporation
14 September 2004 (Class 704/228); filed 22 January 2001

This very brief patent devotes three full paragraphs to the ''Detailed Description'' section, describing the patented device for measuring the speech transmission index. An off-the-shelf spectrum analyzer has been adapted by adding a control chip to preprogram an analysis of the particular audio source signal used. A separate, handheld audio generator may be a CD, tape, MP3, or other suitable player.—DLR

6,850,555

43.60.Dh SIGNALLING SYSTEM

Michael John Barclay, assignor to Scientific Generics Limited
1 February 2005 (Class 375/141); filed in the United Kingdom 16 January 1997

The inventor proposes an interesting cross between spread spectrum transmission and audio. The specific application is the updating of electronic price tags in a supermarket, but the overall idea is more general.—MK

6,853,869

43.60.Dh METHOD AND APPARATUS FOR GENERATING SURROUND-SOUND DATA

Kei Nishioka, assignor to Rohm Company, Limited
8 February 2005 (Class 700/94); filed in Japan 17 November 1999

The use of ''surround sound'' in this patent is something of a misnomer, inasmuch as the patent deals primarily with a single audio channel ''looping'' circuit, in which a signal is fed back on itself multiple times. Such elements as these may be used as building blocks in larger surround-sound-synthesis programs. The basic circuit is shown in the figure. Here,

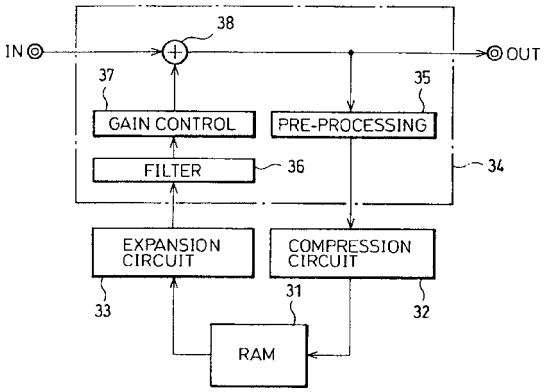

complementary compression and expansion (known as ''compansion'') are used to preserve signal-to-noise integrity when multiple passes are made through the loop. In other embodiments, digital technology is used to maintain the integrity of multiple passes through the use of noise shaping.—JME

6,857,312

43.60.Dh SYSTEMS AND METHODS FOR SENSING AN ACOUSTIC SIGNAL USING MICROELECTROMECHANICAL SYSTEMS TECHNOLOGY

Howard C. Choe and Emel S. Bulat, assignors to Textron Systems Corporation
22 February 2005 (Class 73/170.13); filed 29 October 2003

Hot-wire anemometers are arrayed in front of a miniature condenser microphone to provide wind velocity data. These data are processed to predict pressure fluctuations due to wind. It all happens on board in an ASIC that delivers a clean audio signal in real time. The devices are not integrated into a single silicon assembly, and one wonders how well the cancellation can be done in real time, considering the randomness of turbulence. A significant part of the patent is devoted to describing arrays of narrow-band microphones for use as signal classifiers, which is tangential to the former topics. There is a lot of detail on how such structures would be fabricated.—JAH

6,850,621

43.60.Lq THREE-DIMENSIONAL SOUND REPRODUCING APPARATUS AND A THREE-DIMENSIONAL SOUND REPRODUCTION METHOD

Hiromi Sotome *et al.*, assignors to Yamaha Corporation
1 February 2005 (Class 381/17); filed in Japan 21 June 1996

Here is yet another method for deriving a ''three-dimensional'' effect from a single audio channel. As seen in the figure, a stereo effect is first simulated from a single input channel, and the two outputs are further fil-

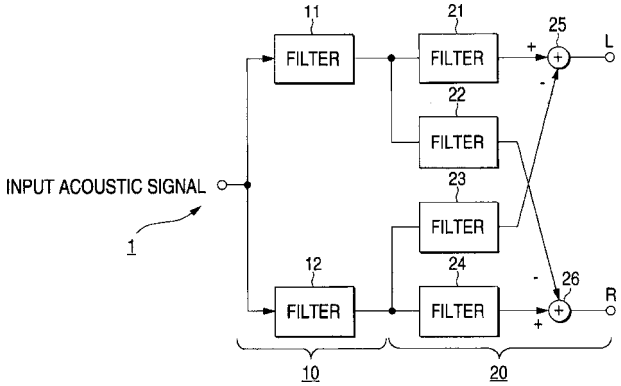

tered (delayed) and cross-fed left to right and *vice versa* to create some degree of out-of-bounds imaging. The effect is intended to enhance close-in listening to a variety of electronic musical instruments.—JME

6,850,622

43.60.Lq SOUND FIELD CORRECTION CIRCUIT

Yoshimichi Maejima, assignor to Sony Corporation
1 February 2005 (Class 381/22); filed in Japan 29 May 1997

A ''virtualizer'' circuit is used to create a family of playback cues over two loudspeakers for subsequent psychoacoustical localization at a variety of virtual positions (left, front, right, and rear) for television and video disk viewing. The primary ''steering'' tools here are sets of approximated

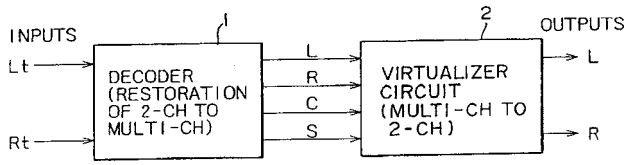

HRTFs. As can be seen in the figure, the incoming signals from the program source already consist of a set of intended directional signals, via Dolby surround matrix encoding. These are mixed back to two channels with subsequent spatial reassignment via HRTFs.—JME

6,853,732

43.60.Lq CENTER CHANNEL ENHANCEMENT OF VIRTUAL SOUND IMAGES

William Clayton Scofield, assignor to Sonics Associates, Incorporated
8 February 2005 (Class 381/27); filed 1 June 2001

According to the patent text, the reproduction of center channel (in-phase) program information over normal two-channel stereo loudspeakers may suffer from ''hole in the middle'' or ''in the head'' localization. The patent suggests the use of a center loudspeaker, fed a properly processed signal, for alleviating these ills. The patent further suggests that the use of a center loudspeaker can also alleviate similar localization problems employing headphones. The amount and variety of signal processing required to do all of this appears complex beyond all reason.—JME

6,851,048

43.66.Ts SYSTEM FOR PROGRAMMING HEARING AIDS

Scott T. Armitage, assignor to Micro Ear Technology, Incorporated
1 February 2005 (Class 713/1); filed 10 September 2002

A host computer sends and receives serial data and control signals to/from a hearing aid programming device via a PCMCIA, USB, RS-232,

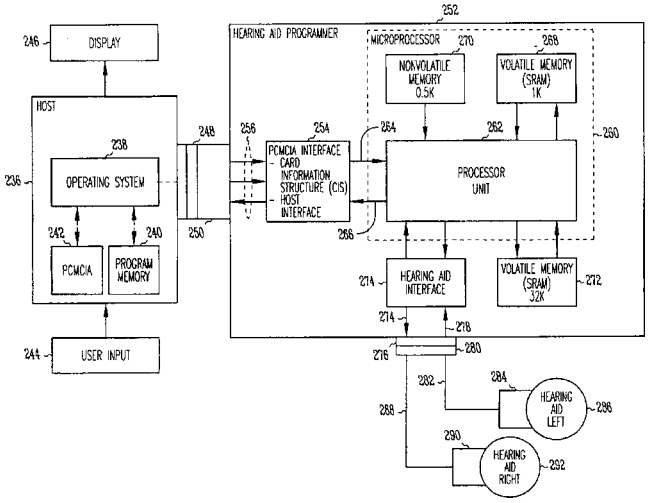

SCSI, IEEE 1394 Firewire, or wireless communication interface. The hearing aid programming interface is portable but also electrically isolates the host computer from the hearing aid.—DAP

6,850,775

43.66.Ts FITTING-ANLAGE

Christian Berg, assignor to Phonak AG
1 February 2005 (Class 455/556.1); filed 18 February 2000

Parameter settings and signal processing algorithms stored in a hearing aid are updated from a server via a cell phone or personal digital assistant (PDA). This allows the fitting to be optimized based on the individual wearer's comments and performance. The link between the cell phone or PDA and hearing aid may be wired or wireless. Either the wearer or fitting specialist may update the hearing aid.—DAP

6,855,104

43.66.Ts IMPLANTABLE TRANSDUCER FOR HEARING AIDS AND PROCESS FOR TUNING THE FREQUENCY RESPONSE OF ONE SUCH TRANSDUCER

Christoph Schmid *et al.*, assignors to Phonak AG
15 February 2005 (Class 600/25); filed in the European Patent Office 20 November 2002

A hermetically sealed electromagnetic implantable transducer may act

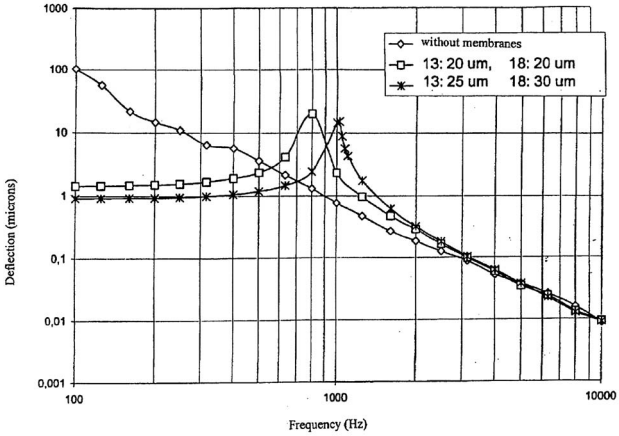

as a sensor or actuator. A flexible membrane connects the static and dynamic portions of the transducer and enables tuning the frequency response.—DAP

6,850,882

43.70.Jt SYSTEM FOR MEASURING VELAR FUNCTION DURING SPEECH

Martin Rothenberg, Dewitt, New York
1 February 2005 (Class 704/211); filed 23 October 2000

A slight updating is presented for the famous ''Rothenberg mask'' in its particular application to the measurement of the nasal/oral airflow ratio, and thereby, velar function. An optimized form of the mask apparatus is suggested, by which nasal and oral airflows are separated and measured using resistance screens (which convert the flow variations to pressure variations) and pressure transducers. This much is not new; the innovation involves the notion of then bandpass filtering the airflow transducer signal to encompass the voice fundamental frequency as closely as possible, or alternatively, a wider and higher bandwidth encompassing the first formant frequency. The idea is to filter out the subsonic airflow components, which are inordinately influenced by articulator movements and do not accurately reflect the true oral/nasal division of the actual speech airflow. It is suggested that the fundamental-frequency band best reflects the true oral/nasal airflow ratio, and various *ad hoc* methods are suggested for determining this band for the subject wearing the mask.—SAF

6,796,798

43.71.Ft DYNAMIC READING INSTRUCTION

Thomas Sanocki, assignor to University of South Florida
28 September 2004 (Class 434/156); filed 27 March 2003

The premise here is that it will be easier to learn to read if additional associations can be evoked leading to connections between articulation, sound, and meaning, especially given certain learning deficiencies. The

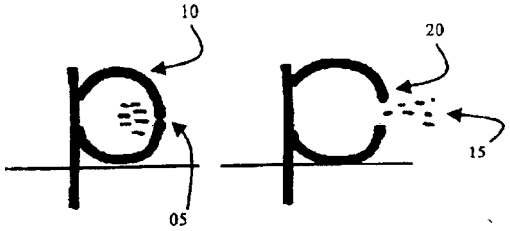

premise is almost certainly valid. The value of this particular implementation remains to be seen. The letter shown would be animated so that the puff of air is unmistakable. According to the cited references, the patent author published related materials in the early 1990s.—DLR

6,785,652

43.72.Ar METHOD AND APPARATUS FOR IMPROVED DURATION MODELING OF PHONEMES

Jerome R. Bellegarda and Kim Silverman, assignors to Apple Computer, Incorporated
31 August 2004 (Class 704/266); filed 19 December 2002

This patent is a continuation of United States Patent 6,553,344, reviewed in J. Acoust. Soc. Am. **115**, 2701 (2004). The phoneme duration model described here is essentially the same as in the earlier patent. Some of the factors considered in the weightings include preceding and following phonemes, duration to the utterance end, number of phonemes to utterance end, position of the phoneme in the word, and position of the word in the utterance, just to name a few.—DLR

6,850,884

43.72.Ar SELECTION OF CODING PARAMETERS BASED ON SPECTRAL CONTENT OF A SPEECH SIGNAL

Yang Gao and Huan Yu-Su, assignors to Mindspeed Technologies, Incorporated
1 February 2005 (Class 704/224); filed 14 February 2001

A general method is outlined for modifying a digital encoding of speech in accordance with detected variations in the spectrum of the input speech signal. Various specific embodiments are run through to exemplify the process, including the adaptive selection of different LPC parameters for encoding (by means of different bandwidth expansion constants) in response to particular spectral slopes of the input speech, or the adaptive selection of weight constants for perceptual weighting filters applied to the encoding, again in response to particular spectral slopes of the input speech. The patent seems sufficiently detailed to inform the experienced reader.—SAF

6,845,379

43.72.Gy SOUND DATA PROCESSING SYSTEM AND PROCESSING METHOD

Fumiaki Ito *et al.*, assignors to Canon Kabushiki Kaisha
18 January 2005 (Class 707/102); filed in Japan 30 March 2000

In order to simultaneously process audio outputs and sounds presented from a wide variety of unexpected sources across networks, a methodology

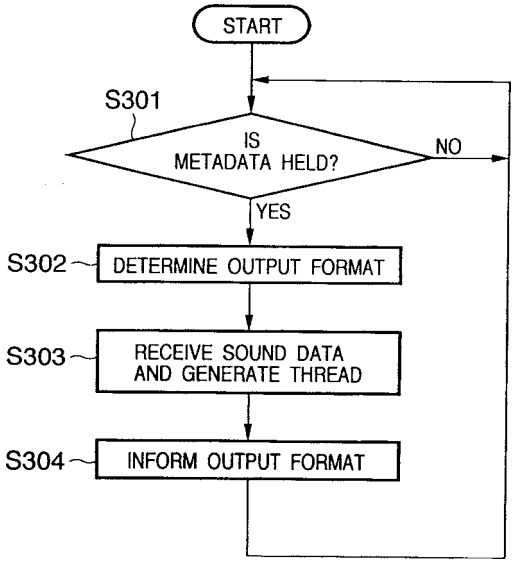

using metadata is proposed that would set the output format corresponding to the contents of a sound, regardless of the source of that sound.—DAP

6,792,407

43.72.Ja TEXT SELECTION AND RECORDING BY FEEDBACK AND ADAPTATION FOR DEVELOPMENT OF PERSONALIZED TEXT-TO-SPEECH SYSTEMS

Nicholas Kibre *et al.*, assignors to Matsushita Electric Industrial Company, Limited
14 September 2004 (Class 704/260); filed 30 March 2001

This is a system for collecting speech recordings for the purpose of training a speech synthesizer. The concatenative synthesis uses a large database of speech fragments to construct the synthesized speech output. In order to minimize the time required for making the training recordings, a selection algorithm finds the shortest subset of the provided texts that will cover the phonetic inventory required by the training procedure. This ''greedy'' snippet selection algorithm is described in some detail.—DLR

6,801,894

43.72.Ja SPEECH SYNTHESIZER THAT INTERRUPTS AUDIO OUTPUT TO PROVIDE PAUSE/SILENCE BETWEEN WORDS

Yoshihisa Nakamura and Hiroaki Matsubara, assignors to Oki Electric Industry Company, Limited
5 October 2004 (Class 704/258); filed in Japan 23 March 2000

This patent pertains to the playback of recorded speech phrases that have been stored in a ROM memory device. The speech is stored using a standard ADPCM coding and all playback systems are well-known prior art. The sole issue here is that unless the stored phrases are extremely well matched, the playback would be enhanced by including a certain length of pause between items. However, it is expensive to store silences, even in ADPCM coding. So extra hardware is added to silence the output for specified periods. In other words, there is nothing new here.—DLR

6,785,650

43.72.Ne HIERARCHICAL TRANSCRIPTION AND DISPLAY OF INPUT SPEECH

Sara H. Basson *et al.*, assignors to International Business Machines Corporation
31 August 2004 (Class 704/235); filed 16 March 2001

This automatic transcription system is based on a speech recognizer with a typical phonetic analysis, but that uses a detailed linguistic model to produce output in the form of phonemes, syllables, and parsed word structures, rather than the typical text strings. Intended as a tutor for reading skills and to teach lip reading, the system includes several levels of well-known statistical analyses, optionally producing *n*-best lists of possible recognition results. The results are presented in a multilevel scheme in which words are displayed if the confidence is high, syllables if the words do not meet the criteria, and phonetic elements if the syllables do not make it.—DLR

6,789,065

43.72.Ne SYSTEM, METHOD AND COMPUTER PROGRAM PRODUCT FOR POINT-TO-POINT VOICE-ENABLED DRIVING DIRECTIONS

Mikael Berner *et al.*, assignors to BeVocal, Incorporated
7 September 2004 (Class 704/275); filed 24 January 2001

This system uses a speech recognition component as part of an automobile navigation assistant. Recognition is used to enter the destination address into the system. The starting point may be determined by further recognition or by another means, such as a GPS device. A surprising portion of the short patent text is given to touting the merits of various computer languages used in constructing a travel route from point A to point B, a topic not mentioned in the single, short claim.—DLR

6,792,096

43.72.Ne DIRECTORY ASSISTANCE DIALOG WITH CONFIGURATION SWITCHES TO SWITCH FROM AUTOMATED SPEECH RECOGNITION TO OPERATOR-ASSISTED DIALOG

John M. Martin *et al.*, assignors to SBC Technology Resources, Incorporated
14 September 2004 (Class 379/218.01); filed 11 April 2002

A system is described in which a speech recognizer is used to assist a human operator in providing a telephone directory assistance function. The recognition architecture is arranged so the human operator can easily take over the dialog at any of several points of the transaction. Part of the motivation for providing the close human/machine interaction seems to be intended as an aspect of training the speech recognizer. So the human operator is acting as a tutor for the machine operator.—DLR

6,792,409

43.72.Ne SYNCHRONOUS REPRODUCTION IN A SPEECH RECOGNITION SYSTEM

Heribert Wutte, assignor to Koninklijke Philips Electronics N.V.
14 September 2004 (Class 704/276); filed in the European Patent Office 20 December 1999

This automated dictation system operates in two phases. In the initial step, word recognition is performed, while the user's speech input is also being recorded and tagged to the recognized word sequence. In the second phase, the recorded speech is played back while each recognized word is highlighted on a display. That much is prior art. This system offers a smoother control structure, allowing the user to easily stop the playback and correct a word, reenter specific words or phrases, or specify repeats, and then continue in either mode. The patent text includes a very brief description of the recognition technology.—DLR

6,795,806

43.72.Ne METHOD FOR ENHANCING DICTATION AND COMMAND DISCRIMINATION

James R. Lewis and Kerry A. Ortega, assignors to International Business Machines Corporation
21 September 2004 (Class 704/260); filed 20 September 2000

This patent describes a control system for an automated dictation recognizer. The emphasis here is on a novel system in which an eye tracker helps to identify the operator's intent; whether a speech utterance is intented

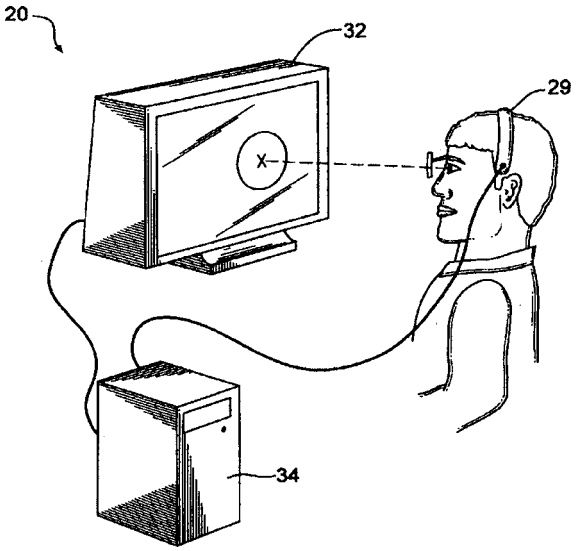

as a control phrase or as further dictation content. Curiously, the patent says little about specific screen layouts to be used with the eye tracker.—DLR

6,850,602

43.72.Ne METHOD AND APPARATUS FOR ANSWERING MACHINE DETECTION IN AUTOMATIC DIALING

Wu Chou, assignor to Avaya Technology Corporation
1 February 2005 (Class 379/80); filed 27 March 2002

To facilitate telemarketing, a methodology is described to identify whether a response to automatic dialing is a machine or not. The system

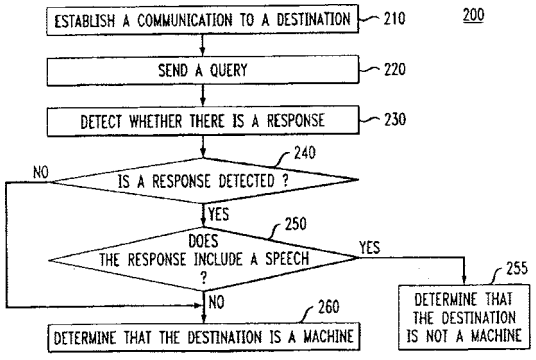

determines within a predetermined time interval whether a tone or speech is present in the response and, if speech, whether a dialog can occur.—DAP

6,801,891

43.72.Ne SPEECH PROCESSING SYSTEM

Philip Neil Garner and Jason Peter Andrew Charlesworth, assignors to Canon Kabushiki Kaisha
5 October 2004 (Class 704/254); filed in the United Kingdom 20 November 2000

This patent describes a step in a speech recognition process in which sequences of subword units are optimally combined so as to form the words being recognized. Various subword units are considered, including phonemes, syllables, or Japanese katakana. The patent includes an extensive and well-written discussion of the matching process, based on the probabilities of insertions and deletions, much of which is repeated in the 70 detailed claims. A standard dynamic programming approach is used to walk through the matrix of possibilities.—DLR

6,801,893

43.72.Ne METHOD AND APPARATUS FOR EXPANDING THE VOCABULARY OF A SPEECH SYSTEM

Gerhard Backfried and Hubert Crépy, assignors to International Business Machines Corporation
5 October 2004 (Class 704/257); filed in the European Patent Office 30 June 1999

This patent addresses the issue of adding new vocabulary to a large-vocabulary speech recognition system. Specifically, it includes steps intended to deal with ''special'' words that do not fit a typical language model, such as acronyms, names, and expressions. When the system first ''hears'' a new word, it first asks the user to type in that word. A letter-to-sound system then attempts to reconstruct the pronunciation of the word as it was spoken by the user. If the match is close enough, the new word is simply added to the vocabulary. If not, a variety of strategies is described by which the system attempts to model the word as spoken and as spelled.—DLR

6,845,251

43.72.Ne ADVANCED VOICE RECOGNITION PHONE INTERFACE FOR IN-VEHICLE SPEECH RECOGNITION APPLICATIONS

Charles A. Everhart *et al.*, assignors to Visteon Global Technologies, Incorporated
18 January 2005 (Class 455/563); filed 29 November 2000

A phone number is entered into an automobile speech recognition system using a voice command, dialed with a second voice command, and

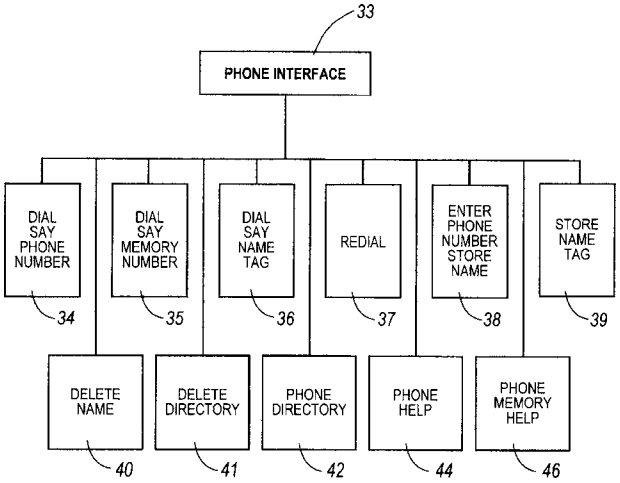

associated with a tag using a third voice command. The tag is then stored into a phone directory with a fourth voice command.—DAP

6,801,890

43.72.Ne METHOD FOR ENHANCING RECOGNITION PROBABILITY IN VOICE RECOGNITION SYSTEMS

Ulrich Kauschke *et al.*, assignors to DeTeMobil, Deutsche Telekom MobilNet GmbH; Deutsche Telekom AG
5 October 2004 (Class 704/243); filed in Germany 3 February 1998

A prior patent cited here is said to describe a method of speech recognition in which, after the successful recognition of a word, the stored analysis results for previous utterances of the same word are updated. This updating is referred to as post-training. Exactly how it was to be done in the earlier patent is not described here, but is criticized as being ineffective. In fact, what is described here is not the post-training process, *per se*, but rather the decision process by which a recognition is deemed to have been successful. This reviewer finds that to be curious, in that the claims seem to hang on the ''characterization'' of the post-training, while saying only that it would be ''based on a comparison through correlation,'' without further discussion.—DLR

6,856,956

43.72.Ne METHOD AND APPARATUS FOR GENERATING AND DISPLAYING N-BEST ALTERNATIVES IN A SPEECH RECOGNITION SYSTEM

Chris Thrasher and Fileno A. Alleva, assignors to Microsoft Corporation
15 February 2005 (Class 704/251); filed 12 March 2001

A number of recent patents from competing corporations all present variations on this same theme, so this one will be reviewed as representative. The idea, which involves a statistical computation and not an acoustic innovation, is to improve the response of a standard speech recognition system when there is high uncertainty about the recognized string or word by computing an *N*-best list of alternative words at each point in the string from a recognizer confidence score. When a string of words is to be considered, a set of hypothesis paths through the various alternatives can be provided in the form of a ''hypothesis lattice.'' The hypothesis alternative paths can then be confidence scored and ranked for a presentation to the user as alternatives that they might have said. It is further suggested that the *N*-best alternatives need not be computed until the user highlights incorrectly recognized text. It seems to this reviewer that all of the recent patents (three this month and one last month) involving this idea overlap to a very high degree, making it difficult to determine who in fact holds the patent on the idea.—SAF

6,850,885

43.72.Ne METHOD FOR RECOGNIZING SPEECH

Daniela Raddino *et al.*, assignors to Sony International (Europe) GmbH
1 February 2005 (Class 704/236); filed in the European Patent Office 13 December 2000

This patent confronts a common problem in ''word-spotting'' speech recognition systems, in which the likelihood provided by the ''garbage model'' for out-of-vocabulary items exceeds that provided by a keyword model, when a known keyword was actually uttered. The simple solution here is to associate a variable penalty, depending upon the specifics of the application, with a selection of the garbage model, thereby encouraging the selection of the best keyword model.—SAF

6,853,971

43.72.Ne TWO-WAY SPEECH RECOGNITION AND DIALECT SYSTEM

George W. Taylor, assignor to Micron Technology, Incorporated
8 February 2005 (Class 704/10); filed 21 June 2002

To reduce time for reliably transcribing speech from multiple users into text, user queries are paired with a dialectal database to help determine

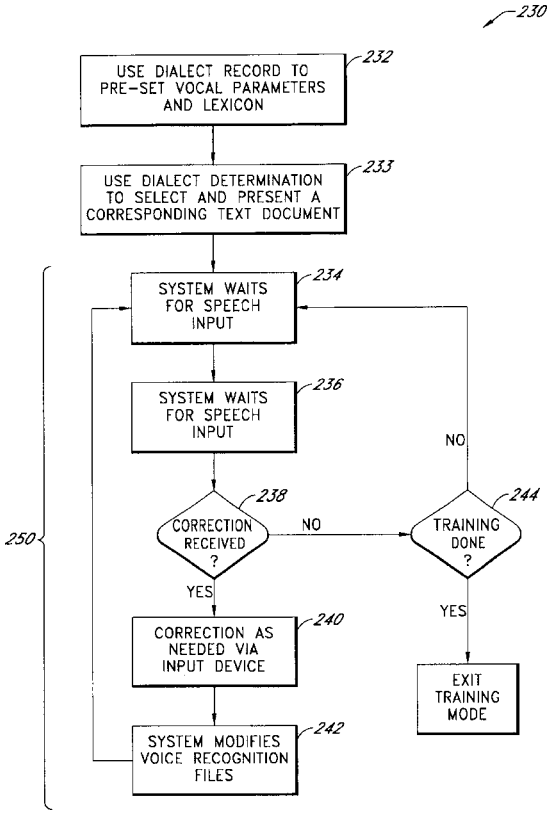

the likely dialect of a user prior to training the speech recognition system. —DAP

6,838,607

43.75.Hi MOTORIZED PERCUSSION DEVICES

Daniel J. Elliot and George T. Foster, assignors to Elliot Rudell
4 January 2005 (Class 84/422.4); filed 28 February 2001

One of the very first tasks for a beginning percussion student is to develop a fine drum roll. Well, why not just use a battery powered drumstick vibrator? Surely all jazz drummers would shake their heads in amazement.—MK

6,838,604

43.75.Kk WOODEN BARS ARRANGED FOR PERCUSSION INSTRUMENTS

Hiroyasu Abe *et al.*, assignors to Yamaha Corporation
4 January 2005 (Class 84/402); filed in Japan 7 September 2001

Pitched percussion instruments, such as the marimba, used to depend on the availability of rare and unusual woods. These woods are now impossible to find or extremely expensive. The solution presented here is the lamination of a base wood, a plastic layer, and a top hardwood. The patent includes various details about grain variation and is all in all very readable.—MK

6,835,886

43.75.Wx TONE SYNTHESIS APPARATUS AND METHOD FOR SYNTHESIZING AN ENVELOPE ON THE BASIS OF A SEGMENT TEMPLATE

Motoichi Tamura and Yasuyuki Umeyama, assignors to Yamaha Corporation
28 December 2004 (Class 84/627); filed in Japan 19 November 2001

The envelope shape is of critical importance in computer synthesis of musical instruments. This particular patent presents an arbitrary selection of envelopes for use in a synthesis setting. The patent describes how these envelope segments can be used to create larger gestures.—MK

6,835,887

43.75.Wx METHODS AND APPARATUS FOR PROVIDING AN INTERACTIVE MUSICAL GAME

John R. Devecka, Clifton, New Jersey
28 December 2004 (Class 84/743); filed 4 March 2002

Once again, it is man versus machine—this time it is a percussion drum set in an arcade setting. Other patents have examined similar situations, e.g., United States Patent 6,342,665 [reviewed in J. Acoust. Soc. Am. **112**, 803 (2002)].—MK

6,848,537

43.80.Qf STETHOSCOPE

Richard J. Deslauriers, Robert T. Potash, and S. Windsor, both of Woodbury, Connecticut
1 February 2005 (Class 181/131); filed 20 July 2001

The apparent difference of this stethoscope from prior models is that it features a second layer of insulation over an inner layer of insulation in the tube running from the head assembly to the earpiece assembly in an effort to better isolate the heart signals from outside noise.—DRR

6,855,116

43.80.Qf ESOPHAGEAL STETHOSCOPE WITH CARRIER MEMBERS FOR CARDIAC PACING AND OXIMETRY

John L. Atlee III, Hartland, Wisconsin
15 February 2005 (Class 600/528); filed 6 February 2003

This device is an esophageal probe for performing recording, monitoring, or stimulation functions from or within the esophagus, such as transesophageal monitoring of cardiac activity, transesophageal cardiac stimulation, such as cardiac pacing, or esophageal oximetry. It includes a tubular

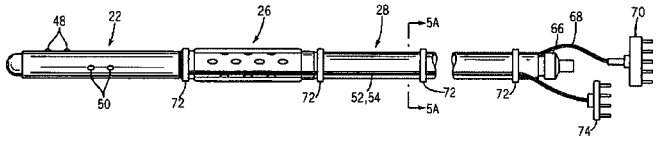

flexible body having an acoustic input region. The carrier member carries one or more devices for providing esophageal recording, monitoring, or stimulation functions. For transesophageal cardiac pacing, electrodes are attached to the carrier member, which enables the device to function as a pacer.—DRR

6,849,047

43.80.Sh INTRAOSTEAL ULTRASOUND DURING SURGICAL IMPLANTATION

Mark R. Goodwin, assignor to Cutting Edge Surgical, Incorporated
1 February 2005 (Class 600/437); filed 28 March 2003

Intraosteal ultrasound is the application of acoustical energy to facilitate "real time" manipulation and navigation of a device for intraosseous placement of synthetic or biological implants and to diagnose the condition into which the implant is being emplaced. Examples of such applications include the placement of bone screws or other implants through vertebral pedicles during spinal fusion surgery. Devices performing such procedures can create a lumen or channel into the bone at the desired site, and may include a probe for providing realtime feedback of differences in the density of the tissue, typically differences in acoustical impedance between cancellous and cortical bone. These devices may also include a means for monitoring the feedback such as an imaging screen that can be used by the surgeon as he/she creates the channel, and/or an audible signal that indicates the presence of different tissues. The system can also be used for diagnostic purposes.—DRR

6,855,123

43.80.Sh THERAPEUTIC ULTRASOUND SYSTEM

Henry Nita, assignor to Flow Cardia, Incorporated
15 February 2005 (Class 604/22); filed 2 August 2002

This is a device for ablating obstructions from tubular anatomical structures, such as blood vessels. It is an ultrasound system that incorporates a catheter consisting of a flexible catheter body containing at least one lumen extending longitudinally inside that body. The catheter also includes an ultrasound transmission member extending longitudinally through the lumen of the catheter body. The ultrasound transmission member's proximal

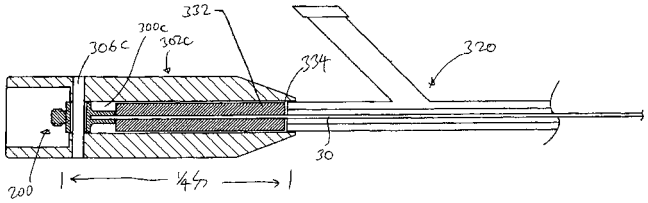

end is connected to a separate ultrasound generator and its distal end is coupled to the distal end of the catheter body, which is flexible. The transmission member is connected through a sonic connector to an ultrasound transducer. This system also provides a method for reverse irrigation and removal of particles.—DRR

6,852,081

43.80.Vj VOLUME RENDERING IN THE ACOUSTIC GRID METHODS AND SYSTEMS FOR ULTRASOUND DIAGNOSTIC IMAGING

Thilaka Sumanaweera *et al.*, assignors to Siemens Medical Solutions USA, Incorporated
8 February 2005 (Class 600/443); filed 13 March 2003

Volume rendering is accomplished using a graphic accelerator card and acoustic data in a grid to reduce or eliminate scan conversion prior to rendering.—RCW

6,853,856

43.80.Vj DIAGNOSTIC IMAGING INTERVENTIONAL APPARATUS

Jeffrey H. Yanof *et al.*, assignors to Koninklijke Philips Electronics N.V.
8 February 2005 (Class 600/417); filed 21 November 2001

A mechanical arm is used along with an imaging apparatus to accomplish an interventional procedure. The arm includes a number of jointed segments and a means to grip and release a surgical instrument during the procedure. The imaging system can be an x-ray CT scanner, a magnetic resonance imaging system, or an ultrasonic imaging system.—RCW

6,858,009

43.80.Vj ULTRASONIC ANGIOSCOPE SYSTEM

Satoshi Kawata *et al.*, assignors to Japan Science and Technology Corporation
22 February 2005 (Class 600/439); filed in Japan 18 July 2000

This system consists of a laser **11** that is outside the body, a probe **20** that delivers the laser beam into blood vessel **1**, a lens **14** that focuses the beam, a water chamber **15** in which the focused beam produces ultrasonic

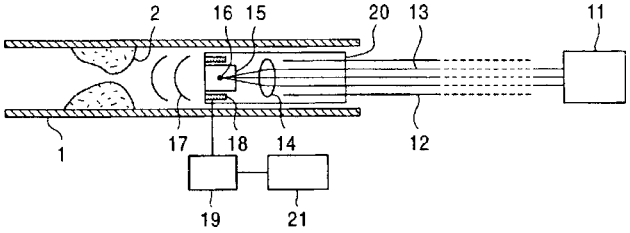

waves **17**, hydrophones **18** that receive reflections of the emitted ultrasonic waves, and a means **21** to form a three-dimensional image by using a synthetic aperture method.—RCW

6,858,010

43.80.Vj IDENTIFYING CLINICAL MARKERS IN SPATIAL COMPOUNDING ULTRASOUND IMAGING

Ismayil M. Guracar and Wayne J. Gueck, assignors to Siemens Medical Solutions USA, Incorporated
22 February 2005 (Class 600/443); filed 6 May 2003

Clinical markers such as bright areas or shadowed regions that are often visible in single images but made less visible by compounding are preserved by displaying both a single image and a compound image or by adding the clinical marker information back into a compound image.—RCW

LETTERS TO THE EDITOR

This Letters section is for publishing (a) brief acoustical research or applied acoustical reports, (b) comments on articles or letters previously published in this Journal, and (c) reply by the article author to criticism by the Letter author in (b). Extensive reports should be submitted as articles, not in a letter series. Letters are peer-reviewed on the same basis as articles, but usually require less review time before acceptance. Letters cannot exceed four printed pages (approximately 3000–4000 words) including figures, tables, references, and a required abstract of about 100 words.

On the performance of automated porpoise-click-detectors in experiments with captive harbor porpoises (*Phocoena phocoena*) (L)

Frank Thomsen[a)]
Biologisch-landschaftsökologische-Arbeitsgemeinschaft (biola), Gotenstrasse 4, D-20097 Hamburg, Germany and Biozentrum Grindel, Universität Hamburg, Martin-Luther-King-Platz 3, D-20146 Hamburg, Germany

Niels van Elk
Research and Rehabilitation Centre, Dolfinarium Harderwijk, Strandboulevard Oost 1, NL-3840 GC Harderwijk, Netherlands

Vilmut Brock and Werner Piper
Biologisch-landschaftsökologische-Arbeitsgemeinschaft (biola), Gotenstrasse 4, D-20097 Hamburg, Germany

(Received 13 December 2004; revised 25 April 2005; accepted 27 April 2005)

Recently, automated porpoise-click-detectors (T-PODs, Chelonia-Marine-Research) have been used intensively in monitoring harbor porpoises (*Phocoena phocoena*) in the wild. However, the automated click-detection-mechanism of the T-POD leads to questions on the characteristics of the detection process. We undertook experiments with six captive harbor porpoises (four subadult males in one pool, two adult males in another) at the Dolfinarium Harderwijk (Netherlands). One T-POD was placed for over a week in each pool, while the behavior of the porpoises was logged by visual observation. Data were analyzed using the T-POD software. A total of 725 431 clicks in 30 090 trains were recorded with 32% of the trains classified as CET HI, 27% as CET LO, and 41% as DOUBTFUL. All three train classes differed significantly in all parameters, except for click duration. We conclude that T-PODs perform generally well in detecting click trains of harbor porpoises but that in any future study trains classified as being of lower probability should be investigated very carefully to avoid the risk of losing valuable information. © *2005 Acoustical Society of America.* [DOI: 10.1121/1.1937347]

PACS number(s): 43.80.−n, 43.80.Ev, 43.80.Ka [WA] Pages: 37–40

I. INTRODUCTION

Underwater acoustic has become an important tool for long-term monitoring of cetaceans in the wild. Fixed hydrophone installations at strategic sites can provide a means of remotely monitoring the presence of a particular species throughout the year, day and night and in all weather conditions. Recently, a variety of automated click detectors have been developed that hold great potential for acoustically monitoring the distribution and movements of harbor porpoises (*Phocoena phocoena*; reviews in Evans and Hammond, 2004; Gordon and Tyack, 2002). One such device is the T-POD (porpoise-detector; Chelonia Marine Research), which has been used in several field studies (e.g., Teilmann *et al.*, 2002a; Koschinski *et al.*, 2003; Verfuss *et al.*, 2004; Carlström, 2005). The crucial part of the T-POD system is an algorithm which identifies click trains using an estimate of their probability of arising by chance if the prevailing rate of arrival of clicks was from random or non train producing sources such as rain or propeller cavitations. Based on this principle the software classifies all trains in different classes according to their probability of coming from porpoises. This fully automated mechanism leads to questions on the characteristics of the classification process. For example, it is uncertain how to deal with the "less-probable" train categories. Should they be included in quantitative analysis or better left out? In the present study we tested the performance of T-PODs in experiments with six harbor porpoises in captivity. Results of click-train-classification and temporal parameters of trains will be presented. Based

[a)]Electronic mail: drthomsen@web.de

TABLE I. T-POD-settings used in the experiments (scan limit: first number=settings for T-POD 199, second number=settings for T-POD 247).

Scan	1	2	3	4	5	6
A-filter frequency (kHz)	130	130	130	130	130	130
B-filter frequency (kHz)	90	90	90	90	90	90
Selectivity (ratio A/B)	4	4	4	4	4	4
A-integration period	Short	Short	Short	Short	Short	Short
B-integration period	Long	Long	Long	Long	Long	Long
Sensitivity	4	4	4	4	4	4
Scan limit	160/240	160/240	160/240	160/240	160/240	160/240

on our results, the feasibility of T-PODs will be discussed.

II. METHODS

A. General description of T-PODs

A detailed description of the T-PODs and the T-POD software, including a manual for data acquisition and analysis, can be found at http://www.chelonia.demon.co.uk/PODhome.html (for a German introduction on the method see Thomsen and Piper, 2004). The T-POD consists of a transducer, an analogue click detector, a digital timer, and a duration logger. The data are transferred via parallel port to the PC for train detection. Sonar clicks of porpoises are detected by the comparison of the outputs of two bandpass filters. The T-POD hardware settings can be reconfigured six times each minute. In each of these "scans" the T-POD logs for 9.3 s using selected values for different parameters. *(a) The target (A) and the reference (B) filter frequency*. Filter A is set to the peak spectral frequency of clicks of the target species, in harbor porpoises 130 kHz (Verboom and Kastelein, 1995; Au *et al.*, 1999; Teilmann *et al.*, 2002b). Filter B is set away from the center-frequency. *(b) The ratio of energy from A filter compared with the B filter*. The ratio can be altered in steps of arbitrary value from 1 to 16. Setting the minimum ratio between A and B low increases sensitivity while setting it high makes the system select more narrowband clicks. *(c)* Successive versions of the T-POD have allowed variation of *the sharpness (Q factor)* of each filter, or the *integration period* used in the comparison and the most efficient settings have subsequently been embodied in the hardware. *(d) The minimum intensity threshold of filter A*. This value can be set from 0 to 15. *(e) Maximum number of clicks to log in each scan*. This value can be set in steps of 20 from 0 (no limit) to 240 to conserve memory space when this might to be appropriate (e.g., in areas with a high density of porpoises).

B. Facility and subjects

The study was carried out from July 4 to 10 2003 at the Research and Rehabilitation Centre of the Dolfinarium Harderwijk, Netherlands. Six male harbor porpoises (age 1–6) were used in the experiments. Four subadult males were housed in one pool (A), two adult males in another (B). The pools in the facility are indoor, concrete, and oval shaped (8.6 m $\times$ 6.3 m; water depth: 1.2–1.6 m). The water level is held constant with an average temperature of 19.5 °C and an average salinity of 2.2% NaCl.

C. Data collection

We used two T-PODs (identification Nos.: 199 and 247) for the experiments. Prior to the installation, the porpoises from pool A were removed for medical examination, which provided an opportunity to test if there was any ambient noise which the POD 247 would detect. First, the T-POD was set and deployed with the pump shut off for 15 min. The pump then was turned on. After another 15 min the porpoises were reintroduced into the pool one by one. Each T-POD was tied to a weight and placed in the center of pool A (POD 247) and pool B (POD 199), respectively. Both T-PODs floated in upright position approximately 50 cm below the surface. The T-POD 247 collected data from 4 July (12:10) to 10 July (13:00), the T-POD 199 from 4 July (11:30) to 10 July (13:00). During cleaning of the pool A T-POD 247 was removed for a short period (09.07.03 11:00–13:00). Table I gives an overview over the settings used. Since we anticipated more signals from pool A (four animals) than from pool B (two), we set the corresponding limits of clicks per scan to 240 and 160, respectively. All other settings were identical (Table I).

D. Data analysis

The analysis of the data was done with the T-POD software (version 7.41). The software first creates "pdc" files which contain all clicks recorded. Then a "pdt" file is created by processing a pdc file to detect trains. For a direct comparison of the data of both T-PODs, the pdt file of T-POD 247 was reprocessed using the same limit of clicks per scan as the T-POD 199 (160). The train-detection-algorithm classifies trains in various categories: (1) CET HI: trains with a high probability of coming from porpoises. They should be reliable as porpoise trains, (2) CET LO: less distinctive trains that may be unreliable in noisy places, (3) DOUBTFUL: these are often porpoise trains but are unreliable in noisy environments, (4) VERY DOUBTFUL: these include trains resembling chance sequences arising from random sources or regular sequences from boat sonar, (5) FIXED RATE/BOAT SONAR: these are trains showing very little drift in click rate, often containing long clicks and having a strong resemblance to a boat sonar. For our analysis, we concentrated on

TABLE II. Statistics of trains and clicks for pools A and B combined (CET HI=high probability being from porpoises, $n=9914$; CET LO=less distinctive, $n=8256$; DOUBTFUL=doubtful, $n=12\,739$; ICI=interclick interval; shown are mean±SD; three asterisks=significant differences among all train classes; two asterisks =significant differences only between CET HI and the other two classes, no difference between CET LO and DOUBTFUL).

	Train duration (ms)	Clicks per train	Min ICI (ms)	Max ICI (ms)	Click duration (μs)
CET HI	421.5 (360.5)	43.4 (27.2)	10.0 (8.8)	19.5 (18.1)	88.3 (26.7)
CET LO	231.6 (166.0)	12.9 (6.0)	19.8 (18.3)	29.2 (26.5)	71.2 (32.9)
DOUBTFUL	251.6 (212.7)	14.7 (16.4)	23.0 (24.3)	33.7 (35.9)	71.2 (33.4)
H-test	$H=1658$ $P<0.001$	$H=15\,600$ $P<0.001$	$H=4622$ $P<0.001$	$H=1916$ $P<0.001$	$H=2778$ $P<0.001$
Dunn's method ($P<0.05$)	***	***	***	***	**

the first three classes of trains. Groups of clicks closely spaced in time are reduced by the software to a single click marking the cluster. If echoes of clicks from either the pool sides or the surface, or from refraction produce large clusters, they will be automatically rejected by the train-detection algorithm. The T-POD software offers three display options: duration of clicks and trains, interclick intervals (ICI) and pulse-repetition-frequencies between clicks of a train. It can be set to "high resolution" from 20 μs to 100 ms per pixel along the x axis. The "low resolution" mode shows click counts over periods from 1 min to 12 h. Clicks of different categories are counted by the software over the entire logging period. In a first step, data from both T-PODs were visually inspected using these different display options. For the quantitative analysis, characteristics from all trains of the CET HI, CET LO, and DOUBTFUL classes were exported as "txt" files via the T-POD software. The data included the following parameters for each train: *train duration (ms), total number of clicks, minimum interclick interval (ms), maximum interclick interval (ms), mean duration of clicks* (μs). We exported all trains of each class from each recording. Data from the two pools were first analyzed independently and later pooled since the results in both pools were similar. We compared the parameters across the three train classes using a one-way ANOVA (H-test, Kruskal Wallis). If means differed we performed a multiple comparison after Dunn's method (Zar, 1996).

III. RESULTS

In the absence of porpoises, T-POD 247 (pool A) did not detect any signals with the pump shut down (0–15 min) or the pump working (15–30 min). As soon as the first porpoise was introduced in the pool, clicks were detected. Both T-PODs logged continuously during the deployment period with battery power well above threshold throughout the data acquisition period (247: 8.99 V–8.45 V; 199: 9.32 V –8.07 V). T-POD 199 recorded 52 399 scans with 47% "full." T-POD 247 recorded 51 550 scans with only 34% "full." A total of 725 431 clicks in 30 090 trains were recorded with 32% trains classified as CET HI, 27% as CET LO, and 41% as DOUBTFUL. T-POD 247 classified a much higher proportion of trains as CET HI than T-POD 199 (37% vs 24%). Table II gives an overview over the statistics for each train class in both pools combined. It can be seen all three train classes differed significantly in all parameters, except for click duration. CET HI clicks were significantly longer than both CET LO and DOUBTFUL ones, whereas the duration of CET LO and DOUBTFUL trains was almost identical. CET HI trains ranged from 18.8 to 2800 ms in duration, contained between 13 and 159 single clicks, ranged in interclick interval from 0.63 to 145 ms (maximum pulse-repetition-frequency=1587/s) and single clicks had duration between 12 and 254 μs.

IV. DISCUSSION AND CONCLUSIONS

Our study shows that T-PODs perform generally well in detecting click trains in the presence of harbor porpoises. However, a relatively high proportion of trains were classified as CET LO and DOUBTFUL. This is puzzling, if we consider that the parameters of all train classes matched those reported for harbor porpoises (Verboom and Kastelein, 1995; Au *et al.*, 1999; Teilmann *et al.*, 2002b). The relatively short interclick intervals found in this study, especially in the CET HI train class, have also been described elsewhere (Verfuss *et al.*, 1999) and most likely represent near-target echolocation, in our case close investigation of the T-POD in the pool. One possible reason for the high amount of CET LO and DOUBTFUL trains might be the algorithm at work: we found significant differences in the temporal parameters between the train classes, most prominently between CET HI and the two other ones. CET HI classified trains are longer in general because of the probability model used: a long train has a lower probability of having arisen by chance than a short one. In this study, both CET LO and DOUBTFUL trains were almost always closely associated with CET HI ones, indicating that they were part of the same "acoustic bout." Therefore, in any study using T-PODs, these "lower" classes of trains, especially those clustered with CET HI ones, should be examined very carefully and considered for further analysis to reduce the risk of losing valuable information. However, this is often constrained by time, since in this case large data sets have to be analyzed in more detail. It is therefore desirable that future generations of the T-POD algorithm should be trained for a more rigid detection of porpoise trains.

The finding that the two T-PODs classified a different proportion of trains as being "certain" might be a further point of concern. It is possible that these differences were due to external factors (acoustic properties of the pools, number of animals and interferences of signals, etc.). Another possibility might be that the algorithm classified trains differently based on the proportion of "full" scans which was different between T-PODs. Finally, it is quite possible that the two T-PODs were designed differently and therefore also reacted differently to incoming signals. Further tests using two devices simultaneously in one position are currently under way both in captivity and in the field to investigate the feasibility of T-PODs for monitoring studies in more detail.

ACKNOWLEDGMENTS

We would like to thank Jolanda Meerbeck and all the members from the team at Harderwijk for their assistance during data acquisition. We also thank Nick Tregenza for his help with data acquisition and analysis and for valuable comments on an earlier version of this paper.

Au, W. W. L., Kastelein, R. A., Rippe, T, and Schooneman, N. M., (**1999**). "Transmission beam pattern and echolocation signals of a harbor porpoise (*Phocoena phocoena*)," J. Acoust. Soc. Am. **196**, 3699–3705.

Carlström, J., (**2005**). "Diel variation in echolocation behaviour of wild harbor porpoises," Marine Mammal Sci. **21**, 1–12.

Evans, P. G. H., and Hammond, P. S., (**2004**). "Monitoring cetaceans in European waters," Mammal. Rev. **34**, 131–156.

Gordon, J., and Tyack, P. L., (**2002**). "Acoustic techniques for studying cetaceans," in *Marine Mammals: Biology and Conservation*, edited by P. G. H. Evans and T. Raga (Kluwer Academic/Plenum, New York), pp. 293–324.

Koschinski, S., Culik, B. M., Henriksen, O. D., Tregenza, N., Ellis, G. E., Jansen, C., and Kathe, G., (**2003**). "Behavioral reactions of free-ranging harbor porpoises and seals to the noise of a simulated 2 MW wind-power generator," Mar. Ecol.: Prog. Ser. **265**, 263–273.

Teilmann, J., Henriksen, O. D., Carstensen, J., and Skov, H., (**2002a**). "Monitoring effects of offshore windfarms on harbour porpoises using PODs (porpoise detectors)," Technical report to the Ministry of the Environment Denmark, 95 pp.

Teilmann, J., Miller, L. A., Kirketerp, T., Kastelein, R. A., Madsen, P. T., Nielsen, B. K., and Au, W. W. L., (**2002b**)."Characteristics of echolocation signals used by a harbour porpoise (*Phocoena phocoena*) in a target detection experiment," Aquatic Mammals **28**, 275–284.

Thomsen, F., and Piper, W., (**2004**). "Methodik zur Erfassung von Schweinswalen (*Phocoena phocoena*) mittels Klickdetektoren (T-PODs)," Natur- und Umweltschutz **3**, 47–52.

Veerbom, W. C., and Kastelein, R. A., (**1995**). "Acoustic signals by harbour porpoises (*Phocoena phocoena*)," in *Harbour Porpoises—Laboratory Studies to Reduce Bycatch*, edited by P. E. Nachtigall, J. Lien, W. W. L. Au, and A. J. Read (De Spil, Woerden, Netherlands), pp. 343–362.

Verfuss, U. K., Miller, L. A., and Schnitzler, H. U., (**1999**). "The echolocation behaviour of the harbour porpoise (*Phocoena phocoena*) during prey capture," in Abstracts of the 13th Biennial Conference on the Biology of Marine Mammals, Wailea, Maui, Hawaii, Nov. 28–Dec 03, 1999, Society for Marine Mammalogy, p. 193.

Verfuss, U. K., Honnef, C., Kilian, A., and Benke, H., (**2004**). "Relative abundance of harbour porpoises (*Phocoena phocoena*) and its seasonal variation in the German Baltic Sea monitored with porpoise detectors (T-PODs)," in Abstracts of the 18th Annual Conference of the ECS, Kolmarden, 28–31 March 2004, European Cetacean Society, p. 15.

Zar, J. H., (**1996**). *Biostatistical Analysis*, 3rd ed. (Prentice–Hall, Englewood Cliffs, NJ).

Comparing *F*0 discrimination in sequential and simultaneous conditions (L)

Christophe Micheyl[a] and Andrew J. Oxenham
Research Laboratory of Electronics, Massachusetts Institute of Technology, Cambridge, Massachusetts 02139-4307

(Received 1 December 2004; revised 12 April 2005; accepted 18 April 2005)

In an influential study, Carlyon and Shackleton [J. Acoust. Soc. Am. **95**, 3541–3554 (1994)] measured listeners' performance (d') in fundamental-frequency (*F*0) discrimination between harmonic complex tones (HCTs) presented simultaneously in different spectral regions and compared their performance with that found in a sequential-comparison task. In this Letter, it is suggested that Carlyon and Shackleton's analysis of the simultaneous-comparison data did not adequately reflect their assumption that listeners were effectively comparing *F*0's across regions. A reanalysis consistent with this assumption is described. The new results suggest that under the assumption that listeners were effectively comparing *F*0 across regions, their performance in this task was substantially higher than originally estimated by Carlyon and Shackleton, and in some conditions much higher than expected from the performances measured in a traditional *F*0-discrimination task with sequential HCTs. Possible explanations for this outcome, as well as alternative interpretations, are proposed. © *2005 Acoustical Society of America.*
[DOI: 10.1121/1.1929228]

PACS number(s): 43.66.Ba, 43.66.Fe, 43.66.Hg [RAL] Pages: 41–44

I. INTRODUCTION

Signal detection theory (SDT) provides a unifying framework for comparing results across studies involving different psychophysical paradigms, tasks, or procedures (Green and Swets, 1966; Jesteadt and Sims, 1974; Jesteadt and Bilger, 1975). Such comparisons may then be used to gain more insight into the mechanisms of perception than could be obtained with comparisons restricted to data all gathered using the same paradigm.

An interesting illustration of this approach can be found in an influential study by Carlyon and Shackleton (1994). In that study, the same listeners were tested in two experiments that were both thought to involve fundamental-frequency (*F*0) discrimination abilities. One experiment (experiment 3a in Carlyon and Shackleton's article) was a basic two-interval two-alternative forced choice (2I2AFC) *F*0-discrimination experiment, in which listeners were asked to indicate which of two consecutive harmonic complex tones (HCTs) had a higher *F*0. The other experiment (experiment 3b in Carlyon and Shackleton's article) involved comparing two consecutive pairs of simultaneous HCTs filtered into different spectral regions. In one of the two pairs, the two HCTs had the same *F*0; in the other pair, the two HCTs had different *F*0's. The listener's task was to indicate in which of the two pairs the two simultaneous HCTs had different *F*0's.

In order to compare performance in the two experiments, Carlyon and Shackleton transformed the proportion of correct responses into d'. They found that, when the two HCTs being compared both contained peripherally resolvable harmonics, the d''s measured in the experiment with simultaneous HCTs were not significantly different from those predicted based on the results of the experiment with only sequential HCTs. In contrast, when one of the two simultaneous HCTs contained resolved harmonics and the other did not, the d''s measured in the experiment with simultaneous HCTs were significantly lower than predicted. Carlyon and Shackleton noted that this pattern of results was consistent with the hypothesis that the *F*0's of resolved and unresolved harmonics are processed by different mechanisms, the outputs of which cannot be directly compared. They suggested that the necessary "translation" of these outputs into a common format caused performance in *F*0 comparisons between resolved and unresolved harmonics to be limited by some internal "translation noise." Because of its important implications for pitch perception theories, Carlyon and Shackleton's study has generated much interest in recent years (Meddis and O'Mard, 1998; Grimault *et al.*, 2002; Plack and Carlyon, 1995; Gockel *et al.*, 2004; Micheyl and Oxenham, 2004).

In this note, we suggest that Carlyon and Shackleton's SDT analysis of the results of their experiment with simultaneous HCTs is not consistent with their assumption that listeners were comparing *F*0's across regions in that experiment. We propose a reanalysis of the experimental data that is consistent with this assumption and, on the basis of the results of this reanalysis, point out alternative interpretations of the data.

II. SIGNAL-DETECTION-THEORETIC CONSIDERATIONS

Central to the present reanalysis is the question of what strategy listeners could use for optimal task performance in Carlyon and Shackleton's two experiments.[1] The optimal

[a]Electronic mail: cmicheyl@mit.edu

(likelihood-ratio) strategy determines the relationship between d' and proportion correct in the considered experiment.[2]

For the sequential $F0$-discrimination experiment, the answer is obvious. Since this experiment involved a basic two-interval, two-alternative forced-choice (2I2AFC) paradigm with a roving standard, the optimal strategy is to subtract the perceived $F0$ in the first interval from that in the second interval, and respond "interval 2" if the resulting difference was larger than zero or "interval 1" otherwise (Green and Swets, 1966; Macmillan and Creelman, 1991). With this decision rule, the relationship between d' and the proportion of correct responses, P_C, is given by Green and Swets (1966) (see also: Macmillan and Creelman 1991)

$$d' = \sqrt{2}\Phi^{-1}(P_C), \tag{1}$$

where Φ^{-1} denotes the inverse of the cumulative standard normal.

The optimal strategy in the experiment involving two pairs of HCTs is less obvious. Although this experiment superficially involved a 2I2AFC task, each observation interval in fact contained two (simultaneous) HCTs. In one of the observation intervals, the two $F0$'s were the same, while in the other they were different. If it is assumed that the listeners have access to the $F0$'s of the two HCTs in each interval, and that they compare these $F0$'s, the experiment is more accurately described as a dual-pair comparison or four-interval AX (4IAX) task.

Possible strategies for the 4IAX paradigm have been described in earlier publications (Macmillan *et al.*, 1977; Kaplan *et al.*, 1978; Noreen, 1981; Rousseau and Ennis, 2001). The strategies available to listeners depend on the specifics of the experimental design. If the design is such that it prevents listeners from relying on absolute judgments of the observations, and instead forces them to rely on comparisons between observations, then the best that listeners can do is compare the absolute value of the differences between the two observations in each pair, and select the pair for which the absolute difference is larger; this is the so-called differencing strategy for the 4IAX paradigm (Rousseau and Ennis, 2001).

Two implementation features of Carlyon and Shackleton's experiment with simultaneous HCTs constrained which strategy the listeners could use in order to perform optimally. First, the baseline stimulus $F0$ was roved widely across trials, which drastically limited the use of a fixed internal reference, and produced highly correlated sensory observations. Second, in the stimulus pair containing HCTs with different $F0$'s, the higher-$F0$ HCT was assigned randomly to the lower or to the higher spectral region; thus, the sign of the difference between the two observations in each pair was irrelevant to the task. It can be demonstrated that under these circumstances, the differencing strategy is the optimal strategy (Micheyl and Messing, unpublished).

Under the differencing strategy, the relation between proportion correct and d' in the 4IAX paradigm is (Macmillan *et al.*, 1977)

$$P_C = [\Phi(d'/2)]^2 + [1 - \Phi(d'/2)]^2, \tag{2}$$

where Φ is the cumulative standard normal. Different (but equivalent) formulations of the relationship between proportion correct and d' for the differencing strategy in the 4IAX design can be found elsewhere (e.g., Rousseau and Ennis, 2001).

Thus, the relationship between d' and proportion correct in Carlyon and Shackleton's experiment using simultaneous pairs of HCTs should, in theory, be that described in Eq. (2). Instead, Carlyon and Shackleton treated both experiments as standard 2I2AFC paradigms and, accordingly, used Eq. (1) or an equivalent of it, in order to transform into d' the proportion-correct values measured in their two experiments. However, the relationship between d' and proportion correct described by Eq. (1) is based on the assumption that listeners made only two observations and only one comparison on each trial, which is inconsistent with Carlyon and Shackleton's tacit assumption that listeners compared $F0$ across spectral regions in each of the two observation intervals from each trial. Accordingly, we reanalyzed the data from Carlyon and Shackleton's experiment involving two pairs of harmonic complexes using Eq. (2).

III. REANALYSIS OF CARLYON AND SHACKLETON'S DATA

The d' values shown in Fig. 7 of Carlyon and Shackleton's article were converted to proportions of correct responses using the inverse form of Eq. (1). The resulting proportions were then transformed back into d' using the inverse form of Eq. (2).[3] The recomputed d' values are plotted in Fig. 1 as open symbols connected by solid lines. These can be compared to the d' values originally calculated by Carlyon and Shackleton for this task, which are shown here as filled symbols connected by solid lines. The d' values that were predicted by Carlyon and Shackleton based on the results of the sequential $F0$-discrimination task are also replotted here as open symbols connected by dotted lines.

It can be seen that the recomputed d' values are systematically and markedly ($\sim$80%) larger than the d' values originally calculated by Carlyon and Shackleton. This suggests that if listeners really compared $F0$ across spectral regions in the simultaneous case, Carlyon and Shackleton's (1994) calculations substantially underestimated performance in this task. Furthermore, when the recomputed d' values are compared to those predicted based on the results of the basic sequential $F0$-discrimination experiment, it is found that in three of the four conditions tested, the predictions fall below the recomputed d' values. Leaving aside the MIDHI 88-Hz condition (for which Carlyon and Shackleton indicated a strong reason to expect higher performance, based on pitch-pulse asynchrony cues), planned comparisons (two-way repeated-measures ANOVAs contrasting the predicted and recomputed d' values, with the $F0$ difference included as a factor) showed a significant difference between the predicted and the recomputed d' values for the LOMID 250-Hz condition [$F(1,2)=921.054, p=0.01$], as well as for

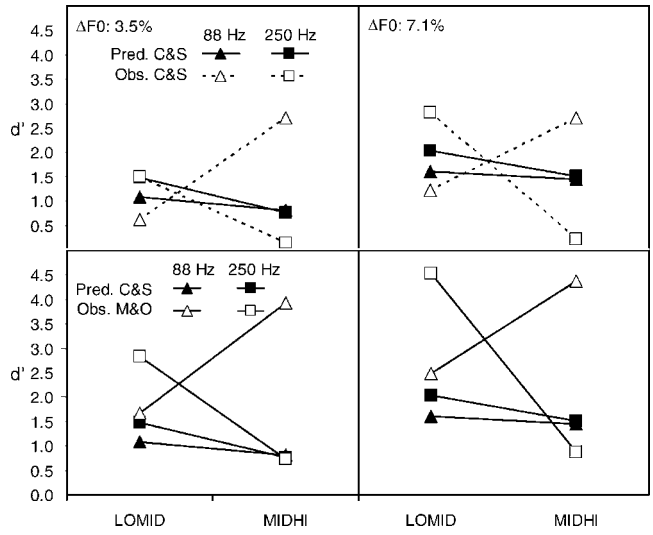

FIG. 1. Comparison between the d' values calculated by Carlyon and Shackleton (1994) and those calculated in the present reanalysis. The top panels show the observed and predicted d' values replotted from Carlyon and Shackleton (1994). The format of these panels is the same as that of their Fig. 9: the "observed" d' values, which were calculated based on the measured proportion of correct responses in the experiment with simultaneous HCTs, are shown as filled symbols connected with solid lines; the "predicted" d' values, which were calculated based on the results of the sequential $F0$-comparison experiment, are represented by empty symbols connected with short-dashed lines. Triangles are used to represent data obtained with a nominal $F0$ of 88 Hz, squares to represent data obtained with a nominal $F0$ of 250 Hz. The left-hand panel shows data obtained using an $F0$ separation ($\Delta F0$) of 3.5%, while the right-hand panel shows data obtained with a $\Delta F0$ of 7.1%. The spectral regions into which the stimuli were filtered are indicated in the abscissa. The lower panels show the recalculated "observed" d' values that resulted from the present reanalysis of Carlyon and Shackleton's data. The recalculated values are shown as empty symbols connected by solid lines. Carlyon and Shackleton's original predictions are also replotted here to facilitate comparisons; they are the same as in the upper panels, and are again shown as filled symbols connected by solid lines.

the LOMID 88-Hz condition $[F(1,2)=94.881, p=0.010]$, but not for the MIDHI 250-Hz condition $[F(1,2)=0.108, p=0.774]$.

IV. DISCUSSION

The present results can be interpreted in two main ways, depending on whether or not one is willing to accept that Carlyon and Shackelton's experiment with two pairs of simultaneous HCTs filtered into different spectral regions involved basically the same $F0$-comparison mechanisms as the more traditional sequential $F0$-discrimination experiment. If it is assumed that this was the case, then the results of the present reanalysis indicate that simultaneous $F0$ comparisons between HCTs filtered into different spectral regions can be significantly more accurate than $F0$ comparisons between sequential HCTs filtered into the same spectral region, even when one of the two simultaneous complexes contains resolved harmonics while the other does not (see the results of the LOMID 88-Hz condition). This conclusion is the opposite of that drawn by Carlyon and Shackleton (1994), who concluded (based on the same data) that performance was systematically *poorer* than predicted in conditions involving simultaneous comparisons between resolved and unresolved harmonics.

Nevertheless, the new analysis remains consistent with Carlyon and Shackleton's main finding that $F0$ comparisons between resolved and unresolved harmonics are less accurate than comparisons between harmonics of the same resolvability status. Indeed, even with the recomputed data shown in Fig. 1, the amount by which observed performance exceeds predicted performance is somewhat larger in resolved–unresolved conditions (LOMID-88 Hz and MIDHI-250 Hz) than in resolved–resolved conditions (LOMID-250 Hz). This is consistent with relatively more noise being present in the former than in the latter conditions, regardless of whether the sequential listening conditions involved more noise than the simultaneous ones or not (see footnote 3 in Carlyon and Shackleton). Two possible reasons for which simultaneous $F0$ comparisons may be more accurate than sequential comparisons are, first, that sequential comparisons involve memory noise while simultaneous comparisons do not (Durlach and Braida, 1969; see footnote 3 in Carlyon and Shackleton, 1994), and second, that instantaneous across-region comparisons are immune to correlated noise across peripheral channels (Durlach *et al.*, 1986; Dai and Green, 1992). Another possible explanation, which is more specific to the considered experiments by Carlyon and Shackleton, is that in these experiments the $F0$ of the stimuli varied over time (it was modulated over 5% at a rate of 2.5 Hz). This variation in $F0$ over time may have limited listeners' ability to make sequential $F0$ comparisons, as it may have required that the estimated $F0$ tracks from the two HCTs be temporally aligned prior to being compared. In contrast, when the HCTs to be compared were simultaneous, the $F0$ modulation being phase coherent, listeners could compare $F0$'s across spectral region on a moment-by-moment basis. This could explain the higher performance in simultaneous across-region comparisons than in sequential within-region comparisons.

While there are some reasons to expect sequential $F0$ comparisons between HCTs filtered into the same spectral region to involve sources of internal noise to which simultaneous $F0$ comparisons between HCTs filtered into different regions may be immune, there are as many if not more reasons to expect the converse. For instance, the salient timbre differences between complexes filtered into different spectral regions may have a detrimental effect on the ability to make fine $F0$ discrimination between these complexes (e.g., Faulkner, 1985; Moore and Glasberg, 1990; Micheyl and Oxenham, 2004). Furthermore, due to pitch-shift effects, differences in spectral region may cause complexes having the exact same $F0$ to sound like they have a different pitch (Chuang and Wang, 1978; Singh and Hirsh, 1992). Finally, it has recently been shown (Gockel *et al.*, 2004) that the perception of the $F0$ of a harmonic complex filtered in a spectral region can be adversely affected by the simultaneous presence of another complex in a different region, especially when the $F0$'s of the two complexes are relatively close. In the light of these earlier results, the conclusion that performance in simultaneous $F0$ comparisons across different

spectral regions is generally better than performance in sequential *F*0 comparisons within the same region may appear difficult to accept.

An alternative interpretation of the current results is that the two considered experiments of Carlyon and Shackleton involved different perceptual mechanisms. Although both experiments probably required the extraction of *F*0-related information at some stage, it is quite possible that this *F*0 information was utilized very differently in the two experiments. For instance, task performance in the experiment with simultaneous complexes could be based primarily on the output of *F*0-based grouping/segregation processes, whereby simultaneous HCTs having different *F*0's were perceived as less well-fused than HCTs having the same *F*0 (Darwin, 1992). Although grouping and segregation processes possibly involve some implicit comparison of *F*0 information across spectral regions, they may not necessarily engage the same *F*0-comparison mechanisms as a sequential task.[4] Like Carlyon and Shackleton's (1994) original analysis, the present reanalysis is based on the assumption that the sequential and simultaneous "*F*0-discrimination" experiments involved the same type of *F*0-comparison mechanisms. Without this assumption, it becomes unclear how performance obtained in these two types of tasks can be meaningfully compared in order to elucidate the nature of the underlying pitch mechanisms.

In any case, the present reanalysis and the resulting reversal of the conclusions regarding relative task difficulty illustrate the importance of selecting the correct decision models when comparing performance across different tasks.

ACKNOWLEDGMENTS

This work was supported by the National Institutes of Health (NIDCD Grant R01 DC 05216). The authors are grateful to Robert Carlyon, Laurent Demany, Joshua Bernstein, David Messing, and an anonymous reviewer for helpful comments on earlier versions of the manuscript.

[1]These two experiments are described as experiment 3a and experiment 3b in Carlyon and Shackleton's (1994) article.

[2]Throughout this article, d' is meant as the standard index of performance from signal-detection-theory, traditionally defined in reference to the basic yes/no (YN) paradigm as the distance beteen the means of the two (Gaussian) internal probability density functions corresponding to the two possible stimulus alternatives. This d' is sometimes referred to in the psychophysical literature as the "true" d'. One important feature of d', when it is defined in this way is that, all other things being equal, its value will not depend on the experimental paradigm that is used to measure it.

[3]The inverse form of Eq. (2) can be found by completing the square. When this is done, it is found that $d'=2\Phi^{-1}(1/2+\sqrt{x})$, with $x=P_C/2-1/4$. P_C, d', and Φ^{-1} are as defined above. Note that the domain over which this formula is applicable is $0.5<P_C<1$.

[4]In fact, there is some evidence that the auditory grouping/segregation mechanisms related to the perception of mistuning operate partly independently from pitch-perception mechanisms. For instance, the grouping of simultaneous frequency components appears to be governed by spectral regularity, not just harmonicity (Roberts and Brunstrom, 2003). Other arguments for the notion that the detection of mistuning between simultaneous tones may involve other processes than explicit pitch comparisons can be found in Demany and Semal (1992).

Carlyon, R. P., and Shackleton, T. M. (**1994**). "Comparing the fundamental frequencies of resolved and unresolved harmonics: Evidence for two pitch mechanisms," J. Acoust. Soc. Am. **95**, 3541–3554.

Chuang, C. K., and Wang, W. S. (**1978**). "Psychophysical pitch biases related to vowel quality, intensity difference, and sequential order," J. Acoust. Soc. Am. **64**, 1004–1014.

Dai H., and Green, D. M. (**1992**). "Auditory intensity perception: Successive versus simultaneous, across-channel discriminations," J. Acoust. Soc. Am. **91**, 2845–2854.

Darwin, C. J. (**1992**). "Listening to two things at once," in *The Auditory Processing of Speech, from Sounds to Words*, edited by M. E. H. Schouten (Mouton de Gruyer, New York), pp. 133–145.

Demany, L., and Semal, C. (**1992**). "Detection of inharmonicity in dichotic pure-tone dyads," Hear. Res. **61**, 161–166.

Durlach, N. I, and Braida, L. D. (**1969**). "Intensity perception. I. Preliminary theory of intensity resolution," J. Acoust. Soc. Am. **46**, 372–383.

Durlach, N. I., Braida, L. D., and Ito, Y. (**1986**). "Towards a model for discrimination of broadband signals," J. Acoust. Soc. Am. **80**, 63–72.

Faulkner, A. (**1985**). "Pitch discrimination of harmonic complex signals: Residue pitch of multiple component discrimination?" J. Acoust. Soc. Am. **78**, 1993–2004.

Gockel, H., Carlyon, R. P., and Plack, C. J. (**2004**). "Across-frequency interference effects in fundamental frequency discrimination: Questioning evidence for two pitch mechanisms," J. Acoust. Soc. Am. **116**, 1092–1104.

Green, D. M., and Swets, J. A. (**1966**). *Signal Detection Theory and Psychophysics* (Wiley, New York).

Grimault, N., Micheyl, C., Carlyon, R. P., and Collet, L. (**2002**). "Evidence for two pitch encoding mechanisms using a selective auditory training paradigm," Percept. Psychophys. **64**, 189–197.

Jesteadt, W., and Bilger, R. C. (**1974**). "Intensity and frequency discrimination in one- and two-interval paradigms," J. Acoust. Soc. Am. **55**, 1266–1276.

Jesteadt, W., and Sims, S. L. (**1975**). "Decision processes in frequency discrimination," J. Acoust. Soc. Am. **57**, 1161–1168.

Kaplan, H. L., Macmillan, N. A., and Creelman, C. D. (**1978**). "Tables of d' for variable-standard discrimination paradigms," Behav. Res. Methods Instrum. **10**, 796–813.

Macmillan, N. A., and Creelman, C. D. (**1991**). *Detection Theory: A User's Guide* (Cambridge University Press, Cambridge, UK).

Macmillan, N. A., Kaplan, H. L., and Creelman, C. D. (**1977**). "The psychophysics of categorical perception," Psychol. Rev. **84**, 452–471.

Meddis, R., and O'Mard, L. (**1997**). "A unitary model of pitch perception," J. Acoust. Soc. Am. **102**, 1811–1820.

Micheyl, C., and Messing, P., "Likelihood ratio, optimal decision rules, and correct-response probabilities in the 4IAX paradigm".

Micheyl, C., and Oxenham, A. J. (**2004**). "Sequential *F*0 comparisons between resolved and unresolved harmonics: No evidence for translation noise between two pitch mechanisms," J. Acoust. Soc. Am. **116**, 3038–3050.

Moore, B. C. J., and Glasberg, B. R. (**1990**). "Frequency discrimination of complex tone with overlapping and non-overlapping harmonics," J. Acoust. Soc. Am. **87**, 2163–2177.

Noreen, D. L. (**1981**). "Optimal decision rules for some common psychophysical paradigms, in *Mathematical Psychology and Psychophysiology (Proceedings of the Symposium in Applied Mathematics of the American Mathematical Society and the Society for Industrial and Applied Mathematics, Vol. 13)*, edited by S. Grossberg (American Mathematical Society, Providence, RI), pp. 237–279.

Plack, C. J., and Carlyon, R. P. (**1995**), "Differences in frequency modulation detection and fundamental frequency discrimination between complex tones consisting of resolved and unresolved harmonics" J. Acoust. Soc. Am. **98**, 1355–1364.

Roberts, B., and Brunstrom, J. M. (**2003**). "Spectral pattern, harmonic relations, and the perceptual grouping of low-numbered components," J. Acoust. Soc. Am. **114**, 2118–2134.

Rousseau, B., and Ennis, D. M. (**2001**). "A Thurstonian model for the dual pair (4IAX) discrimination method," Percept. Psychophys. **63**, 1083–1090.

Singh, P. G., and Hirsh, I. J. (**1992**). "Influence of spectral locus and *F*0 changes on the pitch and timbre of complex tones," J. Acoust. Soc. Am. **92**, 2650–2661.

Estimation of the location of a farfield acoustic source

Jay C. Hardin, Mikhail Gilinsky, and Vitali Khaikine
Hampton University, Hampton, Virginia 23668

(Received 19 July 2004; revised 17 December 2004; accepted 14 April 2005)

A backward integration method for estimating the location of a source of sound waves in the atmosphere is presented. This geometric acoustics method is based upon the analysis of microphone array measurements to determine the incoming ray direction in three dimensions. The equations governing the propagation of the ray are then integrated backward in time. The sound source lies somewhere along the calculated ray path. The intersection of such loci from more than one array would provide an estimate of the source location. The method appears to be very rapid to implement and, assuming the time delays to be accurately measured, limited in accuracy only by the timeliness of the input sound speed and velocity profiles in the atmosphere. © *2005 Acoustical Society of America.* [DOI: 10.1121/1.1926007]

PACS number(s): 43.28.Gq, 43.28.Js [AJZ] Pages: 45–50

I. INTRODUCTION

Techniques for determining the location of the source of sound waves in the atmosphere have many applications. One area of particular interest is locating weather phenomena. As an example, in the 1980s, a study was carried out at NASA's Langley Research Center of sound generation by microbursts (intense, local downflows of air) as an aircraft alert system.[1] If an aircraft encounters a microburst on landing approach, the aircraft experiences more lift in which case the pilot has a tendency to reduce the angle of attack in order to remain on the proper glide slope. Upon exiting the microburst, the aircraft may then not have sufficient lift to remain aloft, and crashes have resulted. The idea was that acoustic arrays could be installed at airports to alert pilots to such dangers. Although other means for aircraft safety alerts were subsequently installed on aircraft, the study demonstrated the feasibility of locating atmospheric phenomena by monitoring their acoustic emissions. A similar potential application could be to the monitoring of aircraft wake vortices near airports, which is of considerable current interest.[2] The interaction of the vortices with the ground plane produces a characteristic infrasonic acoustic signature that could be employed to track the vortices. In addition, a source of audible sound has also been observed and is now being studied for the purpose of tracking.[3] Studies of another application, the detection of bolides (meteors) entering our atmosphere from space were carried out in the 1990s, particularly by Los Alamos National Laboratory.[4]

The approach presented herein envisions utilizing data from an array of five microphones, four in the form of a cross with a fifth at the center. From this single array, it is shown that it is possible to determine the direction of the incoming sound. This information is then utilized as initial conditions for the backward integration of the three-dimensional ray equations with variable sound speed and velocity vector to determine the loci of possible source positions. The intersection of such loci from more than one such array would then determine the source position. The idea of utilizing such data for source location is certainly not new. In fact, the Prototype International Data Center, in operation since 1998, has been developing an automatic and interactive data processing system for highly impulsive sources in any terrestrial environment.[5] That system, as presently implemented, determines source location based upon intersecting azimuths from more than one array, as well as travel-time tables.

II. ESTIMATION OF APPARENT SOURCE ELEVATION

Consider an acoustic source at the point (x,y,z) in an ambient medium and three microphones, one each at the origin, the point $(d,0,0)$, and the point $(0,d,0)$, respectively, in a Cartesian coordinate system, as shown in Fig. 1.

Without loss of generality, to be explained later, assume that x, y, and z are all greater than or equal to zero. The source generates acoustic waves that travel out in all directions from the source at constant speed c. An acoustic wave generated by the source at time $t=0$ will arrive at the origin at time t, at the point $(d,0,0)$ at time $t+\Delta t_1$, and at the point $(0,d,0)$ at time $t+\Delta t_2$. These time differences Δt_1 and Δt_2 will be assumed to be measured and known.

Applying the distance formula to this geometry yields the three equations,

$$x^2+y^2+z^2=c^2t^2,$$

$$(x-d)^2+y^2+z^2=c^2(t+\Delta t_1)^2, \tag{1}$$

$$x^2+(y-d)^2+z^2=c^2(t+\Delta t_2)^2,$$

which govern the location of the source position. The first two of equations (1) may be solved for the travel time t, yielding

$$t=\frac{d^2-2dx-c^2\,\Delta t_1^2}{2c^2\,\Delta t_1}\geqslant 0, \tag{2}$$

while the first and third may be solved to yield

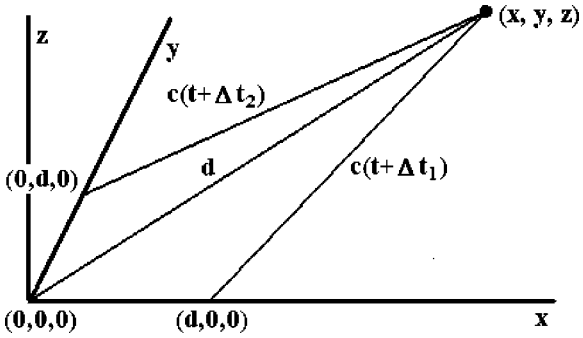

FIG. 1. Source location geometry.

$$t = \frac{d^2 - 2dy - c^2\,\Delta t_2^2}{2c^2\,\Delta t_2} \geqslant 0. \tag{3}$$

These two solutions must be equal, which provides a causality requirement on the source position. Introducing the normalized variables $\tilde{x}=x/d$, $\tilde{y}=y/d$, and $\tilde{z}=z/d$ as well as the parameters $a=d/c\,\Delta t_1$ and $b=d/c\,\Delta t_2$ and equating (2) and (3) shows that

$$\frac{ct}{d} = -a\left(\tilde{x} - \frac{1}{2} + \frac{1}{2a^2}\right) = -b\left(\tilde{y} - \frac{1}{2} + \frac{1}{2b^2}\right) \geqslant 0, \tag{4}$$

which must be satisfied at the normalized source position $(\tilde{x},\tilde{y},\tilde{z})$.

A. Delay time constraints

Note that Eq. (4) implies that if $\tilde{x} > 1/2 - 1/2a^2$, as will usually be the case in applications, then $a<0$. Similarly, if $\tilde{y} > 1/2 - 1/2b^2$, then $b<0$. The parameters a and b are, of course, not independent. Considering Fig. 2 and applying the law of cosines to the triangle passing through the origin, the source position, and the point $(d,0,0)$ shows that $a^2 \geqslant 1$. Similarly, applying the law of cosines to the triangle passing through the origin, the source position and the point $(0,d,0)$ shows that $b^2 \geqslant 1$. Finally, let α, β, and γ be the direction cosines of the vector from the origin to the source point. An

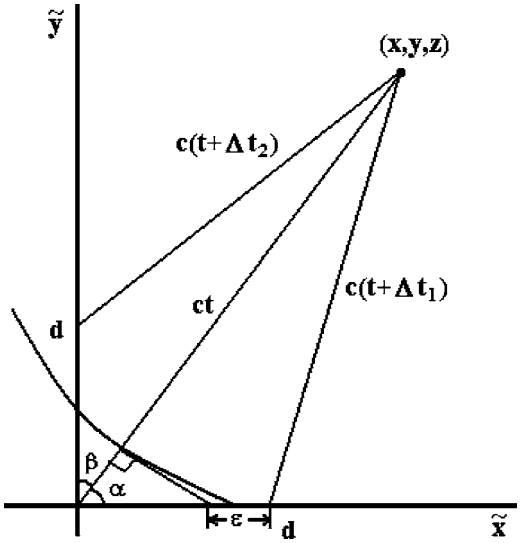

FIG. 2. Delay time constraints.

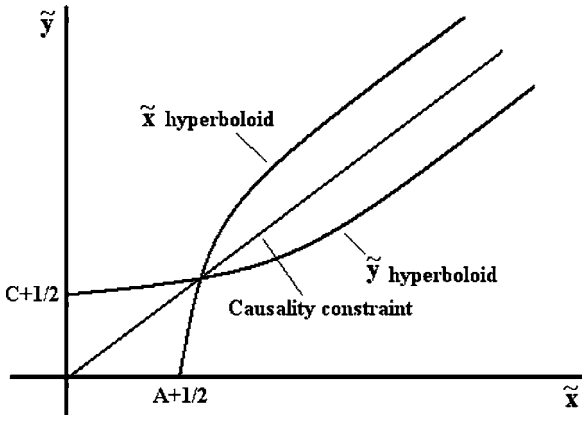

FIG. 3. Source location relations in the $\tilde{x}$-$\tilde{y}$ plane.

arc of radius $c(t+\Delta t_1)$ from the source point intersects this vector at a distance of $c|\Delta t_1|$ from the origin. The tangent line to this arc at the intersection crosses the x axis at $d-\varepsilon$. Hence, it can be seen that

$$\cos\alpha = \frac{c|\Delta t_1|}{d-\varepsilon} > \frac{c|\Delta t_1|}{d} = \frac{1}{|a|}.$$

Similarly, $\cos\beta > 1/|b|$. Thus, the constraint that

$$\frac{1}{a^2} + \frac{1}{b^2} < \cos^2\alpha + \cos^2\beta \leqslant \cos^2\alpha + \cos^2\beta + \cos^2\gamma = 1 \tag{5}$$

can be obtained.

B. Source location hyperboloids

Utilizing Eq. (2) in the first or second of Eqs. (1) yields

$$\left(\tilde{x} - \frac{1}{2}\right)^2 \Big/ A^2 - \tilde{y}^2/B^2 - \tilde{z}^2/B^2 = 1, \tag{6}$$

where $A^2=1/4a^2$ and $B^2=(a^2-1)/4a^2$. Equation (6) may be recognized as a hyperboloid with the $\tilde{x}$ axis as the transverse axis. The source position must lie on this hyperboloid. Similarly, utilizing Eq. (3) in the first or third of Eqs. (1) yields

$$\left(\tilde{y} - \frac{1}{2}\right)^2 \Big/ C^2 - \tilde{x}^2/D^2 - \tilde{z}^2/D^2 = 1, \tag{7}$$

where $C^2=1/4b^2$ and $D^2=(b^2-1)/4b^2$. Equation (7) may be recognized as a hyperboloid with the $\tilde{y}$ axis as the transverse axis. Likewise, the source position must lie on this hyperboloid. Hence, the source position must lie on the intersection of the two hyperboloids given by Eqs. (6) and (7). Further, the source position must satisfy the causality constraint given by Eq. (4), which, in terms of the parameters A, B, C, and D, becomes

$$(\tilde{y} - 2D^2) = \frac{C}{A}(\tilde{x} - 2B^2). \tag{8}$$

This relation as well as the projections in the $\tilde{x}-\tilde{y}$ plane of the hyperboloids given by Eqs. (6) and (7) are shown in Fig. 3.

Note that the linear equation (8) defines the source plane (the plane in which the source must lie) as well as two of the direction cosines to the source from any point on the line in the $\tilde{x}-\tilde{y}$ plane, i.e.,

$$\cos \alpha_S = \frac{A}{\sqrt{A^2 + C^2}} \sin \gamma_S$$

and

$$\cos \beta_S = \frac{C}{\sqrt{A^2 + C^2}} \sin \gamma_S, \tag{9}$$

where γ_S is the angle that the incoming ray from the source makes with the z axis.

C. Intersection of hyperboloids

The source location has been shown above to lie on the intersection of the two hyperboloids and to satisfy the causality constraint. In order to determine the form of the intersection, consider the change of variables,

$$\tilde{x} = 2B^2 + \frac{A\eta - C\varsigma}{\sqrt{A^2 + C^2}},$$

$$\tilde{y} = 2D^2 + \frac{C\eta + A\varsigma}{\sqrt{A^2 + C^2}},$$

$$\tilde{z} = \tilde{z},$$

which places the origin of the η-ς coordinate system at the point $(\tilde{x},\tilde{y})=(2B^2,2D^2)$ and then rotates it through an angle $\theta=\tan^{-1} C/A$ with respect to the $\tilde{x}$-$\tilde{y}$ axes. Thus, the η axis is in the direction of the causality constraint, given by Eq. (8), along which the intersection will lie, and the ζ axis is perpendicular to it. Utilizing this change of variables in either Eq. (6) or Eq. (7) and setting $\zeta=0$ yields

$$\frac{(\eta - \eta_0)^2}{S^2} - \frac{\tilde{z}^2}{R^2} = 1, \tag{10}$$

where

$$\eta_0 = \frac{2(AB^2 + CD^2)\sqrt{A^2 + C^2}}{B^2 - C^2},$$

$$R^2 = B^2 + \frac{4B^2(AC + D^2)^2}{B^2 - C^2},$$

and

$$S^2 = \frac{(A^2 + C^2)R^2}{B^2 - C^2}.$$

Note that R^2 and S^2 are both non-negative since

$$B^2 - C^2 = \frac{(a^2 - 1)}{4a^2} - \frac{1}{4b^2} = \frac{1}{4}\left(1 - \frac{1}{a^2} - \frac{1}{b^2}\right) > 0,$$

by Eq. (5). Thus, Eq. (10) may be recognized as a hyperbola, as shown in Fig. 4, which must be satisfied by the altitude of the source. Note that for large distances, which will ordinarily be the case in practice, the hyperbola approaches its asymptote given by

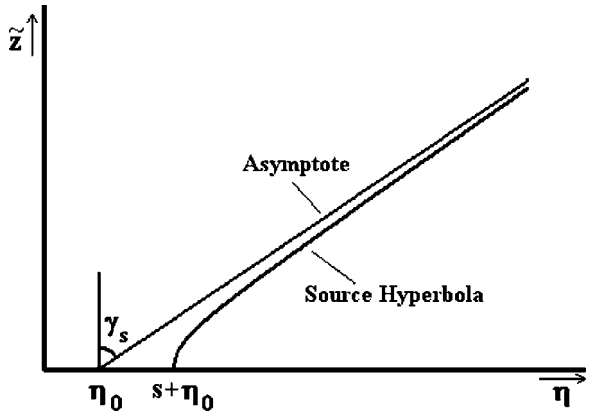

FIG. 4. Altitude hyperbola in source plane.

$$\tilde{z} = \frac{R}{S}(\eta - \eta_0). \tag{11}$$

Thus, the direction cosine toward a distant source from the point $(\eta,\varsigma,\tilde{z})=(\eta_0,0,0)$ is given by

$$\cos \gamma_S = \frac{R}{\sqrt{R^2 + S^2}}. \tag{12}$$

This relation, along with Eqs. (9), completely define the direction to a distant source from the point

$$\tilde{x} = x/d = 2B^2 + \frac{A\eta_0}{\sqrt{A^2 + C^2}},$$

$$\tilde{y} = y/d = 2D^2 + \frac{C\eta_0}{\sqrt{A^2 + C^2}}, \tag{13}$$

$$\tilde{z} = z/d = 0.$$

This fact will be utilized in the development of the backward integration method.

III. THE BACKWARD INTEGRATION METHOD

At this point, one might well question what the previous analysis for an ambient medium with a constant speed of sound has to do with the real atmosphere, where there are winds and where the temperature and, hence, the sound speed varies with position. In actuality, this ambient analysis will be employed only to produce initial conditions for the backward integration method to determine the location of the source of incoming radiation. Note that the parameters a and b and, hence, the parameters A, B, C, D, R, and S depend only upon the microphone spacing and the measured time delays. Further, the wind velocity near the ground is ordinarily on the order of $0.01c$. Thus, one can imagine replacing the real source, wherever it might be, by a nearby source producing the same time delays. The direction to this nearby source in an ambient medium would be the same as the local apparent direction to the real source in the variable atmosphere. Thus, it is only necessary that the medium be reasonably ambient in the vicinity of the microphone array.

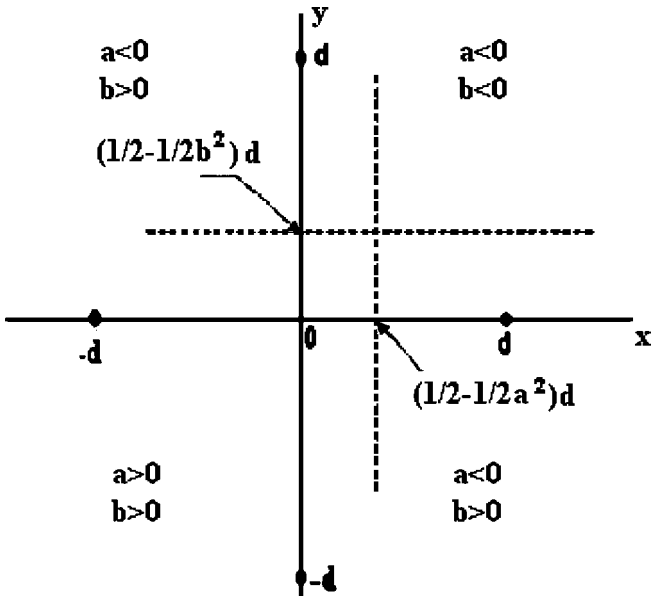

FIG. 5. Assumed microphone array.

Imagine a set of five microphones in the form of a cross, as shown in Fig. 5. Considering only the microphones at the origin, at the point $(d,0,0)$ and at the point $(0,d,0)$ for the moment, if the parameters a and b are measured, then the quadrant in which the source lies is essentially determined by the signs of a and b. As can be seen in Fig. 5, the causality constraint, Eq. (4), shows that unless $0 \leqslant x \leqslant (1/2-1/2a^2)d$ or $0 \leqslant y \leqslant (1/2-1/2b^2)d$ or both, which is unlikely, the source quadrant can be assigned based upon a knowledge of the signs. Once the source quadrant has been determined, then one can consider only the three microphones in that quadrant and the previous analysis applies. Hence, this array of five microphones allows the previous analysis to be applied, regardless of the position of the source with respect to the microphone array. However, a similar analysis could be developed for other arrays of microphones.

A. Numerical iteration technique

The backward integration technique utilizes a ray acoustics approach. Ray acoustics is based upon the idea that sound moves through the medium at the speed of sound plus the speed of the medium. Thus, if $\mathbf{v}(\mathbf{x},t)$ and $c(\mathbf{x},t)$ are the wind velocity and speed of sound, respectively, at the point $\mathbf{x}$ in the medium at time t, then the velocity of a point on a wave front is given by[6]

$$\frac{d\mathbf{x}}{dt} = \mathbf{v}(\mathbf{x},t) + \mathbf{n}(\mathbf{x},t)c(\mathbf{x},t), \tag{14}$$

where $\mathbf{n}(\mathbf{x},t)$ is the normal vector to the wave front. The change in the normal vector as the wave front propagates satisfies[7]

$$\frac{d\mathbf{n}}{dt} = -\nabla c - \nabla \mathbf{v}\cdot\mathbf{n} + \mathbf{n}(\mathbf{n}\cdot\nabla c + \mathbf{n}\cdot(\nabla \mathbf{v}\cdot\mathbf{n})). \tag{15}$$

From Eq. (14), it can be seen that if the initial normal vector lies in a plane through which there is no crosswind, i.e., the wind velocity vector lies in the same plane, then the velocity of the point on the wave front will also be in that plane. In this case, a sound ray from the source would travel from the source to a receiver at the point given by Eq. (13) in the source plane given by Eq. (8). Further, as can be seen from Eq. (15), if the speed of sound and the wind velocity were constant, the normal vector would not change and the ray paths would be straight lines.

The backward integration technique proposed herein can be shown to be equivalent to a forward integration technique with the velocity vector reversed. However, the authors prefer the backward integration as the more physically intuitive. The calculations required are essentially the same. In order to implement the backward integration method, the best available sound speed and velocity data as a function of space and time are utilized in Eqs. (14) and (15). Thus, all the complications of variable sound speed and wind velocity are included, in particular, any crosswind component through the source plane. These ordinary differential equations are then integrated backward in time, utilizing the position and angle of the incoming ray developed in Eqs. (9), (12), and (13). The accuracy of the technique in determining the true source location is highly dependent upon the timeliness and accuracy of the sound speed and wind velocity data as well as the accuracy of the time delay measurements.

In this general discussion, the velocity vector and speed of sound have been allowed to be time dependent. However, such data is typically not available for the atmosphere. In a further analysis, the velocity vector and speed of sound will be taken to depend only upon altitude although more complex dependencies are readily handled by the same techniques if the relevant data is available.

B. Examples

In order to demonstrate the technique, some examples have been devised and numerically computed. The assumed sound speed and velocity profiles depend only upon altitude and, for simplicity, the wind velocity will be assumed to only have a component in the x direction. Thus, the governing ray tracing equations, given by Eqs. (14) and (15) become

$$\frac{dl}{d\tilde{t}} = n/F, \quad \frac{d\tilde{x}}{d\tilde{t}} = \tilde{u} + l\tilde{c},$$

$$\frac{dm}{d\tilde{t}} = nmF, \quad \frac{d\tilde{y}}{d\tilde{t}} = m\tilde{c}, \tag{16}$$

$$\frac{dn}{d\tilde{t}} = (n^2-1)F, \quad \frac{d\tilde{z}}{d\tilde{t}} = n\tilde{c},$$

where $\tilde{u}=u/c(0)$, $\tilde{c}=c/c(0)$, $\tilde{t}=c(0)t/d$, and $F=l(d\tilde{u}/d\tilde{z}) + (d\tilde{c}/d\tilde{z})$.

Example 1: To illustrate the technique, consider the problem of determining the position of the source of audible vortex sound produced by an aircraft on the landing approach. This sound is apparently generated[3] when a length of the wake vortices becomes unstable. Although not a point source, this source may be treated as such since the microphones are normally in both the acoustic, i.e., more than a

wavelength away, and geometric, i.e., far enough away that the source distribution appears as a point source, farfields of the the source. For this example, the sound speed has been taken as constant, $c=330$ m/s, and the wind velocity profile is the typical boundary layer profile,

$$u(z) = V(z_0) \cdot \left(\frac{z}{z_0}\right)^n,$$

where $n=1/7$, $z_0=10$ m, and $V(z_0)=5$ m/s.

Suppose the ground track of the aircraft landing approach lies parallel to the y axis of the microphone array and the aircraft is landing in the positive y direction. The origin of the array will be taken to be at a distance of 1 mile $=1609.35$ m to the left of the flight path and the microphone spacing, d, will be taken as 200 ft$=60.98$ m. The measured time difference between the arrival of the sound at the microphone located at the origin and that located at $(d,0,0)$ was found to be -0.1823 s, that located at $(0,d,0)$ was found to be -0.0138 s, that located at $(-d,0,0)$ was found to be 0.1826 s and that located at $(0,-d,0)$ was found to be 0.0207 s. Since the first two time differences are negative, the source is determined to lie in the first quadrant of the microphone array. Thus, only that quadrant will be considered further. It should be mentioned that the source location technique is sensitive to the accuracy of these measured time differences, particularly for very small time differences.

With $\Delta t_1=-0.1823$ s *and* $\Delta t_2=-0.0138$ s, performing the calculations described previously yields the estimated angles to the distant source, i.e.

$$\alpha_S = 7.96\,^\circ,$$

$$\beta_S = 85.7\,^\circ,$$

$$\gamma_S = 83.38\,^\circ,$$

from the point $x=2.32d=141.46$ m, $y=0.67d=40.85$ m, and $z=0$. Recalling that the incoming ray is in the direction opposite to the direction to the source, the incoming ray has a direction vector given by

$$\mathbf{n} = -\cos\alpha_S\mathbf{i} - \cos\beta_S\mathbf{j} - \cos\gamma_S\mathbf{k}$$
$$= -0.990\mathbf{i} - 0.075\mathbf{j} - 0.115\mathbf{k}.$$

Thus, all initial conditions for the backward integration program have been developed. Here, the equations (16) were integrated in dimensional form backward with $\Delta t=0.5$ s. The results are shown in Fig. 6. The source location is expected to be along the flight path of the aircraft. Thus, note that at $t=-4.6$ s, $x=1609$ m, which is one mile from the center of the array, $y=154$ m, and $z=212$ m, which is the estimated source location.

Example 2: For this example, an infrasonic source whose rays can travel great distances before dissipation is imagined. The speed of sound in the atmosphere has been assumed, given by the expression

$$c(z) = 0.012z^2 - 5.3z + 340,$$

in meters per second where z is in kilometers. This profile is shown in Fig. 7, which is somewhat reminiscent of the typical profile in the lower atmosphere.[6] The wind velocity profile has been assumed to be linear, i.e.,

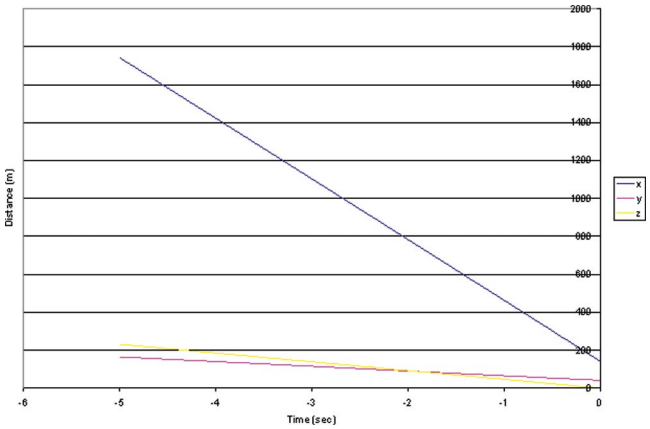

FIG. 6. Wake vortex source location.

$$u(z) = -0.83z,$$

with z in kilometers, as shown in Fig. 8. Note that the wind speed reaches values of the order of Mach number 0.1 near the altitude of 40 km.

The microphones have been taken to be separated by the distance $d=2$ km, which is on the order of the proposed monitoring stations[4] and to each measure a time delay of 3.39 s, i.e., $\Delta t_1=\Delta t_2=-3.39$ s. Thus, $a=b=-\sqrt{3}$ and the direction cosines to the source from the position $(\tilde{x},\tilde{y},\tilde{z})=(1,1,0)$, given by Eq. (13), are $\cos\alpha_S=\cos\beta_S=\cos\gamma_S=1/\sqrt{3}$, as shown by Eqs. (9) and (12). Note that the source plane makes an angle of 45° with both the x and y axes, and thus the velocity only in the x direction assumed above will represent a cross wind through the source plane. For this example, a turning point exists near an altitude of 50 km.

The incoming ray has direction vector given by

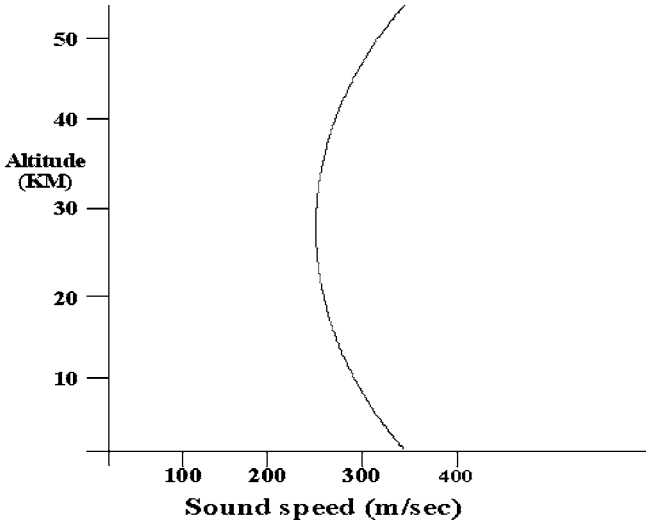

FIG. 7. Sound speed profile.

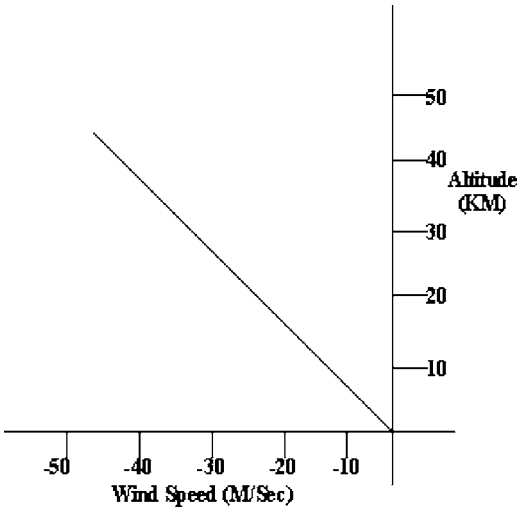

FIG. 8. Sound speed profile.

$$\mathbf{n} = -\cos\alpha\mathbf{i} - \cos\beta\mathbf{j} - \cos\gamma\mathbf{k} = -\frac{1}{3}(\mathbf{i}+\mathbf{j}+\mathbf{k}),$$

since the direction cosines determined were toward the source. Equations (16) were integrated in nondimensional form backward in time with $\Delta\tilde{t}=0.5$ from the final position given by Eq. (13). The results are shown in Fig. 9, which depicts the nondimensional ray position at times previous to its arrival at the microphone array.

Note that the maximum altitude of the ray is near a nondimensional height of 25 that corresponds to the turning point near 50 km. The ray path deviates from the apparent source plane where $x=y$ due to the cross-flow through the source plane. The integration was terminated when the ray position returned to the surface of the earth. If the source was in the atmosphere, its location would lie along the ray path shown in Fig. 9. If the source was on the surface of the Earth and the ray path does not include a reflection from the surface, the results indicate that its position lies at the nondimensional point $\tilde{x}=63.16, \tilde{y}=55.88$ from the center of the array. The sound would have taken 102 nondimensional time units to propagate from the source to the array. If reflection from the surface was expected, the boundary condition of angle of incidence=angle of reflection could be imposed and the subsequent ray path followed by further backward integration.

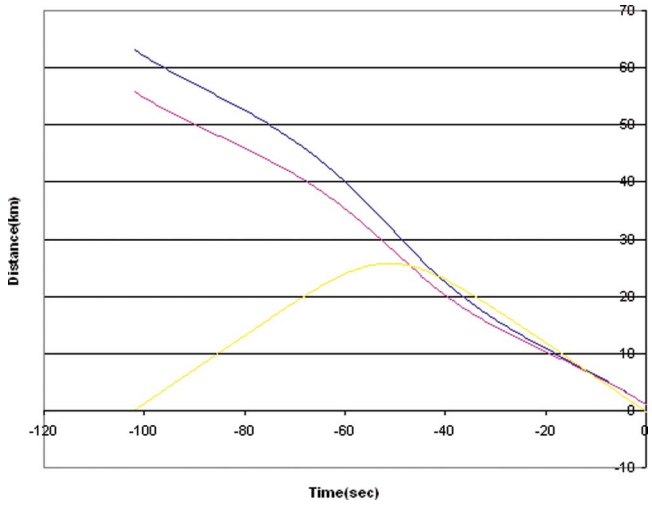

FIG. 9. Backward integration results.

IV. CONCLUSION

In this paper we have developed a backward integration method for locating the source of atmospheric radiation based upon acoustic data from a standard array of microphones. The analysis determines the direction cosines to the apparent source location; not only is the azimuthal direction but also the apparent elevation of the source is defined. The backward integration fully accounts for turning points in the atmosphere and employs the best available information on wind velocity and sound speed. An array of five microphones in the shape of a cross appears to be preferable in terms of simplifying the data analysis. The technique is readily implemented and should decrease the uncertainty in source location. The accuracy is limited only by the timeliness of the wind velocity and sound speed data, assuming accuracy of the time delay measurements.

ACKNOWLEDGMENTS

We would like to acknowledge the NASA Glenn and Langley Research Centers for interest and support of our research. This research was partially conducted under the NASA Grants No. NAG-3-2249 and No. 2422.

[1]A. J. Zuckerwar, "Infrasonic emissions from local meteorological events: A summary of data taken throughout 1984," NASA TM 87686, 1986.
[2]D. C. Alix, P. D. Simich, H. Wassaf, and F. Y. Wang, "Acoustic characterization of wake vortices in ground effect," AIAA Paper No. 2005-0260, 2005.
[3]R. P. Dougherty, F. Y. Wang, E. R. Booth, M. E. Watts, N. Fenichel, and R. E. D'Errico, "Aircraft wake vortex measurements at Denver International Airport," AIAA Paper No. #2002-2880, 2002.
[4]D. O. ReVelle and R. W. Whitaker, "Infrasonic detection of a leonid bolide: 1998 November 17," Meteorit. Planet. Sci. **34**, 995–1005 (1999).
[5]D. J. Brown, J. Wang, C. N. Katz, A. Gault, and R. LeBras, "Infrasonic processing at the prototype international data center," 21st Seismic Research Symposium, Las Vegas, NV, 21–24 September, 1999.
[6]A. D. Pierce, *Acoustics* (Acoustical Society of America, Woodbury, NY, 1991).
[7]W. D. Hayes, R. C. Haefeli, and H. E. Kulsrud, "Sonic boom propagation in a stratified atmosphere, with computer program," NASA CR-1299, 1969.

Ultrasonic wave propagation across a thin nonlinear anisotropic layer between two half-spaces

Jeff Sadler,[a] Brian O'Neill, and Roman Gr. Maev
Department of Physics, University of Windsor, Windsor, Ontario, N9B 3P4, Canada

(Received 2 April 2004; revised 13 April 2005; accepted 17 April 2005)

Boundary conditions and perturbation theory are combined to create a set of equations which, when solved, yield the reflected and transmitted wave forms in the case of a thin layer of material that is perfectly bonded between two isotropic half-spaces. The set of perturbed boundary conditions is created by first using the fully bonded boundary conditions at each of the two interfaces between the thin layer and the half-spaces. Then, by restricting the layer's thickness to be much smaller than an acoustic wavelength, perturbation theory can be used on these two sets of boundary equations, producing a set of equations which effectively treat the thin layer as a single interface via a perturbation term. With this set of equations, the full range of incident and polar angles can be considered, with results general enough to use with a layer that is anisotropic, nonlinear, or both anisotropic and nonlinear. Finally the validity of these equations is discussed, comparing the computer simulation results of this theory to results from standard methods, and looking at cases where the results (or various properties of the results) are known or can be predicted. [DOI: 10.1121/1.1929227]

PACS number(s): 43.20.Bi, 43.20.El, 43.25.Dc [MFH] Pages: 51–59

I. INTRODUCTION

In this paper, the situation of a thin layer between two isotropic half-spaces is considered. The thin layer is perfectly bonded to each of the half-spaces, is restricted to have a thickness much less than an acoustic wavelength, and may be linear or nonlinear, and isotropic or anisotropic. The restriction to a thin layer allows a perturbation method to be used to create a set of boundary equations in which the thin layer is effectively treated as a single interface, instead of two separate interfaces. In addition, by using the stress–strain relation and the acoustic equation of motion, the terms dealing with the acoustic waves in the interface can be related to the acoustic waves in the half-spaces. This gives this theory the advantage that it accounts for the multiple reflections of the acoustic waves internal to the thin layer via a single term, which does not contain any direct references to the fields inside the thin layer. The perturbed boundary equations also allow for non-normal incident angle waves to be considered, and for the addition of both nonlinearity and anisotropy to the thin layer. In addition, the final boundary conditions require only minimal information about the thin layer and the half-spaces.

Most literature examining the case of a thin layer of material tends to be concerned with either anisotropy or nonlinearity alone, and the nonlinear examinations are typically only concerned with normal incident waves. In the case of an anisotropic thin layer, a boundary condition approach has been used by Nicklasson *et al.*[1,2] to consider guided waves in an anisotropic thin layer between two half-spaces,[1] and also in the case of a thin layer coating on an isotropic half-space.[2] Rokhlin and Huang[3,4] also consider the case of a thin layer bonded between two media, but choose to use a transfer matrix approach to examine the reflected and transmitted waves in the case where all the media anisotropic. The case of a nonlinear thin layer between two half-spaces has been described by Rothenfusser *et al.*,[5] and Hedberg and Rudenko.[6] Hedberg and Rudenko[6] use a finite element model to solve the problem and add nonlinearity to the thin layer by using a nonlinear density (the density is dependent on pressure). On the other hand Rothenfusser *et al.*[5] use a finite element model and add nonlinearity to the thin layer via the stress–strain relation using an expansion on the strain terms. This paper and our previous paper[7–9] all describe the situation of a thin layer between two isotropic half-spaces, where thin layer can be both nonlinear and anisotropic, and examine the resulting reflected and transmitted waves due to an incident wave. Of the various options to include nonlinearity[5,6,10,11] this paper chooses to add nonlinearity via the stress–strain relation.

II. THEORY

As mentioned in Sec. I the situation being considered consists of two half-spaces (referred to as media I and II) connected by a thin layer (L) of size δ, where δ is much smaller than an acoustic wavelength. The boundary between the half-spaces and the thin layer is assumed to be perfectly bonded. In the following sections, perturbation theory is used to create boundary conditions, which will be used to describe the reflected and transmitted waves in the half-spaces and accounts for the waves internal to the thin layer via a single term. The thin layer may be isotropic, or anisotropic, and linear or nonlinear, and has its orientation defined by the unit vector **n**, which is perpendicular to the interface (Fig. 1). To begin the process, the boundary conditions at each interface are found, then a perturbation expansion is used to create a

[a]Electronic mail: sadler1@uwindsor.ca

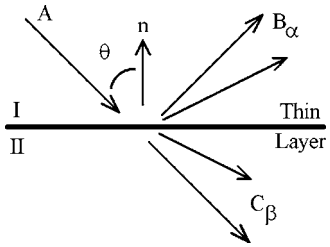

FIG. 1. Setup of thin layer between two half spaces showing the normal (**n**), the incident wave (A), the reflected waves (B_α), and the transmitted waves (C_β). There may be up to three reflected and transmitted waves.

set of perturbed boundary conditions. Next, any reference to waves internal to the thin layer will be eliminated, then the required alterations due to nonlinearity will be added to the boundary conditions. Finally the method for solving these equations in terms of the reflected (B_α) and transmitted (C_β) wave forms will be examined (α and β are possible polarizations of the waves) to create a solution proportional to the incident wave (A) of any polarization, and is not restricted to being a plane wave.

A. Perturbed boundary conditions

As each interface is assumed to be perfectly bonded, this requires the displacement components (u_i) and the stress components (T_{ij}) perpendicular to the interface to be continuous across each boundary. The boundary conditions that satisfy these continuity requirements at each interface are

$$u_i^{\mathrm{I}}(0,t) = u_i^L(0,t), \tag{1}$$

$$u_i^L(\delta n_k,t) = u_i^{\mathrm{II}}(\delta n_k,t), \tag{2}$$

$$n_j T_{ij}^{\mathrm{I}}(0,t) = n_j T_{ij}^L(0,t), \tag{3}$$

$$n_j T_{ij}^L(\delta n_k,t) = n_j T_{ij}^{\mathrm{II}}(\delta n_k,t), \tag{4}$$

where δ is the thickness of the layer, n_k is the k component of the unit vector **n**, the subscripts i and j follow Einstein summation convention and are valued 1, 2, or 3, and the superscripts denote the half-spaces (I and II) and the thin layer (L). To relate the displacement and stress on each side of the thin layer, perturbation theory can be used to expand the displacement and stress about δ to obtain

$$u_i^L(\delta n_k,t) = u_i^L(0,t) + n_p \frac{\partial u_i^L(0,t)}{\partial x_p}\delta, \tag{5}$$

$$T_{ij}^L(\delta n_k,t) = T_{ij}^L(0,t) + n_p \frac{\partial T_{ij}^L(0,t)}{\partial x_p}\delta. \tag{6}$$

Equations (5) and (6) combined with Eqs. (1)–(4) create the set of "perturbed boundary conditions"

$$u_i^{\mathrm{II}}(\delta n_k,t) - u_i^{\mathrm{I}}(0,t) = n_p \frac{\partial u_i^L(0,t)}{\partial x_p}\delta, \tag{7}$$

$$n_j(T_{ij}^{\mathrm{II}}(\delta n_k,t) - T_{ij}^{\mathrm{I}}(0,t)) = n_j n_p \frac{\partial T_{ij}^L(0,t)}{\partial x_p}\delta, \tag{8}$$

where the evaluation points in Eqs. (7) and (8) will be understood implicitly from this point on. The actual evaluation at the position δ can either be performed exactly, or by using an expansion similar to that in Eqs. (5) and (6). It is worth noting that such an expansion, for linear media, effectively introduces a small phase shift in the signal. In a practical sense, such a phase shift is unmeasurable, unless some type of mode conversion or harmonic conversion is also going on. It is therefore not of great importance, in many cases, whether the u^{II}, or T^{II} is taken strictly at $x=\delta n_k$ or at $x=0$. The displacement and stress in media I and II are defined with respect to the reflected (B_α) and transmitted (C_β) waves, and the incident wave form. The coefficients are obtained by setting $\delta=0$ in Eqs. (7) and (8) producing a set of equations[9] which can be solved using the typical matrix methods either symbolically or numerically. In the case of the thin layer (L), the displacement and stress must be approximated with respect to the zeroth-order results (no thin layer). It is noted, that if one wished, the terms relating to the thin layer can also be written as being evaluated at $(n_k\delta,t)$, or the average of the two positions (i.e., $[f(0,t)+f(n_k\delta,t)]/2$), by choosing alternative expansions for Eqs. (5) and (6). These various options though will yield results which do not differ significantly from one another.

B. Displacement and stress internal to the thin layer

Relating the displacement and stress internal to the thin layer cannot be done by simply changing the index L in Eqs. (7) and (8) to the index I. Any derivatives of displacement or stress with components in the **n** direction create results that are discontinuous across the interfaces (these will be referred to as discontinuous derivatives). However, derivatives of displacement or stress with components perpendicular to **n** give results that are continuous across the interface and can thus be related directly to the equivalent derivative in the half-spaces (i.e., this is a "continuous derivative" and the index can be changed from L to I or II). Because the derivatives in Eqs. (7) and (8) are projected into the direction **n** they are discontinuous and must be related to other quantities. To begin this process, consider Hooke's law

$$T_{ij} = c_{ijkl}\epsilon_{kl} = c_{ijkl}\frac{\partial u_k}{\partial x_l}, \tag{9}$$

and the acoustic equation of motion

$$\rho\frac{\partial^2 u_i}{\partial t^2} = \frac{\partial T_{ij}}{\partial x_j}. \tag{10}$$

To separate the continuous derivatives in Eqs. (9) and (10), from those which are discontinuous, the projection onto the plane perpendicular to **n** (or more simply the projection into plane of the thin layer) will be used. This projection (ξ) is defined as

$$\xi_{lp} \equiv \delta_{lp} - n_l n_p. \tag{11}$$

Considering the thin layer specifically, and using Eq. (11) to separate the continuous and discontinuous derivatives in Hooke's Law [Eq. (9)] yields

$$T_{ij}^L = c_{ijkl}^L n_l n_p \frac{\partial u_k^L}{\partial x_p} + c_{ijkl}^L \frac{\partial u_k^L}{\partial x_p} \xi_{lp}, \tag{12}$$

where it should be noted that the second displacement derivative is continuous at both interfaces. The derivatives in the acoustic equation of motion [Eq. (10)] can also be separated using Eq. (11), and then be rearranged to obtain

$$n_j n_p \frac{\partial T_{ij}^L}{\partial x_p} = \rho \frac{\partial^2 u_i^{\mathrm{I}}}{\partial t^2} - \frac{\partial T_{ij}^L}{\partial x_p} \xi_{jp}, \tag{13}$$

which may be used directly as the right-hand side of Eq. (8). In Eq. (13) it is valid to change the medium index on the time derivative of displacement from L to I, because if u_i is continuous at the boundary so must $\dot{u}_i$ and $\ddot{u}_i$ as frequency does not change at the boundaries. To discover the unknown stress derivative in Eq. (13) and the displacement derivative in Eq. (7) the altered form of Hooke's law [Eq. (12)] must be considered further. To begin, Eq. (12) is multiplied by an overall factor of n_j so that a change of index from L to I on stress becomes possible via Eq. (3). Combined with a change of index from L to I on the continuous displacement term yields

$$n_j T_{ij}^{\mathrm{I}} = n_j c_{ijkl}^L n_l n_p \frac{\partial u_k^L}{\partial x_p} + n_j c_{ijkl}^L \frac{\partial u_k^{\mathrm{I}}}{\partial x_p} \xi_{lp}. \tag{14}$$

Equation (14) can then be rearranged to solve for $\partial u_i^L / \partial x_p$ obtaining

$$n_p \frac{\partial u_k^L}{\partial x_p} [n_s n_t c_{iskt}^L]^{-1} n_j \left(T_{ij}^{\mathrm{I}} - c_{ijmn}^L \frac{\partial u_m^{\mathrm{I}}}{\partial x_p} \xi_{np} \right), \tag{15}$$

where indices on the stiffness tensors and the displacement derivatives have been changed so as not to imply unwanted summations. It should also be noted that in Eq. (15) the expression $[n_s n_t c_{iskt}^L]^{-1}$ is an inverse matrix and not a single numerical value. With the displacement derivative expressed in terms of known quantities [Eq. (15)], the altered form of Hooke's Law [Eq. (12)] is now used to find the stress derivatives needed in Eq. (13). Taking the necessary position derivative Hooke's Law [Eq. (12)], and multiplying by the projection ξ yields

$$\xi_{jq} \frac{\partial T_{ij}^L}{\partial x_q} = c_{ijkl}^L n_l n_p \xi_{jq} \frac{\partial}{\partial x_q} \frac{\partial u_k^L}{\partial x_p} + c_{ijkl}^L \xi_{jq} \frac{\partial}{\partial x_q} \frac{\partial u_k^{\mathrm{I}}}{\partial x_p} \xi_{lp}, \tag{16}$$

where the medium index on the last derivative is valid to change from L to I as both of the derivatives are continuous. To summarize, the final perturbed boundary conditions are

$$u_k^{\mathrm{II}} - u_k^{\mathrm{I}} = [n_s n_t c_{iskt}^L]^{-1} n_j \left(T_{ij}^{\mathrm{I}} - c_{ijmn}^L \frac{\partial u_m^{\mathrm{I}}}{\partial x_p} \xi_{np} \right) \delta, \tag{17}$$

$$n_j (T_{ij}^{\mathrm{II}} - T_{ij}^{\mathrm{I}}) = \left(\rho \frac{\partial^2 u_i^{\mathrm{I}}}{\partial t^2} - c_{ijkl}^L \left(n_i n_p \xi_{jq} \frac{\partial}{\partial x_q} \frac{\partial u_k^L}{\partial x_p} + \xi_{jq} \frac{\partial}{\partial x_q} \frac{\partial u_k^{\mathrm{I}}}{\partial x_p} \xi_{lp} \right) \right) \delta, \tag{18}$$

where $n_l (\partial u_k^L / \partial x_p)$ may also be replaced using Eq. (15) because the operator $\xi_{jq}(\partial / \partial x_p)$ produces continuous results. It should be pointed out that the displacement and stress components in Eqs. (17) and (18) are continuous in the zeroth order of the approximation. Thus the superscript I on the right-hand side may be replaced with the superscript II with little effect, if one finds this arrangements simpler to work with. The best approximation might come from averaging the two, that is using $\frac{1}{2}(u^{\mathrm{I}} + u^{\mathrm{II}})$ and $\frac{1}{2}(T^{\mathrm{I}} + T^{\mathrm{II}})$. One should recall, however that quantities in media II are evaluated at the position $(n_k \delta, t)$.

C. Alterations due to nonlinearity in thin layer

Considering a classical nonlinearity added to Hooke's law via a power series expansion about strain allows the stress of the layer to be found in a very similar way as the previous section. Again the process begins by considering Hooke's law, but now in the nonlinear form. To obtain this form first consider the expansion of the free energy (E) about powers of strain[12] to obtain the relation

$$T_{ij} = \frac{\partial E}{\partial \epsilon_{ij}} = c_{ijkl} \epsilon_{kl} + \frac{1}{2} c_{ijklmn} \epsilon_{kl} \epsilon_{mn} + \cdots, \tag{19}$$

which can be written as

$$T_{ij}^{\mathrm{NL}} = c_{ijkl}^L \epsilon_{kl} (1 + \beta_{mn} \epsilon_{mn} + \chi_{mnop} \epsilon_{mn} \epsilon_{op} + \cdots), \tag{20}$$

where the superscript NL denotes that the stress is nonlinear. Using the definition of strain, and rewriting the nonlinear portion into a single function (F^L), Eq. (20) can be rewritten as

$$T_{ij}^{\mathrm{NL}} = c_{ijkl}^L \epsilon_{kl}^L (1 + F^L) = T_{ij}^L (1 + F^L), \tag{21}$$

where $F^L = (\beta_{mn} \epsilon_{mn} + \chi_{mnop} \epsilon_{mn} \epsilon_{op} + \cdots)$, and it is recalled that the superscript L denotes quantities in the thin layer. To consider the changes due to nonlinearity in the thin layer the perturbed boundary condition for the stress [Eq. (8)] must now be written in terms of this nonlinear stress (T^{NL}) in the thin layer,

$$n_j (T_{ij}^{II} - T_{ij}^{\mathrm{I}}) = n_j n_p \frac{\partial T_{ij}^{\mathrm{NL}}}{\partial x_p} \delta. \tag{22}$$

Taking the necessary derivative of stress in Eq. (21) with respect to position yields

$$\frac{\partial T_{ij}^{\mathrm{NL}}}{\partial x_n} = \frac{\partial T_{ij}^L}{\partial x_n} (1 + F^L) + T_{ij}^L \frac{\partial F^L}{\partial x_n}, \tag{23}$$

where the term $\partial T_{ij}^L / \partial x_n$ is the linear quantity, and the remainder of the equation is due to the nonlinearity. Finally, taking the necessary projections yields the perturbed nonlinear boundary conditions whose linear part is the same as in Eq. (8), and includes an additional part involving the nonlinearity,

$$n_j(T_{ij}^{II} - T_{ij}^{I}) = n_j n_p \frac{\partial T_{ij}^{L}}{\partial x_p}(1 + F^L)\delta + n_j n_p T_{ij}^{L} \frac{\partial F^L}{\partial x_p}\delta. \quad (24)$$

This allows the solution for the reflected and transmitted waves to be broken down into linear and nonlinear parts, thus making it essentially a third level in a perturbation expansion. The nonlinear function F^L can be evaluated exactly from the strains, evaluated from the displacements using separate continuous and discontinuous derivatives,

$$\frac{\partial u_k^L}{\partial x_l} = n_l n_p \frac{\partial u_k^L}{\partial x_p} + \xi_{lp} \frac{\partial u_k^{\mathrm{I}}}{\partial x_p}, \quad (25)$$

where $n_p(\partial u_k^L/\partial x_p)$ is known via Eq. (15). To evaluate $n_p(\partial F/\partial x_p)$, exactly the same separation as in Eq. (25) can be used, and the derivative $\partial/\partial x_p$ can be taken first to yield

$$n_p \frac{\partial}{\partial x_p}\frac{\partial u_m^L}{\partial x_n} = \left(n_n n_q \frac{\partial}{\partial x_q} + \xi_{nq}\frac{\partial}{\partial x_q}\right) n_p \frac{\partial u_m^L}{\partial x_p}. \quad (26)$$

The derivative $\xi_{nq}(\partial/\partial x_q)$ produces continuous results and can be combined with Eq. (15), while the derivative $n_n n_q(\partial/\partial x_q)$ can be evaluated by taking an additional position derivative of Eq. (12), and rearranging to yield

$$n_q n_p \frac{\partial^2 u_k^L}{\partial x_p \partial x_q} = [n_s n_t c_{iskt}^L]^{-1} n_q n_j \left(\frac{\partial T_{ij}^L}{\partial x_q} - c_{ijmn}^L \frac{\partial}{\partial x_p}\frac{\partial u_m^L}{\partial x_q}\xi_{np}\right). \quad (27)$$

This result, although rather complicated in appearance, contains only known quantities evaluated in the half-spaces.

III. PERTURBATION TYPE SOLUTION FOR SINGLE HARMONIC PLANE WAVES AT NORMAL INCIDENCE

As a general solution for the problem could be quite lengthy and may require a description in the form of a numerical treatment, it is beneficial to use a plane wave solution so that the mathematical detail in the problem can be shown more easily. It should be noted that even though this solution is presented only for a harmonic plane wave, the theory itself does not necessarily require this restriction. As the theory to this point has been presented as a perturbation type expansion this approach will be continued in this section, though other alternative solutions are possible and perhaps easier depending upon the reader's point of view. To begin with a perturbation type solution it is ideal to be able to express the wave in a three level expansion such as

$$\text{Wave} = \text{zeroth order} + \text{Linear perturbation term} + \text{Nonlinear term}, \quad (28)$$

where each term corresponds in turn to a set of equations as follows, the zeroth-order equations [Eqs. (7) and (8) with $\delta = 0$], the perturbed boundary equations [Eqs. (7) and (8)], and the nonlinear equation [Eq. (24)]. This perturbation approach provides the advantage of allowing each level of the expansion separately, thus only the changes due to the thin layer can be examined. If the entire problem were solved the "background" of the two layer solution would need to be subtracted to examine the changes due to the thin layer. In the wave forms the perturbation term corresponds to the waves crossing the additional thin layer region, thus a small phase shift (ϕkd) must be added to each wave form

$$B_\alpha(\omega t + k_i^\alpha x_i) \rightarrow B_\alpha(\omega t + k_i^\alpha x_i + \phi_\alpha(t) n_j k_j^\alpha \delta), \quad (29)$$

$$C_\beta(\omega t - k_i^\beta x_i) \rightarrow C_\beta(\omega t - k_i^\beta x_i + \phi_\beta(t) n_j k_j^\beta \delta), \quad (30)$$

where B_α and C_β are the reflected and transmitted waves, respectively, and k_i^α is a component of the wave vector, with polarization α. It should be noted that the repetition of Greek letters does not imply summation; any summation of polarizations will be written explicitly. Taking the phase change from crossing the thin layer to be very small allows the wave forms to be expanded to first order in δ to obtain:

$$B_\alpha(\omega t + k_i^\alpha x_i) = B_0^\alpha(\omega t + k_i^\alpha x_i) + \phi_\alpha(t) n_j k_j^\alpha \delta \times B_0'^\alpha(\omega t + k_i^\alpha x_i), \quad (31)$$

$$C_\beta(\omega t - k_i^\beta x_i) = C_0^\beta(\omega t - k_i^\beta x_i) + \phi_\beta(t) n_j k_j^\beta \delta \times C_0'^\beta(\omega t - k_i^\beta x_i), \quad (32)$$

where B_0^α and C_0^β are the zeroth-order solutions, and $B_0'^\alpha$ and $C_0'^\beta$ are derivatives with respect to the argument. The assumption that the phase shift (ϕkd) is small is noted to mean that both d, the thickness of the thin layer, as well as the quantity ϕ are small, where ϕ is related to the change in the impedance between the two layers and the thin layer.[7] These wave forms in Eqs. (31) and (32) are known to be directly proportional to the incident wave, (A), via the reflection (R_α) and transmission (T_β) coefficients.[8,9] Thus, it is found that

$$B_\alpha(0,t) = R_\alpha A(0,t) + \phi_\alpha(t) n_j k_j^\alpha \delta R_\alpha A'(0,t), \quad (33)$$

$$C_\beta(\delta,t) = T_\beta A(\delta,t) + \phi_\beta(t) n_j k_j^\beta \delta T_\beta A'(\delta,t), \quad (34)$$

where A is the incident wave of some polarization, and A' is the first derivative with respect to the argument. In the case of a nonlinear thin layer, it is simplest to add a third term to the wave expansion to deal with the nonlinear boundary conditions [Eq. (24)]. Thus, the parameter ϕ is expanded into linear and nonlinear terms

$$\phi_\alpha(t) \rightarrow \phi_\alpha + \phi_\alpha^{\mathrm{NL}}(t), \quad (35)$$

$$\phi_\beta(t) \rightarrow \phi_\beta + \phi_\beta^{\mathrm{NL}}(t). \quad (36)$$

Considering the fact that ϵ_{ij} can be related directly to A', it is expected that, in the case of classical nonlinearity [Eq. (20)] the nonlinear factor will have the form

$$\phi^{\mathrm{NL}}(t) \propto (C_1 A'(t) + C_2(A'(t))^2 + \cdots), \quad (37)$$

allowing the solutions of the wave forms [Eqs. (33) and (34)] to be expanded further. However, the classical nonlinearity represents just a specific case; a more general nonlinearity would result in a different form.

The displacement is the sum of the partial waves, which in this one-dimensional case of a normal incident longitudinal wave is

$$u_z^{\mathrm{I}}(0,t) = (1 + R)A(0,t) + \phi_R k_z^{\mathrm{I}} \delta R A'(0,t), \quad (38)$$

$$u_z^{\mathrm{II}}(\delta,t) = TA(\delta,t) + \phi_T k_z^{\mathrm{II}} \delta TA'(\delta,t), \tag{39}$$

which in turn can be used to define the stress

$$T_{zz}^{\mathrm{I}}(0,t) = \omega Z_{\mathrm{I}}(-1+R)A'(0,t) + \omega Z_{\mathrm{I}} \phi_R k_z^{\mathrm{I}} \delta RA''(0,t), \tag{40}$$

$$T_{zz}^{\mathrm{II}}(\delta,t) = -\omega Z_{\mathrm{II}} TA'(\delta,t) + \omega Z_{\mathrm{II}} \phi_T k_z^{\mathrm{II}} \delta TA''(\delta,t), \tag{41}$$

where Z is the impedance, k_z is the wave number in the direction z which has arbitrarily been chosen to be perpendicular to the sample (that is the vector **n** used in the theory to be in the direction z), and the unwritten polarizations are implicitly longitudinal. In this one-dimensional situation the initial boundary conditions [Eqs. (5) and (6)] can be rewritten as

$$u_z^{\mathrm{II}}(\delta,t) - u_z^{\mathrm{I}}(0,t) = \frac{\partial u_z^L(0,t)}{\partial x_z}\delta, \tag{42}$$

$$T_{zz}^{\mathrm{II}}(\delta,t) - T_{zz}^{\mathrm{I}}(0,t) = \frac{\partial u_z^L(0,t)}{\partial x_z}\delta, \tag{43}$$

where all other components are zero. In the final boundary conditions [Eqs. (17) and (18)], the only factors which yield nonzero results are u_z^{I}, T_{iz}^{I}, and derivatives with respect to $\partial/\partial x_z$. Thus the much simplified boundary conditions are

$$u_z^{\mathrm{II}} - u_z^{\mathrm{I}} = [c_{izzz}^L]^{-1} T_{iz}^{\mathrm{I}} \delta, \tag{44}$$

$$T_{zz}^{\mathrm{II}} - T_{zz}^{\mathrm{I}} = \rho \frac{\partial^2 u_z^{\mathrm{I}}}{\partial t^2}\delta. \tag{45}$$

Inserting Eqs. (38)–(41) into the boundary conditions [Eqs. (44) and (45)] creates equations with derivatives of the incident wave with respect to both position and time, to relate these two derivatives we utilize the relation

$$\ddot{A}(0,t) = \omega^2 \frac{\partial^2 A(0,t)}{\partial (wt)^2} = \omega^2 A''(0,t). \tag{46}$$

Thus, eliminating the first-order solution and common factors, the boundary conditions can be written as

$$\phi_T k_z^{\mathrm{II}} T - \phi_R k_z^{\mathrm{I}} R = [c_{zzzz}^L]^{-1} \omega Z_{\mathrm{I}}(-1+R) + k_z^{\mathrm{II}} T, \tag{47}$$

$$Z_{\mathrm{II}} \phi_T k_z^{\mathrm{II}} T - Z_{\mathrm{I}} \phi_R k_z^{\mathrm{I}} R = \rho\omega(1+R) - Z_{\mathrm{II}} k_x^{\mathrm{II}} T, \tag{48}$$

which can be solved via the usual matrix methods either symbolically or numerically for the quantities $\phi_R k_z^{\mathrm{I}} R$ and $\phi_T k_z^{\mathrm{II}} T$. It should be noted that the final terms on the right-hand side of Eqs. (47) and (48) are the result from expanding the incident wave $A(\delta,t)$ about delta so that common factors of $A(0,t)$ could be eliminated.

Multiple harmonic plane waves

In the case of an incident wave which is not made up of a single harmonic, this perturbation expansion solution is still useful as the equations can again be written in terms of the incident wave form, and the necessary derivatives, without the need for a decomposition in terms of individual harmonics. To begin the initial wave forms can be expressed as a sum of many single harmonic plane waves

$$B_\alpha(x,t) = \sum_m b_m^\alpha (c_m \omega_0 t + c_m k_i^\alpha x_i), \tag{49}$$

where b_m are single harmonic plane wave forms of varying amplitudes, and c_m are positive nonzero constants relating the frequencies in the total wave form B. Adding the phase change from crossing the thin layer and expanding to first order

$$B_\alpha(x,t) = \sum_m b_0^\alpha (c_m \omega_0 t + c_m k_i^\alpha x_i) + \phi_\alpha(t) n_j k_j^\alpha \delta \sum_m c_m b'^\alpha (c_m \omega_0 t + c_m k_i^\alpha x_i), \tag{50}$$

which can be rewritten as

$$B_\alpha(x,t) = B_0^\alpha(x,t) + \phi_\alpha(t) n_j k_j^\alpha \delta B_0'^\alpha(x,t). \tag{51}$$

Thus the expression of the wave forms in terms of harmonics is not needed and the final form of the wave forms in Eqs. (33) and (34) is still valid. The solution continues as before with the same final result, but with respect to the reference values ω_0 and $k^\alpha = \omega_0/c^\alpha$, where c^α is the acoustic velocity of a wave with polarization α. It should be noted that this reference ω_0 has only been used so that the notation in the previous section could be maintained, mathematically it is easiest to set this to 1 making c_m the individual angular frequencies. This same perturbation solution approach can be expanded to the nonlinear case and again allows the problem to be solved without the need of an expansion in terms of harmonics. This allows for the use of incident wave forms which are difficult to express in terms of an expansion of harmonics.

IV. COMPARISON TO TRANSFER MATRIX METHOD (REFS. 3 AND 4)

It can be shown that by restricting the incident wave to a harmonic wave, the boundary conditions [Eqs. (17) and (18)] of this theory are identical to the second-order boundary conditions found via the transfer matrix method[4] (where in this case an orthotropic thin layer is considered). We begin by using the coordinate system described by Rokhlin[4] (the vector **n** in the direction z, and the plane of incidence in the xz plane), the boundary conditions in Eqs. (17) and (18) then become

$$u_k^{\mathrm{II}} - u_k^{\mathrm{I}} = [c_{izkz}^L]^{-1} \left(T_{iz}^{\mathrm{I}} - c_{izmn}^L \frac{\partial u_m^{\mathrm{I}}}{\partial x_p} \xi_{np} \right) \delta, \tag{52}$$

$$T_{iz}^{\mathrm{II}} - T_{iz}^{\mathrm{I}} = \left(\rho \frac{\partial^2 u_i^{\mathrm{I}}}{\partial t^2} - c_{ijkz}^L \xi_{jq} \frac{\partial}{\partial x_q} \frac{\partial u_k^L}{\partial x_p} + c_{ijkl}^L \xi_{jq} \frac{\partial}{\partial x_q} \frac{\partial u_k^{\mathrm{I}}}{\partial x_p} \xi_{lp} \right) \delta. \tag{53}$$

Restricting the stiffness matrix to an orthotropic system the displacement condition simplifies to

$$u_x^{\mathrm{II}} - u_x^{\mathrm{I}} = \left(s_{xzxz}^L T_{xz}^{\mathrm{I}} - \frac{\partial u_z^{\mathrm{I}}}{\partial x_x} \right) \delta, \tag{54}$$

$$u_y^{\mathrm{II}} - u_y^{\mathrm{I}} = s_{yzyz}^L T_{iz}^{\mathrm{I}} \delta, \tag{55}$$

$$u_z^{\mathrm{II}} - u_z^{\mathrm{I}} = \left(s_{zzzz}^L T_{iz}^{\mathrm{I}} - \frac{c_{zzxx}^L}{c_{zzzz}^L} \frac{\partial u_x^{\mathrm{I}}}{\partial x_x} - \frac{c_{zzyx}^L}{c_{zzzz}^L} \frac{\partial u_y^{\mathrm{I}}}{\partial x_x} \right) \delta, \tag{56}$$

where due to the diagonal in the lower half of the compliance and stiffness matrix for an orthotropic system we were able to use the property

$$s_{ijij} = [c_{ijij}]^{-1} = \frac{1}{c_{ijij}} \ (i \neq j). \tag{57}$$

When we assume the incident wave is a harmonic wave (that is $A = e^{i(kx \pm wt)}$) we obtain

$$u_x^{\mathrm{II}} - u_x^{\mathrm{I}} = (s_{xzxz}^L T_{xz}^{\mathrm{I}} - ik_x u_z^{\mathrm{I}}) \delta, \tag{58}$$

$$u_y^{\mathrm{II}} - u_y^{\mathrm{I}} = s_{yzyz}^L T_{yz}^{\mathrm{I}} \delta, \tag{59}$$

$$u_z^{\mathrm{II}} - u_z^{\mathrm{I}} = \left(s_{zzzz}^L T_{zz}^{\mathrm{I}} - ik_x \frac{c_{zzxx}^L}{c_{zzzz}^L} u_x^{\mathrm{I}} - ik_x \frac{c_{zzyx}^L}{c_{zzzz}^L} u_y^{\mathrm{I}} \right) \delta, \tag{60}$$

which are identical to those by Rokhlin.[4] It is noted that in Rokhlin's paper the displacement and stress on the right-hand side are written using the averages of materials I and II, but as previously mentioned, the continuity of the stress and displacement will ensure components labeled I, II and the average of I and II are all approximately the same. Although the stress equations are more complicated, the two theories again yield identical results. Thus, this theory will have the same level of error as the transfer matrix method for harmonic waves, while allowing for a more general range of wave forms. This allows the consideration of a nonlinear thin layer in the time domain, thereby encompassing the broadest possible range of nonlinear behavior.

V. VALIDATION CASES

In this section, we explore the validity of the proposed approximation using special cases where certain characteristics may be inferred beforehand. By comparing the results of this theory to results from other models, the amount of error resulting from the perturbation method may be inferred, or at least estimated. The analysis will begin by examining the deviation of the results from an energy conserving state, then results will be compared to the exact solution for a linear three layer system at normal incidence, and finally the case of an anisotropic layer will be used to look at the influence of symmetry on the waves. As each case contains different restrictions on materials and angles, these restrictions will be detailed in the appropriate section, and the specific numerical values used for the material properties can be found in Tables I and II. While reading the proceeding sections, one should keep in mind that due to the restriction of the layer thickness being much less than the acoustic wavelength (required so that the perturbation approach remain valid), any classical bulk nonlinearity is going to have little impact. It more likely should be thought of as representing a very thin layer of adhesion bonding (sometimes referred to as the interphase region) between the two materials, or any other small region possessing different material properties than the half-spaces.

TABLE I. Isotropic material properties.

Material	Density (kg/m^3)	Velocity (m/s) (longitudinal)	Velocity (m/s) (transverse)
Aluminum	2700	6420	3040
Acrylic	1190	2750	1375
Steel	7900	5960	3235
Epoxy	1100	2700	1300
Epoxy (type II)	1150	2400	1200

A. Conservation of energy

The perturbation method used to approximate the wave forms [Eqs. (33) and (34)] in this theory results in an expansion where energy conservation is not possible. Despite this, it is useful to calculate the total energy as a measure of the error inherent in the approximation. In general, when materials with similar properties (velocity and density) are used, the results show very small deviations from an energy conserving state as the incident angle or layer thickness is changed. Larger discrepancies from an energy conserving state are typically found in cases where the thin layer material properties differ considerably from those of the bulk media (such as a plastic half space, and a metal thin layer). For example, a simulation with an acrylic–epoxy–acrylic sample (with 10 μm thin layer 1.0 MHz incident longitudinal wave) produces a negligible deviation (0.0005% at normal incidence, increasing to 0.001% at 85°) from an energy conserving system as the angle of incidence in changed. Increasing the size of the thin layer, in this case, also yields negligible deviation from an energy conserving state. In fact a 1% deviation is not yet reached at 18.5% of the longitudinal wavelength and a 2% deviation is only reached at roughly 26% of the longitudinal wavelength. Even though the energy is largely conserved at these sizes, the layer size is becoming a significant fraction of a wavelength and another expansion should likely be tested if one wishes to use these larger layer thickness. Alternatively, the case aluminum–epoxy–aluminum sample (with 10 μm thin layer, 1.0 MHz incident longitudinal wave) has half-spaces with much different properties than the thin layer, and is found to deviate much faster from an energy conserving state. Figure 2 shows the total energy as the angle of incidence is altered, while Fig. 3 shows the total energy as the layer thickness is increased for this case. The deviation from an energy conserving state is very small as the incident angle is changed, beginning with 0.7% deviation at normal incidence and reaching only 3% deviation at 80°. As the size of the thin layer is increased, with the angle of incidence restricted to 0°, the system moves more quickly away from an energy conserving state as the layer thickness increases, reaching a 10% deviation at roughly 1.3% of the longitudinal wavelength. Though a 10%

TABLE II. Anisotropic material properties.

Material	Density (kg/m^3)	Stiffness (GN/m^2)
Boron (hexagonal anisotropy)	1157	c_{11}=13.5 c_{33}=125.9 c_{12}=5.5 c_{13}=6.3 c_{44}=6.2

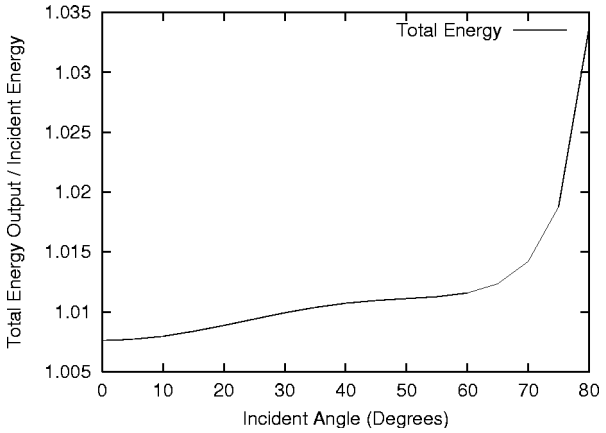

FIG. 2. Total energy change with incident angle.

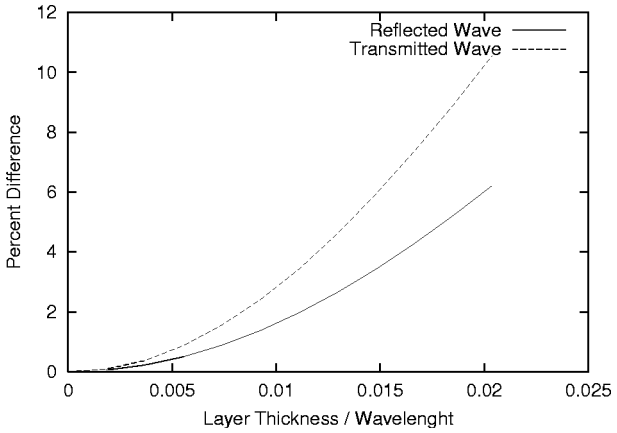

FIG. 4. Percent difference between the exact three layer solution and the thin layer approximation at normal incidence for the reflected and transmitted longitudinal waves.

error is reached rather quickly when the layer thickness is changed, a layer thickness of less than 1% of a wavelength has fairly minor deviations, only 5% at roughly 1% wavelength.

B. Comparison with the exact solution of a linear three layer system

Here a special case is considered to compare the results of the thin layer approximation to the exact results from a three layer linear system. To simplify the mathematics of the three layer system, this comparison will use only normal incidence longitudinal waves. In this three layer system, each layer is of arbitrary size, and the boundary conditions at each of the two interfaces must be considered. After some mathematics, a recursive time domain solution is used to find the reflected and transmitted waves. In general, it is discovered that the individual error in the reflected and transmitted waves are, as one would expect, found to be lower than the deviation from conservation of energy. In addition the amount of error in the two waves typically rises at different rates, though it was not possible to determine if the reflected or transmitted wave would produce the greater error in a given specific case. Again considering the case of an acrylic–epoxy–acrylic sample, the change in the percent difference between the three layer system and the thin layer approximation is considered as the size of the thin layer increases.

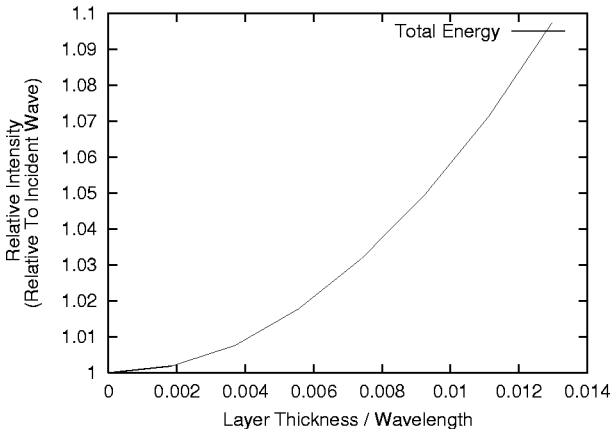

FIG. 3. Total energy change with layer size.

Here, both the reflected and the transmitted waves produce negligible error even at 4% of an acoustic wave-length. (The transmitted wave is approaching a 0.5% error, while the reflected wave is approaching a 1% error.) In the case of the aluminum–epoxy–aluminum sample (Fig. 4) the increase in error is much quicker, with the transmitted wave reaching a 10% difference at roughly 2% of an acoustic wavelength. It is noted that, due to the limit on the size of the epoxy layer, a real sample made of two aluminum plates bonded by a layer epoxy of some thickness is likely better represented by this simulation as a theoretical aluminum–epoxy–epoxy example, treating the thin epoxy layer as variable to represent the adhesion region between the aluminum and epoxy. In addition, this approach results in near negligible errors due to the thin layer having similar material properties to one of the half-spaces. Finally, it is possible to link a pair of these simulations together if both epoxy–aluminum interfaces require it.

C. Linear anisotropic thin layer

By adding anisotropy to the thin layer it is expected that the displacement amplitude of the waves change with polar angle, in addition, mode converted waves will be created. The symmetry of the displacement amplitude versus polar angle depends on the anisotropy and orientation of the layer. As an example to test for the correct symmetry consider a theoretical steel–boron fiber rod–steel sample, where the boron rod thin layer is a 10-μm-thick hexagonal anisotropic material orientated so that the axis of symmetry lies parallel to the interface. This creates an angular dependence that is expected to repeat every 180°. As expected, the theory produces mode converted horizontal quasi-shear waves that possess amplitude variations that repeat every 180° versus the polar angle (Fig. 5, which used an incident longitudinal wave of frequency 1.0 MHz). It is also possible to see the changes in the plot of the transmitted shear vertical wave versus incident angle at various polar angles (Fig. 6). Other anisotropic materials also produce the expected angular dependence, while the analogous change in the displacement amplitude for the quasi-longitudinal and vertical quasi-shear

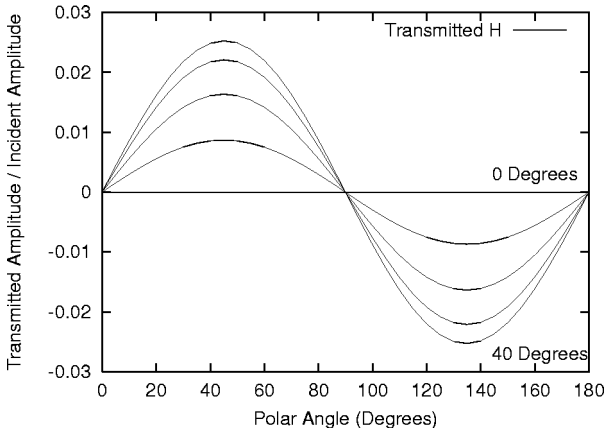

FIG. 5. Transmitted shear horizontal wave: Change in amplitude vs polar angle, for a hexagonal anisotropic thin layer. Each line represents a 10° change of incident angle.

waves is often very small, and in some cases, almost negligible in comparison to changes with the incident angle.

D. The nonlinear thin layer

One of the great advantages of the techniques developed here is the fact that the expressions do not rely on a harmonic decomposition. Nowhere is this more important than in the case of nonlinearity, where the superposition principle becomes suspect. The nonlinearity of Sec. II C was introduced using the layer stress–strain relation in the form of a classical expansion around small strains. It should be very clear, however, that the nonlinear effects introduced by a thin layer of a classically nonlinear material are likely to be negligible in most cases. There is no reason to believe, however, that this theory is somehow restricted to dealing with classical bulk materials. In fact, the stress–strain relation of the layer may take virtually any form and be based on any set of parameters without changing the mathematics significantly, because the expansion is in terms of the layer thickness instead of harmonics. This aspect makes this theory ideal for modeling strongly nonlinear situations. A highly relevant example of such a situation is the "interphase" region in the neighborhood of an adhesive bond interface. Given that any

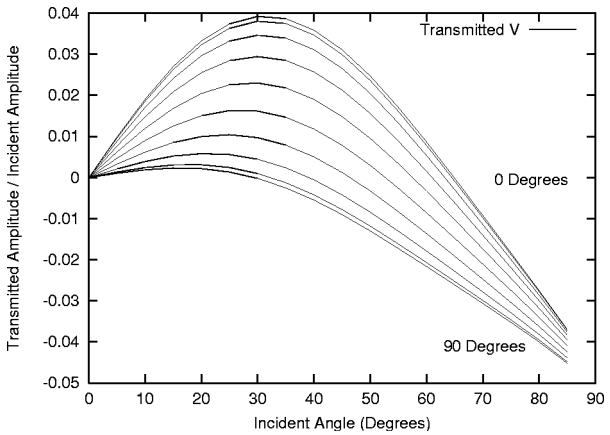

FIG. 6. Transmitted shear vertical wave: Change in amplitude vs incident angle, for a hexagonal anisotropic thin layer. Each line represents a 10° change of polar angle.

TABLE III. Harmonics from various nonlinear expansions.

Nonlinear function (F_{kl})	Harmonics of expansion	Harmonics produced
$\beta\epsilon_{kl}^2$	0,2	0,2
$\chi\epsilon_{kl}^3$	1,3	1,3
$\delta\epsilon_{kl}^4$	0,2,4	0,2,4
$\beta\epsilon_{kl}^2+\chi\epsilon_{kl}^3$	0,1,2,3	0,1,2,3

real interface may be physically viewed as a region of transition from one material to another, with its own strength and failure properties, this formulation may be much more relevant than it might appear at first glance—as a general continuum model of the material interface. However, as there is not sufficient space here to explore these issues in any depth, the following consideration is restricted to analyzing the classical nonlinearity only.

To verify that the theory produces the expected nonlinear results, the second and third-order nonlinear parameters β and ξ in the nonlinear stress–strain expansion [Eq. (20)]

$$T_{ij}^{\mathrm{NL}} = c_{ijkl}^{L}\epsilon_{kl}(1 + \beta_{mn}\epsilon_{mn} + \chi_{mnop}\epsilon_{mn}\epsilon_{op} + \cdots),$$

are defined to be simple diagonal matrices where $\beta_{mn} = C_1\delta_{mn}$, and $\xi_{mnop} = \xi_{\alpha\beta} = C_2\delta_{\alpha\beta}$ ($\xi_{\alpha\beta}$ is written in the standard Voight notation). From the solution for the additional nonlinear factor [Eq. (37)] it is expected that the additional harmonics created will correspond exactly to the higher order parameters in the nonlinear expansion. Taking the Fourier transform of the reflected and transmitted waves obtains the results for the harmonics in these waves summarized in Table III. As expected, the additional harmonics found in the reflected and transmitted wave forms have an exact correspondence with the higher order terms in the nonlinear expansion. The magnitude of the harmonics are found to change linearly with the constants C_1 and C_2, and as expected from Eqs. (33) and (34), the magnitude is also linear with respect to changes in size of the thin layer. In addition, a summation of expansion terms is found to produce the harmonics from each individual term combined, as is expected due to superposition of the expansion terms.

Along with the ability to examine the size of the harmonics, the simulation allows for the examination of the change in the harmonic response with angle of incidence. This gives the possibility of finding the angle of incidence which will yield the maximum harmonic response for each acoustic wave polarization generated. Figure 7 shows the response of the amplitude of the second harmonic (with respect to the amplitude of the incident wave) for a theoretical aluminum–epoxy–epoxy(type II) sample, where the thin layer of epoxy has the nonlinear properties, and has slightly different material properties than the bulk epoxy. Here the simulation has used a 1.0 MHz incident longitudinal sinusoidal wave, and a 10 μm thin layer with the nonlinear parameter $\beta_{mn} = 10\delta_{mn}$. Increasing the nonlinear parameter is found to linearly increase the amplitude of the additional harmonics over the entire range of incident angles. In this case we see that for the longitudinal waves there is some advantage to using higher incident angles to increase the size of the nonlinear response. In addition, reflected and transmit-

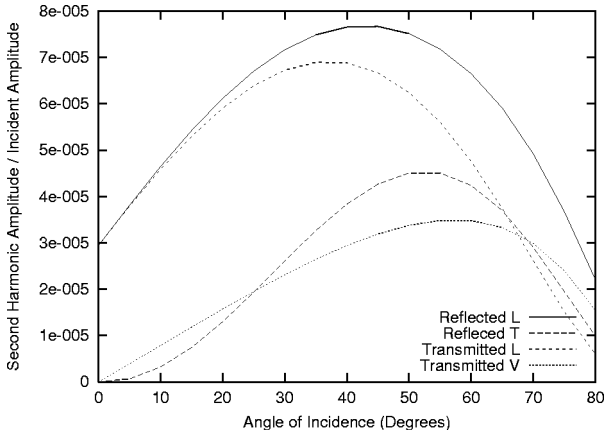

FIG. 7. Second harmonic change with incident angle for reflected and transmitted longitudinal (L) and shear vertical (V) waves.

ted waves of the same polarization are found to give similar nonlinear responses over the range of incident angles, with the longitudinal waves producing the larger response. Examining the reflected longitudinal wave it is found that the amplitude level of the second harmonic lies roughly 75–85 dB below the wave's first harmonic. The response of the third harmonic produces approximately the same curves as in the case of the second-order response, but with amplitudes an order of 10^{-3} the size even with $\xi_{\alpha,\beta}=10\delta_{\alpha\beta}$, where reducing ξ an order of magnitude reduces the harmonics an order of magnitude as well. This, however, is a specific case, and other cases, such as an aluminum–epoxy–aluminum sample, produce results with a response an order of magnitude higher in all modes. Again, the reflected and transmitted longitudinal waves give approximately the same nonlinear response over the range of incident angles, but now this nonlinear response decreases at larger angles of incidence. It is, of course, possible to further explore the nonlinear response with different configurations for the nonlinear parameters, but the intent here is to validate the model and show the results for some simple cases.

VI. CONCLUSIONS

In the first two validation methods, both the comparison with the exact solution for a linear three layer system at normal incidence and the examination of energy conservation show the simulation gives reasonably accurate results as long as an appropriately sized thin layer is used. For the case of samples where the material properties in thin layer differ significantly from the half-spaces, this limit was about 1% of the longitudinal acoustic wavelength, while cases with similar properties produce results with little error allowing for layers at 10% of a wavelength, or possibly more, to be considered. With these two comparisons available, the output from the simulation can easily be checked to quickly ensure the simulation does not venture outside the parameters of the theory. The final two validation methods tested the anisotropy and nonlinearity in the thin layer by using situations where certain properties of the reflected and transmitted wave forms were known. In the case of an anisotropic thin layer, the simulation was found to produce both the expected mode converted waves, as well as reproducing the expected polar symmetry. In the case of a nonlinear thin layer, the simulation was found to produce the expected harmonics, in cases where individual terms of the the nonlinear expansion were considered. In addition, the total nonlinear expansion was also found to result in the expected harmonics

ACKNOWLEDGMENTS

The authors would like to express gratitude to the NSERC for providing funding for this research which was completed thorough the NSERC Industrial Research Chair at the University of Windsor.

[1] A. Niklasson, S. Datta, and M. Dunn, "On ultrasonic guided waves in a thin anisotropic layer lying between two isotropic layers," J. Acoust. Soc. Am. **108**, 2005–2011 (2000).
[2] A. Niklasson, S. Datta, and M. Dunn, "On approximating guided waves in plates with thin anisotropic coatings by means of effective boundary conditions," J. Acoust. Soc. Am. **108**, 943–993 (2000).
[3] S. Rokhlin and W. Huang, "Ultrasonic wave interaction with thin anisotropic layer between two anisotropic solids: Exact and asymptotic boundary condition methods," J. Acoust. Soc. Am. **92**, 1729–1743 (1992).
[4] S. Rokhlin and W. Huang, "Ultrasonic wave interaction with a thin anisotropic layer between two anisotropic solids II. Second order asymptotic boundary conditions," J. Acoust. Soc. Am. **94**, 3405–3420 (1993).
[5] M. Rothenfusser, M. Mayer, and J. Baumann, "Acoustic nonlinearities in adhesive joints," Ultrasonics **38**, 322–326 (2000).
[6] C. M. Hedberg and O. V. Rudenko, "Pulse response of a nonlinear layer," J. Acoust. Soc. Am. **100**, 2340–2350 (2001).
[7] B. O'Neill, J. Sadler, F. Severin, and R. G. Maev, "Theoretical and experimental study of the acoustic nonlinearities and an interface with poor adhesive bonding," Acoust. Imaging **26**, 309–317 (2002).
[8] B. O'Neill, J. Sadler, F. Severin, and R. G. Maev, "Development of a nonlinear boundary condition approach as a new model for the nonlinear acoustic interface problem," Nonlinear Acoustics at the Beginning of the 21st Century **1**, 29–32 (2002).
[9] J. Sadler, B. O'Neill, and R. G. Maev, "Characterization and imaging of thin, highly oriented layers: Theory and experiment," Acoust. Imaging **27**, 341–348 (2004).
[10] I. Solodov and R. G. Maev, "Overview of opportunities for nonlinear acoustic applications in material characterization and NDE," Proceedings of the 2nd International Conference on Emerging Technologies in NDE, edited by D. Van Hemlrijk, A. Anastassopoulos, and T. Philippidis, Rotterdam, 2000, pp. 137–144.
[11] L. A. Ostrovsky and P. A. Johnson, "Dynamic nonlinear elasticity in geomaterials," La Rivista Del Nuovo Cimento della Societa Italiania di Fisica **94**, 1–46 (2001).
[12] L. Landow and E. M. Liftshitz, *Theory of Elasticity*, 3rd ed. (Permagon, New York, 1986).

An inherently stable boundary-condition-transfer algorithm for muffler analysis

T. Kar and M. L. Munjal[a)]
Facility for Research in Technical Acoustics, Department of Mechanical Engineering, Indian Institute of Science, Bangalore-560 012, India

(Received 2 December 2004; revised 13 March 2005; accepted 25 April 2005)

Wave coupling exists in the wave propagation in multiple interacting ducts within a waveguide. One may use the segmentation approach, decoupling approach, eigenvalue approach, or the matrizant approach to derive the overall transfer matrix for the muffler section with interacting ducts, and then apply the terminal boundary conditions to obtain a two-by-two transfer matrix. In such instances, a boundary condition applied to a vector is given as a linear combination of its components. Spatial dimensions along with parameters like impedance of the perforated interface may yield numerical instability during computation leading to inaccurate prediction of the acoustic performance of mufflers. Here, an inherently stable boundary-condition-transfer approach is discussed to analyze the plane wave propagation in suchlike mufflers and applied to waveguides of variable cross-sectional area. The concept of pseudo boundary conditions applied to the state vector at an intermediate point is outlined. The method is checked for self-consistency and shown to be stable even for extreme geometries. © *2005 Acoustical Society of America.* [DOI: 10.1121/1.1931847]

PACS number(s): 43.20.Bi, 43.20.Mv [DKW] Pages: 60–71

I. INTRODUCTION

Waveguides or mufflers with perforated elements are extensively used for various practical purposes. In any such acoustical element, waves propagating in different ducts may interact to build a coupled standing wave. There exists a vast pool of literature covering the analytical prediction of the acoustical performance of several probable configurations. Many of them have been corroborated experimentally.

Acoustical modeling of interacting perforated pipes, on the basis of plane wave propagation, is largely done by either the eigenfunction expansion method[1] or the segmentation method.[2] The solution for either case is in the form of a transfer matrix, subjected to certain boundary conditions. A complete discussion on the decoupling method has been narrated in the literature.[3–8] Solution to such problems is attained by applying boundary conditions to the linear operator, a transmission matrix, of the state vectors. The transfer matrix is basically generated by the decoupling analysis. An alternate way of analysis was presented by Dokumaci,[9] where he made use of the concept of matrizant[10,11] approach to analyze a muffler, comprising any number of parallel perforated ducts communicating with each other through perforated walls along a common length. This approach enjoys the advantage of retaining the first-order fundamental continuity and momentum equations of each of the control volumes; one does not have to derive and solve their corresponding second-order wave equations. This matrizant method has been applied by the authors to plane-wave propagation in a variable area concentric tube resonator,[12] where the differential coefficients are continuous functions of the axial coordinate. In the matrizant analysis the Peano-Baker series of mean coefficients is used for producing the transfer matrix. Recently a generalized algorithm for analysis of any such configuration has been presented.[13]

However, all these investigations are restricted to a muffler of length short enough to remain under the computational limitation. The computational stability of the existing method remains uncertain when applied to longer elements. The other spatial parameter of a resonator that may create instability is the effective cross-sectional area of wave propagation for the individual ducts. The computational stability offered by the existing approach for predicting the acoustical performance, like transmission loss (TL) spectrum over a frequency range of mufflers, while varying any single parameter over a wider range, is doubtful. Porosity of the perforated ducts also plays a vital role over performance. Unfortunately, extreme values of these parameters have not been dealt with in the existing literature, probably due to lack of practical application.

Here, an inherently stable algorithm involving a new boundary-condition-transfer (BCT) approach is presented to overcome the aforesaid limitations of the existing methods. In the next section, the phenomenon of wave coupling is studied in order to identify the source of computational errors. Then, the BCT approach is outlined and a general algorithm is developed for implementation thereof. In the following section, the algorithm is successfully applied to the study of the variable-area waveguides for a wide range of geometrical parameters.

II. ACOUSTICAL WAVE COUPLING

Before the boundary-condition-transfer (BCT) approach is worked out in detail, the wave coupling or the wave interaction across the perforated interface of the interacting ducts within a waveguide will be described in order to identify the

a)Author to whom correspondence should be addressed. Electronic mail: munjal@mecheng.iisc.ernet.in

 0001-4966/2005/118(1)/60/12/$22.50

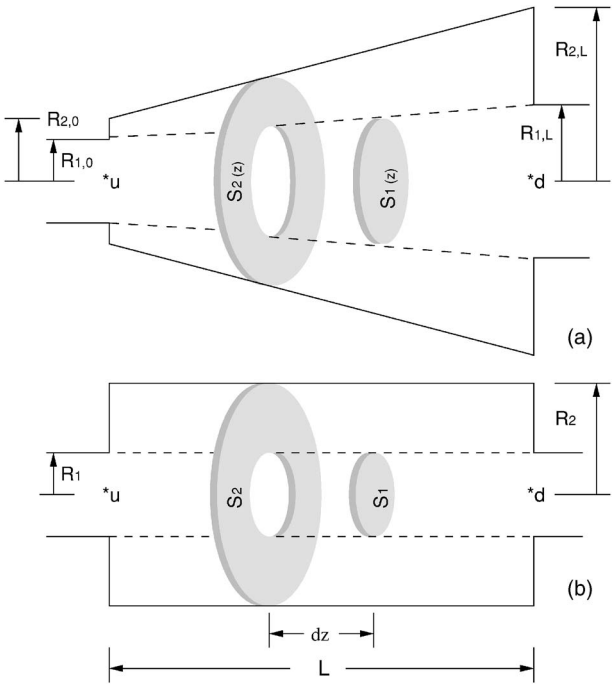

FIG. 1. Line diagrams of (a) conical concentric-tube resonator and (b) simple concentric-tube resonator.

computational limitations. The simplest among them is a two-duct conical concentric-tube resonator (CCTR) shown in Fig. 1, which is known to attenuate the odd harmonics.[12] A plane wave propagation in both the interacting variable area ducts, and a grazing mean flow through the inner tube of radius $R_1(z)$, is assumed. A rigorous mathematical modeling is avoided by assuming the absence of temperature gradients and viscous effect of the medium. However, the viscous effect is included in the acoustic impedance of the perforate. Thus, for an incompressible moving medium in the duct of variable cross-sectional area $S_i(z)$, the mass continuity equations are given as[12]

$$\frac{D\rho_i}{Dt} + \rho_0 \frac{\partial u_i}{\partial z} + u_i \rho_0 \frac{dS_i(z)}{S_i(z)dz} + \frac{2\pi R_1(z) u^* \rho_0}{S_i(z)} = 0, \quad i = 1 \text{ and } 2, \tag{1}$$

where ρ_i is the space average density perturbation over the mean air density ρ_0 in the ith duct. Similarly u_i is the corresponding particle velocity perturbation, and $S_1(z) = \pi R_1^2(z)$ and $S_2(z) = \pi[R_2^2(z) - R_1^2(z)]$ are the variable effective cross-sectional areas of the tube and the cavity, respectively. The particle velocity through the perforation u^*, which acts along the radial direction, is due to the pressure difference across the perforated plate of negligible thickness as compared to the radial dimension of the waveguide. Hence,

$$u^* = \frac{p_1(z) - p_2(z)}{\rho_0 c_0 \zeta} \tag{2}$$

where ζ is the dimensionless specific acoustic impedance of the perforate and c_0 is the speed of sound in air. The expression for the acoustic impedance ζ is empirical in nature and does not get involved during the analytical development of the wave propagation. With the assumption of no momentum transfer across the dynamically passive interface, the corresponding conservation of momentum equations may be given as

$$\rho_0 \left[\frac{Du_i}{Dt} \right] + \frac{\partial p_i}{\partial z} - (\rho_0 u_i + \rho_i U_i) \frac{U_i dS_i(z)}{S_i(z)dz} = 0, \quad i = 1 \text{ and } 2 \tag{3}$$

Variables p_1 and p_2 are acoustic pressures averaged over areas $S_1(z)$ and $S_2(z)$, respectively. For plane wave propagation in fluids, the acoustic pressure, density, and velocity perturbations are all harmonic functions of time. Working in the frequency domain, the time dependence of all variables may be taken as harmonic ($e^{i\omega t}$). Using the condition of isentropicity, the density and the pressure perturbations are related by

$$p_i = \rho_i c_0^2, \quad i = 1,2. \tag{4}$$

A. Solution

Although the set of four coupled differential equations, Eqs. (1) and (3), can be solved by different numerical methods for constant differential coefficients, a brief description of the matrizant analysis will be rendered here in view of the variable coefficients for the aforementioned case of CCTR. Equation (4) may be used to replace the density perturbations ρ_i's by the corresponding acoustic pressures p_i's. Thus, the derivative of each state variable may be rearranged as a linear combination of the state variables (acoustic pressure and particle velocity) for further analysis. Thus,

$$\frac{d\{\mathbf{Y}\}_i}{dz} = \sum_{j=1}^{4} [\upsilon]_{ij} \{\mathbf{Y}\}_j, \quad i = 1 \text{ to } 4, \tag{5}$$

where the state vector $\{\mathbf{Y}\}$ of Eq. (5) may be written in the normalized form:

$$\{\mathbf{Y}\} = [p_1 \quad p_2 \quad (\rho_0 c_0) u_1 \quad (\rho_0 c_0) u_2]^T. \tag{6}$$

Although the constituent elements of the square matrix $[\upsilon]$ are given in Appendix A, details of the process of obtaining them are left out of the current manuscript. Properties of individual matrix elements with respect to different physical conditions and their corelationships can be gleaned from the literature.[12] Here, the emphasis has been given to identification of the multifarious limitations of the existing solutions and development of an inherently stable approach to overcome them.

As the elements $[\upsilon]_{ij}$ are continuous functions of the axial coordinate z, there exists a definite integral and thus an approximated solution for the first-order differential equation of Eqs. (5) over the variable range z_s, where z_s is a subset of z. Error associated with the approximation depends upon both the path length represented by z_s and characteristics of the functions $[\upsilon]_{ij}$. The total path of the variable z may be segmented into a finite number, $\mathbf{N}$, of intervals of length $L_s = (L/\mathbf{N})$, and the functions for each of these segments are to

be independently worked out as given below. Thus, for any such interval that spans (z_0, z_1), the state vectors at the boundaries are related as[12]

$$\{\mathbf{Y}\}_{z=z_0} = \mathbf{e}^{[\mathbf{\Gamma}]}\{\mathbf{Y}\}_{z=z_1}; \quad [\mathbf{\Gamma}] = -\int_{z_0}^{z_1} [\upsilon] dz, \tag{7}$$

where $(z_1 - z_0) = L_s$. The transfer matrix $\mathbf{e}^{[\mathbf{\Gamma}]}$, which acts as a linear operator between the downstream and upstream state vectors of one segment, may be expanded using the Maclaurin's series

$$\mathbf{e}^{[\mathbf{\Gamma}]} = [\mathbf{I}_N] + \sum_{n=1}^{\infty} \frac{[\mathbf{\Gamma}]^n}{n!} \equiv [\mathbf{\Phi}] \quad \text{(say)}. \tag{8}$$

The transfer matrix $\mathbf{e}^{[\mathbf{\Gamma}]}$ is diagonalized using the corresponding modal matrix $[\mathbf{\Psi}]$ and the eigenvalues of the matrix $[\mathbf{\Gamma}]$ as follows:

$$[\mathbf{\Gamma}] = [\mathbf{\Psi}][\lambda][\mathbf{\Psi}]^{-1}, \quad [\mathbf{\Phi}] = [\mathbf{\Psi}][\mathbf{e}^{\lambda}][\mathbf{\Psi}]^{-1}, \tag{9}$$

where

$$[\mathbf{e}^{\lambda}]_{ik} = \begin{cases} \mathbf{e}^{\lambda_i} & \text{if } i = k, \\ 0 & \text{if } i \neq k, \end{cases} \tag{10}$$

where λ_i is the ith latent root. The process is repeated for all segments and the corresponding transfer matrices are determined and sequentially multiplied to produce the overall transfer matrix:

$$[\mathbf{\Omega}] = \left[\prod_{i=1}^{\mathbf{N}} [\mathbf{\Phi}]_i \right]. \tag{11}$$

The above procedure would apply equally for any general configuration. The difference lies with the boundary conditions associated with different muffler elements. Application of boundary conditions in succession to the transfer matrix $[\mathbf{\Omega}]$ leads to a four-pole parameter transmission matrix $[\mathbf{T}]$ that relates the acoustic pressures and particle velocities at the inlet and the outlet of the muffler. Transmission loss (TL) can be evaluated from the absolute sum of the four-pole parameters:[3]

$$\text{TL} = 20 \log_{10}\left[\frac{1}{2}\left(\frac{S_d}{S_u}\right)^{0.5}\left(\frac{1+M_u}{1+M_d}\right)|T_{11} + T_{12} + T_{21} + T_{22}| \right], \tag{12}$$

where S_d and S_u are the cross-sectional areas of, and M_d and M_u are the mean flow Mach numbers at the downstream end (outlet) and the upstream end (inlet) points, respectively.

Figure 2 shows the TL spectrum predicted as per the existing transfer matrix method for the configuration of Fig. 1(a), where the uniform inner perforated tube has radius of 25 mm, whereas the radial dimensions of the cavity R_{20} and R_{2L} are 26 and 75 mm, respectively. Henceforth, this set of radial dimensions will be taken default unless mentioned explicitly. In these sample TL spectra, exact numerical values are of little significance; rather, numerical instabilities in the form of spectral irregularities and hence the corresponding erroneous predictions, which are prominent in the subplots of Fig. 2 for longer elements, are the matter of concern here. Factors other than axial dimension will be discussed later.

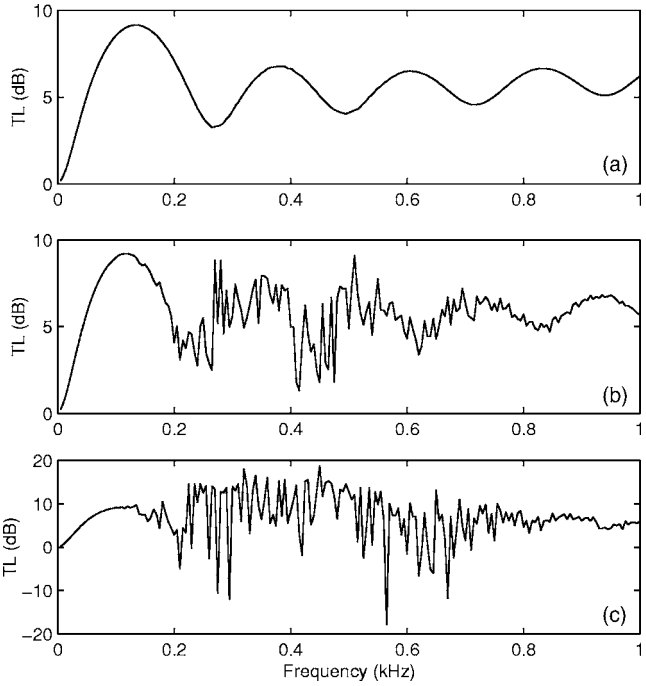

FIG. 2. Predicted TL spectrum for various values of length (L) of a two-duct CCTR for the configuration of Fig. 1. (a) 0.75 m, (b) 0.85 m, and (c) 0.9 m.

B. Source of errors

Figure 3 shows a schematic block diagram of the events involved in the conventional method to reach the solution. Event $\mathbf{A}_1$ symbolizes Eq. (11), which represents the sequential multiplication of segmental transfer matrices to get the overall transfer matrix $[\mathbf{\Omega}]$. Application of the boundary conditions is represented by the event $\mathbf{A}_2$, which yields the desired 2×2 transfer matrix $[\mathbf{T}]$. Finally $\mathbf{A}_3$ stands for determining the TL. This subsection presents a systematic backward investigation to trace the source of numerical instability.

As far as the analysis is concerned, the differential coefficients $[\upsilon]_{i,j}$ are continuous functions of the independent variable z. Therefore, it is expected and indeed has been observed that elements of intermediate transmission matrices $[\mathbf{\Phi}]_i$ and the overall transfer matrix $[\mathbf{\Omega}]$ are continuous as well. However, numerical instability manifests itself in all the four-pole parameters of the 2×2 transfer matrix $[\mathbf{T}]$ and hence in TL. Although all the elements suffer from similar

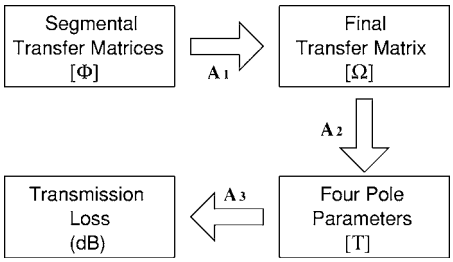

FIG. 3. Block diagram to show the steps to the solution for the conventional method. Arrows represent the analytical events.

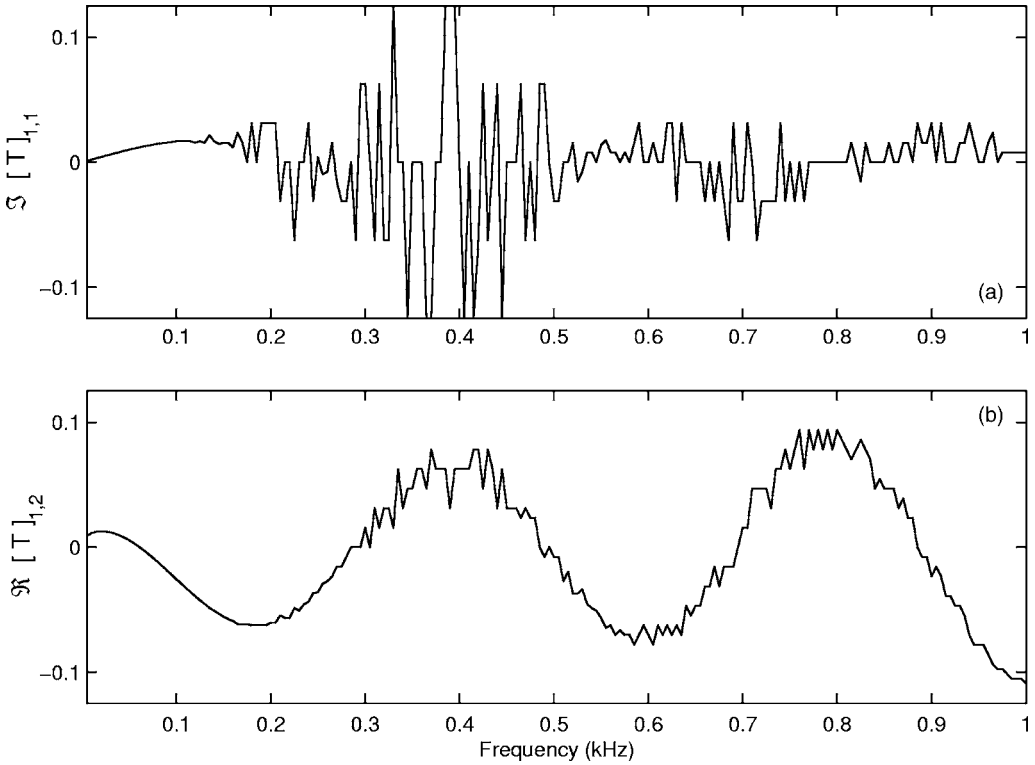

FIG. 4. Real and imaginary parts of two different elements of the four pole transfer matrix $[\mathbf{T}]$ for length L=0.85 m. (a) $\Im[\mathbf{T}]_{1,1}$ and (b) $\Re[\mathbf{T}]_{1,2}$.

instability like the TL spectrum, only a single case of real and imaginary parts for two different elements of the four pole matrix $[\mathbf{T}]$ has been plotted in Fig. 4. Significantly, elements of the matrix $[\mathbf{\Omega}]$ do not suffer similarly. Both the real and imaginary parts of a diagonal $[\mathbf{\Omega}]_{1,1}$ and an offdiagonal element $[\mathbf{\Omega}]_{2,3}$, are plotted in subplots (a) and (b), respectively, in Fig. 5. It can be seen that all the curves are smooth and continuous over a given frequency range. But the individual elements of the overall transfer matrix $[\mathbf{\Omega}]$ are of the order of 10^{15}. Numerical instabilities creep in while

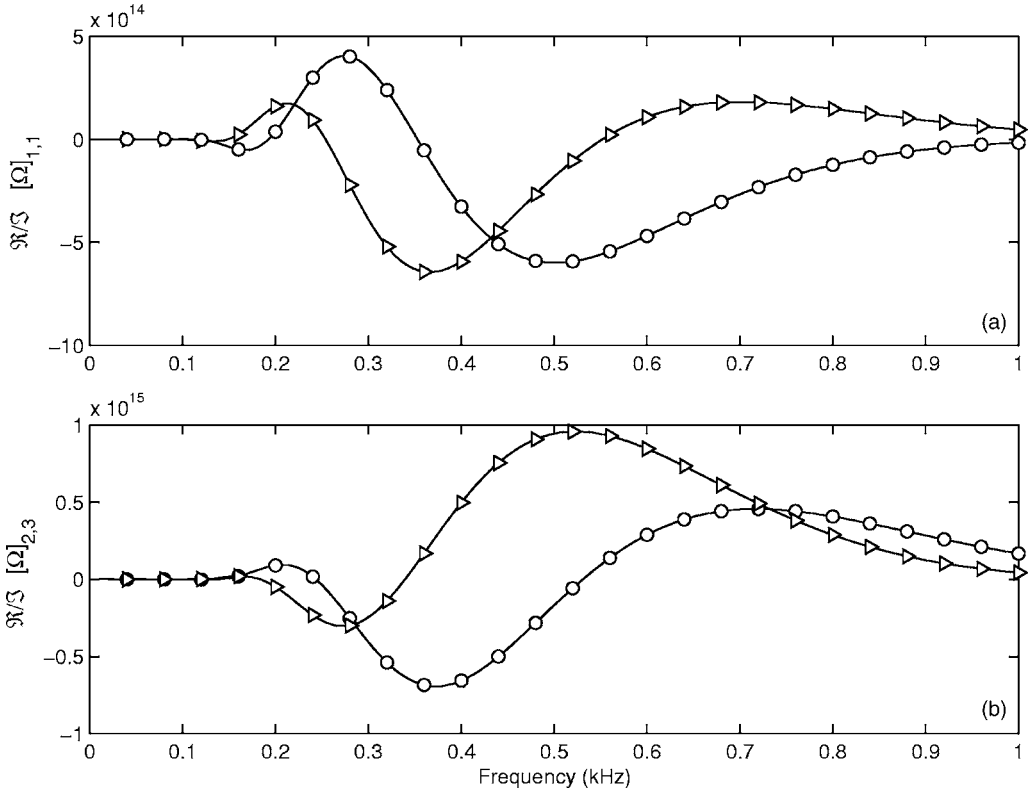

FIG. 5. Real (○—○—○) and imaginary parts (▷—▷—▷) for different elements of the overall matrix $[\mathbf{\Omega}]$ for length L=0.85 m. (a) $[\mathbf{\Omega}]_{1,1}$ and (b) $[\mathbf{\Omega}]_{2,3}$.

working with such large numbers. The conventional method of normalizing the field variables with appropriate scales fails to avert this problem. Normalizing the matrix elements would enlarge the vector components of only one end by the same factor. Thus, it does not solve the problem as those astronomical numbers will appear during the algebraic reduction of the system matrix to four-pole parameter transfer matrix. Thus it may be concluded safely that errors are brought forth while applying the boundary conditions; i.e., in the event $\mathbf{A}_2$ in Fig. 3. Application of boundary conditions is basically a reduction process to produce the four-pole parameters, which are of the order of unity. Thus, even minute fractional round-off errors in $[\mathbf{\Omega}]$, which are generated during the multiple operations over the system matrix $[\mathbf{\Gamma}]$, have an amplified impact on the elements of the four-pole transmission matrix $[\mathbf{T}]$. These become more acute for larger $[\mathbf{\Omega}]_{i,j}$'s.

Instability in the conventional methods[1,4,12] can never be overcome by judicious choice of the number of segments $\mathbf{N}$. Better accuracy would be ensured with an increasing number of segments,[12] provided there were no instabilities. In the conventional method, segmental matrices are multiplied prior to the application of boundary conditions. Thus, the order (magnitudes) of the transfer matrix elements, on which the boundary conditions are applied, remain more or less the same. Instabilities originate in the algebraic calculations comprising large numbers. Thus, an approach that deals with such astronomical numbers can never overcome the instabilities.

III. METHODOLOGY: A GENERAL ALGORITHM

This section deals with a boundary-condition-transfer (BCT) approach, a completely novel method applied to state vectors, constituted at each of the confluence points between two subintervals, over a finite but continuous interval. As elaborated in the previous section, it is assumed here that components of the state vectors are functions of a single variable. The number of subintervals, where the analysis is performed independently over each of them, may be chosen arbitrarily. Let the interval (the length of the perforated section) be divided into "$\mathbf{N}$" segments and each of them be defined by two unique state vectors at its boundaries, where equality of subintervals of the independent variable is not a constraint. The interface of two consecutive segments may be considered as a vector plane, a plane normal to the path of the independent variable. In such systems, a couple of sequential vectors (jth and $(j+1)$th) may be related as

$$\{\mathbf{Y}\}^j = [\mathbf{\Phi}]^j \{\mathbf{Y}\}^{j+1} \quad \text{for } j = 1,2,\ldots,\mathbf{N}, \tag{13}$$

where $[\mathbf{\Phi}]^j$ is the appropriate transfer matrix and hence a linear operator that transforms the jth vector to the $(j+1)$th vector along the variable "z," and represents the coefficients of a set of simultaneous linear equations. Figure 6 renders a schematic view of the ordered transformation, where thick blocks, represented as segmental transmission matrices, establish a mapping between two vectors, represented by $\{\mathbf{Y}\}^1, \{\mathbf{Y}\}^2$, etc.

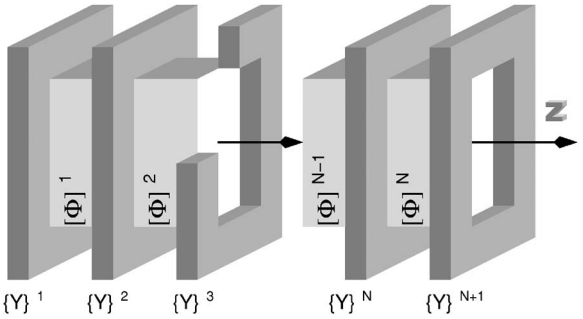

FIG. 6. A schematic diagram constituting the vectors and the transmission matrices, presented by thin plates and thick blocks, respectively.

In practice, several boundary conditions need to be applied to the terminal vectors before arriving at the overall 2×2 transfer matrix. The general approach for arriving at the solution is to generate a final transfer matrix between the vectors at the extreme ends before applying the boundary conditions, which may be given as

$$\{\mathbf{Y}\}^1 = \prod_{i=1}^{\mathbf{N}} [\mathbf{\Phi}]^i \{\mathbf{Y}\}^{\mathbf{N}+1}. \tag{14}$$

This approach induces numerical instabilities as described above from the computational point of view. The inception of such erroneous computation that leads to some of the most undesirable results will be shown in the next section. Justification of the method outlined here will become clear in the following sections, where comparative studies will be made to demonstrate the stabilizing potential of the boundary-condition-transfer (BCT) method.

This paragraph describes the basic concept of transferring the boundary conditions from the end vectors, where they are defined, to the intermediate vector planes, across the segmental transfer matrices (see Fig. 6). Here a boundary condition should be seen as a relationship among the components of the corresponding vector. Thus any one component of an "n"th-order vector may be expressed in terms of the remaining "$n-1$" components. Such a relationship for a unique vector may be given as

$$\{\mathbf{Y}\}_{\tilde{k}}^j = f(\{\mathbf{Y}\}_i^j | \ \forall\, i = 1 \text{ to } n,\ i \neq \tilde{k}), \tag{15}$$

where $\{\mathbf{Y}\}_{\tilde{k}}^j$ is the $\tilde{k}$th component of the vector $\{\mathbf{Y}\}^j$. Thus, the collection of the functions f's of Eq. (15) that equals the number of BCs applied over a domain will form a set $\mathbf{X}^j = \{\mathbf{Y}\}^{j\{\mathbf{Y}\}^j}$ and denotes a finite set of maps from $\{\mathbf{Y}\}^j$ to $\{\mathbf{Y}\}^j$. Function f in Eq. (15) can take any form, but from the acoustical point of view here, a simple case of the more generic function f will be discussed, where the function is a linear combination of the variables. Then, Eq. (15) corresponding to the ℓth function f_ℓ may be written in the form

$$\{\mathbf{Y}\}_{\tilde{k}}^j = \sum_{\phi=1}^{n} (\mathbf{C}_{f_\ell})_\phi^j \{\mathbf{Y}\}_\phi^j \quad (\phi \neq \tilde{k}), \tag{16}$$

where $(\mathbf{C}_{f_\ell})_\phi^j$'s are complex constants. Here we explicate a linear operation by expressing a component of a vector as a

linear combination of the rest of the components. In view of the fact that the transmission matrix is itself a linear operator, this boundary condition, expressed as a linear operation, may well be transmitted across the vector planes. Though there exists no boundary at the intermediate points on the path of the independent variable, here it is possible to reason out a similar relationship among the vector components at any intermediate point. This relationship may be looked upon as a pseudo boundary condition. Now, the ϕth component of the vector $\{\mathbf{Y}\}^j$ in Eq. (13) may be given as

$$\{\mathbf{Y}\}^j_\phi = \sum_{i=1}^{n} [\mathbf{\Phi}]^j_{\phi,i} \{\mathbf{Y}\}^{j+1}_i. \tag{17}$$

The functions f's of Eq. (15) representing the boundary conditions are mere repetitive and hence the total algorithm. Thus, from here onwards the complex coefficients $(\mathbf{C}_{f\ell})^j_\phi$ of Eq. (16) will be given as $\mathbf{C}^j_\phi$ in a generic manner. Applying Eq. (17) to both the sides of the equality, Eq. (16) may be given as

$$\sum_{i=0}^{n} [\mathbf{\Phi}]^j_{\tilde{k},i} \{\mathbf{Y}\}^{j+1}_i = \sum_{\phi=1}^{n} \mathbf{C}^j_\phi \sum_{i=1}^{n} [\mathbf{\Phi}]^j_{\phi,i} [\mathbf{Y}]^{j+1}_i \quad (\phi \neq \tilde{k}). \tag{18}$$

It can be noticed that both sides of Eq. (18) involve only the components of vector $\{\mathbf{Y}\}^{j+1}$, so any $\tilde{q}$th component of the vector $\{\mathbf{Y}\}^{j+1}$ can be singled out and be given in terms of the rest of the components:

$$\{\mathbf{Y}\}^{j+1}_{\tilde{q}} = \sum_{i=1}^{n} \mathbf{C}^{j+1}_i \{\mathbf{Y}\}^{j+1}_i \quad (i \neq \tilde{q}), \tag{19}$$

where $\mathbf{C}^{j+1}_i$'s are the output coefficients of the transmission matrix $[\mathbf{\Phi}]^j$. They can be given in terms of the corresponding input coefficients $\mathbf{C}^j_i$'s:

$$\mathbf{C}^{j+1}_i = \frac{\left[\sum_{\phi=1}^{n} \mathbf{C}^j_\phi [\mathbf{\Phi}]^j_{\phi i}\right] - [\mathbf{\Phi}]^j_{\tilde{k}i}}{[\mathbf{\Phi}]^j_{\tilde{k}\tilde{q}} - \sum_{\phi=1}^{n} \mathbf{C}^j_\phi [\mathbf{\Phi}]^j_{\phi\tilde{q}}} \quad \begin{cases} \phi \neq \tilde{k}, \\ i \neq \tilde{q}. \end{cases} \tag{20}$$

The process of determining the pseudo boundary conditions and hence a set of coefficients at each of the intermediate vector planes defined at discrete points on the path of the variable begins at one end and moves sequentially until it reaches the other end. For convenience and algorithmic simplicity it is desirable to place the vector component, on which the boundary condition is defined, down the order. Thus, there appears a pseudo boundary condition for any two consecutive vector planes $\{\mathbf{Y}\}^j$ and $\{\mathbf{Y}\}^{j+1}$, which may be applied on the corresponding transfer matrix $[\mathbf{\Phi}]^j$ independently. Consequently, if applied, a boundary condition is responsible for reducing the order of the square matrix $[\mathbf{\Phi}]^j$ by one. A muffler subjected to multiple boundary conditions would produce different sets of coefficients. Thus, they form a set of linearly independent linear algebraic equations, related to the vector components of an intermediate vector, in terms of the derived coefficients. If an "n"th-order vector is subjected to "m" ($m<n$) boundary conditions, then the set of simultaneous linear equations may be given as

$$\{\mathbf{Y}\}^{j+1}_n = \sum_{i=1}^{n-1} (\mathbf{C}_\ell)^{j+1}_i \{\mathbf{Y}\}^{j+1}_i \quad (\ell = 1,2,\ldots,m). \tag{21}$$

Thus, similar to the application of a single boundary condition, Eqs. (21), when applied to the intermediate state vectors across each of the segmental matrices $[\mathbf{\Phi}]$'s for the respective value of j, would reduce the order of the square matrix $[\mathbf{\Phi}]^j$ of Eq. (8) by "m." The procedure for applying the rhs boundary conditions is similar to their lhs counterparts. Here, the functional relationship among the components of an intermediate vector plane is worked out from the inverse of the segmental transfer matrices. Then the equivalent expression for Eq. (13), for two consecutive vector planes $\{\mathbf{Y}\}^{j+1}$ and $\{\mathbf{Y}\}^j$, may be given as

$$\{\mathbf{Y}\}^{j+1} = [\mathbf{\Phi}]^{j-1} \{\mathbf{Y}\}^j, \quad \text{for } j = 1,2,\ldots,\mathbf{N}.$$

The rest of the algorithm will be applied as it is. Segmental transfer matrices are reduced to second-order square matrices by the aforementioned reduction process. The set of simultaneous linear equations $[\mathbf{\Phi}]$ of Eq. (8) for a given j may be reduced to a four-pole parameter transfer matrix each and may be written as

$$[p_1 \quad u_1]^T_z = [T]^j [p_1 \quad u_1]^T_{z+L_s}, \quad \{j{:}1 \leqslant j \leqslant \mathbf{N}\}. \tag{22}$$

The overall four-pole parameters between the ends are produced by the sequential multiplication of these reduced segmental transfer matrices:

$$[T]_1 = \left[\prod_{i=1}^{\mathbf{N}} [T]^j\right]. \tag{23}$$

The application of the algorithm is illustrated in Appendix B.

IV. RESULTS AND DISCUSSION

This section will show the advantage of the boundary-condition-transfer approach when applied to the acoustical analysis of various concentric tube resonators. Results and the corresponding discussions will be limited to a set of default parametric values. Unless a completely different configuration is referred to, the configuration shown in Fig. 1(a) will be analyzed. The porosity (σ) is fixed at 0.05, whereas the hole diameter (d_h) and the thickness of the perforated tube (t_h) have the default values of 3 and 1 mm, respectively. Besides, the default dimensions for the two-duct CCTR of Fig. 1 will remain the same as mentioned earlier in Sec. II A.

The number of segments **N**, used in the calculation, and the magnitude of the matrix elements $[\mathbf{\Phi}]_{ij}$ are reciprocally connected and hence case sensitive. The number of segments, **N**, affects the convergence of the matrizant method. Here, the proposed concept of transferring the boundary condition to the hypothetical intermediate vectors uses the same value of **N**. But it is not necessary that they have to be the same.[11] Thus, it seems to have no methodical selection of **N** but it should be large enough to provide desired numerical stability as well as the convergence of the matrizant method. Here, it has been selected on a case to case basis. All numeri-

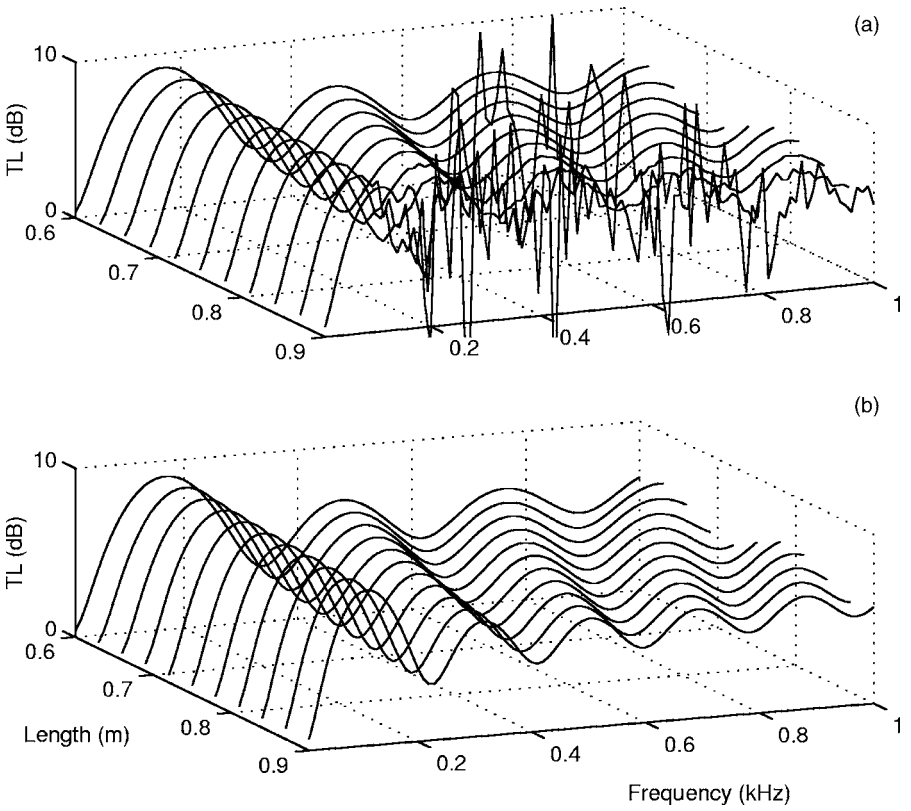

FIG. 7. TL surface plot for (CCTR). (a) Conventional approach[12] and (b) the BCT algorithm.

cal computations, unless mentioned explicitly, were performed for sonic speed of 340 m/s and 10 segments ($N=10$).

A. Length of the muffler

Being the sole independent variable for the plane wave propagation in any muffler, axial dimension of the tubular elements is the parameter of utmost significance. This subsection deals with the computational evaluation of the acoustic performance of longer elements with appropriate boundary conditions. Keeping the radial dimension invariant, the TL spectrum for the configuration of Fig. 1(a) is drawn in Fig. 7 for different values of length L. The length of the sample muffler is increased until the TL spectrum develops numerical instability, from 0.6 to 0.9 m in steps, and the TL spectrum for each step is generated by both the conventional and the boundary-condition-transfer (BCT) approaches.

Figure 7(a) shows the predicted TL spectra for various lengths analyzed by the traditional approach where boundary conditions are applied on the overall transfer matrix $[\boldsymbol{\Omega}]$, whereas the corresponding one based on the BCT algorithm is shown in Fig. 7(b). Though the conventional method works well up to a certain length, instability builds up for higher values of the axial dimension. The TL contour plot for the same element is shown in Fig. 8 where the abscissa and ordinate represent the length and the frequency range, respectively. Numerical instabilities are exemplified by the abrupt changes in TL contours for higher values of length. It may be noticed that the instabilities have a peculiar relationship with the exciting frequency, as they span only a finite range of intermediate frequencies, which is evident from Figs. 2, 7, and 8.

Figure 9 plots the TL contour for a simple concentric-tube resonator of Fig. 1(b). The perforated tube and the cavity have radii of 25 and 75 mm, respectively. The length of the tube has been varied from 0.8 to 1.0 m in steps. Results with the conventional approach[3] and with the BCT algorithm have been plotted in different subplots. Small circular patches in both the subplots of Fig. 9 correspond to the sharp troughs and hence the harmonics of the resonant frequency for different lengths of the resonator. These patches are missing in Fig. 8 due to the raised troughs, which is an inherent property of the CCTR.[12] The locus that may pass through a set of points denoted by a string of patches in Fig. 9 would relate the harmonic frequency to the length of the resonator, where the frequency times the resonator length equals a constant. Similarly, the algorithm has been applied successfully for a 0.5-m-long three-duct CCTR of Fig. 10 and the corresponding TL contour is shown in Fig. 11. Radial dimensions at the inlet are 25, 26, and 27 mm, respectively, whereas the corresponding ones at the outlet are 25, 50, and 75 mm. Although the overall size remains the same for both the elements, in the case of the three-duct CCTR, instability commences at a much shorter length when compared to the corresponding two-duct CCTR.

B. Radial dimension

Similar to the length, radial dimension may play a role towards inaccurate computation. But unlike its axial counter-

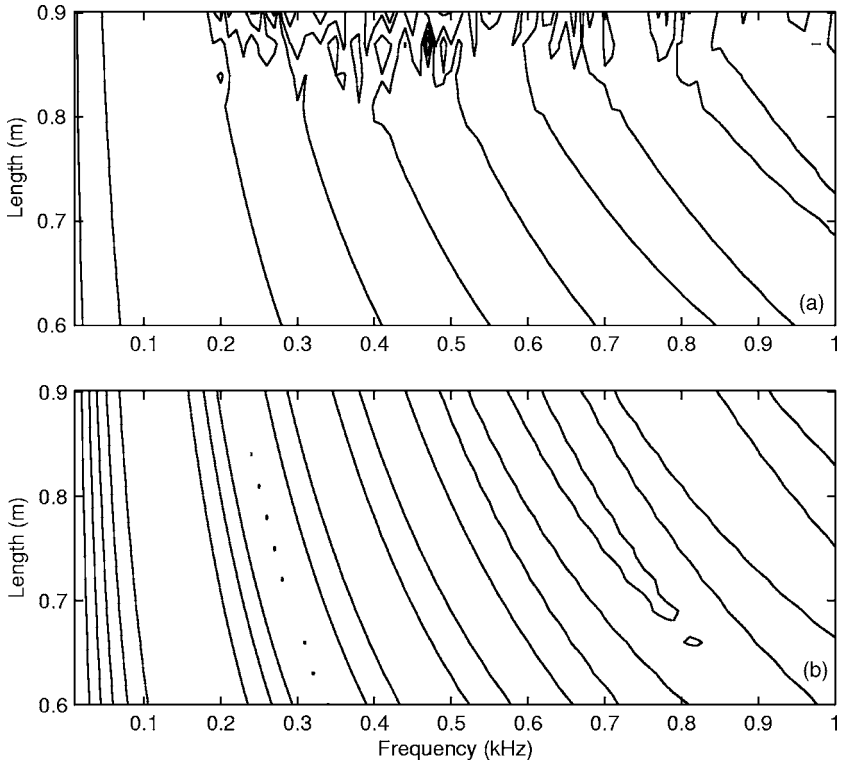

FIG. 8. TL contour plot for (CCTR). (a) Conventional approach[12] and (b) the BCT algorithm.

part, smaller dimensions for certain configurations lead to erroneous predictions. A case of a three-duct CCTR has been analyzed to study the impact of the effective cross-sectional area of the variable area cavities over the computational stability. Areas $S_2(z)$ and $S_3(z)$ are varied by changing $R_{2,L}$, the outlet radius of the intermediate perforated duct. The associated TL contours are shown in Fig. 12. Cross-sectional area of a cavity reduces drastically when $R_{2,L}$ approaches either $R_{3,L}$ or $R_{1,L}$. Both the cases run to inaccurate prediction and the results are shown in Figs. 12(a) and 12(b), respectively. Figure 12(c) is the corresponding result obtained by means of the BCT algorithm. Variation of the radial dimension of

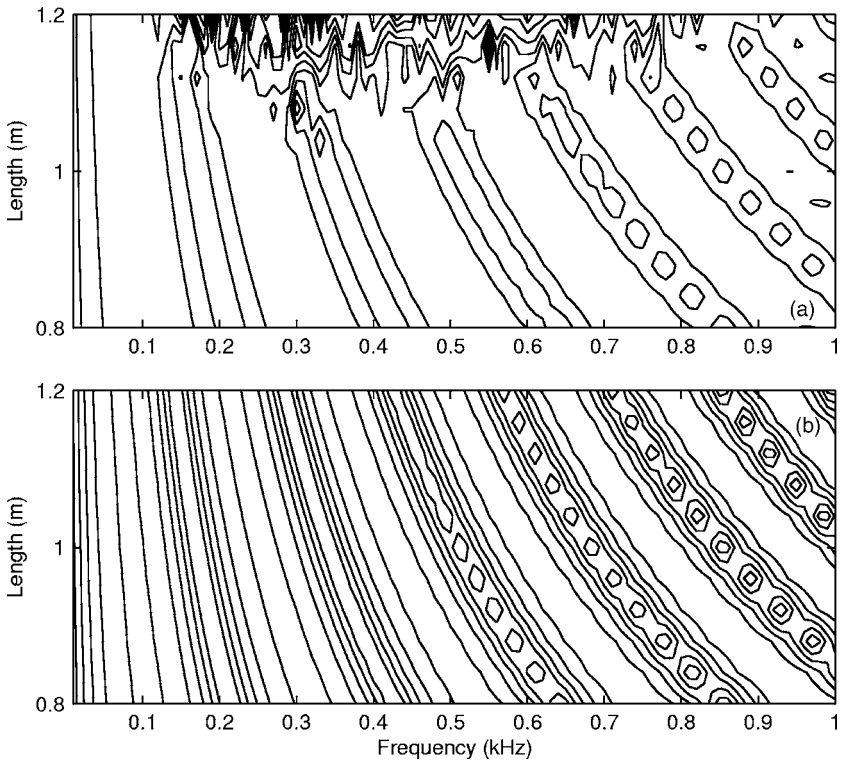

FIG. 9. TL contour plot for uniform duct CTR. (a) Conventional approach[3] and (b) the BCT algorithm.

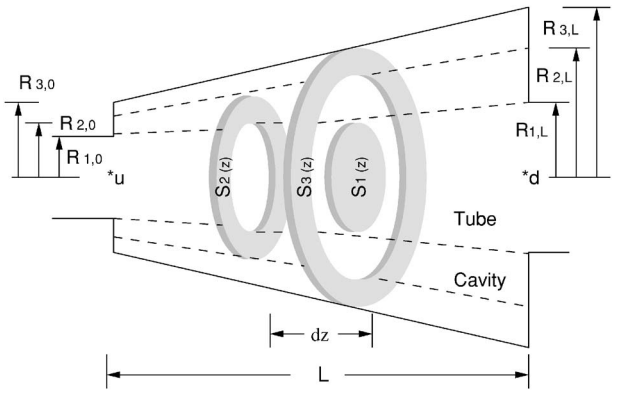

FIG. 10. A line diagram of a conical concentric-tube resonator with three interacting ducts.

the intermediate perforated shield simply alters the space shared by both the cavities. Thus the contours are bound to be straight lines, irrespective of the values of $R_{2,0}$ and $R_{2,L}$, with a slight exception, however, at higher frequencies.

C. Perforate impedance

Apart from the spatial parameters discussed earlier, factors like perforate impedance may restrict the utility of computational methods to a narrow band of parametric values. The present day analysis of acoustical elements always uses empirical formulas for the acoustical impedance offered by the perforated interface.[14] Although they have been in use for predicting the performance of several muffler elements, their theoretical validity, from the numerical stability point of view, has not been tested as yet beyond a certain range of porosity. One of these limiting cases is the complete transparency of the perforated interface. The stability of the existing computational methods may be questioned when the admittance at the perforated interface is increased considerably to look at the transparency of the shield. For an absolute transparent system, with porosity nearing the value of one, the element should behave as if the concerned perforate duct

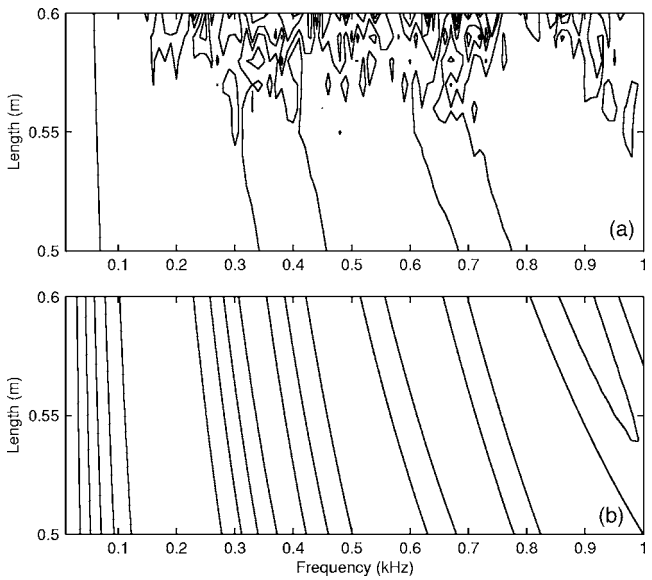

FIG. 11. TL contour plot for three-duct CCTR. (a) Conventional approach[12] and (b) the BCT algorithm.

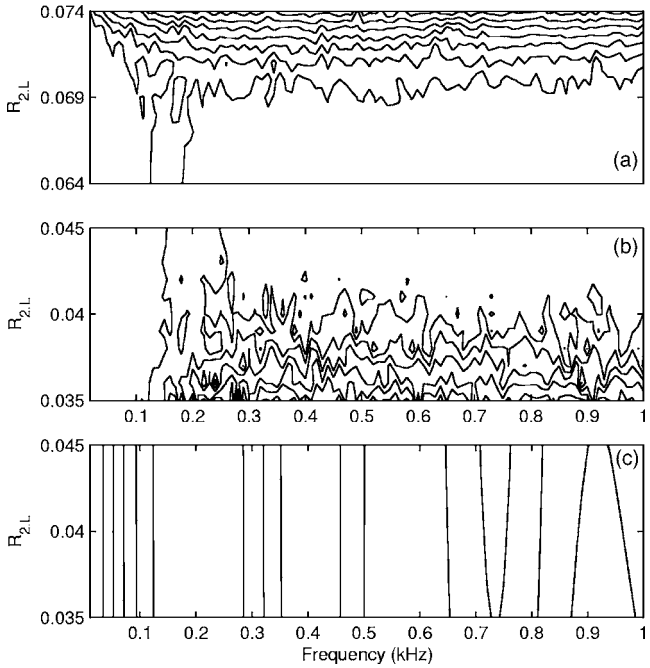

FIG. 12. TL contour plot for three-duct CCTR for various values of $R_{2,L}$. (a) and (b) the conventional approach and (c) with the BCT algorithm.

is absent. Results for such extreme criterion are not attainable by simple extrapolation due to the empirical nature of the perforate impedance expressions. But the strength of the BCT algorithm allows one to analyze CTRs with small values of perforate impedance. The unstable spectrum of Fig. 13(a) relates to the TL of a CCTR shown in Fig. 1 for a porosity of merely 0.15. Numerical computations become highly unstable with decreasing impedance. This is due to the astronomically large values associated with the individual complex elements of the overall transfer matrix $[\mathbf{\Omega}]$. Therefore, application of boundary conditions leads to computational errors. The $[\mathbf{\Omega}]_{ij}$'s are of the order of 10^{35} for an impedance of 0.1 times the impedance offered by the default parametric values (ζ_d). For 0.01 times the default impedance (1% of ζ_d), it becomes 10^{110}. As mentioned earlier, conventional approaches[12] would fail while working with such enormously large numbers. Although it may look unnecessary from the practical point of view, the corresponding TL spectra for the same configuration but with smaller impedances are shown in Fig. 13(b) to demonstrate the extreme credibility of the BCT approach presented here.

V. CONCLUDING REMARKS

It has been shown above that in the conventional transfer matrix approach instabilities result from application of boundary conditions to the product transfer matrix of perforate elements like uniform/simple CTRs as well as conical CTRs. Transfer of boundary conditions from segment to segment helps in overcoming the problem. The credibility of the boundary-condition-transfer (BCT) approach is made apparent through a detailed comparative study and hence should be used to overcome the limitations posed by the conventional transfer matrix approach. By rectifying numerical instabilities, if at all there are any, it is always feasible to make

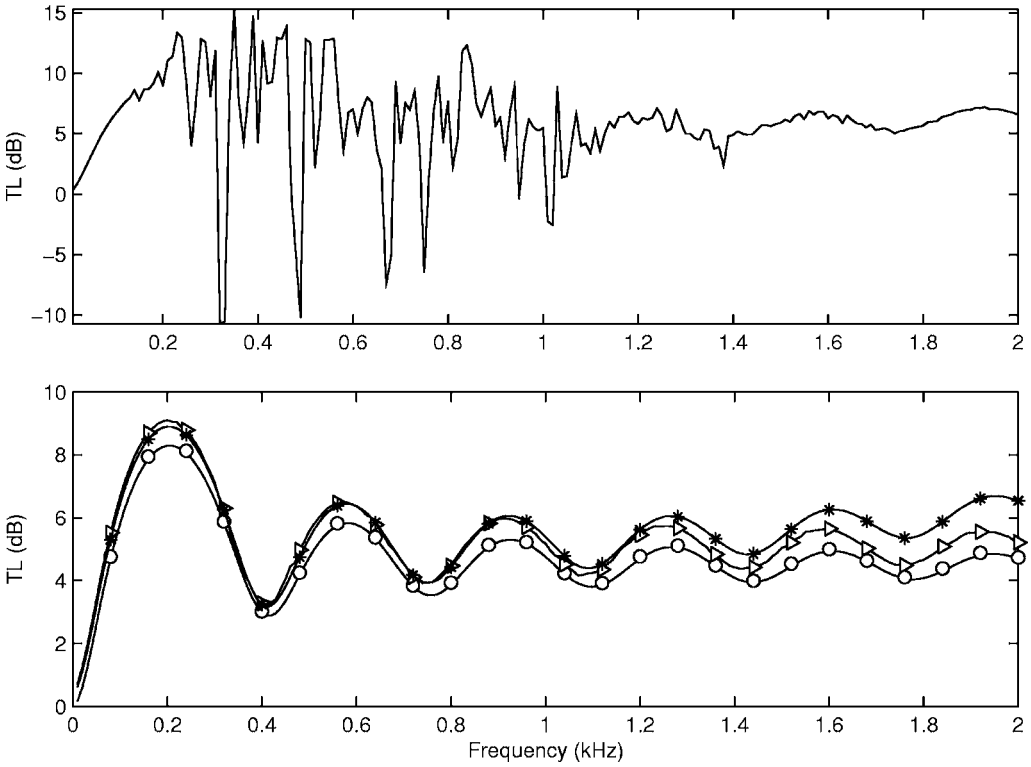

FIG. 13. TL spectrum of the two-duct CCTR (L=0.5 m) for different perforate impedances; (a) the conventional approach and (b) the BCT algorithm. *—*—*, $\zeta=\zeta_d$, $\mathbf{N}=10$; ▷—▷—▷, $\zeta=0.1\times\zeta_d$, $\mathbf{N}=10^2$; and ○—○—○, $\zeta=0.01\times\zeta_d$, $\mathbf{N}=10^3$.

inroads into better solutions. Although it is applied here to acoustical problems, the BCT approach may find a significant role in other forms of wave phenomena, particularly in the analysis of multiply-connected muffler elements used in automobiles. Due to its complex structure, the three-duct configuration of Fig. 10 is certainly of least use from the application point of view, but it narrates a different facet of the BCT algorithm. This algorithm can be made use of for analyzing the performance of the long acoustic wedges, where the instability is even more severe due to the wave propagation in the porous sound absorbing material.

The large numbers associated with the system matrix are not necessarily functions of the spatial dimensions. Low perforate impedance at the interface, as mentioned earlier, yields astronomically large numbers. The concept of such hypothetical low perforated impedances can be used while predicting the acoustic performance of a wedge of an anechoic chamber. For instance, the wedges that are unwrapped (without the protection of perforated plates) may be modeled with a perforated screen of infintesimally small value of acoustic impedance at the perforated interface. This forms the subject matter of another paper.

ACKNOWLEDGMENTS

The authors would like to place on record their appreciation of the financial sponsorship of FRITA by the Department of Science and Technology of the Government of India.

APPENDIX A: ELEMENTS OF THE SYSTEM MATRIX $[\upsilon]$

The square matrix $[\upsilon]$ associated with the matrix equations (5) has generalized elements $[\upsilon]_{ij}$ for any arbitrary concentric tube resonator (CTR) configuration, provided no singularity is encountered there during analytical modeling. Neglecting the M_1^3 and higher order terms, the matrix elements are given by

$$[\upsilon]_{11}=\gamma_1[jk_0M_1+M_1^2(\ln S_1)']-[\upsilon]_{12}, \tag{A1}$$

$$[\upsilon]_{12}=2\gamma_1\frac{M_1}{\zeta r(z)}, \tag{A2}$$

$$[\upsilon]_{13}=\gamma_1[-jk_0+2M_1(\ln S_1')], \tag{A3}$$

$$[\upsilon]_{21}=2\pi\gamma_2\frac{M_2r(z)}{\zeta S_2(z)}, \tag{A4}$$

$$[\upsilon]_{22}=\gamma_2[jk_0M_2+M_2^2(\ln S_2')]-[\upsilon]_{21}, \tag{A5}$$

$$[\upsilon]_{24}=\gamma_2[-jk_0+2M_2(\ln S_2')], \tag{A6}$$

$$[\upsilon]_{31}=-jk_0\gamma_1-[\upsilon]_{32}, \tag{A7}$$

$$[\upsilon]_{32}=\frac{2\gamma_1}{\zeta r(z)}, \tag{A8}$$

$$[\upsilon]_{33}=\gamma_1[jk_0M_1-(1+M_1^2)(\ln S_1')], \tag{A9}$$

$$[\upsilon]_{41} = \gamma_2 \frac{2\pi r(z)}{\zeta S_2(z)}, \tag{A10}$$

$$[\upsilon]_{42} = -jk_0\gamma_2 - [\upsilon]_{41}, \tag{A11}$$

$$[\upsilon]_{44} = \gamma_2[jk_0M_2 - (1+M_2^2)(\ln S_2')], \tag{A12}$$

where $r(z)=R_1(z)$ is the radius of tube. The rest of the matrix elements are identically equal to zero, and

$$\gamma_i = \frac{1}{1-M_i^2}, \quad i=1,2. \tag{A13}$$

Though γ_i in Eq. (A13) depends on z, it may be assumed to be invariant on the basis of an averaged mean flow velocity over a segment, for simplification.

APPENDIX B: APPLICATION OF THE BCT ALGORITHM

Here the methodology for applying the BCT algorithm is presented with an example in the form of the CCTR of Fig. 1(a). The boundary conditions may be given in terms of zero admittance (zero normal particle velocity) at both the axial boundaries of the cavity. For the sake of illustration, let us assume that the muffler comprises two ($\mathbf{N}=2$) equal segments. Let the transmission matrix $[\mathbf{\Phi}]$ of Eq. (8) for the first segment, spanning $z=0$ to $z=L/2$, be given as $[\mathbf{A}]$ and the corresponding one for the second segment ($z=L/2$ to $z=L$) be denoted as $[\mathbf{B}]$. Thus, there is a set of three state vectors $\{\mathbf{Y}\}^1$, $\{\mathbf{Y}\}^2$, and $\{\mathbf{Y}\}^3$ of the form of Eq. (6) defined at $z=0$, $z=L/2$, and $z=L$, respectively. Matrix $[\mathbf{A}]$ connects $\{\mathbf{Y}\}^1$ to $\{\mathbf{Y}\}^2$ whereas $[\mathbf{B}]$ operates between $\{\mathbf{Y}\}^2$ and $\{\mathbf{Y}\}^3$.

The essential task is to determine the coefficients $(\mathbf{C}_{f_\ell})_\phi^j$'s of Eq. (16) for the vectors, other than the one where the boundary condition is defined, across the segmental transmission matrices $[\mathbf{\Phi}]$'s. Applying the boundary condition $u_{2,(z=0)}=0$ on the state vector $\{\mathbf{Y}\}^1$, u_2^1 may be given in terms p_1^1, p_2^1, and u_1^1 by

$$u_2^1 = (\mathbf{C}_{f_1})_1^1 p_1^1 + (\mathbf{C}_{f_1})_2^1 p_2^1 + (\mathbf{C}_{f_1})_3^1 u_1^1, \tag{B1}$$

where the coefficients $(\mathbf{C}_{f_1})_1^1$, $(\mathbf{C}_{f_1})_2^1$, and $(\mathbf{C}_{f_1})_3^1$ are identically equal to zero. Components of the vector $\{\mathbf{Y}\}^1$ can be expressed in terms of $\{\mathbf{Y}\}^2$ and the transfer matrix $[\mathbf{A}]$:

$$\begin{aligned} p_1^1 &= \mathbf{A}_{11}p_1^2 + \mathbf{A}_{12}p_2^2 + \mathbf{A}_{13}u_1^2 + \mathbf{A}_{14}u_2^2, \\ p_2^1 &= \mathbf{A}_{21}p_1^2 + \mathbf{A}_{22}p_2^2 + \mathbf{A}_{23}u_1^2 + \mathbf{A}_{24}u_2^2, \\ u_1^1 &= \mathbf{A}_{31}p_1^2 + \mathbf{A}_{32}p_2^2 + \mathbf{A}_{33}u_1^2 + \mathbf{A}_{34}u_2^2, \\ u_2^1 &= \mathbf{A}_{41}p_1^2 + \mathbf{A}_{42}p_2^2 + \mathbf{A}_{43}u_1^2 + \mathbf{A}_{44}u_2^2. \end{aligned} \tag{B2}$$

It may be noted that the superscript here indicates the location or the section, and not power of the state variables. Applying the expressions for p_1^1, p_2^1, and u_1^1 of Eqs. (B2) in Eqs. (B1) and equating the resulting u_2^1 with that of Eqs. (B2), a linear relationship among the components of the vector $\{\mathbf{Y}\}^2$ may be developed. Thus, u_2^2 may be given in terms of p_1^2, p_2^2, u_1^2 and a set of respective coefficients $(\mathbf{C}_{f_1})_j^2$, $j=1$, 2, and 3. The coefficients $(\mathbf{C}_{f_1})_1^2$, $(\mathbf{C}_{f_1})_2^2$, and $(\mathbf{C}_{f_1})_3^2$ for vector $\{\mathbf{Y}\}^2$ are functions of the coefficients $(\mathbf{C}_{f_1})_1^1$, $(\mathbf{C}_{f_1})_2^1$, and $(\mathbf{C}_{f_1})_3^1$ and matrix $[\mathbf{A}]$. Making use of the coefficients of the vector $\{\mathbf{Y}\}^2$ and matrix $[\mathbf{B}]$, the above procedure would be repeated to determine the corresponding relationship and hence the coefficients $(\mathbf{C}_{f_1})_1^3$, $(\mathbf{C}_{f_1})_2^3$, and $(\mathbf{C}_{f_1})_3^3$ for vector $\{\mathbf{Y}\}^3$. Basically, each of the above boundary conditions brings about a set of coefficients for each of the intermediate state vector.

Similarly, the other boundary condition $u_{2,(z=L)}=0$ will generate a different set of coefficients at each of the state vectors. Let the relationships among the components of the vector $\{\mathbf{Y}\}^2$ corresponding to both the boundary conditions be given as

$$u_2^2 = (\mathbf{C}_{f_1})_1^2 p_1^2 + (\mathbf{C}_{f_1})_3^2 p_2^2 + (\mathbf{C}_{f_1})_4^2 u_1^2, \tag{B3a}$$

$$u_2^2 = (\mathbf{C}_{f_2})_1^2 p_1^2 + (\mathbf{C}_{f_2})_2^2 p_2^2 + (\mathbf{C}_{f_2})_3^2 u_1^2. \tag{B3b}$$

Equating the expressions for u_2^2 of Eqs. (B3b) and (B3a), p_2^2 and u_2^2 may be expressed in terms of p_1^2 and u_1^2:

$$p_2^2 = \mathbf{C}_1 p_1^2 + \mathbf{C}_2 u_1^2 \quad \text{and} \quad u_2^2 = \mathbf{D}_1 p_1^2 + \mathbf{D}_2 u_1^2. \tag{B4}$$

Thus, the regular expression for p_1^1 and u_1^1 of Eqs. (B2) may be given in terms of p_1^2 and u_1^2:

$$\begin{aligned} p_1^1 &= (\mathbf{A}_{11} + \mathbf{C}_1\mathbf{A}_{12} + \mathbf{D}_1\mathbf{A}_{14})p_1^2 + (\mathbf{A}_{13} + \mathbf{C}_2\mathbf{A}_{12} \\ &\quad + \mathbf{D}_2\mathbf{A}_{14})u_1^2, \\ u_1^1 &= (\mathbf{A}_{31} + \mathbf{C}_1\mathbf{A}_{32} + \mathbf{D}_1\mathbf{A}_{34})p_1^2 + (\mathbf{A}_{33} + \mathbf{C}_2\mathbf{A}_{32} \\ &\quad + \mathbf{D}_2\mathbf{A}_{34})u_1^2, \end{aligned} \tag{B5a}$$

or,

$$[p_1^1 \quad u_1^1]^T = [T]^1[p_1^2 \quad u_1^2]^T. \tag{B5b}$$

Equations (B5b) represent the 2×2 transfer matrix $[T]^1$ of Eq. (22) for the first segment. Similarly, the second-order transfer matrix $[T]^2$ corresponding to the second segment may be determined. The product of the two transfer matrices $[T]^1$ and $[T]^2$ yields the overall transfer matrix $[T]_1$ of Eq. (23).

[1] J. W. Sullivan and M. J. Crocker, "Analysis of concentric tube resonators having unpartitioned cavities," J. Acoust. Soc. Am. **64**, 207–215 (1978).
[2] J. W. Sullivan, "A method for modeling perforated tube muffler components. I. Theory," J. Acoust. Soc. Am. **66**, 772–778 (1979).
[3] M. L. Munjal, *Acoustics of Ducts and Mufflers* (Wiley, New York, 1987).
[4] M. L. Munjal, K. N. Rao, and A. D. Sahasrabudhe, "Aeroacoustic analysis of perforated muffler components," J. Sound Vib. **114**(2), 173–188 (1987).
[5] K. S. Peat, "A numerical decoupling analysis of perforated pipe silencer elements," J. Sound Vib. **123**(2), 199–212 (1988).
[6] G. R. Gogate and M. L. Munjal, "Analytical and experimental aeroacoustic studies of open-ended three-duct perforated elements used in mufflers," J. Acoust. Soc. Am. **97**(5), 2919–2927 (1995).
[7] M. L. Munjal, "Analysis of a flush-tube three-pass perforated element muffler by means of transfer matrices," Int. J. Acoust. Vib. **2**(2), 63–68 (1997).
[8] M. L. Munjal, "Muffler Acoustics," Chapter K in *Formulas of Acoustics*, edited by F. P. Mechel (Springer-Verlag, Berlin, 2002).
[9] E. Dokumaci, "Matrizant approach to acoustic analysis of perforated multiple pipe mufflers carrying mean flow," J. Sound Vib. **191**(4), 505–518 (1998).
[10] H. F. Baker, "On the integration of the linear differential equations," Proc. London Math. Soc. XXXV, 333–378 (1902).
[11] R. A. Frazer, W. J. Duncan, and A. R. Collar, *Elementary Matrices and*

Some Applications to Dynamics and Differential Equations (Cambridge U. P., Cambridge, 1952).
[12]T. Kar and M. L. Munjal, "Analysis and design of conical concentric tube resonators," J. Acoust. Soc. Am. **116**(1), 74–83 (2004).
[13]T. Kar and M. L. Munjal, "Generalized analysis of a muffler with any number of interacting ducts," J. Sound Vib. (in press).
[14]T. H. Melling, "The acoustic impedance of perforates at medium and high sound level," J. Sound Vib. **29**(1), 1–65 (1973).

Analysis of sound propagation in a fluid through a screen of scatterers

Y. C. Angel[a)]
Therapeutic Applications of Ultrasound Laboratory, INSERM UMR 556, Université Claude Bernard Lyon 1, 151, Cours Albert Thomas, 69424 Lyon Cedex 03, France

C. Aristégui[b)]
Laboratoire de Mécanique Physique, CNRS UMR 5469, Université Bordeaux 1, 351, Cours de la Libération, 33405 Talence Cedex, France

(Received 26 July 2004; revised 18 April 2005; accepted 24 April 2005)

A multiple scattering analysis in a nonviscous fluid is developed in detail in order to predict the coherent sound motion in the presence of disordered heterogeneities, such as particles, fibers, bubbles, or contrast agents. Scatterers can be homogeneous, layered, shell-like with encapsulated liquids or gas, nonabsorbing, or absorbing, and can take a wide variety of shapes. *A priori* imposed limitations or physical assumptions are absent in the derivation, whether they concern the expected response of the fluid-scatterer mixture, the scatterer size relative to wavelength, or the scatterer concentration or the screen thickness. However, as in any multiple scattering formulation, a closure assumption is invoked. Closed-form results for the backscattered and forward-scattered wave motions on either side of the screen of scatterers are obtained. The fluid-scatterer mixture is shown to behave as an effective dissipative medium from the standpoint of the coherent motion. It is found that the effective medium is fully described once two parameters are determined: the effective wave number and the reflection coefficient for the associated half-space screen. Remarkably, both parameters depend only on the far-field scattering properties of a *single* scatterer. © *2005 Acoustical Society of America.* [DOI: 10.1121/1.1931088]

PACS number(s): 43.20.Gp, 43.20.Fn [ANN] Pages: 72–82

I. INTRODUCTION

In biological tissue, in structural materials, or in the ocean, ultrasonic signals are often subjected to scattering by small inhomogeneities, such as hard grains, contrast agents, solid particles, fibers, pores, or bubbles. Each scatterer exchanges acoustic energy with all the others, and multiple transport paths are possible in the sample.[1,2] This causes experimental difficulties, as in the construction of images, and also fundamental difficulties, as in the construction of analytical models.

This paper attempts to provide fundamental understanding that is lacking concerning wave propagation in the presence of multiple scatterers. We focus attention on the coherent wave motion.[3,4] It is, by definition, the statistical average of all motions corresponding to all possible configurations of the scatterers. Experimentally, this average on disorder can be performed either by using receivers with large active areas or by moving the emitting and receiving transducers relative to the sample to be inspected.[5]

Coherent backscattered motions are usually accessible in practice. They cannot be used to extract information on the exact position of each scatterer. However, they contain information on the concentration as well as on the material and geometrical properties of the scatterers. For example, to count bubbles and determine their average size *in vivo* during high-temperature cancer treatments,[6] the analysis of this paper could prove a very useful tool.

We provide here a detailed analytical derivation of the coherent motion, when the scatterers form a screen of finite thickness and are uniformly distributed in a nonviscous fluid. Since viscosity is neglected, only pressure waves can propagate in the fluid. We show that the analysis yields explicit expressions for the waves propagating outside and inside the screen. Further, we observe from the results that two parameters are required to describe completely this system of waves.

We call these parameters K and Q. By K we denote the effective wave number, and by Q we denote a frequency-dependent dimensionless parameter that characterizes the screen "boundaries." We use here the term "boundary" for lack of a better term since, for any fixed configuration of scatterers, it is possible to walk in and out of the screen while staying in the fluid.

Our derivation yields an expression for the effective wave number that is independent of the screen thickness, which makes it an intrinsic property of the fluid-scatterer mixture. This result is consistent with the notion of an effective medium. We also find that the effective wave number is identical to that found elsewhere for a semi-infinite screen.[7]

The parameter Q has appeared elsewhere either explicitly or implicitly,[8–11] but the expression that is derived in this paper is not to be found in those references. The reason for this discrepancy is that the earlier derivations for Q make use of continuity conditions for both velocity and pressure at the

[a)]Electronic mail: angel@univ-lyon1.fr
[b)]Electronic mail: c.aristegui@lmp.u-bordeaux1.fr

 0001-4966/2005/118(1)/72/11/$22.50

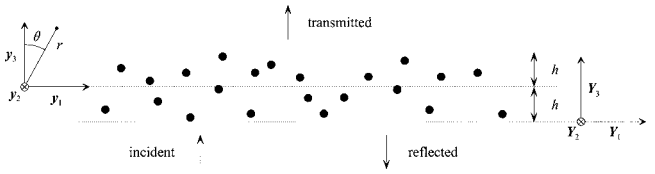

FIG. 1. Layer of scatterers and system of acoustic waves.

screen "boundaries." However, pressure continuity can be written only if an effective mass density is assumed for the fluid-scatterer mixture in the screen. Thus, it is assumed in those works that the screen behaves *a priori* like an effective medium.

Our derivation shows that the coherent wave motion outside and inside the screen can be determined independently of any continuity assumption, and therefore of any mass density assumption. We demonstrate that the screen is indeed equivalent to an effective medium.

We have chosen to perform our analysis in the context of the theory proposed by Waterman and Truell,[7] whose predictions have stood the test of multiple cross examinations.[12] The theory applies to anisotropic scatterers and is considered to be valid for low scatterer concentration.

The presentation of the paper is as follows. In Sec. II, we describe a distribution of identical cylindrical or spheroidal scatterers immersed in a nonviscous fluid. We assume that the fluid occupies the entire space, but the scatterers occupy positions inside a layer of finite thickness. The cylinder problem (2D case) and the spheroid problem (3D case) are analyzed in parallel in the remainder of the paper.

The coherent displacement field in the fluid is defined in Sec. III, and the various fields that are needed for its determination are described in Secs. IV and V. This approach yields a system of equations that is not closed, as is typical in multiple scattering problems.[1,2] A closure assumption, which is discussed in detail in Sec. VI, allows us to determine the coherent wave motion in closed form outside and inside the screen.

Formulas for the effective wave number K, the dimensionless parameter Q, and the amplitudes of the various displacement fields are given in Secs. VII and VIII. The limiting case of a semi-infinite screen, partly studied by Waterman and Truell,[7] is examined in Sec. IX. Then we infer that the parameter Q can be interpreted as the reflection coefficient at the "boundary" of the associated semi-infinite screen of scatterers. Predictions for the special case of a screen of isotropic scatterers are obtained in Sec. X. Finally, we summarize the analysis in Sec. XI.

II. SCREEN OF SCATTERERS

We consider a layer of scatterers in a nonviscous fluid subjected to the action of a wave, as shown in Fig. 1.

The scatterers, of identical geometry and elastic properties, are uniformly and randomly distributed in the layer of thickness $2h$, where their number concentration is n_0. Interaction with the scatterers causes the incident wave to be reflected on one side of the layer and transmitted on the other.

The wave motion in the fluid is the superposition of the incident wave and the waves multiply scattered by all the scatterers. For a given incident wave and a given number concentration n_0, there exist an infinite number of scatterer configurations and an infinite number of corresponding wave motions. The average of these wave motions is a weighted sum, where the weight represents the probability of finding a given configuration among all possible configurations.

The scatterers have either cylindrical geometry, with constant cross section along the y_2 direction of Fig. 1, or spheroidal geometry. Thus, we consider, respectively, two- and three-dimensional problems. We assume further that, in the 2D case, the cross sections are symmetrical with respect to axes parallel to the y_3 axis. In the 3D case, we assume that the scatterers have a symmetry of revolution with respect to those axes.

It follows from the preceding assumptions on the distribution and geometry of the scatterers that the wave system in Fig. 1, after averaging on disorder, is one-dimensional. These waves cause the fluid particles to move with displacement u_3 in the y_3 direction, where u_3 is measured from equilibrium. The particle velocity in the context of linear acoustics, the density variation, and the pressure variation from equilibrium values, respectively, are given by

$$v_3 = \frac{\partial u_3}{\partial t}, \quad \rho = -\rho_0 \frac{\partial u_3}{\partial y_3}, \quad p = c_0^2 \rho, \tag{1}$$

where ρ_0 denotes the equilibrium mass density and c_0 is the speed of sound in the fluid.

If the time dependence is of the form $\exp(-i\omega t)$ and the regime is continuous, the three waves of Fig. 1 are represented, respectively, by the three displacements

$$u_3^i = u_0 e^{ iky_3}, \quad u_3^r = -u_0 R e^{-iky_3}, \quad u_3^t = u_0 T e^{iky_3}, \tag{2}$$

where $k = \omega / c_0$ is the wave number, u_0 is an amplitude factor, R is the reflection coefficient, T is the transmission coefficient, and the factor $\exp(-i\omega t)$ has been omitted. The waves (2) propagate in the fluid outside the layer. Observe that a minus sign is used to represent the reflected motion. Inside the layer, where the scatterers are distributed, there is a system of two waves traveling, respectively, in the forward and backward directions.

The coefficients R and T in (2) represent, respectively, averages on disorder of the backscattered and forward-scattered amplitudes on either side of the screen. These amplitudes depend *a priori* on frequency, number concentration n_0, scatterer properties, the density and speed of sound in the surrounding fluid, and on the layer thickness $2h$. Another parameter is the angle of incidence, but in this work we focus attention on normal incidence.

The scattering properties of a single scatterer are described in 2D and 3D, respectively, by sets of coefficients C_n and S_n, where the letter C is used for "cylindrical" and the letter S for "spheroidal." Calling Φ the displacement potential[13] of the scattered motion in the fluid, one can write

$$\Phi(r,\theta) = \sum_{n=0}^{+\infty} \varepsilon_n A_n^{(2)} C_n H_n^{(1)}(kr) \cos(n\theta), \quad \text{in 2D}, \tag{3}$$

$$\Phi(r,\theta)=\sum_{n=0}^{+\infty}(2n+1)A_n^{(3)}S_n h_n^{(1)}(kr)P_n(\cos\theta),\quad \text{in 3D}. \tag{4}$$

These equations represent outgoing solutions of the Helmholtz equation. They are written in terms of the cylindrical and spherical Hankel functions, respectively, $H_n^{(1)}$ and $h_n^{(1)}$, and of the Legendre polynomials P_n. In Eq. (3), the Neumann factor is defined by $\varepsilon_0=1$ and $\varepsilon_n=2$, for all values of n greater than zero. The coefficients $A_n^{(2)}$ and $A_n^{(3)}$ characterize the displacement potential of the exciting motion on the scatterer. In Eqs. (3) and (4), the pairs of variables (r,θ) are, respectively, local cylindrical and spherical coordinates centered on the scatterer.

Let $\boldsymbol{\xi}$ denote the position of the scatterer in the coordinate system of Fig. 1. Then, the distance r is defined by either $r^2=(y_3-\xi_3)^2+(y_1-\xi_1)^2$ or $r^2=(y_3-\xi_3)^2+(y_1-\xi_1)^2+(y_2-\xi_2)^2$, depending on the dimension. In either case, however, the angle θ is such that $\cos\theta=(y_3-\xi_3)/r$. Corresponding to the incident wave of (2), one finds that the coefficients $A_n^{(2)}$ and $A_n^{(3)}$ of (3) and (4) are

$$A_n^{(2)}=A_n^{(3)}=-u_0 \mathrm{i}^{n+1}\mathrm{e}^{\mathrm{i}k\xi_3}/k. \tag{5}$$

These coefficients are those of the incident displacement potential Φ^i in the expressions

$$\Phi^i(r,\theta)=\sum_{n=0}^{+\infty}\varepsilon_n A_n^{(2)}J_n(kr)\cos(n\theta),\quad \text{in 2D}, \tag{6}$$

$$\Phi^i(r,\theta)=\sum_{n=0}^{+\infty}(2n+1)A_n^{(3)}j_n(kr)P_n(\cos\theta),\quad \text{in 3D}, \tag{7}$$

where J_n and j_n denote, respectively, the cylindrical and spherical Bessel functions.

The rule (3) and (6) says that the nth exciting mode of amplitude $A_n^{(2)}$ is scattered away from the local origin $r=0$, where the scatterer is centered, with amplitude $A_n^{(2)}C_n$. The coefficient C_n acts as an amplification factor and is dimensionless. Further, each scattered mode has a Log r $(n=0)$ or r^{-n} $(n\geqslant 1)$ singularity as r approaches zero. Analogous comments can be made concerning the rule (4) and (7) in the 3D case, except that the singularity is of the type r^{-n-1} as r approaches zero.

Observe that the origin $r=0$ is inside the scatterer and the scattered field is defined outside the scatterer. Thus there is no singularity in the region where (3) or (4) holds. The coefficients C_n and S_n depend on frequency, as well as on the properties of the scatterer and of the fluid outside. In particular, scatterers can be nonabsorbing or absorbing.[14,15]

In the next section, we shall reduce the geometry of each scatterer to a line (in 2D) or a point (in 3D). To this line, we associate the scattered potential (3), where the coefficients C_n are evaluated by imposing appropriate boundary conditions on the *real-size* cylinder. Thus, we shall replace the real scatterer with a new scattering object, such that the geometry is modified but the scattering properties are preserved. This geometrical simplification, however, causes the singularity of (3) to be no longer embedded inside the scatterer. The scattered potential of (3) is now a singular solution of the 2D Helmholtz equation in the fluid. Similar remarks can be made concerning the 3D scatterer, the potential of (4), the coefficients S_n, and the r^{-n-1} singularity.

III. COHERENT MOTION

The coherent motion in the fluid of Fig. 1 is, according to the Foldy-Twersky approach, the sum of the incident motion and of the wave motions scattered by all the scatterers.[1,7] In terms of the displacement components in the y_3 direction, one has[16]

$$u_3^{(2)}(y_3)=u_3^i(y_3)+n_0\int_{-h}^{h}\int_{-\infty}^{+\infty}u_3(y_3,y_1;\xi_3,\xi_1)d\xi_3\,d\xi_1,\quad \text{in 2D}, \tag{8}$$

$$u_3^{(3)}(y_3)=u_3^i(y_3)+n_0\int_{-h}^{h}\int_{-\infty}^{+\infty}\int_{-\infty}^{+\infty}u_3(y_3,y_1,y_2;\xi_3,\xi_1,\xi_2)\times d\xi_3\,d\xi_1\,d\xi_2,\quad \text{in 3D}. \tag{9}$$

The second term on the right-hand side of (8) represents the global contribution of all scatterers located at all possible positions (ξ_3,ξ_1) in the layer of thickness $2h$, under the assumption that the distribution is random and uniform. The same interpretation holds for the second term on the right-hand side of (9), except that scatterers occupy positions (ξ_3,ξ_1,ξ_2) and an additional integration has to be performed in the ξ_2 direction. The dimensions of the number densities n_0 in (8) and (9) are, respectively, an inverse area and an inverse volume.

The term $u_3(y_3,y_1;\xi_3,\xi_1)$ in (8) is an average displacement corresponding to the wave motion scattered by the line at (ξ_3,ξ_1). The average on disorder is taken over all configurations keeping the line at (ξ_3,ξ_1) fixed. Thus, it is a partial average. The coordinate y_1 is integrated out on the right-hand side of (8) owing to the translational invariance in the y_1 direction.

The corresponding term $u_3(y_3,y_1,y_2;\xi_3,\xi_1,\xi_2)$ in (9) is likewise an average displacement corresponding to the wave motion scattered by the point at (ξ_3,ξ_1,ξ_2) when this point is kept fixed. Both coordinates y_1 and y_2 are integrated out on the right-hand side of (9).

When all the scatterers occupy deterministic positions, each scatterer "sees" an exciting wave motion that is the result of scattering processes of all orders (single, double, triple,…)[1,2] inside the screen. Keeping the scatterer fixed and averaging these exciting wave motions, one defines the average exciting motion and the corresponding displacement potential Φ^E. Assuming that this potential is a *bounded* solution of the Helmholtz equation in the fluid, one finds that the most general expression of Φ^E corresponding to a scatterer fixed at $\boldsymbol{\xi}$ is

$$\Phi^E(y_3,y_1;\xi_3,\xi_1)=u_0\sum_{n=0}^{+\infty}\varepsilon_n E_n^{(2)}(\xi_3)J_n(k|\mathbf{y}-\boldsymbol{\xi}|)\times\cos(n\theta),\quad \text{in 2D}, \tag{10}$$

$$\Phi^E(y_3,y_1,y_2;\xi_3,\xi_1,\xi_2) = u_0\sum_{n=0}^{+\infty}(2n+1)E_n^{(3)}(\xi_3)j_n(k|\mathbf{y}-\boldsymbol{\xi}|) \times P_n(\cos\theta), \quad \text{in 3D}, \tag{11}$$

where the angle θ is defined by $\cos\theta=(y_3-\xi_3)/|\mathbf{y}-\boldsymbol{\xi}|$ and the distance $|\mathbf{y}-\boldsymbol{\xi}|=r$ is defined as in (3) and (4). The coefficients $E_n^{(2)}$ and $E_n^{(3)}$ in (10) and (11), respectively, depend only on ξ_3, owing to the translational invariance in the y_1 and y_2 directions.

Next we recall the scattering rule (3) and (6) in 2D and the analogous rule (4) and (7) in 3D. Thus, we infer that the average scattered potentials corresponding to (10) and (11), respectively, are given by

$$\Phi(y_3,y_1;\xi_3,\xi_1) = u_0\sum_{n=0}^{+\infty}\varepsilon_n C_n E_n^{(2)}(\xi_3)H_n^{(1)}(k|\mathbf{y}-\boldsymbol{\xi}|) \times\cos(n\theta), \quad \text{in 2D}, \tag{12}$$

$$\Phi(y_3,y_1,y_2;\xi_3,\xi_1,\xi_2) = u_0\sum_{n=0}^{+\infty}(2n+1)S_n E_n^{(3)}(\xi_3)h_n^{(1)} \times(k|\mathbf{y}-\boldsymbol{\xi}|)P_n(\cos\theta), \quad \text{in 3D}. \tag{13}$$

The average scattered components u_3 on the right-hand sides of (8) and (9) are obtained by differentiating (12) and (13), respectively, with respect to y_3. We differentiate the combinations $H_n^{(1)}\cos(n\theta)$ and $h_n^{(1)}P_n(\cos\theta)$ in (12) and (13) with respect to y_3 by using the chain rule relative to the local coordinates $r=|\mathbf{y}-\boldsymbol{\xi}|$ and θ, and by using properties of the derivatives of the Hankel functions and Legendre polynomials.[17,18] After differentiation, rearranging terms in the series (12) and (13), and substituting the results into (8) and (9), respectively, one finds that

$$u_3^{(2)}(y_3) = u_0e^{ik y_3} + n_0u_0k\sum_{n=0}^{+\infty}\int_{-h}^{h}(C_{n+1}E_{n+1}^{(2)}(\xi_3) - C_{n-1}E_{n-1}^{(2)} \times(\xi_3))\varphi_n^{(2)}(y_3-\xi_3)d\xi_3, \quad \text{in 2D}, \tag{14}$$

$$u_3^{(3)}(y_3) = u_0e^{ik y_3} + n_0u_0k\sum_{n=0}^{+\infty}\int_{-h}^{h}((n+1)S_{n+1}E_{n+1}^{(3)}(\xi_3) - nS_{n-1}E_{n-1}^{(3)}(\xi_3))\varphi_n^{(3)}(y_3-\xi_3)d\xi_3, \quad \text{in 3D}. \tag{15}$$

Observe that to keep expressions compact in (14) and (15), we have defined $C_{-1}=0$, $S_{-1}=0$, $E_{-1}^{(2)}(\xi_3)=0$, and $E_{-1}^{(3)}(\xi_3)=0$. The quantities $\varphi_n^{(2)}$ and $\varphi_n^{(3)}$ on the right-hand sides of (14) and (15), respectively, are defined by

$$\varphi_n^{(2)}(y_3-\xi_3) = \int_{-\infty}^{+\infty}H_n^{(1)}(k|\mathbf{y}-\boldsymbol{\xi}|)\cos(n\theta)d\xi_1, \quad \text{in 2D}, \tag{16}$$

$$\varphi_n^{(3)}(y_3-\xi_3) = \int_{-\infty}^{+\infty}\int_{-\infty}^{+\infty}h_n^{(1)}(k|\mathbf{y}-\boldsymbol{\xi}|) \times P_n(\cos\theta)d\xi_1\,d\xi_2, \quad \text{in 3D}. \tag{17}$$

The integrals (16) and (17) are evaluated, respectively, over the entire real line and the entire plane. They can be evaluated by mathematical induction, which yields the results[9,19,20]

$$\varphi_{2n}^{(2)}(y_3-\xi_3) = (-1)^n\frac{2}{k}e^{ik|\xi_3-y_3|}, \tag{18}$$

$$\varphi_{2n+1}^{(2)}(y_3-\xi_3) = i(-1)^n\frac{2}{k}\,\mathrm{sgn}(\xi_3-y_3)e^{ik|\xi_3-y_3|}, \tag{19}$$

$$\varphi_n^{(3)}(y_3-\xi_3) = \frac{\pi}{k}\varphi_n^{(2)}(y_3-\xi_3), \tag{20}$$

where $n=0,1,2,\ldots$ and sgn denotes the sign function. It follows from (14)–(20) that the coherent displacements in the fluid are given by

$$u_3^{(q)}(y_3) = u_0e^{ik y_3} + n_0u_0k\int_{-h}^{h}\sigma_1^{(q)}(\xi)e^{ik|\xi-y_3|}\,d\xi + in_0u_0k\int_{-h}^{h}\sigma_2^{(q)}(\xi)\mathrm{sgn}(\xi-y_3)e^{ik|\xi-y_3|}\,d\xi, \tag{21}$$

where $q=2$ and $q=3$ correspond, respectively, to the 2D and 3D cases. The functions $\sigma_1^{(q)}(\xi)$ and $\sigma_2^{(q)}(\xi)$ in (21) are defined by

$$\sigma_1^{(2)}(\xi) = \frac{2}{k}\sum_{j=0}^{+\infty}(-1)^j(C_{2j+1}E_{2j+1}^{(2)}(\xi) - C_{2j-1}E_{2j-1}^{(2)}(\xi)),$$
$$\sigma_2^{(2)}(\xi) = \frac{2}{k}\sum_{j=0}^{+\infty}(-1)^j(C_{2j+2}E_{2j+2}^{(2)}(\xi) - C_{2j}E_{2j}^{(2)}(\xi)), \tag{22}$$

$$\sigma_1^{(3)}(\xi) = \frac{2\pi}{k^2}\sum_{j=0}^{+\infty}(-1)^j((2j+1)S_{2j+1}E_{2j+1}^{(3)}(\xi) - 2jS_{2j-1}E_{2j-1}^{(3)}(\xi)),$$
$$\sigma_2^{(3)}(\xi) = \frac{2\pi}{k^2}\sum_{j=0}^{+\infty}(-1)^j((2j+2)S_{2j+2}E_{2j+2}^{(3)}(\xi) - (2j+1)S_{2j}E_{2j}^{(3)}(\xi)). \tag{23}$$

The two integrals on the right-hand side of (21) represent the contribution of all the scattering processes taking place inside the layer. If all the scatterers are removed ($n_0=0$), this contribution vanishes and only the incident wave propagates in the fluid.

It follows from (21) that the reflected coherent motion is a plane wave of wave number k and amplitude $u_0R^{(q)}$ and the transmitted coherent motion is a plane wave of wave number k and amplitude $u_0T^{(q)}$, as in (2). Expressions for the coefficients $R^{(q)}$ and $T^{(q)}$ are obtained by setting, respectively, $y_3<-h$ and $y_3>h$ on the right-hand side of (21). We find that

$$R = -n_0 k \int_{-h}^{h} (\sigma_1(\xi) + \mathrm{i}\sigma_2(\xi)) \mathrm{e}^{\mathrm{i}k\xi}\, d\xi, \tag{24}$$

$$T = 1 + n_0 k \int_{-h}^{h} (\sigma_1(\xi) - \mathrm{i}\sigma_2(\xi)) \mathrm{e}^{-\mathrm{i}k\xi}\, d\xi. \tag{25}$$

For simplicity, the superscript q has been omitted on R, T, σ_1, and σ_2 in (24) and (25).

The transmitted coherent wave is the sum of the incident wave and all the forward-scattered waves, whereas the reflected coherent wave is constructed only from the backscattered waves. Inside the layer, where $-h<y_3<h$, one infers from (21) that the coherent displacement u_3 is the sum of one term with an $\exp(iky_3)$ factor and another term with an $\exp(-iky_3)$ factor. Both terms have "amplitudes" that depend on y_3. In this form, the coherent motion inside the layer looks rather complicated. To write it in a more interesting form, we need to determine the functions $E_n(\xi)$, which are still unknown at this point in our discussion.

IV. SCATTERED MOTION

For $-h<y_3<h$, we write each of the two integrals in (21) as a sum of two integrals over the intervals $(-h, y_3)$ and (y_3, h), respectively. Then, we write $y_3-\xi=y_3-\zeta_3+\zeta_3-\xi$, where ζ_3 is the coordinate along the y_3 direction of an arbitrary fixed point $\boldsymbol{\zeta}$ inside the layer. On each integration interval, we use the expansions

$$\mathrm{e}^{\mathrm{i}k(y_3-\zeta_3)} = \sum_{n=0}^{+\infty} \varepsilon_n \mathrm{i}^n J_n(k|\mathbf{y}-\boldsymbol{\zeta}|)\cos(n\alpha), \quad \text{in 2D}, \tag{26}$$

$$\mathrm{e}^{\mathrm{i}k(y_3-\zeta_3)} = \sum_{n=0}^{+\infty} (2n+1)\mathrm{i}^n j_n(k|\mathbf{y}-\boldsymbol{\zeta}|)P_n(\cos\alpha), \quad \text{in 3D}, \tag{27}$$

where the angle α is defined by $\cos\alpha=(y_3-\zeta_3)/|\mathbf{y}-\boldsymbol{\zeta}|$. After some rather lengthy but straightforward calculations, one finds that (21) can be written, for $-h<y_3<h$, in the equivalent form

$$u_3^{(2)}(y_3) = u_0\mathrm{e}^{\mathrm{i}ky_3} + n_0u_0k\sum_{n=0}^{+\infty} \varepsilon_n G_n^{(2)}(y_3,\zeta_3)J_n(k|\mathbf{y}-\boldsymbol{\zeta}|) \times\cos(n\alpha), \quad \text{in 2D}, \tag{28}$$

$$u_3^{(3)}(y_3) = u_0\mathrm{e}^{\mathrm{i}ky_3} + n_0u_0k\sum_{n=0}^{+\infty} (2n+1) G_n^{(3)}(y_3,\zeta_3)j_n(k|\mathbf{y}-\boldsymbol{\zeta}|) \times P_n(\cos\alpha), \quad \text{in 3D}. \tag{29}$$

In these equations, the term $G_n^{(q)}$ can be written as the sum of a term that depends only on ζ_3 and another term that depends on both ζ_3 and y_3. Thus, omitting the superscript q on F_n, D_n, σ_1, and σ_2, one has

$$G_n(y_3,\zeta_3) = F_n(\zeta_3) + D_n(y_3,\zeta_3), \tag{30}$$

with $|y_3|<h$ and $|\zeta_3|<h$. For even and odd values of the subscript, one finds that

$$F_{2n}(\zeta_3) = (-1)^n F_0(\zeta_3), \quad F_{2n+1}(\zeta_3) = (-1)^n F_1(\zeta_3), \tag{31}$$

$$D_{2n}(y_3,\zeta_3) = (-1)^n D_0(y_3,\zeta_3), \quad D_{2n+1}(y_3,\zeta_3) = (-1)^n D_1(y_3,\zeta_3), \tag{32}$$

$$F_0(\zeta_3) = \int_{-h}^{h} \sigma_1(\xi)\mathrm{e}^{\mathrm{i}k|\xi-\zeta_3|}\, d\xi + \mathrm{i}\int_{-h}^{h} \sigma_2(\xi)\mathrm{sgn}(\xi-\zeta_3) \times \mathrm{e}^{\mathrm{i}k|\xi-\zeta_3|}\, d\xi, \tag{33}$$

$$F_1(\zeta_3) = -\mathrm{i}\int_{-h}^{h} \sigma_1(\xi)\mathrm{sgn}(\xi-\zeta_3)\mathrm{e}^{\mathrm{i}k|\xi-\zeta_3|}\, d\xi + \int_{-h}^{h} \sigma_2(\xi)\mathrm{e}^{\mathrm{i}k|\xi-\zeta_3|}\, d\xi, \tag{34}$$

$$D_0(y_3,\zeta_3) = -2\mathrm{i}\int_{\zeta_3}^{y_3} \sigma_1(\xi)\sin(k(\xi-\zeta_3))d\xi - 2\mathrm{i}\int_{\zeta_3}^{y_3} \sigma_2(\xi)\cos(k(\xi-\zeta_3))d\xi, \tag{35}$$

$$D_1(y_3,\zeta_3) = 2\mathrm{i}\int_{\zeta_3}^{y_3} \sigma_1(\xi)\cos(k(\xi-\zeta_3))d\xi - 2\mathrm{i}\int_{\zeta_3}^{y_3} \sigma_2(\xi)\sin(k(\xi-\zeta_3))d\xi. \tag{36}$$

We observe that G_0 and G_1 determine G_n for all values of n. Further, the series expansions in (28) and (29) can be decomposed according to (30) into two series expansions. The series with the coefficients F_n are solutions of the Helmholtz equation in the fluid with wave number k. The series with the coefficients D_n are not in general solutions of that equation, because the D_n depend on y_3.

Observe that representations for u_3 analogous to (28) and (29) hold also in $y_3>h$ and $y_3<-h$. In these intervals, the coefficients G_n are independent of y_3, and exact expressions can be obtained readily from (21), (26), and (27). These remarks will be useful later when we approximate the exciting motion on a fixed scatterer.

V. EXCITING MOTION

When all the scatterers occupy deterministic positions, a scatterer at $\boldsymbol{\zeta}$ "sees" an exciting wave motion that is the sum of the incident motion and of the motions scattered by all the other scatterers.[1,7] Averaging on disorder, keeping the scatterer at $\boldsymbol{\zeta}$ fixed, one finds that the exciting displacement potentials are given by

$$\Phi^E(y_3,y_1;\zeta_3,\zeta_1) = \Phi^i(y_3) + n_0\int_{-h}^{h}\int_{-\infty}^{+\infty} \Phi(y_3,y_1;\xi_3,\xi_1;\zeta_3,\zeta_1) \times d\xi_3\, d\xi_1, \quad \text{in 2D}, \tag{37}$$

$$\Phi^E(y_3,y_1,y_2;\zeta_3,\zeta_1,\zeta_2) = \Phi^i(y_3) + n_0\int_{-h}^{h}\int_{-\infty}^{+\infty}\int_{-\infty}^{+\infty}\Phi(y_3,y_1,y_2;\xi_3,\xi_1,\xi_2;\zeta_3,\zeta_1,\zeta_2) \times d\xi_3\, d\xi_1\, d\xi_2, \quad \text{in 3D}. \tag{38}$$

On the right-hand side of (37), the term in the integrand represents the average potential scattered by the line at (ξ_3,ξ_1) when the line at (ζ_3,ζ_1) is also held fixed. The integral of this potential over all positions (ξ_3,ξ_1) in the layer of Fig. 1 represents the total contribution of all scattered motions knowing that the line at (ζ_3,ζ_1) is held fixed. The point at which the wave motion is evaluated is (y_3,y_1). The average exciting potential on the left-hand side of (37) is given by (10), where (ξ_3,ξ_1) must be replaced by (ζ_3,ζ_1). Similar comments apply to Eqs. (38) and (11), where a point is kept fixed at $(\zeta_3,\zeta_1,\zeta_2)$.

The potentials Φ^E and Φ^i are bounded solutions of the Helmholtz equation in the fluid with wave number k, where derivatives in that equation are taken with respect to the $\mathbf{y}$ coordinates. It follows that the two integrals in (37) and (38), respectively, are bounded solutions of the Helmholtz equation in the fluid with wave number k. Thus, we write (37) and (38) in the equivalent form

$$\Phi^E(y_3,y_1;\zeta_3,\zeta_1) = \Phi^i(y_3) + n_0u_0\sum_{n=0}^{+\infty}\varepsilon_n M_n^{(2)}(\zeta_3) \times J_n(k|\mathbf{y}-\boldsymbol{\zeta}|)\cos(n\alpha), \quad \text{in 2D}, \tag{39}$$

$$\Phi^E(y_3,y_1,y_2;\zeta_3,\zeta_1,\zeta_2) = \Phi^i(y_3) + n_0u_0\sum_{n=0}^{+\infty}(2n+1)M_n^{(3)} \times(\zeta_3)j_n(k|\mathbf{y}-\boldsymbol{\zeta}|) \times P_n(\cos\alpha), \quad \text{in 3D}. \tag{40}$$

The coefficients $M_n^{(2)}$ and $M_n^{(3)}$ in (39) and (40), respectively, depend only on ζ_3, owing to the translational invariance in the y_1 and y_2 directions. The angle α is defined as in (26) and (27).

The average exciting potential Φ^E is expanded in (39) by using (10), where $(\boldsymbol{\xi},\theta)$ are replaced with $(\boldsymbol{\zeta},\alpha)$, and in (40) by using (11), where the same replacements are made. The incident potentials Φ^i in (39) and (40) are expanded by using (6) and (7), respectively, where $(\boldsymbol{\xi},\theta)$ are replaced with $(\boldsymbol{\zeta},\alpha)$. All the terms in (39) and (40) are now series on the bases of functions $J_n(k|\mathbf{y}-\boldsymbol{\zeta}|)\cos(n\alpha)$ and $j_n(k|\mathbf{y}-\boldsymbol{\zeta}|)P_n(\cos\alpha)$, respectively. Equating the coefficients on either side of (39) and (40), one finds that

$$E_n^{(q)}(\zeta_3) = -\frac{1}{k}\mathrm{i}^{n+1}\mathrm{e}^{\mathrm{i}k\zeta_3} + n_0M_n^{(q)}(\zeta_3), \tag{41}$$

where $q=2$ and $q=3$ correspond, respectively, to the 2D and 3D cases.

In Eq. (41), the quantities $E_n(\zeta_3)$ represent the exciting potential on a fixed scatterer at $\boldsymbol{\zeta}$ averaged on the disorder of all the other scatterers. The quantities $n_0M_n(\zeta_3)$ represent a global scattered potential, where the potential scattered by a scatterer at $\boldsymbol{\xi}$ is averaged on the disorder of all the other scatterers except those at $\boldsymbol{\zeta}$ and $\boldsymbol{\xi}$ and, subsequently, all the positions $\boldsymbol{\xi}$ are taken into account by integrating over the layer of thickness $2h$. At this stage, neither E_n nor M_n are known.

In analogy to (37) and (38), we write the average exciting displacement u_3^E on a scatterer fixed at $\boldsymbol{\zeta}$ in the form

$$u_3^E(y_3,y_1;\zeta_3;\zeta_1) = u_3^i(y_3) + n_0\int_{-h}^{h}\int_{-\infty}^{+\infty}u_3(y_3,y_1;\xi_3,\xi_1;\zeta_3,\zeta_1)d\xi_3\, d\xi_1, \quad \text{in 2D}, \tag{42}$$

$$u_3^E(y_3,y_1,y_2;\zeta_3,\zeta_1,\zeta_2) = u_3^i(y_3) + n_0\int_{-h}^{h}\int_{-\infty}^{+\infty}\int_{-\infty}^{+\infty}u_3(y_3,y_1,y_2;\xi_3,\xi_1,\xi_2;\zeta_3,\zeta_1,\zeta_2) \times d\xi_3\, d\xi_1\, d\xi_2, \quad \text{in 3D}. \tag{43}$$

The components u_3^E on the left-hand sides of (42) and (43) are obtained by differentiating (39) and (40), respectively, with respect to y_3. In these equations, we differentiate the combinations $J_n\cos(n\alpha)$ and $j_nP_n(\cos\alpha)$ with respect to y_3 by using the chain rule relative to the local coordinates $r=|\mathbf{y}-\boldsymbol{\zeta}|$ and α, and by using properties of the derivatives of the Bessel functions and Legendre polynomials.[17,18] Then after differentiation, rearranging terms in the series, one finds that (39) and (40) yield

$$u_3^E(y_3,y_1;\zeta_3,\zeta_1) = u_3^i(y_3) + n_0u_0k\sum_{n=0}^{+\infty}(M_{n+1}^{(2)}(\zeta_3) - M_{n-1}^{(2)} \times(\zeta_3))J_n(k|\mathbf{y}-\boldsymbol{\zeta}|)\cos(n\alpha), \quad \text{in 2D}, \tag{44}$$

$$u_3^E(y_3,y_1,y_2;\zeta_3,\zeta_1,\zeta_2) = u_3^i(y_3) + n_0u_0k\sum_{n=0}^{+\infty}((n+1)M_{n+1}^{(3)} \times(\zeta_3) - nM_{n-1}^{(3)}(\zeta_3))j_n(k|\mathbf{y}-\boldsymbol{\zeta}|) \times P_n(\cos\alpha), \quad \text{in 3D}, \tag{45}$$

where we have defined $M_{-1}^{(2)}(\zeta_3)=0$ and $M_{-1}^{(3)}(\zeta_3)=0$.

In the 2D case, we can also obtain an expression for the average exciting displacement u_1^E by differentiating (10) with respect to y_1. Likewise, in the 3D case, we can obtain expressions for u_1^E and u_2^E, respectively, by differentiating (11) with respect to y_1 and y_2. It can be shown, by using the chain rule to differentiate the combinations $J_n\cos(n\theta)$ and $j_nP_n(\cos\theta)$, that (10) and (11) yield series from $n=1$ to infinity with coefficients of the form $E_{n+1}+E_{n-1}$, respectively, on the bases of functions $J_n\cos(n\theta)$ and $j_nP_n(\cos\theta)$.

Since the translational invariance in the y_1 and y_2 directions imposes that the average displacements u_1^E and u_2^E be equal to zero, we infer that the coefficients $E_{n+1}+E_{n-1}$ must vanish for $n=1,2,3,\ldots$. Omitting the superscript q, one has

$$E_{2n}(\zeta_3) = (-1)^n E_0(\zeta_3), \quad E_{2n+1}(\zeta_3) = (-1)^n E_1(\zeta_3). \quad (46)$$

Then, combining (41) and (46), one finds that

$$M_{2n}(\zeta_3) = (-1)^n M_0(\zeta_3), \quad M_{2n+1}(\zeta_3) = (-1)^n M_1(\zeta_3). \quad (47)$$

With the conditions (47), one finds that (44) and (45) yield

$$u_3^E(y_3, y_1; \zeta_3, \zeta_1) = u_0 e^{ik y_3} + n_0 u_0 k \sum_{n=0}^{+\infty} \varepsilon_n M_{n+1}^{(2)}(\zeta_3) \times J_n(k|\mathbf{y} - \boldsymbol{\zeta}|)\cos(n\alpha), \quad \text{in 2D}, \quad (48)$$

$$u_3^E(y_3, y_1, y_2; \zeta_3, \zeta_1, \zeta_2) = u_0 e^{ik y_3} + n_0 u_0 k \sum_{n=0}^{+\infty} (2n+1) M_{n+1}^{(3)} \times (\zeta_3) j_n(k|\mathbf{y} - \boldsymbol{\zeta}|) \times P_n(\cos\alpha), \quad \text{in 3D}. \quad (49)$$

VI. GLOBAL CLOSURE ASSUMPTION

Equation (37) expresses the exciting potential on a fixed $\boldsymbol{\zeta}$ in terms of the scattered potential corresponding to two fixed $\boldsymbol{\xi}$ and $\boldsymbol{\zeta}$. Similarly, one can write an equation for the exciting potential corresponding to two fixed $\boldsymbol{\zeta}$ and $\boldsymbol{\nu}$ in terms of the scattered potential keeping three scatterers fixed at $\boldsymbol{\xi}$, $\boldsymbol{\zeta}$, and $\boldsymbol{\nu}$. Repeating this process, one can construct a sequence of equations such that an additional scatterer is held fixed at each step. Eventually, all the scatterers are fixed. This approach would in principle allow us to determine the quantities $E_n^{(2)}$ of (10) exactly but, unfortunately, it is too complicated and cannot be implemented in practice.[7] Similar comments apply to Eq. (38) and to the determination of the quantities $E_n^{(3)}$ of (11).

As an alternative to the approach described above, we make a closure assumption to determine the quantities E_n.

One possible assumption corresponds to the situation of simple scattering, where the scatterers are sufficiently distant from each other and the interactions between them can be neglected. In this case, the exciting field on each scatterer is assumed to be equal to the incident field. The coefficients E_n corresponding to simple scattering are obtained from (41) by setting the second term on the right-hand side of that equation equal to zero. Substituting the resulting expressions for E_n into (21)–(23), one finds the corresponding coherent displacements and, substituting into (24) and (25), one finds the reflection and transmission coefficients.

When interactions between scatterers cannot be neglected, one must take into account multiple scattering effects. These effects are represented in our formulation by the quantities M_n in (41).

The terms M_{n+1} in (48) and (49), respectively, can be viewed as representations of the integrals on the right-hand sides of (42) and (43). Likewise, the G_n in (28) and (29) can be viewed as representations of the integrals on the right-hand sides of (8) and (9).

Comparing the integral in (8) with that in (42), we recall that the former is *not* a solution of the Helmholtz equation with wave number k in the interval $|y_3| < h$ and the latter is indeed a solution of the Helmholtz equation with wave number k for all y_3. Otherwise, both integrals represent the same global scattered displacement averaged on disorder, except that in (42) one of the scatterers is fixed at $\boldsymbol{\zeta}$ and in (8) no scatterer is fixed. Similar remarks can be made in the 3D case concerning (9) and (43).

In view of the preceding discussion, we assume that the integrals in (42) and (43) are equal, respectively, to the parts of the integrals in (8) and (9) that are solutions of the Helmholtz equation in the fluid. Thus, referring to (28)–(30), (48), and (49), we leave out the D_n and we write as an approximation

$$M_{n+1}(\zeta_3) = F_n(\zeta_3), \quad (50)$$

for $n = 0, 1, 2\ldots$. We observe from (32), (35), and (36) that the D_n approach zero as the observation point at y_3 approaches the fixed scatterer at ζ_3.

Equation (50) is our global closure assumption. It will allow us to determine the coherent motion. For $n=0$ and $n=1$, respectively, one finds that (41) and (50) yield

$$E_0(\zeta_3) = -\frac{i}{k} e^{ik\zeta_3} - n_0 F_1(\zeta_3) \quad (51)$$

and

$$E_1(\zeta_3) = \frac{1}{k} e^{ik\zeta_3} + n_0 F_0(\zeta_3), \quad (52)$$

where (31), (46), and (47) have been used. Observe that the superscript q has been omitted on E_0, E_1, F_0, and F_1 in (51) and (52).

VII. EFECTIVE WAVE NUMBER

Equation (46) allows us to write the functions $\sigma_1(\xi)$ and $\sigma_2(\xi)$ in (22) and (23) only in terms of E_0 and E_1. Omitting the superscript q, we find that

$$\sigma_1(\xi) = \sigma_1 E_1(\xi) \quad \text{and} \quad \sigma_2(\xi) = -\sigma_2 E_0(\xi), \quad (53)$$

where the factors σ_1 and σ_2 are independent of ξ and are given by

$$\sigma_1^{(2)} = \frac{4}{k} \sum_{j=0}^{+\infty} C_{2j+1}, \quad \sigma_2^{(2)} = \frac{2}{k} \sum_{j=0}^{+\infty} \varepsilon_{2j} C_{2j}, \quad (54)$$

and

$$\sigma_1^{(3)} = \frac{2\pi}{k^2} \sum_{j=0}^{+\infty} (4j+3) S_{2j+1}, \quad \sigma_2^{(3)} = \frac{2\pi}{k^2} \sum_{j=0}^{+\infty} (4j+1) S_{2j}. \quad (55)$$

Substituting (53) into (33) and (34), one can write F_0 and F_1 in terms of E_0 and E_1. It follows that (51) and (52) represent a system of two coupled integral equations for the unknown functions E_0 and E_1.

To simplify the notation, we use the variable x in the place of ζ_3. Then, omitting the superscript q on E_0, E_1, σ_1, and σ_2, we find that the system of equations for E_0 and E_1 has the form

$$E_0(x) = -\frac{\mathrm{i}}{k}\mathrm{e}^{\mathrm{i}kx} + n_0\sigma_2\int_{-h}^{h} E_0(\xi)\mathrm{e}^{\mathrm{i}k|\xi-x|}\,d\xi + \mathrm{i}n_0\sigma_1\int_{-h}^{h} E_1(\xi)\mathrm{sgn}(\xi-x)\mathrm{e}^{\mathrm{i}k|\xi-x|}\,d\xi, \tag{56}$$

$$E_1(x) = \frac{1}{k}\mathrm{e}^{\mathrm{i}kx} - \mathrm{i}n_0\sigma_2\int_{-h}^{h} E_0(\xi)\mathrm{sgn}(\xi-x)\mathrm{e}^{\mathrm{i}k|\xi-x|}\,d\xi + n_0\sigma_1\int_{-h}^{h} E_1(\xi)\mathrm{e}^{\mathrm{i}k|\xi-x|}\,d\xi. \tag{57}$$

We differentiate (56) and (57) two times with respect to x, keeping the variable x in the interval $(-h,h)$. We use the properties that the derivatives of $\mathrm{sgn}(x)$ and $\mathrm{e}^{|x|}$, respectively, are $2\delta(x)$ and $\mathrm{sgn}(x)\mathrm{e}^{|x|}$, where $\delta(x)$ denotes the Dirac delta function. Thus, we find that

$$\frac{d^2}{dx^2}E_0(x) = -K^2E_0(x) \quad \text{and} \quad \frac{d^2}{dx^2}E_1(x) = -K^2E_1(x). \tag{58}$$

The coefficient K is independent of x and of the screen thickness $2h$. Omitting the superscript q on K, σ_1, and σ_2, one has

$$K^2 = (k - 2\mathrm{i}n_0\sigma_1)(k - 2\mathrm{i}n_0\sigma_2). \tag{59}$$

Thus, E_0 and E_1, respectively, are solutions of second-order ordinary differential equations. The general solutions of the differential equations (58) are

$$E_0(x) = V_0\mathrm{e}^{\mathrm{i}Kx} + W_0\mathrm{e}^{-\mathrm{i}Kx}, \tag{60}$$

$$E_1(x) = V_1\mathrm{e}^{\mathrm{i}Kx} + W_1\mathrm{e}^{-\mathrm{i}Kx}, \tag{61}$$

where the coefficients V_0, W_0, V_1, and W_1 are independent of x and will be determined in closed form in the next section.

We now infer from (21), (53), and (57) that the coherent displacements in the interval $|y_3|<h$ are given by

$$u_3^{(q)}(y_3) = u_0 k E_1^{(q)}(y_3). \tag{62}$$

Equations (61) and (62) show that, inside the layer where the scatterers are distributed, there is one wave traveling in the forward direction and a second wave traveling in the backward direction. Both waves are characterized by the effective wave number K of (59). In general, the wave number K is complex valued and depends on frequency. It follows that the two waves inside the screen are dispersive and undergo attenuation as they propagate.

It is customary to write K in terms of the far-field potential scattered by a *single* scatterer.[7] To arrive at the usual formula for K, we recall that the cylindrical and spherical Hankel functions are given in the far field as r tends to infinity by the expressions

$$H_n^{(1)}(kr) = (-\mathrm{i})^n\sqrt{\frac{2}{\pi kr}}\mathrm{e}^{\mathrm{i}(kr-\pi/4)}, \tag{63}$$

$$h_n^{(1)}(kr) = (-\mathrm{i})^{n+1}\frac{1}{kr}\mathrm{e}^{\mathrm{i}kr}. \tag{64}$$

Substituting (5) and (63) into (3), and then (5) and (64) into (4), respectively, one finds that

$$\Phi(r,\theta) = \Phi_0\sqrt{\frac{2\pi}{kr}}\mathrm{e}^{\mathrm{i}(kr+\pi/4)}f^{(2)}(\theta), \quad \text{in 2D}, \tag{65}$$

$$\Phi(r,\theta) = \Phi_0\frac{1}{r}\mathrm{e}^{\mathrm{i}kr}f^{(3)}(\theta), \quad \text{in 3D}, \tag{66}$$

where $\Phi_0 = -\mathrm{i}u_0/k$ is the amplitude factor of the incident potential. When the scatterer is located at $\boldsymbol{\xi}=\mathbf{0}$, the angular shape functions $f^{(2)}$ and $f^{(3)}$ in (65) and (66), respectively, are given by

$$f^{(2)}(\theta) = \frac{1}{\mathrm{i}\pi}\sum_{n=0}^{+\infty}\varepsilon_n C_n\cos(n\theta), \quad \text{in 2D}, \tag{67}$$

$$f^{(3)}(\theta) = \frac{1}{\mathrm{i}k}\sum_{n=0}^{+\infty}(2n+1)S_nP_n(\cos\theta), \quad \text{in 3D}. \tag{68}$$

We can see from Fig. 1 that, relative to the incident wave, the forward direction corresponds to $\theta=0$ and the backward direction to $\theta=\pi$. It follows that $f(0)$ and $f(\pi)$, respectively, are measures in the forward and backward directions of the field scattered by a single scatterer. Using the properties $P_n(1)=1$ and $P_n(-1)=(-1)^n$, and omitting the superscript q on $f(0)$, $f(\pi)$, σ_1, and σ_2, we infer from (54), (55), (67), and (68) that

$$\sigma_1 = \frac{\mathrm{i}\pi}{k}(f(0) - f(\pi)) \quad \text{and} \quad \sigma_2 = \frac{\mathrm{i}\pi}{k}(f(0) + f(\pi)). \tag{69}$$

Equation (69) shows that the factors σ_1 and σ_2 depend only on the far-field amplitudes scattered by a single scatterer in the forward and backward directions, apart from the wave number k in the fluid. Substituting (69) into (59), and rearranging terms, one finds the well-known result[7]

$$K^2 = k^2\left(1 + n_0\frac{2\pi}{k^2}f(0)\right)^2 - k^2\left(n_0\frac{2\pi}{k^2}f(\pi)\right)^2. \tag{70}$$

The 2D formula (70) has been given elsewhere correctly, but without detail, for circular cylinders and SH waves.[21] A formula similar in form, but not identical, to (59) has also been obtained previously.[9]

VIII. REFLECTION AND TRANSMISSION

We determine the coefficients V_0, W_0, V_1, and W_1 by substituting (60) and (61) into (56) and (57). The four integrals over the interval $(-h,h)$ in (56) and (57) are evaluated in closed form, with the variable x in the interval $(-h,h)$. The integrations are performed separately on $(-h,x)$ and (x,h). Then, (56) and (57) yield a system of two equations of the form

$$a_{m1}e^{iKx} + a_{m2}e^{-iKx} = a_{m3}e^{ikx} + a_{m4}e^{-ikx}, \tag{71}$$

where $m=1$ and $m=2$ correspond, respectively, to (56) and (57). The eight coefficients a_{mn}, where $m=1,2$ and $n=1,2,3,4$, depend linearly on V_0, W_0, V_1, and W_1. We find by using the expression (59) for the effective wave number that the four coefficients a_{2n} are related to the four coefficients a_{1n}. One has

$$a_{21} = Pa_{11}, \quad a_{22} = -Pa_{12}, \quad a_{23} = ia_{13}, \quad \text{and} \quad a_{24} = -ia_{14}, \tag{72}$$

where the factor P is defined by

$$P = -\frac{i\sigma_2 K}{\sigma_1(k - 2in_0\sigma_2)}. \tag{73}$$

We infer now from (72) that, for $m=1$ and $m=2$, (71) represents a system of two equations for the four unknowns a_{1n}. These two equations hold for all x in $(-h,h)$. We differentiate them with respect to x, which yields two additional equations that hold also for all x in $(-h,h)$. We now have a total of four equations, in which we set $x=0$. This yields a linear system of four homogeneous equations for the four unknowns a_{1n}. We have verified that the 4×4 determinant of this system does not vanish. Thus, we conclude that the four coefficients a_{1n} must vanish.

These four conditions yield in turn a linear system of four inhomogeneous equations for the four unknowns V_0, W_0, V_1, and W_1. We have solved this system in closed form by using Cramer's rule.

Next, we use these solutions, together with (53), (60), and (61), to determine the reflection and transmission coefficients of (24) and (25). Integrating the exponential functions in closed form, we find that

$$R = -\frac{Qe^{-2ikh}}{1 - Q^2e^{4iKh}}(1 - e^{4iKh}), \tag{74}$$

$$T = \frac{1 - Q^2}{1 - Q^2e^{4iKh}}e^{2i(K-k)h}, \tag{75}$$

where

$$Q = \frac{1 - Z}{1 + Z} \quad \text{and} \quad Z = \frac{k - 2in_0\sigma_1}{K} = \frac{K}{k - 2in_0\sigma_2}. \tag{76}$$

For simplicity, the superscript q has been omitted on R, T, Q, K, Z, σ_1, and σ_2 in (74)–(76), which hold for either the 2D problem or the 3D problem. The quantities σ_1 and σ_2 are defined in terms of the scattering coefficients C_n and S_n by (54) and (55), or by (69) in terms of the forward and backward scattering amplitudes $f(0)$ and $f(\pi)$.

From (61) and (62), and the solutions for V_1 and W_1, we infer that the coherent displacements in the interval $|y_3|<h$ are given by

$$u_3(y_3) = u_0A_+e^{iKy_3} - u_0A_-e^{-iKy_3}, \tag{77}$$

where the amplitudes A_+ and A_- are given by

$$A_+ = kV_1 = \frac{1 + Q}{1 - Q^2e^{4iKh}}e^{i(K-k)h}, \tag{78}$$

$$A_- = -kW_1 = \frac{Q(1 + Q)}{1 - Q^2e^{4iKh}}e^{i(3K-k)h}. \tag{79}$$

Observe that a minus sign is used to represent the backward-propagating wave. For completeness, we also record here the solutions for the coefficients V_0 and W_0 of (60) in the form

$$V_0 = -iZV_1, \quad \text{and} \quad W_0 = iZW_1, \tag{80}$$

where Z is defined in (76). For simplicity in (77)–(80), the superscript q has been omitted on u_3, A_+, A_-, V_1, W_1, V_0, W_0, Z, Q, and K.

The preceding results provide a complete evaluation of the system of coherent waves generated in the fluid of Fig. 1 by a plane incident wave of amplitude u_0. Outside the layer, the reflected and transmitted waves have amplitudes $-u_0R$ and u_0T, respectively, where R and T are given by (74) and (75). Inside the layer, the forward- and backward-propagating waves have amplitudes u_0A_+ and $-u_0A_-$, respectively, where A_+ and A_- are given by (78) and (79).

The factor Q in (74), (75), (78), and (79) is defined by (76). We observe that Q depends on the effective wave number K, the wave number k in the fluid, and either the factor $n_0\sigma_1$ or the factor $n_0\sigma_2$. It is not possible in general to write either $n_0\sigma_1$ or $n_0\sigma_2$ only in terms of the wave numbers K and k. Thus, the factor Q of (76) is not, in general, a function of only K and k.

The formulas (74), (75), (78), and (79) for the reflected, transmitted, forward, and backward waves, respectively, apply to a homogeneous fluid layer.

To see this, replace in Fig. 1 the layer containing scatterers with a homogeneous nonviscous or viscous fluid layer of thickness $2h$ and mass density ρ_1. In this fluid, we call k_1 and c_1, respectively, the wave number and speed of pressure waves at the angular frequency ω. Observe that $c_1=\omega/k_1$, and both c_1 and k_1 are complex valued if the fluid is dissipative. In this context, one finds that the amplitudes of the four waves generated by the incident wave of (2) are still given by (74), (75), (78), and (79), provided that K is replaced with k_1 and Q is replaced with

$$Q = \frac{\rho_0c_0 - \rho_1c_1}{\rho_0c_0 + \rho_1c_1}. \tag{81}$$

The factor Q in (81) is a ratio of acoustic impedances, which is complex valued when the fluid layer is viscous. This shows that the system of waves propagating in the presence of scatterers in Fig. 1 is formally identical to that propagating outside and inside a homogeneous fluid layer. What distinguishes the two cases from each other is the factor Q, which is given by (76) in the first case and by (81) in the second one. Observe that the factor Q in (81) is the amplitude factor for the reflected wave at the interface of two homogeneous fluid half-spaces.

We note that expressions for the reflected and transmitted amplitudes similar to (74) and (75) have been obtained in the special case where the far-field approximation is used for the scattered motion.[22] Reflection and transmission have also been evaluated by using a distance of closest approach between scatterers and ignoring transition region complications.[23,24] Finally, we observe that earlier expres-

sions for R and T, obtained in other contexts, can be cast in the form (74) and (75), provided that appropriate expressions for Q are introduced.[16,20]

IX. COMPARISON WITH WATERMAN AND TRUELL

We introduce in Fig. 1 the system of axes (Y_3, Y_1), where the Y_3 axis has its origin at the lower boundary of the layer of thickness $2h$. Thus, the y_3 and Y_3 coordinates are related by $y_3 = Y_3 - h$. The incident, reflected, and transmitted waves of (2), which are represented as functions of y_3, can also be represented as functions of Y_3. One has

$$u_3^i = U_0 e^{ikY_3}, \quad u_3^r = -U_0 R_W e^{-ikY_3}, \quad \text{and } u_3^t = U_0 T_W e^{ikY_3}. \tag{82}$$

Likewise, inside the layer, the forward-propagating wave and the backward-propagating wave of (77) can be represented as

$$u_3(Y_3) = U_0 A_{W+} e^{iKY_3} - U_0 A_{W-} e^{-iKY_3} \quad (0 < Y_3 < 2h). \tag{83}$$

In Eqs. (82) and (83), the subscript W is used for "Waterman." We find that

$$U_0 = u_0 e^{-ikh}, \quad R_W = R e^{2ikh}, \quad T_W = T, \tag{84}$$

$$A_{W+} = A_+ e^{-i(K-k)h}, \quad A_{W-} = A_- e^{i(K+k)h}, \tag{85}$$

where R, T, A_+, and A_- are given, respectively, by (74), (75), (78), and (79). In their paper,[7] Waterman and Truell consider scatterers distributed in a half-space, as shown in their Fig. 3 (Ref. 7, p. 522). Their situation corresponds to that of our Fig. 1 as the upper boundary of the layer is seen by the incident wave as receding toward infinity.

Thus, the system of waves propagating in the fluid of Fig. 1, in the limit when scatterers are distributed in the half-space $Y_3 > 0$, is obtained for each frequency by taking the limit of (84) and (85) as Kh tends to infinity.

We recall here that the effective wave number K is complex valued and is given by (59) or (70). We assume that K^2 lies in the first or second quadrant of the complex plane, and we call K the root that lies in the first quadrant. It follows that the attenuation, which is represented by the imaginary part of K, is positive.

With the assumption $\mathrm{Im}(K) > 0$, we take the limit of the amplitudes R_W, T_W, A_{W+}, and A_{W-} in (84) and (85) as Kh tends to infinity. Substituting the results into (82) and (83), we find that the system of waves in the half-space problem is defined by

$$u_3^i = U_0 e^{ikY_3}, \quad u_3^r = U_0 Q e^{-ikY_3} \quad (Y_3 < 0), \tag{86}$$

$$u_3 = U_0(1+Q) e^{iKY_3} \quad (Y_3 > 0). \tag{87}$$

In the limit, both T_W and A_{W-} vanish. Thus, there is no transmission across the scatterer region (which extends to infinity) and there is no wave propagating in the backward direction through the scatterer region. There is a reflected wave in the fluid, which is given by (86), and there is a wave propagating in the forward direction through the scatterer region, which is given by (87).

In the paper mentioned above,[7] it is shown that the forward-propagating wave is characterized by the effective wave number K, as in (87), but the amplitude factor $(1+Q)$ is not determined. The amplitude factor $-Q$ of the reflected wave in (86) is not determined either.

Equation (86) shows that the factor Q, which is defined in (76), can be interpreted within a minus sign as the amplitude factor for the wave reflected by a half-space region of scatterers.

X. ISOTROPIC SCATTERERS

There is one particular case, which is that of isotropic scattering,[20] where Q reduces to a function of K and k. In this case, the only nonzero scattering coefficients are, respectively, C_0 in 2D and S_0 in 3D. Thus, the scattering shape functions f of (67) and (68) are independent of θ, and it follows from (22) and (23) that

$$\sigma_1^{(2)}(\xi) = \sigma_1^{(3)}(\xi) = 0, \quad \sigma_2^{(2)}(\xi) = -\frac{2}{k} C_0 E_0^{(2)}(\xi),$$

$$\text{and} \quad \sigma_2^{(3)}(\xi) = -\frac{2\pi}{k^2} S_0 E_0^{(3)}(\xi). \tag{88}$$

Using (88) and the method of the preceding sections, we have determined the coherent displacement outside and inside the screen. We find that (2) and (77) hold as before. In these equations, the coefficients R, T, A_+, and A_- are still given, respectively, by (74), (75), (78), and (79), provided that K and Q are redefined. The appropriate expression for the effective wave numbers is

$$K^2 = k^2 - 2ikn_0\sigma_2, \tag{89}$$

where $\sigma_2^{(2)} = 2C_0/k$ and $\sigma_2^{(3)} = 2\pi S_0/k^2$. The appropriate expression for the factor Q is

$$Q = \frac{K-k}{K+k}. \tag{90}$$

Observe that the superscript q has been omitted on σ_2, Q, and K in (89) and (90). This result shows that Q depends only on the wave number k in the fluid and on the effective wave number K inside the screen.

XI. SUMMARY

Using the Foldy-Twersky approach for multiple scattering, we have determined the coherent wave motion in a nonviscous fluid containing either cylindrical or spheroidal scatterers. The scatterers are distributed in a screen of finite thickness, so that two "boundaries" exist in the medium.

Displacement potentials are used throughout to describe the various wave fields in the fluid. For example, we call E_n the scalar coefficients that represent the average exciting potential on a fixed scatterer, and we show that the coherent displacement in the fluid is entirely determined by these coefficients—Eqs. (14) and (15). Likewise, we call M_n the scalar coefficients that represent the average exciting potential on a fixed scatterer, knowing that another scatterer is also held fixed. We find that E_n and M_n are related through the

incident wave field by Eq. (41), which is an exact equation. In addition, we infer from the translational invariance of the problem that the E_n for all values of the index n are determined by E_0 and E_1 and likewise all the M_n are determined by M_0 and M_1—Eqs. (46) and (47).

To determine E_0 and E_1, we use the closure assumption (50), which says that global scattering in the layer, when one scatterer is held fixed, is equal to *a part* of global scattering in the layer when no scatterer is held fixed. That part is a solution of the Helmholtz equation in the fluid. In this approach, we do not use translational addition theorems for cylindrical or spherical wavefunctions,[7,23] which cloud the physical meaning of the issue.

This closure assumption allows us to obtain in Eqs. (74), (75), (78), and (79), respectively, amplitude factors for the reflected, transmitted, forward-scattered, and backscattered waves in the medium. These amplitudes are written in terms of four parameters: k, the wave number in the fluid; $2h$, the screen thickness; K, the effective wave number; and $-Q$, the reflection coefficient for the associated semi-infinite screen. In our derivation, we do not assume *a priori* the existence of the wave number K.

This paper shows that the "boundaries" of the layer can be treated as real acoustical boundaries from the point of view of the coherent motion, provided that the fluid-scatterer mixture in the layer is replaced with an equivalent dissipative effective medium. The effective medium is defined in general by the two independent parameters K and Q.

We see that K and Q, which are given by Eqs. (70) and (76), respectively, depend on k and n_0. The parameter n_0 is the number of cylinders per unit area or the number of spheroids per unit volume.

Apart from their dependence on k and n_0, K and Q are both completely determined when the backscattered and forward-scattered amplitudes of a *single* scatterer are known. If these two amplitudes, which are denoted $f(\pi)$ and $f(0)$, respectively, in the text, can be determined either analytically, numerically, or experimentally, then the screen problem is solved.

In an analytical approach, the scattering coefficients C_n and S_n of Eqs. (3) and (4) are determined by writing appropriate continuity conditions at the boundary between the external fluid and the scatterer. Additional continuity conditions are required in the case of shell-like or layered scatterers. Our analysis applies to a wide variety of scatterer shapes. Scatterers may have noncircular cross sections in 2D and may be nonspherical in 3D.

[1] A. Ishimaru, *Wave Propagation and Scattering in Random Media* (IEEE, Piscataway, NJ, 1997).

[2] P. Sheng, *Introduction to Wave Scattering, Localization and Mesoscopic Phenomena* (Academic, New York, 1995).

[3] A. Lagendijk and B. A. van Tiggelen, "Resonant multiple scattering of light," Phys. Rep. **270**, 143–215 (1996).

[4] A. Derode, A. Tourin, and M. Fink, "Random multiple scattering of ultrasound. I. Coherent and ballistic waves," Phys. Rev. E **64**, 036605 (2001).

[5] A. Tourin, A. Derode, A. Peyre, and M. Fink, "Transport parameters for an ultrasonic pulsed wave propagating in a multiple scattering medium," J. Acoust. Soc. Am. **108**, 503–512 (2000).

[6] F. Chavrier, J.-Y. Chapelon, A. Gelet, and D. Cathignol, "Modeling of high-intensity focused ultrasound-induced lesions in the presence of cavitation bubbles," J. Acoust. Soc. Am. **108**, 432–440 (2000).

[7] P. C. Waterman and R. Truell, "Multiple scattering of waves," J. Math. Phys. **2**(4), 512–537 (1961).

[8] E. L. Carstensen and L. L. Foldy, "Propagation of sound through a liquid containing bubbles," J. Acoust. Soc. Am. **19**, 481–501 (1947).

[9] R. J. Urick and W. S. Ament, "The propagation of sound in composite media," J. Acoust. Soc. Am. **21**, 115–119 (1949).

[10] V. Twersky, "Acoustic bulk parameters of random volume distributions of small scatterers," J. Acoust. Soc. Am. **36**, 1314–1329 (1964).

[11] K. W. Commander and A. Prosperetti, "Linear pressure waves in bubbly liquids: Comparison between theory and experiments," J. Acoust. Soc. Am. **85**, 732–746 (1989).

[12] R. E. Challis, J. S. Tebbutt, and A. K. Holmes, "Equivalence between three scattering formulations for ultrasonic wave propagation in particulate mixtures," J. Phys. D **31**, 3481–3497 (1998).

[13] Y. C. Angel, "On the static and dynamic equilibrium of concentrated loads in linear acoustics and linear elasticity," J. Elast. **24**, 21–42 (1990).

[14] M. Born and E. Wolf, *Principles of Optics*, 5th ed. (Pergamon, Oxford, 1975).

[15] H. C. van de Hulst, *Light Scattering by Small Particles* (Dover, New York, 1981).

[16] Y. C. Angel and Y. K. Koba, "Complex-valued wavenumber, reflection and transmission in an elastic solid containing a cracked slab region," Int. J. Solids Struct. **35**, 573–592 (1998).

[17] I. S. Grashteyn and I. W. Ryzhik, *Tables of Integrals, Series and Products*, 5th ed. (Academic, New York, 1994).

[18] P. M. Morse and K. U. Ingard, *Theoretical Acoustics* (Mc Graw-Hill, New York, 1968).

[19] A. R. Aguiar and Y. C. Angel, "Antiplane coherent scattering from a slab containing a random distribution of cavities," Proc. R. Soc. London, Ser. A **456**, 2883–2909 (2000).

[20] C. Aristégui and Y. C. Angel, "New results for isotropic point scatterers: Foldy revisited," Wave Motion **36**(4), 383–399 (2002).

[21] R.-B. Yang and A. K. Mal, "Multiple scattering of elastic waves in a fiber-reinforced composite," J. Mech. Phys. Solids **42**(12), 1945–1968 (1994).

[22] C. Javanaud and A. Thomas, "Multiple scattering using the Foldy-Twersky integral equation," Ultrasonics **26**, 341–343 (1988).

[23] J. G. Fikioris and P. C. Waterman, "Multiple scattering of waves. II. 'Hole corrections' in the scalar case," J. Math. Phys. **5**(10), 1413–1420 (1964).

[24] P.-Y. Le Bas, F. Luppé, and J.-M. Conoir, "Reflection and transmission by randomly spaced elastic cylinders in a fluid slab-like region," J. Acoust. Soc. Am. **117**, 1088–1097 (2005).

Acoustic power measurements of a damped aeroacoustically driven resonator[a)]

W. V. Slaton
Department of Physics and Astronomy, The University of Central Arkansas, 201 Donaghey Avenue, Conway, Arkansas 72035-0001

J. C. H. Zeegers
Department of Applied Physics, Eindhoven University of Technology, P.O. Box 513, 5600 MB Eindhoven, The Netherlands

(Received 3 October 2004; revised 21 March 2005; accepted 13 April 2005)

Strong self-sustained acoustic oscillations may occur in a gas pipe network under certain gas flow velocities within the network. The pipe network under consideration consists of a main pipe, with a variable mean airflow, with two closed coaxial side branches of variable but equal length joined to the main pipe. Coupling between resonant acoustic standing waves and instabilities of the shear layers separating the flow in the main pipe from the stagnant gas in the closed side branches leads to strong acoustic oscillations at a frequency corresponding to the half-wavelength acoustic mode defined by the total side-branch length. An acoustic damper consisting of a variable acoustic resistance and compliance is used to dissipate power from the resonating mode. The response of the aeroacoustically driven resonator to variable damping will be examined for different fluid flow regimes as well as side-branch geometries. © *2005 Acoustical Society of America.* [DOI: 10.1121/1.1925907]

PACS number(s): 43.20.Ks, 43.25.Vt, 43.28.Ra [RR] Pages: 83–91

I. INTRODUCTION

Sound excitation in closed side branches due to vortex shedding by a mean flow of gas over the mouth of the branch has been extensively studied.[1–5] In an industrial setting, these flow-induced pulsations in gas networks are undesirable.[6,7] Methods of predicting[8] and/or eliminating[4] these flow-induced resonances have been an ongoing research goal for the aeroacoustic community. High-amplitude pressure waves in gas networks can lead to fatigue in pipes, valves,[9] or welds, spurious mean flow measurements, or equipment shutdown due to excessive vibration. However, not all flow-induced pulsations are considered a nuisance; examples include whistling,[10] musical instruments like the flute,[11] or the common whistling teakettle.[12]

Accurate modeling of the aeroacoustic response of a gas network to mean flow depends on good estimates of the acoustic field generated by the shed vortices. The shed vortices drive the acoustic resonance in the side branches; and the resonance triggers the shedding of the next vortex. Theoretical[13–19] and experimental[20–27] work has been carried out to quantify acoustic-vortex coupling at low amplitude. However, the high-amplitude behavior of the coupling is poorly understood. The authors have measured high-amplitude pressure oscillations of 20% of the mean pressure at 10 bar and consequently the acoustic power in the resonance is difficult to predict at these amplitudes from linear theory. In this investigation we describe experimental tests used to quantify the vortex-acoustic source power at high acoustic amplitude. Of interest is the response of the aeroacoustic source to controlled damping at a fixed flow rate and fixed frequency. By dissipating the acoustic power through known loss mechanisms, an estimate of the total power available from the aeroacoustic source can be found. The controlled damping of the resonance is achieved by a variable flow resistance in series with a compliant volume. The benefit of this technique is that it allows for a modification of the energy balance of the system during an experimental run. A side benefit is the discovery that the flow-induced resonance may be eliminated entirely with this type of damper.

The experimental setup used in this investigation is described in detail in Sec. II. Basic concepts of aeroacoustics in closed side branches as well as acoustic power loss mechanisms are discussed in Sec. III. The results of the investigation are found in Sec. IV with an analysis in Sec. V. Conclusions may be found in Sec. VI.

II. EXPERIMENTAL APPARATUS

In this section we detail several experimental setups that have been used to investigate the aeroacoustics of internal flows. A high-pressure flow setup at the Technical University at Eindhoven (TU/e) was utilized to study the aeroacoustic phenomena. The aeroacoustic behavior of closed coaxial cylindrical side branches of various geometries is investigated with this setup in several different experimental configurations. The high-pressure flow setup is first described including details of the aeroacoustic whistle and side branches; then an acoustic damper is described that was used to dissipate power from the acoustic field.

The high-pressure and high-flow velocity air system at the TU/e can maintain 10 bar absolute pressure and flow

[a)]Portions of this work have been presented in W. V. Slaton and J. C. H. Zeegers, "Systematic loading of an aeroacoustic whistle," J. Acoust. Soc. Am. 113, p. 2283 (2003).

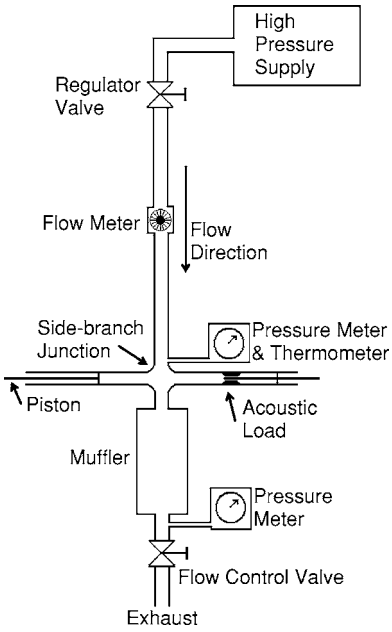

FIG. 1. Experimental flow setup used for these tests. The high-pressure supply can provide ~50 bar of air. The flow velocity of the air through the setup is controlled by the valve near the exhaust to room pressure at the bottom of the figure. The side-branch length may be adjusted with sliding pistons.

rates up to 50 m/s. At a typical operating setting (10 bar and 30 m/s flow) the system uses over 750 standard cubic meters of air per hour. The system, illustrated in Fig. 1, consists of a main pipe with flow and two closed coaxial side branches. The main pipe has an inner diameter of 30 mm and the side branches have an inner diameter of 25 mm. As indicated in the figure, the system is instrumented with a flow meter, several mean pressure sensors, a thermometer, as well as interchangeable flow control valves with varying flow resistances. The temperature and pressure of the flowing gas is measured and used to calculate the values of gas transport and thermodynamic properties. The muffler acts to dampen escaping acoustic waves generated by the junction as well as to isolate the junction from sound generated by flow through the exit control valve. The side-branch junction is the site of aeroacoustic sound generation. The closed side branches act as a resonating chamber driven by vortex shedding. The length of the side branches may be varied independently by moving the indicated pistons. For all work that is presented in this paper, the side-branch lengths will be equal.

Varying the side-branch length changes the resonant frequency of the cavity. Figure 2 illustrates one instant in time for the half-wavelength standing wave resonant mode for the acoustic pressure amplitude by $|p|$ and acoustic velocity by $|u|$ in the coaxial side branches. There is an acoustic pressure node in the middle of the side-branch junction and antinodes at the side-branch ends; conversely, there is an acoustic velocity antinode in the center of the side-branch junction. The periodic acoustic velocity at the side-branch openings act to shed vortices from the main flow at regular intervals. The coupling of resonant acoustic modes in the side branches and instabilities of the shear layer results in self-sustained acoustic oscillations. A model 116A PCB pressure transducer is installed in the piston of one of the side branches, as illustrated by Mic. 1 in the figure.

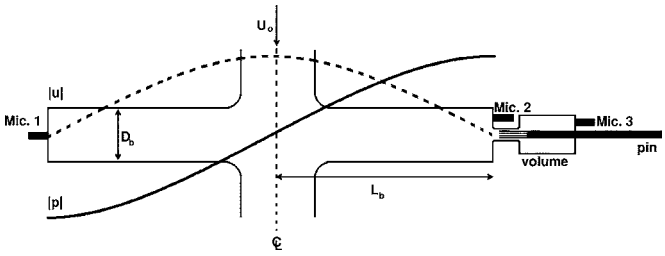

FIG. 2. Schematic detail of the side-branch system. The mean flow of air, U_0, passes past the open mouths of the co-axial side-branches of branch length L_b. The acoustic pressure, $|p|$, (solid line) and velocity, $|u|$, (dashed line) for the half-wavelength acoustic mode within the side branches is illustrated during one instant of the acoustic cycle. The structure in the right side-branch illustrates the acoustic damper.

Figure 2 also illustrates the acoustic damper at the end of one of the side branches. This type of damper has been used in the thermoacoustic literature to measure acoustic power.[28–30] The device is simply a resistance and compliance network instrumented with model 105C02 PCB microphones, illustrated by Mic. 2 and Mic. 3 in the figure. The resistance is provided by a pin with slits through which gas can oscillate. This resistance can be varied by changing the depth to which the pin penetrates into the neck of the load. Also, pins with varying numbers of slits and slit widths have been constructed to offer a wide range of resistances. The compliant volume behind the neck can also be varied, however, in these investigations the volume is kept at 7.73 cm^3. The length of the neck is 30 mm and the slit length is 25 mm, enabling the valve to be effectively closed when the pin is fully inserted into the neck. In the fully inserted position the pin does not make a perfect seal against the valve. The tiny gap does allow for gas flow and hence dissipation but this is a small effect, as will be seen later. Also, both ends of the valve neck have rounded edges.

The geometry of the side branches affect the aeroacoustic sound source's performance. Figure 3 illustrates the four geometries investigated all with a side-branch inner diameter of D_b=25 mm: the cross junction with coaxial side branches, a forked junction with side branches making an angle of 20°, and two trident-shaped side branches with a large (r_{cl}/D_b =1.7) and a small (r_{cl}/D_b=0.7) centerline radii of curvature. The mouths of the side branches are rounded (r_j/D_b=0.2) for the cross junction and both trident junctions. The forked junction did not give any aeroacoustically excited resonances under any flow conditions, thus, it will not appear in the data that follows. The remaining junctions are examined with the side-branch arms aligned along and against the direction of the gas flow in the main pipe.

III. THEORY

The Strouhal number is a dimensionless number that is important for characterizing aeroacoustic phenomena. The Strouhal number can be thought of as a dimensionless ratio of the time for the main pipe flow to pass the side branch to the period of the acoustic disturbance. Thus,

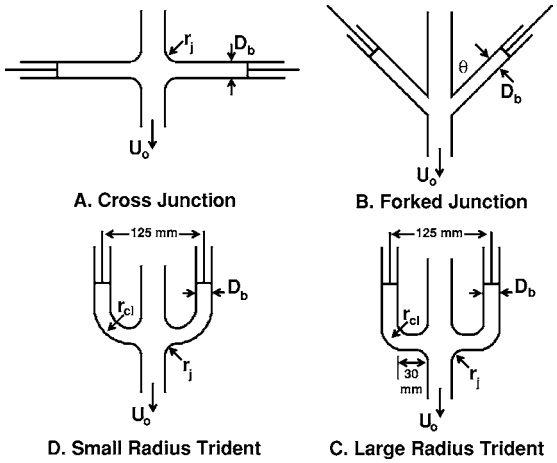

FIG. 3. A. The cross junction composed of variable length coaxial side-branches joining the main flow pipe with a mouth rounding of $r_j/D_b=0.2$. B. The forked junction consists of variable length side-branches mounted to the main pipe at an angle of 20°. C. The large radius trident consists of variable length side-branches bent to a center-line radius of curvature equal to $r_{cl}/D_b=1.7$ with a mouth rounding of $r_j/D_b=0.2$. D. The small radius trident consists of variable length side-branches bent to a radius of curvature equal to $r_{cl}/D_b=0.7$ with a mouth rounding of $r_j/D_b=0.2$.

$$\mathrm{St}=\frac{fW_{\mathrm{eff}}}{U_0}, \tag{1}$$

where f is the frequency of the periodic phenomena (the shedding of vortices or equivalently the frequency of the acoustic wave), W_{eff} is the effective diameter of the side-branch opening to the main pipe, and U_0 is the mean flow velocity of gas in the main pipe grazing over the side-branch opening. This dimensionless number will be used to characterize the performance of the aeroacoustic sound. The effective diameter of the circular side-branch pipe with rounded edges joining the main pipe is defined as

$$W_{\mathrm{eff}}=\frac{\pi}{4}D_b+r_j, \tag{2}$$

with D_b as the diameter of the side branch and r_j is the radius of curvature of the upstream edge of the mouth of the junction[2] that has been defined earlier.

For standing wave phasing the acoustic pressure is out of phase with the acoustic velocity. The acoustic pressure excited by aeroacoustic phenomena is measured by Mic. 1 at an antinode of the excited mode, P_{ac}. The acoustic velocity at the junction is inferred from $u_{\mathrm{ac}}=P_{\mathrm{ac}}/\rho c$, where ρ is the gas density and c is the speed of sound calculated from the temperature and pressure measured at the junction. The dimensionless ratio of acoustic velocity to main flow velocity, u_{ac}/U_0, at the junction is a useful and common method of displaying aeroacoustic sound amplitude. Bruggeman *et al.*[1,31] distinguish these regimes:

- $u_{\mathrm{ac}}/U_0<10^{-3}$: small acoustic amplitude, the growth of disturbances in the shear layer can be described by theory that is linear in the acoustic amplitude.
- $10^{-3}<u_{\mathrm{ac}}/U_0<10^{-1}$: moderate amplitude, the linear theory is valid for the initial shear layer disturbances. Nonlinear effects begin that limit the growth of shear layer perturbations.
- $u_{\mathrm{ac}}/U_0=O(1)$: high-amplitude, vortex generation and power of sound source strongly influenced by the amplitude of the acoustic field.

The acoustic power generated by shed vortices at the mouth of the side branches accumulates in the half-wavelength mode of the resonator. The conservation of energy dictates that all the flow-induced source power must be dissipated by loss mechanisms. The loss mechanisms traditionally considered in the literature have been due to viscous/thermal attenuation in the side branches and nonlinear wave steepening. In this investigation we include the power dissipated in the acoustic load. These loss mechanisms are explained in the following paragraphs.

Acoustic waves propagating in a pipe are attenuated by viscous/thermal effects between the gas and the stationary isothermal pipe wall. This attenuation is well known and in the boundary layer limit, the area-averaged power dissipated by a resonating standing wave in a pipe of constant cross-sectional area is given by[32]

$$P_{v-\mathrm{th}}=\frac{1}{4}\left(\frac{P_{\mathrm{ac}}}{P_0}\right)^2\frac{\rho c^3}{\gamma^2}\pi^2R\left[\delta_k(\gamma-1)\left(1+\frac{2R\omega}{c\pi}\right)+\delta_\nu\right]. \tag{3}$$

In Eq. (3) the following terms are identified: γ is the ratio of specific heats, ω is the angular acoustic frequency, ρ is the density, c is the speed of sound, R is the radius of the resonator, and P_{ac}/P_0 is the ratio of the acoustic standing wave amplitude to the ambient pressure. The viscous penetration depth is defined as, $\delta_\nu=\sqrt{2\mu/\omega\rho}$, with μ as the gas viscosity, and the thermal penetration depth is defined as $\delta_\kappa=\sqrt{2\kappa/\omega\rho c_p}=\delta_\nu/\sqrt{N_p}$, where κ is the gas thermal conductivity, c_p is the gas isobaric heat capacity, N_p is the Prandtl number, and the other symbols are the same as defined before.

Constant frequency large-amplitude traveling waves will develop a higher harmonic content with increased propagation distance.[33] This phenomenon is sometimes called "nonlinear wave steepening" in the literature, and this description follows the work of Peters, Dequand, and Hoffmans. It should be noted that even harmonics generated in this manner will be radiated away because the main pipe acts as a pressure release surface—this effect constitutes a loss mechanism for the half-wavelength mode. The ratio, $\sigma=x/x_s$, where x is the distance traveled by the wave and x_s is the shockwave formation distance plays an important role in higher harmonic generation. It is given by Pierce as

$$\sigma=\frac{\beta k_0P_{\mathrm{ac}}^{\mathrm{trav}}x}{\rho c^2}, \tag{4}$$

where β is given by $(\gamma+1)/2$ for an ideal gas, $P_{\mathrm{ac}}^{\mathrm{trav}}$ is the initial amplitude of the traveling wave, k_0 is the wave number given by ω/c, and the other symbols are as defined before. Pierce derives simplified expressions for the amplitude of the fundamental, $P_1^{\mathrm{trav}}=P_{\mathrm{ac}}^{\mathrm{trav}}(1-\sigma^2/8)$, and the second harmonic, $P_2^{\mathrm{trav}}=P_{\mathrm{ac}}^{\mathrm{trav}}\sigma/2$, for small σ (for all data presented later, $\sigma\leqslant 0.45$). Knowing the acoustic pres-

sure of the first radiating mode allows for a calculation of the radiated acoustic power,

$$P_{\text{rad}} = \frac{A_{\text{main}} P_2^2}{\rho c}, \tag{5}$$

since the oscillating pressure of the even mode generates an in-phase acoustic velocity, $u_{\text{ac}}^{\text{trav}} = P_{\text{ac}}^{\text{trav}}/\rho c$, and this power is radiated along both directions of the main pipe of cross-sectional area, A_{main}. Thus, the area-averaged radiation loss is given by

$$P_{\text{rad}} = \frac{\rho c^3 \pi^2 (\gamma+1)^2 A_{\text{main}}}{256\gamma^4}\left(\frac{P_{\text{ac}}}{P_0}\right)^4, \tag{6}$$

where we have used the fact that the standing wave in the side branches is composed of two superimposed traveling waves of amplitude, $P_{\text{ac}}^{\text{trav}} = P_{\text{ac}}/2$, and that we can express the mean pressure with the following for an ideal gas: $P_0 = \rho c^2/\gamma$. The traveling wave propagates down the length of one side branch and back to the junction, allowing us to write $k_0 x = \pi$.

Lastly, the acoustic load may be characterized in the following way. The measurement of the magnitude and phase of the acoustic pressure at the mouth of the load and in the cavity allows a calculation of the power dissipated in the load. This is accomplished by noting the acoustic impedance of a cavity,[34] $Z_A = -i1/\omega C_A$, where $Z_A = P_{\text{ac}}/U_{\text{vol}}$ and $C_A = V_0/\gamma P_0$, with U_{vol} denoting the volume velocity into the cavity. The cavity volume, V_0, and the mean pressure, P_0, are specified, and so the measurement of acoustic pressure in the cavity yields the volume velocity into the cavity, which must have flowed through the neck resistance. The acoustic power dissipated in the resistance is now calculated as

$$P_{\text{load}} = \frac{1}{2}\,\text{Re}[P_{\text{ac},2}\tilde{U}_{\text{vol},3}] = \frac{1}{2}\frac{\omega V_0}{\gamma P_0} P_{\text{ac},2} P_{\text{ac},3}\sin[\theta_2 - \theta_3], \tag{7}$$

where the overtilde denotes complex conjugation and where $P_{\text{ac},2}$ and θ_2 are the magnitude and phase of the acoustic pressure outside the valve measured by Mic. 2 and $P_{\text{ac},3}$ and θ_3 are the magnitude and phase of the acoustic pressure inside the cavity measured by Mic. 3. Thermal dissipation within the cavity has been ignored in this derivation.

The sum of these loss mechanisms should give an estimate of the acoustic power generated by the aeroacoustic source at the junction for given flow conditions,

$$P_{\text{source}} = P_{v-\text{th}} + P_{\text{rad}} + P_{\text{load}}. \tag{8}$$

By varying the damping occurring in the load, it is possible to change the amplitude of the resonance. In this way the performance of the aeroacoustic sound source at different amplitudes may be observed. Numeric computations of the vortex-acoustic interaction in the junction have been carried out by Kriesels.[5] These computations allow for the calculation of the acoustic source power that drives the resonance phenomena. For low to moderate amplitude ($u_{\text{ac}}/U_0 < 0.2$), the acoustic source power is thought to be linear in the acoustic amplitude. The source power for the cross junction for this amplitude regime is reproduced in Fig. 4(a) from Ref. 5. This figure displays the dimensionless source power for different roundings of the edge of the side-branch mouth as a function of the Strouhal number. Note that the vortex-acoustic source power is made dimensionless by $\rho U_0^2 u_{\text{ac}} A_b$, where A_b is the cross-sectional area of the side branch. This is done to eliminate the linear amplitude dependence of the source power. As suggested earlier, the functional dependence of the source power on amplitude changes with increasing amplitude. This dependence is presented in Fig. 4(b) for sharp edges ($r_j/D_b = 0$), which is also taken from Ref 5. Note that the vortex-acoustic source power is made dimensionless by $\rho U_0^3 A_b$, with A_b defined as before. This is done to illuminate the functional dependence of the source power on amplitude at fixed Strouhal number. We will use these numerical simulations to compare with the experimental results obtained with the setup described in Sec. II.

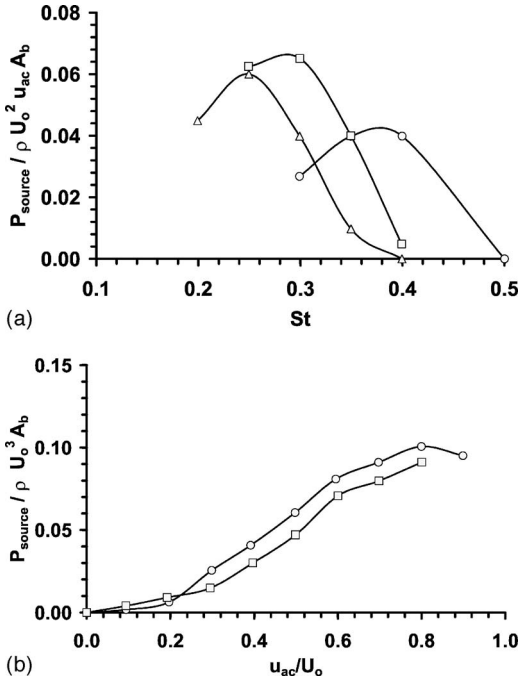

FIG. 4. (a) Numerically calculated dimensionless vortex-acoustic source power versus the Strouhal number for various edge roundings of the mouth of the side-branch/main pipe junction from Ref. 5. Circles denote sharp edges, $r_j/D_b = 0$, squares denote rounded edges of $r_j/D_b = 0.2$, triangles denote rounded edges of $r_j/D_b = 0.4$. (b) Numerically calculated dimensionless vortex-acoustic source power versus relative acoustic velocity amplitude for various Strouhal numbers from Ref. 5 for the cross-junction with sharp edges. Circles denote St=0.1 and Squares denote St=0.4.

IV. EXPERIMENTAL RESULTS

The aeroacoustically excited resonance in the experimental setup described in Sec. II may now be studied. The pressure amplitude of the resonance for different half-wavelength frequencies and mean flow velocities is measured at a pressure antinode. From this the dimensionless ratio of acoustic velocity to mean flow velocity at the junction is calculated. The measured acoustic pressure amplitude is also used to calculate the various loss mechanisms described earlier. By summing these loss mechanisms, Eq. (8),

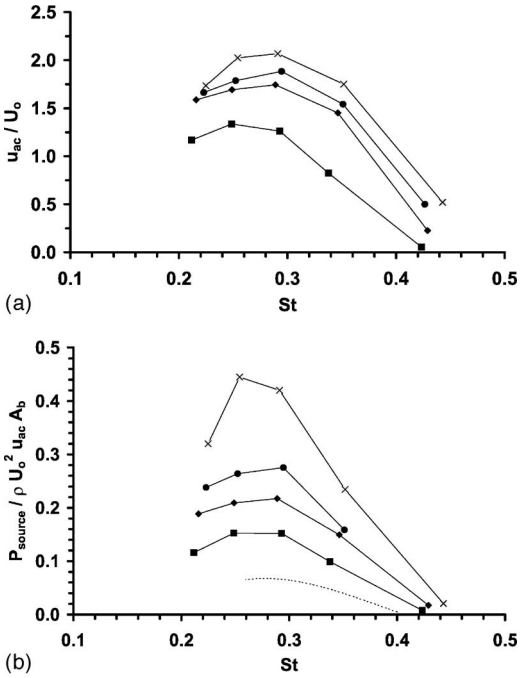

FIG. 5. (a) Relative acoustic velocity amplitude at the junction versus the Strouhal number at 10 bar absolute pressure for the cross-junction at various half-wavelength frequencies. Squares denote 200 Hz, diamonds denote 300 Hz, circles denote 400 Hz and X's denote 540 Hz. (b) Dimensionless vortex-acoustic source power versus Strouhal number at 10 bar absolute pressure for the cross-junction at various half-wavelength frequencies. Squares denote 200 Hz, diamonds denote 300 Hz, circles denote 400 Hz, X's denote 540 Hz and the dashed line reproduces the data for the r_j/D_b =0.2 mouth edge rounding from Ref. 5.

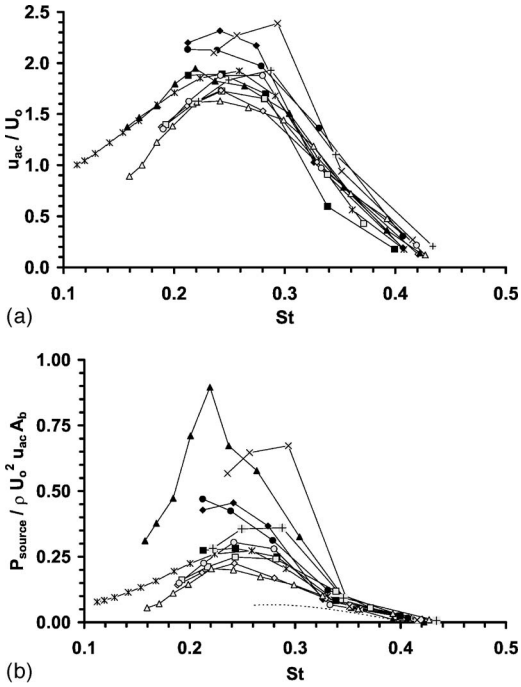

FIG. 6. (a) Relative acoustic velocity amplitude at the junction versus the Strouhal number at 10 bar absolute pressure for the large radius trident at various half-wavelength frequencies. Filled symbols denote data taken with the trident arms orientated with the mean flow velocity, empty symbols denote data taken with the arms against the mean flow. Squares denote 200 Hz, ∗'s denote 260 Hz with arms orientated with the mean flow, diamonds denote 300 Hz, triangles denote 350 Hz, circles denote 400 Hz, X's denote 540 Hz with arms orientated with the mean flow and +'s denote 540 Hz with arms orientated against the mean flow. (b) Dimensionless vortex-acoustic source power versus Strouhal number at 10 bar absolute pressure for the large radius trident at various half-wavelength frequencies. Filled symbols denote data taken with the trident arms orientated with the mean flow velocity, empty symbols denote data taken with the arms against the mean flow. Squares denote 200 Hz, ∗'s denote 260 Hz with arms orientated with the mean flow, diamonds denote 300 Hz, triangles denote 350 Hz, circles denote 400 Hz, X's denote 540 Hz with arms orientated with the mean flow, +'s denote 540 Hz with arms orientated against the mean flow and the dashed line reproduces the data for the r_j/D_b=0.2 mouth edge rounding from Ref. 5.

an estimate of the vortex-acoustic source power may be calculated at a given acoustic amplitude, frequency, Strouhal number, or junction geometry. The use of the acoustic load in an aeroacoustic-excited resonator allows for variable damping of the acoustic wave. Experimental results for the performance of the aeroacoustic sound source with and without load damping for different mean pressures, flow velocities, and frequencies (side-branch lengths) follow in this section. All lines through the data should be considered as guides for the eye and unless otherwise stated the absolute air pressure is 10 bar.

A. No acoustic load damping

The aeroacoustic response of the cross junction without load damping at different half-wavelength acoustic mode frequencies appears in Figs. 5(a) and 5(b). Figure 5(a) displays the dimensionless acoustic amplitude, u_{ac}/U_0, versus the Strouhal number. The cross junction side branches resonate over a range of Strouhal numbers between 0.5 and 0.15. Of note in Fig. 5(a) is that the peak of the response falls near St=0.27 for all frequencies examined. The measured relative acoustic velocity amplitude is extremely large for this configuration, ranging from 0 to 2. The dimensionless vortex-acoustic source power, $P_{source}/\rho U_0^2 u_{ac} A_b$, for the data in Fig. 5(a) is presented in Fig. 5(b) as calculated by Eq. (8) with P_{load} small but not zero. Due to the imperfect seal made by the pin in the valve there is a small amount of dissipation in the valve, even when it is considered closed. This is why the power dissipated in the load is not exactly zero when the valve is closed; however, this constitutes only 0.2% of the total loss at the highest amplitudes. Near the peak of the dimensionless aeroacoustic power, St=0.27, the estimated source power shows a variation of a factor of 3 from low to high frequency. This is because at high amplitude the radiation loss, Eq. (6), is the dominant effect and depends on the amplitude to the fourth power. Thus, at St=0.27 the range of acoustic pressure amplitude from low to high frequency varies by a factor of 1.3; this raised to the fourth power is the observed factor of 3 in the power plot. The dashed line in Fig. 5(b) denotes Kriesels' dimensionless vortex-acoustic source power for cross-junction side-branch mouth roundings of r_j/D_b=0.2 from Fig. 4(a). The discrepancy between Kriesels' numeric results and the data could be due to the low-amplitude ($u_{ac}/U_0 < 0.2$) used by Kriesels. However, the same general shape of the data as well as the location of the maximum agrees with Kriesels' predictions.

Similar plots for the large-radius trident appear in Figs. 6(a) and 6(b) with closed symbols indicating that the trident

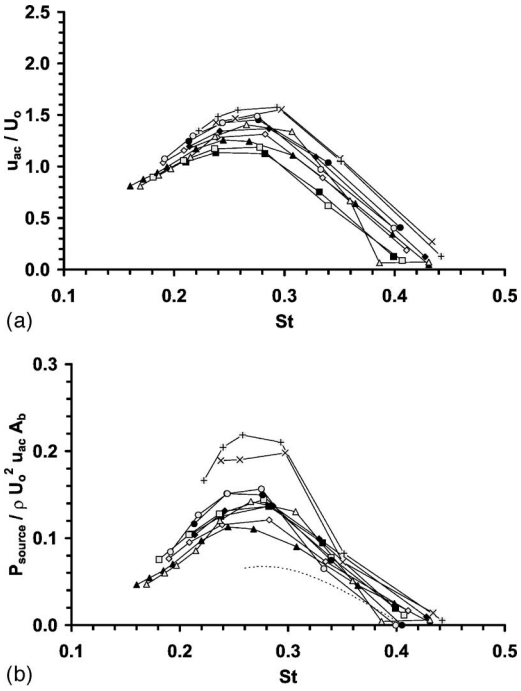

FIG. 7. (a) Relative acoustic velocity amplitude at the junction versus the Strouhal number at 10 bar absolute pressure for the small radius trident at various half-wavelength frequencies. Filled symbols denote data taken with the trident arms orientated with the mean flow velocity, empty symbols denote data taken with the arms against the mean flow. Squares denote 200 Hz, diamonds denote 300 Hz, triangles denote 350 Hz, circles denote 400 Hz, X's denote 540 Hz with arms orientated with the mean flow and +'s denote 540 Hz with arms orientated against the mean flow. (b) Dimensionless vortex-acoustic source power versus Strouhal number at 10 bar absolute pressure for the small radius trident at various half-wavelength frequencies. Filled symbols denote data taken with the trident arms orientated with the mean flow velocity, empty symbols denote data taken with the arms against the mean flow. Squares denote 200 Hz, diamonds denote 300 Hz, triangles denote 350 Hz, circles denote 400 Hz, X's denote 540 Hz with arms orientated with the mean flow, +'s denote 540 Hz with arms orientated against the mean flow and the dashed line reproduces the data for the $r_j/D_b=0.2$ mouth edge rounding from Ref. 5.

arms are aligned with the direction of the main pipe flow velocity and open symbols indicating the arms are aligned against the main flow direction. Note that the range of Strouhal numbers corresponding to resonance is similar to the cross junction with a peak near St=0.25 for most. An extremely high relative acoustic velocity amplitude could be excited in the large-radius trident configuration. The approximate factor of 2 spread in amplitude near St=0.25 results in approximately a factor of 8 spread in the calculated power, Fig. 6(b). The dashed line in Fig. 6(b) denotes Kriesels dimensionless vortex-acoustic source power for cross-junction side-branch mouth roundings of $r_j/D_b=0.2$ from Fig. 4(a). The numerical source power for the cross junction is included with the data for the large-radius trident for comparison purposes only.

Data for the small-radius trident is displayed in Figs. 7(a) and 7(b). Again, the range of Strouhal numbers corresponding to resonance is similar to the cross junction and the large-radius trident. The relative acoustic velocity amplitude for the small-radius trident is noticeably smaller than the cross junction or the large-radius trident, Fig. 7(a), with closed symbols indicating that the trident arms are aligned with the direction of the main pipe flow velocity and open symbols indicating the arms are aligned against the main flow direction. The orientation of the side branches with or against the mean flow velocity does not seem to be a large effect for the small-radius trident. The peak in the dimensionless velocity amplitude still occurs for a Strouhal number near 0.27. The computed source power for the amplitude data in Fig. 7(a) appears in Fig. 7(b). A decreased relative acoustic velocity amplitude implies decreased source power. The dashed line of Kriesels for the cross junction from Fig. 4(a) is included for comparison purposes only.

The data presented in Figs. 5–7 show that bent side branches will resonate over the same range of Strouhal numbers as straight-coaxial side branches. The plots not only illustrate the effect of the radius of curvature of the bent side branch but also the effect of the orientation of the bent branches: either along or against the direction of the main flow velocity. The small trident's performance seems to be independent of the side-branch alignment. However, the large trident suffers a decrease in performance when the branches are aligned against the flow direction. Curiously, the small trident resonates at a lower amplitude than the larger trident or cross-junction side branches. This decrease in acoustic amplitude could be due to acoustic-driven vortex shedding at the site of the bend in the side branch. This loss mechanism is not included in the analysis presented in Sec. I. The comparison of all power data to the numerical results of Kriesels indicates a discrepancy, probably due to the fact that the recorded acoustic amplitude is a factor of 10 larger than that assumed by Kriesels for his low-amplitude calculation in a cross-junction geometry.

B. Acoustic load damping

The acoustic load may be used in two ways. First, the load may be set to have a constant resistance by fixing the position of the slotted pin in the neck of the valve. By varying the flow velocity over the mouths of the side branches, the aeroacoustic response at fixed damping may be investigated. Conversely, the flow velocity may be set to a fixed value (i.e. fixed Strouhal number) and the damping within the load may be varied. This second method of using the acoustic load is helpful to observe how much acoustic power beyond the traditional loss mechanisms described earlier may be extracted from the aeroacoustic source before the sound is extinguished. Results using these methods are described below.

1. Variable mean flow rate

The relative acoustic velocity amplitude for the cross junction at 350 Hz and 2 and 10 bar absolute pressure with fixed damping as a function of the Strouhal number appears in Fig. 8(a). A valve setting of "0 mm" indicates that the slotted pin within the neck of the load is removed 0 mm (this is the valve-closed position), "25 mm" indicates that the pin is removed to 25 mm from the 30 mm long neck. Interestingly, the data demonstrates higher dimensionless acoustic velocity amplitude at higher pressure, with a maximum amplitude of approximately 1.4 for 10 bar and approximately 1

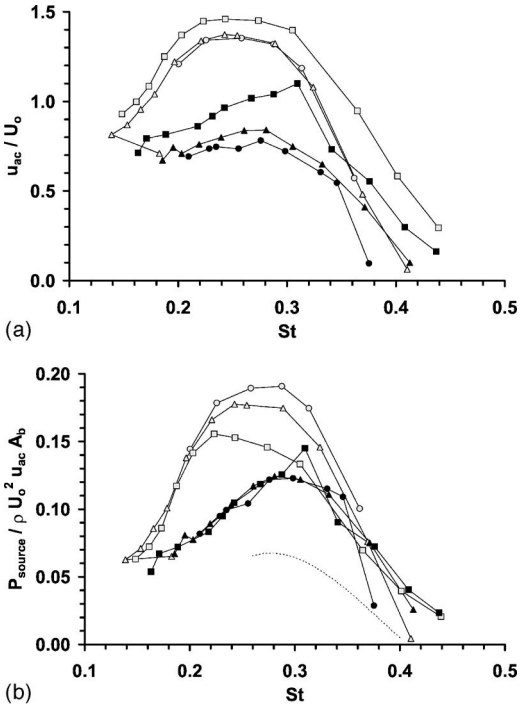

FIG. 8. (a) Relative acoustic velocity amplitude at the junction versus the Strouhal number for the cross-junction at 350 Hz with acoustic load damping. Filled symbols denote data at 2 bar and empty symbols denote data at 10 bar absolute pressure. Squares denote a pin extraction distance of 0 mm, triangles denote a pin extraction distance of 25 mm, and circles denote a pin extraction distance of 28 mm. (b) Dimensionless vortex-acoustic source power versus the Strouhal number for the cross-junction at 350 Hz with acoustic load damping. Filled symbols denote data at 2 bar and empty symbols denote data at 10 bar absolute pressure. Squares denote a pin extraction distance of 0 mm, triangles denote a pin extraction distance of 25 mm, circles denote a pin extraction distance of 28 mm, and the dashed line reproduces the data for the r_j/D_b=0.2 mouth edge rounding from Ref. 5.

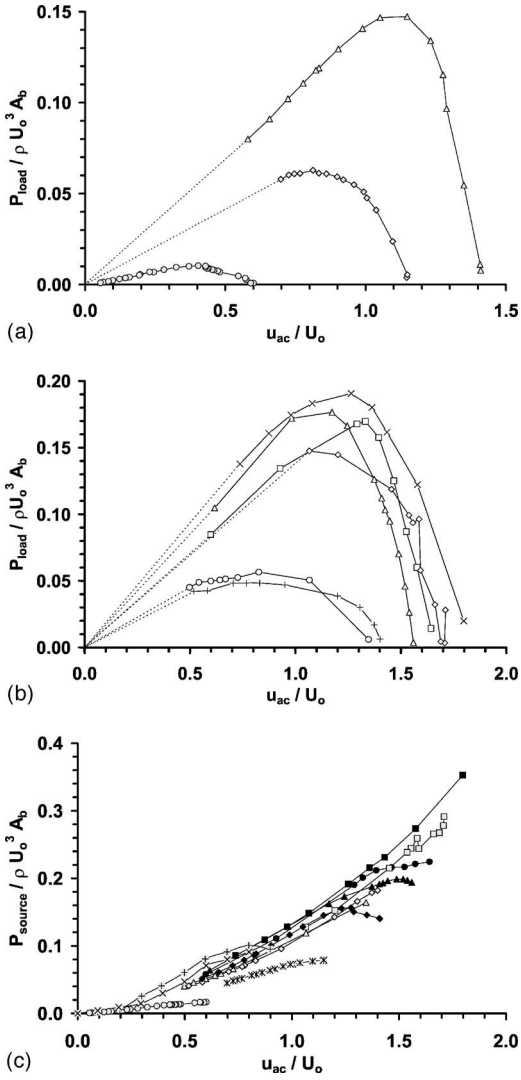

FIG. 9. (a) Dimensionless power dissipated in the acoustic load versus the relative acoustic velocity amplitude at the cross-junction at 350 Hz and 10 bars absolute pressure for various Strouhal numbers. Circles—St=0.4, triangles—St=0.26, and squares—St=0.18. (b) Dimensionless power dissipated in the acoustic load versus the relative acoustic velocity amplitude at the cross-junction for various half-wavelength frequencies and Strouhal numbers. +'s—178 Hz and St=0.26, circles—200 Hz and St=0.28, squares—300 Hz and St=0.29, triangles—400 Hz and St=0.28, diamonds—500 Hz and St=0.29, X's—525 Hz and St=0.29. (c) Dimensionless vortex-acoustic source power versus the relative acoustic velocity amplitude at the cross-junction for various half-wavelength frequencies and Strouhal numbers. Open circles—350 Hz and St=0.4, closed circles—300 Hz and St=0.29, open squares—500 Hz and St=0.29, closed squares—525 Hz and St=0.29, open triangles—200 Hz and St=0.28, closed triangles—400 Hz and St=0.28, open diamonds—178 Hz and St=0.26, closed diamonds—350 Hz and St=0.26, *'s—350 Hz and St=0.18, +'s—Kriesels with St=0.3, X's—Kriesels with St=0.4.

for 2 bar. The mean pressure not only affects the magnitude of the loss mechanisms but also affects the hydrodynamic power of the mean flow, and this influences the vortex-acoustic source strength. The relative acoustic velocity amplitude is decreased when the acoustic load is used to dissipate additional power from the resonance. The additional damping caused by the load does not significantly shift the peak of the dimensionless amplitude plot at a given pressure that occurs near St=0.25 at 10 bar and closer to 0.3 at 2 bar. The total dimensionless vortex-acoustic source power ratio calculated using Eq. (8) for this data is presented in Fig. 8(b) along with the numerical analysis of Kriesels from Fig. 4(a). Of note in Fig. 8(b) is how the vortex-acoustic source power at 2 bar collapses to one curve for the different acoustic damping settings, however, the 10 bar data does not. This could be indicative of an unaccounted loss mechanism or a different acoustic amplitude dependence, which is assumed to be linear for a comparison with Kriesels. The discrepancy between the total vortex-acoustic power available represented by the data and the dashed line of Kriesels indicates that the energy balance calculation embodied in Eq. (8) is lacking for high mean pressures and large relative acoustic velocity amplitudes.

2. Variable resistance

Figure 9(a) displays the ratio of dimensionless power dissipated in the load, $P_{\text{load}}/\rho U_0^3 A_b$, versus the dimensionless acoustic velocity amplitude at the cross junction for a frequency of 350 Hz and various Strouhal numbers (various mean flow velocities) for the cross junction. The rightmost data point of each data series corresponds to the acoustic load valve being effectively closed. As before, due to the imperfect seal made by the pin in the valve, there is a small amount of dissipation in the valve, even when it is consid-

ered closed. This is why the power dissipated in the load is not exactly zero when the valve is closed. As this valve is slowly opened, the load dissipates more and more power, this dissipation decreases the relative acoustic velocity amplitude within the resonator. Since the relative acoustic velocity amplitude in the side branch drives the power dissipation in the load as well as the vortex-acoustic source power, we expect the decreasing amplitude to result in a maximum in the data series in Fig. 9(a). This maximum corresponds to the maximum amount of excess power that can be dissipated for the resonant mode for the given flow conditions. The maximum at a Strouhal number of 0.4 corresponds to an acoustic pressure amplitude of 3.5% of the ambient pressure and a power dissipation in the load of 0.4 W. However, the maximum at a Strouhal number of 0.26 corresponds to an acoustic pressure amplitude of 15.4% of the mean pressure, resulting in 21.7 W being dissipated in the load. Finally, the maximum at a Strouhal number of 0.18 corresponds to an acoustic pressure amplitude of 15.2% of the mean pressure, resulting in 26.0 W being dissipated in the load. The dashed line segments extending the data series to zero relative acoustic velocity amplitude and zero power dissipation illustrate the abrupt extinguishing of the aeroacoustic sound source due to excessive damping. Data could be taken in this region if the load had a finer control of its resistance. Oftentimes this abrupt extinction of the resonance occurred when the acoustic load valve was almost completely open.

The amount of power that can be dissipated in the load also depends on how much power has been dissipated elsewhere. Figure 9(b) displays the dimensionless power dissipated in the acoustic load, $P_{\text{load}}/\rho U_0^3 A_b$, versus the acoustic velocity ratio for different half-wavelength resonant frequencies and constant fixed Strouhal numbers between 0.26 and 0.29 for the cross junction. Low frequencies correspond to long side-branch lengths and large viscous/thermal penetration depths, which imply more power loss due to damping in the sidebranch pipe compared to short/high-frequency side branches. The data generally demonstrates that more power can be extracted with the damper from the short/high-frequency side branches than from the long/low-frequency side branches. The data also displays the same functional dependence on amplitude as in Fig. 9(a). Also, the dashed line segments have the same meaning as in the discussion as before.

The total power loss calculated by Eq. (8) including the contributions of the load for this data appears in Fig. 9(c). In this figure the source power is made dimensionless by $\rho U_0^3 A_b$. Included in this figure is the numerical calculation of the vortex-acoustic source power by Kriesels, Fig. 4(b), for the cross junction with sharp edges. It can be seen that for low relative acoustic velocity amplitudes and a Strouhal number of 0.4 the data agrees with the numerics in the magnitude and in the linear dependence on u_{ac}/U_0. At higher amplitudes, above $u_{\text{ac}}/U_0=0.5$, the numerical work overpredicts the available source power but the general functional dependence of the source power on the amplitude is similar. This overestimation of the available source power was observed by Kriesels as well.

Figure 10(a) displays the dimensionless power dissipated in the load at a half-wavelength frequency of 350 Hz and a Strouhal number of 0.27 for the large and small tridents orientated with and against the mean flow direction as well as the cross junction for comparison. Surprisingly, more power may be dissipated in the load when installed in a side branch of the large-radius trident orientated with the main flow direction than compared with the other junction geometries. The maximum power dissipated for the large-radius trident was almost 32 W in the load at an acoustic amplitude that was 17.5% of the mean pressure. The dependence of the power extracted from the resonance by the load on the side branch geometry and orientation indicates an unaccounted for the loss mechanism that is dissipating power from the resonance and making that power unavailable for the acoustic load. This unaccounted loss mechanism could be due to acoustic-driven vortex shedding at the site of the 90° bends in the trident side-branch arms.

Calculating the total power dissipated by all loss mechanisms, Eq. (8), for the data in Fig. 10(a) appears as a function of acoustic amplitude in Fig. 10(b). Included in this figure is the low-amplitude numerical calculation of vortex-acoustic source power by Kriesels from Fig. 4(b) at Strouhal numbers of 0.3 and 0.4. The data from Fig. 10(a) for the tridents and cross junction seem to approach the same source power near

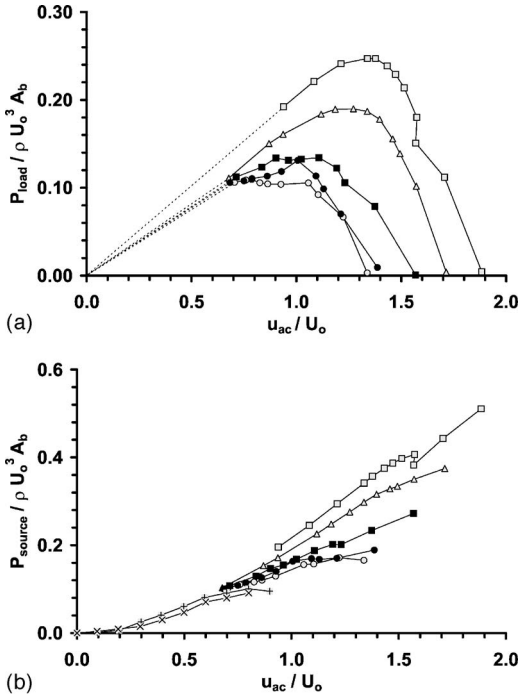

FIG. 10. (a) Dimensionless power dissipated in the acoustic load versus the relative acoustic velocity amplitude at 350 Hz and a Strouhal number of 0.27 for the different junction geometries. Open triangles—cross junction, open circles—small trident arms aligned with main pipe flow, closed circles—small trident arms aligned against the main pipe flow, open squares—large trident arms aligned with the main pipe flow, closed squares—large trident arms aligned against the main pipe flow. (b) Dimensionless vortex-acoustic source power versus the relative acoustic velocity amplitude at 350 Hz and a Strouhal number of 0.27 for the different junction geometries. Open triangles—cross junction, open circles—small trident arms aligned with main pipe flow, closed circles—small trident arms aligned against the main pipe flow, open squares—large trident arms aligned with the main pipe flow, closed squares—large trident arms aligned against the main pipe flow.

a relative acoustic velocity amplitude of 0.75; these data also agree with Kriesels predictions for the source power at this amplitude. However, as the amplitude increases, the data series diverge. Again, this diverging series of data indicates an unaccounted-for loss mechanism in the theoretical framework of Sec. III. However, while the spread in the calculated source power is a factor of 2 at a relative acoustic velocity amplitude of 1.25, it still may be used to estimate acoustic amplitudes for similar networked gas flow situations in industrial or laboratory settings.

V. CONCLUSIONS

The available source power from the aeroacoustic excitation of a resonance in a gas network has been estimated at a high relative acoustic velocity amplitude for three coaxial side-branch geometries: straight branches, branches with a large 90° bend and branches with a small 90° bend. The investigation of the available source power has been extended by the use of a coupled resistance and compliance placed at a pressure antinode to dissipate power in a controlled manner. It has been observed that this load can dissipate a large fraction of the power within the resonance and can even silence the resonance. Silencing unwanted aeroacoustic excitations in industrial gas networks by inserting a valve and compliant volume is a simple solution to a complex and possibly dangerous problem. Also, by measuring the fraction of the resonance's power that can be extracted before the resonance is silenced allows for the optimization of devices to extract this power from natural gas pipelines for the generation of electricity downwell or in remote locations or for other uses.[35]

ACKNOWLEDGMENTS

The authors would like to thank Han Crijns for participating in this project as well as Jan Willems for constructing the high-pressure flow setup. Also, a special thanks goes to Avraham Hirschberg for aeroacoustic expertise, which was invaluable for this project to succeed. Lastly, the authors appreciate the support of Alex van der Spek, who supplied funding through Shell's International Exploration and Production B. V. department.

[1]J. C. Bruggeman, "Flow induced pulsations in pipe systems," Ph.D. dissertation, Department of Applied Physics, Technical University at Eindhoven, The Netherlands, 1987.
[2]M. C. A. M. Peters, "Aeroacoustic sources in internal flows," Ph.D. dissertation, Department of Applied Physics, Technical University at Eindhoven, The Netherlands, 1993.
[3]S. Dequand, "Duct aeroacoustics: from technological applications to the flute," Ph.D. dissertation, Department of Applied Physics, Technical University at Eindhoven, The Netherlands, 2001.
[4]J. C. Bruggeman, A. Hirschberg, M. E. H. van Dongen, A. P. J. Wijnands, and J. Gorter, "Self-sustained aeroacoustic pulsations in gas transport systems: experimental study of the influence of closed side branches," J. Sound Vib. **150**, 371–393 (1991).
[5]P. C. Kriesels, M. C. A. M. Peters, A. Hirschberg, A. P. J. Wijnands, A. Iafrati, G. Riccardi, R. Piva, and J. C. Bruggeman, "High amplitude vortex-induced pulsations in a gas transport system," J. Sound Vib. **184**, 343–368 (1995); P. C. Kriesels, "Vortex induced pulsations in gas transport systems: prediction method and data on the acoustic source power," Report R-1307-D, Vakgroep Transportfysica TUE, 1994.
[6]D. Rockwell and E. Naudascher, "Review—Self-sustained oscillations of flow past cavities," J. Fluids Eng. **100**, 152–165 (1978).
[7]D. Rockwell, "Oscillations of impinging shear layers," AIAA J. **21**, 645–664 (1983).
[8]T. D. Mast and A. D. Pierce, "Describing-function theory for flow excitation of resonators," J. Acoust. Soc. Am. **97**, 163–172 (1995).
[9]R. M. Baldwin and H. R. Simmons, "Flow-induced vibration in safety relief valves," J. Pressure Vessel Technol. **108**, 267–272 (1986).
[10]T. A. Wilson, G. S. Beavers, M. A. DeCoster, D. K. Holger, and M. D. Regenfus, "Experiments on the fluid mechanics of whistling," J. Acoust. Soc. Am. **50**, 366–372 (1971).
[11]M. S. Howe, "Contributions to the theory of aerodynamic sound, with application to excess jet noise and the theory of the flute," J. Fluid Mech. **71**, 625–673 (1975).
[12]R. C. Chanaud, "Aerodynamic whistles," Sci. Am. **222**, 40–60 (1970).
[13]S. A. Elder, "Self-excited depth-mode resonance for wall-mounted cavity in turbulent flow," J. Acoust. Soc. Am. **64**, 877–891 (1978).
[14]M. Meissner, "Acoustic modes induced by flow in a pipe with two closed side-branches," Appl. Acoust. **63**, 1071–1083 (2002).
[15]M. S. Howe, "Contributions to the theory of aerodynamic sound, with application to excess jet noise and the theory of the flute," J. Fluid Mech. **71**, 625–673 (1975).
[16]M. S. Howe, "The dissipation of sound at an edge," J. Sound Vib. **70**, 407–411 (1980).
[17]M. S. Howe, "The influence of mean shear unsteady aperture flow, with application to acoustical diffraction and self-sustained cavity oscillations," J. Fluid Mech. **109**, 125–146 (1981).
[18]M. S. Howe, "Edge cavity and aperture tones at very low Mach numbers," J. Fluid Mech. **330**, 61–84 (1997).
[19]P. A. Nelson, N. A. Halliwell, and P. E. Doak, "Fluid dynamics of a flow excited resonance, Part II: Flow acoustic interaction," J. Sound Vib. **91**, 375–402 (1983).
[20]S. A. Elder, T. M. Farabee, and F. C. DeMetz, "Mechanisms of flow-excited cavity tones at low Mach number," J. Acoust. Soc. Am. **72**, 532–549 (1982).
[21]S. A. Elder, "Forced oscillations of a separated shear layer with application to cavity flow-tone effects," J. Acoust. Soc. Am. **67**, 774–781 (1980).
[22]S. Ziada and S. Shine, "Strouhal numbers of flow-excited acoustic resonance of closed side branches," J. Fluids Struct. **13**, 127–142 (1999).
[23]S. Ziada, "A flow visualization study of flow-acoustic coupling at the mouth of a resonant side-branch," J. Fluids Struct. **8**, 391–416 (1994).
[24]A. Cummings, "The response of a resonator under a turbulent boundary layer to a high amplitude non-harmonic sound field," J. Sound Vib. **115**, 321–328 (1987).
[25]P. Shakkottai, E. Y. Kwack, and L. H. Back, "Aeroacoustic flow sensor," Rev. Sci. Instrum. **62**, 2205–2212 (1991).
[26]P. Shakkottai, E. Y. Kwack, and L. H. Back, "Tone generation by aeroacoustic sources in pipes with flow," J. Acoust. Soc. Am. **87**, 1489–1496 (1990).
[27]B. E. Walker and A. F. Charwat, "Correlation of the effects of grazing flow on the impedance of Helmholtz resonators," J. Acoust. Soc. Am. **72**, 550–555 (1982).
[28]A. M. Fusco, W. C. Ward, and G. W. Swift, "Two-sensor power measurements in lossy ducts," J. Acoust. Soc. Am. **91**, 2229–2235 (1992).
[29]G. W. Swift, *Thermoacoustics—A Unifying Perspective For Some Engines and Refrigerators* (Acoustical Society of America, New York, 2002), Chap. 9.
[30]R. Smith, "High efficiency two kilowatt acoustic source for a thermoacoustic refrigerator," MS thesis, Department of Acoustics, Pennsylvania State University, 2000.
[31]J. C. Bruggeman, A. Hirschberg, M. E. H. van Dongen, A. P. J. Wijnands, and J. Gorter, "Flow induced pulsations in gas transport systems: analysis of the influence of closed side branches," J. Fluids Eng. **111**, 484–491 (1989).
[32]G. W. Swift, "Thermoacoustic engines," J. Acoust. Soc. Am. **84**, 1145–1180 (1988).
[33]A. D. Pierce, *Acoustics: An Introduction to Its Physical Principles and Applications* (Acoustical Society of America, New York, 1989), Chap 11.
[34]L. Beranek, *Acoustics* (Acoustical Society of America, New York, 1996), Chap 5.
[35]W. V. Slaton and J. C. H. Zeegers, "An aeroacoustically driven thermoacoustic heat pump," submitted to the J. Acoust. Soc. Am. 2004.

Directional radiation pattern in structural–acoustic coupled system

Hee-Seon Seo[a] and Yang-Hann Kim[b]
Center for Noise and Vibration Control (NOVIC), Department of Mechanical Engineering, Korea Advanced Institute of Science and Technology (KAIST), Science Town, Daejon, 305-701, Korea

(Received 10 March 2004; revised 24 March 2005; accepted 11 April 2005)

In this paper we demonstrate the possibility of designing a radiator using structural-acoustic interaction by predicting the pressure distribution and radiation pattern of a structural-acoustic coupling system that is composed by a wall and two spaces. If a wall separates spaces, then the wall's role in transporting the acoustic characteristics of the spaces is important. The spaces can be categorized as bounded finite space and unbounded infinite space. The wall considered in this study composes two plates and an opening, and the wall separates one space that is highly reverberant and the other that is unbounded without any reflection. This rather hypothetical circumstance is selected to study the general coupling problem between the finite and infinite acoustic domains. We developed an equation that predicts the energy distribution and energy flow in the two spaces separated by a wall, and its computational examples are presented. Three typical radiation patterns that include steered, focused, and omnidirected are presented. A designed radiation pattern is also presented by using the optimal design algorithm.
 [DOI: 10.1121/1.1925850]

PACS number(s): 43.20.Tb, 43.40.Rj [EGW] Pages: 92–103

I. INTRODUCTION

In order to reduce noise generated by structural–acoustic interaction, numerous studies (for example, see Refs. 1–28) have been performed to understand the coupling mechanism between the structure and the space. Many investigations have also been conducted (for example, see Refs. 1, 2, and 7–19) under the assumption of weakly coupled or larger structural impedance in comparison to that of contained fluid. For example, structural vibration is not affected by acoustic pressure distribution of the medium, and this is valid in many practical situations. However, if the structure is either a membrane or thin plate or if the medium has significantly high impedance (for example, water), then this assumption is no longer valid. In this case, structural vibration is affected by the pressure distribution on the structure or the other way around, and we call this a "full coupling problem." Figure 1(a) shows a coupling problem in which a wall separates two unbounded spaces and Fig. 1(b) is another typical example of a coupling problem that has a structure and two bounded spaces. These kinds of problems are common and solutions are available,[1–4] but if the wall separates bounded and unbounded spaces, as shown in Fig. 1(c), then the wall's role in transporting the acoustic characteristics is not well defined.

Numerous numerical and experimental investigations have been conducted to understand the physical mechanism between structural vibration and fluid pressure distribution over the structure by many researchers [see Refs. 1–37]. Reviewing the previous work is divided several categories that start with the general approach of the structural–acoustic coupled problem to sound radiation associated with coupling. Dowell, Gorman, and Smith[4] presented a general theoretical model for interior sound fields in a structural–acoustic coupling system with absorbing material. To obtain high computational efficiency, they proposed solutions for the coupled responses in terms of an *in vacuo* structural wall and (rigid wall) acoustic cavity natural modes. Junger[5,6] introduced a general approach to structural–acoustic coupling problems in his paper[5] and book.[6]

The effect of structural–acoustic interaction on structural vibration has been studied in previous works.[7–11] Maidanik[7] studied the response of ribbed panels to reverberant acoustic fields, showing that the acceleration spectrum of the vibration field is related to the pressure spectrum. Dowell and Voss[8] studied the effect of a rectangular box on plate vibration. The free and forced vibration of a rectangular panel backed by a closed rectangular cavity was studied theoretically by Pretlove.[9,10] Guy and Pretlove[11] also studied the cavity-backed panel resonance.

Sound transmission in a structural–acoustic coupling problem has been studied in previous research.[12–17] Lyon[12] investigated noise reduction in case of a rigid enclosure with one flexible wall. Guy and Bhattacharya[13] studied the influence of a finite cavity backing a finite panel on the transmission of sound through the panel. Guy[14] also used multimodal analysis to study the transmission of sound at normal and oblique incidences through a flexible panel backed by a finite rectangular cavity. In order to reduce the noise transmitted through the panel into the cavity, an active noise control technique was proposed by Pan *et al.*[15,16] and Kim *et al.*[17]

Possible shapes of the coupling system, other than rectangular, have been studied in previous research.[6,18–21] Fuller and Fahy[18] investigated the structural–acoustic coupling in cylindrical elastic shells filled with fluid. A FEM-based

[a]Electronic mail : sonar@kaist.ac.kr
[b]Electronic mail : yanghannkim@kaist.ac.kr

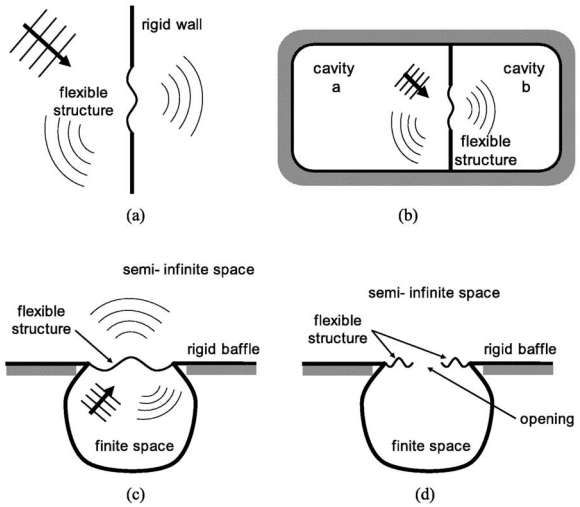

FIG. 1. The typical examples of the coupling systems: (a) unbounded spaces separated by the wall; (b) two bounded spaces separated by the wall; (c) bounded and unbounded spaces separated by the wall; and (d) bounded and unbounded spaces separated by two walls with an opening.

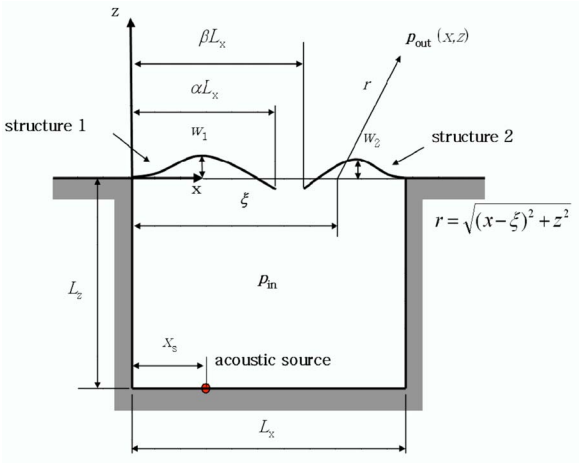

FIG. 2. The mathematical model of a coupled cavity used in the study. The cavity is rectangular and its size is L_x by L_z. The plates have length αL_x and $(1-\beta)L_x$, respectively. The source is located at the bottom of cavity ($z=-L_z$, $x=x_s$).

model to discover the structural–acoustic coupling mechanism in an irregular-shaped system was studied by Craggs[19,20] and Nefske *et al.*[21]

Researchers have also studied the sound radiation associated with structural–acoustic interaction.[22–36] Smith[22] investigated the response to sound and consequent sound radiation for one linear resonant mode of a partial structure. Feit and Liu[23] studied the near-field response of a line-driven fluid-loaded plate using numerical evaluation of the Fourier integral representations of the solution for frequencies below and above coincidence. Ko[24] investigated the modal contribution of a finite elastic plate, submerged in fluid and simply supported at both ends, to the power spectrum. Pan *et al.*[25–28] investigated coupling in high- and low-frequency ranges and an analytical model for bandlimited responses. Recently, to explain more general structure-acoustic coupling mechanism, Kim and Kim[29,30] performed theoretical and experimental study of a partially opened two-dimensional membrane–cavity system that has two different modally reacting boundary conditions. A typical example of such a general coupling problem can be observed in a musical instrument like the guitar, which has vibrating plates and an echoing cavity with an opening.[31–36]

The previous studies, however, were not attempted to design the distribution of external pressure field using a structural–acoustic interaction. To design an efficient radiator, one has to obtain various insights of the coupling system. Analytical methods including the modal expansion method can display the dependence of the model behavior on its nondimensional parameters and can easily check the limiting case of the system. However, these methods are not generally to derive analytic expressions, especially the terms in the series for the modal expansion method, because of the complexity of the system modeled. A finite element method may be applied to any physical system, including the structural–acoustic coupled problem of which the behavior is described by a set of partial differential equations. However, the number of degree of freedom is limited, so FEM is more useful for enclosed volumes than for unbounded fluid volume. In this paper, modal expansion methods are adopted as the basic analysis tool because the method shows us how the coupling phenomenon is affected by each subsystem's natural mode characteristics. The previous works have seen the system to find a good noise control means. Therefore, implicitly they are interested in getting a weak coupling. In this paper we aim to show the possibility of designing an efficient radiator using a structural–acoustic interaction by predicting the pressure distribution and radiation pattern of a structural–acoustic coupling system depicted in Fig. 1(d) and a design example of an efficient radiator that has high emission power and low side level has been presented by using the optimal design algorithm.

In order to understand the general coupling mechanism, we chose a finite space and a semi-infinite space separated by a flexible structure, as shown in Fig 1(d). Figure 1(d) shows an acoustic cavity covered by two finite-sized structures. The acoustic field is divided by the structure into two parts: One is a finite and highly reverberant space, and the other is a semi-infinite field without any reflection. In order to introduce more general coupling phenomena, we added an opening. The structure represents a "volume interaction" element, and the opening can be considered as a "pressure interaction" element. For its simplicity, without losing generality, we

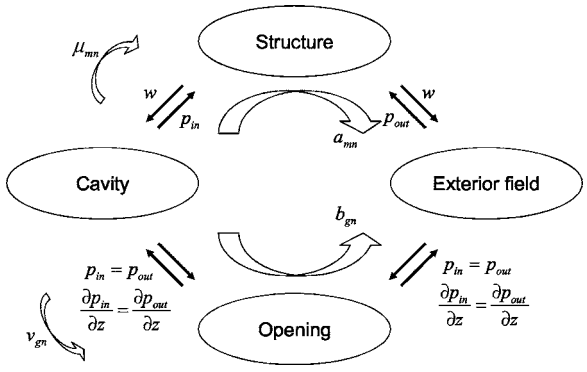

FIG. 3. The role of coupling coefficients between the subsystems.

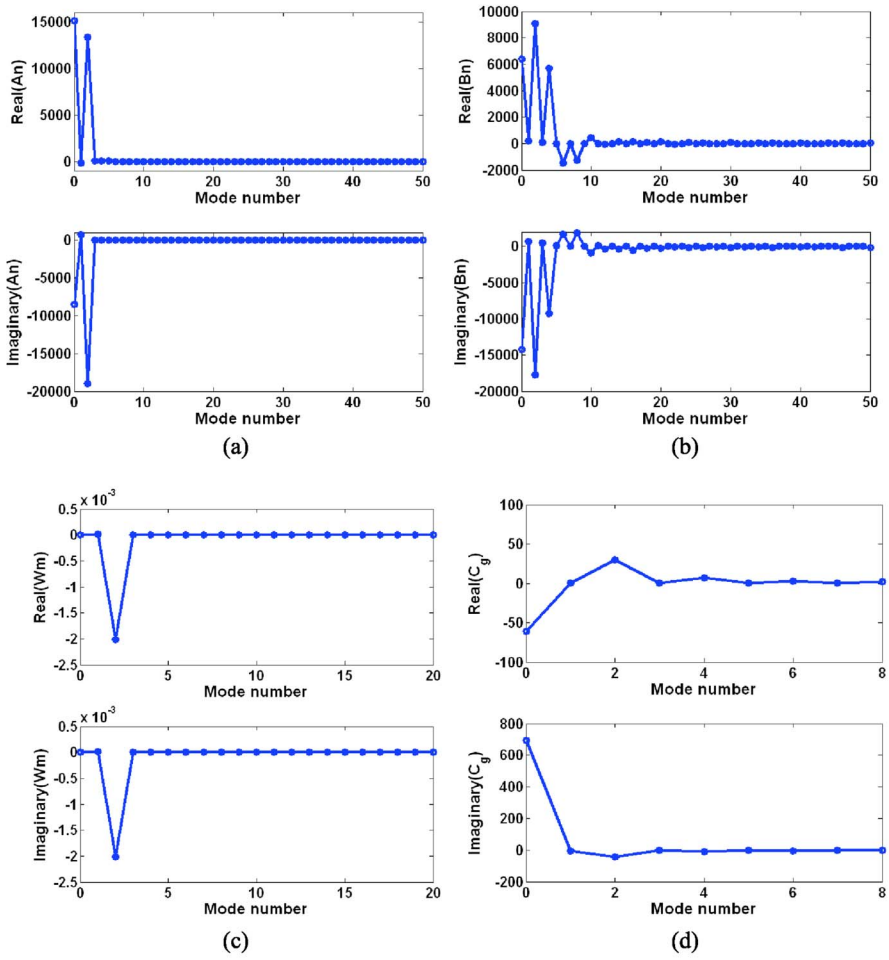

FIG. 4. Modal coefficient of subsystems at the fifth acoustic-dominated mode (2530 Hz): (a) forward pressure in the cavity; (b) backward pressure in the cavity; (c) plate; (d) opening.

used a rather simplified model (Fig. 2) instead of the one depicted in Fig. 1(d).

II. THEORETICAL APPROACH

A. Description of system

As shown in Fig. 2, we considered a partially open cavity that is coupled with a semi-infinite exterior field by having two plates and an opening. The size of the cavity is L_x by L_z, and its walls are assumed to be acoustically rigid, except for the top wall. The top side of the cavity is covered with two plates, and their flexural stiffnesses are D_1 and D_2, respectively. The length of each plate is αL_x and $(1-\beta)L_x$. We can vary the size and material property for each plate. To obtain mathematical simplicity, we assumed that the system does not change in the y direction. The boundaries of the plates are clamped on the wall and are free at the opening. Their thickness is regarded as negligible compared to the shortest wavelength of interest, but their flexural rigidity is governed by the thickness of each plate. The system is excited by a monopole source of strength Q that is located at the bottom of the cavity ($z=-L_z$, $x=x_s$).

B. Governing equations and boundary conditions

Assuming harmonic time dependence, the two-dimensional homogeneous wave equation for the acoustic field is

$$\left(\frac{\partial^2}{\partial x^2}+\frac{\partial^2}{\partial z^2}+k^2\right)p_{\text{in,out}}(x,z)=0, \tag{1}$$

where p_{in} and p_{out} are the pressure inside and outside the cavity, respectively, and k is the wave number. The equation for the plate's displacement with harmonic time dependence is given by

$$\left(\frac{\partial^4}{\partial x^4}-\kappa_i^4\right)w_i(x)=\frac{1}{D_i}\{p_{\text{in}}(x,0)-p_{\text{out}}(x,0)\},\quad i=1,2, \tag{2}$$

where w represents the plate's displacement. κ and D are the wave number and flexural rigidity of the plate, defined as

$$\kappa_l=(\rho_{m,i}\omega^2/D_i)^{1/4},\quad i=1,2, \tag{3a}$$

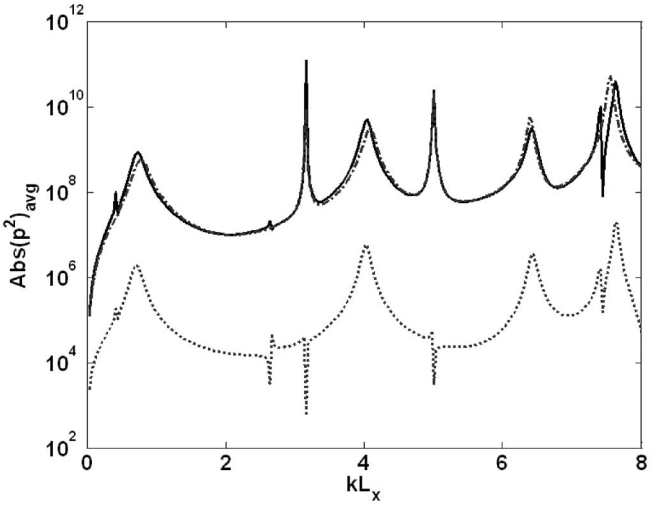

FIG. 5. The spatially averaged sound pressure level; Solid line: inside the cavity, dotted line: outside the cavity of the coupled system, and dash dotted line: inside the cavity of the uncoupled system.

$$D_i = E_i h_i^3/12(1-\nu_i^2), \quad i=1,2, \tag{3b}$$

where $\rho_m=\rho_s h$ is the mass per unit area, ρ_s is the density, and h is the thickness of the plate. E is the Young's modulus and ν is the Poisson's ratio of the plate.

The boundary conditions at the bottom of the cavity can be written as

$$\left.\frac{\partial p_i}{\partial z}\right|_{z=-L_z} = -jk\rho cQ\delta(x-x_s), \tag{4}$$

where ρ is the density and c is the sound speed of the fluid. The boundary condition on the rigid wall is zero pressure gradients. It is noteworthy that the plate's velocity has to be the same as both the inside and outside fluid particle velocities. The pressure and fluid particle velocity are continuous at the opening (see Fig. 2). We now have three governing equations and related boundary conditions.

C. Modal solution

The pressure inside the cavity can be expressed by the superposition of positive- and negative-going parts of x and z directional waves. By applying the left and right rigid wall boundary conditions inside the cavity, the pressure inside the cavity is represented by

$$p_{\text{in}}(x,z) = \sum_{n=0}^{\infty} \psi_n(x)(A_n e^{-jk_{zn}z} + B_n e^{jk_{zn}z}), \tag{5}$$

where $\psi_n(x)$ is a modal function of pressure inside the cavity in the x direction, and k_{zn} is the z directional wave number of the nth mode. A_n and B_n are positive- and negative-going modal coefficients of the nth mode, respectively. Pressure outside the cavity can be derived from the Kirchhoff–Helmholtz integral equation. We assume that an imaginary source is located at $z=0$ on a rigid baffle. We may choose the Green's function, which satisfies the Neumann boundary condition at $z=0$ and apply the velocity continuity condition at the boundary. The pressure outside the cavity can be written using the pressure gradient inside the cavity as

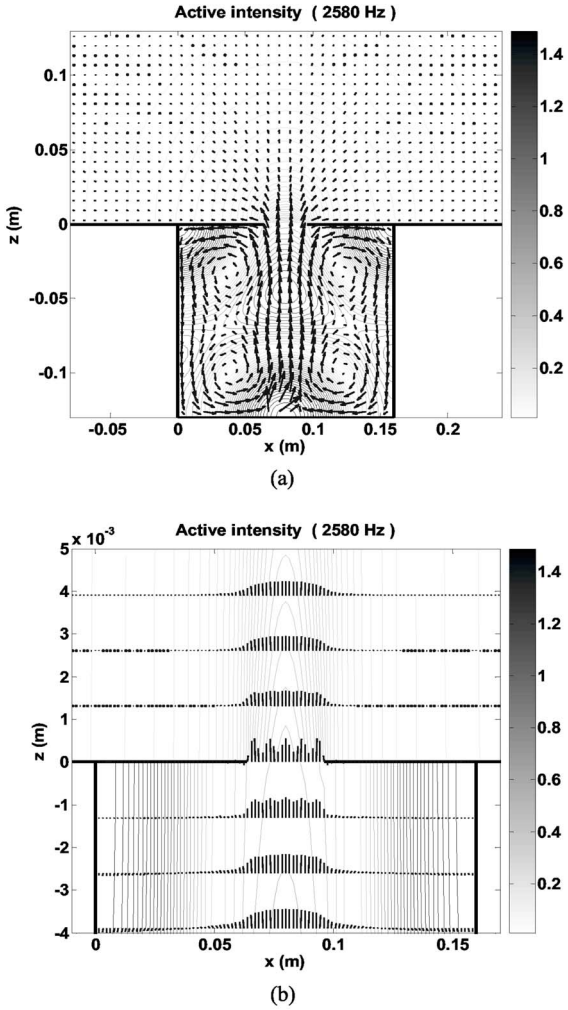

FIG. 6. The pressure and active intensity of two acoustic spaces [(a) whole cavity and external space; (b) near the opening] at the fifth acoustic-dominated mode. The pressure and intensity are normalized by $\sqrt{\langle (p_{\text{in}})^2\rangle}$ and $\langle (p_{\text{in}})^2\rangle/2\rho c^2$, respectively.

$$p_{\text{out}}(x,z) = -\int_0^{L_x} G_N(x,z|\xi,0)\frac{\partial p_{\text{in}}(\xi,0)}{\partial \zeta}d\xi. \tag{6}$$

The plate's displacement can be represented as the sum of *in vacuo* modes. That is,

$$w_i(x) = \sum_{m=0}^{\infty} W_{il}\phi_l(x), \quad i=1,2, \quad l=m,h, \tag{7}$$

where $\phi_m(x)$ and $\phi_h(x)$ are the modal functions of displacements of plate 1 and 2, respectively. W_{1m} and W_{2h} are the unknown coefficients to be determined. The pressure distribution in the opening can also be represented as the sum of modal functions. That is,

$$p_h(x) = \sum_{g=0}^{\infty} C_g\varphi_g(x), \tag{8}$$

where $\varphi_g(x)$ are arbitrary modal functions that are complete sets for representing any pressure in the opening. The expan-

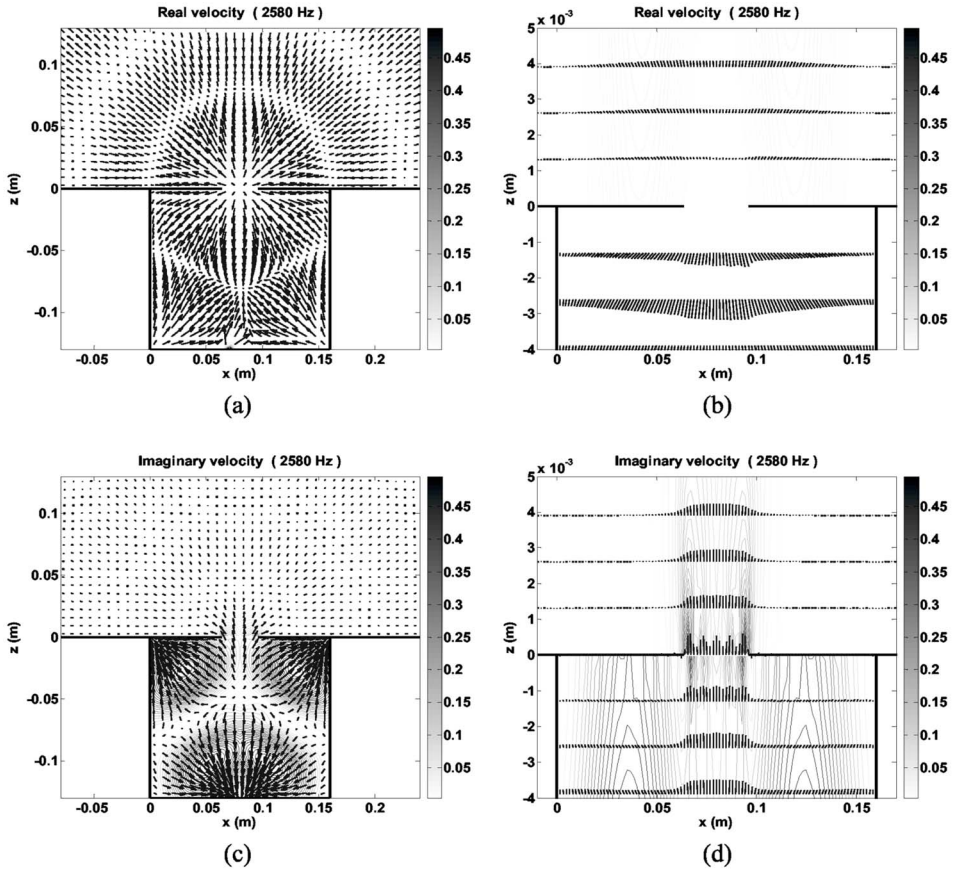

FIG. 7. The velocity distribution of two acoustic spaces at the fifth acoustic-dominated mode about the uncoupled system. (a) The real part of whole cavity and external space; (b) the real part near the opening; (c) the imaginary part of the whole cavity and external space; (d) the imaginary part near the opening.

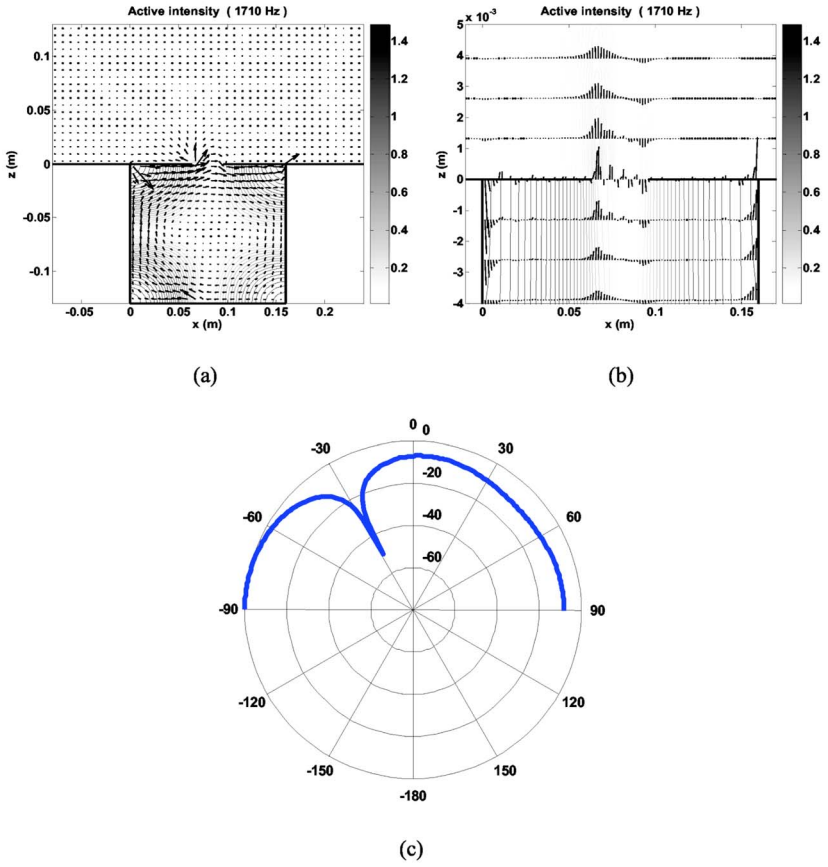

FIG. 8. The pressure and active intensity of two acoustic spaces (1710 Hz) [(a) whole cavity and external space; (b) near the opening]; (c) steered radiation pattern at the third acoustic-dominated mode.

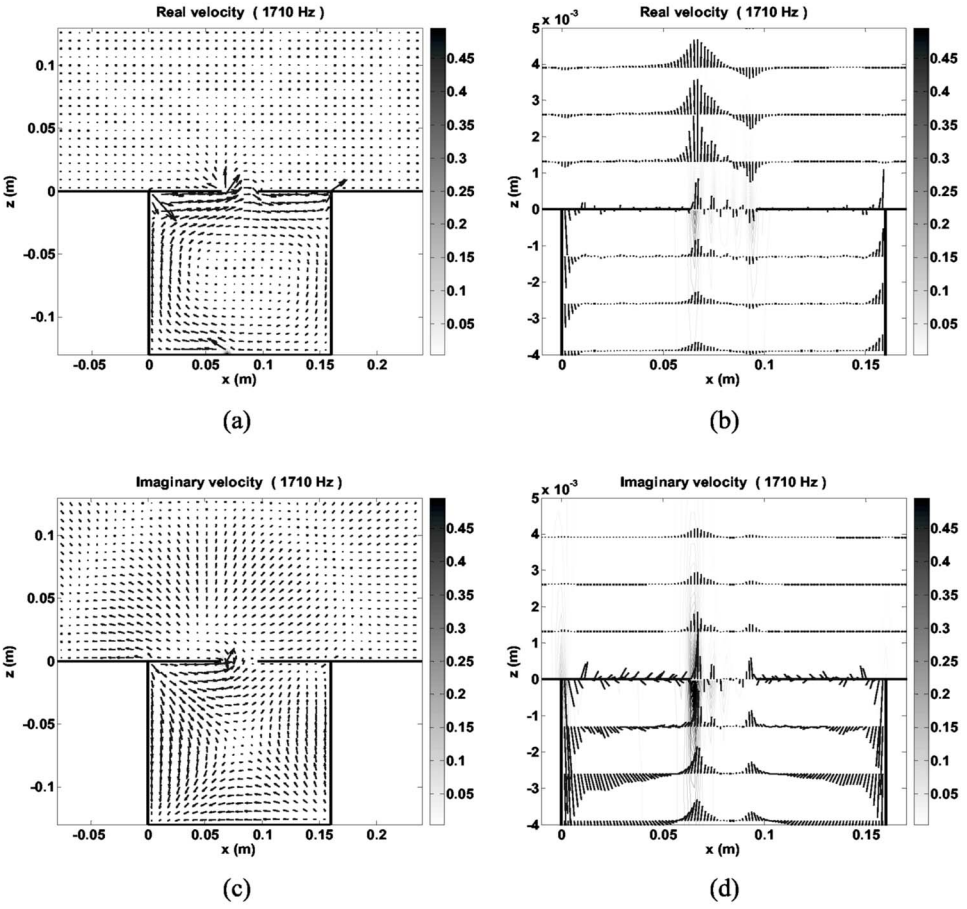

FIG. 9. The velocity distribution of two acoustic spaces at the third acoustic-dominated mode (1710 Hz) about the coupled system. (a) The real part of the whole cavity and external space; (b) the real part near the opening; (c) the imaginary part of the whole cavity and external space; (d) the imaginary part near the opening.

sion function in the opening is assumed a Fourier cosine series. That is,

$$\varphi_g(x) = \sqrt{2-\delta_{g0}}\cos\frac{g\pi}{(\beta-\alpha)L_x}(\beta L_x - x), \quad g = 0,1,2. \quad (9)$$

The procedure to get the modal coefficients developed by Kim and Kim[30] is about a partially opened two-dimensional membrane–cavity system that has two different modally reacting boundary conditions. In this paper, we expand this procedure to a partially opened two-dimensional plate–cavity system that has three different modally reacting boundary conditions.

Using this procedure, we can obtain the following equations for the modal coefficients. The relation between A_n and B_n can be written as

$$A_n = B_n e^{-2jk_{zn}L_z} + \frac{k\rho cQ\psi_n(x_s)}{k_{zn}L_x}e^{-jk_{zn}L_z}. \quad (10)$$

The equation for the modal coefficient B_n is given by

$$\sum_{n=0}^{\infty}[jk_{zn}S_{il}(1-e^{-2jk_{zn}L_z})\mu_{ln} - (1+e^{-2jk_{zn}L_z})\mu_{ln} - j(1-e^{-2jk_{zn}L_z})k_{zn}L_x a_{ln}]B_n = \sum_{n=0}^{\infty}\left[\frac{k\rho cQ\psi_n(x_s)}{k_{zn}L_x}(jk_{zn}S_{il}\mu_{ln} + \mu_{ln} - jk_{zn}L_x a_{ln})e^{-jk_{zn}L_z}\right], \quad i = 1,2, \quad l = m,h, \quad (11a)$$

$$\sum_{n=0}^{\infty}[(1+e^{-2jk_{zn}L_z})\nu_{gn} + j(1-e^{-2jk_{zn}L_z})k_{zn}L_x b_{gn}]B_n = -\sum_{n=0}^{\infty}\frac{k\rho cQ\psi_n(x_s)}{k_{zn}L_x}e^{-jk_{zn}L_z}(\nu_{gn} - jk_{zn}L_x b_{gn}), \quad (11b)$$

where the four nondimensional coupling coefficients are defined by

$$\mu_{ln} \equiv \frac{1}{\Lambda_l}\int_{\Lambda_l}\phi_l(x)\psi_n(x)dx, \quad l = m,h, \quad (12)$$

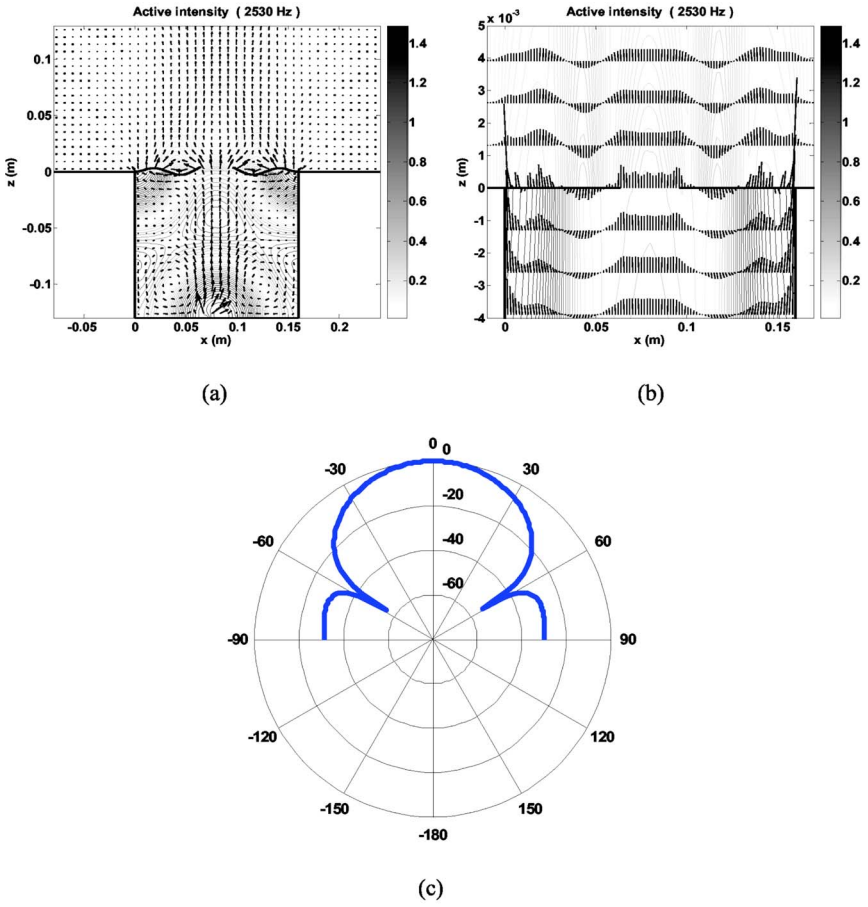

FIG. 10. The pressure and active intensity of two acoustic spaces (2530 Hz) [(a) the whole cavity and external space; (b) near the opening]; (c) focused radiation pattern at the fifth acoustic-dominated mode.

$$a_{ln} \equiv \frac{1}{\Lambda_l \Lambda} \int_{\Lambda} d\xi \int_{\Lambda_l} dx \times \left(\phi_l(x)\psi_n(\xi) \times \frac{-j}{2} H_0^{(2)}(k|x-\xi|) \right), \quad l = m,h, \tag{13}$$

$$\nu_{gn} \equiv \frac{1}{\Lambda_g} \int_{\Lambda_g} \varphi_g(x)\psi_n(x)dx, \tag{14}$$

$$b_{gn} \equiv \frac{1}{\Lambda_g \Lambda} \int_{\Lambda} d\xi \int_{\Lambda_g} dx \times \left(\varphi_g(x)\psi_n(\xi) \times \frac{-j}{2} H_0^{(2)}(k|x-\xi|) \right), \tag{15}$$

and S_{il} is

$$S_{il} = \frac{D_i(\kappa_l^4 - \kappa_i^4)}{\rho\omega^2} = \frac{Eh^3(\kappa_l^4 - \kappa_i^4)}{12(1-\nu^2)\rho\omega^2}, \quad i = 1,2, \quad l = m,h, \tag{16}$$

where $H_0^{(2)}(kr)$ is the second kind Hankel function of order zero that satisfies the Neumann boundary condition at $z=0$. Λ refers to the total radiating domain just like L_x in this paper, and Λ_l is the spatial domain of each plate. μ_{mn} represents the component of the mth plate mode for the nth cavity mode for the first plate, and μ_{hn} is a similar representation for the second plate. a_{mn} expresses modal contributions of the mth modal component to the nth cavity mode when it propagates. The coefficients ν_{gn} and b_{gn} have similar characteristics to μ_{hn} and a_{mn}, but they express the role of the opening and the cavity. Figure 3 captures the role of the coupling coefficients between subsystems in detail.

To get modal coefficients B_n, we express Eq. (11a) and (11b) to a simple form using a matrix notation as

$$[Y_1]_{MN}\{B\}_N = \{Q_1\}_M, \qquad [Y_3]_{HN}\{B\}_N = \{Q_3\}_H, \tag{17a}$$

$$[Y_2]_{GN}\{B\}_N = \{Q_2\}_G. \tag{17b}$$

Equations (17a) and (17b) can be rewritten as a single matrix equation as

$$[Y]_{MN}\{B\}_N = \{Q\}_N, \tag{18}$$

where

$$[Y]_{NN} = \begin{bmatrix} [Y_1]_{MN} \\ [Y_2]_{GN} \\ [Y_3]_{HN} \end{bmatrix} \quad \text{and} \quad \{Q\}_N = \begin{Bmatrix} \{Q_1\}_M \\ \{Q_2\}_G \\ \{Q_3\}_H \end{Bmatrix}. \tag{19}$$

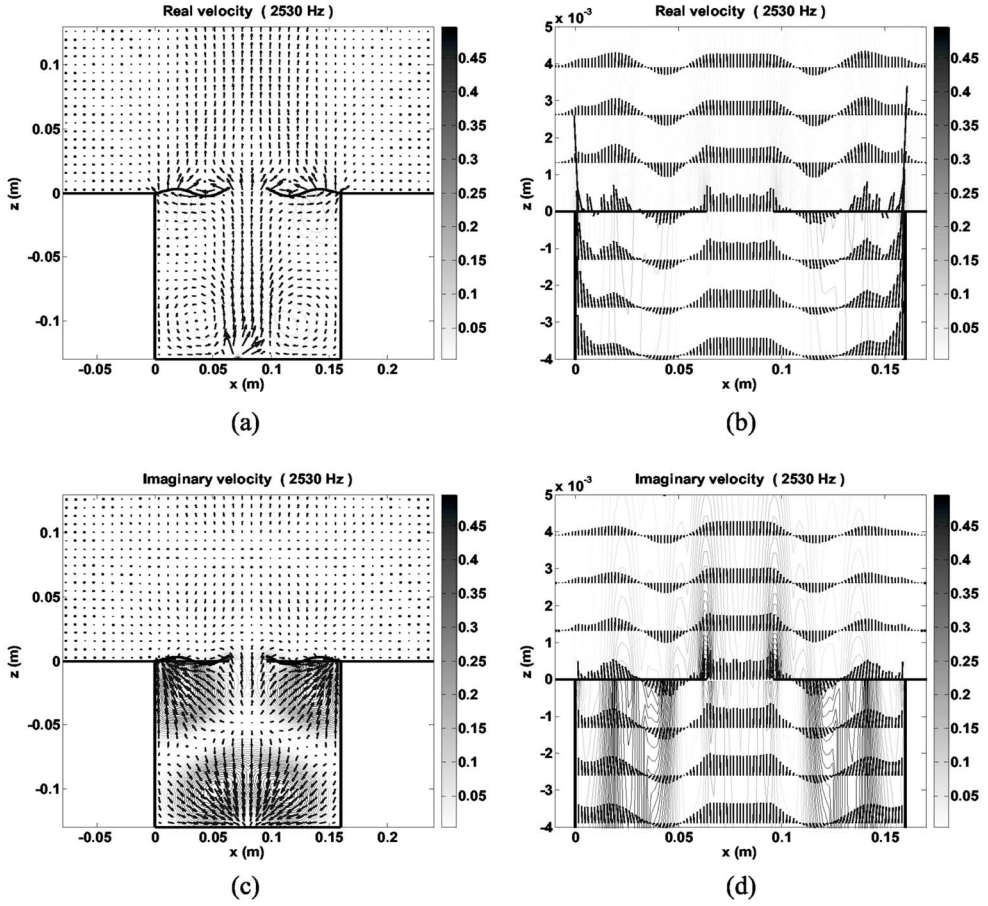

FIG. 11. The velocity distribution of two acoustic spaces at the fifth acoustic-dominated mode (2530 Hz) about the coupled system. (a) The real part of the whole cavity and external space; (b) the real part near the opening; (c) the imaginary part of the whole cavity and external space; (d) the imaginary part near the opening.

We can solve this problem by using the same number of modes and equations. If we want to consider $N+1$ modes in the cavity, $M+1$ modes in plate 1, and $H+1$ modes in plate 2, then we have to use $G=N-M-H-1$ modes in the opening to obtain a matrix of full rank. Therefore, the coefficient vector $\{B\}_N$ or B_n can be solved and A_n can be obtained from Eq. (10). The pressure inside and outside the cavity can be obtained using Eq. (5) and Eq. (6).

III. COMPUTATIONAL EXAMPLES AND DISCUSSION

A. Descriptions of examples and convergence of solution

In order to visualize the coupling mechanism using the equation derived and observe the possibility of designing radiator directivity or noise control means using a directional radiation pattern due to the structural–acoustic interaction, several numerical simulations were performed. The cavity size of $0.16\ \text{m} \times 0.13\ \text{m}$ was selected to excite only the modes in the frequency band of interest. The aspect ratio of the cavity was selected to avoid modal overlap in the frequency band of interest for clear results. The position of the monopole source was set at $x_s=0.07$ m in the bottom. The material for the plate is steel, and its thickness is 0.67 mm. To examine the effects of the structural–acoustic coupling phenomena, an uncoupled system that is composed by rigid walls instead of the plate. The opening occupied 20% of the top wall and was placed at the center.

The normal mode expansion method is known to have poor convergence about a highly damped system. The flexible structure and the opening in the coupled system act as a damping with respect to the finite cavity. So, the modal coefficients should be determined that acoustic characteristics of two spaces may converge. The pressure and velocity distribution of two spaces (inside and outside the cavity) can be calculated using Eqs. (5) and (6). To get an acceptable solution, the convergence of coefficients A_n and B_n are the most important. Therefore, the convergence criterion is decided on the convergence trend of coefficients A_n and B_n. The modal coefficients of higher-order terms can be truncated when the coefficients are sufficiently small compared to the dominant coefficient. Figures 4(a) and 4(b) show real and imaginary parts of the coefficients A_n and B_n. In this paper, we assumed that modal coefficients smaller than $1/100$ compared to the largest modal coefficient can be truncated. Modal coefficients higher than the 22nd mode satisfy the criterion. So, we need at least 22 modes to calculate the pressure inside and outside the cavity. To properly represent the displacement of the plate and the pressure in the opening, the convergence of $W_{m,h}$ and C_g also should be considered. Figures 4(c) and 4(d)

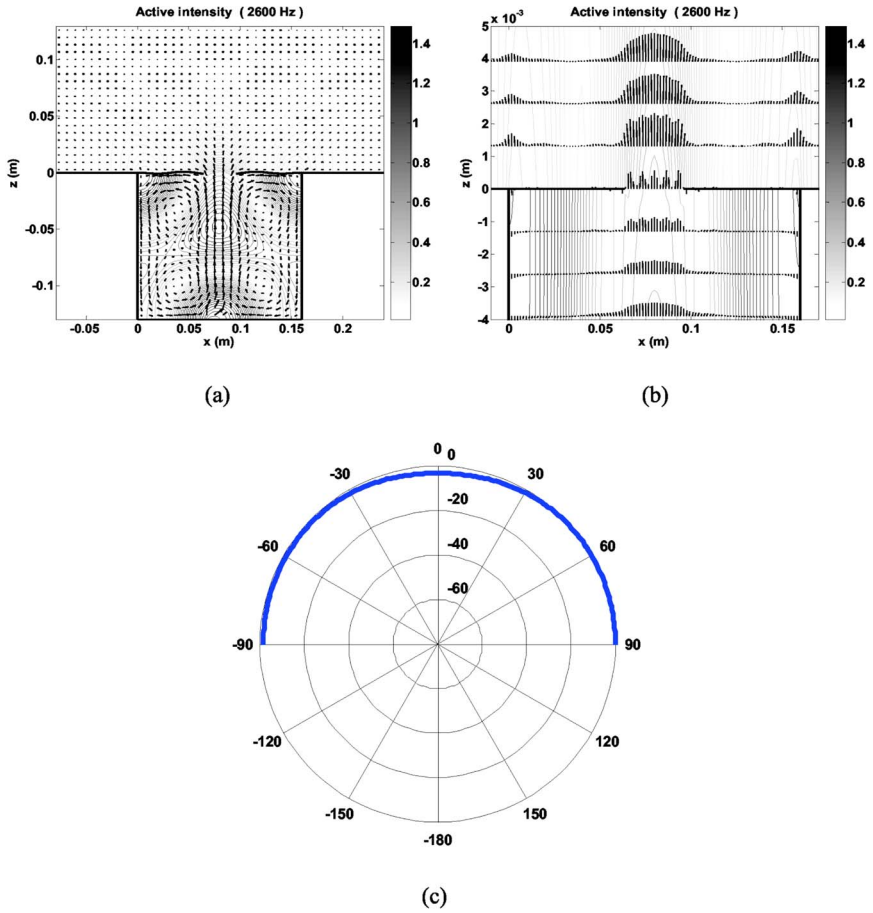

FIG. 12. The pressure and active intensity of two acoustic spaces (2600 Hz) [(a) the whole cavity and external space; (b) near the opening]; (c) the omnidirected radiation pattern at the sixth acoustic-dominated mode.

show real and imaginary parts of the coefficients W_m and C_g. W_h is omitted because it is very similar to W_m.

B. Spatially averaged sound pressure

To examine the effects of structural–acoustic coupling phenomena, an uncoupled system that has rigid walls instead of flexible structures and an opening between the rigid walls is selected for the reference model. Figure 5 shows spatially averaged sound pressure squared levels inside and outside of the cavity as a function of the normalized wave number about the uncoupled and coupled system. The inside averaged pressure is averaged over the cavity. The outside averaged pressure is an averaged select region that correspond to double the cavity's width and the cavity's height. As can be seen in this figure, the frequency region can be separated into two parts in which kL_x is higher and lower than 3. In a lower frequency region, we can observe a broad peak near $kL_x \sim 0.73$ that occurs because the air mass around the opening is balanced by the cavity stiffness, and that is known by the Helmholtz mode that occurs naturally in the case of a cavity with an opening at low frequency. The sharp peaks and troughs occur near the *in vacuo* mode of the structure due to coupling and are known as structure-dominated modes which can be seen clearly compared to the uncoupled system. The peak at $kL_x \sim 0.41$ corresponds to the inside and outside of the cavity, but the peak inside the cavity at $kL_x \sim 2.64$ corresponds to the trough outside the cavity, and *vice versa*. These are the same results as the experimental output presented in Ref. 29. In a higher-frequency region, we can observe five or six peaks corresponding to the cavity modes known as acoustic-dominated modes. The modes near $kL_x \sim 3.14$ and 5 have small bandwidths compared to other modes. In acoustic-dominated modes, a small amount of pressure is formed near the opening, and a large amount of pressure is trapped inside the cavity, so the small amount of pressure is radiated. It is clear that the farfield pressure is small for these modes, as shown in the figure. Some modes have broad bandwidths and large pressure outside the cavity. This is because a large amount of pressure is efficiently radiated to the semi-infinite field through the opening. We can conclude that the position of the opening is important when a certain frequency is dominant.

C. Uncoupled system

Figures 6 visualizes pressure contour and active intensity vector of the two acoustic spaces at the fifth acoustic-dominated mode as functions of the two spatial coordinates about the uncoupled system. The pressure in the figure is normalized by square root of the mean square cavity pressure ($\sqrt{\langle (p_{\mathrm{in}})^2 \rangle}$), and the active intensity is normalized by $\langle (p_{\mathrm{in}})^2 \rangle / 2\rho c^2$. The operator $\langle \cdot \rangle$ indicates a spatial average over the cavity. Some of the energy is trapped in the cavity

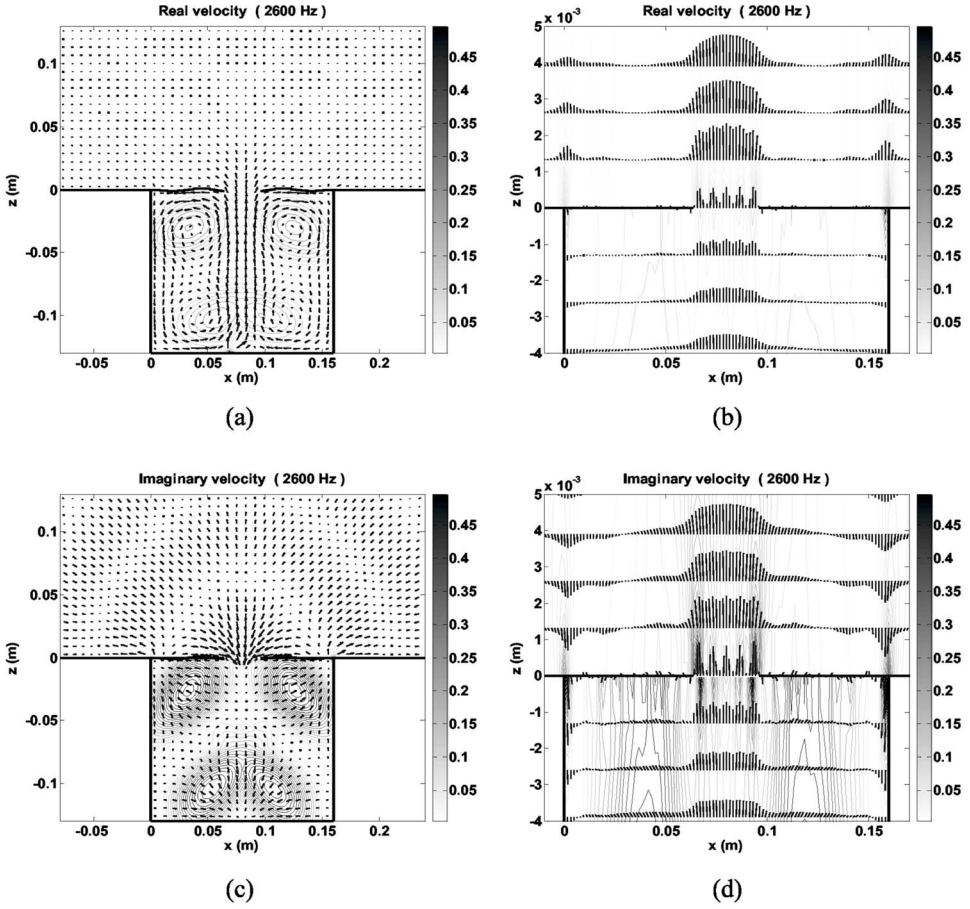

FIG. 13. The velocity distribution of two acoustic spaces at the sixth acoustic-dominated mode (2600 Hz) about the coupled system. (a) The real part of the whole cavity and external space; (b) the real part near the opening; (c) the imaginary part of the whole cavity and external space; (d) the imaginary part near the opening.

and the other is emitted through the opening, as shown in Fig. 6(a). Figure 6(b) is a detailed view of the pressure contour and active intensity near the opening [Compare x and z scaled to Fig. 6(a)]. This figure shows the variation of the active intensity distribution near the opening. The active intensity is zero at the cutting edge, and the distribution on the opening can be observed. We also examine the velocity field, as shown in Figs. 7(a) and 7(b) (real part) and 7(c) and 7(d) (imaginary part). The contour is real and imaginary velocity square normalized by the maximum velocity in the cavity. The imaginary part of the velocity shows interesting results, Figs. 7(c) and 7(d), which shows standing wave characteristics in the cavity and singular-like features near and outside the cutting edge, as was pointed out by Bouwkamp[37] and was shown by Williams.[38] So we can conclude that the modal expansion method is a suitable solution method to analyze the system with a cutting edge.

D. Steered, focused, and omnidirected radiation pattern

Figure 8(a) visualizes the plate's displacement, pressure contour, and active intensity vector of the two acoustic spaces at the third acoustic-dominated mode as functions of the two spatial coordinates. Internal energy is emitted through the opening as well as the plate, and the energy flow is developed in an oblique direction. The detailed view of Fig. 8(a) near the opening is shown in Fig. 8(b). The distribution of the active intensity near the opening is very complicated, but its shape is simple as far as the opening. Figure 8(c) gives an example of a possibility of a steered radiation pattern due to a structural–acoustic interaction. The null occurs 30° from the center axis, and the main axis occurs on the right axis. The side lobe level is about 6 dB, meaning that the noise generated from the cavity can be oriented to a specific direction using the structural–acoustic interaction for the purpose of noise control. Figure 9 shows the velocity distribution of two acoustic spaces at the third acoustic-dominated mode (1710 Hz) about the coupled system. (a) The real part of whole cavity and external space; (b) the real part near the opening; (c) the imaginary part of the whole cavity and external space; (d) the imaginary part near the opening. The velocity at the cutting edge is almost zero, but it has singular-like features near the cutting edge, as shown in Fig. 9(d).

Figure 10 shows the possibility of a focused beam. As can be seen in this figure, the energy flow is formed like a column or focused in accordance with the center axis. This type of focused beam is very useful in designing an efficient radiator using a structural–acoustic interaction. The hydrodynamic short-circuiting phenomena can be easily observed in

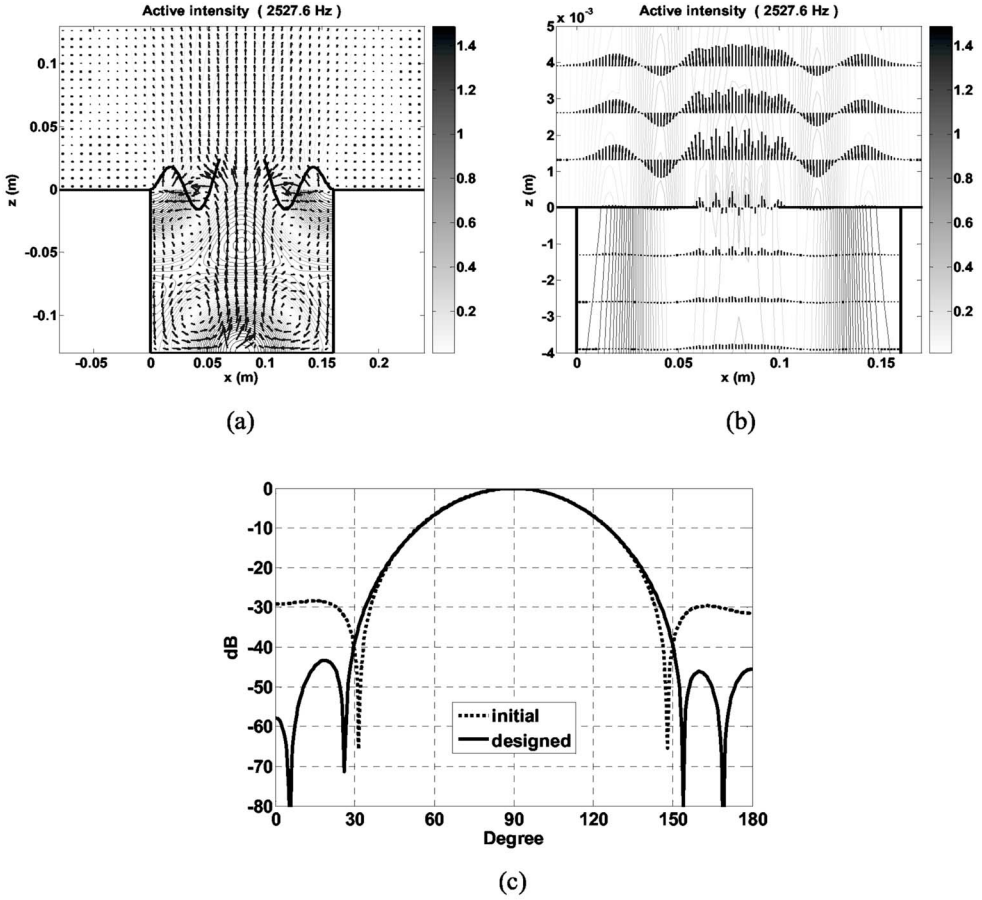

FIG. 14. The pressure and active intensity of two acoustic spaces [(a) the whole cavity and external space; (b) near the opening]; (c) radiation pattern of the designed system.

this figure. Figure 10(b) is a detailed distribution of the active intensity of Fig. 10(a) near the opening. The largest active intensity occurs at the cutting edge because the fluid rushes from one side of the edge to the other to fill in the vacuum created by the edge motion. Figure 10(c) shows the beam pattern; the 3 dB beam width is about 40°, the side lobe level is −27 dB, and the main energy is focused on the main axis. Figure 11 shows the velocity distribution of two acoustic spaces at the fifth acoustic-dominated mode (2530 Hz) about the coupled system. The velocity at the cutting edge is maximum value and it has singular-like features near the cutting edge, as shown in Fig. 11(d), as shown by Williams.[38]

Figure 12 shows the possibility of an omnidirected beam. As can be seen in this figure, the energy flow is formed like a monopole source. This type of omnidirected beam is useful in designing an omnidirectional source at high frequency using structural–acoustic coupling. Figure 13 shows the velocity distribution of two acoustic spaces at the sixth acoustic-dominated mode (2600 Hz) about the coupled system. The velocity at the cutting edge is nearly zero, but it has singular-like features near the cutting edge, as shown in Fig. 13(d).

E. Radiator design example

Radiation pattern in a semi-infinite space has a nonlinear relation to the geometry of the walls and excitation frequency. In this paper, we aim to maximize the radiation power ($P_{\max}$) and minimize the side lobe level (SLL) simultaneously, and subject to the direction of the main axis ($\theta_{\max}$). The mathematical formulation of this aim is

$$\text{minimize } F(\mathbf{x}) = W_1 \times \text{SLL} - W_2 \times |P_{\max}|^2, \text{subject to } \theta_1 \leqslant \theta_{\max} \leqslant \theta_2, \tag{20}$$

where θ_1 and θ_2 are the lower and upper limits of the main axis, respectively. W_1 and W_2 are a weighting of the each objective. The design variables are the plate's thickness, the normalized plate's length, and the excitation frequency. The initial values of the optimal problem are the same values using in Sec. III D. The initial and designed variables are

$$\{x\}^T = (\text{normalized plate's length, plate's thickness, excitation frequency}),$$

$$\{x\}^T_{\text{initial}} = (0.68 \text{ mm}, 0.4, 2530 \text{ Hz}), \quad \{x\}^T_{\text{designed}} = [0.695 \text{ mm}, 0.4045, 2527.6 \text{ Hz}]. \tag{21}$$

Figure 14 shows the designed field distribution and beam pattern. The maximum power increases 1.73 times and the sidelobe level decreased 15 dB in comparison to the initial value. This figure shows that the radiator with high radiation

power and low sidelobe level can be designed using the structural–acoustic interaction.

IV. CONCLUSIONS

The study has examined the possibility of designing radiator directivity using structural–acoustic interaction by predicting the pressure distribution and radiation pattern of a structural–acoustic coupling system and the behavior of the general coupling mechanism has been explained. We have used the finite space and semi-infinite space separated by two flexible structures and one opening. The structure represents a "volume interaction" element, and the opening represents "pressure interaction." An approximated solution that predicts energy distribution and energy flow in the two spaces separated by the structures and an opening has been developed, and its computational examples are presented. The energy distribution (pressure) and energy flow (active intensity) of the two spaces have been visualized to describe the coupling system's behavior. Three typical radiation patterns (steered, focused, and omnidirected) have been presented. The steered beam can be applied for noise control, and the focused beam can be used for designing an efficient radiator or directivity pattern. The design example that is a focused radiator with high radiating power and low sidelobe level has been presented by using the optimal design algorithm.

ACKNOWLEDGMENTS

This study was partly supported by the NRL (National Research Laboratory) project of KISTEP (Korea Institute Of Science and Technology Evaluation and Planning), and the BK21(Brain Korea 21) project initiated by the Ministry of Education and Human Resources Development of Korea. The authors wishes to thank Dr. E. G. Williams for valuable comments.

[1]P. M. Morse, "Transmission of sound through a circular membrane in a plane wall," J. Acoust. Soc. Am. **40**, 354–366 (1966).
[2]V. Mason, "On the coupling of a membrane with an incident sound wave," J. Sound Vib., **4**, 9–17 (1966).
[3]P. M. Morse and K. U. Ingard, *Theoretical Acoustics* (McGraw-Hill, New York, 1968), pp. 679–688.
[4]E. H. Dowell, G. F. Gorman, and D. A. Smith, "Acoustoelasticity: General theory, acoustic natural modes and forced response to sinusoidal excitation, including comparisons with experiment," J. Sound Vib. **52**, 519–542 (1977).
[5]M. C. Junger, "Approaches to acoustic fluid-elastic structure interactions," J. Acoust. Soc. Am. **82**, 1115–1121 (1987).
[6]M. C. Junger and D. Feit, *Sound, Structures, and Their Interaction* (The MIT Press, Cambridge, MA, 1986).
[7]G. Maidanik, "Response of ribbed panels to reverberant acoustic fields," J. Acoust. Soc. Am. **34**, 809–826 (1962).
[8]E. H. Dowell and H. M. Voss, "The effect of a cavity on panel vibration," AIAA J. **1**, 476–477 (1963).
[9]A. J. Pretlove, "Free vibrations of a rectangular panel backed by a closed rectangular cavity," J. Sound Vib. **2**, 197–209 (1965).
[10]A. J. Pretlove, "Forced vibrations of a rectangular panel backed by a closed rectangular cavity," J. Sound Vib. **3**, 252–261 (1966).
[11]R. W. Guy and A. J. Pretlove, "Cavity-backed panel resonance," J. Sound Vib. **27**, 128–129 (1973).
[12]R. H. Lyon, "Noise reduction of rectangular enclosures with one flexible wall," J. Acoust. Soc. Am. **33**, 1791–1797 (1963).
[13]R. W. Guy and M. C. Bhattacharya, "The transmission of sound through a cavity-backed finite plate," J. Sound Vib. **27**, 203–223 (1973).
[14]R. W. Guy, "The steady state transmission of sound at normal and oblique incidence through a thin panel backed by a thin panel backed by a rectangular room—a multi-modal analysis," Acustica **43**, 295–304 (1979).
[15]J. Pan, C. H. Hansen, and D. A. Bies, "Active control of noise transmission through a panel into a cavity: I. Analytical study," J. Acoust. Soc. Am. **87**, 2098–2108 (1990).
[16]J. Pan and C. H. Hansen, "Active control of noise transmission through a panel into a cavity: I. Analytical study," J. Acoust. Soc. Am. **90**, 1488–1492 (1991).
[17]S. M. Kim and M. J. Brennan, "Active control of harmonic sound transmission into an acoustic enclosure using both structural and acoustic actuators," J. Acoust. Soc. Am. **107**, 2523–2534 (2000).
[18]C. R. Fuller and F. J. Fahy, "Characteristics of wave propagation and energy distributions in cylindrical elastic shells filled with fluid," J. Sound Vib. **81**, 501–518 (1982).
[19]A. Craggs, "The transient response of a coupled plate-acoustic system using plate and acoustic finite elements," J. Sound Vib. **15**, 509–528 (1971).
[20]A. Craggs, "An acoustic finite element approach for studying boundary flexibility and sound transmission between irregular enclosures," J. Sound Vib. **30**, 343–357 (1973).
[21]D. J. Nefske, J. A. Wolf, JR and L. J. Howell, "Structural-acoustic finite element analysis of the automobile passenger compartment: A review of current practice," J. Sound Vib. **80**, 247–266 (1982).
[22]P. W. Smith, Jr., "Response and radiation of structural modes excited by sound," J. Acoust. Soc. Am. **34**, 640–647 (1962).
[23]D. Feit and Y. N. Liu, "The nearfield response of a line-driven fluid-loaded plate," J. Acoust. Soc. Am. **78**, 763–766 (1985).
[24]S. H. Ko, "Modal contributions of a finite plate to power spectra," J. Acoust. Soc. Am. **87**, 1948–1954 (1990).
[25]J. Pan and D. D. Bies, "The effect of fluid-structural coupling on sound waves in an enclosure-theoretical part," J. Acoust. Soc. Am. **87**, 691–707 (1990).
[26]J. Pan, S. J. Elliott, and K.-H. Back, "Analysis of low frequency acoustic response in a damped rectangular enclosure," J. Sound Vib. **223**, 543–566 (1999).
[27]J. Pan and D. D. Bies, "The effect of fluid-structural coupling on acoustical decays in a reverberation room in the high-frequency range," J. Acoust. Soc. Am. **87**, 718–727 (1990).
[28]K. S. Sum and J. Pan, "An analytical model for bandlimited response of acoustic-structural coupled systems. I. Direct sound field excitation," J. Acoust. Soc. Am. **103**, 911–923 (1999).
[29]S.-M. Kim and Y.-H. Kim, "Structural-acoustic coupling in a partially opened plate-cavity system: Experimental observation by using nearfield acoustic holography," J. Acoust. Soc. Am. **109**, 65–74 (2001).
[30]S.-M. Kim and Y.-H. Kim, "Solution of coupled acoustic problems: A partially opened cavity coupled with a membrane and a semi-infinite exterior field," J. Sound Vib. **254**, 231–244 (2002).
[31]T. D. Rossing, *The Science of Sound* (Addison-Wesley, New York, 1989), pp. 187–213.
[32]I. M. Firth, "Physics of the guitar at the Helmholtz and first top-plate resonances," J. Acoust. Soc. Am. **61**, 588–593 (1977).
[33]O. Christensen and B. B. Vistisen, "Simple model for low-frequency guitar function," J. Acoust. Soc. Am. **68**, 758–766 (1980).
[34]E. A. G. Shaw, "Cavity resonance in the violin: Network representation and the effect of damped and undamped rib holes," J. Acoust. Soc. Am. **87**, 398–410 (1990).
[35]M. J. Eljabarrieta, A. Ezcurra, and C. Santamaria, "Coupled modes of the resonance box of the guitar," J. Acoust. Soc. Am. **111**, 2283–2292 (2002).
[36]G. Bissinger, "Modal analysis of a violin octet," J. Acoust. Soc. Am. **113**, 2105–2113 (2003).
[37]C. J. Bouwkamp, "A note on singularities occurring at sharp edges in electromagnetic diffraction theory," Physica **12**, 467–474 (1946).
[38]E. G. Williams, "Numerical evaluation of the radiation from unbaffled, finite plates using the FFT," J. Acoust. Soc. Am. **74**, 343–347 (1983).

Acoustic radiation impedance and directional response of rectangular pistons on elliptic cylinders

Jeffrey E. Boisvert
NAVSEA Newport, Newport, Rhode Island 02841-5047

A. L. Van Buren
Middletown, Rhode Island 02842

(Received 24 November 2004; revised 29 March 2005; accepted 13 April 2005)

The self- and mutual radiation impedances and the farfield directional response of rectangular pistons conformal to a rigid elliptic cylindrical baffle are formulated. The pistons are assumed to vibrate with uniform normal velocity and the solution for the acoustic pressure is expressed in terms of a modal series representation in Mathieu functions. The Mathieu functions are obtained using computer programs that have been recently developed to provide accurate values of the functions at high frequencies. Results for the normalized self- and mutual radiation resistance and reactance and the directional response of acoustic radiation are presented over a wide frequency range for different piston sizes and elliptic cylinder cross section shapes. [DOI: 10.1121/1.1925927]

PACS number(s): 43.20.Rz, 43.30.Jx, 43.38.Hz [SFW] Pages: 104–112

I. INTRODUCTION

The acoustic radiation impedance and directional response of sources on baffles has been considered in the literature for various geometries, including planes, spheres, cylinders, and prolate spheroids.[1–9] In this paper we address sources on elliptic cylindrical baffles. Cylindrical structures with an elliptic cross section are commonplace with examples given by aircraft fuselages, marine vehicles, acoustic transducers, and mufflers. An important consideration is in the design of transducers and arrays on such structures. However, published results appear to be limited to scattering and radiation from full elliptic cylinders. The authors have found no references pertaining to acoustic radiation impedance and directivity patterns of sources on an elliptic cylindrical baffle. In the present work we consider first the general case of the acoustic pressure and radiation impedance of sources on a rigid elliptic cylindrical baffle. The special case of the self- and mutual acoustic radiation impedance of rectangular pistons conformal to a rigid elliptic cylindrical baffle is then formulated. An expression for the farfield directional response is derived from the general expression for the acoustic pressure. Finally, numerical results for the radiation impedance and directional response of rectangular pistons on elliptic cylinders are presented for several elliptic cross section shapes, including the limiting case of the circular cylinder.

II. MATHEMATICAL FORMULATION

The elliptic cylindrical coordinate system (u,ϑ,z) is related to Cartesian coordinates by

$$x=\frac{d}{2}\cosh u\cos\vartheta,$$

$$y=\frac{d}{2}\sinh u\sin\vartheta,$$

$$z=z, \tag{1}$$

where d is the interfocal distance of the elliptic cross section, and the ranges of variables are

$$0\leqslant u<\infty,$$

$$0\leqslant\vartheta\leqslant 2\pi, \tag{2}$$

$$-\infty\leqslant z\leqslant\infty.$$

In place of u, it is convenient to define the radial coordinate (or so-called shape parameter) ξ equal to $\cosh u$, giving $1\leqslant\xi\leqslant\infty$. The coordinate system (ξ,ϑ,z) is illustrated in Fig. 1. The surface of constant ξ is a right cylinder oriented along the z axis with an elliptic cross section defined by a major axis ξd and a minor axis $(\xi^2-1)^{1/2}d$. Varying the value of the cross section shape parameter ξ produces a wide range of shapes for the elliptic cylinder ranging from a strip ($\xi=1$) of width d, to a circular cylinder ($\xi\to\infty$).

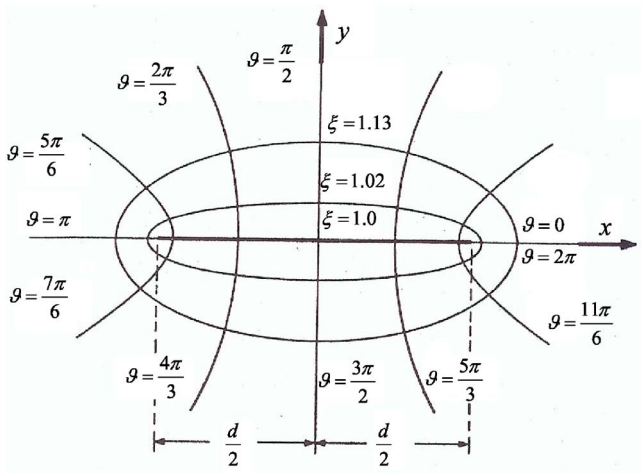

FIG. 1. Elliptic cylindrical coordinate system.

Consider a conformal region S_i that is assumed to vibrate with normal velocity ν_i on an otherwise rigid elliptic cylindrical baffle ($\xi=\xi_0$), immersed in an unbounded fluid of density ρ and sound speed c. Note that (script) i is employed throughout to designate a region to avoid confusion with (text) $\mathrm{i}=\sqrt{-1}$. Assuming time harmonic ($e^{\mathrm{i}\omega t}$) wave fields, the acoustic field exterior to ($\xi=\xi_0$) is governed by the Helmholtz equation

$$\nabla^2\Psi + k^2\Psi = 0, \tag{3}$$

where ∇^2 is the Laplacian in elliptic cylindrical coordinates, $k=\omega/c$, ω is the angular frequency, and $\Psi(u,\vartheta,z)$ denotes the spatial portion of the acoustic velocity potential. The solution of Eq. (3) is facilitated by the application of the Fourier integral transform,

$$\tilde{\Psi}(u,\vartheta,k_z) = \int_{-\infty}^{+\infty} \Psi(u,\vartheta,z)e^{\mathrm{i}k_z z}\,dz, \tag{4}$$

yielding

$$\frac{\partial^2\tilde{\Psi}}{\partial u^2} + \frac{\partial^2\tilde{\Psi}}{\partial\vartheta^2} + (\cosh^2 u - \cos^2\vartheta)\gamma^2\tilde{\Psi} = 0, \tag{5}$$

where $\gamma^2=(d/2)^2(k^2-k_z^2)$, and the overtilde $\sim$ denotes Fourier transform. Using the radial coordinate ξ in place of u, one can express the solution of Eq. (5) for outgoing waves in an eigenfunction expansion of Mathieu functions,

$$\tilde{\Psi}(\xi,\vartheta,k_z) = \sum_{m=0}^{\infty} [A_m Mc_m^{(4)}(\gamma,\xi)ce_m(\gamma,\vartheta) + B_m Ms_m^{(4)}(\gamma,\xi)se_m(\gamma,\vartheta)], \tag{6}$$

where

$$\begin{aligned} Mc_m^{(4)}(\gamma,\xi) &= Mc_m^{(1)}(\gamma,\xi) - \mathrm{i}Mc_m^{(2)}(\gamma,\xi), \\ Ms_m^{(4)}(\gamma,\xi) &= Ms_m^{(1)}(\gamma,\xi) - \mathrm{i}Ms_m^{(2)}(\gamma,\xi), \end{aligned} \tag{7}$$

denote, respectively, the even and odd Mathieu radial functions of the fourth kind, written in terms of the even and odd Mathieu radial functions of the first and second kinds, $ce_m(\gamma,\vartheta)$ and $se_m(\xi,\vartheta)$ denote, respectively, the even and odd Mathieu angle functions of the first kind, and $\gamma=(d/2)\times(k^2-k_z^2)^{1/2}$ for $k_z<k$ and $\gamma=-\mathrm{i}(d/2)(k_z^2-k^2)^{1/2}$ for $k<k_z$.

The boundary condition of the continuity of normal particle velocity at the elliptic cylinder–fluid interface ($\xi=\xi_0$) is given by

$$\frac{1}{h_\xi}\left(\frac{\partial\Psi}{\partial\xi}\right)_{\xi=\xi_0} = \begin{cases} \nu_i(\vartheta,z), & \text{on } S_i, \\ 0, & \text{elsewhere}, \end{cases} \tag{8}$$

where $h_\xi=(d/2)[(\xi^2-\cos^2\vartheta)^{1/2}/(\xi^2-1)^{1/2}]$ denotes the scale factor in the ξ direction. Taking the Fourier integral transform of Eq. (8) results in

$$\left(\frac{\partial\tilde{\Psi}}{\partial\xi}\right)_{\xi=\xi_0} = h_\xi\tilde{\nu}_i, \tag{9}$$

where

$$\tilde{\nu}_i = \int_z \nu_i(\vartheta,z)e^{\mathrm{i}k_z z}\,dz. \tag{10}$$

The substitution of Eqs. (6) and (10) into Eq. (9) yields

$$(d/2)\frac{(\xi_0^2-\cos^2\vartheta)^{1/2}}{(\xi_0^2-1)^{1/2}}\tilde{\nu}_i = [A_m Mc_m^{(4)\prime}(\gamma,\xi_0)ce_m(\gamma,\vartheta) + B_m Ms_m^{(4)\prime}(\gamma,\xi_0)se_m(\gamma,\vartheta)], \tag{11}$$

where the prime on each radial function denotes the first derivative with respect to ξ. The A_m coefficients are obtained by the multiplication of both sides of Eq. (11) by $ce_p(\gamma,\vartheta)$ and integrating over ϑ from 0 to 2π, yielding

$$A_m = \frac{(d/2)\iint_{S_i}\nu_i(\vartheta,z)(\xi_0^2-\cos^2\vartheta)^{1/2}ce_m(\gamma,\vartheta)e^{\mathrm{i}k_z z}\,d\vartheta\,dz}{(\xi_0^2-1)^{1/2}Mc_m^{(4)\prime}(\gamma,\xi_0)Nc_m} = \frac{(d/2)I_{cz}^{im}(\gamma,k_z)}{(\xi_0^2-1)^{1/2}Mc_m^{(4)\prime}(\gamma,\xi_0)Nc_m}, \tag{12}$$

where $I_{cm}^{im}(\gamma,k_z)$ denotes the integral over S_i in (12) and

$$Nc_m = \int_0^{2\pi}[ce_m(\gamma,\vartheta)]^2\,d\vartheta = \pi \tag{13}$$

defines the normalization of the even Mathieu angle functions. In a similar manner, utilizing the orthogonality of the odd Mathieu angle functions, the B_m coefficients are given by

$$B_m = \frac{(d/2)\iint_{S_i}\nu_i(\vartheta,z)(\xi_0^2-\cos^2\vartheta)^{1/2}se_m(\gamma,\vartheta)e^{\mathrm{i}k_z z}\,d\vartheta\,dz}{(\xi_0^2-1)^{1/2}Ms_m^{(4)\prime}(\gamma,\xi_0)Ns_m} = \frac{(d/2)I_{sz}^{im}(\gamma,k_z)}{(\xi_0^2-1)^{1/2}Ms_m^{(4)\prime}(\gamma,\xi_0)Ns_m}, \tag{14}$$

where $I_{sm}^{im}(\gamma,k_z)$ denotes the integral over S_i in (14) and

$$Ns_m = \int_0^{2\pi}[se_m(\gamma,\vartheta)]^2\,d\vartheta = \pi. \tag{15}$$

Now the solution for the spatial variation of the acoustic velocity potential is obtained by the Fourier inversion of Eq. (6) following the substitution of Eq. (12) and Eq. (14),

$$\Psi(\xi,\vartheta,z) = \frac{1}{2\pi}\int_{-\infty}^{+\infty}\tilde{\Psi}(\xi,\vartheta,k_z)e^{-\mathrm{i}k_z z}\,dk_z. \tag{16}$$

Since the acoustic pressure is related to the velocity potential by

$$p_i(\xi,\vartheta,z) = -\rho\frac{\partial\Psi}{\partial t} = -\mathrm{i}\omega\rho\Psi(\xi,\vartheta,z), \tag{17}$$

the general solution for the acoustic pressure may be written as

$$p_i(\xi,\vartheta,z) = \frac{-\mathrm{i}\omega\rho}{2\pi^2}\frac{(d/2)}{(\xi_0^2-1)^{1/2}} \times\sum_{m=0}^{\infty}\left\{\int_{-\infty}^{+\infty}\left[\frac{Mc_m^{(4)}(\gamma,\xi)ce_m(\gamma,\vartheta)I_{cz}^{im}(\gamma,k_z)}{Mc_m^{(4)\prime}(\gamma,\xi_0)} + \frac{Ms_m^{(4)}(\gamma,\xi)se_m(\gamma,\vartheta)I_{sz}^{im}(\gamma,k_z)}{Ms_m^{(4)\prime}(\gamma,\xi_0)}\right]e^{-\mathrm{i}k_z z}\,dk_z\right\}. \tag{18}$$

Equation (18) thus represents the general form of the acoustic pressure for a source of arbitrary shape and location vibrating on a rigid elliptic cylindrical baffle.

A piston is defined by the special case where the source on the baffle vibrates with uniform normal velocity, $v_i(\vartheta,z)=V_i$. Thus for a piston, Eq. (18) is expressible as

$$p_i(\xi,\vartheta,z) = \frac{-\mathrm{i}\omega\rho V_i d}{4\pi^2(\xi_0^2-1)^{1/2}} \times\sum_{m=0}^{\infty}\left[\int_{-\infty}^{+\infty}\left(\frac{Mc_m^{(4)}(\gamma,\xi)ce_m(\gamma,\vartheta)I_{cz}^{im}(\gamma,k_z)}{Mc_m^{(4)\prime}(\gamma,\xi_0)} + \frac{Ms_m^{(4)}(\gamma,\xi)se_m(\gamma,\vartheta)I_{sz}^{im}(\gamma,k_z)}{Ms_m^{(4)\prime}(\gamma,\xi_0)}\right)e^{-\mathrm{i}k_z z}\,dk_z\right], \tag{19}$$

where

$$I_{cz}^{im}(\gamma,k_z) = \iint_{S_i}(\xi_0^2-\cos^2\vartheta)^{1/2}ce_m(\gamma,\vartheta)e^{\mathrm{i}k_z z}\,d\vartheta\,dz,$$
$$I_{sz}^{im}(\gamma,k_z) = \iint_{S_i}(\xi_0^2-\cos^2\vartheta)^{1/2}se_m(\gamma,\vartheta)e^{\mathrm{i}k_z z}\,d\vartheta\,dz. \tag{20}$$

It is noted that the integrals residing in Eq. (20) define the size, shape, and location of the piston on the elliptic cylindrical baffle.

Consider a second region S_j (distinct from S_i) located on the surface of the elliptic cylinder. The acoustic force F_{ij} acting on region S_j due to the pressure originating from region S_i is given by

$$F_{ij} = \int_{S_j} p_i(\xi,\vartheta,z)\big|_{\xi=\xi_0}\,dS, \tag{21}$$

where the area element on the elliptical cylindrical surface is defined by

$$dS = (d/2)(\xi_0^2-\cos^2\vartheta)^{1/2}\,d\vartheta\,dz. \tag{22}$$

The acoustic mutual radiation impedance is defined by

$$Z_{ij} = F_{ij}/V_i, \tag{23}$$

and this quantity represents the acoustic impedance (force per unit normal velocity) acting on region S_j due to the motion of region S_i with uniform velocity. The self-radiation impedance Z_{ii} is defined by the condition when S_i and S_j are the same region, and represents the acoustic radiation force per unit normal velocity acting on region S_i due to its own uniform motion.

The normalized acoustic mutual radiation impedance z_{ij} is defined by

$$z_{ij} = \frac{Z_{ij}}{\rho cA_j} = \frac{1}{\rho cA_jV_i}\int_{S_j} p_i(\xi,\vartheta,z)\big|_{\xi=\xi_0}\,dS, \tag{24}$$

where A_j is the area given by the integration of Eq. (22) over region S_j, i.e.,

$$A_j = (d/2)\iint_{S_j}(\xi_0^2-\cos^2\vartheta)^{1/2}\,d\vartheta\,dz. \tag{25}$$

The substitution of Eq. (19) into Eq. (24) yields

$$z_{ij} = \frac{-\mathrm{i}hd}{4\pi^2(\xi_0^2-1)^{1/2}A_j} \times\sum_{m=0}^{\infty}\left[\int_{-\infty}^{+\infty}\left(\frac{Mc_m^{(4)}(\gamma,\xi_0)I_{cz}^{im}(\gamma,k_z)I_{cz}^{jm^*}(\gamma,k_z)}{Mc_m^{(4)\prime}(\gamma,\xi_0)} + \frac{Ms_m^{(4)}(\gamma,\xi_0)I_{sz}^{im}(\gamma,k_z)I_{sz}^{jm^*}(\gamma,k_z)}{Ms_m^{(4)\prime}(\gamma,\xi_0)}\right)dk_z\right], \tag{26}$$

where the I_{cz}^{jm} and I_{sz}^{jm} integrals are given by Eq. (20), with i replaced by j, $h=kd/2$, and $*$ denotes the complex conjugate. Equation (26) is the generalized expression for the mutual acoustic radiation impedance between two piston sources on a rigid elliptic cylindrical baffle. The impedance is dependent upon the size, shape, and location of each of the two pistons. It depends implicitly on their separation through the products of the integrals $I_{cz}^{im}I_{cz}^{jm^*}$ and $I_{sz}^{im}I_{sz}^{jm^*}$ appearing in Eq. (26).

III. RECTANGULAR PISTONS

A. Acoustic radiation impedance

Of special interest in this paper is the case where the pistons are rectangular in shape, and conformal to the surface of the elliptic cylinder. A piston is defined by the center-point location (ϑ_c,z_c), angular width $\Delta\vartheta_i$, and axial length Δz_i, where the piston sides are parallel to the coordinate axes, as shown in Fig. 2. Now the expression for I_{cz}^{im} in Eq. (20) becomes

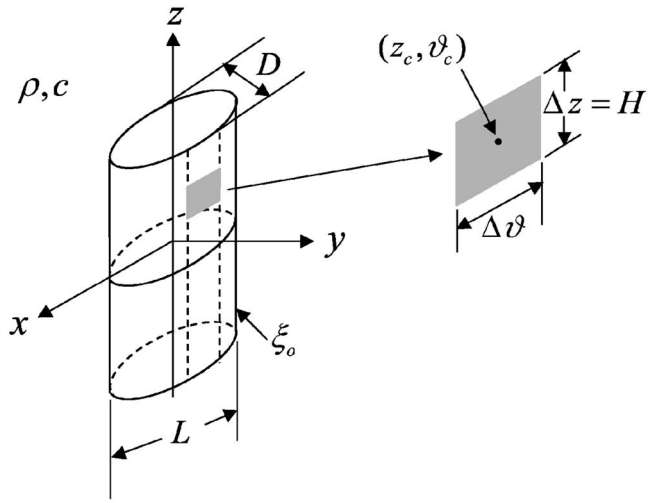

FIG. 2. Rectangular piston conformal to a rigid elliptic cylindrical baffle.

$$I_{cz}^{im}(\gamma,k_z)=\int_{z_{c_i}-(\Delta z_i/2)}^{z_{c_i}+\Delta z_i/2} e^{\mathrm{i}k_z z}\,dz\int_{\vartheta_{c_i}-(\Delta\vartheta_i/2)}^{\vartheta_{c_i}+\Delta\vartheta_i/2}(\xi_0^2-\cos^2\vartheta)^{1/2}\times ce_m(\gamma,\vartheta)\,d\vartheta$$
$$=\frac{e^{\mathrm{i}k_z(z_{c_i}+\Delta z_i/2)}-e^{\mathrm{i}k_z(z_{c_i}-\Delta z_i/2)}}{\mathrm{i}k_z}\times\int_{\vartheta_{c_i}-(\Delta\vartheta_i/2)}^{\vartheta_{c_i}+\Delta\vartheta_i/2}(\xi_0^2-\cos^2\vartheta)^{1/2}ce_m(\gamma,\vartheta)\,d\vartheta$$
$$=F_i(k_z)Ic_m^i(\gamma). \tag{27}$$

Similarly,

$$I_{sz}^{im}(\gamma,k_z)=\int_{z_{c_i}-\Delta z_i/2}^{z_{c_i}+\Delta z_i/2} e^{\mathrm{i}k_z z}\,dz\int_{\vartheta_{c_i}-\Delta\vartheta_i/2}^{\vartheta_{c_i}+\Delta\vartheta_i/2}(\xi_0^2-\cos^2\vartheta)^{1/2}\times se_m(\gamma,\vartheta)\,d\vartheta$$
$$=F_i(k_z)Is_m^i(\gamma), \tag{28}$$

and the $I_{cz}^{im^*}$ and the $I_{sz}^{im^*}$ integrals are given by

$$I_{cz}^{im^*}(\gamma,k_z)=\int_{z_{c_j}-\Delta z_j/2}^{z_{c_j}+\Delta z_j/2} e^{-\mathrm{i}k_z z}\,dz\int_{\vartheta_{c_j}-\Delta\vartheta_j/2}^{\vartheta_{c_j}+\Delta\vartheta_j/2}(\xi_0^2-\cos^2\vartheta)^{1/2}\times ce_m(\gamma,\vartheta)\,d\vartheta$$
$$=F_j^*(k_z)Ic_m^j(\gamma), \tag{29}$$

and

$$I_{sz}^{im^*}(\gamma,k_z)=\int_{z_{c_j}-\Delta z_j/2}^{z_{c_j}+\Delta z_j/2} e^{-\mathrm{i}k_z z}\,dz\int_{\vartheta_{c_j}-\Delta\vartheta_j/2}^{\vartheta_{c_j}+\Delta\vartheta_j/2}(\xi_0^2-\cos^2\vartheta)^{1/2}\times se_m(\gamma,\vartheta)\,d\vartheta$$
$$=F_j^*(k_z)Is_m^j(\gamma), \tag{30}$$

where $*$ denotes the complex conjugate.

Upon the substitution of Eq. (27), Eq. (28), Eq. (29), and Eq. (30) into Eq. (26), followed by algebraic manipulation, the expression for the mutual radiation impedance can be written as

$$z_{ij}=\frac{-\mathrm{i}hd}{2\pi^2(\xi_0^2-1)^{1/2}A_j}\times\sum_{m=0}^{\infty}\left[\int_0^{\infty}\left(\frac{Mc_m^{(4)}(\gamma,\xi_0)Ic_m^i(\gamma)Ic_m^j(\gamma)}{Mc_m^{(4)'}(\gamma,\xi_0)}+\frac{Ms_m^{(4)}(\gamma,\xi_0)Is_m^i(\gamma)Is_m^j(\gamma,k_z)}{Ms_m^{(4)'}(\gamma,\xi_0)}\right)\Omega_{ij}\,dk_z\right], \tag{31}$$

where

$$\Omega_{ij}=\frac{4\sin(k_z\Delta z_i/2)\sin(k_z\Delta z_j/2)\cos k_z(z_{c_i}-z_{c_j})}{k_z^2}. \tag{32}$$

Now at the transition point $k_z=k$, with the transformation $\alpha=k_z d/2$, Eq. (32) becomes

$$z_{ij}=\frac{-\mathrm{i}hd^2}{\pi^2(\xi_0^2-1)^{1/2}A_j}\sum_{m=0}^{\infty}\left[\int_0^{h}\left(\frac{Mc_m^{(4)}(\kappa,\xi_0)Ic_m^i(\kappa)Ic_m^j(\kappa)}{Mc_m^{(4)'}(\kappa,\xi_0)}+\frac{Ms_m^{(4)}(\kappa,\xi_0)Is_m^i(\kappa)Is_m^j(\kappa)}{Ms_m^{(4)'}(\kappa,\xi_0)}\right)\Omega_{ij}(\alpha)\,d\alpha+\int_h^{\infty}\left(\frac{Mc_m^{(4)}(-\mathrm{i}\kappa^-,\xi_0)Ic_m^i(-\mathrm{i}\kappa^-)Ic_m^j(-\mathrm{i}\kappa^-)}{Mc_m^{(4)'}(-\mathrm{i}\kappa^-,\xi_0)}+\frac{Ms_m^{(4)}(-\mathrm{i}\kappa^-,\xi_0)Is_m^i(-\mathrm{i}\kappa^-)Is_m^j(-\mathrm{i}\kappa^-)}{Ms_m^{(4)'}(-\mathrm{i}\kappa^-,\xi_0)}\right)\Omega_{ij}(\alpha)\,d\alpha\right] \tag{33}$$

where $\kappa=(d/2)(k^2-k_z^2)^{1/2}$, $\kappa^-=(d/2)(k_z^2-k^2)^{1/2}$, and

$$\Omega_{ij}(\alpha)=\begin{cases}\dfrac{\sin(\alpha\,\Delta z_i/d)\sin(\alpha\,\Delta z_j/d)\cos[2\alpha(z_{c_i}-z_{c_j})/d]}{\alpha^2}, & \alpha\neq 0,\\ \dfrac{\Delta z_i\,\Delta z_j}{d^2}, & \alpha=0.\end{cases} \tag{34}$$

Equation (33) is the general expression for the normalized mutual acoustic radiation impedance between two rectangular pistons located on a rigid elliptic cylindrical baffle. It is noted that the first integral corresponds to the resistive portion of the impedance and the second integral corresponds to the reactive portion of the impedance. The normalized acoustic self-radiation impedance is directly obtained from Eq. (33) with the substitution $j=i$.

B. Acoustic directional response

With regard to the directional response of acoustic radiation from a rectangular piston conformal to a rigid elliptic cylindrical baffle, the general expression for the acoustic pressure, Eq. (19), becomes

$$p(\xi,\vartheta,z)=\frac{-\mathrm{i}\omega\rho Vd}{4\pi^2(\xi_0^2-1)^{1/2}}\times\sum_{m=0}^{\infty}\left[\int_{-\infty}^{+\infty}\left(\frac{Mc_m^{(4)}(\gamma,\xi)ce_m(\gamma,\vartheta)Ic_m(\gamma)}{Mc_m^{(4)\prime}(\gamma,\xi_0)}+\frac{Ms_m^{(4)}(\gamma,\xi)se_m(\gamma,\vartheta)Is_m(\gamma)}{Ms_m^{(4)\prime}(\gamma,\xi_0)}\right)F(k_z)e^{-\mathrm{i}k_z z}\,dk_z\right], \tag{35}$$

where the subscript i has been dropped. Now as $\xi\to\infty$, employing the asymptotic form of the Mathieu radial function of the fourth kind,

$$Mc_m^{(4)}(\gamma,\xi)=Ms_m^{(4)}(\gamma,\xi)\to(\gamma\xi)^{-1/2}e^{-\mathrm{i}(\gamma\xi-(2m+1)\pi/4)}, \tag{36}$$

and the relationships $\vartheta=\cos\phi$ and $\xi d/2\to R\sin\theta$, the farfield acoustic pressure is given by

$$p^{\mathrm{far}}(R,\theta,\phi)=\frac{-\mathrm{i}\omega\rho Vd}{4\pi^2}\frac{e^{\mathrm{i}(2m+1)\pi/4}}{(R\sin\theta)^{1/2}}\times\sum_{m=0}^{\infty}\left(\int_{-\infty}^{+\infty}G(k_z)e^{-\mathrm{i}R[(k^2-k_z^2)\sin\theta+k_z\cos\theta]}dk_z\right), \tag{37}$$

where

$$G(k_z)=\left(\frac{ce_m(\gamma,\cos\phi)Ic_m(\gamma)}{Mc_m^{(4)\prime}(\gamma,\xi_0)}+\frac{se_m(\gamma,\cos\phi)Is_m(\gamma)}{Ms_m^{(4)\prime}(\gamma,\xi_0)}\right)\times\frac{F(k_z)}{(\xi_0^2-1)^{1/2}(k^2-k_z^2)^{1/4}}, \tag{38}$$

and (R,θ,ϕ) are the spherical coordinates. Upon the evaluation of the integral in Eq. (37) by the method of stationary phase, the farfield acoustic pressure is written as

$$p^{\mathrm{far}}(R,\theta,\phi)=-\frac{h}{\sqrt{2\pi}}\rho cV\frac{e^{-\mathrm{i}kR}}{kR}f(\theta,\phi). \tag{39}$$

The directional response function in Eq. (39) is defined by

$$f(\theta,\phi)=\frac{e^{\mathrm{i}k\cos\theta(z_c+\Delta z/2)}-e^{\mathrm{i}k_z(z_c-\Delta z/2)}}{(\xi_0^2-1)^{1/2}\cos\theta}\times\sum_{m=0}^{\infty}\mathrm{i}^{m+1}\left(\frac{ce_m(h\sin\theta,\cos\phi)Ic_m(h\sin\theta)}{Mc_m^{(4)\prime}(h\sin\theta,\xi_0)}+\frac{se_m(h\sin\theta,\cos\phi)Is_m(h\sin\theta)}{Ms_m^{(4)\prime}(h\sin\theta,\xi_0)}\right). \tag{40}$$

Using Eq. (40), the farfield directional response of a rectangular piston on an elliptic cylindrical baffle is given by

$$F(\theta,\phi)=f(\theta,\phi)/f(\theta_0,\phi_0), \tag{41}$$

where θ_0,ϕ_0 specify the direction of maximum response. Finally, the amplitude of the directional response may be expressed in decibels by

$$20\log|F(\theta,\phi)|\ \mathrm{dB}. \tag{42}$$

IV. RESULTS AND DISCUSSION

The equations above have been used to calculate the normalized self- and mutual radiation resistance and reactance of rectangular pistons and their directivity patterns as a function of the frequency and piston location for various sized pistons and elliptic cylindrical baffle cross section shapes. The calculation of the (normalized) self- and mutual radiation impedance for rectangular pistons by the use of Eq. (33) requires values of the radial Mathieu functions $Mc_m^{(4)}$, $Ms_m^{(4)}$ their first derivatives, and values of the angular Mathieu functions ce_m and se_m. Since an objective of the present effort is to obtain results at high frequencies (large acoustic size), a parallel effort to develop algorithms to calculate Mathieu functions over a wider range of parameters than previously available has been undertaken, with the results of that study to be reported in the future.[10] The newly developed algorithms were employed in the present study.

The elliptic cylindrical baffle cross section is defined by major axis L, and minor axis D; see Fig. 2. The effect of cross-section eccentricity on the radiation impedance and directional response will be considered by keeping L fixed and varying D. Four cross section shapes are chosen: $L/D=1.000\,05$, 2, 4, and 10, as shown in Fig. 3. Since an elliptic cylinder approaches a circular cylinder as $L/D\to1$, it is noted that the results for $L/D=1.000\,05$ may be regarded as equivalent to those for a circular cylinder. In all cases that follow, the piston is square with a height $H=\Delta z$ that is equal to the arclength of the subtended angle $\Delta\vartheta$. Unless noted otherwise, the piston has a relative size given by $H/L=0.1$; that is, the piston height (and width) is equal to one-tenth of the baffle cross-section major axis.

Figures 4 and 5 give examples for the normalized self-radiation resistance r_{ii} [the real part of Eq. (33) evaluated with $j=i$] and reactance x_{ii} [the imaginary part of Eq. (33) evaluated with $j=i$] for a square piston with relative size $(H/L=0.1)$ located on the elliptic cylinder at $(\vartheta_c=0°, z_c=0)$, as a function of dimensionless frequency kH. Results are given for four cross-section shapes. Figure 4 shows that the resistance is small for low values of kH and increases as

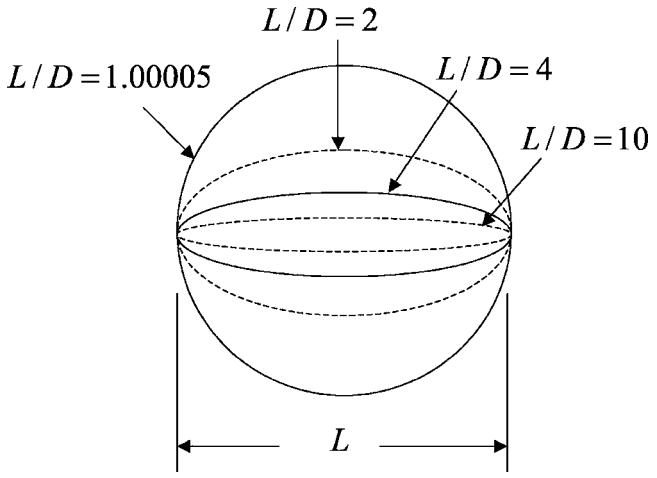

FIG. 3. Baffle cross-section aspect ratios.

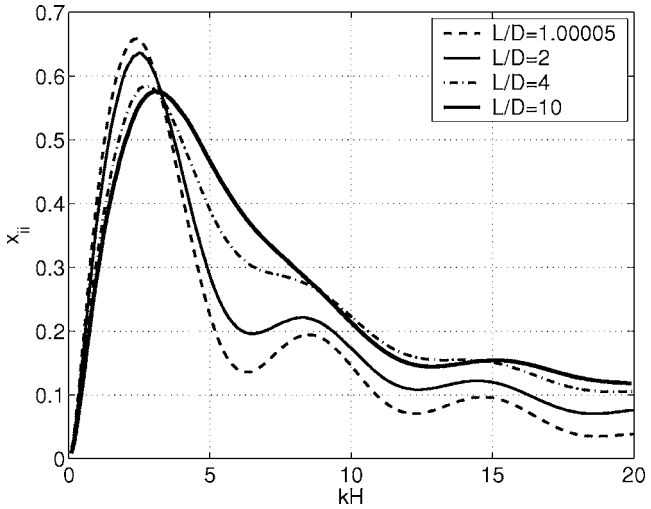

FIG. 5. Normalized self-radiation reactance versus kH of a square piston of relative size $H/L=0.1$ located at $(\vartheta_c=0°, z_c=0)$ as a function of the baffle cross-section aspect ratio.

kH increases. The rate of increase becomes larger as L/D decreases and the cross section becomes more circular. It is also seen that as the cross section becomes less circular, the first peak in the resistance and the subsequent oscillatory behavior (corresponding to constructive and destructive interference) is reduced, due to the increased curvature at the tip where the piston resides. The reactance, while larger than the resistance for small values of kH, rises to a peak value somewhat smaller than unity then decreases as kH increases. It is noted that as the baffle cross-section aspect ratio increases, the reactance above the first peak falls off more slowly (with substantial differences in the region $4 \leqslant kH \leqslant 8$), and, also, the reactance approaches zero more slowly as kH increases. In all cases, when the piston becomes acoustically large, the radiation resistance tends to unity, and the radiation reactance tends to zero, a result consistent with the radiation impedance of pistons on other baffle geometries (planar, spherical, cylindrical, etc.).

Figures 6 and 7 illustrate results for the normalized mutual radiation resistance r_{ij} and reactance x_{ij} for a pair of adjoining square pistons located at the end of the elliptic cylinder, as a function of kH. The first piston is located at the tip $(\vartheta_c=0°, z_c=0)$ of the baffle, and the second piston adjoins the first along its side in the positive ϑ direction, i.e. $(\vartheta_c>0°, z_c=0)$. It is seen that substantial interaction occurs in the region below $kH \approx 5$, and above that, the interaction decreases appreciably and approaches zero, although the reactance approaches zero more slowly when the baffle cross section is noncircular. Hence, although the pistons are adjoining, when the frequency is high enough, the fields are spatially localized. Thus, essentially no acoustic coupling occurs; the pistons "see" only their self-radiation impedance.

Results for the normalized mutual radiation resistance and reactance for square pistons as a function of separation angle ϑ on two different baffle cross sections are shown in Fig. 8, at $kH=2.41$. In all cases, the center point of the first piston is held at $(\vartheta_c=0°, z_c=0)$, and the second piston initially adjoins the first piston, then traverses along the direction of increasing ϑ (at $z_c=0$) around the baffle cross section. The abscissa denotes the absolute separation between the pis-

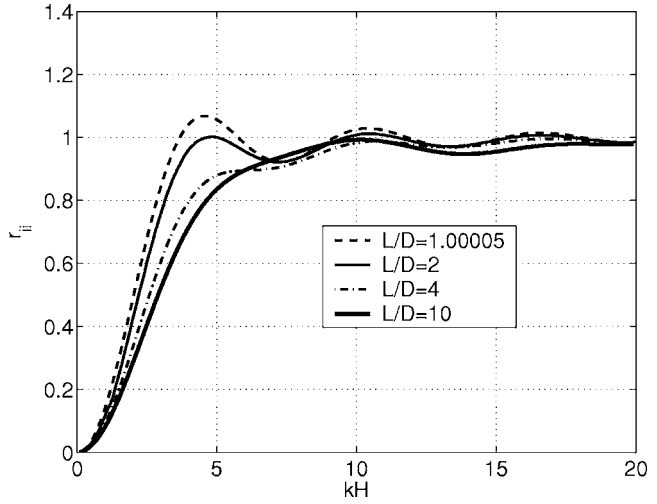

FIG. 4. Normalized self-radiation resistance versus kH of a square piston of relative size $H/L=0.1$ located at $(\vartheta_c=0°, z_c=0)$ as a function of the baffle cross-section aspect ratio.

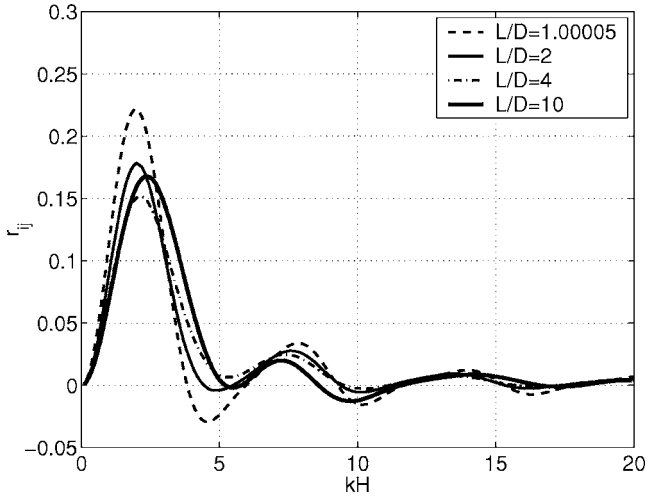

FIG. 6. Normalized mutual radiation resistance versus kH of adjoining square pistons of relative size $H/L=0.1$ located at $(\vartheta_c=0°, z_c=0)$ and $(\vartheta_c>0°, z_c=0)$ as a function of the baffle cross-section aspect ratio.

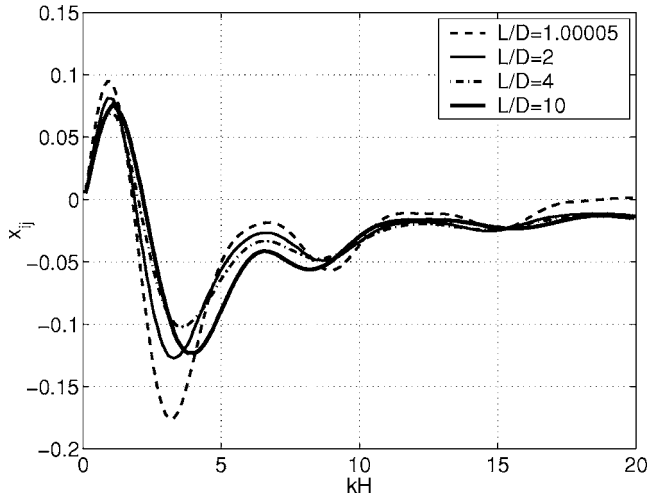

FIG. 7. Normalized mutual radiation reactance versus kH of adjoining square pistons of relative size $H/L=0.1$ located at $(\vartheta_c=0°, z_c=0)$ and $(\vartheta_c>0°, z_c=0)$ as a function of the baffle cross-section aspect ratio.

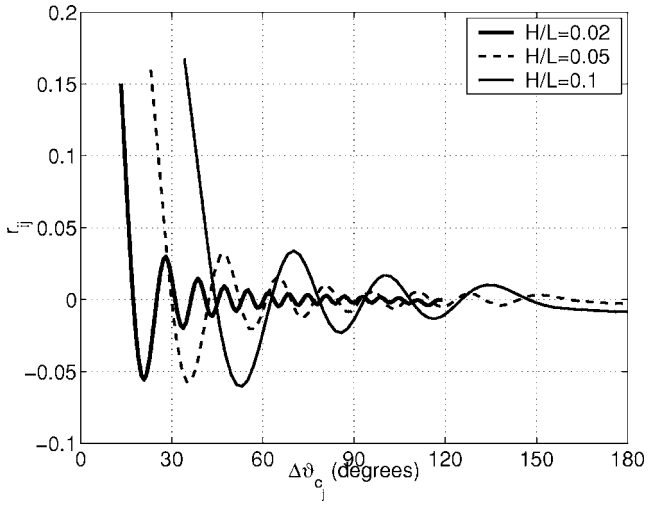

FIG. 9. Normalized mutual radiation resistance versus separation angle ϑ_{c_j} for square pistons on an $L/D=10$ elliptic cylindrical baffle as a function of piston sizes $H/L=0.02$, 0.05, 0.1, at $kH=2.4$.

ton center points in degrees, which in this case is equal to ϑ_{c_j}. It is seen that the interaction decreases more rapidly for the case of the pistons on the circular cross section. Figures 9 and 10 illustrate, respectively, the normalized mutual resistance and reactance versus the separation angle for pistons of various sizes ($H/L=0.02$, 0.05, 0.1) on an elliptic cylindrical baffle defined by $L/D=10$. As before, the center point of the first piston is at $(\vartheta_c=0°, z_c=0)$, and $kH=2.41$ for each piston. It is seen that as the piston gets smaller, a more rapid decrease in the interaction occurs as a function of the separation angle.

To examine the effect of the baffle cross-section aspect ratio upon the amplitude of farfield radiation from (square) pistons, Fig. 11 illustrates the horizontal directional response ($x-y$ plane) as a function of L/D for the piston located at the tip $(\vartheta_c=0°, z_c=0)$ of the baffle, at $kH=2\pi$. It is seen that the piston on the circular cylinder is the most directional, and as L/D increases, the baffle curvature likewise increases, thus the projected area of the piston is reduced and the patterns become less directional. Figure 12 shows results for the same piston located at the midpoint $(\vartheta_c=90°, z_c=0)$ of the baffle cross section at the same frequency. Here the main lobe response is relatively independent of the cross-section aspect ratio, however, the pressure in the back plane is seen to exhibit a decreased baffling effect as the cross section approaches that of a circular cylinder. Conversely, as the cross-section aspect ratio increases, the local curvature at the midpoint of the cross section decreases and becomes more planar, indeed Fig. 13 shows that the $L/D=10$ directivity pattern for the piston (centered at $\vartheta_c=90°, z_c=0$) is very similar to the directivity pattern of the same piston mounted on an infinite planar baffle. Finally to illustrate the effect of piston size relative to a given baffle, Fig. 14 shows the horizontal directional response for various piston sizes all located at the tip $(\vartheta_c=0°, z_c=0)$ of an elliptic cylindrical baffle defined by $L/D=4$, with the acoustic size fixed at $kH=2\pi$ in all cases. These results show that for a given acoustic size, as

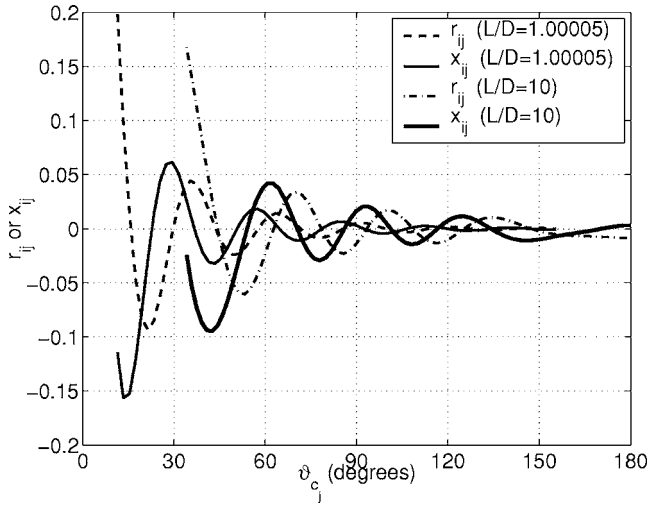

FIG. 8. Normalized mutual radiation impedance versus separation angle ϑ_{c_j} for square pistons with size parameter $H/L=0.1$ as a function of baffle cross-section aspect ratios $L/D=1.000\,05$, 10, at $kH=2.4$.

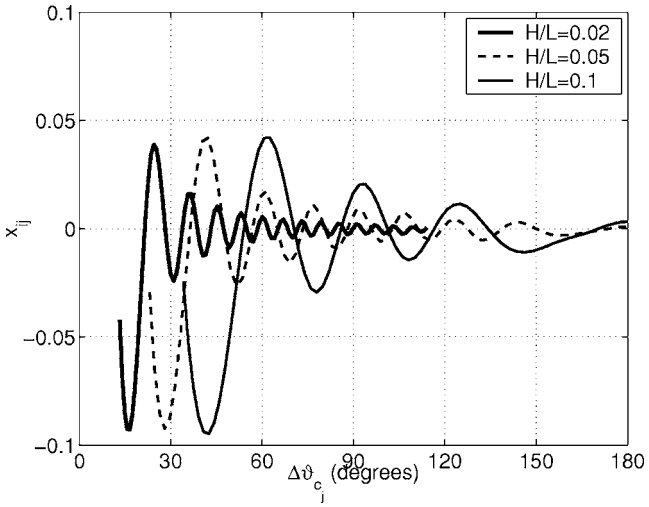

FIG. 10. Normalized mutual radiation reactance versus separation angle ϑ_{c_j} for square pistons on an $L/D=10$ elliptic cylindrical baffle as a function of piston sizes $H/L=0.02$, 0.05, 0.1, at $kH=2.4$.

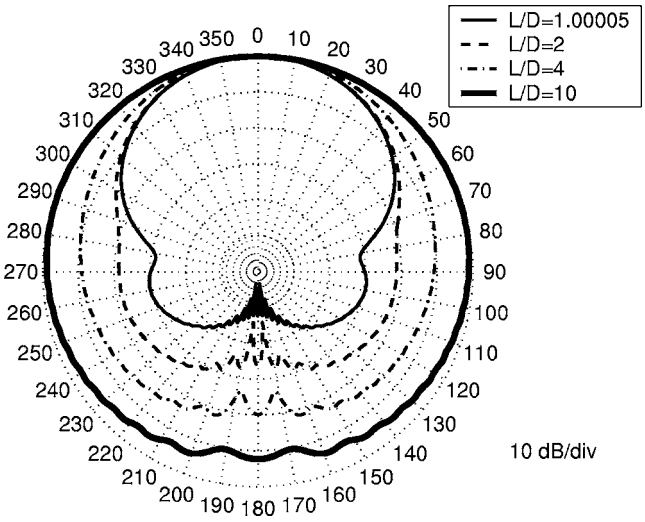

FIG. 11. Horizontal polar directivity pattern of a square piston with size parameter $H/L=0.1$ located at $(\vartheta_c=0°, z_c=0)$ as a function of baffle cross-section aspect ratio at $kH=2\pi$.

the piston extends over more of the tip of the baffle, its projected area becomes smaller, and therefore the farfield patterns become less directional.

V. SUMMARY

Expressions for the directional response and the self- and mutual radiation impedance for piston sources vibrating on a rigid elliptic cylindrical baffle have been developed. The special case of rectangular pistons was derived and is given by Eq. (33) for impedance and Eq. (40) for directional response. Sample results have been presented that illustrate the behavior of the radiation impedance and directional response (amplitude) for different pistons and baffle cross-section shapes as a function of frequency and piston location on the baffle. In addition, results were presented that show the variation of the mutual impedance between two pistons as a function of their angular separation distance. For the following, although no results were presented, it should be noted

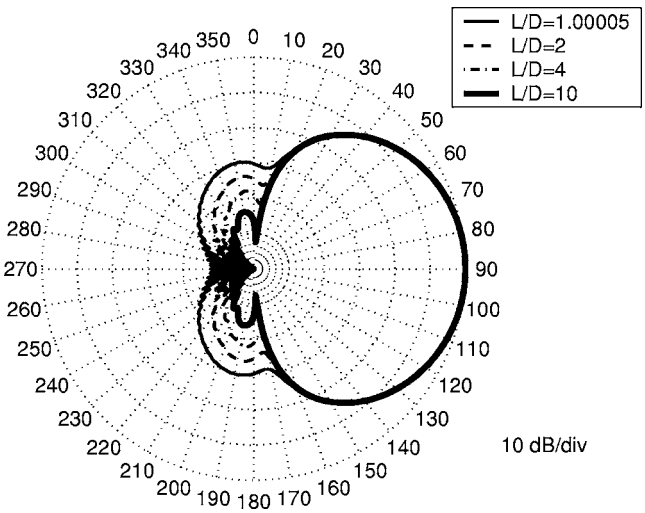

FIG. 12. Horizontal polar directivity pattern of a square piston with size parameter $H/L=0.1$ located at $(\vartheta_c=90°, z_c=0)$ as a function of baffle cross-section aspect ratio at $kH=2\pi$.

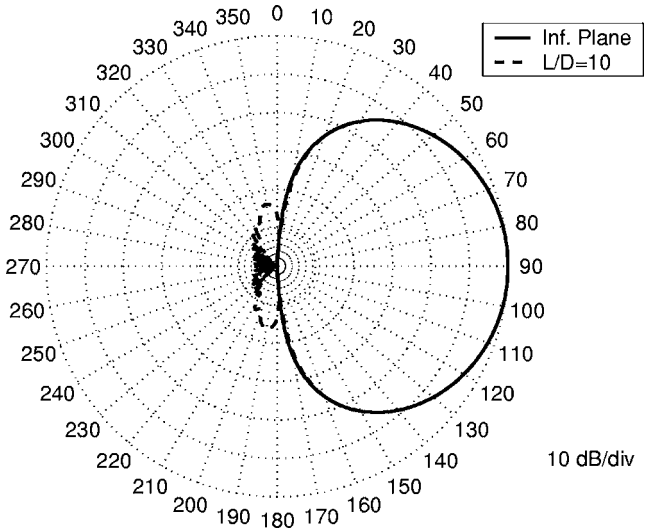

FIG. 13. Horizontal polar directivity pattern of a square piston with size parameter $H/L=0.1$ located at $(\vartheta_c=90°, z_c=0)$ on an $L/D=10$ elliptic cylindrical baffle versus the pattern of the same piston located on an infinite plane, at $kH=2\pi$.

that (a) the mutual radiation impedance between two pistons as a function of arbitrary separation distance is directly obtainable from Eq. (33), (b) the phase of the directional response is directly obtainable from Eq. (40), (c) the radiation impedance and directional response of pistons on the limiting case of the strip is directly obtainable from the equations with $\xi_0=1$, and (d) the directional response of an array of pistons conformal to an elliptic cylindrical baffle is readily obtainable by the superposition of the individual single element responses. Finally, it is noted that the radiation impedance and directional response for pistons of other shapes on elliptic cylindrical baffles is obtainable by the evaluation of Eqs. (27) and (28) with limits of integration appropriate for the piston shape of interest.

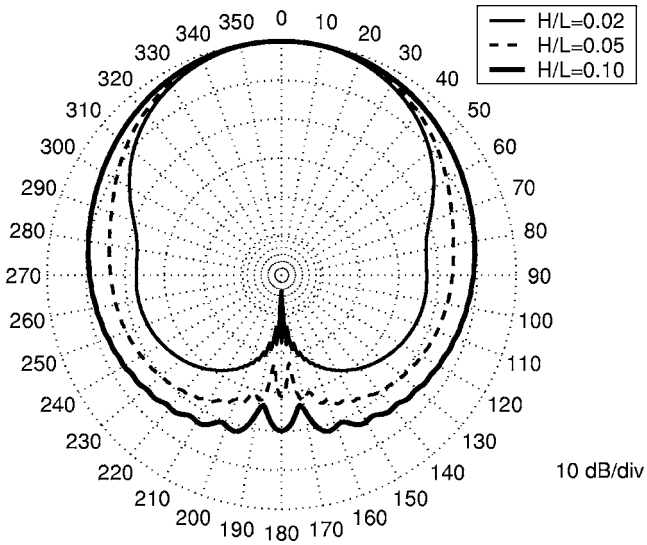

FIG. 14. Horizontal polar directivity pattern of square pistons of varying size located at $(\vartheta_c=0°, z_c=0)$ on an $L/D=4$ elliptic cylindrical baffle at $kH=2\pi$.

ACKNOWLEDGMENTS

This work was supported by the Office of Naval Research Code 321. The development of the algorithms for calculating the Mathieu functions was facilitated by their similarity to algorithms for calculating prolate spheroidal wave functions developed in a parallel effort supported by the NAVSEA Newport ILIR Program.

[1]D. H. Robey, "On the radiation impedance of an array of finite cylinders," J. Acoust. Soc. Am. **27**, 706–710 (1955).
[2]C. H. Sherman, "Mutual radiation impedance of sources on a sphere," J. Acoust. Soc. Am. **31**, 947–952 (1959).
[3]R. L. Pritchard, "Mutual acoustic impedance between radiators in an infinite rigid plane," J. Acoust. Soc. Am. **32**, 730–737 (1960).
[4]J. E. Greenspon and C. H. Sherman, "Mutual-radiation impedance and nearfield pressure for pistons on a cylinder," J. Acoust. Soc. Am. **36**, 149–153 (1964).
[5]E. M. Arase, "Mutual radiation impedance of square and rectangular pistons in an infinite baffle," J. Acoust. Soc. Am. **36**, 1521–1525 (1964).
[6]J. E. Boisvert and A. L. Van Buren, "Acoustic radiation impedance of rectangular pistons on prolate spheroids," J. Acoust. Soc. Am. **111**, 867–874 (2002).
[7]P. M. Morse, *Vibration and Sound* (McGraw-Hill, New York, 1948).
[8]D. T. Laird and H. Cohen, "Directionality patterns for acoustic radiation from a source on a rigid cylinder," J. Acoust. Soc. Am. **24**, 46–49 (1952).
[9]J. E. Boisvert and A. L. Van Buren, "Acoustic directivity of rectangular pistons on prolate spheroids," J. Acoust. Soc. Am. **116**, 1932–1937 (2004).
[10]A. L. Van Buren and J. E. Boisvert, "Improved calculation of the Mathieu radial and angle functions of integer order and their first derivatives," to be submitted to Q. Appl. Math.

Experiments of high-amplitude and shock-free oscillations of air column in a tube with array of Helmholtz resonators

M. Masuda and N. Sugimoto[a)]
Department of Mechanical Science, Graduate School of Engineering Science, University of Osaka, Toyonaka, Osaka 560-8531, Japan

(Received 23 December 2004; revised 20 April 2005; accepted 20 April 2005)

This experimental study is made to verify the weakly nonlinear theory for high-amplitude and shock-free oscillations of an air column developed in the previous paper [Sugimoto *et al.*, J. Acoust. Soc. Am., **114**, 1772–1784 (2003)]. The experiments use a new tube and resonators designed so as to not only avoid higher harmonic resonances and evanescences but also reduce the values of the coefficient of Q in the amplitude equation, and a rubber diaphragm sandwiched by circular plates to drive the air column. The steady-state pressure field in the tube and in the cavities of the resonators is measured, from which Fourier coefficients are obtained. In spite of nonlinearity, higher harmonics are suppressed significantly as designed, and the frequency response measured shows quantitatively good agreement with the one predicted up to about 170 dB (SPL). The first harmonics and the nonoscillatory component in the pressure field are well predicted, though the second harmonics show a quantitative discrepancy with the theory. In view of the good agreement of the frequency response, it is concluded that the theory is valid and useful enough to provide guidelines in designing the tube with the array of resonators. [DOI: 10.1121/1.1929237]

PACS number(s): 43.25.−x, 43.25.Cb, 43.25.Gf, 43.25.Zx [MFH] Pages: 113–123

I. INTRODUCTION

It is known that high-amplitude and shock-free oscillations of an air column are achieved in "dissonant tubes." In fact, oscillations with amplitude higher than 10% of equilibrium pressure (about 170 dB in the sound pressure level) are generated by exciting the air column resonantly.[1–4] The term "dissonant" used in contrast to "consonant" means such a tube that resonance frequencies of the air column are not ordered as integral multiples of the fundamental one.[5] At present, there are two methods available to make a tube dissonant, one being to make a cross section of the tube nonuniform axially[1,2] and the other to exploit wave dispersion.[3]

If dispersion is present, the phase velocity differs from a sound speed and depends on a frequency. Thus a tube becomes naturally dissonant. The dispersion can be introduced by connecting an array of side branches in any form along a tube. Sugimoto *et al.*[3] have made a tube with a periodic array of Helmholtz resonators (called simply resonators hereafter) to demonstrate the annihilation of shocks and the generation of high-amplitude oscillations. Later they have developed a weakly nonlinear theory to seek the pressure and flow field in the tube and the resonators to derive the amplitude equation, from which the frequency response is obtained.[6] But there is a significant discrepancy in the frequency response between the results measured and predicted. One reason for this discrepancy turns out to be that the tube and resonators do not meet the conditions required by the theory. The purpose of this paper is thus to verify the theory by using a new tube and resonators designed in light of the results of the theory.

When the array of resonators is connected to a tube of uniform cross section, there arises an infinite number of pairs of resonance frequencies. In addition, a new mode appears at a frequency just above the resonance frequency of the Helmholtz resonator in which the air column oscillates in unison without exhibiting any axial structure. Focusing on the resonance at the lowest frequency with one pressure node in the middle of tube, the theory assumes no harmonic resonances and evanescences which will occur, respectively, where frequencies of higher harmonics coincide with one of the resonance frequencies of the tube or with the resonance frequency of the Helmholtz resonator.

Although no second harmonic resonance occurs in a strict sense, a situation close to it would be plausible. Then the coefficient Q (not the quality factor) of the nonlinear term in the amplitude equation takes a large value so that the response curve is bent and the peak pressure is suppressed. This is the situation encountered in the previous experiments.[3] Even worse, the frequency of the fifth harmonics happens to coincide with the resonance frequency of the resonator. Such higher harmonic evanescences do not contribute to making the value of Q large. But when they occur, the energy of excitation would be absorbed in the resonators and the peak pressure would also be suppressed. The theory excludes these cases up to the third harmonics. But it is desirable in designing the tube with the array of resonators to avoid them up to any harmonics as much as possible.

In order to generate higher peak pressure, the jet loss of the throat of the resonator should also be reduced. This requires choice of a smaller cavity and a wider throat but has nothing to do with throat length. It turns out that the throat should be lengthened in order to reduce the values of Q as well as of D for the jet loss. The tube and the resonators used

a)Electronic mail: sugimoto@me.es.osaka-u.ac.jp

in the previous experiments are not the ones designed by taking account of the above-mentioned conditions but the existing ones for the experiments of the acoustic solitary waves.[7] In consequence, the frequency response agrees with the theory only up to the peak pressure of a few percent of the equilibrium pressure. Now that these restrictions have been unveiled, a tube and resonators are chosen to avoid them.

As for the method to excite the air column, the previous experiments exploit the bellows mounted at one end of the tube. Although they have a merit of securing the hermetic sealing, nonuniformity in inner diameter gives rise to unignorable effects if a tube is not long enough in comparison with the depth of the bellows. The present experiments use a rubber diaphragm sandwiched by a couple of circular plates, whose center is driven by a linear motor. When the center of the plates is displaced axially, the rubber stretches to form a circular-cone frustum with the plates. This device is different from a plane piston but a flow field near it would be much simpler than that driven by the bellows and closer to the piston. The depth (or height) of the frustum can be related equivalently to the displacement of the piston by equating the volume displaced.

In what follows, Sec. II summarizes the results of the weakly nonlinear theory necessary to comparison with the ones measured. Section III describes the experimental setup. The experiments measure not only the frequency response but also the pressure field in the tube and the resonators. Results of measurements are compared against the theory in Sec. IV and discussions are given in Sec. V. Finally the conclusions are given.

II. SUMMARY OF THE THEORY

A. Outline of formulation

An air column in a tube of radius R and of length l is driven sinusoidally by a plane piston installed at one end of the tube with the other end closed by a flat plate. Identical Helmholtz resonators are connected to the tube in array through the side wall with equal axial spacing d. Each resonator consists of the cavity of volume V and the throat of radius r and of length L. The volume of each resonator is assumed to be small in the sense that the size parameter κ, defined as V/Ad, is much smaller than unity, where A is the cross-sectional area of the tube. The axial spacing is taken much smaller than a wavelength of oscillations so that the continuum approximation may be applied to smear the discrete distribution of the resonators.

A natural angular frequency of the resonator is given by ω_0 $(=\sqrt{\pi a_0^2 r^2/L_e V})$ where a_0 is the sound speed and L is lengthened to L_e $(=L+2\times 0.82r)$ by taking account of the end corrections. Because the volume of the throat is usually negligibly small in comparison with the one of the cavity, no distinction is made between the volume of the cavity and the total volume of the resonator V_r $(=V+\pi r^2 L)$. But when the volume of the throat is small but not negligible, it is found that ω_0 based on V_r instead of V fits better with a measured one.[7]

The Reynolds number $a_0 u_0/\nu\omega$ is so high that effects of viscosity and heat conduction are confined only in a boundary layer on the tube, where u_0, ν, and ω denote, respectively, a typical axial speed of air, its kinematic viscosity, and a typical angular frequency of oscillations. Since the boundary layer is thin and the size parameter is small, the main flow in the outside of the boundary layer and except for the neighborhoods of throat orifices may be regarded as being almost one-dimensional. Assuming the ideal gas for the air and the adiabatic relation in the main flow, one-dimensional, nonlinear wave equation (21) in Ref. 6 is derived from the equations of continuity and of axial motions of air averaged over the cross section of the main flow in terms of the velocity potential $\phi(x,t)$, x and t being, respectively, the axial coordinate along the tube and the time, and the overbar used to designate the dimensionless quantities being suppressed. Effects of the boundary layer and the array of resonators are taken into account in the form of a source term in the equation of continuity.

For response of the resonators, the compressibility of air in the throat is ignored because the throat length is much smaller than the wavelength, and the equation of axial motion along the throat is averaged over it by taking account of a boundary layer on the throat wall. For the air in the cavity, no motions are assumed and only the mass balance is required with the adiabatic relation. To simulate the response of the resonator well, it is of vital importance to consider a jet loss at the throat which occurs when the air flows through it. Using the jet loss in a semi-empirical form, the oscillation equation (95) in Ref. 6 for the excess pressure in the cavity $p_c'(x,t)$ is derived with the excess pressure in the tube $p'(x,t)$ as the forcing term. Of course, p' is derived from ϕ by the Bernoulli's theorem.

B. Assumptions of the theory

It is revealed in the lossless linear theory that the natural oscillations of the air column confined in $0<x<1$ by flat plates at both ends are given in the dimensionless form as follows:

$$\begin{bmatrix} \phi \\ p' \\ p_c' \end{bmatrix} = \begin{bmatrix} i/\pi\sigma \\ 1 \\ s \end{bmatrix} \cos[k(x-1)]\alpha e^{i\pi\sigma t} + \text{c.c.}, \tag{1}$$

where ϕ is normalized by lu_0, p' and p_c' by $\rho_0 a_0 u_0$, x and t by l and l/a_0, respectively, ρ_0 being the density of air in equilibrium; the wavenumber k, given by

$$k^2 = (\pi\sigma)^2(1+\kappa s)$$

with

$$s = \frac{\sigma_0^2}{\sigma_0^2 - \sigma^2}, \tag{2}$$

is chosen to be $m\pi$ $(m=0,1,2,\ldots)$ by the boundary conditions at both ends, from which the dimensionless angular frequency $\sigma(=\omega l/\pi a_0)$ is determined, ω being a dimensional one; α denotes the complex amplitude, and c.c. implies the complex conjugate to all preceding terms. For a given value

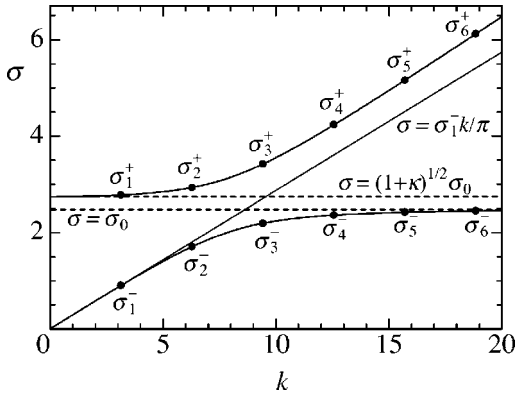

FIG. 1. Graph of the dispersion relation (2) between σ and k in the solid curves and the natural angular frequencies $\sigma_m^{\pm}$ for $k=m\pi$ ($m=1,2,3,\ldots,6$) designated by the closed circles in the case with $\sigma_0=2.5$ and $\kappa=0.2$; for the lowest frequency σ_1^-, all the other frequencies are located off the straight line $\sigma=\sigma_1^- k/\pi$, which indicates the tube is dissonant.

of m, there occurs a pair of the natural angular frequencies $\sigma_m^{\pm}$ given by

$$\sigma_m^{\pm}=\frac{1}{\sqrt{2}}\Big\{m^2+(1+\kappa)\sigma_0^2 \pm\sqrt{[m^2+(1+\kappa)\sigma_0^2]^2-4m^2\sigma_0^2}\Big\}^{1/2}, \tag{3}$$

where σ_0 ($=l\omega_0/\pi a_0$) denotes the dimensionless natural angular frequency of the resonator. Note that $\pi a_0/l$ is the lowest natural angular frequency of the air column in the tube without the array.

In Fig. 1, the solid curves show the graph of the dispersion relation (2) which stipulates σ for an arbitrary value of k in the case with $\sigma_0=2.5$ and $\kappa=0.2$, and the closed circles indicate the natural angular frequencies $\sigma_m^{\pm}$ for $k=m\pi$ ($m=1,2,3,\ldots,6$) selected by imposing the boundary conditions at both ends. By connecting the array of resonators, the dispersion curves are split into two branches, which are separated by the stopping band in the frequency range $\sigma_0<\sigma<(1+\kappa)^{1/2}\sigma_0$. The lower bound corresponds to the evanescence with $k\to\infty$, while the upper one to the resonance with $k\to 0$ mentioned briefly in Sec. I. For the lowest natural angular frequency σ_1^-, the straight line $\sigma=\sigma_1^- k/\pi$ is drawn to indicate that all the other frequencies are located off the line so that the tube is dissonant.

Let one end of the air column be driven by a plane piston at $x=x_p=c\cos(\pi\sigma t)$ with $c=X_p/l\ll 1$ and at a frequency close to one of σ_1^- ($\equiv\sigma_1$) where X_p denotes the dimensional displacement amplitude of the piston surface so the air column occupies the region $x_p<x<1$. Then three quantities come into play. One is a parameter specifying the order of detuning of the driving frequency from the natural one, $\Delta\sigma$ ($|\Delta\sigma|\ll 1$), and another is a parameter for the order of oscillations. While this is given by the maximum excess pressure relative to the equilibrium one, it is the acoustic Mach number ε ($=u_0/a_0\ll 1$) that is used in the theory. Of course, both parameters are comparable in order. The theory assumes such a situation that

$$\varepsilon\approx\frac{c}{|\Delta\sigma|}. \tag{4}$$

In view of the experiments in which c, $\Delta\sigma$, and ε are of order 10^{-3}, 10^{-2} and 10^{-1}, Eq. (4) is satisfied when c is assumed to be of ε^3 while $|\Delta\sigma|$ of ε^2.

The other quantities are parameters specifying the order of dissipation due to the boundary layers on the tube wall and throat wall. They are given, respectively, by δ and δ_r defined as follows:

$$\delta=2\left(1+\frac{\gamma-1}{\sqrt{\mathrm{Pr}}}\right)\frac{\sqrt{\nu l/a_0}}{R^*}\ll 1,\quad \delta_r=2\frac{\sqrt{\nu l/a_0}}{r^*}\ll 1, \tag{5}$$

where γ and Pr denote the ratio of the specific heats and the Prandtl number, respectively, while R^* and r^* denote the reduced radii defined, respectively, as R^* [$=R/(1-\pi r^2R/2Ad)$] and r^* ($=r/c_L$), $c_L=(L+2r)/L_e$. The values of these parameters are regarded as the quantities of ε^2.

The theory assumes no higher harmonic resonances and evanescences up to the third harmonics. If a frequency of the nth higher harmonics, $n\sigma_1$, n being an integer greater than unity, coincides with $\sigma_m^{\pm}$ ($m=0,1,2,\ldots$), i.e.,

$$(m\pi)^2=(n\pi\sigma_1)^2\left[1+\frac{\kappa\sigma_0^2}{\sigma_0^2-(n\sigma_1)^2}\right], \tag{6}$$

then σ_1^2 is determined in terms of σ_0 as

$$\sigma_1^2=\frac{1}{2(n^2-1)}\{m^2-1\pm[(m^2-1)^2-4(m^2-n^2)\times(1-n^{-2})\sigma_0^2]^{1/2}\}. \tag{7}$$

This relation may be transformed into the expression for σ_0^2 in terms of κ as

$$\sigma_0^2=\frac{1}{2(1+\kappa)^2}[-j_{mn}\pm\sqrt{j_{mn}^2-4(1+\kappa)^2m^2}], \tag{8}$$

with

$$j_{mn}=\frac{(m^2-n^4)^2-(1+\kappa)[m^2(n^2-1)^2+(m^2-n^2)^2]n^2}{(m^2-n^2)(n^4-n^2)}, \tag{9}$$

or alternatively into the expression for κ in terms of σ_0^2 as

$$\kappa=\frac{[m^2(n^2-1)^2+(m^2-n^2)^2]n^2\pm k_{mn}}{2(m^2-n^2)(n^4-n^2)\sigma_0^2}-1, \tag{10}$$

with

$$k_{mn}=\sqrt{(m^2-n^4)^2[(m^2-1)^2n^4-4(m^2-n^2)(n^4-n^2)\sigma_0^2]}. \tag{11}$$

As far as σ_0^2 or κ thus obtained is positive, they have physical meanings. If $n\sigma_1$ hits σ_0 for evanescence, κ and σ_0^2 are determined as

$$\sigma_0^2=\frac{n^2-n^4}{1-(1+\kappa)n^2}\ \text{or}\ \kappa=\frac{(n^2-1)(n^2-\sigma_0^2)}{n^2\sigma_0^2}. \tag{12}$$

In order to achieve higher pressure oscillations in reality, it is desirable to avoid these resonances and evanescences beyond

the third harmonics in designing the tube with the array of resonators. Even if these conditions were not satisfied exactly, it is desirable to depart from them as much as possible.

C. Results of the theory

The solutions for the velocity potential in the tube and the pressure in the cavities of the resonators are sought in the asymptotic expansion with respect to ε by the method of multiple (double) time-scales up to the order of ε^2. The main outcome is the amplitude equation which determines a temporal behavior of the complex amplitude α for the dimensionless excess pressure in the tube. The equation is derived from the boundary conditions of ε^2 as [see Eq. (100) in Ref. 6 with the correction (σ_1 on the right-hand side to be removed)]

$$i\mu\frac{\partial\alpha}{\partial t_2}+\frac{S}{\varepsilon^2}\alpha+i\frac{D_0}{\varepsilon}|\alpha|\alpha+Q_0|\alpha|^2\alpha=\frac{\pi\sigma_1 c}{\varepsilon^3}e^{i\pi\sigma' t_2}, \tag{13}$$

where α is assumed to depend on the slow time variable t_2 ($=\varepsilon^2 t$) and μ, S ($=S_{re}+iS_{im}$), D_0 and Q_0 are constants given by

$$\mu=2+2\kappa s_1\left(1+\frac{s_1}{\Omega}\right),$$

$$S_{re}=-S_{im}=-\sqrt{\frac{\pi\sigma_1}{2}}\left(\frac{\delta}{\sigma_1^2}+\frac{\kappa\delta_r s_1^2}{\Omega}\right), \tag{14}$$

$$D_0=\frac{128\kappa\delta_J\sigma_1^3 s_1^3}{9\pi\sigma_0^2},\quad Q_0=Q_1+Q_2+Q_3,$$

with $s_1=\sigma_0^2/(\sigma_0^2-\sigma_1^2)$, $\Omega=\sigma_0^2/\sigma_1^2$, and $\delta_J=(l/\pi\sigma_0 L_e)^2$, σ' being a constant of order unity. For the detailed expressions of Q_1, Q_2, and Q_3, see Eqs. (70) to (72) in Ref. 6.

The experiments measure only the excess pressures in the tube and in the cavities of the resonators, from which the Fourier coefficients are obtained. For the sake of comparison with the experiments, the solutions are rewritten in the form convenient to this purpose. The dimensional excess pressures $\rho_0 a_0 u_0 p'$ and $\rho_0 a_0 u_0 p_c'$ are now renormalized by the equilibrium pressure p_0, and their solutions are rearranged in the form of the Fourier series in t with period $2/\sigma_1$ as follows:

$$\frac{\rho_0 a_0 u_0}{p_0}\begin{bmatrix}p'\\ p_c'\end{bmatrix}=\sum_{n=0}^{\infty}\begin{bmatrix}P_n(x,t_2;\varepsilon)\\ P_{cn}(x,t_2;\varepsilon)\end{bmatrix}e^{in\pi\sigma_1 t}+\text{c.c.} \tag{15}$$

Here note that $\rho_0 a_0 u_0/p_0=\varepsilon\gamma$ with $a_0^2=\gamma p_0/\rho_0$, and P_n and P_{cn} denote the complex Fourier coefficients which depend not only on x but also on t_2 and ε. The Fourier coefficients are related to the coefficients of the asymptotic expansion as follows:

$$P_0=P_{c0}=\varepsilon^2\gamma\left\{\frac{1}{2}\left(1-\frac{1}{\sigma_1^2}\right)+\frac{1}{2}\left(1+\frac{1}{\sigma_1^2}\right)\cos[2\pi(x-1)]\right\}|\alpha|^2, \tag{16}$$

$$\begin{bmatrix}P_1\\ P_{c1}\end{bmatrix}=\varepsilon\gamma\alpha\begin{bmatrix}1\\ s_1\end{bmatrix}\cos[\pi(x-1)]+\varepsilon^3\gamma\begin{bmatrix}F_1^{(2)}\\ G_1^{(2)}\end{bmatrix}+\text{c.c.}+\cdots, \tag{17}$$

$$\begin{bmatrix}P_2\\ P_{c2}\end{bmatrix}=\varepsilon^2\gamma\begin{bmatrix}F_2^{(1)}\\ G_2^{(1)}\end{bmatrix}+\text{c.c.}+\cdots, \tag{18}$$

and so on [see Eqs. (54)–(56), (80), and (82) in Ref. 6 for the explicit expressions].

It is found that $F_1^{(2)}$ contains the term which has the same dependence on x as the lowest solution in the form of $\cos[\pi(x-1)]$. This term may be incorporated into it by defining P instead of α as

$$\varepsilon\gamma\alpha+\varepsilon^3\gamma\left[-\frac{i}{\pi\sigma_1}\frac{\partial\alpha}{\partial t_2}+\frac{1}{2}\left(1-\frac{1}{\sigma_1^2}\right)\mathcal{A}_2|\alpha|^2\alpha\right]=\frac{P}{2}, \tag{19}$$

where $\partial\alpha/\partial t_2$ is given by Eq. (13) and the term of ε^3 is approximated for a large value of Ω. For the explicit expression of $\mathcal{A}_2$, see Eq. (52) in Ref. 6. This relation is expressed inversely as

$$\varepsilon\gamma\alpha=\frac{P}{2}+\frac{i}{2\pi\sigma_1}\frac{\partial P}{\partial t}-\frac{1}{16\gamma^2}\left(1-\frac{1}{\sigma_1^2}\right)\mathcal{A}_2|P|^2P+\cdots, \tag{20}$$

to the present order of approximation where the relation $\varepsilon^2\partial\alpha/\partial t_2=\partial\alpha/\partial t$ has been used. The parameter ε indicating explicitly the smallness is now removed. But it should always be kept in mind that P is the small quantity. Using this replacement, all quantities are expressed in terms of P.

Noting the amplitude equation (13) describes competition between the quantities of order unity, it is transformed without any additional terms into

$$i\mu\frac{\partial P}{\partial t}+SP+iD|P|P+Q|P|^2P=\Gamma e^{i\pi\Delta\sigma t}, \tag{21}$$

with $D=64\kappa\delta_J\sigma_1 s_1^3/9\pi\gamma\Omega$, $Q=Q_0/4\gamma^2$, $\Gamma=2\pi\gamma\sigma_1 c$, and $\varepsilon^2\sigma'=\Delta\sigma$. It is remarked that the amplitude equation is determined by the zeroth and second Fourier coefficients of ε^2 but not by the third one. The frequency response in the steady-state oscillations is given by

$$\Delta\sigma=\frac{1}{\pi\mu}\left[S_{re}+Q|P|^2\pm\sqrt{\frac{\Gamma^2}{|P|^2}-(S_{im}+D|P|)^2}\right]. \tag{22}$$

The peak in the frequency-response curve occurs when the factor in the square root vanishes. Then the magnitude of P is given by

$$|P|_{\text{peak}}=\frac{1}{2D}(-S_{im}+\sqrt{S_{im}^2+4D\Gamma}), \tag{23}$$

at the frequency $\sigma_1+\Delta\sigma_{\text{peak}}$ with the shift given by

$$\Delta\sigma_{\text{peak}}=(S_{re}+Q|P|_{\text{peak}}^2)/\pi\mu. \tag{24}$$

Thus the complex amplitude at the peak is expressed as

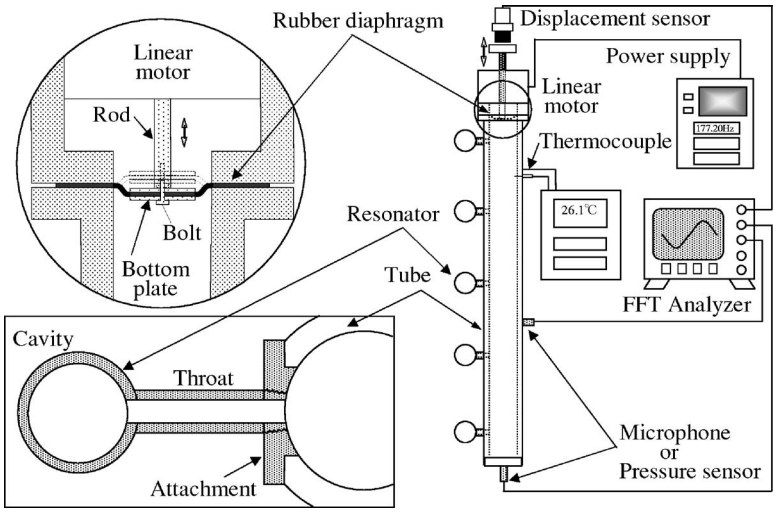

FIG. 2. Illustration of the experimental setup.

$$P = |P|_{\text{peak}} e^{i(\pi\Delta\sigma_{\text{peak}}t-\pi/2)}, \tag{25}$$

[see Eqs. (86) and (87) in Ref. 6 in the case without the jet loss]. When the piston is oscillating at the frequency $\sigma + \Delta\sigma_{\text{peak}}$, the phase in the pressure at $x=1$ lags behind the piston displacement just by $\pi/2$, while the pressure at $x=0$ leads the piston displacement by $\pi/2$. The latter implies that the pressure on the piston surface is just in phase with the piston velocity so that the maximum power may be input into the air column at a given displacement amplitude of the piston.

III. EXPERIMENTAL SETUP

A tube, resonators, and a driver unit are designed carefully so as to meet conditions required by the theory. Especially the higher harmonic resonances and evanescences are avoided as much as possible. In order to generate high pressure amplitude, it is conjectured that the response curve should become symmetric with respect to the peak just as in the linear response. For this, the value of the coefficient Q, responsible for bending of the response curve, should be made as small as possible. This is substantially to suppress the nonlinear effects including the jet loss. The maximum pressure in the tube is set to be about 10% of the equilibrium pressure because the weakly nonlinear theory tends to break down as the pressure increases further. The experimental setup used is illustrated in Fig. 2 and described in the following.

A. Tube and resonators

A stainless-steel tube of inner diameter 37 mm, length 923 mm, and thickness 9 mm is used. The inner surface is polished so smoothly by honing with surface roughness R_z (ISO4287) below 0.6 μm as to meet the assumptions used in the theory for the boundary layer. One end of the tube is closed by a flat plate while the other end is connected to the driver unit. The resonator consists of the spherical cavity and the circular throat, both being made of the stainless steel. The volume of the resonator is 14.7 cm^3, while the throat is of inner diameter 7.1 mm, length 72.3 mm, and volume 2.87 cm^3. The natural frequency of the resonator is calculated to be 325 Hz at temperature 26.1 °C. For reference, the natural frequency of the tube without the array takes 188 Hz at the same temperature.

Five resonators are connected to the tube equidistantly with the axial spacing $d=185$ mm. The resonator nearest to the closed end at $x=1$ is placed at half the axial spacing $d/2$ away from the end. Such an arrangement is suggested by the fact that the boundary condition at the closed end may be replaced by the mirror image.[7] In fact, the axial spacing appears to be uniform if the mirror image is taken. The resonator is connected to the tube through the hole in the tube wall with an attachment (see Fig. 2), which secures flush mounting with the inner surface of the tube. The end surface of the attachment has the same radius of curvature as the tube so that the inner surface of the tube may become smooth everywhere including where the resonators are connected.

B. Driver unit

Although the plane piston is assumed in the theory, it is difficult to seal the air column tightly in reality because no leak of the air through a narrow gap between the piston head and the tube would be guaranteed. Newly devised is a rubber diaphragm of thickness 2 mm sandwiched by a couple of circular plates. The diaphragm is stretched to cover the whole cross section of the tube and clamped at its edge. Two stainless-steel plates of diameter 27 mm and of thickness 0.8 mm each are bolted together at the center as shown in Fig. 2 to the axis of the linear motor.

When the couple of the plates (called simply a bottom plate hereafter) are displaced from the equilibrium position, the diaphragm stretches to form a frustum with the plate. Assuming the lateral surface to be conical, the volume of the frustum is proportional to the displacement of the bottom plate. The ratio of this volume to the cross-sectional area of the tube gives equivalently the displacement of the plane piston x_p in the theory. Denoting the displacement of the bottom plate from the equilibrium position by x_b, this is related to x_p as in the case of the bellows.[3] Taking the greater diameter D_g as the tube diameter and the smaller one D_s as

TABLE I. Experimental conditions and values of constants.

Figure	T_0 (°C)	p_0 (hPa)	a_0 (m/s)	ν (m^2/s)	Pr	S_{im}
3 and 4	22.8	1009.1	345.4	1.538×10^5	0.7096	0.0502
5	26.1	1014.5	347.4	1.560×10^5	0.7086	0.0504
6	24.1	1021.7	346.2	1.530×10^5	0.7092	0.0500
7, 8, 10, and 11	23.8	1024.3	346.0	1.524×10^5	0.7093	0.0499
9	25.8	1004.0	347.2	1.573×10^5	0.7087	0.0507

the diameter of the bottom plate, the piston displacement x_p is given equivalently by $x_p=(1+\chi+\chi^2)x_b/3$ with $\chi=D_s/D_g$. For $\chi=27$ mm/37 mm=0.730, $x_p=0.754x_b$ and the coefficient of proportion is smaller than unity, whereas it takes the value 1.422 in the case of the bellows.

The bottom plate is driven by a linear motor of voice-coil type with the maximum thrust 72 N (Sumitomo Special Metals: type LV25). The motor reciprocates along its axis and its motion is transmitted to the bottom plate by the rod connecting them. This type linear motor can accurately be controlled by varying the input current. The ac power supply (Takasago: AA2000XG) is used to generate sinusoidal currents. The maximum relative errors in the frequency and the wave form from a purely monochromatic wave are less than 5×10^{-3}% and 0.3%, respectively. The magnitude of higher harmonics involved in the displacement of the bottom plate is less than 0.2% of the fundamental one.

C. Measuring instruments

The displacement of the bottom plate is measured by a laser displacement sensor (Keyence: LB-62) with resolution 50 μm up to 3 kHz. Excess pressure in the tube or in the cavity of the resonator is measured by two condenser microphones (Brüel & Kjær: type 4941) with sensitivity 0.085 mV/Pa. The microphones are set flush with the inner surface of the tube. When the pressure in the cavity is measured, the microphone is set at the bottom of the cavity (at a position opposite to the throat).

The nonoscillatory (zeroth harmonics or dc) component is measured by two pressure sensors of strain-gauge type (Kyowa: PGM-05KG) with a natural frequency of 3 kHz because the microphones fail to measure it. They are also mounted flush with the flat plate and the tube wall as well as the microphones. The data are processed by the FFT analyzer (Ono Sokki: CF-3600) with maximum number of sampling points 16384 to obtain Fourier coefficients.

The temperature of the air column and the tube wall are measured by two sheath-thermocouples of K-type and of diameter 0.3 mm. Both thermocouples are positioned at $x=0.25$. One is inserted hermetically into the center axis of the tube, while the other is put on the outer surface of the tube wall where the temperature of the wall may be regarded as the equilibrium temperature of the air in the tube. The atmospheric pressure is taken as the equilibrium one in the tube so the ambient pressure is measured by an aneroid barometer.

D. Evaluation of the parameters

For the tube and the resonators chosen, the various parameters are evaluated. The size parameter κ takes the value 0.0737, which is much smaller than the one 0.198 in the previous experiments. Here it is to be noted that κ is evaluated by using V_r instead of V. The dimensionless angular frequencies σ_0 and σ_1, which are independent of the temperature and dependent of κ only, take the fixed values at 1.73 and 0.951, respectively. The array makes the natural frequency of the tube lower by about 5% than the one in the tube without the array. Given the value of κ, no harmonic resonances with the combinations of m $(=0,1,2,\ldots,8)$ and n $(=2,3,4)$ occur for the value of σ_0 in the range $|\sigma_0-1.73|<0.05$. For the range $|\sigma_0-1.73|<0.01$, m and n may be taken up to 19 and 10, respectively. The higher harmonic evanescences are avoided in the present case.

The values of δ and δ_r depend on the temperature through a_0, ν, and Pr (see Table I and Ref. 3). While the value of γ is taken to be a constant 1.40, the dependence of the sound speed on the temperature is taken into account according to $a_0=331.5+0.61T_0$ m/s for T_0 measured in degrees Celsius. At 26.1 °C, for example, δ and δ_r takes the values 0.0325 and 0.116, respectively, which is to be compared with the previous ones $\delta=0.0282$ and $\delta_r=0.223$. The value of δ_r is reduced but larger than the one assumed. The parameters in the amplitude equation except for S are evaluated by the geometry only as follows: $\mu=2.30$, $D=0.478$, and $Q=-0.735$. For the value of S_{im} $(=-S_{re})$, see Table I. The values of μ, S, and D are close to the ones in the previous experiments ($\mu=2.43$, $S_{im}=0.0430$, $D=0.398$, and $Q=15.2$), but the one of Q is dramatically reduced. Thus we may say that the present tube and resonators are designed so that the nonlinear effects except for the jet loss are suppressed significantly at the cost of slight increase in the values of δ and D.

IV. EXPERIMENTS

The experiments are made with the tube hung vertically and the driver unit on top. The excess pressure in the tube is measured at the position $x=0.17$, 0.38, 0.50, 0.63, 0.83, and 1, while the one in the cavities of the five resonators at $x=0.10$, 0.30, 0.50, 0.70, and 0.90. At the same time, the complex Fourier coefficients are obtained. Measurements are made when the steady state of oscillations appear to be achieved at a frequency of the peak in the response. The peak is identified by observing that the phase in the displacement of the bottom plate is ahead of the one of the pressure at x

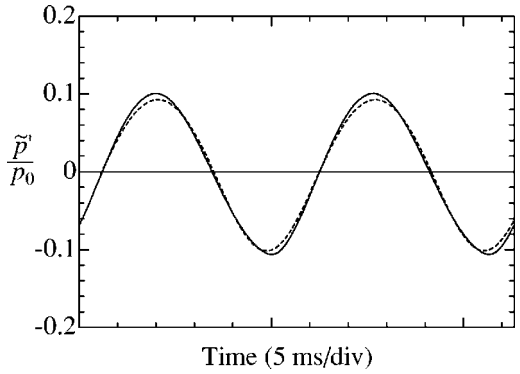

FIG. 3. Temporal profile of the oscillatory component in the pressure measured on the flat plate at the closed end for the displacement amplitude of the bottom plate $X_b=1.39$ mm where $\tilde{p}'$ denotes the dimensional excess pressure p' minus the nonoscillatory component corresponding to $P_0(1)$, and the solid and broken lines represent, respectively, the ratio of $\tilde{p}'$ to the equilibrium pressure p_0 measured and predicted by Eq. (17) with the second harmonics (18) inclusive and the replacement of α by Eq. (20).

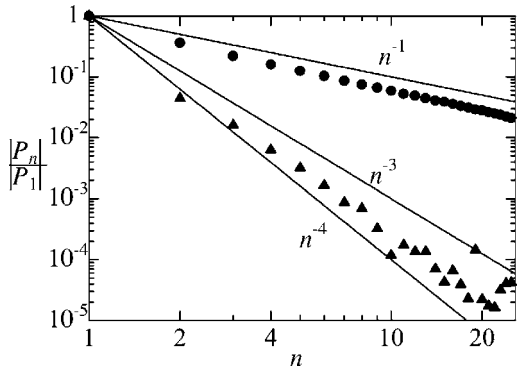

FIG. 4. Decays of the Fourier coefficients $|P_n|$ relative to $|P_1|$ (=0.101) where the triangles and the circles represent, respectively, the data for the profile shown by the solid line in Fig. 3 and a shocked profile measured in a tube without the array.

$=1$ just by $\pi/2$. Since only two microphones are available, measurements are repeated by changing the positions.

Here it should be remarked that the Fourier coefficients measured are different from the ones in Eq. (15). The series (15) is the expansion with period $2/\sigma_1$, while the coefficients to be measured correspond to the ones in the expansion with period $2/(\sigma_1+\Delta\sigma_{\text{peak}})$. Therefore it must be rewritten for comparison. In Eq. (15), the factors $e^{in\pi\Delta\sigma t}$ $(=e^{in\pi\sigma' t_2})$ are taken out of P_n and P_{cn} to form $e^{in\pi(\sigma_1+\sigma' t_2)}$ as follows:

$$\begin{bmatrix} P_n(x,t_2;\varepsilon) \\ P_{cn}(x,t_2;\varepsilon) \end{bmatrix} e^{in\pi\sigma_1 t} = \begin{bmatrix} P_n(x,t_2;\varepsilon)e^{-in\pi\sigma' t_2} \\ P_{cn}(x,t_2;\varepsilon)e^{-in\pi\sigma' t_2} \end{bmatrix} \times e^{in\pi(\sigma_1 t+\sigma' t_2)}, \tag{26}$$

$(n=0,1,2,\ldots)$ where $\varepsilon^2\sigma'$ takes the value $\Delta\sigma_{\text{peak}}$. It is the coefficients in the square brackets on the right-hand side that will be available experimentally. Although the coefficients appear to depend on t_2, this must not be so. The factor $e^{-in\pi\sigma' t_2}$ cancels indeed with the one involved in P_n and P_{cn}. Setting P_n and P_{cn} to be in the following form

$$P_n=|P_n|e^{i\theta_n}, \quad P_{cn}=|P_{cn}|e^{i\theta_{cn}}, \tag{27}$$

the complex coefficients on the right-hand side of Eq. (26) are expressed as

$$P_n e^{-in\pi\sigma' t_2}=|P_n|e^{i\psi_n}, \quad P_{cn}e^{-in\pi\sigma' t_2}=|P_{cn}|e^{i\psi_{cn}}, \tag{28}$$

with $\psi_n=\theta_n-n\pi\Delta\sigma_{\text{peak}}t$ and $\psi_{cn}=\theta_{cn}-n\pi\Delta\sigma_{\text{peak}}t$. Using Eq. (25) and the explicit form of P_n and P_{cn} in terms of P, ψ_n and ψ_{cn} are found to be independent of t.

A. Pressure profiles and Fourier coefficients

Figure 3 shows the temporal profile of the oscillatory component in the pressure measured on the flat plate at the closed end $x=1$ for the displacement amplitude of the bottom plate $X_b=1.39$ mm where $\tilde{p}'$ denotes the dimensional excess pressure p' minus the nonoscillatory component corresponding to $P_0(1)$, and the broken line represents the solution taken up to the second harmonics inclusive, i.e., P_1 in Eq. (17) and P_2 in Eq. (18) with the replacement of α by Eq. (20). It is obvious that the profiles are smooth without any shocks.

For the profile in Fig. 3, Fig. 4 shows how the magnitude of each Fourier coefficient $|P_n|$ decays as n increases up to 25th. The triangles indicate the data relative to $|P_1|$ (=0.101) for the profile in Fig. 3, while the circles indicate, for reference, the decay of the coefficients for a shocked profile measured in the tube without connecting the array. As n increases, the coefficients of the shock-free profile decay very rapidly at rate between n^{-3} and n^{-4} in contrast to the slow decay as n^{-1} for the shocked profile. As will also be seen in Fig. 10, it is found that the magnitude of the second harmonics involved is about 4% relative to $|P_1|$ and the profile in Fig. 3 is very close to a monochromatic wave in spite of the presence of the nonlinearity. But a slight discrepancy between the profiles measured and predicted is considered to result from higher harmonics.

B. Frequency response

In the previous experiments, the frequency response is obtained by measuring the maximum pressure δp at the closed end against the frequency of excitation. In the present experiments, it is obtained from the first Fourier coefficient measured at the closed end. The magnitude of $|P_1(1)|$ is plotted against the dimensional frequency of excitation in Fig. 5 by the open triangles, closed triangles, open circles, and closed circles for four values of $X_b=0.25$, 0.50, 1.00, and 1.75 mm, respectively. It is seen that the data measured fall perfectly on the theoretical curves (22) shown in the solid lines, except for the data designated by the closed circles in the vicinity of the peak. The agreements in the magnitude and the frequency are excellent. Since the value of Q is small, the curves are symmetric with the peak, as expected.

Next we examine the relation between the peak pressure $|P|_{\text{peak}}$ and the displacement amplitude of the piston c $(=X_p/l)$ equivalent to the one of the bottom plate. Figure 6 plots $|P|_{\text{peak}}$ vs c by the circles in the log–log scales. It is already shown in Ref. 6 that for $\Gamma \ll S_{im}^2/4D$, $|P|_{\text{peak}}$ is given by Γ/S_{im} while for $\Gamma \gg S_{im}^2/4D$, $|P|_{\text{peak}}$ is given by $\sqrt{\Gamma/D}$. Thus while Γ, i.e., c is small, the peak pressure is proportional to c, but it becomes proportional to $c^{0.5}$ as c becomes

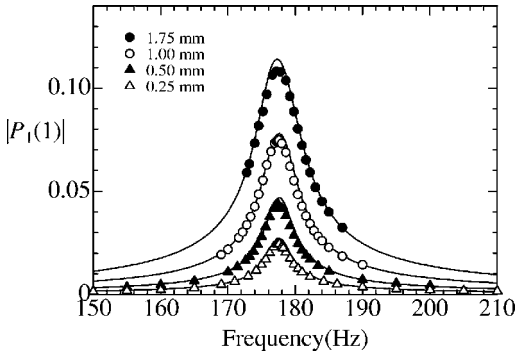

FIG. 5. Frequency response measured and predicted where the open triangles, closed triangles, open circles, and closed circles represent the data measured for the displacement amplitude of the bottom plate X_b=0.25, 0.50, 1.00, and 1.75 mm, respectively and the solid lines represent the theoretical curves calculated by Eq. (22) for the respective amplitudes.

larger. The changeover is defined to occur at $\Gamma = S_{im}^2/4D$, which gives $\Gamma = 1.33 \times 10^{-3}$ and $c = 1.59 \times 10^{-4}$. The data measured lie on the line $c^{0.77}$ approximately, which is located between two lines c and $c^{0.5}$. The data seem to continue on the line $c^{0.77}$ beyond $c = 10^{-3}$.

C. Axial distributions of the first harmonics

Next the pressure field in the tube and in the cavities of the resonator is measured and checked against the theory. Figures 7 and 8 show, respectively, the axial distributions of the first Fourier coefficients $|P_1|e^{i\psi_1}$ and $|P_{c1}|e^{i\psi_{c1}}$ where (a) and (b) represent, respectively, each magnitude and phase in degree. Here the open triangle, closed triangle, open circle, and closed circles represent, respectively, the data for X_b =0.52, 0.82, 1.09, and 1.33 mm, respectively. The solid lines represent the theoretical distributions calculated by P_1 and P_{c1} in Eq. (17) with the replacement of α by Eq. (20). The change in sign of P_1 and P_{c1} with respect to x is taken into the respective phases ψ_1 and ψ_{c1}.

The measured data fall on the curves predicted by the theory. Quantitatively good agreements are seen not only in the tube but also in the cavities. Note that the maximum excess pressure in the cavity is about 50% greater than the one in the tube. It turns out that the terms of $|P|^3$ yield the

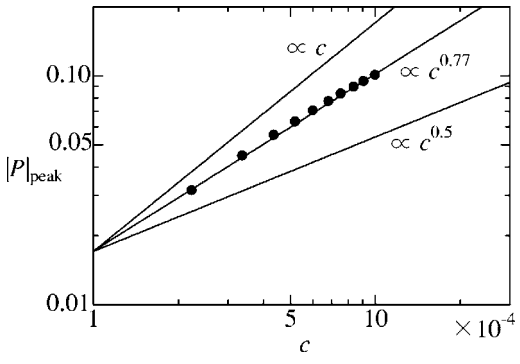

FIG. 6. Relation between the peak amplitude $|P|_{\text{peak}}$ and the displacement amplitude of the piston c ($=X_p/l$) equivalent to the one of the bottom plate, and two reference straight lines proportional to c and $c^{0.5}$ indicate the approximate relations when c is much smaller than the changeover value 1.59×10^{-4} and when c is much greater than it, respectively.

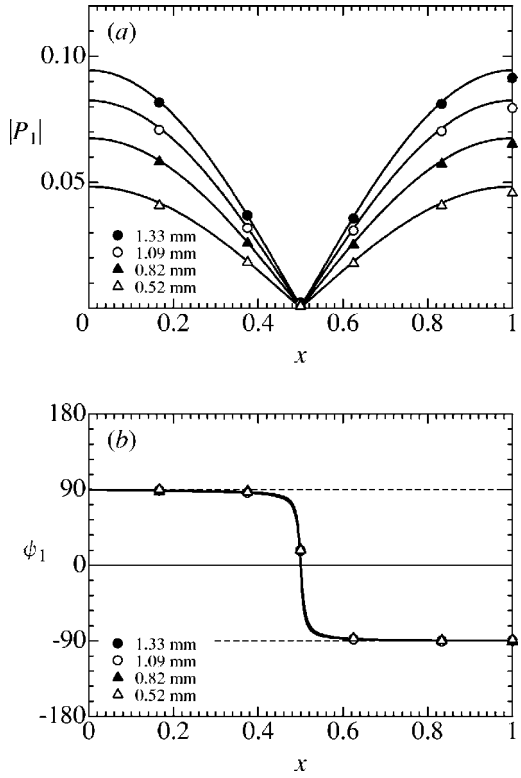

FIG. 7. Axial distributions of the first Fourier coefficient $|P_1|e^{i\psi_1}$ for the pressure profile in the tube where (a) and (b) represent, respectively, the distributions of the magnitude $|P_1|$ and the phase ψ_1 in degree; the open triangles, closed triangles, open circles, and closed circles indicate the data measured for the displacement amplitude of the bottom plate X_b=0.52, 0.82, 1.09, and 1.33 mm, respectively; the solid lines show the theoretical distributions calculated by P_1 in Eqs. (17) with (20).

corrections of a few percent. Thus the nonlinearity is suppressed to be so small that the pressure distributions may be regarded as being close to the linear solutions. The above-noted agreements support the validity of the assumptions of the one-dimensional field in the tube and the continuum approximation for the resonators. There are *only five* resonators that are connected to the tube.

D. Axial distributions of the zeroth and second harmonics

We proceed to check the zeroth (dc) and second harmonic components in the pressure field. At first, the zeroth components P_0 and P_{c0} are measured. Figure 9 shows the axial distributions of ΔP_0 for the deviation of $P_0(x)$ from $P_0(1)$. The symbols in figures correspond to the amplitudes of the bottom plate specified in Figs. 7 and 8, while the solid lines represent the distributions calculated by P_0 in Eq. (16) with Eq. (20). Here it should be remarked that P_0 tends to increase slowly in the course of time because the mean temperature and pressure in the tube increase slowly due to heating by friction on the tube wall. Thus the deviation ΔP_0 is plotted in Fig. 9. The zeroth harmonics is seen to agree well with the theory.

Figures 10 and 11 show, respectively, the axial distributions of the second Fourier coefficients $|P_2|e^{i\psi_2}$ and $|P_{c2}|e^{i\psi_{c2}}$ in the tube and in the cavities where (a) and (b) represent each magnitude and phase in degree. As two nodes are pre-

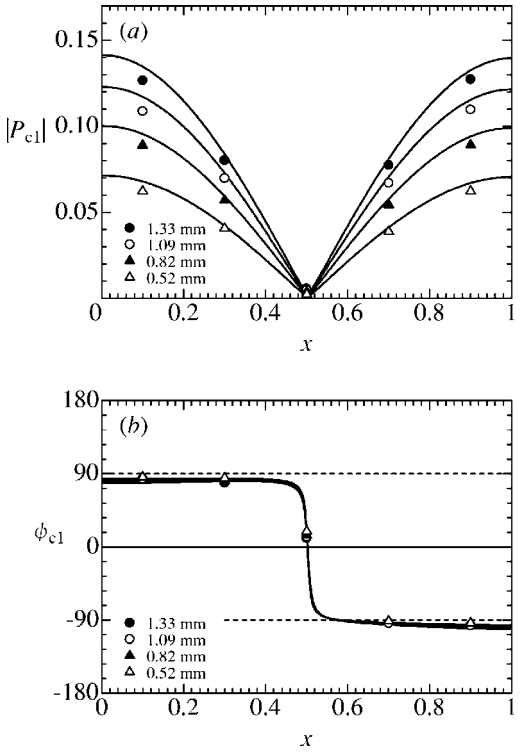

FIG. 8. Axial distributions of the first Fourier coefficient $|P_{c1}|e^{i\psi_{c1}}$ for the pressure in the cavity of the resonator where (a) and (b) represent, respectively, the distributions of the magnitude $|P_{c1}|$ and the phase ψ_{c1} in degree; the open triangles, closed triangles, open circles, and closed circles indicate the data measured for the displacement amplitude of the bottom plate X_b =0.52, 0.82, 1.09, and 1.33 mm, respectively; the solid lines show the theoretical distributions calculated by P_{c1} in Eqs. (17) with (20).

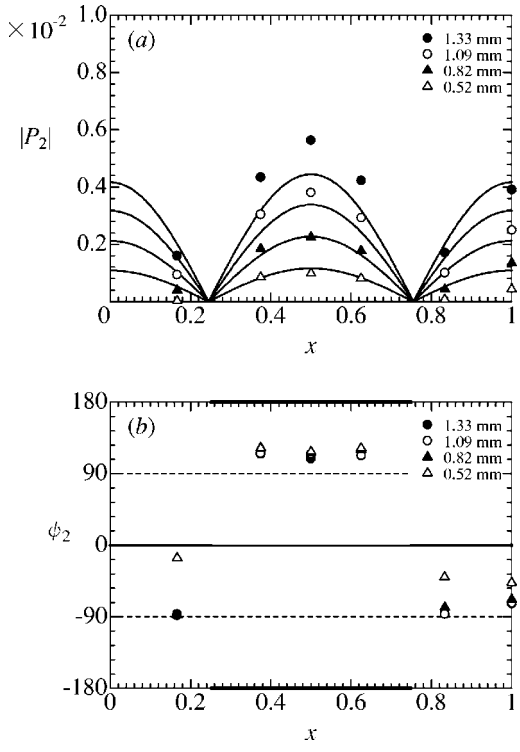

FIG. 10. Axial distributions of the second Fourier coefficient $|P_2|e^{i\psi_2}$ for the pressure profile in the tube where (a) and (b) represent, respectively, the distributions of the magnitude $|P_2|$ and the phase ψ_2 in degree; the open triangles, closed triangles, open circles, and closed circles indicate the data measured for the displacement amplitude of the bottom plate X_b=0.52, 0.82, 1.09, and 1.33 mm, respectively; the solid lines show the theoretical distributions calculated by P_2 in Eqs. (18) with (20).

dicted near x=0.25 and 0.75, the data measured show the axial distributions similar to the theoretical ones calculated by P_2 and P_{c2} in Eq. (18) with Eq. (20). While the amplitude of the bottom plate is small, the data for the magnitude are close to the curve predicted. Generally speaking, however, the data measured are greater than the ones by the theory in the middle of the tube and smaller near both ends. For the second harmonics as well, the magnitude in the cavity is remarkably larger than the one in the tube.

But there is a significant discrepancy in the phase. From the second harmonics of ε^2 [see Eqs. (54) and (55) in Ref. 6], it is found that ψ_2 and ψ_{c2} take the values 0 or π depending on the sign. Because the frequency of the second harmonics exceeds the resonance frequency of the Helmholtz resonator, ψ_{c2} is different from ψ_2 by π. But it is seen that the data measured scatter in between and the phases differ by multiples of 45°.

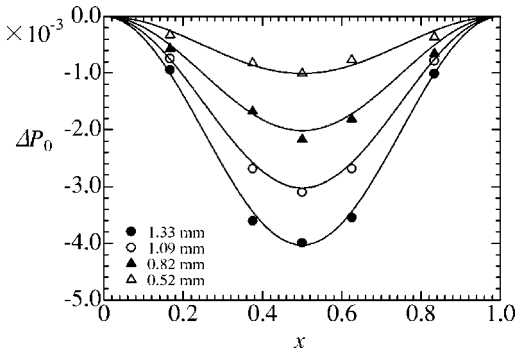

FIG. 9. Axial distributions of the deviation of the zeroth Fourier coefficient ΔP_0 $[=P_0(x)-P_0(1)]$ where the open triangles, closed triangles, open circles, and closed circles indicate the data measured for the displacement amplitude of the bottom plate X_b=0.52, 0.82, 1.09, and 1.33 mm, respectively; the solid lines show the theoretical distributions calculated by P_0 in Eqs. (16) with (20).

V. DISCUSSIONS

In designing the tube and the resonators, higher harmonic resonances and evanescences have been avoided as much as possible. In consequence, higher harmonics are suppressed significantly. It is seen from Eq. (3), however, that as m increases, σ_m^+ approach m, while σ_m^- approach σ_0, so that the effect of dispersion tends to disappear as m increases. Thus it becomes difficult to avoid the harmonic resonances for even higher modes. It would eventually determine the upper limit of the peak pressure how far the state of out-of-resonance can be achieved. Therefore it is essential to postpone the resonance as far as possible in order to yield a higher peak in the frequency response.

All theoretical results used for comparison are calculated by using the size parameter κ and the natural frequency of the resonator ω_0 based on the total volume of the resonator V_r instead of the volume of the cavity V. If those values by the original definitions are used in the frequency response for example, then the peak values are higher by several percent while each curve is shifted upward by a few hertz. In this

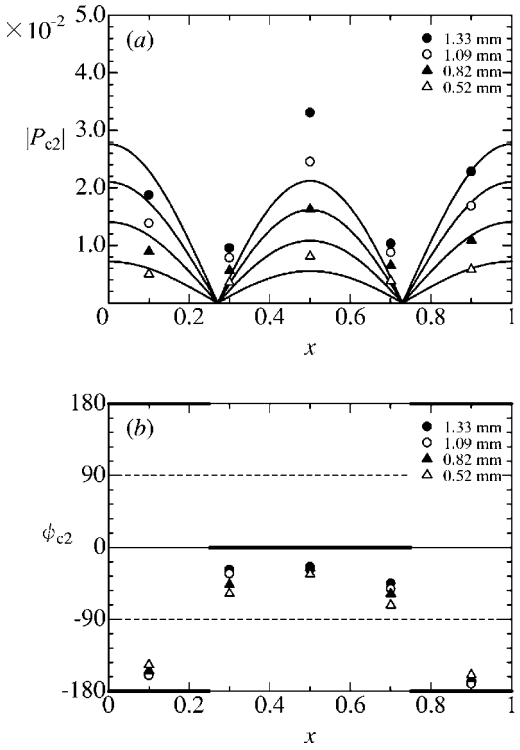

FIG. 11. Axial distributions of the second Fourier coefficient $|P_{c2}|e^{i\psi_{c2}}$ for the pressure in the cavity of the resonator where (a) and (b) represent, respectively, the distributions of the magnitude $|P_{c2}|$ and the phase ψ_{c2} in degree; the open triangles, closed triangles, open circles, and closed circles indicate the data measured for the displacement amplitude of the bottom plate X_b=0.52, 0.82, 1.09, and 1.33 mm, respectively; the solid lines show the theoretical distributions calculated by P_{c2} in Eqs. (18) with (20).

case, it is hard to acknowledge the perfect agreements. This is why V_r has been used in the comparisons that follow. It implies that when the volume of the throat is not negligible, the equation for the conservation of mass in the whole resonator would be more appropriate than the one in the cavity. But it is remarked that if the throat is included, then the definition of the mean pressure in the cavity would become ambiguous.

Next we consider physical origin of the discrepancy of the second Fourier coefficients. It may be attributed to the fact that the value of δ_r (=0.116) for the throat friction takes a larger value than assumed. In the present experiments, most concerned is the reduction of the value of Q whereas the value of δ_r is less concerned because its effect on the parameter S in the amplitude equation is weakened by the factor κ. As the wall friction becomes large, the magnitude of the pressure field is expected to be suppressed in general. Strange enough, however, the pressure in the tube and the cavities measured at the positions in the middle of the tube is higher than the one predicted. The wall friction does not resolve the discrepancy in the magnitude, but it may be promising to explain a phase difference in the multiples of 45°. Because the effect of the wall friction in Eq. (95) in Ref. 6 is expressed in the form of the derivative of three half-order with respect to the time, the factor $i^{3/2}$ $(=e^{3i\pi/4})$ appears, which yields the phase difference by 45°. In fact, a tendency for this deviation is seen in Figs. 9(b) and 10(b) but is not conclusive yet.

The origin may also be attributed to the jet loss taken in the semi-empirical form. The present model does not take account of asymmetry in the jet loss with respect to the direction of flow in the throat. Physically there should be some difference between the jet loss when the air flows from the tube into the small cavity and the one when it flows from the cavity into the tube. Such a difference has not been considered. Imagine that the value of the coefficient of the jet loss depends on the direction of the flow. Then the second harmonics would appear in the solutions of order ε^2 in addition to the odd harmonics for the symmetric jet loss [see Eq. (97) in Ref. 6]. Since the measured data correspond to the solutions including all order in ε, it is likely that the second harmonics due to the asymmetry might contaminate the ones of order ε predicted by the theory. But this is not beyond the speculation as well.

The theoretical framework on the basis of the assumptions (4) and $\delta_r = O(\varepsilon^2)$ is typical and essential to derivation of the amplitude equation (13). If this framework were modified or changed, a different but less typical situation would appear for the resonant excitation. In order to see better agreements of the second coefficient in the present framework, reduction of the values of δ_r and of D for the jet loss is necessary even at the cost of increase of the parameter value of Q.

VI. CONCLUSIONS

The validity of the weakly nonlinear theory for high-amplitude and shock-free oscillations of the air column in the tube with the array of Helmholtz resonators has been checked against the data measured in the experiments. By avoiding the harmonic resonances and evanescences and reducing the value of Q in the amplitude equation, higher harmonics have been suppressed significantly in spite of the presence of nonlinearity. In consequence, the pressure profile appears to be nearly sinusoidal and the curves of the frequency response become symmetric with respect to the peak without any bending just as in the linear case. It has resulted in the quantitatively good agreements with the one predicted by the theory up to the peak pressure of about 170 dB (SPL). In order to achieve shock-free, high-amplitude oscillations, the condition for a tube to be dissonant is necessary but not sufficient. On top of dissonance, it is crucial to guarantee how far harmonic resonances and evanescences can be avoided.

The agreements of the first Fourier coefficients for the pressure field in the tube and in the cavities endorse the validity of the underlying assumptions of the one-dimensional field averaged over the cross section of the main flow and the continuum approximation for the array of resonators. As the slight discrepancy in the frequency response occurs at the peak pressure of about 170 dB (SPL), the weakly nonlinear theory tends to break down near this level and beyond it. Perhaps effects of the acoustic streaming would be pronounced and the flow field would no longer be almost one-dimensional. In addition, the formation of the high-speed jets from the orifices would make the field very complicated. It is unknown yet whether or not these would

be responsible for the quantitative discprepancy in the second Fourier coefficients. In view of the good agreements of the frequency response, however, it may be concluded that the theory is valid and useful enough to provide guidelines in designing accurately the array of Helmholtz resonators up to the present level of excitation.

ACKNOWLEDGMENTS

The authors acknowledge the assistance of H. Horimoto in doing the experiments. This work has been supported partially by the Grants-in-Aid from the Japan Society of Promotion of Science.

[1]C. C. Lawrenson, B. Lipkens, T. S. Lucas, D. K. Perkins, and T. W. van Doren, "Measurements of macrosonic standing waves in oscillating closed cavities," J. Acoust. Soc. Am. **104**, 623–636 (1998).
[2]Y. A. Ilinskii, B. Lipkens, T. S. Lucas, T. W. van Doren, and E. A. Zabolotskaya, "Nonlinear standing waves in an acoustical resonator," J. Acoust. Soc. Am. **104**, 2664–2674 (1998).
[3]N. Sugimoto, M. Masuda, T. Hashiguchi, and T. Doi, "Annihilation of shocks in forced oscillations of an air column in a closed tube," J. Acoust. Soc. Am. **110**, 2263–2266 (2001).
[4]M. A. Hossain, M. Kawahashi, M. Saito, and T. Fujioka, "Application of finite amplitude oscillation of air-column in closed tube to design acoustic compressor," Proceedings of the 18th International Congress on Acoustics, 2004, pp. I-381–384.
[5]A. B. Coppens and A. A. Atchley, "Nonlinear standing waves in cavities," in *Encyclopedia of Acoustics*, edited M. J. Crocker (Wiley, New York, 1997), Vol. **1**, pp. 237–247.
[6]N. Sugimoto, M. Masuda, and T. Hashiguchi, "Frequency response of nonlinear oscillations of air column in a tube with an array of Helmholtz resonators," J. Acoust. Soc. Am. **114**, 1772–1784 (2003).
[7]N. Sugimoto, M. Masuda, K. Yamashita, and H. Horimoto, "Verification of acoustic solitary waves," J. Fluid Mech. **504**, 271–299 (2004).

Re-radiation of acoustic waves from the A_0 wave on a submerged elastic shell[a)]

A. C. Ahyi, Hui Cao, and P. K. Raju
Department of Mechanical Engineering, Auburn University, Auburn, Alabama 36849-5341

Herbert Überall[b)]
Physics Department, Catholic University of America, Washington, DC 20064-0001

(Received 13 February 2003; accepted 2 December 2004)

We consider evacuated thin semi-infinite shells immersed in a fluid, which may be either of cylindrical shape with a hemispherical shell endcap, or formed two-dimensionally by semi-infinite parallel plates joined together by a semi-cylinder. The connected shell portions are joined in a manner to satisfy continuity but with a discontinuous radius of curvature. Acoustic waves are considered incident along the axis of symmetry (say the z axis) onto the curved portion of the shell, where they, at the critical angle of coincidence, generate Lamb and Stoneley-type waves in the shell. Computations were carried out using a code developed by Cao *et al.* [Chinese J. Acoust. **14**, 317 (1995)] and was used in order to computationally visualize the waves in the fluid that have been re-radiated by the shell waves a the critical angle. The frequency range was below that of the lowest Lamb wave, and only the A_0 wave (and partly the S_0 wave) was observed to re-radiate into the fluid under our assumptions. The results will be compared to experimental results in which the re-radiated waves are optically visualized by the Schardin–Cranz schlieren method. [DOI: 10.1121/1.1852548]

PACS numbers: 43.30.Jx, 43.40.Ey [ANN] Pages: 124–128

I. INTRODUCTION

The acoustical properties of thin submerged shells have been investigated for a number of years; see, e.g., the recent review by one of the present authors.[1] The large majority of these studies deals with regular shapes of shells such as infinite cylinders and spheres, although more general objects have also been considered.[2] Some French investigations (among others) concern finite-length cylindrical shells,[3,4] often terminated by hemispherical endcaps (this object being called ''la line'' in the French literature).

In the present investigation we deal with semi-infinite empty, water-immersed cylindrical shells capped by a hemispherical shell or, as closely related, the two-dimensional case of semi-infinite parallel plates joined together by a semi-cylindrical shell. (The connected shell portions are joined in a manner to satisfy continuity although with discontinuous curvature). An acoustic wave is considered axially incident onto the curved portion of the shell.

We adapted an existing computer program[5] that allows us to create visualizations of the acoustic field of an incident plane wave and its interaction with an elastic object, to the two-dimensional case of an evacuated, water-immersed endcapped shell as described above. The visualization illustrates the field rescattered from the object that is characteristic of the elastic material; it shows the clear result that the impact of the incident wave generates, at a critical angle of incidence, an elastic wave that is based in the shell and re-radiates back into the fluid. The type of elastic waves that can re-radiate have been shown to be analogous to those of submerged elastic plates,[1,6–8] and the corresponding terminology is used here also, namely, the Scholte–Stoneley wave (also called the A-wave), and the Lamb waves A_i and S_i ($i=0,1,2,...$, where A stands for antisymetric and S for symmetric relative to a free plate), A_0 and S_0 being interface waves, and A_j and S_j ($j \geqslant 1$) proper Lamb waves.[6] From the calculated dispersion curves of phase velocity vs frequency of these waves, we can show that our visualization corresponds to re-radiated A_0 waves. This wave begins at coincidence frequency and, due to its strong attenuation,[9] was found to be difficult to observe (both directly or via its circumferential resonances[1]), but its observation has recently been achieved[10,11] by optical visualization using the Schardin–Cranz schlieren method. [Other observations of the A_0 wave using different methods have also been carried out, e.g. by Ref. 12, where timing as well as amplitude data were used to verify the wave type. The broad nature of the associated resonances was also noted and analyzed.[9]] What was done by Ref. 10 in order to observe the A_0 wave is to do this immediately after it has been generated, due to its rapid decay. This is also the case in the present situation, where its re-radiation is visualized promptly after its creation.

II. NUMERICAL VISUALIZATION

The computer code of Ref. 5 was applied to the (two-dimensional) water-immersed, evacuated shell of Fig. 1, with the following geometrical parameters: r=outer radius of shell=14 cm, h=shell thickness=0.9 cm (6.4%), $(r-h)/r=0.936$, and material parameters: compressional wave speed $c_L=5000$ m/s, shear speed $c_T=3000$ m/s, shell density $\rho=4$ g/cm^3. This is an artificial material chosen for computational

[a)]Presented at the 142nd Meeting of the Acoustical Society of America, Fort Lauderdale, Florida, 3–7 December 2001.
[b)]Corresponding author; electronic mail: uberallh@msn.com

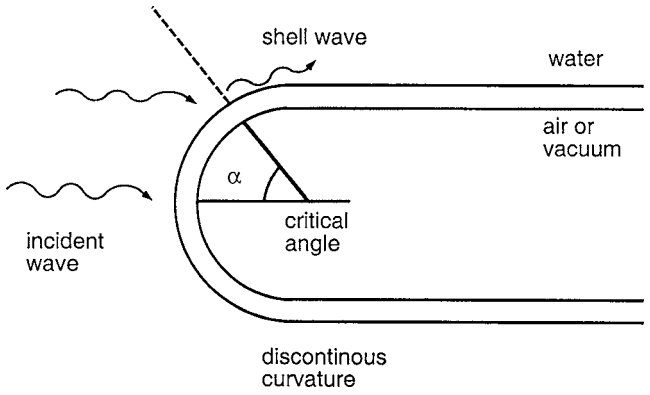

FIG. 1. Endcapped cylindrical shell, with an incident wave creating a shell wave at a critical angle.

convenience, but the material parameters are not vastly different from those of aluminum ($c_L^{\mathrm{Al}}=6400\,\mathrm{m/s}$, $c_T^{\mathrm{Al}}=3100\,\mathrm{m/s}$ and $\rho^{\mathrm{Al}}=2.78\,\mathrm{g/cm^3}$); but it is actually more like brass because the Poisson ratio 3/11 is less than 1/3. For the incident signal (a plane wave), a pulse was used as shown in Fig. 2; its spectrum is centered around 75 kHz.

The result of this calculation is shown in Fig. 3. The plane wave was incident from the left. The heavy vertical lines at the right edge of the figure represent the incident pulse wave front (which at the moment shown has progressed beyond the point of the juncture with the endcap; the timing of this snapshot is 130 μs from the time the incident wave had first hit the tip of the endcap). Comparing with the pulse in Fig. 2, the black bands are recognized as areas of negative pressure, accompanied by white regions of positive pressure. The heavy curved lines which join up with the incident pulse on the right, and which surround the entire graph towards the left, represent the pulse specularly reflected from the shell in its entirety. These are the features expected to be seen in this geometry. Furthermore, outgoing wave fronts from surface wave radiation on a circular surface are shown to diverge from a circular "virtual caustic."[13] Specifically, it is known that isolated wavefronts are the involutes of the circular virtual caustic. Also see Ref. 14. These features may serve to interpret the re-radiated waves in Fig. 3.

The substantial new feature in our visualization of Fig. 3 is a re-radiated pulse (both above and below the center line) which originates from a point on the shell located at an angle $\alpha=47°$ from the horizontal. This wave can be interpreted as the re-radiation, back into the water, from a shell wave generated at a critical angle α_c, the locus of its generation. It is determined unambiguously as the A_0 wave, by satisfying the Cremer rule[15] for the critical angle of the reradiation back into the water. Using calculated phase velocity curves of shell waves for such an analysis, it will be recognized that it is here the A_0 wave as generated in the shell that is responsible for the visualized re-radiated wave, as will be shown in the following section. It can be seen there that, since the A_0 speed surpasses the sound speed in water, the A_0 wave fronts begin pulling ahead of the incident wave. This can be seen also in our experimental figure (Fig. 8, later).

III. ANALYSIS OF VISUALIZED RE-RADIATION

In order to apply Cremer's coincidence condition to a determination of the critical angle of generation of the shell wave whose re-radiation is being visualized, it is necessary to calculate the phase velocities vs frequency (dispersion curves) of the shell waves that can intervene here. We may

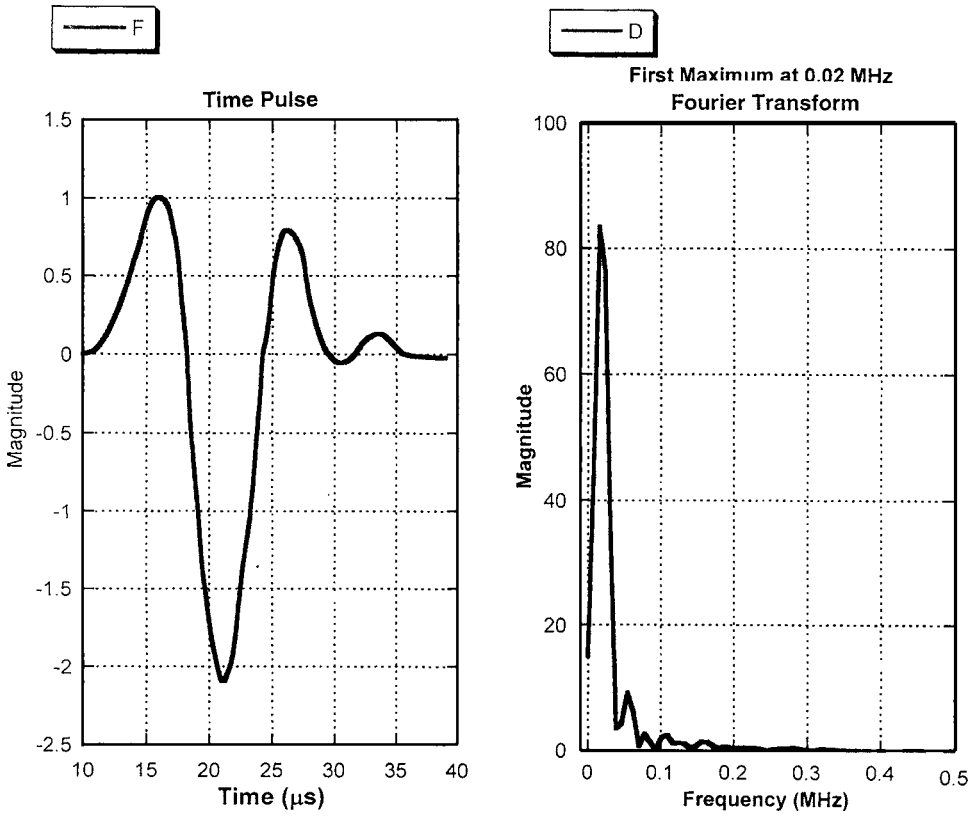

FIG. 2. Assumed form of incident pulse.

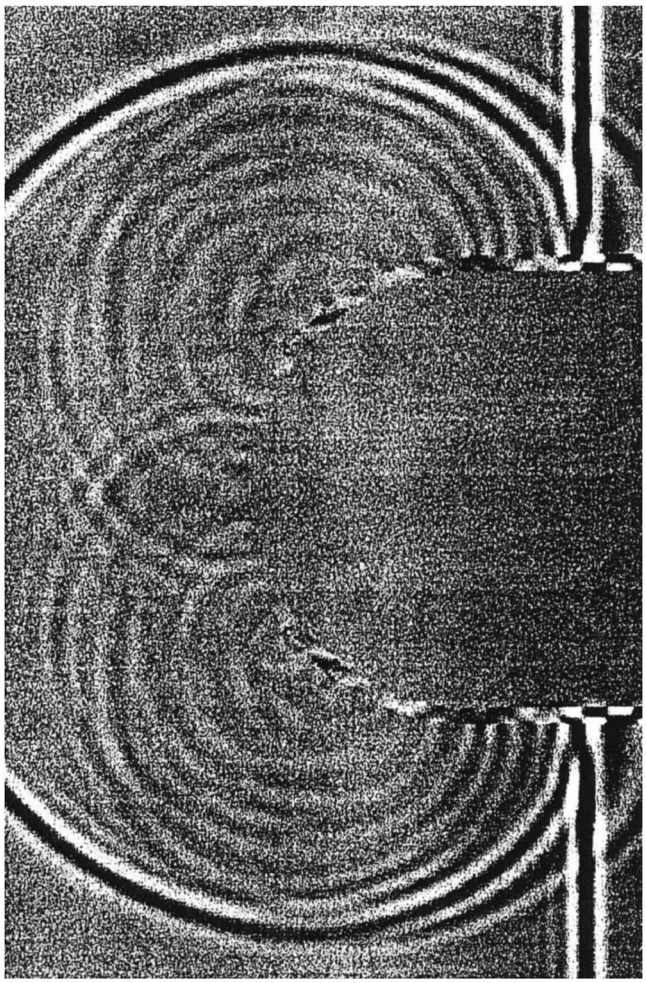

FIG. 3. Computational visualization of plane-wave pulse incident on the shell of Fig. 1, with the reflected pulse and re-radiation from the shell wave.

already state that only the A_0 wave was found to satisfy Cremer's condition leading to the observed critical angle of $\alpha_c = 47°$. This shows that the method utilized here can serve to pinpoint the type of shell wave that is responsible for the observed re-radiation effects.

As to the shell waves that may be considered here, it should be realized that for thin (<10% thick) metal shells (Al, steel...) of fairly slight curvature, the dispersion curves

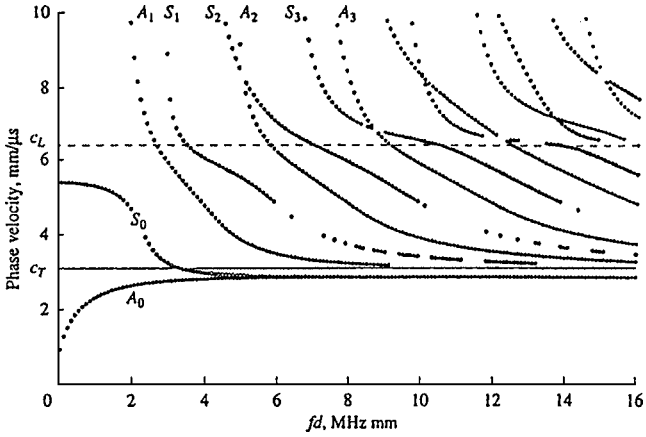

FIG. 4. Lamb wave dispersion curves on a free Al plate of thickness d (from Ref. 6).

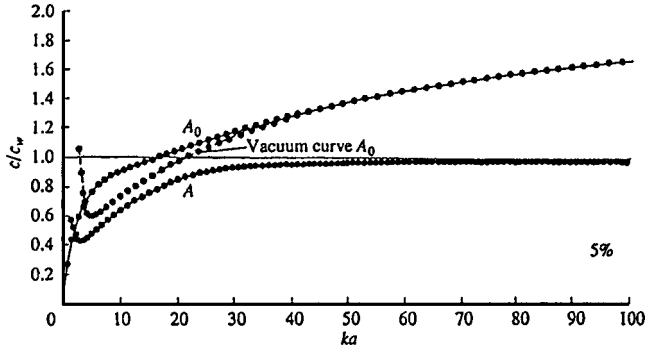

FIG. 5. The A_0 and A wave phase velocity dispersion curves for a 5% thick spherical aluminum shell in water, and of the A_0 wave for a shell in vacuum (from Ref. 6).

differ very little between those of waves on cylindrical or spherical shells or those on plates,[1] so that any of these can be utilized in a semi-quantitative fashion, although it should be realized that for the 6.4% thick shell considered here, some higher-order but non-negligible differences may occur; this is described in Ref. 16. Figure 4 presents, for illustration purposes, the Lamb wave dispersion curves on a free aluminum plate.[6] The only difference is created when the plate (or shell) is fluid-loaded on one or both sides;[17] if on one side, Fig. 5 shows that an additional wave A (the Scholte–Stoneley wave) is present which interacts with the A_0 wave.[6] This latter figure refers to a 5% thick spherical Al shell[18] (water-immersed and evacuated), and is shown here for illustration purposes. The upturn of the A wave at low frequencies (or of the A_0 wave for the sphere in vacuum; both upturning curves being shell-borne waves in the low-frequency region[1,6]) provides a measure, on the frequency scale, for the similarity of plate or curved-shell dispersion curves since the upturn is characteristic for the geometry of the sphere only. It should be noted that this upturn at low frequencies does not let these curves tend to infinity, since it was shown[19] that at even smaller frequencies down to zero, the upturning curves turn down again and tend towards zero at zero frequency.

We here need calculated dispersion curves for the material of the shell (quoted above) on which Fig. 3 is based.

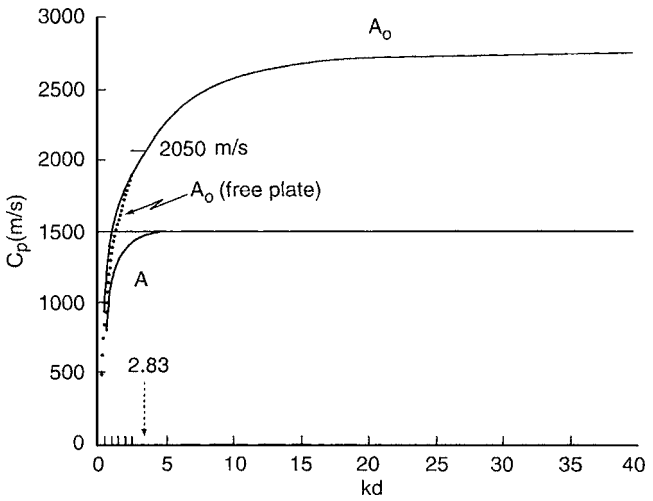

FIG. 6. Dispersion curves of A_0 and A waves for a shell with material parameters given at the beginning of Sec. II.

These are shown in Fig. 6 (A_0 and A for the water-loaded plate and A_0 for the free plate, sufficient for our purposes as stated above), for phase velocities of the shell curves termed c_s. If α is the angle of incidence of the incoming plane wave with the shell surface (measured from the shell normal, this being the same as the angle α in Fig. 1) then $c_{\mathrm{tr}}=c_w/\sin\alpha$ (c_w=sound speed in the ambient water) and the coincidence condition reads $c_{\mathrm{tr}}=c_s$. Using $c_w=1500$ m/s, we have $c_s=2050$ m/s for the shell-wave phase velocity at $\alpha=47°$ (critical angle as read off from Fig. 3). For the A_0 wave, from Fig. 6, this happens at $kd=2.83$ ($k=\omega/c_w$, d=plate thickness =0.9 cm), i.e., at a frequency $f=75$ kHz, which corresponds exactly to the frequency of the spectral maximum of the pulse of Fig. 2 used in the numerical calculation that led to Fig. 3. Needless to say that neither the A wave (Fig. 6) nor the other Lamb waves (Fig. 4) can possibly be involved as causal agents of the re-radiating shell wave generated at the critical angle $\alpha_c=47°$ as it appears in Fig. 3. In fact, as a function of frequency the A_0 wave first appears at coincidence frequency where its phase velocity surpasses the sound speed in water (see Fig. 6), where the A wave weakens and disappears. Our results thus constitute a visualization of the A_0 shell wave (by its re-radiation), similar to the experimental procedure of Refs. 10 and 11. This visualization has been possible in both cases due to the fact that (a) the A_0 wave was observed immediately after its generation, and (b) it got visualized due to its intense re-radiation into the ambient fluid. It is, incidentally, this intense radiation (and rapid intensity decay) which caused it not to form any narrow resonances upon successive circumnavigations of a closed shell,[9] and which previous to the experimental study of Ref. 10 has prevented its detection by experimental means.[1] Prior to this work and that of Ref. 9 earlier attempts to observe the A_0 wave failed because they did not compensate for the rapid decay in time.

The results of our numerical calculation will be complemented here by a visualization similar to that of Fig. 3, but extending further up along the semi-infinitely extended part of the scattering object, much beyond the juncture point with the endcap (Fig. 7). The timing of this snapshot is 60 μs from the time the incident wave had first hit the tip of the end cap. The greater contrast of this figure makes it possible to also visualize a weaker, but very rapidly advancing wave that has far overtaken the incident wave at this point in time, and exhibits a wave front that lies almost tangent to the cylinder surface. A similar analysis as that which led to the previous identification of the A_0 wave, now shows that this weak but fast wave can be ascribed to the S_0 shell wave as generated by the incident pulse. Its dispersion curve, illustrated in Fig. 4, shows its indicated rapid speed, both phase speed as well as its group velocity which, due to the relatively flat portion of the phase velocity in the region of interest, substantially coincides with the group speed. Indeed, at this point both the S_0-wave phase and group velocity equal the plate velocity, which is about three times faster than the A_0 wave at the frequency studied. Due to its high Q value, it rings for a long time, but with a weak amplitude. The group velocity of the S_0 wave at the present 75 kHz is $v_g=5360$ m/s, hence the tilt

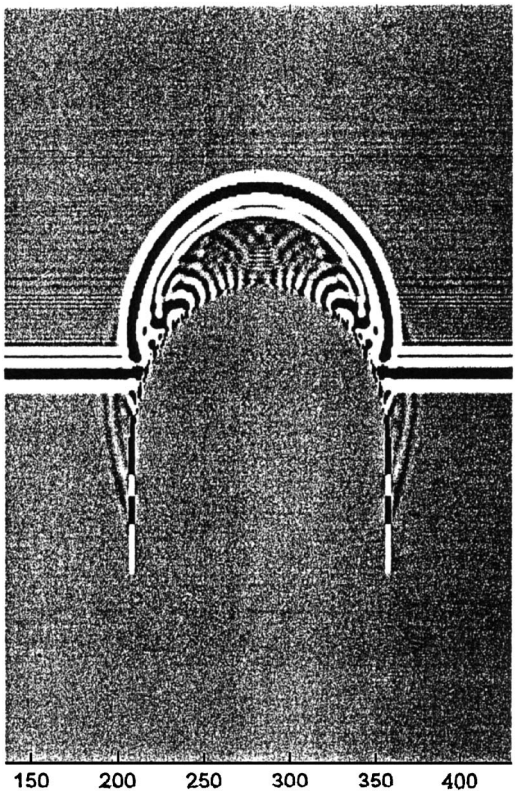

FIG. 7. Similar to Fig. 3 but at a somewhat earlier time; the S_0 wave is also visible here.

of the re-radiation from it is 16.3° which agrees with the visible wavefront in Fig. 7.

IV. ILLUSTRATIONS OF OPTICAL VISUALIZATION

Optical visualization of sound pulses interacting with a (3-dimensional) hemispherically-endcapped evacuated, water-immersed cylindrical glass shell have been carried out at Auburn University, using the Schardin–Cranz schlieren method and extending the work of Refs. 10 and 11. We illustrate preliminary results of ongoing investigations in Fig. 8, which shows an incident wave emanating from a point source, leading to a reflected wave and also exhibiting the A_0 wave reradiation similarly to Ref. 10, and to Figs. 3 and 7. The geometries in Fig. 8 indicate a group velocity to this A_0 wave of about 1950 m/s, which can reasonably be expected. However, the experimental resolution is here not sensitive enough to also visualize the very rapid S_0 wave which was visible in Fig. 7.

V. SUMMARY

We have presented a numerical visualization of acoustic scattering from a water-immersed, evacuated thin semi-infinite shell carrying an endcap, towards which a plane-wave pulse is incident. While these results showed the incident and specularly-reflected pulses as expected, they also indicated the generation of, and its re-radiation from, a shell-borne wave at a critical angle determined by Cremer's coincidence condition. A comparison with calculated shell-wave dispersion curves identified this shell-borne wave as the A_0 wave, the present analysis thus constituting (Fig. 3) a nu-

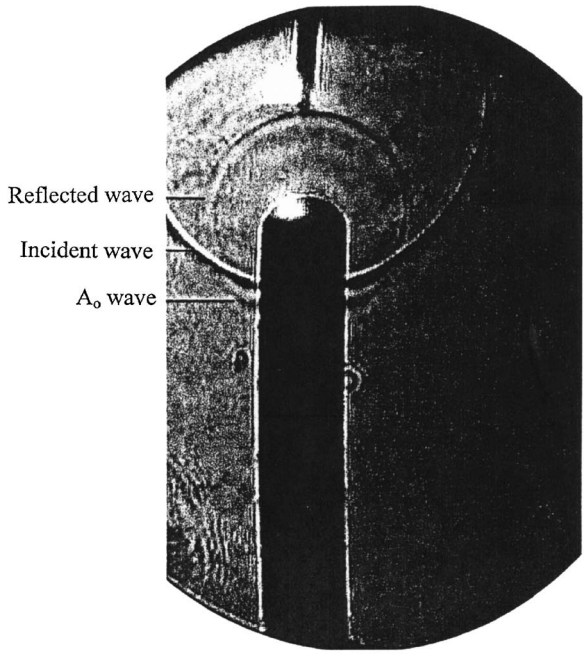

FIG. 8. Optical visualization of incidence and reflection from a glass tube, also showing re-radiation from an A_0 wave.

merical visualization of the acoustic generation of the A_0 wave, in addition to the preceding experimental demonstration of this shell wave by optical visualization.[10,11] This is significant since earlier experimental attempts to observe the generation of the A_0 wave had been unsuccessful.[1] In addition, we could also numerically visualize the generation of the S_0 wave (Fig. 7) which, however, had already been seen in previous experiments.[1] The experimental results shown here satisfy the objectives of the present investigation, and are supported by our numerical predictions. As discussed in Sec. IV, they are of a preliminary nature at this time, and shall be more fully reported in due course.

[1] H. Überall, "Acoustics of shells," Akust. Zh. **47**, 149–177 (2001) (in Russian). [English translation: Acoust. Phys. **47**, 115–139 (2001)].
[2] L. M. Lyamshev, "Nonspecular reflection, resonance scattering and radiation of sound by plates and shells in water," Acoust. Phys. **45**, 619–642 (1999).
[3] G. Maze, F. Lecroq, D. Décultot, J. Ripoche, S. K. Numrich, and H. Überall, "Acoustic scattering from finite cylindrical elastic objects," J. Acoust. Soc. Am. **90**, 3271–3278 (1991).
[4] X. L. Bao, H. Überall, J. Niemiec, D. Décultot, F. Lecroq, G. Maze, and J. Ripoche, "The resonances of finite-length elastic cylinders and elastic spheroids excited by sound scattering," J. Acoust. Soc. Am. **102**, 49–54 (1997).
[5] H. Cao, V. F. Humphrey, and H. O. Berktay, "Sound pulse scattering from an edge of thick elastic plates: experimental and numerical investigations," Chin. J. Acoust. Soc. **14**, 317–329 (1995).
[6] H. Überall, B. Hosten, M. Deschamps, and A. Gérard, "Repulsion of phase velocity dispersion curves and the nature of plate vibrations," J. Acoust. Soc. Am. **96**, 908–917 (1994).
[7] M. F. Werby and H. Überall, "The analysis and interpretation of some special properties of higher-order symmetric Lamb waves: The case for plates," J. Acoust. Soc. Am. **111**, 2686–2691 (2002).
[8] M. F. Werby and H. Überall, "A systematic study of water-filled submerged elastic spherical shells and the resolution of elastic- and water-included resonances," J. Acoust. Soc. Am. **112**, 896–905 (2002).
[9] M. Talmant, H. Überall, R. D. Miller, M. F. Werby, and J. W. Dickey, "Lamb waves and fluid-borne waves on water-loaded thin spherical shells," J. Acoust. Soc. Am. **86**, 278–289 (1989).
[10] A. C. Ahyi, P. Pernod, O. Gatti, V. Latard, A. Merlen, and H. Überall, "Experimental demonstration of the Pseudo-Rayleigh (A_0) wave," J. Acoust. Soc. Am. **104**, 2727–2732 (1998).
[11] A. Ahyi, P. Pernod, V. Latard, and A. Merlen, "Diffraction d'une impulsion acoustique par un tube et une cible de type Line immergés," *Proceedings of the 4th Congress on Acoustics*, French Acoustic Society, Marseilles, France, 1997, pp. 789–792.
[12] S. G. Kargl and P. L. Marston, "Observations and modeling of the backscattering of short tone bursts from a spherical shell: Lamb wave echoes, Glory, and axial reverberations," J. Acoust. Soc. Am. **85**, 1014–1028 (1989).
[13] P. L. Marston, "Quantitative ray methods for scattering," in *Encyclopedia of Acoustics*, edited by M. J. Crocker (Wiley, New York, 1997), pp. 483–492.
[14] W. G. Neubauer, "Pulsed circumferential waves on aluminum cylinders in water," J. Acoust. Soc. Am. **45**, 1134–1144 (1969).
[15] L. M. Brekhovskikh, *Waves in Layered Media*, 1st ed. (Academic, New York, 1960).
[16] P. L. Marston, "Phase velocity of Lamb waves on a spherical shell: Approximate dependence on curvature from kinematics," J. Acoust. Soc. Am. **85**, 2663–2665 (1989).
[17] J. P. Sessarego, J. Sageloli, C. Gazanhes, and H. Überall, "Two Scholte–Stoneley waves on doubly fluid-loaded plates and shells," J. Acoust. Soc. Am. **101**, 135–142 (1997).
[18] G. S. Sammelmann, D. H. Trivett, and R. H. Hackman, "The acoustic scattering by a submerged spherical shell I." J. Acoust. Soc. Am. **85**, 114–124 (1989).
[19] G. Kaduchak, C. S. Kwiatkowski, and P. L. Marston, "Measurement and interpretation of the impulse response for backscattering by a thin spherical shell using a broad-band width source that is nearly acoustically transparent," J. Acoust. Soc. Am. **97**, 2699–2708 (1995).

On the relationship between signal bandwidth and frequency correlation for ocean surface forward scattered signals[a)]

R. Lee Culver[b)] and David L. Bradley
Applied Research Laboratory and Graduate Program in Acoustics, The Pennsylvania State University, State College, Pennsylvania 16801

(Received 21 June 2004; revised 18 March 2005; accepted 26 March 2005)

The relationship between the bandwidth of a signal and the correlation of that signal with its ocean surface reflected arrival, a quantity we term *frequency correlation*, has been investigated experimentally and compared with two theories. Decorrelation of wideband surface scattered signals is a direct consequence of time spread. The acoustic measurement utilized a very short pure tone signal, from which time spread has been estimated, and four broadband signals with different bandwidths, for which correlation with the transmitted signal has been measured. An environment-driven model developed by Dahl was used to predict time spread, which agreed favorably with our time spread measurements. The model was also employed in two theories that predict frequency correlation. The first, a theory published by Reeves in 1974, is based upon the ratio of signal temporal resolution to total time spread. This theory compared well with our measurements for 1 kHz bandwidth signals, but is not applicable for signal bandwidths greater than about 2 kHz. The second, a theory developed by Ziomek, models ocean acoustic propagation as transmission through a linear system. This theory agreed well with our frequency correlation measurements for signal bandwidths of 1–22 kHz.
[DOI: 10.1121/1.1914266]

PACS numbers: 43.30.Hw, 43.30.Re, 43.30.Zk, 43.30.Pc [DRD] Pages: 129–138

I. INTRODUCTION

There have been widespread efforts in recent years to increase the bandwidth of sonar systems and components (e.g., transducers) in an effort to improve system performance against noise or interference. [For example, see the presentation by D. H. Johnson entitiled ''Littoral ASW FNC Overtiew,'' Proceedings of the Office of Naval Research: Ocean, Atmosphere and Space Uncertainty Department Research Initiative (DRI) Review, June 19-20, 2002, Scripps Institution of Oceanography, San Diego, CA, available at http://www.onr.navy.mil/sci_tech/ocean/321_sensing/cuwg/proceedings.asp.] A relevant question therefore is ''How much bandwidth will an ocean acoustic channel accommodate before frequency-dependent effects begin to degrade coherent processing?'' This paper addresses that question for acoustic signals that have been forward-scattered by the ocean surface.

Fortuin[1] and Ogilvy[2] have provided insightful overviews of early ocean surface scattering research that focused on understanding how the mean forward scattered energy varied with sea state, grazing angle, and frequency. More recently, significant progress has been made toward understanding the effects of changes in receive array geometry and the sea surface environment, or the *spatial coherence* of the forward scattered field, in order to understand the limits of acoustic array performance.[3] The focus of our research is on how the structure of the forward scattered signal is affected by signal bandwidth, referred to as *frequency correlation*, to determine the limits of broadband sonar performance.

The term *correlation* has been used in a number of different circumstances, so for clarity we define our use of this term. Consistent with Bendat and Piersol,[4] the term *correlation* in this paper refers to the operation

$$RC(l,\beta)=\left\langle \int_0^T y(t+l)x^*(t)dt \right\rangle, \tag{1}$$

where $y(t)$ is the received signal, $x(t)$ is usually related to the transmitted signal, and T and β are the duration and bandwidth, respectively, of the transmitted signal. Also, t is time, l is the time lag between $y(t)$ and the time of signal transmit, and $\langle\ \rangle$ indicates an ensemble average (our use of the term *ensemble average* is also consistent with Bendat and Piersol). We use the notation $RC(l,\beta)$ for correlation because $x(t)$ will be a replica of the transmitted signal and we will refer to Eq. (1) as *replica correlation* in this paper. Also, we will use the subscript β with $x(t)$ and $y(t)$ to be explicit about the bandwidth of those signals.

In this paper, the term *correlation coefficient* refers to the correlation normalized by the square root of the energies in $x(t)$ and $y(t)$ over a duration T:

$$\rho(l,\beta)=\left\langle \frac{\int_0^T y(t+l)x^*(t)dt}{[\int_0^T|y(t+l)|^2dt]^{1/2}[\int_0^T|x(t)|^2dt]^{1/2}} \right\rangle. \tag{2}$$

The value of $\rho(l,\beta)$ must be between -1 and 1. We will use the term *frequency correlation coefficient*, or sometimes sim-

[a)]Portions of this work were presented at the High Frequency Ocean Acoustics Conference, San Diego, CA, 2–5 March 2004.
[b)]Electronic mail: rlc5@psu.edu

ply *frequency correlation*, to refer to the dependence of $\rho(l,\beta)$ on signal bandwidth β.

We will make use of a model developed by Dahl[5–7] for the bistatic scattering cross section of the ocean surface. The model can be used to compute the intensity impulse response function $I_{\text{imp}}(\tau)$, which characterizes how surface scattering spreads the signal in time. The intensity impulse function can be convolved with the envelope of the transmit pulse to produce the ensemble-averaged intensity of a pulse that has been forward scattered from the sea surface. This average intensity is called the *time spread*. Using $I_{\text{imp}}(\tau)$, Dahl defines a *characteristic time spread* for the sea-surface bounce path

$$L=\frac{[\int_0^\infty I_{\text{imp}}(\tau)d\tau]^2}{\int_0^\infty I_{\text{imp}}^2(\tau)d\tau}\ \text{s}, \tag{3}$$

which provides "a measure of the energy-containing region of support" for $I_{\text{imp}}(\tau)$. Further, he predicts that the inverse of the characteristic time spread, L^{-1}, with units of cycles/s (Hz), provides "a measure ... of the *frequency coherence bandwidth* associated with the sea-surface bounce channel." Dahl has calculated L^{-1} for a number of environmental circumstances, and in this paper we compute L^{-1} for our data and compare it with our frequency correlation measurements.

In Sec. II, we briefly review a theory published by Reeves[8] that relates frequency correlation to the fraction of ocean surface facets that contribute to the time spread during the temporal resolution of the transmitted signal, with facet contributions weighted by a Gaussian distribution of surface slopes. We apply the theory using $I_{\text{imp}}(\tau)$ as the sum of weighted facet contributions. We then develop a second theory by modeling acoustic propagation through the ocean as a linear, time and space varying system. Linear system theory is shown to predict that frequency correlation is the integrated product of the Fourier transform of $I_{\text{imp}}(\tau)$ and a frequency domain version of the signal ambiguity function.

In Sec. III we describe our environmental and acoustic measurements. We then focus on one segment of the acoustic data and a single projector-hydrophone pair, and calculate $I_{\text{imp}}(\tau)$ for our measurement frequencies. We compare our measurements of time spread, which are ~300 ping ensemble averages, with time spread estimates obtained by convolving $I_{\text{imp}}(\tau)$ with the signal envelope and find good agreement. Next we compare our measurements of frequency correlation, which are derived from ~300 ping ensemble averages of the peak correlation coefficient for different bandwidth signals, with theoretical predictions for frequency correlation made using $I_{\text{imp}}(\tau)$ and the two theories discussed above. The comparison is discussed in Secs. IV and V. We show that the theory published by Reeves compares favorably with our measurements for 1 kHz bandwidth signals, and that the prediction derived from linear systems theory matches our measurements quite well for all signal bandwidths considered, up to 22 kHz.

II. THEORIES PREDICTING FREQUENCY CORRELATION

We begin with a theory published by Reeves in 1974 that relates the decorrelation of an ocean surface forward scattered arrival to the bandwidth of the signal.[8] That theory was based upon the *time spread* of an acoustic signal caused by scattering from multiple facets at or near the ocean surface. Drawing upon earlier work by Martin[9] and Weston,[10] Reeves related frequency correlation to the fractional number of sea surface facets which contribute to the received signal during an interval corresponding to the temporal resolution of the signal. Based upon optical glitter measurements by Cox and Munk,[11] Reeves assumed a Gaussian distribution of ocean surface slopes, and his model weighted the contribution of each facet by the probability associated with the slope required for that facet to reflect sound toward the receiver. The sum of all contributions, N_T, is proportional to the total temporal elongation of the received signal. The sum of the contributions that occur during the interval corresponding to the signal temporal resolution, $1/\beta$, is denoted N, and the frequency correlation estimate is taken as the ratio N/N_T. The theory thus predicted that increasing bandwidth (which decreases temporal resolution and lowers N) results in decreased correlation. In Ref. 8, Reeves shows that the signal resolution to total temporal elongation ratio (henceforth referred to as SIRTER) theory compared favorably with correlation measurements for signal bandwidths up to 2 kHz, which was the maximum bandwidth attainable with equipment available in the early 1970s.

We move now to a second theoretical approach, which draws upon linear systems theory to predict frequency correlation from the spreading of the signal in time. Ziomek[12,13] draws upon three decades of radar and sonar signal processing work[14–25] to characterize "the ocean medium (in general) as a *linear, time-variant, space-variant, random filter*." The filter *transfer function* $H(f,t)$ depends on frequency and can vary with time, and the *transfer function correlation*

$$R_H(\Delta f,\Delta t)=E\left|H(f,t)H^*(f+\Delta f,t+\Delta t)\right| \tag{4}$$

describes how ocean surface scattering decorrelates the envelopes of signals separated in time Δt and/or frequency Δf. It is the width of $R_H(\Delta f,\Delta t)$ in Δf that determines frequency correlation, while the width in Δt determines the temporal correlation. If $R_H(\Delta f,\Delta t)$ is broad in Δf, broadband signals will suffer minimal decorrelation; if $R_H(\Delta f,\Delta t)$ is narrow in Δf, correlation will drop off rapidly as signal bandwidth is increased. We now review the linear systems equations that lead up to Eq. (4).

Given a source and receiver, the transmitted signal $x(t)$ and the received signal $y(t)$ are related through convolution with the linear time varying *impulse response function* $h(\tau;t)$ or its Fourier transform with respect to t, the *spreading function* $S(\tau;\phi)$:

$$\begin{aligned} y(t)&=\int x(t-\tau)h(\tau;t)d\tau \\ &=\int\int x(t-\tau)S(\tau;\phi)\exp(j2\pi\phi t)d\tau d\phi. \end{aligned} \tag{5}$$

Here t is absolute time, τ is delay time (or time since transmit), and ϕ is the rate of change of the impulse response in hertz.[13] In Eq. (5), the source directionality and receiver spatial response have been absorbed into $h(\tau;t)$ and $S(\tau;\phi)$. Since the ocean surface is a random distribution of scatterers, the impulse response and the spreading functions are likewise random. From Eq. (5), the mean square received signal is

$$\begin{aligned} E\{|y(t)|^2\} &= \int\int\int\int x(t-\tau)x^*(t-\tau')\exp[j2\pi(\phi \\ &\quad -\phi')t]E\{S(\tau;\phi)S^*(\tau';\phi')\}d\phi d\tau d\phi' d\tau' \\ &= \int\int\int\int x(t-\tau)x^*(t-\tau')\exp[j2\pi(\phi \\ &\quad -\phi')t]R_s(\tau,\tau';\phi,\phi')d\phi d\tau d\phi' d\tau' \\ &= \int\int |x(t-\tau)|^2 R_s(\tau,\phi)d\phi d\tau. \end{aligned} \tag{6}$$

To write the last line of Eq. (6) and obtain mathematically tractable results, we have assumed that the spreading function $S(\tau,\phi)$ is *uncorrelated* with $S(\tau',\phi')$ for all values of $\tau \neq \tau'$ and $\phi \neq \phi'$. Then $R_s(\tau,\phi) \equiv E\{|S(\tau;\phi)|^2\}$ is the *scattering function*, which describes the average amount of spread that an input signal's power will undergo as a function of time delay τ and frequency ϕ. As expressed by Ziomek,[13] "the condition of uncorrelated spreading in time delay τ ... [and] frequency ϕ ... is equivalent to a condition of wide-sense stationarity in ... frequency Δf ... [and] time Δt..., respectively." This is referred to as the *wide-sense stationary uncorrelated spreading (WSSUS)* condition. The wide-sense stationary assumption means that the scattering process depends only upon Δt and Δf and not on the absolute values of t or f. For the ocean surface, this seems reasonable for periods of at least several minutes and modest bandwidths. The physical meaning of uncorrelated scattering in τ and ϕ is that scattering from different patches of the surface or bubbles, which contribute to the scattering function for different values of τ and ϕ, is, on average, uncorrelated $(E\{S(\tau;\phi)S^*(\tau';\phi')\} = R_s(\tau;\phi)\,\delta(\tau-\tau')\,\delta(\phi-\phi'))$. This is not an unreasonable assumption since the scattering patches are physically separate areas of the ocean surface.

We can integrate over frequency ϕ on the right-hand side of Eq. (6), and from the definition of $I_{\text{imp}}(\tau)$ given in the introduction above, it must be equal to that integral:

$$I_{\text{imp}}(\tau) = \int R_s(\tau,\phi)d\phi. \tag{7}$$

The spectrum of the transmitted signal is

$$X(f) = \int x(t)\exp(-j2\pi ft)dt \tag{8}$$

and the acoustic path *transfer function* is[13]

$$H(f,t) = \int h(\tau,t)\exp(-j2\pi f\tau)d\tau. \tag{9}$$

Using the transmitted signal as the replica in Eq. (1), the *replica correlator output* can be written in terms of the spectrum $X(f)$ and the channel transfer function:

$$\begin{aligned} RC(l,\beta) = \Big\langle \int\int\int H(f,t)X_\beta(f)X_\beta^*(g)\exp(j2\pi ft) \\ \times\exp(-j2\pi g(t-l))df\,dg\,dt \Big\rangle, \end{aligned} \tag{10}$$

where g and f are frequencies in the transmitted signal spectrum and β is the bandwidth of the transmitted signal. Under WSSUS conditions, and using Eq. (4), the peak of the mean square replica correlator output is

$$|RC(\beta)|^2_{\text{peak}} = \int\int R_H(\Delta f,\Delta t)|\Gamma_\beta(\Delta f,\Delta t)|^2 d\Delta f d\Delta t, \tag{11}$$

where Δf and Δt are frequency and time separations, respectively, and we have introduced the *spectral ambiguity function (SAF)*,

$$\Gamma_\beta(\Delta f,\Delta t) \equiv \int X_\beta(f)X_\beta^*(f+\Delta f)\exp(-j2\pi f\Delta t)df, \tag{12}$$

which describes the fundamental resolution of the signal in frequency and time. We can normalize the signal spectrum such that $|\Gamma_\beta(\Delta f,\Delta t)|^2$ integrates to unity, and scale $R_H(\Delta f,\Delta t)$ to unity at the origin $(\Delta f = \Delta t = 0)$. Under these conditions, Eq. (11) approaches unity as the SAF approaches the delta function product $\delta(\Delta f)\cdot\delta(\Delta t)$ and thus provides a means of predicting the correlation coefficient for comparison with received signals that have been processed according to Eq. (2).

Notice that the operation indicated by Eq. (11) amounts to multiplying $|\Gamma_\beta(\Delta f,\Delta t)|^2$ times $R_H(\Delta f,\Delta t)$ and integrating over all Δf and Δt. For the sake of illustration, take $R_H(\Delta f,\Delta t)$ to be rectangular in shape and constant over some band B, and take $\Gamma_\beta(\Delta f,\Delta t)$ to be broad in Δf but to be very narrow in Δt, approaching $\delta(\Delta t)$. Then the integral of Eq. (11) will be unity as long as the width of $|\Gamma_\beta(\Delta f,\Delta t)|^2$ is less than or equal to B, in which case we could say that signal bandwidth is less than channel bandwidth. However, if the width of $|\Gamma_\beta(\Delta f,\Delta t)|^2$ is greater than B, the result of the integral will be less than unity, and we could say that the signal bandwidth is now greater than the channel bandwidth. This is a key to understanding the linear systems theory based predictions, as well as the SIRTER model. Note that this illustration does not apply if $|\Gamma_\beta(\Delta f,\Delta t)|^2$ has sufficient extent in Δt such that the temporal decorrelation due to the nonzero width of $R_H(\Delta f,\Delta t)$ in Δt would occur.

From linear system theory and under WSSUS conditions, the transfer function correlation $R_H(\Delta f,\Delta t)$ can be calculated by Fourier transforming the scattering function[13]

$$\begin{aligned} R_H(\Delta f,\Delta t) = \int\int R_S(\tau,\phi)\exp(j2\pi(\phi\Delta t \\ -\Delta f\tau))d\tau\,d\phi. \end{aligned} \tag{13}$$

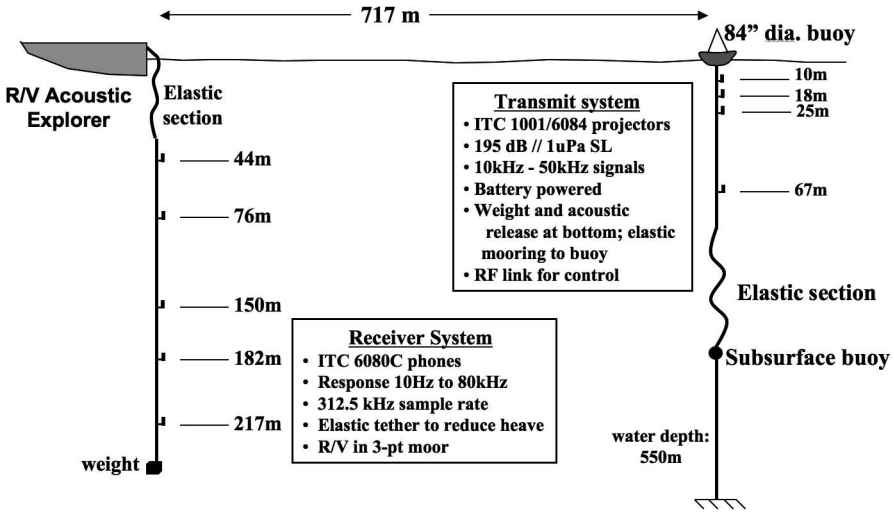

FIG. 1. Measurement geometry, August 2002, 2500 m east of San Clemente Island, CA. Projectors were suspended from a bottom-moored surface buoy using an elastic section to reduce the watch circle. Receive hydrophones were suspended from the R/V Acoustic Explorer in a 3-pt moor.

The variable bandwidth signals used in our frequency correlation measurement were all 10 ms or less in duration, so that like the above-noted illustration, the spectral ambiguity function is broad in Δf and narrow in Δt. This means that to utilize Eq. (11), we only need the transfer function correlation $R_H(\Delta f, \Delta t)$ at $\Delta t = 0$. This we obtain from Eq. (13), with $\Delta t = 0$, and with reference to Eq. (7), that

$$R_H(\Delta f, 0) = \int I_{\text{imp}}(\tau) \exp(-j2\pi \Delta f \tau) d\tau. \tag{14}$$

Equations (11), (12), and (14) constitute the linear systems-based method by which the frequency correlation can be predicted for short duration, wideband signals.

III. MEASUREMENTS OF TIME SPREAD AND FREQUENCY CORRELATION

An ocean acoustic measurement was conducted in August 2002 with the primary objective of measuring whether the direct and surface reflected paths become less correlated with the transmitted pulse when the signal bandwidth is increased. Ocean surface wave height directional spectra, wind speed and direction, ocean current, and sound speed versus depth were measured concurrently to investigate the physical mechanisms associated with signal decorrelation. The experiment location was 32° 38.2′N, 117° 57.4′W, which is about 2.5 km east of San Clemente Island and about 80 km west of San Diego, CA. Water depth was approximately 500 m.

A. Acoustic measurement instrumentation

The measurement geometry is shown in Fig. 1. Signals were transmitted from International Transducer Corporation (ITC) 1001 and 6084 acoustic projectors attached to the riser of a bottom-moored surface buoy. The buoy mooring included an elastic section composed of bungee cords that served to reduce the buoy watch circle to a few tens of meters. Transmit electronics were housed in the surface buoy. Inside the buoy, a computer controlled signal transmission in response to commands from the research vessel via 900 MHz and 2.4 GHz rf links. Marine batteries provided power for several days of continuous operation. Signals were generated at 250 k samples/s and amplified using an Instruments Inc. L6 power amplifier that was controlled via the remote interface. Only one projector was active at a time, with projector selection accomplished remotely.

Signals were received at ITC 6080C hydrophones suspended from the research vessel Acoustic Explorer, which was in a three-point moor. Elastic tethers were used to decouple the hydrophones from ship heave. Received signals were filtered and sampled at 312.5 k samples/s.

B. Environmental measurements

Figure 2 shows a sound speed profile calculated from a conductivity and temperature versus depth (CTD) drop made during the experiment. It shows a very shallow mixed layer and a strong downward refracting region to about 100 m; below, the water is approximately isothermal. A ray-trace made using the Comprehensive Acoustic System Simulation/Gaussian Ray Bundle (CASS/GRAB) acoustic propagation model[26] for the 67-m-deep projector and 217-m-deep receiver shows a slightly refracted direct path and a surface reflected path. For this projector-hydrophone pair, the difference in travel time between the direct and surface reflected paths is about 19 ms.

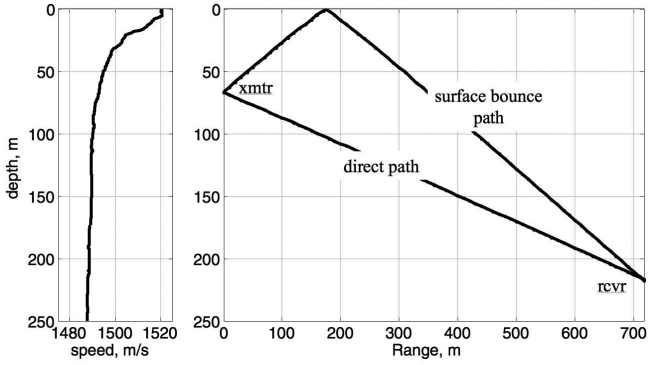

FIG. 2. Measured sound speed profile and ray trace between the 67-m-deep projector and 217-m-deep hydrophone. Direct and surface bounce paths are shown.

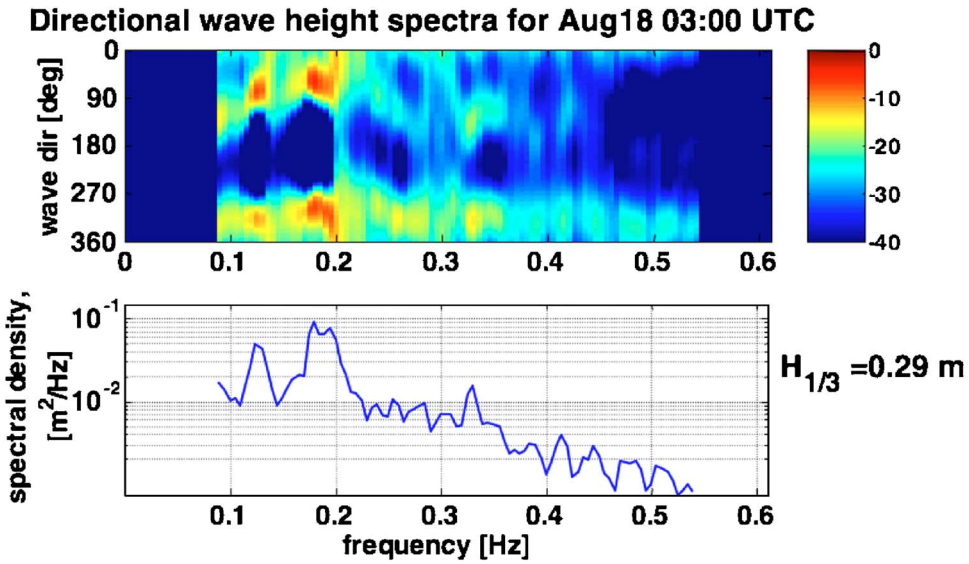

FIG. 3. (Color online) Upper panel: Directional wave height spectra recorded Aug 18 0300 UTC 2500 m east of Wilson Cove, San Clemente Island, CA. Lower panel: Directional spectra in the upper panel integrated over all wave directions. As discussed in the text, energy below about 0.085 Hz is an artifact caused by the total absence of swell, and has been removed from the data.

The measurement site was very much in the lee of San Clemente Island, which affected wind speed and direction and significantly reduced wave height and direction. The wind at the site of the experiment was from the north-northwest at 5–7 m/s while the measurements presented in this paper were made. However, a NOAA buoy west of San Clemente Island recorded higher winds and more from the west, confirming that the island was significantly affecting the wind at the experiment site.

Directional wave height spectra were measured during the experiment using an AXYS Technologies Triaxys wave rider buoy. Figure 3 shows average wave height measured at 0300 on 18 August, 2002 (UTC). The upper panel shows the distribution of surface wave height energy by frequency and direction of arrival, while the bottom panel shows the energy integrated over all directions. The surface waves came from the northwest and northeast. Significant wave height ($H_{1/3}$) was 0.29 m and rms wave height was less than 0.1 m, corresponding to sea state 0. Comparing wind speed and wave height measurements indicates significantly reduced fetch and significantly less than fully developed seas. The energy below about 0.085 Hz is an artifact.[27] The manufacturer has determined that low freq ($f<0.085$ Hz) interference can be introduced into the buoy data when LF energy is quite low (as in the complete absence of swell). No swell was present during the measurement, so we have presumed that the data are valid only for $f>0.085$ Hz. The upper frequency limit for the wave height spectrum is 0.54 Hz.

A surface wave height wave number spectrum is needed to provide the environmental input to Dahl's model. In forward scattering geometries, the spectrum must extend to ocean surface wave numbers of about $k/4$, where k is the acoustic wave number.[28,7] Using the method developed by Dahl,[6] and the wave height wave number spectrum model of Plant[29] (the "D" spectrum) which uses wind speed and fetch as inputs, the measured wave height spectrum was extended to frequencies well above those measured by the wave rider buoy. In applying Plant's model, a 4 km fetch was used because it is the approximate distance from the northwest end of San Clemente Island to the experiment site.

C. Acoustic measurements

The signals that were transmitted are identified in Table I. Two continuous wave (cw) pulses and four linear frequency modulated (LFM) pulses were transmitted at two different center frequencies. Note that the bandwidth of a cw pulse is approximately one over the pulse length. Each signal was transmitted from one projector at a time using a 10 Hz repetition rate for 30 s. The short cw signals were designed to estimate time spread. Figure 4 shows 300 short cw pulses transmitted from the 67-m-deep projector and received at the 217-m-deep hydrophone at about 0230 UTC on 18 Aug 2002. The received signals were match filtered to enhance signal-to-noise ratio. The vertical band in the left half of each panel is the direct path (DP) arrival; the second much wider vertical band, about 20 ms later, is the surface bounce (SB) arrival. Several features are evident. First, there is some jitter in the arrival times of both the DP and SB arrivals. This is due partly to relative movement between the projector and receiver but also to variation in the medium. Second, a fully refracted path may be seen just after the DP arrival. Third, the background level is about 10 dB lower in the 40 kHz band than in the 20 kHz band, and fourth, the DP arrival is sharp and distinct, but the SB arrival is composed of a first arrival corresponding to specular return followed by a series of arrivals extending for 8–10 ms. The arrivals that follow the specular return are termed *time spread*.

TABLE I. Signals transmitted at center frequencies of 20 kHz and 40 kHz.

Signal type	Duration	Bandwidth	Time-bandwidth product
CW pulse	0.14 ms[a]	7.0 kHz	1.0
CW pulse	1.0 ms	1.0 kHz	1.0
LFM	8.0 ms[b]	1.0 kHz	8
LFM	8.0 ms[b]	7.0 kHz	56
LFM	8.0 ms[b]	13.0 kHz	104
LFM	8.0 ms[b]	22.0 kHz	176

[a]Pulse length and bandwidth were 0.25 ms and 4.0 kHz for projector 4 only.
[b]Pulse length was 10.0 ms for projector 3 only.

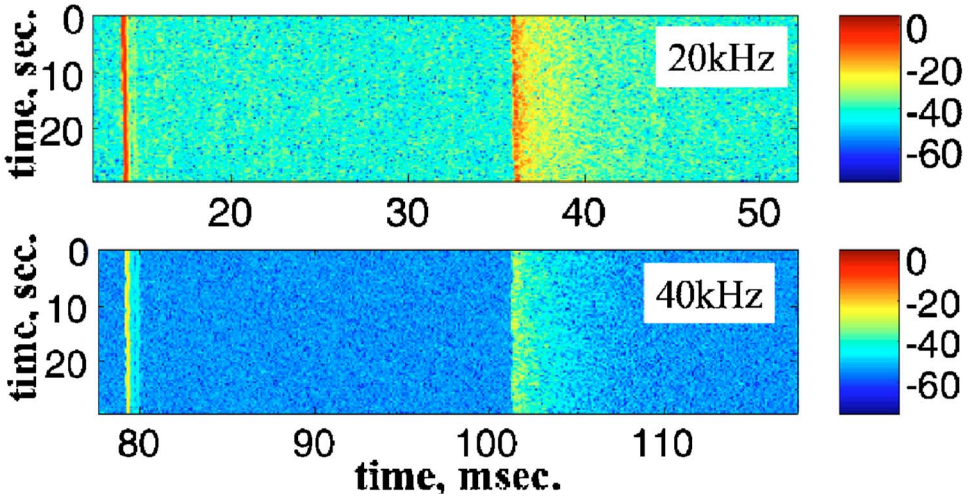

FIG. 4. (Color online) Acoustic data recorded at approximately 0230 on 18 Aug 2002 (UTC). Each panel contains ~300 short cw pulses transmitted from the 67-m-deep projector and received at the 217-m-deep hydrophone. In each panel, the vertical band on the left is the direct path; the vertical band near the center of each panel is the surface reflected path; and the smattering of arrivals following the surface reflected path is time spread.

IV. MODEL: MEASUREMENT COMPARISON

To estimate the time spread of the surface bounce path from the data shown in Fig. 4, we align the SB arrivals by their leading edges and ensemble average them. The resulting time spread measurements are shown in Fig. 5. On average, the received signal drops 20 dB in about 3 ms at 20 kHz, but takes about 6 ms to drop the same amount at 40 kHz. The later arrivals are due to scattering from parts of the surface that are farther from the specular point, where the grazing angles are increasingly shallow, and where the shorter wavelength results in higher scattering.

For the time spread prediction, we first utilize Dahl's model[5–7] to obtain an intensity impulse response function $I_{\text{imp}}(\tau)$. Transmit and receive beam patterns must be used in this calculation. The intensity impulse response function was then convolved with the envelope of the transmitted signal and a noise floor was added to obtain the time spread prediction, which is shown in Fig. 5. The agreement is reasonably good at both frequencies, which provides confidence in the validity of the $I_{\text{imp}}(\tau)$ function.

The frequency correlation measurement is obtained using the LFM time series. The data were separated into the DP and SB paths and the correlation coefficient calculated separately for each path using Eq. (2). An actual direct path received signal was used as the replica in order to account for frequency dependent acoustic absorption. The peak DP and SB path correlation coefficients were found for each ping and ensemble averaged. The dotted lines in Fig. 6 denote the measured correlation coefficient for the DP signals transmitted by the 67-m-deep projector and received at the 217-m-deep receiver between 0200 and 0300 UTC on 18 August 2002. Vertical lines denote error bars. The correlation coefficient of the DP arrivals is very high for all bandwidths measured, indicating that propagation through the ocean medium over this range had little effect on signal structure. The solid lines with error bars in Fig. 6 denote the measured correlation coefficient for the SB arrivals. The reduction in correlation with increasing bandwidth indicates that reflection at the ocean surface does impact signal structure in a manner which depends upon signal bandwidth. These results are consistent with measurements reported by Reeves[8] and Keranen.[30]

To obtain the frequency correlation predicted by the SIRTER theory, we use the intensity impulse response function $I_{\text{imp}}(\tau)$. and calculate the ratio

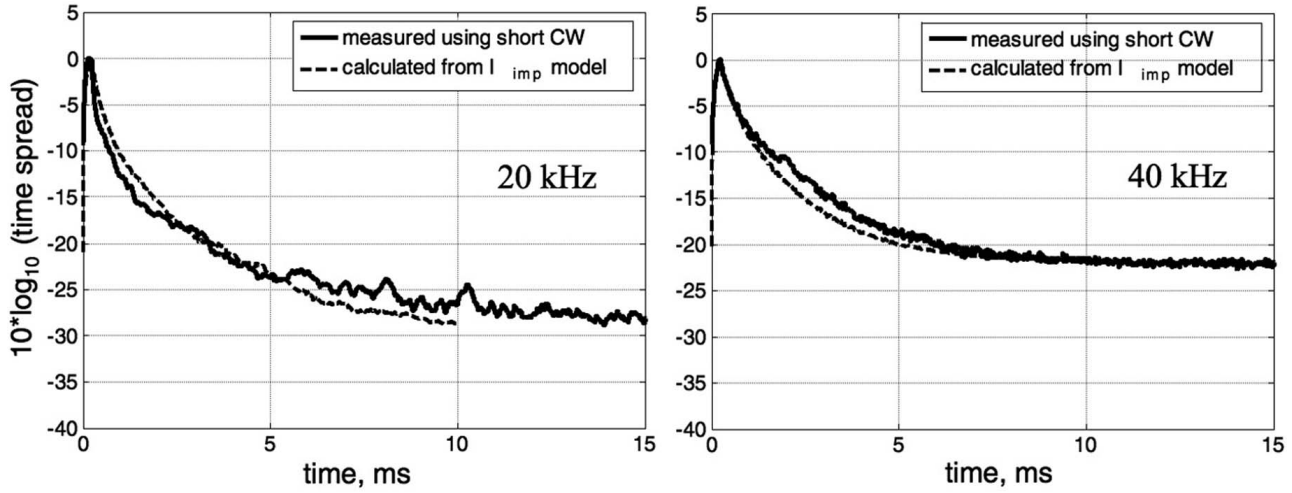

FIG. 5. Measured (solid line) and predicted (dashed line) time spread for the short cw pulses transmitted from the 67-m-deep projector and received at the 217-m-deep hydrophone at approximately 0230 on 18 Aug 2002 (UTC).

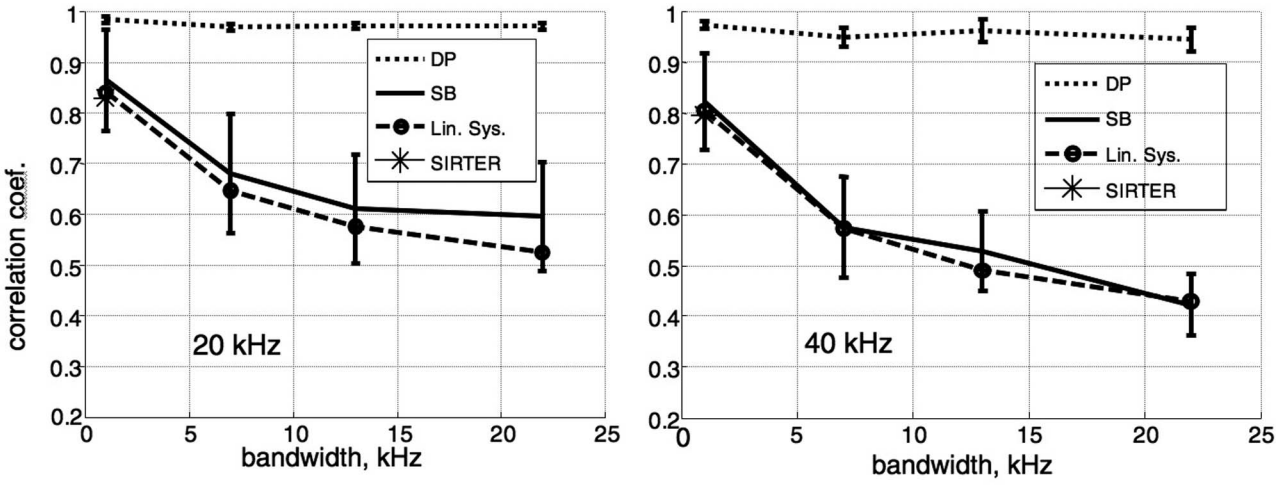

FIG. 6. Frequency correlation for the 67-m-deep projector and received at the 217-m-deep hydrophone. Shown are the direct path (DP) and surface bounce path (SB) measurements, and the linear systems and signal resolution to total temporal elongation ratio (SIRTER) theoretical predictions.

$$RC_{\mathrm{SIRTER}}(\beta)=\frac{\int_0^{\beta^{-1}} I_{\mathrm{imp}}(\tau)\,d\tau}{\int_0^{\infty} I_{\mathrm{imp}}(\tau)\,d\tau}, \tag{15}$$

where the upper integration limit in the numerator is the temporal resolution of the signal. The SIRTER predictions for 1 kHz bandwidth signals are indicated by asterisks at 1 kHz bandwidth in Fig. 6. The prediction is virtually identical to the frequency correlation measured using a 1 kHz bandwidth LFM. Reeves recommended against extension of the theory to bandwidths greater than 2 kHz,[8] thus we did not compare his theory to larger bandwidth measurements. However Keranen reported frequency correlation measurements using bandwidths up to 13 kHz signals, and found the SIRTER prediction to be lower than measured values for bandwidths above 2 kHz.[30]

To apply the linear systems theory, we begin by calculating the ocean surface forward reflection transfer function correlation function using Eq. (14) and the first 5 ms of the intensity impulse response function $I_{\mathrm{imp}}(\tau)$. $10\log_{10} R_H(\Delta f,0)$ is plotted in Fig. 7 for the two center frequencies used in the measurements (only the positive halves of the transforms are shown). According to Fig. 7, forward scattering by the ocean surface will reduce by 5 dB the cross-correlation between envelopes of signals near 20 kHz but different in frequency by 2 kHz [that is, $R_H(\Delta f,0)$ will be reduced by a factor of about 3]. Figure 7 also indicates that the envelopes of signals near 20 kHz and separated by 20 kHz will be decorrelated by about 10 dB [$R_H(\Delta f,0)$ is reduced by a factor of 10]. The coherence bandwidth estimates calculated using $I_{\mathrm{imp}}(\tau)$ and Eq. (3) are 2.06 and 1.19 kHz, respectively, for 20 and 40 kHz, and are marked with asterisks in Fig. 7. Figure 7 shows that the coherence bandwidth estimate L^{-1} corresponds to the frequency separation that causes a 5 dB drop in the transfer function correlation function.

Next, Eq. (12) was used to compute $|\Gamma_\beta(\Delta f,0)|^2$ for the four LFM signals used in the measurement. Figure 8 shows $10\log_{10}|\Gamma_\beta(\Delta f,0)|^2$ for the four signals, all normalized to unit energy, together with $R_H(\Delta f,0)$ for 20 kHz. It is clear from Fig. 8 that $R_H(\Delta f,0)$ is relatively narrow in Δf, so that

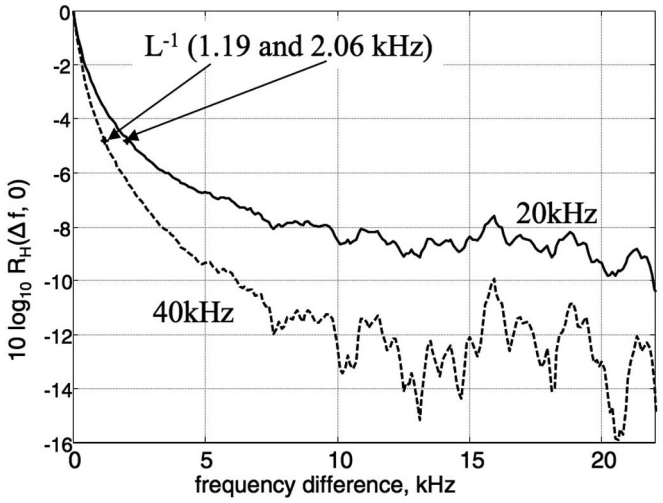

FIG. 7. $10\log_{10} R_H(\Delta f,0)$ calculated using Eq. (14) for 20 and 40 kHz center frequencies. Asterisks mark the coherence bandwidth (L^{-1}) values calculated using Eq. (3).

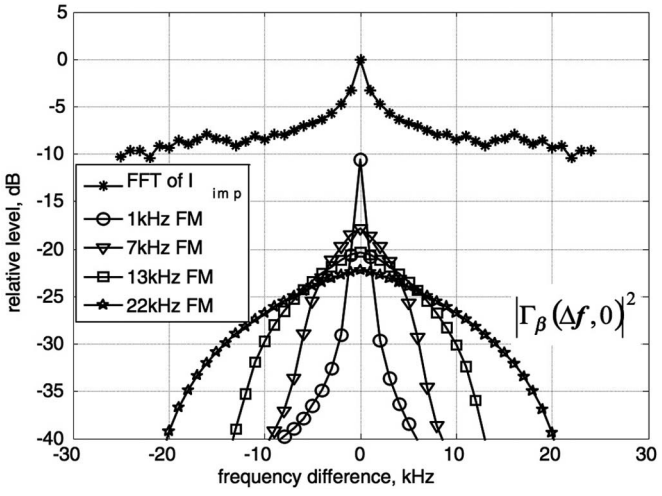

FIG. 8. Transfer function correlation function $R_H(\Delta f,0)$ (uppermost curve) and spectral ambiguity functions $|\Gamma_\beta(\Delta f,0)|^2$ for the four LFM signals used in the experiment.

the integral in Eq. (11) can be expected to fall off as the level of $|\Gamma_\beta(0,0)|^2$ decreases. Finally, Eq. (11) was applied to calculate the frequency correlation prediction, which is shown by the dashed lines in Fig. 6. The linear systems theory prediction is within the error bars of the measured frequency correlation for all bandwidths considered.

V. DISCUSSION

Our results depend a great deal upon the validity of the intensity impulse response function $I_{\text{imp}}(\tau)$, which was calculated using Dahl's model and a wave height spectrum derived from wave rider buoy measurements. The $I_{\text{imp}}(\tau)$ calculation takes into account the receive hydrophone 3 dB beam widths, which are 75° at 20 kHz and 41° at 40 kHz. The 67-m-deep projector is omnidirectional. The specular angle for the 67-m-deep transmitter and 217-m-deep receiver was 16°, which means that $I_{\text{imp}}(\tau)$ is impacted by the receive beam pattern more at 40 kHz than at 20 kHz. Our confidence in the validity of the $I_{\text{imp}}(\tau)$ prediction is based upon the good agreement obtained between the measured and modeled time spread at 20 and 40 kHz (Fig. 5). However, the $I_{\text{imp}}(\tau)$ calculation does not take into account shadowing of the ocean surface, which might become important under higher sea state conditions.

The function $I_{\text{imp}}(\tau)$ was used to predict frequency correlation directly utilizing the SIRTER theory developed by Reeves. The theory was motivated by Weston's analysis of pulses whose shape, after being scattered, was on average Gaussian, for which he suggested that the reduction in correlator output was proportional to the ratio of the signal temporal resolution (equal to one over the signal bandwidth) to the total temporal spread of the signal. Reeves found Weston's prediction to be "in qualitative agreement" with his own data, by which he meant that the reduction in correlator output he measured was likewise proportional to the ratio of the signal temporal resolution to the total temporal spread of the signal.[8] He found good agreement between his theory and the measurement results for bandwidths to 1 kHz, but found the correlation of 2 kHz bandwidth signals to be somewhat above that predicted by the theory. In the conclusions, he predicted that the theory would be "limited ... by the condition in which individual highlights all become resolved. Beyond this point the correlation loss should become independent of bandwidth." We found good agreement with the SIRTER theory for 1 kHz bandwidth LFM signals, and as shown in Fig. 6, found that frequency correlation at greater bandwidths showed considerably less bandwidth dependence.

Guided by linear systems theory, the function $I_{\text{imp}}(\tau)$ was also Fourier transformed to obtain the transfer function correlation function $R_H(\Delta f,0)$. The assumptions that led to that operation were that (1) the wide-sense stationary uncorrelated scattering (WSSUS) condition was met, and (2) $R_H(\Delta f,\Delta t)$ changed slowly in Δt compared to the 10 ms duration of the transmitted signal. These assumptions are deemed reasonable based upon physical considerations, and strong support is demonstrated by the good agreement between the measured and modeled frequency correlation coefficient shown in Fig. 6.

It is tempting to conclude from the present work that the SB path is useful for coherent signal processing of very wideband signals, in that the correlation loss was found to be quite small relative to the noise suppression obtainable from replica correlation [approximately $10\log_{10}(2T\beta)$ for pulse length T and bandwidth β]. However, there are two significant limitations to the present results. First, our measurements were made under fairly benign surface conditions; frequency correlation has not been measured under higher sea state conditions. Second, our broadband LFM pulses were very short, such that temporal decorrelation due to reflection at the ocean surface was not significant; longer pulses would certainly experience additional correlation loss. We hope to investigate these two issues theoretically and experimentally in the future.

We now seek to clarify the relationship between coherence bandwidth and the frequency correlation coefficient. First note that the transfer function correlation function $R_H(\Delta f,0)$, which Adams and Doubek refer to as the *two-frequency correlation function*,[31] characterizes the degree of correlation between the envelopes of two pure tone signals separated in frequency by Δf. Therefore, second-order-measures of the transfer function correlation function, such as the coherence bandwidth, specify the value of Δf at which the transfer function correlation is reduced by a certain amount, e.g., 5 dB. However, according to Eq. (11), the output of the replica correlation receiver is a function of $R_H(\Delta f,0)$, not a second-order-measure of $R_H(\Delta f,0)$. Both the theory and measurements shown in Fig. 6 indicate that the correlation coefficient remains high for signal bandwidths that are much greater than the coherence bandwidth. For example, from Fig. 6 we predict that (for our surface conditions) the replica correlator receiver response to a SB 22 kHz bandwidth signal centered at 20 kHz will be, on average, only about 3 dB lower than the response to a DP signal. However, the coherence bandwidth prediction, based upon $R_H(\Delta f,0)$ alone, is 2.06 kHz. The same drop in receiver output is predicted to occur for 17 kHz bandwidth signals centered at 40 kHz, although the coherence bandwidth prediction is 1.19 kHz. The reason that the coherence bandwidth is much lower than the bandwidth that is evidently available for use by the sonar can be seen from Eq. (11), which shows that the receiver output is the result of integration of $R_H(\Delta f,0)^*|\Gamma_\beta(\Delta f,0)|^2$ over all frequency separations. Since coherence bandwidth is a second-order measure of the transfer function correlation function, and the latter is required to compute frequency correlation, there appears to be no simple relationship between coherence bandwidth and frequency correlation. However, it may be possible to obtain useful results by guessing at the shape of $R_H(\Delta f,0)$ and fitting it to a coherence bandwidth.

One other relevant point is that our frequency correlation results, which were obtained using a DP arrival as the replica of the transmitted signal, will not, in general, be realized by other broadband acoustic systems unless frequency-dependent absorption is accounted for in forming the replica.

VI. SUMMARY

We have presented ocean surface forward scatter time spread and frequency correlation measurements made in August 2002, about 2500 m east of San Clemente Island, CA, under a very modest sea state. The time spread measurements have been compared with predictions derived from a model by Dahl[5–7] that uses the surface wave height spectrum as environmental input. Time spread predicted using the model was found to compare quite well with the time spread measurements at two frequencies (20 and 40 kHz).

Measurements of frequency correlation, or the reduction in correlation resulting from increased signal bandwidth, were compared with two theoretical predictions. First, the intensity impulse response function $I_{\mathrm{imp}}(\tau)$ calculated using Dahl's model was used with a theory developed by Reeves[8] that relates frequency correlation to the signal (temporal) resolution to total time elongation ratio (SIRTER). Consistent with Reeves' own measurements, we found that that his theory matches our measured correlation well for 1 kHz signal bandwidths. The theory is not applicable to higher bandwidth signals.

Second, linear systems theory was used to predict frequency correlation for very short signals using the Fourier transform of $I_{\mathrm{imp}}(\tau)$ and the spectral ambiguity function of the transmitted signal. The theory depends upon the assumption that scattering by the sea surface is wide-sense stationary and uncorrelated in delay and frequency (the WSSUS condition). We found that the linear systems based frequency correlation prediction matched the measurements quite well, indicating that the theory and assumption appear to be valid. We find the correlation loss associated with the ocean surface bounce to be approximately 3 dB for 22 kHz bandwidth signals centered at 20 kHz, which is small compared with the 25 dB processing gain available from such large time-bandwidth signals. However, our measurements were made under benign sea state conditions using very short pulses, and our results are applicable to those conditions. Greater correlation loss due to ocean surface reflection may be expected under higher sea state where the time spread will be greater, and using longer pulses such that temporal decorrelation becomes important.

Finally, our analysis has clarified the relationship between frequency correlation and the *coherence bandwidth* parameter, which has been tabulated by Dahl for a number of environmental conditions. Coherence bandwidth is a second-order measure of the intensity impulse response function, and is the frequency separation at which the transfer function correlation is reduced by 5 dB. However, the intensity impulse response function itself is required in order to predict frequency correlation.

ACKNOWLEDGMENTS

We sincerely appreciate our sponsors, Dr. J. Tague [Code 321US at the Office of Naval Research (ONR)] and CAPT. Jim Binford USN (ret.) [PMS 415J at the Naval Sea Systems Command (NAVSEA)]. The at-sea measurements were successful in large part due to considerable assistance from many people at the Marine Physical Laboratory (MPL) of Scripps Institution of Oceanography, especially Dr. Gerald D'Spain and CAPT. Bill Gaines (USN-Ret). Acoustics graduate students Steven Lutz, Rachel Romond, and Tom Weber did superb work at sea and their contributions are appreciated, as are those of ARL staff member Mike Vanatta. We especially thank the Captains and crews of the R/V *Acoustic Explorer* and M/V *Independence* for their professionalism and "can-do" attitudes. Jon Reeves provided many valuable comments and useful insight into the physics of scattering by the ocean surface. Bill Plant provided us his model for the surface wave height spectrum, and Peter Dahl spent many hours explaining details of his very fine work and excellent papers.

[1] L. Fortuin, "Survey of literature on reflection and scattering of sound waves at the sea surface," J. Acoust. Soc. Am. **47**, 1209–1228 (1969).
[2] J. A. Ogilvy, *Theory of Wave Scattering from Random Rough Surfaces* (Institute of Acoustics, Bristol, UK, 1991).
[3] P. H. Dahl, "Forward scattering from the sea surface and the van Cittert-Zernike theorem," J. Acoust. Soc. Am. **115**, 589–599 (2004).
[4] J. S. Bendat and A. G. Piersol, *Random Data: Analysis and Measurement Procedures*, 2nd ed. (Wiley, New York, 1986).
[5] P. H. Dahl, "On the spatial coherence and angular spreading of sound forward scattered from the sea surface: Measurements and interpretive model," J. Acoust. Soc. Am. **100**, 748–757 (1996).
[6] P. H. Dahl, "On bistatic sea surface scattering: Field measurements and modeling," J. Acoust. Soc. Am. **105**, 2155–2169 (1999).
[7] P. H. Dahl, "High-frequency forward scattering from the sea surface: The characteristic scales of time and angle spreading," IEEE J. Ocean. Eng. **26**, 141–151 (2001).
[8] J. C. Reeves, "Distortion of acoustic pulses reflected from the sea surface," Ph.D. Dissertation, University of California, Los Angeles, 1974.
[9] J. J. Martin, "Time and frequency characteristics of an acoustic signal reflected from a rough boundary," J. Acoust. Soc. Am. **43**, 405–417 (1968).
[10] D. E. Weston, "Correlation loss in echo ranging," J. Acoust. Soc. Am. **37**, 119–124 (1965).
[11] C. S. Cox and W. H. Munk, "Statistics of the sea surface derived from sun glitter," J. Mar. Res. **13**, 198–227 (1954).
[12] L. J. Ziomek, "A scattering function approach to underwater acoustic detection and signal design," Ph.D. thesis, The Pennsylvania State University, State College, PA, 1981.
[13] L. J. Ziomek, *Underwater Acoustics: A Linear Systems Theory Approach* (Academic, Orlando, 1985).
[14] L. A. Zadeh, "Frequency analysis of variable networks," Proc. IRE **38**, 291–299 (1950).
[15] L. A. Zedeh and C. A. Desoer, *Linear Systems Theory* (McGraw-Hill, New York, 1963).
[16] T. Kailath, "Channel characterization: Time-variant dispersive channels," in *Lectures on Communication System Theory*, edited by E. J. Baghdady (McGraw-Hill, New York, 1961).
[17] A. W. Ellinthorpe and A. H. Nuttall, "Theoretical and empirical results on the characterization of undersea acoustic channels," IEEE First Annual Communications Convention, 1965.
[18] K. A. Sostrand, "Mathematics of the time-varying channel," Proceedings of NATO Advanced Study Institute on Signal Processing with Emphasis on Underwater Acoustics, Vol. II, Enschede, The Netherlands, 1968.
[19] J. Johnsen, "Spectrum analysis of reverberations," in *Signal Processing*, edited by J. W. R. Griffiths, P. L. Stocklin, and C. Van Schooneveld (Academic, New York, 1973).
[20] R. Laval, "Sound propagation effects on signal processing," in Ref. 19.
[21] P. A. Bello, "Characterization of randomly time-variant linear channels," IEEE Trans. Commun. Sys. **11**, 360–393 (1963).
[22] A. Papoulis, *Signal Analysis* (McGraw-Hill, New York, 1977).
[23] A. Ishimaru, *Wave Propagation and Scattering in Random Media* (Academic, New York, 1978), Vol. 1.
[24] R. S. Kennedy, *Fading Dispersive Communication Channels* (Wiley-Interscience, New York, 1969).
[25] H. L. Van Trees, *Detection, Estimation and Modulation Theory* (Wiley, New York, 1971), Pt. III.

[26] H. Weinberg and R. E. Keenan, ''Gaussian ray bundles for modeling high-frequency propagation loss under shallow-water conditions,'' J. Acoust. Soc. Am. **100**, 1421–1431 (1996).
[27] P. H. Dahl (private communication).
[28] S. T. McDaniel and D. F. McCammon, ''Composite-roughness theory applied to scattering from fetch-limited seas,'' J. Acoust. Soc. Am. **82**, 1712–1719 (1987).
[29] W. J. Plant, ''A stochastic, multiscale model of microwave backscatter from the ocean,'' J. Geophys. Res. **107**, 3-1–3.21 (2002).
[30] J. G. Keranen, ''Effect of the ocean environment on the coherence of broadband signals,'' MS thesis, The Pennsylvania State University, State College, PA, 2001.
[31] S. L. Adams and J. W. Doubek, ''Frequency coherence and time coherence in random multipath channels,'' J. Acoust. Soc. Am. **62**, 286–294 (1977).

A robust spatial filtering technique for multisource localization and geoacoustic inversion

S. A. Stotts
Applied Research Laboratories, The University of Texas at Austin, P.O. Box 8029, Austin, Texas 78713-8029

(Received 5 November 2004; revised 15 March 2005; accepted 16 March 2005)

Geoacoustic inversion and source localization using beamformed data from a ship of opportunity has been demonstrated with a bottom-mounted array. An alternative approach, which lies within a class referred to as spatial filtering, transforms element level data into beam data, applies a bearing filter, and transforms back to element level data prior to performing inversions. Automation of this filtering approach is facilitated for broadband applications by restricting the inverse transform to the degrees of freedom of the array, i.e., the effective number of elements, for frequencies near or below the design frequency. A procedure is described for nonuniformly spaced elements that guarantees filter stability well above the design frequency. Monitoring energy conservation with respect to filter output confirms filter stability. Filter performance with both uniformly spaced and nonuniformly spaced array elements is discussed. Vertical (range and depth) and horizontal (range and bearing) ambiguity surfaces are constructed to examine filter performance. Examples that demonstrate this filtering technique with both synthetic data and real data are presented along with comparisons to inversion results using beamformed data. Examinations of cost functions calculated within a simulated annealing algorithm reveal the efficacy of the approach. [DOI: 10.1121/1.1904404]

PACS numbers: 43.30.Ma, 43.30.Pc, 43.30.Wi, 43.30.Bp, 43.30.−k [AIT] Pages: 139–162

I. INTRODUCTION

Isolating a single source within an ocean of sources continues to be an important and challenging problem. The ultimate goal is the ability to perform source detections and to simultaneously determine source and environmental characteristics using no *a priori* information about the environment, except perhaps water sound-speed profiles (SSP). A general, possibly iterative, inversion method would use sources of opportunity to obtain these characteristics and has recently been established.[1] The filtering method described here can be used in both range-independent and range-dependent environments. One of the main purposes of this paper is to demonstrate an automated and robust method to circumvent the rank deficiency of the pseudoinverse for the filtering. The method is based on the number of effective elements of the array. The application of this method to both uniformly and nonuniformly spaced array elements will be presented. For the nonuniformly spaced elements, a high-frequency cutoff must be invoked for the number of singular values retained from the pseudoinverse. Throughout this study, the emphasis is on filter performance and not on inversion for geoacoustics, although this goal dictates the approach of this analysis.

To begin, the ocean is divided into bearing space segments, and a spatial filter is applied to isolate a source of interest within one bearing region. A subset of the overall problem is first considered using simulated data with the assumptions that the environment is known and that a single source is to be isolated in the presence of one loud interferer.[2] Solving a subset of the general problem allows the details of the filtering technique to be more thoroughly investigated. In addition, an inversion for two of the source parameters, range and bearing, with actual data is performed. The real data contain a dominant source in the presence of several interferers of varying strengths and locations. Inversions are performed using element level data, both before and after the filter has been applied, with various forward model choices in a simulated annealing algorithm. These include normal modes,[3,4] parabolic equation (PE RAM),[5,6] and a recently developed combination of ray trace[7–9] plus plane-wave reflection coefficient (PWRC) model.[10] For the work discussed in this paper, the ORCA (Ref. 3) normal-mode model is used exclusively.

The spatial filtering method described here was originally introduced in the context of optimization as a useful approach to filter design involving short data records.[11–14] For those applications, filters were constructed by specifying passband, transition band, and stop band values. An added constraint was imposed on the filter shape to yield the desired response, which was then compared to a Hilbert transform response and showed significantly lower error for the filter. Another recent application involved the design of the frequency response of FIR bandpass equiripple filters.[15]

The advantage of using the filter method lies in the transformation procedure, whereby filtered element level data (up to the full aperture) are used in the inversion process. This is in contrast to first forming subarrays which are then beamformed prior to performing the inversion.[1] The latter method often requires an iterative procedure to select optimum elements to include in the subarrays.

For much of this study, a cost function was evaluated at specific locations in the defined search space on a parameter space grid. The coherent cross-spectral broadband cost function defined in Sec. III D 1 has a basis in matched-field processing approaches.[16] For a recent application of this approach to geoacoustic inversion, see Ref. 17 and related references cited therein.

Section II contains a brief background of the spatial filtering technique. In Sec. III details of a robust approach to filter construction for both uniformly and nonuniformly spaced array elements are presented and compared to alternative methods using ambiguity surfaces to benchmark the filter performance. Applications of the filtering approach to real data are given in Sec. IV. The paper is concluded in Sec. V.

II. SPATIAL FILTERING APPROACH

Recently, the spatial filter approach, referred to as matrix filtering, has been applied to isolate sources in ocean acoustic environments.[13,14] The optimization criterion chosen, the least-squares method, is used to construct the filter in bearing space, subject to the constraint of a unit response within a defined bearing sector. The filters are designed to isolate sources within the given bearing sector with respect to the array axis.

A horizontal, bottom-mounted line array is assumed for purposes of this discussion, although the principles are not limited to this array type. Element spacings considered here are both uniform and nonuniform. The approach taken continues this development by analyzing in detail the filter construction to improve the performance. A robust automated method was developed to ensure stability across a broad range of frequencies and for general array designs.

The concept of the filtering technique is basically that element level data are transformed to beam data and a bearing window filter is applied to isolate a given sector. Finally, an inverse transform is applied to obtain filtered element level data.[13] The transform is accomplished by constructing a steering matrix, Y_{nm}, consisting of the matrix of plane-wave phase delays for a given beam direction m at a given receiver n. This is given by

$$Y_{nm} = \exp\{i\omega[x_n \cos(\phi_m) + y_n \sin(\phi_m)]/c\}, \tag{1}$$

where ϕ_m is the steering angle defined as the angle of the incoming wave measured relative to the line of the array. For frequency f, $\omega = 2\pi f$, and c is the sound speed at the depth of the array. The element coordinates for a uniformly spaced horizontal array can be written as $x_n = (n-1)d$, where d is the element spacing, and where $y_n = 0$ for the line arrays considered here. An incoming plane wave produces a field of the form $e^{i\omega[x_n \cos(\phi_{m,})/c - t]}$.

For the work presented here, no weighting of the steering matrix elements has been used. Thus, the transformation involves unshaded conventional beamforming (CBF). A well-known alternative method, adaptive beamforming (ABF), has a similar goal of isolating sources by nulling out the loud interferers.

Adaptive beamforming has a long history in ocean acoustics processing for multisensors, as well as many other areas of signal processing.[18,19] Indeed, this subject continues to be an important topic of interest with regard to source detections and performance predictions.

The basis for ABF lies in the estimation of the cross-spectral matrices (CSMs).[20] The correspondence between the largest eigenvalues of the CSM and dominant sources in an environmental field has been established and utilized to reduce the noise field by discriminating against the loudest sources.[21–23]

The ABF method can be classified as statistically optimal beamforming, whereas the matrix filter method is a data-independent approach. Quantifying a comparison between the ABF approach[18] and the matrix filtering technique presented here is a current topic of interest. Comparisons between these two approaches will substantiate the matrix filter's usefulness but lies beyond this work.

In solving a multisource problem, several approaches may be employed. These include nulling out the loud sources (such as with ABF), applying a notch filter (constructed from the method described here) to suppress loud sources,[24] or building a filter around a source of interest while suppressing interferers. The latter method is the approach considered in this paper. In this approach, commonly referred to as an ''onion peeling'' process, the loudest source would first be used in the inversion. In principle, determining the important environmental variables such as SSPs and bottom properties would then allow the use of backpropagation to acquire the characteristics of the source.[25] The contribution of this source would then be removed from the field. Subsequently, the same procedure would be applied to the next strongest source for additional environmental inversion information and/or determining this source's characteristics. These steps would then be repeated for each remaining source in the field.

It is this onion peeling solution to the multisource problem which is the motivation for the work presented here. Performing the inversions with element level data is the main focus. After a CBF transformation is used to construct the filter, a final transformation back to the element level data is performed. This is a preprocessing step applied prior to the inversion. The inversion results using this filtering technique are compared in Secs. III and IV to inversions performed without filtering and to results obtained by dividing the array into subarrays using CBF with Taylor shading.[26] One advantage of the matrix filter method, as compared to inversions using subarrays, is that it may be applied to any subset of elements.

The beamforming and filtering methods introduced here have their basis in a least-squares optimization problem given by[13,27]

$$\min_g \|GY - YD\|^2 = \min_g \|Y^\dagger G^\dagger - DY^\dagger\|^2, \tag{2}$$

where a dagger (†) denotes the adjoint (complex conjugate transpose), g corresponds to the elements of the filter G, and D is the bearing filter window.

A unit response is invoked in the filtered bearing sector. This is achieved by constructing the bearing filter window, D, to be a square matrix with dimension equal to the number of beams, with unit entries in the diagonal terms corresponding to the desired bearing filter sector and zeros elsewhere.

The general filter equation which is implemented in this paper is defined in terms of the equivalent conjugate form given by

$$G_{ln} = \sum_{m=1}^{M} Y_{lm} D_{mm} (Y^{\dagger})^{-1}_{mn}, \tag{3}$$

where the pseudoinverse of the beam steering matrix is defined by

$$(Y^{\dagger})^{-1} = [YY^{\dagger}]^{-1} Y, \tag{4}$$

and M is the number of beams.

In general, the number of beams exceeds the number of array elements, N. For example, in this paper, $M = 181$ for 1-deg increments in ϕ, and either $N = 52$ or $N = 65$ elements. Therefore, the inverse is rank deficient and undefined, which can cause contamination from the noise subspace into the signal subspace.[28,29] The conditioning of the beam matrix Y has been discussed previously in regards to the pseudoinverse of Y within the least-square optimization approach.[27] For the present application an algorithm for the effective number of elements is invoked to address the rank deficiency as discussed in Sec. III.

For this work the inverse is calculated using a singular value decomposition algorithm. Routines for solving the inverse are found in the LAPACK software package.[30] In this form, the steering matrix adjoint can be written as

$$Y^{\dagger} = U \Sigma V^{\dagger}, \tag{5}$$

where U and V are unitary matrices, and Σ is a diagonal matrix containing the singular values, $S_k \equiv \Sigma_{kk}$. The pseudoinverse of the adjoint of the nonsquare beam steering matrix is $(Y^{\dagger})^{-1} = V \Sigma^{-1} U^{\dagger}$. In component form this is given by

$$(Y^{\dagger}_{ij})^{-1} = \sum_{k=1}^{r_{\max}} V_{ik} \Sigma^{-1}_{kk} U^{*}_{jk}, \tag{6}$$

where $r_{\max} \leqslant$ rank of the matrix is the number of singular values used in the inverse and is not to be confused with a range value.

For efficiency, the components of Y and $(Y^{\dagger})^{-1}$ are stored for each frequency, at a given time segment, along with the window D. Subsequently, G is applicable to all FFT time windows. This filter component storage would also allow the filter windowing to change with time in an efficient manner, by generalizing the window to be time dependent, i.e., $D = D(t)$.

Two methods of bearing discretization were investigated for computing $Y^{\dagger}$. At first, 181 beams were sampled in equal $\sin(\phi)$ space; however, similar results were obtained by using 181 beams equally spaced in ϕ. Except for an initial demonstration of the filtering method discussed in Sec. III A, all remaining filter constructions use an equal ϕ sampling.

III. EFFECTIVE ELEMENT METHOD AND FILTER PERFORMANCE

The problems associated with the pseudoinverse in Eq. (6) are a result of having singular values which are too small, making the inverse ill-defined and the filter in Eq. (3) unstable. In this section, an algorithm for the number of effective elements for both uniformly and nonuniformly spaced array elements will be applied to stabilize the pseudoinverse. To demonstrate the effectiveness of this method, some comparisons will be made for simulated data using two alternative methods, a fixed singular value threshold and a method referred to as polar decomposition.[29] Then, in Sec. IV using real data, inversions with the effective element method will be compared to the fixed threshold approach and to inversions with CBF beamforming using subarrays.

The effective element method, referred to here as the N_{λ} method, accounts for the frequency dependence on the array performance in setting the maximum number of singular values used in the filter construction, $r_{\max}$. Since a separate filter must be constructed for each frequency used in the inversion, having an automated approach to determine $r_{\max}$ is essential for broadband analysis. The N_{λ} method is based on the degrees of freedom of the array, given by

$$N_{\lambda} = \frac{L}{\lambda/2}, \tag{7}$$

which is the number of half wavelengths along an array of length L. This approach directly links the signal physics in the array performance to the construction of the filter by choosing $r_{\max} = N_{\lambda}$ for frequencies at or below the design frequency, for which $N_{\lambda} \leqslant N$, of an equally spaced array. For frequencies greater than the design frequency, $r_{\max}$ is set to N

$$r_{\max} = \begin{cases} N_{\lambda}; & N_{\lambda} \leqslant N \\ N; & N_{\lambda} > N. \end{cases} \tag{8}$$

For nonuniformly spaced array elements, an alternative algorithm for $r_{\max}$ is necessary, as discussed in Sec. III C.

A. Alternative filtering methods

The N_{λ} method was compared to two alternative techniques for building the pseudoinverse in the spatial filter. One technique is to set a frequency-independent threshold for the singular values in the pseudoinverse calculation. The other technique is derived from a separation of rotational and dilatational components of the steering matrix given in Eq. (5).

In the fixed threshold method all eigenvectors with singular values greater than the threshold are used in the pseudoinverse calculation. Thus

$$r_{\max} = N_t, \tag{9}$$

where N_t is the number of singular values greater than a specified threshold, t. The problem with this method is setting the threshold value to optimize filter performance. The optimal threshold can depend on the array design. Some frequency dependence is inherent with a constant threshold value, since the number of singular values above a given threshold does change with increasing frequency. However, the problem of setting the threshold for the singular values remains because the optimum threshold can vary by three orders of magnitude between uniform and nonuniform array spacings.

The other method, referred to as the polar decomposition method,[29] separates the beam transformation into a rotational and dilatational part, similar to the polar representation of a complex number, $z = re^{i\theta}$. To apply this method, a pseudoidentity matrix, I_{nm}, is inserted into the beam transformation matrix. In component form

$$Y^{\dagger}_{mn} = U_{mm}\Sigma_{mn}V^{\dagger}_{nn} = U_{mm}(I_{mn}V^{\dagger}_{nn}V_{nn}I_{nm})\Sigma_{mn}V^{\dagger}_{nn}$$
$$= (U_{mm}I_{mn}V^{\dagger}_{nn})(V_{nn}I_{nm}\Sigma_{mn}V^{\dagger}_{nn}), \quad (10)$$

where I_{nm} is a matrix of n 1's along the diagonals with 0's elsewhere. Also, the unitarity of the U and V matrices has been used in the form $V^{\dagger}V = I$ in Eq. (10). The quantity in the first parenthesis of the last line in Eq. (10) is the rotational part, and the quantity in the second parenthesis is the dilatational part. In the polar decomposition method only the rotational part is used in the transformation, i.e.,

$$\tilde{Y}^{\dagger}_{mn} = U_{mm}I_{mn}V^{\dagger}_{nn}. \quad (11)$$

It is also noted that this result can be obtained by simply setting all the singular values in Eq. (5) to 1, i.e., $\Sigma_{kk} = 1 \forall k$, thus avoiding the instability of the filter due to the rank-deficient inverse. However, the price paid in this approach is that the transformation data do not preserve the overall amplitude and phase, which may affect the results depending on the cost function.

B. Arrays with uniform element spacings

To illustrate the filtering procedure and to discuss the various methods, a simulation was constructed with four moving sources. A sample multisource field was calculated to demonstrate the effect of filtering a single source in a realistic environment. The approach is similar to that in Ref. 31, except here all the sources are near the surface.

The fields from the sources were generated using ORCA. The field from each source track position is calculated to each array element using a realistic water sound-speed profile, sketched in Fig. 1(a), and a bottom which contains two layers with the sound speed, density, and attenuation values listed in Table I. Mode functions on the complex k plane were generated to compute the data, whereas for the forward propagation model in the inversions the real k-plane option of ORCA was used to simulate a realistic inversion problem. The real k-plane approach for inversions is at least an order of magnitude faster than the complex k-plane method. The accuracy of using the real k-plane option for inversions was demonstrated previously.[17]

The horizontal receiver array was located on the bottom and was aligned along the horizontal axis in the sketch in Fig. 1(b), where the source locations are marked. For the 65 elements in the first example the spacing is uniform at 4 m, giving an array length of 256 m. The broadband source levels were S1=125 dB, S2=130 db, S3=140 dB, and S4=125 dB in the band of 10–250 Hz, although the source spectra were tapered down to 110 dB at 250 Hz.

For this example the sources are well separated, i.e., their minimum azimuthal spacing exceeded 20°. The filter bearing width was 20° for all the examples presented in this paper, and is large enough to include multipath effects inside the bearing window. A study of the inversion results for varying filter window widths showed this to be adequate.[32] Also, multiple time sequences are needed to obtain inversions of source speeds and course headings; however, single time sequences will be used for all of the results presented in this paper since bearing, range, and depth localizations only are sufficient to illustrate the procedure and to examine the filter performance. Only the range and bearing localizations will be discussed here since surface sources are used in both simulations and real data analysis. Other work is currently underway with simultaneous inversion of geoacoustic data and source localizations.[24,33,34]

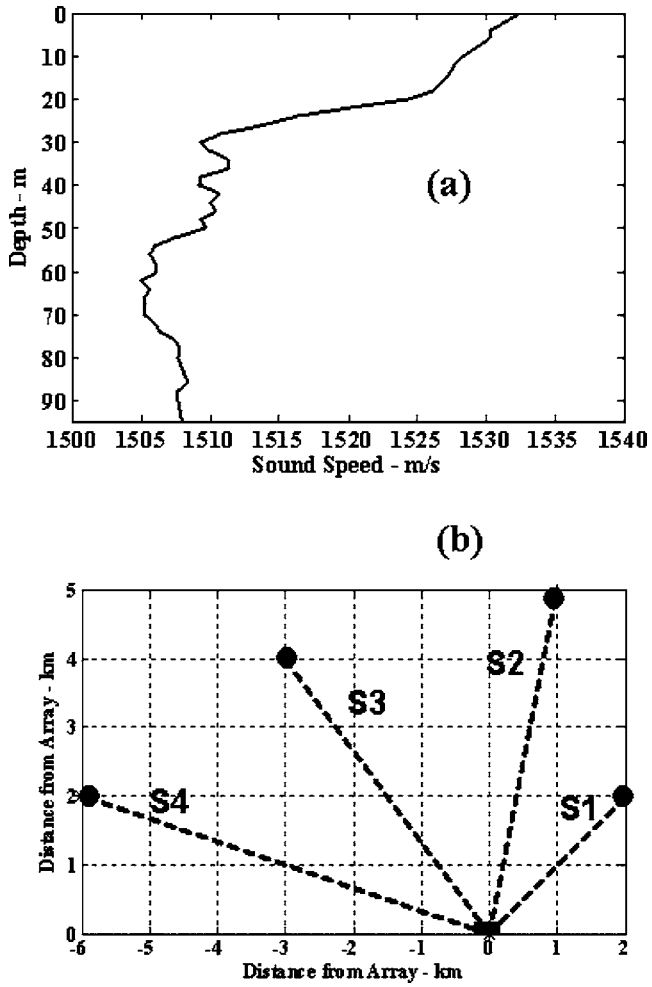

FIG. 1. (a) Geo-acoustic environment used in normal-mode simulation. (b) Positions of the sources for the simulated multisource field for demonstrating the spatial filtering technique.

A beam projection image of both the filtered and unfiltered data as a function of frequency from 10–250 Hz can be used to determine the ability to filter a single source in the presence of other sources well separated from the source of interest and having levels comparable to, or less than, the filtered source. An example is shown in Fig. 2 of the magnitude of both the unfiltered and filtered beam projections. The

TABLE I. Bottom parameters used in the simulations for the source–receiver geometry shown in Fig. 1.

Parameter	Layer 1	Layer 2	Substrate
Thickness—m	25.0	50.0	
C_{top}—m/s	1510.0	1750.0	2100.0
C_{bot}—m/s	1535.0	1760.0	
ρ—g/cm^3	1.37	2.0	2.2
α_{top}—dB/m-kHz	0.005	0.06	0.1
α_{bot}—dB/m-kHz	0.008	0.12	

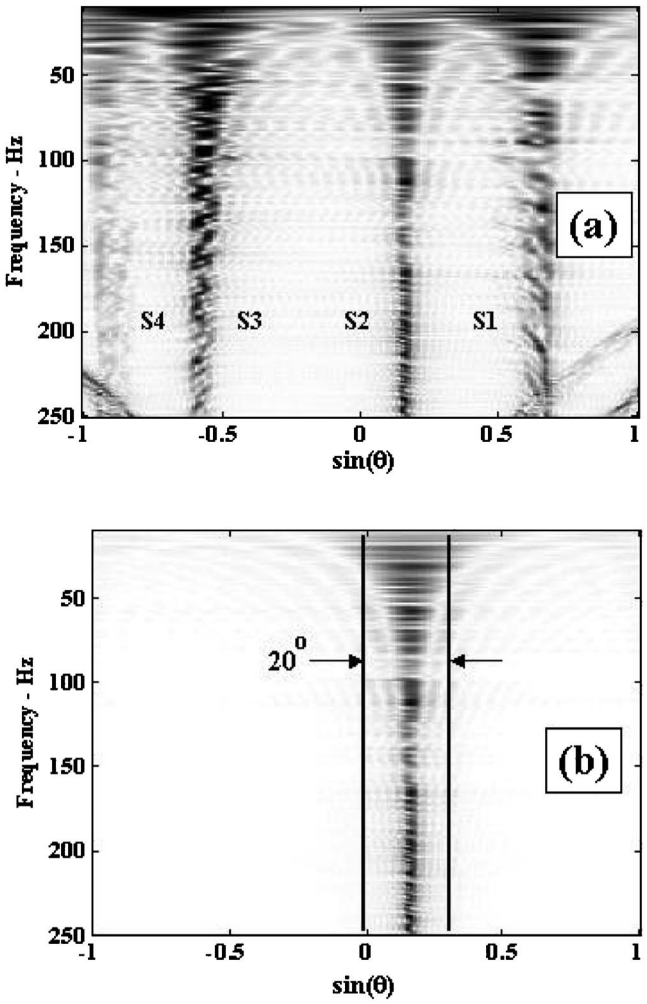

FIG. 2. Beam projection of (a) unfiltered data and (b) data from the N_λ filter for a simulation based on Fig. 1.

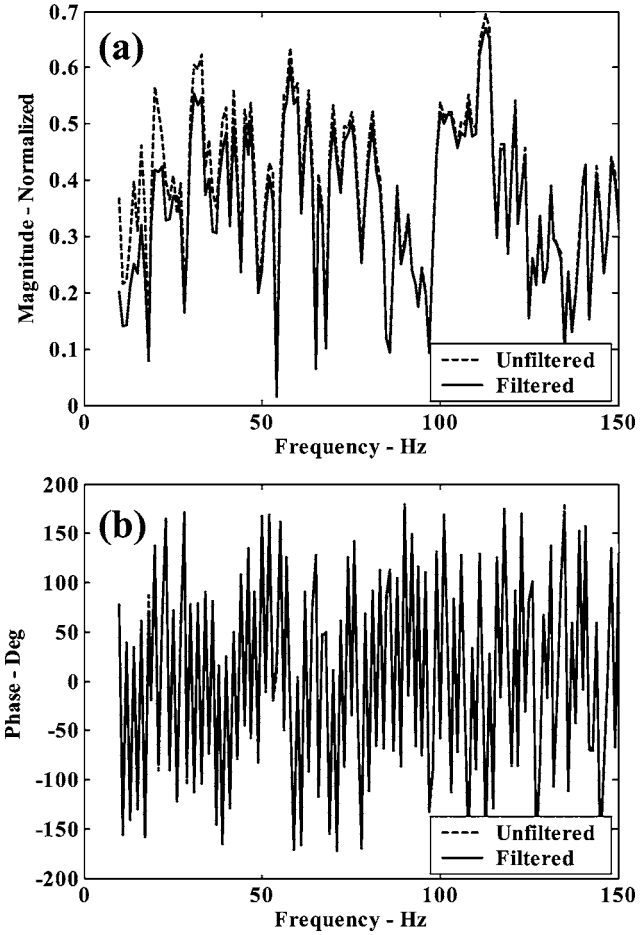

FIG. 3. Magnitude (a) and phase (b) at a bearing of 45° (through the source of interest) of unfiltered data and from N_λ filtered data.

beam projections are defined here to be the unfiltered data norms of $Y^\dagger \mathbf{x}$ with components

$$|Y^\dagger \mathbf{x}|_i = \sqrt{\left(\sum_j Y_{ij}^\dagger x_j \right)^2}, \tag{12}$$

where i is the bearing index. The corresponding norms for the filtered data are $|Y^\dagger G \mathbf{x}|_i$.

Beam projections plotted as a function of frequency (as in Fig. 2) are depicted in waterfall fashion, whereby increasing frequency is shown from top to bottom of the page. Similarly, bearing-time displays depicted below are with increasing time from top to bottom of the page.

The N_λ filter works well for frequencies below and above the design frequency of approximately 188 Hz for this array. The magnitude and phase of the complex beam output $\Sigma_j Y_{ij}^\dagger x_j$, where i is the index of the beam centered on the bearing of the source at 45°, are shown in Fig. 3 for the unfiltered data and the N_λ filtered data. [Bearing is 0° at broadside, vertical up in Fig. 1(b), and 90° horizontally to the right.] The result is that the filtering affects the magnitude of the data only for these normalized data obtained from the 4-m element spacing at frequencies well below the design frequency. The phase remains unchanged between the unfiltered and filtered data for this example. This is in contrast to the result (not shown) from the fixed threshold approach. The data were normalized prior to filtering in order to put them on the same scale for Fig. 3. In the remaining applications of the filtering, no initial normalization of the data is performed, unless stated otherwise.

To understand the filter performance for arrays with uniform element spacings, it is useful to examine the frequency dependence of the singular values that are used in constructing the filter. The singular value spectrum for the same array used in the simulation in Fig. 1 is shown in Fig. 4. (The standard singular value routine used here returns the singular values in descending order.[30]) There are 65 elements in the array, and the beams are steered every degree from $-90°$ to 90°. All the singular values greater than 1×10^{-4} are shown.

Several points about the singular decomposition eigenvalue spectral structure are worth noting. First, for uniformly spaced array elements the singular values increase with increasing frequency. The second point is that the break points, or knee, of each curve occur at eigenvalue number $k = N_\lambda$ for the uniformly spaced element arrays below the design frequency. Note that the eigenvalues at the knee are greater than 1 for all frequencies shown in Fig. 4. As previously mentioned, for uniformly spaced arrays at frequencies greater than the ideal design frequency, $r_{\max} = N$. The frequency dependence of $r_{\max}$ is illustrated in Fig. 5(a) for the 4-m spaced array with 65 elements and is consistent with the first N

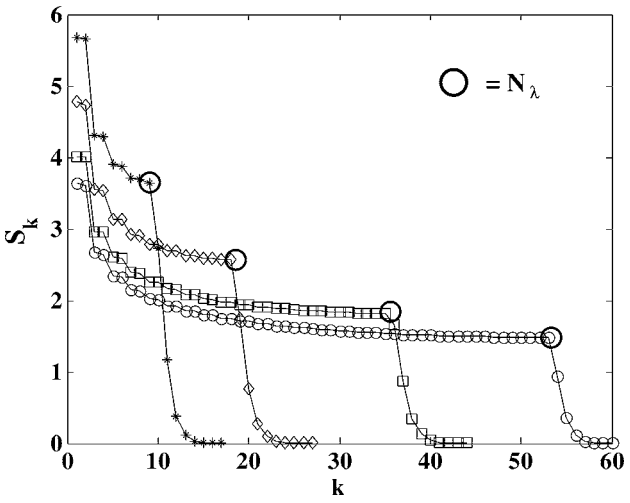

FIG. 4. Singular values of the steering matrix at several frequencies for an array of uniformly spaced elements: 25 Hz—asterisks; 50 Hz—diamonds; 100 Hz—squares; 150 Hz—circles.

singular values being larger than 1 for frequencies above the design frequency for this array.

Simulations using the sources in Fig. 1 can be used to demonstrate the limiting value of the threshold for the particular array with 4-m element spacings. The beam projections for the unfiltered data are shown in Fig. 2(a). Filtered data with a threshold of 1×10^{-4} are shown in Fig. 6(a) and for a threshold of 1×10^{-6} in Fig. 6(b). The threshold 1×10^{-4} was found to be approximately the lowest value that should be set for a stable and well-behaved filter. The value 1×10^{-6} gives poor results for the beam projection of the source, as shown in Fig. 6(b). The filter has become unstable since the tolerance was set too low. A threshold of 1×10^{-5} was also checked and found to give worse results than a threshold of 1×10^{-4} because it produced an unstable filter for several frequencies.

The magnitude and phase at a beam direction of 45° as a function of frequency were examined using the fixed threshold method with the threshold set to 1×10^{-4}. The magnitudes of the unfiltered and filtered data agree well; however, the phase is not as well preserved by the fixed threshold method compared to the N_λ method. The effect this phase difference has on the cost function for general array designs has not yet been investigated.

To determine a limiting minimum threshold required to maintain a stable filter, it is helpful to compare the total received energy in the filtered and unfiltered data, as given by

$$\mathcal{R}=\frac{\Sigma_i|\Sigma_j G_{ij}x_j|^2}{\Sigma_j|x_j|^2}. \tag{13}$$

The requirement for energy conservation is that $\mathcal{R}\leqslant 1$. This ratio is exhibited in Fig. 7 at several threshold values for the multisource simulated data used to give Fig. 2. For the N_λ method with uniformly spaced elements, conservation of energy is maintained for each frequency considered since $r_{\max}$ for the N_λ method corresponds to a fixed threshold much

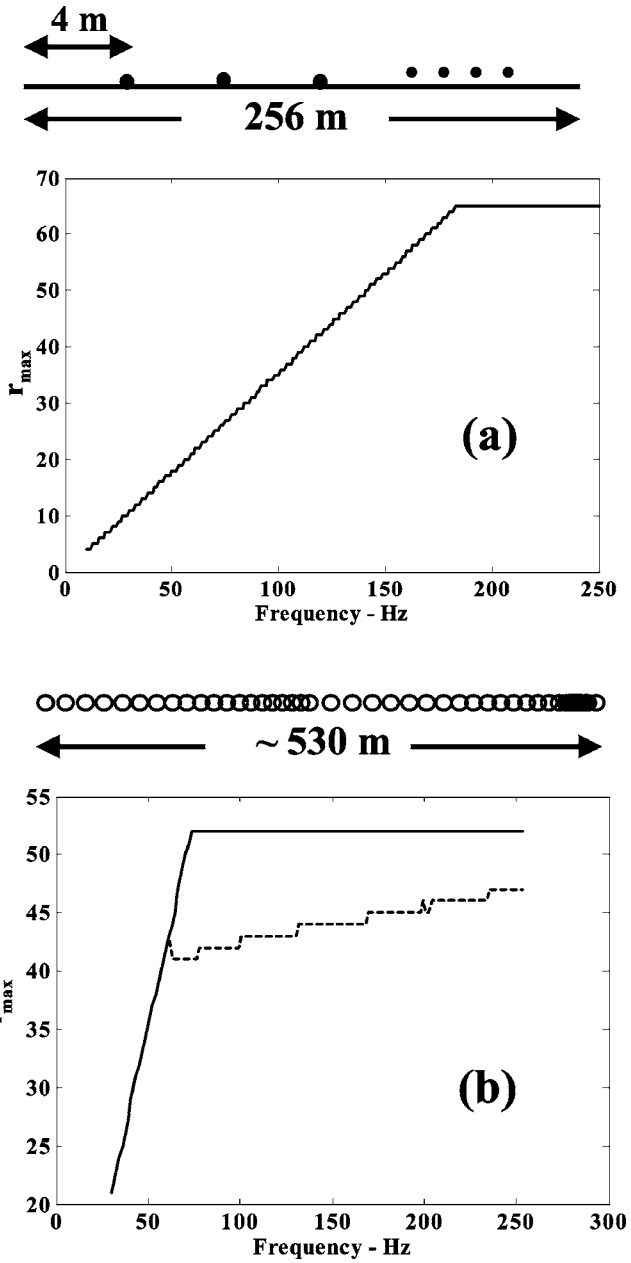

FIG. 5. Number of singular values for the pseudoinverse used in constructing the effective element filter. (a) Uniform element spacing. (b) Nonuniform element spacing. The solid line is from Eq. (8), and the dashed line is $r_{\max}$ for the modified N_λ filter as described in Sec. III C.

greater than those shown in Fig. 7, as discussed in Sec. III D 1.

C. Arrays with nonuniform element spacings

Equation (8) is not necessarily valid when considering arrays with nonuniform element spacings. Some of the singular values $k\leqslant N$ are too small when N_λ approaches N. Thus, the filter construction based on N_λ in Sec. II A must be altered for arrays with nonuniform element spacings in order to assure filter stability. This conclusion was based on results for a bottom-mounted horizontal line array with nonuniform element spacings.

The nonuniform array considered is a double-tapered array, depicted at the top of Fig. 5(b), and was used to collect the data discussed in Sec. IV. The behavior of $r_{\max}$ is shown in Fig. 5(b). The solid line shows the values used if the

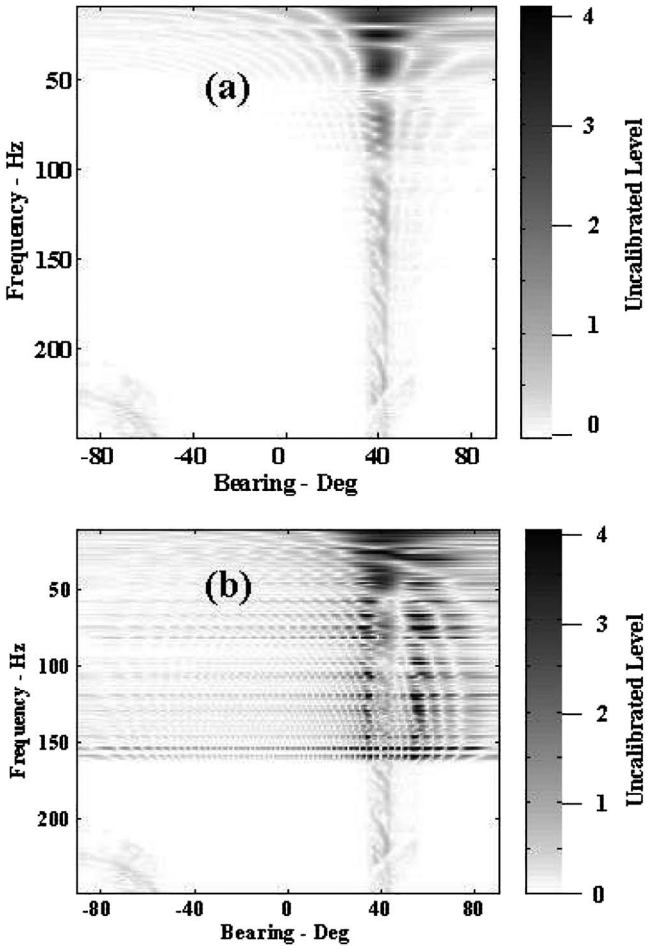

FIG. 6. Beam projection of filtered data using the fixed threshold filter for the simulation based on Fig. 1 with thresholds set to (a) 1×10^{-4} and (b) 1×10^{-6}.

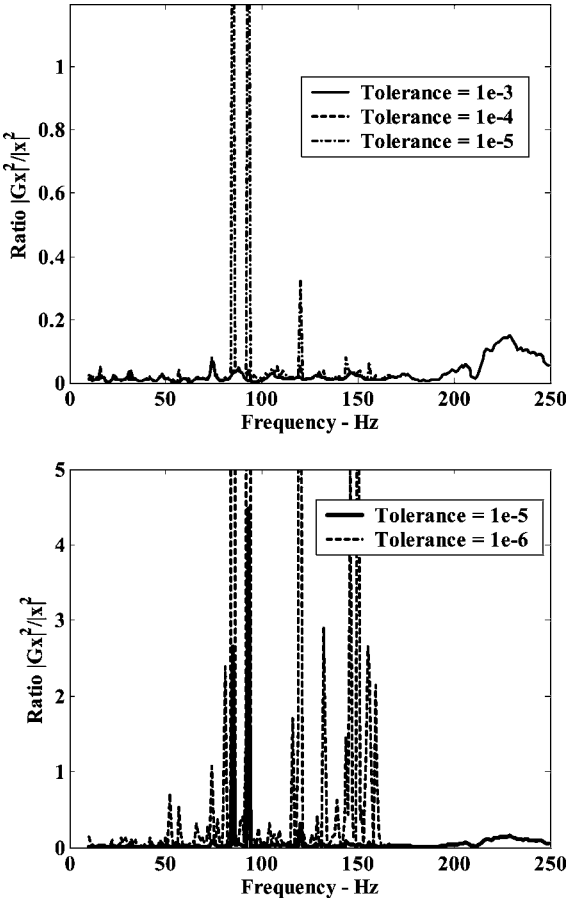

FIG. 7. Ratio of filtered data energy to unfiltered data energy for uniformly spaced elements.

method for the uniformly spaced arrays is applied, i.e., Eq. (8). The dashed line gives the actual $r_{\max}$ values that will be used instead for frequencies near or above the average design frequency, as discussed in the remainder of this section.

A threshold method is constructed to determine $r_{\max}$ above the average design frequency. Initially, two of the smallest singular values are excluded and this results in the initial discontinuity at approximately 50 Hz as shown in Fig. 5(b). Also, the nonuniform spacing of the elements results in the discontinuity shown at 200 Hz in Fig. 5(b), where one of the smallest singular values is excluded at this frequency. Neither of these discontinuities affects the filter design significantly.

Before discussing this high-frequency limitation of $r_{\max}$, it is useful to examine the operational frequency range of the nonuniformly spaced array. For illustration, the spacings between adjacent elements were assembled, and an ideal frequency for each pair was defined by $d=\lambda/2$. Figure 8 shows the ideal frequency for each pair. The close element spacings near the end of the array result in the high-frequency values beyond element pair 35.

An approximate design frequency for the nonuniform array is obtained by calculating the design frequency for the average element spacing, i.e.,

$$f_{\mathrm{AVG}}=c(N-1)/(2L). \tag{14}$$

For the array shown in Fig. 5(b), f_{AVG} is approximately 66 Hz.

A comparison between uniform and nonuniform element spacings of the behavior of the singular value spectrum shows why the rank must be limited. Figure 9 shows singular values for several frequencies. The overall shape of the spec-

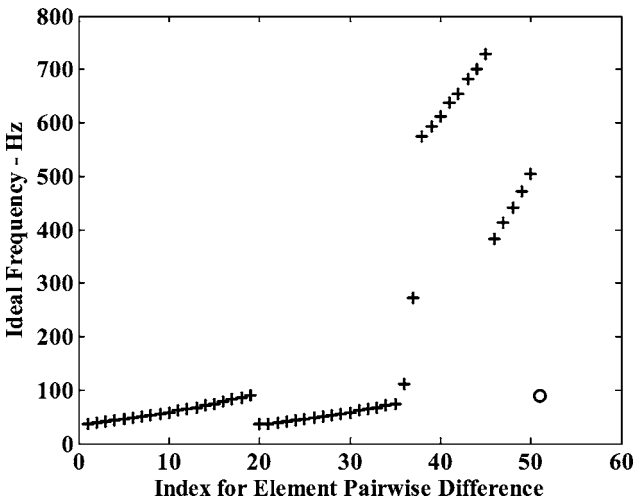

FIG. 8. Ideal frequency for pairs of consecutive elements in the nonuniform array (+) and average for tapered endfire subaperture (○).

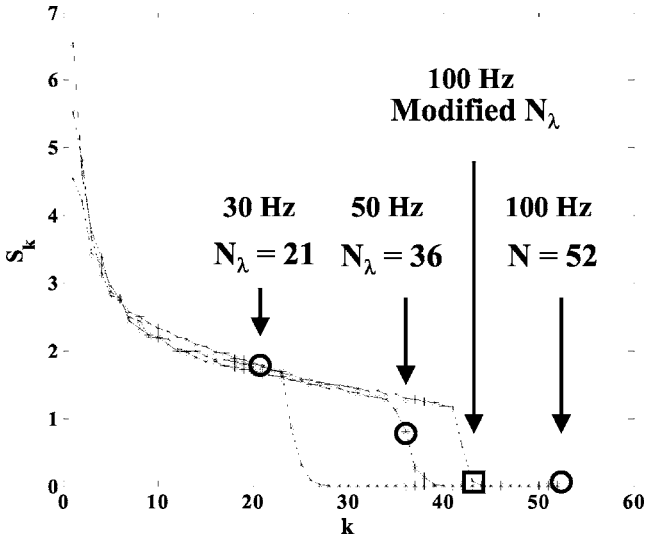

FIG. 9. Singular values as a function of frequency for the nonuniformly spaced elements. The $r_{\max}$ values from Eq. (8) are $N_\lambda = 21$ (30 Hz), $N_\lambda = 36$ (50 Hz), and modified N_λ (100 Hz).

tra is similar to that for uniform element spacings; however, the distribution as a function of frequency is changed and will depend on the array design. The circles in Fig. 9 indicate the N_λ points as in Fig. 4. For frequencies below f_{AVG}, N_λ can be used for $r_{\max}$. For frequencies above f_{AVG}, such as the 100-Hz example shown in Fig. 9, using $r_{\max}$ from Eq. (8) includes too many singular values. Thus, the filter will be contaminated (information from the noise subspace will be included in the signal subspace) and will fail.

To solve this problem, the knee is permitted to define $r_{\max}$. To search for the knee, the pairwise difference of the singular values is constructed. Monitoring the ratio of the pair difference to the first value of the pair easily identifies the location of the knee. The ratio being calculated is given by

$$R_s = |S_{k+1} - S_k| / S_k . \tag{15}$$

The ratios from Eq. (15) for 100 Hz are shown in Fig. 10. The sudden discontinuity which identifies the knee is apparent in Fig. 10. A somewhat arbitrary threshold of 1 was set

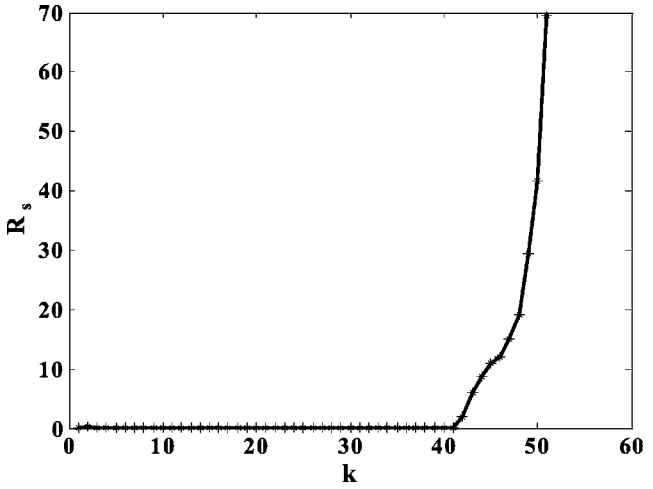

FIG. 10. Ratio, R_s, [Eq. (15)] used to identify the knee of the spectrum.

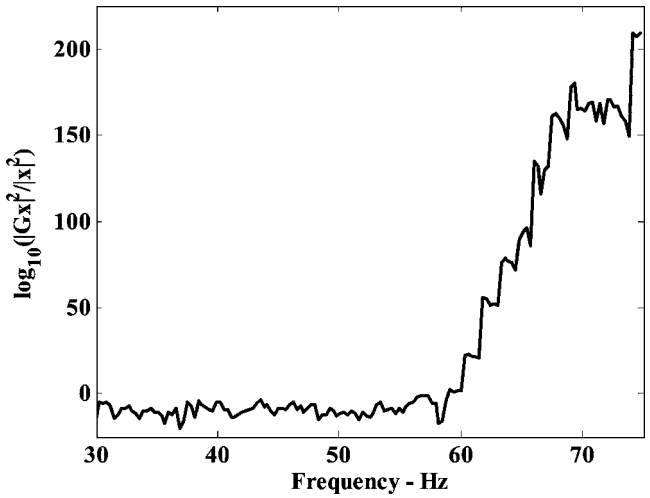

FIG. 11. Ratio of filtered data energy to unfiltered data energy for nonuniformly spaced elements.

for R_s to automate the detection of this knee. Note that this threshold value does not depend on frequency and is more robust than choosing $r_{\max}$ with a fixed singular value threshold.

The position of $r_{\max}$ is adjusted to include two additional singular values that have magnitudes less than the magnitude of the singular value at the knee, as long as these two singular values have $S_k > 10^{-4}$. These two additional singular values guarantee that all of the signal subspace is present in the pseudoinverse, while preserving the stability of the filter. The $r_{\max}$ value from the knee method is indicated by the square in Fig. 9 for 100 Hz.

The importance of applying the cutoff criteria at higher frequency for the nonuniformly spaced elements is established by Fig. 11, showing the ratio $\mathcal{R}$ from Eq. (13) for the N_λ method using Eq. (8) without a cutoff at high frequency. For values above f_{AVG}, $\mathcal{R}$ becomes much greater than 1 if no cutoff is included.

For the remainder of this work, filters constructed for nonuniformly spaced arrays will be referred to as modified N_λ filters, and it will be understood that the knee search and cutoff is being applied, unless stated otherwise.

D. Weak source in presence of loud interferer

The performance of the various filters is measured by evaluating the cost function at each interferer bearing. In this paper the cost function used for most of the simulations and all of the data analysis has the form[1]

$$1 - C = 1 - N_{\mathrm{REF}}^{-1} \sum_{s=1}^{N_{\mathrm{seq}}} \sum_{f_c=1}^{N_c} \sum_{\substack{i,j=1 \\ i \neq j}}^{N_e} \left(\frac{1}{N_f} \sum_{f=f_c-N_f/2}^{f_c+N_f/2} \frac{D_i D_j^*}{|D_{\mathrm{REF}}|^2} \right) \times \frac{M_i M_j^*}{|M_{\mathrm{REF}}|^2}, \tag{16}$$

where N_{seq} is the number of segments, N_c is the number of center frequencies, N_e is the number of elements, N_f is the number of bins averaged over each center frequency, D_i are the received pressure data, and M_i are the corresponding

received model pressures. Note that only the nondiagonal elements pairs are summed in the cost function construction.

The normalizations in Eq. (16) are defined for each frequency bin by

$$|D_{\mathrm{REF}}|^2=\sum_{i}^{N_e}|D_i|^2/N_e, \tag{17}$$

$$|M_{\mathrm{REF}}|^2=\sum_{i}^{N_e}|M_i|^2/N_e, \tag{18}$$

$$N_{\mathrm{REF}}=\left(\sum_{s=1}^{N_{\mathrm{seq}}}\sum_{f_c=1}^{N_c}\sum_{\substack{i,j=1\\ i\neq j}}^{N_e}\left|\frac{1}{N_f}\sum_{f=f_c-N_f/2}^{f_c+N_f/2}\frac{D_iD_j^*}{|D_{\mathrm{REF}}|^2}\right|^2\right.$$
$$\left.\times\sum_{s=1}^{N_{\mathrm{seq}}}\sum_{f_c=1}^{N_c}\sum_{\substack{i,j=1\\ i\neq j}}^{N_e}\left|\frac{M_iM_j^*}{|M_{\mathrm{REF}}|^2}\right|^2\right)^{1/2}. \tag{19}$$

For this cost function definition, the highest correlation C between data and model cross spectra gives a cost function value of 0. Also, $0\leqslant|C|\leqslant 1$, so that the cost function values range from 0 to 2, and the inversion seeks the minimum cost function.

1. Uniform element spacing

To demonstrate the filtering capability of the N_λ method compared to alternative methods, a weak source is filtered from a simulated acoustic field which includes one loud interferer. The weak source is located at 45° and at a range of 2800 m, whereas the interferer, which is 20 dB louder, is kept at a constant range of 3500 m. The interferer bearing was varied in 10° increments from −90° to 90° as depicted in Fig. 12(a). The simulated data were calculated for the same environment and array described in Sec. III B. To simulate a typical inversion, the real k-plane option of ORCA was used to generate the forward model inputs.

The cost function is shown in Fig. 12(b) as a function of interferer bearing location. The results from three filters (N_λ, fixed threshold, and polar decomposition) are shown, along with the result obtained if no filtering is first performed on the data.

Several comments regarding Fig. 12(b) are in order. First, the cost function is evaluated at the range and bearing of the quiet source. Second, for the unfiltered data, the presence of the loud interferer produces a very high cost function value, such that the quiet source is undetectable for all interferer bearings. Third, the high cost function value from the unfiltered data decreases as the interferer gets closer to the quiet source, but this occurs because the field from the interferer contains more of the same components as the field from a quiet source along the same bearing, and not because the quiet source is more distinguishable at those interferer bearings. Within the window region, the cost function value from the filtered data approaches the unfiltered value, which shows that the cost function is dominated by the interferer and not the quiet source, even at the range corresponding to the quiet source.

An important observation regarding Fig. 12 is that all three filters produce similar results. As shown in Fig. 12(b), data from each filter give cost function values below 0.3 for interferer bearings less than approximately 20°. The lowest cost function values are obtained from the fixed threshold data; however, several searches were made in order to set the threshold as discussed in Sec. III B, making this method onerous to implement for different array designs. For example, increasing the threshold by 4 orders of magnitude, to 1.0, gives cost function values comparable to the N_λ filtered data in Fig. 12(b). Data from the N_λ filter give a low cost function value, and the N_λ filter is stable for all interferer bearings. The plane-wave polar decomposition filter gives a cost function behavior similar to the N_λ filter since the singular values included in the N_λ filter have values greater than

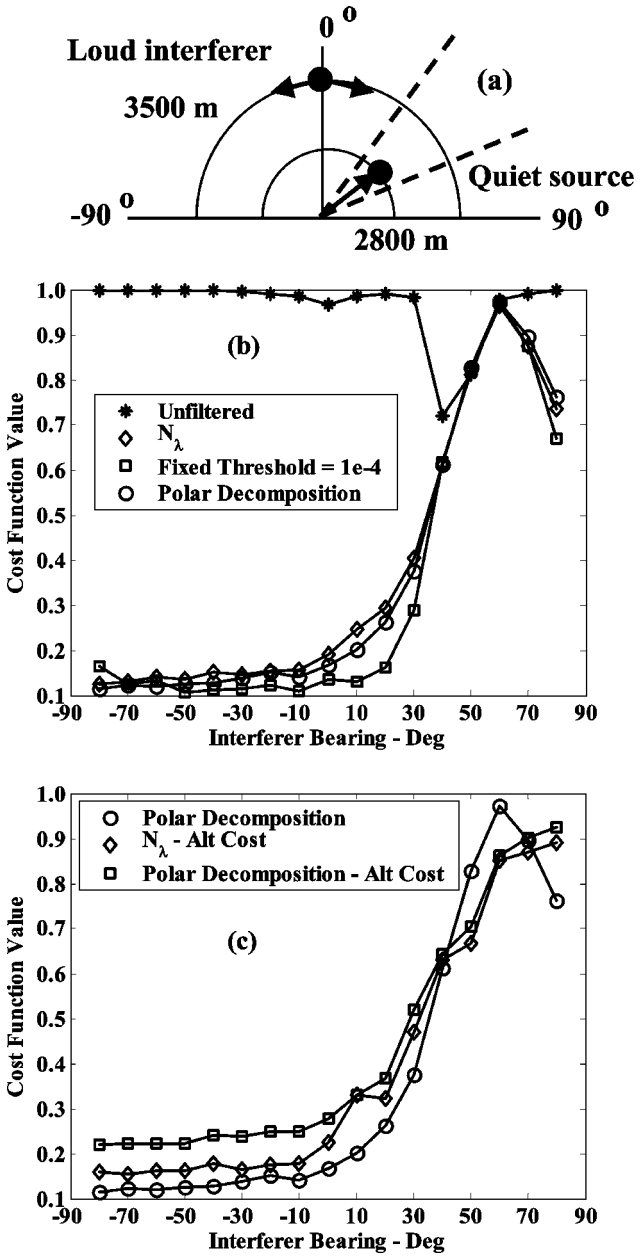

FIG. 12. Cost function at the weak source position in the presence of a loud interferer. (a) Loud interferer and quiet source geometry. (b) Comparison of unfiltered, N_λ filtered, fixed threshold filtered, and polar decomposition methods. (c) N_λ and polar decomposition method using an alternate cost function compared to polar decomposition result reproduced from (b).

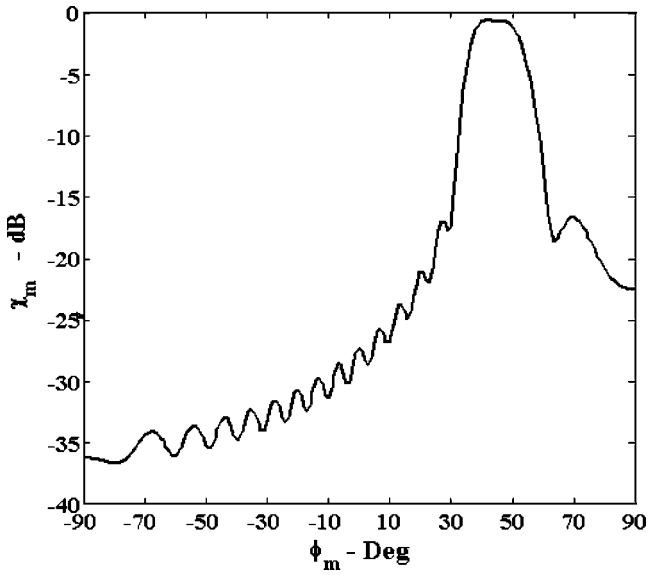

FIG. 13. Filter response of a 20° N_λ filter window centered on a bearing of 45° for the equally spaced array depicted in Fig. 5(a).

1.0, as shown in Fig. 4. A fixed threshold filter with a theshold of 1.0 also gave cost function behavior similar to the N_λ filter.

The plane-wave polar decomposition filter produces cost function values which are somewhat sensitive to the normalization. This is illustrated in Fig. 12(c), where an alternate cost function was constructed by applying an overall normalization of the cross-phone correlations only after averaging over the frequency bins, in contrast to Eq. (16). Filtering with the plane-wave polar decomposition method gives data that produce greater sensitivity to the form of the cost function than the data from the other filters. Applying a plane-wave polar decomposition filter to real data may be disadvantageous if cost function robustness is important for localizing sources of interest and thus may be too restrictive, whereas the N_λ and fixed threshold methods are less sensitive to the differences in the two cost functions.

The behavior of the cost function, as the interferer approaches the filter window from either side, is understood by considering the filter response shown in Fig. 13. The filter response is produced by calculating the norm of $Y^\dagger G$, the projection of the filter onto beam space

$$\chi_m = \sqrt{\sum_{n=1}^{N} \left(\sum_k Y_{mk}^\dagger G_{kn} \right)^2}, \tag{20}$$

where χ_m is the response at a given beam direction ϕ_m. For filter responses exceeding -20 dB, the interferer (20 dB louder than the quiet source) affects the filtered data and the cost function, i.e., for bearings between 20° and 70°.

The example in Fig. 12 of the effect of a single loud interferer serves as a good test of the filter performance since the relative energy level between the quiet and loud source is comparable to the sidelobe level of the filter response shown in Fig. 13.

To demonstrate that an inversion would give the cost function minimum at the actual quiet source range and depth, the range–depth ambiguity surface was constructed by calculating the cost function value over a vertical slice at the quiet source bearing of 45° with a loud interferer at bearing 0°, as depicted in Fig. 12(a). Figure 14 shows the resulting ambiguity surfaces from unfiltered and N_λ filtered data. The ranges are sampled every 20 m and the depths every 1 m. For the unfiltered data, the cost function values range from 0.97 to 0.988, again demonstrating that the quiet source is undetectable. For the filtered data, the cost function values span 0.12 to 0.85, and the minimum is located at the correct range of 2800 m at the near-surface source depth.

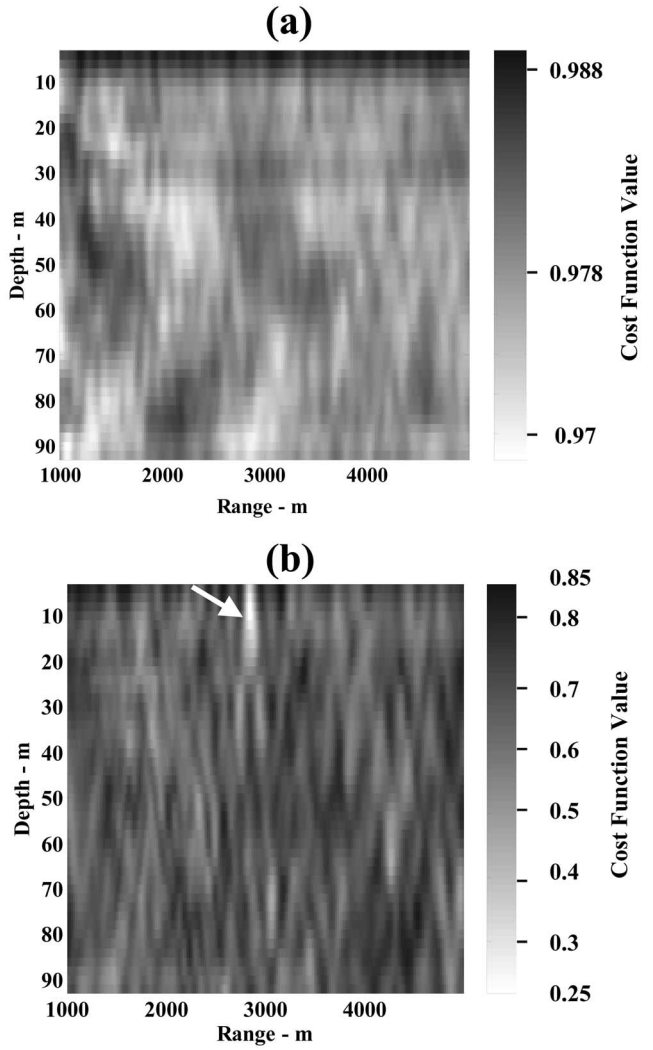

FIG. 14. Range–depth ambiguity surface for two sources positioned as depicted in Fig. 12(a). Cost function values from (a) unfiltered data and (b) N_λ filtered data.

2. Nonuniform element spacing

One problem associated with filtering weak sources in the presence of loud interferers for arrays with nonuniformly spaced elements has to do with the unweighted beam transformation, Eq. (1). Grating lobes can appear which inhibit the ability to isolate the source of interest. The acoustic field at the nonuniform array in Fig. 5(b) was simulated, and the beam projections of the filter were computed for an interferer 20 dB louder than the source of interest. This source was held constant at a bearing of 45° and a range of 2800 m, and

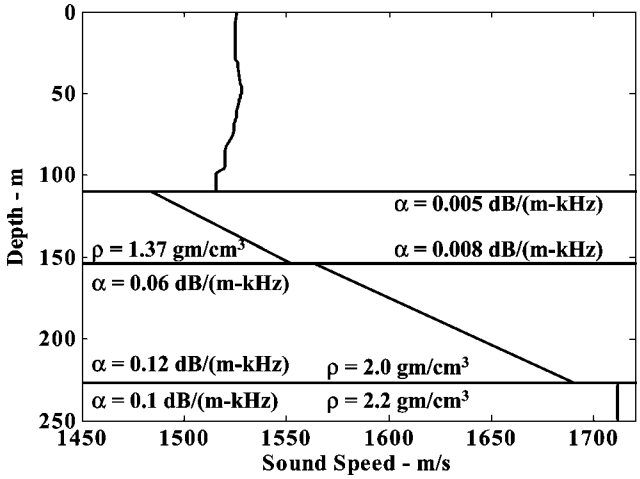

FIG. 15. The environment obtained from an inversion analysis of data taken during the Gulf of Mexico (GOM) experiment.

the interferer was placed at a bearing of 0° and a range of 3500 m, as shown in Fig. 12(a). The environment used in these simulations is representative of the environment for the data analysis discussed in Sec. IV and is depicted in Fig. 15. Also, a frequency band of 120–195 Hz was used for the simulation considered here, as well as for the data analysis in Sec. IV. For cost function calculations with Eq. (16) center frequencies at approximately 7 Hz spacings were used with averaging over 5 bins about each center frequency.

The beam projections for this array are shown in Fig. 16 for unfiltered and modified N_λ filtered data. The approximate width of the filter in bearing space is also designated by the vertical bars in Fig. 16(b). For the unfiltered data in Fig. 16(a) both sources are observed at frequencies below approximately 125 Hz. In the filtered data at frequencies below the average design frequency, $f_{\mathrm{AVG}} \approx 65\,\mathrm{Hz}$, defined in Eq. (14), the loud source has been successfully filtered out. Well above the design frequency, for frequencies greater than approximately 125 Hz, grating lobes cause the data inside the filter to be dominated by the loud interferer and will prohibit the localization of the weak source. These origins of the strong signals appearing in the filter window were identified by removing the quiet source from the simulation and then applying the filter. The resulting beam projection (not shown) is nearly identical to the one in Fig. 16(b) for frequencies above f_{AVG}. At frequencies below f_{AVG} no source appears in the filter window with the quiet source removed.

The effects on the cost function of varying the frequency band, as well as the strength of the interferer relative to the quiet source, are shown in Fig. 17. The interferer and source are located at the same positions as they were for Fig. 16. In Fig. 17(a) for the 120–195-Hz band, the cost function minimum value increases from 0.3 with a 5-dB louder interferer to 0.8 with a 20-dB louder interferer. For the 30–105-Hz band, the minimum in Fig. 17(b) is approximately 0.24 for the 5-dB louder interferer and only increases to 0.5 for the 20-dB louder source. Of course, lowering the band to combat aliasing and improve the localization will not help if the source does not emit much energy there! In the analysis of

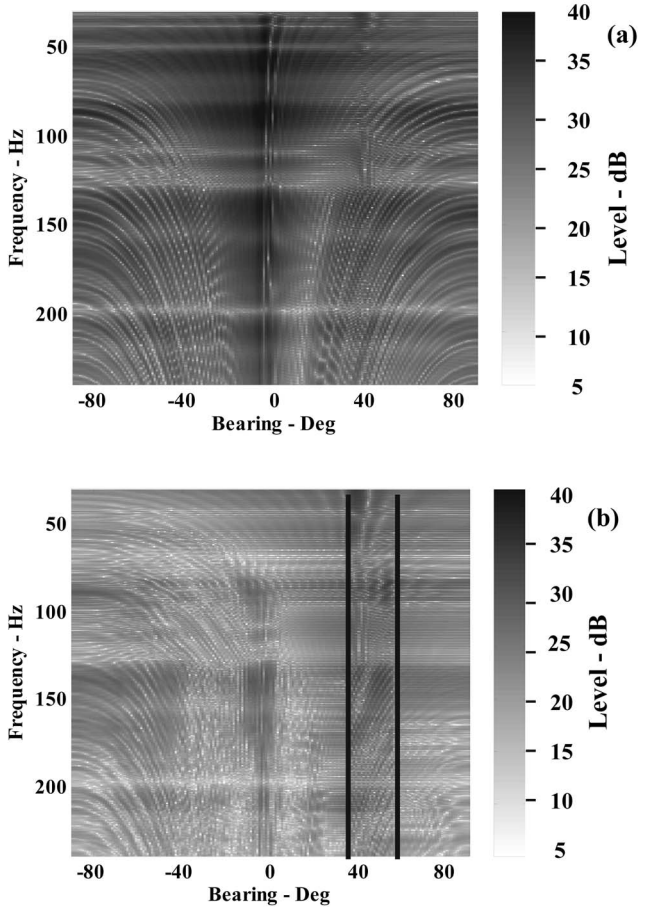

FIG. 16. Beam projections of the (a) unfiltered and (b) N_λ filtered data from a simulation with the nonuniform array in the GOM environment. Interferer bearing 0°, quiet source bearing 45°.

the real data in Sec. IV the seismic sources were also dominant below 120 Hz.

The problem of nulling out loud sources has a long history in adaptive beamforming (ABF). For a given beam sector, the spatial filter constructed here does not change with respect to time even if the interferers move, unlike an ABF filter, which is constructed from the noise field. Still, it might be interesting to apply ABF weights in the filter construction, but that is not discussed here.

The simulations presented here were intended to study the performance limits on the filter response and to represent the extreme case. In the next section, however, the importance of filtering will be demonstrated for localizing a surface ship, in the presence of several interferers, during several data segments of an actual experiment.

IV. APPLICATION TO REAL DATA

Data were collected in the Gulf of Mexico (GOM) using a horizontal line array (HLA) of nonuniformly spaced elements (the nonuniform array examined in Sec. III C) located on the bottom. Inversions of the geoacoustic parameters were obtained using implosive sources.[35] In this section these geoacoustic parameter values will be used to localize the source of interest, the RV LONGHORN (research vessel used in the experiment) in a range-independent environment. Also,

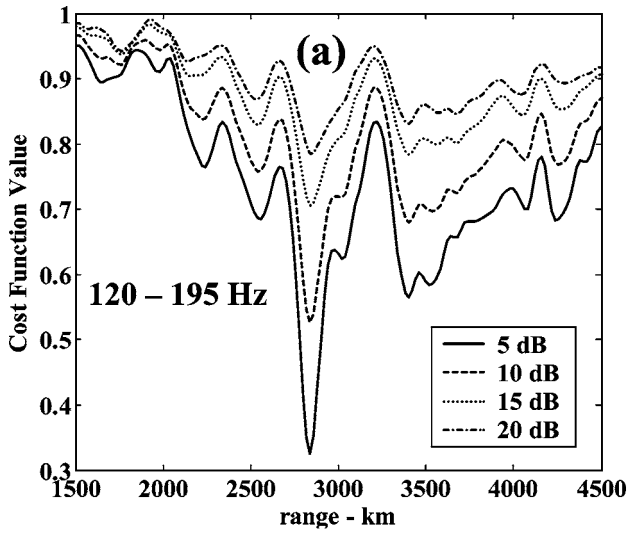

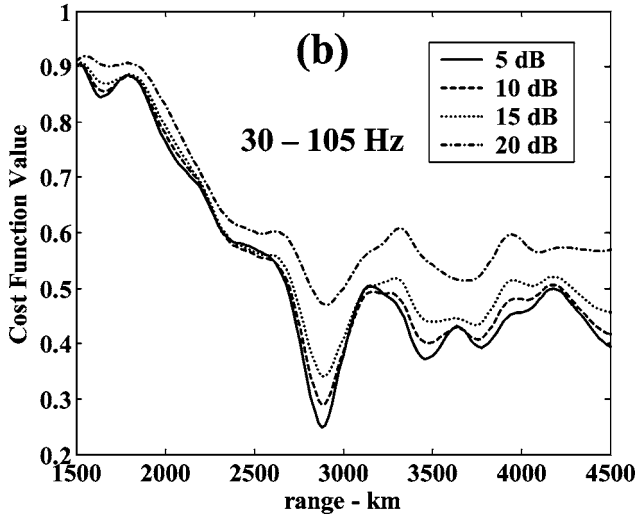

FIG. 17. Dependence of cost function on SNR for (a) 120–195-Hz band and (b) 30–105-Hz band.

the localizations for individual time segments are examined in detail to compare the inversion results for the unfiltered, modified N_λ filtered, CBF subarray beamformed, and threshold filtered data. In addition, ambiguity surfaces at each segment are analyzed to further understand the localization results, and these will be discussed.

The analysis presented in Secs. IV C–E will emphasize the robustness of the modified N_λ filter over the other filters. Three main points are revealed in the analysis. First, the cost function minimum values and the locations of the minima in range-bearing space depend on the type of filter applied to the data being used in the cost function. This observation is especially applicable to subaperture data, for which the ambiguity surface depends on the subarray selection. Second, the modified N_λ filter avoids having to optimize either a threshold or the subarray selection and is thus more efficient and robust. Finally, depending on the total length of the subapertures, additional improvements with subaperture data can be realized by first filtering the data prior to beamforming.

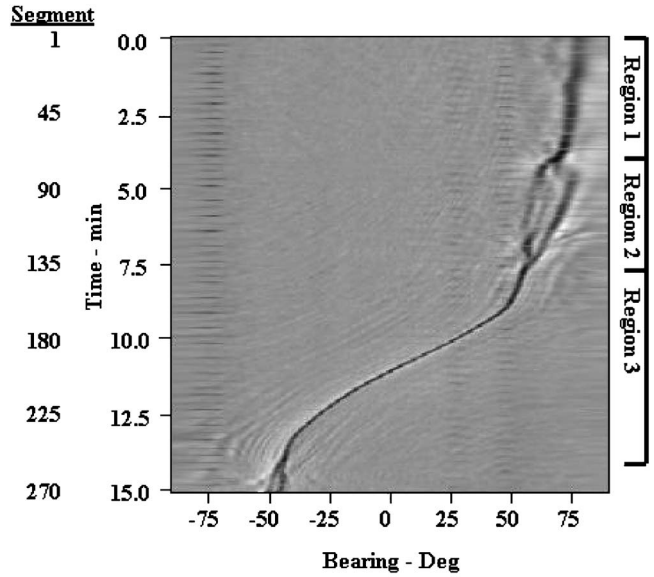

FIG. 18. Bearing-time display from the RV LONGHORN for the example data from the GOM experiment.

A. Experiment

The environment obtained from the inversions of previous work is depicted in Fig. 15. The water depth is approximately 110 m in this range-independent environment. The first bottom layer has an initial sound speed lower than the water sound speed at the water–sediment interface, so that no critical angle exists for propagation in this layer. The sound speed at the top of the second layer is larger than the sound speed at the bottom of the first layer, so that a critical angle effect is produced at that interface. These layer sound-speed differences lead to a large separation of the multipaths when the source approaches a critical range of approximately 2 km, as shown in region 2 of the bearing-time display in Fig. 18.[23] A moving source model, based on ORCA,[3] and incorporating broadband levels, was used to calculate the field to the same array geometry as the experiment. This model reproduced the close range multipath effects shown in Fig. 18. In this region, refraction of paths penetrating into the bottom layers was verified by modeling the same source in an environment with the bottom layers removed.[24]

Figure 18 spans the time period in which localizations were performed. The array axis was oriented at approximately 66° East of North (E of N), and the source is approaching the array from endfire starting at the top of the bearing-time display. The dominant source track corresponds to the RV LONGHORN, as mentioned previously. Bursts from seismic profilers are also apparent in the display at several other bearings (−75°, 25°, and 50°); therefore, this is an example of a multisource environment. Each data segment in Fig. 18 is built from an 8-K FFT of digitized data sampled at 2457.6 Hz.

The projection onto beam data of the unfiltered and filtered data, using all the elements of the array, for a sample data segment near 0 min in Fig. 18 is shown in Fig. 19 as a function of frequency. The single dominant source during this time segment, the RV LONGHORN, is at bearing 80° near endfire of the array. A comparison of the unfiltered, Fig.

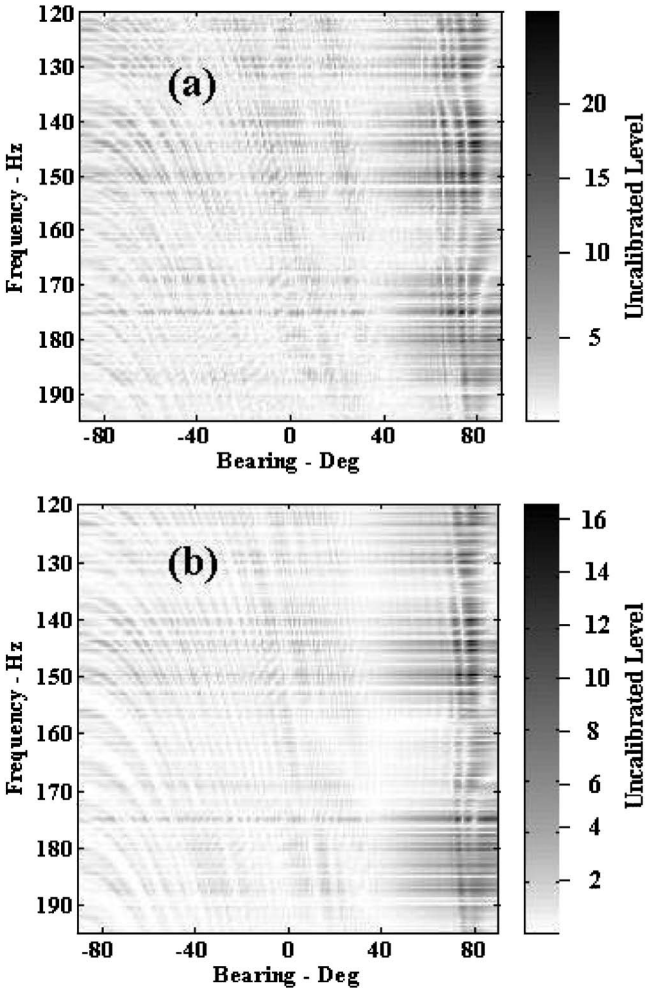

FIG. 19. Multipath structure in the beam projection of the GOM data. (a) Unfiltered and (b) modified N_λ filtered.

19(a), and the filtered, Fig. 19(b), data shows that some, but not all, of the energy in the multipath structure is retained by the filter process. The filter window was 20° with one window boundary at 90°.

The data in Fig. 18 are divided into three regions as shown. In regions 1 and 3 a 20° window allowed enough energy to be retained such that the global minima in constructed range-bearing ambiguities occurred at the correct source localizations, as will be discussed in Secs. IV B and IV C. In region 2, however, the soft surficial sediment supports many refracted arrivals, and at ranges near 1.4 to 2.2 km, the multiple arrivals are strong compared to the waterborne paths and arrive at well-separated angles as shown in Fig. 18. (Multipaths with unique vertical angles arrive on conical HLA beams, which are in turn projected onto distinct horizontal bearings and diverge as range decreases.) Thus, in Secs. IV B and IV C for processing in region 2, the filter window was increased to 30° to include more energy from the separated multipaths. Region 3 was similar to region 1, and a 20° window shifted by 10° towards broadside (0°) from the window used for processing region 1 was used for localizations in region 3. However, the emphasis in this paper is on filter performance in regions 1 and 2, and region 3 is omitted from the analyses presented in this section. The 30° window could be used in regions 1 and 3, but this also increases the interferer noise in the filtered data.

B. Demonstration of inversion

For a demonstration of the application of filtering to inversions with real data, the RV LONGHORN near endfire (90°) of the array was localized in range and bearing using all the elements of the array for time segment 57 (near the middle of region 1 in Fig. 18). A 6-m source depth was assumed in the forward model calculations. The ambiguity surfaces in Figs. 20 (filtered data) and 21 (unfiltered data) for time segment 57 were obtained by varying the range in 20-m increments and the bearing in 1-deg increments. One consideration for these figures is that the matrix filtering technique works for real data, giving a source localization at the correct range and bearing, as seen in Fig. 20(a). For this region 1 segment, having no dominant interferer permits the localization of the source from the unfiltered data, but the cost function value is near 0.4 (Fig. 21) as compared to 0.15 (Fig. 20) from the modified N_λ filtered data. Thus, another conclusion is that the N_λ filter for the nonuniform array produces data that give a much lower cost function value, by filtering out the noise, than is obtained from unfiltered data.

The importance of applying the correct filter (modified N_λ) for the nonuniform array is demonstrated in Fig. 21. Applying the N_λ filter given in Eq. (8) for the uniform array to the nonuniform array in the real dataset fails due to the filter instability discussed in Sec. III. The data from the unmodified N_λ filter give high cost function values (dashed line) near 0.75, and the source is not localized because, as shown in Fig. 21(b), the minimum cost function value does not occur at the correct range.

To analyze the filter performance in more detail, and to demonstrate that correct source localization is obtained from inversions with filtered data, several data segments were used in an actual inversion at ranges before, during, and after the well-separated multipath ranges, i.e., through regions 1–3, respectively. The RV LONGHORN was initially located at approximately 3000 m and was approaching the array from endfire for these inversions. A simulated annealing algorithm was used to successfully localize the range and bearing for several individual data segments using all the elements of the array. An initial search range within ±200 m of the determined ground truth position was used and the bearing search was restricted to a 70°–90° bearing window (the filter window width) in the inversion. The ground truth was obtained from GPS sensors located on the source, and a GPS reading was recorded at the site of the array during deployment. The frequency band used in the filter construction and inversion is the band 120–195 Hz used in the simulations presented in Sec. III D 2. This will also be the band used throughout the data analysis in Secs. IV C–E.

The cost function values from the filtered data are lower than from the unfiltered data by approximately 0.2 for most of the time segments. Both unfiltered and modified N_λ filtered inversions tracked the source in regions 1–3. More detailed analysis shows the improvements obtained from filtering the data, since in a realistic inversion restrictions on

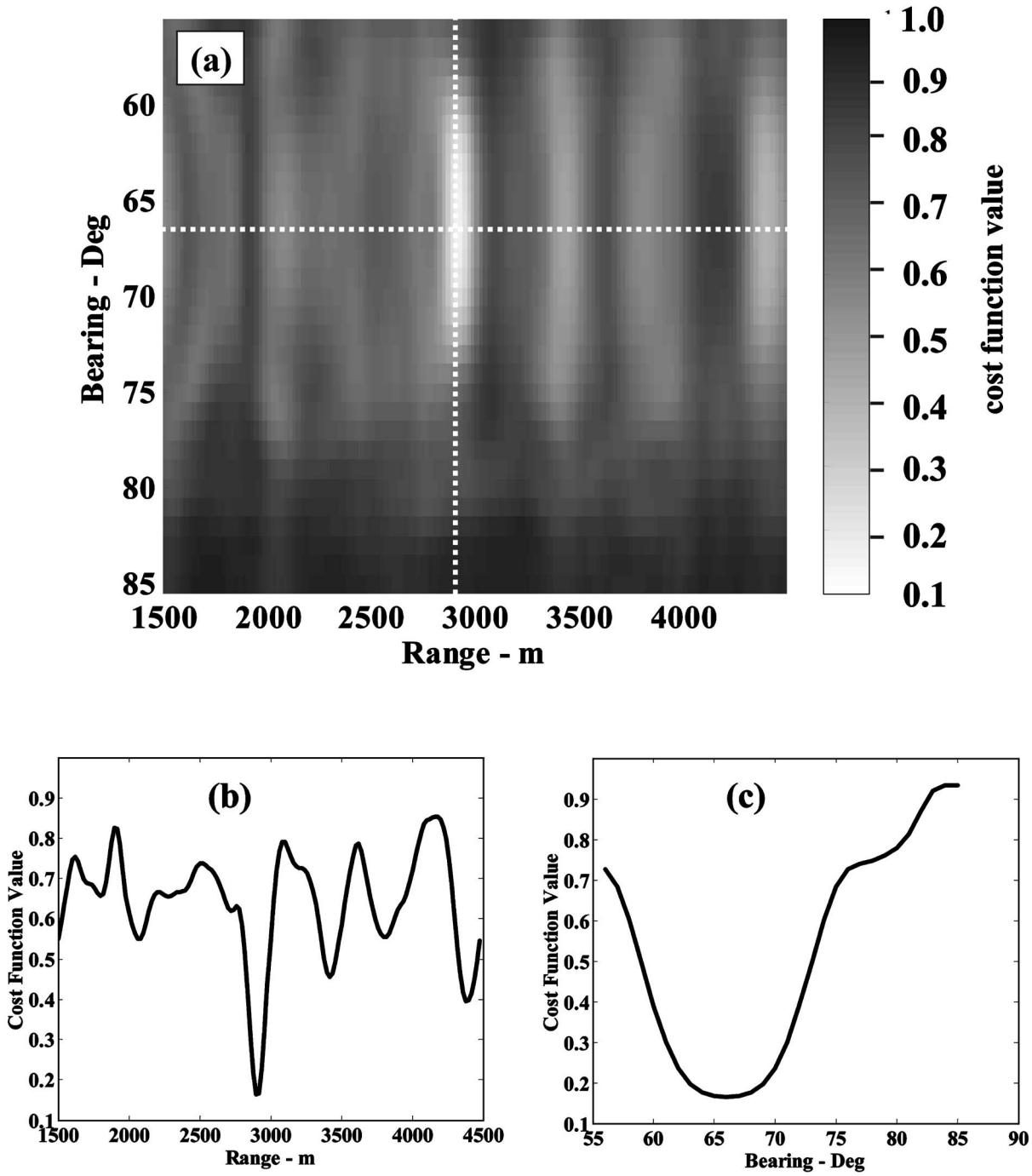

FIG. 20. (a) Range-bearing ambiguity surface for the GOM example using data from the modified N_λ filter. (b) Range and (c) bearing cost function slices through the minimum of the ambiguity surface.

the search space may not be available. Sections IV C–E contain more discussion of results with filtered data.

C. Filter performance summary

Details of the localization, including the effects of the multipath arrivals on the localization, were examined by considering range-bearing ambiguities and expanding the search space to represent a realistic search for unknown source locations. Four kinds of data were studied with the localizations: unfiltered, modified N_λ filtered, threshold filtered, and subaperture data. For the subaperture data several element subsets of the array were CBF beamformed, as discussed in more detail in Sec. IV D.

Energy paths that penetrate into the higher sound-speed sediment layers are manifested as sidelobe ambiguities in range and bearing. Some arrivals other than the waterborne paths produce sidelobes at ranges approximately 800 m closer than the actual positions. Other arrivals are projected as emanating from a source at farther ranges. In addition, other sources present in the data can produce minima in the ambiguity surface or turn multipath sidelobes into global

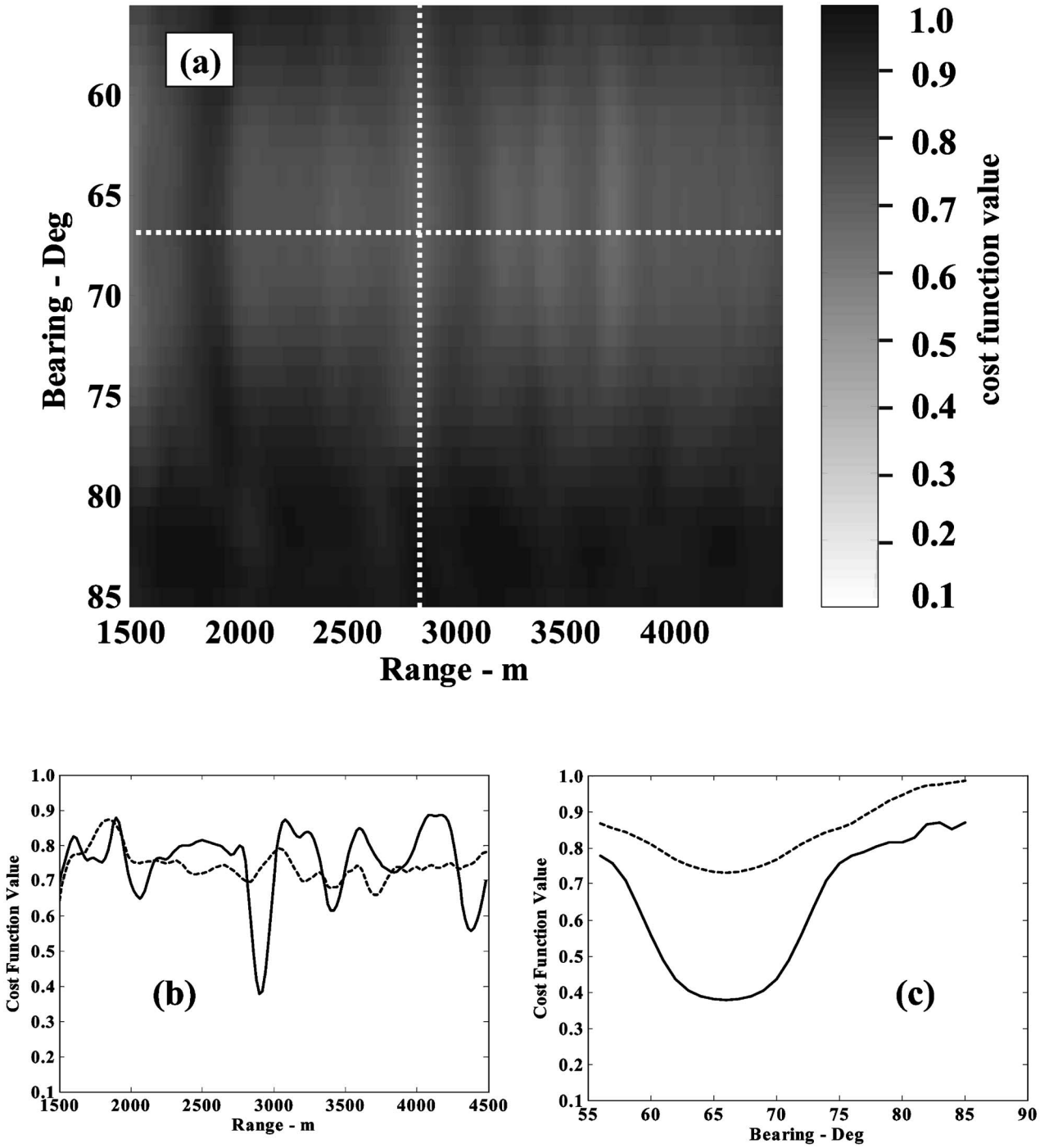

FIG. 21. (a) Range-bearing ambiguity surface for the GOM example with unfiltered data. (b) Range and (c) bearing cost function slices through the minimum of the ambiguity surface from unfiltered (solid) and Eq. (8) N_λ filtered (dashed) data.

minima. Since the frequency band is above the design frequency of the array, the alias lobes discussed in Sec. III D 2. could also result in additional false minima. No attempt will be made here to identify all the types of the minima seen in the ambiguity surfaces.

Ambiguity surfaces from the unfiltered and modified N_λ filtered data are shown in Fig. 22 for time segment 89, near the middle of region 2. The actual source location is approximately 1700 m in range and 76.4° bearing E of N. For purposes of analysis and discussion, the ambiguity surface was bracketed into 2 subsurfaces, e.g., as shown by the horizontal line at the 1500-m range in Figs. 22(a) and (b). An examination of the cost function values is made at ranges and bearings above and below the arbitrary line. The minimum in each subsurface was found separately and compared among the unfiltered, filtered, subaperture, and filtered-subaperature data. The latter two types of data are discussed in more detail in Sec. IV D. The minima in the two ambiguity subsurfaces will be called close-range and far-range ambiguities, respectively. As the source approaches the array the minimum corresponding to the actual source position should shift from the far-range subsurface to the close-range subsurface near time

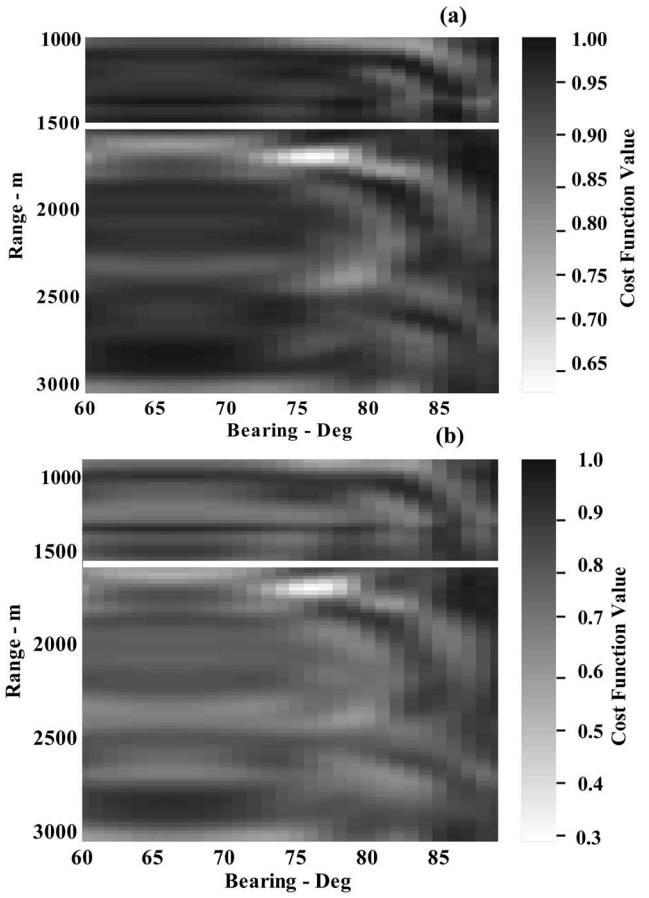

FIG. 22. Range-bearing ambiguity surfaces and the division into close and far subsurfaces for time segment 89 in region 2 with (a) unfiltered and (b) modified N_λ filtered data.

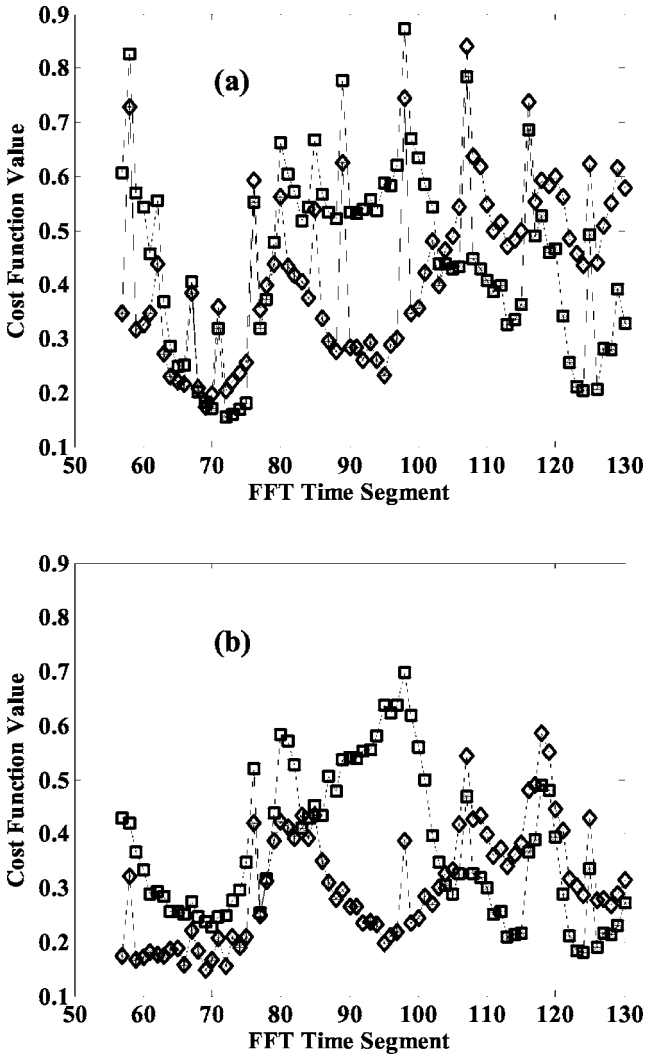

FIG. 23. Cost function values at the minimum on each ambiguity subsurface and the values at the global minimum for (a) unfiltered and (b) modified N_λ filtered data. Minima in the subsurface with ranges less than 1500 m (squares), in the subsurface with ranges greater than 1500 m (diamonds), and the global minimum over the entire ambiguity surface (asterisks).

segment 110. The structure of the ambiguity surface depends on the kind of data and on the time segment. Analyzing each ambiguity surface segment by segment revealed the time evolution of the minima and aided in the analysis. The value of the cost function at the minimum in Fig. 22(b) with the modified N_λ filtered data is much lower than the minimum value in Fig. 22(a) and permits the correct localization for the source. For example, the ratio of the cost function value of the global minimum to the cost function value of the close range ambiguity for time segment 89 is 0.552 for the filtered data as compared to 0.803 for the unfiltered data. (There are also intrinsic ambiguities due to the symmetry of the line array, which are expected and are not discussed here.)

The ambiguity surfaces for other time segments look similar to those in Fig. 22 but have differing structure with respect to range, especially in region 2, where the multipath effects become apparent. During propagation, the relative energy between the paths fluctuates, due to the bottom interaction at closer ranges, as discussed previously, and this manifests itself as more complicated ambiguity structure in region 2. Near the end of region 2 (segments 122–130), propagation effects resulting from possible mismatches between the data and the assumed geoacoustic model produce additional minima near the actual source position.

The cost function minimum values from the ambiguity subsurfaces, compared to each other and to the global minimum found over the entire search space, are shown in Fig. 23 for time segments from regions 1 and 2. The cost function values from the filtered data are consistently lower than from the unfiltered data, and the global minimum from the filtered data for each FFT time segment corresponds to the actual source position through most of region 2. During the multipath splitting (region 2, FFT time segments 75–100), the cost function values increase for both the filtered and unfiltered data.

Further insight is gained by examining Fig. 24, which contains the range localizations from the subsurface minimum and from the global minimum found in Fig. 23. The unfiltered data from portions of segments 67–79 produce incorrect source positions. For the modified N_λ filtered data the correct source position corresponds to the global minima throughout region 2, demonstrating the importance of the filter.

The position of the global minima for bearing localizations obtained from the unfiltered data is shown in Fig. 25(a) and exhibits greater variation than the bearings from the fil-

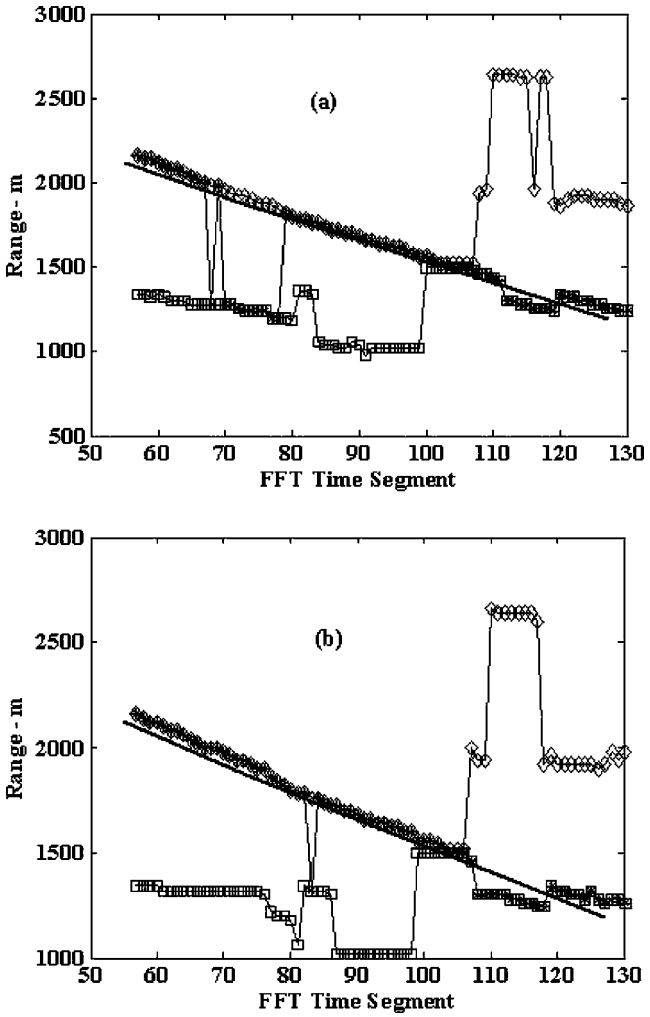

FIG. 24. Ranges at the global and ambiguity subsurface minima in Fig. 23 for (a) unfiltered and (b) modified N_λ filtered data. Symbols used as in Fig. 23. Ground truth source track ranges (line) from the GPS recordings.

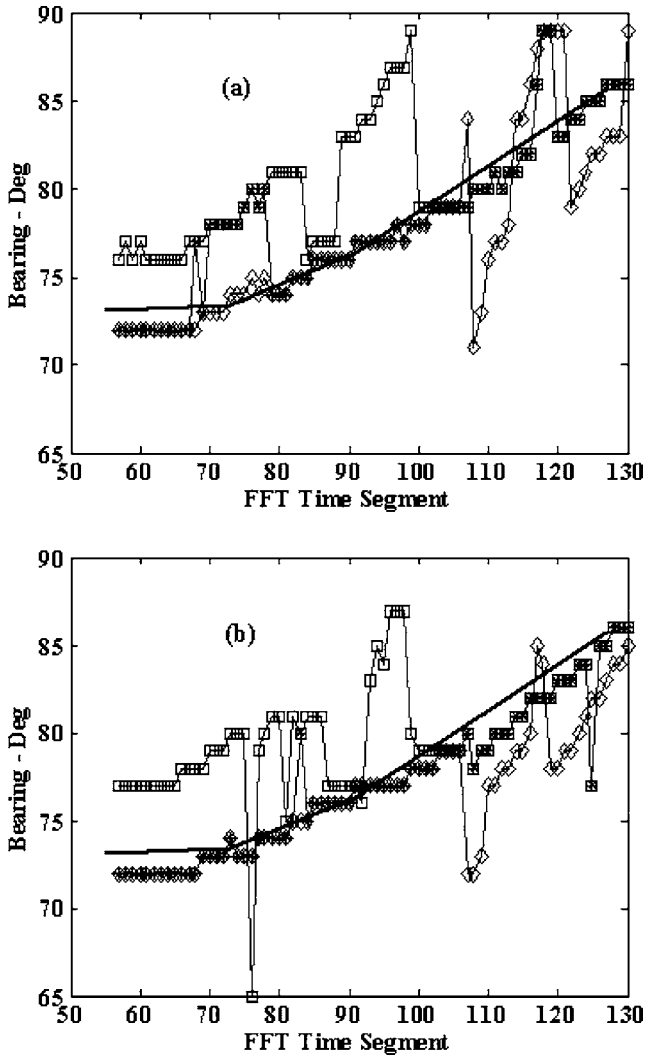

FIG. 25. Bearings at the global and ambiguity subsurface minima in Fig. 23 for (a) unfiltered and (b) modified N_λ filtered data. Symbols used as in Fig. 23. Ground truth source track ranges (line) from the GPS recordings.

tered data shown in Fig. 25(b). Further, the global minima for the filtered data track the source to within 2° almost throughout and are closer to the actual source bearing than the bearings from the unfiltered data for region 2 time segments 67–79.

The importance of the filter window width is shown in Fig. 26 for the ambiguity surface at time segment 100. The minimum of the cost function at the source position for the 30° window is much lower relative to the minimum from the 20° window due to the inclusion of more multipath energy in the cost function.

The filtering does suppress most of the energy due to the seismic interferers. The performance of the filter in suppressing interferers was examined by calculating the energy in the band 120–195 Hz. The energy was averaged over each center frequency and each receiver element. This value was calculated for each FFT time segment from both the unfiltered and filtered data, and then the ratio $\bar{\mathcal{R}}$ of the filtered data energy to the unfiltered data energy was evaluated to test the energy conservation of the filter. The ratio was less than 0.5 throughout regions 1 and 2, except for two time segments 60 and 61 where both unfiltered and filtered energy levels were low, but $\bar{\mathcal{R}}$ was greater than 1. The seismic sources are active at least every 10 segments in Fig. 23(a), where high cost function values are seen for the unfiltered data during these segments. The filtered data significantly reduced the large peaks from the seismic profilers. This demonstrates the filter's ability to isolate a source of interest in real data containing multiple sources.

Next, the fixed threshold filter (with a threshold of 0.1) was evaluated. Evaluating the cost function and comparing its minima to the cost function values in Fig. 23(b) shows this threshold filter to be comparable to the modified N_λ filter for the nonuniform array. Also, the accuracy of range and bearing determinations with the data from this fixed threshold filter are comparable to those in Figs. 24(b) and 25(b), respectively. The threshold of 0.1 is 3 orders of magnitude higher than the threshold used for the uniform array, 1×10^{-4}. If the 1×10^{-4} threshold is used for the nonuniform array, the fixed threshold filter becomes unstable and gives erroneous values for the source ranges and bearings for all the time samples, as exemplified by the range determinations shown in Fig. 27. The cost function values are approximately 0.8 throughout all the time segments shown in Fig. 27.

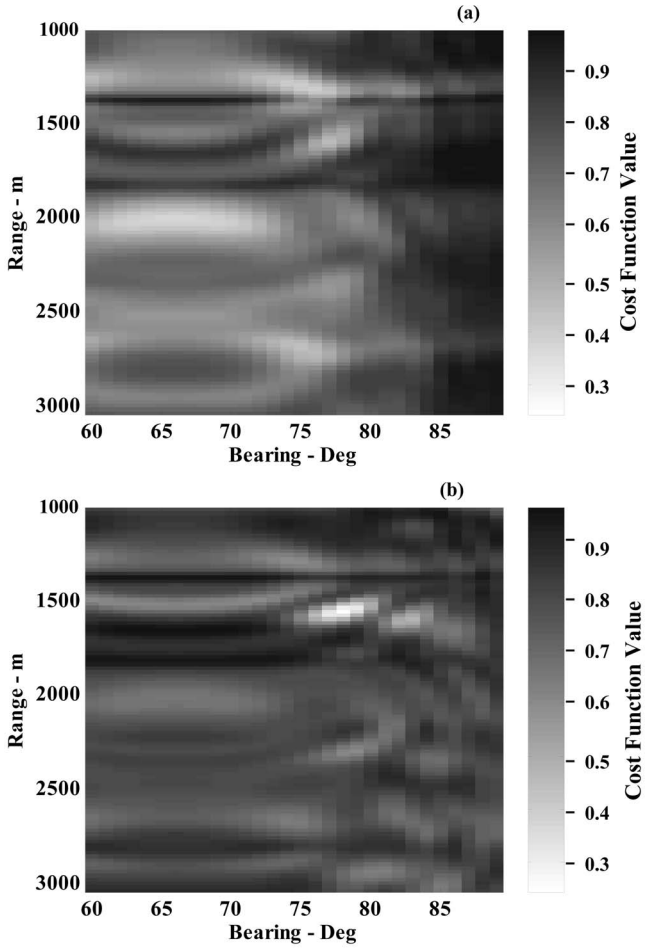

FIG. 26. Range-bearing ambiguity surface at time segment 100 for the modified N_λ filtered data with (a) 20° window and (b) 30° window.

Figures 23–25 demonstrate the stability and accuracy of inversions using the modified N_λ filtered data as compared to the unfiltered data. Both methods used all the elements of the array in the inversion and thus spanned the total aperture. In Sec. IV D the dependence on the aperture length is examined.

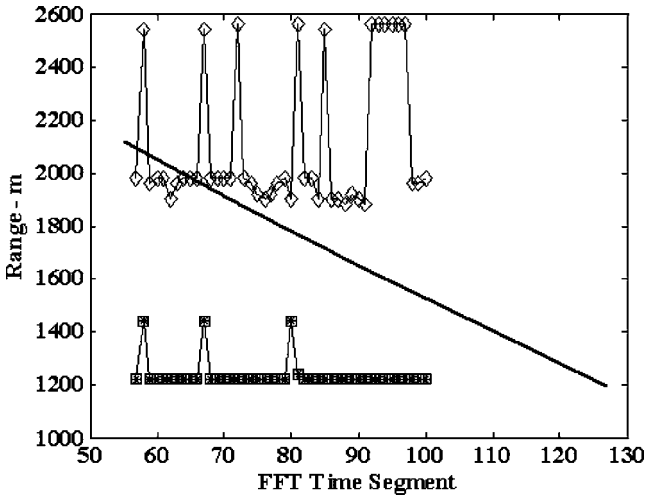

FIG. 27. Range localizations with fixed threshold filtered data for a threshold of 1×10^{-4}. Symbols used as in Fig. 23. Ground truth source track ranges (line) from the GPS recordings.

TABLE II. Subarrays used for subaperture data.

Subarray elements	Length—m	Average spacing—m
20–24	79.41	19.85
25–29	62.00	15.50
30–34	48.40	12.10
36, 38, 47, 52	35.96	11.99
1–4	58.06	19.35
5–9	62.0	15.50
10–14	48.4	12.10
15–19	37.79	9.45

D. Processing with subapertures

The ideal frequency curve shown in Fig. 8 could be used for inversions, using only the subaperture data without filtering, to optimize the number of receivers included in each subarray, as well as the number of subarrays included. Knowing the frequency regimes for the different element spacings could aid in element selection and tailoring the subarrays to the data frequencies used in the cost function. Here, the elements were chosen by trying to maintain approximately constant element spacings for the first four subarrays listed in Table II.

Several subapertures were selected to compare the performance of the modified N_λ filter data to the subaperature data. Varying the subaperture configurations produces variations in the relative levels of the cost function value minima for the ambiguity subsurfaces. This will be discussed in more detail in Sec. IV D 2 with the results of localizations obtained using eight subapertures, spanning the full length of the array, compared to those obtained with four subapertures that span half the array length. In addition, filtering the data prior to subarray processing was also examined and will be discussed using both four and eight subapertures.

Table II lists subaperture lengths in addition to the corresponding subarrays used to process the data. Taylor shading with 25-dB suppression on 5 equal sidelobes was used for each subarray.[26] Instead of a track beam approach, where subarrays are steered along a bearing-time track, CBF beamforming for the subaperture data is used here with beams constructed for each subarray at the angle corresponding to the current source location being sampled in the range-bearing surface. The model contributions to the cost function are evaluated for the field propagated to a single element located at the phase center of the subarray. This method was found to be accurate and efficient for source track inversions.[1]

1. Four subapertures

In this section cost function values are generated with the data from the first four subarrays listed in Table II. Ambiguity surfaces and localization performance with data from these subapertures are compared to results obtained in Sec. IV C with the filtered and unfiltered data from the entire array and with filtered data from only the elements in these four subarrays.

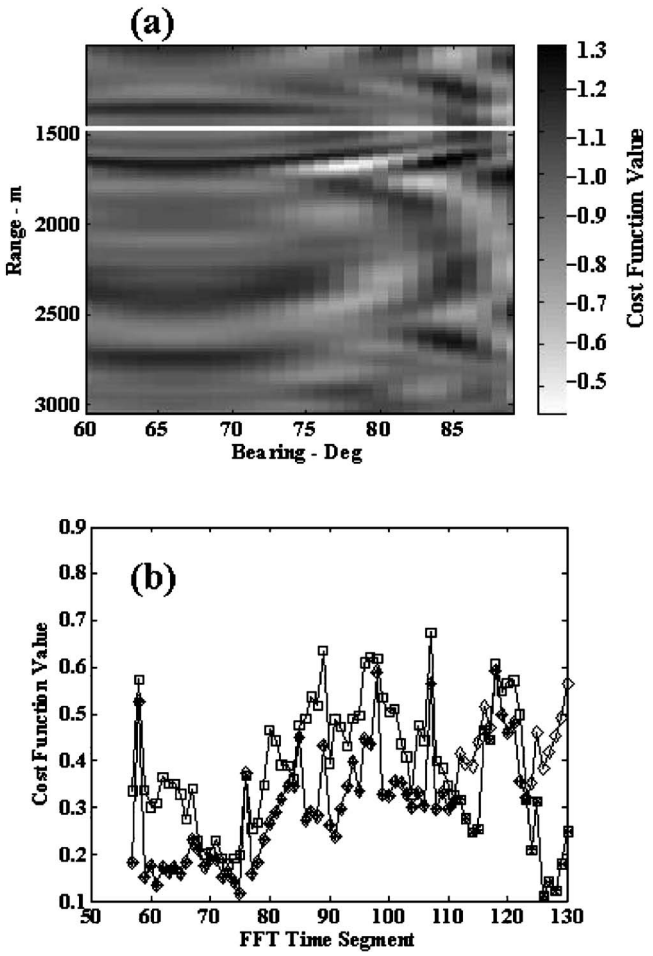

FIG. 28. (a) Range-bearing ambiguity from subaperture data. (b) Cost function values at the minimum on each ambiguity subsurface and the values at the global minimum with subaperture data from four subarrays. Symbols used as in Fig. 23.

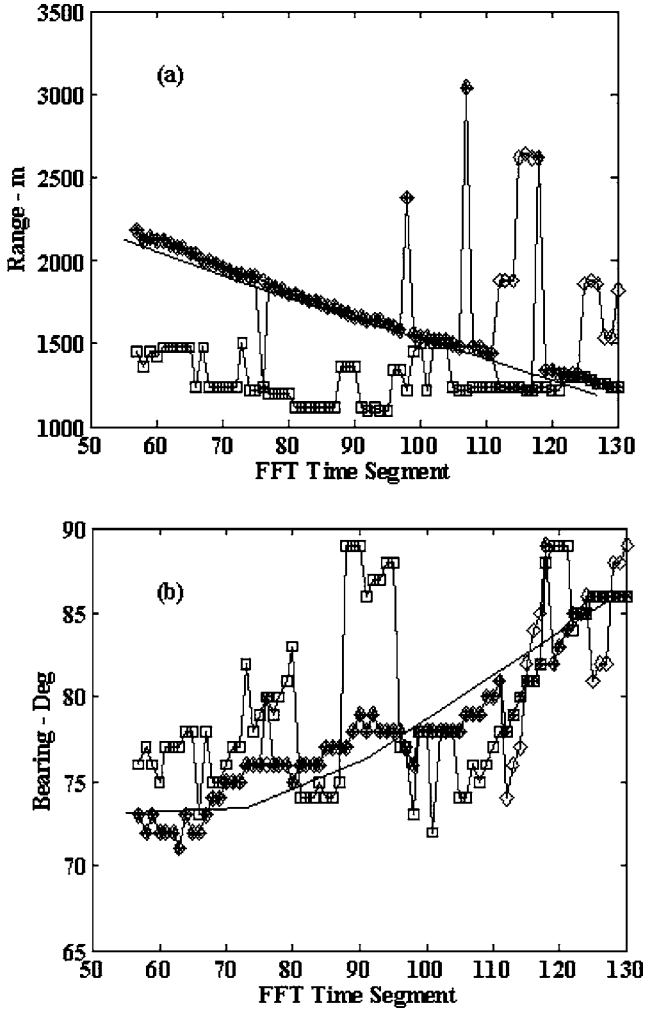

FIG. 29. Ranges (a) and bearings (b) at the global and ambiguity subsurface minima in Fig. 28 for the subaperture data. Symbols used as in Fig. 23. Ground truth source track ranges (line) from the GPS recordings.

For the same time segment used in Fig. 22, the ambiguity surface obtained from the four subaperture data is shown in Fig. 28(a). The cost function global and ambiguity subsurface minima, as described in Sec. IV C, are shown in Fig. 28(b) as a function of time segment. The range and bearing at the global and ambiguity subsurface minima from the subaperture data are shown in Fig. 29. These results are similar to those from the modified N_λ filtered data except that some effects of the profilers remain in region 2 as compared to the filtered data in Fig. 23(b), as evidenced in Fig. 28(b) by the numerous spikes in the cost function values at the global minima. The bearing values at the global minima also show more variation in Fig. 29(b) than in Fig. 25(b).

For a more direct comparison of results with unfiltered and modified N_λ filtered data, only data from the elements in the first four subarrays were used to generate filtered data and to evaluate the cost function. Applying the modified N_λ filter to the elements of the first four subarrays and then evaluating the cost function with data from only these filtered single elements also gave results similar to those in Fig. 29, except for the end of region 2 (time segments 125–130) where the modified N_λ filtered data found the global minimum at the farther range ambiguity. The unfiltered data, using only the elements of the first four subarrays in Table II, gave similar results to Fig. 24(a) for time segments 68–78, whereas the global minimum with the subaperature data from the first four subarrays is at the actual source for all of these same time segments, except for time segment 75.

The difference in the ambiguity surfaces from subaperture data and modified N_λ filtered data from only the 19 elements from the first four subapertures is shown in Fig. 30 for time segment 122. The subaperture data give an ambiguity surface structure in Fig. 30(a) similar to the structure in Fig. 30(b) from the modified N_λ filtered data, but the cost function value of the minimum at the actual source position (range 1300 m, bearing 84°) is lower for the subaperture data. For the filtered data, several minima all have approximately the same cost function values. In segment 122 the source is near the boundary of the filter window. Of course, the filter performance is dependent on the location of the window, as well as the number of elements used in constructing the filter. It may be possible to adjust the filter window for the reduced set of elements to put the source at the global minimum, but no attempt was made to do so.

Filtering the data prior to beamforming was also investigated. For instance, for the time segments shown in Fig. 29 the modified N_λ filter was applied to the data of the elements

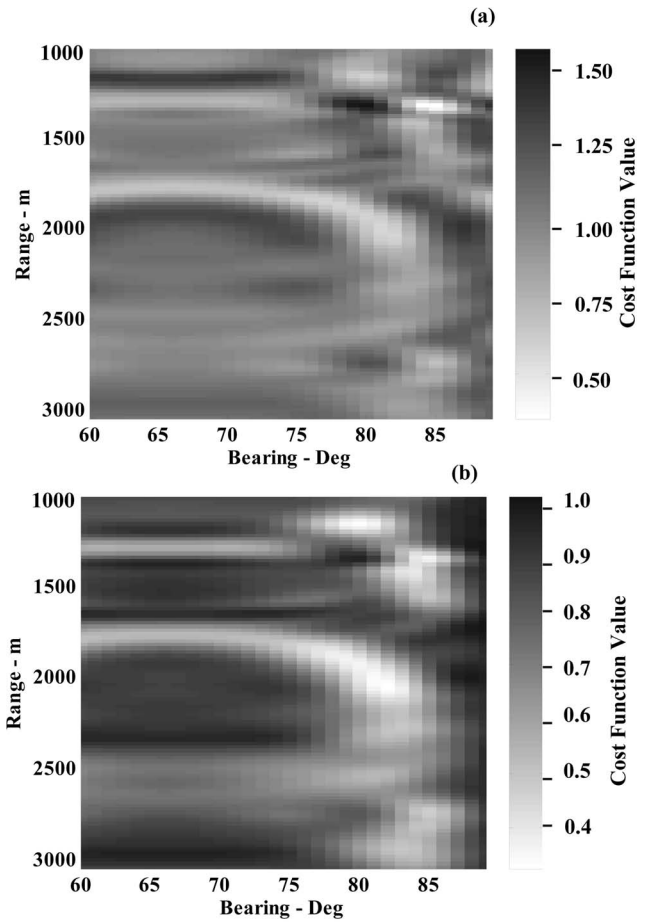

FIG. 30. Range-bearing ambiguity surface at time segment 122 in region 2 from the (a) subaperture data and (b) modified N_λ data.

of the first four subarrays prior to forming the subaperture beam data. This will be called the filter+subaperture method. The results were similar to those in Figs. 29(a) and (b). However, data from the filter+subaperature method resulted in improved range localization for the time segments 125–130 to within 200 m of the actual source.

The effects of filtering on the beamforming can be further quantified by calculating the ratio of the global cost function minima from the modified N_λ filtered+subaperture data to the global cost function minima in Fig. 28(b) of the subaperture data. These ratios are shown in Fig. 31(a). A ratio less than 1 indicates that filtering the data before beamforming has reduced the cost function. In region 2, time segments 73–92, the ratio initially increases slightly due to the multipathing effects. At the end of region 2, time segments 124–130, the ratio again increases, though similar localizations were achieved in both regions for the two methods.

2. Eight subapertures

The subarray set used for Figs. 28–31(a) did not span the full aperture of the array. To examine localizations using the full aperture and for more direct comparisons with respect to results shown in Figs. 22–27, all eight subapertures listed in Table II were used. The FFT time segments from regions 1 and 2 were evaluated with this new subaperture set. With the additional four subapertures with their larger element spacing, the ambiguity surfaces formed with data from eight subapertures were actually degraded, i.e., a number of global minima in region 2 did not correspond to the actual source position as they do in Fig. 28(b). Range localization results with eight subaperture data for time segments 57–100

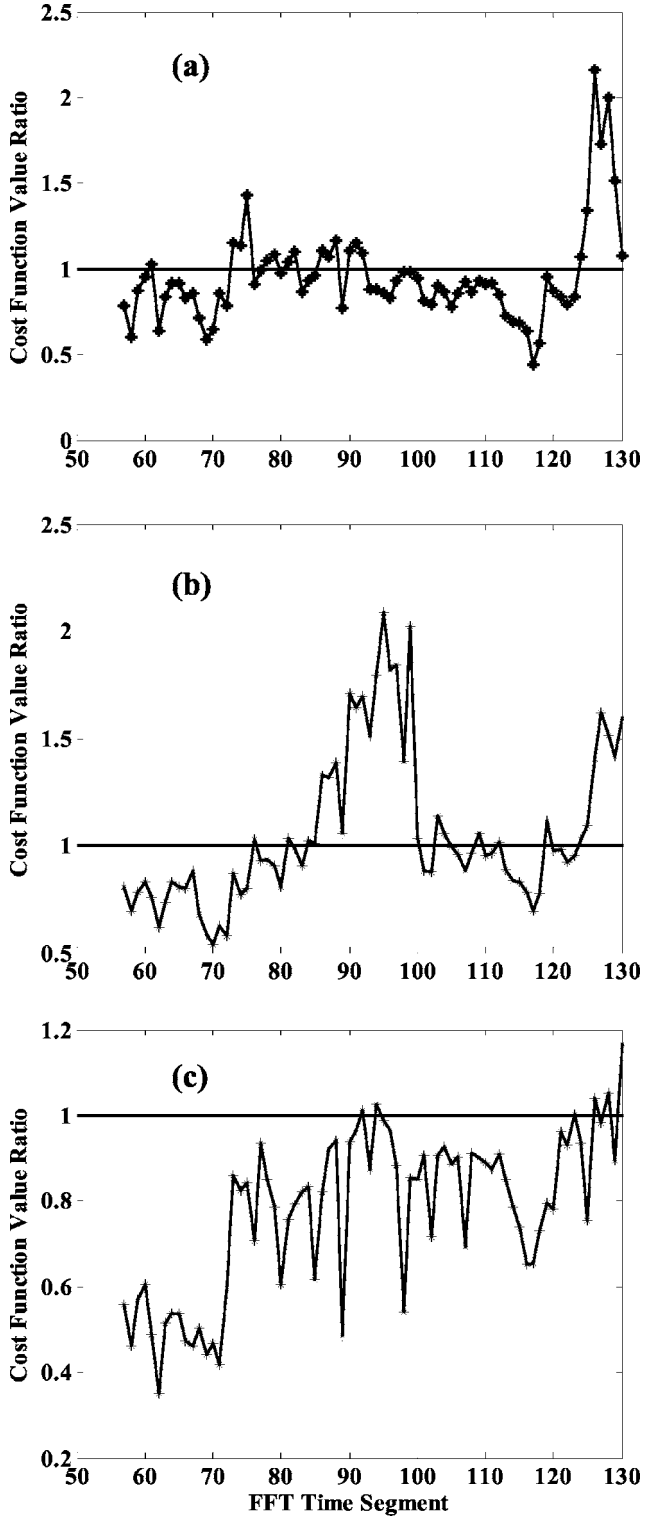

FIG. 31. Ratio of cost function global minimum value from filter + subaperture data to the cost function global minimum value from subaperture data for (a) four and (b) eight subarrays. (c) Ratio of the cost function global minimum values from modified N_λ filtered data with all the elements to the cost function global minimum values from the unfiltered data.

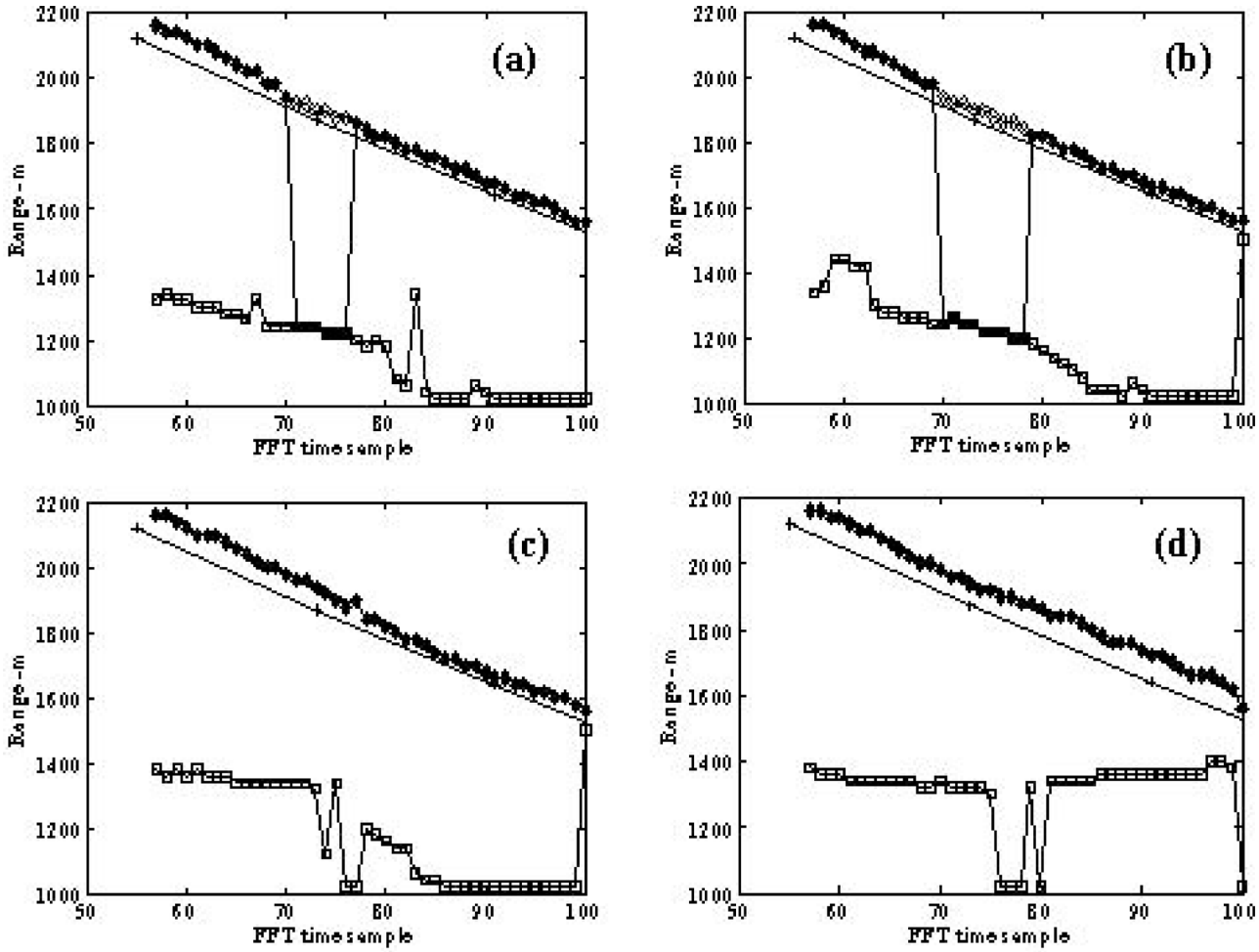

FIG. 32. Ranges at the global and ambiguity subsurface minima using elements from eight subarrays to produce (a) subaperture data; (b) unfiltered data; (c) modified N_λ filtered data; and (d) data from filter + subaperture method. Symbols used as in Fig. 23. Ground truth source track ranges (line) from the GPS recordings.

are shown in Fig. 32(a). As in Fig. 24(a) and in Fig. 32(b) from unfiltered data with the 38 elements of the eight subarrays, the ranges of the global cost function minima in Fig. 32(a) are in the close-range ambiguity surfaces for time segments 70–78 instead of the actual source position. In none of the examples considered in this study did using the unfiltered data produce the correct source localizations for time segments 70–78.

Next, the modified N_λ filter was applied to the data of only the elements in the eight subarrays. Correct range localizations were obtained in regions 1 and 2, including the time segments 57–100 shown in Fig. 32(c). Also, as shown in Fig. 32(d), the filter+subaperture data restore the correct source localizations missed with the subaperture data shown in Fig. 32(a). This result demonstrates that additional gain is achieved by applying the filter to the data, no matter how the data are subsequently used in evaluating the cost function.

The ratio of the global cost function minima from the filter+subaperture data with eight subarrays to the minima from subaperture data with eight subarrays is shown in Fig. 31(b). Notice that in region 1 and early in region 2 (time segments $\leqslant$85), the cost function values from the filter +subaperture data are lower than the corresponding cost function values from the subaperture data, including the time segments 70–80 where the filter+subaperture data facilitates localization. In region 2 for time segments greater than 85, the increased filter window width, in addition to the multipath effects, gave a higher value for the ratio because the cost function values for the filter + subaperture data increased to approximately 0.4, whereas for the subaperture data the cost function values were approximately 0.2. The increase in the cost function values from the filter + subaperture data may be due to a profiler being contained in the filter in this region, as seen in Fig. 18.

The effects of filtering the data prior to applying the subaperture method are further demonstrated in Fig. 33 for time segment 73 in region 2, where the unfiltered subaperture data do not correctly localize the source. The cost function values are shown in Fig. 33(a) as a function of range on the constant bearing slice through the global cost function minimum. For the modified N_λ filter + subaperture data, this minimum is at the correct source bearing of 73°. For the subaperture data the global cost function minimum value is at 78°, i.e., a 5° error. The range at the global minimum for the subaperture data is 1240 m, as shown in Fig. 33(a), compared to 1940 m at the global minimum for the filter +subaperture data, much closer to the actual source range. Figure 33(b) shows that the cost function value minimum

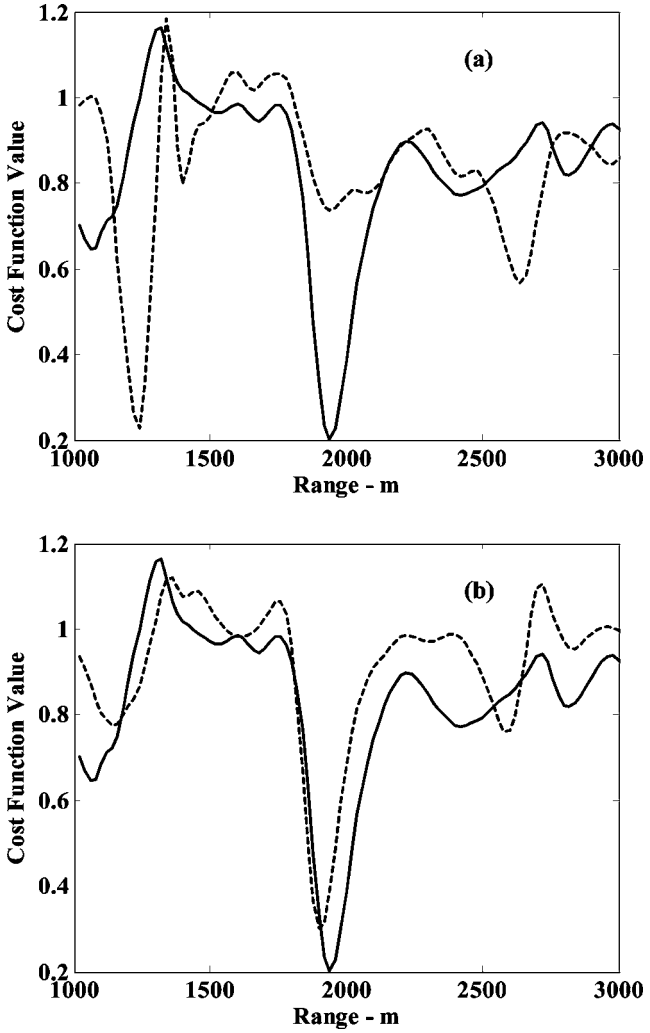

FIG. 33. Cost function values using eight subarrays (a) evaluated at the bearing of the global minimum with the subaperture method (dashed line) and modified N_λ + subaperture method (solid line). (b) Cost function values at the bearing corresponding to the actual source for the subaperture method (dashed line) and modified N_λ + subaperture method (solid line).

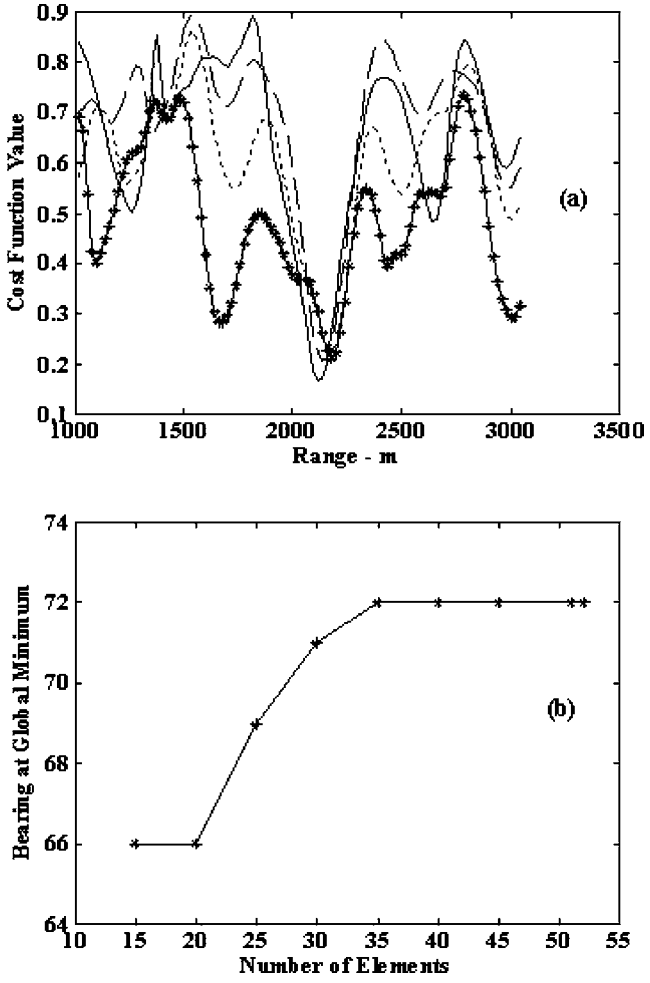

FIG. 34. (a) Range localizations for time segment 59 for receivers 1–51 (solid line), 1–35 (dashed), 1–25 (dotted), and 1–15 (asterisks). (b) Dependence on number of elements of the bearing at the cost function minimum.

through a source bearing of 73° in the subaperture data is greater than the cost function value at the global minimum for the modified N_λ + subaperture data [repeated from Fig. 33(a)] by approximately 0.07. This accounts for the region 2 localization errors shown in Fig. 32(a).

Finally, for the elements used in the eight subarrays, the ratio of the cost function values for the modified N_λ filtered data and the unfiltered data is shown in Fig. 31(c). In segments 55–75 the ratio values in Fig. 31(c) are substantially less than 1, but for some time segments the cost function values of the filtered data approach the cost function values of the unfiltered data.

3. Dependence on total aperture

A final study of the effect of the total aperture size was made by starting with the total aperture and then decreasing the number of elements used in both the filter construction and in subsequent cost function evaluations. This was done for a starting source range of 2120 m and bearing of 72° at time segment 59. Bearing and range slices through the location of the global minimum were constructed for each set of elements used in the cost function evaluation.

The closely spaced elements at the east endfire were removed from the cost function one by one, and the filter was constructed in each instance with the 20° window centered 10° off of array endfire. The global cost function minimum corresponded to the actual source position until the total number of elements was significantly reduced, down to 10 elements, with an aperture of 151.24 m, approximately 2/7 of the full array and 1.5 water depths. The cost function values as a function of range at the bearing of the global minimum are shown in Fig. 34(a) as a function of the number of elements. As the number of elements decreases the cost function value at the minimum at the actual source position increases, while the cost function values at other minima decrease. For instance, in Fig. 34(a) the minimum value changes from 0.166 for 52 elements to 0.228 for 20 elements. The cost function value actually decreases again slightly to 0.210 for 15 elements.

The bearings for the global minimum cost function values shown in Fig. 34(a) are shown in Fig. 34(b) as a function of the number of elements used to construct the cost function. The bearing values start to degrade with fewer than 34 elements, and the error with 10 elements is approximately 6°.

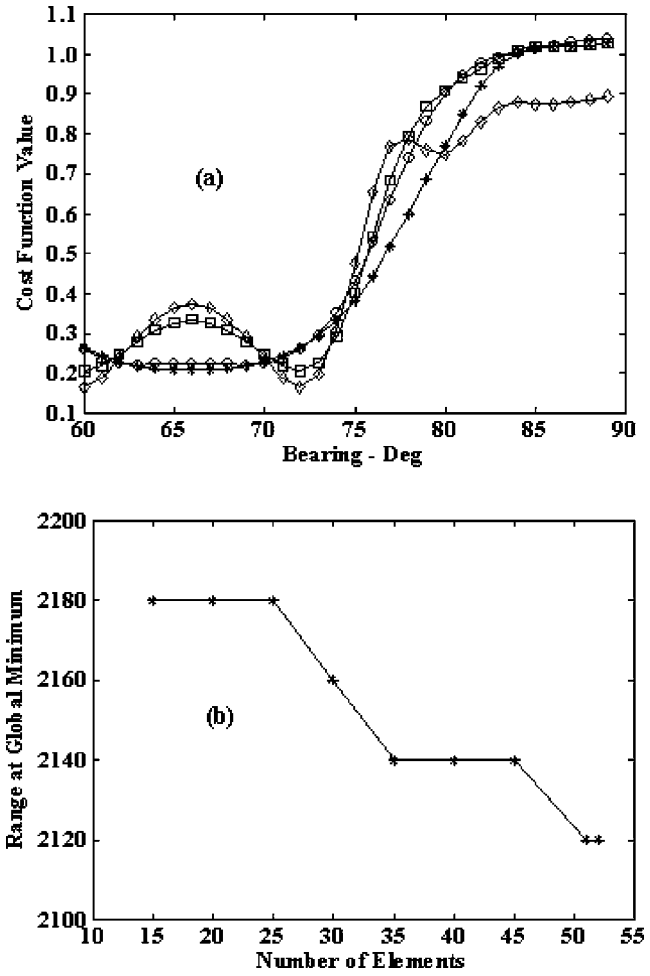

FIG. 35. Bearing localizations for time segment 59 as a function of the number of elements using receivers 1–51 (diamonds), 1–35 (squares), 1–25 (circles), and 1–15 (asterisks). (b) Dependence on number of elements of the range at the cost function minimum.

The cost function values for the bearing slices are evaluated at the ranges shown in Fig. 35(b) as a function of the number of elements. The minima at the actual source location in the ambiguity surfaces become more shallow as the number of elements is decreased, as seen in Fig. 35(a), and the locations of the minima shift to smaller bearing angles. The shape of the curve tends to flatten as the number of receivers decreases.

The values of the cost function minima as a function of the number of elements, as shown in Fig. 34(a), depend on the segments considered. For example, in region 2 the multipath effects alter the cost function values of the local minima as shown in Fig. 30. The minima in Fig. 34(a) are seen to be very dependent on the number of elements used.

V. CONCLUSION

A robust method for constructing a matrix filter was presented. The matrix filters are constructed at each frequency by transforming the elements to beam data using a CBF transformation, windowing on a bearing sector of interest, and then inverse transforming back to element level data using a singular value decomposition for the inverse transform.

Details of filter design and performance for both uniformly and nonuniformly spaced elements were discussed. Filter robustness is achieved by limiting the number of singular values in the inverse based on the effective number of elements of the array. Simulated data were constructed using a normal-mode model in a realistic environment, and filter performance was demonstrated by filtering for a single source in the presence of a loud interferer. Comparisons of the effective element methods, N_λ or modified N_λ, to alternative methods, such as fixed threshold and polar decomposition, showed the utility of having an automated procedure in constructing the filter. For the nonuniformly spaced elements the optimum threshold for the singular values to include in the filter differed by several orders of magnitude from the number for the uniformly spaced elements. In both cases, the effective element method gave comparable results to both the fixed threshold and polar decomposition methods.

Detailed analyses of an inversion experiment were used to demonstrate the application of the filtering method to real data. Inversions were performed using a simulated annealing algorithm to verify that correct source localizations could be obtained for this dataset. Source range and bearing estimates in the presence of interferers (seismic profilers) were improved with modified N_λ filtered data relative to the estimates with unfiltered data. The modified N_λ filter was compared to the fixed threshold filter and to subarray beamforming with the result that either comparable or improved localizations are achieved with the modified N_λ filter using all the elements of the array. The modified N_λ filter method thus avoids the problem of subaperture selection in a subarray processing method. The performance of the filter was demonstrated by showing comparable localizations between the modified N_λ filter data, constructed from the elements used in the subaperture data, and the subaperture data. Finally, localizations were improved by applying the modified N_λ filter prior to the subarray processing with subarrays that spanned the length of the array.

ACKNOWLEDGMENTS

The author expresses his appreciation to Dr. R. A. Koch, Dr. D. P. Knobles, Dr. E. A. Honda, Dr. B. L. Lacour, and Dr. G. R. Wilson for many helpful discussions.

[1] R. A. Koch and D. P. Knobles, "Geoacoustic inversion with ships as sources," J. Acoust. Soc. Am. **117**, 626–637 (2005).
[2] S. A. Stotts and R. A. Koch, "Unified inversion using isolated moving sources," J. Acoust. Soc. Am. **113**, 2217 (2003).
[3] E. K. Westwood, C. T. Tindle, and N. R. Chapman, "A normal mode model for acousto-elastic ocean environments," J. Acoust. Soc. Am. **100**, 3631–3645 (1996).
[4] R. B. Newman and R. A. Koch, "Software description for the NAUTILUS subroutine," Applied Research Laboratories, The University of Texas, ARL:UT Technical Report, ARL-TL-EV-03-09, April, 2003. See references cited therein.
[5] F. D. Tappert, "The parabolic equation method," in *Wave Propagation and Underwater Acoustics*, edited by J. B. Keller and J. S. Papadakis (Springer, New York, 1977).
[6] M. D. Collins, "A split-step Padé solution for the parabolic equation method," J. Acoust. Soc. Am. **93**, 1736–1742 (1993).
[7] E. K. Westwood and P. J. Vidmar, "Eigenray finding and time series simulation in a layered-bottom ocean," J. Acoust. Soc. Am. **81**, 912–924 (1987).

[8] E. K. Westwood and C. T. Tindle, ''Shallow water time-series simulation using ray theory,'' J. Acoust. Soc. Am. **81**, 1752–1761 (1987).
[9] T. L. Foreman, ''Ray Modeling Methods for Range Dependent Ocean Environments,'' Applied Research Laboratories, The University of Texas, ARL:UT Technical Report, ARL-TR-83-41 (1983).
[10] S. A. Stotts, D. P. Knobles, R. A. Koch, D. E. Grant, K. C. Focke, and A. J. Cook, ''Geoacoustic inversion in range-dependent ocean environments using a plane wave reflection coefficient approach,'' J. Acoust. Soc. Am. **115**, 1078–1102 (2004).
[11] R. J. Vaccaro and B. F. Harrison, ''Optimal matrix filter design,'' IEEE Trans. Signal Process. **44**, 705–709 (1996).
[12] R. J. Vaccaro and B. F. Harrison, ''Matrix Filters for Passive SONAR,'' Proc. ICASSP 2001 Int. Conf. Acoust., Speech, and Sig. Process., Salt Lake City, Utah, 2001.
[13] C. S. MacInnes, ''Source localization using subspace estimation and spatial filtering,'' IEEE J. Ocean. Eng. (submitted).
[14] T. B. Neilsen and C. S. MacInnes ''Source localization from multi-target broadband horizontal line array data,'' IEEE J. Ocean. Eng. (submitted).
[15] C. S. MacInnes, ''The Design of Equiripple Matrix Filters,'' in Proceedings of the ICASSP 2001 International Conference on Acoustics, Speech, and Signal Processing, Salt Lake City, Utah, May 2001.
[16] E. K. Westwood, ''Broadband matched-field source localization,'' J. Acoust. Soc. Am. **91**, 2777–2789 (1992).
[17] D. P. Knobles, R. A. Koch, S. A. Stotts, and T. B. Neilsen, ''A Numerical study of geoacoustic inversion in range-dependent ocean environments,'' IEEE J. Ocean. Eng. **28**, 355–369 (2003).
[18] H. Cox, R. M. Zeskind, and M. M. Owen, ''Robust adaptive beamforming,'' IEEE Trans. Acoust., Speech, Signal Process. **ASSP-35**, 1365–1376 (1987).
[19] N. L. Owsley, ''Sonar Array Processing,'' in *Array Signal Processing*, edited by S. Haykin (Prentice-Hall, Englewood Cliffs, NJ, 1985), Chap. 3.
[20] D. E. Grant, J. H. Gross, and M. Z. Lawrence, ''Cross-spectral matrix estimation effects on adaptive beamforming,'' J. Acoust. Soc. Am. **98**, 517–524 (1995).
[21] D. A. Abraham and N. L. Owsley, ''Beamforming with dominant mode rejection,'' Naval Underwater Systems Center, Newport, Rhode Island, NUSC Report 8751 (11 July, 1990).
[22] T. R. Messerschmitt, ''Evaluation of the dominant mode rejection beamformer,'' ARL Tech. Report No. 96-2 (ARL-TR-96-2), Appl. Res. Lab., The Univ. of Texas at Austin (January 1996).
[23] T. M. Redheendran and R. A. Gramann, ''Initial evaluation of the dominant mode rejection beamformer,'' J. Acoust. Soc. Am. **104**, 1331–1344 (1998).
[24] E. A. Ritterman, ''Geoacoustic Inversion in Multiple Source Environments,'' Masters thesis, The University of Texas at Austin, May 2004.
[25] R. A. Koch and D. P. Knobles, ''Inversion for source levels and environmental and source track parameters,'' J. Acoust. Soc. Am. **114**, 2401 (2003).
[26] T. T. Taylor, ''Design of line-source antennas for narrow beamwidth and low side lobes,'' IRE Trans. Antennas Propag. **AP-3**, 16–28 (1955).
[27] B. D. Van Veen and K. M. Buckley, ''Beamforming: a versatile approach to spatial filtering,'' IEEE ASSP Magazine **5-2**, 4–24 (1988).
[28] G. Strang, *Introduction to linear Algebra* (Wellesley-Cambridge Press, Cambridge, MA, 1993).
[29] E. Honda (unpublished).
[30] E. Anderson, Z. Bai, and C. Bischof, J. Demmel, J. Dongarra, J. DuCruz, A. Greenbaum, S. Hammarling, A. McKenney, S. Ostrouchov, and D. Sorensen, ''LAPACK Users Guide,'' SIAM (1995).
[31] T. B. Neilsen and C. S. MacInnes, ''Localization of multiple acoustic sources in the shallow ocean,'' J. Acoust. Soc. Am. (submitted).
[32] A. J. Cook, S. A. Stotts, and R. A. Koch, ''Comparisons of multisource localization and spatial filtering techniques,'' J. Acoust. Soc. Am. **114**, 2400 (2003).
[33] E. A. Rittermann, R. A. Koch, S. A. Stotts, and D. P. Knobles, ''Matched field processing in a multisource environment,'' J. Acoust. Soc. Am. **114**, 2400 (2003).
[34] R. Newman and R. Koch, ''Localization and environmental inversion in a soft sediment environment using rotated coordinates,'' J. Acoust. Soc. Am. **114**, 2400 (2003).
[35] D. P. Knobles, R. A. Koch, L. A. Thompson, and P. E. Eisman, ''Broadband sound propagation in shallow water and geoacoustic inversion,'' J. Acoust. Soc. Am. **113**, 205–222 (2002).

Remote sensing of sediment density and velocity gradients in the transition layer

Charles W. Holland[a)]
The Pennsylvania State University, Applied Research Laboratory, State College, Pennsylvania 16804-0030

Jan Dettmer and Stan E. Dosso
School of Earth and Ocean Sciences, University of Victoria, Victoria, BC, Canada

(Received 10 January 2005; revised 13 April 2005; accepted 13 April 2005)

The geoacoustic properties of marine sediments, e.g., bulk density and compressional velocity, commonly exhibit large variations in depth near the water–sediment interface. This layer, termed the transition layer, is typically of $O(10^{-1}-10^{0})$ m in thickness. Depth variations within the transition layer may have important implications for understanding and modeling acoustic interaction with the seabed, including propagation and reverberation. In addition, the variations may contain significant clues about the underlying depositional or erosional processes. Characteristics of the transition layer can be measured directly (e.g., coring) or remotely. Remote measurements have the advantage of sampling without disturbing the sediment properties; they also have the potential to be orders of magnitude faster and less expensive than direct methods. It is shown that broadband seabed reflection data can be exploited to remotely obtain the depth dependent density and velocity profiles in the transition layer to high accuracy. A Bayesian inversion approach, which accounts for correlated data errors, provides estimates and uncertainties for the geoacoustic properties. These properties agree with direct (i.e., core) measurements within the uncertainty estimates. © *2005 Acoustical Society of America.* [DOI: 10.1121/1.1925988]

PACS number(s): 43.30.Pc, 43.30.Ma, 43.20.El [AIT] Pages: 163–177

I. INTRODUCTION

Geoacoustic properties commonly exhibit large variations as a function of depth near the water–sediment interface. These gradients may arise due to various mechanisms, including overburden pressure, wherein porosity decreases as a function of depth (even when the grain size distribution is constant with depth). In addition, the gradients may be induced by depositional, erosional, and/or biological processes (e.g., Refs. 1 and 2), resulting in a grain size distribution that is a function of depth. In the classical deposition process, coarse grains are deposited first and the fines last, so that a decrease in porosity (the ratio of interstitial water volume to total volume) with increasing depth might be expected. However, other processes exist where the grain size decreases and the porosity increases with depth (e.g., Ref. 3). This upper zone of the sediment column is often referred to as a transition layer, suggestive of a layer of smoothly varying properties between the water above and another layer(s) below. Transition layers (or layers with smoothly varying properties) may of course exist at any point in the sediment column, however, in this paper we use the term (consistent with its general usage) to mean that layer commencing at the water–sediment interface.

Gradients in the transition layer are known to have a significant effect on acoustic reflection and scattering from the seabed. Robins[4–7] provides analytic solutions for the plane-wave reflection coefficient for various forms of velocity and density gradients. He shows substantial deviations from the homogeneous assumption (i.e., no gradient) that are a complex function of frequency and angle, but, in general, scale with the nondimensional quantity $k_z h$, where k_z is the vertical component of the wave number and h is the thickness of the transition layer. His results put in a broader perspective the conclusions in Ref. 8, which indicated that the effect of density gradients at low frequencies (50 Hz) would be observed primarily at high angles.

Carbó[9] studied 1–400 kHz normal incidence reflectivity from a seabed with a density and velocity gradient for a sandy and silty-clay sediment. He concluded that transitional layers induce a strong frequency dependence on normal incidence reflectivity, thus single frequency reflection measurements inverted using the common homogeneous half-space assumption may yield poor estimates of velocity and density. Lyons and Orsi[10] studied the effect of density gradients in the transition layer on 1–100 kHz reflection and scattering (their definition of forward loss is identical to reflection loss). Using gradients estimated from core data, they show that density gradients affect both the reflected and scattered field. Consistent with Robins,[4] the effects were largest at the highest frequencies and grazing angles. An analysis of measured backscattering at 140 kHz[11] from various seabed types in water depths $O(10^{1})$ m appeared to also underscore the importance of transition layer gradients. Using measured reflection loss data[12] showed that the effects of the density profile in the transition layer can be important.

Given the apparent importance of these gradients, the question is raised, "how well can the gradients in the transi-

a)Electronic mail: holland-cw@psu.edu

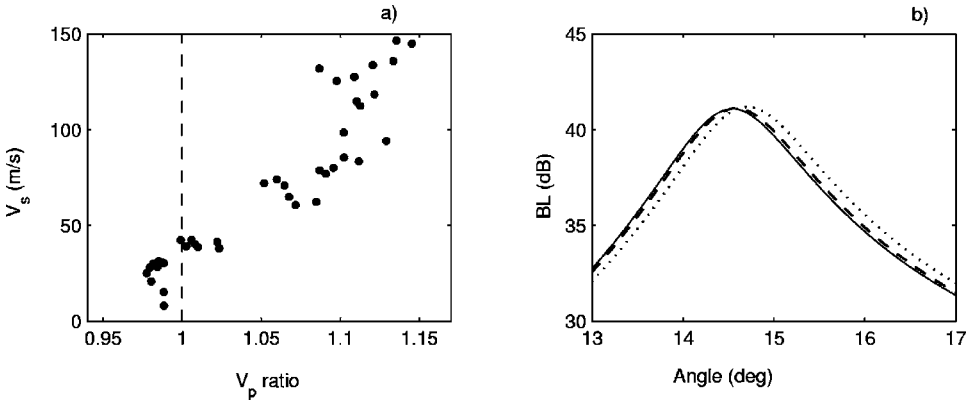

FIG. 1. Shear waves in fine grained sediments; (a) *in situ* compressional and shear velocity data from Ref. 13; (b) the effect of shear velocity on the reflection coefficient is small and occurs around the angle of intromission: no shear (solid), Vs=25 m/s (dashed), Vs=50 m/s (dotted).

tion layer be measured?" The answer to that question may have significance not only for the ocean acoustics community, but also for the sediment transport community for whom the transition layer contains a wealth of information on both erosional and depositional processes. In this paper, we attempt to address that question by using a remote sensing technique, employing a particular inversion approach on a specific set of measurements. While this approach falls short of completely answering the general question, its value is in demonstrating what can be done currently as well as perhaps shedding light on what might be done. The focus of the paper is on the potential for using seabed reflection data with a Bayesian inversion strategy to estimate gradients in the transition layer.

The paper is organized as follows. In Sec. II, the forward reflection model is discussed. In Sec. III we provide a brief overview of the measured reflection data and in Sec. IV we describe the inversion technique. The main results of this paper are contained in Sec. V, where the inversion technique is applied to the measurements and the density and velocity gradients are estimated. The estimated transition profiles are compared with core measurements and the implications discussed. The final section contains a summary and conclusions.

II. REFLECTION MODEL

Our inversion approach (fully discussed in Sec. IV) requires iterations on a forward model, which is discussed below. First, the rationale for simplifying approximations pertaining to the forward reflection model are provided. Second, the mathematical form of the velocity and density profiles are given. Finally, a sensitivity study is presented, showing the effects of the transition layer on seabed reflectivity.

In this study, we use reflection data from an area with fine-grained sediments. Some of the simplifying approximations and assumptions pertain specifically to this sediment type. This does not mean that the method cannot be applied to other sediment types. Indeed, the measurement technique and the inversion technique are quite general and can be applied to a variety of sediment types. For other sediment types, the approximations in the forward model may be somewhat different than those used here for fine-grained sediments.

A. Approximations and assumptions

The reflection model (and associated inversion) can be simplified by ignoring poroviscoelastic effects and treating the sediment as a lossy fluid. For fine-grained sediments, the fluid approximation seems justified because of the low shear velocities generally associated with such sediments. For example, *in-situ* measurements of compressional and shear velocity[13] (Fig. 1) show that for fine-grained sediments (Vp ratio <1) the mean shear velocity is 21 m/s and the maximum is 42 m/s. The effect of shear velocities of 25 and 50 m/s on the reflection coefficient is small and only occurs near the angle of intromission, δ [Fig. 1(b)]. In agreement with this, prior inversion modeling treating the sediment as a homogeneous half-space (Ref. 14) has shown that (1) the reflectivity is quite insensitive to the shear properties, and (2) that ignoring the shear properties does not result in any bias to the lossy fluid properties (i.e., density, compressional velocity, and attenuation). We assume that for a transition layer, the shear gradients would also be small and that compressional-to-shear coupling would be negligible.

Using Biot theory[15] as a guide, the characteristic frequency (the frequency at which we might expect dispersive effects to become apparent) can be estimated. For a typical silty-clay sediment, the characteristic frequency $O(10^6)$ MHz, is far above the present frequency range of interest (300–2000 Hz). Thus, we assume that effects due to the two-phase nature of the sediment can also be neglected.

The geometry of the experiment (point source, point receiver) means that the measurement quantity is the spherical wave reflection coefficient. However, spherical wave reflection coefficient computations are time consuming (relative to plane wave computations). For fine-grained sediments, the spherical wave reflectivity is nearly identical to the plane wave reflectivity, except at low frequencies in the vicinity of the angle of intromission δ (see Fig. 2). Above about 300 Hz, the difference between the plane and spherical wave reflection coefficients are less than 1 dB at the angle of intromission; away from the angle of intromission the plane and spherical wave coefficients are essentially identical. Calculations have shown that the results shown in Fig. 2 for a half-space are also representative of the results for a transition layer (when the attenuation is higher/lower than that used in the simulation, the frequency at which the plane and spherical wave coefficients are the same decreases/increases).

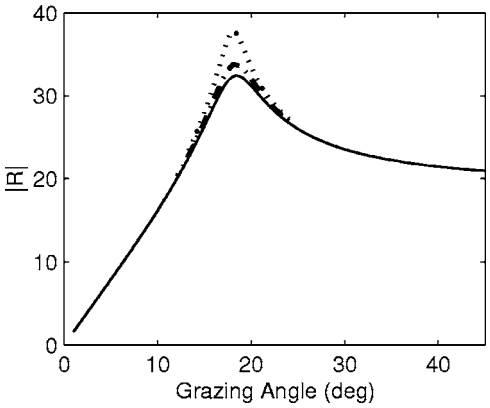

FIG. 2. A comparison of modeled plane wave (solid) and spherical wave reflection loss (100 Hz dotted; 300 Hz dash–dotted). For the spherical wave calculations source and receiver heights above the seabed were 102 and 41 m, respectively, corresponding to the experimental geometry. The sound velocity and density ratios are 0.973 and 1.26; attenuation is 0.38 dB/λ.

Thus, we exploit the computational advantage of a plane wave forward model in the inversion and use only data above 300 Hz, accepting a small bias in the attenuation estimates at low frequencies (see the discussion in Sec. II C 4).

Finally, we make the assumption that the gradients are in the vertical direction only. For the reflection data, this assumes that lateral variability for scales less than $O(10^2)$ m is negligible.

B. Transition layer profiles

Parametrized velocity and density profiles are required for the inversion process. In order to have the greatest probability of finding the "true" but unknown profile, a very general parametrization is desirable, i.e., a profile that will fit a wide range of environments.

As a concrete example of transition layer profiles, Fig. 3 shows various density and sound velocity profiles in the transition layer in the Italian littoral from gravity core data. Note that the density and velocity in the upper several centimeters of core data are often biased due to near-interface effects (see Sec. V B). Nevertheless, the density shows very high gradients $O(10^{-2})$ g/cm^4 in the upper few decimeters, gradually decreasing to a near constant gradient below about 25 cm. The velocity, on the other hand, shows a roughly constant gradient. While the sound velocity gradient is sometimes negative and sometimes positive, the gradients in sound velocity are much smaller (with respect to the mean values) than for density. In the transition layer profiles of Fig. 3, some fine-scale fluctuations $O(10^{-2}-10^{-1})$ m (i.e., fine-scale layers) are visible. The intent (in this paper) is to recover the smooth gradients and not the fine-scale fluctuations.

There are several forms of the velocity and density profiles [see Fig. 4(a)] for which analytic solutions to the reflection coefficient are known (e.g., Refs. 4 and 5). While the mathematical forms of the velocity gradient (typically linear k^2), fit a wide range of core measurements reasonably well, the mathematical forms of the density profile, in general, do not. That is not to say that they do not fit any core measurements, it is only to say that there are many core measurements that are not well described by the assumed profile (especially large near-surface gradients). A notable exception is a density profile based on Bessel functions,[6]

$$\rho(z) = AJ_\mu(\gamma(z+\lambda)^s) + BY_\mu(\gamma(z+\lambda)^s), \tag{1}$$

where J and Y are Bessel functions of the first and second kind, z is normalized depth, and the other variables are fitting parameters. This equation is extremely flexible and parameters can be found that fit density profiles that we have encountered. Thus, it is a powerful tool for forward modeling. However, using Eq. (1) for inversions leads to instabilities since small changes in the parameters can lead to very large and highly nonlinear changes in the density profile.

Instead, we propose a form of the density gradient that is quite general and also stable for use in inversions,

$$\rho(z) = \rho_t + (\rho_t - \rho_b)\sin^\nu(z\pi/2), \tag{2}$$

where the parameters ρ_t and ρ_b have a physical meaning (i.e., the densities at the top and bottom of the layer, respectively), ν is a nondimensional parameter related to the gradient,

$$\frac{\partial\rho}{\partial z} = \nu\sin^{\nu-1}(z\pi/2)\cos(z\pi/2)(\rho_b - \rho_t)\pi/2, \tag{3}$$

and z is depth normalized by layer thickness h. Figure 4(b) shows some of the profiles for various values of ν. Small values of ν give large near-surface gradients. The profile of Eq. (2) appears to be general enough to fit a wide range of profiles, including measured profiles we have observed in our core measurements.

There is no known analytic solution to the reflection coefficient for the density profile of Eq. (2). Instead, the reflection coefficient is computed by discretizing the transition layer into many thin layers, each with constant density and sound velocity using an iterative approach (Ref. 16, Eq. 3.38). By reducing the layer thickness (with respect to the

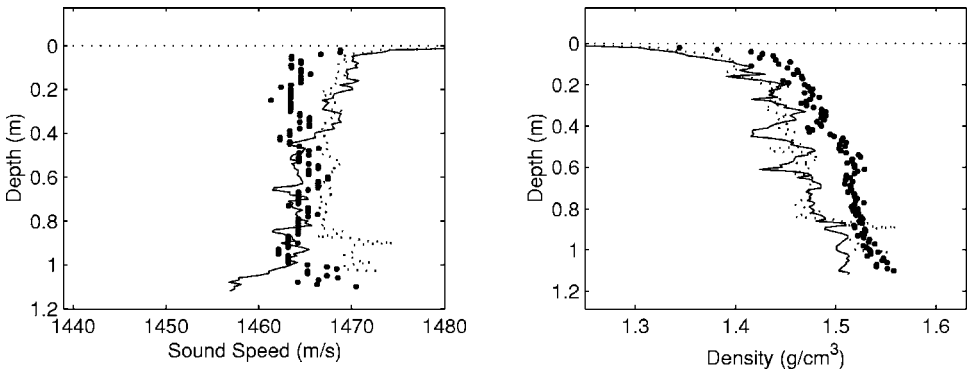

FIG. 3. Examples of measured transition layer at 100 m water depth. The three cores are from various locations in the Strait of Sicily and the North Tuscany shelf. The sound velocity at the base of the water column varies from site to site but is approximately 1510 m/s. The density in the water column is 1.029 g/cm^3.

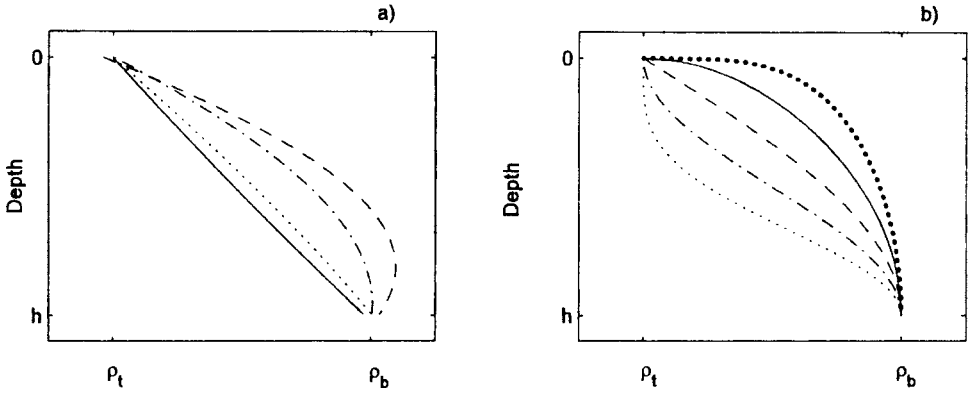

FIG. 4. Density profiles using (a) the generalized exponential profile from Ref. 4 and (b) Eq. (2), with $\nu = 0.25, 0.5, 1, 2, 4$ corresponding to the bold dotted, solid, dashed, chain-dashed, and thin dotted lines, respectively. The ratio between the density at the top and bottom of the layer is $\rho_t/\rho_b = 1.154$. Negative gradients are also possible and are symmetric with those shown.

wavelength) the discretization errors can be made arbitrarily small. As an example of the kinds of errors introduced by discretization, the exact solution for an exponential density profile[5] was compared with a discretized version. Figure 5(a) shows the errors in the magnitude of the plane-wave pressure reflection coefficient, R, due to discretization of a 1 m layer. The largest errors occur at the angle of intromission and increase with increasing frequency. For this discretization interval (2.5 cm), the largest errors are quite small, $O(10^{-5})$ for the reflection coefficient and less than 1 dB for the reflection loss ($-20\log_{10}|R|$) difference [see Fig. 5(b)]. In the inversion (described in Sec. IV), the maximum frequency was 1600 Hz, the number of layers employed was 10 and the largest discretization errors were roughly 0.5 dB. Later, the impact of small errors in reflection loss at the angle of intromission will be addressed and shown to be of negligible import.

A possible alternative to the parametrization of Eq. (2) could be the use of empirical orthogonal functions (EOFs) as a set of basis functions to be fit to the data. However, computing appropriate EOFs requires a set of representative sediment profiles that encompass the possible profile shapes for the data at hand. Such a profile set may often not be available. Further, the six parameters used here to represent density and sound-speed profiles in a flexible manner should be at least as efficient as EOF expansions of these two profiles.

C. Effect of gradients on $|R|$, sensitivity study

The sensitivity of reflectivity to the density and velocity profiles in the transition layer are examined in order to demonstrate which features of the reflection data are likely to contain information about the shape of the profiles. The effects of the density and velocity profiles are first treated separately and then together.

A previous paper[17] showed that the density and sound velocity for a fine-grained sediment (homogeneous) half-space could be obtained using the position of the angle of intromission. The angle of intromission, δ, is defined as the angle at which reflection coefficient $R=0$ for a lossless medium:

$$\cos\delta = \left[\frac{1-\left(\frac{\rho_0 c_0}{\rho c}\right)^2}{1-\left(\frac{\rho_0}{\rho}\right)^2}\right]^{1/2}; \quad \frac{\rho c}{\rho_0 c_0} > 1 \quad \text{and} \quad \frac{c}{c_0} < 1 \quad \text{or} \quad \rho c \rho 0 c 0 < 1 \quad \text{and} \quad cc0 > 1, \tag{4}$$

where the subscript 0 refers to the seawater properties in the upper half-space, and the angles are referenced to grazing, i.e., 0° is grazing incidence. For fine-grained marine sediments, it is the first condition of Eq. (4) that gives rise to the angle of intromission. In real materials (where the attenuation is nonzero) the $|R(\delta)|$ is small but not identically zero.

For a homogeneous half-space, the angle of intromission is independent of frequency [Fig. 6(a)]. However, a gradient in density or velocity (or both) produces an angle of intromission that depends upon frequency. For fine-grained sediments it is largely this frequency dependence that provides the opportunity to remotely measure the transition layer gradients.

1. Effect of density gradients on $|R|$

The effect of various density profiles on reflectivity (with a constant sound velocity) from the transition layer is shown in Figs. 6(d)–6(f). Note the frequency dependence of the angle of intromission. At low frequencies ($k_z h \ll 1$), the

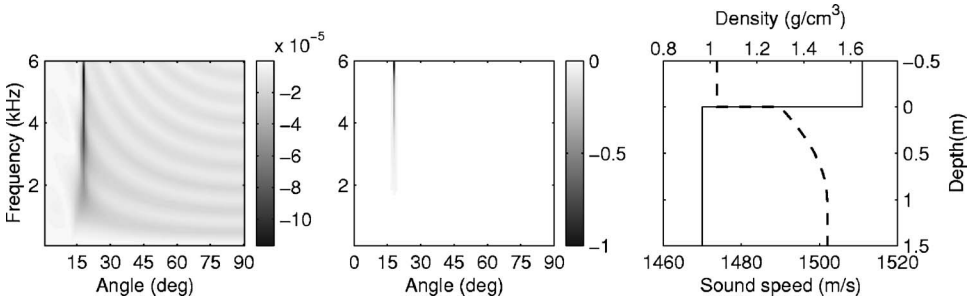

FIG. 5. Discretization errors for the reflectivity, (a) in amplitude, (b) in dB, (c) the sound velocity (solid) and density (dashed) profiles. 40 layers were used in the simulation.

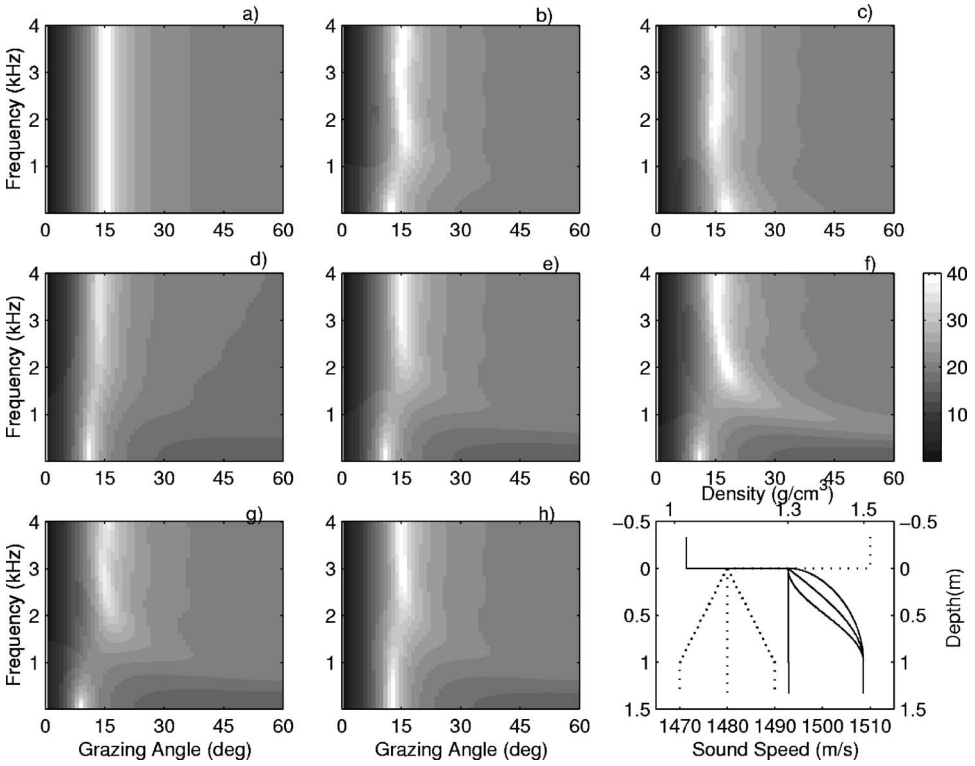

FIG. 6. Sensitivity of reflection loss (dB) to transition layer velocity and density gradients: (a) half-space; (b) velocity gradient of 10 s^{-1}; (c) velocity gradient of -10 s^{-1}; (d)–(f) density gradients with $\nu=0.5,1,2$, respectively (see Fig. 4); (g)–(h) density gradient of $\nu=1$, velocity gradient of 10 s^{-1} and -10 s^{-1}, respectively; (i) density (solid) and velocity (dashed) transition layer profiles used in the sensitivity study. The water column sound velocity and density are 1510 m/s and 1.03 g/cm^3.

transition layer is acoustically "invisible" and the angle of intromission asymptotically approaches $\sim 11°$, which can be calculated, assuming the seabed is a homogeneous half-space [see Eq. (4)] using the properties at the base of the transition layer. At high frequencies ($k_z h \gg 1$), the acoustic field essentially interacts only with the water sediment interface so that $\delta \sim 15°$, which is consistent with reflection from a homogeneous half-space described by the properties at the top of the transition layer. The detailed behavior of $|R|$ between the low-and high-frequency asymptotes ($k_z h \sim 1$) depends upon the density profile. The reflectivity differences observed in Figs. 6(d)–6(f) give an indication of the sensitivity of $|R|$ to the shape of the density profile (which are shown in the lower-right panel of the figure).

2. Effect of sound velocity gradients on $|R|$

The effect of a positive and negative sound velocity gradient on reflectivity (with a constant density) is shown in Figs. 6(b) and 6(c). The frequency dependence of the angle of intromission can be understood in the same manner as for the density profile. At low frequencies ($k_z h \ll 1$) the transition layer is acoustically "invisible" and the seabed is essentially a homogeneous half-space. For the positive gradient [Fig. 6(b)] $\delta \sim 12°$, which can be calculated from Eq. (4) using the velocity at the base of the transition layer. At high frequencies ($k_z h \gg 1$), the acoustic field essentially interacts only with the water sediment interface so that $\delta \sim 15°$, which is consistent with reflection from a homogeneous half-space described by the properties at the top of the transition layer. For the negative sound velocity gradient [Fig. 6(c)], the low-frequency asymptote of the angle of intromission is $\delta \sim 18°$, which corresponds to reflection from a half-space composed of the properties at the base of the transition layer.

3. Effect of sound velocity and density gradients on $|R|$

Since the density and velocity both affect the angle of intromission in similar ways, it may be impossible to separate (i.e., uniquely determine) the effects of the velocity and density gradient by measuring only the angle of intromission.

The frequency dependence of the reflectivity at high angles (approximately greater than 45°), however, provides independent data to separate the effects of density and velocity. Note that the velocity gradients [Figs. 6(b) and 6(c)] have a relatively minor effect on the high angle reflectivity (i.e., $|R|$ is nearly frequency independent) since the relative variation of the velocity is small (less than 1%). However, the density profile has a substantially larger effect on high angle reflectivity [see, e.g., Fig. 6(d)] because the relative variation is $\sim 15\%$. Thus, by using observations both near the intromission angle and at high angles, the effects of velocity and density profiles can be separated. The combined effects of the density ($\nu=1$) and sound velocity profiles are shown in Figs. 6(g) and 6(h). A comparison of Figs. 6(g) and 6(h) with Fig. 6(e) indicates that the density profile and velocity profiles can be separated by making measurements both near the angle of intromission and at high angles. Though the sensitivity study has identified specific angle regimes of importance, the inversion technique (see Sec. IV) uses the data across the entire angular aperture of the measurements (10–80°).

The sensitivity of reflectivity both to layer thickness as well as the magnitude of the gradients can be understood by simple scaling arguments. Changing the sediment thickness changes the frequency scaling via the nondimensional parameter $k_z h$. In other words, the larger the layer thickness, the smaller the low- and high-frequency asymptotes, and *vice*

versa. In Fig. 6, differences of 0.2 g/cm^3 and 10 m/s were used at the top and bottom of the layer. Increasing/decreasing these differences (i.e., larger/smaller gradients) increase/decrease the difference in both the low- and high-frequency asymptote for the angle of intromission and $|R|$ at high angles. In practice, the low- and high-frequency asymptotes of the angle of intromission (i.e., the frequency required to accurately determine the upper or lower layer properties) are roughly $k_z h \leqslant \pi/10$ and $k_z h \geqslant \pi$, respectively (see the Appendix). The ability to resolve small velocity and/or density gradients, clearly depends on the bandwidth as well as the angular resolution, and reflection loss measurement accuracy (discussed in Sec. III).

In the sensitivity study results, only positive density gradients were shown, however, Eq. (4) is general enough so that negative density gradients are permitted. The sensitivity of $|R|$ to negative density gradients is completely commensurate with that shown for positive gradients.

In summary, the sensitivity study has shown that the reflection coefficient is sensitive to both velocity and density gradients. Most of the information for the shape of the gradients is in the neighborhood of $k_z h \sim 1$. Measurements of the low- $k_z h \ll 1$ and high- $(k_z h \gg 1)$ frequency asymptotes are required to estimate layer thickness and the properties at the upper and lower boundaries of the layer. Separating the effects of velocity and density gradients requires reflection coefficient measurements at high angles ($>45°$).

4. Effect of attenuation on $|R|$

In a homogeneous silty-clay half-space, the attenuation profile only has an effect at and near the angle of intromission. The effect of increasing the attenuation is to increase the reflection coefficient (decrease the reflection loss) at the angle of intromission. The reflection coefficient is also proportional to the attenuation at the angle of intromission in the presence of a transition layer, with the largest effects in the intermediate frequency regime $(k_z h \sim 1)$. In principle, the data near the angle of intromission in the intermediate frequency regime could be used to estimate the attenuation profile. However, since the quantity of interest for attenuation $(|R(\delta f)|)$ is so close to zero, other effects can easily mask the effect of the attenuation profile, like scattering from minute density or velocity fluctuations (e.g., see the Appendix of Ref. 18). Hence, it is believed that attenuation estimates from these data will be effective rather than intrinsic attenuation and the effective attenuation is assumed constant over the layer.

III. REFLECTION MEASUREMENTS AND DATA PROCESSING

Seabed reflection measurements were made using a broadband geophysical source and a single fixed hydrophone. The footprint of the experiment is of order 100 m, i.e., spatial averaging in range is of that order. The geometry for the experiment is given in Fig. 7. The source (Uniboomer with bandwidth $\sim 10^4$ Hz) is towed near the surface with a repetition rate of 1 pulse per second and a tow speed of ~ 4 knots giving an angular resolution as shown in Fig. 8(a). The

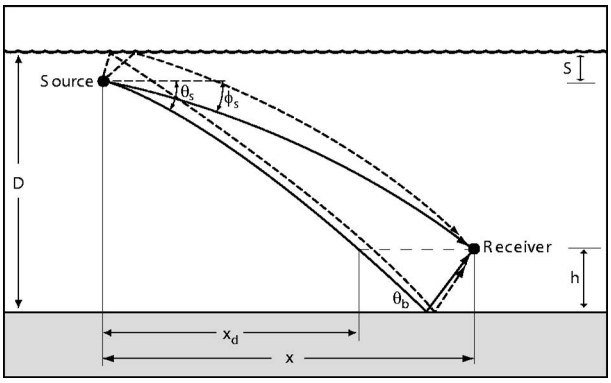

FIG. 7. Geometry of seabed reflection experiment.

dataset used here was collected on the mid-shelf region of the Malta Plateau at 36 ° 32.25′*N* 14 ° 49.30′*E*. In Ref. 17, the average sound speed and density were estimated using a single (frequency-averaged) estimate of the angle of intromission. In this paper, the frequency dependence of the reflectivity is exploited to obtain the depth-dependent properties.

Details of the data processing are given in Refs. 12 and 19 and are briefly summarized here. The magnitude of the pressure reflection coefficient is obtained by

$$|R(\theta_b,f)| = \left| \frac{p_r(x,f)}{p_d(x,f)} \right| \frac{q_d(x,f)}{q_d(x_d,f)} \frac{\gamma_d}{\gamma_0}, \tag{5}$$

where the first factor is a ratio of measured amplitudes, the second factor is a ratio of source amplitude fitting functions, and the third is a ratio of transmission factors. The subscript *r* indicates a path reflected from the seabed and the subscript *d* indicates a direct path from source to receiver. The ratio of measured levels means that there is no bias from uncertainties in the hydrophone or receiving electronics calibrations. The main source of measurement uncertainty (random not a bias error) in the reflectivity data comes from source amplitude variability. Uncertainties for the dataset used in the following section are shown in Fig. 9 (see Refs. 19 for details on how the uncertainty is estimated). The lowest uncertainties are in the band from 315–1600 Hz. This band was used in the inversion because below 300 Hz, the plane-wave assumption breaks down and the data above 1600 Hz are sensitive to fine-scale (centimeter scale) fluctuations in the sediment properties. The interest in this paper rather is to explore the smoothly varying sediment properties.

There is also uncertainty associated with the estimate of the incident/reflected angle, which arises from uncertainties in the experiment geometry and propagation paths. Reference 19, provides the equations for estimating the angle uncertainty (and provides measurement evidence of its adequacy). For the dataset considered here, the angular uncertainty is given in Fig. 8(b).

Another important aspect of the data processing is that the data can be time windowed around a specific interface or layer, so that the reflection coefficient can be obtained for just that interface or layer (as opposed to the more common total energy reflection processing that includes energy from

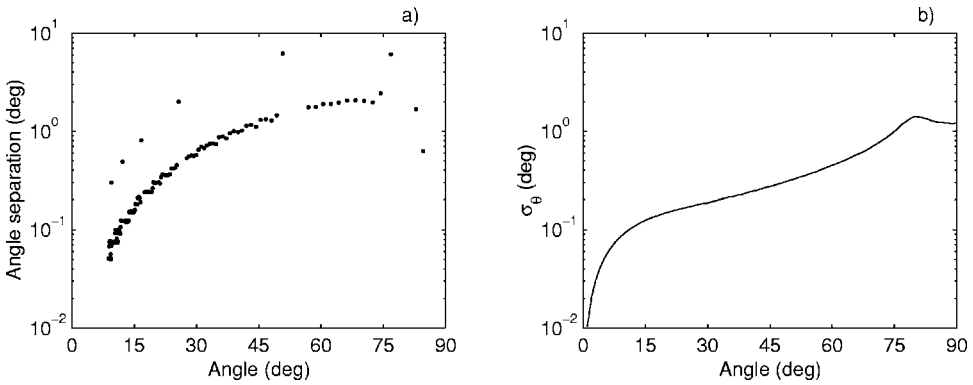

FIG. 8. (a) Angular separation of seabed reflection measurements and (b) standard deviation of the angle estimates.

all the sub-bottom layers). For this paper, the data are time windowed around the transition layer (i.e., the upper few meters of the sediment column).

The smallest gradients that could be measured by this method depend (in part) on the angular resolution, η_θ (i.e., the difference in angles between two adjacent measurements) and angular uncertainty σ_θ at the angle of intromission, i.e.,

$$\min|\delta_{LF} - \delta_{HF}| \cong 2\max(\eta_\theta, \sigma_\theta), \tag{6}$$

where the subscripts on δ indicate the low- and high-frequency asymptotes, respectively. Above about 11° grazing the angular resolution dominates:

$$\eta_\theta = \frac{v \sin^2 \theta}{\varpi(D - S + h)}, \tag{7}$$

where v is ship speed, ϖ is the pulse repetition rate, and D, S, and h are water depth, source depth, and receiver height (see Fig. 7). Note that Eq. 17 in Ref. 19 has a typo; ϖ should be in the denominator. Equations (6) and (7) lead to a transcendental equation, and estimates of the minimum observable differences in velocity/density can be estimated thereby. As an example, assume that the mean $\delta \sim 15°$ and the data have a sufficient bandwidth to estimate δ_{LF} and δ_{HF}. Using the angular resolution of the data [see Fig. 8(a)], Eq. (6) predicts that density/velocity differences (i.e., the difference from the top to the bottom of the transition layer) as small as 0.012 g/cm^3 and 1.5 m/s can be measured. This estimate is a lower bound since uncertainties in $|R|$ also lead to uncertainties in the estimation of δ, and are not accounted for in Eq. (6). Furthermore, these lower bound estimates assume that density and velocity differences occur independently. A better estimate of the lower bound is made in the following section using the density and velocity uncertainties themselves.

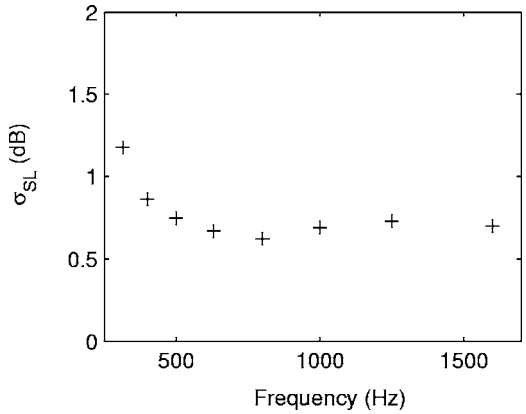

FIG. 9. Uncertainties in source level for the reflection measurements.

IV. INVERSION TECHNIQUE

A. Bayesian inversion

In this section we provide a brief overview of the Bayesian formulation used here to estimate geoacoustic model parameters of the transition layer; more complete treatments of Bayesian theory can be found in Refs. 20 and 21. Bayes' rule can be written as

$$P(\mathbf{m}|\mathbf{d}) = \frac{\mathfrak{L}(\mathbf{d}|\mathbf{m})P(\mathbf{m})}{P(\mathbf{d})}, \tag{8}$$

where $m \in \mathbb{R}^M$ and $d \in \mathbb{R}^N$ are random variables that represent the model parameters and data, respectively. $P(\mathbf{m}|\mathbf{d})$ is the posterior probability density (PPD), $\mathfrak{L}(\mathbf{d}|\mathbf{m})$ is the likelihood function, $P(\mathbf{m})$ is the model prior distribution, and $P(\mathbf{d})$ is the data prior (a constant factor once the data are measured). The likelihood function can generally be expressed as $\mathfrak{L}(\mathbf{m}) \propto \exp(-E(\mathbf{m}))$, where $E(\mathbf{m})$ is an appropriate error function (considered later). Equation (1) then becomes

$$P(\mathbf{m}|\mathbf{d}) = \frac{\exp(-\phi(\mathbf{m}))}{\int_{\mathfrak{M}} \exp(-\phi(\mathbf{m}'))d\mathbf{m}'}, \tag{9}$$

where the integration is over the model space $\mathfrak{M} \subset \mathbb{R}$ and $\phi(\mathbf{m})$ is the generalized misfit

$$\phi(\mathbf{m}) = E(\mathbf{m}) - \log_e P(\mathbf{m}). \tag{10}$$

The PPD represents the full solution to the inverse problem in the Bayesian formulation. However, due to the PPD's multidimensional nature, interpretation is not trivial and properties such as the maximum *a posteriori* (MAP) estimate $\hat{\mathbf{m}}$, the model covariance matrix $\mathbf{C}^{(\mathbf{m})}$, and marginal probability distributions $P(m_i|\mathbf{d})$, must be calculated to provide parameter estimates, uncertainties, and inter-relationships:

$$\hat{\mathbf{m}} = \mathrm{Arg}_{\max} P(\mathbf{m}|\mathbf{d}), \tag{11}$$

$$\mathbf{C}^{(\mathbf{m})} = \int_{\mathfrak{M}} (\mathbf{m}' - \hat{\mathbf{m}})(\mathbf{m}' - \hat{\mathbf{m}})^T P(\mathbf{m}'|\mathbf{d}) d\mathbf{m}', \tag{12}$$

$$P(m_i|\mathbf{d}) = \int_{\mathfrak{M}} \delta(m_i' - m_i) P(\mathbf{m}'|\mathbf{d}) d\mathbf{m}', \tag{13}$$

where δ denotes the Dirac delta function. Higher-dimensional joint marginal distributions can be defined similar to Eq. (13). Uncertainties of parameter estimates can also be quantified in terms of highest probability density (HPD) intervals. The $\beta\%$ HPD interval is defined as the interval of minimum width that contains $\beta\%$ of the area of the marginal probability distribution. While analytic solutions to Eqs. (11)–(13) exist for linear inverse problems, solutions for nonlinear problems must be found numerically.

The MAP model [Eq. (11)] can be found by numerical optimization such as a hybrid algorithm (e.g., adaptive simplex simulated annealing[22]). The above integrals are the moments of the PPD and are computationally challenging. They have the general form

$$I = \int_{\mathfrak{M}} f(\mathbf{m}') P(\mathbf{m}'|\mathbf{d}) d\mathbf{m}', \tag{14}$$

where $f(\mathbf{m})$ represents the characteristic term for each moment. I can be efficiently estimated by importance sampling, which preferentially draws random samples from those regions of the model space that contribute most to the integral by using a sampling function. The Gibbs distribution, which describes the state of energy of a system of many atoms in statistical mechanics, is used as a sampling function in Gibbs sampling, and is given by

$$P_G(\mathbf{m}) = \frac{\exp(-\phi(\mathbf{m})/T)}{\int_{\mathfrak{M}} \exp(-\phi(\mathbf{m}')/T) d\mathbf{m}'}. \tag{15}$$

T is a factor that resembles the temperature in statistical mechanics. For $T=1$, Eq. (15) has the form of the PPD [Eq. (9)]. Using importance sampling with $P_G(\mathbf{m})$ as the sampling function at $T=1$ approximates Eq. (14) as

$$I \approx \frac{1}{Q} \sum_{i=1}^{Q} f(\mathbf{m}_i), \tag{16}$$

providing an unbiased estimate of the integral based on a sample of Q models. Further, it can be shown, using Markov chain analysis that the Metropolis algorithm (MA) converges to the Gibbs distribution for large Q and can provide an unbiased estimate of the PPD.[21] In this paper, an efficient Gibbs sampling algorithm, fast Gibbs sampling (FGS[23]), is used to sample the PPD.

B. Likelihood and data errors

Formulating the likelihood function $\mathfrak{L}(\mathbf{m})$ requires specifying the data uncertainty distribution. Data uncertainties must include both measurement errors due to experimental processes (discussed in Sec. III) and theory errors due to model parametrization and simplifications in the forward model. In general, the Bayesian inversion outlined above can be applied with arbitrary uncertainty distributions. In practice, however, the lack of information about the error distribution often suggests a mathematically simple distribution be assumed. In this work, Gaussian and double-sided exponential distributions are considered, with the statistical parameters estimated from the data.

A common assumption in geoacoustic inversion is that the data errors are uncorrelated. In practice, however, strong error correlations can be present. It is important to verify whether or not significant error correlations are present in Bayesian inversion, since neglecting these can result in unreasonably tight uncertainty bounds for the model parameters. One approach to treat correlated errors is to downsample the data below the correlation length, with an obvious loss of information. In this paper we apply a rigorous approach to analyze data residuals to test for randomness and incorporate error correlations into the inversion without losing information. A full data covariance matrix is estimated from the data residuals and applied in the error function of the Bayesian inversion.

For N_i data $\mathbf{d}_i$ at each of F frequencies f_i and M model parameters $\mathbf{m}$, the likelihood function $\mathfrak{L}(\mathbf{m})$ for unbiased Gaussian-distributed random errors uncorrelated from frequency to frequency is

$$\mathfrak{L}(\mathbf{m}) \propto \prod_{i=1}^{F} \exp\left(-\frac{1}{2} (\mathbf{d}_i - \mathbf{d}_i(\mathbf{m}))^T \mathbf{C}_i^{-1} (\mathbf{d}_i - \mathbf{d}_i(\mathbf{m})) \right), \tag{17}$$

where $\mathbf{C}_i$ are the F $N_i \times N_i$ data covariance matrices. In this case, the data misfit for known $\mathbf{C}_i$ is given by the L_2 norm

$$E_2(\mathbf{m}) = \sum_{i=1}^{F} \frac{1}{2} (\mathbf{d}_i - \mathbf{d}_i(\mathbf{m}))^T \mathbf{C}_i^{-1} (\mathbf{d}_i - \mathbf{d}_i(\mathbf{m})). \tag{18}$$

In many cases, the $\mathbf{C}_i$ are not known, but can be estimated as follows. Initially assuming uncorrelated errors over angle, the data covariance can be written as $\mathbf{C}_i = \sigma_i^2 \mathbf{I}$, where $\mathbf{I}$ is the identity matrix. The likelihood function then becomes

$$\mathfrak{L}(\mathbf{m}) \propto \prod_{i=1}^{F} \exp\left(-\sum_{j=1}^{N_i} \frac{(d_{i;j} - d_{i;j}(\mathbf{m}))^2}{2\sigma_i^2} \right), \tag{19}$$

where $d_{i;j}$ represents the jth datum at the ith frequency. A ML estimate for the σ_i can be found by maximizing $\mathfrak{L}(\mathbf{m})$ over σ_i and $\mathbf{m}$ to yield

$$\tilde{\sigma}_i = \left(\frac{1}{N_i} \sum_{j=1}^{N_i} (d_{i;j} - d_{i;j}(\tilde{\mathbf{m}}))^2 \right)^{1/2}, \tag{20}$$

where the ML estimate $\tilde{\mathbf{m}}$ is found by minimizing

$$\tilde{E}(\mathbf{m}) = \prod_{i=1}^{F} \sum_{j=1}^{N_i} (d_{i;j} - d_{i;j}(\mathbf{m}))^2. \tag{21}$$

With the estimates σ_i, another minimization is carried out using Eq. (18) with $\mathbf{C}_i = \tilde{\sigma}_i^2 \mathbf{I}$ to produce the MAP estimate $\hat{\mathbf{m}}^{(1)}$. The data covariance matrices at each frequency can then be estimated by calculating the autocovariance function

of the data residuals $\mathbf{n}_i^{(1)}=\mathbf{d}_i-\mathbf{d}_i(\hat{\mathbf{m}}^{(1)})$. The autocovariance is defined as an ensemble average. However, the data provide only a single, finite subset of the random process. For uniform sampling in angle, the ensemble average can be replaced by an average over the N_i angles, assuming an ergodic process. For nonuniform spacing in angle, estimating the autocovariance function is more difficult and a nonparametric approach is applied here. First, the main diagonal of the covariance matrix is computed as

$$C_{i;jj}=\frac{1}{N_i}\sum_{j=1}^{N_i} n_{i;j}^2, \tag{22}$$

where $n_{i;j}$ is the jth residual at the ith frequency. Then the product for every unique data pair $c_{i;j,k}=n_{i;j}n_{i;k}$ $(k\neq j, k>j)$ and their differences in angle $\Delta\theta_{i;j,k}=|\theta_{i;j}-\theta_{i;k}|$ are calculated and sorted according to increasing angle difference. The sorted $c_{i;l}$, where $l=1,\ldots,Q_i$, and $Q_i=(N_i(N_i+1)/2)-N_i+1$ is the number of pairs that equals the number of off-diagonal elements for the symmetric covariance matrix, are smoothed with a running cosine window that varies in width from 4° to 10° with increasing $\Delta\theta$. To ensure the covariance matrix estimate is positive definite, the smoothed autocovariance estimate is damped with an exponential factor,

$$x_{i;l}=\exp\left(-\kappa_i\frac{l}{Q_i}\right), \tag{23}$$

where κ_i is an empirical factor for each frequency to obtain $\bar{c}_{i;l}$.

After smoothing and damping, the $\bar{c}_{i;l}$ are sorted back to the original order of the $\Delta\theta_{i;j,k}$ to obtain $\bar{c}_{i;j,k}$ that fill an initial symmetric data covariance matrix estimate $\hat{\mathbf{C}}_{(i,1)}$ according to $\hat{C}_{(i,1);jk}=\bar{c}_{i;j,k}$. This covariance matrix can then be applied in a subsequent inversion for a MAP estimate $\hat{\mathbf{m}}^{(2)}$. If the covariance matrix computed for $\hat{\mathbf{m}}^{(2)}$ using the above procedure is sufficiently close to $\hat{\mathbf{C}}_{(i,1)}$, the method can be considered to have converged. If not, further iterations can be performed. Synthetic data examples showed that the recovered estimate of the covariance matrix converged after the second iteration. The final estimate for the covariance can be incorporated into the FGS algorithm using Eq. (18).

Assuming a Gaussian distribution for data errors leads to L_2-norm inversion. One of the strengths of a numerical approach is that data misfit functions for different error distributions can be applied. For instance, L_1-norm inversion corresponds to a double-sided exponential error distribution with an error function,

$$E_1(\mathbf{m})=\sum_{i=1}^{F}\sum_{j=1}^{N_i}|\mathbf{L}_i^{-1}(\mathbf{d}_i-\mathbf{d}_i(\mathbf{m}))_j|, \tag{24}$$

where $\mathbf{L}$ is the lower triangular matrix of the Cholesky decomposition of the covariance matrix,

$$\mathbf{C}_i=\mathbf{L}_i\mathbf{L}_i^T. \tag{25}$$

The effect of taking covariances into account while inverting the data can be examined by transforming the data residuals at each frequency with the Cholesky decomposition $\mathbf{L}_i$ from Eq. (25) according

$$\tilde{\mathbf{n}}_i=\mathbf{L}_i^{-1}\mathbf{n}_i. \tag{26}$$

To test whether the transformed data residuals satisfy the initial assumptions, qualitative methods, and rigorous statistical tests can be applied. The autocorrelation function can be used to visualize the randomness of the residuals. Independent random errors should produce a narrow peak at zero lag. The wider the peak, the longer the correlation length of the errors. To quantify randomness, a runs test (one-tailed median delta test[24]) can be applied. The runs test tests the null hypothesis H_0 that the residuals are random against the alternative hypothesis H_1 that the residuals are correlated by counting the number of runs on either side of the median. The output is a p value that indicates the level of confidence against H_0. Values of $p\geqslant 0.05$ are generally accepted as little evidence against H_0.

The Kolmogorov–Smirnov (KS) test can be applied to test whether the residuals are drawn from a particular distribution.[25] It compares the cumulative distribution of the residuals to the theoretical cumulative distribution (e.g., Gaussian or double-sided exponential) based on the maximum difference between the distributions. A p value quantifies the evidence against the null hypothesis that the residuals are from the particular distribution.

V. ACOUSTIC INVERSION RESULTS AND COMPARISON WITH CORE SAMPLES

Measured seabed reflection data and the inversion results for density and velocity profiles in the transition layer are presented here. The remotely sensed results are compared with core data.

A. Acoustic inversion results

Seabed reflection measurements were conducted during the SCARAB98 experiment, April 1998. The data were time windowed so that only the upper 1.5 m of the sediment column contribute to the reflectivity and were processed in 1/3 octave frequency bands (see Fig. 10). In the Bayesian inversion approach, uniform priors were employed over a wide range of parameters, i.e., assuming no prior knowledge of the sediment properties (see Table I). Figure 10 shows the fit of the replica data, generated for the MAP model $\hat{\mathbf{m}}$, to the measured data. The measured data include one standard deviation ML error estimates quantifying both theory and measurement errors. The good agreement between data and replica indicates a reasonable parametrization. However, the plot also indicates correlated errors. Rows 1 and 3 in Fig. 11 give the autocorrelation function of the raw data residuals $\mathbf{n}_i$ at each frequency and show that every frequency features a wide peak around lag zero indicating strong error correlations. Hence, a full covariance matrix for every frequency was estimated as described in Sec. IV B and applied in the misfit function. This produced a second MAP model $\hat{\mathbf{m}}^{(2)}$ and residuals $\mathbf{n}_i^{(2)}$. The result of applying the data covariance matrix estimate to the data is shown in rows 2 and 4 of Fig. 11 for the residuals $\tilde{\mathbf{n}}_i^{(2)}$, prewhitened according to Eq. (26). The

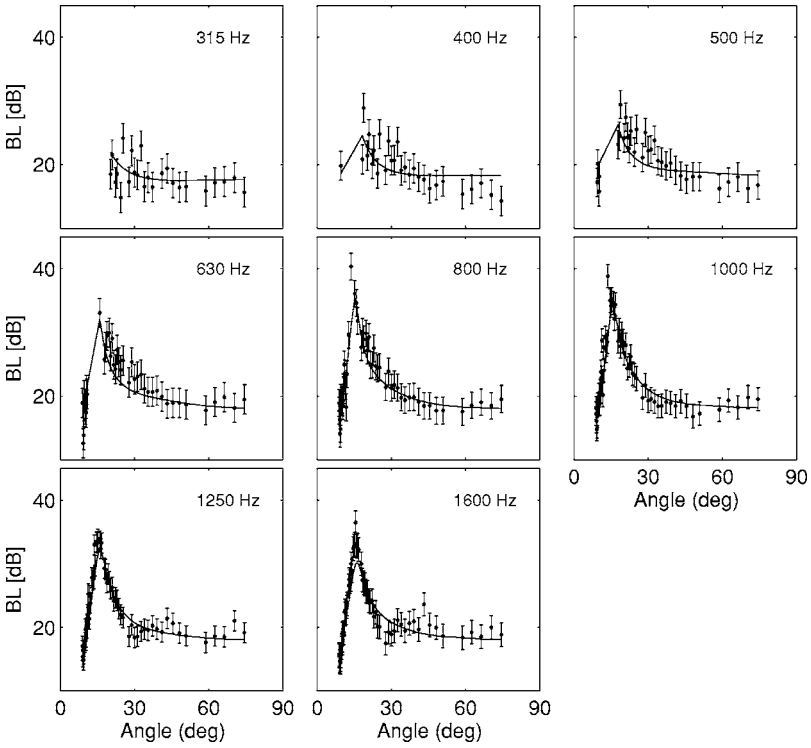

FIG. 10. Fit of the MAP estimate (solid line) to the measured data that includes one standard deviation ML error estimates. For clarity, only every second data point is shown. Correlated data errors are indicated by consecutive data points on one side of the solid line.

peaks of the autocorrelation function of $\mathbf{n}_i^{(2)}$ are narrow and there are virtually no oscillations at greater lags.

To quantify the randomness of the residuals, a runs test was performed and p values calculated for every frequency before and after applying the data covariance matrix estimate according to Eq. (26). Before taking covariances into account, the residuals had p values of $p<10^{-3}$ to $p=0.059$; all but one frequencies fail at the $p>0.05$ confidence level. After taking correlations into account, the test produced values between $p=0.002$ and $p=0.737$; five out of eight frequencies pass the test at the $p>0.05$ confidence level. The p values are given in Fig. 11.

To quantify the effect of the data covariance matrix estimate on the statistical distribution of the residuals, the KS test was applied to $\mathbf{n}_i$ and $\tilde{\mathbf{n}}_i^{(2)}$. Figure 12 shows cumulative distributions for the data residuals (solid line) and for a theoretical Gaussian distribution (dashed lines). Rows 1 and 3 are for the raw residuals $\mathbf{n}_i$ and rows 2 and 4 are for residuals $\tilde{\mathbf{n}}_i^{(2)}$, prewhitened according to Eq. (26). The match between the theoretical distributions and the data residuals appears to be good for most frequencies before and after applying the covariances. The p values that the KS test produced, given in Fig. 12, show that 4 frequencies pass at the $p>0.05$ confidence. In one case, $f=1000$ Hz, the p value changes from $p=0.13$ for $\mathbf{n}_i$ to $p=0.03$ for $\tilde{\mathbf{n}}_i^{(2)}$. In all other cases, applying the covariance matrix does not change the statistics of the residuals significantly. At all frequencies, the cumulative distributions appear close to the theoretical curves.

The complete inversion procedure, including covariance estimation, was also carried out for the assumption of double-sided exponential error distributions with similar results (not shown). The KS test produced higher p values for residuals at some frequencies. However, the applied KS test is not very sensitive in the tails of a distribution. The double-sided exponential distribution features heavier tails than the Gaussian distribution. Histograms of the data residuals showed that the peaks were better represented by the double-sided exponential distribution but the tails were not heavy enough. Comparing these results provides confidence in the method applied as it appears to be more important to incorporate error correlations than finding the best match for the error distribution.

The parameter estimates from the inversion along with their uncertainties are given in Table I and the marginal distributions in Fig. 13. One of the significant results of the inversion (see Table I and Fig 13) is that the upper and lower values of the density in the transition layer are clearly resolved, i.e., the parameter uncertainties are smaller than the density difference. The upper and lower values of the velocity are also resolved, but just barely. The joint marginal distributions between several parameters indicate coupling between density, velocity, layer thickness, and ν (Fig. 14).

TABLE I. Geoacoustic parameter estimates from inversion with uncertainties. The bounds defining uniform prior distributions are also provided.

Parameter	Prior bounds	MAP estimate	95% credibility interval
Thickness (m)	0.5–3.5	1.67	1.48–1.86
ρ_t (g/cm^3)	1.1–1.6	1.356	1.346–1.363
c_t (m/s)	1450–1550	1472.7	1471.3–1474.1
ν	0–1.5	1.00	0.88–1.10
ρ_b (g/cm^3)	1.2–1.8	1.55	1.50–1.60
c_b (m/s)	1450–1550	1465.9	1460.3–1471.0
α (dB/λ)	0–0.8	0.38	0.35–0.42

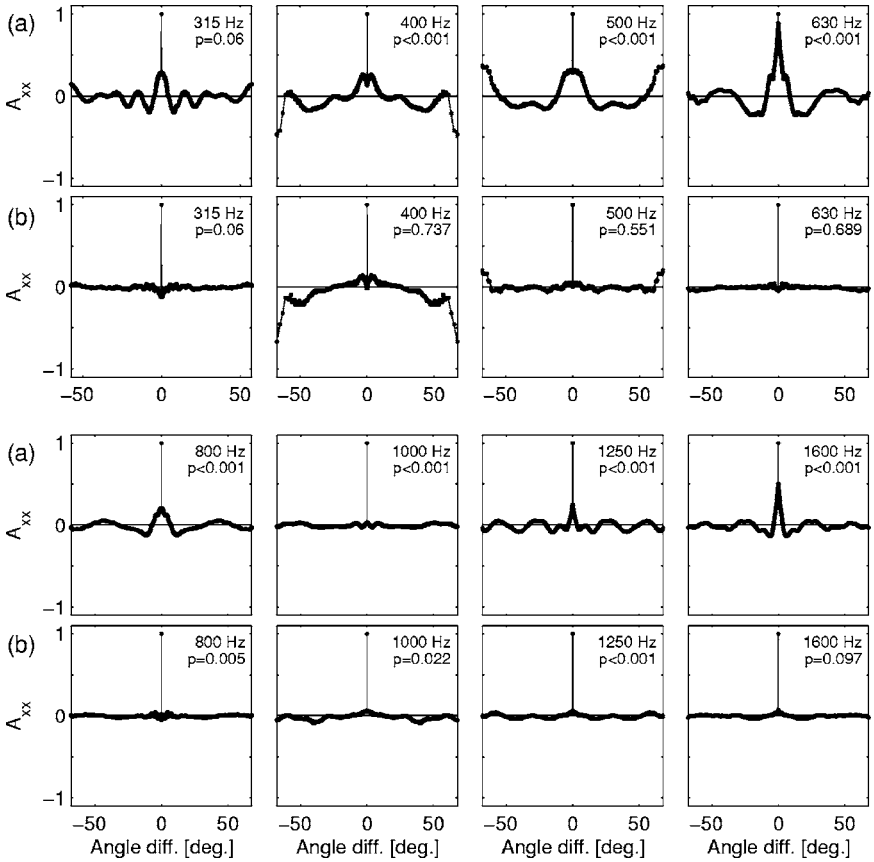

FIG. 11. Estimate of the autocovariance for (a) raw data residuals n_i and (b) pre-whitened data residuals $\tilde{\mathbf{n}}_i^{(2)}$. Run test results are given as p values.

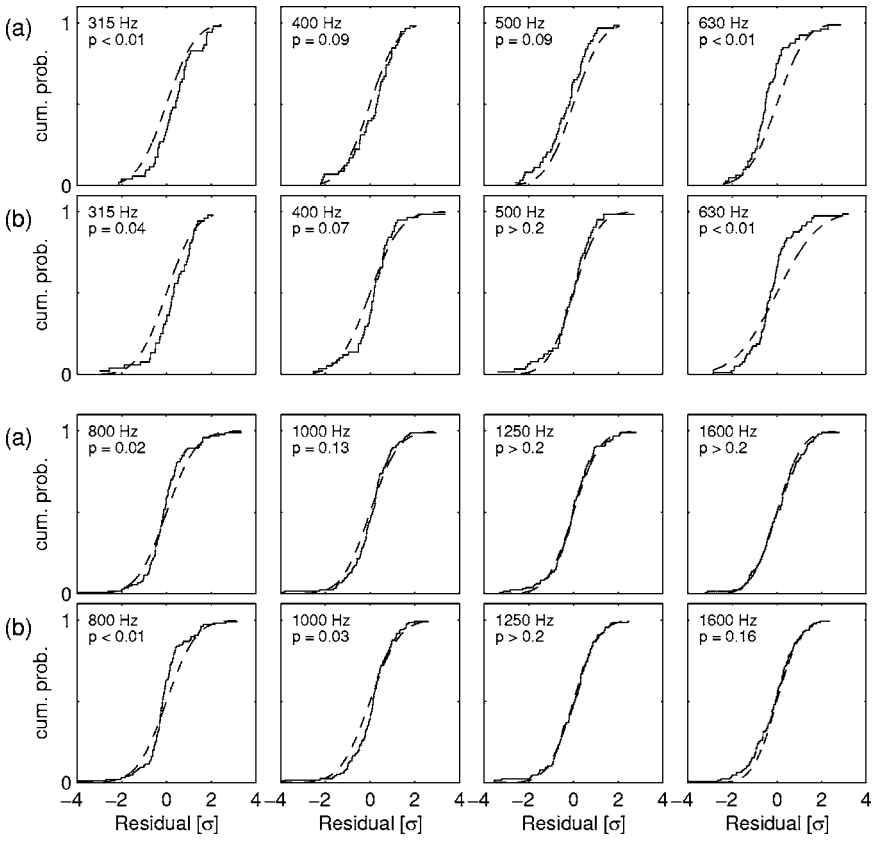

FIG. 12. Cumulative probability distributions for (a) raw data residuals n_i and (b) pre-whitened data residuals $\tilde{\mathbf{n}}_i^{(2)}$. Results of the K–S test are given as p values. Dashed lines represent theoretical Gaussian cumulative probability distributions.

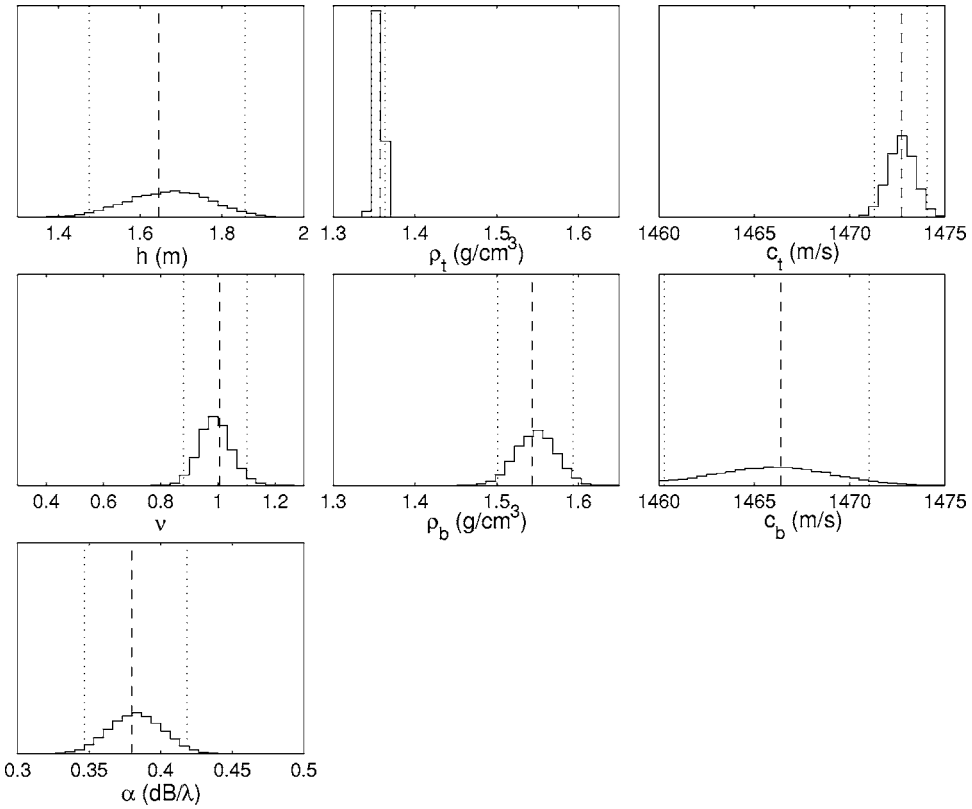

FIG. 13. Marginal probability distributions for geoacoustic parameters computed using the full data covariance matrix. Also shown are the MAP estimates (dashed lines) and the 95% HPD intervals (dotted lines).

B. Gravity core data

In order to have an independent measurement of the transition layer properties, two gravity cores were collected at this site. The cores were collected using a 1.3 m long, 110 mm diameter thin-walled core barrel with a sphincter closure device, designed to minimize sampling disturbance. The weights on the core head were adjusted until ~10–20 cm of seawater was retained on top of the core. The motivation for this procedure was to minimize disturbance of the sediment interface properties and to obtain *in situ* seawater for calibration purposes. Following retrieval, the cores were capped and stored upright for several hours until the cores reached an ambient temperature. Compressional velocity (at 200 kHz) and density measurements (gamma ray attenuation) were then conducted at 1 cm intervals using a Geotek Multi-Sensor Core Logger (MSCL). Errors in the velocity and density measurements come from two main sources: (1) a sampling disturbance that would include disturbance during core penetration, sphincter closing, core recovery and capping, and core storage (possible compaction due to ship heave and roll) and (2) MSCL measurement errors that would include calibration errors, plus uncertainties in picking the time of flight for the velocity and uncertainties in the empirical relations used to relate gamma ray attenuation with bulk density. The MSCL developer has estimated the latter errors to be ~6 m/s and 2% of density at 2 standard deviations. Though manufactured to a close tolerance, we have found additional velocity errors to be related to small variations of the core liner thickness. We have no estimates for errors associated with the sampling disturbance.

Two cores were collected at this site, ~140 m apart, as a gross attempt to bound random sampling errors plus lateral variability (the two effects can not be separated with these data). The two cores (see Fig. 15) are quite similar, though there are minor differences in the small (cm) scale variability that may be due to lateral variability or sampling errors or both. The largest difference is observed in the velocities below 1 m depth. It is believed that the velocities below 1 m are unreliable due to effects from the sphincter closing or end capping, or both.

The core data are also unreliable in the upper 3 cm due to three factors: (a) there is a very fine layer of surficial sediment that is highly disturbed in the core operation; when the core is recovered on deck, the fines are clearly in suspension in the seawater (visible through the clear liner) and several hours to a day are required for settlement, (b) there is an inherent measurement resolution of 1–2 cm in depth, and (c) the water–sediment interface of the cores is not perfectly flat; generally there is a ~1 cm variation (sometimes as great as 2 cm) in either small mounds, depressions, and/or the overall slope of the interface. So the first factor means that some disturbance is inherent in the uppermost layer (roughly 0.005 m), almost certainly reducing its density relative to the *in situ* value. The second two factors together mean that near the sediment interface, the gamma rays and acoustic pulse traverse a path that is partly sediment and partly water. Such a path will bias the density low and the velocity high (since in this case the water has a higher sound velocity than the sediment) until ~0.03 m below the interface. The bias would clearly be a function of depth, that is, the greatest errors would be near the water–sediment interface and the errors would decrease with increasing depth, leading to a steeper gradient than actually exists. The data could be partially corrected if the exact shape of the core surface were measured,

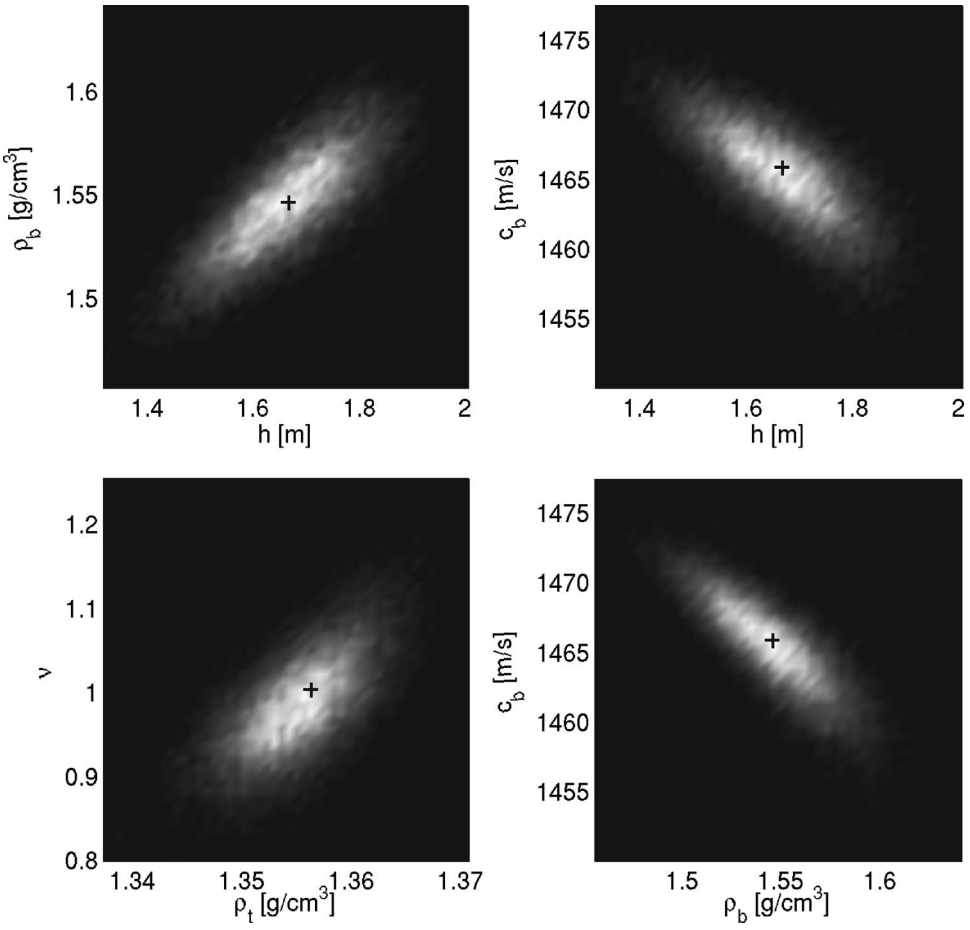

FIG. 14. Joint marginal distributions for selected parameter pairs. The black cross indicates the MAP model result.

but this has not been done. Thus, the high positive gradient in the upper 0.03 m in density is too large and the large negative velocity gradient is also in error.

C. Comparison of inversion results with gravity cores data

The properties of the transition layer obtained from the acoustic inversion are compared with the core data in Fig. 15. The most important point regarding the comparison is that the agreement is quite good, i.e., there is overlap in the uncertainties of the two methods. An aspect of the comparison that seems particularly promising is the similarity of the shape of the profiles between the remote sensing and the core measurement. For the density profile, recall that there is a wide variation of allowable profiles by varying ν [see Eq. (2) and Fig. 4]; thus the agreement seems excellent. The remote sensing technique was also capable of measuring a small negative velocity gradient (-6 s^{-1}) in the upper meter.

The remote sensing results agree very well with the core data at the bottom of the core (discounting core end effects).

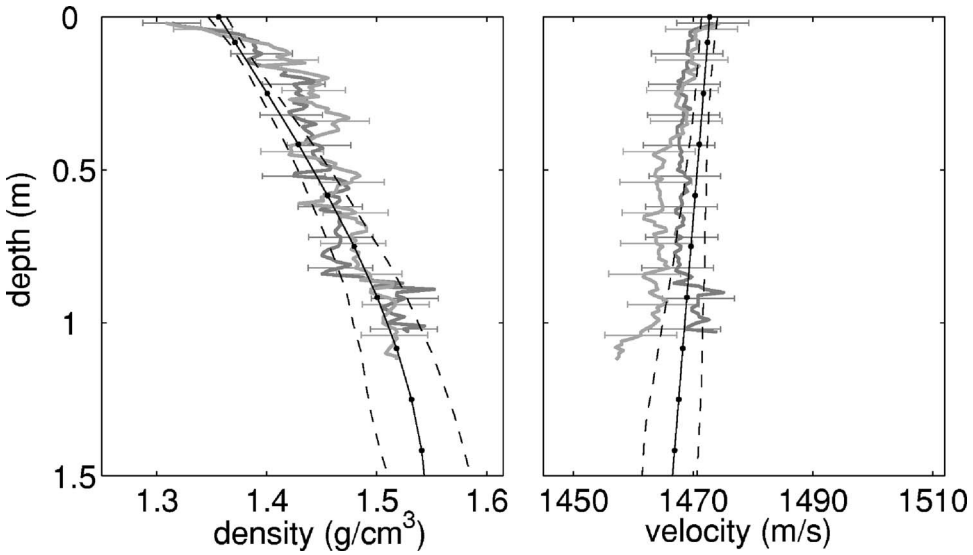

FIG. 15. A comparison of remotely sensed results (MAP estimate; dashed lines are 95% confidence bounds) with two core measurements (heavy gray lines with 2 standard deviations every tenth datum).

At the top of the core (in the top 3 cm), the density and velocity gradients are known to be in error. We now examine the possibility of error in the remote sensing results at the water–sediment interface. In order to estimate the properties at the interface, the frequency has to be large enough to sample the high-frequency asymptote of the angle of intromission, δ_{HF}. In the Appendix it is shown that δ_{HF} can be resolved at $k_z h \sim \pi$. For the properties in Table I, at 1600 Hz (the largest frequency used in the inversion) $k_z h = 3$ at the angle of intromission, so it appears that the frequency is high enough to make a good estimate of the surficial properties. If the density were lower and the velocity higher at the water–sediment interface (as the biased core data suggest), it would lead to a higher angle of intromission and an even higher $k_z h$. In other words, the frequency range of the data appear to be sufficient to estimate density gradients near the water–sediment interface. Thus, the remote sensing values of velocity and density at the water–sediment interface are properly estimated, at least with respect to the frequency range criterion and the assumed parametrization. As a check on the parametrization, the core data was fit to Eq. (2). The fit between the parametrized core and the core measurements is very good (misfit $\sim 1\%$), indicating that the parametrization is appropriate for these sediments.

There are no independent measurements of the attenuation with which to compare the inversion results. However, it is believed that the attenuation estimate is biased due to several factors. First, the reflection coefficient at the angle of intromission is nearly zero and thus small effects (e.g., scattering from small density or velocity fluctuations or noise) can lead to biases. Second, the forward model has a small bias at the angle of intromission at low frequencies (see Fig. 2). Third, there may be an attenuation gradient (which has been ignored). Effects from the first factor mentioned above almost certainly dominate and the authors believe that the attenuation estimate is biased high, by an order of magnitude (for attenuation estimates in similar sediments see, for example, Refs. 26 and 27).

VI. SUMMARY AND CONCLUSIONS

Marine sediments often exhibit continuous changes of geoacoustic properties within a distinct sedimentary layer. A particularly important example of continuous variation occurs at the water–sediment interface, called the transition layer. We have demonstrated a method for remotely obtaining the density and velocity gradients within this layer. Although the transition layer from a fine-grained sediment was treated in the present analysis, the method (measurement and inversion) is quite general and could be used for sandy sediment fabrics as well (e.g., see Ref. 14). Also note that, in principle, this technique could be applied to any layer within the sediment column, whether it was at or below the water–sediment interface. In order to analyze a layer below the water–sediment interface, the layer would be isolated in time so that the reflection coefficient would apply just to that layer boundary. The properties of the layer immediately above the target layer would also have to be known, and could be obtained by a layer-stripping approach, as in Ref. 12.

The method exploits the frequency and angular dependence of the reflection coefficient to estimate the sediment geoacoustic parameters by a Bayesian inversion approach. The density and velocity profiles obtained via inversion agree well with core measurements within the uncertainties of both methods. The advantages of the remote-sensing method over the traditional coring approach are that (1) there is no sediment disturbance, which is particularly important for fragile fine-grained sediments, (2) measurements are substantially faster (and less expensive) and can be performed in a survey mode with a towed receiver, (3) has as low or lower uncertainties than coring. The velocity uncertainties were lower for the remote-sensing than the coring, the density uncertainties at the top of the transition layer were lower than the core data uncertainties, but higher than the core uncertainties at the base of the layer. However, this comparison only uses the known uncertainties in the core measurement process. There are additional, but unknown, uncertainties that exist in the sampling, recovery, and storage that increase the core uncertainties.

In any inversion it is important to check the validity of the underlying assumptions by examining the statistics of the data residuals *a posteriori*. In particular, neglecting correlations between data errors can result in significantly underestimating uncertainties in the inversion results.[28] For the data considered here, the residuals from an initial inversion were approximately Gaussian distributed, but were clearly correlated over angles. Hence, a Bayesian inversion algorithm was developed that included a rigorous treatment of data error correlations, which has not been applied previously in geoacoustic inversion. A full error covariance matrix was estimated iteratively from the residuals and included in the likelihood function. Statistical tests (runs test) applied to the resulting prewhitened residuals indicated a substantial decrease in correlation effects.

It is worth noting that the uncertainty bounds computed here represent the confidence in the parameter values obtained in the inversion; this depends on the particular parametrization applied, and does not preclude the possibility that the actual seabed properties vary outside these bounds (this is true for any inverse problem). For example, the core measurements include fine-scale fluctuations with depth. Since these fluctuations are beyond the resolution of reflectivity data at the frequencies considered here, the parametrization applied represents density and sound speed as smooth, monotonic functions of depth that purposefully excludes any unresolvable small-scale structure. The particular choice of parametrization represents an application of prior information to the inverse problem, which is reflected in the Bayesian uncertainty bounds. The bounds constrain the average behavior of the profiles that is consistent with the parametrization, but do not necessarily encompass the full (small-scale) variability that is possible in the sediment structure.

This remote-sensing technique could be employed for a variety of applications, including the measurement of crucial geoacoustic properties required for shallow water propagation and reverberation studies. In addition, because it predicts density variations to high accuracy, it can also be used to predict the burial depth of objects placed or dropped on

the seabed. Finally, the transition layer properties may reveal aspects of the underlying depositional or erosional processes that have important implications in other branches of marine science, e.g., sediment transport, benthic biology, or pollutant monitoring.

ACKNOWLEDGMENTS

We gratefully acknowledge the support of the Office of Naval Research (Code OA321) and the NATO Undersea Research Center for their support.

APPENDIX: APPROXIMATE HIGH- AND LOW-FREQUENCY LIMITS FOR REFLECTION FROM A TRANSITION LAYER

The high- and low-frequency limits for acoustic reflection from a transition layer at the seabed can be approximated by considering reflection from a layer in which there is no discontinuity in density at the boundary and where the sound speed is constant.

The reflection coefficient for this case can be written[4] as

$$|R|^2 = \frac{(\alpha h)^2 \sin^2(\beta h)}{(k_z h)^2 \sin^2(\beta h) + (\beta h)^2 \cos^2(\beta h)}; \qquad \alpha = \log\left(\frac{\rho_1}{\rho_0}\right) h;\ \beta = (k_z^2 - \alpha^2/4)^{1/2}. \tag{A1}$$

At high frequencies, $k_z \gg \alpha$,

$$|R|^2 = (\alpha h)^2 \frac{\sin^2(k_z h)}{(k_z h)^2}. \tag{A2}$$

At infinite frequency the sinc function and hence the reflection coefficient goes to zero, as expected. A practical value for the high-frequency limit is the first zero crossing of the sinc function, or $k_z h \sim \pi$. That this is a reasonable value even when the interface has a discontinuity in the density and sound speed can be seen in Fig. 6. For example, in Fig. 6(b), the reflection loss is essentially constant above 2400 Hz, where $k_z h \sim \pi$ at the angle of intromission.

The low-frequency limit to Eq. (A1) can be obtained as

$$(k_z h)^2 \ll \frac{1}{4}(\alpha h)^2 \coth^2(\alpha h/2), \tag{A3}$$

and if we require the left-hand side of Eq. (A3) to be one order of magnitude smaller than the right-hand side, the low-frequency limit is

$$k_z h < \frac{1}{2\sqrt{10}} \log\left(\frac{\rho_1}{\rho_0}\right) \frac{\rho_1 + \rho_0}{\rho_1 - \rho_0}, \tag{A4}$$

which for many values of ρ_1/ρ_0 leads to the estimate of the low-frequency asymptote at approximately $k_z h < \pi/10$.

[1] R. Wheatcroft and D. Drake, "Post-depositional alteration and preservation of sedimentary event layers on continental margins; I, The role of episodic sedimentation," Mar. Geol. **199**, 123–137 (2003).
[2] S. Bentley and A. Sheremet, "New model for the emplacement, bioturbation, and preservation of fine-scaled sedimentary strata," Geology **31**, 725–728 (2003).
[3] B. M. Hand, "Inverse grading resulting from coarse-sediment transport lag," J. Sediment Res. **67**, 124–129 (1997).
[4] A. Robins, "Reflection of plane acoustic waves from a layer of varying density," J. Acoust. Soc. Am. **87**, 1546–1552 (1990).
[5] A. Robins, "Reflection of a plane wave from a fluid layer with continuously varying density and sound speed," J. Acoust. Soc. Am. **89**, 1666–1696 (1991).
[6] A. Robins, "Exact solutions of the Helmholtz equation for plane wave propagation in a medium with variable density and sound speed," J. Acoust. Soc. Am. **93**, 1347–1352 (1993).
[7] A. Robins, "Plane-wave reflection from a solid layer with non-uniform density, sound speed, and shear speed," J. Acoust. Soc. Am. **103**, 1337–1345 (1998).
[8] S. Rutherford and K. Hawker, "Effects of density gradients on bottom reflection loss for a class of marine sediments," J. Acoust. Soc. Am. **63**, 750–757 (1978).
[9] R. Carbó, "Wave reflection from a transitional layer between the seawater and the bottom," J. Acoust. Soc. Am. **101**, 227–232 (1997).
[10] A. Lyons and T. H. Orsi, "The effect of a layer of varying density on high frequency reflection, forward loss, and backscatter," IEEE J. Ocean. Eng. **23**, 411–421 (1998).
[11] E. Pouliquen and A. Lyons, "Backscattering from bioturbated sediments at high frequency," IEEE J. Ocean. Eng. **27**, 388–402 (2002).
[12] C. W. Holland and J. Osler, "High resolution geoacoustic inversion in shallow water: A joint time and frequency domain technique," J. Acoust. Soc. Am. **107**, 1263–1279 (2000).
[13] M. D. Richardson, In-situ shallow water sediment geoacoustic properties, in *Shallow Water Acoustics*, edited by R. Zhang and J. Zhou (China Ocean Press, City, 1997).
[14] S. E. Dosso and C. W. Holland, "Geoacoustic uncertainties from viscoelastic inversion of seabed reflection data," IEEE J. Ocean. Eng. (in press).
[15] M. A. Biot, "Generalized theory of acoustic propagation in porous dissipative media," J. Acoust. Soc. Am. **34**, 1254–1264 (1962).
[16] L. M. Brekovskikh, *Waves in Layered Media*, 2nd ed. (Academic, New York, 1980), p. 502.
[17] C. W. Holland, "Geoacoustic inversion for fine-grained sediments," J. Acoust. Soc. Am. **111**, 1560–1564 (2002).
[18] C. W. Holland, "Shallow water coupled scattering and reflection measurements," IEEE J. Ocean. Eng. **27**, 454–470 (2002).
[19] C. W. Holland, Seabed reflection measurement uncertainty, J. Acoust. Soc. Am. **114**, 1861–1873 (2003).
[20] A. Tarantola, *Inverse Problem Theory* (Elsevier, Amsterdam 1987).
[21] M. K. Sen and P. L. Stoffa, *Global Optimization Methods in Geophsyical Inversion* (Elsevier, Amsterdam, 1995).
[22] S. E. Dosso, M. J. Wilmut, and A.-L. S. Lapinski, "An adaptive-hybrid algorithm for geoacoustic inversion," IEEE J. Ocean. Eng. **26**, 324–336 (2001).
[23] S. E. Dosso, "Quantifying uncertainty in geoacoustic inversion. I. A fast Gibbs sampler approach," J. Acoust. Soc. Am. **111**, 129–142 (2002).
[24] J. E. Freund, *Modern Elementary Statistics* (Prentice–Hall, Englewood Cliffs, NJ, 1967).
[25] F. J. Massey, "The Kolmogorov–Smirnov test for goodness of fit," J. Am. Stat. Assoc. **46**, 68–78 (1951).
[26] S. K. Mitchell and K. Focke, "New measurements of compressional wave attenuation in deep ocean sediments," J. Acoust. Soc. Am. **67**, 1582–1589 (1980).
[27] G. Frisk, J. Doutt, and E. Hayes, "Bottom interaction of low-frequency acoustic signals at small grazing angles in the deep ocean," J. Acoust. Soc. Am. **69**, 84–94 (1981).
[28] D. C. Montgomery and E. A. Peck, *Introduction to Linear Regression Analysis*, 2nd ed. (Wiley, New York, 1992).

A suppressor to prevent direct wave-induced cavitation in shock wave therapy devices[a)]

Thomas J. Matula,[b)] Paul R. Hilmo, and Michael R. Bailey
Applied Physics Laboratory, University of Washington, 1013 NE 40th Street, Seattle, Washington 98115

(Received 20 October 2004; revised 6 April 2005; accepted 26 April 2005)

Cavitation plays a varied but important role in lithotripsy. Cavitation facilitates stone comminution, but can also form an acoustic barrier that may shield stones from subsequent shock waves. In addition, cavitation damages tissue. Spark-gap lithotripters generate cavitation with both a direct and a focused wave. The direct wave propagates as a spherically diverging wave, arriving at the focus ahead of the focused shock wave. It can be modeled with the same waveform (but lower amplitude) as the focused wave. We show with both simulations and experiments that bubbles are forced to grow in response to the direct wave, and that these bubbles can still be large when the focused shock wave arrives. A baffle or "suppressor" that blocks the propagation of the direct wave is shown to significantly reduce the direct wave pressure amplitude, as well as direct wave-induced bubble growth. These results are applicable to spark-gap lithotripters and extracorporeal shock wave therapy devices, where cavitation from the direct wave may interfere with treatment. A simple direct-wave suppressor might therefore be used to improve the therapeutic efficacy of these devices. © *2005 Acoustical Society of America.* [DOI: 10.1121/1.1937205]

PACS number(s): 43.35.Ei, 43.80.Vj, 43.25.Yw [RR] Pages: 178–185

I. INTRODUCTION

Shock wave lithotripsy (SWL) has been and remains the principal treatment for uncomplicated, upper urinary tract calculi.[1] Upward of 70% of symptomatic cases of upper urinary tract stones are treated by SWL, even at a time when alternative procedures such as ureteroscopy and percutaneous nephrostolithotomy are on the rise.[2] Some of the physical mechanisms associated with stone comminution include spallation,[3] squeezing,[4] superfocusing,[5] and dynamic fatigue.[6] Cavitation, in particular, has been shown to play a major role in SWL. Cavitation facilitates stone comminution,[7,8] but it has also been implicated as a mechanism for tissue injury.[9,10] We thus recognize the dual nature of cavitation as having both beneficial *and* detrimental bioeffects.

Cavitation plays three important roles: (1) Cavitation bubbles help erode the stone to a passable size by generating liquid jets or shock waves that hammer the stone,[11,12] causing pits along the surface and initiating cracks; (2) however, at high pulse repetition frequencies (PRFs), undissolved cavitation bubbles may actually shield the stone from subsequent shock waves;[13] (3) cavitation bubbles also appear to be a major factor in observed tissue damage.[14] These observations suggest that cavitation effects can be optimized for stone comminution, while minimizing tissue injury. The motivation for this work is to understand how the direct wave may create or enhance cavitation that we speculate could contribute to some of these effects.

In this paper, we consider the direct unfocused wave that propagates directly from the shock wave source to the focus ahead of the focused shock wave, and associated cavitation. This is relevant to specific shock wave devices that generate a direct wave, such as spark-gap (electrohydraulic) lithotripters and musculoskeletal therapy machines. The direct wave has received very little attention because its amplitude is much smaller than the focused shock wave. However, we find that the direct wave yields significant bubble growth, and thus deserves further study.

The paper is presented as follows: We begin with a discussion of the shape and the temporal location of the direct wave relative to the focused shock wave. Experimental evidence of the direct wave is shown, and bubble growth due to the direct wave is shown using a light scattering technique. We then show how a direct wave suppressor can eliminate the direct wave and associated bubble dynamics. We also discuss how a direct wave suppressor can be used to improve shock wave therapy.

II. THEORY

A spark-gap lithotripter such as the Dornier HM3 operates by discharging a high voltage between a pair of electrodes under water at the primary focus F1 of an ellipsoidal reflector. The discharge generates an outgoing spherically spreading shock wave, a portion of which is reflected to a secondary focus F2 (Fig. 1). At F2, the focused shock wave pressure amplitude can be 30 MPa or higher.[15] In addition to the focused shock wave, there exists a direct spherically expanding shock wave that passes directly from F1 to F2. The direct wave has a much smaller amplitude, but it can exceed 1 MPa.[16] This is not inconsequential; consider that single-bubble sonoluminescence—whereby a microsized bubble

[a)]Portions of this work were presented in "Influence of the direct wave on bubbles in electrohydraulic lithotripters: *In vitro* observations," *Proceedings of the International Symposium on Nonlinear Acoustics*, 16th ISNA, Moscow, Russia, August 2002.

[b)]Electronic mail: matula@apl.washington.edu

 0001-4966/2005/118(1)/178/8/$22.50

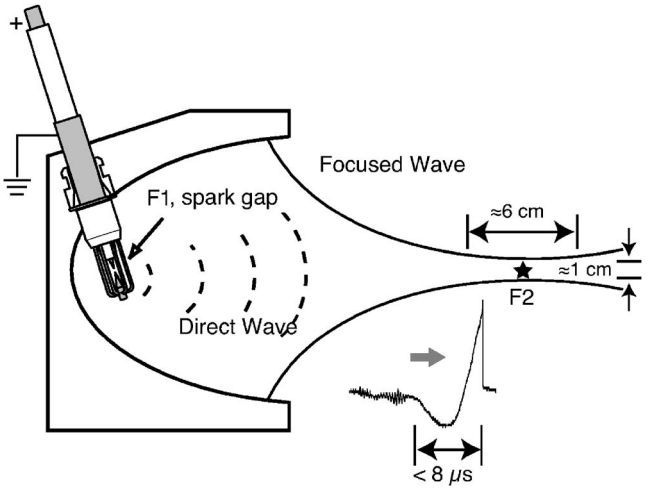

FIG. 1. Lithotripter illustration. A spark discharge at F1 generates an outgoing pressure pulse. The direct wave propagates directly from F1 to the focus F2. A portion of the direct wave is reflected to the focus, producing the focused wave. The focal zone of the focused wave is approximately 6 cm long by 1 cm diameter. The inset shows a spatial view of the shock wave generated by the lithotripter.

undergoes extremely violent collapses leading to the emission of electromagnetic radiation—only requires about 0.13 MPa.[17]

A. The pressure profiles

Models for the pressure–time profile of the direct and focused shock waves are well known. There is *a priori* justification for modeling the direct wave as an underwater explosion: a discontinuous jump in pressure, which then decays exponentially in time.[18] However, as the wave propagates outward, a tensile region (negative tail) develops. From hydrophone measurements of the direct wave, we will *a posterori* assume that at the focus the direct wave has a shape similar to that of the focused shock wave, with a reduced amplitude (evidence is provided later). We thus model both the direct and focused shock waves as[19]

$$P(t) = 2P_a e^{-\alpha t}\cos(\omega t + \pi/3), \tag{1}$$

where the peak pressure amplitude is P_a (whose amplitude depends on the particular shock wave, direct or focused), α describes the decay of the positive pressure, and $\omega = 2\pi f$ is a frequency that describes the extent of the negative tail. We neglect the finite rise time of the spike, and assume it occurs instantaneously. The finite rise time of the pulse is not important for our purposes of studying bubble growth, which is due to the negative portion of the pressure pulse.

In our models we use $\alpha = 3.5 \times 10^5$ for the decay constant of the positive pressure spike for both shock waves, and $f = 50$ kHz for defining the negative tail (again, equal for both shock waves). These values differ from the original parameters given in Ref. 19, because we believe that experimental measurements of the negative tail can be truncated prematurely when water separates from the hydrophone, leading to a less accurate measurement.[20] An example of the elongated shock wave generated by our electrohydraulic research lithotripter is shown in Fig. 2.[21] The arrival time relationship

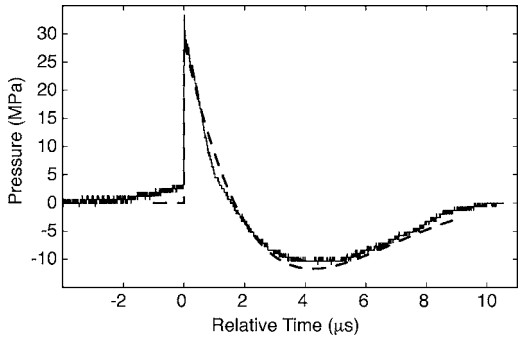

FIG. 2. HM-3-generated shock wave measured by PVDF membrane hydrophone (solid line), elongated based on published comparisons to fiberoptic hydrophone measurements (Ref. 20). A fit using Eq. (1) is shown as a dashed line. (See Ref. 22.)

between the direct and reflected focused shock wave at the focus F2 depends on the geometry of the ellipsoidal reflector. In the HM3, the direct wave precedes the focused shock wave by almost 30 μs. Figure 3 illustrates a simulation of the separation and amplitude relationship between the two shock waves at F2, assuming that the direct wave is ten times smaller in amplitude than the focused shock wave.

B. Bubble dynamics

With the arrangement of the direct and focused shock waves, we can now examine how a preexisting bubble will evolve. A common model used to investigate bubble dynamics in SWL is the Gilmore–Akulichev model, first implemented in SWL by Church,[19] although modified Rayleigh-Plesset models can also be used.[22] For our purposes of qualitative understanding, the accuracy of the model is not too important, but it is worth discussing these issues briefly. Bubble dynamics models accurately capture the growth and collapse of the bubble, but they predict unrealistic pressures at bubble collapse unless an accounting of the diffusion of gas and vapor into and out of the bubble is made. Even then they overestimate the measured pressures generated in collapse, and they fail to accurately capture the amplitude, period, or decay of the bubble's afterbounces.[22,23] Furthermore, the single-bubble model fails to correctly relate observed maximum bubble sizes to bubble collapse times, an effect indicative of the important role of multibubble interactions.[24]

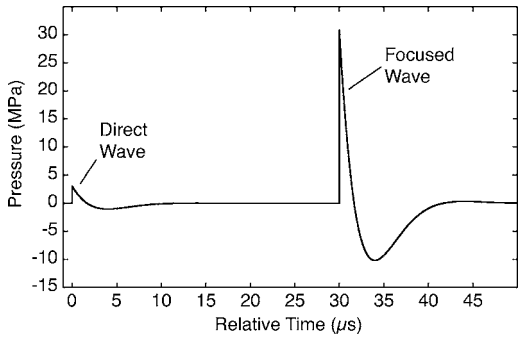

FIG. 3. Simulated direct wave and focused shock wave. The relative displacement between the two pulses depends on the geometry of the ellipsoidal reflector. In this plot, we assume that the direct wave amplitude is ten times smaller than the focused shock wave; its profile remains the same.

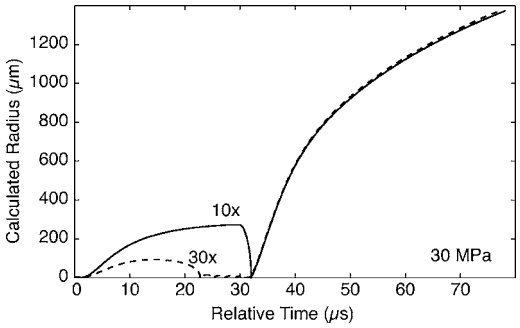

FIG. 4. Illustrative simulations of a bubble's response to a direct wave followed by a focused shock wave. The simulated peak pressure amplitude of the focused wave is 30 MPa. The solid line corresponds to a direct wave amplitude that is 10 times (labeled 10×) smaller than the focused shock wave, corresponding to 3 MPa, or 0.5 MPa peak negative pressure. The dashed line is for a direct wave amplitude that is 30 times (labeled 30×) smaller than the focused shock wave, corresponding to 1 MPa, or 0.15 MPa peak negative pressure.

In spite of these failings, and because detailed knowledge of bubble–bubble interactions is unknown (and difficult to model), we will rely on the single-bubble model to guide us in understanding how bubbles forced into a premature growth from the direct wave are affected when the focused shock wave arrives.

We solve the Gilmore equation[19] for an initial bubble radius of 5 μm and a peak positive pressure amplitude (for the focused wave) of 30 MPa. Parameters not given here can be found in the literature (we do not include gas diffusion in these calculations, but we acknowledge that this would be an important addition in a more thorough analysis). An example of how a bubble responds to the direct wave followed by the focused shock wave is illustrated in Fig. 4. Notice that the negative tail associated with the direct wave causes the preexisting bubble to grow, antecedent to bubble growth from the focused wave. The duration and extent of growth depends on the negative pressure amplitude of the direct wave, which in turn depends on the amplitude of the shock wave generated by the spark discharge. For a direct wave pressure amplitude of 1 MPa, where the bubble response is small, the bubble will grow and collapse prior to the arrival of the main focused wave (dashed line). We would then predict that the direct wave should be of little or no consequence. That is, memory of the direct wave will be lost.

However, at higher pressure amplitudes, antecedent bubble growth due to the direct wave continues even as the focused shock wave arrives (solid line). In this case, the growing bubble is forced into a premature collapse by the positive pressure spike of the focused wave. After the premature collapse, the bubble then grows again in response to the negative tail of the focused shock wave ($t > 32$ μs).

To reiterate, in the low-amplitude case (designated by 30× in the figure, because the direct-wave amplitude is 30 times smaller than the focused wave), the direct wave-induced bubble has collapsed back to its ambient size before the arrival of the focused shock wave. In the large-amplitude case (designated by 10× in the figure), the bubble is large when the focused shock wave arrives. The "critical" amplitude is approximately 1.5 MPa (20×). Direct-wave amplitudes greater than this will cause the antecedent bubble to interfere with the arrival of the focused shock wave, while amplitudes smaller than 1.5 MPa will result in antecedent bubble collapse prior to the arrival of the focused shock wave.

In Fig. 4, subsequent bubble growth ($t > 32$ μs) is nearly the same whether the bubble collapses before the focused wave arrives or as a result of it. This is because bubble growth due to the negative tail of the focused wave is nearly independent of bubble size,[19] as long as antecedent bubble growth is not too large. (The potential also exists that, but the model does not predict whether, bubble fission occurs in the premature breakup, which would increase cavitation nuclei seen by the focused wave.) Nevertheless, these results do suggest that the direct wave produces or enhances cavitation *before the focused shock wave arrives*. This antecedent cavitation field may interact with the focused wave in a number of ways. At lower-pressure amplitudes, where the direct wave amplitude is also lower, the antecedent field may simply serve to seed the region with additional cavitation nuclei. The direct wave would then act as a mechanism to enhance the total cavitation field.

At relatively high-pressure amplitudes however, the focused wave may be incident on much larger bubbles. If the number density is large, then the antecedent bubble field may present a highly shielded environment for a stone, inhibiting effective stone comminution.[25] In addition, the direct wave may initiate additional cavitation nuclei in the vasculature, increasing tissue injury. These issues are discussed later.

C. Light scattering

Measuring antecedent bubble growth is difficult because the bubbles are small, and their lifetimes short. Light scattering provides a means for visualizing these bubbles. Light scattering was originally used to size stationary bubbles in water[26,27] and to quantify radial instabilities in water. These techniques have now been refined to measure nonlinear pulsations of bubbles, including the highly nonlinear oscillations of sonoluminescing bubbles,[17,28] ultrasound contrast microbubbles,[29] and bubbles generated by lithotripters.[22]

In essence, the intensity I of scattered light depends strongly on the observation angle. Marston[26] recommended that for an air bubble in water, the observation angle should be near the critical angle $\theta_c \approx 82.8°$ from forward scattering. The recommendation was based on a physical-optics approximation, which predicts that the scattered light intensity is a monotonic function of bubble size, with a nearly R^2 dependence. The approximation apparently breaks down near a minimum size parameter of $kR=25$,[30] where k is the optical wave number ($\lambda = 2\pi/k = 632$ nm in our experiments) and R is the bubble radius. Thus, the approximation is valid for $R \gg 2.5$ μm. We will assume that the approximation is valid, and take $R \propto \sqrt{I - I_0}$, where I_0 is the background light intensity. In the experiments we use a lens to increase the scattered light intensity, so the collection angle spans the range approximately 75°–100°. This range is a compromise that provides a relatively good signal/noise ratio.

We are making two assumptions about light scattering:

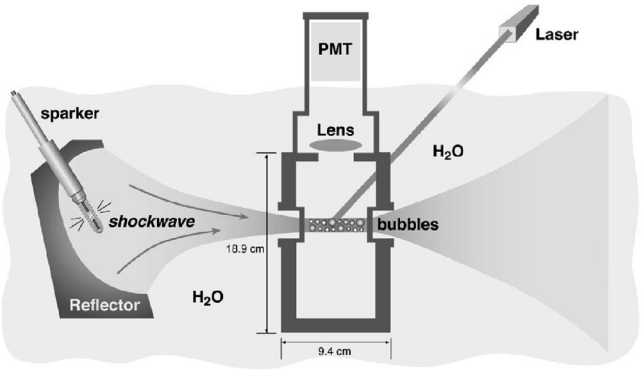

FIG. 5. Measurements are performed in a light-tight box so that the spark discharge does not saturate the photodetector (PMT). The box is made of TPX; approximately 95% of acoustic energy passes through the box. A small optically transparent opening in the side allows the 10 mW HeNe laser light to pass through. After passing through the lithotripter water tank and measurement box, the laser beam waist is estimated to be less than 5 mm diameter. Light scattered off the bubbles is focused by a lens, through a HeNe laser line filter, and onto the PMT.

First, that the bubble remains spherical, and second, the detected signal corresponds to a single bubble. This second assumption is most probably not valid because the device is operated at 2 Hz pulse repetition frequency (PRF), a setting where it is known that cavitation bubbles generated by one shock wave do not completely dissolve before the next shock wave arrives. It would therefore be difficult to quantify bubble dynamics associated with either the direct wave or the focused shock wave. Nevertheless, we can obtain *qualitative* information on bubble dynamics with light scattering. This is our main objective in this paper: To show that cavitation can be generated by the direct wave, and to call attention to some of the consequences associated with the interaction of these antecedent bubbles with the focused shock wave.

III. EXPERIMENTAL METHODS AND RESULTS

All experiments are performed in a research electrohydraulic shock wave lithotripter, modeled after the Dornier HM3. Detailed characterizations of this lithotripter can be found in the literature.[15,31] An example of the PVDF-measured focused waveform at the center of its 6-cm long by 1-cm diameter focus is shown in Fig. 2.

Bubble response experiments are carried out in a specially designed underwater chamber (Fig. 5). The detailed description can be found elsewhere.[22] The lithotripter is operated at 2-Hz PRF, which has been a common clinical rate and likely has the effect of creating unstabilized bubbles that fail to dissolve between focused shock waves. The sparker voltage was varied between 16–22 kV.

A. Hydrophone measurements

Hydrophone measurements of the direct and focused shock waves (in the free field, in the absence of a box) are shown in Fig. 6. The measurements are obtained with an uncalibrated (Sonic Industries, Hatboro, PA) PVDF membrane hydrophone. Because the shape of the direct wave looks like a smaller version of the focused shock wave, we

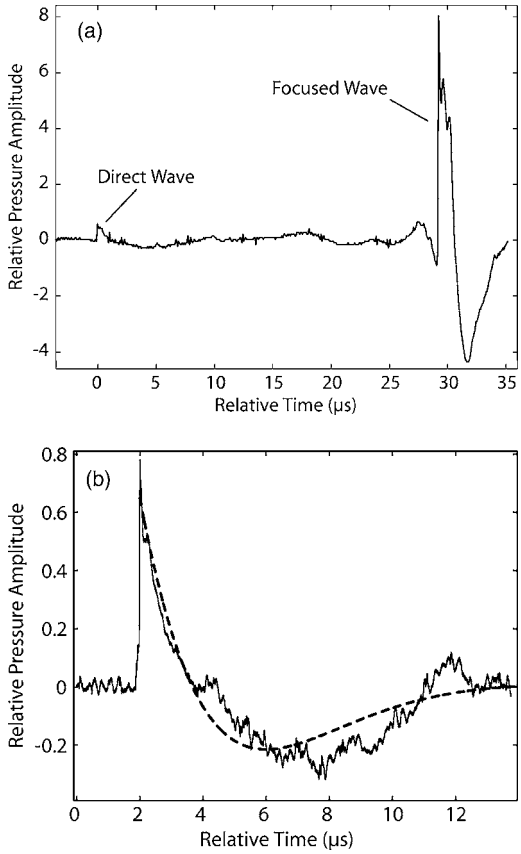

FIG. 6. (a) Uncalibrated hydrophone measurement of shock wave showing a direct wave and a focused shock wave. A series of five waveforms were averaged together to obtain this curve. The oscillations that follow the peak of the focused wave is a hydrophone artifact. (b) A series of ten measurements of the direct wave were averaged together to improve the S/N. The dashed line is a fit to Eq. (1).

model it using Eq. (1) [Fig. 6(b)]. Although the pressure amplitude (both peak positive and peak negative) is much smaller than the focused shock wave, the negative pressure is not inconsequential—bubbles subjected to the direct wave should undergo significant growth before the focused shock wave arrives. As an example, the peak positive amplitude of the direct wave in Fig. 6 appears to be about 15 times smaller than the focused wave. If we assume the peak positive and negative amplitudes of the focused wave are 30 MPa and 11 MPa, respectively (measured at 18 kV[15]), then the peak positive and negative amplitudes of the direct wave would be about 2 MPa and 0.73 MPa, respectively.

B. Light scattering measurements

Light scattered from the bubbles is focused onto a photomultiplier tube (PMT; Thorn EMI 9956KB, 12 ns response) using a 5 cm diameter biconvex lens mounted near the top of the enclosure (see Fig. 5). The output of the PMT (−900 V supply) is terminated directly into the 50 Ω impedance of an oscilloscope (Lecroy LC334 AL, 500 MHz). Further details can be found in the literature.[32]

1. Bubble response to the direct wave

The first indication that the direct wave causes antecedent expansion of preexisting bubbles can actually be found in

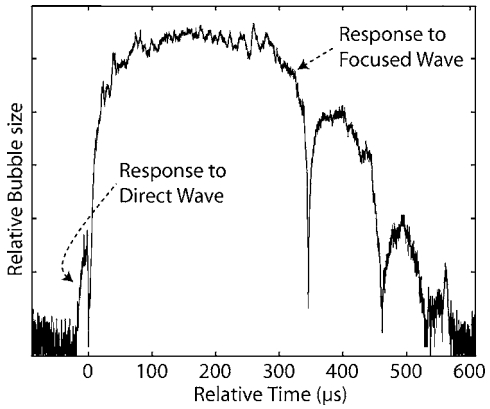

FIG. 7. Light scattering signal corresponding to a bubble's response to a single lithotripter shock wave. Experimental details for generating single bubble-response curves are given in the literature Ref. 22. The precursor (labeled here as "Response to Direct Wave") to the main growth and collapse sequence (labeled "Response to Focused Wave") can also be seen in Refs. 22 and 25.

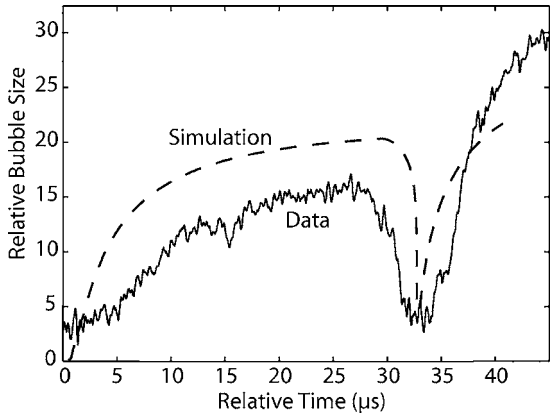

FIG. 9. A comparison of light-scattering data (solid line) and the simulation of bubble response to the direct wave (dashed line). Note the similarities in the asymmetry of the curves. These results suggest that antecedent bubble growth is prematurely terminated when the focused shock wave arrives.

light-scattering data from Figs. 6 and 7 of Ref. 22, or from Fig. 3 of Ref. 25. These figures show a precursor to the main growth and collapse sequence of a bubble. We show in Fig. 7 of this paper an illustrative example of a precursor associated with the direct wave. We understand now that this precursor signal is a bubble's response to the arrival of the direct wave. Further evidence was obtained with an additional set of experiments shown in Fig. 8: Increasing the applied voltage to the sparker unit increases the direct and focused wave amplitudes and correspondingly increases the amplitude of the precursor signals. The main "bubble growth" phase occurs when one or more preexisting bubbles are subjected to the large negative tensile pressure from the focused shock wave.[22] The higher the voltage (and therefore focused wave amplitude), the larger and more rapid the bubble growth. Ahead of this growth phase is the precursor, whose amplitude also depends on the discharge voltage. The precursor occurs at a time when the expected direct wave should arrive and corresponds to bubble growth resulting from the direct wave.

In Fig. 9 we compare an experimental direct wave-induced bubble response with a corresponding simulation of the bubble response to the direct wave. There is good qualitative agreement in the asymmetry of the curves. The asymmetry suggests that the bubble collapses prematurely, in response to the arrival of the focused shock wave. This supports the notion that the direct wave creates an antecedent cavitation field that grows ahead of the focused shock wave's arrival, and that the field can be made to collapse prematurely when the focused shock wave arrives.

Later we will discuss how the direct wave and associated antecedent cavitation cloud may have implications for effective shock wave therapy. First, we describe how to suppress the direct wave and associated antecedent bubble cloud.

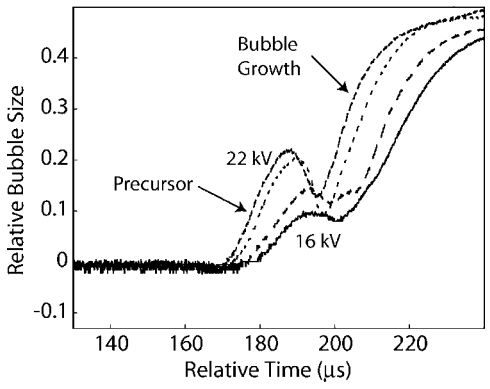

FIG. 8. Light scattering signal showing precursor signals at various spark-discharge voltages. The amplitude of the precursor signal (antecedent bubble growth) increases with discharge voltage.

2. Direct wave suppression

We have investigated two direct wave suppressor designs, an irregularly shaped "suppressor disk" and a press-fit "suppressor clip." Our original design utilized a 3.8 cm diameter disk with an irregularly shaped edge (metal, plastic, or rubber) placed a few cm (adjustable) from the spark source [see Fig. 10(a)]. The major reason for making the disk irregular is that it reduces the coherence of the diffracted wave, resulting in reduced pressure.[33] However, to an observer very far from the disk, the irregularities will disappear, making the disk appear circular. Because of this, and because of the desire to make such a disk reasonably simple for manufacturers and suppliers, we have tested a suppressor clip that can be press-fitted, or clipped onto the cage of the electrode, an example of which is shown in Fig. 10(b). An added advantage of the suppressor clip is that the focused shock wave does not appear to be affected. The following data is associated with using the suppressor clip.

An example of how the suppressor clip decreases the direct wave amplitude is shown in Fig. 11(a). A potential source of error was in aligning the clip so that complete blockage of the direct wave would occur. Alignment is accomplished by rotating the sparker until the clip is directly in line between F1 and F2. A marketable realization of the suppressor clip would necessitate an alignment notch so that the

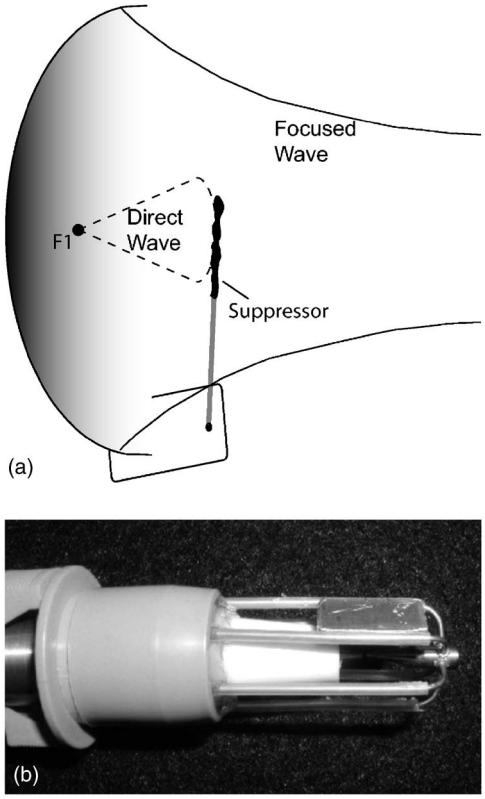

FIG. 10. (a) Original version of the disk suppressor. An irregularly shaped disk is mounted near the sparker unit. (b) A new version of the suppressor incorporates a small rectangular aluminum disk with a groove cut into the sides so that the disk can be press fitted into the cage of the sparker unit. This design is more convenient, but not necessarily optimized.

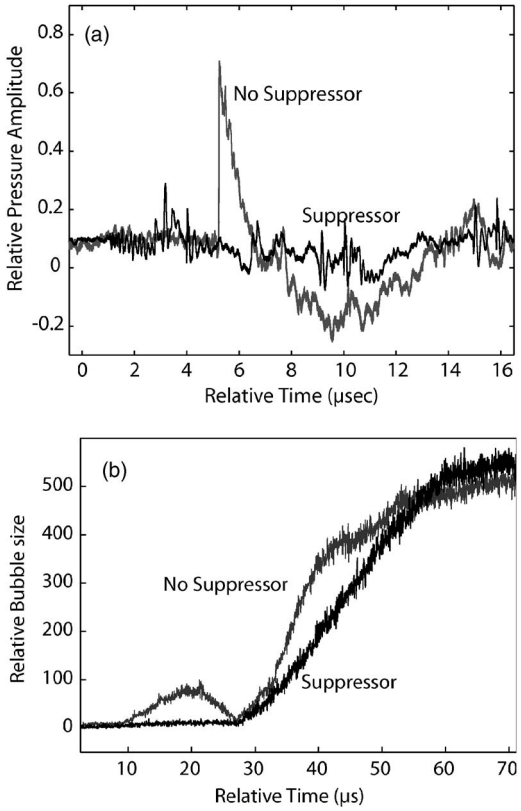

FIG. 11. Comparisons of (a) direct wave pressure pulse and (b) direct wave-induced bubble dynamics with, or without a disk suppressor placed in front of the spark discharge source. When the suppressor is inserted, the direct wave is significantly reduced, and bubble dynamics due to the direct wave is not observed (the difference in the slope between the two bubble growths may be due to multiple-bubble effects).

clip is always aligned correctly. Note that with the clip in place, there is no noticeable change of the focused shock wave.

The measure of effectiveness for a suppressor is to reduce or eliminate antecedent bubble growth; that is, with a significantly reduced direct wave, preexisting bubbles should not respond to the same degree as without a suppressor. Figure 11(b) shows an example of how antecedent bubble growth can be significantly reduced when the suppressor is installed.

3. Discussion

Measurements of the direct wave (and suppressor effects) are presented for free-field conditions; however, the relevancy is for generating an antecedent cavitation cloud in the vicinity of a kidney stone (or within the vasculature) before the focused shock wave arrives. If the PRF is sufficiently high, this cloud could shield a stone from the focused shock wave, or act as additional cavitation nuclei. Such nuclei in the vasculature could lead to tissue injury.

In addition to providing shielding that reduces stone comminution effectiveness, or adding nuclei in the vasculature, the antecedent cavitation field can also interact strongly with the positive pressure spike associated with the focused shock wave. The positive pressure spike forces preexisting bubbles to collapse, and this initial cavitation collapse has been shown to be by some measures more energetic than the ensuing inertial collapse that follows bubble growth; e.g., the resulting sonoluminescence emission can be much greater than during the latter inertial collapse.[32] Bubble compression, or collapse, associated with this oft-ignored pressure spike may have important consequences to stone comminution and/or tissue injury, and direct wave-induced cavitation may significantly influence these effects. In future studies, we plan to use high-speed optical imaging to study antecedent bubble growth in the free field, and on model kidney stones. Such studies will help quantify cavitation generated by the direct wave.

A direct-wave suppressor will limit cavitation activity, and thus potentially enhance stone comminution and reduce tissue injury. Our investigation of a suppressor is only preliminary, and a couple of comments regarding the clip (also relevant to a suppressor disk) are worth noting.

First, the thickness of the clip should be considered. We have tested two aluminum samples, 3.175 mm thick, and 9.5 mm thick. Both were 9.65 mm wide (to accommodate the separation between supporting cage bars). No difference in suppressor ability was observed. Second, the size of the clip should be considered relative to the wavelength of the negative tail (about 3 cm; $f=50$ kHz). The wavelength is larger than the width of the clip, suggesting that the clip should not strongly block the negative tail. However, waveform measurements are made at the focus. Near the source, the waveform is probably much different (recall that the explosion is typically modeled as a discontinuous pressure

jump that decreases exponentially in time). It may be that the clip interferes with the expanding pressure pulse and inhibits the formation of a nicely shaped wave form. Such an analysis is beyond the scope of this paper. Thus, there will be some compromise between the size and shape of a suppressor, and the resulting amplitude of the direct wave, while having a minimal effect on the focused wave.

As a final comment, in this paper we consider the direct wave associated with a spark-gap shock wave therapy device, specifically, a lithotripter. Spark-gap devices are also in use for musculoskeletal therapy, including plantar fasciitis (heel pain), lateral epicondylitis (tennis elbow), shoulder tendonitis, and nonunion fractures. These devices are physically smaller than typical lithotripters and so the separation in time between the arrival of the direct wave and the focused shock wave will be shorter. Because of the smaller separation and the fact that orthopedic machines often operate at higher voltages (measured peak amplitudes of 50 MPa[34]) and PRFs (up to 4 Hz) than lithotripters, antecedent bubble growth associated with the direct wave may have more of an influence on the focused shock wave. Furthermore, we have recently observed, for the first time, cavitation during the treatment of plantar fasciitis.[34] Thus, this research is also applicable to such devices.

IV. CONCLUSIONS

Some shock wave therapy devices (e.g. spark-gap devices) generate a direct (unfocused) wave. Although the positive and negative pressure amplitude is much smaller than the focused shock wave, the direct wave can force a preexisting bubble cloud into growth, ahead of the arrival of the focused shock wave. This represents a new mechanism that can affect the efficacy of shock wave therapy devices, and presents a new opportunity for controlling the cavitation field. There is strong evidence that cavitation evolves over the course of treatment, implying that the direct wave can enhance stone shielding and tissue injury, especially toward the end of lithotripsy treatment. Reducing the direct wave amplitude effectively eliminates cavitation due to the direct wave. Further research is necessary in order to quantify the degree to which premature direct-wave cavitation affects stone comminution and/or tissue injury, and to what extent musculoskeletal therapy is affected by the direct wave.

ACKNOWLEDGMENTS

We wish to thank S. Kargl at APL and members of the Center for Shock Waves in Medicine (CSWM) for many helpful discussions. This research is funded by NIH Grants No. DK43881 and No. DK55674.

[1]D. Gravenstein, "Extracorporeal shock wave lithotripsy and percutaneous nephrolithotomy," Anesthesiol. Clin. North America **18**, 953–971 (2000).
[2]K. Kerbl, J. Rehman, J. Landman, D. Lee, C. Sundaram, and R. V. Clayman, "Current management of urolithiasis: Progress or regress?," J. Endourol **16**, 281–288 (2002).
[3]C. Chaussy, W. Brendel, and E. Schmiedt, "Extracorporeally induced destruction of kidney stones by shock waves," Lancet **2**, 1265–1268 (1980).
[4]W. Eisenmenger, "The mechanisms of stone fragmentation in ESWL," Ultrasound Med. Biol. **27**, 683–693 (2001).
[5]D. Howard and B. Sturtevant, "In vitro study of the mechanical effects of shockwave lithotripsy," Ultrasound Med. Biol. **23**, 1107–1122 (1997).
[6]B. Sturtevant, in *Smith's Textbook of Endourology*, edited by A. D. Smith, G. H. Badlani, D. H. Bagley, R. V. Clayman, G. H. Jordan, L. R. Kavoussi, J. E. Lingeman, G. M. Preminger, and J. W. Segura (Quality Medical Publishing, Inc., St. Louis, 1996), pp. 529–552.
[7]S. Zhu, F. H. Cocks, G. M. Preminger, and P. Zhong, "The role of stress waves and cavitation in stone comminution in shock wave lithotripsy," Ultrasound Med. Biol. **28**, 661–671 (2002).
[8]M. Delius, F. Ueberle, and W. Eisenmenger, "Extracorporeal shock waves act by shock wave–gas bubble interaction," Ultrasound Med. Biol. **24**, 1055–1059 (1998).
[9]P. Zhong, I. Cioanta, S. L. Zhu, F. H. Cocks, and G. M. Preminger, "Effects of tissue constraint on shock wave-induced bubble expansion in vivo," J. Acoust. Soc. Am. **104**, 3126–3129 (1998).
[10]A. P. Evan, L. R. Willis, B. A. Connors, Y. Shao, J. E. Lingeman, J. J. C. Williams, J. A. McAteer, N. S. Fineberg, M. R. Bailey, and L. A. Crum, "Kidney damage and renal functional changes are minimized by waveform control that suppresses cavitation in SWL," J. Urol. (Baltimore) **168**, 1556–1562 (2002).
[11]J. E. Field, "The physics of liquid impact, shock wave interactions with cavities, and the implications to shock wave lithotripsy," Phys. Med. Biol. **36**, 1475–1484 (1991).
[12]P. Zhong, C. J. Chuong, and G. M. Preminger, "Propagation of shock waves in elastic solids caused by cavitation microjet impact II: Application in extracorporeal shock wave lithotripsy," J. Acoust. Soc. Am. **94**, 29–36 (1993).
[13]R. F. Paterson, D. A. Lifshitz, J. E. Lingeman, J. C. Williams, D. L. Rietjens, A. P. Evan, B. A. Connors, M. R. Bailey, L. A. Crum, R. O. Cleveland, Y. A. Pishchalnikov, I. V. Pishchalnikova, and J. A. McAteer, "Slowing the pulse repetition frequency in shock wave lithotripsy (SWL) improves stone fragmentation in vivo," *Proceedings of the 17th International Congress on Acoustics*, 2001.
[14]D. Dalecki, C. H. Raeman, S. Z. Child, D. P. Penney, R. Mayer, and E. L. Carstensen, "The influence of contrast agents on hemorrhage produced by lithotripter fields," Ultrasound Med. Biol. **23**, 1435–1439 (1997).
[15]R. O. Cleveland, M. R. Bailey, N. Fineberg, B. Hartenbaum, M. Lokhandwalla, J. A. McAteer, and B. Sturtevant, "Design and characterization of a research electrohydraulic lithotripter patterned after the Dornier HM3," Rev. Sci. Instrum. **71**, 2514–2525 (2000).
[16]A. J. Coleman, J. E. Saunders, R. C. Preston, and D. R. Bacon, "Pressure waveforms generated by a Dornier extra-corporeal shock-wave lithotripter," Ultrasound Med. Biol. **13**, 651–657 (1987).
[17]T. J. Matula, "*Inertial cavitation and single-bubble sonoluminescence*," in Philos. Trans. R. Soc. London, Ser. A, edited by J. R. Blake (The Royal Society, London, 1999) **357**, pp. 225–249.
[18]D. S. Campbell, H. G. Flynn, D. T. Blackstock, C. Linke, and E. L. Carstensen, "The acoustic fields of the Wolf electrohydraulic lithotripter," J. Lithotripsy and Stone Disease **3**, 147–156 (1991).
[19]C. C. Church, "A theoretical study of cavitation generated by an extracorporeal shock wave lithotripter," J. Acoust. Soc. Am. **86**, 215–227 (1989).
[20]J. Staudenraus and W. Eisenmenger, "Fibre-optic probe hydrophone for ultrasonic and shock-wave measurements in water," Ultrasonics **31**, 267–273 (1993).
[21]M. R. Bailey, Ph.D. thesis, University of Texas, Austin, 1997.
[22]T. J. Matula, P. R. Hilmo, B. D. Storey, and A. J. Szeri, "Radial response of individual bubbles subjected to shock wave lithotripsy pulses in vitro," Phys. Fluids **104**, 913–921 (2002).
[23]R. O. Cleveland, O. A. Sapozhnikov, M. R. Bailey, and L. A. Crum, "A dual passive cavitation detector for localized detection of lithotripsy-induced cavitation in vitro," J. Acoust. Soc. Am. **107**, 1745–1758 (2000).
[24]M. Tanguay and T. Colonius, "Progress in modeling and simulation of shock wave lithotripsy (SWL)," *5th International Symposium on Cavitation*, 2003.
[25]T. J. Matula, P. R. Hilmo, and M. R. Bailey, "*Influence of the direct wave on bubbles in electrohydraulic lithotripters*," International Symposium on Nonlinear Acoustics **1**, 387–390 (2002).
[26]D. S. Langley and P. L. Marston, "Critical-angle scattering of laser light from bubbles in water: measurements, models, and application to sizing of bubbles," Appl. Opt. **23**, 1044–1054 (1984).
[27]G. M. Hansen, "Mie scattering as a technique for the sizing of air bubbles," Appl. Opt. **24**, 3214–3220 (1985).
[28]B. P. Barber and S. J. Putterman, "Light scattering measurements of the repetitive supersonic implosion of a sonoluminescing bubble," Phys. Rev. Lett. **69**, 3839–3842 (1992).

[29]J. Guan and T. J. Matula, "Using light scattering to measure the response of individual ultrasound contrast microbubbles subjected to pulsed ultrasound in vitro," J. Acoust. Soc. Am. **116**, 2832–2842 (2004).
[30]D. L. Kingsbury and P. L. Marston, "Mie scattering near the critical angle of bubbles in water," J. Opt. Soc. Am. **71**, 358–361 (1981).
[31]M. R. Bailey, D. T. Blackstock, R. O. Cleveland, and L. A. Crum, "Comparison of electrohydraulic lithotripters with rigid and pressure-release ellipsoidal reflectors. II. Cavitation fields," J. Acoust. Soc. Am. **106**, 1149–1160 (1999).
[32]T. J. Matula, P. R. Hilmo, M. R. Bailey, and L. A. Crum, "In vitro sonoluminescence and sonochemistry studies with an electrohydraulic shockwave lithotripter," Ultrasound Med. Biol. **28**, 1199–1207 (2002).
[33]P. Menounou, M. R. Bailey, and D. T. Blackstock, "Edge wave on axis behind an aperture or disk having a ragged edge," J. Acoust. Soc. Am. **107**, 103–111 (2000).
[34]T. J. Matula, unpublished data.

On the meaning of Lamb mode nonpropagating branches

F. Simonetti and M. J. S. Lowe
Department of Mechanical Engineering, Imperial College, London SW7 2AZ, United Kingdom

(Received 31 January 2005; revised 29 April 2005; accepted 2 May 2005)

The modes of vibration of an elastic plate are usually divided into propagating and nonpropagating kinds. While nonpropagating modes characterize local vibration nearby a perturbation source, which can be either an external force or a geometrical discontinuity, propagating modes carry energy along the waveguide and account for the vibration far away from the perturbation source. In this paper, by considering that the modes of an absorbing plate are always propagating, it is shown that each elastic mode consists of propagating and nonpropagating branches, which turn into a single propagating mode as soon as internal absorption is considered. Moreover, it is shown how introducing a little material damping leads to a rigorous differentiation of elastic modes when they are connected. A similar result can be obtained by loading the plate with a light fluid [Rokhlin *et al.*, J. Acoust. Soc. Am. **85**, 1074–1080 (1989)]. © *2005 Acoustical Society of America.* [DOI: 10.1121/1.1938528]

PACS number(s): 43.35.Mr, 43.35.Zc [YHB] Pages: 186–192

I. INTRODUCTION

The propagation of stress waves in plates has been extensively studied since Rayleigh and Lamb established the secular equation for the free vibrations of infinite elastic plates in 1889. The study of the dispersion characteristics of propagating modes was initiated by Lamb who first investigated the lowest symmetric and antisymmetric modes. In the following half a century, researchers had focused their efforts on the characterization of the higher order propagating modes by analyzing the dispersion of the real roots (wave numbers) of the Rayleigh–Lamb equation, see Fay.[1] Only in 1955 Lyon[2] calculated the purely imaginary roots of the secular equation which correspond to modes of infinite wavelength starting at the cutoff frequencies of the Lamb modes. Remarkable is the work done by Mindlin who established the existence of modes at the cutoff frequencies whose amplitudes vary linearly with the propagation distance[3] and also demonstrated the presence of complex roots of the Rayleigh–Lamb equation, Mindlin.[4,5] A rather complete picture of the topology of real, imaginary, and complex wave number dispersion is provided by Mindlin.[6]

Modes associated with nonreal wave numbers appear to be substantially different from those corresponding to real wave numbers as they do not carry energy[7] and are exponentially damped with distance (therefore they are generally referred to as nonpropagating modes). As a consequence, there is ground for a sharp separation between propagating and nonpropagating modes on the basis of a strong physical argument such as the energy propagation. However, this separation may lead to a misleading interpretation of the nature of these two families of modes which are representative of the same physical phenomenon, i.e., plate vibrations. This common nature is suggested by the fact that nonpropagating modes, at each frequency, provide the infinity of eigenmodes which, jointly with the finite number of propagating modes, results in a complete set of orthogonal eigenmodes.[8] This, for instance, allows the response of the plate to an arbitrary body force to be studied by expanding the force in terms of the infinite number of plate eigenmodes, both propagating and nonpropagating, according to the modal analysis theory.[9,10]

The aim of this paper is to clarify and enforce the link between propagating and nonpropagating modes by abandoning the hypothesis of elasticity and introducing internal damping mechanisms. It is already known that the topology of the modes of lossless plates or cylindrical shells loaded with fluid provides insight into the relationship between propagating and nonpropagating branches of the free waveguide.[11] However, when considering waveguides with complicated cross sections, adding material absorption can lead to a simpler interpretation of the mode topology since fluid loading introduces modes which do not belong to the free waveguide (see for instance the appearance of the Scholte-Stoneley mode in fluid loaded plates[12]) and anomalous behavior of certain modes as in the case of the fundamental antisymmetric mode of a fluid loaded plate.[13]

In Sec. II the Rayleigh–Lamb equation for absorbing plates is briefly presented. By observing that the modes of an absorbing plate are always propagating,[14] Sec. IV demonstrates that as the material damping vanishes, the propagating modes of the attenuative plate, which are studied in Sec. III, break down into propagating and nonpropagating branches. Therefore, a nonpropagating mode should be regarded as part of a mode which also has propagating branches, rather than a mode itself. Moreover, Sec. V shows that the phase velocity dispersion curves of an attenuative waveguide contain branches which, on one hand do not belong to the propagating modes of the so-called elastic waveguide but on the other hand, can be ascribed to the so-called nonpropagating modes of the elastic waveguide.

II. DISPERSION EQUATION

Viscoelasticity is an effective model for introducing material damping, being able to represent the hysteretic nature of several attenuative materials. This subject has attracted considerable attention over the past century and a comprehensive treatise is provided by Christensen.[15] In this paper,

 0001-4966/2005/118(1)/186/7/$22.50

TABLE I. Material parameters used for the free plate.

	c_S (m/ms)	c_L (m/ms)	k_S (np/wl)	k_L (np/wl)	ρ (kg/m^3)
Lossless plate	3.26	5.96	0.1	0.1	7932

the material damping is modelled according to the theory of linear viscoelasticity which leads to linear equations of motion and is representative of several materials as verified experimentally in a recent paper.[16]

Let us consider a homogeneous, isotropic viscoelastic plate of thickness $2b$ and infinite extent. The motion is independent of the $\hat{x}_2$ direction and takes place in two directions, $\hat{x}_1$, $\hat{x}_3$, the origin being taken in the middle surface of the plate. The traction-free condition holds over the planes $x_3 = \pm b$. The Fourier transformed displacement field, $\mathbf{u}$, can be written as

$$\mathbf{u} = \mathbf{h}(x_3)e^{i\xi x_1}, \tag{1}$$

where $\mathbf{h}(x_3)$ is the mode shape and ξ is the wave number which satisfies the Rayleigh–Lamb equation

$$\frac{\tan \beta b}{\tan \alpha b} + \left[\frac{4\xi^2\alpha\beta}{(\xi^2-\beta^2)^2}\right]^{\pm 1} = 0, \tag{2}$$

where the plus and minus signs refer to symmetric and antisymmetric modes, respectively. The quantities α and β can be related to the angular frequency ω, and the complex sound velocities a_L and a_S

$$\alpha^2 = \frac{\omega^2}{\alpha_L^2} - \xi^2, \tag{3}$$

$$\beta^2 = \frac{\omega^2}{a_S^2} - \xi^2, \tag{4}$$

the subscripts L and S refer to longitudinal and shear, respectively. The complex sound velocities can be obtained from the rheological properties of the material[17]

$$a_{L,S} = \frac{c_{L,S}}{1 + i\dfrac{k_{L,S}}{2\pi}}, \tag{5}$$

where $c_{L,S}$ are the material bulk velocities and $k_{L,S}$ are the bulk attenuations in Nepers per wavelength (np/wl).

III. DISPERSION LOCI

Here, a simple rheological model based on the hypothesis that the bulk velocities do not vary with frequency and that the bulk attenuations vary linearly with frequency is assumed. Moreover, the numerical solution to Eq. (2) is obtained by using the software Disperse.[17,18]

It has already been shown that for a waveguide made of a linear viscoelastic plate rigidly bonded to an elastic plate the decay of the average energy flow can be related to the average dissipated power according to[14,19]

$$\Delta P + p_d = 0, \tag{6}$$

where, P is the average energy flow through a cross section of the waveguide over a period, Δ refers to the difference calculated between two consecutive cross sections of the waveguide, and p_d is the dissipated power within the volume comprised between the two cross sections. This implies that if there were nonpropagating modes ($P=0$) the dissipated power would vanish which is physically impossible. As a consequence, it can be concluded that nonpropagating modes do not exist in absorbing waveguides. Moreover, the frequencies where the guided mode wavelength is infinite do not correspond to mode cutoff since, at these frequencies, ξ is purely imaginary and α and β have nonzero imaginary component (while for a nonpropagating mode α and β are always real).

A few symmetric modes of the plate whose properties are summarized in Table I are shown in Fig. 1(a), the frequency and wave number being normalized according to

$$\Omega = \frac{2b\omega}{c_S\pi}, \tag{7}$$

$$\bar{\xi} = \frac{2b\xi}{\pi}. \tag{8}$$

Note that the mode labels in Fig. 1 have negative subscript if the energy flux is opposite to the wave number vector according to the notation proposed by Auld,[7] this being discussed later in this section. Figure 1(b) shows the dispersion curves for the propagating modes of an elastic plate with the same bulk velocities as the attenuative plate but zero bulk

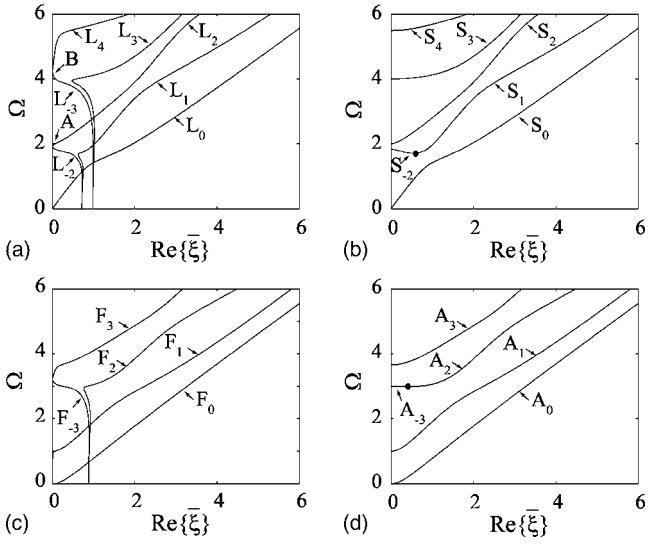

FIG. 1. Real wave number dispersion curves; (a) attenuative symmetric modes; (b) elastic symmetric modes; (c) attenuative antisymmetric modes; (d) elastic antisymmetric modes.

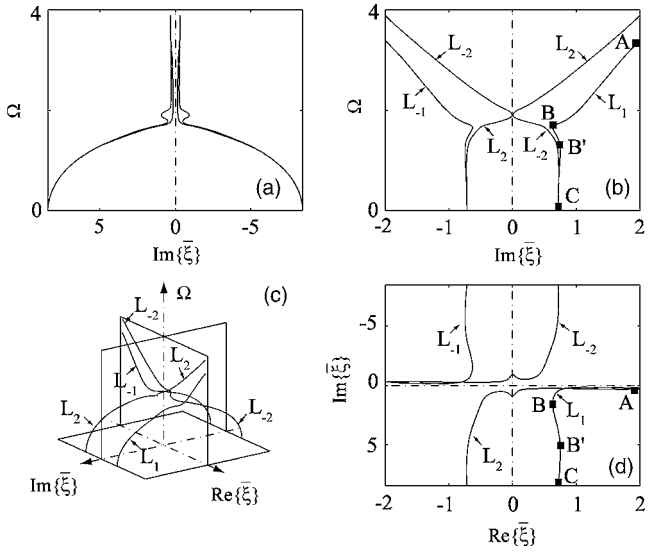

FIG. 2. Three-dimensional dispersion curves for the lossy plate (c) and projections over the planes: (a) $\mathrm{Re}\{\bar{\xi}\}=0$; (b) $\mathrm{Re}\{\bar{\xi}\}=0$; (d) $\Omega=0$.

attenuations. Note that the separation between the S_1 mode and the backward mode S_2, which appear to be connected (black dot), is due to the change in energy velocity sign as was originally explained by Mindlin,[6] and discussed by many other authors[7,11,20] more recently. It can be observed that the two sets of dispersion curves shown in Figs. 1(a) and 1(b) are very similar except for the zones labelled A and B where the spectrum of the attenuative plate exhibits some extra branches. Moreover, some modes appear to join each other at infinite wavelength (see, for instance, L_2 and L_{-2}). The same considerations hold for the antisymmetric modes which are shown in Figs. 1(c) and 1(d) for the attenuative and elastic plate, respectively. For this reason, in the following, only symmetric modes are considered.

The understanding of the topology of the dispersion curves can only be gained by considering the dispersion of both the real and imaginary parts of the wave number. This leads to a three-dimensional representation of the dispersion loci in the space $(\mathrm{Im}\{\bar{\xi}\},\mathrm{Re}\{\bar{\xi}\},\Omega)$ as originally proposed by Mindlin. Figure 2(c) shows such a representation for the modes L_1, L_2, and L_{-2}. Figures 2(a)–2(d) are the projections of the mode trajectories over the planes $\mathrm{Re}\{\bar{\xi}\}=0$, $\mathrm{Im}\{\bar{\xi}\}=0$, and $\Omega=0$, respectively. As was previously observed, the imaginary part of the wave number is always non-null [see Fig. 2(d)].

Consider the trajectory of the L_1 mode. For large values of the frequency [branch AB Fig. 2(d)], $\mathrm{Re}\{\bar{\xi}\}$ is dominant with respect to $\mathrm{Im}\{\bar{\xi}\}$. However, as the frequency decreases, $\mathrm{Im}\{\bar{\xi}\}$ becomes significant (branch B′C). The topological characteristics of the L_1 mode are the same as those of the mode labelled S_1 in Ref. 12 for a plate loaded with a light fluid. Interesting is the slope of the function $\Omega(\mathrm{Re}\{\bar{\xi}\})$ which is negative along the branch BB′ at whose edges the derivative $d\Omega/d\,\mathrm{Re}\{\bar{\xi}\}$ is singular [Fig. 2(b)]. As a consequence, a question arises: is this derivative representative of the group velocity? It can be observed that the original conception of group velocity, introduced by Rayleigh,[21] is to predict the speed of a wave packet whose harmonic components travel at different speeds. Such a velocity for a conservative system can be related to the wave number, k, according to

$$V_{\mathrm{gr}}=\frac{d\omega}{dk}. \tag{9}$$

Note that the wave number is real since the system is conservative. A natural, but not necessarily correct, way of defining the group velocity for propagation in lossy media, is to consider the real part of the wave number, i.e.,

$$V_{\mathrm{gr}}=\frac{d\omega}{d\,\mathrm{Re}\{k\}}. \tag{10}$$

Such a definition, for the attenuative plate, would lead to both negative (branch BB′) and supersonic (higher than the material longitudinal velocity) group velocities around the point B and B′ of the L_1 mode. Studies on the propagation of electromagnetic waves have shown that the definition (10) leads to "abnormal" velocities when the material absorption is taken into account, as in any medium there would be frequencies where the group velocity is superluminal, infinite or negative.[22] The debate on whether these abnormal cases are unphysical[23–25] or not[26,27] is still open. In the acoustic field, there has been little work on this subject and at the time of writing there are no theoretical evidences which suggest a correct and sensible definition of the velocity of a wave packet. However, a possibility is to consider the velocity of energy transport which is defined as the ratio of energy flow to mechanical energy density. While for a conservative system, group velocity and velocity of energy transport are coincident,[28] when material absorption is taken into account, the two velocities differ. In particular, Bernard et al.[29] showed experimentally for the L_3 mode that where a group velocity singularity occurs the velocity of the wave packet tends to the velocity of energy transport rather than the group velocity.

Moreover, the sign of the velocity of energy transport characterizes the modes since for each of them it remains unchanged.[11,20] This can be proved by observing that the propagation direction of a mode has to be constant along the path of the mode [note that here "the path of the mode" refers to the continuous locus of points solutions to Eq. (2) in the space $(\mathrm{Im}\{\bar{\xi}\},\mathrm{Re}\{\bar{\xi}\},\Omega)$]. If there was a propagation direction inversion, then either a frequency where the energy flow is zero or discontinuous would exist. However, a zero energy flow frequency is not possible as a mode is always propagating. On the other hand, a discontinuous change in the energy flow would imply that at the frequency where the discontinuity occurs, the mode propagates in both directions $(\pm\hat{x}_1)$ with the same wave number. This is not possible as it would require the existence of two different mode shapes, $\mathbf{h}(x_3)$, for the same mode at the same frequency [see Eq. (1)]. As a result, for one mode, it can be concluded that the sign of the velocity of energy transport has to be constant for all frequencies.

It has to be emphasized that at a given frequency the same perturbation can propagate in the positive or negative

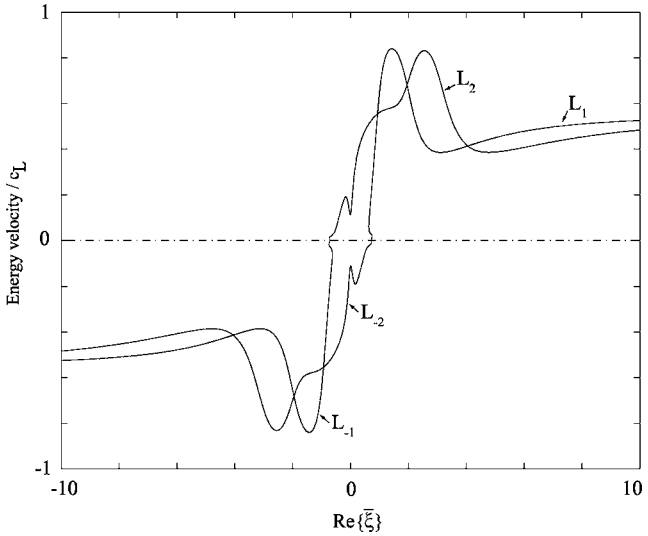

FIG. 3. Velocity of energy transport versus real wave number.

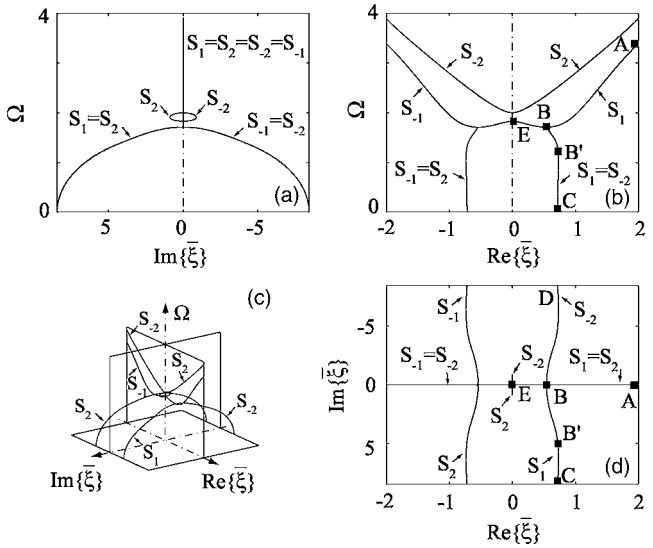

FIG. 4. Three-dimensional dispersion curves for the elastic plate (c) and projections over the planes: (a) Re{$\bar{\xi}$}=0; (b) Im{$\bar{\xi}$}=0; (d) Ω=0.

direction, which is confirmed by the fact that only the square of the wave number is involved in Eq. (2). Therefore, the roots ξ and $-\xi$ must equally be solutions to Eq. (2). However, in the space (Im{$\bar{\xi}$},Re{$\bar{\xi}$},Ω), these roots lie over different paths. As an example, in Fig. 2(d), L_1 corresponds to a mode propagating along $\hat{x}_1$ while L_{-1} represents the same type of vibration propagating in the opposite direction, as can be deduced from the signs of the velocity of energy transport shown in Fig. 3. Note that the velocity of energy transport is always subsonic.

While for L_1 the real part of the wave number is always positive, as the frequency decreases, the L_2 mode crosses the plane Re{$\bar{\xi}$}=0 [Figs. 2(b) and 2(d)]. The same happens for the corresponding mode of an elastic plate loaded with a light fluid (S_2 mode in Ref. 12). At the frequency where the intersection occurs, the wavelength is infinite, but in contrast with the cutoff modes of an elastic plate free or loaded with fluid, the mode still carries energy along $\hat{x}_1$. As the frequency decreases further, Re{$\bar{\xi}$} becomes negative while Im{$\bar{\xi}$} is still positive. Since the velocity of energy transport is always positive (Fig. 3), the mode still propagates in the direction $\hat{x}_1$. However, when Re{$\bar{\xi}$}<0 the energy flow is in the opposite direction to the phase velocity. This type of propagation is known as backward-wave motion and was first theoretically predicted by Tolstoy *et al.* [(J. Accoust. Soc. Am. **29**, 37–42 (1956)] and experimentally observed by Meitzler,[30] Wolf *et al.*[31] and more recently by Hosten and Castaings[32] for elastic plates and cylinders. It should be noticed that the topology of the modes of an absorbing plate is very similar to that of a plate loaded with a low density fluid,[11] since the fluid induces energy radiation which results in the mode attenuation. However, the spectrum of the fluid loaded plate contains extra modes which do not belong to the free plate (see, for instance, the Scholte–Stoneley mode).

IV. ATTENUATIVE VERSUS LOSSLESS PLATE

The understanding of the topology of the dispersion curves of an attenuative plate, provides a clear picture of the structure of the dispersion curves of the elastic case.

Figure 4, which is equivalent to Fig. 2, shows a few symmetric modes of the elastic plate whose dispersion curves are shown in Fig. 1(b) as first derived by Mindlin.[3] Consider the S_1 mode as the frequency goes to zero. Along the branch AB [Figs. 4(b) and 4(d)] the mode is propagating along $\hat{x}_1$ and its trajectory is entirely contained in the plane Im{$\bar{\xi}$}=0. At point B, the mode breaks into three more branches, BC, BD, and BE. Along the branches BC and BD the mode is nonpropagating, while along BE the group velocity is negative. However, among these branches only BC belongs to S_1. Mindlin clarified that the branch BE is not part of S_1 on the basis of the negativity of the group velocity (hence, of the energy flow). However, it is not clear why the branch BC has to belong to S_1 rather than BD or even being a different mode. It is usually argued that a nonpropagating mode is a vibration which does not propagate and decays from the source. As a consequence, if the S_1 mode propagates in the $\hat{x}_1$ direction, the nonpropagating mode which decays in the same direction (branch BC), is associated with it. In these terms, this would be a mere convention which does not provide a valid motivation for considering the branch BC as a part of S_1 rather than an independent mode.

The physical reason why the branch BC has to belong to the S_1 mode lays in the dispersion curves of the attenuative plate. Since the trajectories of the attenuative plate modes tend to those of the elastic case as the material damping vanishes (see limiting absorption principle[33]), it follows that for very low material damping the modes of the attenuative plate mark the trajectories of the elastic plate. For instance, the L_1 mode tends to embrace the branches AB and BC [compare Figs. 2(d) and 4(d)]. Therefore, it can be concluded that since the two branches AB and BC of the elastic plate correspond to the limit toward which the trajectory of only one mode (L_1) tends, they belong to the same mode indeed. In a similar fashion, the branches BD and BE belong to the S_{-2} mode since the L_{-2} mode tends to them as the absorption vanishes [compare Figs. 2(d) and 4(d)]. Moreover, a nonpropagating mode decays along the propagation direction of

TABLE II. Material parameters used for the bilayer.

	c_S (m/ms)	c_L (m/ms)	k_S (np/wl)	k_L (np/wl)	ρ (kg/m^3)	Thickness (mm)
Viscoelastic layer	0.90	1.70	0.01	0.01	1250	9.00
Lossless layer	3.26	5.96	0	0	7930	8.00

the corresponding mode of the attenuative plate. This discussion suggests that it would be more appropriate to refer to the nonpropagating branch of a mode rather than to a nonpropagating mode. An equivalent conclusion can be drawn by considering the fluid loaded case in the limit as the fluid density goes to zero.[11]

It is worth noticing that for a mode of the attenuative plate, the branch of it which approaches the nonpropagating branch of the corresponding elastic mode is characterized by large guided wave attenuation ($\mathrm{Im}\{\xi\}$). As a consequence, the L_1 mode at very low frequency is rapidly attenuated with distance, and from a practical point of view behaves as a nonpropagating mode. This consideration holds for the other higher order modes in the regions where they approach the elastic nonpropagating mode branches.

V. LAMB WAVES IN BILAYERED PLATES

In order to show how intimate the link between propagating and nonpropagating branches is, the analysis of the bilayer studied in a previous work[19] is carried out, the bilayer consisting of an elastic plate coated with a viscoelastic layer. The acoustic properties and the geometry are summarized in Table II.

Figure 5 is the spectrum of the first five Lamb modes of the bilayer. For simplicity only the curves with positive $\mathrm{Re}\{\bar{\xi}\}$ have been represented. Solid lines refer to modes propagating along the $\hat{x}_1$ direction, while the dashed line represents a backward mode. On the other hand, Fig. 6 shows the dispersion loci when the material absorption in the viscoelastic layer is neglected. In this case all the propagating modes lie on the plane $\mathrm{Im}\{\bar{\xi}\}=0$. Note that the only nonpropagating branches are AD, AD′, and the loops CB, GF, and EO. While the trajectories of M_0 and M_1 are quite similar to those of $\bar{M}_0$ and $\bar{M}_1$, the paths of the other modes exhibit significant changes. In particular, the modes of the elastic bilayer are all connected through complex branches, whereas the modes of the attenuative bilayer are well separated. As in the case of a free plate, the mode paths of the elastic bilayer can be thought of as the limit condition toward which the modes of the attenuative bilayer tend as the material attenuation goes to zero.

An interesting feature of the dispersion loci of the elastic bilayer is the presence of a complex loop with diameter BC one half of which belongs to the mode M_3 (space $\mathrm{Im}\{\bar{\xi}\}>0$, solid line) and the other half to M_{-4} (space $\mathrm{Im}\{\bar{\xi}\}<0$, dashed line) as depicted in the zoom at the top of Fig. 6. This loop

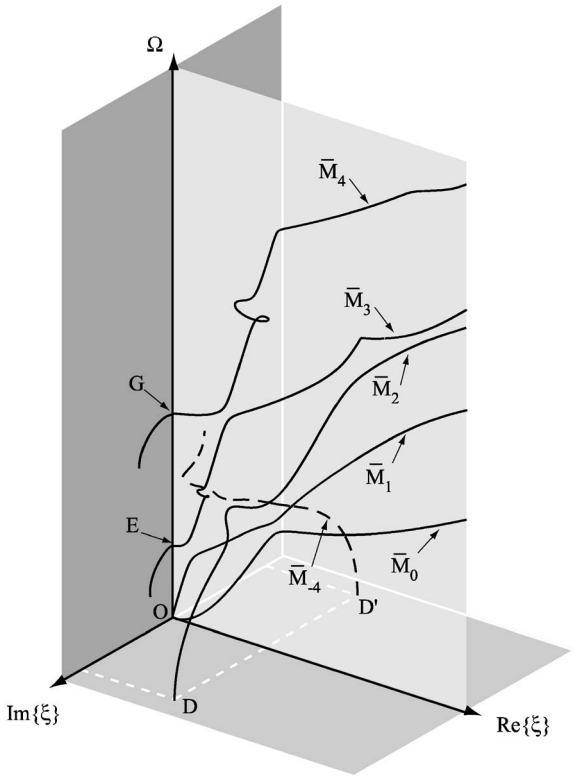

FIG. 5. Three-dimensional Lamb wave dispersion curves for the bilayer described in Table II with $k_S=k_L=0.01$ np/wl.

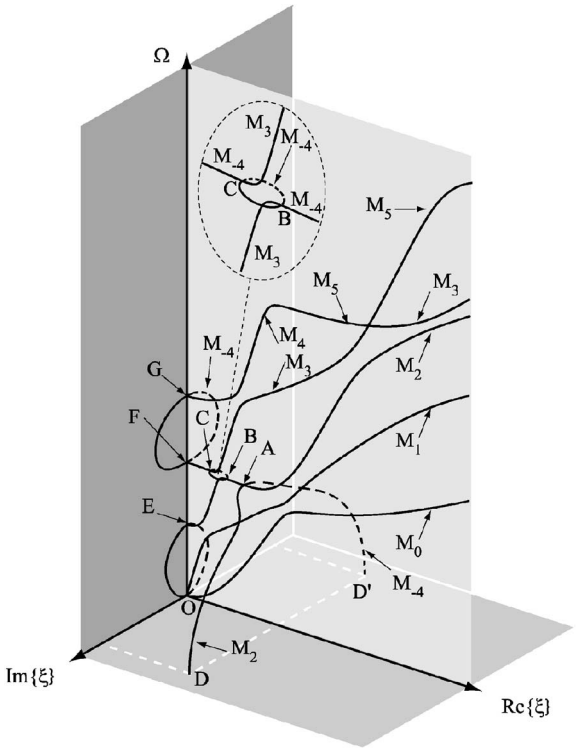

FIG. 6. Three-dimensional dispersion curves for the equivalent elastic bilayer of Table II.

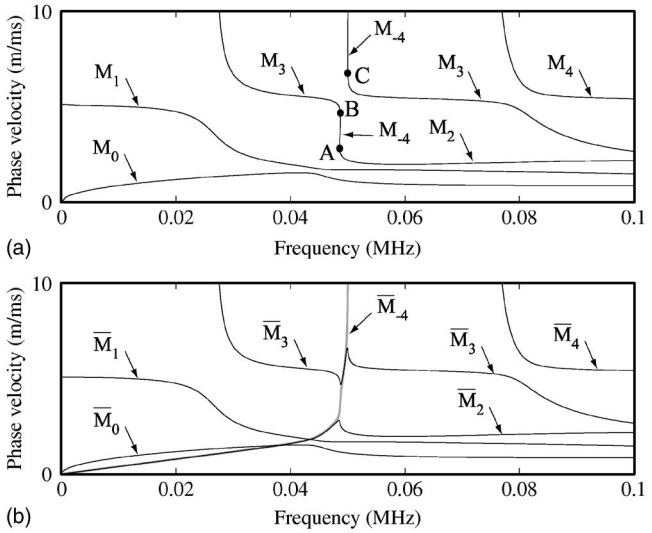

FIG. 7. Lamb wave phase velocity dispersion curves for the bilayer described in Table II: (a) elastic case; (b) $k_S=k_L=0.01$ np/wl.

causes the M_3 mode to split into two different branches in the phase velocity versus frequency plane shown in Fig. 7(a). The apparent separation is due to the fact that the half loop belonging to M_3 is not visible since it is nonpropagating. However, as the attenuation in the viscoelastic layer is considered, the loop becomes propagating and the two branches join together Fig. 7(b). Moreover, due to the shape of the loop, a maximum in the guided wave attenuation, $\mathrm{Im}\{\xi\}$, occurs. Also the branch AD of M_2 and the branches CB, BA and AD, of M_{-4} appear in the phase velocity dispersion curves as soon as the material absorption is taken into account, Fig. 7(b).

VI. CONCLUSIONS

The nature of the nonpropagating modes of an elastic plate has been investigated by considering the elastic case as a restriction of the more general viscoelastic problem. It has been emphasized that the existence of nonpropagating branches in the dispersion curves of an elastic plate is due to the elastic hypothesis. In other words, once energy absorption within the material is considered, nonpropagating branches begin to carry energy and become a continuous extension of the original elastic propagating mode. As a consequence, a nonpropagating mode should be regarded as a mode branch which forms a mode jointly with one or more propagating branches, rather than being a mode itself. An equivalent conclusion can be drawn by considering the fluid loaded case in the limit as the fluid density goes to zero.[11]

This interpretation enables a clear separation of the modes of complex waveguides such bilayered plates. In this case, it has been shown that branches which appear to be totally unconnected in the phase velocity-frequency plane do indeed belong to the same mode due to the existence of nonpropagating branches which lead to a single continuous propagating mode as material absorption is considered.

[1] R. D. Fay and O. V. Fortier, "Transmission of sound through steel plates immersed in water," J. Acoust. Soc. Am. **23**(3), 339–346 (1951).
[2] R. H. Lyon, "Response of an elastic plate to localized driving forces," J. Acoust. Soc. Am. **27**(2), 259–265 (1955).
[3] R. D. Mindlin, "Vibrations of an infinite elastic plate at its cutoff frequencies," in *Proceedings of the Third U.S. National Congress of Applied Mechanics*, 1958, p. 225.
[4] R. D. Mindlin and M. Onoe, "Mathematical theory of vibrations of elastic plates," in *Proceedings of the Eleventh Annual Symposium of Frequency Control*, U.S. Army Signal Engineering Laboratories, New Jersey, 1957, p. 17–40.
[5] R. D. Mindlin and M. A. Medick, "Extensional vibrations of elastic plates," J. Appl. Mech. **26**, 561–569 (1959).
[6] R. D. Mindlin, "Waves and vibrations in isotropic, elastic plates," in *Structural Mechanics*, J. N. Goodier and N. J. Hoff (Pergamon, New York, 1960), pp. 199–232.
[7] B. A. Auld, *Acoustic Fields and Waves in Solids* (Krieger, Malabar, 1990), Vol. 2.
[8] W. B. Fraser, "Orthogonality relation for the Rayleigh–Lamb modes of vibration of a plate," J. Acoust. Soc. Am. **59**(1), 215–216 (1976).
[9] R. L. Weaver and Y. Pao, "Axisymmetric elastic waves excited by a point source in a plate," J. Appl. Mech. **49**, 821–836 (1982).
[10] C. Scandrett and N. Vasudevan, "The propagation of time harmonic Rayleigh–Lamb waves in a bimaterial plate," J. Acoust. Soc. Am. **89**, 1606–1614 (1991).
[11] S. I. Rokhlin, D. E. Chimenti, and A. H. Nayfeh, "On the topology of the complex wave spectrum in a fluid-coupled elastic layer," J. Acoust. Soc. Am. **85**(3), 1074–1080 (1989).
[12] J. P. Sessarego, J. Sageloli, C. Gazanhes, and H. Uberall, "Two Scholte–Stoneley waves on doubly fluid-loaded plates and shells," J. Acoust. Soc. Am. **101**(1), 135–142 (1997).
[13] A. Freedman, "Anomalies of the a_0 leaky lamb mode of a fluid-loaded, elastic plate," J. Sound Vib. **183**(4), 719–737 (1995).
[14] F. Simonetti and P. Cawley, "On the nature of shear horizontal wave propagation in elastic plates coated with viscoelastic materials," Proc. R. Soc. London A **460**, 2197–2221 (2004).
[15] R. M. Christensen, *Theory of Viscoelasticity: An Introduction* (Academic, New York, 1971).
[16] M. Castaings and B. Hosten, "Guided waves propagating in sandwich structures made of anisotropic, viscoelastic, composite materials," J. Acoust. Soc. Am. **113**(5), 2622–2634 (2003).
[17] M. J. S. Lowe, "Matrix techniques for modelling ultrasonic waves in multilayered media," IEEE Trans. Ultrason. Ferroelectr. Freq. Control **42**, 525–542 (1995).
[18] B. N. Pavlakovic, M. J. S. Lowe, D. N. Alleyne, and P. Cawlev, "Disperse: A general purpose program for creating dispersion curves," in *Review of Progress in Quantitative NDE*, edited by D. O. Thompson and D. E. Chimenti (Plenum, New York, 1997), Vol. 16, pp. 185–192.
[19] F. Simonetti, "Lamb wave propagation in elastic plates coated with viscoelastic materials," J. Acoust. Soc. Am. **115**, 2041–2053 (2004).
[20] P. Marston, "Negative group velocity lamb waves on plates and applications on the scattering of sound by shells," J. Acoust. Soc. Am. **113**, 2659–2662 (2003).
[21] Lord Rayleigh, *The Theory of Sound* (Dover, New York, 1945), Vol. 1.
[22] E. L. Bolda, R. Y. Chiao, and J. C. Garrison, "Two theorems for the group velocity in dispersive media," Phys. Rev. A **48**, 3890–3894 (1993).
[23] K. Suchy, "Real Hamilton equations of geometrical optics for media with moderate absorption," Radio Sci. **16**, 1179–1182 (1981).
[24] D. Censor, "Alternative methods for ray propagation in absorbing media," Proc. IEEE **69**, 750–751 (1981).
[25] I. Gurwich, "On the pulse velocity in absorbing and nonlinear media and parallels with the quantum mechanics," Electromagn. Waves **33**, 69–96 (2001).
[26] C. G. B. Garrett and D. E. McCumber, "Propagation of Gaussian light pulse through an anomalous dispersion medium," Phys. Rev. A **1**(2), 305–313 (1970).
[27] S. Chu and S. Wong, "Linear pulse propagation in an absorbing medium," Phys. Rev. Lett. **48**(11), 738–741 (1982).
[28] M. A. Biot, "General theorems on the equivalence of group velocity and energy transport," Phys. Rev. **105**(4), 1129–1137 (1957).
[29] A. Bernard, M. J. S. Lowe, and M. Deschamps, "Guided waves energy velocity in absorbing and nonabsorbing plates," J. Acoust. Soc. Am. **110**(1), 186–196 (2001).
[30] A. H. Meitzler, "Backward-wave transmission of stress pulses in elastic

cylinders and plates," J. Acoust. Soc. Am. **38**, 835–842 (1965).
[31]J. Wolf, T. D. K. Ngoc, R. Kille, and W. G. Mayer, "Investigation of lamb waves having a negative group velocity," J. Acoust. Soc. Am. **83**(1), 122–126 (1988).
[32]B. Hosten and M. Castaings, "Parabolic mirror and air-coupled transducer for multimodal plate detection," in *Review of Progress in Quantitative NDE*, edited by D. O. Thompson and D. E. Chimenti (American Institute of Physics, New York, 2003), Vol. 22, pp. 1243–1250.
[33]D. Eidus, "The limiting absorption principle," Russ. Math. Surveys **24**, 97–167 (1969).

Errors in two-point sound reproduction[a)]

P. A. Nelson[b)] and J. F. W. Rose
Institute of Sound and Vibration Research, University of Southampton, Highfield, Southampton SO17 1BJ, United Kingdom

(Received 6 August 2004; revised 14 April 2005; accepted 18 April 2005)

This paper deals with the problem of reproducing two signals at two points in space by using two acoustic sources. While much is now known about the techniques available for the design of matrices of inverse filters that enable this objective to be achieved in practice, it is still the basic physics of the sound field produced that controls the effectiveness of such systems and which ultimately dictates their design. The basic physical processes involved in producing the cross-talk cancellation that enables the reproduction of the desired signals is revisited here by using a simple two source/two field point free field model. The singular value decomposition is used to identify those frequencies where the inversion problem becomes ill-conditioned and to explain physically the origin of the ill-conditioning. As observed previously, it is found that cross-talk cancellation becomes problematic when the path length difference between the two sources and one of the field points becomes equal to one half the acoustic wavelength. The ill-conditioned frequencies are also found to be associated with a limited spatial region of cross-talk cancellation and with large source outputs manifested in the time domain by responses of long duration. © *2005 Acoustical Society of America.* [DOI: 10.1121/1.1928787]

PACS number(s): 43.38.Md, 43.60.Tj, 43.60.Pt [AJZ] Pages: 193–204

I. INTRODUCTION

The introduction of low cost digital signal processing into widespread use offers the opportunity of more sophisticated approaches to sound reproduction than has ever been possible. A fundamental problem in this field is the need to reproduce at the ears of the listener those acoustic signals that would have been produced by a specific source of sound located at a particular position relative to the listener. The sound reproduction is undertaken by loudspeakers whose input signals are manipulated in order to generate the ear signals associated with this specific "virtual source."[1,2] The signal manipulation is accomplished through the use of matrices of inverse filters whose design may be deduced by using procedures outlined previously.[3–5] It was pointed out by Ward and Elko[6] that this inversion problem becomes ill-conditioned (in the two source/two field point case) when the path length difference between the two sources (loudspeakers) and the field points (listeners ears) is equal to one half of the acoustic wavelength. This result helps explain the apparent effectiveness of virtual acoustic imaging systems based on the "Stereo Dipole"[7,8] where the loudspeakers subtend an angle at the listener in the region of 10°. More recently,[9–12] it has been shown that the bandwidth of operation of such systems may be considerably expanded by deploying a number of pairs of loudspeakers each transmitting sound in a different frequency range. The high frequency loudspeakers subtend a small angle at the listener, while the low frequency loudspeakers subtend a large angle at the listener. In principle, most effective results are obtained by an "optimal source distribution"[13] that transmits the entire audio frequency range with a continuous dependence on angle relative to the listener.

The purpose of the current paper is to point out the connection between the condition number of the inversion problem, the extent of the spatial region over which cross-talk cancellation is achieved, and the response of the reproduction system in the time domain. The two-source/two-field-point problem is analyzed using the singular value decomposition (SVD) of the free-field transfer function matrix relating the outputs of two point acoustic sources to the sound pressures produced at two points in space representing the ears of a listener. At frequencies where the problem is well-conditioned, the spatial effectiveness of cross-talk cancellation is greatest and, most important, the time domain response of the system is of limited duration. The results are illustrated with computer simulation of the wave field generated in a number of geometrical arrangements.

II. THE FREE FIELD FREQUENCY RESPONSE FUNCTION

A simple analysis of the problem of reproducing sound at two positions in space using two free field point monopoles illuminates the basic difficulties associated with the system inversion. Using the geometry illustrated in Fig. 1, the relationship between the vector of acoustic pressures $\mathbf{p}=[p_1,p_2]^T$ and the vector of source volume acceleration $\mathbf{v}=[\nu_1,\nu_2]^T$ can be written as $\mathbf{p}=\mathbf{C}\mathbf{v}$ where the matrix $\mathbf{C}$ is given

$$\mathbf{C}=\frac{\rho_0 e^{-jkl_1}}{4\pi l_1}\begin{bmatrix}1 & ge^{-jk\Delta l}\\ ge^{-jk\Delta l} & 1\end{bmatrix}, \tag{1}$$

where l_1 and l_2 are the path lengths between the sources and field points such that the path length difference $\Delta l=l_2-l_1$

[a)]This paper is the text of the principle author's keynote lecture entitled "Active control for virtual acoustics" presented at *Active 2002, the 2002 International Symposium on Active Control of Sound and Vibration*, held in Southampton during July 2002.

[b)]Electronic mail: pan@isvr.soton.ac.uk

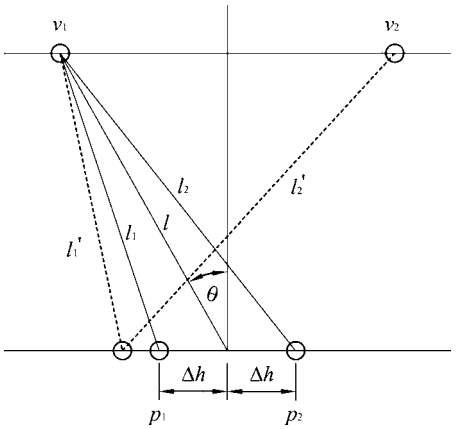

FIG. 1. Geometry of the free field model where sources of strength ν_1 and ν_2 produce pressures p_1 and p_2 at the two field points.

and the path length ratio $g=l_1/l_2$. The density is given by ρ_0 and the acoustic wave number $k=\omega/c_0$ where ω is the frequency and c_0 the sound speed.

It will prove useful to work with the normalized matrix $\mathbf{C}_N=\mathbf{C}(4\pi l_1/\rho_0 e^{-jkl_1})$. It can be shown[10] that the singular value decomposition (SVD) of the normalized matrix can be written as

$$\mathbf{C}_N=\mathbf{U}\Sigma\mathbf{V}^{\mathrm{H}}, \tag{2}$$

where H denotes the conjugate transpose, the diagonal matrix of singular values is given by

$$\Sigma=\begin{bmatrix}\sqrt{(1+ge^{jk\Delta l})(1+ge^{-jk\Delta l})} & 0\\ 0 & \sqrt{(1-ge^{jk\Delta l})(1-ge^{-jk\Delta l})}\end{bmatrix}, \tag{3}$$

and the matrices of left and right singular vectors are given, respectively, by

$$\mathbf{U}=\frac{1}{\sqrt{2}}\begin{bmatrix}\sqrt{\frac{1+ge^{-jk\Delta l}}{1+ge^{jk\Delta l}}} & \sqrt{\frac{1-ge^{-jk\Delta l}}{1-ge^{jk\Delta l}}}\\ \sqrt{\frac{1+ge^{-jk\Delta l}}{1+ge^{jk\Delta l}}} & -\sqrt{\frac{1-ge^{-jk\Delta l}}{1-ge^{jk\Delta l}}}\end{bmatrix}, \tag{4}$$

$$\mathbf{V}=\frac{1}{\sqrt{2}}\begin{bmatrix}1 & 1\\ 1 & -1\end{bmatrix}. \tag{5}$$

The behavior of the singular values as a function of frequency is shown in Fig. 2, where the two singular values are denoted by

$$\sigma_{\mathrm{in}}=\sqrt{(1+ge^{jk\Delta l})(1+ge^{-jk\Delta l})}, \tag{6}$$

$$\sigma_{\mathrm{out}}=\sqrt{(1-ge^{jk\Delta l})(1-ge^{-jk\Delta l})}. \tag{7}$$

Note that peaks in σ_{in} occur at frequencies given by $k\Delta l=0,2\pi,4\pi,\ldots$ (corresponding to $\Delta l=0\lambda,\lambda,2\lambda,\ldots$) where λ is the acoustic wavelength) whereas peaks in σ_{out} occur at frequencies given by $k\Delta l=\pi,3\pi,5\pi,\ldots$ (corresponding to $\Delta l=\lambda/2,3\lambda/2,4\lambda/2,\ldots$).

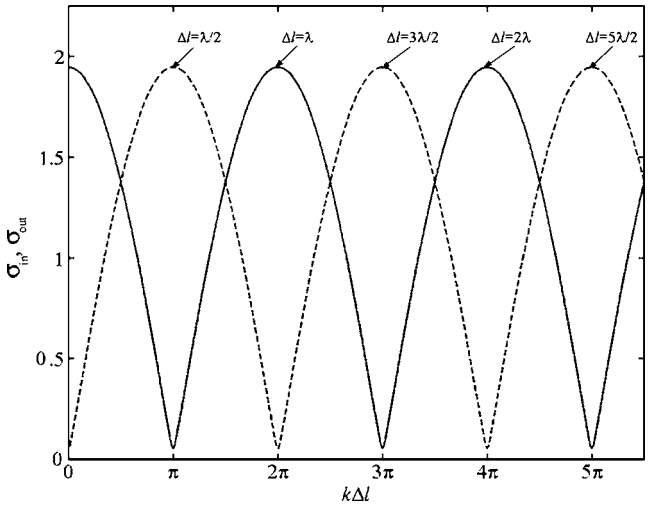

FIG. 2. The variation of the singular values σ_{in} (—) and σ_{out} (---) as a function of the path length difference Δl.

The structure of the singular value decomposition at these frequencies is also informative. First, note that the relationship between the acoustic pressure and the source volume accelerations can be written as

$$\mathbf{p}_N=\mathbf{C}_N\mathbf{v}, \tag{8}$$

where $\mathbf{p}_N$ denotes the normalized pressure defined by $\mathbf{p}(4\pi l_1/\rho_0 e^{-jkl_1})$, which is the acoustic pressure expressed relative to that produced at one of the field points by the furthest source. Since the matrix $\mathbf{U}$ is unitary (and has the property $\mathbf{U}^{\mathrm{H}}\mathbf{U}=\mathbf{I}$ where $\mathbf{I}$ is the identity matrix), then use of the SVD shows that

$$\mathbf{U}^{\mathrm{H}}\mathbf{p}_N=\Sigma\mathbf{V}^{\mathrm{H}}\mathbf{v}. \tag{9}$$

At frequencies where $\Delta l=0\lambda,\lambda,2\lambda,\ldots$ and at frequencies where $\Delta l=\lambda/2,3\lambda/2,5\lambda/2,\ldots$ the matrix $\mathbf{U}$ reduces to

$$\mathbf{U}=\frac{1}{\sqrt{2}}\begin{bmatrix}1 & 1\\ 1 & -1\end{bmatrix}. \tag{10}$$

Thus at frequencies where $\Delta l=0\lambda,\lambda,2\lambda,\ldots$ Eq. (9) can be written as

$$\begin{bmatrix}1 & 1\\ 1 & -1\end{bmatrix}\begin{bmatrix}p_{N1}\\ p_{N2}\end{bmatrix}=\begin{bmatrix}(1+g) & 0\\ 0 & (1-g)\end{bmatrix}\begin{bmatrix}1 & 1\\ 1 & -1\end{bmatrix}\begin{bmatrix}\nu_1\\ \nu_2\end{bmatrix} \tag{11}$$

and at frequencies where $\Delta l=\lambda/2,\lambda,3\lambda/2,\ldots$ Eq. (9) can be written as

$$\begin{bmatrix}1 & 1\\ 1 & -1\end{bmatrix}\begin{bmatrix}p_{N1}\\ p_{N2}\end{bmatrix}=\begin{bmatrix}(1-g) & 0\\ 0 & (1+g)\end{bmatrix}\begin{bmatrix}1 & 1\\ 1 & -1\end{bmatrix}\begin{bmatrix}\nu_1\\ \nu_2\end{bmatrix}. \tag{12}$$

Note that the premultiplication of $\mathbf{p}_N$ by $\mathbf{U}^{\mathrm{H}}$ and the premultiplication of $\mathbf{v}$ by $\mathbf{V}^{\mathrm{H}}$ may be regarded as transform operations such that the transformed normalized pressure $\tilde{\mathbf{p}}_N=\mathbf{U}^{\mathrm{H}}\mathbf{p}$, and the transformed volume acceleration $\tilde{\mathbf{v}}=\mathbf{V}^{\mathrm{H}}\mathbf{v}$. This then shows that the transformed variables are related by the diagonal matrix Σ of singular values such that $\tilde{\mathbf{p}}_N=\Sigma\tilde{\mathbf{v}}$.

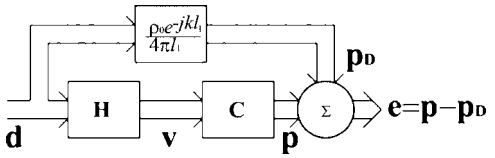

FIG. 3. Block diagram of the free field sound reproduction problem. The difference between the desired pressures $\mathbf{p}_D$ and the reproduced pressures $\mathbf{p}$ is denoted by a vector of errors $\mathbf{e}$.

At frequencies where $\Delta l=0,\lambda,2\lambda,\ldots$ it follows from Eq. (11) that

$$(p_{N1}+p_{N2})=(1+g)(\nu_1+\nu_2), \tag{13}$$

$$(p_{N1}-p_{N2})=(1-g)(\nu_1-\nu_2). \tag{14}$$

These relationships can be written as

$$\tilde{p}_{N\mathrm{in}}=(1+g)\tilde{v}_{\mathrm{in}}, \tag{15}$$

$$\tilde{p}_{N\mathrm{out}}=(1-g)\tilde{v}_{\mathrm{out}}, \tag{16}$$

where $\tilde{\mathbf{p}}_N=[\tilde{p}_{N\mathrm{in}},\ \tilde{p}_{N\mathrm{out}}]$ and $\tilde{\mathbf{v}}=[\tilde{v}_{\mathrm{in}},\ \tilde{v}_{\mathrm{out}}]$. Thus when the path length difference $\Delta l=0\lambda,\lambda,2\lambda,\ldots$ then the "in-phase" pressure component at the field points is well coupled to the "in-phase" volume accelerations of the sources (by the factor $1+g$) but the "out-of-phase" component of the pressure is only weakly coupled to the out-of-phase component of the volume acceleration (by the factor $1-g$). Conversely, at frequencies where $\Delta l=\lambda/2,3\lambda/2,5\lambda/2,\ldots$ it follows from Eq. (12) that

$$(p_{N1}+p_{N2})=(1-g)(\nu_1+\nu_2), \tag{17}$$

$$(p_{N1}-p_{N2})=(1+g)(\nu_1-\nu_2), \tag{18}$$

which can be written as

$$\tilde{p}_{N\mathrm{in}}=(1-g)\tilde{v}_{\mathrm{in}}, \tag{19}$$

$$\tilde{p}_{N\mathrm{out}}=(1+g)\tilde{v}_{\mathrm{out}}. \tag{20}$$

Thus at these frequencies, the in-phase components of the acoustic pressure are only weakly coupled (by $1-g$) to the in-phase component of the volume acceleration, whereas the out-of-phase component of the pressure is strongly coupled (by $1+g$) to the out-of-phase component of the volume acceleration. These observations have a crucial bearing on the ability of a system of two loudspeakers to reproduce the signals desired at two points in space (and indeed, at the ears of a listener).

III. THE PERFORMANCE OF INVERSE FILTERS

With reference to the block diagram of Fig. 3, assume that the objective of the free field sound reproduction system is to produce pressures defined by the vector $\mathbf{p}_D=[p_{D1},p_{D2}]^T$ at the field points. Also assume that these pressures are expressed in terms of the signals $\mathbf{d}=[d_1,d_2]^T$ where $\mathbf{p}_D=\mathbf{d}(\rho_0 e^{-jkl_1}/4\pi l_1)$. The signals $\mathbf{d}$ are input to a matrix $\mathbf{H}$ of inverse filters designed to produce the requisite source volume acceleration vector $\mathbf{v}$ that ensures the reproduction of the pressures $\mathbf{p}_D$ at the field points. Thus, we require that $\mathbf{p}=\mathbf{p}_D$, which leads to $\mathbf{Cv}=\mathbf{p}_D$ and therefore that

$$\mathbf{CHd}=\frac{\rho_0 e^{-jkl_1}}{4\pi l_1}\mathbf{d}. \tag{21}$$

Using the definition of the normalized matrix $\mathbf{C}_N$ then shows that we require

$$\mathbf{C}_N\mathbf{H}=\mathbf{I}. \tag{22}$$

The matrix of inverse filters is therefore given by

$$\mathbf{H}=\mathbf{C}_N^{-1}=\mathbf{V}\Sigma^{-1}\mathbf{U}^{\mathrm{H}}, \tag{23}$$

where the properties $\mathbf{U}^{\mathrm{H}}\mathbf{U}=\mathbf{V}^{\mathrm{H}}\mathbf{V}=\mathbf{I}$ have been used to express $\mathbf{H}$ in terms of the singular value decomposition of the matrix $\mathbf{C}_N$.

Now observe the requirements of the inverse filters at the particular frequencies at which the path length difference Δl is an integer number of half-wavelengths. First, note that the source volume accelerations are given by $\mathbf{v}=\mathbf{Hd}$, which can be written as

$$\mathbf{v}=\mathbf{V}\Sigma^{-1}\mathbf{U}^{\mathrm{H}}\mathbf{d} \tag{24}$$

or alternatively in the form

$$\mathbf{V}^{\mathrm{H}}\mathbf{v}=\Sigma^{-1}\mathbf{U}^{\mathrm{H}}\mathbf{d}. \tag{25}$$

Thus when $\Delta l=0,\lambda,2\lambda,\ldots$, this relationship becomes

$$\begin{bmatrix}1 & 1\\ 1 & -1\end{bmatrix}\begin{bmatrix}\nu_1\\ \nu_2\end{bmatrix}=\begin{bmatrix}(1+g)^{-1} & 0\\ 0 & (1-g)^{-1}\end{bmatrix}\begin{bmatrix}1 & 1\\ 1 & -1\end{bmatrix}\begin{bmatrix}d_1\\ d_2\end{bmatrix} \tag{26}$$

or in terms of transformed variables

$$\tilde{v}_{\mathrm{in}}=(1+g)^{-1}\tilde{d}_{\mathrm{in}}, \tag{27}$$

$$\tilde{v}_{\mathrm{out}}=(1-g)^{-1}\tilde{d}_{\mathrm{out}}, \tag{28}$$

where $\tilde{d}_{\mathrm{in}}=d_1+d_2$ and $\tilde{d}_{\mathrm{out}}=d_1-d_2$.

Similarly, when $\Delta l=\lambda/2,3\lambda/2,5\lambda/2,\ldots$, Eq. (25) becomes

$$\begin{bmatrix}1 & 1\\ 1 & -1\end{bmatrix}\begin{bmatrix}\nu_1\\ \nu_2\end{bmatrix}=\begin{bmatrix}(1-g)^{-1} & 0\\ 0 & (1+g)^{-1}\end{bmatrix}\begin{bmatrix}1 & 1\\ 1 & -1\end{bmatrix}\begin{bmatrix}d_1\\ d_2\end{bmatrix} \tag{29}$$

and therefore

$$\tilde{v}_{\mathrm{in}}=(1-g)^{-1}\tilde{d}_{\mathrm{in}}, \tag{30}$$

$$\tilde{v}_{\mathrm{out}}=(1+g)^{-1}\tilde{d}_{\mathrm{out}}. \tag{31}$$

Thus at integer numbers of half wavelengths in the path length difference, the in-phase and out-of-phase components of the source accelerations have alternately to compensate for their relative weak coupling to the in-phase and out-of-phase pressure components at the field points. A simple example demonstrates the point. Suppose that the objective of the sound reproduction system is to produce pressures at the field points specified by $d_1=1$, $d_2=0$. Both $\tilde{d}_{\mathrm{in}}$ and $\tilde{d}_{\mathrm{out}}$ have

a value of unity and therefore the source outputs can be described by

$$\left.\begin{aligned}\tilde{v}_{\text{in}} &= (1+g)^{-1}\\ \tilde{v}_{\text{out}} &= (1-g)^{-1}\end{aligned}\right\} \quad \text{when } \Delta l = 0\lambda, \lambda, 2\lambda, \ldots, \tag{32}$$

$$\left.\begin{aligned}\tilde{v}_{\text{in}} &= (1-g)^{-1}\\ \tilde{v}_{\text{out}} &= (1+g)^{-1}\end{aligned}\right\} \quad \text{when } \Delta l = \lambda/2, 3\lambda/2, 5\lambda/2, \ldots . \tag{33}$$

At these particular frequencies, therefore, the ratio of the in-phase to out-of-phase components of the source strength is at a maximum and either the in-phase or out-of-phase component of the desired signals is maximally amplified by the inverse filters. In short, it is at these frequencies at which the sources have to "work hardest" to achieve their objective of reproducing the desired signals at the field points.

It is also worth noting that at frequencies between those associated with an integer number of half wavelengths in the path length difference, the source strengths required are at a minimum. This occurs when $\Delta l = \lambda/4, 3\lambda/4, 5\lambda/4, \ldots$. At these frequencies the matrix of singular values reduces to

$$\Sigma = \begin{bmatrix} \sqrt{(1+jg)(1-jg)} & 0 \\ 0 & \sqrt{(1+jg)(1-jg)} \end{bmatrix}. \tag{34}$$

The matrix $\mathbf{U}$ however takes different values depending on the number of quarter-wavelength path length differences. When $\Delta l = \lambda/4, 5\lambda/4, 9\lambda/4, \ldots$ the matrix is given by

$$\mathbf{U} = \frac{1}{\sqrt{2}} \begin{bmatrix} \sqrt{\dfrac{(1-jg)}{(1+jg)}} & \sqrt{\dfrac{(1+jg)}{(1-jg)}} \\ \sqrt{\dfrac{(1-jg)}{(1+jg)}} & -\sqrt{\dfrac{1+jg}{1-jg}} \end{bmatrix} \tag{35}$$

and when $\Delta l = 3\lambda/4, 7\lambda/4, 11\lambda/4, \ldots$ the matrix is given by

$$\mathbf{U} = \frac{1}{\sqrt{2}} \begin{bmatrix} \sqrt{\dfrac{(1+jg)}{(1-jg)}} & \sqrt{\dfrac{(1-jg)}{(1+jg)}} \\ \sqrt{\dfrac{(1+jg)}{(1-jg)}} & -\sqrt{\dfrac{(1-jg)}{(1+jg)}} \end{bmatrix}. \tag{36}$$

Substitution of these values into Eq. (25) and again assuming that the desired signals are specified by $d_1 = 1$, $d_2 = 0$ shows that

$$\left.\begin{aligned}\tilde{v}_{\text{in}} &= (1-jg)^{-1}\\ \tilde{v}_{\text{out}} &= (1+jg)^{-1}\end{aligned}\right\} \quad \text{when } \Delta l = \lambda/4, 5\lambda/4, 9\lambda/4, \ldots, \tag{37}$$

$$\left.\begin{aligned}\tilde{v}_{\text{in}} &= (1+jg)^{-1}\\ \tilde{v}_{\text{out}} &= (1-jg)^{-1}\end{aligned}\right\} \quad \text{when } \Delta l = 3\lambda/4, 7\lambda/4, 11\lambda/4, \ldots . \tag{38}$$

Note that at these frequencies, the moduli of the in-phase and out-of-phase components are the same and the desired reproduction of the sound at the field points is comfortably achieved. Thus to emphasize the point, for example

$$\left|\frac{\tilde{v}_{\text{in}}}{\tilde{v}_{\text{out}}}\right|^2 = 1 \quad \text{when } \Delta l = \lambda/4, \tag{39}$$

$$\left|\frac{\tilde{v}_{\text{in}}}{\tilde{v}_{\text{out}}}\right|^2 = \frac{(1+g)^2}{(1-g)^2} \quad \text{when } \Delta l = \lambda/2. \tag{40}$$

IV. THE SIGNIFICANCE OF THE CONDITION NUMBER

It is well known that in any problem involving the inversion of a matrix it is the condition number of the matrix that dictates the sensitivity to errors of the resulting solution.[14] In the case considered here, for example, the objective is to reproduce accurately the desired acoustic pressures at the two spatial positions and it is important to evaluate the sensitivity of the source outputs deduced to errors in the measurement or specification of these pressures and errors in the estimation of the frequency response function to be inverted. Working with the normalized acoustic pressure and frequency response function matrix such that $\mathbf{v} = \mathbf{C}_N^{-1}\mathbf{p}_N$, one proceeds by assuming that errors in $\mathbf{v}$ (denoted by $\delta\mathbf{v}$) that result from errors in $\mathbf{C}_N$ and $\mathbf{p}_N$ (denoted, respectively, by $\delta\mathbf{C}_N$ and $\delta\mathbf{p}_N$) are related by

$$(\mathbf{p}_N + \delta\mathbf{p}_N) = (\mathbf{C}_N + \delta\mathbf{C}_N)(\mathbf{v} + \delta\mathbf{v}). \tag{41}$$

It then follows that (see Golub and Van Loan[14] for details)

$$\frac{\|\delta\mathbf{v}\|}{\|\mathbf{v}\|} \leqslant \kappa(\mathbf{C}_N)\left[\frac{\|\delta\mathbf{C}_N\|}{\|\mathbf{C}\|} + \frac{\|\delta\mathbf{p}_N\|}{\|\mathbf{p}_N\|}\right], \tag{42}$$

where $\|\cdot\|$ denotes the 2-norm. Note that the 2-norm of a vector is the square root of the sum of the squared elements and the 2-norm of a matrix is the square root of its largest singular value. The rms error in the solution for $\mathbf{v}$ is thus seen to be bounded by the condition number $\kappa(\mathbf{C}_N)$ of the frequency response function matrix $\mathbf{C}_N$. Errors in the specification of either $\mathbf{C}_N$ or $\mathbf{p}_N$ are thus amplified by the condition number. If $\kappa(\mathbf{C}_N)$ is large, then large errors in the specification of the source volume accelerations can result. The condition number of $\mathbf{C}_N$ is given by the ratio of the maximum to the minimum singular value. Since the two singular values σ_{in} and σ_{out} given by Eqs. (6) and (7) are oscillatory functions of frequency, the condition number is also strongly frequency dependent.

Of particular interest are the frequencies identified above at which the path length difference Δl is an integer number of half (or quarter) wavelengths. It follows from Eqs. (6) and (7) that

$$\kappa(\mathbf{C}_N) = \frac{1+g}{1-g} \quad \text{when } \Delta l = 0\lambda, \lambda/2, \lambda, 3\lambda/2, \ldots, \tag{43}$$

$$\kappa(\mathbf{C}_N) = 1 \quad \text{when } \Delta l = \lambda/4, 3\lambda/4, 5\lambda/4, 7\lambda/4, \ldots . \tag{44}$$

The matrix of frequency response functions is thus intrinsically ill-conditioned when the path length difference Δl is an integer number of half wavelengths (and at infinite wavelength, or zero frequency when $\Delta l = 0\lambda$). Conversely, when $\Delta l = \lambda/4, 3\lambda/4, 5\lambda/4, \ldots$ the matrix is optimally conditioned;

it has the smallest possible value of condition number of unity (since the two singular values are identical at these frequencies). These results suggest that the process of sound reproduction is therefore intrinsically more error prone at the frequencies when $\Delta l = 0\lambda, \lambda/2, \lambda, \ldots$, but more robust to errors when $\Delta l = \lambda/4, 3\lambda/4, 5\lambda/4, \ldots$. Of course, these are precisely the two sets of conditions identified earlier when cross-talk cancellation requires either large or small source volume accelerations.

These observations hold for any symmetrical arrangement of two sources and two field points. However, more insight into the dependence of the system on geometrical factors can be gained by observing the dependence of the condition number on the angle subtended by the sources at the midpoint of the two field points.[6] With reference to the geometry of Fig. 1, it follows that the path length l_1 is related to the length l and the angle θ by

$$l_1^2 = l^2 + \Delta h^2 - 2\Delta h l \sin\theta. \tag{45}$$

This relationship can be written in the form

$$l_1 = l\left[1 + \left(\frac{\Delta h}{l}\right)^2 - 2\left(\frac{\Delta h}{l}\right)\sin\theta\right]^{1/2}, \tag{46}$$

which on use of the binomial expansion $(1+x)^{1/2} = 1 + \frac{1}{2}x - \frac{1}{8}x^2 \cdots$ shows that when $\Delta h \ll l$ we may write

$$l_1 = l\left[1 - \frac{\Delta h}{l}\sin\theta + O\left[\left(\frac{\Delta h}{l}\right)^2\right]\cdots\right] \tag{47}$$

and therefore to leading order in $\Delta h/l$,

$$l_1 = l - \Delta h \sin\theta. \tag{48}$$

By exactly similar reasoning

$$l_2 = l + \Delta h \sin\theta. \tag{49}$$

Thus under the conditions that Δh is smaller than the distance l, the path length difference Δl is given by

$$\Delta l = l_2 - l_1 = 2\Delta h \sin\theta. \tag{50}$$

Using this expression for the path length difference in the expressions for the singular values given by Eqs. (6) and (7) allows the condition number $\kappa(\mathbf{C}_N)$ to be plotted as a function of the source span 2θ for a given choice of the distance Δh. When $2\Delta h$ is chosen to be the typical value of the distance between the ears of a human head, the condition number can be plotted as a function of both frequency and source span 2θ as illustrated in Fig. 4. This shows $\kappa(\mathbf{C}_N)$ plotted on a logarithmic grayscale. The lighter bands show the regions of small condition number while the darker bands show the regions of high condition number.

Also shown in Fig. 4 is a vertical line corresponding to a source span 2θ of 10°. The significance of this angle is that the frequency range of approximately 300 Hz–3 kHz is best conditioned when this choice of source span is made. This is precisely the range in which most speech signals (and many other signals of practical interest) fall. Thus, the so-called Stereo Dipole[7,8] virtual sound imaging system (which has been found in practice to exhibit desirable properties[15]) is

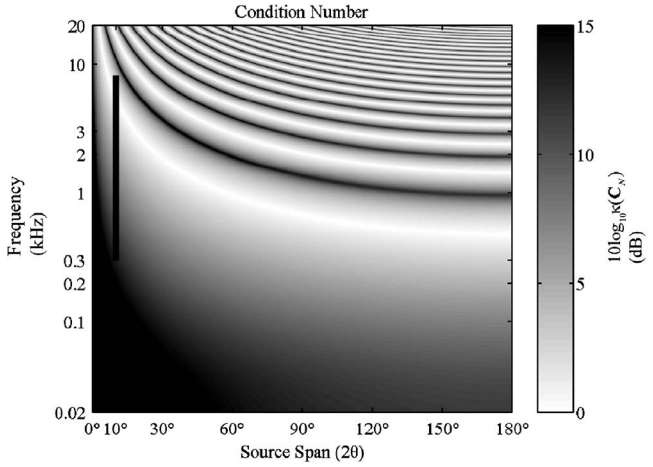

FIG. 4. Condition number $\kappa(\mathbf{C}_N)$ as a function of frequency and source span 2θ. The vertical line defines the bandwidth of operation of the Stereo Dipole, which operates with a source span in the region of 10°.

therefore associated with a particular loudspeaker arrangement that enables cross-talk cancellation to be readily achieved over an important frequency range.

It is also worth pointing out that there is a direct link between the frequencies at which the matrix $\mathbf{C}_N$ is well-conditioned and the degree to which the desired signals can be reproduced over an extensive spatial region. This in turn is directly related to the "sweet-spot" size of a virtual acoustic imaging system. As an illustration of this, with reference to the geometry of Fig. 1, it is possible to calculate the distribution of sound pressure produced in the region of the field points when a particular combination of desired signals is chosen. Consider first the source volume accelerations required to produce desired signals d of $d_1 = 1$ and $d_2 = 0$ at the two field points when the frequency corresponds to a "badly conditioned" case when $\Delta l = \lambda/2$. It follows from Eq. (33) that the individual source outputs at this frequency are given by

$$\nu_1 = \frac{1}{1-g^2}, \quad \nu_2 = \frac{g}{1-g^2}. \tag{51}$$

The pressure p_1' in the region of the field point at which the desired pressure $p_1 = \rho_0 e^{jkl_1}/4\pi l_1$ can be written as

$$p_1' = \frac{\nu_1 \rho_0 e^{-jkl_1'}}{4\pi l_1'} + \frac{\nu_2 \rho_0 e^{-jkl_2'}}{4\pi l_2'}, \tag{52}$$

where l_1' and l_2' are the distances from the sources ν_1 and ν_2, respectively, to a point displaced laterally from the field point as illustrated in Fig. 1. It also follows from the above-described geometrical considerations that

$$l_1' = l - (\Delta h + \Delta h')\sin\theta = l_1 - \Delta h' \sin\theta, \tag{53}$$

where $\Delta h'$ is the lateral displacement from the field point. Similarly, it follows that

$$l_2' = l + (\Delta h + \Delta h')\sin\theta = l_2 + \Delta h' \sin\theta. \tag{54}$$

Substitution into Eq. (52) of these relationships together with the source strengths defined by Eq. (51) leads to

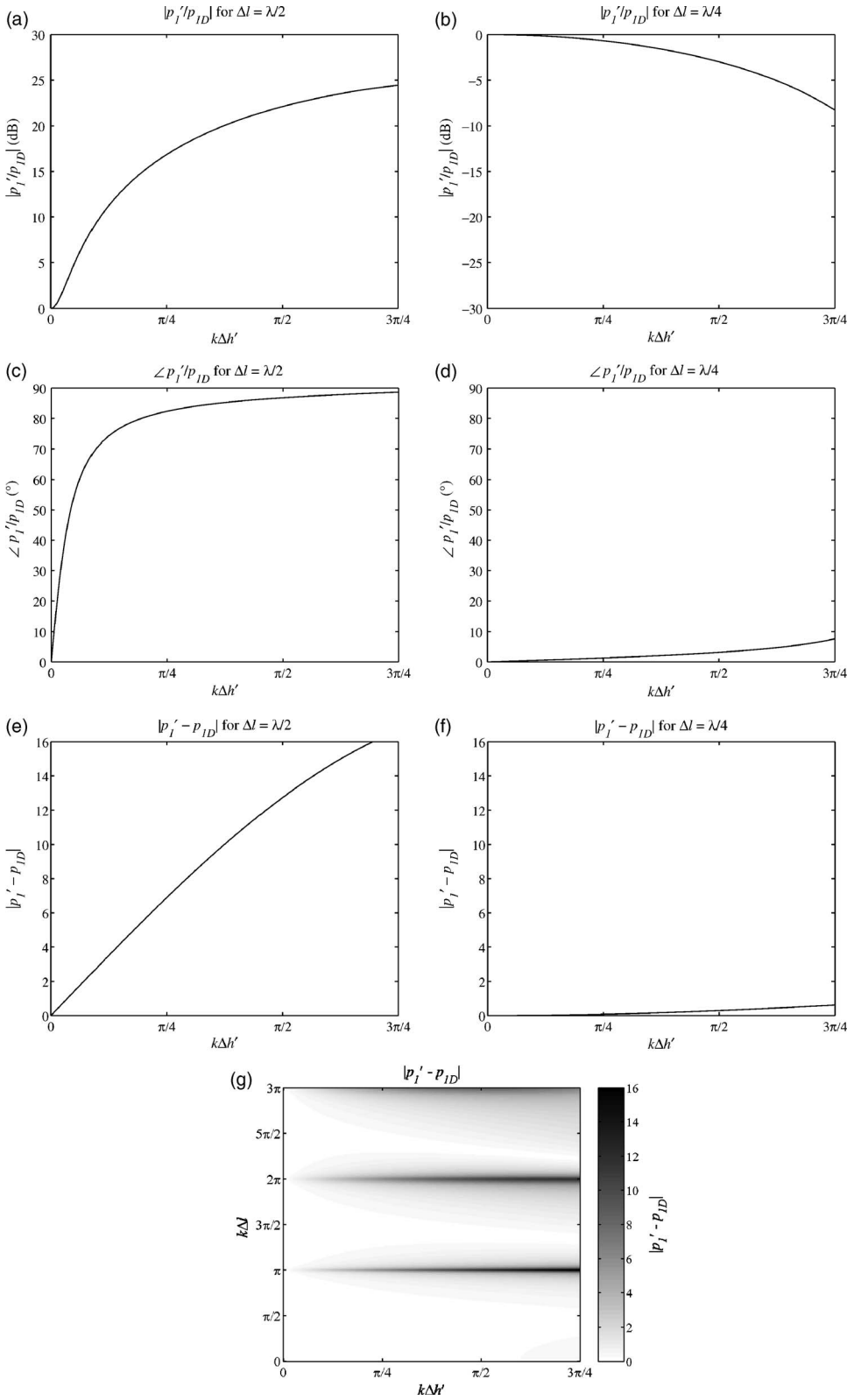

FIG. 5. The dependence of the reproduced pressure p_1' on the lateral displacement $\Delta h'$ from field point 1 in cases (a) $\Delta l = \lambda/2$ and (b) $\Delta l = \lambda/4$. Results are shown relative to the desired pressure $p_{1D} = \rho_0 e^{-jkl_1}/4\pi l_1$ and are given by $20\log_{10}|p_1'/p_{1D}|$. Also shown is the phase difference between p_1' and p_{1D} in the case (c) $\Delta l = \lambda/2$ and (d) $\Delta l = \lambda/4$ and the magnitude of the relative error between p_1' and p_{1D} in cases (e) $\Delta l = \lambda/2$, (f) $\Delta l = \lambda/4$, and (g) $0 \leqslant \Delta l \leqslant 3\lambda/2$.

$$p_1' = \frac{\rho_0 e^{-jkl_1}}{4\pi l_1}\left[\frac{1}{1-g^2}\left(e^{jk\Delta h' \sin\theta} - g^2 e^{-jk\Delta h' \sin\theta}\right)\right], \qquad (55)$$

where l_1' and l_2' have been, respectively, approximated by l_1 and l_2 in the denominators of the terms in Eq. (52). Note that when $\Delta h' = 0$ this expression reduces to the desired value of the pressure at the field point. An exactly similar calculation can be undertaken at a frequency corresponding to a "well-conditioned" case when, for example, $\Delta l = \lambda/4$. In this case, the source strengths that follow from Eq. (37) are given by

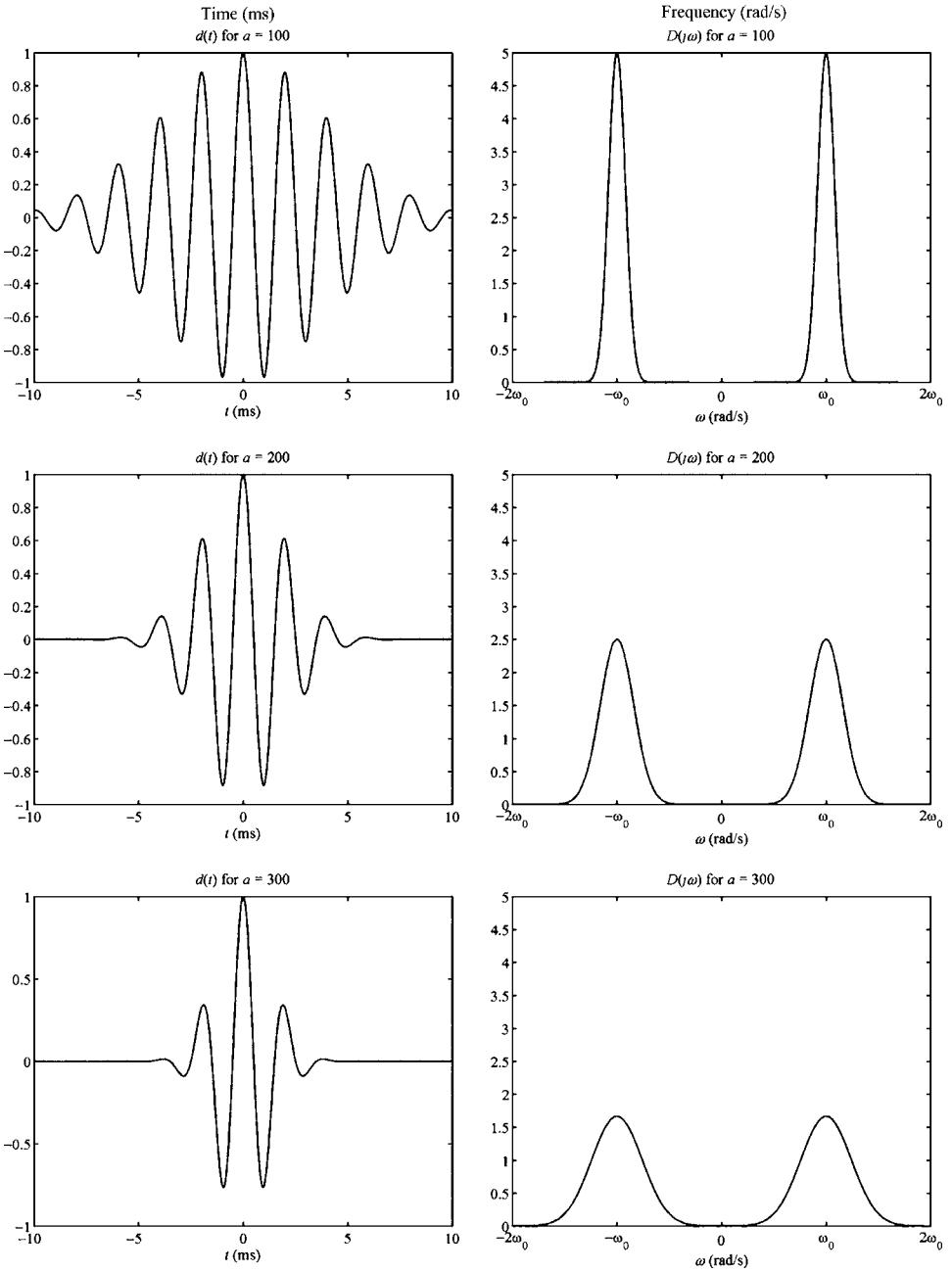

FIG. 6. The time history and spectra corresponding to the Gaussian pulse $d(t)=e^{-\pi(at^2)}\cos\omega_0 t$ for values given by (a) $a=100$, (b) $a=200$, (c) $a=300$.

$$\nu_1=\frac{1}{1+g^2},\quad \nu_2=\frac{jg}{1+g^2}. \tag{56}$$

Use of the same geometrical approximations as used earlier then shows that the reproduced pressure is given by

$$p_1'=\frac{\rho_0 e^{-jkl_1}}{4\pi l_1}\left[\frac{1}{1+g^2}\left(e^{jk\Delta h'\sin\theta}+g^2e^{-jk\Delta h'\sin\theta}\right)\right]. \tag{57}$$

Plots of the dependence of p_1' on $\Delta h'$ are shown in Figs. 5(a)–5(f) for the two cases $\Delta l=\lambda/2$ and $\Delta l=\lambda/4$. The extent to which the desired pressure is maintained in the "well-conditioned" case when $\Delta l=\lambda/4$ is clearly illustrated, whereas the rapid departure spatially of the pressure p_1' from the desired value is clearly shown in the "badly conditioned" case when $\Delta l=\lambda/2$. Figure 5(g) is a two-dimensional plot showing the dependence of the relative error between the reproduced pressure p_1' and the desired pressure p_{1D} on both $\Delta h'$ and frequency. Peaks in the error occur at frequencies where $k\Delta l=\pi,2\pi,3\pi,\ldots$ (or $\Delta l=\lambda/2,\lambda,3\lambda/2,\ldots$), which correspond to the largest ratios between maximum to minimum singular values as shown in Fig. 2. To emphasize the point, series expansions of the exponential terms in Eqs. (55) and (57) yield to leading order in $\Delta h'$

$$p_1'=\frac{\rho_0 e^{-jkl_1}}{4\pi l_1}\left[1+\frac{(1+g^2)}{(1-g^2)}jk\Delta h'\sin\theta\right]\quad(\Delta l=\lambda/2), \tag{58}$$

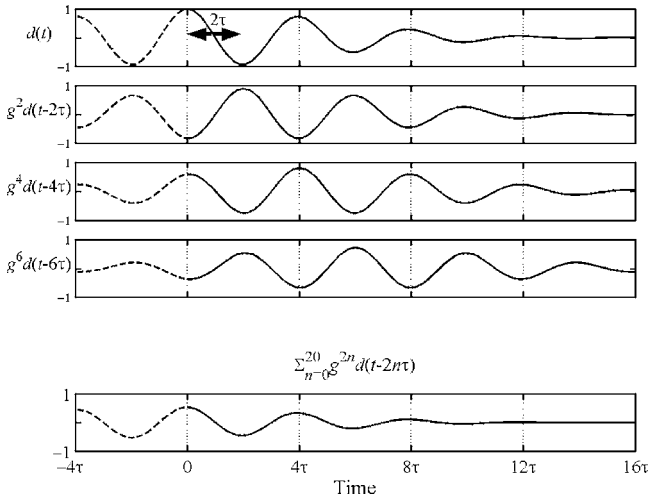

FIG. 7. An illustration of the time history $\nu_1(t)$ that results from a succession of pulses whose frequency is centered on one half of the "ringing frequency." The lower graph shows the sum of 20 terms in the series given by Eq. (5.7).

$$p_1' = \frac{\rho_0 e^{-jkl_1}}{4\pi l_1}\left[1 + \frac{(1-g^2)}{(1+g^2)} jk\Delta h' \sin\theta\right] \quad (\Delta l = \lambda/4). \tag{59}$$

The ill-conditioned frequencies are therefore clearly shown to be associated with rapid departure from the desired pressure (and a small "sweet spot") while the well-conditioned frequencies lead to more extensive spatial regions of desired pressure.

V. THE SOLUTION IN THE TIME DOMAIN

It is also useful to note the relationship between the frequencies at which the problem is badly conditioned and the response of the system in the time domain when producing cross-talk cancellation. First, note that the inverse of the normalized matrix $\mathbf{C}_N$ can be written as

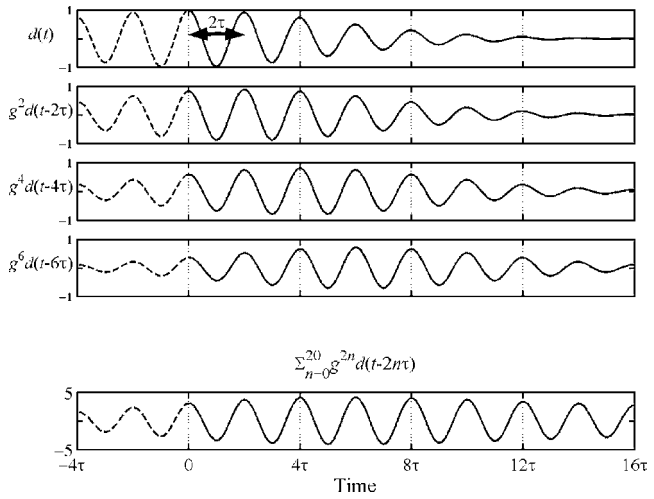

FIG. 8. An illustration of the time history $\nu_1(t)$ that results from a succession of pulses whose frequency is centered on the ringing frequency. The lower graph shows the sum of 20 terms in the series given by Eq. (5.7).

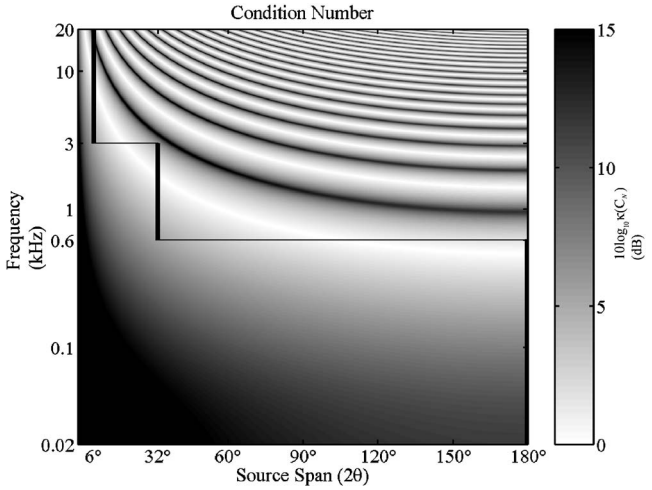

FIG. 9. The dependence of condition number $\kappa(\mathbf{C}_N)$ showing the choice of source span 2θ associated with the optimal source distribution.

$$\mathbf{C}_N^{-1} = \frac{1}{1-g^2e^{-2jk\Delta l}}\begin{bmatrix} 1 & -ge^{-jk\Delta l} \\ -ge^{-jk\Delta l} & 1 \end{bmatrix} \tag{60}$$

and this therefore specifies the frequency response function matrix $\mathbf{H}$ of the inverse filters in accordance with Eq. (22). Note that this expression can be written in terms of the time delay $\tau = \Delta l / c_0$, which is the time taken for sound to travel one path length difference. Thus,

$$\mathbf{C}_N^{-1} = \frac{1}{1-g^2e^{-2j\omega\tau}}\begin{bmatrix} 1 & -ge^{-j\omega\tau} \\ -ge^{-j\omega\tau} & 1 \end{bmatrix}. \tag{61}$$

If the desired pressure signals are written as

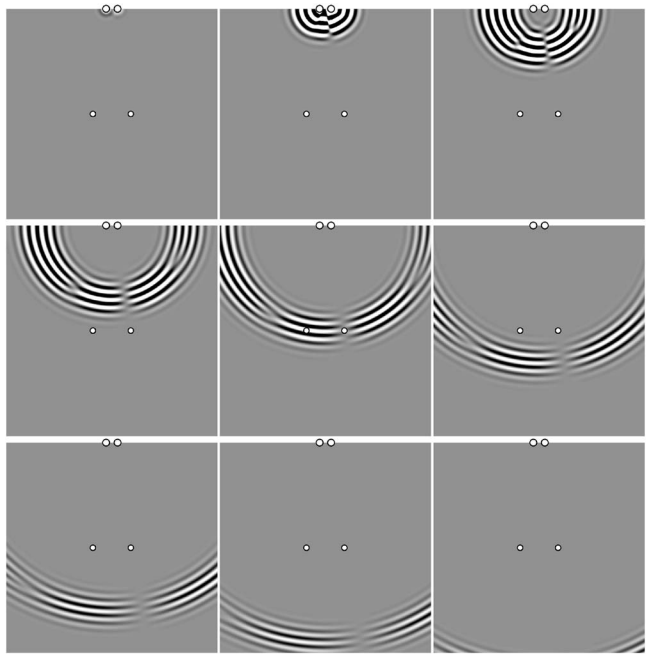

FIG. 10. The wave field generated by two sources subtending an angle 2θ of 6° at the two field points when the desired pulse at the left field point has the spectrum illustrated in Fig. 14(a) while silence is required at the right field point ($\Delta h = 9$ cm, $l = 0.5$ m, $a = 3000$, $\omega_0 = 56\,000$ rad/s).

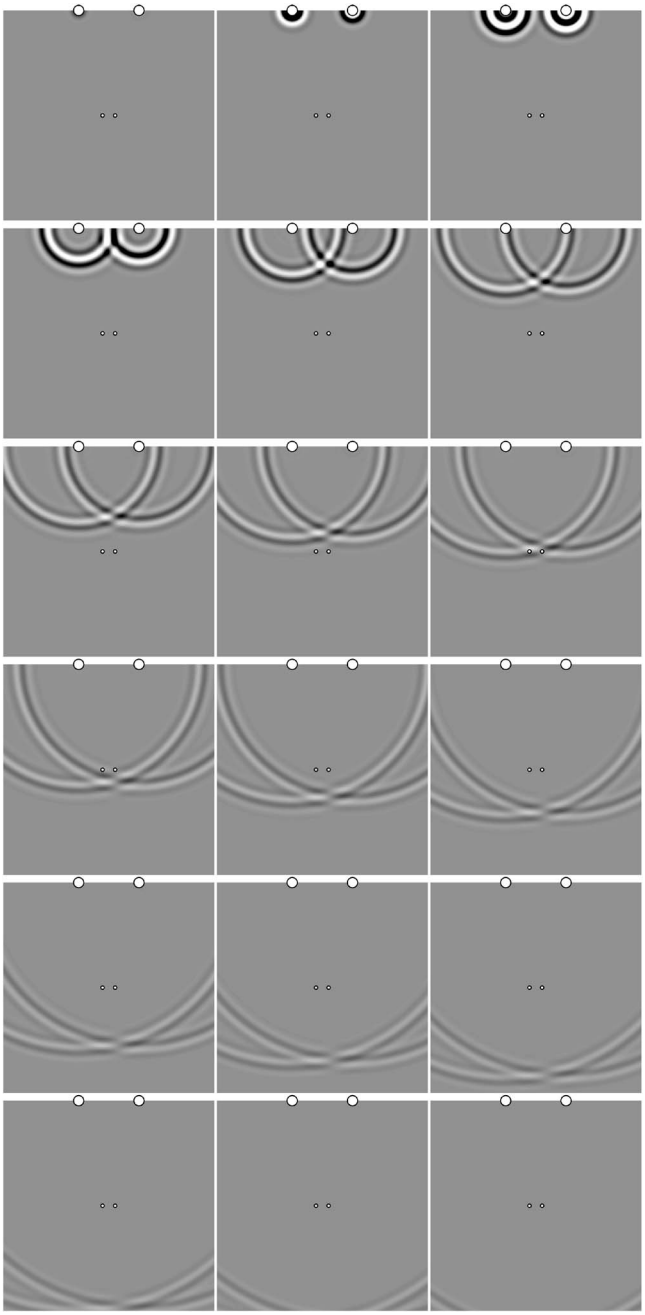

FIG. 11. The wave field generated by two sources subtending an angle 2θ of 32° at the two field points when the desired pulse at the left field point has the spectrum illustrated in Fig. 14(b) (centered on the frequency range of low condition number) while silence is required at the right field point (Δh=9 cm, l=1.56 m, a=1200, ω_0=11 000 rad/s).

$$\mathbf{p}_D = \frac{\rho_0 e^{-jkl_1}}{4\pi l_1}\begin{bmatrix} D(j\omega) \\ 0 \end{bmatrix}, \tag{62}$$

where $D(j\omega)$ specifies the frequency content of the signal derived at position 1 in the sound field, then since $\mathbf{d}=[D(j\omega),0]^T$ and $\mathbf{v}=\mathbf{H}\mathbf{d}=\mathbf{C}_N^{-1}\mathbf{d}$ it follows that the solution for the source strengths can be written as

$$\mathbf{v} = \frac{D(j\omega)}{1-g^2e^{-2j\omega\tau}}\begin{bmatrix} 1 \\ -ge^{-j\omega\tau} \end{bmatrix}. \tag{63}$$

Since it follows from the expansion

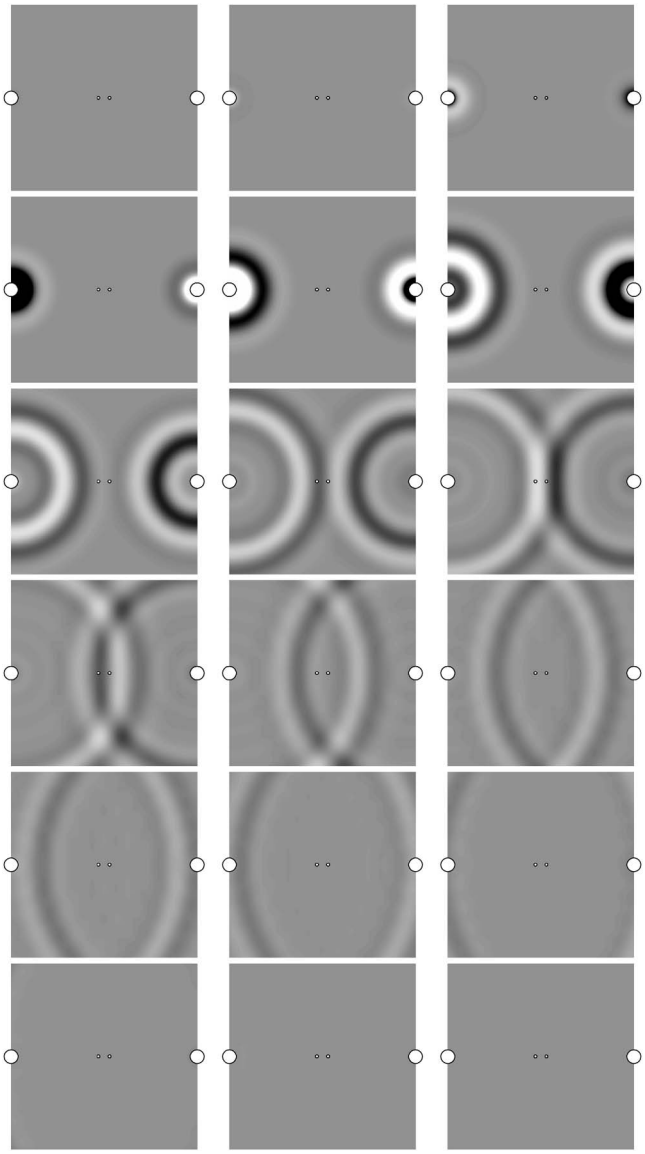

FIG. 12. The wave field generated by two sources subtending an angle 2θ of 180° at the two field points when the desired pulse has the spectrum illustrated in Fig. 14(c) while silence is required at the right field point (Δh =9 cm, l=1.5 m, a=400, ω_0=3000 rad/s).

$$(1-x)^{-1} = \sum_{n=0}^{\infty} x^n \quad \text{for } |x| < 1 \tag{64}$$

that

$$\mathbf{v} = D(j\omega)\sum_{n=0}^{\infty} g^{2n}e^{-2nj\omega\tau}\begin{bmatrix} 1 \\ -ge^{-j\omega\tau} \end{bmatrix}, \tag{65}$$

then the solution for the source strengths in the time domain can be written as

$$\nu_1(t) = d(t)^*[1 + g^2\delta(t-2\tau) + g^4\delta(t-4\tau) \ + \cdots, \tag{66}$$

$$\nu_2(t) = -gd(t-\tau)^*[1 + g^2\delta(t-2\tau) + g^4\delta(t-4\tau) \ + \cdots, \tag{67}$$

where $d(t)$ is the time domain representation of the signal $D(j\omega)$ desired at field point 1 and the asterisk denotes con-

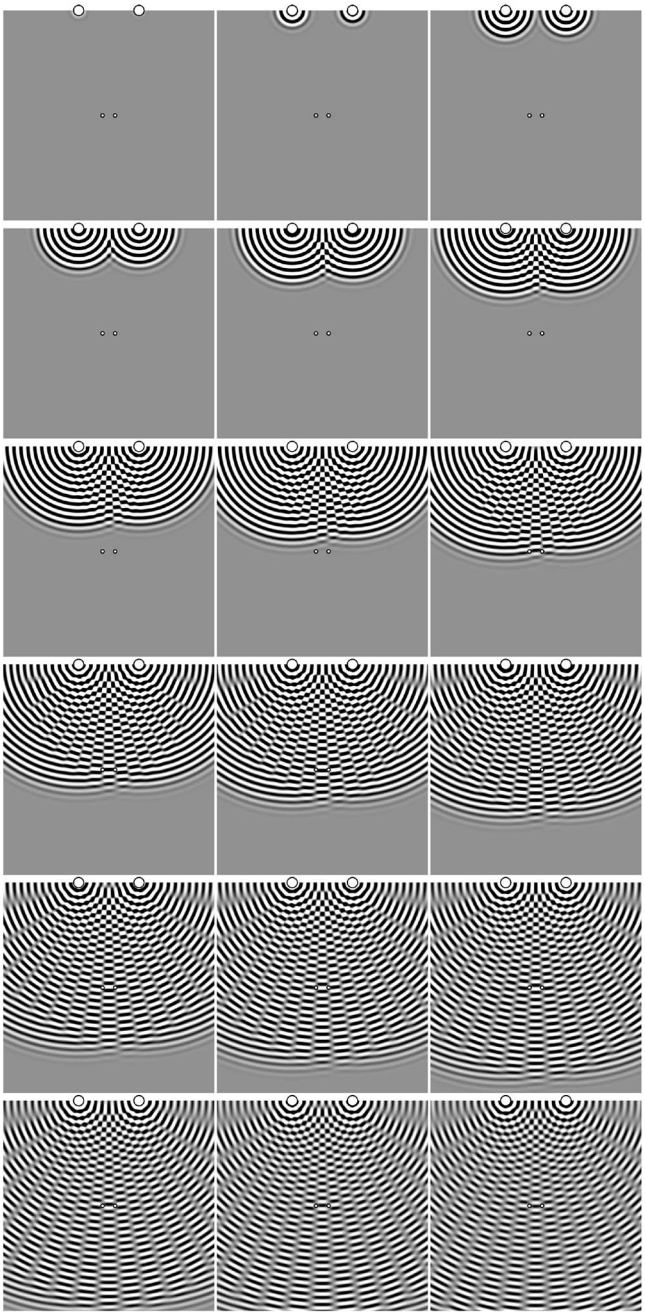

FIG. 13. The wave field generated by two sources subtending an angle 2θ of 32° at the two field points when the desired pulse has the spectrum illustrated in Fig. 14(b) (centered on the ringing frequency) while silence is required at the right field point (Δh=9 cm, l=1.56 m, a=1200, ω_0 =22 000 rad/s).

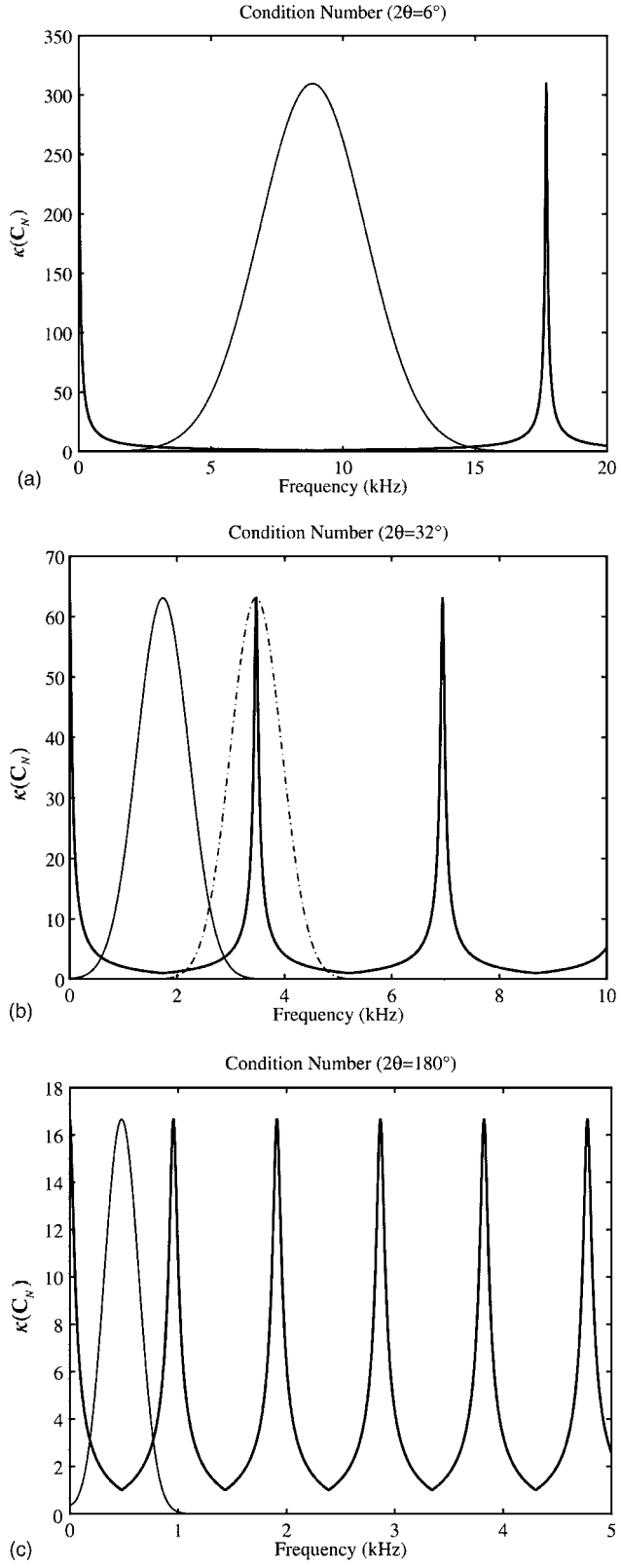

FIG. 14. Plots showing the frequency dependence of the condition number $\kappa(\mathbf{C}_N)$ and the spectra of the Gaussian pulses used in the simulations shown in Figs. 10–13 for (a) 2θ=6°, (b) 2θ=32°, (c) 2θ=180°.

volution. The above-mentioned result follows since $e^{j\omega t}$ and $\delta(t-\tau)$ are a Fourier transform pair, $\delta(\ )$ denoting the Dirac delta function. The recursive nature of this solution has already been described in some detail previously.[7] It is interesting to note that the reciprocal of the time 2τ has previously been used to denote the "ringing frequency" in the reproduced sound field and that since $(1/2\tau)=c_0/2\Delta l$, this denotes the frequency at which the path length difference Δl becomes equal to one half wavelength. The ringing frequency therefore defines the first frequency at which the inversion problem becomes ill-conditioned.

It has previously been noted when describing the Stereo Dipole system[8,15] that a reduction in the span of the angle 2θ produces an increase in the ringing frequency $1/2\tau$ such that the source outputs necessary to produce cross-talk cancella-

tion are of short duration. This argument can be developed further by considering the source outputs necessary to achieve cross-talk cancellation for a pulse of both limited time duration and limited bandwidth. Assume that the pulse in question has the time history given by

$$d(t) = e^{-\pi(at)^2} \cos \omega_0 t. \tag{68}$$

Since $e^{-j\pi(at)^2}$ has the Fourier transform given by $e^{-\omega^2/4\pi a^2}/|a|$ and the Fourier transform of a function $f(t)\cos \omega_0 t$ is given by $(1/2)[F(\omega-\omega_0)+F(\omega+\omega_0)]$ where $F(\omega)$ is the Fourier transform of $f(t)$, then

$$D(j\omega) = \frac{1}{2|a|}[e^{-(\omega-\omega_0)^2/4\pi a^2} + e^{-(\omega+\omega_0)^2/4\pi a^2}]. \tag{69}$$

The time history $d(t)$ and the Fourier spectrum $D(j\omega)$ are plotted in Fig. 6 for illustration. Note that both the duration of $d(t)$ and the bandwidth of $D(j\omega)$ are controlled by a; smaller a means "longer" $d(t)$ but "narrower" $D(j\omega)$ and vice-versa. It is also perhaps worth noting that this particular choice of pulse has the minimum product of bandwidth and duration necessary to satisfy the uncertainty principle.[16]

Now assume that the frequency ω_0 of the pulse is chosen to be one half of the "ringing frequency." This of course means that the frequency corresponds to the "well-conditioned" frequency where cross-talk cancellation is naturally easy within the sound field. Figure 7 illustrates the succession of pulses produced by source 1 in accordance with Eq. (66). Note that the separation time 2τ between the pulses is one half of the period 4τ associated with the frequency ω_0 (which is one half of the ringing frequency). As a consequence, when all the pulses are added together, a pulse of short duration results since the positive and negative parts of the successive pulses cancel. By contrast, if ω_0 is chosen to be equal to the ringing frequency, the source outputs ring on for a long duration, since the positive parts of the successive pulses are all aligned because the underlying period of the pulse is 2τ. A net output of long duration therefore results. This is illustrated in Fig. 8.

It is therefore evident that provided the frequency content of the pulse to be reproduced lies within the range of frequencies over which the inversion problem is well-conditioned, then cross-talk cancellation can be produced with a well-defined wave-field of relatively short duration. This may have psychoacoustical benefits since it is well known that the human auditory system relies on interaural time differences for localization, especially at low frequencies, while interaural envelope shifts are regarded as being important at high frequencies. Returning to Fig. 4 it is evident that there is a relatively simple relationship between the "well-conditioned" frequency range and the angle of source span 2θ. This also suggests that one may wish to use sources of narrow span for high frequencies and wider span for lower frequencies. This observation has led to the development of the "optimal source distribution" (OSD), which ideally consists of transducers that transmit different frequencies as a continuous function of angle subtended at the listener. It is also of course a more practical alternative to attribute difference frequency bands to different source spans. This is illustrated in Fig. 9, which shows the particular choice of span and bandwidth associated with a "3-way" OSD system that has been built and tested as described by Takeuchi *et al.*[11]

Figures 10–12 depict the wave fields generated by sources, respectively, at spans 2θ of 180°, 32°, and 6°. In each case the center frequency ω_0 of the pulse $d(t)$ defined by Eq. (68) was chosen to be at the center of the operational bandwidth associated with the given span. Thus since the "well-conditioned" frequencies correspond to $\Delta l = 2\Delta h \sin\theta = \lambda/4$, then the frequency $\omega_0 = 2\pi c_0/\lambda$ is given by

$$\omega_0 = \frac{\pi c_0}{4\Delta h \sin\theta}. \tag{70}$$

Note also that the value of "a" chosen in each case was modified to ensure that the pulses had a frequency content which lay in the operational bandwidth associated with each span. It is evident that cross-talk cancellation is efficiently achieved in each frequency range. By contrast, Fig. 13 depicts the wave field generated in the case of $2\theta = 32°$ when the center frequency of the pulse coincides with the "ringing frequency." This clearly illustrates the consequences of attempting cross-talk cancellation at such a frequency. The frequency content of each of the pulses used in these simulations is illustrated in Fig. 14, which also shows the condition number of $\mathbf{C}_N$ as a function of frequency in each case.

VI. CONCLUSIONS

The source of ill-conditioning in a two source/two field point model has been shown to be associated with dominance of either the "in-phase" or "out-of-phase" modes of the transfer function matrix relating the acoustic pressures at the field points to the source volume accelerations. At these specific frequencies, the spatial extent of the regions over which cross-talk cancellation is effective are found to be limited, while at well-conditioned frequencies the spatial extent of cross-talk cancellation is found to be much greater. In addition, the ill-conditioned frequencies are found to be associated with source outputs (and inverse filter impulse responses) that are of long duration in the time domain, whereas at well-conditioned frequencies, the source outputs are well-contained in time and result in "simpler" interference fields in the time domain. It is these basic principles that lead naturally to the design of virtual acoustic imaging systems such as the Stereo Dipole[7,8] that uses a source span of about 10° in order to cover an important range of audio frequencies and to the optimal source distribution[10–12] that uses a number of transducer spans to capture almost the entire audio frequency range.

[1] B. S. Atal and M. R. Schroeder, "Apparent sound source translator," US Patent No. 3,236,949 (1966).

[2] D. H. Cooper and J. L. Bauck, "Prospects for transaural recording," J. Audio Eng. Soc. **37**, 3–19 (1989).

[3] P. A. Nelson, H. Hamada, and S. J. Elliott, "Adaptive inverse filters for stereophonic sound reproduction," IEEE Trans. Signal Process. **40**, 1621–1632 (1992).

[4] P. A. Nelson, F. Orduna-Bustamante, and D. Engler, "Multi-channel signal processing techniques in the reproduction of sound," J. Audio Eng. Soc. **44**, 973–989 (1996).

[5]O. Kirkeby, P. A. Nelson, H. Hamada, and F. Orduna-Bustamante, "Fast deconvolution of multichannel systems using regularisation," IEEE Trans. Speech Audio Process. **6**, 189–194 (1998).
[6]D. B. Ward and G. W. Elko, "Effect of loudspeaker position on the robustness of acoustic crosstalk cancellation," IEEE Signal Process. Lett. **6**, 106–108 (1999).
[7]P. A. Nelson, O. Kirkeby, T. Takeuchi, and H. Hamada, "Sound fields for the production of virtual acoustic images," Letters to the Editor of the Journal of Sound and Vibration **204**, 386–396 (1997).
[8]O. Kirkeby, P. A. Nelson, and H. Hamada, "The Stereo Dipole—A virtual source imaging system using two closely spaced loudspeakers," J. Audio Eng. Soc. **46**, 387–395 (1998).
[9]J. L. Bauck, "A simple loudspeaker array and associated crosstalk canceller for improved 3D audio," J. Audio Eng. Soc. **49**, 3–13 (2001).
[10]T. Takeuchi and P. A. Nelson, "Optimal source distribution for virtual acoustic imaging," ISVR Tech. Rep. No. 288, University of Southampton, 2000.
[11]T. Takeuchi, M. Teschl, and P. A. Nelson, "Subjective evaluation of the optimal source distribution system for virtual acoustic imaging," Proceedings of the 19th Audio Engineering Society International Conference, Schloss Elmau, Germany, 2001.
[12]T. Takeuchi and P. A. Nelson, "Optimal source distribution for virtual acoustic imaging," Audio Engineering Society 110th Convention, Amsterdam, preprint No. 5372 (2001).
[13]T. Takeuchi, "Systems for virtual acoustic imaging using the binaural principle," Ph.D. thesis, University of Southampton, Southampton, UK, 2001.
[14]G. H. Golub and C. F. Van Loan, *Matrix Computations* (The Johns Hopkins University Press, Baltimore, MD, 1996).
[15]O. Kirkeby and P. A. Nelson, "Local sound field reproduction using two closely spaced loudspeakers," J. Acoust. Soc. Am. **104**, 1973–1981 (1998).
[16]D. Gabor, "Theory of communication," Journal of the Institute of Electrical Engineers (London), **93**, 429–457 (1946).

Airflow noise in telephone handsets and methods for its reduction[a)]

Michael R. Stinson,[b)] Gilles A. Daigle, and John F. Quaroni
Institute for Microstructural Sciences, National Research Council, Ottawa, Ontario K1A 0R6, Canada

(Received 1 December 2004; revised 20 April 2005; accepted 22 April 2005)

The noise in a telephone handset produced by the bursts of airflow that accompany plosive sounds such as a "p" or "t" has been investigated. Measurements have been made on a series of modified handsets, using various arrangements of ports and tubes between microphone and the exterior of the telephone mouthpiece. A narrow stream of air was used to probe the mouthpiece and the signal picked up by the microphone recorded. The use of one, two, and multiple exterior holes was considered. Two-hole approaches alleviate the static pressure buildup that occurs when a single microphone hole is used and in many cases they result in reduced noise generation; for some directions of incident airflow, though, noise can be markedly increased. This was found to be due to interaction between intersecting streams of air. By using a large number of small (less than 0.5 mm) exterior holes, the airflow noise can be reduced by over 30 dB for all incident directions of airflow. It is also beneficial to ensure that none of the exterior holes is in direct line with the sound tube leading to the microphone. [DOI: 10.1121/1.1931087]

PACS number(s): 43.38.Si, 43.70.Aj, 43.50.Ed, 43.28.Ra [AJZ] Pages: 205–212

I. INTRODUCTION

There can be significant airflow accompanying certain sounds, such as the plosive sounds "p" and "t." For example, Isshiki and Ringel[1] reported airflow rates of approximately 1000 cm^3/s during production of the stop consonant /p/. During use of a telephone, the talker's mouth is generally quite close to the mouthpiece of the telephone and this airflow can generate aerodynamic noise that is picked up by the microphone in the handset and is then audible to a listener at the remote end of the communication line.[2] Appropriate design of the mouthpiece, whether by intent or by luck, can minimize the generation of noise, so that it is not audible above other sources of noise. But this is not always the case.

Discussion of airflow noise in telephone handsets and methods for its reduction are found mainly in the patent literature. Adapting designs for windscreens that surround a microphone with various materials or structures, some approaches make use of porous or fibrous materials to reduce the noise generation.[3,4] These materials may deteriorate with time and, so, may be inappropriate. Rabe[5] makes use of a shaped sound tube between the exterior of handset and the microphone; this enables frequency shaping of the signal and reduction of certain bands of noise, but it does not prevent the formation of acoustical noise. Komoda and Murata[6] describe a telephone mouthpiece for which the distance between the single entrance hole and the microphone is increased using a transverse duct, claiming that the wind noise levels will decrease more rapidly than speech signals as the duct length is increased. Dou *et al.*[7] reduce airflow noise by placing a microphone within a recessed area of the mouthpiece and covering the recess with a thin film. Without no exposed entrance holes, there will be no noise generated. This approach is unsuitable for telephone handsets, though, because of fabrication challenges and the need to have the microphone located a considerable distance inside the shell of the handset for prevention of electrostatic discharge. Noise cancellation approaches[8,9] can be applied, although these do not reduce the noise generation at the source. There has been considerable work on the acoustical radiation of air jets and their interaction with flat surfaces and implications to wind-driven musical instruments,[10] but nothing directly relevant to the noise produced in handset entrance holes.

A design that has found its way into existing telephone handsets is that of Oku.[11] He suggests the use of a plurality of outer microphone holes in a mouthpiece casing leading into an air chamber and an inner microphone hole leading to the microphone. There is no restriction placed on the size of outer holes and, in fact, there is no mention of airflow noise at all. More recently, Choi *et al.*[2] specifically addressed the "air blow" noise due to plosive consonants. His solution to this problem can be applied to cell phones. An array of small holes, referred to as a wind filter, allows airflow to pass right through a thin "flip-style" plate in which microphones are located away from the airflow. There is no static pressure buildup during periods of airflow and no significant noise generation. This approach, though, would not be immediately applicable to the handset used with a conventional desktop telephone without considerable modification to allow air to pass freely through the interior of the handset.

In this article, the mechanisms of airflow noise generation will be examined, making use of a series of handsets having different configurations of holes and chambers between the exterior of the mouthpiece and the microphone inside. Measurements of noise will be made using a stable airflow simulator. Mouthpieces having one, two, and mul-

[a)]Portions of this work were presented at the 148th Meeting of the Acoustical Society of America as paper 4pEA4, entitled "Reduction of airflow noise in telephone handsets."

[b)]Electronic mail: mike.stinson@nrc-cnrc.gc.ca

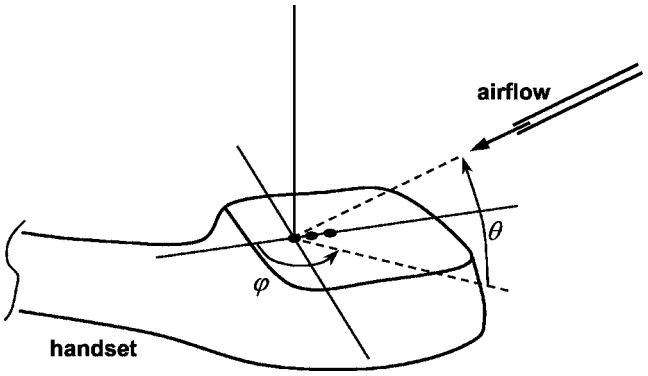

FIG. 1. Sketch of the approach used to generate airflow noise at the mouthpiece of a telephone handset. An airstream from the nozzle can be aimed at desired locations. The direction of flow is specified through the azimuthal angle ϕ and the elevation angle θ.

tiple exterior holes will be considered in turn. The optimal approaches identified will be shown to reduce noise generation by over 30 dB.

II. MEASUREMENT OF AIRFLOW NOISE

An airflow simulator was constructed to simulate the gusts of air that project from the mouth while talking (see Fig. 1). The source of air was a compressed air line with a pressure reduction valve. The exit nozzle was stainless steel tubing (3 mm o.d./2 mm i.d.). The apparatus produced a collimated stream of air that made no perceptible noise. The direction of the flow, relative to each test telephone handset, is specified through an azimuthal angle φ and an elevation angle θ. By having a narrow stream of air, specific features on the mouthpiece can be selected for acoustical excitation.

The collimation is shown in Fig. 2. A TSI hot wire anemometer has been used to measure the flow velocity as a function of transverse position. At a distance of 20 mm from the nozzle, the air stream has a width of 2 mm. Additional measurements showed that the integrity of the stream was

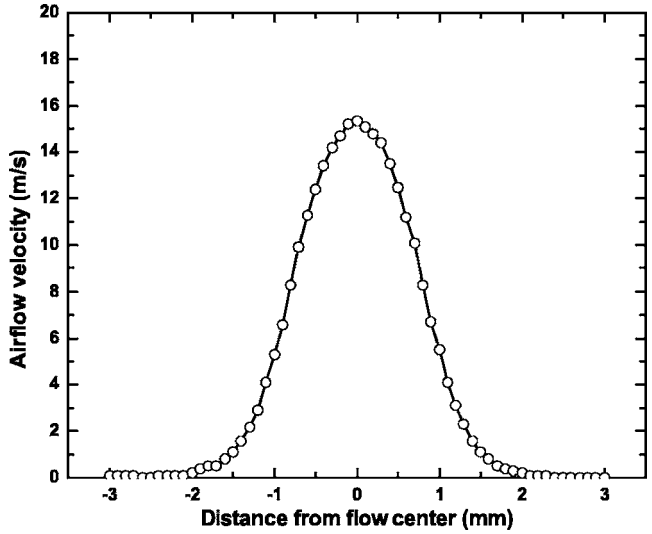

FIG. 2. The collimation of the airstream as measured with a hot wire anemometer. Flow velocity as a function of transverse position is shown, at a distance of 20 mm from the nozzle. The air stream has a width of 2 mm here.

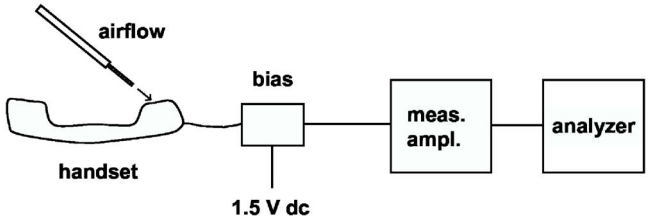

FIG. 3. The measurement system used to obtain noise spectra in response to airflow impinging on the exterior microphone ports.

maintained for a distance of approximately 50 mm. The anemometer was also used to survey the velocity of air flowing from the mouth when a talker produced a "p" sound. A range of values was obtained that depended on the strength of the plosive sound and how long it was sustained. At a distance of 20 mm from the mouth, air speeds of 6–18 m/s were found. These speeds are comparable to those produced by the airflow simulator. The gusts of air produced during plosive sounds are also collimated: Widths of these airstreams are 2–4 mm in width at a distance of 20 mm from the mouth, roughly comparable to the simulator airflows.

For all measurements, the nozzle was 20 mm away from the mouthpiece. Both handset and airflow simulator were positioned on tripods located some distance from other objects that might affect the local airflow. There is a wide range of positions in which a handset might be held during typical usage. The mouth of a user might be directed normally at the face of the mouthpiece (elevation angle 90°) or at more grazing incidence (an elevation angle of perhaps 30°). The azimuthal position of the mouth (as defined by the angle φ in Fig. 1) will depend on several factors, such as the size and shape of the handset, the handedness of the user, and how the user fits the earpiece to his pinna. For a mouth located closer to the earpiece than the mouthpiece, we have an azimuthal angle of 0°. This might be considered fairly typical, but users can often be observed with their mouths off to the side of the mouthpiece, at ±90°; when used as part of an intercom system, handsets are sometimes used upside down (with an azimuthal angle of 180°). Our challenge is to provide reductions in airflow noise for all manners of usage. Thus, it is necessary to consider airflow from nearly every possible direction.

The airflow over the mouthpiece holes generates broadband noise, clearly audible. To quantify these observations, noise spectra were obtained. The measurement system is shown in Fig. 3. The signal generated at the microphone was fed to a HP 3567A spectrum analyzer via a bias circuit and amplifier. There was ample signal, relative to ambient background noise levels, and no gain from the measuring amplifier (Brüel & Kjær 2610) was required. The power spectrum was determined at 400 linearly spaced frequencies between 0 and 12.8 kHz. Averaging was enabled in the data acquisition to ensure good signal-to-noise: each spectrum is the direct rms average of 16 consecutive spectra.

An equivalent noise level can be obtained from each measured power spectrum, for comparison. The different frequency components need to be weighted according to their importance to the listener—here, we adopt an A-weighting.

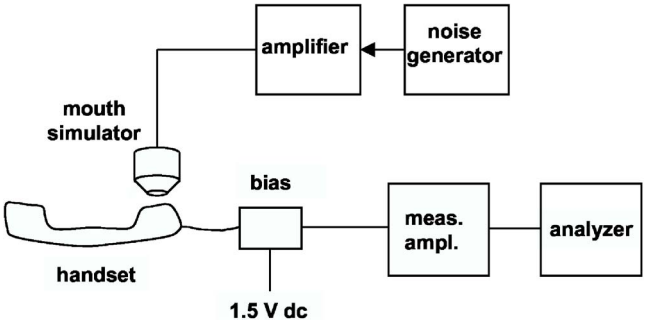

FIG. 4. The measurement approach used to determine speech transmission of the telephone handset.

For a measured spectrum V_n (dB) and an A-weighting function W_n (dB), with n being the frequency index, the total power is proportional to

$$P = \sum_n 10^{(V_n - W_n)/10}. \quad (1)$$

Conversion to equivalent sound pressure level requires specification of the microphone sensitivity s. Subsidiary measurements on the various microphone assemblies used in this study gave a typical sensitivity of $s = 18$ mV/Pa. The equivalent noise level (in dB) is then

$$N = 10 \log[P/(p_0 s)^2], \quad (2)$$

where p_0 is the reference sound pressure level of 20 μPa.

III. MEASUREMENT OF SPEECH TRANSMISSION

We will be considering several different configurations of cavities and tubes between microphone and outside of handset. An approach that successfully reduces the airflow noise might also reduce the transmission of speech into the microphone. To monitor this possibility, speech transmission was measured using the arrangement sketched in Fig. 4. White noise from a Brüel & Kjær 1405 noise generator drives a Brüel & Kjær 4227 mouth simulator, located 25 mm from the mouthpiece of the test handset. The handset is oriented so that the center of the mouth simulator, relative to the center of the mouthpiece of the handset, is at an azimuth of 270° and an elevation of 45°. The electrical signal picked up by the microphone is measured with the HP spectrum analyzer. This measurement arrangement was designed for quick interchange with the noise measurement of Sec. II—it was not intended to follow any specific ITU standards recommendations.[12]

IV. SINGLE-HOLE APPROACHES

Several mouthpiece arrangements having a single microphone hole on the outside of the mouthpiece will be considered. The telephone handset sketched in Fig. 5 was used as the starting point. This handset A1, with side and top views shown on the two left panels, has a single hole that leads from the exterior of the handset to the microphone. The hole is 20 mm long, with a diameter of 2.0 mm at the entrance and 2.3 mm at the inner end. (There are two other holes present in this configuration, but they are purely decorative and not involved in the transmission of sound to the microphone.) The physical separation between microphone and the exterior of the handset reduces the possibility of electrostatic discharge. Note that the detailed internal construction is not shown, only the features relevant to the acoustical performance are included.

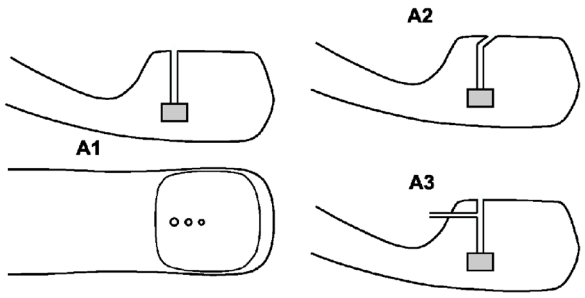

FIG. 5. Telephone handsets having a single exterior microphone hole in the mouthpiece. Side and top views of handset A1 are shown to the left. This handset has a single straight hole to the microphone. The two holes indicated on the top view are decorative and not relevant acoustically. Handsets A2 and A3, shown to the right, introduce an angled bend and a side vent, respectively.

Measured noise spectra for this handset are shown in Fig. 6, for airflow directed at the entrance hole along several combinations of azimuthal and elevation angles. All spectra are fairly flat up to about 2 kHz and roll off rapidly at higher frequencies. Repeat measurements (not shown here) indicate that the overall level of the spectra is quite sensitive to the targeting of airflow at the entrance hole—variations of up to 5 dB can arise as the airflow is shifted marginally about the entrance hole position and are indicative of the repeatability of the measurements. In these and all other measurements, the airflow nozzle was adjusted to maximize the noise being produced. For this mouthpiece configuration, there is little dependence on azimuthal angle φ. There is a significant dependence on the angle of elevation θ, with the highest levels of noise found for an angle of 60°. Equivalent noise levels have been computed from the measured spectra using Eq. (1). The results for handset A1 are summarized in Table I.

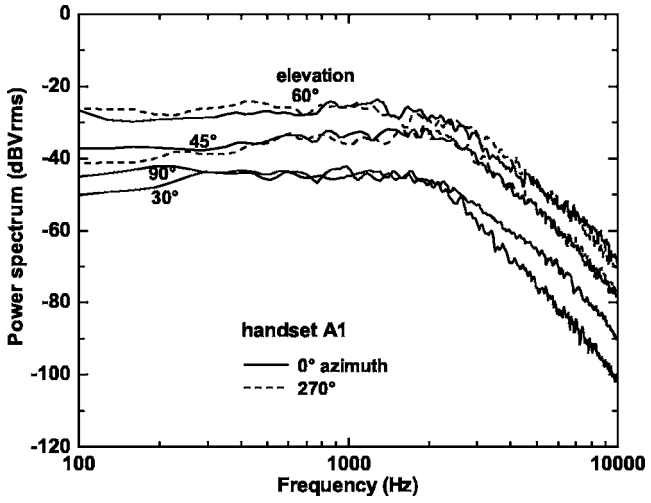

FIG. 6. Measured noise spectra for handset A1, for several directions of incident airflow. Results for this handset are essentially independent of the azimuthal angle.

TABLE I. Measured equivalent noise levels for airflow directed at the microphone port of telephone handset A1. No dependence on azimuthal direction of airflow was noted, so measured levels at different azimuths and repeat measurements have all been listed for each elevation angle.

Elevation (°)	Equivalent noise levels (dB)	Mean level (dB)
0	88.1	88
30	97.4	97
33	94.5	95
45	107.5, 112.5, 112.0, 107.6, 109.7	110
60	116.2, 116.4, 112.8, 115.8, 118.2, 112.9, 114.9	115
90	94.2, 101.6	98

The multiple entries for some of the elevation angles correspond to both repeat measurements and different azimuthal angles—we are assuming that there is no dependence on azimuthal direction of airflow for this handset, so measured levels at different azimuths can be treated as repeat measurements. For elevation angles of 45°, 60°, and 90°, mean noise levels of 110, 115, and 98 dB, respectively, are obtained: These results can be used as a baseline measure of performance when other mouthpiece configurations are considered.

Also sketched in Fig. 5 are two other approaches that make use of a single exterior microphone hole. For handset A2, there is a 40° bend in the microphone hole, approximately 3.5 mm from the outside surface, with the bend angled toward the 180° azimuth. The rationale for this approach is to modify the manner in which an airflow interacts with the entrance port. Model A3 considers a different approach for reducing airflow noise: a vent located 5 mm from the entrance leads out the side of the mouthpiece, at an azimuthal angle of 295°—the vent intends to prevent pressure buildup in the microphone hole and the subsequent generation of turbulent flow.

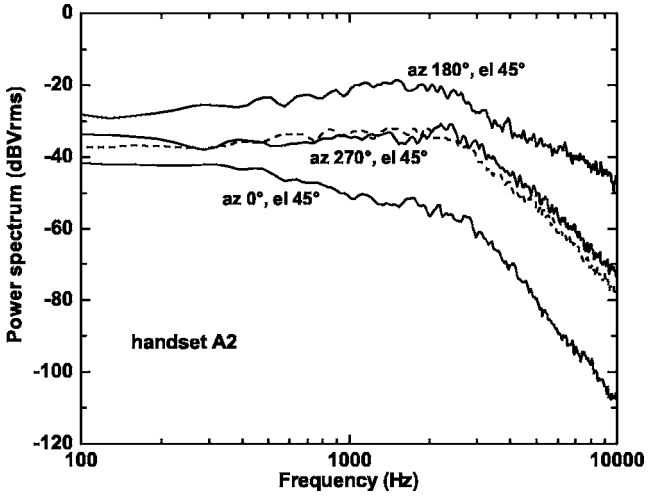

FIG. 7. Measured noise spectra for handset A2, shown as the solid curves, for azimuths of 0°, 180°, and 270° and for an elevation angle of 45°. The dashed curve shows the result for handset A1 at 270° azimuth and 45° elevation.

Some measured spectra for handset A2 are shown in Fig. 7 as the solid curves, all for an elevation angle of 45°. The noise spectrum for the baseline handset A1 is included as the dashed curve. There is a significant variation with azimuthal orientation of the airflow for this handset. For an azimuth of 0°, the spectrum is significantly lower than the corresponding measurement for handset A1. The angling of the microphone hole is clearly beneficial in this case. However, when the airflow is from an azimuth of 180°, the spectrum is higher than the baseline. The observations are confirmed by computation of the equivalent noise levels, giving 98 dB for 0° azimuth and 123 dB for 180° azimuth. The equivalent noise levels for these and all other measurements are tabulated in Table II.

Measured noise spectra for handset A3 are shown in Fig. 8. The solid and dotted curves both correspond to an eleva-

TABLE II. Measured equivalent noise levels (in dB) for all telephone handsets tested, for different orientations (azimuthal and elevation angles) of airflow. The numbers for the baseline handset A1 are the mean values presented in Table I. The results for the multiple-hole configurations C1–C4 are independent of azimuthal angle.

	az 0°		az 90°		az 180°		az 270°		
Configuration	el 45°	el 60°	el 45°	el 60°	el 45°	el 60°	el 45°	el 60°	el 90°
One hole									
A1	112	115	110	115	110	115	110	115	98
A2	92	112			123	112	110	113	106
A3	98	96					102	103	107
Two hole									
B1	93	99	102	95			120	113	102
B2	89	96	81	90	111	107	116	118	100
B3	120	119			100	106	94	103	107
B4	120	118			109	110	101	99	111
B5	94	100			107	108	102	111	108
Multiple hole									
C1							84	90	91
C2							81	63	51
C3							75		
C4							46	48	46

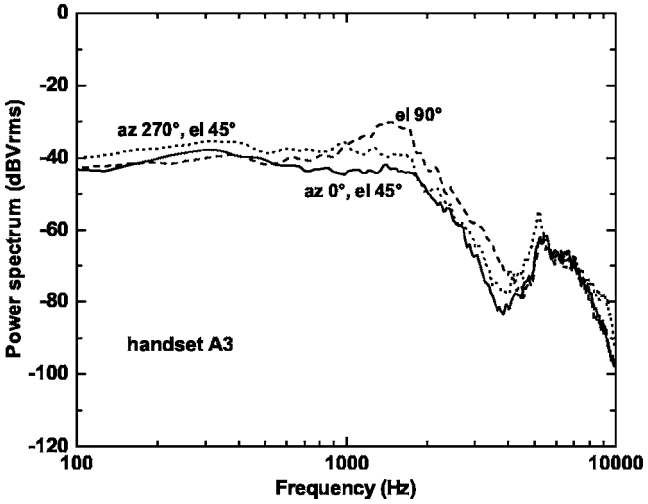

FIG. 8. Measured noise spectra for handset A3. The solid and dotted curves correspond to azimuths of 0° and 270°, respectively, and an elevation angle of 45°. The dashed curve shows the result for airflow normally incident, i.e., a 90° elevation.

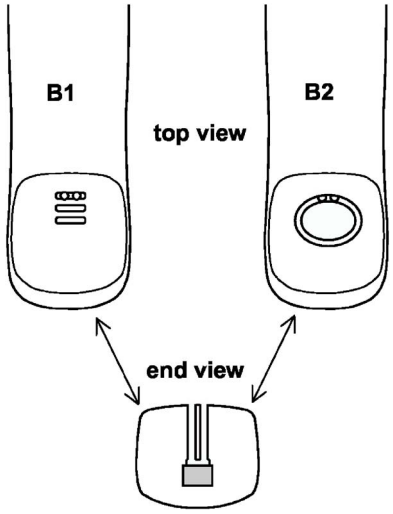

FIG. 9. Two handsets that have two exterior microphone holes. The 2.5-mm holes lead to a cavity immediately in front of the microphone. For handset B1, the microphone holes originate in one of three shallow depressions; for handset B2, the microphone holes originate in a shallow elliptical depression. For all measurements on these handsets, the airstream was directed at the hole on the side toward the 90° azimuth.

tion angle of 45°, for azimuths of 0° and 270°, respectively. Their similarity indicates azimuthal symmetry for this microphone hole configuration. Equivalent noise levels are about 10 dB lower than those obtained for handset A1. For an elevation of 60°, noise levels were about 15 dB lower. For normal incidence (90° elevation), though, the measured spectrum (shown as the dashed curve in Fig. 8) yields noise levels 10 dB higher than handset A1.

V. TWO-HOLE APPROACHES

Several two-hole approaches were investigated as a means for reducing airflow noise. The idea is that a gust of air striking one microphone hole can flow down the hole and out the other hole; there is no pressure buildup and no obstruction of the incident stream, so the generation of noise may be reduced.

Two variants are shown in Fig. 9. Both make use of two 2.5-mm-diam holes leading from the exterior of the mouthpiece to a cavity immediately in front of the microphone. The holes are arranged transverse to the long axis of the handset, i.e., along the 90°/270° azimuth, and are 2 mm apart. For handset B1, the microphone holes originate in one of three shallow depressions (10 mm long, 2 mm wide, and 1 mm deep). For handset B2, the microphone holes originate in a shallow elliptical depression, approximately 1 mm deep and 2 mm wide. For all measurements on these handsets, the airstream was directed at the hole on the side toward the 90° azimuth. The cavity in front of the microphone had a diameter of 10 mm and depth of 2 mm.

Figure 10 shows measured noise spectra for handset B1. Various directions of airflow, indicated on the figure, have been used. The dashed curve corresponds to the baseline handset A1, for azimuth 0° and elevation 45°. There is significant reduction of noise, in some cases. For example, the equivalent noise level (Table II) for this handset at azimuth 0° and elevation 45° is 17 dB lower than for handset A1. For an azimuth of 270°, however, levels are actually quite a bit higher. A hypothesized explanation for this behavior is sketched in Fig. 11. When the airflow is from an azimuth of 90°, the airstreams in towards the incident microphone hole and out from the other hole do not intersect, and relatively smooth flow lines develop, as sketched in panel (a). However, when the airflow is from an azimuth of 270° and directed at the left hole as shown in panel (b), the airstream outgoing from the right hole is going to cross the path of the ingoing flow. Unsteady, turbulent flow and increased noise generation are anticipated. To test this hypothesis, a deflector flap (width 8 mm at attachment point and increasing to 22 mm over its 35 mm length) was put in place as shown in panel (c) and the measurements repeated. The results are displayed in Fig. 12, comparing spectra with and without deflector. There is a large reduction of the noise, nearly

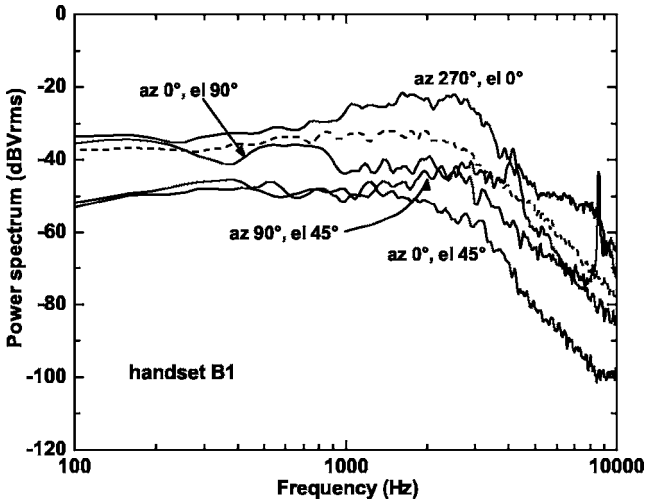

FIG. 10. Measured noise spectra for handset B1, the first in a series of handsets having two exterior microphone holes, for several combinations of azimuthal and elevation angles. For comparison, the spectrum measured for the one-hole handset A1 at 270° azimuth and 45° elevation are shown as the dashed curve.

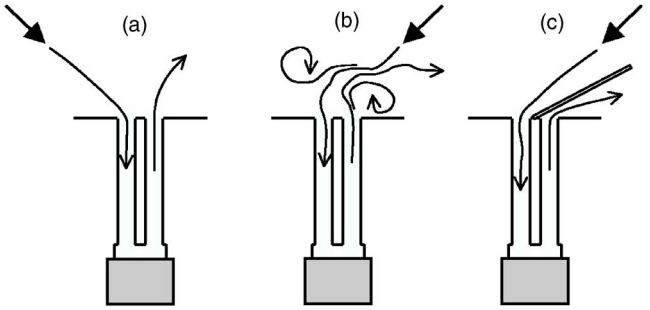

FIG. 11. Mechanism of increased noise for a two-hole handset when airstreams intersect. When the airflow is from an azimuth of 90°, as shown in panel (a), the airstreams in towards the incident microphone hole and out from the other hole do not intersect. When the airflow is from an azimuth of 270°, as shown in panel (b), the airstream outgoing from the right hole crosses the path of the ingoing flow. Unsteady, turbulent flow and increased noise generation are anticipated. A deflector was put in place as shown in panel (c) to test this hypothesis.

20 dB, when the deflector is in place. It is concluded that intersecting flow streams need to be avoided.

Three other two-hole configurations have been considered, designated B3, B4, and B5. For handset B3, two microphone holes aligned along the 0°/180° azimuth and spaced 4.5 mm apart lead inwards through the handset shell, about 2 mm, to a circular chamber, then along a single hole to the microphone. Top and side views of this handset are shown on the left half of Fig. 13. The chamber is 10 mm in diameter and 0.5 mm in depth. Handset B4 is the same as B3, except that the chamber is somewhat larger, being a conical volume with a depth of 3 mm. For handset B5, there are two slots 1.6×5 mm^2 leading through 3 mm of a teflon inset to the inner chamber; they are angled at 45° toward the 180° azimuth. The chamber is 2 mm deep. The single hole leading to the microphone is also angled somewhat, to avoid lining up with one of the slots. This handset is shown on the right half of Fig. 13. In all measurements on these three handsets, the airflow was directed at the 180° azimuth hole (to the right, in Fig. 13).

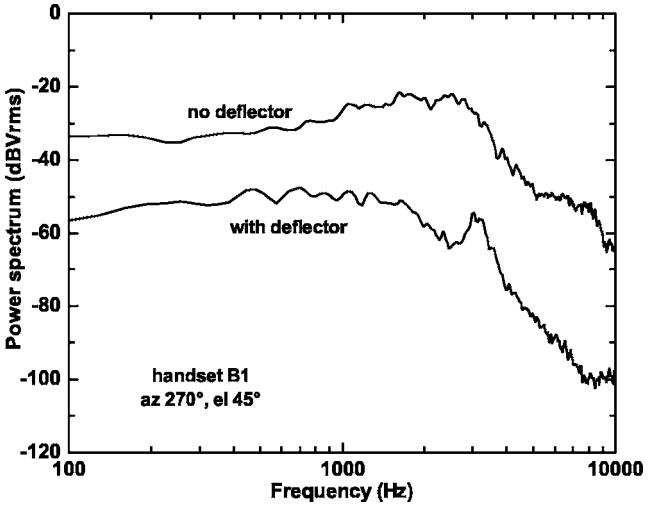

FIG. 12. Measured noise spectra for handset B1, with airflow directed from an azimuth angle of 270° and an elevation angle of 45°. The top curve corresponds to situation (b) in Fig. 11, without a deflector; the bottom curve corresponds to situation (c) with a deflector.

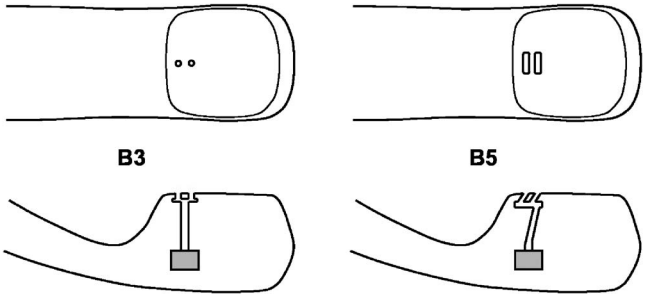

FIG. 13. Top and side views of two other handsets, B3 and B5, that make use of two exterior microphone holes. Handset B4 is similar to B3, except the mixing chamber is larger. In all measurements on these three handsets, the airflow was directed at the 180° azimuth hole (to the right, as shown here).

The range of noise spectra obtained for the two-microphone-hole approaches is indicated in Fig. 14. For each of the five handsets, the spectra having the highest noise level and the spectra having the lowest noise level, for an elevation angle of 45°, are shown. All handsets show approximately the same range of results—some azimuth angles are good for reducing the airflow noise, others lead to increased flow stream interactions and increased noise. The equivalent noise levels for these handsets are tabulated in Table II. An acceptable solution needs to work for all incident angles of the airflow, not just some.

VI. MULTIPLE-HOLE APPROACHES

The use of a large number of small exterior microphone holes can reduce considerably the problem of interacting flow streams. Outgoing airflow will be distributed between several smaller airstreams, lessening the possibility and strength of interaction. Four configurations were investigated. For handset C1, an array of 15 holes, each 0.97 mm in diameter, led through the handset casing to a cylindrical chamber 3 mm deep. A single hole 2 mm in diameter led from there to the microphone; this hole was angled slightly so it would not be in line with incoming airflow through any

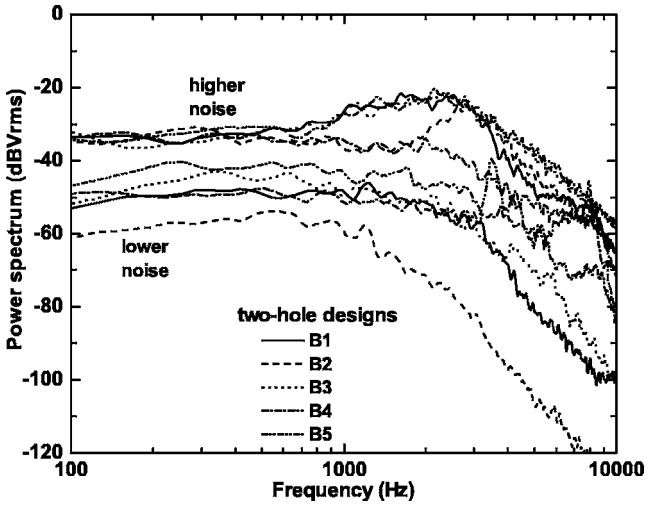

FIG. 14. Measured noise spectra for the two-hole handsets, B1–B5. For each handset, the spectra having the greatest noise and the lowest noise are shown.

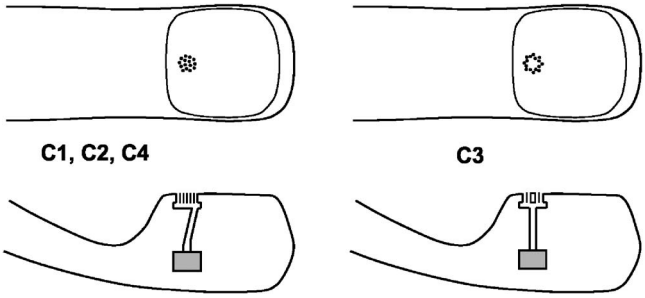

FIG. 15. Multiple-hole approaches for airflow noise reduction. Handsets C1, C2, and C4 make use of 15 exterior holes of diameter 0.97, 0.57, and 0.34 mm, respectively. Handset C3 has 16 exterior holes of diameter 0.57 mm arranged in an annular pattern.

of the exterior holes. This construction is sketched on the left side of Fig. 15, showing top and side views. Handsets C2 and C4 had the same construction except for the size of holes: handset C2 used 0.57-mm-diam holes and handset C4 used 0.34-mm-diam holes. Handset C3 had 16 holes of 0.57 mm diameter arranged in an annular pattern, as shown on the right side of Fig. 15. The inner microphone hole was not angled in this configuration; airflow through any of the outer holes was not directly incident on this inner hole.

Figure 16 shows the noise spectra for handset C1 for several directions of airflow. Computed equivalent noise levels, for this and the other multiple-hole handsets, are included in Table II. The noise levels are considerably less than those obtained with the baseline handset A1. Nearly 25 dB of noise reduction is obtained for elevation angles of 45° and 60° and about 7 dB for 90° elevation. No significant dependence on azimuthal angle was found. The use of multiple holes is clearly advantageous.

In Fig. 17, some noise spectra for handsets C2 (solid curves) and C3 (dashed curve), both having 0.57-mm-diam outer holes, are shown. The airflow noise is lower with these smaller holes than with the 0.97-mm diameter of handset C1. The use of an annular pattern of holes to avoid any airstreams from the outer holes entering the inner hole gives 6 dB of extra reduction. In Fig. 18, noise spectra are shown

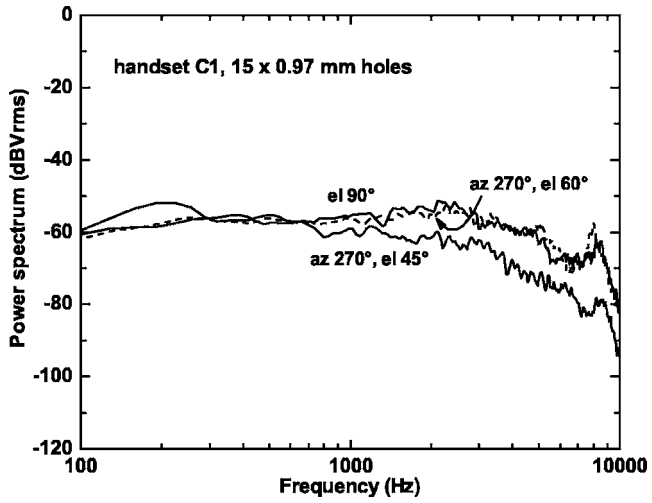

FIG. 16. Measured noise spectra for handset C1, for several directions of incident airflow. There are 15 exterior holes of diameter 0.97 mm.

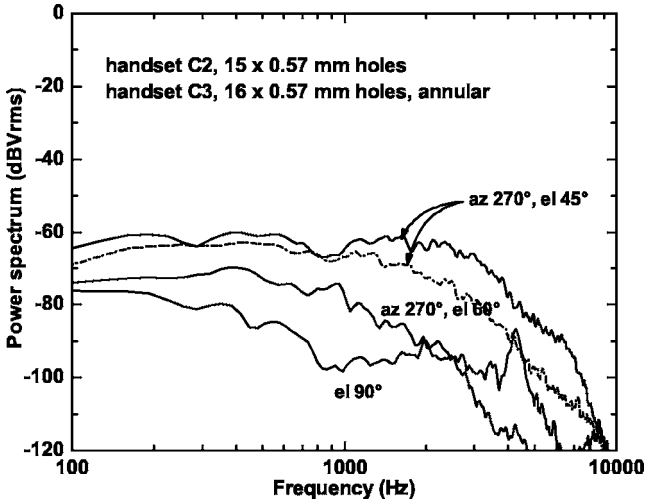

FIG. 17. Measured noise spectra for handsets C2 (solid curves) and C3 (dashed curve). Both make use of 0.57 mm diameter exterior holes.

for handset C4, outer holes 0.34 mm in diameter. Airflow noise is reduced even further. For comparison, the spectrum for the original handset A1, at azimuth of 270° and elevation of 45°, is also shown. This handset is more than 50 dB quieter than handset A1, for all angles of incidence that were measured (Table II).

VII. SPEECH TRANSMISSION

The very large reductions of airflow noise achieved with the multiple-hole configurations must not be accompanied by a loss of speech transmission. To verify that this is not the case, speech transmission curves were obtained as described in Sec. III. These are shown in Fig. 19 for handsets A1 and B1, as representatives of the one- and two-hole approaches, and for the multiple-hole handsets C1, C2, C3, and C4. All the transmission curves are clustered together up to 2.5 kHz. At higher frequencies, handset B1 shows somewhat reduced

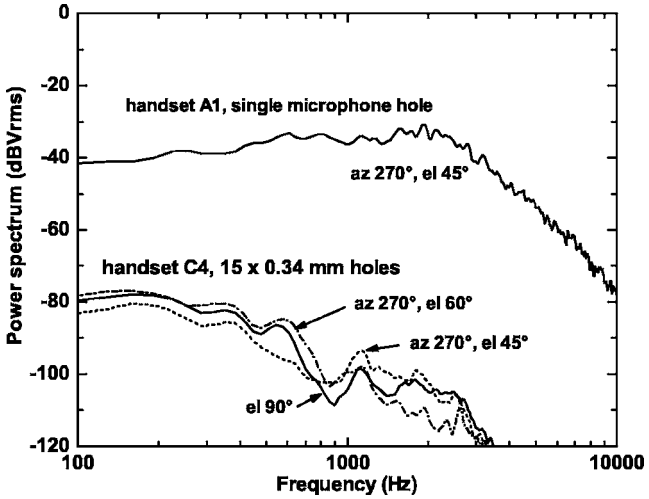

FIG. 18. Measured noise spectra for handset C4 for several directions of incident airflow. There are 15 exterior holes of 0.34-mm diameter. Noise levels are greater than 50 dB below those obtained with the one-hole handset A1.

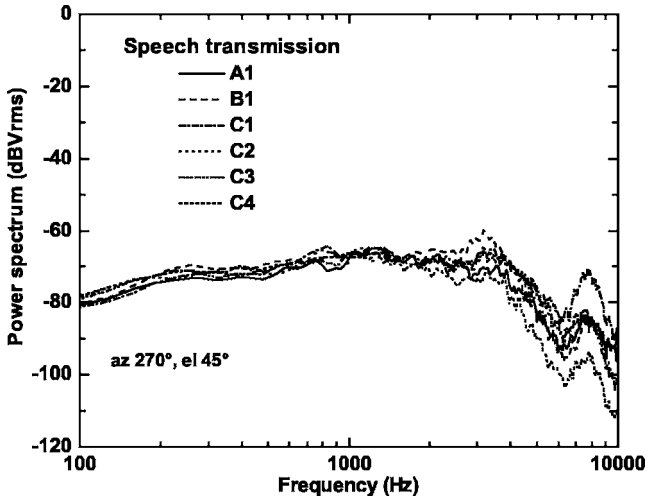

FIG. 19. Measured speech transmission spectra for the one-hole handset A1, for the two-hole handset B1, and for the multiple-hole handsets C1–C4. White noise was played through a mouth simulator and the handset response measured.

speech transmission. However, the multiple-hole configurations have not lost any speech transmission performance relative to the baseline handset A1.

VIII. CONCLUDING REMARKS

A variety of approaches have been investigated to reduce the noise produced in telephone handsets by the gusts of air produced by persons talking into the mouthpiece.

With a single microphone hole leading from the mouthpiece exterior to the internal microphone, there is a temporary pressure buildup within the hole causing instability in the oncoming airflow and leading to turbulent noise. Angling of the microphone hole can help for some directions of airflow incidence but not others. In consideration of the different ways that a handset is held by different users, a solution is desired that is effective for all angles of incidence.

By using two exterior microphone holes, merging in a common chamber somewhere before the microphone, the pressure buildup problem can be avoided. A gust of air striking one of the holes can travel down the hole and out the other hole. Several two-hole approaches were considered. Significant reduction of airflow noise was obtained, for some directions of incident airflow. For other directions, however, the noise was greater. A problem was identified: If the air stream exiting the second hole crosses the path of the incoming stream, considerable noise can be generated in the interaction region and transmitted to the microphone.

It was found that the use of a large number of entrance holes reduced this problem of interacting air streams. An array of 15 entrance holes, each 0.97 mm in diameter, leading into a chamber 2 mm inside the mouthpiece, with a single inner hole leading to the microphone, was found to be effective at reducing airflow noise for all directions of incident airflow. Reductions of 25 dB were obtained. The use of an array of holes was suggested by Oku[11] although he set no restriction on size of hole—from his figures, a diameter of 2 mm is suggested, too large to effectively reduce airflow noise. It was noted that the entrance holes should not be in direct line with the inner hole leading to the microphone. Further improvement was obtained by reducing the size of the entrance holes more. With 15 entrance holes, each 0.34 mm in diameter, the airflow noise is reduced by over 50 dB for all incident directions of airflow. The transmission of speech, from talker to the microphone, was maintained for these multiple-hole approaches. Whether additional noise reduction is possible with even smaller holes remains a topic for future investigation.

ACKNOWLEDGMENTS

The authors would like to acknowledge Mitel Networks for providing a number of telephone handsets and for funding some of this work. Discussions with Philippe Moquin are appreciated.

[1]N. Isshiki and R. Ringel, "Air flow during the production of selected consonants," J. Speech Hear. Res. **7**, 233–244 (1964).
[2]S. Choi, W. Moon, and J. H. Lee, "A new microphone system for near whispering," J. Acoust. Soc. Am. **114**, 801–812 (2003).
[3]G. W. Plice, "Wind and breath noise protector for microphones," U.S. Patent No. 4,887,693 (19 December 1989). A brief review appears in J. Acoust. Soc. Am. **90**, 1217 (1991).
[4]N. Toki, "Transmitter structure for limiting the effects of wind noise on a microphone," U.S. Patent No. 6,091,830 (18 July 2000). A brief review appears in J. Acoust. Soc. Am. **110**, 2822 (2001).
[5]K. W. Rabe, "Radiotelephone having a non-resonant wave guide acoustically couple to a microphone," U.S. Patent No. 5,890,072 (30 March 1999).
[6]M. Komoda and Y. Murata, "Telephone mouthpiece for preventing wind noises and method for reducing wind noises input thereto," U.S. Patent No. 5,701,354 (23 December 1997).
[7]X. Dou, J. Castaneda, X. Wu, D. Zak, C. Yeh, and K. W. Wyatt, "Flush-porting method and device for reduction of wind-induced noise in a microphone," U.S. Patent No. 5,905,803 (18 May 1999).
[8]P. L. Regen and W. H. Kingsley II, "Noise cancelling apparatus for a telephone handset," U.S. Patent No. 5,239,578 (24 August 1993).
[9]A. S. Nasar, C. Birman, and D. R. Raichel, "Considerations in applying noise cancellation techniques to telephones," J. Acoust. Soc. Am. **99**, 2505–2529 (1996).
[10]R. Khosropour and P. Millet, "Excitation of a Helmholtz resonator by an air jet," J. Acoust. Soc. Am. **88**, 1211–1221 (1990).
[11]H. Oku, "Transmitter for communication equipment," U.S. Patent No. 5,144,656 (1 September 1992).
[12]For example, International Telecommunication Union ITU-T Recommendation P.64 "Determination of sensitivity/frequency characteristics of local telephone systems."

Noise screening effects of balconies on a building facade

S. K. Tang[a)]
Department of Building Services Engineering, The Hong Kong Polytechnic University, Hong Kong, China

(Received 3 May 2004; revised 21 April 2005; accepted 25 April 2005)

The insertion loss and its spectrum due to a rectangular balcony on a building facade in the presence of sound reflection and scattering from adjacent balconies were examined using a scale model. The front panel of the balcony dictates the screening performance, while the side walls of the balcony are found to be insignificant. Balconies without a front panel do not provide acoustic protection in the presence of upper balcony reflection, especially for a distant noise source. Sound amplifications are also observed in many cases. In addition, the shapes of the insertion loss spectra are found to depend on the elevation angle of the balcony. Significant correlations between the A-weighted balcony insertion losses with this angle are found in the absence of upper balcony reflections. With such reflection, an angle defined using the balcony configuration and source position correlates within engineering tolerance to the insertion losses. © *2005 Acoustical Society of America.* [DOI: 10.1121/1.1931887]

PACS number(s): 43.50.Gf, 43.50.Rq [DKW] Pages: 213–221

I. INTRODUCTION

Buildings in a densely populated city like Hong Kong are very often erected close to ground transportation lines. Many people have chosen to live in the countryside and the provision of transportation to these new residential areas is essential. This eventually leads to even more careful noise control planning as the background noise levels there are considerably lower than those in the urban areas.

Architectural features, like balconies and fins, are believed to be able to control the acoustical energy actually falling on the noise sensitive parts of a building, which in most cases are the windows. This topic has attracted the attention of many researchers in the past few decades. Both computational studies and scale model measurements have been carried out (for instance, Hothersall *et al.*,[1] Mohsen and Oldham,[2] and Hossam El-Dien and Woloszyn[3]). Several different forms of the balconies have been tested as well.[2–4] The Government of the Hong Kong Special Administration Region has considered the balcony as a form "Green features" and encourages building developers and architects to consider adopting such features in their designs by exempting the areas occupied by balconies from the calculations of "Gross Floor Area" and "Site Coverage Ratio."[5] However, the effectiveness of the balcony on a building facade as a screening device for ground transportation noise is still subject to debate. A clarification of its acoustical performance is therefore essential for future development of building design.

Many studies in the existing literature deal with the screening effect of a single balcony (for instance, Mohsen and Oldham,[2] Hammad and Gibbs,[4] and Cheng *et al.*[6]), but a standalone balcony can rarely be found in a high-rise city in reality. The reflection of noise from the upper balcony will probably deteriorate the original screening effect provided by the lower balcony. The reflection and scattering of noise by nearby balconies on the same building facade[7] have also added to the complexity of the subject. Wave interaction inside the balconies in the presence of a top reflection may lead to the amplification of noise. May[8] investigated the effects of acoustic linings on reducing noise levels inside a high-rise balcony well above a nearby freeway, but the actual insertion loss is difficult to estimate as the reference noise data in May's study were affected by the other balconies on the building facade. Besides, the form of the balcony will affect the noise reflection and scattering. However, the extent of these effects is unclear.

In the present study, a scale model was set up to study the acoustic protection offered by balconies inside of a balcony array, which simulated better the real scenario in a high-rise city. Four different balcony forms, which are commonly found in Hong Kong, were considered. It is hoped that the results can provide useful information on the application to balconies and help the future development of noise control plan.

II. THE SCALE MODEL AND THE MEASUREMENTS

Similar to the study of Mohsen and Oldham,[2] a 1:10 scale-down model was used in the present investigation. The scale model was made of half-inch-thick plywood with varnished surfaces, which were acoustically hard enough to simulate the concrete building facade of negligible sound absorption. Figure 1(a) illustrates the dimensions and construction of the present scale model. A balcony array of nine equispaced balconies was adopted. Each element of the model balconies, such as the side wall and front panel, could be detached from the balcony assembly if necessary. All the measurements were carried out inside an anechoic chamber of workable floor area and height of 4 m × 5 m and 3 m, respectively. The air temperature and relative humidity inside the chamber were maintained at 22 °C and 50%, respectively. It is believed that the performance of the balconies will depend on several important angles, which are defined in Fig. 1(b). They will be discussed further later.

a)Electronic mail: besktang@polyu.edu.hk

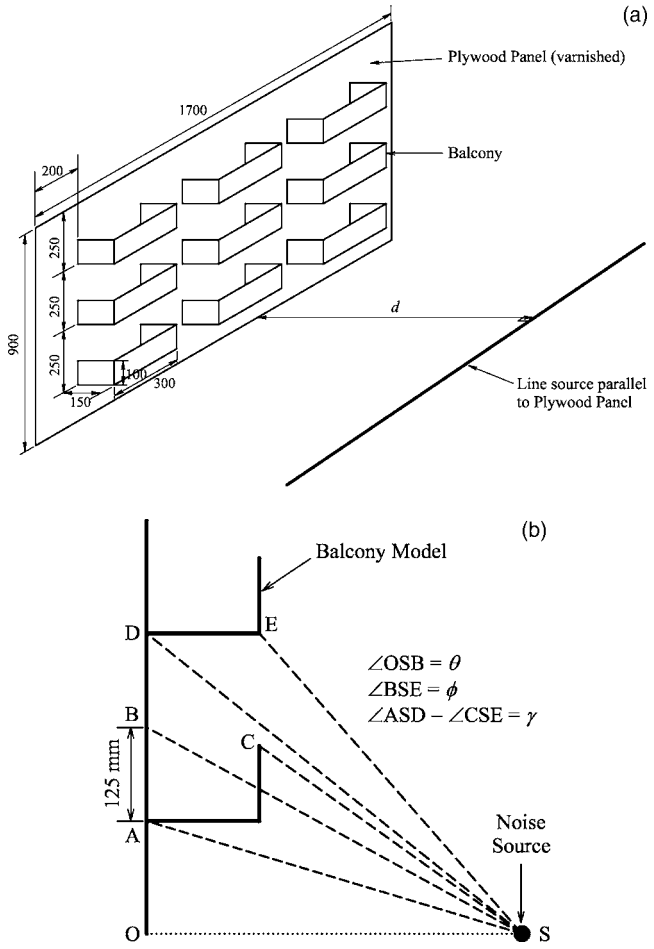

FIG. 1. (a) Dimensions of the scale model and the nomenclature adopted. (b) Definitions of important angles.

Four different balcony forms commonly found in Hong Kong were considered in the present study, as shown in Fig. 2, together with photographs of real life examples. The first one is the "Closed" form, which is similar to that of Mohsen and Oldham.[2] The second one is the "Front-Bottom," which represents the case where the balcony is made up of a solid hard front wall with fences installed between it and the building facade. The fences are acoustically transparent to sound propagation. This is also the type of balcony studied by Hossam El-Dien and Woloszyn.[3] The third one is the "Side-Bottom" configuration, wherein the balcony is made up of hard side walls with a fence in the front. The last one is the canopy-like "Bottom," which represents the case wherein fences form the three sides of the balcony.

The noise source adopted was a linear loudspeaker array consisting of a 4 m long wooden rod of triangular cross section with 54 identical small loudspeakers mounted on each of its two exposed surfaces (Fig. 3). Although these small loudspeakers could not produce much low-frequency noise, their operation frequency ranges fitted the 1:10 scale model requirement. Noise frequency range considered in the present measurements was from 1 to 20 kHz, which corresponds with the range of 100 Hz to 2 kHz for the full scale balconies. The loudspeaker array was set parallel with the model throughout the experiments. Its normal distance from the

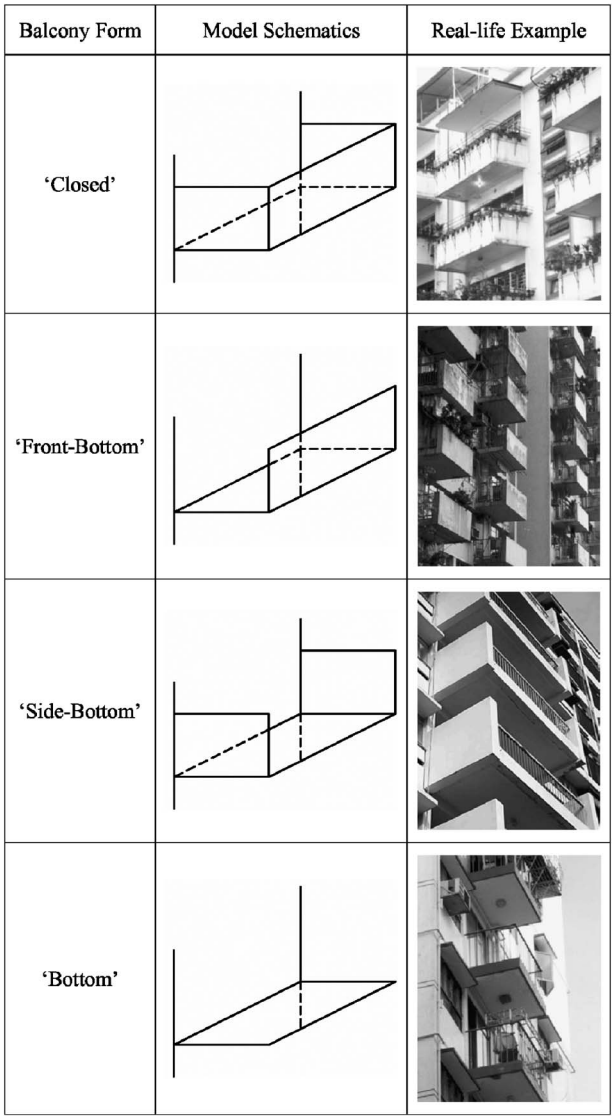

FIG. 2. Balcony forms and real life examples.

scale model (d) was varied from 0.5 to 2 m in the present study. The angles defined in Fig. 1(b) varied accordingly.

Noise spectra were recorded at 25 equally spaced locations behind the middle column balconies with and without the balconies by a Brüel & Kjœr Type 4935 0.25 in. microphone mounted flush with the plywood panel surface (dark points on the middle balcony column in Fig. 3) and the NORSONIC RTA840 real time frequency analyzer. The frequency resolution in the spectrum sampling was 62.5 Hz. The power supplied to the noise source was chosen so that the noise spectra over the frequency range considered were all higher than the background by at least 10 dB. In the foregoing discussions, the frequencies are scaled down already, such that the frequency resolution of the spectra presented later is ~6 Hz.

III. NOISE SOURCE CHARACTERISTICS

Figure 4 illustrates the noise spectrum measured at d = 1 m with a height of 0.6 m. It is normalized by the 1/3 octave band level at 1 kHz. Its shape falls within the spectral boundaries of vehicle noises shown in Berglund *et al.*[9] The

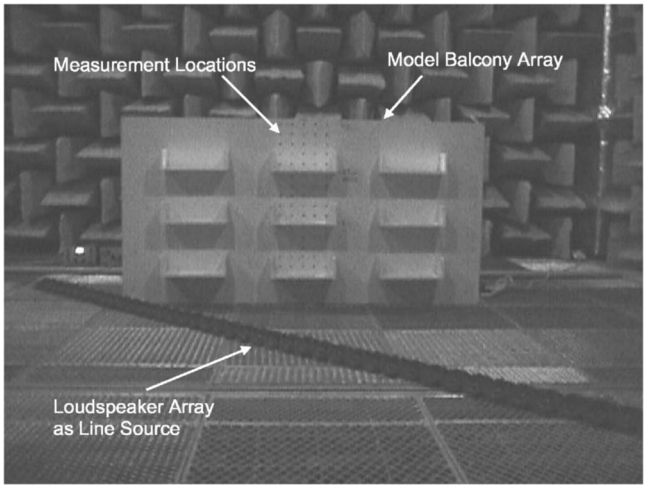

FIG. 3. The scale model and noise source (Side-Bottom model balconies are shown).

higher band levels within the 500 and 630 Hz bands are also not worse than those of the loudspeaker array employed by Hammad and Gibbs.[4,10] However, it deviates from the typical tire noise spectrum[11] and the standard traffic noise spectrum.[12] The latter appears to agree well with that of freely flowing traffic noise in Hong Kong obtained from a separated study of the author (not presented here). Therefore, a special weighting relative to the standard traffic noise spectrum has to be applied to the present measurement so that a more relevant A-weighted insertion loss can be calculated as in Mohsen and Oldham.[2] The variation of the spectra along the length of the model is less than 2 dB, which is reasonable as compared with that of Hammad and Gibbs.[10]

Some directivity patterns of the sound source at radii of 1 and 2 m are given in Fig. 5. In general, the deviations of the noise levels from the mean values are less than 1.5 dB and those for the 1/3 octave bands below 500 Hz and the A-weighted levels are even around or below 1 dB. The radiations at an angle less than 6° are less uniform, but these have insignificant influence to the results presented later as only around 6% of the measurements at $d=2$ m were done at

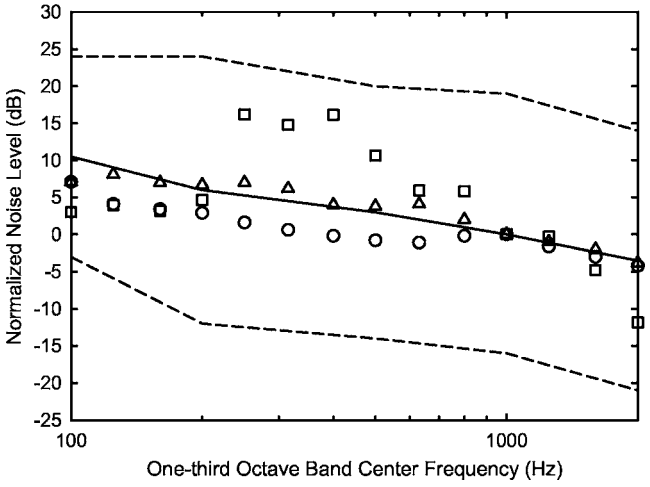

FIG. 4. Noise spectrum of the source. ○: ISO717;[12] △: Delany *et al.* (Ref. 4); □: present data; – – –: boundaries of Berglund *et al.* (Ref. 9); —: midpoint between boundaries of Berglund *et al.* (Ref. 9).

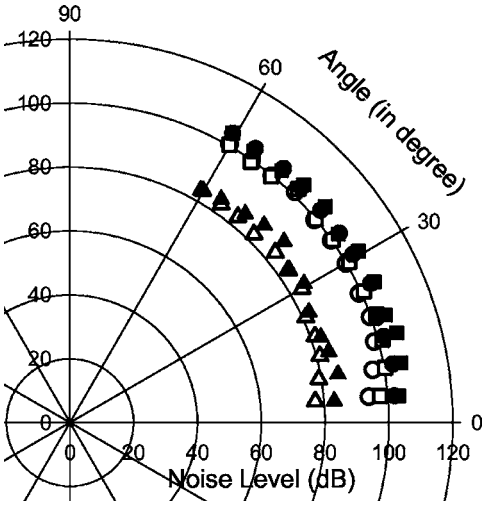

FIG. 5. Directivity patterns of the noise source in different 1/3 octave bands. ○: 250 Hz; □: 500 Hz; △: 1 kHz. Closed symbol: at radius 1 m; open symbol: at radius 2 m.

these angles. Real traffic noise is neither a two-dimensional nor a point source. The A-weighted and 1/3 octave band noise levels generated by the present loudspeaker array drop 3 to 4 dB when the radius is increased from 1 to 2 m. The noise level thus falls off with distance to the power ~1 to 1.33. This appears acceptable.

It is found in a preliminary experiment using the Closed form balcony that the introduction of an upper balcony to the middle balcony in the absence of the two side balcony columns results in an A-weighted noise level increase of ~6 dB at $d=0.5$ m. This increase drops to ~4 dB at $d=1$ m. The introduction of the side balcony column gives rise to a very slight decrease in the insertion loss of the middle and bottom balconies (~0.2 dB). However, such a decrease is around 1 to 2 dB behind the top balconies. This effect of the side balcony columns is expected to be more serious when the "Bottom" form balconies are installed because of the edge scattering.

IV. RESULTS AND DISCUSSIONS

There were five rows of equally spaced measurement points behind each middle column balcony, with two of them above, two below, and one leveled with the edge of the front panel of the Closed balcony form (Fig. 3). A-weighted sound pressure levels are adopted here to describe the general screening effects of the balconies as in many references; for instance, Mohsen and Oldham[2] and Hammad and Gibbs.[4] Insertion loss (IL) is defined as the drop in sound pressure level after the installation of the balconies. A negative IL thus means sound amplification. Since the maximum path difference due to the balcony in the present study is less than 10 cm, the air absorption will result in a noise attenuation of at the most 0.05 dB at 20 kHz (~0.5 dB/m and even less at lower frequencies[13]). This is comparable to noise measurement uncertainty and thus correction for air absorption to IL is not necessary here.

Various angles defined in Fig. 1(b) are expected to be important to the ILs of the balconies and their correlations

TABLE I. Various angles of the balconies.

d (m)	Position	θ (rad)	ϕ (rad)	γ^{a} (rad)
	Top	0.9978	⋯	⋯
0.5	Middle	0.8098	0.2670	0.1236 (C,FB) 0.0155 (B,SB)
	Bottom	0.5028	0.3491	0.1515 (C,FB) −0.0637 (B,SB)
	Top	0.6594	⋯	⋯
1.0	Middle	0.4835	0.1695	0.0747 (C,FB) −0.0171 (B,SB)
	Bottom	0.2684	0.1714	0.0778 (C,FB) −0.0335 (B,SB)
	Top	0.4768	⋯	⋯
1.5	Middle	0.3367	0.1121	0.0543 (C,FB) −0.0124 (B,SB)
	Bottom	0.1813	0.1068	0.0560 (C,FB) −0.0164 (B,SB)
	Top	0.3697	⋯	⋯
2.0	Middle	0.2567	0.0812	0.0429 (C,FB) −0.0080 (B,SB)
	Bottom	0.1367	0.0763	0.0440 (C,FB) −0.0094 (B,SB)

[a]C: Closed; FB: Front-Bottom; B: Bottom; SB: Side-Bottom.

with the ILs will be discussed in detail in the following subsections. Table I illustrates the values of these angles for different balcony and noise source positions.

A. A-weighted attenuation

Figures 6(a)–6(l) illustrate the average IL at the five different height levels behind the balconies at various perpendicular distances of the loudspeaker array from the model. For the top balcony [Figs. 6(a)–6(d)], there is no reflection from its top.

For d=0.5 m, the Bottom balcony form provides the weakest protection, which is very much expected. The Closed form gives the best acoustic protection at heights at or above the edge level of the balcony front panel, but the extent of the attenuation is reduced at lower height levels within the balcony. A similar phenomenon is observed for the Front-Bottom balcony form. This will be discussed further. The Side-Bottom form offers the best attenuation at lower height levels inside the balconies. This is reasonable as the multiple noise reflections inside the balconies is significantly weakened in the absence of the front panel.

The effects of the side walls can be found by a comparison between the performance of the Bottom and Side-Bottom balconies and between that of the Closed and Front-Bottom ones. The side walls usually result in maximum 1 dB higher noise attenuation at or above the edge level of the front panel (which is also that of the side wall). Below this edge level, they have negligible effects in the presence of the front panel, but have substantial contributions once the front panel is taken off. The overall 4 to 8 dB noise attenuation appears consistent with the results of Hammad and Gibbs.[4]

The effects of top reflection become important when the middle balconies are concerned [Figs. 6(e)–6(h)]. The strong reflection at short distance from the noise source result in amplification of sound at nearly all height levels inside the balconies. While such amplification is not dependent on the balcony form at levels close to the top reflecting surface, less amplification is observed inside the Closed and Front-

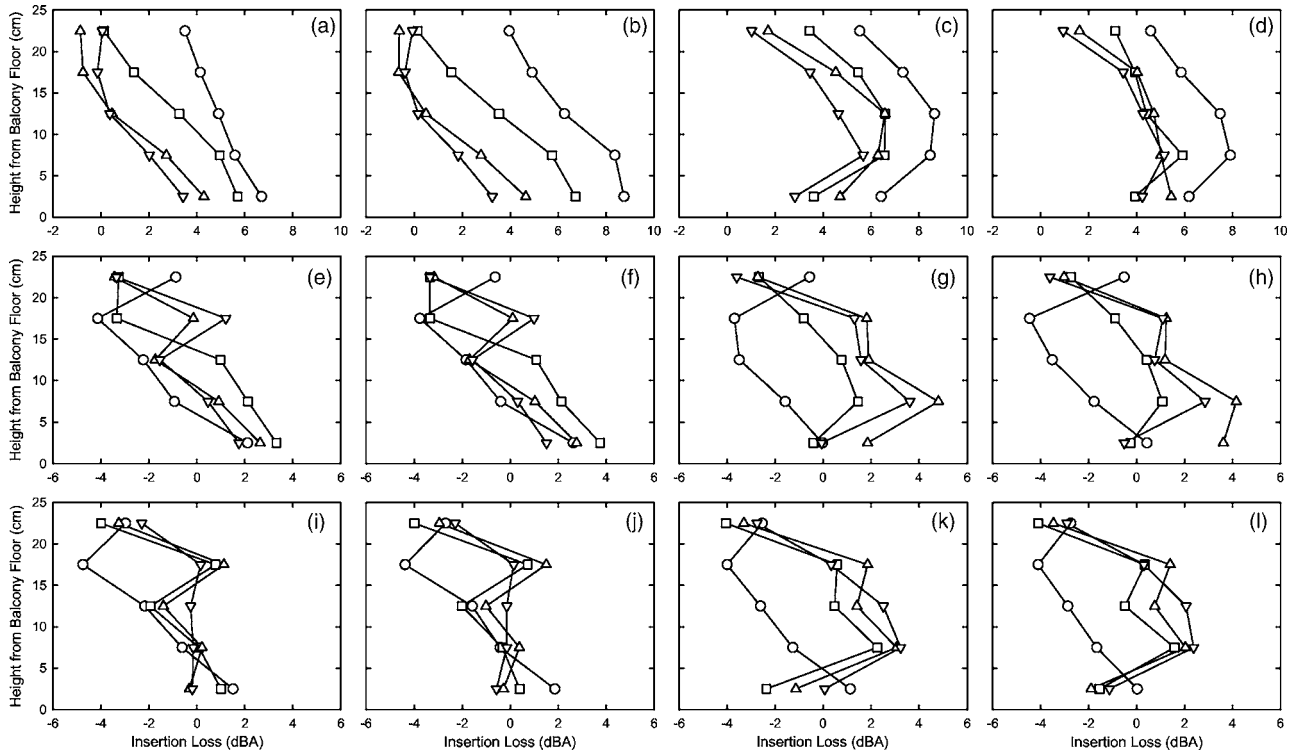

FIG. 6. Vertical variations of A-weighted noise level insertion loss within balconies. Top balcony: (a) Bottom; (b) Side-Bottom; (c) Closed; (d) Front-Bottom. Middle balcony: (e) Bottom; (f) Side-Bottom; (g) Closed; (h) Front-Bottom. Bottom balcony: (i) Bottom; (j) Side-Bottom; (k) Closed; (l) Front-Bottom. ○: d=0.5 m; □: d=1 m; △: d=1.5 m; ▽: d=2 m.

Bottom balconies at other height levels, especially those close to the balcony floor. Largely similar observations can be made inside the bottom balcony. It is noted that the magnitudes of the noise amplification in the presence of upper balcony reflection obtained in the present study with noise source close to the model are less than the equivalent sound pressure level differences measured by May[8] without acoustic linings. Using the noise level outside the balcony as a reference, as in May,[8] may not reflect the true insertion loss.

The increase in the distance of the noise source from the balconies from 0.5 to 1 m results in an overall reduction in sound attenuation inside the top balcony. Although the screening patterns of the four different balcony forms basically follow those for $d=0.5$ m, their differences have been reduced in general. Significant changes in these patterns are observed within the middle balconies. Stronger sound attenuation than in the previous case of $d=0.5$ m is observed for all balcony forms, but the reverberation due to the front panels in the Closed and Front-Bottom balconies does not allow higher sound attenuation near to the balcony floor. The situation within the bottom balcony appears to be a combination of those observed within the two upper balconies and the vertical IL distribution becomes irregular. The serious top reflection in the bottom balcony still results in strong sound amplification near to the ceilings of the balconies. The increase in the suspended angle of the balcony ceiling from the noise source [$\angle$DSE in Fig. 1(b)] does not improve the IL close to the balcony floors.

There is a continuous reduction of the IL across the highest measurement row in the top balconies as d increases for the Bottom and Side-Bottom balconies, while those related to the other two forms become negligible as d increases further from 1.5 to 2 m. The screening patterns within the middle balconies are similar to those within the bottom balconies at small d. It can also be observed that there is an overall small increase in the IL within the bottom balcony as d increases from 1.5 to 2 m. The screening patterns are smoother at increased d and these are expected to observe within the middle balcony when d is further increased. At these distances, the side walls of the balconies do not have significant effects on the IL. However, the top reflections within the middle and bottom balconies still result in sound amplification. The approximately 3 dB amplification at $d=2$ m appears to be reasonable as the upper balcony reflects the diffracted and scattered sound at the edges of the front panel or the bottom panel onto the wooden panel behind the balcony. The wave front of the noise is more or less planar when it arrives at the model balcony, which is not the case at small d.

One can notice that the screening effects provided by the Bottom and Side-Bottom balconies at the bottom of the scale model are not good. The patterns at $d=2$ m, which eventually will be those within the middle balconies at larger d, suggest slight noise amplification. The bottom panels/floors of these balconies cannot offer acoustic protection for distant noise sources.

Figure 7 illustrates the variation of the overall A-weighted sound pressure level reduction behind the middle column top balconies with the elevation angle θ.

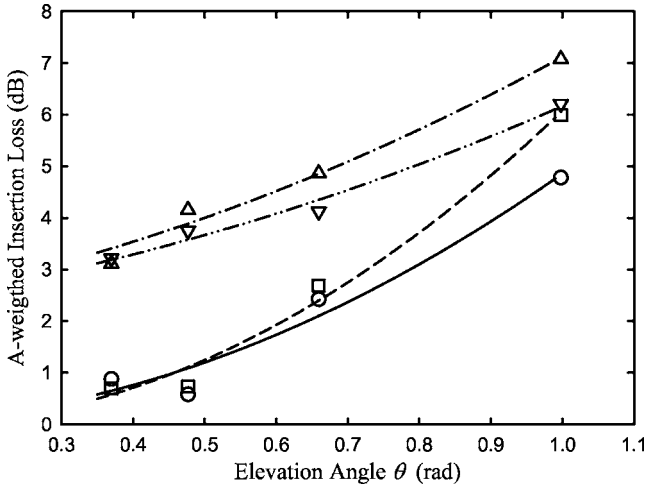

FIG. 7. Effects of elevation angle on overall A-weighted noise level insertion loss of top balconies. ○: Bottom; □: Side-Bottom; △: Closed; ▽: Front-Bottom. Regression lines:—: Bottom; – –: Side-Bottom; –·–: Closed; –··–: Front-Bottom.

These overall ILs are calculated from the average of the 25 measured noise spectra behind each balcony. The high sound attenuation behind the top balconies at larger θ is not surprising. The Bottom and Closed form balconies offer the weakest and strongest acoustic protection, respectively. As d increases, the sound path differences due to the configurations of the balconies become less, reducing the ILs as in the case of noise barrier.[14] At large d and thus small θ, these path differences will become small, and the trends shown in Fig. 7 indicate some degrees of convergence of the IL. The IL drops to about 0.5 dB for the Bottom and Side-Bottom balconies and ~3 dB for the other two balcony forms. This tends to suggest that the front panel of the balcony accounts for a 2.5 dB sound reduction at large d. Theoretically when $\theta \rightarrow 0$, the Bottom and Side-Bottom balconies will not offer any acoustic protection, while the front panels of the other two balcony forms will approximately stop 40% of the noise propagation (excludes the diffraction at the panel edge) as the height of the panel is 40% of the distance between two balconies in a column. The latter will result in an IL of 2.2 dB. This is independent of d. One can observe that the ILs shown in Fig. 7 follow quadratic variations with θ. The associated empirical formulae, the correlation coefficients, and the standard errors are given in Table II. Significant correlations are observed.

Overall A-weighted noise amplifications are observed in the middle and bottom balconies of all forms, but they do not scale on θ because of the reflections from the upper balconies. Figure 8 illustrates the variations of these ILs with the

TABLE II. Variations of top balcony insertion loss with elevation angle θ given in radians.

Balcony	Empirical formula	R^2	Standard error (dBA)
Closed	$IL=2.63\theta^2+2.29\theta+2.2$	0.99	0.2
Front-Bottom	$IL=2.07\theta^2+1.90\theta+2.2$	0.99	0.1
Side-Bottom	$IL=7.18\theta^2-1.10\theta$	0.99	0.2
Bottom	$IL=4.93\theta^2-0.07\theta$	0.97	0.3

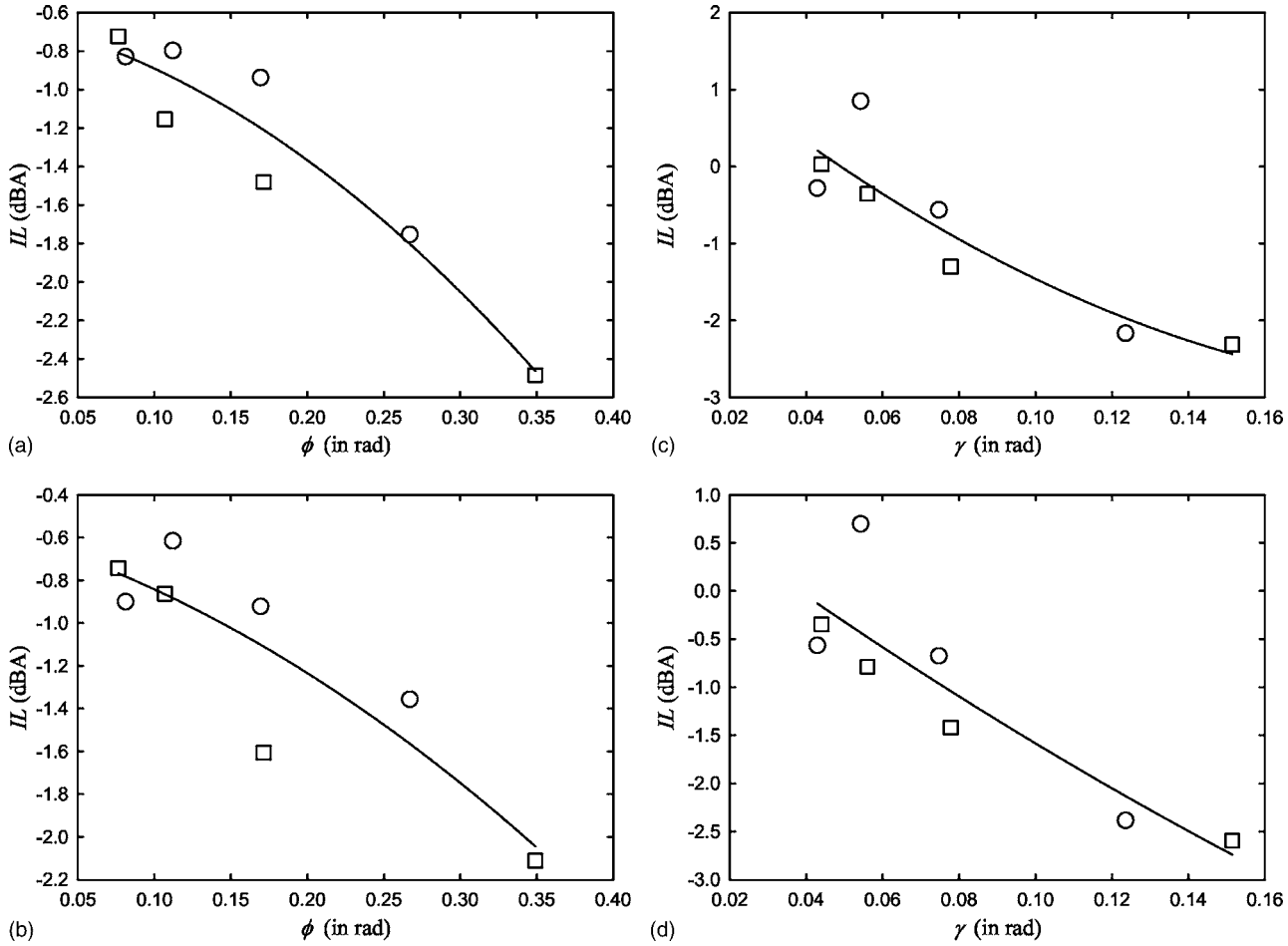

FIG. 8. Dependence of A-weighted noise level insertion loss on angle differences. (a) Bottom, ϕ; (b) Side-Bottom, ϕ; (c) Closed, γ; (d) Front-Bottom, γ. —: regression lines.

angles defined in Fig. 1(b). The corresponding empirical formulae, the correlation coefficients and the standard errors are given in Table III. It is found that the ILs of the Bottom and Side-Bottom form balconies do not correlate with γ, and the corresponding results are not presented. Those of the Closed and Front-Bottom balconies scale slightly better with γ. Their corresponding IL variations are curved downwards [Figs. 8(c) and 8(d)], suggesting slower IL variation at larger angle differences. Those for the Bottom and Side-Bottom ones varying with ϕ are opposite. Since all the ILs correlate with ϕ reasonably well, this angle appears to be more useful for design purposes.

One can also notice from Fig. 8 that the amplifications are slightly more serious for the Bottom and Side-Bottom balconies. The consistently higher amplification inside the Front-Bottom balcony than in the Closed balcony manifests that the side walls offer more diffraction loss than enhancing the reverberation.

TABLE III. Variations of balcony insertion loss with ϕ and γ given in radians.

Balcony	Empirical formula	R^2	Standard error (dBA)
Closed	$\mathrm{IL}=9.57\phi^2-13.92\phi-1.21$	0.78	0.5
	$\mathrm{IL}=94.41\gamma^2-42.73\gamma+1.87$	0.81	0.4
Front-Bottom	$\mathrm{IL}=-1.13\phi^2-9.20\phi+0.56$	0.74	0.5
	$\mathrm{IL}=28.06\gamma^2-25.51\gamma-1.09$	0.77	0.5
Side-Bottom	$\mathrm{IL}=-6.10\phi^2-2.09\phi-0.57$	0.77	0.2
Bottom	$\mathrm{IL}=-10.39\phi^2-1.65\phi-0.62$	0.91	0.2

B. Spectral analysis

This section will be focused on the frequency characteristics of the insertion loss. The frequencies presented in the foregoing discussions are scaled back to the real size of the balcony. One should note that the IL spectra are not affected by the spectral shapes of the noises.

Figures 9(a)–9(c) show the variations of ILs with frequency behind the top, middle, and bottom balconies, respectively, at $d=0.5$ m. Broadband attenuation of sound is observed behind the top balconies, resulting in high ILs [Fig. 9(a)]. The spectral performance of the middle and bottom balconies does not depend much on the forms of the balconies, implying further that the floors of the balconies play a determining role in the IL where the source is close to the balconies. The spectral amplification patterns within the middle and bottom balconies are also alike, with relatively more significant attenuations or less sound amplifications at around 680, 1000, 1250, and 2200 Hz. The amplifications at frequency below 400 Hz are believed to be due to the standing waves in the vertical direction inside the balconies.

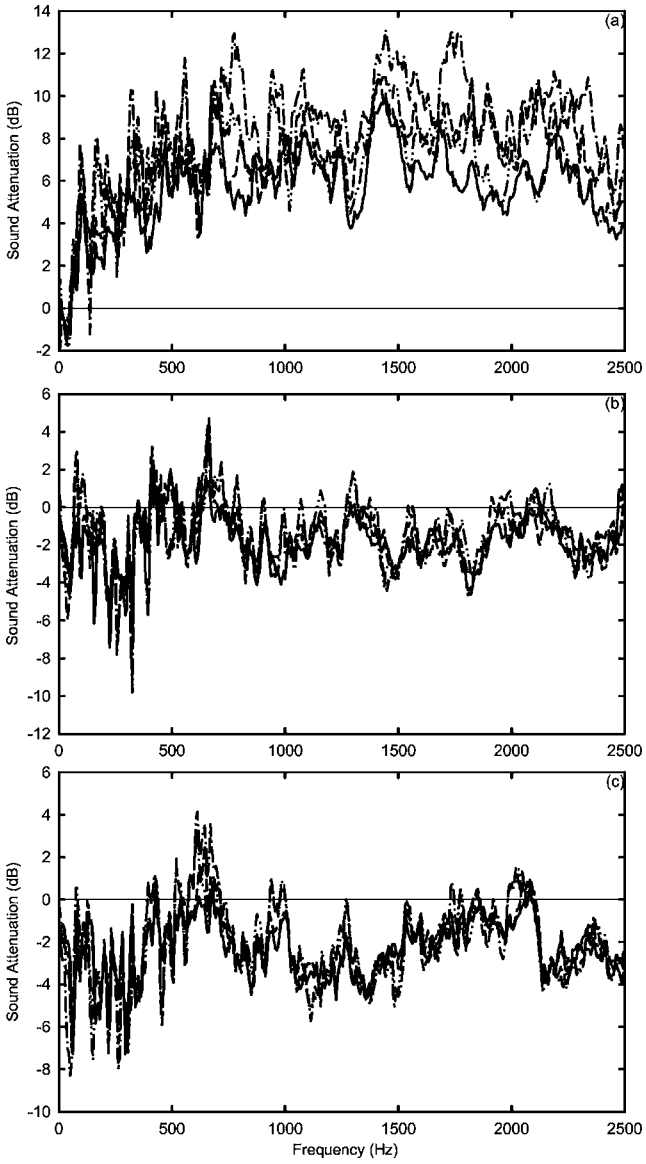

FIG. 9. Spectral characteristics of the noise screening at $d=0.5$ m. (a) Top balcony; (b) middle balcony; (c) bottom balcony. —: Bottom; – –: Side-Bottom; –·–: Closed; –··–: Front-Bottom.

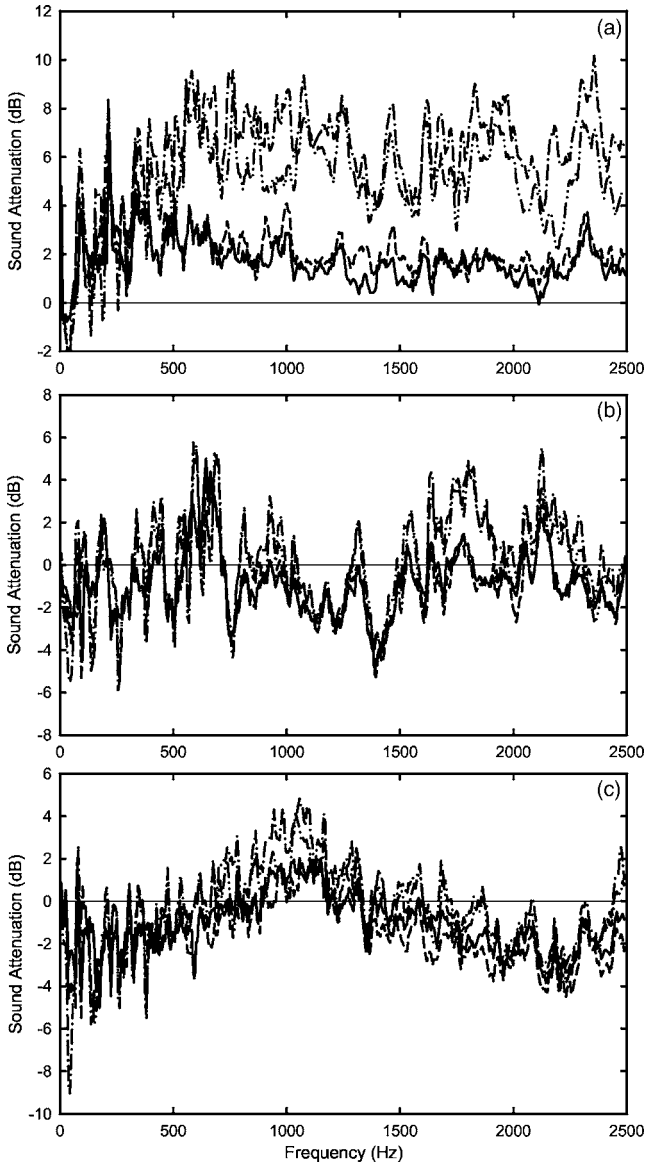

FIG. 10. Spectral characteristics of the noise screening at $d=1$ m. (a) Top balcony; (b) middle balcony; (c) bottom balcony. Legends: same as those in Fig. 9.

The increase in the distance of the noise source from the model to 1 m results in a nearly broadband drop of sound attenuation within the top balconies [Fig. 10(a)], but such drops at frequencies higher than 400 Hz within the balconies with a front panel are much more rapid. Within the middle balconies [Fig. 10(b)], the spectral performances of different balcony forms are similar, except that there are relatively higher attenuations at the frequencies round 1800 and 2200 Hz for balconies with a front panel (Closed and Front-Bottom). The overall A-weighted broadband attenuation inside these middle balconies is negative (Fig. 8), suggesting that the amplifications at frequencies below 1500 Hz dominate the overall screening property. One can observe that the spectral shapes of the ILs shown in Figs. 9(c) and 10(b) are similar, suggesting that θ plays a role in affecting the balcony screening, apart from the balcony form. The spectral performance of the bottom balconies does not depend much on the balcony form, except that a slightly higher noise attenuation at frequencies about 1000 Hz is achieved in the presence of a front wall panel [Fig. 10(c)].

As the source distance increases, a further drop of the IL within the top balconies at high frequency is expected [Fig. 11(a)]. The IL associated with a balcony without a front panel is around 1 dB across the whole frequency range of the present study. The two sharp amplification peaks at around 50 and 140 Hz associated with the Closed and Front-Bottom balconies, respectively, are believed to result from the acoustic modes within the balconies. The former is closed to the (1,0) mode and the other the (1,1) or (2,1) modes. One can observe these peaks in Figs. 9 and 10, but they are very prominent in Fig. 11. Such peaks are also found in the results with $d=1.5$ m (not shown here).

The spectral shapes of the IL within the middle balconies at the source distance of 2 m, shown in Fig. 11(b), are similar to those illustrated in Fig. 10(c). This further con-

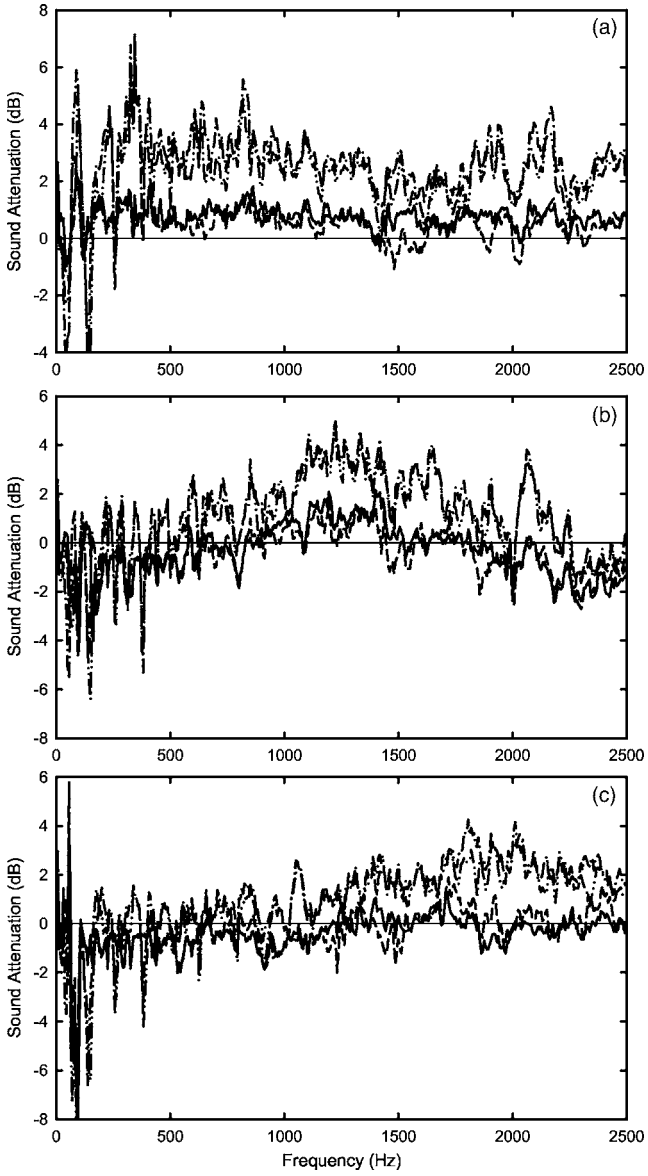

FIG. 11. Spectral characteristics of the noise screening at $d=2$ m. (a) Top balcony; (b) middle balcony; (c) bottom balcony. Legends: same as those in Fig. 9.

firms the importance of θ discussed previously. A broader frequency band of noise attenuation is observed in Fig. 11(b) compared to that in Fig. 10(c). Among the bottom balconies, relatively more significant attenuation can only be found at higher frequency within the Closed and the Front-Bottom balconies. Figure 11(c) indicates clearly that the balconies without a front panel will not offer any acoustic protection over the whole frequency range of concern when the noise source is far away from them. The reflection from the upper balcony makes thing worse, especially in the low-frequency range.

There have been consistent IL peaks at certain frequencies in Figs. 9–11 for the cases in which reflections from upper balconies are expected. For instance, the broadband IL peaks at around 650 Hz in Figs. 9(c) and 10(b), those at around 1000 Hz in Figs. 10(c) and 11(b), and the narrower band IL peak at around 2200 Hz in Figs. 10(b) and 11(b). The latter can also be observed in Fig. 9(c), although the corresponding magnitude is weak. The reasons for these observations are still not clear and these frequencies may change with the balcony dimensions. While the sharp IL peaks or troughs at frequencies below 200 Hz as discussed before can be ascribed to the effects of acoustic modes within the balconies, those above 400 Hz are difficult to explain in similar terms as the modal overlapping becomes very serious in this frequency range. Above 400 Hz, each data point may include contributions from one or more eigenfrequencies of the balcony, making the experimental isolation of modes difficult.[15] A numerical investigation with a large number of node points on the balcony surfaces and in the balcony voids is required for such mode isolations.

V. CONCLUSIONS

A scale model study on the acoustic protection offered by balconies on a building facade was carried out with reflections and scattering from adjacent balconies taken into account. Four different forms of rectangular balcony, which are commonly found in Hong Kong and many other cities around the world, were included. Effects of the distance between noise source and the balconies and some special angles defined using the balcony configurations and the noise source positions on the insertion loss were also discussed. The noise source was kept parallel to the balcony models throughout the experiment.

It is found that when the source is close to the balconies, the reflections from the upper balconies and the screening effects of the balcony floors have the major contributions to the insertion loss. However, the front panel gradually becomes the determinant member of the balcony in affecting the A-weighted insertion loss and the spectral characteristics of the screening as the distance between the source and the balconies increases. At large source distances, the balcony without a front panel does not offer any noise screening, while the one with a front panel still manages to provide limited noise attenuation at high frequency. There is significant noise amplification due to reflection from upper balcony at low frequency at such source distances. Sound amplification is observed near the upper balcony floor for all balcony forms.

The elevation angle of the balcony correlates very well with the A-weighted insertion loss produced by the balcony in the absence of top reflections. There is also evidence that the elevation angle influences the spectral shapes of the insertion loss (not the exact values). However, in the presence of top reflections, an angle defined using the midheight of the balcony and the bottom corner of the associated upper balcony appears to have good correlations with the A-weighted insertion loss, at least to engineering tolerance.

Spectral peaks of amplification and attenuation are found on the frequency variation of insertion loss. Those at low frequencies are related to the acoustic modes within the balconies, but those at high frequencies remain difficult to explain precisely through experiments because of modal overlapping. Numerical study with large number of node points is suggested as a follow-up of the present investigation.

ACKNOWLEDGMENTS

The financial support from the Research Committee of The Hong Kong Polytechnic University under Grant No. GYD-41 is gratefully acknowledged. The author would also like to thank K. C. Vong and W. L. Chan for carrying out the experiment, and Dr. C. F. Ng of the Civil and Structural Engineering Department, the Hong Kong Polytechnic University for his constant interest in the work.

[1]D. C. Hothersall, K. V. Horoshenkov, and S. E. Mercy, "Numerical modeling of the sound field near a tall building with balconies near a road," J. Sound Vib. **198**, 507–515 (1996).

[2]E. A. Mohsen and D. J. Oldham, "Traffic noise reduction due to the screening effect of balconies on a building facade," Appl. Acoust. **10**, 243–257 (1977).

[3]H. Hossam El-Dien and P. Woloszyn, "Prediction of the sound field into high-rise building facades due to its balcony ceiling form," Appl. Acoust. **63**, 431–440 (2004).

[4]R. N. S. Hammad and B. M. Gibbs, "The acoustic performance of building facades in hot climates: Part 2—Closed balconies," Appl. Acoust. **16**, 441–454 (1983).

[5]*Green and Innovative Buildings*, Joint Practice Note No. 1, Building Department, Lands Department and Planning Department, the Government of the Hong Kong Special Administration Region, China.

[6]W. F. Cheng, C. F. Ng, and K. C. Fung, "The theoretical model to optimize noise barrier performance at the window of a high-rise building," J. Sound Vib. **238**, 51–63 (2000).

[7]R. Makarewicz and P. Kokowski, "Reflection of noise from a building's facade," Appl. Acoust. **43**, 149–157 (1994).

[8]D. N. May, "Freeway noise and high-rise balconies," J. Acoust. Soc. Am. **65**, 699–704 (1979).

[9]B. Berglund, P. Hassmén, R. F. S. Job, "Sources and effects of low-frequency noise," J. Acoust. Soc. Am. **99**, 2985–3002 (1996).

[10]R. N. S. Hammad and B. M. Gibbs, "The acoustic performance of building facades in hot climates: Part 1—Courtyards," Appl. Acoust. **16**, 121–137 (1983).

[11]M. E. Delany, A. J. Rennie, and K. M. Collins, *Scale Model Investigation of Traffic Noise Propagation* (National Physical Laboratory Report AC 58, 1972).

[12]BS EN ISO717, *Acoustics—Rating of Sound Insulation in Buildings and of Building Elements. Part 1: Airborne Sound Insulation* (BSI, London, 1997).

[13]ISO 9613, *Acoustics—Attenuation of Sound During Propagation Outdoors. Part 1: Calcuation of Absorption of Sound by the Atmosphere* (ISO, Geneva, 1993).

[14]U. J. Kurze, "Noise reduction by barriers," J. Acoust. Soc. Am. **55**, 504–518 (1974).

[15]H. Kuttruff, *Room Acoustics* (Elsevier, London, 1991).

Toward a theory of wave energy transport in large irregular structures

Nicholas L. Wolff and Richard L. Weaver[a)]
Department of Theoretical and Applied Mechanics, University of Illinois at Urbana-Champaign, 216 Talbot Lab, 104 S. Wright Street, Urbana, Illinois 61801

(Received 28 November 2004; revised 1 April 2005; accepted 8 April 2005)

An ansatz is proposed by which the energy transport behavior observed at early times in a direct numerical simulation (DNS) of a large irregular structure may be extrapolated to arbitrary times. In the slow-transport limit, this ansatz leads to a diffusion-like equation, similar to that of time-domain statistical energy analysis (SEA), but it does not require substructuring. The model is successfully used to extract diffusion parameters from simulated data of unambiguously diffusive character. The model is then successfully used to extract diffusion parameters from data obtained in a DNS of a simple undamped two-room structure of a kind typically analyzed by SEA or room acoustics.
 [DOI: 10.1121/1.1925847]

PACS number(s): 43.55.Br, 43.40.Dx, 43.40.Hb, 43.60.Cg [ANN] Pages: 222–231

I. INTRODUCTION

A. Background

Direct numerical simulations (DNS) are commonly employed to obtain the dynamical response of large structural acoustic systems. Though always possible in principle and often straightforward, such simulations are subject to widely recognized limitations. These include high computational costs, especially burdensome if fine spatial or time resolution is required, or if the late-time solution is required. Moreover, interpretation is problematic due to the inevitable sensitivity to fine details of the structure. A detailed numerical solution to the dynamics of one system is therefore of limited value for describing the dynamics of another system with slightly different structure. Prompted by these limitations there has long been interest in statistical theories to predict dynamic responses.

Statistical energy analysis (SEA) is one such theory. A monograph[1] and several journal articles[2–4] review that subject and related theories.[5] Conventional SEA estimates the steady-state energy density for a band-limited response in the presence of dissipation. SEA models assume a partition of the system into weakly coupled substructures; they also assume that there is equipartition of energy among modes to justify using a modal average for "coupling loss factors," the coefficients that determine energy flow between the substructures. A predictive SEA model therefore requires modal densities and dissipation estimates for each substructure, and estimates for these coupling loss factors.

SEA is one of a class of energy transport models analogous to heat conduction or diffusion. Diffusive models have been used for vibrational and acoustic energy flow in solid mechanics,[6] heterogeneous fluids,[7,8] granular materials,[9] and room acoustics.[10] Lyon in his original work (Ref. 1, and references within), and many others since, have gone to great effort to justify energy conduction laws for structural vibrational systems, often using statistical arguments.

Chief amongst the difficulties associated with SEA is the need to develop methods to estimate the required parameters, especially coupling loss factors. Direct finite element numerical simulations[11–13] have been used to estimate these, though more commonly they are estimated using analytic models[14] or experimental observations. Once these parameters have been determined, one solves the resulting set of simple differential equations. SEA requires substructuring, but the correct way to substructure a system is not always obvious; some systems may not admit substructuring at all. Moreover, SEA considers only average modal energy density in substructures. It does not account for local variations in impedance within a substructure. Finally, the variables in SEA, like energy density and energy flux between structures, are not directly measurable. It would be preferable to have a model with variables, like force and displacement, that are directly measurable in experiment or DNS.

Time-dependent SEA[15,16] and some hybrid methods[17] have been developed in recent years. Coupling loss factors in coupled beam structures,[13,18,19] coupled plate structures,[11,12,20] and a building plan[21] have been extracted from data obtained using the finite element method and receptance theory. SEA results have been obtained by asymptotic modal analysis and compared to direct numerics.[22] Gregory and Keltie[23] have used experimental data and extracted SEA parameters using the Eigensystem Realization Algorithm.[24] Langley and others[25] have developed SEA for periodically stiffened plates widely used in industry. Vibro-Acoustic Sciences, which markets the software package AUTOSEA©, has an ongoing effort developing semi-analytic techniques for estimating SEA parameters.

The present work is part of a project[26,27] seeking methods to predict mean square responses (e.g., energies) using information gleaned from direct numerical simulations. Weaver[26] showed that DNSs of undamped systems over modest times comparable to the inverse of the desired frequency resolution permit good estimates of mean square re-

a)Author to whom correspondence should be addressed; electronic mail: r-weaver@uiuc.edu

sponses at infinite time. The technique did not lend itself to predictions of energy flow. Wolff and Weaver[27] sought to extend the work by attempting to fit a diffusion model to DNS-like data using nonlinear least squares. The method explored there was, at best, awkward: nonlinear fits are notoriously unstable.

Section I B provides a review of some of the relevant previous work. Section II presents a description of an alternative approach that reduces to diffusion in the limit that transport is slow. Section III applies this approach to data taken from a solution to a diffusion-like equation. Section IV describes application to data obtained from a direct numerical simulation of a wave equation. We conclude in Sec. V and propose future work.

B. Relevant previous work

Weaver[26] estimated band-limited mean-square late-time responses in large undamped systems by

$$\Psi_{rs,B}(t=\infty)=\frac{E_{r,B}E_{s,B}}{\mathcal{N}}, \tag{1}$$

where

$$\mathcal{N}=2\pi^3 f_c^2 D(2\pi f_c)\int B^2(t)dt \tag{2}$$

is related to global modal density $D(\omega)=dN/d\omega$, and

$$E_{s,B}=\int_0^{T_B} B(t)\left[\frac{d}{dt}\int_0^t (\{s\}^T[\mathbf{G}(t-\tau)]\{s\})B(\tau)d\tau\right]dt \tag{3}$$

can loosely be referred to as the admittance at site s. $E_{s,B}$ is the work done by a band-limited, short-time source $B(t)$ with spatial distribution $\{s\}$, center frequency f_c, and duration T_B. Diagonal elements of the Green's function $[\mathbf{G}(t)]$ for each receiver and source of interest for only short times $t<T_B$ are required. [These elements are "diagonal" in the sense $\mathbf{G}_{ss}(t)=\{s\}^T[\mathbf{G}(t)]\{s\}$.] The superscript T denotes transpose.

Weaver's previous work[26] showed that the early time dynamics predicts late-time mean-square responses. It did not address energy flow at moderate times and was thus of limited utility. In particular, it was inapplicable to dissipative systems. But early time responses also describe a degree of transport which, if observed in a DNS, could in principle be extrapolated to later times and/or applied to estimate steady state responses in dissipative systems. The statistical energy ansatz supposes that energy transport is diffusive. If the parameters of that diffusion model can be taken from the behavior of short-time-scale direct numerical simulations, it may be that energy flow can be extrapolated to long times using the diffusion parameters apparent at early times.

We note, like Weaver,[26] that a diffusion model need not require substructuring or involve quantities—like modal energy density in substructures—that are poorly related to measurable quantities like displacement. This is in contrast to SEA. For our first attempts[27] to estimate the envelope of the complex dynamics of a vibrational system, we adopted a diffusion-like governing differential equation for slowly evolving band-limited energy. (The term energy is used generically to refer to any mean square field amplitude.) The equation governed slowly time-varying mean square displacement Ψ at each of R receivers, where R denotes the total number of sites (receivers and potential sources). In the absence of dissipation, the equation takes the form[27]

$$[\mathbf{H}]\frac{\partial}{\partial t}\{\Psi(t)\}=\{\hat{\Pi}(t)\}-[\mathbf{D}]\{\Psi(t)\}, \tag{4}$$

where the diffusion parameters $[\mathbf{H}]$ and $[\mathbf{D}]$ are symmetric and $R\times R$, $\{\Psi\}$ is $R\times 1$, and $\{\hat{\Pi}\}$ contains the average band-limited forcings squared and is also $R\times 1$, as a source acts through each receiver. We may anticipate that $[\mathbf{H}]$ should be diagonal; otherwise a source at one site leads instantaneously to a response at another site. Similarly one might expect elements of $[\mathbf{D}]$ between distant sites to vanish.

It may be emphasized that $\{\Psi\}$ and $\{\hat{\Pi}\}$, unlike the quantities encountered in SEA (power and energy), are directly measurable quantities. The close relationship between Eq. (4) and SEA is discussed elsewhere.[27]

Considering the generalized eigenvalue problem $[\mathbf{D}]\times\{\mathbf{U}\}=\Lambda[\mathbf{H}]\{\mathbf{U}\}$ yields eigenpairs $(\Lambda_r,\{\mathbf{V}\}^r)$, $r=1,2,\ldots,R$. The solution to Eq. (4) is given by an expansion in the eigenvectors. Previously,[27] we sought to extract the diffusion parameters $[\mathbf{H}]$ and $[\mathbf{D}]$ or, equivalently, Λ's and $\{\mathbf{V}\}$'s from data $\{\hat{\Pi}\}$ and $\{\Psi\}$ obtained over short times t by means of a direct fit to that solution.

A brute-force nonlinear least-squares fit of the model of Eq. (4) was applied to noisy data with underlying diffusive character.[27] The data were constructed by evaluating the solution to Eq. (4) and adding noise by a procedure discussed in the following. Results were mixed. Fits were good—Λ's and $\{\mathbf{V}\}$'s were recovered accurately—for small two substructure systems, but convergence was difficult for larger systems. In conclusion the method explored there was impractical due to the instability of the fits. Other fit algorithms might have performed better, but here we consider a different approach, and the remainder of this paper explores this promising alternative.

II. A CONCATENATION ANSATZ

A. The model

Toward the end of extracting $[\mathbf{H}]$ and $[\mathbf{D}]$, we now present a different model, which we call the "concatenation ansatz." Consider a set of receivers in an undamped structure, each of which may in principle also act as a source. The intensity Ψ_{rs} at receiver r from a unit band-limited impulsive[28] source at s $\Pi_s(t)=\langle F^2(t)\rangle=\delta(t)$, i.e., the squared displacement response smoothed over time, over a frequency band, and possibly over nearby receivers, is denoted as $\hat{\mathbf{J}}_{rs}(t)$. Now consider a version of $\hat{\mathbf{J}}$ with limited information

$$\hat{\mathbf{J}}^{\Delta}_{rs}(t)=\hat{\mathbf{J}}_{rs}(t)e^{-\Delta t}. \tag{5}$$

This $\hat{\mathbf{J}}^{\Delta}$ is sensitive only to transport at short times $t<\mathcal{O}(1/\Delta)$. The information in $\hat{\mathbf{J}}^{\Delta}_{rs}(t)$ may be generated directly in the frequency domain as described in Sec. V. As an alternative, $e^{-\Delta t}$ might be replaced by a rectangular window

$\Theta(1/\Delta - t)$, in which case $\hat{\mathbf{J}}^{\Delta}_{rs}(t)$ is probably generated most efficiently by a time domain DNS. Either an exponential or a rectangular window emphasizes early times over late times, and $\hat{\mathbf{J}}^{\Delta}_{rs}$ can be obtained at small computational cost.

The proposed *ad hoc* concatenation ansatz attempts to construct the intensity at later times by "relaunching" the decayed intensity continuously in time by some weight, $\mathbf{Q}_{rs}$, for each source/receiver. Formally,

$$\hat{\mathbf{J}}^{\text{concat}}_{rs}(t) = \hat{\mathbf{J}}^{\Delta}_{rs}(t) + \int_0^t \hat{\mathbf{J}}^{\Delta}_{r\sigma}(t-\tau)\mathbf{Q}_{\sigma\rho}\hat{\mathbf{J}}^{\text{concat}}_{\rho s}(\tau)d\tau. \tag{6}$$

Equation (6) may be solved by iteration

$$\hat{\mathbf{J}}^{\text{concat}} = \hat{\mathbf{J}}^{\Delta} + \hat{\mathbf{J}}^{\Delta} \otimes \mathbf{Q}\hat{\mathbf{J}}^{\Delta} + \hat{\mathbf{J}}^{\Delta} \otimes \mathbf{Q}\hat{\mathbf{J}}^{\Delta} \otimes \mathbf{Q}\hat{\mathbf{J}}^{\Delta} + \cdots, \tag{7}$$

where $\otimes$ represents a convolution. Each term of Eq. (7) is a concatenation of short time propagations, $\hat{\mathbf{J}}^{\Delta}$. After taking a Fourier transform[29]

$$\mathbf{J}_{rs}(\Omega) = \int_{-\infty}^{\infty} \hat{\mathbf{J}}_{rs}(t)e^{-i\Omega t}dt \tag{8}$$

and shifting to matrix notation, Eq. (6) becomes

$$[\mathbf{J}^{\text{concat}}(\Omega)] = [\mathbf{J}^{\Delta}(\Omega)] + [\mathbf{J}^{\Delta}(\Omega)][\mathbf{Q}][\mathbf{J}^{\text{concat}}(\Omega)]. \tag{9}$$

Its solution is

$$\begin{aligned}[\mathbf{J}^{\text{concat}}(\Omega)] &= (\mathbf{I}_S - [\mathbf{J}^{\Delta}(\Omega)][\mathbf{Q}])^{-1}[\mathbf{J}^{\Delta}(\Omega)] \\ &= ([\mathbf{J}^{\Delta}(\Omega)]^{-1} - [\mathbf{Q}])^{-1},\end{aligned} \tag{10}$$

where $\mathbf{I}_S$ is the $S \times S$ identity matrix, and S is the total number of sources. Thus, $[\mathbf{J}^{\text{concat}}]$ is readily constructed for all times, not only $t < \mathcal{O}(1/\Delta)$.

The weights $[\mathbf{Q}]$ of relaunching are determined by solving (details are left to Appendix A)

$$(\mathbf{I}_S - [\mathbf{J}^{\Delta}(0)][\mathbf{Q}])\{E\} = 0. \tag{11}$$

The array $\{E\}$ contains the admittances given by Eq. (3). Equation (11) assures that $[\hat{\mathbf{J}}^{\text{concat}}(t \to \infty)]$ will have the relative intensity distribution demanded by equipartition.[26]

Explicit reference to the argument $\Omega = 0$ will be dropped unless needed for clarity. Equation (11) has a unique solution if $[\mathbf{Q}]$ is assumed Ω independent and diagonal. This implies that the intensity relaunched from receiver r depends only on the intensity observed at receiver r, and only on the intensity observed at the same instant as the relaunching. It is reassuring that large Δ corresponds to small $\mathbf{J}^{\Delta}$ [cf. Eq. (5)] and large $[\mathbf{Q}]$ [cf. Eq. (6)], thus requiring stronger relaunching to compensate for the rapid decay Δ. Formal solution of Eq. (11) for $[\mathbf{Q}]$ is awkward. A column array $\{\mathbf{Q}\}$ consisting of the diagonal elements of $[\mathbf{Q}]$ is obtained by

$$\{\mathbf{Q}\} = [E_{\text{inv}}][\mathbf{J}^{\Delta}]^{-1}\{E\}, \tag{12}$$

where $[E_{\text{inv}}]$ is a diagonal matrix with elements $1/E_s$.

Requiring the $[\hat{\mathbf{J}}^{\text{concat}}(t \to \infty)]$ to reproduce the correct relative intensities $\{E\}$ leads to the condition Eq. (11). Requiring the correct absolute intensities Eq. (1) leads to (details are left to Appendix B)

$$\mathcal{N} = -\{E\}^T[\mathbf{J}^{\Delta}]^{-1}[\mathbf{J}^{\Delta}]'[\mathbf{Q}]\{E\}, \tag{13}$$

where $[\mathbf{J}(\Omega)]' \equiv (\partial/\partial i\Omega)[\mathbf{J}(\Omega)]$ and i is the imaginary unit. This is a condition on the concatenation ansatz. It is interesting that the right-hand side of Eq. (13) may be calculated with no knowledge of the size of the structure, to which $\mathcal{N}$ is proportional. Thus Eq. (13) is a nontrivial condition. Presumably, if all important information is implicit in the limited data $[\mathbf{J}^{\Delta}]$ and $\{E\}$, then $\mathcal{N}$ obtained by Eq. (13) will be identical to an independently obtained estimate from, e.g., a Weyl series. If not, then some important information has not been accounted for, perhaps by neglecting to place a receiver in some substructure.

B. Diffusion limit

In the low Ω limit, the solution Eq. (10) of Eq. (6) may be recognized as the solution of a diffusion equation like Eq. (4). We wish to enforce the equality

$$[\mathbf{J}^{\text{concat}}(\Omega)] = ([\mathbf{J}^{\Delta}(\Omega)]^{-1} - [\mathbf{Q}])^{-1} = (i\Omega[\mathbf{H}] + [\mathbf{D}])^{-1} \tag{14}$$

as $\Omega \to 0$. After expanding the left-hand side in $i\Omega$, one identifies

$$[\mathbf{D}] = [\mathbf{J}^{\Delta}(0)]^{-1} - [\mathbf{Q}], \tag{15a}$$

$$[\mathbf{H}] = -[\mathbf{J}^{\Delta}(0)]^{-1}[\mathbf{J}^{\Delta}(0)]'[\mathbf{J}^{\Delta}(0)]^{-1}. \tag{15b}$$

Thus the parameters $[\mathbf{H}]$, $[\mathbf{D}]$ of a diffusion model follow directly from raw data $[\mathbf{J}^{\Delta}]$.[30]

If those raw data happen to be exactly diffusive,[31] one deduces that the parameters $[\mathbf{H}]$ and $[\mathbf{D}]$ are recovered exactly. We take the data to be the solution of Eq. (4) with matrices $[\mathbf{d}]$ and diagonal $[\mathbf{h}]$, so

$$[\mathbf{J}^{\Delta}(\Omega)] = ((i\Omega + \Delta)[\mathbf{h}] + [\mathbf{d}])^{-1}. \tag{16}$$

It follows from Eq. (15b) that

$$\begin{aligned}[\mathbf{H}] &= -[\mathbf{J}^{\Delta}(0)]^{-1}[\mathbf{J}^{\Delta}(0)]'[\mathbf{J}^{\Delta}(0)]^{-1} \\ &= ([\mathbf{J}^{\Delta}]^{-1})'|_{\Omega=0} = [\mathbf{h}],\end{aligned} \tag{17}$$

which shows that $[\mathbf{H}]$ is correctly recovered by the concatenation ansatz. It also follows from Eq. (15a) that

$$[\mathbf{D}] = [\mathbf{J}^{\Delta}(0)]^{-1} - [\mathbf{Q}] = \Delta[\mathbf{h}] + [\mathbf{d}] - [\mathbf{Q}]. \tag{18}$$

Thus, $[\mathbf{D}] = [\mathbf{d}]$ if $[\mathbf{Q}] = \Delta[\mathbf{h}]$. We confirm that the diagonal matrix $[\mathbf{Q}] = \Delta[\mathbf{h}]$ satisfies Eq. (11):

$$\begin{aligned}(\mathbf{I}_S - [\mathbf{J}^{\Delta}]\Delta[\mathbf{h}])\{E\} &= (\mathbf{I}_S - [\mathbf{J}^{\Delta}](-[\mathbf{d}] + [\mathbf{J}^{\Delta}]^{-1}))\{E\} \\ &= -[\mathbf{J}^{\Delta}]([\mathbf{D}]\{E\}) = 0.\end{aligned} \tag{19}$$

That $[\mathbf{D}]\{E\}$ is zero follows from identifying $\{E\}$ with the first eigenvector $\{\mathbf{V}\}^1$.

Finally, the condition, Eq. (13), is satisfied exactly:

$$\begin{aligned}\mathcal{N} &= -\{E\}^T[\mathbf{J}^{\Delta}]^{-1}[\mathbf{J}^{\Delta}]'[\mathbf{Q}]\{E\} \\ &= \{E\}^T([\mathbf{J}^{\Delta}]^{-1})'[\mathbf{J}^{\Delta}][\mathbf{Q}]\{E\} \\ &= \{E\}^T([\mathbf{J}^{\Delta}]^{-1})'\{E\} = \{E\}^T[\mathbf{H}]\{E\} = 1.\end{aligned} \tag{20}$$

In summary, closed form expressions for the parameters $[\mathbf{H}]$, $[\mathbf{D}]$ of a diffusion model have been obtained. They depend on data describing energy flow on short time scales. If the data are perfectly diffusive, the diffusion parameters the method extracts are exact (and, thus, invariant under Δ, as they ought to be to have meaning and usefulness). Moreover, a generalization to nondiffusive regimes is predicted for Ω away from the low Ω limit.

Weaknesses of the above-mentioned model include an assumption of diffusion: the model is set up to extract diffusion parameters in the zero Ω limit. If diffusion fails at $\Omega \rightarrow 0$ (e.g., Anderson localization[32]), the model must fail also. Also, with a view toward DNS simulations where receivers are relatively inexpensive compared to sources, there is a question of how to make use of receivers not allowed to act as sources so that E_r is unknown. One answer may be to use receivers that are close to sources such that their admittances can be estimated to be the same as those of the sources. Finally, it may be remarked that this concatenation method uses only magnitude information, i.e., the mean squares of the DNS responses. Relative phases are ignored; it is not yet clear what, if any, useful information is thereby neglected.

The present approach is tested in the following two sections. In Sec. III the model is tested on contrived data with known underlying diffuse character and noise superimposed. In Sec. IV the model is tested on DNS data from a system typically studied with SEA.

III. DATA WITH KNOWN DIFFUSIVE CHARACTER

Our desire is to be able to fit short-time DNS measured data to a diffusion model in order to be able to predict transport dynamics over longer times. Toward this end we here generate data artificially and attempt to use the equations of Sec. II to recover the parameters of diffusion.

We consider a simple case study of the strict substructuring class, which maps well onto SEA. It has two substructures (rooms). For these studies admittances (i.e., the elements of $\{E\}$) are taken as known, as if they have been evaluated by a procedure like that of Weaver[26] for sites with a source. Forcing $\{\Pi\}$ is also known as it would be in a DNS.

A. Description of data

The data to be fit is constructed by solving a time-domain SEA equation like Eq. (4) in a simple two substructure system. With a view toward application to data gleaned from a DNS, with inevitable stochastic fluctuations, we then add noise. Wolff and Weaver[27] contains the details of the noise construction method. Noise is generated independently at each r, t such that $\{\Psi\}$ has fixed fractional standard deviation σ. This is typical in stochastic wave systems. Moreover the fractional standard deviation is $\sigma = 1/\sqrt{\Delta f \Delta f}$ in real DNS applications or measurements where Δf is the bandwidth, and Δt is the duration of the time window over which energies are averaged. There is a theoretical argument[33] for this estimate, and some experimental studies are discussed by Davy.[34] Studying fluctuations from the mean is an area of active research. Some years ago there was a series of papers by Lyon[35] and Davy,[34,36,37] and more recently by Lobkis *et al.*[38] and Langley and others.[39–41]

For a sample interesting structure, the following parameters were chosen:

$$[\mathbf{H}] = \begin{bmatrix} 1 & 0 \\ 0 & \frac{1}{2} \end{bmatrix}, \quad [\mathbf{D}] = \begin{bmatrix} 1 & -\frac{1}{2} \\ -\frac{1}{2} & \frac{1}{4} \end{bmatrix} \tag{21}$$

corresponding to a system where one room is twice the size of the other. This results in parameters

$$\lambda_1 = 0, \quad \lambda_2 = 1.5, \tag{22a}$$

$$\{\mathbf{V}\}^1 = \begin{Bmatrix} 1 \\ 2 \end{Bmatrix} \Big/ \sqrt{3}, \quad \{\mathbf{V}\}^2 = \begin{Bmatrix} 1 \\ -1 \end{Bmatrix} \Big/ \sqrt{1.5}. \tag{22b}$$

The array of admittances was taken to be $\{E\} = \{\mathbf{V}\}^1$.

The fundamental solution $[\hat{\mathbf{J}}(t)]$ of Eq. (4) was constructed for times t out to $T = 100/\lambda_2$, i.e., 100 times the characteristic diffusion time. Data points were spaced by $\delta t = 10^{-2}/\lambda_2$. The information window $e^{-\Delta t}$ was restricted to emphasize time ranges from one time step ($\Delta = 100\lambda_2$) to the full domain ($\Delta = \lambda_2/100$). A few noise amplitudes were considered, $\sigma = 0\%$, 10%, 20%, 30%. Explicitly,

$$\hat{\mathbf{J}}_{rs}(t) = (\mathbf{V}_r^1 \mathbf{V}_s^1 + \mathbf{V}_r^2 \mathbf{V}_s^2 e^{-\lambda_2 t}) \times \chi_{rs}(t), \tag{23}$$

where χ is a chi-square distributed random number with unity mean and σ standard deviation.

The Fourier transforms needed for Eqs. (15a) and (15b) are calculated as follows:

$$[\mathbf{J}^{\Delta}(0)] = \int_0^T [\hat{\mathbf{J}}(t)] e^{(-i\Omega - \Delta)t} dt \big|_{\Omega=0} = \int_0^T [\hat{\mathbf{J}}(t)] e^{-\Delta t} dt, \tag{24}$$

$$[\mathbf{J}^{\Delta}(0)]' = \frac{\partial}{\partial i\Omega} \int_0^T [\hat{\mathbf{J}}(t)] e^{(-i\Omega - \Delta)t} dt \big|_{\Omega=0} = \int_0^T -t[\hat{\mathbf{J}}(t)] e^{-\Delta t} dt. \tag{25}$$

Estimated matrices $[\mathbf{Q}]$, $[\mathbf{D}]$, and $[\mathbf{H}]$ are then obtained from Eqs. (12), (15a), and (15b).

B. Results and discussion

A plot of the recovered first nontrivial eigenvalue of the estimated $[\mathbf{D}]$ and $[\mathbf{H}]$ matrices is shown in Fig. 1. The recovered value is accurate except at exceptionally small values of Δ. This is related to the cutoff in the numerical time integration. The error stemming from the cutoff is

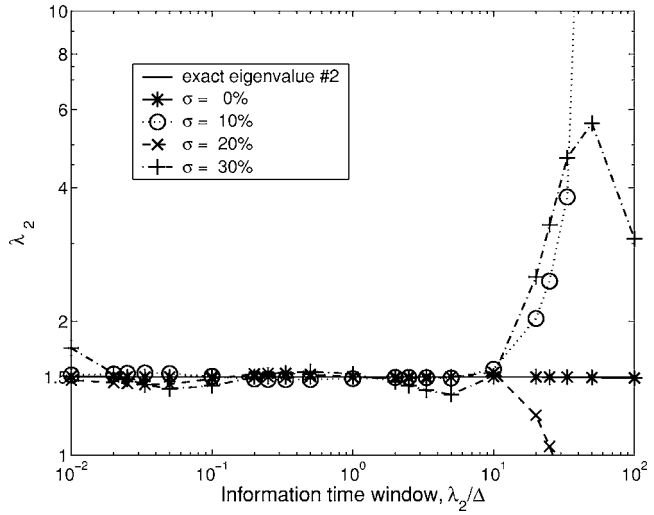

FIG. 1. First nontrivial eigenvalue for the artificial system is plotted vs a nondimensional measure of the duration of the information window $e^{-\Delta t}$. The extracted eigenvalue is good when sufficient information is retained. The method fails at low Δ because of an uninteresting cutoff in the numerical integration. Even with large Δ, corresponding to little information retained, the extracted eigenvalue is close to the known value.

$$\frac{\int_0^\infty te^{-\Delta t}dt - \int_0^T te^{-\Delta t}dt}{\int_0^\infty te^{-\Delta t}dt} = T\Delta e^{-T\Delta} + e^{-T\Delta}, \tag{26}$$

which is about 10% when $T\Delta$ is about 3.9. This explains the low Δ behavior of Fig. 1. That said, this error is uninteresting: it simply means that simulations [Eq. (23)] need to extend over some minimum multiple of $1/\Delta$ to achieve accuracy in the time integrations in Eqs. (24) and (25). In any case, small Δ is irrelevant to ultimate applications.

What is more striking is the accuracy for large Δ. As noted earlier, the largest value of Δ considered corresponds to retaining information in $[\mathbf{J}^\Delta]$ only through times of order $1/100\lambda_2$. Even with so little data effectively being used in the extraction of the diffusion parameters, both in an absolute sense and in a sense relative to how much information there is about the diffusion in the data, the program nevertheless extracts the correct eigenvalue. The implication is that Δ needs be chosen small enough only to capture the earliest stages of diffusive transport.

The condition, Eq. (13), is plotted in Fig. 2. The quantity $\mathcal{N}$ should be unity, and the recovered value is close to unity for a broad range of Δ. The uninteresting discrepancy for small Δ is present here as in Fig. 1. A discrepancy for large Δ is also observed. The discrepancy's weakness is striking, however, considering how little information is used in the calculations.

Finally, a plot of the prediction based on the recovered diffusion parameters $[\mathbf{H}]$ and $[\mathbf{D}]$ is shown in Fig. 3 superimposed on the original noisy data. This is for one of the extreme cases suggested by Figs. 1 and 2 of $\Delta/\lambda_2=50$ (corresponding to retention of information through time $1/50\lambda_2$) and $\sigma=20\%$. The diffusion parameters recovered by the concatenation calculations represent the data well.

With a view toward adding extra receivers in DNS, this suggests a figure of merit of the following form:

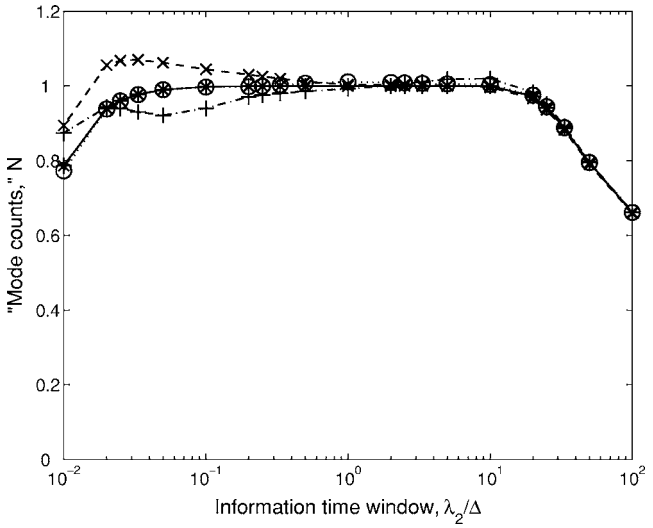

FIG. 2. Condition of Eq. (13). The check fails at low Δ because of the uninteresting cutoff in the numerical integration. It fails at high Δ only when $1/\Delta$ is less than two time steps of data, i.e., 1/50 of a diffusion time $1/\lambda_2$. Legend is the same as in Fig. 1.

$$\text{figure of merit(f.o.m.)} = \frac{1}{\sigma}\sqrt{\frac{R}{S}N_t}, \tag{27}$$

where R/S is the number of receivers per source, and $N_t = 1/\delta t\Delta$ is the number of uncorrelated time points within the information window. Fluctuations can be effectively reduced by averaging the signal from several nearby receivers. The f.o.m. takes a value of 7.1 with the parameters of Fig. 3.

IV. APPLICATION TO DNS DATA

The concatenation ansatz is now applied to imperfectly diffusive data. The analysis here differs from that of Sec. III in that the data are generated by DNS; thus, it is not necessarily described by the solution of a diffusion equation like

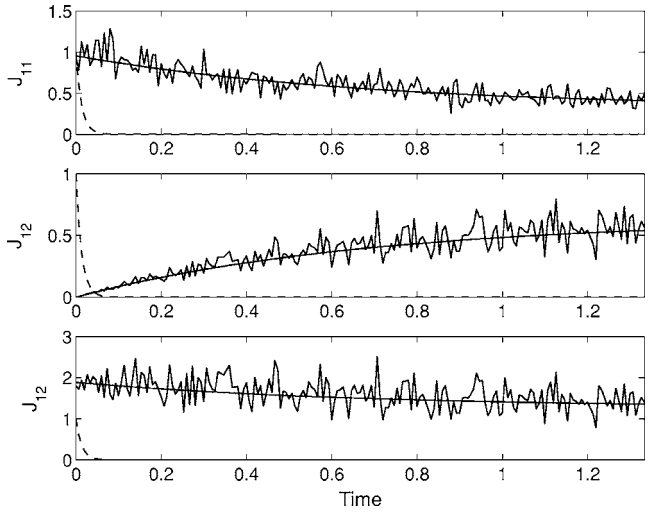

FIG. 3. Fit of intensity calculated from the recovered diffusion parameters along with original noisy artificial data. Data are plotted out to $t_{max}=1.33=2/\lambda_2$=two diffusion times. Noise amplitude $\sigma=20\%$; $\Delta/\lambda_2=50$. The smooth solid lines represent the solutions based on $[\mathbf{H}]$ and $[\mathbf{D}]$, calculated from $[\hat{\mathbf{J}}^\Delta]$, equal to data (jagged lines) multiplied by $e^{-\Delta t}$. The dashed curve shows $e^{-\Delta t}$.

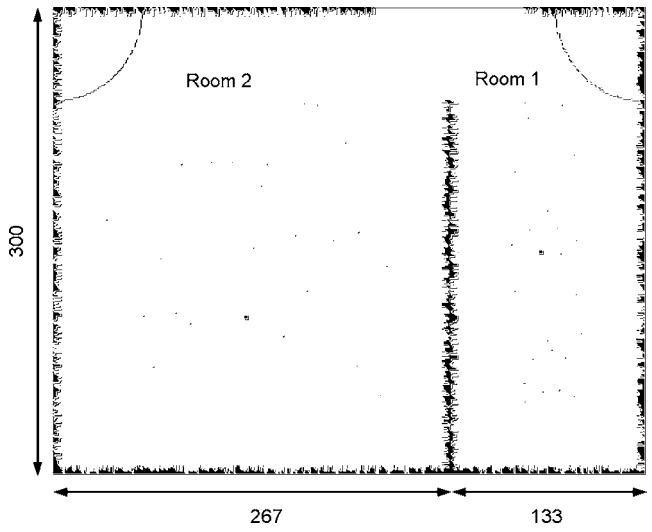

FIG. 4. Geometry of the system analyzed with DNS. There are two rooms with 25 receivers in each room. Scatterers and roughened walls are used to randomize the flow of energy and more rapidly establish a diffuse energy state. The two receivers acting as sources are indicated with heavy dots.

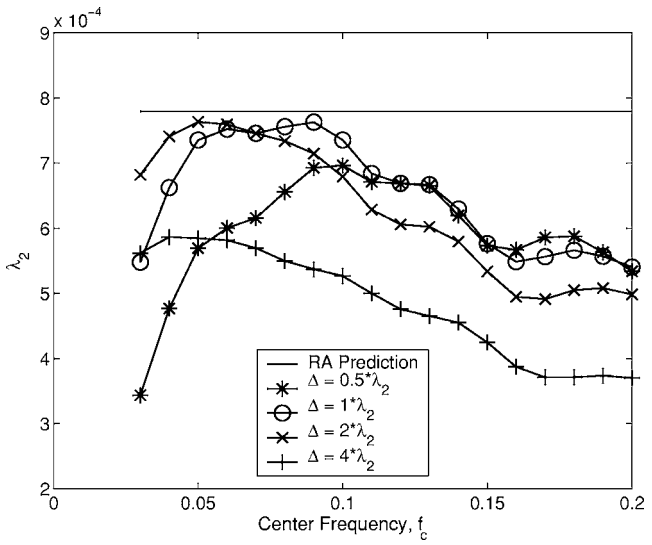

FIG. 5. First nontrivial eigenvalue obtained from the DNS data for various center frequencies and Δ's. The Δ is in units of the theoretical room acoustics (RA) prediction. Smallest $\Delta=0.5\lambda_2$ corresponds to about five information windows in total time. The largest Δ corresponds to about one transit time, before a diffuse field is established.

Eq. (4). Also, the noise amplitude cannot be controlled directly; instead, data are smoothed (averaged) over frequency and over nearby receivers where admittances are equal to the admittance at the source. The weak Anderson localization[42] enhanced backscattering effect is first divided out of the intensity at the source site. These nearby receivers thus define a "cloud" of equivalent receivers associated with the source. This smoothing results in noise with fixed fractional standard deviation over the data set. Data are also considered for different center frequencies.

A. Time domain solutions

The system considered is pictured in Fig. 4. It consists of a 400×300 membrane, with nominal wave speed $c=1$, divided into two substructures (133×300 and 267×300) coupled by a window of length 60. In practice, this window must be small for the "weak-coupling" demanded by SEA but larger than a few wavelengths to avoid localization.[26,32] Scatterers are placed, and the walls are roughened, to scatter the reflecting waves. This enhances randomization and more rapidly establishes a diffuse field in each substructure. In particular, two large rigid (Dirichlet) quarter circles are placed opposite the windows to de-focus rays. A total of 50 source/receiver locations are marked in the figure, 25 placed randomly in each room. The two locations acting as sources are marked with a heavier dot.

The DNS is obtained by solving central difference equations in space and time. The time step used is $\delta t=0.4$. Two solutions are obtained directly, one with an impulsive source at the source site in room one, the other with an impulsive source at the source site in room two. For each source a total of 50 wave forms, one for each receiver, are recorded.

Filtered solutions are obtained by convolving the impulse response with a finite duration sinusoidal filter

$$B(t)=\begin{cases}0, & t<-\dfrac{T_B}{2}\\ B_0\left(1+\cos\dfrac{2\pi t}{T_B}\right)\cos(2\pi f_c t), & -\dfrac{T_B}{2}<t<\dfrac{T_B}{2},\\ 0, & t>\dfrac{T_B}{2}\end{cases} \tag{28}$$

where f_c is the center frequency of the tone burst, $T_B=60$ is the filter duration, and the coefficient B_0 is such that $\int B^2(t)dt=1$. Center frequencies were considered over a range $f_c=0.03-0.20$. The full width at half power of $B(t)$, calculated numerically, is $\Delta f=0.0239$. This corresponds to a correlation time in the filtered responses of $\Delta t=1/\Delta f=41.8$. These filtered solutions are then squared and averaged over the several (25) nearby receivers in each cloud.

The filter duration was chosen so that there are no reflections from the walls or other scatterers within the duration of the filter. This implies that the admittances $\{E\}$ calculated directly from Eq. (3) are identical for each receiver. This precludes the need to locate a source at each receiver site.

B. Results and discussion

The nontrivial eigenvalue recovered from the concatenation calculations is shown in Fig. 5 as a function of center frequency f_c and for various Δ's. The f.o.m.$=\sqrt{R/S\times\Delta f/\Delta}$ ranges from 14–39 as Δ ranges from $4\lambda_2$ to $0.5\lambda_2$. This is perhaps a slight overestimate, as the receivers are not fully independent. The simple theoretical room acoustics prediction λ_2 is also shown for comparison. The room acoustic prediction is obtained by solving the eigenvalue problem with

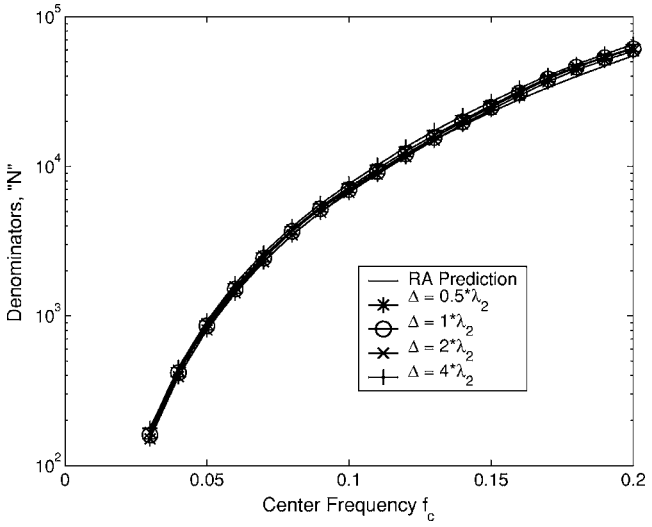

FIG. 6. Check of Eq. (13). The check fails strongly at low Δ because of the uninteresting cutoff in the numerical integration (not shown), but is reasonable at high Δ in spite of $1/\Delta$ being insufficient time to establish a diffuse field.

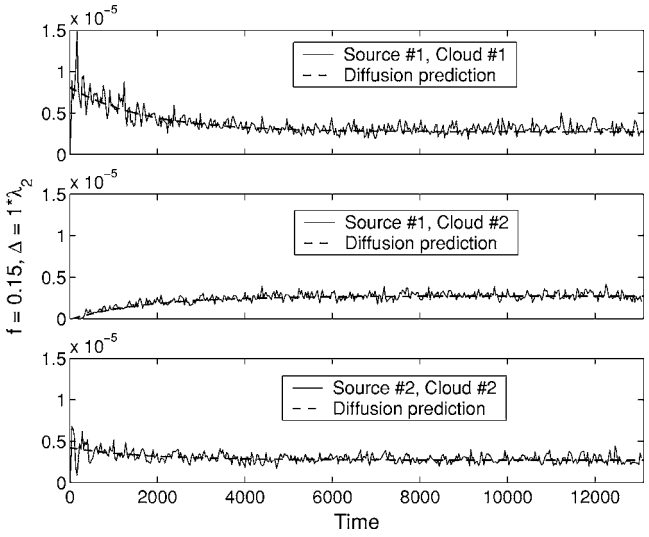

FIG. 7. Prediction of intensity calculated from the recovered diffusion parameters along with original noisy data (averaged over time and nearby receivers) for a "good" choice of Δ.

$$[\mathbf{H}] = \begin{bmatrix} A_1 & 0 \\ 0 & A_2 \end{bmatrix}, \quad [\mathbf{D}] = \frac{cl}{\pi}\begin{bmatrix} 1 & -1 \\ -1 & 1 \end{bmatrix}, \tag{29}$$

where A_r is the area of room r, the wave speed c is unity in nondimensional units, and $l=60$ is the window width. Corrections to the areas are made for the wall roughness and other scatterers. The eigenvalues are

$$\lambda_1 = 0, \quad \lambda_2 = \frac{cl}{\pi}\frac{A_1 + A_2}{A_1 A_2} \approx 7.79 \times 10^{-4}. \tag{30}$$

The extracted eigenvalue differs from the room acoustics estimate. The validity of this room acoustics estimate is in question here: the extracted values of the diffusion parameters represent the data better.

The extracted eigenvalue is independent of Δ over a range of moderate Δ, but differs for either small or large Δ. Deviations can be explained by realizing that the energy in the structure is not fully diffuse at the short times implicit in large Δ. Also, for smaller Δ, $[\mathbf{J}^{\Delta}(0)]$ and $[\mathbf{J}^{\Delta}(0)]'$ are in error because of the uninteresting cutoff in time integration (not shown).

The condition, Eq. (13), is shown in Fig. 6 along with a Weyl series estimate based on the geometry for comparison. This estimate was confirmed to be correct by direct comparison to late time mean square displacement using the methods of Weaver[26] (not shown). The denominator, $\mathcal{N}$, is plotted against frequency for various Δ's. The recovered value for $\mathcal{N}$ is reasonably close to the estimate even for largest value of Δ shown in the figure, but not for small Δ (not shown).

The smooth behavior that underlies the fluctuations is recovered from the extracted diffusion parameters by the solution to Eq. (4). It represents the filtered, smoothed data well, as shown in Fig. 7. The data shown are for a representative center frequency ($f=0.150$) and information window ($\Delta = 1 \times \lambda_2$) from within the good range of Δ. The data have been smoothed in time over a window of width $T_B/2$ in order to reduce the fluctuations. If the simple room acoustics estimate had been used, the fit would not have represented the data well.

The recovered underlying behavior extracted using a large Δ is plotted against the same filtered, smooth data in Fig. 8. The large value used there ($1/\Delta = 321$) corresponds to retention of information over approximately one transit time (time for the first wave front to reach the middle receiver from the other source ≈ 300). The correct value of the response at late times is predicted, consistent with the reasonable value of $\mathcal{N}$ seen in Fig. 6. However, the rate at which this value is achieved is markedly slow, corresponding to the underprediction of the eigenvalue seen in Fig. 5. We ascribe the discrepancy to the imperfectly diffuse character of the wave field at those short times ~ 300. Indeed, very little sig-

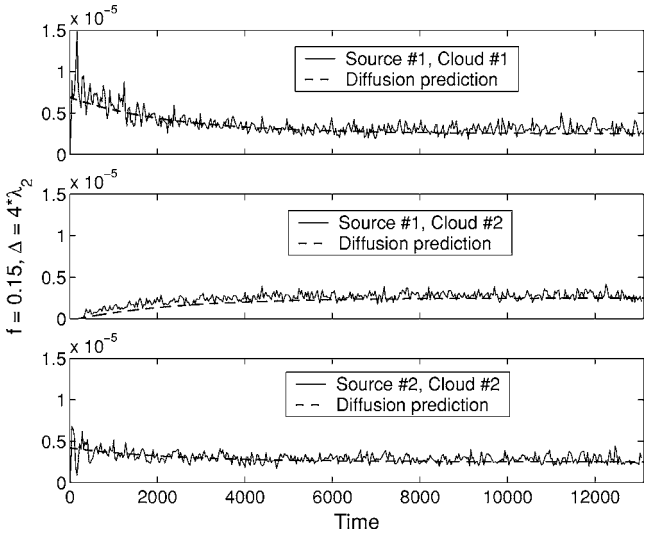

FIG. 8. Prediction of intensity calculated from the recovered diffusion parameters along with original noisy data (averaged over time and nearby receivers) for a "bad" choice of Δ. The late time response is predicted correctly corresponding to a reasonable value of $\mathcal{N}$ in Fig. 6. The diffusion rate is slow, corresponding to the incorrect value in Fig. 5.

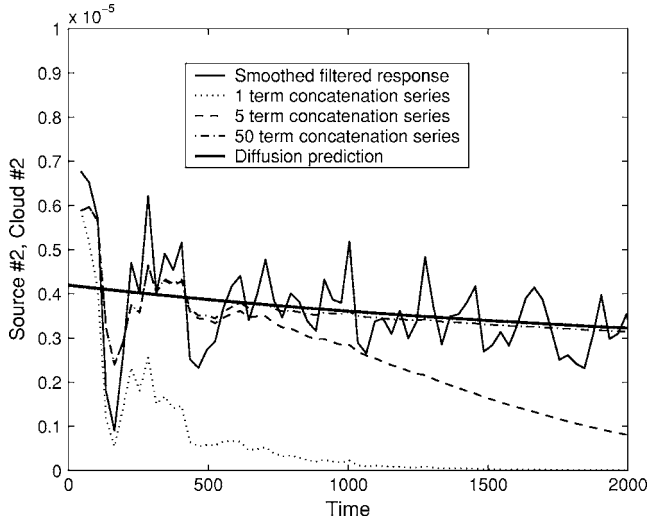

FIG. 9. Prediction from the concatenation series of Eq. (7) at early times. The parameters are $f_c=0.15$ and $\Delta=4\lambda_2$. The solid jagged line is the smoothed filtered response at receivers in room 2 from the source in room 2, $\hat{\mathbf{J}}_{22}$; the lowest data (dotted line) are a one term concatenation series, $\hat{\mathbf{J}}_{22}^{\Delta}$; and the smooth solid line is the diffusion prediction from $[\mathbf{H}]$ and $[\mathbf{D}]$. The concatenation series represents the data well during the early time, nondiffusive, regime; the diffusion prediction represents the data well after a sufficient time has passed to establish a diffusive field.

nal has yet arrived at distant receivers. It is perhaps surprising that the fits are as good as they are. If Δ had been even slightly larger, $[\mathbf{J}^{\Delta}]$ would be virtually diagonal, and the ansatz would fail. The f.o.m. for this case is 14, larger than the 7.1 found adequate in Sec. III B. A larger f.o.m. is needed here because information is needed covering the early stages of diffusion.

We note that a nondiffusive regime is predicted for early times. This is most easily explored by eschewing the $\Omega\rightarrow 0$ limit and evaluating the concatenation series for $\hat{\mathbf{J}}_{22}^{\text{concat}}$ [Eq. (7)]. Figure 9 shows intensity at early times (smoothed in time over a window of width $T_B/2$) as given by a one-term series $\hat{\mathbf{J}}_{22}^{\Delta}$, five-term series, and by a fifty-term series. We judge by visual inspection the series Eq. (7) to have converged over the time range shown. The diffusion prediction is also plotted. The concatenation series represents the response at early times $t<600$ better than the diffusion prediction. In particular, it captures the undulations of period ~ 150 due to reverberations off the walls. After this early time, the diffusion prediction represents the data well.

One might object that the substructuring is being used explicitly in the selection of source/receiver sites. The authors have carried out similar analysis with receivers more closely spaced, eschewing knowledge of substructuring. In particular, the receivers were placed in one cloud—in each room close to the respective source—each a five by five array with receivers spaced 15 grid spacing apart. Results (not shown) were almost as good. In particular, the denominator, $\mathcal{N}$, was somewhat underpredicted for large Δ. This lead to an overshooting of the prediction for late time response, suggesting that the method was seeing the structure as smaller than it really was. The more random placement of receivers leads to a better sampling of energy density throughout the structure.

V. CONCLUSIONS

We have proposed a procedure for extracting diffusion parameters from cost-effective DNS data. The method readily extracts diffusion parameters for any application for which the energy transport is anticipated to be diffusive, including any application suitable for SEA. The $[\mathbf{J}^{\Delta}]$ and $[\mathbf{J}^{\Delta}]'$ matrices are obtained from (band-limited squared) raw data from Eqs. (24) and (25). These yield the weights $[\mathbf{Q}]$ by Eq. (11) and, finally, the parameters $[\mathbf{D}]$ and $[\mathbf{H}]$ of Eq. (4), the governing diffusion equation, by Eqs. (15a) and (15b).

Behavior over the full time range is successfully predicted from analysis of DNS data acquired at short times only. The method extracts the correct eigenvalues of the $[\mathbf{D}]$ and $[\mathbf{H}]$ matrices, and an independent check of the global modal density is satisfied. Finally, the explicit solution to the diffusion equation, Eq. (4), represents the DNS data well. There are no fit parameters. The method is robust for the simple systems studied in this paper. Future work extending the technique is indicated.

A possible way to further reduce computational burden may be to use a rectangular window instead of an exponential $e^{-\Delta t}$. The latter de-emphasizes late times as desired, but does so rather inefficiently. In addition, the cutoff in numerical integration to calculate the Fourier transforms is problematic. This is particularly the case in $[\mathbf{J}^{\Delta}]'$ because of the extra factor of t in the integrand. An effort to examine the effect of a rectangular window in lieu of $e^{-\Delta t}$ is therefore indicated.

Recasting the DNS problem from the time domain to the frequency domain may be helpful. Most other work is done in the frequency domain. We note that the quantity $\mathbf{J}^{\Delta}(\Omega)$ is readily constructed in frequency domain DNS by evaluating responses at complex inner frequencies $\omega\pm i\Delta/2\pm\Omega/2$.[6]

Structures that do not admit substructuring should be studied. To date, we have examined only what may be more properly called "conduction" in systems which can be clearly divided into two rooms. Diffusion itself is expected to govern systems with enough scatterers to establish a diffuse vibrational energy field, but without walls and windows to separate the system into clearly defined rooms.[6,7,9]

One possibly subtle complication will be incorporating systems that admit local resonances, e.g., receivers inside a cavity or near a wall for which admittances are strong functions of frequency.[26] One way to deal with such cases is to have a source at each receiver site and calculate the admittance explicitly. This is computationally demanding so there may be value in seeking rational ways to estimate all admittances with fewer sources.

ACKNOWLEDGMENT

This work was supported in part by NSF Grant No. CMS-0201346.

APPENDIX A: DERIVATION OF [Q] FORMULA

To obtain $[\mathbf{Q}]$ we constrain $\hat{\mathbf{J}}^{\text{concat}}$ to have a specified steady state (late time) value.

$$\hat{\mathbf{J}}_{rs}^{\text{concat}}(t) = \hat{\mathbf{J}}_{rs}^{\text{steady-state}}(t) + \hat{\mathbf{J}}_{rs}^{\text{trans}}(t), \tag{A1a}$$

$$= \frac{E_r E_s}{\mathcal{N}} \Theta(t) + \hat{\mathbf{J}}_{rs}^{\text{trans}}(t), \tag{A1b}$$

where $\hat{\mathbf{J}}_{rs}^{\text{steady-state}}$ is the late-time steady state response which can be predicted accurately by Ref. 26 and $\hat{\mathbf{J}}_{rs}^{\text{trans}}$ is the transient response (which vanishes at $t \to \infty$). It is this transient response which this proposal is attempting to recover. This is an extension of the theory in Ref. 26.

Taking a Fourier transform and considering the zero frequency limit results in

$$\mathbf{J}_{rs}^{\text{concat}}(\Omega) = \frac{E_r E_s}{\mathcal{N} i\Omega} + \mathbf{J}_{rs}^{\text{trans}}(\Omega), \tag{A2}$$

where i is the imaginary unit and the second term on the right-hand side is bounded for all Ω. Shifting to matrix notation and substituting from Eq. (10),

$$(\mathbf{I}_S - [\mathbf{J}^{\Delta}][\mathbf{Q}])^{-1}[\mathbf{J}^{\Delta}] = \frac{\{E\}\{E\}^T}{\mathcal{N} i\Omega} + [\mathbf{J}^{\text{trans}}]. \tag{A3}$$

So,

$$[\mathbf{J}^{\Delta}(\Omega)] = (\mathbf{I}_S - [\mathbf{J}^{\Delta}][\mathbf{Q}]) \frac{\{E\}\{E\}^T}{\mathcal{N} i\Omega} + (\mathbf{I}_S - [\mathbf{J}^{\Delta}][\mathbf{Q}])[\mathbf{J}^{\text{trans}}]. \tag{A4}$$

The left-hand side is bounded as $\Omega \to 0$, so

$$\lim_{\Omega \to 0} (\mathbf{I}_S - [\mathbf{J}^{\Delta}][\mathbf{Q}])\{E\} = \{\mathbf{A}\} i\Omega \tag{A5}$$

for some vector $\{\mathbf{A}\}$. So, defining $[\mathbf{J}(\Omega)]' \equiv (\partial / \partial i\Omega)[\mathbf{J}(\Omega)]$,

$$(\mathbf{I}_S - [\mathbf{J}^{\Delta}(0)][\mathbf{Q}])\{E\} = 0, \tag{A6a}$$

$$[\mathbf{J}^{\Delta}(0)]'[\mathbf{Q}]\{E\} = -\{\mathbf{A}\} \tag{A6b}$$

are conditions on $[\mathbf{Q}]$ and $\{\mathbf{A}\}$. Equation (11) is thus derived, and Eq. (A6b) is used in the following.

APPENDIX B: DERIVATION OF $\mathcal{N}$ CONDITION

Substituting Eq. (A6b) into Eq. (A4), and evaluation as $\Omega \to 0$, one finds

$$[\mathbf{J}^{\Delta}] = -\frac{[\mathbf{J}^{\Delta}]'[\mathbf{Q}]\{E\}\{E\}^T}{\mathcal{N}} + (\mathbf{I}_S - [\mathbf{J}^{\Delta}][\mathbf{Q}])[\mathbf{J}^{\text{trans}}]. \tag{B1}$$

Multiplying on the left by $[\mathbf{J}^{\Delta}(0)]^{-1}$,

$$\mathbf{I}_S = -\frac{[\mathbf{J}^{\Delta}]^{-1}[\mathbf{J}^{\Delta}]'[\mathbf{Q}]\{E\}\{E\}^T}{\mathcal{N}} + ([\mathbf{J}^{\Delta}]^{-1} - [\mathbf{Q}])[\mathbf{J}^{\text{trans}}]. \tag{B2}$$

Multiplying on the left by $\{E\}^T$, the second term vanishes by Eq. (11), and

$$\{E\}^T = \frac{(-\{E\}^T[\mathbf{J}^{\Delta}]^{-1}[\mathbf{J}^{\Delta}]'[\mathbf{Q}]\{E\})\{E\}^T}{\mathcal{N}}. \tag{B3}$$

The term in parentheses is, evidently, $\mathcal{N}$:

$$\mathcal{N} = -\{E^T\}[\mathbf{J}^{\Delta}]^{-1}[\mathbf{J}^{\Delta}]'[\mathbf{Q}]\{E\}, \tag{B4}$$

which is Eq. (13).

[1] R. H. Lyon and R. G. DeJong, *Theory and Application of Statistical Energy Analysis*, 2nd ed. (Butterworth-Heimann, Boston, 1995).
[2] F. J. Fahy, "Statistical energy analysis: A critical overview," Philos. Trans. R. Soc. London, Ser. A **346**, 431–447 (1994).
[3] J. Woodhouse, "An approach to the theoretical background of statistical energy analysis applied to structural vibration," J. Acoust. Soc. Am. **69**, 1695–1709 (1981).
[4] J. Woodhouse, "An introduction to statistical energy analysis of structural vibration," Appl. Acoust. **14**, 455–469 (1981).
[5] C. H. Hodges and J. Woodhouse, "Theories of noise and vibration transmission in complex structures," Rep. Prog. Phys. **49**, 107–170 (1986).
[6] R. L. Weaver, "Diffusivity of ultrasound in polycrystals," J. Mech. Phys. Solids **38**, 55–86 (1990).
[7] A. Tourin, A. Derode, A. Peyre, and M. Fink, "Transport parameters for an ultrasonic pulsed wave propagating in a multiple scattering medium," J. Acoust. Soc. Am. **108**, 503–512 (2000).
[8] A. Tourin, A. Derode, P. Roux, B. A. Tiggelen, and M. Fink, "Time-dependent coherent backscattering of acoustic waves," Phys. Rev. Lett. **79**, 3637–3639 (1997).
[9] X. Jia, C. Caroli, and B. Velicky, "Ultrasound propagation in externally stressed granular media," Phys. Rev. Lett. **82**, 1863–1866 (1999).
[10] V. O. Knudsen and C. M. Harris, *Acoustical Designing in Architecture* (Wiley, New York, 1950).
[11] B. R. Mace and P. J. Shorter, "Energy flow models from finite element analysis," J. Sound Vib. **233**, 369–389 (2000).
[12] C. R. Fredo, "SEA-like approach for the derivation of energy flow coefficients with a finite element model," J. Sound Vib. **199**, 645–666 (1997).
[13] K. Shankar and A. J. Keane, "Vibrational energy flow analysis using a substructure approach: The application of receptance theory to FEA and SEA," J. Sound Vib. **201**, 491–513 (1997).
[14] R. S. Langley and P. J. Shorter, "The wave transmission coefficients and coupling loss factors of point connected structures," J. Acoust. Soc. Am. **113**, 1947–1964 (2003).
[15] M. L. Lai and A. Soom, "Prediction of transient vibration envelopes using statistical energy analysis techniques," Ind. Math. **122**, 127–137 (1990).
[16] R. J. Pinnington and D. Lednik, "Transient SEA of an impulsively excited two oscillator system," J. Sound Vib. **189**, 249–264 (1996).
[17] R. S. Langley and P. G. Bremner, "A hybrid method for the vibrational analysis of complex structural-acoustic systems," J. Acoust. Soc. Am. **105**, 1657–1671 (1999).
[18] K. Shankar and A. J. Keane, "Energy flow predictions in a structure of rigidly joined beams using receptance theory," J. Sound Vib. **185**, 867–890 (1995).
[19] K. Shankar and A. J. Keane, "A study of the vibrational energies of two coupled beams by FEM and receptance methods," J. Sound Vib. **181**, 801–838 (1995).
[20] C. Simmons, "Structure-borne sound transmission through plate junctions and estimates of SEA coupling loss factors using the finite element method," J. Sound Vib. **144**, 215–227 (1991).
[21] J. A. Steel and R. J. M. Craik, "Statistical energy analysis of structure-borne sound transmission by FEM," J. Sound Vib. **178**, 553–561 (1994).
[22] E. H. Dowell and Yuji Kubota, "Asymptotic modal analysis and SEA of dynamical systems," J. Appl. Mech. **52**, 949–957 (1985).
[23] J. W. Gregory and R. F. Keltie, "SEA system identification using transient vibration data," in Proceedings of the Second International AutoSEA Users Conference, Detroit-Troy Marriott, Troy, MI, 2002.
[24] J.-N. Juang and R. S. Pappa, "An eigensystem realization algorithm for modal parameter identification and model reduction," J. Guid. Control Dyn. **8**, 620–627 (1985).
[25] R. S. Langley, J. R. D. Smith, and F. J. Fahy, "Statistical energy analysis of periodically stiffened damped plate structures," J. Sound Vib. **208**, 407–426 (1997).
[26] R. L. Weaver, "Equipartition and mean-square responses in large undamped structures," J. Acoust. Soc. Am. **110**, 894–903 (2001).
[27] N. L. Wolff and R. L. Weaver, "Towards a diffusion model of acoustic energy flow in large undamped structures," J. Sound Vib. (to be published).

[28] The term "impulsive" applied to band limited mean square forcings is a short-duration tone burst on the inner fast time scale.
[29] The Fourier transform variable is the outer frequency Ω of the slow-time

energy transport. This is not the inner frequency ω of displacement data obtained in a DNS of the system.
[30]It is interesting that [**H**] need not be diagonal, nor must [**D**] have support only between physically connected substructures.
[31]That is, a solution to Eq. (4) without fluctuations.
[32]R. L. Weaver and O. I. Lobkis, "Anderson localization in coupled reverberation rooms," J. Sound Vib. **231**, 1111–1134 (2000).
[33]D. E. Newland, *An Introduction to Random Vibrations and Spectral Analysis*, 2nd ed. (Longman House, New York, 1984).
[34]J. L. Davy, "The ensemble variance of random noise in a reverberation room," J. Sound Vib. **107**, 361–373 (1986).
[35]R. H. Lyon, "Statistical analysis of power injection and response in structures and rooms," J. Acoust. Soc. Am. **45**, 545–565 (1967).
[36]J. L. Davy, "The relative variance of the transmission function of a reverberation room," J. Sound Vib. **77**, 455–479 (1981).
[37]J. L. Davy, "Improvements to formulae for the ensemble relative variance of random noise in a reverberation room," J. Sound Vib. **115**, 145–161 (1987).
[38]O. I. Lobkis, R. L. Weaver, and I. Rozhkov, "Power variances and decay curvature in a reverberant system," J. Sound Vib. **237**, 281–302 (2000).
[39]R. S. Langley and V. Cotoni, "Response varience prediction in the statistical energy analysis of built-up structures," J. Acoust. Soc. Am. **115**, 706–718 (2004).
[40]R. S. Langley and A. W. M. Brown, "The ensemble statistics of the energy of a random system subjected to harmonic excitation," J. Sound Vib. **275**, 823–846 (2004).
[41]R. S. Langley and A. W. M. Brown, "The ensemble statistics of the band-averaged energy of a random system," J. Sound Vib. **275**, 847–857 (2004).
[42]R. L. Weaver and J. Burkhardt, "Weak Anderson localization and enhanced backscatter in reverberation rooms and quantum dots," J. Acoust. Soc. Am. **96**, 3186–3190 (1994).

Sound propagation and energy relations in churches

Ettore Cirillo and Francesco Martellotta[a)]
Dipartimento di Fisica Tecnica, Politecnico di Bari, via Orabona 4, I-70125 Bari, Italy

(Received 28 January 2005; revised 15 April 2005; accepted 20 April 2005)

The results of an acoustic survey carried out in a group of Italian churches differing in style, typology, and location were used in order to study how the acoustic energy varies inside this kind of space. The effect of different architectural elements on sound propagation was investigated by means of three-dimensional impulse responses measured using a B-format microphone with sweep signals. Side chapels, columns, and trussed roofs appeared to scatter the reflections, so that the purely diffuse exponential sound decay begins after a time interval which grows with the source–receiver distance and with the complexity of the church. The results of the measurements were then compared with predictions given by existing theoretical models to check their accuracy. In particular a model previously proposed by the authors for a specific type of Romanesque churches was further refined taking into account the new findings and making some simplifications. Its application to the wider sample of churches under analysis showed that strength, clarity, and center time can be predicted with reasonable accuracy.
 [DOI: 10.1121/1.1929231]

PACS number(s): 43.55.Br, 43.55.Gx [NX] Pages: 232–248

I. INTRODUCTION

The prediction of acoustical parameters for the purposes of architectural acoustics is a task currently carried out almost exclusively using computer programs. These give detailed and reliable results but require a three-dimensional (3D) model of the room in question. However, researchers and professionals often welcome the availability of simple prediction formulas because they can provide reference values with little calculation effort and also aid the general understanding of room acoustics.

The success of the reverberation time as a measure relies not only on its correlation with perceived subjective quality, but also on its being appropriate for a whole space, and, above all, on its predictability with some simple formulas[1,2] which cover most of the cases (or at least those having even absorption and mixing geometries[3]). When dealing with individual position parameters things become more complex, but, at least for sound strength and clarity, Barron and Lee[4] propose a "revised theory" which, assuming that the reflected sound cannot arrive earlier than direct sound, makes both parameters decrease as a function of the distance. In concert halls and other proportionate spaces this theory provides considerably better predictions of the real behavior of strength and clarity than any classical formula based on constant reverberant field theory.[5] A further modification of this theory has been proposed by Vörlander[6] for reverberant chambers, and this method is commonly used to account for a decrease in reflected level due to sound absorbed at the first reflection.

Unfortunately, several studies show that churches and other places of worship can hardly be included among the "proportionate" spaces. Measurements of both strength and clarity carried out in Gothic-Mudejar churches,[7,8] in Mosques,[9] and in Italian churches[10,11] show that reflected sound levels generally fall below those predicted by the revised theory. Possible explanations for this behavior may be found in the "disproportionate" nature of these kinds of buildings, and in the effect of columns, side aisles, chapels, high vaults, and other architectural elements which scatter or hinder the sound, especially affecting early reflections.[10] However, several works show that, despite some fluctuations, the acoustic parameters under investigation are well related to source–receiver distance, allowing the development of prediction equations based on simple regression models,[12,13] or leading to modifications of the revised theory in order to fit the measured data[7,10] better. However, the model proposed by Sendra *et al.*[7] introduces an attenuation of the reflected energy (based on regression analyses), which equally affects early and late reflections, improving the prediction accuracy for sound level but not for early-to-late energy indices.[8]

The model proposed by Cirillo and Martellotta[10] for Apulian-Romanesque churches assumes that the early reflected energy varies linearly within a time interval proportional to the source–receiver distance, after which the reverberant sound follows a purely exponential decay. The present paper further investigates this model by taking into account a wider group of churches, spanning different architectural styles (from Early-Christian to Modern), and different typologies (basilica plan, single nave, central plan). The whole set of collected data was analyzed in order to validate some of the assumptions on which the modified theory is based. Then, taking into account both the new and the old results, the modified theory was refined in order to remove some of the weakest links. In fact, as observed by Chiles and Barron,[5] the first formulation of the theory requires some approximations that could make its application difficult or, in some ways, subjective. Finally, the reliability of the model was

[a)]Electronic mail: f.martellotta@poliba.it

checked by comparing measured and predicted values of sound strength (G), clarity (C_{80}), and center time (T_s).

II. OVERVIEW OF THEORETICAL MODELS

A. The classical theory

According to the classical theory of sound propagation in enclosed rooms,[1] if the absorption is uniformly distributed and if the sound field is diffuse, the sound pressure level at a point at a distance r from the source (assumed to be omnidirectional) is

$$L(r) = 10 \log\left[\frac{\rho_0 c W}{p_{\text{ref}}^2}\left(\frac{1}{4\pi r^2} + \frac{4}{A}\right)\right] \text{(dB)}, \tag{1}$$

where ρ_0 is the density of the air, c is the sound speed in air, p_{ref} is the standard reference sound pressure, W is the sound power of the source, and A is the total acoustic absorbing area (including both wall absorption and air absorption). A can be expressed as a function of the reverberation time (T) and of the room volume (V) by means of Sabine's equation ($A=0.161\ V/T$). If the sound pressure level is measured in relative terms, that is assuming the level L_{10} of the direct sound at a distance of 10 m from the source as a reference, Eq. (1) becomes

$$G(r) = L(r) - L_{10} = 10 \log(100/r^2 + 31\ 200T/V)\ \text{(dB)}. \tag{2}$$

According to the classical theory, when a perfectly exponential decay follows an interrupted steady-state excitation, then the energy decay after an impulse sound also decays exponentially with the same time constant (equal to $T/13.8$). The instantaneous energy density of the reverberant field following a power impulse $W\cdot\Delta t$ (Δt being the pulse duration) is given by

$$D_r(t) = (W\Delta t/V)\cdot e^{-13.8\cdot t/T}\ (\text{J/m}^3). \tag{3}$$

Consequently, the integral of Eq. (3) divided by Δt equals the steady-state energy of the reverberant sound field generated by a continuous sound source radiating the same power W. The energy density may be conveniently expressed in relative terms by dividing Eq. (3) by the energy density of an impulsive sound at a distance of 10 m:

$$D_{d10} = W\Delta t/(400\pi c)\ (\text{J s/m}^3), \tag{4}$$

so the relative energy density of the reflected sound is

$$g(t) = D_r(t)/D_{d10} = (13.8\cdot 31\ 200/V)\cdot e^{-13.8\cdot t/T}\ (\text{s}^{-1}), \tag{5}$$

and becomes dimensionless after integration. All the energy-based acoustic parameters may be calculated using Eq. (5), but the main drawback of the classical theory is that beyond the reverberation radius the predicted variation in total level and in every other acoustic parameter is small compared to the actual measured values.

B. The revised theory

Barron and Lee[4] proposed a model to account for the larger variations of acoustic parameters observed in real rooms. They noticed that the concert hall situation differed from diffuse requirements in several aspects. However, they found that the sound level decay was linear soon after the direct sound in the majority of the halls, the main discrepancy being observed in the decrease in the reflected sound level with increasing source–receiver distance. So, they proposed a model based on the following assumptions. The direct sound is followed by linear level decay at a rate corresponding to the reverberation time. During a decay the instantaneous level of the late decaying sound is uniform throughout the space, so that decay traces for all receiver positions are superimposed. The time $t=0$ corresponds to the time the signal is emitted from the source, therefore the direct sound reaches a point at a distance r from the source after a time $t_D=r/c$. In this way the integrated energy decreases when the source–receiver distance increases, while the early/late reflected energy ratio remains constant. The integrated value for the reflected sound level is assumed to be, at $t=0$, equal to the value predicted by the classical theory [Eq. (2)].

The application of Barron's revised theory allows the calculation of the integrated relative energy from time t to infinity, given by

$$i(t) = \int_t^\infty g(\Theta)d\Theta = (31\ 200T/V)e^{-13.8t/T}, \tag{6}$$

where Θ is a dummy variable. In order to predict the total sound-pressure level and the clarity index, the sound energy is divided into three components: the direct sound (d), the early reflected sound (from 0 to 80 ms, E_0^{80}), and the late reflected sound (from 80 ms to infinity, E_{80}^{∞}). From Eq. (6), the corresponding energies of each of them become

$$d(r) = 100/r^2, \tag{7}$$

$$E_0^{80}(r) = (31\ 200T/V)e^{-0.04r/T}(1 - e^{-1.11/T}), \tag{8}$$

$$E_{80}^{\infty}(r) = (31\ 200T/V)e^{-0.04r/T}e^{-1.11/T}. \tag{9}$$

So the relative sound level is given by

$$G(r) = 10 \log(d + E_0^{80} + E_{80}^{\infty}), \tag{10}$$

and the clarity index is given by

$$C_{80}(r) = 10 \log[(d + E_0^{80})/E_{80}^{\infty}]. \tag{11}$$

The center time is the first-order momentum of the acoustic energy and, taking into account that for a purely exponential decay the distance of the center of gravity from the origin (i.e., the starting point of the decay t_D) is independent of r and is equal to $T/13.8$, it is given by

$$T_s(r) = T(E_0^{80} + E_{80}^{\infty})/[13.8(d + E_0^{80} + E_{80}^{\infty})]. \tag{12}$$

Barron and Lee compared measured and predicted values, proving the suitability of the revised theory in many concert halls. They remarked, however, that in the presence of highly diffusing ceilings the model tends to overestimate the early energy.

C. The present work ("modified" theory)

The analysis of the results obtained in a group of Romanesque churches[10] showed that the basic hypothesis of the revised theory, namely the uniformity of the reverberant sound field throughout the space, was generally satisfied. However, the time at which the decay began to be linear was later, the farther the measurement position was from the source. Furthermore, at points near the source the early reflections were stronger than the ideal classical reverberant field [as given by Eq. (5)], while, conversely, when the distance from the source grew the early reflections became weaker.

In order to fit with these observations two modifications were introduced. The first one was to assume the reverberant sound field to be uniform, as it is in Barron's theory, but that linear level decay starts with a certain delay (t_R) after the arrival of the direct sound. The measurements showed that this delay was proportional to the source–receiver distance, therefore, in general, it could be written as $t_R=\rho r$. The ρ coefficient depended on the room characteristics and was estimated by assuming that the delay at the farthest point of each room could not exceed the time necessary to have a sufficiently high reflection density. However, the relationship between ρ and the room characteristics was weakened by the arbitrary assumption about the reflection density. Therefore, in order to provide a more reliable and physically acceptable hypothesis based on experimental results, the onset time of the reverberant sound field was investigated as described in detail in the next sections.

The second modification was to schematize the early reflected sound arriving between the direct sound and the reverberant sound field. This part of the sound decay is characterized by discrete reflections which are more or less spaced in time according to the geometry of the room. The magnitude of these reflections is proportional to that of the direct sound according to the characteristics of the room surfaces. In order to simplify the model, the energy of the discrete reflections was schematized by means of a continuous linear function varying from an initial value (at the time t_D), proportional through a factor γ to the energy of the direct sound, and a final value (at time t_D+t_R), equal to the energy of the reverberant field at the same time. The factor γ was introduced to account for two different aspects of the early reflections: their magnitude and their spacing in time.

When a sound hits a wall, part of its energy is absorbed, part is scattered, and the rest is specularly reflected. The first is lost, the second is "distributed" in the space, and the third propagates according to geometrical reflection laws (depending on the wavelength). The first reflections are expected to contain only the fraction of the direct sound energy corresponding to the specularly reflected energy. So, the factor γ was assumed to be proportional to $(1-\alpha)(1-s)$, where α and s are, respectively, the mean absorption coefficient and the mean scattering coefficient of the room surfaces. The estimation of the mean scattering coefficient was the other weakest link of the model due to its mostly subjective assessment. More precise guidelines to estimate this parameter are proposed below on the basis of the results of the present survey.

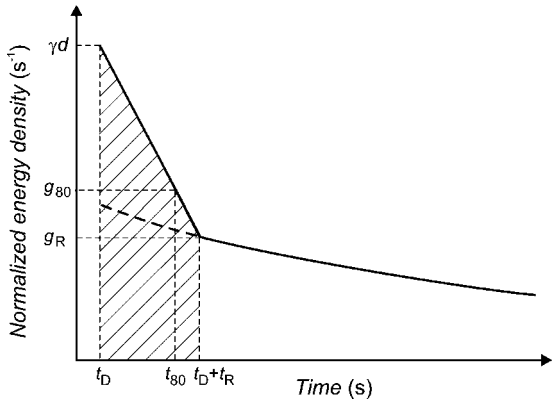

FIG. 1. Plot of the theoretical distribution of energy density of the reflected sound against the time according to the modified theory. The sound is emitted at time $t=0$, and reaches the receiver at t_D. From t_D to t_D+t_R the energy density follows a linear function, and then starts the purely exponential decay.

Finally, the factor γ must be inversely proportional to a time constant in order to transform the energy of the first discrete reflection in a continuous function. The time interval $\Delta\tau$ between the direct sound and the first reflection is actually a complex function of the geometry of the room and cannot be easily calculated. However, as proposed by Vorlander,[6] a reasonable estimate of the average arrival time of the first reflection is given by the time for sound to travel the mean free path equal to $4V/S$, where S is the room surface area. Consequently, $\Delta\tau$ is equal to

$$\Delta\tau = 4V/cS, \tag{13}$$

and the factor γ is given by

$$\gamma = (1-\alpha)(1-s)/\Delta\tau. \tag{14}$$

In order to conclude the definition of the theoretical impulse response, the instantaneous value of the reverberant field energy at the time t_D+t_R was calculated from Eq. (5) expressing the time as a function of the distance:

$$g_R(r) = g(t_D+t_R) = (31\,200\cdot 13.8/V)e^{-(0.04+13.8\rho)r/T}. \tag{15}$$

The resulting theoretical distribution of the energy density impulse response is shown in Fig. 1.

In order to calculate both strength and clarity, it was necessary to integrate the energy contributions previously described. The integrated early reflected energy i_E was calculated as a trapezium area (see Fig. 1), and was given by

$$i_E(r) = t_R(\gamma d + g_R)/2. \tag{16}$$

The integrated reverberant energy was obtained by putting $t=t_D+t_R$ into Eq. (6):

$$i_L(r) = i(t_D+t_R) = (31\,200T/V)e^{-(0.04+13.8\rho)r/T}. \tag{17}$$

Since the direct sound energy d is still given by Eq. (7), the total energy can be calculated by adding d, i_E, and i_L. However, depending on the t_R value, different formulas must be used to calculate the early (E_0^{80}) and late (E_{80}^{∞}) energy with reference to the 80 ms time limit. The simplest method is to

TABLE I. Basic details of the twelve churches surveyed. Reverberation time (T_{30}) is measured at 1 kHz octave band.

Church	Period	Style	Volume (m^3)	Total area (m^2)	Length (m)	T_{30} (s)
St. Sabina Basilica, Rome	432	Early-Christian	17 500	6 000	52	4.1
St. Apollinare in Classe, Ravenna	549	Byzantine	22 500	7 200	57	3.6
Modena Cathedral (Duomo)	1099	Romanesque	20 000	8 000	62	5.0
St. Nicholas Basilica, Bari	1197	Romanesque	32 000	10 500	59	4.4
Lucera Cathedral	1301	Gothic	33 100	10 500	64	5.3
St. Petronius Basilica, Bologna	1390	Gothic	160 000	42 000	130	9.8
San Lorenzo Basilica, Florence	1419	Renaissance	39 000	18 000	82	7.9
The Holy Name of Jesus Church, Rome	1568	Renaissance	39 000	13 000	68	5.1
St. Luke and Martina, Rome	1664	Baroque	8 700	3 500	35	3.1
St. Martin Basilica, Martina Franca	1763	Baroque	16 400	6 500	45	6.9
Concattedrale, Taranto	1970	Modern	9 000	6 200	50	4.2
S. Maria Assunta Church, Riola	1978	Modern	5 500	3 700	35	6.1

calculate E_0^{80} when $t_R > 80$ ms, so that the early reflected energy follows the linear law during the whole interval and, after 80 ms, is equal to

$$g_{80}(r) = \gamma d - 0.08(\gamma d - g_R)/(\rho r). \tag{18}$$

So, the integrated early reflected energy is given by the trapezium area (see Fig. 1):

$$E_0^{80}(r) = 0.08(\gamma d + g_{80})/2. \tag{19}$$

Conversely, when $t_R < 80$ ms, it is the late energy that follows the exponential law throughout the interval and, consequently E_{80}^{∞} may be expressed using Eq. (9).

In this way when $t_R > 80$ ms, E_0^{80} is given by Eq. (19) and $E_{80}^{\infty} = i_E + i_L - E_0^{80}$, when $t_R < 80$ ms then E_{80}^{∞} is given by Eq. (9) and $E_0^{80} = i_E + i_L - E_{80}^{\infty}$. Consequently G and C_{80} may be calculated as usual by means of Eqs. (10) and (11), while the center time requires a different formula to take into account the modified early energy (Fig. 1). The trapezium may be divided into a square having area $g_R \cdot t_R$, centered at $t_R/2$, and a triangle having area $(\gamma d - g_R) \cdot t_R/2$, centered at $t_R/3$. The center of the late energy is, again, at $T/13.8$ after the starting point (which, this time, is t_R). So the first-order momentum yields

$$T_s(r) = \lfloor (\gamma d/2 + g_R) t_R^2/3 + (t_R + T/13.8) i_L \rfloor / (d + i_E + i_L). \tag{20}$$

III. THE ACOUSTIC SURVEY

A. The churches surveyed

Twelve Catholic churches were analyzed during the present survey. Churches of different period and geographic area were included in the survey in order to have a sample varying in architectural style, typology, and dimensions, as reported in Table I and Fig. 2. All the churches were unoccupied during the measurements and their floors were only covered with pews (and sometimes groups of seats) according to the layout reported in Fig. 2. Pews were made of wood and in none of the cases were covered with cushions or any other absorbing material. Only in few cases [Figs. 2(c), 2(f), and 2(k)] large floor surfaces near the altar were covered with carpets. A short description of the churches surveyed is provided below.

Santa Sabina Basilica [Fig. 2(a)] is an Early-Christian church built at the beginning of the fifth century. It has a basilica plan with a large apse. The nave is covered with a flat wooden ceiling, while the side aisles are roofed. The walls are flat and finished in plaster.

St. Apollinare in Classe [Fig. 2(b)] is a Byzantine church, with a basilica plan without transept and with a large apse. Both the nave and the aisles are covered with a trussed roof. The walls are flat and decorated with mosaics, and the chancel area is raised about 1 m above the floor.

Modena Cathedral [Fig. 2(c)] is a Romanesque church with a basilica plan without transept and with three apses. The walls and the cross-vaults that cover both the nave and the aisles are made of brick and are smooth. The chancel area was, originally, located above the crypt which communicates with the main volume of the church by means of wide openings. Nowadays the altar is located in front of the crypt in the main nave.

St. Nicholas Basilica in Bari [Fig. 2(d)] is the prototype of the Apulian Romanesque style, it has a transept with three apses. Two columns separate the transept and the nave. There are roofed women's galleries, while the nave ceiling is wooden with large painted canvases. The side aisles are cross-vaulted.

Lucera Cathedral [Fig. 2(f)] is a large church built in Angevine-gothic style. It has a cross-shaped plan with a transept and three apses. The high nave and the aisles are covered with a wooden roof with trusses. The walls and the apses are finished in plaster, while the columns are made of rough stone.

St. Petronius Basilica [Fig. 2(e)] in Bologna is the fifth largest church in the world. It is built in gothic style, even though it was completed in the renaissance period. The church has a central nave (which terminates with an apse in the choir), with aisles and deep chapels. The high cross-vaults (more than 40 m) that cover the nave, and those covering the aisles and the chapels are plastered, as are the walls, while the ribbed columns are made of bricks.

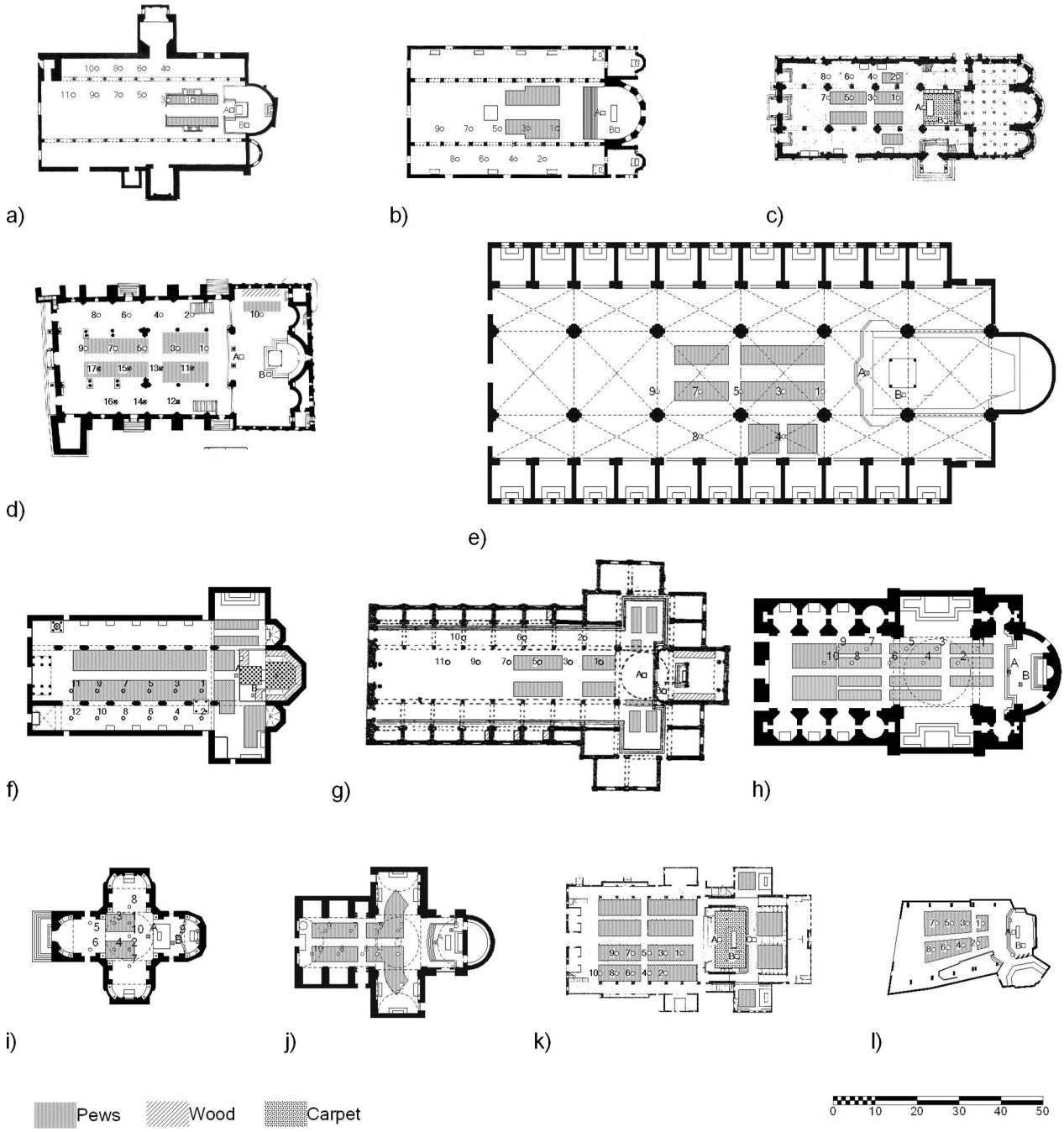

FIG. 2. Plans of the twelve churches surveyed: (a) Santa Sabina Basilica in Rome, (b) St. Apollinare in Classe, (c) Modena Cathedral, (d) St. Nicholas Basilica in Bari, (e) St. Petronius Basilica in Bologna, (f) Lucera Cathedral, (g) San Lorenzo Basilica in Florence, (h) The Holy Name of Jesus in Rome, (i) St. Luca e Martina in Rome, (j) St. Martin Basilica in Martina Franca, (k) Concattedrale of Taranto, (l) S. Maria Assunta in Riola. (Same scale for all the churches.)

San Lorenzo Basilica in Florence [Fig. 2(g)] was built between 1419 and 1470 by Brunelleschi. It has a cruciform plan, with the main nave and the transept covered with a flat wooden ceiling and side aisles covered with vaults. The walls are flanked by chapels. The walls are scarcely decorated and are finished in plaster.

The church of the Holy Name of Jesus in Rome [Fig. 2(h)] was built in the late Renaissance style by Jacopo da Vignola. The church has a Latin-cross plan, with a dome over the crossing and barrel vaults to cover the nave and the transept braces. Chapels flank the main nave. The walls and the vaults are covered with decorations and paintings.

The church of the Saints Luca and Martina in Rome [Fig. 2(i)] was built in 1635–1664 by Pietro da Cortona as a domed cruciform church, according to the Baroque style. The walls and the vaults are finished in plaster and richly decorated.

St. Martin Basilica in Martina Franca [Fig. 2(j)] was built from 1747 to 1763 in baroque style. The church has a single nave with a large transept with a dome above the crossing. The nave is covered with a barrel vault and flanked by deep chapels. Walls and vaults are finished in plaster and abundantly decorated.

The Cathedral of the Blessed Virgin Mary in Taranto

[Fig. 2(k)], also known as the "Concattedrale," was built in 1970 by Giò Ponti. The church has a large nave with narrow aisles. The ceiling is flat with beams and is finished in rough plaster, as are the walls. The chancel area is raised and is covered by a higher ceiling. The floor area is tightly fitted with wooden pews.

The church of Our Lady Assumed into Heaven in Riola [Fig. 2(l)] was designed by Alvar Aalto in 1966 and completed in 1978. The church is an asymmetrical room (nearly fan-shaped) with an asymmetrical vault supported by concrete arches. The walls and the vault are finished in smooth plaster.

B. Measurement technique

The measurements were carried out using an omnidirectional sound source made of twelve 120 mm loudspeakers (with a flat response up to 16 kHz) mounted on a dodecahedron, together with an additional sub-woofer to cover the frequencies from 40 to 100 Hz. A calibrated measurement chain made by a GRAS 40-AR omni-directional microphone together with a 01 dB Symphonie system was used to measure the sound pressure levels. A MLS signal was used to get the calibrated impulse responses to obtain the strength values. The other acoustic parameters were obtained using high-quality impulse responses collected using a Soundfield Mk-V microphone, an Echo Audio Layla 24 sound card, and a constant envelope equalized sine sweep[14] to excite the room.

Two source positions were used in each church, one on the axis of symmetry and one off the axis, both in the chancel area. The source was placed 1.5 m above the floor. Nine receiver positions were used on average. In very large but symmetrical churches the receivers were only placed in one half of the floor, otherwise they were spread to cover the whole floor area uniformly (Fig. 2). The microphone was placed 1.2 m from the floor surface.

All the measurements and the calculations of the indices were carried out according to ISO-3382 standard.[15] In particular for the measurement of the sound strength (G) the sound power of the source was calibrated in a reverberation chamber, employing the same measurement chain and the same settings used during the on site survey. For the sake of brevity, in the following analysis only 1 kHz octave band results are presented.

IV. EXPERIMENTAL RESULTS

A. Spatial distribution of sound levels

The measurements of the relative sound level performed in the churches surveyed showed that the level decreases as a function of the source–receiver distance. However, in agreement with the results shown in other works,[7,9–11] the decrease appears steeper than it is in auditorium spaces and the like. So the agreement with the revised theory is also quite unsatisfactory. In particular, the mean values are predicted with acceptable accuracy (with a mean error of 0.6 dB, and a maximum error of 1.2 dB), but the predicted rate of decay is generally lower than measured (by about 1 dB/10 m), underestimating the values near the source, and overestimating the values far from the source (Fig. 3). At this level of investigation it cannot be stated whether the level decay depends on weaker late reflections, or, more likely, on a lack of early reflections. In order to better understand this issue, the time distribution of the reflections must be taken into account.

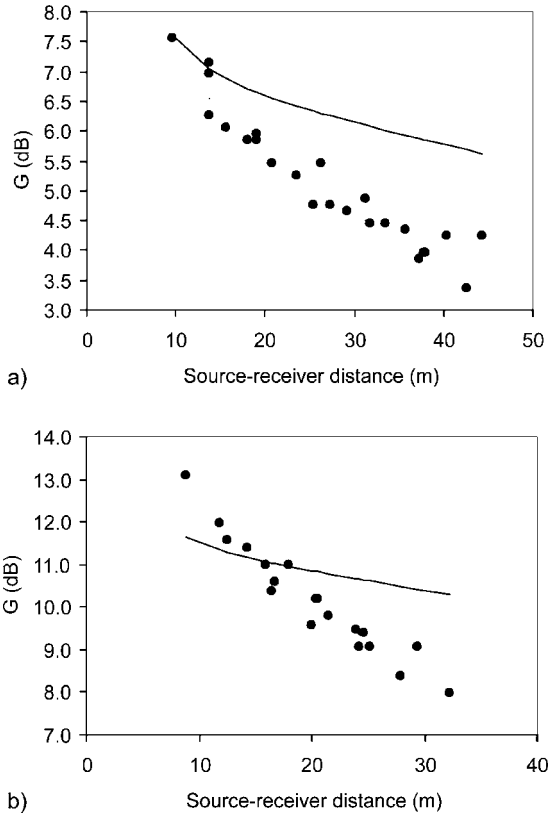

FIG. 3. Plot of measured (●) and Barron's (—) values of the relative sound level at 1 kHz octave inside Lucera Cathedral (a), and the Concattedrale in Taranto (b).

B. Spatial distribution of early and late sound

The first approach to investigate the time distribution of the reflections was the analysis of the early and late reflected levels assuming 80 ms as the time limit between the early and late part. Figure 4 shows that the early sound (from 5 to 80 ms) is quite scattered, proving its strong dependence on single reflections. However, the correlation with source–receiver distance is significant and points out a clear decreasing trend with a rate of decay higher than that predicted by the model. This means that the reflections arriving at the farthest receivers within 80 ms are both few and weak. The late reflected level is less scattered but again shows a decreasing trend with a slope steeper than that predicted by the model. This lack in energy at the farthest points can be explained by taking into account that early reflections continue to arrive well after the 80 ms limit, with a weaker energy and a smaller density than predicted by the classical theory.

Evidence supporting this hypothesis comes from the plot of the early and late reflected levels when assuming a time limit of 500 instead of 80 ms. After this time the late reflections should behave reasonably in a purely statistical (i.e., diffuse) way, and the agreement with predicted values should be better. Figure 5 confirms this, showing a good match be-

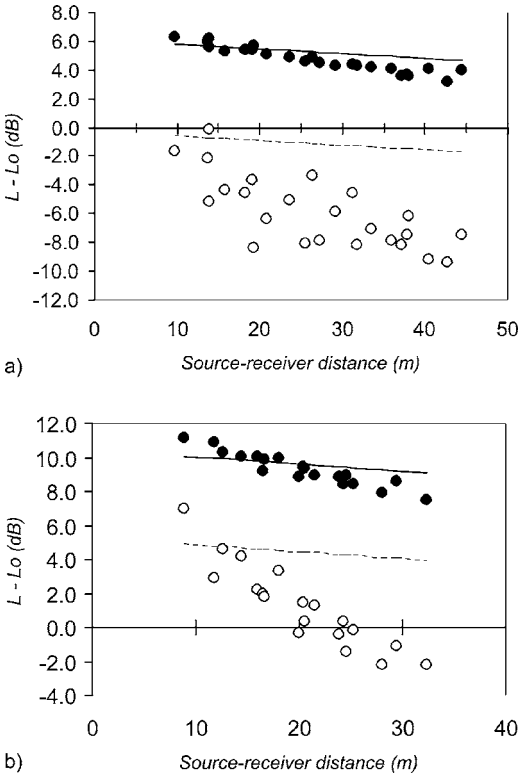

FIG. 4. Plot of predicted (using Barron's model) and measured early and late reflected sound level at 1 kHz octave against the source–receiver distance for Lucera Cathedral (a), and the Concattedrale in Taranto (b). (●) Measured late level, (○) measured early sound level, (—) predicted late sound level, (---) predicted early sound level. Early–late limit is assumed at 80 ms and direct sound is excluded.

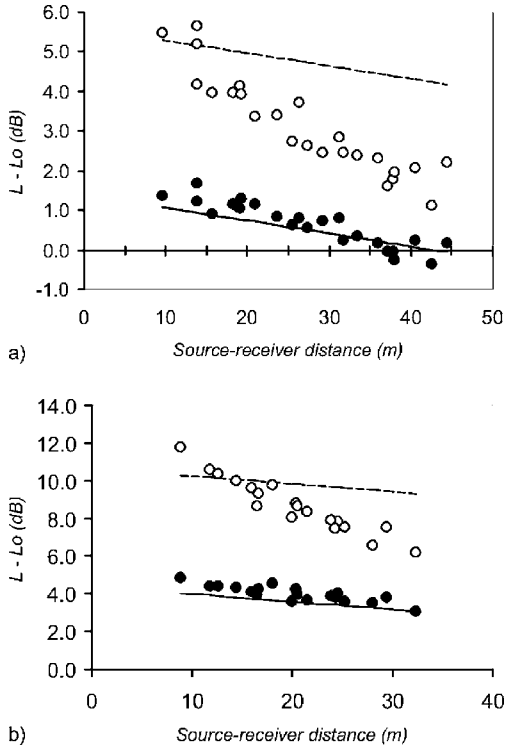

FIG. 5. Plot of predicted (using Barron's model) and measured early and late reflected sound level at 1 kHz octave against the source–receiver distance for Lucera Cathedral (a), and the Concattedrale in Taranto (b). (●) Measured late level, (○) measured early sound level, (—) predicted late sound level, (---) predicted early sound level. Early–late limit is assumed at 500 ms and direct sound is excluded.

tween measured and predicted late levels, while the early level decreases almost linearly with a greater slope than predicted.

Further evidence of the late transition to the purely reverberant sound field comes from analyzing the early decay traces relative to receivers at different distances from the source (Fig. 6). According to the revised theory the instantaneous level must be the same at all positions during a sound decay. Therefore the measured sound decay should coincide, provided that $t=0$ is the time at which the sound is emitted and the relative levels are taken into account when plotting the decay curves. Figure 6 shows that the starting point of each decay can be identified quite clearly and depends on the effective source–receiver distance. The early reflections appear soon after the direct sound as the more or less evident steps following the direct sound. After a certain time the curves converge, showing the later reflected sound to be reasonably uniform throughout the space. It can be seen that perfect convergence is hardly obtained. However, the convergence point, assumed to be the time at which all the decay curves are aligned and the following decay is linear, can be quite easily detected by visual inspection and appears only about 0.5 s after the direct sound.

C. The directional characteristics of the early reflections

The analysis of the early and late part of the reflected sound showed that the critical point of the application of Barron's model to the churches is represented by the prediction of the early reflected energy. In fact, taking into account only the late reverberant sound (arriving at least 0.5 s after the direct sound) the agreement between the measurements and the model is good. On the contrary, the same analysis pointed out that there is a clearly distinct early part where, depending on the energy and on the density of the reflections arriving, the integrated energy may be higher or lower than predicted. Figures 4 and 5 clearly show that the closer the receiver to the source, the stronger the reflections, and vice versa, with the early reflections becoming weaker as the source–receiver distance grows.

This behavior is due, according to Barron and Lee,[4] to highly diffusing surfaces which reflect the sound energy in nonspecular directions so that, on average, they act according to Lambert's Law, sending less energy to the rear of the room (far from the source) than to the front. In the surveyed churches there are trusses on the roof, cross-vaults, columns along the nave, niches or deeper chapels, and other architectural elements which scatter the incident sound and might lead to the observed behavior.

This hypothesis can be verified by taking advantage of the three-dimensional (3D) impulse responses obtained using the B-Format recording technique. The directional components (X,Y,Z) were combined with the omni-directional component (W) to provide a 3D impulse response. Polar plots representing the energy content arriving from discrete directions represented by azimuthal and zenithal angles projected on the same plane were used to make the information

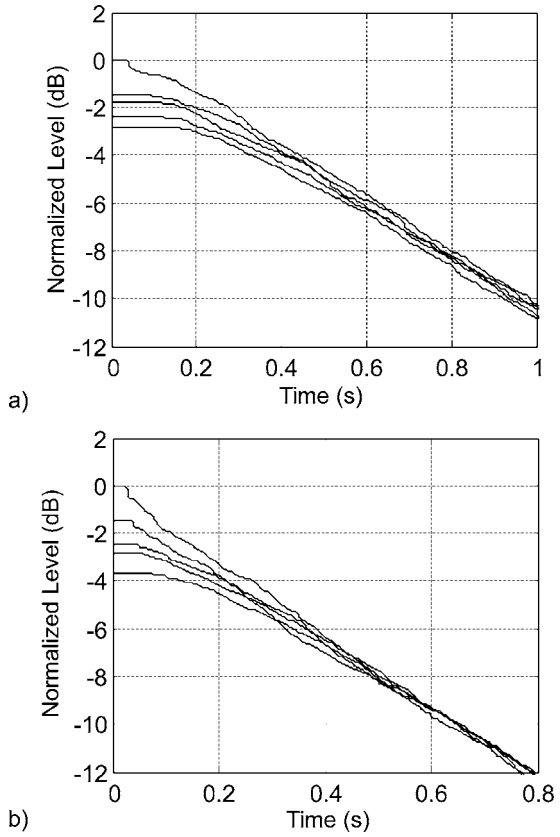

FIG. 6. Early decay traces at 1 kHz octave, measured in different points of the nave of (a) Lucera Cathedral, and (b) the Concattedrale in Taranto. Sound is emitted is $t=0$ on the time axis.

more easily accessible. Then, in order also to take the time distribution into account, three time slices were considered: from 5 to 80 ms (so excluding the direct sound), from 80 to 500 ms, and from 500 to 1000 ms. For each plot the level of the reflections was normalized by assuming the maximum energy value for that slice as a reference.

A quantitative measure which can be conveniently used in this analysis is the directional diffusion δ, defined, for each time slice, as:[1,16]

$$\delta = (1 - \mu/\mu_0) \times 100\% \tag{21}$$

with μ computed from

$$\mu = \frac{1}{\bar{e}} \sum |e_i - \bar{e}|, \tag{22}$$

where e_i is the energy content associated to the direction i, and $\bar{e}$ is the mean energy over all directions. The quantity μ_0 is the value for single plane wave incidence and depends on the number of subdivisions, so δ can vary between 0% (anechoic) to 100% (isotropic). In the present case δ was calculated with reference to the horizontal/azimuthal distribution (δ_h) and to the vertical/zenithal distribution (δ_v).

Figure 7 reports the polar plots for a representative sample of churches. In order to make coherent comparisons only the farthest points from the source were considered, and in all the cases the source was at the center of the chancel.

In the first case, the church of St. Apollinare in Classe, the reflections arriving within 80 ms are scarcely diffuse ($\delta_h=65\%$, $\delta_v=65\%$), and come mostly from the front, probably because of the flat and reflecting surfaces of the chancel. The effect of the highly diffusing ceiling is particularly evident in the lack of strong early reflections from the top. In fact, there are mostly frontal reflections until 500 ms, even though the diffusion is increased. The later part presents diffuse reflections ($\delta_h=91\%$, $\delta_v=81\%$) coming quite evenly in the horizontal plane, and with a prevalence from above (due to the microphone position) in the vertical plane.

In the second case, Modena Cathedral, the naves are covered with cross vaults instead of a wooden roof. From 5 to 80 ms the sound comes mostly from the front-top quadrant and is scarcely diffuse ($\delta_h=59\%$, $\delta_v=56\%$), also because of a strong lateral reflection. From 80 to 500 ms the reflections are more evenly distributed even though they appear to be mostly lateral on the horizontal plane, while in the vertical plane there is a certain dominance of purely perpendicular reflections probably because the chancel area is unable to reflect the sound. In fact, the late reflections are clearly diffuse in the horizontal plane ($\delta_h=90\%$), while on the vertical plane the reflections keep on coming quite perpendicularly from the top ($\delta_v=75\%$). In this case the cross-vaults are wide (due to the large span of the nave) and not very high, so they behave in a mixed mode, partly scattering the sound (when the curvature is perpendicular to the nave), and partly reflecting it (when the curvature is parallel to the nave).

In the third case, the church of the Holy Name of Jesus, the barrel vault provides strong reflections from the front-top quadrant until 500 ms. The early reflections are scarcely diffuse ($\delta_h=59\%$, $\delta_v=56\%$), and even the reflections arriving between 80 and 500 ms are less diffuse than in other churches because of a lack of lateral reflections. In fact, the side walls, due to their decorations and deep chapels, scatter and absorb the sound almost completely so that the lateral reflections are very weak compared to those from the front. After 500 ms the sound field becomes diffuse ($\delta_h=90\%$, $\delta_v=74\%$) but on the vertical plane the behavior is similar to Modena, with reflections coming almost perpendicularly from the top.

In the last case, the church in Riola, the very early reflections are weakly diffuse ($\delta_h=52\%$, $\delta_v=44\%$), and come mostly from the front-top quadrant due to the large reflecting surfaces that surround the source. However, soon after, the sound field becomes nearly diffuse ($\delta_h=91\%$, $\delta_v=81\%$) with an almost uniform distribution of the reflections from the sides and from the top.

The analysis of the directional characteristics of the early reflections shows that the depth and the decorations of the side chapels strongly affect the lateral energy because the sound is reflected according to complex paths that prevent the sound from coming back into the nave. A comparable effect, although not so dramatic, is due to side aisles and decorated walls that reduce the lateral reflections, making them weaker and scattered, as if the surface acted according

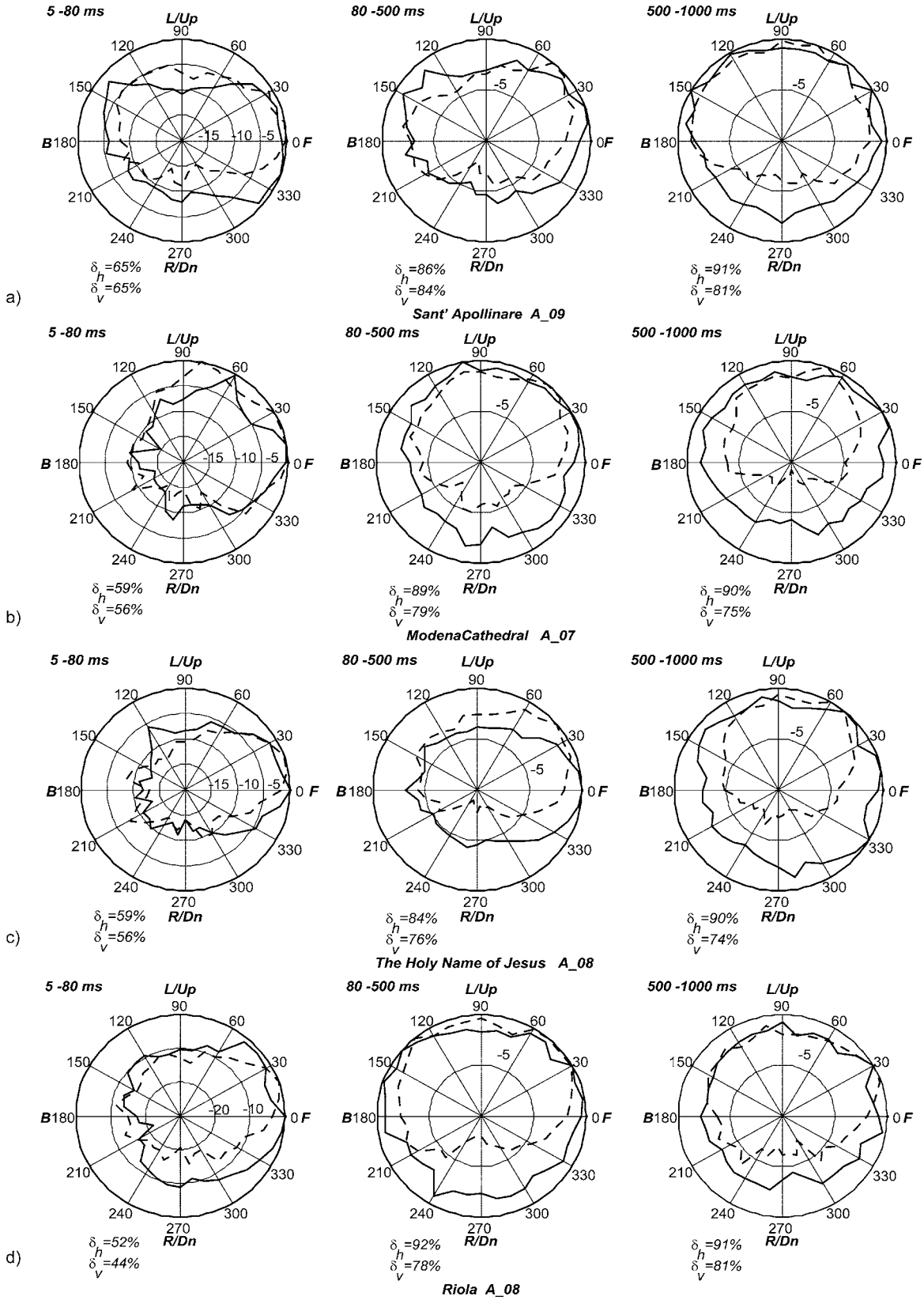

FIG. 7. Polar plots of the directional distribution of the energy content of the reflections at 1 kHz. Reflection levels are normalized with reference to the maximum energy content for each time slice. (---) Energy level in the vertical plane; (—) energy level in the horizontal plane.

to Lambert's law. Similar behavior is observed in the vertical plane in the presence of trussed roofs and highly diffusing ceilings, while vaults, especially barrel vaults, provide stronger reflections.

D. The time distribution of the early reflections

The scattering of early reflections observed in the previous section is also responsible for the slower build up of the

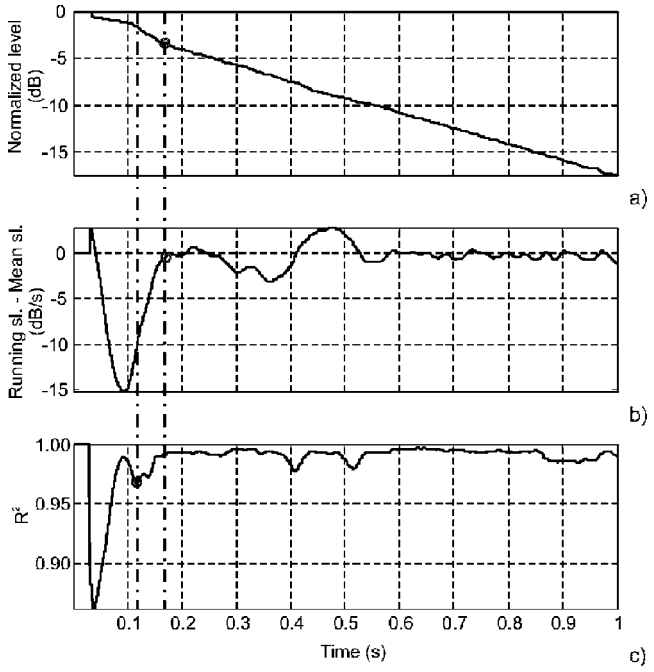

FIG. 8. Example of calculation of the onset time of the reverberant sound field. (a) Plot of the decay curve; (b) plot of the difference between running slope calculated over a 100 ms interval and mean slope; (c) plot of the correlation coefficient of the best fit line.

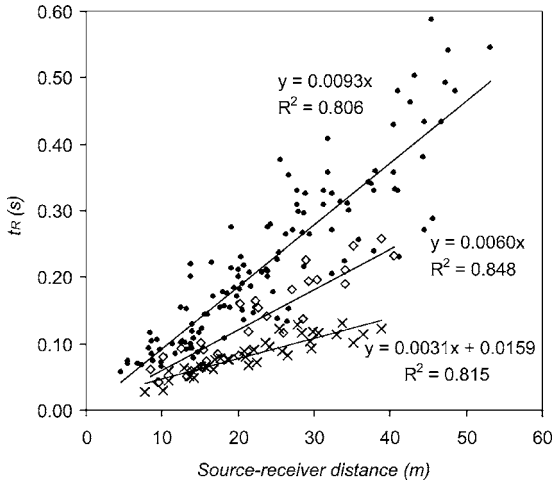

FIG. 9. Scatterplot of the onset times as a function of the source–receiver distance. (×) Simple shape churches (Santa Sabina, Sant'Apollinare, and Riola); (◇) basilica-plan churches (Modena Cathedral, St. Nicholas Basilica); (●) complex shape churches.

purely reverberant sound field. In fact, it was observed that in most of the cases the sound appeared fully diffuse only after 500 ms (Fig. 6). However, this value is the time limit after which all the decay curves became linear, so it cannot be excluded that it might be shorter in some cases. It can be reasonably supposed that the onset time of the reverberant sound field might be room-dependent and, inside each church, position-dependent. In order to investigate this hypothesis the onset time of the reverberant sound was determined by means of the running slope of the level decay curves.

The running slope at time t was defined as the slope of the best-fit line calculated over the 100 ms portion of the decay curve following t. The determination coefficient R^2 of the best-fit line was also calculated, because lower values may easily indicate the presence of steps or sudden slope changes in the decay curve. The onset time was finally assumed to be the time at which the running slope equals for the first time the mean slope of the decay curve (based on T calculation), provided that R^2 shows a relative minimum shifted (ideally) 50 ms earlier (Fig. 8), meaning that the slope is actually changing.

The whole set of the onset time values was plotted as a function of the source–receiver distance, as this was the simpler and more significant parameter to describe individual position differences. The plot, reported in Fig. 9, shows that the correlation between the onset times and the distance is good, provided that three different subsets of data are considered. The subsets were obtained by grouping all the onset times belonging to churches showing the same trend on the plot. In all the cases, the best regression models proved to be linear (as can be confirmed by a simple visual inspection of the plot). In addition, in order to avoid equations yielding negative t_R values, in two cases the regression lines were forced by the origin at the expense of a slightly worse correlation coefficient. The first group included the churches of Santa Sabina, Sant'Apollinare in Classe and the parish church in Riola. The regression line was statistically significant ($R^2=0.815; p=0.05$), and its equation was $t_R=0.0031r+0.0159$. The second group included St. Nicholas Basilica ad Modena Cathedral. The regression line was statistically significant ($R^2=0.848, p=0.05$), and its equation was $t_R=0.0060r$. The third group included all the other churches and showed some scatter of the data but, thanks to the large number of observations, the regression line had the highest statistical significance ($R^2=0.806, p=0.03$), and its equation was $t_R=0.0093r$.

The above-presented results confirm that, as proposed by Cirillo and Martellotta,[10] the onset time of the reverberant field depends on the source–receiver distance. However, the identification of a group of linear equations valid for a range of churches, suggests a simpler dependence on the room characteristics than was originally proposed. In fact, the churches of the first group share large flat reflecting surfaces and simple geometries, while the churches in the third group share complex volume articulation. So it can be reasonably supposed that the coefficient of proportionality between t_R and r might be simply chosen as a function of the general room characteristics.

A further interpretation of the results may be obtained by expressing t_R as a function of the direct sound delay t_D. For the first group of churches the equation becomes $t_R=1.06\cdot t_D+0.016$, for the second it becomes $t_R=2.06\cdot t_D$, and for the third it becomes $t_R=3.19\cdot t_D$. According to the equations reported the ratio t_R/t_D should be constant in each church, but the spread of the data reported in Fig. 9 suggests that there might be significant fluctuations. The mean ratio t_R/t_D was calculated for each church together with the standard deviation of the individual position values. The results, reported in Table II, show that the mean values for each church do not differ much from the group values and, above all, the standard deviations are relatively small and vary be-

TABLE II. Mean values of the onset time t_R and of the ratio t_R/t_D.

Church	t_R/t_D	
	Mean	St. Dev.
S. Sabina Basilica, Rome	1.45	17%
St. Apollinare in Classe	1.24	16%
Duomo of Modena	1.90	26%
St. Nicholas Basilica, Bari	2.13	24%
St. Petronius Basilica	2.84	26%
Lucera Cathedral	3.54	28%
San Lorenzo Basilica, Florence	3.25	18%
Jesus Church, Rome	2.97	21%
St. Luca and Martina, Rome	3.30	28%
St. Martin Basilica, Martina Fr.	2.99	19%
Concattedrale, Taranto	3.42	16%
S. Maria Assunta, Riola	1.48	21%

tween 16% and 28%. In addition, the values of t_R/t_D show no specific trend and no significant correlation with the distance, confirming that the hypothesis of a constant t_R/t_D for a given church is reasonable.

Further evidence of the reliability of this hypothesis can be obtained by plotting predicted and measured late levels assuming the onset time of the reverberant sound to be proportional to t_D according to the values reported in Table II.

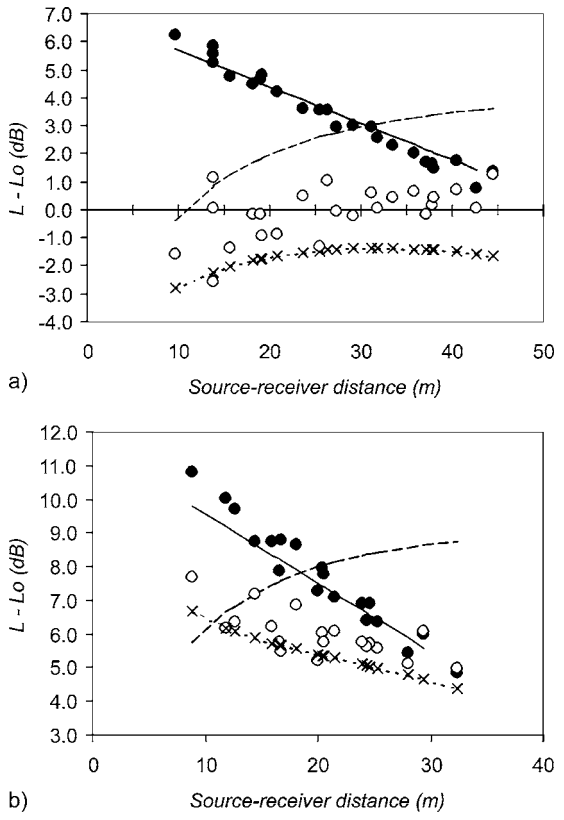

FIG. 10. Plot of predicted (using Barron's model) and measured early and late reflected sound level at 1 kHz octave against the source–receiver distance for Lucera Cathedral (a), and the Concattedrale in Taranto (b). (●) Measured late level, (○) measured early sound level, (—) predicted late sound level, (---) predicted early sound level, (-×-) early sound level predicted using the modified theory. Early–late limit is assumed proportional to the direct sound delay.

The plot, reported in Fig. 10, shows that the agreement between the late levels is as good as that observed in Fig. 5, where a constant t_R was assumed. Predicted and measured values of the early levels are significantly different. However, due to the importance of the early reflections this issue is discussed in detail in Sec. IV E.

E. The energy of the early reflections

In the previous sections the early reflections were analyzed both in terms of directional properties, and of time distribution. This allowed better understanding of the effect of highly scattering room surfaces, which produce weaker early reflections and cause a slower build up of the purely reverberant sound field. However, no information was obtained about the intensity of the early reflections. Some clues can be obtained by comparing Figs. 4, 5, and 10. Figure 4 reports the early reflection level assuming 80 ms as the time limit, here there are the largest variations, with the level decreasing rapidly as the distance grows, showing that at the farthest points the reflections arriving within 80 ms are both few and very weak. Figure 5 assumes a longer time limit of 500 ms, showing that the early level still decreases as the distance grows but the slope is smaller than before. This behavior can be explained by taking into account the hypothesis that t_R is proportional to t_D. In fact, a constant t_R would imply that at points near the source a part of the reverberant energy is included in the early interval, so that measured values appear more stable and similar to predicted ones and the contribution of the exponential decay becomes weaker at points far from the source. Finally, Fig. 10 shows the early level calculated assuming a variable time limit (proportional to t_D, according to the values reported in Table II). Here the data show, in one case, a tendency to grow with distance with an asymptotic trend, and in the other a tendency to decrease with distance. Figure 11 explains this, showing that in Lucera Cathedral at points near the source there was a lack of reflections within the first 50–100 ms after the direct sound so that the level of the integrated sound increases as the distance, and hence the time interval, grows. On the contrary in the Concattedrale the first reflections were stronger (their intensity is virtually the same as the direct sound), and their decrease as a function of the distance determines the behavior observed in Fig. 10.

An observation that supports the proposed modification to Barron's model is that between the direct sound and the onset of the reverberant sound the energy density appears to vary, with some unavoidable fluctuations, according to a linear function starting from the energy density of the very first reflection and ending with the energy of the reverberant field (Fig. 11).

V. REFINING THE MODEL

When the "modified theory" was presented in Sec. II D two aspects were left open. The first was the estimation of the coefficient ρ required to define the onset time of the purely reverberant sound field, and the second was the estimation of the mean scattering coefficient s necessary to define the energy of the early reflections.

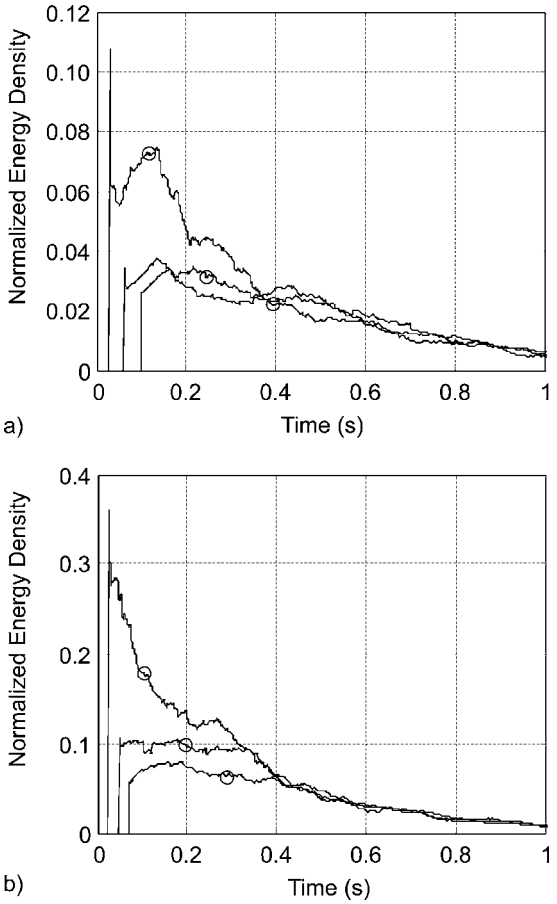

FIG. 11. Plot of the energy density at 1 kHz octave for Lucera Cathedral (a), the Concattedrale in Taranto (b). Circles correspond to the early–late limit assumed proportional to the direct sound delay.

The analysis of the experimental results reported in Sec. IV showed that the onset time of the purely reverberant sound field t_R could be reasonably assumed to be proportional to the direct sound delay t_D. The proportionality factor, given by the ratio t_R/t_D, was reported for each church in Table II, showing that the values varied in a relatively narrow range from 1.24 to 3.54. However, the analysis of the whole sample of data showed that the churches could be divided into three groups with t_R/t_D ratios equal to 1.06 for churches having a simple shape, 2.06 for churches having a proportionate basilica plan, and 3.19 for churches having disproportionate shapes and strongly diffusing surfaces. Finally, in order to make the choice of the ρ values easier and less arbitrary, the three t_R/t_D ratios were rounded to the nearest integer and assigned to a specific set of architectural features according to the classification reported in Table III. According to this classification, the revised theory may be considered as a the limiting case in which ρ equals zero.

The definition of the mean scattering coefficient s cannot rely on measured experimental data because the early reflections depend on such a large number of factors as to prevent any extrapolation of the individual contribution of the scattering. However, some considerations on the propagation of the sound from the sources to the receivers may help in defining a set of suitable values for the scattering coefficient. First of all, it is reasonable to assume that the most important

TABLE III. Values of ρ according to the architectural typology.

Architectural typology	$k=t_R/t_D$	$\rho=k/c$
Auditorium-like churches and churches with large reflecting surfaces and small chancel area	1	0.029
Typical basilica-plan churches, with transept, side aisles, columns, and diffusing ceiling or roof	2	0.058
Basilica-plan churches with very high ceiling and churches with strongly scattering surfaces (deep side aisles or lateral chapels)	3	0.087

contribution to the early reflections is given by the surfaces near the source and near the receivers. The receivers are, in most of the cases, distributed in the church according to a standardized pattern so that they are far from strongly reflecting surfaces, apart from the floor which is generally covered with pews or chairs (in fact, the polar distribution of the reflections reported in Fig. 7 clearly shows that both the early and late reflections rarely come from the bottom). Consequently, the scattering coefficient is mostly dependent on the characteristics of the "sending end" (i.e., the chancel area) of each church, and may be defined in order to include other effects not strictly dependent on scattering. The elements which may influence the scattering of sound are the height of the chancel (that reduces the risk of interference due to grazing propagation), the presence of flat reflecting walls and their distance from the source, and the presence of obstacles between the source and the receivers (such as rails and columns which may hinder the propagation toward given directions). According to these considerations a set of values associated to four groups of chancel typologies, as reported in Table IV, was proposed in order to provide a simple criterion to choose the scattering coefficient.

In this way all the parameters required to apply the new model may be easily calculated or assigned provided that the architectural features of the church are known.

VI. VALIDATION OF THE MODEL

The modified theory was finally applied to the churches surveyed in order to be validated. The geometrical data (such as volume, surface area, etc.) were used together with the reverberation time (see Table I) to determine the coefficients α and $\Delta\tau$, while s and ρ resulted from the classifications reported in Tables III and IV. A summary of the additional parameters used to apply the modified theory in each church is reported in Table V. Then, for each church, the early and

TABLE IV. Values of the mean scattering coefficient according to the chancel typology.

Chancel typology	s
Raised, or bounded by very close hard, flat surfaces	0.20
Slightly raised, bounded by relatively flat reflecting walls with few obstacles between source and walls	0.40
Very slightly raised, bounded by scattering (decorated) walls with some obstacles between source and walls	0.60
Not raised, bounded by far reflecting walls and full of scattering furniture	0.80

TABLE V. Summary of the values required by the new model for each church surveyed.

Church	MFP (m)	$\Delta\tau$ (ms)	α	s	γ (s^{-1})	ρ (s/m)	t_R/t_D
S. Sabina Basilica, Rome	11.7	34	0.11	0.40	5.2	0.0029	1.0
St. Apollinare in Classe, Ravenna	12.5	36	0.14	0.20	18.9	0.0029	1.0
Modena Cathedral	10.0	29	0.08	0.60	12.6	0.0058	2.0
St. Nicholas Basilica, Bari	12.2	36	0.11	0.60	10.0	0.0058	2.0
St. Petronius Basilica, Bologna	15.2	44	0.06	0.20	16.9	0.0087	3.0
Lucera Cathedral	12.5	36	0.09	0.80	5.0	0.0087	3.0
San Lorenzo Basilica, Florence	8.7	25	0.04	0.40	22.7	0.0087	3.0
The Holy Name of Jesus Church, Rome	12.0	35	0.09	0.40	15.5	0.0087	3.0
St. Luca and Martina, Rome	9.9	29	0.13	0.60	12.0	0.0087	3.0
St. Martin Basilica, Martina Franca	10.1	29	0.06	0.20	25.6	0.0087	3.0
Concattedrale, Taranto	5.8	17	0.06	0.20	44.6	0.0087	3.0
S. Maria Assunta Church, Riola	11.0	20	0.07	0.20	23.1	0.0029	1.0

late levels defined assuming t_R as the early/late limit, as well as the values of G, C_{80}, and T_s were calculated for every source–receiver combination using both the revised and the modified theory. The results of the calculations were then compared with the data measured in each church by means of four indices: the difference between mean values, the *just noticeable difference* (JND), the prediction accuracy, and the slope difference. The JND was estimated as the mean ratio between the mean absolute difference between measured and predicted values in each source–receiver combination, and the difference limen for the given parameter. The difference limens commonly adopted for the selected parameters are 1 dB for both G and C_{80}, and 10 ms for T_S.[17,18] The prediction accuracy was estimated by the mean rms error between measured and predicted values for each source–receiver combination. Finally, linear regressions for parameter values against the source–receiver distance were performed and the difference between the measured and predicted values of the slopes was determined. Mean values were calculated excluding the cases where the correlations were not significant at the 5% level.

A. Early and late sound

The first test of the reliability of the new model is the analysis of the early and late components of the reflected sound defined under the assumption of a t_R proportional to t_D. In particular Fig. 10 showed that this hypothesis allows a better estimation of the purely reverberant sound field. Table VI reports the difference between mean values, the rms error, and the slope difference for both early and late reflections. It can be observed that the agreement between the measured and predicted late levels is good, with a mean rms error of 0.57 dB, and a mean slope difference of −0.41 dB/10 m which confirms that, despite the modifications, the theory still tends to underestimate the real slope.

The prediction of the early sound is influenced, as can be observed in Fig. 10, by a larger spread of the measured values (especially near the source). Furthermore, the growth with distance of the early interval gives rise to decreasing or increasing trends depending on the intensity of the very early reflections. In fact, when these reflections are weak the early level tends to grow as a function of the distance [Fig. 10(a)],

TABLE VI. Relationship between measured and calculated values (according to modified theory) of the early and late sound assuming t_R as the early–late limit. Mean level differences, rms error, and slope differences between measured and theoretical values at 1 kHz frequency band.

	Mean (dB)		rms error (dB)		Slope (dB/10 m)	
Church	Early	Late	Early	Late	Early	Late
St. Sabina Basilica, Rome	1.32	0.33	2.13	0.54	0.46	−0.19
St. Apollinare in Classe, Ravenna	1.05	−0.14	1.49	0.54	0.72	−0.58
Duomo of Modena	−1.17	−0.22	1.88	0.57	−1.29	−0.60
St. Nicholas Basilica, Bari	−1.59	−0.87	1.75	0.97	−0.55	−0.33
St. Petronius Basilica, Bologna	0.97	0.53	1.50	0.73	0.66	−0.28
Lucera Cathedral	−1.28	0.10	1.53	0.33	0.38	−0.20
San Lorenzo Basilica, Florence	−0.74	−0.22	1.09	0.40	0.50	−0.11
The Holy Name of Jesus Church, Rome	−0.59	0.16	1.10	0.87	−0.21	−0.66
St. Luca and Martina, Rome	0.24	0.43	1.15	0.52	0.94	−0.36
St. Martin Basilica, Martina Franca	−0.39	−0.51	1.14	0.54	0.43	−0.30
Concattedrale, Taranto	−0.30	−0.23	0.62	0.45	−0.37	−0.54
S. Maria Assunta Church, Riola	0.33	−0.02	1.21	0.43	−0.41	−0.78
Mean	−0.18	−0.05	1.38	0.57	0.10	−0.41

TABLE VII. Relationship between measured and theoretical values of sound strength based on linear regression with source–receiver distance. Mean level differences, JND error, rms error, and slope differences between measured and theoretical values at 1 kHz frequency band.

Church	Mean (dB)		JND		rms error (dB)		Slope (dB/10 m)	
	Revised	Modified	Revised	Modified	Revised	Modified	Revised	Modified
S. Sabina Basilica, Rome	0.8	0.4	0.9	0.6	1.1	0.7	−0.38	−0.12
St. Apollinare in Classe, Ravenna	0.3	−0.1	0.6	0.4	0.7	0.4	−0.72	−0.40
Modena Cathedral	0.1	−0.3	0.7	0.5	0.9	0.7	−1.15	−0.68
St. Nicholas Basilica, Bari	0.7	−0.2	0.9	0.3	1.0	0.4	−0.81	−0.29
St. Petronius Basilica, Bologna	0.9	0.6	1.1	0.7	1.2	0.8	−0.55	−0.13
Lucera Cathedral	1.2	−0.1	1.2	0.3	1.4	0.4	−0.53	0.11
San Lorenzo Basilica, Florence	0.2	−0.4	0.5	0.4	0.7	0.5	−0.54	−0.05
The Holy Name of Jesus Church, Rome	1.2	0.1	1.6	0.5	1.8	0.7	−1.09	−0.38
St. Luca and Martina, Rome	0.9	0.2	1.1	0.5	1.2	0.5	−1.66	−0.52
St. Martin Basilica, Martina Franca	0.0	−0.5	0.5	0.6	0.6	0.6	−0.76	−0.23
Concattedrale, Taranto	0.7	−0.2	1.0	0.4	1.2	0.5	−1.44	−0.55
S. Maria Assunta Church, Riola	0.2	0.0	0.4	0.4	0.5	0.4	−0.99	−0.80
Mean	0.6	−0.1	0.9	0.4	1.0	0.6	−0.88	−0.34

while when the reflections are strong the level decreases with the distance [Fig. 10(b)]. It is interesting to observe that the new model follows the different behavior with reasonable accuracy as shown by the values of the slope difference that are generally below 1.0 dB/10 m. The rms error is higher, as could be expected due to the scatter of the measured values, but, on average, it is 1.38 dB. The largest differences are observed in churches where the mean values are also significantly different, suggesting a constant difference which could be explained by some strong early reflections not accounted for by the model.

B. Sound strength

As stated earlier, the prediction of the total sound level, or of the strength G, which is the same, was acceptable even when the classical revised theory was used. The mean predicted values were in good agreement with the measured values even though the slope was systematically underestimated, providing significant discrepancies at points far from the source. Table VII reports the results of the four accuracy indices calculated in each church with both models. The improvement brought by the new model is significant from all points of view (Fig. 12). The difference between mean values is generally below 0.5 dB. Similarly, also the mean JND is always lower than one unit, showing that the model could be used for individual position prediction. The same result is given by the rms error which is always below 1 dB, nearly halving the error obtained using Barron's model. The slope predicted using the proposed model is generally underestimated (it is slightly overestimated in only two cases), but the difference with the measured value is reduced, on average, to one-third of the value obtained using the classical revised theory.

C. Clarity index

The clarity index depends largely on the early energy level, so the new model is expected to improve the prediction accuracy. Table VIII confirms this, showing that all the indices are considerably improved when the new model is used. The difference between mean values is generally below 0.5 dB with two exceptions: St. Petronius and The Holy Name of Jesus, where the difference is about 2 dB. Both these churches show similar values even for JND and for the rms error, even though the other churches show much better values below one unit for JND and of about 1 dB for the rms error, reducing, on average, the error to one-third of the value obtained using the classical revised theory. The slope is also predicted with good accuracy independent of the church considered. The bad behavior shown by the two aforesaid churches can be related to their dimensions. In fact, they are the longest churches and the largest differences are observed at the farthest points from the sources where, apparently, the clarity assumes values as low as −15 dB because useful reflections are strongly attenuated (Fig. 12). In the church of The Holy Name of Jesus it is possible to observe a slight rise in the clarity possibly due to reflections from the back wall, as seems to be confirmed by the plateau observed in the plot of the T_S values as a function of the distance.

D. Center time

Center time is an acoustic parameter which is more suitable than clarity to check the reliability of the model. In fact, a single reflection arriving at about 80 ms could make quite a difference to the index, depending on which side of the boundary it falls. Clear evidence of this is given by the large scatter shown for clarity values (Fig. 12). On the contrary center time is less influenced by single reflections and consequently is more stable, less scattered, and, above all, is more suited to checking a model where single early reflections are schematized by a continuous function.

The analysis of the results related to the center time shows (Table IX) an astonishing improvement in the prediction of the mean values which, in most cases, are reduced to one-tenth of the value obtained using Barron's model. The slope, which was systematically underestimated by the old method, is now predicted with better accuracy. Lucera cathedral shows comparable slope differences, although of oppo-

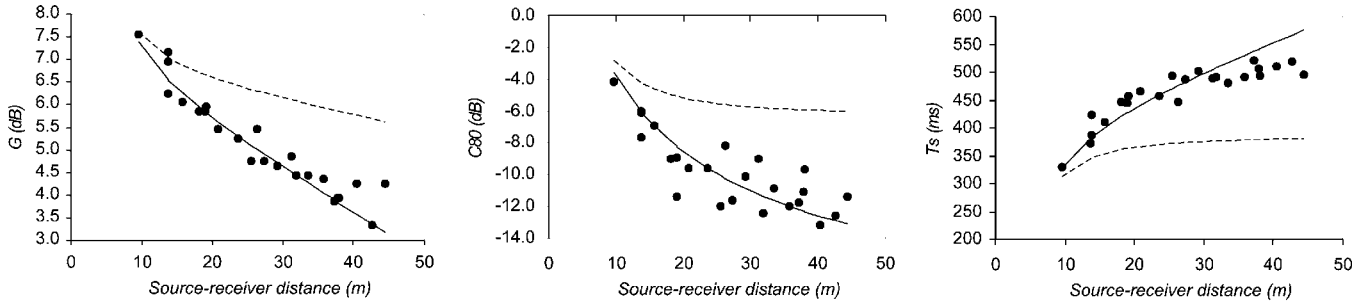

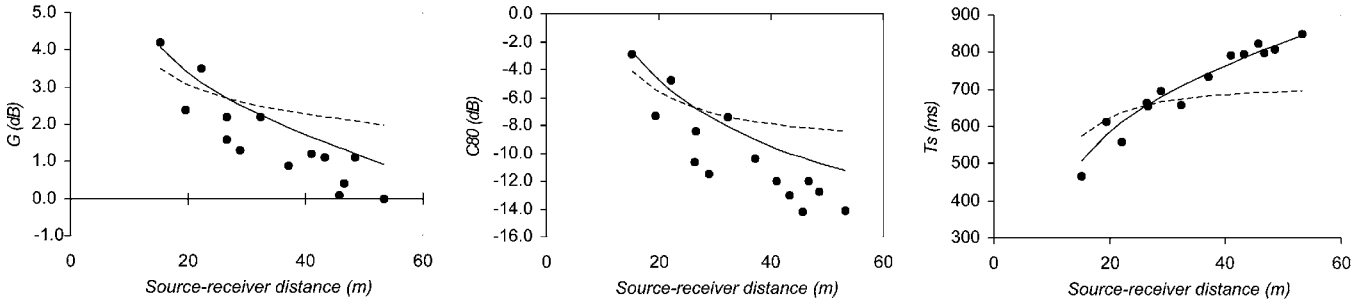

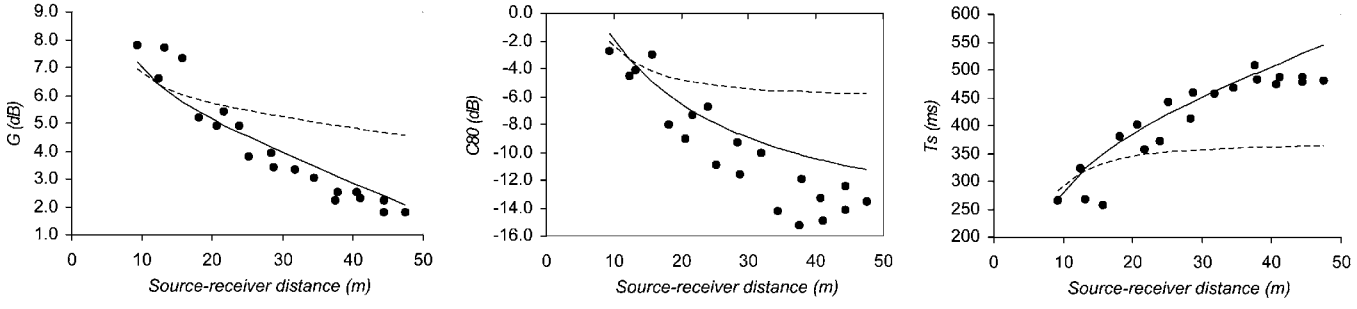

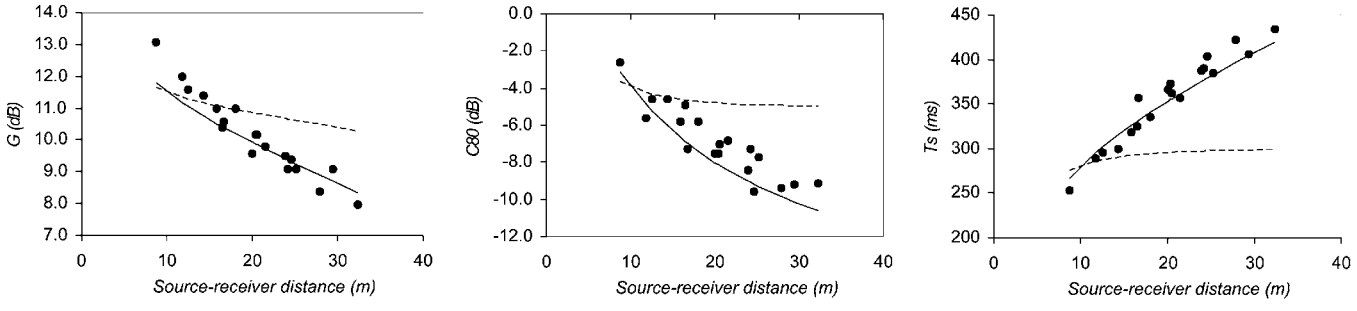

FIG. 12. Plot of measured (●) and predicted values of the strength (left), clarity (center), and center time (right) index at 1 kHz vs source–receiver distance according to the revised theory (---) and the modified theory (—).

site sign, due to lower T_S values observed at the farthest points. So, as was observed in Jesus Church, also in this case the back wall may have provided some early reflections. The analysis of rms errors shows that, on average, the discrepancy between measured and predicted values is of about 20 ms, which, on average, corresponds to an error smaller than 5% of the measured value. The largest error is observed, again, in the Holy Name of Jesus, where the error is 37 ms, corresponding to an average error of 9% of the measured values. But, as explained in Sec. VI C, this behavior mostly depends on the farthest points which are influenced by early reflections coming from the back wall.

The mean JND error is about 1.9 units, with a minimum of 0.9 and a maximum of 2.90 (observed in the Holy Name of Jesus), which would suggest the new model should not be used to calculate individual position values. However it is worth observing that the JND for center time is just 10 ms, but this value was derived[17] using an artificial system that

TABLE VIII. Relationship between measured and theoretical values of clarity based on linear regression with source–receiver distance. Mean level differences, JND error, rms error, and slope differences between measured and theoretical values at 1 kHz frequency band.

	Mean (dB)		JND		rms error (dB)		Slope (dB/10 m)	
Church	Revised	Modified	Revised	Modified	Revised	Modified	Revised	Modified
S. Sabina Basilica, Rome	2.7	−0.6	2.7	1.1	3.1	1.4	−1.24	0.28
St. Apollinare in Classe, Ravenna	2.0	0.5	2.0	0.9	2.2	1.0	−0.51	0.97
Modena Cathedral	2.2	0.2	2.6	1.0	3.1	1.2	−2.76	−0.39
St. Nicholas Basilica, Bari	3.5	0.4	3.5	0.8	3.9	1.1	−1.51	0.36
St. Petronius Basilica, Bologna	2.9	2.0	3.3	2.2	3.7	2.5	−1.57	−0.43
Lucera Cathedral	4.5	0.0	4.5	1.0	4.8	1.3	−1.15	0.66
San Lorenzo Basilica, Florence	1.9	−0.6	2.3	1.2	2.6	1.3	−1.32	0.57
The Holy Name of Jesus Church, Rome	4.8	1.9	5.0	2.1	5.8	2.5	−2.39	−0.80
St. Luca and Martina, Rome	1.8	−0.4	2.1	0.8	2.7	0.9	−4.04	−0.43
St. Martin Basilica, Martina Franca	2.6	−0.1	2.9	0.9	3.4	1.2	−3.00	−0.37
Concattedrale, Taranto	2.3	−0.9	2.4	1.0	2.8	1.1	−2.30	0.29
S. Maria Assunta Church, Riola	0.9	−0.1	1.3	0.7	1.6	0.8	−2.30	−0.95
Mean	2.7	0.2	2.9	1.1	3.3	1.4	−2.01	−0.02

simulated an "average" concert hall with 2 s reverberation time and a clarity index of 3 dB. The JND proved to be motif-dependent so that a slower and legato motif gave a longer limen (11.4±2.7 s) so it is reasonable to suppose that in churches having an average T of 5 s the difference limen for center time would be longer than 10 ms. If it were only doubled, the actual JND error could be halved, meaning that the prediction would be reliable in most of the churches. However, a visual inspection of Fig. 12 confirms the good agreement between predictions made using the proposed model and measurements.

VII. CONCLUSIONS

A sample of twelve churches was surveyed in order to investigate how sound propagates in this kind of complex space. The churches chosen differed in size (from 5500 to 160 000 m^3), in architectural style (from Early-Christian to Modern), and in typology (basilica, central, cruciform, and so on), in order to provide a representative sample. All the churches were analyzed in unoccupied conditions by using two source positions and an average of nine receivers.

The analysis of the measurements showed that the sound in churches propagates following complex paths so that, in most of the cases, the early reflections reach the farthest points with a negligible energy content. In fact, the relative sound level decreases as a function of the distance, as happens in concert halls and other proportionate spaces, but the rate of decrease is significantly steeper in churches.

The analysis of early and late reflected energy showed that the observed behavior mostly depends on the early part. In particular, it appeared that different architectural elements (such as columns, chapels, vaults, roofs, and so on) affect the early reflections so that their intensity and their density is reduced in a way that makes the purely exponential sound decay start with a significant delay after the direct sound arrival. In particular deep side chapels appear to reflect the sound according to complex paths, while side aisles and

TABLE IX. Relationship between measured and theoretical values of center time based on linear regression with source–receiver distance. Mean level differences, JND error, rms error, and slope differences between measured and theoretical values at 1 kHz frequency band.

	Mean (ms)		JND error		rms error (ms)		Slope (ms/10 m)	
Church	Revised	Modified	Revised	Modified	Revised	Modified	Revised	Modified
S. Sabina Basilica, Rome	−33	−6	3.8	1.9	43	21	21.6	4.12
St. Apollinare in Classe, Ravenna	−29	−7	3.0	0.9	35	14	25.5	7.7
Modena Cathedral	−27	5	4.6	2.4	55	31	64.2	28.1
St. Nicholas Basilica, Bari	−71	−16	7.2	2.0	80	24	34.1	−0.8
St. Petronius Basilica, Bologna	−42	5	7.3	2.1	88	27	63.7	6.3
Lucera Cathedral	−96	9	9.6	2.5	102	31	28.0	−23.9
San Lorenzo Basilica, Florence	−58	13	7.7	2.1	89	25	58.5	1.0
The Holy Name of Jesus Church, Rome	−66	20	8.0	2.9	91	37	47.4	−4.4
St. Luca and Martina, Rome	−21	10	3.0	1.3	35	18	53.8	1.7
St. Martin Basilica, Martina Franca	−52	3	5.9	2.0	67	27	51.6	−5.4
Concattedrale, Taranto	−63	−5	6.5	1.2	76	14	67.7	13.2
S. Maria Assunta Church, Riola	−12	4	2.7	1.9	32	23	50.7	32.0
Mean	−47	3	5.8	1.9	66	24	47.2	5.0

decorated walls reduce the lateral reflections, making them weaker and scattered. Trussed roofs and highly diffusing ceilings show similar behavior, while vaults, especially barrel vaults, provide stronger reflections.

A more detailed analysis of the onset time t_R of the reverberant sound field as a function of the distance showed that it grows with the source–receiver distance and it can be reasonably assumed to be proportional to the direct sound delay t_D. The analysis of the ratios t_R/t_D showed that similar values were found in similar churches.

All these results were then used in order to refine a prediction model previously tested only in Apulian-Romanesque churches. In particular, simpler rules to assign the parameters ρ and s (an aspect which was quite critical in the first formulation) were proposed as a function of the architectural characteristics of the rooms.

Finally, the refined model was applied to the churches surveyed. The input parameters were derived from the geometry (V,S,r), from the reverberation time measurements (T,α), or were estimated according to the proposed classifications (s,ρ). Strength, clarity, and center time were calculated and compared with both Barron's theory and our measured values in order to check the reliability of the modified theory. The results were investigated in the terms of difference between mean values, mean rms error, mean JND error, and slope difference. The proposed model predicted relative sound level values with good accuracy. The JND error was always below one unit, with a mean value of 0.4, nearly halving the error given by the revised theory. Clarity was predicted with less accuracy, mostly because measured values (that are influenced by single reflections) are more scattered than strength. The mean JND error was 1.1 units, but it is remarkable that this value is nearly one-third of the error obtained using Barron's model. The prediction of the center time was, apparently, less accurate than the others, with the JND error being 1.9 units. However, it is strongly dependent on the difference limen for center time which is likely to be longer than 10 ms in such large reverberant spaces. In any case, the error is less than one-third of the error given by the revised theory and, for most churches, it corresponds to a difference of about 5% of the measured value.

In conclusion, the proposed relations proved to be a simple instrument to predict energy parameters in churches. Even though measured parameters are scattered due to individual position characteristics, it is significant that the model manages to predict both mean values and the slope with good accuracy.

ACKNOWLEDGMENTS

This study has been carried out within the national interest program of scientific research "*The acoustic of spaces for music*," funded by the Italian Ministry of Instruction and University Research. The authors wish to thank all the parish priests and church management for allowing access to their churches. Special thanks are due to Bengt-Inge Dalembäk and Stephen Chiles for their precious comments and their kind collaboration in reviewing this paper. The authors are finally grateful to the technicians Michele D'Alba and Francesco Settembrini for their valuable cooperation during all phases of the survey.

[1]H. Kuttruff, *Room Acoustics*, 3rd ed. (E & FN Spon, London, 1991).
[2]L. Cremer and H. A. Muller, *Principles and Applications of Room Acoustics* (Applied Science, London, 1982), Vol. **1**.
[3]M. Hodgson, "When is diffuse-field theory applicable?" Appl. Acoust. **49**, 197–207 (1996).
[4]M. Barron and L. J. Lee, "Energy relations in concert auditoriums. I," J. Acoust. Soc. Am. **84**, 618–628 (1988).
[5]S. Chiles and M. Barron, "Sound level distribution and scatter in proportionate spaces," J. Acoust. Soc. Am. **116**, 1585–1595 (2004).
[6]M. Vorlander, "Revised relation between the sound power and the average sound pressure level in rooms and consequences for acoustic measurements," Acustica **81**, 332–343 (1995).
[7]J. J. Sendra, T. Zamarreño, and J. Navarro, "Acoustics in churches," in *Computational Acoustics in Architecture*, edited by J. J. Sendra (Computational Mechanics, Southampton, 1999), pp. 133–177.
[8]M. Galindo, T. Zamarreño, and S. Giron, "Clarity and definition in Mudejar-Gothic Churches," Build. Acoust. **6**, 1–16 (1999).
[9]N. Prodi, M. Marsilio, and R. Pompoli, "On the prediction of reverberation time and strength in mosques," in Proceedings of the 17th ICA, Rome, 2001.
[10]E. Cirillo and F. Martellotta, "An improved model to predict energy-based acoustic parameters in Apulian-Romanesque churches," Appl. Acoust. **64**, 1–23 (2003).
[11]A. Magrini and P. Ricciardi, "Churches as auditoria: Analysis of acoustical parameters for a better understanding of sound quality," Build. Acoust. **10**, 135–158 (2003).
[12]E. Cirillo and F. Martellotta, "Acoustics of Apulian-Romanesque churches: Correlations between architectural and acoustic parameters," Build. Acoust. **10**, 55–76 (2003).
[13]A. P. O. Carvalho, "Relationship between objective acoustical measures and architectural features in churches," Proceedings of the W. C. Sabine Centennial Symposium, 127th Acoustical Society of America Meeting, Cambridge, MA, 1994, pp. 311–314.
[14]S. Müller and P. Massarani, "Transfer-function measurement with sweeps," J. Audio Eng. Soc. **49**, 443–471 (2001).
[15]ISO-3382, "Acoustics–Measurement of the reverberation time of rooms with reference to other acoustical parameters," ISO, Geneva, Switzerland, 1997.
[16]B. N. Gover, J. G. Ryan, and M. R. Stinson, "Measurements of directional properties of reverberant sound fields in rooms using a spherical microphone array," J. Acoust. Soc. Am. **116**, 2138–2148 (2004).
[17]T. J. Cox, W. J. Davies, and Y. W. Lam, "The sensitivity of listeners to early sound field changes in auditoria," Acustica **79**, 27–41 (1993).
[18]I. Bork, "A comparison of room simulation software—The 2nd round robin on room acoustical computer simulation," Acust. Acta Acust. 86, 943–956 (2000).

Perceptual compensation for effects of reverberation in speech identification

Anthony J. Watkins[a)]
School of Psychology, The University of Reading, Reading RG6 6AL, United Kingdom

(Received 29 April 2004; revised 4 April 2005; accepted 7 April 2005)

Listeners were asked to identify modified recordings of the words "sir" and "stir," which were spoken by an adult male British-English speaker. Steps along a continuum between the words were obtained by a pointwise interpolation of their temporal-envelopes. These test words were embedded in a longer "context" utterance, and played with different amounts of reverberation. Increasing only the test-word's reverberation shifts the listener's category boundary so that more "sir"-identifications are made. This effect reduces when the context's reverberation is also increased, indicating perceptual compensation that is informed by the context. Experiment 1 finds that compensation is more prominent in rapid speech, that it varies between rooms, that it is more prominent when the test-word's reverberation is high, and that it increases with the context's reverberation. Further experiments show that compensation persists when the room is switched between the context and the test word, when presentation is monaural, and when the context is reversed. However, compensation reduces when the context's reverberation pattern is reversed, as well as when noise-versions of the context are used. "Tails" that reverberation introduces at the ends of sounds and at spectral transitions may inform the compensation mechanism about the amount of reflected sound in the signal. © *2005 Acoustical Society of America.* [DOI: 10.1121/1.1923369]

PACS number(s): 43.55.Hy, 43.71.Gv, 43.71.Es, 43.71.An [PFA] Pages: 249–262

I. INTRODUCTION

Speech can become less intelligible when it is distorted by reverberation in rooms (Knudsen, 1929; Lochner and Burger, 1961; Santon, 1976). The distortion comes about as reflections from the room's boundaries mix with the sound that arrives at the listener directly from the sound's source. This degrades information conveyed by the wave form's temporal-envelope (Houtgast and Steeneken, 1973) as decaying "tails" are added at sounds' offsets. In continuous utterances, offsets are relatively rare in the wideband signal, but they are more common in the narrowband channels from "auditory filters," which arise through frequency analysis in the auditory periphery. Offsets and onsets can appear in auditory filters during a continuous utterance where the sound's spectrum changes, at "spectral transitions" (Furui, 1986), with offsets occurring at the transitions that reduce the power in a filter. Reverberation adds tails at these offsets and so distorts the sound's temporal-envelopes. The Fourier transform of the temporal envelope, the modulation spectrum, indicates distortion from reverberation by the attenuation of modulation. Measures of a communication channel's attenuation of the modulation in different frequency-bands have led to reliable predictors of speech intelligibility in diverse surroundings (Houtgast *et al.*, 1980).

The detrimental effects of reverberation on speech intelligibility have been attributed to two types of masking (Nábělek *et al.*, 1989). These authors measured identification errors of the consonants /p,t,k,f,m,n,l,w/ spoken in /s-at/ context. They found evidence of "overlap masking," whereby a preceding phoneme can mask a subsequent segment, and of a "self-masking" of cues within consonants that have time-varying characteristics. Certain other detrimental effects of reverberation can arise from a perceptual "fusion," whereby spectral properties of the reflected sound become incorporated with the direct sound (Watkins, 1999). This fusion can give "coloration," which distorts the spectral-envelope cues for phonemes such as vowels and some fricatives (Watkins and Holt, 2000).

Perceptual mechanisms can serve to resist various forms of distortion that arise from reflections, so that the effects are not as severe as they might otherwise be. For example, binaural listening can reduce overlap- and self-masking in speech identification (Nábělek and Robinson, 1982), while the binaural precedence effect in the lateralization of clicks (Wallach *et al.*, 1949) indicates a resistance to distortion of spatial information. There is evidence of a monaural mechanism that is effective with coloration (Watkins, 1991), which seems to be "extrinsic" (Nearey, 1989), in that compensatory influences on a particular syllable arise from information that occurs beyond that syllable, in neighboring speech. Neighboring sounds also seem to influence the precedence effect, as it increases over a series of clicks (Clifton *et al.*, 1994). These authors suggest that listeners develop expectations about the inter-aural characteristics of reflections over the series of clicks, and that these expectations serve to diminish the influence of the reflections on spatial judgments.

There is some evidence of a perceptual resistance to the distorting effects of reflections on sounds' temporal-envelopes. Watkins (1992) used a distinction between test words that was effected by changing only the wideband temporal envelope. The test words were identical except that one began with [s] while the other began with an [s]-stop cluster.

[a)]Electronic mail: syswatkn@reading.ac.uk

These test words were played in synthetic reverberation, which adds a "tail" to the offset of the [s]. The reverberant tail seemed to be perceptually incorporated with the rest of the sound, as it was hard for listeners to discern whether there was a stop-consonant following the [s]. Consequently, listeners had difficulty in distinguishing between the two test words in these conditions. However, this detrimental effect of reverberation diminished when the test words were heard within a longer "context" utterance that contained the same reverberation. This result suggests that there is a perceptual compensation for the test-word's temporal-envelope distortion that is "extrinsic," since it seems to be informed by the presence of reverberation in the neighboring context.

Neighboring sounds also seemed to be influencing temporal-envelope processing in an experiment by Stecker and Hafter (2000) on loudness perception. These authors used tones or broadband noises whose temporal envelopes were shaped to make them similar to those of impulsive sounds with reverberation. This was done by giving the sound an abrupt onset, followed by a slowly decaying offset resembling a reverberant tail. For comparison conditions, these sounds were played backwards, giving a "time reversal" of the envelope that makes the offset abrupt and unlike a reverberant tail. The loudness of the sounds with slowly decaying offsets was found to be lower than the loudness of their time-reversed counterparts. From this result, it seems that slow offsets in these sounds are perceptually attributed to the tails that are introduced by a reverberant environment, so that there is an associated reduction in the contribution of the tail's energy to listeners' assessments of the sounds' loudness. These loudness reductions were only obtained on trials that were preceded by a trial with a sound that had a slow offset, and not when preceded by a trial with a time-reversed abrupt-offset sound. This influence from neighboring sounds suggests that the perceptual processing responsible for these effects is also "extrinsic."

In some respects, the results of Stecker and Hafter (2000) are similar to the earlier findings on compensation for reverberation in speech perception (Watkins, 1992), and it might be that they share a common perceptual origin. Experiments in the present study explore this possibility. They ask whether effects on test words are due to the incorporation of reverberant energy with the direct sound in forming the listener's perception of the sound's source. The experiments also ask whether extrinsic compensation works by reducing the amount of reverberation that is perceptually incorporated.

In the present experiments, listeners identify test words drawn from a "sir" to "stir" continuum, which are each embedded in a longer "context" utterance. When reverberation is applied to the test words, it will add a tail to the [s]. If listeners perceptually incorporate the reverberation with the direct sound, then the tail on the [s] might obscure the [t] and cause some of the continuum steps to sound more like"sir" than "stir." This effect might reduce through extrinsic perceptual compensation when the same reverberation is applied to the context. Experiment 1 of the present study asks if there is any such evidence of extrinsic compensation with naturally occurring levels of reverberation.

Compensation for coloration is disrupted when there is evidence that the context and the test word have come through different transmission channels (Watkins, 1991). A change in the inter-aural time-difference that moves the test-word's bearing away from the context's bearing is sufficient to reduce the compensation effect. Similar changes, that alter the inter-aural characteristics of reflection-patterns, also disrupt the build up of the precedence effect (Clifton *et al.*, 1994). Experiment 2 here asks whether compensation for temporal-envelope distortion by reflections is similarly affected by evidence of a change in transmission channel. Reverberation from two rooms is used, and the room is switched between the context and the test word to effect a change in transmission channel. If the compensation mechanism is sensitive to this change then there should be less compensation in conditions with a room-switch than there is in unswitched conditions.

Binaural factors are informative about room conditions (Bronkhorst and Houtgast, 1999), and much of this information arises from patterns of lateral reflections that vary with distance within a room as well as between rooms. It is therefore possible that binaural factors have some influence on extrinsic compensation for reverberation. This possibility is tested in experiment 3, which measures effects of the context's reverberation in monaural conditions to see if compensation is less than it is in dichotic conditions. As binaural factors reduce masking effects of reverberation (Nábělek and Robinson, 1982), they might also bring about some "intrinsic" reduction in the influence of reverberation on test-words' temporal-envelopes. Experiment 3 also checks for such intrinsic effects, by comparing influences of reverberation on test words in monaural and dichotic conditions.

Extrinsic compensation for coloration reduces markedly when the contexts are changed into a "signal-correlated" noise (Watkins, 1991). This noise preserves the long-term spectrum and the wideband temporal-envelope of the original signal. However, the temporal-envelopes that arise in auditory filters all become the same as the signal's wideband envelope, and there are no spectral transitions. As these transitions are likely to be informative about the amount of reverberation in the context, they might also be important in extrinsic compensation for temporal-envelope distortion. Experiment 4 asks whether this is the case with a comparison of compensation from signal-correlated noise and speech contexts.

Finally, experiment 5 measures the effects of reversing the context's reverberation. This manipulation removes the tails from the offsets of sounds and puts gradually increasing "heads" at onsets instead. In the present experiments' contexts, such effects will arise in auditory filters at spectral transitions. If tails are as salient for compensation in speech perception as they seem to be in loudness perception (Stecker and Hafter, 2000) then any effects of the context's reverberation on test words should be reduced by reversing the reverberation.

II. EXPERIMENT 1

The test words for this experiment are produced by amplitude modulating a token of "sir" so that it receives the

wideband temporal-envelope of a token of "stir." The depth of modulation is varied to form an 11-step continuum, increasing from "sir" at step 0 to "stir" at step 10. Test words are embedded in a longer context utterance and played to listeners for them to identify. From listeners' responses a "category boundary" is obtained, which is directly proportional to the total of "sir"-identifications over all the members of a continuum. Reverberation is varied by changing the distance between the sound source and the receiver in a room. In experimental sounds, reverberation from different distances is applied independently to the test word and to the context. If reverberation is perceptually incorporated with the direct sound in test words it should act to attenuate effects of the amplitude modulation that is used to form the continuum. Thus, increases in the test-word's distance should increase "sir"-identifications and shift the category boundary to a higher step-number. Any extrinsic compensation for such an effect of reverberation should result in an opposing decrease in the category boundary when the context's distance is also increased.

Realistic listening-conditions are obtained by recording reverberation in two rooms of moderate sizes, using transducers that have the directional characteristics of human heads. The resulting reverberation is likely to be relatively mild, so its distorting effects on speech might not be very large. For this reason, conditions are included that aim to boost effects of the test-word's distance. This is done by constructing some of the test words with tokens spoken fairly rapidly, where the temporal-envelope cues are likely to be shorter and so more vulnerable to distortion. Additionally, attempts are made to gauge an effect of room volume by using two rooms that differ somewhat in this respect. Effects of the test-word's distance might be more substantial in the bigger room, where there is more reverberation at a given distance.

A. Method

1. Binaural room impulse responses

To provide conditions with different levels of reverberation, binaural room impulse responses (BRIRs) (Zahorik, 2002) were obtained at different source to receiver distances in real rooms. The BRIRs were then convolved with "dry," nonreverberant sounds, and the resulting signals were played to listeners over headphones. Effects of real-room listening were achieved by matching the signals at listeners' eardrums to those at the eardrums of a representative listener in the room. In order to achieve this matching, BRIRs were obtained so that they capture the directional characteristics of human talkers, whose mouths tend to project sound forwards better than in other directions (Dunn and Farnsworth, 1939), as well as the two-eared and directional head-related transfer characteristics of the human receiver. These characteristics were obtained by playing a measurement sound from a dummy head with an acoustic transducer at its mouth (Bruel & Kjaer 4128 head and torso simulator), while recordings were made using a dummy-head receiver (KEMAR), which has Bruel & Kjaer 4134 microphones in its ears. Signals from KEMAR were recorded on digital audio tape (HHB PDR 1000) using a sampling frequency of 48 kHz with a 16 bit resolution, and transferred from this tape in digital form with the PCI sound card of a Silicon Graphics O_2 computer.

BRIRs were found here by "deconvolution" (Wightman and Kistler, 1989), using the complex fast Fourier transforms (FFTs) of two signals. Accordingly, the FFT of a sound that has been played in the room was divided by the FFT of the same sound before it was played in the room. Denominator zeros were avoided by using a maximum length sequence of samples (at plus or minus $2^{15}-1$), which was derived from a center-tapped 24 bit register. Linear deconvolution was effected with the sequence-doubling method (Gardner and Martin, 1994), using sequences of 2^{23} samples. Synchronization of the sequences used for the numerator and the denominator FFTs was achieved by recording them both simultaneously for each measurement through two channels of the analogue to digital converter on the HHB PDR 1000 recorder.

Impulse responses resulting from this deconvolution have an initial series of samples that correspond to the time taken for sound to travel through the room over the distance from the source to the receiver. These initial samples can be used to indicate the noise level of impulse responses, as ideally there is silence here (Gardner and Martin, 1994). Each measurement was replicated six times in succession and averaged. Noise in the resulting impulse responses was found to be below −42 dB, and was set to zero by reducing the resolution to 7 bits. A further check on the effectiveness of this noise reduction was obtained from energy decay curves, plotted as dB versus time, which are computed by reverse integration of the impulse response (Schroeder, 1965). Noise shows here as a gradual reduction in slope that starts as the signal level of the integrated impulse-response approaches the noise level (Zahorik, 2002). Figure 1(a) shows that this indicator of noise is largely absent in the present measurements above their −42 dB noise-floor.

The frequency-response characteristics of the dummy head talker and of the listener's Sennheiser HD480 headphones were removed from the experimental sounds using a filter with the inverse frequency-response. The dummy talker's characteristics used here were the factory calibration. The headphones' characteristics were measured on KEMAR in an IAC 1201 booth, using the above-described deconvolution method, and averaged over five placements. After convolution with BRIRs the experimental sounds were delivered to listeners' headphones at a peak level of 42 dB SPL.

The BRIR measurements were made in a corridor and in an L-shaped room of a disused office building. This corridor was 2 m wide, and about 35 m long, with a ceiling height of approximately 3.4 m. The floor was uncarpeted linoleum, the walls were painted brick, and the ceiling was painted concrete. There were numerous irregularities in the general structure, including open doorways, roof beams, and furniture. The L-shaped room here had a greater volume, comprising a 6×7 m rectangle and a 4×3 m rectangle with a ceiling height of about 3.4 m, but again with numerous irregularities and clutter. Its floor was carpeted, but otherwise its surfaces were similar to those in the corridor. The dummy head transducers of the talker and listener faced each other,

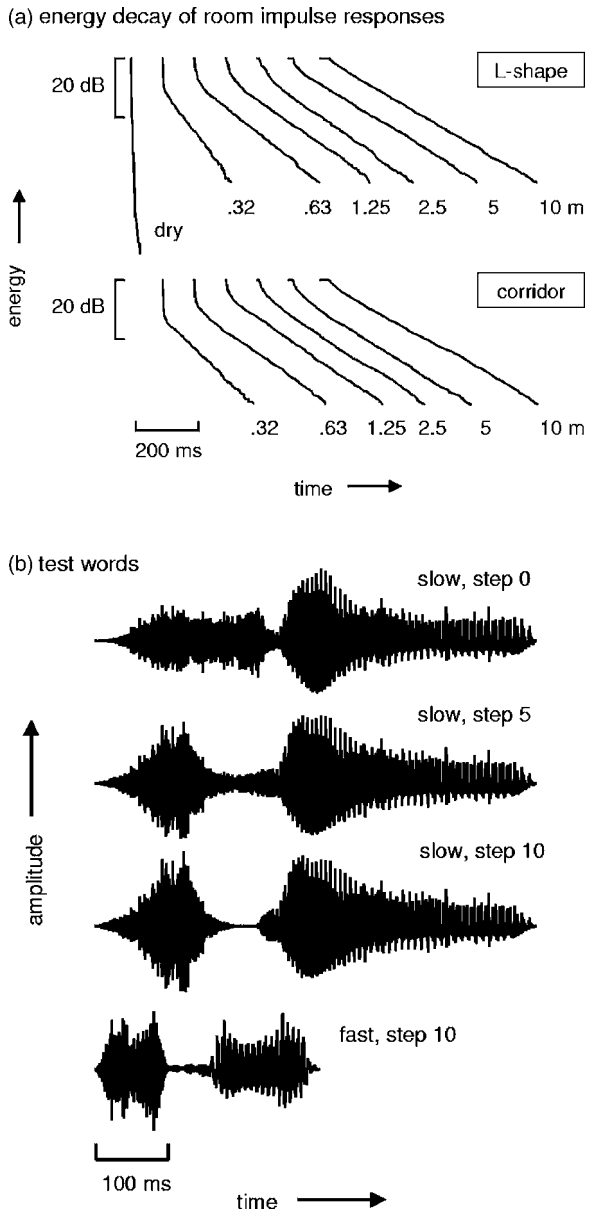

FIG. 1. (a) Characteristics of room impulse responses at the six distances, recorded from the left ear of the KEMAR dummy head. The energy shown on the ordinate is computed from the impulse response using the reverse integration method of Schroeder (1965). The decay of reflected sound-energy is practically linear after the initial drop from the direct sound's level. The flat part at the start is the travel time of the direct sound from its source, so this feature becomes more prominent with increasing distance. The "dry" trace is from the impulse response of the microphone and booth where the context and test words were spoken. (b) These wave forms are steps from test-word continua, which are formed by appropriate amplitude modulation of tokens of "sir" (step 0), spoken rapidly (fast) and more slowly (slow). Test words become more like "stir" (step 10) as the depth of modulation is increased from one step to the next. The rooms' reverberation is likely to oppose effects of this modulation.

while the talker's position was varied to give distances of 0.32, 0.64, 1.25, 2.5, 5.0, or 10 m. Figure 1(a) indicates the prominence of the direct sound at these distances by the length of the vertical part of the trace. This can be seen to decrease monotonically with distance in both rooms, so that there is an accompanying increase in the proportion of reverberant sound as distance is increased.

2. Test-word continua

Recordings were obtained for conditions with fast or with slow test words, played in context sentences that are appropriate for the rate of the test-word's articulation. Tokens of the end points of the test-word continua, "sir" and "stir," were spoken in their contexts by an adult male talker (AJW) with a southern British dialect. These sounds were recorded in the IAC booth with a Sennheiser MKH 40 P48 cardioid microphone. Reverberation in the booth at this microphone was measured by the above-described deconvolution method, using the dummy talker as a sound source. Figure 1(a) plots the resulting energy decay curve where the reverberation in these "dry" conditions can be seen to decay very rapidly and to be substantially below the −42 dB noise floor of the rooms' BRIRs.

For slow test-words, AJW said, "next you'll get sir to click on" and "next you'll get stir to click on," placing moderate stress on the "sir" or "stir." The resulting tokens of the test words were both 577 ms long. The context used with these slow test words had originally been spoken with "sir," where the duration of "next you'll get…" was 685 ms and "…to click on" was also 685 ms. For fast test-words, the same talker said "OK, next you'll get sir to click on" and "OK, next you'll get stir to click on," this time stressing "OK," while the remaining words were spoken rapidly with little stress on any of them. This resulted in shorter tokens of "sir" and "stir," each lasting 294 ms. The context used here had again originally been spoken with "sir." Its first part, "OK next you'll get …," was 1.15 s long, including an "OK" of 550 ms, while its second part, "…to click on," lasted 605 ms.

The fast and slow test-word continua were formed from the corresponding recordings. To obtain wideband temporal envelopes of the sounds, the "sir" and "stir" tokens were first isolated and time aligned at the onset of the periodic, voiced part of these utterances, where the noise-like frication of the consonant segment gives way to the following vowel. The envelopes of both words were then obtained by playing the full-wave rectified wave forms through a low-pass filter with a cut-off frequency of 50 Hz, while maintaining the time alignment between the envelope and the wave form. Interpolations between these end-point envelopes were then used to obtain an 11-step continuum of sounds extending from one end point to the other. For this interpolation, each point in the envelope of "stir" was divided by the temporally corresponding point in the envelope of "sir" to obtain an "envelope ratio." A value of interpolation, k, was then chosen, from the range between 0.0 and 1.0, and then each point in the envelope ratio was multiplied by k, followed by the addition of $1-k$ to give a modulation function. The original recording of "sir" was then multiplied by the modulation function to obtain test words at steps of the continuum.

Continuum steps are numbered with the integers, n, from 0 to 10. Pilot observations indicated that a linear relationship between k and n gives continua where more than half of the steps sound like "sir," which restricts the range of reverberation effects that can be measured. To extend this range, an arcsine root relationship was used, with values of k at each step being chosen so that

$$2\sin^{-1}\left(\frac{1+k}{2}\right)^{0.5} = \frac{\pi}{2} + \frac{n\pi}{20}. \quad (1)$$

Wave forms of some steps from the continua are shown in Fig. 1(b).

3. Same- and mixed-distance phrases

To provide conditions with various combinations of the test-word's distance and the context's distance, test words were re-embedded in the "context" part of the original utterance. This re-embedding was performed by adding two wave forms, one of these being a context with silence replacing the original "sir," the other being the test word with silence where there was originally the context. In this way it was possible to apply different BRIRs to the context and the test word before adding their wave forms, giving same- or different-distance phrases as a result. The rms levels of same-distance phrases were equalized, and the resulting amplitudes of test words and contexts were used for these components in the mixed-distance phrases. BRIRs for all six distances were applied to the contexts, while BRIRs for the 0.32 and 10 m distances were applied to the test words in the continuum. This was done with BRIRs from both of the rooms and for both test-word rates.

4. The category boundary

Listening tests confirmed that test words from both the fast and the slow continuum were heard as "sir" at the lower step numbers, with a switch to "stir" for higher steps. This gives rise to a category boundary that was measured by asking listeners to identify test words from each step. Each of the 11 steps of a continuum was presented three times. Pilot observations showed that this number of repetitions is sufficient to give standard errors of category boundaries that are comparable to values reported for other speech continua. The step corresponding to the category boundary was found from the total number of "sir" responses to all of a continuum's steps. The calculation assumes that the identification function is the cumulative form of a symmetrical distribution (Watkins, 1991), so that an increase in the boundary by one step causes the total of number of "sir" responses to increase by 3. When this total is half of its maximum, the boundary is assumed to be at the mid-point of the continuum. Hence, the boundary here is found by dividing the total number of "sir" responses by 3 before subtracting 0.5, giving a boundary step-number between −0.5 and 10.5. Category boundaries calculated in this way are shown with the corresponding identification functions for one listener in Fig. 2(a).

5. Design

Listeners were opportunistic selections from Reading University's Psychology undergraduates, who had had previous experience with category boundary experiments in their practical classes. They were native or fluent non-native English-speakers and none of them reported any hearing problems. Listeners had not heard the stimuli used in this experiment before, but they were familiar with the voice used, as its owner ran the experiment and conversed with them beforehand.

There were four groups with 6 listeners in each. Two of the groups identified speech with BRIRs from the corridor

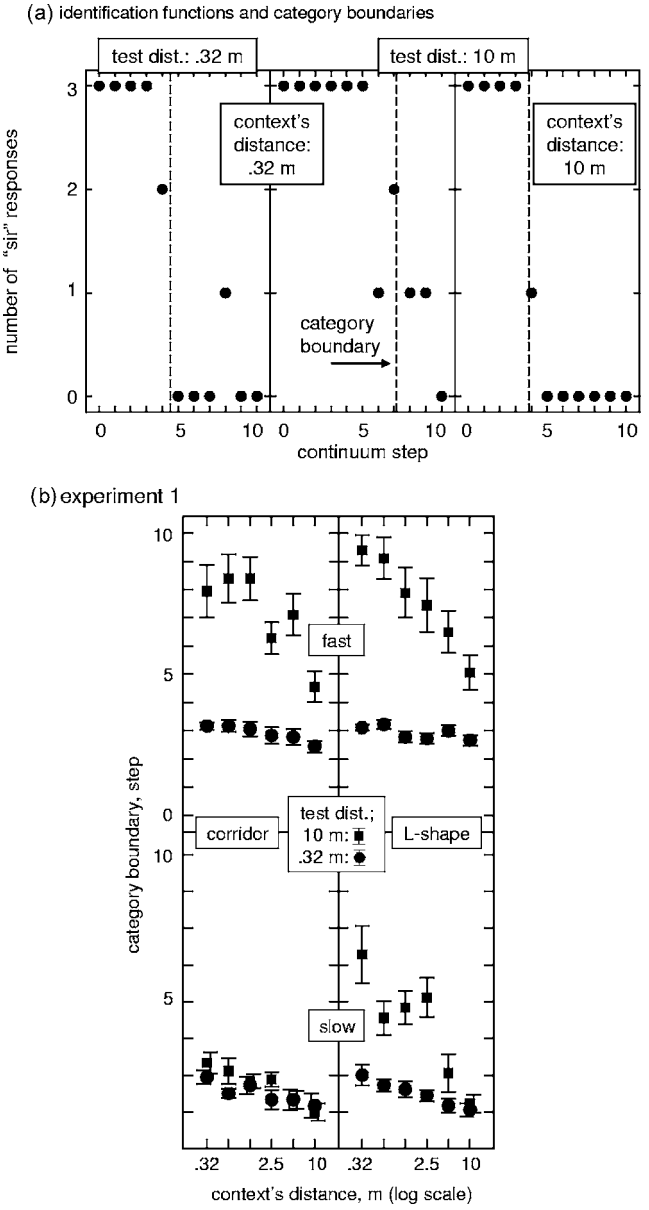

FIG. 2. (a) One listener's identifications of steps from the slowly spoken test-word continuum. Reverberation at the two distances was applied independently to the context and to the test word. The context's distance is 0.32 m in both the left and the center panels. Here, changing the test-word's distance (test dist) from 0.32 m to 10 m increases the test-words' reverberation and causes some of them to sound more like "sir" than "stir." Consequently the category boundary moves to the right. When the context's distance is also increased to 10 m in the right panel, there is a perceptual compensation that moves the category boundary back leftwards to near its original position. (b) Results of experiment 1, showing means (data points) and standard errors (bars) of category boundaries from the four groups of six listeners. Different groups identified test words that were rapidly spoken (fast) or spoken more slowly (slow), which were embedded in a speech context and played through the L-shaped room or the corridor by convolving with appropriate BRIRs. The effect of reverberation on the test word is shown by the increases in category boundary with the test-word's distance. Compensation for this is shown by the reductions in the category boundary as the context's distance is increased.

while the other two groups identified speech with BRIRs from the L-shaped room. For each room, one of the groups identified the fast test-words while the other identified the slow test-words. Over a sequence of trials, listeners heard all combinations of the 6 context distances with the 2 test-word distances. This gives 6 context distances $\times$ 2 test-word distances $\times$ 11 continuum steps $\times$ 3 repeats = 396 trials for each of the listeners, who each received them in a different randomized order.

6. Procedure

The Silicon graphics O_2 computer administered the experiment in individual sessions to listeners who heard the sounds through the Sennheiser headphones in the otherwise quiet conditions of the IAC booth. On each trial, a context with an embedded test-word was presented. Lsteners identified the test word with a click of the computer's infrared mouse, which they positioned while looking through the booth's window at the "sir" and "stir" alternatives displayed on the computer's screen. The computer waited for the listener to respond before presenting the following trial. Before the experimental trials, listeners were informally given some randomly selected practice trials. This acquainted listeners with the sounds and the setup, whilst checking that they could readily identify the test words.

B. Results

Figure 2(b) shows means of category boundaries across the six listeners in each group. A four-way analysis of variance was performed on the category boundaries. Test-word rate and room are between-subject factors that have two levels each, while context distance and test-word distance are within-subject factors that have six levels and two levels, respectively.

When reverberation is applied to test words by increasing the BRIR's distance from 0.32 to 10 m there are accompanying increases in the category boundaries as test words sound more like "sir." This shows in the analysis as a main effect of the test-word's distance where $F(1,20)=115.19$, and $p<0.0001$. This effect of the test-word's distance is more pronounced at the fast test-word rate, as shown by the interaction of test-word rate with test-word distance, where $F(1,20)=43.94$, and $p<0.0001$, and by the main effect of test-word rate where $F(1,20)=13.14$, and $p<0.0017$.

There appears to be an extrinsic compensation for the effects of reverberation on the test word, and it increases as the context's distance moves from 0.32 out to 10 m. This is indicated by a main effect of the context's distance, where $F(5,100)=65.03$, Huynh–Feldt epsilon $=0.8259$ and $p<0.0001$. This compensation is more pronounced at the fast test-word rate, giving an interaction of the effects of the context's distance and test-word rate, with $F(5,100)=6.5$, Huynh–Feldt epsilon $=0.8259$, and $p<0.0001$. There is also an interaction between the effects of the room and the context's distance, with $F(5,100)=5.18$, Huynh–Feldt epsilon $=0.8259$, and $p<0.0008$, indicating that the compensation effect is more pronounced in the L-shaped room.

Compensation arising from context's reverberation has a substantial influence on the identification of test words that contain reverberation from the distant, 10 m BRIR. However, compensation is less influential when the test-word's BRIR is closer at 0.32 m, where there is much less reverberation. This is shown in the analysis by an interaction between the effects of the context's distance and the test word's distance where $F(5,100)=6.5$, Huynh–Feldt epsilon $=0.9138$, and $p<0.0001$. This result pattern is more pronounced at the fast test-word rate as well as in the L-shaped room, giving corresponding three-way interactions. The interaction of context's distance, test word's distance, and test-word rate gives $F(5,100)=6.06$, Huynh–Feldt epsilon $=0.9138$, and $p<0.0001$, and the interaction of context's distance, test word's distance, and room gives $F(5,100)=6.06$, Huynh–Feldt epsilon $=0.9138$, and $p<0.0001$. There are no other significant F-ratios.

C. Discussion

These results show that realistically mild reverberation is sufficient to influence identification of these test words through distortion of their temporal envelopes. Substantial effects of test-words' reverberation occur when the context is at 0.32 m, where it acts to oppose the amplitude modulation that forms the continuum. This is consistent with the hypothesis that the tails added by reverberation are sometimes incorporated with the direct sound in forming the listener's perception of the test words. As a result, category boundaries increase as the [t] in some test words is obscured. The effects are not large in the corridor's reverberation when the test words are spoken slowly [lower left panel in Fig. 2(b)], but they increase when reverberation is from the larger L-shaped room [lower right panel in Fig. 2(b)], and when more rapidly spoken test-words are heard [upper panels in Fig. 2(b)].

There is also evidence of an extrinsic compensation, deriving from the context, which appears to reduce the influence of the distortion in test words at 10 m. This is consistent with the hypothesis that compensation works by reducing the amount of reverberation that is perceptually incorporated with the direct sound in the test word. This may happen as tails from reverberation come to be perceived more correctly as being due to the distortion that the room introduces. The compensation is not complete for the fast test-words [upper panels in Fig. 2(b)], as in this condition the category boundaries for the 0.32 m same-distance conditions lie below those in the 10 m same-distance conditions.

As the context's distance becomes nearer than 10 m its reverberation reduces, and there is an associated reduction in the compensation effect. This might come about if compensation for effects of distortion in the test word were governed by the amount of distortion in the context. However, an alternative possibility is that the reverberation difference between the context and the test word makes them sound as if they have arrived through different transmission channels, and compensation reduces as a result.

The influence of the context's reverberation on test words at 0.32 m is less substantial than it is with the 10 m test-words, with much smaller changes in the category

boundary as the context's reverberation changes. This might happen because the effects of reverberation are not diametrically opposed to the effects of amplitude modulation. Consequently, the relatively dry "sir" test words at 0.32 m are likely to contain features that do not resemble the effects of reverberation on a "stir." The observed lack of influence of the context's reverberation on the drier test words is therefore consistent with compensation being confined to effects of reverberation in the test word.

III. EXPERIMENT 2

The findings of experiment 1 are unclear about the factors that reduce compensation as the context's reverberation is decreased. One possibility is that compensation reduces because the reverberation difference between the context and test word indicates a change in transmission channel. Experiment 2 asks whether other indicators of a change in the transmission channel reduce the compensation. This is done by keeping the distances of the context and test word the same, while the transmission channel is switched between them by changing the room used for the reverberation.

A problem with using this room switching to give a transmission-channel change is that its effects are confounded with effects of differences in rooms' characteristics, such as their volumes, which also arise in unswitched conditions. Also, experiment 1 has shown that these rooms' characteristics give substantial differences in category boundaries. For this reason, experiment 2 is designed against the confound by using a statistical test that pools the two types of room-switch between the context and the test word. That is, switches from the corridor to the L-shaped room are pooled with switches from the L-shaped room to the corridor. Compensation in these switched conditions is then compared within listeners to the compensation in unswitched conditions, which are also pooled across rooms for this comparison. Switched conditions are likely to contain indicators of a transmission-channel difference, which might include monaural factors, such as coloration, as well as binaural factors, such as the inter-aural relationships of lateral reflections. If the compensation mechanism is sensitive to such indicators, then compensation will be reduced in the switched conditions. The rapidly spoken test-words and their contexts are used in this experiment, as these give substantial compensation effects in both of the rooms in the conditions of experiment 1.

A. Method

In this experiment, the factors for the test-word's distance and the context's distance both had two levels, which were 0.32 or 10 m. For each of the six listeners there were two blocks of trials, and the room of the context's BRIR was kept the same throughout a block. Three of the listeners heard contexts from the corridor in their first block, followed by a block with contexts from the L-shaped room. The other three listeners heard the blocks in the opposite order. In a trial of an unswitched condition the test word's BRIR was from the same room as the context's BRIR, while in a trial of a switched condition the BRIRs of the two rooms were different. Steps of continua were presented 3 times each per block, so that each block contains 2 context distances $\times 2$ test-word distances$\times 2$ switched or unswitched $\times 11$ continuum steps$\times 3$ repeats=264. The remaining factor in this design is the test-word's room, which was either L-shaped or corridor. Other aspects of the method were the same as in experiment 1.

B. Results

Figure 3(a) shows means of category boundaries in the different conditions across the six listeners. A four-way analysis of variance was performed on the category boundaries using the two-level factors described above, which are all within-subject.

Several effects emerge that replicate findings of experiment 1. Increasing the distance of the test-word's BRIR from 0.32 to 10 m increases category boundaries giving a main effect of the test-word's distance, where $F(1,5)=32.64$, and $p<0.0023$. There is again extrinsic compensation for this effect of reverberation on the test word, which gives a main effect of the context's distance with $F(1,5)=44.71$, and $p<0.0011$. This compensation is less substantial when the test-word's BRIR is closer at 0.32 m, giving an interaction between the effects of the context's distance and the test word's distance with $F(1,5)=18.76$, and $p<0.0075$.

The central test here is of the prediction that extrinsic compensation should decrease when the context's BRIR is switched to a different room from the test-word's BRIR. This is supported by the analysis. The interaction that tests whether the effect of the context's distance varies between switched and unswitched conditions is significant, with $F(1,5)=12.71$, and $p<0.0161$, with a reduction in the effect in conditions where the rooms are switched. However, this reduction in compensation is relatively small, as a substantial influence of the context's distance remains in switched conditions. At the same time, there is confirmation that the rooms' acoustics are sufficiently dissimilar to bring about differences in their effects on the test word. Effects of the L-shaped room's reverberation are the more pronounced here as they were in experiment 1. There is a main effect of the test-word's room with $F(1,5)=118.76$, and $p<0.0001$, along with an increase in this effect at the farther distance that gives an interaction between the test-word's distance and the test-word's room, with $F(1,5)=31.89$, and $p<0.0024$. There are no other significant F-ratios.

C. Discussion

The bulk of the compensation persists when there are indicators of a transmission-channel difference due to a switch between rooms. These indicators include a mismatch between the level of reverberation in the context and the test word. Therefore, it would now seem that effects of such mismatches in experiment 1 are probably insufficient for any substantial reductions in compensation. It may be that compensation would reduce more markedly if there were other indicators of a channel difference, such as a change in the direct-sound's bearing (Watkins, 1991). Even so, a substantial amount of compensation remains in the room-switched

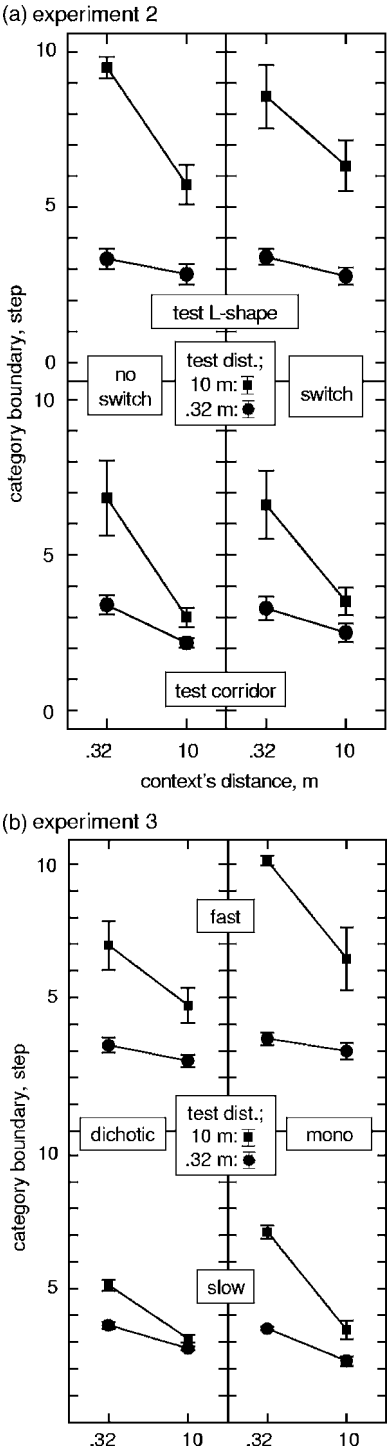

FIG. 3. (a) Results of experiment 2, showing means and standard errors of category boundaries from the six listeners who identified rapidly spoken test-words. The test words and their contexts were played in the L-shaped room or in the corridor by convolving with appropriate BRIRs. In unswitched conditions (no switch) the context's BRIR was from the same room as the test word while in switched conditions (switch) the context's BRIR was from the other room. (b) Results of experiment 3, showing means and standard errors of category boundaries from the two groups of six listeners who identified test words and their contexts presented in monaural (mono) and dichotic conditions. The different groups heard test words that were rapidly spoken (fast) or spoken more slowly (slow). These test words and their contexts were convolved with BRIRs from the L-shaped room.

conditions of experiment 2. This compensation seems to rely on aspects of the reverberation that are shared by the two rooms, such as the tails that reverberation adds at spectral transitions.

IV. EXPERIMENT 3

The room-switched conditions of experiment 2 are likely to have introduced differences between the context and the test word in their inter-aural relationships, particularly in their patterns of lateral reflections. However, extrinsic compensation for reverberation was hardly affected. This result seems unlike effects found with spatial judgments (Clifton *et al.*, 1994), where reflections become substantially more prominent when their inter-aural relationships are changed, so that there is less compensation for spatial distortion. It may be that larger differences between rooms than there are in experiment 2 would bring about more pronounced reductions in compensation. However, it could simply be that extrinsic compensation is insensitive to binaural information. To test the second possibility, experiment 3 compares effects of the context's distance in dichotic and monaural conditions. If compensation is binaurally informed then effects of the context's distance should reduce in monaural conditions.

Binaural factors might also have "intrinsic" effects on test words, perhaps by reducing effects of reverberant overlap and self-masking (Nábělek and Robinson, 1982). To check for such a reduction, experiment 3 also compares effects of the test-word's distance in dichotic and monaural conditions. Test words at both the slow and the fast rates are used, while reverberation is from BRIRs in the L-shaped room that give substantial compensation effects at both of the test-word rates in the conditions of experiment 1.

A. Method

The context's distance and the test-word's distance were both two-level factors, using BRIRs at 0.32 or 10 m. Listening in a dichotic condition was the same as in the conditions of experiment 1. In monaural conditions, listeners heard sounds at one ear. These monaural signals were either a left- or a right-BRIR channel, played to the corresponding ear of the listener. The left ear was used on half of the monaural trials, and the right ear on the others. The monaural signals were played 6 dB above the single-ear level of a dichotic signal, so that their loudness was about the same.

There were two levels of test-word's rate, as in experiment 1, and this factor was tested between two groups of six listeners. Listeners in each group heard 2 context distances $\times 2$ test-word distances $\times 2$ dichotic or monaural $\times 11$ continuum steps $\times 4$ repeats=352 trials. Category boundaries were calculated by dividing a continuum's total of "sir" responses by 4 before subtracting 0.5. Other aspects of the method are the same as in experiment 1.

B. Results

Figure 3(b) shows means of category boundaries in the different conditions across the six listeners in each of the two groups that heard different test-word rates. A four-way analysis of variance was performed on the category boundaries.

Test-word rate is a two-level between-subject factor, while dichotic or monaural is a two-level within-subject factor. Context's distance and test-word's distance are both two-level within-subject factors as before.

If the compensation mechanism is binaurally informed then there should be less extrinsic compensation in the monaural conditions than there is when presentation is dichotic. Inspection of Fig. 3(b) shows that the reverse is the case. The effects of the context's distance turn out to be larger in monaural conditions, and the interaction that tests whether the effect of the test-word's distance varies between monaural and dichotic conditions is significant, with $F(1,10)=5.70$, and $p<0.0383$.

There are effects here that replicate the findings of the preceding experiments. Increasing the distance of the test-word's BRIR from 0.32 to 10 m increases category boundaries giving a main effect of the test-word's distance, where $F(1,10)=166.22$, and $p<0.0001$. This effect is more pronounced in conditions with the faster test words, giving an interaction between test-word rate and test-word's distance with $F(1,10)=28.04$, and $p<0.0004$, along with a main effect of test-word rate with $F(1,10)=8.2$ and $p<0.0169$. There is again extrinsic compensation for this effect of reverberation on the test word, which gives a main effect of the context's distance with $F(1,10)=58.51$, and $p<0.0001$. Also, the compensation is less influential when the test-word's BRIR is closer at 0.32, giving an interaction between the effects of the context's distance and the test-word's distance with $F(1,10)=25.42$, and $p<0.0005$.

Monaural listening tends to increase the influence of reverberation on test words, giving a main effect of dichotic-or-monaural where $F(1,10)=47.72$ and $p<0.0001$. This increased influence tends also to magnify the result pattern found in earlier experiments. This is shown by a two-way interaction between the dichotic-or-monaural factor and the test-word's distance, where $F(1,10)=71.63$ and $p<0.0001$, as well as by a three-way interaction between dichotic-or-monaural, context's distance, and test-word's distance, where $F(1,10)=5.02$ and $p<0.049$. The effect of test-word rate is also increased under monaural conditions giving a two-way interaction between these factors, where $F(1,10)=12.90$ and $p<0.005$. There are no other significant F-ratios.

C. Discussion

The extrinsic compensation does not seem to use binaural information, indicating that listeners' expectations about inter-aural relationships (Clifton *et al.*, 1994) are not involved. Compensation effects are actually more prominent under monaural conditions [right-side panels in Fig. 3(b)]. For slow test-words this increased prominence appears to arise partly because compensation is complete [lower right panel in Fig. 3(b)], as was also found in experiment 1. Consequently, the extent of compensation is limited to the extent of the effects of reverberation on test words. As these effects are larger in monaural conditions, compensation is correspondingly greater. However, for more rapidly spoken test-words compensation is still incomplete in same-distance conditions at 10 m [upper panels in Fig. 3(b)]. Here, the compensation seems to be limited in the amount of distortion that it can handle.

Although the extrinsic compensation effects appear to be monaural, the results do show an "intrinsic" advantage for dichotic listening. This advantage can be seen from effects of the test-word's distance, which are less pronounced in dichotic conditions [left-side panels in Fig. 3(b)]. These results indicate that intrinsic effects are not alone sufficient for complete compensation, although the extrinsic effects seem to augment the intrinsic effects.

V. EXPERIMENT 4

Extrinsic compensation for coloration is reduced when the contexts' spectral transitions are removed by turning them into a signal-correlated noise (Watkins, 1991). Experiment 4 asks whether the extrinsic compensation for reverberation that is observed in the preceding experiments is similarly reduced by this signal manipulation. The resulting noise-contexts are then played in a room by convolving them with appropriate BRIRs. The effect of this is to simulate a sound source that produces the noise in the room, which preserves the inter-aural relationships of reflections that arrive laterally. In a second type of noise manipulation, these relationships are scrambled, by applying the noise processing after the speech context has been convolved with a BRIR. The experiment uses rapidly spoken test-words and their contexts in the L-shaped room, as these conditions gave substantial compensation effects in the preceding experiments.

A. Method

Noise versions of contexts were made by reversing the polarity of a randomly selected half of the signal's samples before applying a filter to give them the same long-term average spectrum as the original (Watkins and Makin, 1996). For noise-before conditions, BRIRs were convolved with noise versions of the contexts. For noise-after conditions, BRIRs were first convolved with speech contexts, and the resulting signals were then turned into the noise, using independent noise-sources for the left and right channels. The context's distance and the test-word's distance were both two-level factors, made with BRIRs from the L-shaped room at 0.32 or 10 m. Listening in a "speech" condition was the same as in experiment 1. Listeners heard 2 context distances $\times 2$ test-word distances $\times 3$ noise conditions (speech, noise before or after) $\times 11$ continuum steps $\times 3$ repeats $=396$ trials. Other aspects of the method are as in experiment 1.

B. Results

Figure 4(a) shows means of category boundaries in the different conditions across the six listeners. A three-way analysis of variance was performed on the category boundaries using within-subject factors, which are noise condition, with three-levels, along with two-level factors for the test-word's distance and the context's distance.

Effects here replicate the findings of the preceding experiments. Increasing the distance of the test-word's BRIR from 0.32 to 10 m increases category boundaries giving a

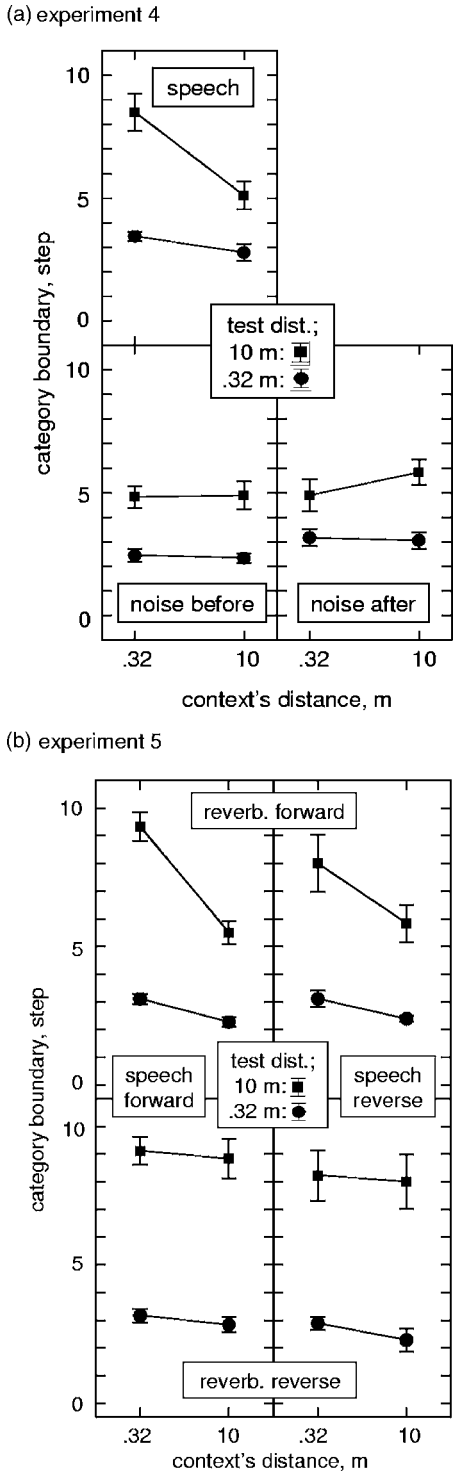

FIG. 4. Means and standard errors of category boundaries from experiments 4 and 5 where the 6 listeners in each experiment identified rapidly spoken test-words and where the contexts were played through BRIRs from the L-shaped room. (a) Data from experiment 4, where the effects of the context's distance and of the test-word's distance are both sharply reduced when contexts are processed to turn them into speech-shaped signal-correlated noise. This reduction happens in the condition where the noise processing is applied before convolution with the BRIR (noise before) as well as in the condition where this processing is applied after this convolution (noise after). The speech condition is a control without any noise processing of the contexts. (b) Data from experiment 5, where the effects of the context's distance are markedly reduced when the context's reverberation pattern is reversed (reverb reverse), but not when the context's speech is reversed (speech reverse). Large effects of the test-word's distance are still apparent in the reversed reverberation conditions, while effects of the context's distance are reduced.

main effect of the test-word's distance, where $F(1,5)=17.13$, and $p<0.009$. There is again extrinsic compensation for this effect of reverberation on the test word, which gives a main effect of the context's distance with $F(1,5)=37.75$, and $p<0.0017$.

Effects of the distances of the test word and of the context are largely due to their prominence in the speech condition. Effects of reverberation on test words are much less prominent in both of the conditions where the contexts are noise. This gives an interaction between test-word's distance and noise condition with $F(2,10)=6.95$, Huynh–Feldt epsilon$=0.7371$, and $p<0.025$. In contexts that are noise the extrinsic compensation effect is not evident. Here, increases in the context's distance do not reduce the effect of the test-word's distance as they do in the speech condition. This gives an interaction between the context's distance and noise condition with $F(2,10)=38.32$, Huynh–Feldt epsilon>1.0, and $p<0.0001$. Effects of the context's distance are more prominent for test sounds at 10 m than they are at 0.32 m, as found previously, but here again this result pattern is confined to the speech condition, giving a three-way interaction between context's distance, test-word's distance, and noise condition with $F(2,10)=25.08$, Huynh–Feldt epsilon$=0.7090$, and $p<0.0009$. Overall there is a main effect of noise condition with $F(2,10)=16.62$, Huynh–Feldt epsilon>1.0, and $p<0.0007$. There are no other significant F-ratios.

C. Discussion

Effects of the context's distance are not apparent when spectral transitions are removed from the context by this experiment's noise processing. This may be because signal characteristics that arise at spectral transitions, such as the tails added by reverberation, are necessary for compensation. However, it is also possible that compensation is reduced here for some other reason, perhaps because it is somehow informed by the context's words, which are not heard in noise versions of contexts. Another possibility is that extrinsic compensation only affects test words that are sequentially grouped with the context (Bregman, 1990), and a noise context might not group with a test word if these sounds are heard as if they have come from different sources.

Results in the speech conditions seem to indicate that the boundary value for 10 m same-distance phrases [upper panel of Fig. 4(a)] is influenced by extrinsic compensation, but similar boundary-values for 10 m test words are found when contexts are noise [lower panels of Fig. 4(a)]. The boundaries for noise contexts might be this low because there is an intrinsic form of compensation in these conditions, deriving perhaps from the reverberant tail on the test-word's vowel. Such compensation might assess the signal's reverberation from only the test word, and exclude the context if it is noise. The parts of the signal that are included in such assessments of reverberation may depend on the extent to which they are perceptually grouped with the test word.

There is a further possible reason for the low boundaries with 10 m test words in the noise conditions. These test words may be influenced by an extrinsic compensation from

the 0.32 m noise-context. Such an influence might occur if effects of the noise-manipulation are in some way similar to the effects of increasing reverberation. One such similarity arises as noise processing generates the relatively smooth, wideband temporal-envelope in all of the auditory filters. Consequently, when the noise processing removes spectral transitions it might effectively extend offsets in auditory filters, as happens when reverberation adds tails.

Effects of the context's distance are not apparent in the noise-before conditions, so it is hard to assess any additional effects of the scrambling of reflections' interaural relationships through the noise-after manipulation. However, there is one slight difference between the two types of noise processing, which is that category boundaries for the 0.32 m test words are lower in the noise-before condition [lower left panel of Fig. 4(a)] than they are in the noise-after and speech conditions [lower right and upper panels of Fig. 4(a)]. The reasons for this are not readily apparent, but it is speculated that some of the test-word's initial frication could be perceptually attributed to a continuation of the preceding noise context, and thereby lower the category boundary.

VI. EXPERIMENT 5

Results of experiments 1–4 are consistent with an extrinsic compensation that is informed by the tails that reverberation adds in the context, so that when these tails are present in auditory filters, a tail on the test word's [s] is not incorporated with the rest of that sound. The origins of these effects might therefore be similar to those that gave rise to the results of Stecker and Hafter (2000) where the tail on a test sound does not contribute to its loudness when a preceding sound also has a reverberation-like tail. For comparison conditions, Stecker and Hafter used time-reversal of sounds that had asymmetric temporal-envelopes, which generates sounds with slowly or rapidly decaying tails that are matched in other respects. Experiment 5 uses analogous comparison conditions for continuous-speech contexts, where onsets and offsets occur in auditory filters at spectral transitions. Compensation is measured with contexts convolved with time-reversed BRIRs. This manipulation gives slowly increasing "heads" at spectral-transition onsets, while the corresponding offsets no longer have a slowly decaying "tail," but remain as rapid as they are in dry conditions. Time reversals of the BRIR's reverberation pattern and of the context's speech were varied orthogonally. This design allows assessment of effects that are due to the time-direction of the tails that reverberation adds, and can separate these from any effects that might come from the temporal asymmetry of the context's speech-signal. The design also controls for effects of words being identifiable or not, which may have been responsible for effects in experiment 4. The experiment tests for reductions in compensation in reversed-reverberation conditions.

A. Method

The experiment used the rapidly spoken test-words and their contexts. The context's distance and the test-word's distance were again both two-level factors, which were made by convolution of dry sounds with BRIRs from the L-shaped room at 0.32 or 10 m. Listening in conditions with forwards-reverberation and forwards-speech was the same as in the conditions of experiment 1. Time reversals of the BRIR and of the context were effected before BRIRs were applied, so that these two types of reversal were separate factors with two levels each, i.e., reversed and forwards. Context reversals were performed separately for the parts that come before and after the test word. Test words were forwards with forwards-reverberation in all conditions. Listeners heard 2 context distances $\times 2$ test-word distances $\times 2$ forwards--or--reversed reverberation conditions $\times 2$ forwards--or--reversed speech conditions $\times 11$ continuum steps $\times 3$ repeats=528 trials. Other aspects of the method are the same as for experiment 1.

B. Results

Figure 4(b) shows means of category boundaries in the different conditions across the six listeners. A four-way analysis of variance was performed on the category boundaries using within-subject factors that have two levels each. The factors include one for conditions with forwards-or-reversed speech, and another for conditions with forwards-or-reversed reverberation. The other two factors are test-word's distance and context's distance as before.

Effects here replicate the findings of the preceding experiments. Increasing the distance of the test-word's BRIR from 0.32 to 10 m increases category boundaries giving a main effect of the test-word's distance, where $F(1,5)=129.41$, and $p<0.0001$. There is again extrinsic compensation for this effect of reverberation on the test word, which gives a main effect of the context's distance with $F(1,5)=31.07$, and $p<0.0027$.

The above effect of the context's distance is largely due to its prominence in the forwards-reverberation conditions, giving an interaction between context's distance and forwards-or-reversed reverberation, with $F(1,5)=10.45$, and $p<0.0233$. Effects of the test-word's distance are reduced by the increase in the context's distance as before, but here this mainly occurs only when the context's reverberation is forwards, giving an interaction between forwards-or-reversed reverberation and test-word's distance, with $F(1,5)=6.99$, and $p<0.0459$. This reduction in the effects of the test-word's distance is more prominent in 10 m test words than in 0.32 m test words as found previously, but this result pattern is less evident when reverberation patterns are reversed. This gives a three-way interaction between forwards-or-reversed reverberation, test-word's distance, and context's distance, with $F(1,5)=9.91$, and $p<0.0255$. Overall there is a main effect of forwards-or-reversed reverberation, with $F(1,5)=8.38$, and $p<0.0341$.

Reversing the context's speech reduces the effects of compensation on 10 m test words a little, giving an interaction between context's distance, test word's distance, and forwards-or-reversed speech, with $F(1,5)=7.01$, and $p<0.046$. There are no other significant F-ratios.

C. Discussion

Compensation is substantial with forwards-reverberation contexts in both the forwards- and reversed-speech conditions [upper panels of Fig. 4(b)], but it is markedly reduced in reversed-reverberation contexts [lower panels of Fig. 4(b)]. It would seem from this that the tails at offsets are primarily responsible for providing the information about reverberation for extrinsic compensation. When reverberation is reversed, tails at offsets are eliminated, and this would appear to indicate an absence of reverberation to the compensation mechanism. As a result, the effects of such contexts are to increase the amount of reverberation in the test word that is perceptually incorporated with the direct sound.

The presence of reversed reverberation in the context gives a sound that contrasts with test words that have forwards reverberation, so this contrast might reduce effects of perceptual grouping between the two sounds. This was also considered as a possible basis for the reduced effects of the noise contexts in experiment 4. Although the context manipulations used in experiments 4 and 5 do both reduce compensation, in other respects their effects are different. In experiment 4 there was a relatively small effect of reverberation on the 10 m test words heard in the noise contexts [lower panels of Fig. 4(a)], but here in experiment 5 the effects are substantial with the reversed-reverberation contexts [lower panels of Fig. 4(b)]. The reversed-reverberation contexts seem to be included with the test word in the assessment of reverberation in the overall signal, so effects of perceptual grouping in experiment 5 would seem to be maintained across conditions where compensation is reduced.

There is a small reduction in compensation in the forwards-reverberation condition when the context's speech is reversed [upper right panel of Fig. 4(b)]. However, a fairly substantial effect remains. Thus, reversed speech is also included to assess reverberation in the overall signal by the compensation mechanism.

Therefore, although this reversed speech is not heard as a series of words, this is not sufficient to abolish the extrinsic compensation. Reversed contexts do still contain speech-like spectral transitions however, and this seems the likely reason for their influence here. Similarly, it now seems unlikely that the reductions in compensation with noise contexts (experiment 4) come about because words are not heard.

VII. GENERAL DISCUSSION

A. Summary of main findings

In the experiments reported here, listeners identified test words from steps of a "sir" to "stir" continuum played in different amounts of reverberation. In some conditions, the reverberation perceptually distorts the test-word's temporal envelope. As a result, listeners make more "sir" responses, and their category boundaries shift to higher step-numbers. This effect occurs when there is more reverberation in the test word than there is in an abutting speech context. Experiment 1 increased this context's reverberation and found evidence of an "extrinsic" compensation for the distortion. As the context's reverberation approaches the level of reverberation in the test word, the perceptual compensation opposes the category-boundary shifts. This compensation is more prominent in rapid speech and in the larger of two rooms. The effects of compensation appear to be confined to those aspects of test words that could plausibly have arisen from reverberation.

Experiment 2 found that the compensation for reverberation was maintained when the room was switched between the context and the test-word. There is a substantial amount of compensation in these conditions, which seems to come from aspects of the reverberation that both of the rooms share.

Experiment 3 found evidence indicating that extrinsic compensation comes from a monaural mechanism, as its effects are actually less pronounced in dichotic conditions than they are in monaural listening. Experiment 3 also found an effect of dichotic listening that served to reduce the category-boundary shifts in comparison with monaural listening. This effect could be related to advantages of binaural listening found in measurements of speech intelligibility (Nábělek and Robinson, 1982). Such effects are not brought about by changes in the context's reverberation, so they are "intrinsic." Other aspects of the results show that the extrinsic mechanism operates to augment the intrinsic effects.

Experiment 4 did not find the above-mentioned effects of extrinsic compensation when contexts were noise versions that have no spectral transitions. This may be because compensation requires information from spectral transitions. However, there was a possibility that information for compensation becomes confined to the test word when the contexts are noise, perhaps because these noise contexts are not sequentially grouped (Bregman, 1990) with the test words. A further possibility is that effects of the noise processing might resemble effects of increasing reverberation, in that the processing acts to extend the offsets in auditory filters as spectral transitions are removed.

Experiment 5 reversed the context's reverberation so that tails at spectral transitions become sharp offsets. Effects of sequential grouping between the context and test word seemed to be maintained in these conditions, but there was nevertheless a marked reduction in the extrinsic compensation.

B. Perceptual grouping

It is possible that the extrinsic compensation observed in the present experiments happens among sounds that are sequentially grouped (Bregman, 1990). The results of experiment 5 indicate that such a grouping should include forwards speech along with speech that is time reversed, consistent with grouping that uses aspects of the signal that are more primitive than representations of words.

Perceptual mechanisms that are informed by primitive aspects of signals have been proposed in order to account for groupings among sounds that come from the same source (Bregman, 1990), or through the same transmission channel (Watkins, 1991). Transmission-channel grouping is consistent with observations that sounds with a similar level of reverberation are sometimes grouped together (Hartmann and Johnson, 1991). However, any grouping involved in ex-

trinsic compensation seems to be maintained across various indicators of a transmission-channel difference between the test word and the context. These indicators include mismatches in the level of reverberation (experiments 1 and 2), mismatches of room characteristics (experiment 2), and mismatches of the reverberation's time-direction (experiment 5). From these results, it seems unlikely that compensation arises through transmission-channel grouping. However, compensation might depend on indications that the context and test word have come from the same source, where the indicators might include the voice characteristics of the talker (Darwin and Hukin, 2000). The findings of experiment 4 are consistent with a reduction in effects of such source grouping when speech contexts are turned into noise.

When contexts are speech in experiments 1–5, their reverberation characteristics have an influence, even when those characteristics are actually misleading about the reverberation in the test word. This might indicate that extrinsic compensation arises through an "obligatory" form of perceptual processing that is effected among sounds when they are grouped (Vliegen, *et al.*, 1999).

C. Attenuation of modulation

The amount of reverberation in speech can be gauged from its modulation characteristics. Since modulation is generally attenuated as the amount of reverberation increases (Houtgast and Steeneken, 1973; Houtgast *et al.*, 1980), it is possible that the context's modulation depth could indicate the amount of reverberation to the extrinsic compensation mechanism. This would be consistent with the findings of experiment 2, as the attenuation of modulation is a characteristic of reverberation that is shared among signals in different rooms. However, experiment 5 showed substantial variations in compensation across conditions with reversed and forwards reverberation. Across these conditions, the context's depth of modulation is the same. This finding did not seem to be due to reductions in effects of sequential grouping in the reversed-context conditions. Other conditions from experiment 5 used contexts with different amounts of reversed reverberation. This manipulation produces substantial variations in modulation depth, but this barely influenced the compensation effects. Therefore, it would seem that modulation depth does not serve to indicate reverberation for the purposes of extrinsic perceptual compensation.

D. Tails from reverberation

Reverberation adds tails at sounds' offsets, and in the contexts used here, which are continuous speech, tails arise at spectral-transition offsets in auditory filters. The results of experiment 5 show that the compensation mechanism is sensitive to the characteristic time-direction of reverberation effects, so signal-characteristics associated with tails might carry the information that it uses. Tails seemed also to signal the presence of reverberation to the listeners who judged sounds' loudness in the experiments of Stecker and Hafter (2000). Such characteristics tend to arise in diverse rooms, including the two used in the room-switching conditions of experiment 2.

Binaural aspects of reverberant tails can serve to distinguish them from the part of the signal that travels directly from the sound's source. The inter-aural correlation tends to be low in the tail, while for the direct sound it is higher. This has been a basis for schemes designed to remove reverberation for the purposes of speech enhancement (Allen, *et al.*, 1977; Bloom, 1982), and listeners seem also to be able to pick up this information in order to assess a sound's distance (Bronkhorst and Houtgast, 1999). However, binaural factors such as this do not seem to be providing information used by the extrinsic compensation mechanism that is responsible for effects in the present experiments. Although binaural factors might work in an intrinsic manner, to reduce the effects of reverberation in experiment 3, the effects of extrinsic compensation are actually larger in monaural conditions.

The present experiments indicate that monaural aspects of tails signal the presence of reverberation to the extrinsic compensation mechanism. Recent measurements have shown that tails from reverberation generally decay more slowly than do the offsets of sounds in dry speech (Ratnam, *et al.*, 2003). It is therefore likely that this distinguishing characteristic underlies the perceptual salience of tails in extrinsic compensation.

ACKNOWLEDGMENTS

This work was supported by a grant to the author from the BBSRC. Elizabeth Hallum and Nigel Holt helped make recordings in the rooms. The author is grateful to Peter Assmann for his editorial critique and John Culling and Simon Makin for their thoughts on an earlier version of the paper.

Allen, J. B., Berkley, D. A., and Blauert, J. (**1977**). "Multimicrophone signal-processing technique to remove room reverberation from speech signals," J. Acoust. Soc. Am. **62**, 912–915.

Bloom, P. J. (**1982**). "Evaluation of a dereverberation process by normal and impaired listeners," in *IEEE, 1982, International Conference on Acoustics, Speech, and Signal Processing* (IEEE, New York), pp. 500–503.

Bregman, A. S. (**1990**). *Auditory Scene Analysis* (MIT, Cambridge).

Bronkhorst, A. W. and Houtgast, T. (**1999**). "Auditory distance perception in rooms," Nature (London) **397**, 517–520.

Clifton, R. K., Freyman, R. L., Litovsky, R. Y., and McCall, D. (**1994**). "Listeners' expectations about echoes can raise or lower echo threshold," J. Acoust. Soc. Am. **95**, 1525–1533.

Darwin, C. J. and Hukin, R. W. (**2000**). "Effects of reverberation on spatial, prosodic, and vocal-tract size cues to selective attention," J. Acoust. Soc. Am. **108**, 335–342.

Dunn, H. K. and Farnsworth, D. W. (**1939**). "Exploration of pressure field around the human head during speech," J. Acoust. Soc. Am. **10**, 184–199.

Furui, S. (**1986**). "On the role of spectral transition for speech perception," J. Acoust. Soc. Am. **80**, 1016–1025.

Gardner, B. and Martin, K. (1994). "HRTF measurements of a KEMAR dummy-head microphone," MIT Media Lab. Perceptual Computing - Technical Report No. 280.

Hartmann, W. M. and Johnson, D. (**1991**). "Stream segregation and peripheral channeling," Music Percept. **9**, 155–184.

Houtgast, T. and Steeneken, H. J. M. (**1973**). "The modulation transfer function in acoustics as a predictor of speech intelligibility," Acustica **28**, 66–73.

Houtgast, T., Steeneken, H. J. M., and Plomp, R. (**1980**). "Predicting speech intelligibility in rooms from the modulation transfer function. I. General room acoustics," Acustica **46**, 60–72.

Knudsen, V. O. (**1929**). "The hearing of speech in auditoriums," J. Acoust. Soc. Am. **1**, 56–82.

Lochner, J. P. A. and Burger, J. F. (**1961**). "The intelligibility of speech under reverberant conditions," Acustica **7**, 195–200.

Nábělek, A. K., Litowski, T. R., and Tucker, F. M. (**1989**). "Reverberant

overlap- and self-masking in consonant identification," J. Acoust. Soc. Am. **86**, 1259–1265.
Nábělek, A. K. and Robinson, P. K. (**1982**). "Monaural and binaural speech perception in reverberation for listeners of various ages," J. Acoust. Soc. Am. **71**, 1242–1248.
Nearey, T. M. (**1989**). "Static, dynamic, and relational properties in vowel perception," J. Acoust. Soc. Am. **85**, 2088–2113.
Ratnam, R., Jones, D. L., Wheeler, B. C., O'Brian Jr., W. D., Lansing, C. R., and Feng, A. S. (**2003**). "Blind estimation of reverberation time," J. Acoust. Soc. Am. **114**, 2877–2892.
Santon, F. (**1976**). "Numerical prediction of echograms and of the intelligibility of speech in rooms," J. Acoust. Soc. Am. **59**, 1399–1405.
Schroeder, M. (**1965**). "New method of measuring reverberation time," J. Acoust. Soc. Am. **37**, 409–412.
Stecker, G. C. and Hafter, E. R. (**2000**). "An effect of temporal asymmetry on loudness," J. Acoust. Soc. Am. **107**, 3358–3368.
Vliegen, J. V., Moore, B. C. J., and Oxenham, A. J. (**1999**). "The role of spectral and periodicity cues in auditory stream segregation, measured using a temporal discrimination task," J. Acoust. Soc. Am. **106**, 938–945.
Wallach, H., Newman, E. B., and Rosenzweig, M. R. (**1949**). "The precedence effect in sound localization," J. Exp. Psychol. **27**, 339–368.
Watkins, A. J. (**1991**). "Central, auditory mechanisms of perceptual compensation for spectral-envelope distortion," J. Acoust. Soc. Am. **90**, 2942–2955.
Watkins, A. J. (**1992**). "Perceptual compensation for effects of reverberation on amplitude-envelope cues to the 'slay'-'splay' distinction," Proc. Inst. Acoust. **14**, 125–132.
Watkins, A. J. (**1999**). "The influence of early reflections on the identification and lateralization of vowels," J. Acoust. Soc. Am. **106**, 2933–2944.
Watkins, A. J. and Holt, N. J. (**2000**). "Effects of a complex reflection on vowel identification," Acust. Acta Acust. 86, 532–542.
Watkins, A. J. and Makin, S. J. (**1996**). "Some effects of filtered contexts on the perception of vowels and fricatives," J. Acoust. Soc. Am. **99**, 588–594.
Wightman, F. L. and Kistler, D. J. (**1989**). "Headphone simulation of free-field listening. I. Stimulus synthesis," J. Acoust. Soc. Am. **85**, 858–867.
Zahorik, P. (**2002**). "Assessing auditory distance perception using virtual acoustics," J. Acoust. Soc. Am. **111**, 1832–1846.

Performance analysis of adaptive equalization for coherent acoustic communications in the time-varying ocean environment

James C. Preisig[a)]
Department of Applied Ocean Physics and Engineering, Woods Hole Oceanographic Institution, Woods Hole, Massachusetts 02543

(Received 13 December 2004; revised 22 March 2005; accepted 24 March 2005)

Equations are derived for analyzing the performance of channel estimate based equalizers. The performance is characterized in terms of the mean squared soft decision error (σ_s^2) of each equalizer. This error is decomposed into two components. These are the minimum achievable error (σ_o^2) and the excess error (σ_ϵ^2). The former is the soft decision error that would be realized by the equalizer if the filter coefficient calculation were based upon perfect knowledge of the channel impulse response and statistics of the interfering noise field. The latter is the additional soft decision error that is realized due to errors in the estimates of these channel parameters. These expressions accurately predict the equalizer errors observed in the processing of experimental data by a channel estimate based decision feedback equalizer (DFE) and a passive time-reversal equalizer. Further expressions are presented that allow equalizer performance to be predicted given the scattering function of the acoustic channel. The analysis using these expressions yields insights into the features of surface scattering that most significantly impact equalizer performance in shallow water environments and motivates the implementation of a DFE that is robust with respect to channel estimation errors. [DOI: 10.1121/1.1907106]

PACS numbers: 43.60.Dh, 43.60.Mn, 43.30.Re [EJS] Pages: 263–278

I. INTRODUCTION

The use of adaptive coherent equalizers for high rate underwater acoustic communications is increasingly common for a large number of applications. The ability to quantitatively relate the performance of different equalizers to prevailing environmental conditions is important for a number of reasons. First, it allows the relative performance characteristics of different techniques and configurations to be compared and realistic system trade-offs made in the selection and demodulation of demodulation algorithms. Second, it can highlight the factors limiting equalizer performance to guide future research and development efforts. Finally, with the field moving rapidly toward the development of underwater acoustic communications networks using coherent modulation and demodulation techniques, performance predictions as a function of environmental conditions and network topology will be an important input to dynamic network control algorithms.

The paper presents the development and interpretation of quantitative expressions for the performance of three types of channel estimate based adaptive coherent equalizers. Channel estimate based equalizers are those that calculate their filter weights based upon estimates of the time-varying impulse response of the acoustic channel between the transmitter and receiver and the statistics of the ambient noise field. Figure 1 shows the basic structure of channel estimate based equalizers. The three types of equalizers considered here are the channel estimate based decision feedback equalizer (CE-DFE) (Stojanovic *et al.*[1]), the linear MMSE equalizer (L-MMSE), and the passive time-reversal equalizers (P-TR) (Rouseff *et al.*,[2] Flynn *et al.*[3]). In Stojanovic *et al.*[4] expressions were developed for the total error achieved by a CE-DFE that either has perfect knowledge of the channel impulse response or perfect knowledge of the second-order statistics of the channel impulse response estimation errors.

The expressions developed here are new in that they separately quantify the equalizer errors that are due to the realization of the channel impulse response and the ambient noise and the degradation in performance that is due to the equalizer having imperfect estimates of the channel impulse response. This leads to new insights into the factors that can limit equalizer performance and the characteristics of equalizers that are robust with respect to channel estimation errors. The expressions also allow the performance of the CE-DFE, L-MMSE, and P-TR equalizers to be compared within a common framework when each equalizer has the same information regarding the channel impulse response and the statistics of the ambient noise field. This work is an expansion of the work originally presented in Preisig.[5] This work also presents the results of the processing and analysis of field data collected during the SPACE02 experiment. The SPACE02 experiment was conducted 5 km South of Martha's Vineyard, MA in the Fall of 2002. It focused on investigating the impact of surface processes on high frequency acoustic propagation and communications in shallow water environments.

The organization of this paper is as follows. Section II outlines notation as well as the expressions for the modeled channel impulse response and the equalizer filter coefficients. Similar expressions with varying notations for the filter coefficients of channel estimate based equalizers can be found in Stojanovic *et al.*[4] and standard communications textbooks. Section III presents and discusses the derivation

a)Electronic mail: jpreisig@whoi.edu

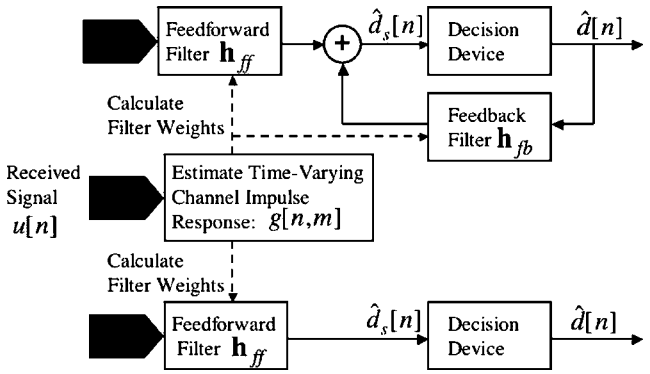

FIG. 1. The structure of channel estimate based coherent equalizers. The received signal, $u[n]$, is processed to generate estimates of the time-varying impulse response of the channel between the transmitter and each receive hydrophone. The impulse response estimates are used to compute the equalizer filter weights. These filter weights are used to implement the equalizer and estimate the desired data symbol. Two different types of equalizers are shown. The upper equalizer is a channel estimate based decision feedback equalizer (CE-DFE) and the lower equalizer is a linear equalizer. The feedforward weights for both filters are denoted here as $\mathbf{h}_{\text{ff}}$ and the feedback weights for the CE-DFE are denoted here as $\mathbf{h}_{\text{fb}}$. In this paper, two different linear equalizers are considered. The first is the linear minimum mean squared error (L-MMSE) equalizer. The filter weights for this equalizer are denoted in the text as $\mathbf{h}_{\text{lin}}$. The second is the passive time-reversal (P-TR) equalizer. The filter weights for this equalizer are denoted in the text as $\mathbf{h}_{\text{tr}}$.

of the expressions for the errors achieved by the channel estimate based equalizers given an estimate of the channel impulse response and the statistics of the ambient noise field and channel estimation errors. Section IV describes the algorithm (the exponentially weighted least-squares estimator) used to estimate the channel impulse response and presents a new expression predicting its performance. Section V describes the relevant characteristics of the SPACE02 experiment during which the data analyzed here was collected.

Section VI presents and analyzes the results achieved when processing communications signals from the SPACE02 experiment with CE-DFE and P-TR equalizers. Predictions of equalizer performance using the expressions derived in Secs. III and IV are shown to closely match the observed performance of the equalizers. Two methods of performance prediction are shown. The first method (Sec. VI A) uses estimates of the statistics of the channel estimation error calculated directly from the processed signals. The results of these predictions validate the expressions derived in Sec. III. The second method (Sec. VI B) uses estimates of the statistics of the channel fluctuations to predict the statistics of the channel estimation errors as described in Sec. IV. These predicted statistics of the channel estimation errors are then used to predict equalizer performance. It is this later approach that must ultimately be fully developed to allow equalizer performance to be rigorously related to environmental conditions. Finally, the performance of CE-DFE and P-TR equalizers is compared in Sec. VI C and a CE-DFE with improved robustness with respect to channel estimation errors is presented in Sec. VII. Section VIII presents conclusions of the paper. Derivations of expressions presented in the body of the paper and the method used to estimate channel scattering functions are described in the appendices.

Throughout this paper, boldface uppercase letters denote matrices, boldface lowercase letters denote vectors (all vectors are assumed to be column vectors), and lowercase letters denote scalar quantities. The superscripts t, $*$, and h denote transpose, complex conjugate, and Hermitian (complex conjugate transpose), respectively. For any square matrix $\mathbf{Q}$, the notation $\tilde{\mathbf{Q}}$ denotes the conjugate symmetric part of $\mathbf{Q}$. That is,

$$\tilde{\mathbf{Q}} \triangleq \frac{\mathbf{Q}+\mathbf{Q}^h}{2}.$$

The symbols $\mathbf{I}$ and $\mathbf{0}$ denote the identity matrix and the matrix or vector of all zeros, respectively. When necessary, the size of the matrices or vectors will be explicitly denoted (e.g., $\mathbf{0}_{N\times M}$ for a matrix of all zeros with N rows and M columns). The caret denotes the estimate of the quantity under the caret (e.g., $\hat{\tilde{\mathbf{g}}}$ denotes the estimate of $\tilde{\mathbf{g}}$).

II. CHANNEL AND EQUALIZER MODEL

All data processing, analysis, and modeling in this paper is done with respect to a sampled baseband received signal. (See Sec. V for a description of this baseband signal.) Thus all discussion is with respect to discrete time signals and processes. The acoustic channel is modeled as a time-varying, discrete time system described by the complex baseband time-varying impulse response. (See Proakis[6] and Van Trees[7]). The received signal at time n is given by

$$u[n]=\sum_{m=-N_a}^{N_c-1} g^*[n,m]d[n-m]+v[n], \tag{1}$$

where $g[n,m]$ is the baseband complex time-varying impulse response relating the input signal at time $(n-m)$ to the output signal at time n, $d[n]$ is the complex baseband transmitted data, and $v[n]$ is complex baseband observation noise. The quantities N_a and N_c denote, respectively, the number of acausal and causal taps in the impulse response.[8] This equation can be put into the vector form of

$$u[n]=\tilde{\mathbf{g}}^h[n]\tilde{\mathbf{d}}[n]+v[n]. \tag{2}$$

where

$$\tilde{\mathbf{g}}[n]\triangleq[g[n,N_c-1],\ldots,g[n,0],\ldots,g[n,-N_a]]^t,$$

and

$$\tilde{\mathbf{d}}[n]\triangleq[d[n-N_c+1],\ldots,d[n],\ldots,d[n+N_a]]^t$$

are samples of the impulse response and transmitted data symbols, respectively. In this section, the received signal is assumed to be sampled at the transmit symbol rate. The extension of the analysis to fractionally spaced systems is conceptually straightforward, but the notation is cumbersome. The final results of the analysis are equally applicable to symbol rate and fractionally spaced systems. Note that the experimental data presented in this paper were fractionally sampled at a rate of 2 samples/symbol (See Sec. V).

The equalizers considered here (Fig. 1) each consist of a linear, finite impulse response (FIR) feedforward filter that filters the received signals and, in the case of the CE-DFE, a FIR feedback filter that filters and feeds back estimates of the transmitted data symbol. The output of the filter is the soft

decision estimate, $\hat{d}_s[n]$, of the transmitted data symbol, $d[n]$. The estimate $\hat{d}_s[n]$ is the input to a decision device that generates the final estimate, $\hat{d}[n]$, of the transmitted data symbol.

For a linear equalizer (e.g., the L-MMSE and P-TR equalizers) the soft decision estimate of the transmitted data symbol, $\hat{d}_s$, is given by

$$\hat{d}_s[n]=\mathbf{h}^h[n]\mathbf{u}[n], \tag{3}$$

where $\mathbf{h}[n]$ is a vector of the feedforward filter coefficients at time n and

$$\mathbf{u}[n]\triangleq[u[n-L_c+1],\ldots,u[n],\ldots,u[n+L_a]]^t. \tag{4}$$

Here, L_c and L_a denote the number of causal and acausal taps, respectively, of the feedforward filter. The notation $\mathbf{h}_{\text{lin}}$ and $\mathbf{h}_{\text{tr}}$ will be used to denote the filter coefficient vectors for the L-MMSE and P-TR equalizers, respectively. For the CE-DFE, $\hat{d}_s$ is given by

$$\hat{d}_s[n]=\mathbf{h}_{\text{ff}}^h[n]\mathbf{u}[n]+\mathbf{h}_{\text{fb}}^h[n]\hat{\mathbf{d}}_{\text{fb}}[n]. \tag{5}$$

Here, $\mathbf{h}_{\text{ff}}$ and $\mathbf{h}_{\text{fb}}$ are vectors of the coefficients of the CE-DFE feedforward and feedback filters, respectively. For a feedback filter of length L_{fb} symbols, $\hat{\mathbf{d}}[n]$ is a vector of estimates of past transmitted data symbols given by $\hat{\mathbf{d}}_{fb}[n]\triangleq[\hat{d}[n-L_{fb}],\ldots,\hat{d}[n-1]]^t$. The span of the feedback filter should be less than or equal to the causal delay spread of the convolution of the channel impulse response and the feedforward filter. Therefore, $L_{\text{fb}}\leq L_c+N_c-2$.[9]

Combining Eqs. (2) and (4) yields

$$\mathbf{u}[n]=\mathbf{G}[n]\mathbf{d}[n]+\mathbf{v}[n], \tag{6}$$

where

$$\mathbf{d}[n]\triangleq[d[n-L_c-N_c+2],\ldots,d[n],\ldots,d[n+L_a+N_a]]^t$$

and

$$\mathbf{v}[n]\triangleq[v[n-L_c+1],\ldots,v[n],\ldots,v[n+L_a]]^t.$$

$\mathbf{G}[n]$ is the channel impulse response matrix with the ith row composed of $\tilde{\mathbf{g}}^h[n-L_c+i]$ packed with leading and trailing zeros to position it in the appropriate columns of the matrix with respect to the elements of the vector $\mathbf{d}[n]$.

The notation presented thus far has been specific to single channel equalizers. Multichannel equalizers are accommodated within this notation by stacking the feedforward filter coefficient vector for each channel into a single larger vector, stacking the received signal vector, $\mathbf{u}$, for each channel into a single larger vector, and stacking the impulse response matrix, $\mathbf{G}$, for each channel into a single matrix with the same number of columns as the original matrix but a greater number of rows.

It is instructive to represent $\mathbf{G}$ using its column vectors indexed in the following manner:

$$\mathbf{G}[n]=[\mathbf{g}_{(N_c+L_c-2)},\ldots,\mathbf{g}_1,\mathbf{g}_0,\mathbf{g}_{-1},\ldots,\mathbf{g}_{-(N_a+L_a)}], \tag{7}$$

The dependence of the columns of $\mathbf{G}[n]$ on the time index n will now be suppressed for notational convenience. Note that the rows of $\mathbf{G}$ are composed of the appropriately positioned versions of the impulse response vector $\tilde{\mathbf{g}}^h$. In this way, each row of $\mathbf{G}$ relates a subset of the elements of the transmitted data vector $\mathbf{d}[n]$ to the corresponding element of the received signal vector $\mathbf{u}[n]$. In contrast, the vector $\mathbf{g}_i$ denoting a particular column of $\mathbf{G}$ is a replica vector for the data symbol $d[n-i]$ in the received signal vector $\mathbf{u}[n]$. That is, it specifies the contribution of one transmitted data symbol symbol $d[n-i]$ to the entire received signal vector.

Partition the transmit data symbols in $\mathbf{d}[n]$ into three groups: $\mathbf{d}_{\text{fb}}[n]\triangleq[d[n-L_{\text{fb}}],\ldots,d[n-1]]^t$, $d[n]$, and $\mathbf{d}_o[n]$ which is composed of the remaining elements of $\mathbf{d}[n]$. Partition the columns of $\mathbf{G}[n]$ into three similarly defined sets: $\mathbf{G}_{\text{fb}}$, $\mathbf{g}_0$, and $\mathbf{G}_o$. Then Eq. (6) can be rewritten as

$$\mathbf{u}[n]=\mathbf{g}_0 d[n]+\mathbf{G}_{\text{fb}}\mathbf{d}_{\text{fb}}[n]+(\mathbf{v}[n]+\mathbf{G}_o\mathbf{d}_o[n]). \tag{8}$$

The first term is the portion of the received signal vector, $\mathbf{u}[n]$, that corresponds to the transmitted data symbol to be estimated, $d[n]$. The second term is the portion of $\mathbf{u}[n]$ that can be canceled by the output of the feedback filter in a CE-DFE, and the terms in the parentheses represent an effective observation noise that the feedforward filter must try to eliminate. Assuming that the data sequence is a zero-mean, white sequence with a variance of one,[10] the data sequence is independent of the channel impulse response and $v[n]$, and that $\mathbf{v}[n]$ is a zero-mean sequence with covariance $\mathbf{R}_v$ that is independent of the channel impulse response, the effective noise correlation matrix, $\mathbf{Q}$, can be written as

$$\mathbf{Q}=\mathbf{R}_v+\mathbf{G}_o\mathbf{G}_o^h. \tag{9}$$

With the model and quantities so defined, a number of approaches can be used to calculate the optimal filter coefficients. One such approach is given in Stojanovic *et al.*[4] In that paper, the effective noise correlation matrix, denoted with the symbol $\mathbf{R}$, includes the impact of channel estimation errors. Therefore, the calculated filter coefficients and subsequent error analysis are valid for the case where the DFE has accurate knowledge of both the noise statistics and the second-order statistics of the channel estimation errors. For the filter calculation and performance analysis presented here, there is no assumption that the DFE knows the statistics of the channel estimation errors.

The filter coefficients for the three equalizers are calculated using estimated quantities for $\mathbf{R}_v$, $\mathbf{G}$, and therefore $\mathbf{Q}$. In the following expressions, these estimated quantities are denoted by the caret (e.g., $\hat{\mathbf{R}}_v$). The filter coefficient vectors for the L-MMSE and CE-DFE equalizers are selected to minimize the mean squared soft decision error ($\text{E}[|\hat{d}_s[n]-d[n]|^2]$) assuming that the estimates of $\mathbf{R}_v$ and $\mathbf{G}$ are accurate and that the statistical assumptions stated in the paragraph before Eq. (9) hold. The expressions for these filter coefficient vectors are

$$\mathbf{h}_{\text{ff}}=\frac{\hat{\mathbf{Q}}^{-1}\hat{\mathbf{g}}_0}{1+\hat{\mathbf{g}}_0^h\hat{\mathbf{Q}}^{-1}\hat{\mathbf{g}}_0},\quad \mathbf{h}_{\text{fb}}=-\hat{\mathbf{G}}_{\text{fb}}^h\mathbf{h}_{\text{ff}}, \tag{10}$$

$$\mathbf{h}_{\text{lin}}=\frac{(\hat{\mathbf{Q}}+\hat{\mathbf{G}}_{\text{fb}}\hat{\mathbf{G}}_{\text{fb}}^h)^{-1}\hat{\mathbf{g}}_0}{1+\hat{\mathbf{g}}_0^h(\hat{\mathbf{Q}}+\hat{\mathbf{G}}_{\text{fb}}\hat{\mathbf{G}}_{\text{fb}}^h)^{-1}\hat{\mathbf{g}}_0}. \tag{11}$$

The P-TR equalizer is a normalized matched filter so its coefficients are given by

$$\mathbf{h}_{\mathrm{tr}}=\frac{\hat{\mathbf{g}}_0}{\hat{\mathbf{g}}_0^h\hat{\mathbf{g}}_0}. \tag{12}$$

See Appendix A for a derivation of Eqs. (10)–(12).

III. EQUALIZER PERFORMANCE PREDICTIONS

Here, equalizer performance is characterized in terms of the variance of the soft decision error $\epsilon_s=(\hat{d}_s[n]-d[n])$. This error will depend on both the estimate of the channel impulse response as well as the error in this estimate. For the analytical results presented here, it is assumed that correct values of the transmitted signal are used to estimate the channel impulse response and as the input to the feedback filter of the CE-DFE. The experimental data were processed in this same manner. That is, the equalizers were run in a ''training mode.'' The impact of the decay in the quality of the channel estimate resulting from using incorrect signal decisions in the estimation algorithm or the feedback of incorrect signal decisions has not been treated here. Thus, the observed and predicted values of the variance of the soft decision error are lower bounds on what could actually be achieved.

Let the true channel impulse response matrix be given by

$$\mathbf{G}[n]=\hat{\mathbf{G}}[n]+\mathbf{E}_G, \tag{13}$$

where $\mathbf{E}_G$ is the error in the estimate of the channel impulse response matrix. Then for the CE-DFE, combining Eqs. (5) and (8) results in

$$\hat{d}_s[n]=\mathbf{h}_{\mathrm{ff}}^h[n](\mathbf{g}_0 d[n]+\mathbf{G}_{\mathrm{fb}}\mathbf{d}_{\mathrm{fb}}[n]+\mathbf{v}[n]+\mathbf{G}_o\mathbf{d}_o[n]) + \mathbf{h}_{\mathrm{fb}}^h[n]\hat{\mathbf{d}}_{\mathrm{fb}}[n].$$

Then, substituting in Eqs. (10) and (13), the soft decision estimate can be written as

$$\hat{d}_s[n]=\mathbf{h}_{\mathrm{ff}}^h[n](\hat{\mathbf{g}}_0 d[n]+\mathbf{v}[n]+\hat{\mathbf{G}}_o\mathbf{d}_o[n])+\mathbf{h}_{\mathrm{ff}}^h[n] \times(\hat{\mathbf{G}}_{\mathrm{fb}}\mathbf{d}_{\mathrm{fb}}[n]-\hat{\mathbf{G}}_{\mathrm{fb}}\hat{\mathbf{d}}_{\mathrm{fb}}[n])+\mathbf{h}_{\mathrm{ff}}^h[n]\mathbf{E}_G\mathbf{d}[n].$$

Assuming that the past symbol decisions that are inputs to the feedback filter are accurate, the second term equals zero and this becomes

$$\hat{d}_s[n]=\mathbf{h}_{\mathrm{ff}}^h[n](\hat{\mathbf{g}}_0 d[n]+\mathbf{v}[n]+\hat{\mathbf{G}}_o\mathbf{d}_o[n]) + \mathbf{h}_{\mathrm{ff}}^h[n]\mathbf{E}_G\mathbf{d}[n]. \tag{14}$$

Subtracting $d[n]$ from both sides of Eq. (14) yields the following expression for the soft decision error of a CE-DFE:

$$\epsilon_s[n]=(\mathbf{h}_{\mathrm{ff}}^h[n](\hat{\mathbf{g}}_0 d[n]+\mathbf{v}[n]+\hat{\mathbf{G}}_o\mathbf{d}_o[n])-d[n]) + \mathbf{h}_{\mathrm{ff}}^h[n]\mathbf{E}_G\mathbf{d}[n]. \tag{15}$$

Similarly, the expression for the soft decision estimate for the L-MMSE and P-TR equalizers can be written as

$$\hat{d}_s[n]=\mathbf{h}^h[n](\hat{\mathbf{g}}_0 d[n]+\mathbf{v}[n]+\hat{\mathbf{G}}_o\mathbf{d}_o[n]+\hat{\mathbf{G}}_{\mathrm{fb}}\mathbf{d}_{\mathrm{fb}}[n]) + \mathbf{h}^h[n]\mathbf{E}_G\mathbf{d}[n], \tag{16}$$

where $\mathbf{h}[n]$ is the appropriate filter coefficient vector ($\mathbf{h}_{\mathrm{lin}}[n]$ or $\mathbf{h}_{\mathrm{tr}}[n]$). Subtracting $d[n]$ from both sides of Eq. (16) yields the following expression for the soft decision error of the L-MMSE and P-TR equalizers:

$$\epsilon_s[n]=(\mathbf{h}^h[n](\hat{\mathbf{g}}_0 d[n]+\mathbf{v}[n]+\hat{\mathbf{G}}_o\mathbf{d}_o[n]+\hat{\mathbf{G}}_{\mathrm{fb}}\mathbf{d}_{\mathrm{fb}}[n]) - d[n])+\mathbf{h}^h[n]\mathbf{E}_G\mathbf{d}[n]. \tag{17}$$

Under the assumption that the estimate of the channel impulse response is a minimum mean squared error estimate, the error matrix $\mathbf{E}_G$ is uncorrelated with the estimated channel impulse response matrix and the received signal and the expectation of $\mathbf{E}_G$ conditioned on $\hat{\mathbf{G}}$ equals zero. Under these conditions, the first and second terms in these expressions are uncorrelated. The variance of the first term represents the minimum achievable error (MAE) of the equalizer and is denoted by σ_o^2. This is the error that will be achieved by the equalizer given that it has perfect estimates of the channel impulse response and the noise statistics. This error depends on the static structure of the channel impulse response and the statistics of the ambient noise but not on the dynamics of the channel impulse response fluctuations. The variance of the second term is the excess error and is denoted by σ_ϵ^2. This error is the additional soft decision error that is due to errors in estimating the channel impulse response. The variance of the soft decision error is given by $\sigma_s^2=\sigma_o^2+\sigma_\epsilon^2$.

The MAE can be calculated by substituting the appropriate expressions for the equalizer coefficients into the first term in Eqs. (15) and (17) and calculating the variance of the resulting term. For the three different equalizers, the variance of the MAE is given by

$$\sigma_{o_{\mathrm{DFE}}}^2=\frac{1}{1+\hat{\mathbf{g}}_0^h\hat{\mathbf{Q}}^{-1}\hat{\mathbf{g}}_0}, \tag{18}$$

$$\sigma_{o_{\mathrm{lin}}}^2=\frac{1}{1+\hat{\mathbf{g}}_0^h(\hat{\mathbf{Q}}+\hat{\mathbf{G}}_{\mathrm{fb}}\hat{\mathbf{G}}_{\mathrm{fb}}^h)^{-1}\hat{\mathbf{g}}_0}, \tag{19}$$

$$\sigma_{o_{\mathrm{tr}}}^2=\frac{\hat{\mathbf{g}}_0^h(\hat{\mathbf{Q}}+\hat{\mathbf{G}}_{\mathrm{fb}}\hat{\mathbf{G}}_{\mathrm{fb}}^h)\hat{\mathbf{g}}_0}{(\hat{\mathbf{g}}_0^h\hat{\mathbf{g}}_0)^2}. \tag{20}$$

See Appendix A for a derivation of these expressions for the variance of the MAE for each type of equalizer.

Comparing Eqs. (18), (19), and (20), it can be shown that

$$\sigma_{o_{\mathrm{DFE}}}^2\leq\sigma_{o_{\mathrm{lin}}}^2\leq\sigma_{o_{\mathrm{tr}}}^2.$$

Furthermore, it can be shown that $\sigma_{o_{\mathrm{DFE}}}^2$ and $\sigma_{o_{\mathrm{lin}}}^2$ will always decrease when the number of received signal channels or the length of the feedforward of feedback filters is increased.

The reduction in MAE when comparing the MAE of the L-MMSE equalizer to the P-TR equalizer is due to the MMSE adaptation of the former equalizer while the reduction in MAE when comparing the CE-DFE to the L-MMSE equalizer is due to the cancellation of the interference energy associated with the ''replica vectors'' corresponding to the columns of $\mathbf{G}_{\mathrm{fb}}$. For all three equalizers, the MAE can be evaluated in terms of the quadratic product of the replica vector associated with the data symbol being estimated, $\mathbf{g}_0$,

and a matrix determined by the observation noise and the outer product of a subset of the columns of $\mathbf{G}$ ($\mathbf{G}_o$ for the CE-DFE, $\mathbf{G}_o$ and $\mathbf{G}_{\mathrm{fb}}$ for the L-MMSE and P-TR equalizers) that are the replica vectors of interfering data symbols. The structure of the channel impulse response matrix impacts the minimal achievable error through these replica vectors.

The variance of the excess error is the variance of the second term in Eqs. (15) and (17). For the three different equalizers, this yields a common form of

$$\sigma^2_{\epsilon_{\mathrm{DFE}}} = \mathbf{h}^h_{\mathrm{ff}} \mathbf{R}_{E_G} \mathbf{h}_{\mathrm{ff}}, \tag{21}$$

$$\sigma^2_{\epsilon_{\mathrm{lin}}} = \mathbf{h}^h_{\mathrm{lin}} \mathbf{R}_{E_G} \mathbf{h}_{\mathrm{lin}}, \tag{22}$$

$$\sigma^2_{\epsilon_{\mathrm{tr}}} = \mathbf{h}^h_{\mathrm{tr}} \mathbf{R}_{E_G} \mathbf{h}_{\mathrm{tr}}, \tag{23}$$

where $\mathbf{R}_{E_G} \triangleq \mathrm{E}[\mathbf{E}_G \mathbf{E}_G^h | \hat{\mathbf{G}}]$. Thus the sensitivity of each equalizer to channel impulse response estimation errors is determined by the magnitude squared of the vector of the equalizer's feedforward filter coefficients and the projection of these coefficient vectors on the eigen-structure of $\mathbf{R}_{E_G}$. In the special case where $\mathbf{R}_{E_G}$ is a scalar times the identity matrix, the sensitivity of each equalizer to channel estimation errors is proportional to the magnitude squared of the feedforward filter weight vector.

The soft decision error expressions derived in this section and used in Sec. VI B assume that the statistics of the channel and data estimation errors are conditioned upon the channel estimate. Thus, the channel estimate is considered to be a deterministic quantity and the actual channel realization a stochastic quantity. This approach is taken for several reasons. First, it yields results that offer better insight into the functional dependence of equalizer performance on the deterministic channel structure and the rate of fluctuation of the channel impulse response than do methods that condition the statistics on the true channel state. Second, unconditional statistics (i.e., conditioned on neither the channel impulse response nor the estimate of the channel impulse response) would not clearly highlight some aspects of the relationship between important physical processes and the performance of the algorithms considered here. An example of such a relationship is the cyclic nature of the soft decision error and the relationship of the time scale of the fluctuation to the dominant surface wave period discussed in Sec. VI A. Third, the expressions presented here can be used to aid in the optimal dynamic configuration of channel estimate based equalizers given channel estimates and estimates of the channel dynamics. In this case, these conditional statistics would be the appropriate ones to use. Finally, the experimental results presented here indicate that the resulting expressions yield results that are relatively accurate to within the limits of our ability to predict the correlation matrix $\mathbf{R}_{E_G}$.

IV. CHANNEL ESTIMATION AND ERROR

The excess error exhibited by any channel estimate based equalizer depends upon the quality of the channel estimate. For the analysis and results presented here, the channel estimation algorithm is the exponentially weighted least squares algorithm. While this algorithm does not yield minimum mean squared error estimates of the channel impulse response and therefore results in a violation of the assumption that the channel esimates and estimation error are uncorrelated, the analysis of experimental data in Sec. VI indicates that the assumption is sufficiently valid for the prediction of excess error.

With the exponentially weighted least squares algorithm, the estimate of the channel impulse response is given by

$$\hat{\tilde{\mathbf{g}}}[n] = \arg\min_{\tilde{\mathbf{g}}} \sum_{m=0}^{n} \lambda^{n-m} |u[m] - \tilde{\mathbf{g}}^h \tilde{\mathbf{d}}[m]|^2, \tag{24}$$

where λ is a constant "forgetting factor" between zero and one. Assume that the channel impulse response, $\tilde{\mathbf{g}}[n]$, is a zero-mean, wide-sense stationary random process with correlation matrix $\mathbf{R}_{\tilde{\mathbf{g}},\tilde{\mathbf{g}}}[m] \triangleq \mathrm{E}[\tilde{\mathbf{g}}[n] \tilde{\mathbf{g}}^h[n+m]]$. Then, the error correlation matrix $\mathbf{R}_{\epsilon,\epsilon}[1] \triangleq \mathrm{E}[(\hat{\tilde{\mathbf{g}}}[n] - \tilde{\mathbf{g}}[n+1])(\hat{\tilde{\mathbf{g}}}[n] - \tilde{\mathbf{g}}[n+1])^h]$ is given by

$$\mathbf{R}_{\epsilon,\epsilon}[1] = \frac{1}{2\pi} \int_{-\pi}^{\pi} \frac{|e^{-j\omega} - 1|^2}{|1 - \lambda e^{-j\omega}|^2} \mathbf{S}_{\tilde{\mathbf{g}},\tilde{\mathbf{g}}}(\omega) d\omega + \frac{(1-\lambda)}{(1+\lambda)} \sigma_v^2 \mathbf{I}, \tag{25}$$

where

$$\mathbf{S}_{g,g}(\omega) = \sum_{m=-\infty}^{\infty} \mathbf{R}_{\tilde{\mathbf{g}},\tilde{\mathbf{g}}}[m] \mathrm{e}^{-j\omega m} \tag{26}$$

is the spectral correlation matrix for the time-varying channel impulse response vector $\tilde{\mathbf{g}}[n]$. Here, the observation noise correlation matrix $\mathbf{R}_v$ is assumed to equal $\sigma_v^2 \mathbf{I}$ and the data symbol variance is assumed equal to one as stated previously. The first term in Eq. (25) is the lag error resulting from the time variation of the channel while the second term is the error variance due to the observation noise. See Appendix B for a derivation of Eq. (25). While experimental data will show that the channel does not exhibit the behavior of a stationary random process, this model is useful for predicting the algorithm dependence on channel behavior over short time periods.

Note that the total mean squared channel estimation error equals the trace of the error correlation matrix. Thus, it is the diagonal elements of this matrix that determine the total mean squared estimation error, and through Eq. (25), this depends on the diagonal elements of the spectral correlation matrix. These diagonal elements are the channel scattering function (See Proakis[6] and Van Trees[7]) defined as a function of delay and Doppler. Figure 2 shows schematically the calculation of the first term in Eq. (25) from the channel scattering function.

The error correlation matrix $\mathbf{R}_{E_G}$ required for the calculation of σ^2_{ϵ} is related to the error correlation matrix $\mathbf{R}_{\epsilon,\epsilon}[1]$ defined in Eq. (25). The matrix is reasonably approximated by a Toeplitz matrix with each element of the ith diagonal of $\mathbf{R}_{E_G}$ equal to the sum of the elements along the ith diagonal of $\mathbf{R}_{\epsilon,\epsilon}[1]$. That is, the terms on the ith diagonal of $\mathbf{R}_{E_G}$ represent the sum of the correlations between the error in estimating all pairs of taps of the channel impulse response

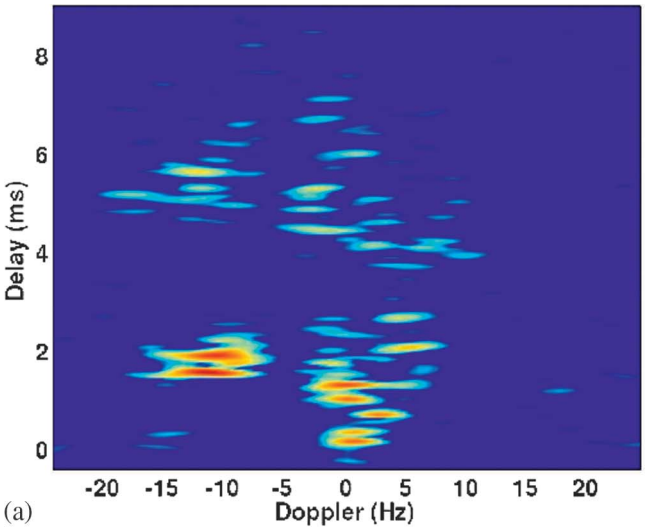

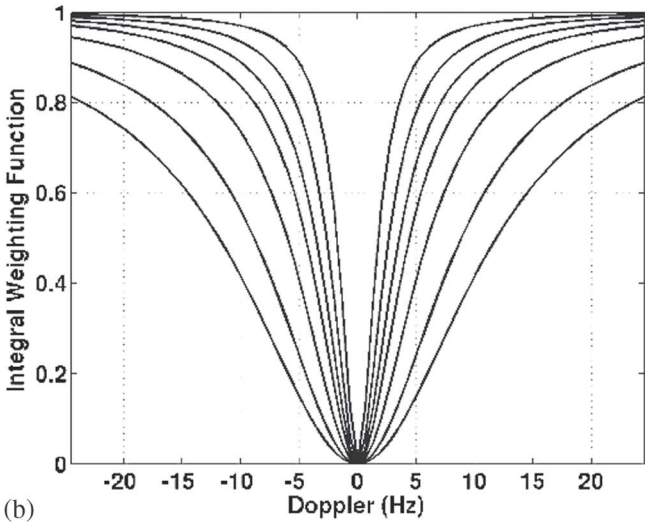

FIG. 2. Graphic representation of the use of a scattering function to predict the lag error [i.e., the first term in Eq. (25)] that is achieved by an exponentially weighted least-squares algorithm used in estimating the time-varying channel impulse response. (a) An estimated scattering function of the channel encountered during the SPACE02 experiment. See Sec. V and Appendix C for descriptions of the experiment and the method used to estimate the scattering function, respectively. This panel is shown in log scale and the range of the color scale is 16 dB. The delay axis is shifted so that a delay of zero corresponds to the peak of the direct path arrival. For each delay tap of the sampled impulse response (the vertical axis on the upper panel), the lag error associated with estimating that tap is a weighted integral across Doppler of the scattering function evaluated at that delay. (b) The weighting function for different values of the exponential weighting factor λ. The bottom curve corresponds to the lowest value of λ (λ=0.9933) with successively higher curves corresponding to successively higher values of λ. The top curve corresponds to a value of λ=0.999. For this figure, a least-squares algorithm update rate of 11.16 kHz is assumed. Note that as λ increases thus increasing the "averaging interval" of the least-squares estimation algorithm, the weighting which determines the contribution of energy at each Doppler frequency to the estimation error increases. Thus, energy at low Doppler frequencies that has an insignificant contribution to the estimation error at low values of λ can make a significant contribution to the estimation error at the highest values of λ.

separated by a delay of i samples. For wide-sense stationary, uncorrelated scattering (WSSUS) channels, $\mathbf{R}_{\epsilon,\epsilon}[1]$ is a diagonal matrix thus resulting in $\mathbf{R}_{E_G}$ equaling the trace of $\mathbf{R}_{\epsilon,\epsilon}[1]$ times the identity matrix. Therefore, evaluation of Eqs. (21)–(23) for this case shows that the excess error for each equalizer equals the trace of $\mathbf{R}_{\epsilon,\epsilon}[1]$ times the magnitude squared of the feedforward filter coefficient vector for each equalizer. Furthermore, for the case of the WSSUS channel the matrix $\mathbf{R}_{E_G}$ can be completely determined from the scattering function of the channel.

This result is independent of the distribution of the channel estimation error among the taps of the channel impulse response vector. While these correlation matrices are not conditioned upon the channel estimate (or equivalently, the calculated feedforward filter weights) as required to properly evaluate Eqs. (21)–(23), they do lend insights into the channel and equalizer characteristics that impact robustness with respect to channel estimation errors. Analysis of data in Sec. VI indicates that in some cases the uncorrelated scattering assumption is sufficiently valid to allow for accurate prediction of the excess error and in other cases the full correlation matrix $\mathbf{R}_{E_G}$ is needed.

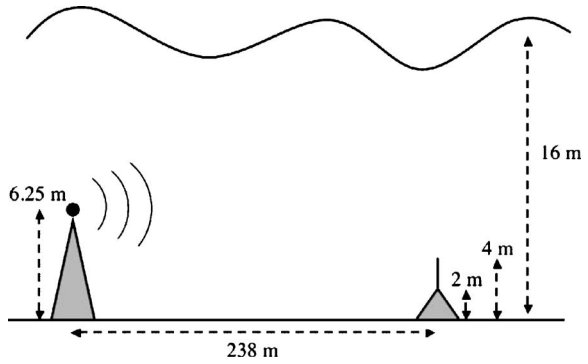

FIG. 3. Side view of the SPACE02 experiment. A source transducer was mounted 6.25 m above the bottom on top of a rigid tripod. The transducer was spherical and had an omni-directional beampattern. A receive hydrophone array was mounted on top of a rigid tripod that was 2 m tall. This vertical, linear array consisted of eight hydrophones with variable spacing and a total aperture of 2.1 m. Data presented in this paper were collected on the center four hydrophones of the array. The spacing between these hydrophones (from bottom to top) was 6.4, 3.7, and 8.4 cm yielding a total aperture of 18.5 cm. The lowermost of the hydrophones was 2.7 m above the bottom. In all cases where results are shown from processing data from just one hydrophone, the hydrophone used is the lowermost of the four. The horizontal range from the transducer to the hydrophone array was 238 m. The bottom was flat in the area of the experiment. The water depth was approximately 16 m during the experiment.

V. THE SPACE02 EXPERIMENT

The experimental data presented in this paper were collected during the Surface Processes and Acoustic Communications Experiment (SPACE02) that took place at the Air Sea Interaction Tower of the Martha's Vineyard Coastal Observatory in the Fall of 2002. A side view of the relevant portion of the experiment and associated physical parameters are shown in Fig. 3. A reference hydrophone was deployed at the same depth as and approximately 1 m from the source transducer to monitor signal transmissions. The sound speed during the experiment was estimated to be approximately 1485 m/s during the time that the data were collected. The signal transmission and data acquisition systems were both driven by a common sampling clock resulting in no clock drift between the two systems. This enabled reliable and precise timing of signal transmissions and receptions. Thus, given

the fact that the source transducer and receive hydrophones were deployed on rigid tripods, all fluctuations or drifts in the received signal relative to the transmitted signal can be attributed to environmental fluctuations.

The transmit and receive signals were sampled at a rate of 44.6428 kHz. Transmit signals were generated with a center frequency of 14 kHz, and were prefiltered to provide an approximately flat system frequency response over a bandwidth of approximately 12 kHz. The signals were transmitted at 56 s intervals with approximately 53.2 s of continuous transmission during each interval. The data presented here are from transmissions of a binary phase shift keyed signal modulated by continuous repetitions of a 4095 point maximum length shift register sequence (m-seq) (see Proakis[6]). The symbol rate of these data was 11160.7 symbols/s. The received signals were modulated to baseband, low pass filtered, and downsampled by a factor of 2 to yield a baseband sample rate of 22.3214 kHz or 2 samples per symbol. This baseband signal was the input to subsequent channel estimation, scattering function estimation, and equalization algorithms.

Data processed here were collected during two different 56 s transmission intervals. The data sets from these two intervals will be referred to as data set 331 and data set 334. The main difference between the two intervals is that significant wave height during the interval corresponding to data set 331 was 0.3 m (very calm conditions) while the significant wave height during the interval corresponding to data set 334 was 3.0 m (very rough conditions). Channel impulse response estimates made using these data are shown in Fig. 4.

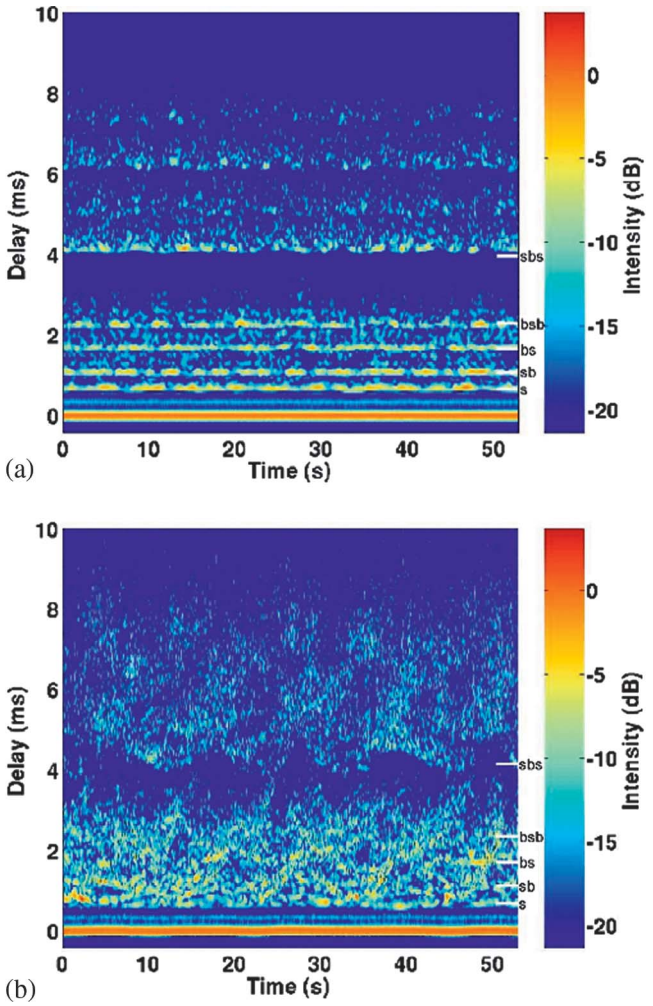

FIG. 4. Intensity of the estimates of the time-varying impulse response of the channel between the transducer and the lowermost of the hydrophones from which data is presented. The estimates were made using exponentially weighted least-squares algorithms. These estimates use data from two different 53.2 s transmission sequences. (a) The estimates made using data collected during a period when the significant wave height was 0.3 m. This is referred to in the paper as data set 331. (b) The estimates made using data collected during a period when the significant wave height was 3.0 m. This is referred to in this paper as data set 334. In (a) and (b), the levels are represented in dB relative to the mean intensity of the direct path arrival during the period. The delay axis has been shifted so that a delay of zero corresponds to the peak of the direct path arrival. The direct and first bottom bounce arrivals make up the thick solid orange line at the bottom of (a) and (b). The white tic marks at the right edge of (a) and (b) represent the predicted arrival time of each successive arrival as labeled on the right-hand side. In order from bottom to top these are the surface, surface/bottom, bottom surface, bottom/surface/bottom, and surface/bottom/surface arrivals. The estimates shown in (a) show a stable arrival pattern and close agreement between predicted and actual arrival times. The estimates in (b) show a highly variable arrival pattern. The arrival time predictions were made assuming two-dimensional propagation in the vertical plane joining the source and receiver and assuming a flat sea surface and bottom. Deviations from this assumption for an arrival due to scattering from a location other than the nominal specular reflection point will almost always result in a greater delay of the arrival (the one exception is the scattering from the trough of a wave at which the sea surface is below the assumed sea surface level). Thus, the predicted arrival times represent the earliest expected arrival time for a particular path. While the estimates in (b) do not line up with the predicted arrival times, the data and the predicted arrival times for the surface and surface/bottom/surface arrivals support this interpretation and represent the earliest arrival times for the single and double surface bounce arrivals, respectively.

VI. EQUALIZER PERFORMANCE ANALYSIS

The data from the SPACE02 experiment was processed using CE-DFE and P-TR equalizers to compare observed and predicted performance. As described previously, the equalizers were run in ''training'' mode. That is, the channel estimation algorithm was given perfect estimates of the transmitted data with which to estimate the channel impulse response. In addition, the data symbols fed back through the feedback filter of the CE-DFE were the true data symbols rather than the estimated data symbols. Note that in channel estimate equalizers, the most up-to-date channel estimate available for calculating filter weights would be the one that could be estimated using data symbols that were demodulated up to that time. This lag between the channel estimate and the data symbols being estimated by the equalizer was enforced in all processing.

In all cases, the length of the impulse response estimate was 175 symbols (350 baseband samples) corresponding to a delay spread of 15.7 ms. The channel estimation algorithm used exponential weighting factors of $\lambda=0.9966$ and $\lambda=0.9933$, respectively, for data sets 331 and 334. The algorithms updated estimates at the symbol rate yielding effective averaging intervals, defined as $1/(1-\lambda)$, of 294 and 149 symbols, respectively. This channel length and these exponential weighting factors offered the best compromise between tracking enough of the channel impulse response to account for the total energy in the received signal and keeping the

estimated channel length small enough to enable tracking of rapid channel fluctuations. The lower value of λ for processing data set 334 was required to enable better tracking of the rapid channel fluctuations. The ability of this trade-off to enable improved overall performance was due in part to the very high signal-to-noise ratio (SNR) of the data set.

The observed SNR was 41 dB. However, the cut off of the estimated impulse response at a delay spread of 15.7 ms resulted in some late arriving energy due to the tail of the channel impulse response appearing as ambient noise from the perspective of the channel estimation and equalization algorithms. When accounting for this energy as part of the ambient noise, the effective SNR dropped to 18.7 dB. In calculating the CE-DFE coefficients, it was assumed that the ambient noise correlation matrix had the form of $\mathbf{R}_v = \sigma_v^2 \mathbf{I}$, where σ_v^2 was based upon either the observed ambient noise level or the observed ambient noise level plus the late arriving energy from the tail of the channel impulse response. These two values are denoted as σ_{va}^2 and σ_{vt}^2, respectively. For the fractionally spaced equalizer used here, the sampled ambient noise is not white because the downsampling filter limits its bandwidth to approximately one half of the full 2π rad/sample of available bandwidth. Thus the model of $\mathbf{R}_v = \sigma_v^2 \mathbf{I}$ is not valid in the MAE expressions. However, at the SNRs observed here, this inaccuracy in the ambient noise model is not expected to significantly affect the results.

The prediction of equalizer performance required estimating both the MAE and the excess error. The excess error calculations required estimates of the error correlation matrix, $\mathbf{R}_{E_G}$. These estimates were made using two different methods. The first was to calculate a running average of the correlation matrix of the residual prediction error of the input signal to the feedforward equalizer. That is

$$\mathbf{e}_{\mathrm{ff}}[n] = \mathbf{u}[n] - \hat{\mathbf{u}}[n] = \mathbf{u}[n] - \hat{\mathbf{G}}[n]\mathbf{d}[n]. \tag{27}$$

This can be rewritten as

$$\mathbf{e}_{\mathrm{ff}} = \mathbf{E}_G \mathbf{d}[n] + \mathbf{v}[n]. \tag{28}$$

Assuming that the observation noise is independent of the channel estimation error and the transmitted data symbol and that $d[n]$ is a white, unit variance data sequence yields

$$\mathbf{R}_{\mathbf{e}_{\mathrm{ff}}} = \mathbf{R}_{E_G} + \mathbf{R}_v . \tag{29}$$

Thus, subtracting the assumed $\mathbf{R}_v$ from the estimated $\mathbf{R}_{\mathbf{e}_{\mathrm{ff}}}$ yields an estimate of $\mathbf{R}_{E_G}$. Results generated using this method are shown in Sec. VI A.

The second method of estimating $\mathbf{R}_{E_G}$ was to estimate the channel scattering function as described in Appendix C. The scattering function estimates were used to calculate the diagonal elements of $\mathbf{R}_{\epsilon,\epsilon}[1]$ using Eq. (25). The estimate of $\mathbf{R}_{E_G}$ then equals the trace of this matrix times the identity matrix. Recall that this method assumes that the channel fluctuations are well modeled as a WSSUS process and the off-diagonal elements of $\mathbf{R}_{\epsilon,\epsilon}[1]$ therefore equal zero. Results generated using this method are shown in Sec. VI B.

The presentation of the experimental data here serves several purposes. The results in Sec. VI A provide experimental verification of the error expressions derived in Sec. III and quantify the relative contributions of MAE and excess error to the soft decision error for the conditions encountered. They also offer some insight into the factors that limit equalizer performance which motivates the modification of the CE-DFE presented in Sec. VII. The results in Sec. VI B verify the applicability of Eq. (25) to predicting channel estimation error and is a further step in the development of quantitative expressions for predicting the performance of equalizers given knowledge of environmental conditions. Finally, the results generated using the CE-DFE and P-TR equalizers are compared which quantifies the improvement realized by the MMSE filter coefficient optimization and DFE structure of the CE-DFE when operating with only a small hydrophone array aperture as is the case here.

A. CE-DFE performance prediction from the residual prediction error correlation matrix ($\mathbf{R}_{\mathbf{e}_{\mathrm{ff}}}$)

Figure 5 shows the predicted and observed estimation errors when processing data set 334 with a one channel CE-DFE. There is close agreement between the observed and predicted soft decision error. For this figure, the assumed noise level was σ_{vt}^2. These data show a rough balance between the MAE and excess error. For comparison, the data were also processed with an equalizer that assumed a noise level of σ_{va}^2. The result of this processing showed a 3 dB increase in excess error but a 2.5 dB drop in MAE. Had the channel fluctuations been slower allowing for the estimation of a larger portion of the channel impulse response, this MAE figure would more accurately represent the true MAE for the equalizer. Thus, in this case, the performance of the equalizer is dominated by the excess error, that is the ability to track the channel.

A striking feature of the data in Fig. 5 is the periodic structure of the fluctuations in the error. The minimum soft decision error in each period is between -5 and -6 dB. By comparison, the processing of data set 331 (data collected during relatively calm conditions) yielded a soft decision error of -6.1 dB. This indicates that even in periods of rough surface conditions, the channel cycles periodically between conditions of a high rate of fluctuation and low rate of fluctuation. The time scale of this cyclic behavior matches that of the dominant surface waves measured during this time interval. In addition, the conditions during a low rate of channel fluctuations are close to as good as those encountered during calm surface conditions. This conclusion is further supported by the analysis in Sec. VI B.

Figure 6 shows comparable data for a four channel CE-DFE processing data set 334. Again, there is close agreement between the observed and predicted soft decision error. In this case, the error is dominated by the excess error. A feature of the data present in Fig. 6 and to a certain extent in Fig. 5 is that the periodic nature of the soft decision error is due primarily to fluctuations in the excess error and not the MAE. In fact, the MAE is relatively constant indicating that the MAE is somewhat insensitive to the particular realization of the channel encountered. Figure 7 shows the bit error rates achieved by the one and four channel equalizers.

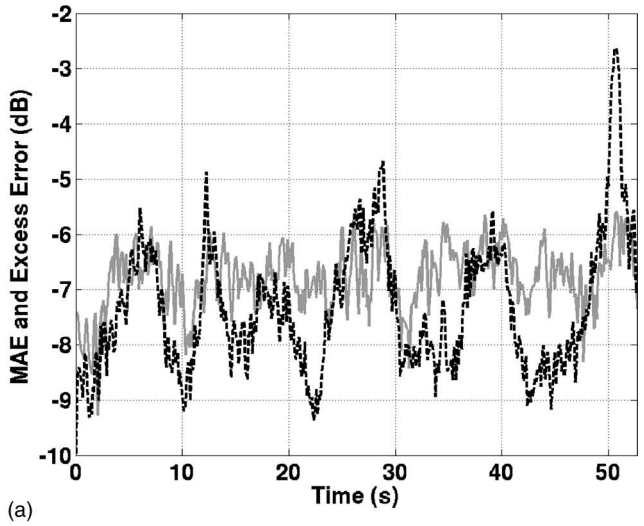

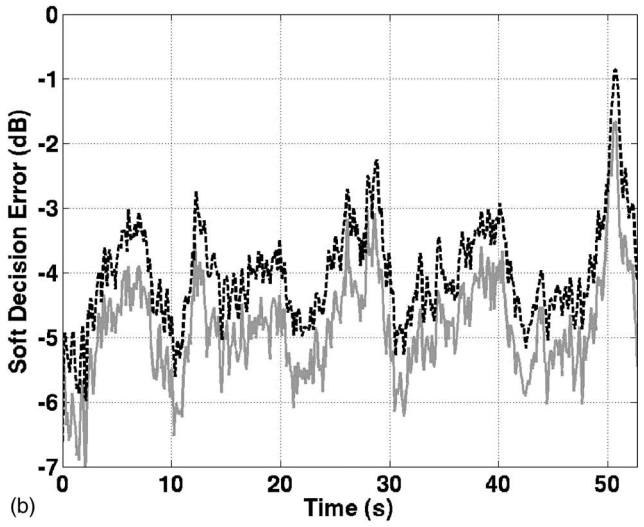

FIG. 5. The predicted and measured data estimation errors are shown for a one channel CE-DFE processing data set 334. All errors are shown in dB relative to the data symbol variance of $\sigma_d^2=1$. (a) The predicted MAE (solid gray line) and excess error (dashed black line). The excess error was calculated using a running average of the full autocorrelation matrix of the feedforward filter residual prediction error. The average used an exponential weighting with an exponential weighting factor of $\lambda=0.999$. Note that the levels of the two different errors are commensurate with the excess error exceeding the MAE during times of rapid channel fluctuations and the reverse being the case at times with no rapid channel fluctuations. (b) The predicted (dashed black line) and observed (solid gray line) soft decision errors. The predicted error shown here is the sum of the predicted MAE and excess error shown in (a). Note the periodic nature of the equalizer soft decision error performance. The data in (a) indicate that the primary source of the periodic variability is the excess error. In addition, the periodicity is in line with the dominant surface wave period of 8.5 s that was measured during the time that these data were collected. Note that the predicted soft decision error consistently exceeds the observed error by up to 1 dB.

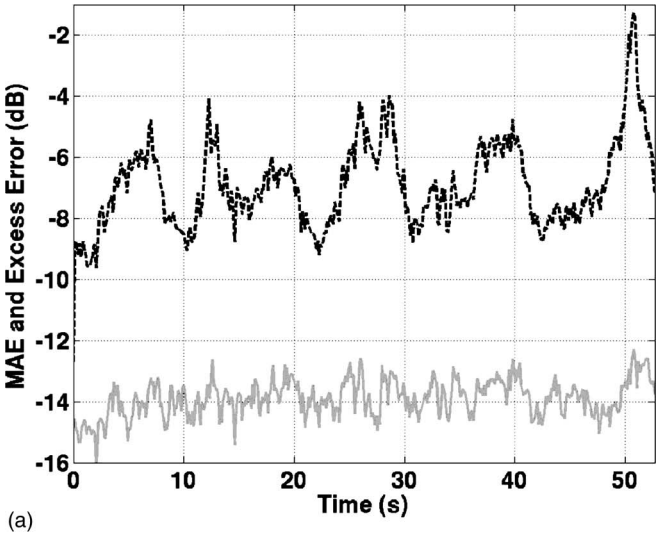

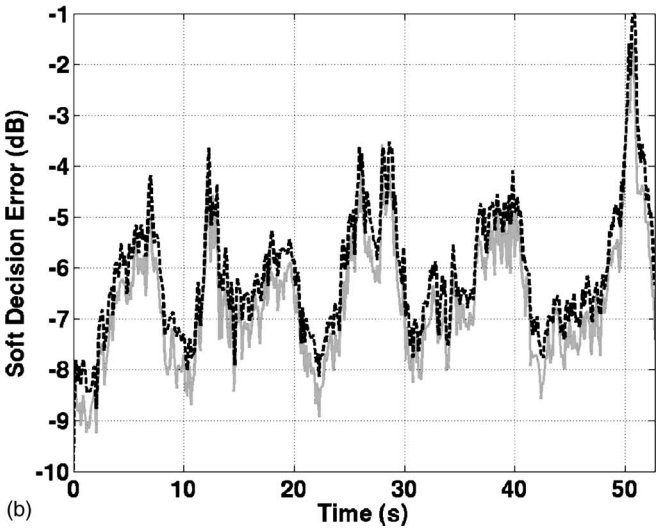

FIG. 6. The predicted and measured data estimation errors are shown for the four channel CE-DFE processing data set 334. All errors are shown in dB relative to the data symbol variance of $\sigma_d^2=1$. (a) The predicted MAE (solid gray line) and excess error (dashed black line). The excess error was calculated using a running average of the full autocorrelation matrix of the feedforward filter residual prediction error. The average used an exponential weighting with an exponential weighting factor of $\lambda=0.999$. Note that the excess error is slightly greater than that shown in Fig. 5(a) for the one channel CE-DFE while the MAE is significantly less than the MAE for the one channel CE-DFE. The limiting factor in this four channel case is the excess error due to a combination of channel estimation errors and a lack of robustness with respect to such errors rather than the MAE which reflects the static channel structure and the ambient noise. (b) The predicted (dashed black line) and observed (solid gray line) soft decision errors. The predicted error shown here is the sum of the predicted MAE and excess error shown in (a). The data here exhibit the same periodicity as that exhibited by the data shown in Fig. 5.

B. Performance prediction using channel scattering functions and the influence of surface scattering

While the use of the observed residual prediction error correlation matrix to predict equalizer performance is effective for understanding the factors limiting performance in a postexperiment data analysis scenario, it is less valuable for the purposes of predicting system performance ahead of time. The capability to predict communications system performance ahead of time based upon assumed or measured environmental conditions is highly desirable for future work on system trade-off studies or the configuration of communications networks. A step in this direction is to be able to predict performance based upon the channel scattering function. The channel scattering function is sufficient to calculate the diagonal elements of the channel estimation error correlation matrix, $\mathbf{R}_{E_G}$. In some cases, these diagonal elements are adequate to yield accurate predictions of equalizer per-

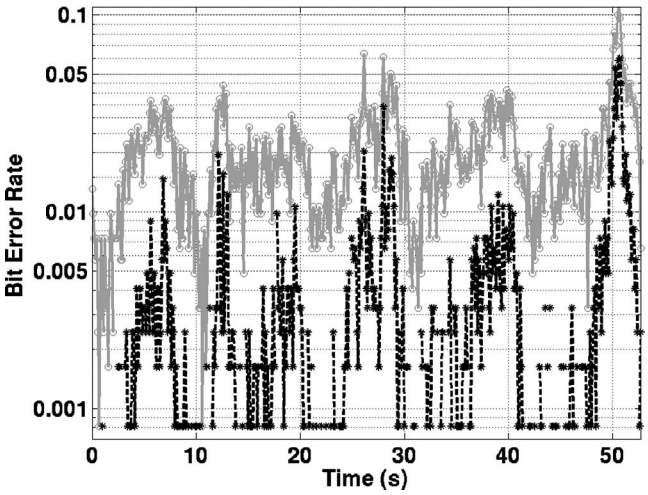

FIG. 7. Bit error rate for the processing of the data set 334 by the one (solid gray line with circles) and four (dashed black line with asterisks) channel CE-DFEs. These bit error rates were calculated over 1230 symbol intervals corresponding to a time interval of 0.1102 s. Thus, the minimum error rate shown is 0.000 81, which corresponds to one demodulation error in a single averaging block. Points in time where successive marks (asterisks for the four channel data) are not connected by lines indicate periods where there were no demodulation errors in a block. The data for both equalizers show periodic increases in bit error rate corresponding to the increases in soft decision error shown in Figs. 5 and 6.

formance. In these cases, a predicted channel scattering function based upon acoustic propagation and scattering models would be the input to the prediction process. In the cases where the diagonal elements of $\mathbf{R}_{E_G}$ are not sufficient to yield accurate performance predictions, additional work needs to be done.

Figure 8 shows the predicted and observed channel and data estimation errors for a one channel CE-DFE processing data set 334 with an estimated noise level of σ_{vt}^2. The predictions in these cases were made using estimates of the channel scattering function and show close agreement with the observed errors. In other cases the agreement was not close. When processing data set 334 with a one channel CE-DFE using an estimated noise level of σ_{va}^2, the predictions of the excess error were 11–16 dB above the values shown in Fig. 5. This resulted in an overprediction of the soft decision error by up to 15 dB. In the case of the four channel CE-DFE processing data set 334, the excess error predictions made using only the diagonal elements of $\mathbf{R}_{E_G}$ resulted in a lower excess error than shown in Fig. 6 and an underprediction of the soft decision error by approximately 2 dB. Thus, additional work needs to be done with respect to predicting the channel estimation error correlation matrix $\mathbf{R}_{E_G}$ from a priori information.

The channel scattering function approach is also useful for determining which channel fluctuations most significantly contribute to the degradation of performance by the equalizers. Figure 9 shows a prediction of the estimation error for each tap of the channel impulse response as a function of time in data set 334. These channel estimation errors are the cause of the degradation of equalizer performance. The data clearly show a periodic structure to the increase in channel estimation errors that results in an increased excess error, soft decision error, and bit error rate in Figs. 5–8. The errors are largest for the single surface bounce paths reflecting higher energy levels of these arrivals and/or a higher rate of fluctuation for these arrivals.

The errors for the single surface bounce paths are also highly localized in delay and time indicating their dependence on conditions in a fairly localized scattering region of the ocean surface. The single surface bounce path errors in the period of high error in the interval of 25–30 s also show a pattern that is characteristic of the surface wave focusing phenomenon reported in Preisig *et al.*[11] Interestingly, the increase in excess error during this period shown in Figs. 5 and 6 shows a distinctive double hump that may be a result of this surface wave focusing.

Comparing the high error region around a time of 50 s in Fig. 9 with the expanded view of the channel impulse estimates shown in Fig. 10 confirms that this region corresponds to a high intensity arrival with a rapidly increasing delay. This analysis indicates that a potential area for the improvement of future channel estimate based equalizers is the improvement of techniques for tracking these rapidly moving impulse response arrivals. While the improvement of the ability to estimate the channel impulse response is one approach to improving equalizer performance, another approach is to improve the robustness of these equalizers with respect to channel estimation errors. Such an approach is presented in Sec. VII.

C. Comparison of adaptive channel estimate decision feedback and passive time reversal equalizers

A passive time reversal equalizer was used to process data set 334 using both one and four channels of data. In both cases, the performance of the equalizer is dominated by the MAE. For the one channel case, the MAE was 4.14 dB resulting in a soft decision error of 4.24 dB and a bit error rate of 0.2. For the four channel processing, the MAE was 2.54 dB, the soft decision error was 2.58 dB, and the bit error rate was 0.17. The predicted and observed soft decision errors in both cases showed excellent agreement.

The error of the P-TR equalizer in this case is completely dominated by the MAE despite the observed large errors in estimating the channel impulse response showing in Fig. 8(a). This result is not surprising since the passive time reversal equalizer relies on near orthogonality of the replica vector for the data symbol to be estimated ($\mathbf{g}_o$) and the remaining columns of the channel impulse response matrix ($\mathbf{G}$) in order to achieve interference cancellation. This orthogonality is difficult to achieve with no spatial aperture (the one channel case) or the 18.7 cm aperture available in the four channel case. However, the results shown in Flynn *et al.*[3] indicate that the performance of passive time reversal systems improves substantially as a significantly wider aperture and more channels of data are available.

VII. ROBUST DECISION FEEDBACK EQUALIZATION USING RESIDUAL PREDICTION ERRORS

The results in Sec. VI show that the excess error resulting from channel estimation errors and the sensitivity of a

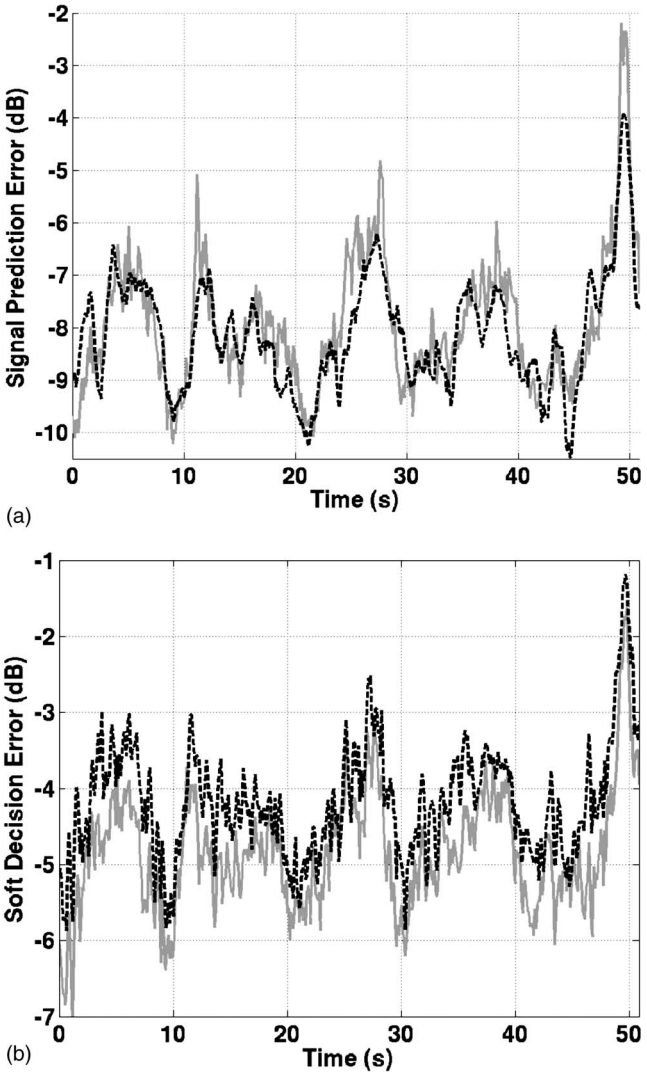

FIG. 8. Comparison of predicted and observed estimation errors for the channel estimation algorithm and the one channel CE-DFE processing data set 334. (a) The predicted (dashed black line) and observed (solid gray line) received signal residual prediction error achieved by the exponentially weighted least-squares algorithm used to estimate that time-varying channel impulse response as shown in Fig. 1. The errors are shown in dB relative to the mean received signal level over the data set. The channel estimate was updated at the symbol rate of 11 161 symbols/s and the exponential weighting factor was $\lambda=0.9933$. The prediction of the residual prediction error is calculated using Eq. (25) and equals the trace of the calculated error correlation matrix. Note that in the periods of slow channel fluctuations when the error is low, the predicted error closely matches the observed error. However, the predicted error is significantly below the observed error in times of rapid channel fluctuations. It is believed that this is due to the inability to accurately estimate the channel scattering function during times when the channel is not only changing rapidly but the channel scattering function is changing rapidly as well. Such a situation has been shown to exist in some situations where signals are scattered off of surface gravity waves (Preisig *et al.*.[11]). The analysis shown in Figs. 9 and 10 indicates that it may exist here as well. (b) The predicted (dashed black line) and observed (solid gray line) soft decision error achieved by the CE-DFE processing data set 334. All errors are shown in dB relative to the data symbol variance of $\sigma_d^2=1$. While the predicted and observed errors show close agreement, the predicted error is based upon an underprediction of channel estimation error as evidenced by the data shown in (a). This indicates that the prediction of soft decision error itself overestimates the error as discussed in the text and is consistent with the data shown in Fig. 5(b).

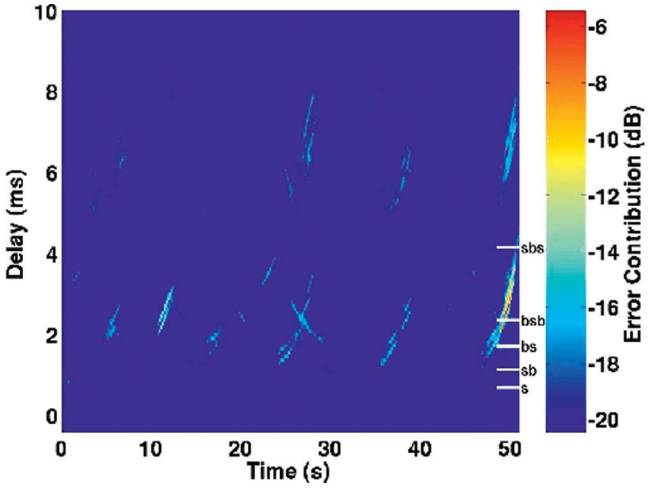

FIG. 9. The predicted estimation error for each tap of the time-varying channel impulse response for the time period corresponding to data set 334. The errors are shown in dB relative to the mean intensity of the direct path arrival. The delay axis has been shifted in the same manner as Figs. 4 and 10 so that a delay of zero corresponds to the peak of the direct path arrival. These predicted errors are calculated based on estimates of the channel scattering function as was the case for the data shown in Fig. 8(a). The white tic marks on the right axis correspond to modeled arrival times for successive propagation paths as described in the caption of Fig. 4. The data clearly show the periodic nature of the increase in channel estimation errors. In addition, the data show moderate coincidence between the time at which the single surface bounce arrivals (the first four arrivals) show high errors and the periods of time at which later arrivals show high error. The most intense sources of error are the single surface bounce arrivals. The coherent steep diagonal structure in the time/delay plane of these errors indicates that they are caused by a single scattered path with a scattering point that is moving rapidly in space resulting in a rapid rate of change of the propagation path length.

traditional CE-DFE to those errors is a major contributor to the overall soft decision error. Thus, a significant performance improvement can be expected by improving the robustness of the CE-DFE with respect to channel estimation

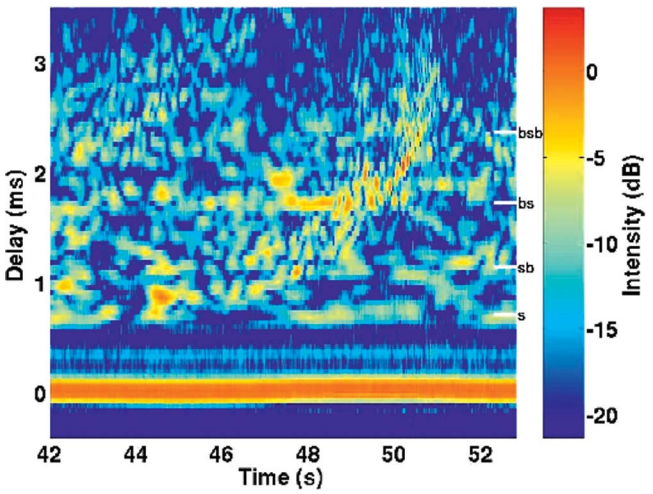

FIG. 10. An expanded view of the intensity of the channel estimates for data set 334 shown in Fig. 4(b). Note the rapid increase in delay of the arrival between the bottom/surface and bottom/surface/bottom marks at around the time of 50 s. The time and delay of this arrival corresponds to the largest source of channel estimation error shown in Fig. 9 and supports the conclusion that the surface scattered arrivals with rapid rates of change of their propagation path lengths comprise a large source of channel estimation error in the data shown here.

errors. The work presented in Stojanovic *et al.*[4] showed that the MMSE CE-DFE equalizer given knowledge of the statistics of the channel estimation errors is one that calculates the filter weights by accounting for these estimation errors in an assumed noise correlation matrix. However, the estimation of the statistics of the channel estimation errors was not addressed.

The residual prediction error of the input signal to the feedforward filter defined in Eq. (27) can be calculated directly by the equalizer and used to estimate the required assumed noise correlation matrix. The equalizer using this approach is referred to here at the residual prediction error DFE (RPE-DFE). The data presented here indicate that this is an effective way of implementing the robust CE-DFE derived in Stojanovic *et al.*[4] and results in a significant performance improvement.

The sample effective noise correlation matrix is this example was calculated as

$$\hat{\mathbf{R}}_{\mathbf{e}_{\mathrm{ff}}}[n]=\sum_{m=0}^{n}\lambda_e^{n-m}\mathbf{e}_{\mathrm{ff}}[m]\mathbf{e}_{\mathrm{ff}}^{h}[m] \tag{30}$$

with an exponential weighting factor of $\lambda_e=0.999$. This effective noise correlation matrix was used in the place of $\mathbf{R}_v$ to estimate the matrix $\mathbf{Q}$ in Eq. (9). The resulting $\mathbf{Q}$ was used in Eq. (10) to calculate the RPE-DFE filter coefficients.

Figure 11 shows the soft decision error and bit error rates achieved by one and four channel RPE-DFEs processing data set 334. The results show the approach improves the robustness of the equalizer but does not completely eliminate the sensitivity to channel estimation errors. A computationally simpler approach was also tried in which $\hat{\mathbf{R}}_{\mathbf{e}_{\mathrm{ff}}}[n]$ was assumed to be the identity matrix times the mean value of the diagonal elements of $\hat{\mathbf{R}}_{\mathbf{e}_{\mathrm{ff}}}[n]$ as defined in Eq. (30). This approach yielded some performance improvement but not nearly as much as that indicated by the data in Fig. 11. This indicates that it is important to properly account for not only the level of the residual prediction error but also the eigenstructure of the residual prediction error correlation matrix.

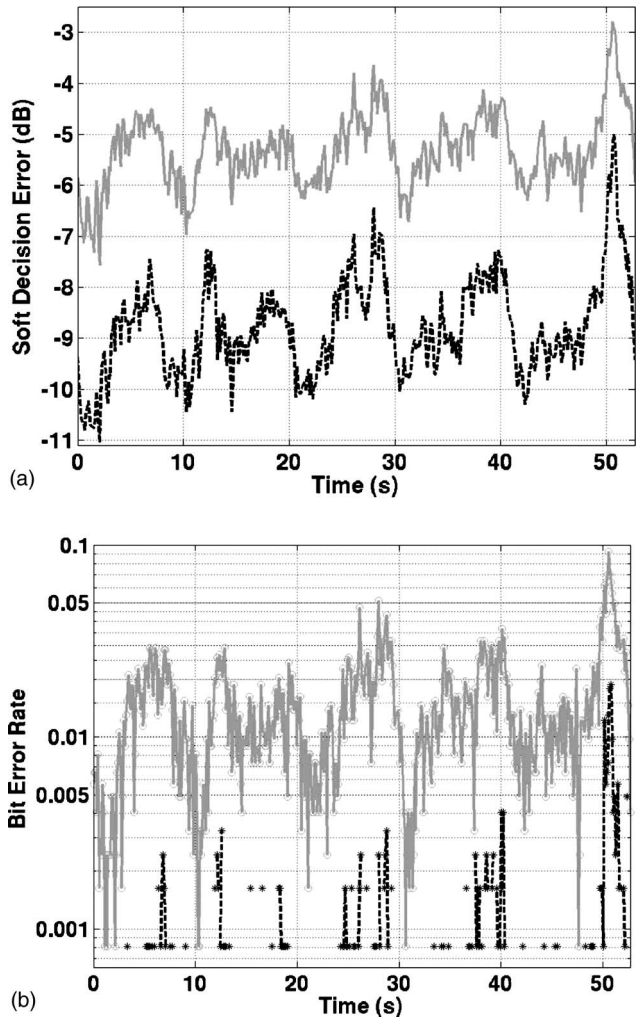

FIG. 11. Estimation error performance with RPE-DFEs processing of data set 334. (a) The soft decision error for the one (solid gray line) and four (dashed black line) channel RPE-DFEs. (b) The bit error rate for the processing achieved the one (solid gray line with circles) and four (dashed black line with asterisks) channel RPE-DFEs. These bit error rates were calculated over 1230 symbol intervals corresponding to a time interval of 0.1102 s. Thus, the minimum error rate shown is 0.000 81, which corresponds to one demodulation error in a single averaging block. Points in time where successive marks (circles for the one channel data, asterisks for the four channel data) are not connected by lines indicate periods where there were no demodulation errors in a block. Note the improvement in performance with respect to the data presented for the standard CE-DFEs in Figs. 5 and 6. This performance improvement is particularly strong in the times when the channel estimation error is poor. This confirms the improvement in equalizer robustness with respect to channel estimation errors afforded by the residual prediction error approach.

VIII. CONCLUSIONS

Expressions for predicting the minimal achievable error and excess error of channel estimated based linear and decision feedback equalizers have been derived and analyzed. The analysis of experimental data verifies that the expressions can accurately predict equalizer performance when the second-order statistics of the errors in the channel impulse response estimates are known. The data also show that the excess error was always a significant contributor to the soft decision error when rough sea surface conditions prevailed. This motivates the use of residual prediction errors to estimate an effective noise correlation matrix that results in an improved robustness of the CE-DFE to channel estimation errors. The expressions for the minimal achievable error allow its interpretation in terms of the projection of the replica vector for the data symbol being estimated onto the replica vectors for the interfering data symbols. This lends insight into the very poor minimal achievable error exhibited by the P-TR equalizer compared to that exhibited by the CE-DFE when using data from a small array aperture.

An expression relating the channel estimation error for an exponentially weighted least-squares algorithm to the spectral correlation matrix of the channel impulse response is presented. For the case of WSSUS channels, this allows for the prediction of equalizer performance based upon the statistics of the fluctuations of the channel impulse response in the form of the channel scattering function. This is an important step toward the eventual goal of quantitatively predicting equalizer performance based upon predictions or observations of environmental conditions. The analysis of data

from the SPACE02 experiment collected during rough weather conditions shows that the equalizer performance characterized by both the excess error and the soft decision error is periodic with the period related to the wave period. Surprisingly, the equalizer performance during the best times of each period is almost as good as the performance achieved when processing data collected during calm weather conditions. If this feature proves to hold for a broad range of shallow water environments, it may be exploitable to improve the overall data throughput of underwater acoustic communications systems.

Finally, the scattering function analysis approach shows the distribution of channel estimation errors as a function of delay in the channel impulse response. The analysis shows a well-defined structure in delay and time. This structure indicates that the primary contributor to the error is the rate of change of the propagation path length for well-defined single surface bounce arrivals. This motivates future work on improving the ability of channel estimation algorithms to track or estimate these arrivals.

ACKNOWLEDGMENTS

This work has been supported by ONR Grant Nos. N00014-00-1-0048 and N00014-02-C-0201. This paper is WHOI Contribution No. 11281.

APPENDIX A: DERIVATION OF EQUALIZER COEFFICIENT AND MAE EXPRESSIONS

The derivation of the equalizer coefficients assumes that the estimates of the channel impulse response are accurate (e.g., $\mathbf{G}=\hat{\mathbf{G}}$) and that past symbol decisions are accurate (e.g., $\mathbf{d}_{\mathrm{fb}}[n]=\hat{\mathbf{d}}_{\mathrm{fb}}[n]$). Therefore, the caret is dropped off of the estimates of these quantities throughout this derivation. Starting with the CE-DFE, let

$$\mathbf{z}[n]=\begin{bmatrix}\mathbf{u}[n]\\ \mathbf{d}_{\mathrm{fb}}[n]\end{bmatrix}, \tag{A1}$$

and

$$\mathbf{h}=\begin{bmatrix}\mathbf{h}_{\mathrm{ff}}\\ \mathbf{h}_{\mathrm{fb}}\end{bmatrix}.$$

Then, from Eq. (5)

$$\hat{d}_s[n]=\mathbf{h}^h\mathbf{z}[n].$$

The equalizer coefficients are the solution to

$$\mathbf{h}_{\mathrm{opt}}=\arg\min_{\mathbf{h}} E[|\mathbf{h}^h\mathbf{z}[n]-d[n]|^2|\mathbf{G}],$$

where the expectation is shown as being conditioned on $\mathbf{G}$. It is straightforward to show that

$$\mathbf{h}_{\mathrm{opt}}=\mathbf{R}_{z,z}^{-1}\mathbf{r}_{z,d}, \tag{A2}$$

and

$$\sigma^2_{o_{\mathrm{DFE}}}=\sigma_d^2-\mathbf{r}_{z,d}^h\mathbf{R}_{z,z}^{-1}\mathbf{r}_{z,d}, \tag{A3}$$

where $\mathbf{R}_{z,z}=\mathrm{E}[\mathbf{z}[n]\mathbf{z}^h[n]|\mathbf{G}]$ and $\mathbf{r}_{z,d}=\mathrm{E}[\mathbf{z}[n]d^*[n]|\mathbf{G}]$. Recall that $d[n]$ is a unit variance and white sequence and is independent of $v[n]$. Then, substituting Eq. (8) into Eq. (A1) and using the result to evaluate these expectations yields

$$\mathbf{r}_{z,d}=\begin{bmatrix}\mathbf{g}_0\\ \mathbf{0}_{L_{\mathrm{fb}}\times 1}\end{bmatrix}, \tag{A4}$$

and

$$\mathbf{R}_{z,z}=\begin{bmatrix}(\mathbf{g}_0\mathbf{g}_0^h+\mathbf{Q}+\mathbf{G}_{\mathrm{fb}}\mathbf{G}_{\mathrm{fb}}^h) & \mathbf{G}_{\mathrm{fb}}\\ \mathbf{G}_{\mathrm{fb}}^h & \mathbf{I}\end{bmatrix}, \tag{A5}$$

where $\mathbf{Q}$ is as defined in Eq. (9). Partition $\mathbf{R}_{z,z}^{-1}$ as follows:

$$\mathbf{R}_{z,z}^{-1}=\begin{bmatrix}\tilde{\mathbf{A}} & \tilde{\mathbf{D}}\\ \tilde{\mathbf{C}} & \tilde{\mathbf{B}}\end{bmatrix},$$

where $\tilde{\mathbf{A}}$ and $\tilde{\mathbf{B}}$ are square matrices with sizes L_a+L_c and L_{fb}, respectively. $\tilde{\mathbf{C}}$ and $\tilde{\mathbf{D}}$ are appropriately sized rectangular matrices. Then, $\mathbf{h}_{\mathrm{ff}}=\tilde{\mathbf{A}}\mathbf{g}_0$, $\mathbf{h}_{\mathrm{fb}}=\tilde{\mathbf{C}}\mathbf{g}_0$, and $\sigma^2_{o_{\mathrm{DFE}}}=1-\mathbf{g}_0^h\tilde{\mathbf{A}}\mathbf{g}_0$. It can be shown that

$$\tilde{\mathbf{A}}=(\mathbf{Q}+\mathbf{g}_0\mathbf{g}_0^h)^{-1}=\mathbf{Q}^{-1}-\frac{\mathbf{Q}^{-1}\mathbf{g}_0\mathbf{g}_0^h\mathbf{Q}^{-1}}{1+\mathbf{g}_0^h\mathbf{Q}^{-1}\mathbf{g}_0}, \tag{A6}$$

and

$$\tilde{\mathbf{C}}=-\mathbf{G}_{\mathrm{fb}}^h\tilde{\mathbf{A}}. \tag{A7}$$

The first equality in Eq. (A6) and the equality in Eq. (A7) follow from the application of the matrix inversion identity for partitioned matrices (Kailath[12]). The second equality in Eq. (A6) follows from the well-known identity for the inverse of a rank one update to a matrix. Using Eqs. (A6) and (A7) to evaluate the expressions for the CE-DFE filter coefficients and MAE yields

$$\mathbf{h}_{\mathrm{ff}}=\tilde{\mathbf{A}}\mathbf{g}_0=\frac{\mathbf{Q}^{-1}\mathbf{g}_0}{1+\mathbf{g}_0^h\mathbf{Q}^{-1}\mathbf{g}_0},$$

$$\mathbf{h}_{\mathrm{fb}}=\tilde{\mathbf{C}}\mathbf{g}_0=-\mathbf{G}_{\mathrm{fb}}^h\mathbf{h}_{\mathrm{ff}},$$

and

$$\sigma^2_{o_{\mathrm{DFE}}}=\frac{1}{1+\mathbf{g}_0^h\mathbf{Q}^{-1}\mathbf{g}_0}.$$

The derivation of similar expressions for the MMSE Linear equalizer starts with $\mathbf{z}[n]=\mathbf{u}[n]$ and $\mathbf{h}=\mathbf{h}_{\mathrm{lin}}$,

$$\mathbf{h}_{\mathrm{opt}}=\mathbf{h}_{\mathrm{lin}}=\mathbf{R}_{z,z}^{-1}\mathbf{r}_{z,d}, \tag{A8}$$

and

$$\sigma^2_{o_{\mathrm{lin}}}=\sigma_d^2-\mathbf{r}_{z,d}^h\mathbf{R}_{z,z}^{-1}\mathbf{r}_{z,d}. \tag{A9}$$

Then,

$$\mathbf{r}_{z,d}=\mathbf{g}_0, \tag{A10}$$

and

$$\mathbf{R}_{z,z}=\mathbf{g}_0\mathbf{g}_0^h+\mathbf{Q}+\mathbf{G}_{\mathrm{fb}}\mathbf{G}_{\mathrm{fb}}^h.$$

Evaluating $\mathbf{R}_{z,z}^{-1}$ yields

$$\mathbf{R}_{z,z}^{-1} = (\mathbf{Q}+\mathbf{G}_{\mathrm{fb}}\mathbf{G}_{\mathrm{fb}}^{h})^{-1} - \frac{(\mathbf{Q}+\mathbf{G}_{\mathrm{fb}}\mathbf{G}_{\mathrm{fb}}^{h})^{-1}\mathbf{g}_0\mathbf{g}_0^{h}(\mathbf{Q}+\mathbf{G}_{\mathrm{fb}}\mathbf{G}_{\mathrm{fb}}^{h})^{-1}}{1+\mathbf{g}_0^{h}(\mathbf{Q}+\mathbf{G}_{\mathrm{fb}}\mathbf{G}_{\mathrm{fb}}^{h})^{-1}\mathbf{g}_0}. \quad \text{(A11)}$$

Substituting Eqs. (A10) and (A11) into Eqs. (A8) and (A9) gives

$$\mathbf{h}_{\mathrm{lin}} = \frac{(\mathbf{Q}+\mathbf{G}_{\mathrm{fb}}\mathbf{G}_{\mathrm{fb}}^{h})^{-1}\mathbf{g}_0}{1+\mathbf{g}_0^{h}(\mathbf{Q}+\mathbf{G}_{\mathrm{fb}}\mathbf{G}_{\mathrm{fb}}^{h})^{-1}\mathbf{g}_0},$$

and

$$\sigma_{o_{\mathrm{lin}}}^{2} = \frac{1}{1+\mathbf{g}_0^{h}(\mathbf{Q}+\mathbf{G}_{\mathrm{fb}}\mathbf{G}_{\mathrm{fb}}^{h})^{-1}\mathbf{g}_0}.$$

For the passive time-reversal equalizer, the filter coefficients are the matched filter normalized so that $\mathbf{h}_{\mathrm{tr}}\mathbf{g}_0 = 1$. Therefore $\mathbf{h}_{\mathrm{tr}} = \mathbf{g}_0/\mathbf{g}_0^{h}\mathbf{g}_0$. This yields a soft decision of

$$\hat{d}_s[n] = \mathbf{h}_{\mathrm{tr}}^{h}\mathbf{u}[n] = d[n] + \frac{\mathbf{g}_0}{\mathbf{g}_0^{h}\mathbf{g}_0}(\mathbf{G}_{\mathrm{fb}}\mathbf{d}_{\mathrm{fb}}[n] + (\mathbf{v}[n] + \mathbf{G}_o\mathbf{d}_o[n])),$$

and a soft decision error of

$$\hat{d}_s[n] - d[n] = \frac{\mathbf{g}_0}{\mathbf{g}_0^{h}\mathbf{g}_0}(\mathbf{G}_{\mathrm{fb}}\mathbf{d}_{\mathrm{fb}}[n] + (\mathbf{v}[n] + \mathbf{G}_o\mathbf{d}_o[n])).$$

Evaluating the expectation of the magnitude squared of this soft decision error yields

$$\sigma_{o_{\mathrm{tr}}}^{2} = \frac{\mathbf{g}_0^{h}(\mathbf{Q}+\mathbf{G}_{\mathrm{fb}}\mathbf{G}_{\mathrm{fb}}^{h})\mathbf{g}_0}{(\mathbf{g}_0^{h}\mathbf{g}_0)^{2}}.$$

APPENDIX B: DERIVATION OF EQ. (25)

The time-varying channel impulse response, $\tilde{\mathbf{g}}^{h}[n]$, is modeled as a zero-mean, wide-sense stationary vector random process with a correlation function

$$\mathbf{R}_{\tilde{g},\tilde{g}}[m] \triangleq \mathrm{E}[\tilde{\mathbf{g}}[n]\tilde{\mathbf{g}}^{h}[n+m]].$$

The vector $\tilde{\mathbf{g}}[n]$ has dimension $N_o \times 1$.

The system identification problem is to estimate $\tilde{\mathbf{g}}[n]$ from observations $u[n]$ where

$$u[n] = \tilde{\mathbf{g}}^{h}[n]\mathbf{d}[n] + v[n]. \quad \text{(B1)}$$

$\mathbf{d}[n]$ is a known zero-mean, white vector time series with $E[\mathbf{d}[n]\mathbf{d}^{h}[n]] = \mathbf{R}_{d,d}$ and is independent of $\tilde{\mathbf{g}}[m]$ for all m and n. $v[n]$ is zero-mean, white observation noise with a variance σ_v^2. $v[n]$ is independent of both $\mathbf{d}[m]$ and $\tilde{\mathbf{g}}[m]$ for all m and n. The estimate is computed as the solution to Eq. (24).

One form of the recursive least-squares solution to Eq. (24) denoted by $\hat{\tilde{\mathbf{g}}}[n]$ is (Haykin[13])

$$\hat{\tilde{\mathbf{g}}}[n] = \hat{\tilde{\mathbf{g}}}[n-1] + \hat{\mathbf{R}}_{d,d}^{-1}[n]\mathbf{d}[n](u[n] - \hat{u}[n])^{*}, \quad \text{(B2)}$$

where

$$\hat{u}[n] = \hat{\tilde{\mathbf{g}}}^{h}[n-1]\mathbf{d}[n], \quad \text{(B3)}$$

and $\hat{\mathbf{R}}_{d,d}[n] = \Sigma_{m=0}^{n}\lambda^{(n-m)}\mathbf{d}[m]\mathbf{d}^{h}[m]$. The quantity of interest is the M-step state prediction error,

$$\boldsymbol{\epsilon}[n+M|n] \triangleq \hat{\tilde{\mathbf{g}}}[n] - \tilde{\mathbf{g}}[n+M], \quad \text{(B4)}$$

and its error correlation matrix

$$\mathbf{R}_{\epsilon,\epsilon}[M] \triangleq \mathrm{E}[\boldsymbol{\epsilon}[n+M|n]\boldsymbol{\epsilon}^{h}[n+M|n]].$$

For the case considered here, the value of $M=1$ is used. While a strict evaluation of the expressions for $\mathbf{R}_{E_G} \triangleq \mathrm{E}[\mathbf{E}_G\mathbf{E}_G^{h}|\hat{\mathbf{G}}]$ requires the evaluation of $\mathbf{R}_{\epsilon,\epsilon}[M]$ at multiple lags greater than one, the results achieved using $M=1$ suffice to demonstrate the techniques presented in this paper.

The derivation of the error correlation equations relies on a state space representation of the process $\tilde{\mathbf{g}}[n]$ as derived in Sec. 1 of Appendix B. The state equation for the estimation error is then derived in Sec. 2 of Appendix B. The state equations for the process and the estimation error are combined in a coupled state model in Sec. 2 a of Appendix B. Sections 2 b and 2 c of Appendix B present the solution of the coupled state equations for required cross-correlation matrices and for $\mathbf{R}_{\epsilon,\epsilon}[1]$.

1. The state space representation of $\tilde{\mathbf{g}}[n]$

For any matrix correlation function $\mathbf{R}_{\tilde{g},\tilde{g}}[m]$ that corresponds to a rational power spectrum, it is possible to define another zero-mean stationary vector random process $\mathbf{g}[n]$ with dimension $N_g \geq N_o$ such that

$$\mathbf{g}[n+1] = \mathbf{A}\mathbf{g}[n] + \mathbf{w}[n], \quad \text{(B5)}$$

$$\tilde{\mathbf{g}}[n] = \mathbf{S}_g\mathbf{g}[n] \quad \text{(B6)}$$

for a selection matrix $\mathbf{S}_g$, [The selection matrix $\mathbf{S}_g$ is an $N_o \times N_g$ matrix with all elements equal to zero except for a single element in each row that equals one], and

$$\mathbf{R}_{\tilde{g},\tilde{g}}[m] = \mathbf{S}_g\mathbf{R}_{g,g}[m]\mathbf{S}_g^{h} \quad \text{(B7)}$$

is the above-specified matrix correlation function. Here, $\mathbf{A}$ is an $N_g \times N_g$ state transition matrix and $\mathbf{w}[n]$ is zero-mean, white process noise with a correlation matrix $\mathbf{R}_w$. $\mathbf{w}[n]$ is independent of $\mathbf{g}[0]$ for all $n \geq 0$ and is independent of $v[m]$ and $\mathbf{d}[m]$ for all n and m. Note that for $M > 0$,

$$\mathbf{R}_{g,g}[M] = \mathbf{R}_{g,g}[0](\mathbf{A}^{M})^{h}. \quad \text{(B8)}$$

2. The error state equation

Equations (B5) and (B6) can be manipulated and combined to yield

$$\tilde{\mathbf{g}}[n+1] = \tilde{\mathbf{g}}[n] - \mathbf{S}_g(\mathbf{I}-\mathbf{A})\mathbf{g}[n] + \mathbf{S}_g\mathbf{w}[n]. \quad \text{(B9)}$$

Substituting Eqs. (B1) and (B3) into Eq. (B2) and substituting Eq. (B4) into the result yields

$$\hat{\tilde{\mathbf{g}}}[n] = \hat{\tilde{\mathbf{g}}}[n-1] + \hat{\mathbf{R}}_{d,d}^{-1}[n]\mathbf{d}[n](v^{*}[n] - \mathbf{d}^{h}[n]\boldsymbol{\epsilon}[n|n-1]). \quad \text{(B10)}$$

Subtracting Eq. (B9) from Eq. (B10), substituting Eq. (B4) into the result, and grouping terms results in the error state equation

$$\boldsymbol{\epsilon}[n+1|n]=(\mathbf{I}-\hat{\mathbf{R}}_{d,d}^{-1}[n]\mathbf{d}[n]\mathbf{d}^h[n])\boldsymbol{\epsilon}[n|n-1]+\mathbf{S}_g(\mathbf{I}-\mathbf{A})\mathbf{g}[n]+\hat{\mathbf{R}}_{d,d}^{-1}[n]\mathbf{d}[n]v^*[n]-\mathbf{S}_g\mathbf{w}[n]. \tag{B11}$$

Equation (B11) is a difference equation with a random time-varying state transition matrix, $(\mathbf{I}-\hat{\mathbf{R}}_{d,d}^{-1}[n]\mathbf{d}[n]\mathbf{d}^h[n])$ and coefficient matrix $\hat{\mathbf{R}}_{d,d}^{-1}[n]$. The direct averaging method (Kushner[14]) may be used to evaluate the convergence behavior of this equation in an average sense. Under the assumption that these matrices vary slowly with time (i.e., λ is close to one), they can be replaced by their expected values. The resulting expression can be used to evaluate the steady state behavior of Eq. (B11) in an average sense. Following the convention adopted in Haykin[13] and Eleftheriou *et al.*[15] $\hat{\mathbf{R}}_{d,d}^{-1}[n]$ is replaced by $(1-\lambda)\mathbf{R}_{d,d}^{-1}$ and $\mathbf{d}[n]\mathbf{d}^h[n]$ is replaced by $\mathbf{R}_{d,d}$. With these substitutions, Eq. (B11) can be rewritten as

$$\boldsymbol{\epsilon}[n+1|n]=\lambda\boldsymbol{\epsilon}[n|n-1]+\mathbf{S}_g(\mathbf{I}-\mathbf{A})\mathbf{g}[n]+(1-\lambda)\mathbf{R}_{d,d}^{-1}\mathbf{d}[n]v^*[n]-\mathbf{S}_g\mathbf{w}[n]. \tag{B12}$$

a. The coupled state equations

The state equations (B5) and (B12) can be written in coupled form as

$$\begin{bmatrix}\mathbf{g}[n+1]\\ \boldsymbol{\epsilon}[n+1|n]\end{bmatrix}=\begin{bmatrix}\mathbf{A} & \mathbf{0}\\ \mathbf{S}_g(\mathbf{I}-\mathbf{A}) & \lambda\mathbf{I}\end{bmatrix}\begin{bmatrix}\mathbf{g}[n]\\ \boldsymbol{\epsilon}[n|n-1]\end{bmatrix}+\begin{bmatrix}\mathbf{I} & \mathbf{0}\\ -\mathbf{S}_g & (1-\lambda)\mathbf{R}_{d,d}^{-1}\mathbf{d}[n]\end{bmatrix}\begin{bmatrix}\mathbf{w}[n]\\ v^*[n]\end{bmatrix}. \tag{B13}$$

For a stable matrix $\mathbf{A}$ and $0<\lambda<1$, the state transfer matrix in Eq. (B13) is stable and the equation describes a zero-mean stationary random process. Therefore

$$\lim_{n\to\infty} E[\boldsymbol{\epsilon}[n+1|n]]=\mathbf{0}. \tag{B14}$$

Define

$$\mathbf{R}_{\boldsymbol{\epsilon},g}[m]\triangleq E[\boldsymbol{\epsilon}[n+1|n]\mathbf{g}^h[n+m]]$$

and let $\mathbf{R}_{g,\boldsymbol{\epsilon}}[m]\triangleq\mathbf{R}_{\boldsymbol{\epsilon},g}^h[m]$. Then, taking the outer product of both sides of Eq. (B13), taking the expectation of both sides, and taking the limit as $n\to\infty$ yields the following four equations that are satisfied by $\mathbf{R}_{g,g}[0]$, $\mathbf{R}_{\boldsymbol{\epsilon},g}[1]$, $\mathbf{R}_{g,\boldsymbol{\epsilon}}[1]$, and $\mathbf{R}_{\boldsymbol{\epsilon},\boldsymbol{\epsilon}}[1]$:

$$\mathbf{R}_{g,g}[0]=\mathbf{A}\mathbf{R}_{g,g}[0]\mathbf{A}^h+\mathbf{R}_w, \tag{B15}$$

$$\mathbf{R}_{\boldsymbol{\epsilon},g}[1]=\lambda\mathbf{R}_{\boldsymbol{\epsilon},g}[1]\mathbf{A}^h+\mathbf{S}_g(\mathbf{I}-\mathbf{A})\mathbf{R}_{g,g}[0]\mathbf{A}^h-\mathbf{S}_g\mathbf{R}_w, \tag{B16}$$

$$\mathbf{R}_{g,\boldsymbol{\epsilon}}[1]=\lambda\mathbf{A}\mathbf{R}_{g,\boldsymbol{\epsilon}}[1]+\mathbf{A}\mathbf{R}_{g,g}[0](\mathbf{I}-\mathbf{A})^h\mathbf{S}_g^h-\mathbf{R}_w\mathbf{S}_g^h, \tag{B17}$$

$$\mathbf{R}_{\boldsymbol{\epsilon},\boldsymbol{\epsilon}}[1]=\lambda^2\mathbf{R}_{\boldsymbol{\epsilon},\boldsymbol{\epsilon}}[1]+\mathbf{S}_g(\mathbf{I}-\mathbf{A})\mathbf{R}_{g,g}[0](\mathbf{I}-\mathbf{A})^h\mathbf{S}_g^h+\lambda\mathbf{R}_{\boldsymbol{\epsilon},g}[1](\mathbf{I}-\mathbf{A})^h\mathbf{S}_g^h+\lambda\mathbf{S}_g(\mathbf{I}-\mathbf{A})\mathbf{R}_{g,\boldsymbol{\epsilon}}[1]+\mathbf{S}_g\mathbf{R}_w\mathbf{S}_g^h+(1-\lambda)^2\sigma_v^2\mathbf{R}_{d,d}^{-1}. \tag{B18}$$

b. Solving the coupled state equations for $\mathbf{R}_{\boldsymbol{\epsilon},g}[1]$ and $\mathbf{R}_{g,\boldsymbol{\epsilon}}[1]$

Equation (B16) can be rewritten as

$$\mathbf{R}_{\boldsymbol{\epsilon},g}[1]=\lambda\mathbf{R}_{\boldsymbol{\epsilon},g}[1]\mathbf{A}^h+\mathbf{S}_g\mathbf{R}_{g,g}[0]\mathbf{A}^h-\mathbf{S}_g(\mathbf{A}\mathbf{R}_{g,g}[0]\mathbf{A}^h+\mathbf{R}_w).$$

Substituting Eq. (B15) into the last term of this equation and rearranging terms yields

$$\mathbf{R}_{\boldsymbol{\epsilon},g}[1]=\mathbf{S}_g\mathbf{R}_{g,g}[0](\mathbf{A}^h-\mathbf{I})(\mathbf{I}-\lambda\mathbf{A}^h)^{-1}. \tag{B19}$$

Since $0<\lambda<1$ and the magnitude of each eigenvalue of $\mathbf{A}$ is less than one, the matrix $\lambda\mathbf{A}$ has eigenvalues all of whose magnitudes are less than one. Therefore (Golub *et al.*[16])

$$(\mathbf{I}-\lambda\mathbf{A}^h)^{-1}=\sum_{m=0}^{\infty}\lambda^m(\mathbf{A}^m)^h. \tag{B20}$$

Substituting Eq. (B20) into Eq. (B19), rearranging terms, and substituting Eq. (B8) into the result yields

$$\mathbf{R}_{\boldsymbol{\epsilon},g}[1]=-\mathbf{S}_g\left(\sum_{m=0}^{\infty}\lambda^m\mathbf{R}_{g,g}[m]\right)(\mathbf{I}-\mathbf{A}^h). \tag{B21}$$

Similarly,

$$\mathbf{R}_{g,\boldsymbol{\epsilon}}[1]=-(\mathbf{I}-\mathbf{A})\left(\sum_{m=0}^{\infty}\lambda^m\mathbf{R}_{g,g}^h[m]\right)\mathbf{S}_g^h. \tag{B22}$$

c. Solving the coupled state equations for $\mathbf{R}_{\boldsymbol{\epsilon},\boldsymbol{\epsilon}}[1]$

Substituting Eqs. (B7), (B8), (B15), (B21), and (B22) into Eq. (B18) and rearranging terms yields

$$\mathbf{R}_{\boldsymbol{\epsilon},\boldsymbol{\epsilon}}[1]=\frac{2}{(1+\lambda)}\left(\mathbf{R}_{\tilde{g},\tilde{g}}[0]-(1-\lambda)\sum_{m=0}^{\infty}\lambda^m\tilde{\tilde{\mathbf{R}}}_{\tilde{g},\tilde{g}}[m+1]\right)+\frac{(1-\lambda)}{(1+\lambda)}\sigma_v^2\mathbf{R}_{d,d}^{-1}. \tag{B23}$$

3. Frequency domain expressions for $\mathbf{R}_{\tilde{g},\tilde{g}}[1]$

Let the function $\lambda_1(m)=\lambda^{-1}\lambda^{|m|}$ when $|m|\geq 1$ and equal 0 for $m=0$. Then, the lag error term (i.e., the first term) in Eq. (B23) may be rewritten as

$$\mathbf{R}_{\text{lag}}[1]=(1+\lambda)^{-1}\left(2\mathbf{R}_{\tilde{g},\tilde{g}}[0]-(1-\lambda)\sum_{m=-\infty}^{\infty}\lambda_1(m)\mathbf{R}_{\tilde{g},\tilde{g}}[m]\right).$$

This can be written in the frequency domain as

$$\mathbf{R}_{\text{lag}}[1]=(1+\lambda)^{-1}\frac{1}{2\pi}\int_{-\pi}^{\pi}(2-(1-\lambda)\mathcal{F}(\lambda_1))\mathbf{S}_{\tilde{g},\tilde{g}}(\omega)d\omega, \tag{B24}$$

where $\mathcal{F}(\lambda_M)$ denotes the Fourier transform of the sequence $\lambda_M(m)$. That is,

$$\mathcal{F}(\lambda_M) = \lambda^{-M} \sum_{|m| \geq M} \lambda^{|m|} e^{-j\omega m}$$

$$= \frac{e^{-j\omega M} + e^{j\omega M} - \lambda(e^{-j\omega(M-1)} + e^{j\omega(M-1)})}{|1 - \lambda e^{-j\omega}|^2}. \tag{B25}$$

Evaluating Eq. (B25) for $M=1$, substituting the result into Eq. (B24), noting that $|1-\lambda e^{-j\omega}|^2 = (1-\lambda e^{-j\omega})(1-\lambda e^{j\omega})$, and combining and rearranging terms yields

$$\mathbf{R}_{\text{lag}}[1] = \frac{1}{2\pi} \int_{-\pi}^{\pi} \frac{|e^{-j\omega} - 1|^2}{|1 - \lambda e^{-j\omega}|^2} \mathbf{S}_{\tilde{g},\tilde{g}}(\omega) d\omega. \tag{B26}$$

This result is seen to generalize the result presented in Lin *et al.*,[17] which is applicable only to channels for which the power spectrum of the fluctuations of the channel taps is the same for all taps. Substituting Eq. (B26) for the first term in Eq. (B23) and recalling that it is assumed that $\mathbf{R}_{d,d} = \mathbf{I}$ yields Eq. (25).

APPENDIX C: SCATTERING FUNCTION ESTIMATION

The acoustic signals received from each of the transmissions were processed to yield estimates of the time-varying scattering function of the acoustic channel (See Proakis[6] and VanTrees[7]). The received signals for the maximum length sequence (m-seq) transmissions (see Sec. V) were modulated to baseband, low-pass filtered, and then downsampled to a rate of two samples per symbol. The channel scattering function was estimated by matched filtering resampled segments of the received baseband signal with a sequence consisting of frequency shifted versions of three repetitions of the transmitted 4095 point m-seq. The resampling of the baseband signal was necessary to account for the fact that the bandwidth of the transmitted signal was too large to allow for modeling the impact of the rate of change of the length of individual propagation paths as a simple frequency (Doppler) shift. Note that the wideband nature of the signal and rate of change of the propagation path lengths results in a violation of the wide-sense stationary channel assumption. However, the framework of the channel scattering function when evaluation over short time intervals is still useful for quantifying and providing insight into the impact of channel fluctuations on the performance of underwater acoustic communications algorithms.

[1] M. Stojanovic, L. Freitag, and M. Johnson, "Channel-estimation-based adaptive equalization of underwater acoustic signals," in Proceedings of the IEEE Oceans'99 Conference, Seattle, WA, 1999, pp. 985–990.

[2] D. Rouseff, D. R. Jackson, W. L. J. Fox, C. D. Jones, J. A. Ritcey, and D. R. Dowling, "Underwater acoustic communications by pasive phase conjugation: Theory and experimental results," IEEE J. Ocean. Eng. **26**, 821–831 (2001).

[3] J. Flynn, J. A. Ritcey, D. Rouseff, and W. L. J. Fox, "Multichannel equalization by decision-directed passive phase conjugation: Experimental results," IEEE J. Ocean. Eng. **29**, 824–836 (2004).

[4] M. Stojanovic, J. Proakis, and J. Catapovic, "Analysis of the impact of channel estimation errors on the performance of a decision-feedback equalizer in fading multipath channels," IEEE Trans. Commun. **COM-43**, 877–886 (1995).

[5] J. Preisig, "The impact of underwater acoustic channel structure and dynamics on the performance of adaptive coherent equalizers," in *High Frequency Ocean Acoustics*, edited by M. Porter, M. Siderius, and W. Kuperman (American Institute of Physics, New York, 2004), pp. 57–64.

[6] J. G. Proakis, *Digital Communications*, 3rd ed. (McGraw-Hill, New York, 1995), Chaps. 13 and 14, pp. 724–729.

[7] H. L. Van Trees, *Detection, Estimation, and Modulation Theory, Part III* (Wiley Inter-Science, New York, 2001), Chap. 13.

[8] Physical underwater acoustic channels are all causal. However, it is sometimes conceptually convenient to think of some point in delay (the variable m) within the impulse response to be the zero delay tap and those points that preceed this point in the delay variable to be acausal taps.

[9] The feedback filter does not need to continuously span the range of past data estimates from $(n-1)$ to $(n-L_{\text{fb}})$. Such feedback filters are said to be "sparse." The modifications to the expressions developed here to handle sparse equalizers are trivial and the conclusions of the analysis are unchanged.

[10] The assumption of unit variance can be made without any loss of generality of the results.

[11] J. Preisig and G. Deane, "Surface wave focusing and acoustic communications in the surf zone," J. Acoust. Soc. Am. **116**, 2067–2080 (2004).

[12] T. Kailath, *Linear Systems* (Prentice-Hall, Englewood Cliffs, NJ, 1980), pp. 656.

[13] S. Haykin, *Adaptive Filter Theory*, 3rd ed. (Prentice-Hall, Upper Saddle River, NJ, 1996).

[14] H. J. Kushner, *Approximation and Weak Convergence Methods for Random Processes With Applications to Stochastic System Theory* (MIT Press, Cambridge, MA, 1984).

[15] E. Eleftheriou and D. Falconer, "Tracking properties and steady-state performance of RLS adaptive filter algorithms," IEEE Trans. Acoust., Speech, Signal Process. **34**, 1097–1109 (1986).

[16] G. H. Golub and C. F. Van Loan, *Matrix Computations*, 3rd ed. (Johns Hopkins University Press, Baltimore, MD, 1996), pp. 58.

[17] J. Lin, J. Proakis, F. Ling, and H. Lev-Ari, "Optimal tracking of time-varying channels: A frequency domain approach for known and new algorithms," IEEE Trans. Selected Areas in Communications **13**, 141–153 (1995).

Characteristics of distortion product otoacoustic emissions in the frog from L_1, L_2 maps

Sebastiaan W. F. Meenderink
Department of Otorhinolaryngology and Head & Neck Surgery, University Hospital Maastricht, P.O. Box 5800, 6202 AZ Maastricht, and Institute for Brain and Behaviour, Maastricht University, The Netherlands

Pim van Dijk
Department of Otorhinolaryngology, University Medical Centre Groningen, P.O. Box 30.001, 9700 RB Groningen and School of Behavioral, and Cognitive Neurosciences, University of Groningen, The Netherlands

(Received 22 November 2004; revised 8 April 2005; accepted 11 April 2005)

For a given set of stimulus frequencies (f_1, f_2), the level of distortion product otoacoustic emissions (DPOAEs) varies with the levels of the stimulus tones. By variation of the stimulus levels, L_1, L_2-maps for DPOAEs can be constructed. Here, we report on L_1, L_2-maps for DPOAEs from the frog ear. In general, these maps were similar to those obtained from the mammalian cochlea. We found a conspicuous difference between the equal-level contour lines for low-level and high-level DPOAEs, which could be modeled by a saturating and an expansive nonlinearity, respectively. The transition from the high-level to the low-level response was accompanied by a DPOAE phase-change, which increased from 0 to π rad with increasing frequency. These results suggest that in the frog low-level and high-level DPOAEs are generated by separate nonlinear mechanisms. Also, there was a conspicuous difference in the growth of the low-level emissions from the two anuran auditory papillae. In the basilar papilla, this growth was expansive for the lowest stimulus levels and saturated for intermediate levels. This is consistent with the behavior of a Boltzman nonlinearity. In the amphibian papilla this growth was compressive, suggesting the additional effect of a compressive amplification mechanism on the generation of DPOAEs. © *2005 Acoustical Society of America.* [DOI: 10.1121/1.1925887]

PACS number(s): 43.64.Bt, 43.64.Jb, 43.80.Lb [BLM] Pages: 279–286

I. INTRODUCTION

Otoacoustic emissions (OAEs) are weak sounds that can be measured in the ear canal, both with and without the presence of an external stimulus. When the stimulus consists of two pure tones, with appropriately chosen frequencies (f_1, f_2) and amplitudes (L_1, L_2), so-called distortion product OAEs (DPOAEs) can be recorded at various intermodulation frequencies of the two stimulus tones (e.g., $2f_1 - f_2$ and $2f_2 - f_1$). To date, most studies of DPOAEs have been on mammals, for which it is generally assumed that (at least for low-level stimuli) electromotility of the outer hair cells (Brownell *et al.*, 1985) is the responsible mechanism for OAE generation. As such, DPOAEs provide a noninvasive tool to investigate the (nonlinear) mechanics of hair cells that are involved in the transduction of sound.

When, for a given combination of stimulus frequencies, the levels of the two stimulus tones are varied, the input/output (I/O) characteristics of DPOAEs may be determined. In such experiments typically both stimulus levels are varied, while keeping the difference $L_1 - L_2$ fixed. The resulting I/O curves exhibit a complex shape, with the rate of DPOAE-amplitude growth dependent on absolute stimulus levels (mammals: Brown, 1987; birds: Froymovich *et al.*, 1995; reptiles: Manley *et al.*, 1993; amphibians: Meenderink and Van Dijk, 2004). One way to explain the shape of these I/O curves (and associated DPOAE phase) is by the interference of two level-dependent components, of which each is dominant over a different range of stimulus levels (Whitehead *et al.*, 1992). The different vulnerability of these components has led to the suggestion that they arise from different mechanisms. The low-level component presumably arises from "active" (i.e., energy is supplied by the ear in such a manner that sound-induced vibration is enhanced) hair cell mechanics, while the component that dominates for high-level stimuli is generated by some "passive" (i.e., no energy is supplied by the ear) nonlinearity, that is not necessarily associated with hair cells (Mills *et al.*, 1993).

Recently, doubt has risen as to whether such a two-source model is necessary to account for DPOAE generation in the mammalian cochlea (Mills, 2002). It seems that the division into a passive high-level and an active low-level component is no longer supported (Mom *et al.*, 2001; Frolenkov *et al.*, 1998). The results from these and other studies in mammals indicate that the generation of low-level and high-level DPOAEs both involve an active nonlinear mechanism that critically depends on the normal functioning of the outer hair cells. In confirmation with this, several I/O characteristics (i.e., differential vulnerability and notches) can be accounted for by models that incorporate only a single, active mechanism for DPOAE generation (Mills, 1997; Lukashkin *et al.*, 2002). Seemingly, only one type of nonlinear mechanism is necessary for DPOAE generation. However, mice lacking the protein prestin in their hair cell's basolateral membrane do generate high-level DPOAEs

(Liberman *et al.*, 2004). Apparently, in contrast to low-level DPOAEs in mice, high-level DPOAEs do not depend on prestin motility and thus must originate from another mechanism.

In frogs, the anatomy of the inner ear deviates considerably from that found in mammals, the most prominent difference being the absence of a cochlea. Instead, the frog inner ear contains two papillae that respond to airborne sound. Of these, the amphibian papilla (AP) shows several similarities with the cochlea. It consists of an elongated strip of sensory epithelium that exhibits tonotopic organization (Lewis *et al.*, 1982). As in the cochlea, the entire epithelium is covered by a tectorial membrane. Hair cells are innervated by both efferent and afferent nerve fibers, the latter having tuning characteristics similar to those found in mammals (Lewis, 1992). The AP may generate both spontaneous and distortion product OAEs (Van Dijk and Manley, 2001). Different from the cochlea are the absence of a basilar membrane and of distinct groups of hair cells (i.e., no inner and outer hair cells).

The structure of the other papilla, the basilar papilla (BP), is much simpler. It consists of a small patch of sensory epithelium, covered by a tectorial membrane. In *R. catesbeiana*, the entire papilla contains between 50 and 100 hair cells whose stereovillar bundles are oriented identically (Lewis, 1978). As in the AP, this papilla lacks a basilar membrane and hair cells are not differentiated into differing groups. The BP lacks tonotopic organization; in individual frogs, the majority of afferent nerve fibers is tuned to a single frequency (Ronken, 1991; Van Dijk *et al.*, 1997). These properties ensure that the entire papilla essentially functions as a single auditory filter (Ronken, 1990; Van Dijk and Manley, 2001). The BP may generate distortion product OAEs, but no spontaneous OAEs have been reported from this papilla.

Recently, we presented I/O curves for DPOAEs from the frog ear that are very similar to I/O curves obtained in other vertebrates (Meenderink and Van Dijk, 2004). We suggested that DPOAEs in the frog are the result from two level-dependent components, with each component arising from a different nonlinear mechanism. Here, we further detail the stimulus-level dependence of DPOAEs in the frog by presenting full L_1,L_2 maps. These maps showed a differential dependence of high-level and low-level DPOAEs, as is evidenced by the different contour lines. Combined with the observed frequency-dependent phase change associated with the transition from low-level to high-level DPOAEs, these results provide further support for the involvement of two separate, level-dependent emission-generation mechanisms in the frog.

II. MATERIALS

Distortion product otoacoustic emissions were recorded from 12 ears of 7 Northern leopard frogs, *Rana pipiens pipiens*; body mass; 37.6–46.8 g (mean: 42.7 g). In order to immobilize the frog during DPOAE recording, it was anaesthetized with an intramuscular injection of pentobarbital sodium solution (diluted Nembutal: 6.0 mg/ml; 10 μl/g body weight) in one of the hind limbs. Approximately 25 min after the administration of the anaesthetic agent, the frog was transferred to a sound-attenuating chamber and placed between wet gauze to prevent dehydration and to facilitate cutaneous respiration.

A custom-built probe assembly was carefully placed with its open end against the skin surrounding the tympanic membrane. A tight seal between the probe and the skin was obtained using vaseline. The probe assembly contained two miniature speakers (E-A-RTONE 3A, Aero Company, IN) for stimulus delivery, and a 1 in. high-sensitivity condenser microphone (B&K type 4179, Brüel & Kjær, Denmark) for emission recording. DPOAEs were evoked by stimulating the ear with two simultaneously played pure tones. These stimulus tones, with frequencies f_1 and f_2 ($f_2>f_1$), were generated from two separate D/A channels (RP2, Tucker-Davis Technologies, Gainesville, FL), attenuated in order to set their levels (PA5, TDT, Gainesville, FL), and each one was played through a separate miniature speaker.

The microphone signal was passed through a low-noise amplifier (B&K type 2660; Brüel & Kjær, Denmark; amplification=20 dB) and a measuring amplifier (B&K type 2610; Brüel & Kjær, Denmark; amplification$\geqslant$0 dB). This amplified microphone signal was recorded using an A/D channel (RP2, TDT, Gainesville, FL) and stored on computer disk for offline analysis. In order to monitor the DPOAEs during the experiment, the frequency spectrum of the amplified microphone signal was viewed online using a spectrum analyzer (SR760, Stanford Research Systems, Sunnyvale, CA). Customized software, written in MATLAB (The Mathworks Inc., Natick, MA) and Rpvds (TDT, Gainesville, FL) was used to control stimulus tone generation and signal recording. The recorded signal was averaged in the time domain after the application of a level-crossing artifact-rejection method. From the averaged signal, both the DPOAEs and the noise floor were calculated using Fourier analysis. For further details concerning data acquisition and analysis we refer to Meenderink and Van Dijk (2004).

Data were collected at various different stimulus frequency combinations (overall range: $313<f_1<3213$ Hz; $f_2/f_1=1.02$, 1.1, or 1.3). For each f_1,f_2 combination, stimulus levels were independently and randomly varied over a 30 dB range in 3 dB steps. This resulted in a square L_1,L_2 matrix, containing 121 points for each stimulus frequency combination.

To determine the distortion of the recording system, additional experiments were performed with the open end of the probe assembly closed by a solid surface. In general, system distortion at the frequencies of the cubic difference tones was approximately 90 dB below the stimulus levels. Only for low stimulus level combinations did this system distortion disappear in the noise floor. Based on these recordings, only DPOAEs for which the amplitude exceeded both the noise floor and the system distortion were arranged in L_1,L_2 matrices. This amounts to the presentation of DPOAEs whose amplitudes exceeded −15 dB SPL. Since the phase of the two stimulus tones was not controlled in the experiments, the DPOAE phase will be given relative to the phase of the

two stimulus tones according to $\Phi_{nf_1-mf_2}=\phi_{nf_1-mf_2}-(n*\phi_1-m*\phi_2)$, where $\phi_{nf_1-mf_2}$ is the recorded DPOAE phase, and ϕ_1 and ϕ_2 are the calculated phases of the two stimulus tones.

All procedures were approved by the animal experiment committee of the Maastricht University.

III. RESULTS

Distortion product otoacoustic emissions (DPOAEs) could be detected in all ears investigated. Although for certain stimulus tone combinations, DPOAEs could be observed at up to 8 different distortion frequencies, here only DPOAEs at frequencies $2f_1-f_2$ and $2f_2-f_1$ will be presented. The DPOAE data were visualized by plotting both the amplitude and the phase of the DPOAE against the levels of both stimulus tones. Within such an L_1,L_2 map, contour lines of equal emission amplitude were calculated at 3 dB intervals. Only data points with amplitudes >-15 dB SPL were included. Phase was represented by arrows, with the phase for the largest L_1,L_2 combination arbitrarily set to zero. As such, absolute phase holds no meaning, but phase changes within each L_1,L_2 map do.

Figure 1 displays results for DPOAEs at $2f_1-f_2$ [Fig. 1(a)] and $2f_2-f_1$ [Fig. 1(b)] obtained from the frog basilar papilla ($f_1=1913$ Hz, $f_2/f_1=1.02$ with L_1 and L_2 between 56 and 86 dB SPL). In this figure, the 3 dB intervals between consecutive amplitude contour lines are coded in gray, with the corresponding DPOAE amplitudes given in the key. Focusing on the amplitude, each L_1,L_2 map could be divided into two principal regions based on the shape of the contour lines. For relatively low stimulus levels, the contour lines were clearly convex. As a result, these lines encompass a more or less pronounced ridge in the L_1,L_2 map that lies approximately parallel to the diagonal $L_1=L_2$. In contrast, when one or both of the stimulus levels were relatively high, the contour lines approximated straight lines, with consecutive contour lines being parallel to each other. The slope of these contour lines depended on the DPOAE frequency: $L_2/L_1=-2$ dB/dB for $2f_1-f_2$ and $L_2/L_1=-0.5$ dB/dB for $2f_2-f_1$.

For the DPOAE phase, the L_1,L_2 maps could be divided into the same two principal regions as the amplitude data (i.e., two relatively low-level stimuli versus at least one relatively high-level stimulus). Within each of these two regions the phase was relatively constant, while between them the phase was different. In the examples shown, this phase difference is approximately 0.7π rad for $2f_1-f_2$ [Fig. 1(a)] and 0.9π rad for $2f_2-f_1$ [Fig. 1(b)]. For clarity, we will refer to the two principal regions in the L_1,L_2 maps as "low level" (relatively low stimulus levels) and "high level" (at least one of the two stimulus levels is relatively high), respectively.

In frogs, DPOAEs arise from either one of the two hearing papillae, depending on the stimulus frequencies used (Van Dijk and Manley, 2001; Meenderink and Van Dijk, 2004). This is reflected in the bimodal shape of the DPOAE audiograms, as illustrated in Figs. 2(a) and 2(b). DPOAEs evoked with low-frequency stimulus tones ($f_1<1250$ Hz for $2f_1-f_2$ and $f_1<1000$ Hz for $2f_2-f_1$, respectively) arise from

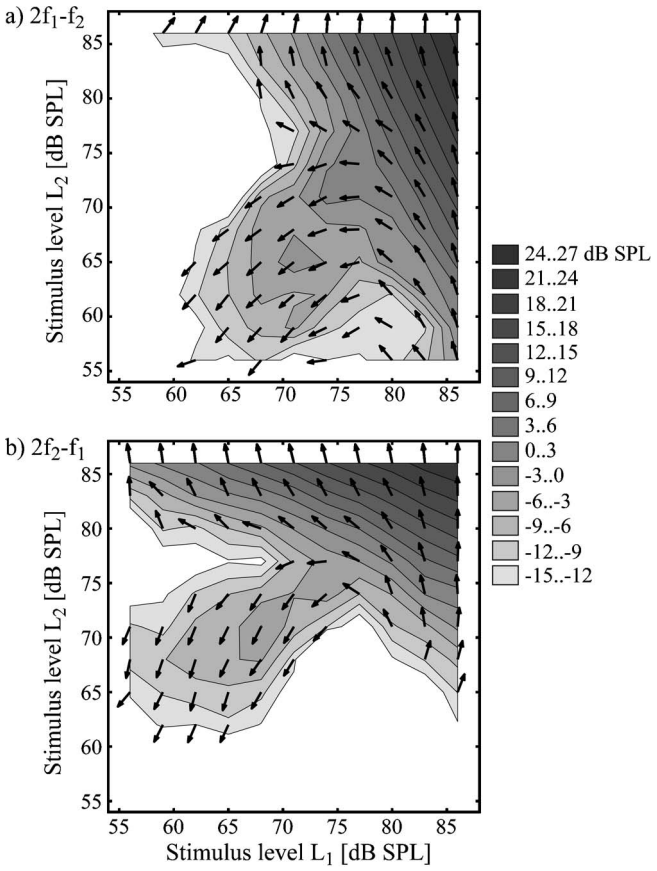

FIG. 1. Amplitude and phase of DPOAEs at (a) $2f_1-f_2$ and (b) $2f_2-f_1$ as function of stimulus levels L_1 and L_2. Shown are data recorded in one frog for $f_1=1913$ Hz and $f_2/f_1=1.02$. This combination of stimulus frequencies results in DPOAEs originating from the frog basilar papilla. The DPOAE amplitude is represented by the equal-amplitude contour lines. The lowest contour lines are at -15 dB SPL and subsequent contour lines are drawn in 3 dB increments. The consecutive intervals between the contour lines are coded in gray, as given in the key. The phase of the DPOAEs is given by the arrows overlaying the contour lines, with a full counterclockwise rotation of the arrows corresponding to a phase lag of 2π rad. The phase is relative to the phase at $L_1=L_2=86$ dB SPL.

the amphibian papilla, while DPOAEs evoked with larger stimulus frequencies originate from the frog basilar papilla. This strict separation between DPOAE generation from the AP and the BP is probably not true. Stimulus frequencies around 1250 Hz presumably evoke an emission component in each papilla. These components will combine, which may result in the amplitude trough commonly seen in DPOAE audiograms.

As an overview, the remaining subplots in Fig. 2 show L_1,L_2 maps at 4 stimulus frequency combinations, all obtained in one ear. For reference, the stimulus frequencies f_1 for which these L_1,L_2 maps were recorded, are illustrated by the vertical dashed lines in Figs. 2(a) and 2(b). These L_1,L_2 maps showed a similar dependence of DPOAEs on stimulus levels as was described for Fig. 1: (1) for all stimulus frequencies, there was a distinction between the stimulus level dependence of low-level and high-level DPOAEs. This is illustrated by the convex shape of equal-amplitude contour lines for the low-level emissions, and the approximately straight contour lines for high-level emissions. (2) The low-level ridge, encompassed by the convex contour lines, ran

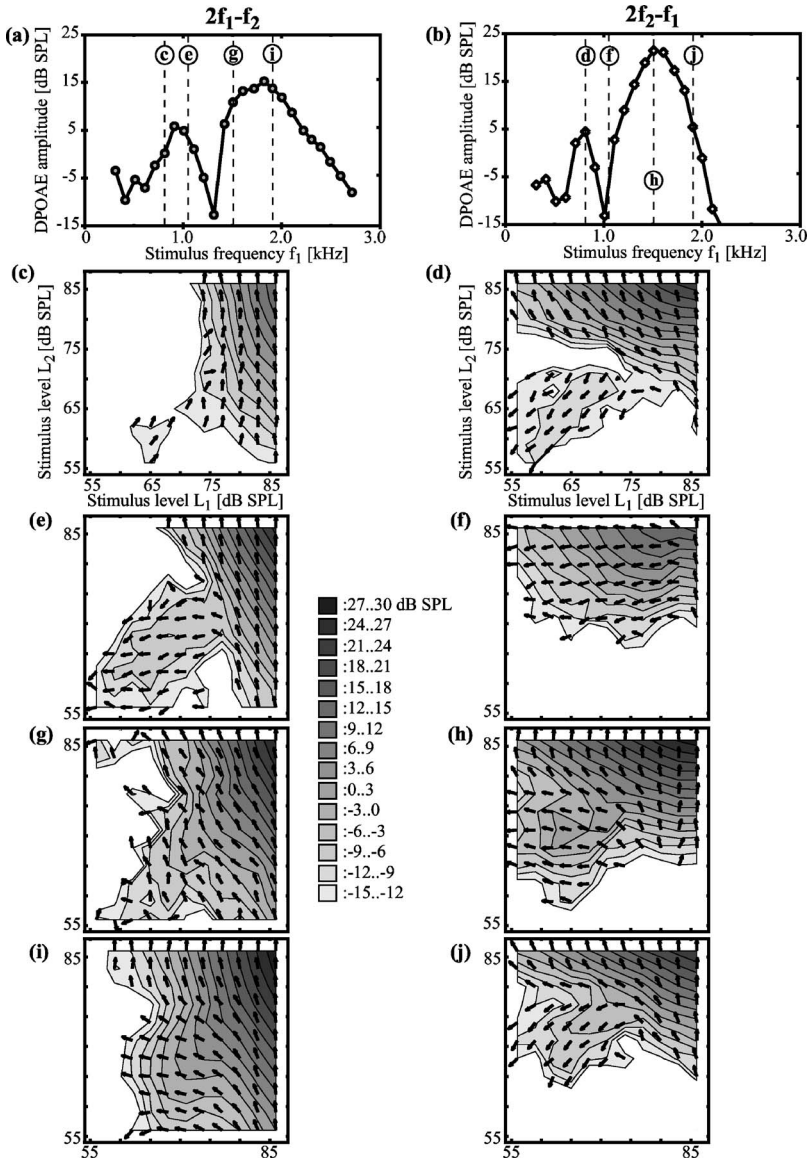

FIG. 2. Overview of the stimulus level dependence of DPOAE amplitude and phase for different stimulus frequencies. All data were obtained in a single ear using $f_2/f_1=1.1$. The left column gives DPOAEs at $2f_1-f_2$, while the right column gives DPOAEs at $2f_2-f_1$. (a)–(b) The DPOAE amplitude as a function of stimulus frequency f_1 obtained with $L_1=L_2=80$ dB SPL. The vertical dashed lines indicate the frequencies ($f_1=814, 1052, 1507, 1907$ Hz) for which L_1, L_2 recordings were made. The labels on the dashed lines refer to the subplots in the figure. (c)–(j) Amplitude and phase of DPOAEs as a function of stimulus levels L_1 and L_2. The layout of the plots is similar to that in Fig. 1. That is, the DPOAE amplitude is represented by equal-amplitude contour lines, drawn at 3 dB intervals. The DPOAE amplitude is represented by shadings of grey, with the corresponding levels given in the key. The DPOAE phase is represented by the arrows overlying the contour lines, with a full counterclockwise rotation of the arrows corresponding to a phase lag of 2π rad. In each subplot, the phase is relative to the phase at $L_1=L_2=86$ dB SPL. As such, phase differences between the different subplots hold no meaning, but changes in phase within each subplot do.

approximately parallel to the diagonal $L_1=L_2$ for both $2f_1-f_2$ and $2f_2-f_1$. (3) The straight high-level contour lines had slopes equal to -2 dB/dB for $2f_1-f_2$ and -0.5 dB/dB for $2f_2-f_1$. (4) Within the low- and the high-level region of the L_1, L_2 maps DPOAE phase was relatively constant, but the transition between both regions was accompanied by a change in phase. Within each papilla, this change increased from close to 0 rad for low frequencies to almost π rad for high frequencies (see Fig. 3). Notice that in the AP the phase difference between low-level and high-level DPOAEs increases more rapidly with frequency than in the BP. A similar difference between the two papillae is found in the group delays of DPOAEs (Meenderink *et al.*, 2005). These differences in DPOAE phase behavior may signify differences in the mechanical filter responses of the two papillae.

Figure 2 shows another clear distinction between DPOAEs from the amphibian papilla and the basilar papilla. In the AP, low-level emissions resulted in an extensive plateau in the L_1, L_2 maps. In contrast, for DPOAEs in the BP this low-level plateau was much smaller or even absent.

The low-level ridge was not always on the diagonal $L_1=L_2$, but its position depends on the stimulus frequency relative to the peak frequency of the DPOAE audiogram. This can be illustrated most clearly for emission measurements at relatively large stimulus frequency ratios. Figure 4 displays results for one subject when $f_2/f_1=1.30$. At this ratio, only DPOAEs from the BP at $2f_2-f_1$ had an amplitude that was sufficient for a systematic evaluation. The DPOAE audiogram contains a single maximum at $f_1=1313$ Hz [Fig. 4(a)]. For a stimulus frequency f_1 at this maximum, the low-level ridge in the L_1, L_2 map is approximately on the diagonal $L_1=L_2$ [Fig. 4(c)]. However, when this stimulus frequency was on the low-frequency slope of the DPOAE audiogram, L_1 needed to be larger that L_2 to obtain a maximum emission amplitude. Consequently, the low-level ridge in the L_1, L_2 map was below the diagonal [Fig. 4(b)]. For a stimulus frequency above the maximum in the DPOAE audiogram, the reverse was true: L_2 needed to be larger than L_1 for a maximum emission amplitude, and the low-level ridge was above

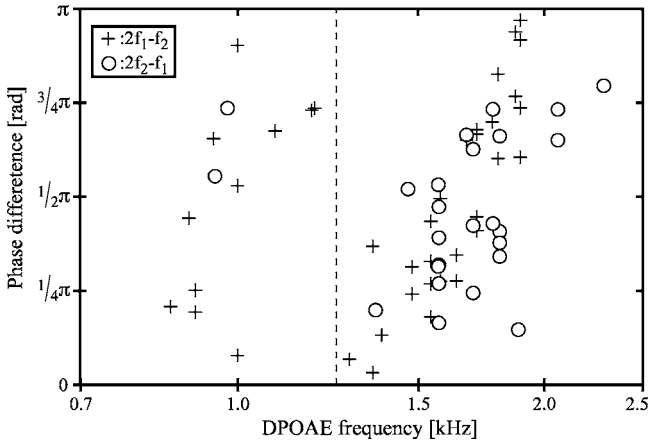

FIG. 3. The difference in phase for DPOAEs at $2f_1-f_2$ (+) and $2f_2-f_1$ (○) evoked with $L_1=L_2=86$ dB SPL and $L_1=L_2=63$ dB SPL as a function of distortion product frequency. Data obtained with $f_2/f_1=1.02$ and 1.10 are combined. The vertical dashed line gives the frequency separation between the amphibian papilla and the basilar papilla (1250 Hz; Ronken, 1991).

the diagonal [Fig. 4(d)]. Nevertheless, for each stimulus frequency combination, the low-level ridge was parallel to the main diagonal $L_1=L_2$.

IV. DISCUSSION

It is currently believed that distortion product otoacoustic emissions (DPOAEs) from the frog arise from both the amphibian papilla (AP) and the basilar papilla (BP), the two end organs in the frog inner ear that are most sensitive to airborne sound. The bimodel shape of DPOAE audiograms is a direct result of this [Figs. 2(a) and 2(b); Van Dijk and Manley, 2001; Meenderink *et al.*, 2005]. In the present work we explored the dependence of DPOAE amplitude and phase on stimulus levels by systematically mapping L_1,L_2 space over a range of stimulus frequencies thus covering the frequency range of highest sensitivity of both papillae. The first obvious result is that across frequencies the L_1,L_2 dependence of DPOAEs is very different for high-level emissions compared to low-level emissions. In the presented L_1,L_2 maps, high-level DPOAEs were characterized by contour

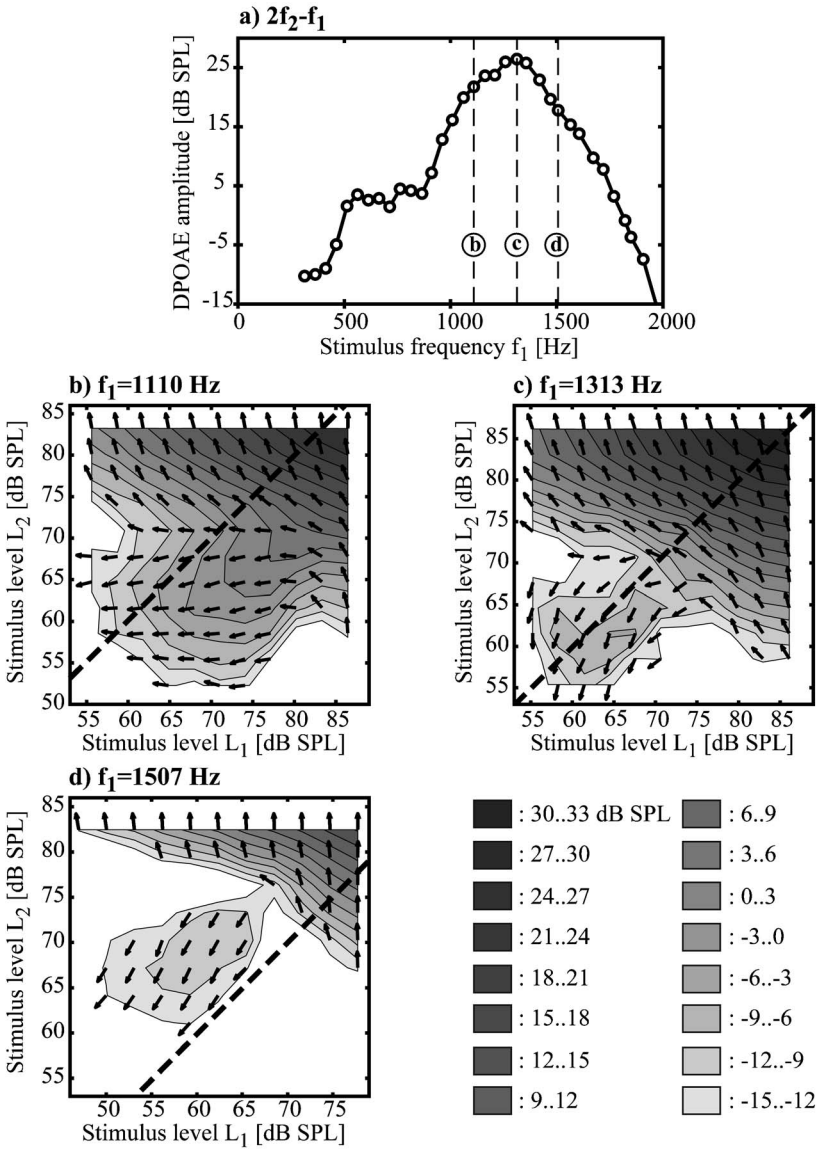

FIG. 4. DPOAEs at $2f_2-f_1$ from the basilar papilla for $f_2/f_1=1.30$. (a) DPOAE amplitude as a function of stimulus frequency f_1 obtained with $L_1=L_2=80$ dB SPL. The vertical dashed lines give the frequencies ($f_1=1110,1313,1507$ Hz) for which L_1,L_2 recordings were made. The labels on these dashed lines refer to the subplots in the figure. (b)–(d) Amplitude and phase of DPOAEs as function of stimulus levels L_1 and L_2. The diagonal dashed line in each subplot corresponds to $L_1=L_2$. The position of the low-level ridge relative to this diagonal depends on the stimulus frequency; compare subplots (b), (c), and (d). DPOAE amplitudes are coded in gray in 3 dB intervals, with the corresponding levels given in the key. The DPOAE phase is represented by the arrows overlying the contour lines, with a full counterclockwise rotation of the arrows corresponding to a phase lag of 2π rad.

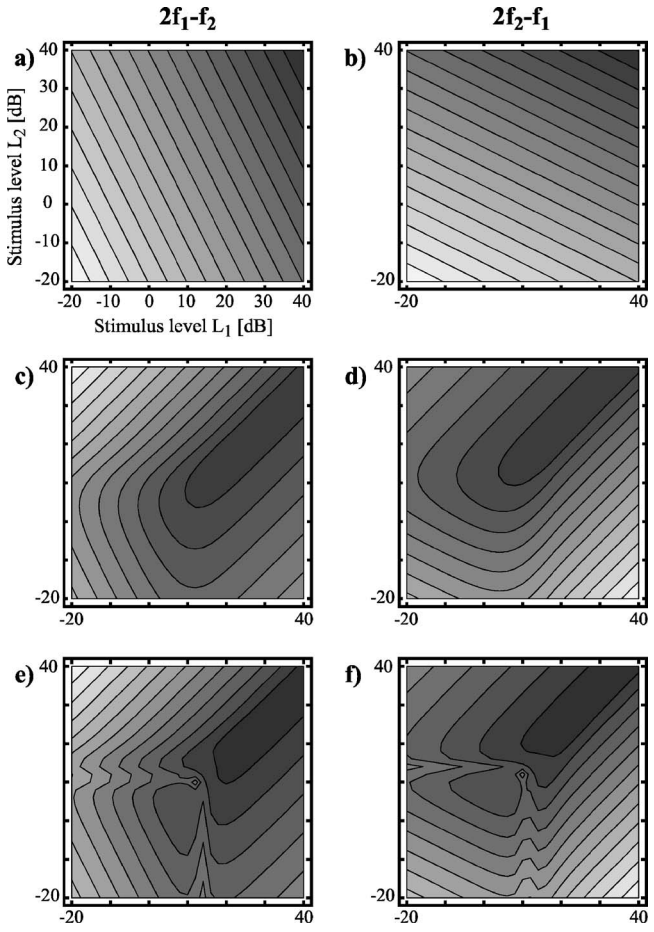

FIG. 5. L_1,L_2 maps for three static nonlinear models. For each model, results are shown for the distortion product at $2f_1-f_2$ (left column) and at $2f_2-f_1$ (right column). Contour lines were calculated at 10 dB intervals. (a) Amplitude at $2f_1-f_2$ for a cubic nonlinearity $y=x^3$. (b) Amplitude at $2f_2-f_1$ for the same nonlinear model. (c) and (d) Results for the Boltzmann function $y=1/(1+\exp(-x))$. (e) and (f) Results for a Boltzmann function with a shifted operation point: $y=1/(1+\exp(-x+3))$. The combination of the cubic nonlinearity [panels (a) and (b)] with a Boltzmann nonlinearity [panels (c) and (d)] may account for the L_1,L_2 maps recorded in the frog. The Boltzmann function with a shifted operation point may describe the transition from low- to high-level emissions. However, in that model the high-level contour lines do not match the approximately linear contour lines observed in the frog.

lines that followed (approximately) straight lines. In contrast, contour lines for low-level DPOAEs were clearly convex (e.g., Fig. 1). In mammals, L_1,L_2 maps show a similar difference between high-level and low-level DPOAEs (Mills *et al.*, 1993; Mills and Rubel, 1994; Whitehead *et al.*, 1995), while DPOAE I/O curves recorded in birds and reptiles indicate similar level-dependent differences in these vertebrate classes (Manley *et al.*, 1993; Kettembeil *et al.*, 1995; Taschenberger and Manley, 1998).

The shape of the contour lines reflects fundamental properties of the nonlinearity that underlies DPOAE generation. For a cubic nonlinear system,

$$y = x^3, \tag{1}$$

contour lines are straight [see Figs. 5(a) and 5(b)], similar to the high-level DPOAEs in both frogs and mammals. Small deviations from straight contour lines may occur for nonlinearities described by $y=\text{sign}(x)|x|^{\nu}$. For $\nu>3$, contour lines are concave while for $\nu<3$ ($\nu\neq 1$) contour lines are convex. The slope of the contour lines for a cubic nonlinearity is $L_2/L_1=-2$ dB/dB for $2f_1-f_2$ and $L_2/L_1=-0.5$ dB/dB for $2f_2-f_1$, which is similar to the slopes of the high-level contour lines found here (e.g., Fig. 1).

If the nonlinearity has an (asymptotic) output clipping level, the contour lines have a shape that is markedly different. As an example, Figs. 5(c) and 5(d) show the L_1,L_2 dependence of distortion product amplitude for a Boltzmann nonlinearity,

$$y = \frac{1}{1+e^{-x}}, \tag{2}$$

which clips to $y=1$ for $x\to\infty$ and $y=0$ for $x\to-\infty$. Here, the contour lines are convex, running parallel to the diagonal $L_1=L_2$ in part of the L_1,L_2 space. Low-level DPOAEs from the frog had a dependence on the stimulus level, which is consistent with a clipping nonlinearity, such as the Boltzmann function.

In mammals, low-level contour lines are also convex, but, in general, the low-level ridge is not parallel to the diagonal $L_1=L_2$ (Whitehead *et al.*, 1992; Kummer *et al.*, 2000; Pibal *et al.*, 2002). Kummer *et al.* (2000) and others interpreted this as being a manifestation of the differential growth of each stimulus amplitude at the presumed location of DPOAE generation, which results from the different growth of basilar membrane vibration at different locations along the cochlea (e.g., Ruggero and Rich, 1991). As such, it reflects the transformation of stimulus amplitudes at the tympanic membrane to stimulus amplitudes at the site of DPOAE generation.

In our results, the low-level ridge was parallel to $L_1=L_2$, suggesting that the stimulus-induced vibration of the tectorial membranes in both the AP and the BP have the same growth rate. In other words, the tectorial membrane response may grow nonlinearly and compressively, but in contrast to the mechanics in the mammalian cochlea, this growth has to be the same for both stimulus frequencies. Note that the finding that the low-level ridge may be shifted away from $L_1=L_2$ (Fig. 4) indicates that equal stimulus levels at the tympanic membrane not necessarily result in equal-amplitude vibrations in the tectorial membrane.

Typically, the observed level dependence of DPOAEs are interpreted as being the result of two level-dependent components (e.g., Kim, 1980; Whitehead *et al.*, 1992). Here, one component is dominant for high-level stimuli, while the second component dominates for low-level stimuli. Based on the differential vulnerability of the two components, it has been suggested that each component arises from a different mechanism (Mills *et al.*, 1993). In this two-source model the low-level component is linked to active hair cell mechanics, while the high-level component arises from a passive nonlinearity, possibly not associated with the hair cells.

Recently, doubt has risen whether the two-source model is applicable to DPOAE generation (Mills, 2002). Frolenkov *et al.* (1998) showed that chemical blocking of the outer hair cell motility abolishes both low-level and high-level DPOAEs in the guinea pig, while Mom *et al.* (2001) provided evidence that the high-level DPOAEs that remain after

cochlear ischemia are highly vulnerable to acoustic overstimulation. These results indicate that the high-level and low-level DPOAEs in mammals depend on active mechanisms. Model studies have shown that a properly configured, single Boltzmann nonlinearity can account for the nonmonotonicities and associated phase shifts seen in mammalian DPOAE I/O data (Lukashkin and Russell, 1998). When such models incorporate feedback they can also reproduce the differential vulnerability of low-level and high-level DPOAEs (Lukashkin *et al.*, 2002). Also, Mills (1997) proposed a model in which one type of active nonlinearity generates DPOAEs. The artificial separation of emissions generated at different locations along the basilar membrane results in the appearance of a "passive" and an "active" component that both arise from the same nonlinearity. In short, the combination of these results imply that both high-level and low-level DPOAEs may arise from one type of active nonlinearity.

However, Liberman *et al.* (2004) showed that mice lacking the protein prestin in their hair cell's basolateral membrane (i.e., the presumed motor molecule of the cochlear amplifier is missing) do generate high-level DPOAEs, indicating that hair cell electromotility is not required for their generation. In addition, they found that after death these high-level DPOAEs disappear rapidly, with a time course similar to the post-mortem disappearance of the cochlear microphonic. Therefore, these "residual" high-level DPOAEs were clearly of biological origin and arose from a second active nonlinear mechanism that is perhaps related to the hair cell stereovillar bundles.

In a single Boltzmann nonlinear model, a transition from low- to high-level DPOAEs is accomplished by a shift of the operation point of the Boltzmann curve (Lukashkin and Russell, 1998). Regardless of the choice of operation point, the Boltzmann nonlinearity is a clipper for large stimulus amplitudes. Thus, a Boltzmann nonlinearity exhibits a transition from low to high levels, but the high-level contour lines are parallel to the main diagonal in the L_1,L_2 maps [see Figs. 5(e) and 5(f)]. This is in sharp contrast with our experimental findings [e.g., Figs. 1(a) and 1(b)]: the frog high-level contour lines were consistent with a cubic-nonlinear function [Eq. (1)]. Thus, we reject a single Boltzmann nonlinearity as a possible model for both low- and high-level DPOAE generation in the frog.

The applicability of the model proposed by Mills (1997) to the frog ear can be excluded *a priori*. Although it results in similar L_1,L_2 maps as in the frog ear, tonotopy is an essential part of the model. Since the basilar papilla is not tonotopically organized, its general applicability to the frog ear is excluded. Also, the frequency dependence of the phase shift between the low-level and the high-level DPOAEs (Fig. 3) suggests that two nonlinear mechanisms are involved in emission generation. These two mechanisms are somehow coupled by a dynamic element (e.g., a spring or a resistor).

There exist important differences in the growth of low-level DPOAEs from the AP and the mammalian cochlea on the one hand, and from the BP on the other hand. The extensive low-level plateaus in the AP indicate that the DPOAE amplitude grows compressively (<1 dB/dB) with increasing low-level stimuli, while at low levels growth in the BP was expansive (>1 dB/dB). The Boltzmann nonlinearity results in expansive growth of the low-level distortion products, in accordance with the expansive growth of low-level DPOAEs in the BP (Meenderink and Van Dijk, 2004; this work). The Boltzmann nonlinearity has been proposed to describe the relationship between the hair bundle deflection and the transduction current in hair cells (Crawford *et al.*, 1989). Thus, DPOAE amplitude in the BP may be proportional to the transduction current in hair cells.

The compressive growth rate in the AP and the mammalian cochlea may be interpreted as being the result of an automatic gain control in these hearing organs. In other words, the generation of DPOAEs may be proportional to the transduction current in hair cells (described by the Boltzmann nonlinearity), but the measured DPOAE amplitude growth may reflect the additive effect of a compressive amplification mechanism.

In conclusion, our L_1,L_2 maps support the notion of two DPOAE-generation mechanisms in the frog. One component dominates for low-level stimuli, while the other is dominant for high-level stimuli. These components differ substantially with respect to their dependence on the stimulus levels, L_1 and L_2. Combined with the finding that the phase difference between the two components varies with frequency, this suggests that different mechanisms underlie their generation.

ACKNOWLEDGMENTS

This work was supported by grants from the Netherlands Organization for Scientific Research (NWO), and the Heinsius Houbolt Foundation.

Brown, A. M. (**1987**). "Acoustic distortion from rodent ears: A comparison of responses from rats, guinea pigs, and gerbils," Hear. Res. **31**, 25–38.

Brownell, W. E., Bader, C. R., Bertrand, D., and de Ribaupierre, Y. (**1985**). "Evoked mechanical responses of isolated cochlear outer hair cells," Science **227**, 194–196.

Crawford, A. C., Evans, M. G., and Fettiplace, R. (**1989**). "Activation and adaptation of transducer currents in turtle hair cells," J. Physiol. (London) **419**, 405–434.

Frolenkov, G. I., Belyantseva, I. A., Kurc, M., Mastroianni, M. A., and Kachar, B. (**1998**). "Cochlear outer hair cell electromotility can provide force for both low and high intensity distortion product otoacoustic emissions," Hear. Res. **126**, 67–74.

Froymovich, O., Rebala, V., Salvi, R. J., and Rassael, H. (**1995**). "Long-term effect of acoustic trauma on distortion product otoacoustic emissions in chickens," J. Acoust. Soc. Am. **97**, 3021–3029.

Kettembeil, S., Manley, G. A., and Siegl, E. (**1995**). "Distortion-product otoacoustic emissions and their anesthesia sensitivity in the European Starling and the chicken," Hear. Res. **86**, 47–62.

Kim, D. O. (**1980**). "Cochlear mechanics: Implications of electrophysiological and acoustical observations," Hear. Res. **2**, 297–317.

Kummer, P., Janssen, T., Hulin, P., and Arnold, W. (**2000**). "Optimal L_1-L_2 primary tone level separation remains independent of test frequency in humans," Hear. Res. **146**, 47–56.

Lewis, E. R. (**1978**). "Comparative studies of the anuran auditory papillae," Scan Electron Microsc. **II**, 633–642.

Lewis, E. R. (**1992**). "Convergence of design in vertebrate acoustic sensors," in *The Evolutionary Biology of Hearing*, edited by D. B. Webster, R. R. Fay, and A. N. Popper (Springer-Verlag, New York), pp. 163–184.

Lewis, E. R., Leverenz, E. L., and Koyama, H. (**1982**). "The tonotopic organization of the bullfrog amphibian papilla, an auditory organ lacking a basilar membrane," J. Comp. Physiol. **145**, 437–445.

Liberman, M. C., Zuo, J., and Guinan, J. J., Jr. (**2004**). "Otoacoustic emissions without somatic motility: Can stereocilia mechanics drive the mammalian cochlea?," J. Acoust. Soc. Am. **116**, 1649–1655.

Lukashkin, A. N., Lukashkina, V. A., and Russell, I. J. (**2002**). "One source

for distortion product otoacoustic emissions generated by low- and high-level primaries," J. Acoust. Soc. Am. **111**, 2740–2748.
Lukashkin, A. N., and Russell, I. J. (**1998**). "A descriptive model of the receptor potential nonlinearities generated by the hair cell mechanoelectrical transducer," J. Acoust. Soc. Am. **103**, 973–980.
Manley, G. A., Köppl, C., and Johnstone, B. M. (**1993**). "Distortion-product otoacoustic emissions in the bobtail lizard. I. General characteristics," J. Acoust. Soc. Am. **93**, 2820–2833.
Meenderink, S. W. F., Narins, P. M., and Van Dijk, P. (**2005**). "Detailed f_1,f_2 area study of distortion product otoacoustic emissions in the frog," J. Assoc. Res. Otolaryngol. **6**, 37–47.
Meenderink, S. W. F., and Van Dijk, P. (**2004**). "Level dependence of distortion product otoacoustic emissions in the leopard frog, *Rana pipiens pipiens*," Hear. Res. **192**, 107–118.
Mills, D. M. (**1997**). "Interpretation of distortion product otoacoustic emission measurements. I. Two stimulus tones," J. Acoust. Soc. Am. **102**, 413–429.
Mills, D. M. (**2002**). "Interpretation of standard distortion product otoacoustic emission measurements in light of the complete parametric response," J. Acoust. Soc. Am. **112**, 1545–1560.
Mills, D. M., Norton, S. J., and Rubel, E. W. (**1993**). "Vulnerability and adaptation of distortion product otoacoustic emissions to endocochlear potential variation," J. Acoust. Soc. Am. **94**, 2108–2122.
Mills, D. M., and Rubel, E. W. (**1994**). "Variation of distortion product otoacoustic emissions with furosemide injection," Hear. Res. **77**, 183–199.
Mom, T., Bonfils, P., Gilain, L., and Avan, P. (**2001**). "Origin of cubic difference tones generated by high-intensity stimuli: effect of ischemia and auditory fatigue on the gerbil cochlea," J. Acoust. Soc. Am. **110**, 1477–1488.
Pibal, I., Drexl, M., and Kössl, M. (**2002**). "Level dependence of optimal stimulus level difference for evoking DPOAEs in the gerbil," Hear. Res. **174**, 260–263.
Ronken, D. A. (**1990**). "Basic properties of auditory-nerve responses from a 'simple' ear: The basilar papilla of the frog," Hear. Res. **47**, 63–82.
Ronken, D. A. (**1991**). "Spike discharge properties that are related to the characteristic frequency of single units in the frog auditory nerve," J. Acoust. Soc. Am. **90**, 2428–2440.
Ruggero, M. A., and Rich, N. C. (**1991**). "Application of a commercially-manufactured Doppler-shift laser velocimeter to the measurement of the basilar-membrane vibration," Hear. Res. **51**, 215–230.
Taschenberger, G., and Manley, G. A. (**1998**). "General characteristics and suppression tuning properties of the distortion-product otoacoustic emission $2f_1-f_2$ in the barn owl," Hear. Res. **123**, 183–200.
Van Dijk, P., and Manley, G. A. (**2001**). "Distortion product otoacoustic emissions in the tree frog *Hyla cinerea*," Hear. Res. **153**, 14–22.
Van Dijk, P., Wit, H. P., and Segenhout, J. M. (**1997**). "Dissecting the frog inner ear with Gaussian noise. I. Application of high-order Wiener-kernel analysis," Hear. Res. **114**, 229–242.
Whitehead, M. L., Lonsbury-Martin, B. L., and Martin, G. K. (**1992**). "Evidence for two discrete sources of $2f_1-f_2$ distortion-product otoacoustic emission in rabbit: I. Differential dependence on stimulus parameters," J. Acoust. Soc. Am. **91**, 1587–1607.
Whitehead, M. L., Stagner, B. B., McCoy, M. J., Lonsbury-Martin, B. L., and Martin, G. K. (**1995**). "Dependence of distortion-product otoacoustic emissions on primary levels in normal and impaired ears. II. Asymmetry in L_1,L_2 space," J. Acoust. Soc. Am. **97**, 2359–2377.

Coherent reflection in a two-dimensional cochlea: Short-wave versus long-wave scattering in the generation of reflection-source otoacoustic emissions

Christopher A. Shera[a)]
Eaton-Peabody Laboratory of Auditory Physiology, Massachusetts Eye and Ear Infirmary, 243 Charles Street, Boston, Massachusetts 02114 and Department of Otology and Laryngology, Harvard Medical School, Boston, Massachusetts 02115

Arnold Tubis
Department of Physics, Purdue University, West Lafayette, Indiana 47907 and Institute for Nonlinear Science, University of California—San Diego, La Jolla, California 92093

Carrick L. Talmadge
National Center for Physical Acoustics, University of Mississippi, University, Mississippi 38677

(Received 22 September 2004; revised 18 February 2005; accepted 1 March 2005)

The theory of coherent reflection filtering explains the empirical form of the cochlear reflectance by showing how it emerges from the coherent ''backscattering'' of forward-traveling waves by impedance perturbations in the mechanics of the cochlear partition. Since the theory was developed using the one-dimensional (1-D) transmission-line model of the cochlea, an obvious logical shortcoming is the failure of the long-wavelength approximation near the peak of the traveling wave, where coherent backscattering is purported to occur. Indeed, existing theory suggests that wave reflection may be strongly suppressed in the short-wave regime. To understand how short-wave behavior near the peak modifies the predictions of the long-wave theory, this paper solves the scattering problem in the 2-D cochlear model. The 2-D problem is reduced to a 1-D wave equation and the solution expressed as an infinite series in which successive terms arise via multiple scattering within the cochlea. The cochlear reflectance is computed in response-matched models constructed by solving the inverse problem to control for variations in mechanical tuning among models of different heights and dimensionality. Reflection from the peak region is significantly enhanced by the short-wave hydrodynamics, but other conclusions of the 1-D analysis—such as the predicted relation between emission group delay and the wavelength of the traveling wave—carry over with only minor modifications. The results illustrate the important role of passive hydromechanical effects in shaping otoacoustic emissions and cochlear tuning. [DOI: 10.1121/1.1895025]

PACS numbers: 43.64.Bt, 43.64.Kc, 43.64.Jb, 43.20.Bi [BLM] Pages: 287–313

I. INTRODUCTION

The theory of coherent reflection filtering describes the coherent backscattering of cochlear traveling waves by distributed mechanical perturbations within the organ of Corti. When combined with a description of sound transmission and reflection by the middle ear, the theory provides a comprehensive account of spontaneous and evoked otoacoustic emissions (OAEs) as well as the microstructure of the hearing threshold (e.g., Shera and Zweig, 1993b; Zweig and Shera, 1995; Talmadge *et al.*, 1998, 2000). Under conditions believed applicable at low and moderate sound levels, the theory predicts that the strongest backscattering occurs within the region about the peak of the traveling-wave envelope. For simplicity, the analysis of cochlear wave reflection that supports this conclusion was performed using the one-dimensional (long-wave) model of the cochlea. An obvious technical defect of this approach, however, is the breakdown of the long-wave assumption in the region near the peak of the traveling wave.

Validity of the long-wave assumption requires that the wavelength λ of the traveling wave be large compared to the dimensions of the scalae. A rough guideline specifies that $\lambda > 2\pi H$, where H is the height (or radius) of the cochlear duct (e.g., Lighthill, 1981; de Boer, 1996). Although the long-wave approximation is believed valid in the basal-most ''tail'' region of the cochlear response where OAEs couple to the middle ear (e.g., Nedzelnitsky, 1980), in the peak region the wavelength of the traveling wave is smaller than the dimensions of the scalae, and the short-wave model is more appropriate. For example, Fig. 1 shows estimates of the ratio $kH \equiv 2\pi H/\lambda$ evaluated at the peak of the traveling wave for both human and guinea pig. Although the values are only approximate, the conclusion is clear: Except perhaps in the apex of the guinea-pig cochlea, the long-wave assumption is everywhere violated at the peak of the traveling wave (see also de Boer, 2001). Since the long-wave assumption fails in precisely the region where coherent backscattering is pre-

a)Electronic mail: shera@epl.meei.harvard.edu

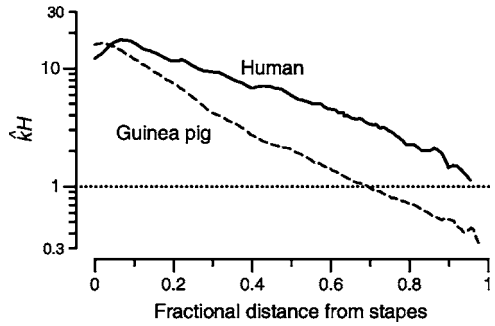

FIG. 1. Violation of the long-wave assumption at the peak of the traveling wave. The figure shows estimates of $\hat{k}H \equiv 2\pi H/\hat{\lambda}$ for the human (solid line) and guinea pig (dashed line) versus fractional distance from the stapes. The wavelength $\hat{\lambda}$ is evaluated at the peak, $\hat{x}(\omega)$, of the traveling wave envelope. For each species, the scala height H was defined as the radius of the equivalent circle (area equal to the combined areas of the scala vestibuli and tympani) as computed from measured scalae dimensions (Thorne *et al.*, 1999). Estimates of $\hat{\lambda}$ were obtained from otoacoustic measurements of stimulus-frequency emission (SFOAE) group delay transformed into equivalent wavelengths using local scaling symmetry and the cochlear map (Shera and Guinan, 2003, Table II). Cochlear maps were adjusted so that the total cochlear length matched the values reported by Thorne *et al.* (1999). Values of $\hat{k}H$ greater than 1 (dotted line) are inconsistent with the long-wave assumption.

dicted to occur, conclusions based on the one-dimensional analysis about the strength and character of wave reflection remain of uncertain validity.

Interestingly, the literature suggests that wave reflection may indeed differ profoundly in long- and short-wave cochlear models. For example, in Siebert's classic formulation of the short-wave model, waves propagating in the two directions satisfy a pair of first-order differential equations, each of which has an exact closed-form solution (e.g., Siebert, 1974; de Boer, 1979, 2001). Siebert's equations for the waves traveling in the two directions are uncoupled, suggesting that wave reflection (e.g., due to rapid spatial variations in the partition impedance) does not occur in a short-wave cochlea (e.g., de Boer, 1983). Zwislocki (1983, 2002) arrives at the same conclusion by an entirely different route. By transforming long- and short-wave models into equivalent transmission lines and analyzing their characteristic impedances, Zwislocki constructs an "unequivocal ... proof" that cochlear wave reflection, although inevitable in the long-wave model, cannot occur in the short-wave regime.

The apparent absence of reflections in the short-wave model has been invoked to explain a puzzle of mammalian cochlear anatomy:[1] Since so much of the important hydromechanical action in the cochlea appears confined to the immediate vicinity of the cochlear partition (e.g., Olson, 2001), why do the scalae vestibuli and tympani grow considerably larger than seems necessary to house the organ of Corti? Because the presence of large reverse-traveling waves would presumably complicate the detection and analysis of sound, perhaps the scalae have evolved their present sizes, so the argument goes, because the hydrodynamics in the peak region need to be short-wave in order to suppress the reflection of traveling waves. If these ideas are correct, and scattering off perturbations in the short-wave region near the peak of the traveling wave is significantly suppressed, or perhaps even nonexistent, then current understanding of OAE generation needs substantial revision.

However, careful examination of the arguments against short-wave reflection suggests that the jury may still be out. Zwislocki's proof, for example, hinges on the validity of his demonstration that in the short-wave limit the characteristic impedance of the equivalent transmission line becomes independent of the partition impedance. But so counter-intuitive is this result that corollary conclusions about wave reflection are hard to credit without independent corroboration. Although Siebert's uncoupled equations might be cited in this regard, closer inspection reveals that they offer no compelling assurances. As Siebert himself makes clear, the derivation of his equations hinges on assumptions that are violated in the presence of irregular perturbations ("roughness") in the mechanics. In particular, Siebert (unlike Zwislocki) assumes that the mechanics of the partition vary so smoothly with position that spatial-frequency components in the partition impedance that unnecessarily complicate his analysis by coupling forward- and reverse-traveling waves can safely be neglected. Without this explicit assumption of mechanical smoothness—an assumption manifestly invalid in the presence of roughness—Siebert's neat decoupling of forward and reverse waves cannot be obtained. Consequently, Siebert's equations cannot be used to understand the nature of wave reflection in the short-wave regime. Although de Boer (2001) has shown that Siebert's two first-order equations can be combined into a single second-order equation that supports both forward- and reverse-traveling waves—and, by implication, the possibility of internal reflection—the procedure remains grounded on equations that apply only in the absence of mechanical perturbations.

The analysis of cochlear wave reflection clearly requires a theory of wave scattering valid in the short-wave regime. Unfortunately, current understanding appears doubly unsatisfactory, for the relevant theories appear mutually exclusive, with no obvious overlapping regions of validity. Whereas the theory of coherent reflection was developed using assumptions about cochlear hydrodynamics that break down in the short-wave regime purported to encompass the region of maximal scattering, the classic theory of the short-wave regime relies on assumptions about the mechanics that fail in the presence of perturbations that might scatter the wave. In this paper, we resolve the dilemma by developing a cochlear scattering formalism for a two-dimensional cochlear model that supports both long and short waves and the transition between the two. Our analysis makes no implicit smoothness assumptions and remains valid in the presence of mechanical perturbations. We apply the formalism to investigate whether—and if so how—the predictions of the long-wave theory of reflection-source OAEs change when the modeling framework is extended to capture the short-wave behavior near the peak of the traveling wave.

Overview

Our argument has three parts and a prologue. After perusing this synopsis, readers interested primarily in the conclusions rather than their logical justification might skip

ahead to part three (Sec. VI) on the assumption that all's well that ends well. For reference, Appendix E contains a list of frequently used symbols.

Preparatory to anything else we begin by reviewing relevant assumptions and deriving the equations for a two-dimensional (2-D) cochlear model with mechanical perturbations (or roughness) in the partition (Sec. II). Our goal is to understand the effects of long- versus short-wave scattering on the properties of reflection-source OAEs. Since bidirectional coupling between the ear canal and the basal, long-wave region of the cochlea is well described by 1-D theory (e.g., Nedzelnitsky, 1980; Shera and Zweig, 1992a; Talmadge *et al.*, 1998; Puria, 2003), our concern here is only to understand the physics that gives rise to reverse-traveling waves within the cochlea (i.e., the mechanisms of emission generation). As viewed from the stapes, backscattering of traveling waves manifests itself as a nonzero value of the cochlear reflectance, R, defined as the ratio of the outgoing to the ingoing pressure waves at the stapes. Our strategy is therefore to calculate R in models of different heights or dimensionality.

The first part of the argument then begins in Sec. III, where we show how the general 2-D problem can be reduced to a 1-D wave equation by considering the pressure averaged over the scalae area, as originally suggested by Duifhuis (1988; see also Zwislocki, 1953). At the base of the cochlea this averaged pressure determines the net force on the stapes and therefore controls how OAEs couple to the middle ear. Traveling-wave solutions in the smooth cochlea permit the definition of "projection operators" that decompose the averaged pressure into components representing forward- and reverse-traveling waves. By introducing the scalae-averaged response to an oscillating point source located on the BM (the "reduced traveling-wave Green's function"), we then show that the model solution in the presence of perturbations takes the form of an infinite series in which successive terms arise physically via multiple wave scattering within the cochlea (Sec. IV). We derive an approximate expression for the reduced traveling-wave Green's function valid in the "far field" at some distance from the source (e.g., near the stapes). Using the projection operators to extract the wave components then yields a first-order perturbative expression for the cochlear reflectance, R.

In the second part we argue that comparing values of R calculated in models of different heights requires compensating for variations in mechanical tuning that would otherwise arise were the BM impedance function held constant (Sec. V). To control for variations in tuning we need to find the BM impedance that yields a given velocity response in a model of specified height, and we develop a new method for solving this cochlear "inverse problem."

In the third and final part we bring everything together and compute the cochlear reflectance in response-matched 1-D and 2-D models of various heights (Sec. VI). We use the results to compare and contrast the nature of wave scattering in long- and short-wave models. We find that the reflection from the peak region—rather than being reduced or even eliminated relative to the long-wave case, as suggested by Zwislocki's analysis—is actually enhanced in the short-wave regime. In effect, the hydrodynamics of the short-wave regime act to magnify the effective size of the perturbations located within the peak of the traveling wave. In other respects, however, the principal conclusions of the 1-D analysis—such as the predicted relation between emission group delay and the wavelength of the traveling wave—survive with only minor modification.

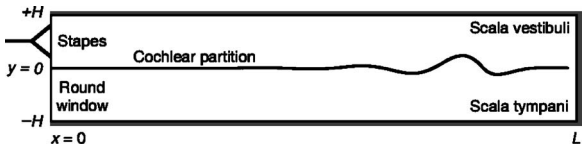

FIG. 2. Sagittal spacetime slice through the two-dimensional box model. The scala vestibuli and scala tympani are assumed to have equal rectangular cross sections of height H. In the z direction perpendicular to the page the width of the scalae is assumed to be everywhere much less than a wavelength so that the model is effectively two dimensional. The cochlear partition, schematized here as a thin membrane partaking in a traveling wave, manifests micromechanical impedance perturbations arising from its discrete cellular architecture. Note that the partition displacement has been grossly exaggerated to make the wave visible on the scale of the figure.

II. A TWO-DIMENSIONAL COCHLEA WITH PERTURBATIONS

A. Assumptions of the model

For clarity of exposition, we make several simplifying assumptions in order to eliminate technical complications that obscure the most important points of the analysis.

First and foremost, we work with the simplest geometry that manifests both long- and short-wave behavior. In particular, we assume a linear, two-dimensional box model of the cochlea with incompressible and inviscid scala fluids (see Fig. 2). The x axis extends longitudinally from the base ($x=0$), and the y axis is oriented perpendicular to the basilar membrane (BM), which is located in the xz plane and spans the entire width, b, of the cochlea (a configuration de Boer has referred to as "wall-to-wall carpeting" with a stereociliary shag). Except at the two windows, we assume that the box is surrounded by rigid bone so that no net fluid enters or leaves the cochlea at acoustic frequencies; the volume displacements of the two windows are therefore equal and opposite.

In the 1-D model, the wavelengths of the waves on the cochlear partition are assumed to be large relative to the heights (and widths) of the scalae so that the pressures and fluid velocities are nearly uniform in any "radial" cross section parallel to the yz plane. Here, we relax this "long-wavelength" assumption and allow the dynamical variables to depend on y, the height above the partition. Effectively, we assume that the width b of the BM—but not necessarily the height H of the scalae—is everywhere much less than a wavelength. Since the pressure field is assumed to be independent of z, the problem is $2+1$ dimensional (2 space, 1 time).

We neglect possible complex spatial variations in the pressure in the immediate vicinity of the oval and round windows at $x=0$; in effect, we assume that the two windows move as rigid pistons with areas that match those of their respective scalae. Furthermore, we assume that the cochlea is

effectively semi-infinite in extent (or, equivalently, that stimulus frequencies are not so low that reflections from the helicotrema and the apical wall contribute significantly to the response). Thus, the only source of apical cochlear wave reflections that we consider is BM roughness, whose perturbative effects are discussed in Sec. IV.

Since the model is linear, its response to any stimulus is completely determined by its response to pure tones. We therefore assume harmonic time dependence and write pressures, velocities, and other dynamical variables as complex Fourier amplitudes representing responses at angular frequency ω [e.g., $v_{\mathrm{BM}}(x,t)=\mathrm{Re}\{V_{\mathrm{BM}}(x,\omega)e^{i\omega t}\}$], where ω is 2π times the stimulus frequency, f. Fourier transformation converts the third (temporal) dimension to frequency; for notational simplicity, we usually leave the functional dependence on frequency implicit and refer to the model as two-dimensional (2-D).

The pressure field in the cochlea can be separated into terms symmetric and antisymmetric about the BM (sum and difference pressures, respectively). Since the two model scalae are symmetric about the BM, the sum and difference pressures are decoupled. We assume that the cochlear partition responds only to the pressure difference across its surface (e.g., Voss *et al.*, 1996), and not to the absolute pressure within the scalae; consequently, we need only consider the pressure difference $P(x,y)$ that gives rise to the classical traveling wave. The difference pressure is defined by $P(x,y)\equiv p(x,y)-p(x,-y)$, where $p(x,y)$ is the scala pressure (i.e., the scala-vestibuli pressure for $y>0$ and the scala-tympani pressure for $y<0$). The pressure difference is antisymmetric about the partition: $P(x,-y)=-P(x,y)$.

B. Synopsis of the model equations

With the exception of an explicit consideration of perturbations in the mechanics of the partition, the equations and boundary conditions describing the model are completely standard (for reviews see Viergever, 1980; de Boer, 1996). All equations follow immediately from Newton's laws; we catalog them here in order to introduce our notation.

Fluid dynamics and boundary conditions. The linearized Euler equation (Newton's second law) and the assumed incompressibility of the cochlear fluids together imply that the pressure difference $P(x,y)$ satisfies Laplace's equation,

$$\nabla^2 P(x,y)=(\partial_x^2+\partial_y^2)P=0, \tag{1}$$

where we have adopted the notational shorthand $\partial_x\equiv\partial/\partial x$. Since the scalae walls are assumed rigid, the normal component of the fluid velocity, and hence the corresponding component of the pressure gradient, must vanish at $y=\pm H$:

$$\partial_y P|_{y=\pm H}=0. \tag{2}$$

Just above the cochlear partition, the fluid velocity must equal the velocity of the BM. Thus,

$$\partial_y P|_{y=0^+}=2i\omega\rho_0 V_{\mathrm{BM}}, \tag{3}$$

where ρ_0 is the density of the cochlear fluids and positive BM displacements are those produced (at $t=0^+$) by positive displacements of the stapes (i.e., positive *into* the scala tympani).

Coupling with the middle ear. Just inside the oval window the x (or longitudinal) component of the fluid velocity must equal the velocity of the stapes. Consequently,

$$U_{\mathrm{sv}}(0)=U_{\mathrm{ow}}, \tag{4}$$

where U_{ow} is the volume velocity of the oval window; $U_{\mathrm{sv}}\equiv\mathbf{U}_{\mathrm{sv}}\cdot\mathbf{e}_x$, with $\mathbf{e}_x$ denoting the unit vector in the longitudinal direction; and $\mathbf{U}_{\mathrm{sv}}(x)$, the scala-vestibuli volume velocity, is given in terms of the fluid particle velocity, $\mathbf{u}_{\mathrm{sv}}(x,y)$, by

$$\mathbf{U}_{\mathrm{sv}}(x)\equiv b\int_0^H \mathbf{u}_{\mathrm{sv}}(x,y)dy. \tag{5}$$

Analogous expressions hold for the longitudinal component of the scala-tympani volume velocity, $U_{\mathrm{st}}(x,y)$.

Equation (4) can be expressed in terms of the pressure by integrating the linearized Euler equation over the scalae to obtain

$$\partial_x\bar{P}=-Z_{\mathrm{f}}U, \tag{6}$$

where $U\equiv(U_{\mathrm{sv}}-U_{\mathrm{st}})/2$ and the average pressure $\bar{P}(x)$ is defined by

$$\bar{P}(x)\equiv\frac{1}{H}\int_0^H P(x,y)dy. \tag{7}$$

The impedance Z_{f} is defined by

$$Z_{\mathrm{f}}\equiv 2i\omega\rho_0/S, \tag{8}$$

where $S\equiv bH$ is the scala area. Z_{f} has units of acoustic impedance per unit length and characterizes the effective acoustic mass of the fluids. Because the cochlear contents and their bony enclosure have been assumed incompressible, $U_{\mathrm{sv}}+U_{\mathrm{st}}=0$ (e.g., Shera and Zweig, 1992b); consequently $U\equiv(U_{\mathrm{sv}}-U_{\mathrm{st}})/2=U_{\mathrm{sv}}$. The stapes boundary condition [Eq. (4)] therefore becomes

$$\partial_x\bar{P}|_{x=0}=-Z_{\mathrm{f}}U_{\mathrm{ow}}. \tag{9}$$

Since our focus here is the physics of wave scattering in the cochlea, we do not employ equations relating intracochlear pressures to those measured in the ear canal. At frequencies well below the maximum characteristic frequency of the partition, the coupling of OAEs into the middle ear involves pressures in the long-wave regime, and the 1-D theory remains valid even if the peak region is short wave. Equations describing sound transmission and reflection by the middle ear are discussed elsewhere (e.g., Shera and Zweig, 1992a,c; Peake *et al.*, 1992; Talmadge *et al.*, 1998; Schairer *et al.*, 2003). Here, we characterize the mechanical and acoustical effects of the external world seen from the cochlea, including the middle ear and any sound sources in the ear canal, by their Thévenin-equivalent source pressure and impedance (e.g., Beranek, 1986). The Thévenin-equivalent impedance can in turn be represented as an equivalent reflection coefficient, R_{stapes}, characterizing the reflection of reverse-traveling waves incident upon the stapes (e.g., Carlin and Giordano, 1964; Shera and Zweig, 1991; Talmadge *et al.*, 1998).

Dynamics of the cochlear partition. The cochlear partition is represented by an effective point impedance function that characterizes the motion induced by the pressure difference across its surface. $\tilde{Z}_{\mathrm{BM}}(x)$ is defined by

$$\tilde{Z}_{\mathrm{BM}}(x) \equiv \frac{P(x,0^+)}{bV_{\mathrm{BM}}(x)}. \tag{10}$$

We have included the factor of b in the definition, thereby giving the impedance units of acoustic impedance times length, so that it matches the definition employed in the 1-D transmission-line model. As explained below, the diacritical tilde indicates the presence of mechanical perturbations. When rewritten in terms of the BM impedance, the BM boundary condition [Eq. (3)] assumes the form

$$\partial_y \ln P\big|_{y=0^+} = \frac{2i\omega\rho_0}{b\tilde{Z}_{\mathrm{BM}}} = HZ_{\mathrm{f}}/\tilde{Z}_{\mathrm{BM}}(x). \tag{11}$$

Note that we have left the functional form of $\tilde{Z}_{\mathrm{BM}}(x)$ completely unspecified. In order to provide a concrete example, we later determine the BM impedance by requiring that the model reproduce a given BM velocity response.

Perturbations in the mechanics. At the micromechanical level, the properties of the cochlear partition presumably vary somewhat irregularly with position (e.g., due to spatial variations in the number, geometry, or mechanical characteristics of the outer hair cells). This micromechanical "roughness" appears superimposed on an overall smooth variation of the mechanics responsible for such things as the cochlear mapping between frequency and position. We represent these micromechanical irregularities as small perturbations, $\Delta Z_{\mathrm{BM}}(x)$, in the impedance of the partition. To indicate that the impedance includes perturbations arising from irregularities in the mechanics, we write $\tilde{Z}_{\mathrm{BM}}(x)$ with a diacritical tilde. Thus,

$$\tilde{Z}_{\mathrm{BM}}(x) = Z_{\mathrm{BM}}(x) + \Delta Z_{\mathrm{BM}}(x), \tag{12}$$

where $Z_{\mathrm{BM}}(x)$ is the "smooth" component of the impedance obtained by "ironing out" the perturbations ΔZ_{BM}.

C. Statement of the problem

Otoacoustic emissions are presumed to indicate the presence of reverse-traveling pressure waves within the cochlea. In a linear cochlea, these waves manifest themselves in the ear canal via their effect on the cochlear input impedance. As discussed in detail elsewhere (e.g., Shera and Zweig, 1993a; Zweig and Shera, 1995; Talmadge *et al.*, 1998), the problem boils down to computing the value of the cochlear reflectance, defined by

$$R \equiv \left.\frac{\bar{P}_l}{\bar{P}_r}\right|_{x=0}, \tag{13}$$

where $\bar{P}_{\{r,l\}}$ are the forward- and reverse-traveling components of the pressure $\bar{P}$ influencing the motion of the stapes. The subscripts $\{r,l\}$ designate waves traveling to the "right" and to the "left," respectively, consistent with the cochlear orientation illustrated in Fig. 2.

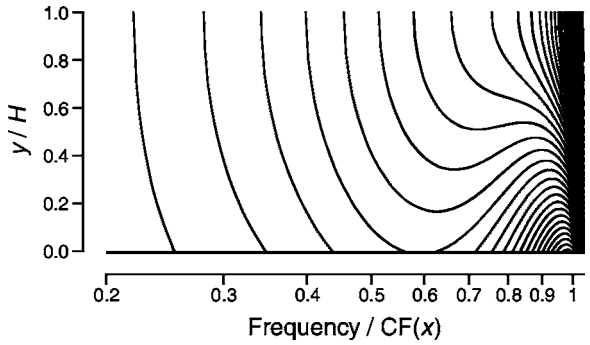

FIG. 3. Amplitude of the pressure field $P(x,y)$ in the scala vestibuli ($y>0$) for a 2-D model cochlea driven from the stapes with a pure-tone stimulus of frequency f. The spatial coordinate x varies along the abscissa and is shown in the form $f/\mathrm{CF}(x)$ so that the peak of the corresponding BM velocity response occurs at the value 1. The y coordinate is normalized by the model height, H (0.7 mm). The BM is represented by the line located along the bottom edge of the plot ($y=0$). Iso-pressure contours are spaced at intervals of 1 dB. The model's BM impedance function, with parameters chosen so that $\hat{k}H \cong 6$ (detailed in Appendix D, Table I), derives from the inverse solution of Zweig (1991) and varies smoothly with position ($\epsilon=0$). $P(x,y)$ was computed numerically using finite differences (e.g., Neely, 1981).

In a nutshell, the problem is to solve Eq. (1) for the pressure $P(x,y)$—subject to boundary conditions at the cochlear walls, stapes, and BM [Eqs. (2), (9), and (11)]—in order to determine how mechanical perturbations $\Delta Z_{\mathrm{BM}}(x)$ affect the cochlear response. By analogy with the scattering of light (e.g., by smoke or density fluctuations in the atmosphere), we expect the perturbations to "scatter" incident traveling waves back toward the stapes, where they contribute to the cochlear reflectance, R. This "scattering problem" has been solved for the 1-D long-wave model (Zweig and Shera, 1995; Talmadge *et al.*, 1998), and our purpose here is not merely to repeat the derivation in 2-D. Rather, our goal is to understand how the results depend on the short- or long-wave behavior of the model, that is, on the value of $\hat{k}H$, where $\hat{k}$ denotes the (real^2) wave number at the peak ($\hat{x}$) of the traveling wave, $\hat{k} \equiv k[\hat{x}(\omega),\omega]$. The character of the waves in the peak region varies inversely with $\hat{k}H$: when $\hat{k}H$ is small, the waves are long wave; when $\hat{k}H$ is large, the waves are short wave. In all cases we assume that the basal-most "tail" region of the cochlear response remains long wave ($k_0 H \ll 1$). This assumption is consistent with pressure measurements made in the basal region of the cochlea, which indicate that at frequencies well below the maximum characteristic frequency of the partition the wavelength of the cochlear traveling wave is large compared to the dimensions of the scalae (e.g., Nedzelnitsky, 1980).

Figure 3 illustrates these remarks by showing the pressure field $P(x,y)$ produced by a pure-tone stimulus in an active 2-D model of the cochlea with parameters chosen so that $\hat{k}H \cong 6$. (Appendix D provides details of the model and a synopsis of our numerical procedures, including the checks used to ensure integrity of the solution.) The iso-pressure contours, spaced at intervals of 1 dB, show that the pressure remains nearly uniform across the scalae in the basal-most tail region near the stapes but becomes highly nonuniform near the characteristic place, where the largest pressures are

found in the immediate vicinity of the BM (cf. Olson, 2001).

To explore the effects of perturbations in the mechanics we could simply assume some convenient form for $\tilde{Z}_{\mathrm{BM}}(x)$ and solve the model equations numerically, as we did for a model without perturbations in Fig. 3. However, understanding any differences between short- and long-wave scattering requires a more considered approach. As we will see, straightforward numerical simulations, if naively interpreted, can introduce spurious sources of variation that seriously compromise the analysis of short- versus long-wave scattering.

III. REDUCTION TO A ONE-DIMENSIONAL WAVE EQUATION

The derivation of a perturbative theory of coherent wave reflections in the 1-D framework is greatly simplified by the existence of an inhomogeneous one-dimensional wave (Helmholtz) equation for the pressure (e.g., Zweig and Shera, 1995; Talmadge *et al.*, 1998). We now derive a generalization of this equation for a 2-D model, based on the work of Duifhuis (1988; Talmadge *et al.*, 2001).

Otoacoustic emissions originating in the cochlea are manifest in the ear canal because of their coupling through the middle ear. As outlined above, this coupling depends on the pressure averaged over the stapes footplate. Our strategy is therefore to consider the quantity $\bar{P}(x)$, defined by Eq. (7) and reproduced below:

$$\bar{P}(x) \equiv \frac{1}{H}\int_0^H P(x,y)\,dy. \tag{14}$$

An equation for $\bar{P}(x)$ can be obtained by averaging $\nabla^2 P$ [Eq. (1)] over the upper duct and applying boundary conditions at the BM and $y=H$ [Eqs. (2) and (11)]. The result is

$$\partial_x^2 \bar{P} + \tilde{k}_{\mathrm{lw}}^2 P_0 = 0, \tag{15}$$

where

$$P_0(x) \equiv P(x,0^+). \tag{16}$$

The function $\tilde{k}_{\mathrm{lw}}(x)$ is given by

$$\tilde{k}_{\mathrm{lw}}^2(x) \equiv -Z_{\mathrm{f}}/\tilde{Z}_{\mathrm{BM}}(x), \tag{17}$$

where the fluid impedance Z_{f} is defined by Eq. (8).

Following Duifhuis (1988) we now introduce the function $\alpha(x)$, defined by

$$\alpha(x) \equiv \frac{P_0(x)}{\bar{P}(x)}. \tag{18}$$

At every location x the function $\alpha(x)$ is the ratio of the pressure driving the cochlear partition to the pressure averaged over the scalae cross section. The value of $\alpha(x)$ depends on the effective dimensionality of the fluid flow at location x. Since the largest pressures are found close to the partition, $|P_0| \geqslant |\bar{P}|$ so that $|\alpha| \geqslant 1$ in the traveling-wave region of the cochlea basal to $\hat{x}(\omega)$. To provide a concrete example, Figs. 4 and 5 show plots of $P_0(x)$, $\bar{P}(x)$, and their ratio, $\alpha(x)$, computed from the pressure field $P(x,y)$ produced by sinusoidal stimulation at the stapes (Fig. 3).

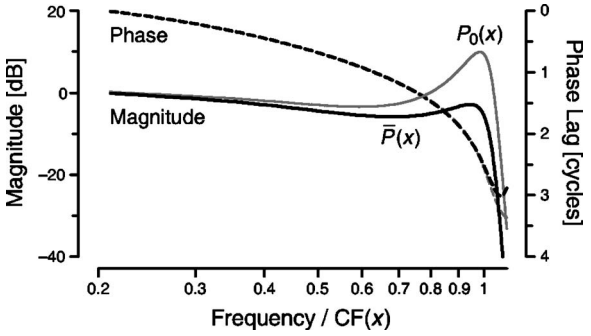

FIG. 4. $P_0(x)$ and $\bar{P}(x)$ computed from the pressure field shown in Fig. 3. Magnitudes (solid lines) are shown in dB (left-hand scale). Phases (dashed lines) are shown in cycles (right-hand scale). Both magnitude and phase are plotted relative to the value of $\bar{P}(0)$.

Rewriting Eq. (15) for $\bar{P}$ using Eq. (18) for α we find that the average pressure $\bar{P}(x)$ satisfies the one-dimensional wave equation

$$(\partial_x^2 + \tilde{k}^2)\bar{P} = 0, \tag{19}$$

where the complex-valued wave number, $\tilde{k}(x)$, is given by

$$\tilde{k}^2(x) \equiv \alpha(x)\tilde{k}_{\mathrm{lw}}^2(x) = -\alpha(x) Z_{\mathrm{f}}/\tilde{Z}_{\mathrm{BM}}(x). \tag{20}$$

Note that $\tilde{k} \to \tilde{k}_{\mathrm{lw}}$ in the long-wave regime where $\alpha \to 1$. For future convenience we write $\tilde{k}^2$ in the form

$$\tilde{k}^2(x) = k^2(x)[1+\epsilon(x)], \tag{21}$$

where $\epsilon(x)$ is related to the perturbations ΔZ_{BM} through the equation $\epsilon = -\delta/(1+\delta)$, with $\delta \equiv \Delta Z_{\mathrm{BM}}/Z_{\mathrm{BM}}$.

Character of the solution in the smooth cochlea

Before pursuing the effects of perturbations, we first explore the character of the solution in the smooth cochlea obtained by taking $\epsilon \to 0$, a process equivalent to ironing out the mechanical perturbations to recover the smooth wave number, $k(x)$. In the smooth cochlea Eq. (19) becomes

$$(\partial_x^2 + k^2)\bar{P} = 0. \tag{22}$$

Because the average pressure $\bar{P}(x)$ satisfies a one-dimensional wave equation, we expect the general solution

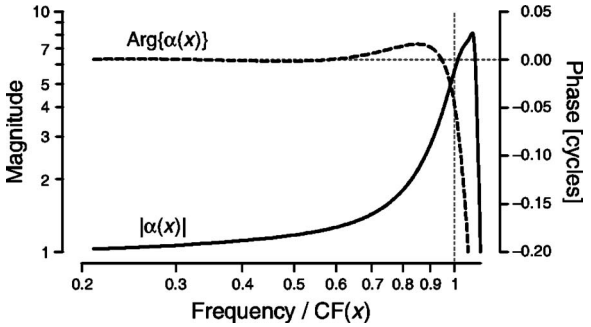

FIG. 5. The function $\alpha(x)$ defined as the ratio $P_0(x)/\bar{P}(x)$ computed from values shown in Fig. 4. Magnitude and phase scales are shown on the left- and right-hand sides of the plot, respectively. For reference, a horizontal dotted line intersects the phase ordinate at 0 cycles. A vertical dotted line locates the peak of the corresponding BM velocity response along the abscissa.

to comprise a superposition of waves traveling in opposite directions with local wavelength $\lambda(x)=2\pi/k(x)$. For example, in the long-wave regime $\alpha\to 1$ and thus $k\to k_{\mathrm{lw}}$. In this regime the impedance $Z_{\mathrm{BM}}(x)$ is dominated by the stiffness of the partition and the wave number $k\cong k_{\mathrm{lw}}$ is therefore essentially real. Equation (22) for $\bar{P}(x)$ thus has the standard Sturm-Liouville form so that its solutions can be presumed oscillatory (e.g., Ince, 1956; Courant and Hilbert, 1953); appropriate linear combinations can then be formed that represent waves traveling independently in opposite directions. Note, however, that the traveling-wave solutions for $\bar{P}(x)$ deduced from Eq. (22) are, at this point, only formal: Eq. (20) indicates that the wave number $k(x)$ depends on $\alpha(x)$, which remains undetermined except in the long-wave regime, where $\alpha\to 1$.

Duifhuis' (1988) procedure for reducing Eq. (15) to a one-dimensional wave equation can only be useful for investigating the reflection of cochlear traveling waves if the process is more than clever sleight-of-hand [for a review, see Jay (2001)]. In particular, the reduction must hold—with the same value of $\alpha(x)$—for waves traveling in both directions. We argue that this is true on general grounds.[3] Suppose we find a solution $P(x,y)$ to the model equations corresponding to a forward-traveling wave. For example, $P(x,y)$ can be computed numerically when the model is driven from the stapes (e.g., Fig. 3). In the basal, long-wave region of the cochlea, the solution will match the standard, one-dimensional solution for a forward-traveling wave. From the solution $P(x,y)$ we can compute the corresponding values of $\alpha(x)$ and $k(x)$, and we will find that the average pressure $\bar{P}(x)$ satisfies Eq. (22) exactly throughout the cochlea. But Eq. (22) is a second-order equation, and it therefore has another, independent solution with the same values of $k(x)$ and $\alpha(x)$. This additional solution has the form of a reverse-traveling wave; like the forward-traveling wave, it transforms smoothly into the standard long-wave solution in the basal region near the stapes.

IV. SOLVING FOR THE COCHLEAR REFLECTANCE

A. Basis waves and projection operators

The two independent traveling-wave solutions in the smooth cochlea constitute "basis waves" that define what is meant by forward- and reverse-traveling waves in a nonuniform medium (Shera and Zweig, 1991; Talmadge *et al.*, 1998). The basis waves, here denoted $W_{\{r,l\}}(x)$, are solutions of the homogeneous wave equation

$$(\partial_x^2+k^2)W_{\{r,l\}}=0. \tag{23}$$

By convention, the basis waves are dimensionless and are normalized so that $W_{\{r,l\}}(0)=1$. Their form can be obtained numerically or analytically using the WKB approximation. In Appendix A we present a procedure for suppressing reflection at the stapes in order to obtain pure forward- and reverse-traveling numerical solutions. We also derive approximate basis waves using the WKB approximation and show that they provide better solutions to Eq. (23) than those obtained from the "standard" WKB solutions for the 2-D model (e.g., Steele and Taber, 1979; Viergever, 1980; de Boer and Viergever, 1982).

The basis waves are central to our analysis because they allow the definition of "projection operators," $\hat{P}_{\{r,l\}}$, that decompose the total pressure at any point into components representing forward- and reverse-traveling waves.[4] The projection operators are defined so that

$$\bar{P}_{\{r,l\}}(x)=\hat{P}_{\{r,l\}}\{\bar{P}(x)\}; \tag{24}$$

they are given in terms of the basis waves $W_{\{r,l\}}(x)$ by the formula (Shera and Zweig, 1991)

$$\hat{P}_{\{r,l\}}=\pm\gamma W_{\{r,l\}}[\partial_x W_{\{l,r\}}-W_{\{l,r\}}\partial_x], \tag{25}$$

where the complex constant γ is the reciprocal of the Wronskian determinant [Eqs. (B5) and (B7)], with dimensions of length. Note that the basis waves $W_{\{r,l\}}(x)$ are eigenfunctions of the projection operators with eigenvalues of either 0 or 1.

Given a solution $\bar{P}(x)$ for the pressure obtained in the presence of mechanical perturbations, the projection operators $\hat{P}_{\{r,l\}}$ enable one to find the forward- and reverse-traveling wave components at any point in the cochlea. In particular, one can use them to determine the cochlear reflectance, defined by Eq. (13). Although the solution $\bar{P}(x)$ can, of course, be obtained numerically, the analytic expression derived in the next section provides crucial insight.

B. Finding the pressure in the presence of perturbations

1. Response to a point source on the BM

We solve the scattering problem by first supposing that we have solved a simpler problem: finding the response in an otherwise smooth cochlea to an isolated point source on the BM. We therefore define the complex-valued 2-D Green's function $G(x,y|x',y')$ as the solution to Poisson's equation,

$$(\partial_x^2+\partial_y^2)G=-\delta(x-x')\,\delta(y-y'), \tag{26}$$

where $\delta(x)$ is the Dirac delta function. Since the product of delta functions vanishes identically except at the point (x',y'), the right-hand side represents an oscillating point source of unit strength located at position (x',y'). The dimensionless Green's function $G(x,y|x',y')$ describes the propagated response at the observation point (x,y) to the source at (x',y') and is understood to satisfy the boundary conditions imposed on the pressure in the cochlea. For example, $G(x,y|x',y')$ depends on the BM impedance via the frequency-dependent boundary condition $\partial_y \ln G=HZ_{\mathrm{f}}/Z_{\mathrm{BM}}$ along the BM [Eq. (11) for a smooth cochlea]. The Green's function is symmetric (reciprocal) under the interchange of source and observation points within the cochlea: $G(x,y|x',y')=G(x',y'|x,y)$. In other words, the response at (x,y) to a source at (x',y') is identical to the response at (x',y') to the same source at (x,y). In our application we take $y'=0^+$ since the sources (perturbations) are presumed to be located on the BM (i.e., at $y=0^+$) rather than somewhere off in the fluid $(y>0)$.

2. An integral equation for the pressure

We now use the Green's function $G(x,y|x',y')$ to obtain an integral representation for the pressure $P(x,y)$. We start with the identity

$$P(x,y)=\frac{1}{b}\iint_{S'} G(x,y|x',y')\partial_{\perp'}P(x',y') - P(x',y')\partial_{\perp'}G(x,y|x',y')dS', \quad (27)$$

where S' is the total boundary surface of the scala vestibuli and $\partial_\perp \equiv (\mathbf{e}_\perp \cdot \nabla)$ represents the derivative in the direction of the local outward normal to the surface (e.g., $\partial_{\perp'} = -\partial_{y'}$ along the BM). Equation (27) is obtained by integrating $G\nabla^2 P - P\nabla^2 G$ over the scala volume and converting the result into a surface integral over S' using Green's theorem (e.g., Courant, 1988).

To evaluate the contributions from the various boundary surfaces we assume that the pressure $P(x',y')$ results from a stimulus applied at the stapes. In the absence of mechanical perturbations, $P(x',y')$ is simply the unperturbed pressure distribution, which we take equal to the forward-traveling wave, $P_r(x',y')$. We now assume, however, that $P(x,y)$ contains effects arising from roughness; near the stapes we therefore expect $P(x',y')$ to comprise both forward- and reverse-traveling wave components. The boundary conditions on $G(x,y|x',y')$ and $P(x',y')$ discussed in Sec. II imply that the only nonzero contributions to the surface integral arise from the basal boundary at the stapes ($x'=0$) and from the lower boundary at the BM ($y'=0^+$). Evaluating these terms yields the integral equation

$$P(x,y)=P_r(x,y)+H\int_0^\infty G(x,y|x',0^+) \times \epsilon(x')k_{\mathrm{lw}}^2(x')P_0(x')dx'. \quad (28)$$

To obtain Eq. (28) we used the fact that along the BM $\partial_{y'}\ln P_0 = HZ_{\mathrm{f}}/\tilde{Z}_{\mathrm{BM}} = (1+\epsilon)Hk_{\mathrm{lw}}^2$ [Eqs. (11), (17), and (21)]; the Green's function $G(x,y|x',0^+)$ is defined in the smooth cochlea and therefore satisfies the same boundary condition with $\epsilon=0$. Note that Eq. (28) for $P(x,y)$ reduces to the unperturbed right-going solution, $P_r(x,y)$, in the absence of roughness.

To obtain an integral equation for the pressure $\bar{P}(x)$ we average Eq. (28) over the scala cross section:

$$\bar{P}(x)=\bar{P}_r(x)+\int_0^\infty \bar{G}_0(x|x')\varrho(x')\bar{P}(x')dx', \quad (29)$$

where $\varrho \equiv \epsilon k^2 \equiv \epsilon\alpha k_{\mathrm{lw}}^2$ and

$$\bar{G}_0(x|x') \equiv \int_0^H G(x,y|x',0^+)dy. \quad (30)$$

The function $\bar{G}_0(x|x')$ has units of length and describes the propagated response, averaged over the duct cross section at the observation point at x, to the BM source at x'. Equation (29) therefore represents the mechanical perturbations as a distribution of BM point sources with strengths that vary with position, x'. At any point x, the scalae-averaged pressure resulting from the distribution of sources is found by adding up the response to each source, $\bar{G}_0(x|x')$, weighted by the corresponding source strength, $\varrho\bar{P}$. In the continuum limit, the summation becomes an integral over the source distribution, where the integration extends over all regions of the cochlea where ϱ is nonzero.

Although the function $\bar{G}_0(x|x')$ defined by Eq. (30) plays a role in Eq. (29) analogous to a one-dimensional Green's function, $\bar{G}_0(x|x')$ is not a conventional Green's function. Note, for example, that $\bar{G}_0(x|x')$ is not symmetric under the interchange of source (x') and observation (x) points within the cochlea. This lack of symmetry is no violation of reciprocity; it simply reflects the basic asymmetry between source and observation inherent in the definition of $\bar{G}_0(x|x')$: Whereas the source occurs on the BM [i.e., at the point $(x',0^+)$] the observation comprises a vertical average over the scalae cross section [i.e., $(x,\int dy)$]. To avoid confusion we refer to $\bar{G}_0(x|x')$ as the "reduced traveling-wave Green's function."

3. An iterative solution

Although Eq. (29) for $\bar{P}(x)$ is purely formal—the first term is known but the unknown solution $\bar{P}(x)$ appears inside the integral—we can construct an explicit solution $\bar{P}(x)$ by iteration. Making the notational substitutions $x'\to x''$ and $x\to x'$ in Eq. (29) yields

$$\bar{P}(x')=\bar{P}_0 W_r(x')+\int \bar{G}_0(x'|x'')\varrho(x'')\bar{P}(x'')dx'', \quad (31)$$

where $\bar{P}_0 \equiv \bar{P}_r(0)$. Inserting this expression for $\bar{P}(x')$ into the integral on the right-hand side of Eq. (29) yields

$$\bar{P}(x)=\bar{P}_0 W_r(x)+\bar{P}_0\int dx'\bar{G}_0(x|x')\varrho(x')W_r(x') + \int dx'\bar{G}_0(x|x')\varrho(x') \times \int dx''\bar{G}_0(x'|x'')\varrho(x'')\bar{P}(x''). \quad (32)$$

The first two terms on the right-hand side of this equation are now known; the unknown function $\bar{P}(x)$ appears only in the third.

By iterating in this fashion we construct the cochlear "Born expansion."[5] Each iteration introduces another power of the perturbations, ϱ. If the perturbations are weak, each additional term is smaller than the one preceding it. Successive iterations then push the unknown function $\bar{P}(x)$ into smaller and smaller terms. Eventually the contribution from this unknown function can be neglected and the solution expressed entirely in terms of known quantities. More formally, let $\bar{P}_1(x) \equiv \bar{P}_0 W_r(x)$ and

$$\bar{P}_{n+1}(x) \equiv \int \bar{G}_0(x|x')\varrho(x')\bar{P}_n(x')dx', \quad (33)$$

for $n=1,2,3,\ldots$. If the series converges, the solution to the integral equation is

$$\bar{P}(x)=\sum_{n=1}^{\infty}\bar{P}_n(x). \tag{34}$$

4. Interpretation as multiple scattering

Series (34) can be interpreted physically as arising from multiple scattering. Each term $\bar{P}_n(x)$ represents the contribution of wavelets scattered $n-1$ times within the cochlea (n is the number of intervals of scatter-free propagation). For example, the term $\bar{P}_3(x)$, defined by the double integral

$$\bar{P}_3(x)=\bar{P}_0\int dx'\,\bar{G}_0(x|x')\varrho(x')\times\int dx''\bar{G}_0(x'|x'')\varrho(x'')W_r(x''), \tag{35}$$

represents the net contribution of all doubly scattered wavelets. The wavelets contributing to $\bar{P}_3$ first propagate freely to x'', where they scatter with strength $\varrho(x'')$. The scattered wavelets then propagate freely to x', where they scatter a second time with strength $\varrho(x')$ before propagating a third and final time to the observation point at x. Since x'' and x' can be located anywhere in the cochlea—in particular, x' can be either apical to or basal to x''—both forward and backward scattering are properly accounted for. The integration over the coordinates x'' and x' thus sums contributions from all pairwise combinations of scattering locations within the cochlea. Finally, summing the terms $\bar{P}_n(x)$ combines wavelets scattered all possible number of times.

C. Approximate form of the reduced traveling-wave Green's function

Practical application of scattering series (34) for $\bar{P}(x)$ requires knowledge of the reduced Green's function, $\bar{G}_0(x|x')$. Ideally one seeks an expression for $\bar{G}_0(x|x')$ valid throughout the cochlea, but to understand the effect of perturbations on the reflectance evaluated at the stapes it suffices to find an approximation valid in the "far field" at some distance from the source at x'. To obtain an approximate form for $\bar{G}_0(x|x')$ valid in this regime we begin by writing $G(x,y|x',y')$ in the form

$$G(x,y|x',y')=G(x|x')Q(y;x|y';x'), \tag{36}$$

where $G(x|x')$ is the traveling-wave Green's function for the equivalent long-wave model (i.e., the long-wave model with the same basis waves) and $Q(y;x|y';x')$ remains undetermined. $G(x|x')$ is defined as the symmetric solution to

$$(\partial_x^2+k^2)G(x|x')=-\delta(x-x'), \tag{37}$$

subject to the appropriate boundary conditions at the base and apex of the cochlea. By writing $G(x,y|x',y')$ in the product form (36) we "factor out" the principal traveling-wave solutions that couple to the stapes. The undetermined function $Q(y;x|y';x')$ thus provides the residual y (and x) dependence. $Q(y;x|y';x')$ has units of reciprocal length and is normalized so that

$$\frac{1}{H}\int_0^H dy\int_0^H dy'\,Q(y;x|y';x')\cong 1. \tag{38}$$

The normalization is exact in the long-wave regime and approximate elsewhere; it guarantees that $G(x,y|x',y')$ reduces to $G(x|x')$ in the limit that the source distribution at x' is independent of y' and the response at x is averaged over y. In the long-wave limit, pressures—and pressure sources—are uniform over the scalae.

According to definition (30), $\bar{G}_0(x|x')$ has the value

$$\bar{G}_0(x|x')=G(x|x')\int_0^H Q(y;x|0^+;x')dy. \tag{39}$$

To obtain an approximate expression for the integrand $Q(y;x|0^+;x')$ we argue physically as follows: When the cochlea is driven from the stapes, the pressure $P_0(x)$ at the BM is $\alpha(x)$ times the "line-averaged" pressure $\bar{P}(x)$ in the fluids above [i.e., $P_0(x)=\alpha(x)\bar{P}(x)$, by Eq. (18)]. In an analogous way, when the driving source at x' is located on the BM ($y=0^+$), we expect the far-field component of the response to be $\alpha(x')$ times the response to a "line source" of equivalent total strength spread out uniformly over the interval $(0,H)$. In other words, we expect that

$$Q(y;x|0^+;x')\cong\alpha(x')\frac{1}{H}\int_0^H Q(y;x|y';x')dy'. \tag{40}$$

Substituting this value into Eq. (39) and applying the normalization (38) yields the approximation

$$\bar{G}_0(x|x')\cong\alpha(x')G(x|x'). \tag{41}$$

We derive a general expression for the 1-D traveling-wave Green's function, $G(x|x')$, in Appendix B. The expression for $G(x|x')$ [Eq. (B8)] is symmetric in x and x' and includes the effect of nonzero reflection from the stapes. Since our goal here is to calculate the cochlear reflectance, a quantity independent of the stapes boundary condition, we assume for simplicity that the stapes presents a perfectly reflectionless boundary ($R_{\text{stapes}}=0$). In this case, the long-wave Green's function $G(x|x')$ reduces to $G_\infty(x|x')$, where the subscript indicates that the cochlea appears infinite in extent to waves incident upon the stapes. According to Appendix B, $G_\infty(x|x')$ is given by

$$G_\infty(x|x')=\gamma W_l(x_<)W_r(x_>), \tag{42}$$

where $x_<(x,x')\equiv\min(x,x')$ and $x_>(x,x')\equiv\max(x,x')$. Derived here on physical grounds, approximation (41) is proved formally in Appendix C for the case when the BM impedance is independent of position; the proof generalizes to yield an approximate expression valid when the smooth component of the BM impedance varies slowly with x.

Figure 6 compares approximation (41) to the "exact" Green's function $\bar{G}_0(x|x')$ computed numerically. As expected, systematic deviations between the two solutions appear when both source and observation points (x and x') are close to the characteristic place (i.e., in the short-wave "near field"). Nevertheless, the approximation is uniformly excellent in the far-field regime ($x\to 0$) relevant here.

D. First-order approximation for the reflectance

Equation (34) constructs the solution $\bar{P}(x)$ in the form of a perturbative "scattering series." When the perturbations

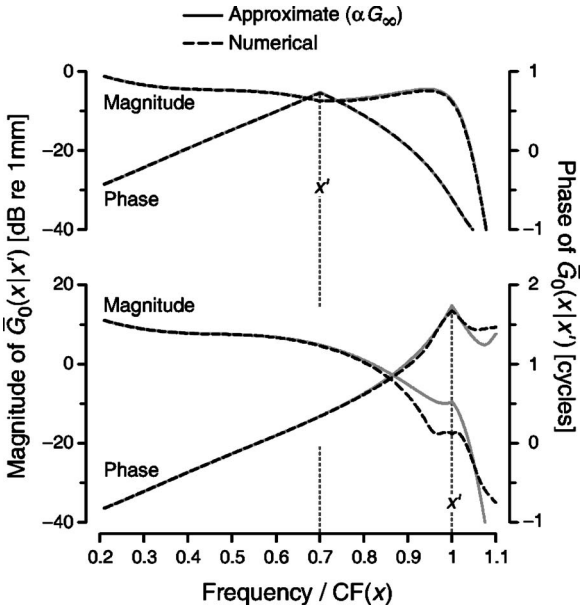

FIG. 6. Reduced traveling-wave Green's functions $\bar{G}_0(x|x')$ for two source locations x'. The observation point x varies along the abscissa and is shown in the form $f/\mathrm{CF}(x)$, where f is the source frequency. When the model is driven from the stapes, the peak of the corresponding BM velocity response occurs at the value 1. Magnitude and phase scales are shown on the left- and right-hand sides of the plot, respectively. Vertical dotted lines mark the two source locations x'. The top panel shows $\bar{G}_0(x|x')$ for an off-peak source located at a point whose CF is more than half an octave above the source frequency $[f/\mathrm{CF}(x')=0.7]$. The bottom panel shows $\bar{G}_0(x|x')$ for a source located at the characteristic place $[f/\mathrm{CF}(x')=1]$. The stapes was assumed perfectly transparent ($R_{\mathrm{stapes}}=0$). The dashed lines show the "exact" Green's functions computed numerically (standard model parameters from Appendix D); the solid lines show the approximate Green's function derived in the text [$\bar{G}_0\cong\alpha G_\infty$, Eqs. (41) and (42)]. The approximation is uniformly excellent as $x\to 0$ and breaks down only when both x and x' are in the short-wave regime close to the characteristic place.

are small one can neglect secondary ($n>2$) scattering by truncating series (34) after the first two terms ($\bar{P}_1+\bar{P}_2$). One then obtains an expression for $\bar{P}(x)$ valid to first order in ϱ (the so-called Born approximation):

$$\bar{P}(x)\cong\bar{P}_0 W_r(x)+\bar{P}_0\int \bar{G}_0(x|x')\varrho(x')W_r(x')dx'. \tag{43}$$

Substitution of the explicit form for $\bar{G}_0(x|x')$ [Eqs. (41) and (42)] yields the approximation

$$\bar{P}(x)\cong\bar{P}_0\left[1+\gamma\int_0^x \varrho\,\alpha W_l W_r\,dx'\right]W_r(x) + \bar{P}_0\left[\gamma\int_x^\infty \varrho\,\alpha W_r^2\,dx'\right]W_l(x). \tag{44}$$

We take the integration to ∞ in the final term as a reminder that we have assumed the cochlea is essentially infinite in extent (i.e., no wave reflection occurs at the helicotrema). In practice, the magnitude of the integrand rapidly falls to zero apical to the peak of the traveling wave; at all but the lowest frequencies the precise value of the upper limit is therefore irrelevant.

The two terms in brackets describe how nonzero perturbations ϱ cause the forward- and reverse-traveling wave amplitudes to vary with position. The cochlear reflectance (13) can be found as the ratio at $x=0$ of the coefficients of $W_l(x)$ and $W_r(x)$ in the series representation of $\bar{P}(x)$. These coefficients can be read off directly from Eq. (44) or, in the more general case, computed by using the projection operators $\hat{P}_{\{r,l\}}$ [Eq. (25)]. To first order in ϱ,

$$R\cong R_{\mathrm{Born}}\equiv\gamma\int_0^\infty \varrho\,\alpha W_r^2\,dx=\gamma\int_0^\infty \epsilon\alpha k^2 W_r^2\,dx. \tag{45}$$

Higher-order approximations to the reflectance that include the effects of multiple scattering are easily derived using series (34). When the various factors in the integrand are replaced by their long-wave equivalents (i.e., $\alpha\to 1$; $k^2\to k_{\mathrm{lw}}^2$; and $W_r^2\to W_{\mathrm{lw},r}^2$), approximation (45) for R reduces to the expression previously derived for the 1-D model (Shera and Zweig, 1993b; Zweig and Shera, 1995; Talmadge *et al.*, 1998).[6]

V. CONTROLLING FOR VARIATIONS IN MECHANICAL TUNING

Before applying our perturbative expression for the cochlear reflectance [Eq. (45)], we need to eliminate spurious sources of variation. Recall that our goal is to understand how the character of the wave scattering in the peak region (i.e., long-wave versus short-wave) modifies the predictions of the theory. We approach the problem via a thought-experiment. Imagine a family of models whose parameters (specifically, the scalae height H and partition impedance function Z_{BM}) differ in ways that yield different values of $\hat{k}H$. In order not to confound our analysis of long- and short-wave scattering, we need to restrict attention to those parameter sets that yield realistic mechanical tuning. In particular, we demand that the BM velocity response for the smooth cochlea, $V_{\mathrm{BM}}(x)$, be held fixed at some predetermined value. Unless $V_{\mathrm{BM}}(x)$ is held fixed, variations in the reflectance that result from changes in mechanical tuning may be mistakenly ascribed to differences between short- and long-wave scattering. Our question thus becomes: How does the reflectance R vary among models of different heights or dimensionality constructed so that they reproduce the same BM velocity response but manifest different values of $\hat{k}H$?

To address this question we must determine how to enforce the constraint of constant tuning. In a nutshell, the problem is to find 1-D and 2-D models that reproduce a given BM velocity response. In other words, we need to solve the cochlear inverse problem. Unfortunately, existing methods (e.g., Zweig, 1991; de Boer, 1995a,b; de Boer and Nuttall, 1999) do not serve our application, and we therefore develop an alternative approach.

A. Finding the wave number from the BM velocity

We first demonstrate that fixing $V_{\mathrm{BM}}(x)$ is equivalent to fixing the wave number, $k(x)$, that appears in the one-dimensional wave equation for $\bar{P}$ [Eq. (19)]. This result makes intuitive sense—since $V_{\mathrm{BM}}(x)$ is the traveling wave, fixing its value necessarily fixes its various properties, among them its wave number, $k(x)$.

We begin by writing Eq. (10) for Z_{BM} in the form

$$P_0 = bZ_{\mathrm{BM}}V_{\mathrm{BM}}. \tag{46}$$

Multiplying both sides by k^2/α and simplifying [using Eqs. (17), (18), and (20)] allows us to rewrite this equation in terms of $\bar{P}$ and k rather than P_0 and Z_{BM}. The result is

$$k^2\bar{P} = -bZ_{\mathrm{f}}V_{\mathrm{BM}}. \tag{47}$$

If we then substitute this expression for $k^2\bar{P}$ into wave equation (22), we obtain an equation for $\bar{P}(x)$ in which the unknown wave number $k(x)$ does not appear:

$$\partial_x^2\bar{P} = bZ_{\mathrm{f}}V_{\mathrm{BM}}. \tag{48}$$

Now, if the function $V_{\mathrm{BM}}(x)$ is known—whether by model or by measurement—Eq. (48) can be solved for $\bar{P}$ by double integration:

$$\bar{P}(x) = bZ_{\mathrm{f}}\int_x^L dx' \int_{x'}^L V_{\mathrm{BM}}(x'')dx''. \tag{49}$$

The constants of integration are chosen to satisfy the boundary conditions (in this case, $\bar{P} = \partial_x\bar{P} = 0$ at the helicotrema). Using our solution (49) for $\bar{P}(x)$ we can then determine the wave number using Eq. (47):

$$k^2(x) = -V_{\mathrm{BM}}(x) \Big/ \int_x^L dx' \int_{x'}^L V_{\mathrm{BM}}(x'')dx''. \tag{50}$$

Thus, the wave number $k(x)$ depends only on the given BM response function, $V_{\mathrm{BM}}(x)$, and is independent of the value of H, the effective height of the model. In other words, fixing $V_{\mathrm{BM}}(x)$ yields the same wave number irrespective of whether the model is everywhere long wave, or short wave, or manifests a transition between the two, as in the real cochlea.

Note that Eq. (50) determines $k(x)$ not by assuming a particular form for $Z_{\mathrm{BM}}(x)$, but by requiring that the model match a given BM-velocity response, $V_{\mathrm{BM}}(x)$. In other words, Eq. (50) provides a partial solution to the inverse problem (partial because it determines k^2 but not Z_{BM}). The wave number inversion procedure derived here is a two-dimensional variant of the procedure suggested by de Boer (1995a). An alternative procedure, analogous to Zweig's (1991) iterative long-wave method, can be developed based on approximate WKB solutions for $\bar{P}(x)$.

B. Finding the partition impedance from the wave number

Controlling for changes in mechanical tuning that would otherwise occur when we vary the height of the model requires varying the model parameters so that the wave number remains independent of H. To accomplish this, and thereby provide a full solution to the inverse problem, we must determine the corresponding BM impedance. Note that our analysis implies that constant mechanical tuning can only be maintained across models of different heights if the BM impedance varies with H. This conclusion should come as no surprise—it merely inverts the more familiar result that $V_{\mathrm{BM}}(x)$ depends on the assumed height of the model when $Z_{\mathrm{BM}}(x)$ is (tacitly) held constant.

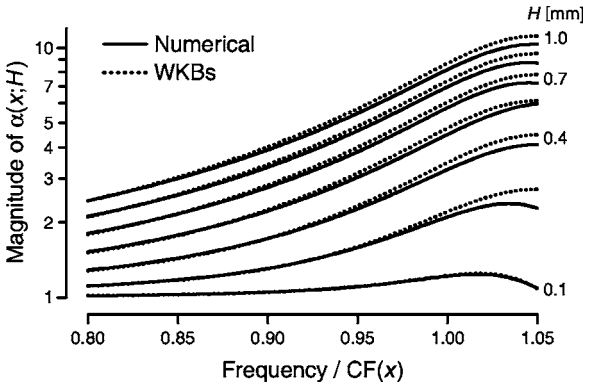

FIG. 7. Magnitude of $\alpha(x;H)$ for various values of H. The figure shows $|\alpha(x;H)|$ near the peak of the BM velocity response, located at the value 1 along the abscissa. Magnitudes are shown at seven equally spaced values of H spanning the interval [0.1,1] mm. Solid lines show $\alpha(x;H)$ computed numerically; dotted lines show the approximate WKB expression $\alpha_{\mathrm{WKBs}}(x;H)$ from Eq. (52). The BM velocity response, $V_{\mathrm{BM}}(x)$, was held fixed using the standard model parameters (Appendix D).

More significantly, the analysis indicates *how* $Z_{\mathrm{BM}}(x)$ must vary with H to maintain constant tuning. According to Eq. (20) the BM impedance and wave number are related by the equation

$$k^2(x) = -\alpha(x)Z_{\mathrm{f}}/Z_{\mathrm{BM}}(x). \tag{51}$$

Equation (51) implies that the ratio $\alpha(x)Z_{\mathrm{f}}/Z_{\mathrm{BM}}(x)$ must be independent of H if $V_{\mathrm{BM}}(x)$ and $k^2(x)$ are to remain invariant. In other words, $Z_{\mathrm{BM}}(x;H)$ must vary with H in exactly the same way as $\alpha(x;H)Z_{\mathrm{f}}$ so that the H dependence cancels in the ratio.

Figure 7 shows how $\alpha(x;H)$ varies with H at fixed $k(x)$. In the process, we compare numerical results with the approximation $\alpha_{\mathrm{WKBs}}(x;H)$ computed from the standard WKB expression for $P(x,y)$ (e.g., Steele and Taber, 1979; Viergever, 1980; de Boer and Viergever, 1982), which yields[7]

$$\alpha(x;H) \cong \alpha_{\mathrm{WKBs}}(x;H) = \frac{k(x)H}{\tanh[k(x)H]}. \tag{52}$$

Although the approximation is generally a good one, systematic deviations are apparent near the peak of the traveling wave. Note that the WKB formula implies that $\alpha(x;H) \cong \alpha[k(x)H]$, a result that makes sense on dimensional grounds: Since $\alpha(x)$ is a dimensionless ratio, it can only be a function of dimensionless products, and the wave number k is the natural quantity with units of inverse length needed to cancel the units of H.

Equation (51)—together with the good but imperfect approximation $\alpha(x) \cong \alpha_{\mathrm{WKBs}}(x)$ illustrated in Fig. 7—suggests an iterative inversion procedure for finding the functions $\alpha(x)$ and $Z_{\mathrm{BM}}(x)$ needed to evaluate Eq. (45) for R and/or to solve the model numerically under the constraint of constant tuning. Figure 8 illustrates the procedure, which begins by using Eq. (50) to find the wave number, $k(x)$, corresponding to the target BM velocity response function, $V_{\mathrm{BM}}(x)$. Then, after using the WKB approximation to provide initial estimates of $\alpha(x)$ and $Z_{\mathrm{BM}}(x)$, the algorithm iteratively improves these estimates, ultimately converging on a self-

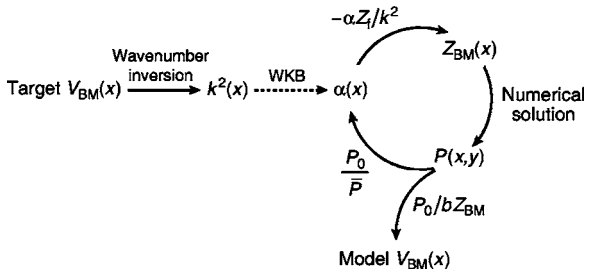

FIG. 8. Iterative inverse method for finding and solving the 2-D model equations that yield a target BM velocity response. The algorithm begins on the left, outside the loop. First, the target $V_{BM}(x)$ is used to determine the corresponding wave number, $k^2(x)$ [Eq. (50)]. An initial estimate of $\alpha(x)$ is then calculated (dotted line) using the standard WKB approximation [Eq. (52)]. Upon entering the loop, the approximate $\alpha(x)$ is used to estimate the corresponding BM impedance, $Z_{BM}(x)$ [Eq. (51)]. Numerical solution of Laplace's equation, with $Z_{BM}(x)$ defining the BM boundary condition, yields the pressure field $P(x,y)$, from which $\bar{P}(x)$, $P_0(x)$, and an improved estimate of $\alpha(x)$ are determined [Eqs. (14), (16), and (18)]. The loop then begins anew, using the improved estimate of $\alpha(x)$ to compute the BM impedance. Iteration continues until the algorithm converges on mutually consistent solutions for $\alpha(x)$, $Z_{BM}(x)$, and $P(x,y)$. The model's BM velocity response [Eq. (46)] then matches the target value.

consistent solution that reproduces the given velocity response. [In practice, no more than two to three iterations are needed to achieve good convergence. If too many iterations are employed, the solution can begin to diverge again just beyond $\hat{x}$. We believe that this instability arises from nonpropagating pressure modes that somehow slink into the solution from their usual innocuous hangout in the cutoff region apical to the characteristic place (e.g., de Boer and Viergever, 1982; Watts, 2000).] Although the initial WKB estimate for $\alpha(x)$ is often a good one (cf. Fig. 7), relatively small changes in $\alpha(x)$ can produce large changes in $V_{BM}(x)$ via their effect on the BM impedance in the region of traveling-wave amplification ($\mathrm{Re}\{Z_{BM}\}<0$) just basal to the peak (see Sec. VII C). The iterative procedure therefore generally improves the overall quality of the solution substantially.

C. The inverse procedure in action

Figure 9 illustrates the application of our inversion procedure. The bottom panel shows two BM impedance functions [$Z^{1d}_{BM}(x)$, dashed line; and $Z^{2d}_{BM}(x)$, solid line] that yield identical velocity responses (top panel) when employed in 1-D and 2-D models, respectively (standard model parameters from Appendix D). We refer to models of different heights or dimensionality that yield the same $V_{BM}(x)$ as "response-matched models." In this case, the target BM velocity response and the impedance Z^{1d}_{BM} were obtained using a variant of the long-wave model of Zweig (1991) as described in Appendix D; Z^{2d}_{BM} was computed using the inverse method diagrammed in Fig. 8.

Although Z^{1d}_{BM} and Z^{2d}_{BM} share a common qualitative form, including a bowl-shaped region of negative resistance in the region basal to the traveling-wave peak,[8] they also manifest important quantitative differences. Since $k^2(x)$ is invariant, Eq. (51) implies that

$$Z^{2d}_{BM}(x)=\alpha(x)Z^{1d}_{BM}(x). \tag{53}$$

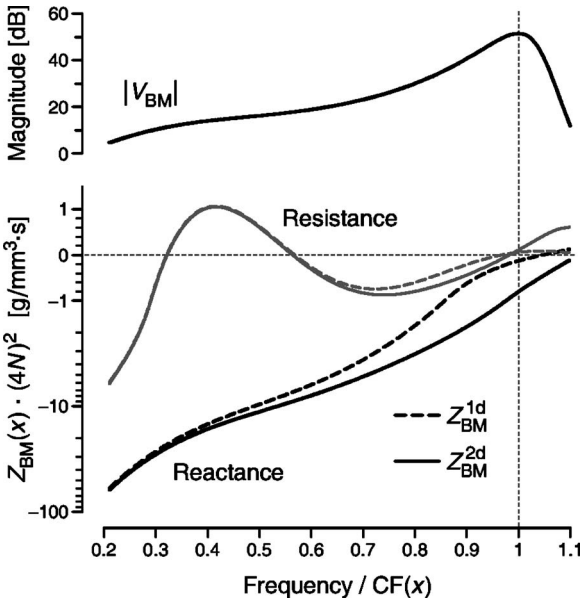

FIG. 9. BM impedance functions (bottom panel) that yield identical mechanical tuning (top panel) in 1-D and 2-D models. The real and imaginary parts of the 2-D impedance, $Z^{2d}_{BM}(x)$ (bottom panel, solid lines), were computed using the inverse procedure outlined in Fig. 8 with a target BM velocity response (magnitude shown in top panel) obtained from a variant of the long-wave model of Zweig (1991) (see Appendix D). The impedance of the 1-D model, $Z^{1d}_{BM}(x)$, is shown with dashed lines. The y-axis scale has been warped to accommodate the wide range of positive and negative impedance values (see Shera *et al.*, 2000, footnote 17); the scale is linear on the interval $[-1,1]$ and logarithmic elsewhere. For reference, a horizontal dotted line intersects the impedance ordinate at 0 and a vertical dotted line locates the peak of the target BM velocity response along the abscissa. The function $\alpha(x)$ corresponding to $Z^{2d}_{BM}(x)$ is shown in Fig. 5 ($\alpha=1$ in the 1-D model).

As expected from the form of $\alpha(x)$ (shown for the same model parameters in Fig. 5), $Z^{1d}_{BM}(x)$ and $Z^{2d}_{BM}(x)$ are essentially indistinguishable in the long-wave region near the stapes but gradually diverge from one another as the traveling wave in the 2-D model enters the short-wave regime. Basal to the characteristic place, $\alpha(x)$ is approximately real and the two impedances therefore differ mostly by a position-dependent scale factor, with $|Z^{2d}_{BM}|>|Z^{1d}_{BM}|$. Just apical to $\hat{x}$, however, the phase of $\alpha(x)$ begins to change rapidly; as a result the relative magnitudes of the resistive and reactive components of the two impedances change. Note, for example, that although $\hat{x}$ is invariant (by design), the "resonant place" of the partition in the 2-D model (as defined by the zero-crossing of the reactance) occurs at a location considerably apical to its 1-D counterpart. (Equivalently, scaling implies that the local "resonant frequency" in the 2-D model appears shifted to higher frequencies.) Thus, the short-wave hydrodynamics in the 2-D model exaggerate an effect already apparent in 1-D: The CF at location x occurs at a frequency well above the *in vacuo* resonant frequency of the partition; in active models (both 1-D and 2-D) the best place is determined more by the zero crossing of the resistance than by the zero crossing of the reactance.

VI. SHORT-WAVE AND LONG-WAVE SCATTERING

Now that we are able to eliminate spurious variations in mechanical tuning, we return to our central question. Figure

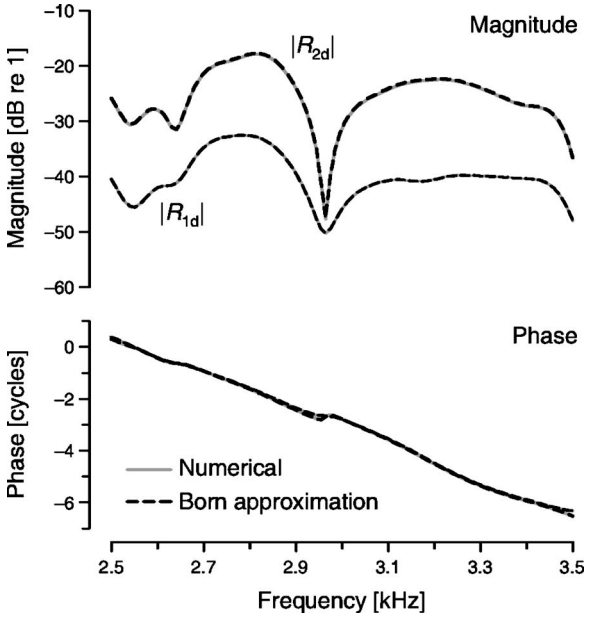

FIG. 10. Cochlear reflectances R_{1d} and R_{2d} versus frequency. The top and bottom panels show reflectance magnitudes and phases as computed in response-matched 1-D and 2-D models [$V_{BM}(x)$ held constant] using identical random impedance perturbations of magnitude $|\epsilon| \sim \mathcal{O}(1/100)$. Nonperturbative numerical calculations are shown with gray solid lines; the first-order Born approximation from Eq. (45) is shown with dashed lines. Standard model parameters are given in Appendix D.

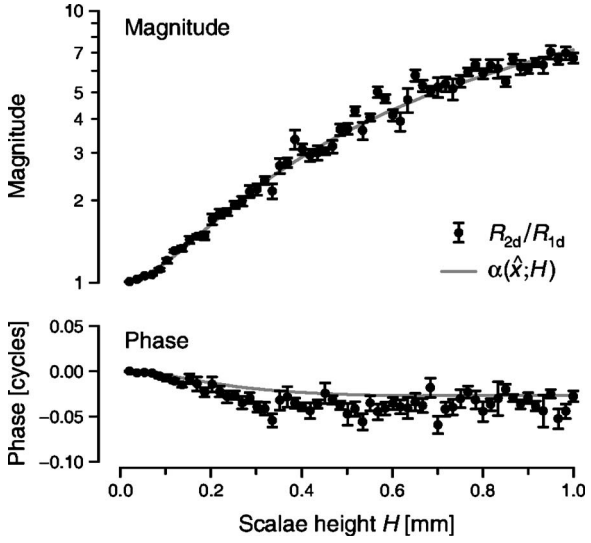

FIG. 11. Reflectance ratio R_{2d}/R_{1d} versus scalae height, H. Data points and error bars represent means and standard deviations of 20 ratios calculated from paired values of R_{1d} and R_{2d} computed numerically in response-matched 1-D and 2-D cochlear models at fixed frequency. Each of the 20 pairs of 1-D and 2-D simulations represented by every point employed a different random realization of the impedance perturbations, $\epsilon(x)$. Ratios were computed at 60 scalae heights spanning the range [0.02,1] mm. The approximation $R_{2d}/R_{1d} \cong \alpha(\hat{x};H)$ from Eq. (55) is shown for comparison (gray line).

10 compares the reflectances R_{1d} and R_{2d} computed in 1-D and 2-D models constructed to have the same BM velocity response (i.e., response-matched models). Identical random impedance perturbations (with $|\epsilon| \sim 1\%$) were used in each case. The reflectances R_{1d} and R_{2d} both share features characteristic of measured stimulus-frequency and transient-evoked OAEs, including a rapidly rotating phase and an amplitude spectrum whose leisurely noodling about is occasionally punctuated by deep notches (reviewed in Shera and Guinan, 1999). Although their phase versus frequency functions are very similar, R_{1d} and R_{2d} differ substantially in overall magnitude, with $|R_{2d}| \gg |R_{1d}|$ for the standard parameters used here. The figure also demonstrates that the first-order perturbative expression for R given in Eq. (45) closely matches the nonperturbative numerical calculation. Our analytic expression for R_{Born} therefore allows us to probe the origin of the differences between R_{1d} and R_{2d}.

A. Relation between 1-D and 2-D reflectances

Figure 11 plots the complex reflectance ratio R_{2d}/R_{1d} as a function of H at fixed frequency. Each data point and its error bar represents the mean and standard deviation of 20 ratios computed from numerical computations of R_{1d} and R_{2d} in response-matched 1-D and 2-D cochlear models of varying height [$V_{BM}(x)$ held constant].[9] Every pair of simulations employed a different random realization of the impedance perturbations, $\epsilon(x)$. As a gross consistency check on the calculations note that $\lim_{H \to 0} R_{2d}/R_{1d} = 1$, as expected. Although the simulations show a small systematic shift in the reflectance phase, the largest effect of the short-wave hydrodynamics is the substantial increase in reflectance magnitude evident at larger values of H.

To understand these results, recall that Eq. (45) for R_{Born} reads

$$R_{Born} = \gamma \int_0^\infty \epsilon \alpha k^2 W_r^2 \, dx. \tag{54}$$

We begin the analysis by asking how the factors in the integrand (i.e., ϵ, α, k^2, and W_r^2) depend on H when $k(x)$ is held fixed. Since we are considering the physically reasonable case where the fractional size of the perturbations ($\Delta Z_{BM}/Z_{BM}$) remains constant, ϵ is independent of H by hypothesis. The factor of k^2 is also clearly independent of H at fixed k, and we have already determined that $\alpha(x;H) \cong \alpha[k(x)H]$ varies with H [see Fig. 7 and Eq. (52)]. What about the factor W_r^2? Since the basis waves $W_{\{r,l\}}(x)$ are solutions of the equation $(\partial_x^2 + k^2) W_{\{r,l\}} = 0$ in which H does not explicitly appear, the basis waves (and the value of γ derived from them) depend only on $k(x)$; consequently, when $k(x)$ is fixed, so too are the basis waves $W_{\{r,l\}}(x)$. We conclude, then, that when $V_{BM}(x)$ is held constant, $\alpha(x;H)$ is the only factor contributing to the reflectance that varies with H. Differences between short- and long-wave scattering thus originate entirely in the function $\alpha(x;H)$.

Roughly speaking, the hydrodynamics encapsulated by $\alpha(x;H)$ can be thought of as modifying the effective strength of the perturbations. For example, Eq. (54) reduces to the 1-D result if the effective perturbations in the 1-D model are taken to be $\epsilon_{eff}(x;H) = \alpha(x;H)\epsilon(x)$. Since $|\alpha| > 1$, the short-wave hydrodynamics act, in effect, to magnify the perturbations, and we therefore expect $|R_{2d}| > |R_{1d}|$, consistent with the results in Figs. 10 and 11. As demonstrated below, the dominant scattering occurs in a region straddling the peak of the integrand, which is generally located close to the characteristic place. [The location of the peak of the integrand is

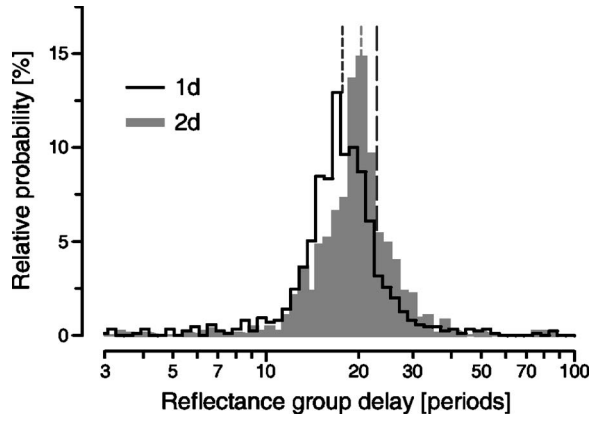

FIG. 12. Reflectance group delays in response-matched 1-D and 2-D models. The figure shows histograms of reflectance group delays (in periods of the stimulus frequency) pooled from 50 simulations, each employing a different random distribution of mechanical perturbations. In each simulation, the stimulus frequency was varied over a small neighborhood about 3 kHz (± 80 Hz in 10-Hz steps), and reflectance group delays (defined as $\tau \equiv -\partial_\omega \angle R$) were found by computing local phase gradients from unwrapped phase responses using centered differences (Shera and Guinan, 2003). The two short-dashed vertical lines that intersect the histogram peaks indicate group delays estimated from the phase gradient of the smooth component of the integrand in Eq. (54), evaluated at its magnitude peak [Eq. (57)]. The long-dashed line on the right shows twice the CF group delay of the corresponding BM velocity transfer function.

somewhat variable because the perturbations $\epsilon(x)$ vary "randomly" from cochlea to cochlea.] To the extent that $\alpha(x;H)$ is roughly constant over the scattering region it can be pulled outside the integral, yielding the approximate relation

$$R_{2\mathrm{d}} \cong \alpha(\hat{x};H)\,\gamma \int_0^\infty \epsilon k^2 W_r^2\, dx \cong \alpha(\hat{x};H) R_{1\mathrm{d}}. \tag{55}$$

In the short-wave region the magnification factor thus has the approximate value $\alpha(\hat{x};H) \cong \hat{k}H$. (Estimated values of $\hat{k}H$ are shown for human and guinea pig cochleae in Fig. 1.) The accuracy of approximation (55) in any given cochlea (or cochlear model) depends on the precise distribution of impedance perturbations. At best, its validity is therefore only statistical. To test Eq. (55), Fig. 11 also plots the function $\alpha(\hat{x};H)$, demonstrating that the approximation captures the dominant trend in the results.

B. Reflectance group delay

The group (or phase-gradient) delay of the cochlear reflectance is the major determinant of the characteristic frequency spacings of OAE fine structure (Shera and Zweig, 1993a; Zweig and Shera, 1995; Talmadge *et al.*, 1998; Shera, 2003a). We have shown previously that integral (54) for R (with $\alpha = 1$) predicts that the reflectance group delay (defined by $\tau \equiv -\partial_\omega \angle R$) is determined by the phase slope of the integrand evaluated near its magnitude peak (e.g., Zweig and Shera, 1995, Appendix D). In the short-wave regime $\alpha(x)$ modifies both the amplitude and phase of the integrand near the peak (see Fig. 5), and we therefore expect reflectance group delays in the 2-D model to differ somewhat from their 1-D values. However, the close match between the phase curves of Fig. 10 suggests that any differences are small.

Figure 12 quantifies group-delay differences between response-matched 1-D and 2-D models using histograms assembled from simulations employing different random distributions of impedance perturbations. Group delays are shown in a dimensionless form representing the number of periods of delay at the emission frequency, which was varied in a small neighborhood about 3 kHz. As expected, the histograms peak at slightly different values, with $\tau_{1\mathrm{d}} < \tau_{2\mathrm{d}}$. Although the modal values are robust, both histograms have substantial width, indicating considerable variability in the results. This variability is manifest both at nearby frequencies in a single (model) ear and between ears at fixed frequency. Similar broad distributions of reflection-source OAE group delay are found experimentally in both human and animal subjects (e.g., Shera and Guinan, 2003, Figs. 1 and 3; Shera, 2003a; Figs. 3 and 4). According to the model, the variability reflects the underlying irregularity in the mechanical perturbations that give rise to the reverse-traveling wave.

To understand the difference between the modal values of $\tau_{1\mathrm{d}}$ and $\tau_{2\mathrm{d}}$, note that the smooth (nonstochastic) component of the integrand ($\mathcal{I}$) in Eq. (54) for R_{Born} can be written in the form

$$\mathcal{I} \equiv \alpha k^2 W_r^2 \sim \alpha \left(\frac{T}{k}\right)^2, \tag{56}$$

where T is the BM mechanical transfer function ($V_{\mathrm{BM}}/V_{\mathrm{stapes}}$) and we have used Eq. (47) with the identification $\bar{P} \sim W_r$. Computing the group delay at the magnitude peak yields

$$\tau \cong \hat{\tau}_{\mathcal{I}} \equiv -\partial_\omega \angle \mathcal{I}|_{\mathrm{peak}} = 2\hat{\tau}_{\mathrm{BM}} - 2\hat{\tau}_k + \hat{\tau}_\alpha, \tag{57}$$

where $\tau_k \equiv -\partial_\omega k$, and so on. In 1-D models, where the peak region is assumed to be long wave, $\alpha \to 1$ and $\tau_\alpha \to 0$. Thus,

$$\tau_{1\mathrm{d}} \cong 2(\hat{\tau}_{\mathrm{BM}} - \hat{\tau}_k). \tag{58}$$

When the peak region is short wave, however, $\alpha \cong \alpha_{\mathrm{WKBs}} \to kH$ [Eq. (52)], so that

$$\tau_{2\mathrm{d}} \cong 2\hat{\tau}_{\mathrm{BM}} - \hat{\tau}_k. \tag{59}$$

The short-dashed lines in Fig. 12 demonstrate that the modal values of $\tau_{1\mathrm{d}}$ and $\tau_{2\mathrm{d}}$ are well approximated by Eqs. (58) and (59).

To determine the sign of $\hat{\tau}_k$, note that wave numbers obtained via inverse analysis in sensitive preparations (e.g., Zweig, 1991; de Boer, 1995b) indicate that $\mathrm{Re}\{k\} > 0$ and that $\mathrm{Im}\{k\}$ goes through a negative-going zero crossing in the vicinity of the response peak (see footnote 2). Using local scaling symmetry to convert these spatial derivatives at fixed frequency into frequency derivatives at fixed position then yields $\hat{\tau}_k > 0$.[10] Consequently,

$$\tau_{1\mathrm{d}} < \tau_{2\mathrm{d}} < 2\hat{\tau}_{\mathrm{BM}}, \tag{60}$$

consistent with the results shown in Fig. 12. Since $\hat{\tau}_k$ is typically only a fraction of $2\hat{\tau}_{\mathrm{BM}}$, the approximation $\tau \cong 2\hat{\tau}_{\mathrm{BM}}$ appears good to within 10%–20%. Inequalities (60) imply that the approximation is improved by short-wave effects within the scattering region. These results are quantitatively consistent with direct and indirect comparisons of SFOAE and BM group delays performed in the basal half of the cochlea (Cooper and Shera, 2004; Shera and Guinan,

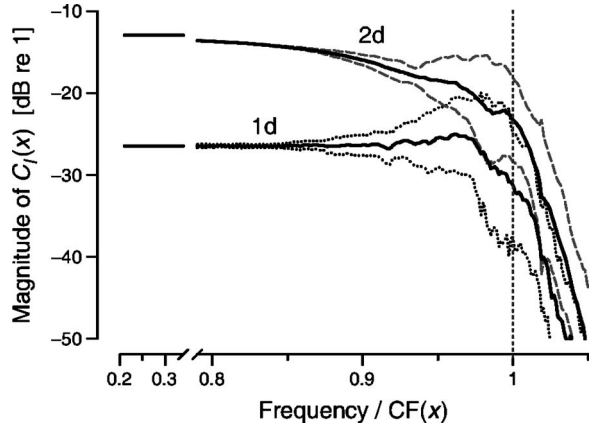

FIG. 13. Wave coefficients $C_l(x)$ in 1-D and 2-D models. Solid lines show the mean magnitudes of 20 numerical computations of $C_l(x)$ computed in response-matched 1-D and 2-D models at fixed frequency. The spatial coordinate x varies along the abscissa; for reference, the peak of the corresponding BM velocity response is marked by the vertical dotted line. In order to emphasize detail in the peak region, the interval (0.34,0.79), over which the functions $C_l(x)$ are almost constant, has been excised from the abscissa. Each of the 20 pairs of 1-D and 2-D simulations employed a different random realization of the impedance perturbations, $\epsilon(x)$. To factor out differences in overall reflectance magnitude due to variations in $\epsilon(x)$, we normalized the functions $C_l(x)$ in each model type to a common value at $x=0$ before computing the mean. Standard deviations about the mean are shown using thinner dashed and dotted lines. Coefficient functions $C_l(x)$ were computed from $\bar{P}(x)$ using the projection operator $\hat{P}_l(x)$ [Eqs. (24) and (25)]. Means and standard deviations were computed after log-transforming the data.

2003). For example, Cooper and Shera (2004) report the relation $\tau_{\mathrm{SFOAE}}=(1.86\pm0.22\,\mathrm{s.d.})\,\hat{\tau}_{\mathrm{BM}}$ based on a comparison of otoacoustic and near-CF mechanical group delays measured in the same ears (ten guinea pigs, one chinchilla).

C. Location of the scattering region

The cochlear reflectance quantifies wave reflection as viewed from just inside the oval window, the intracochlear location where OAEs couple to the middle ear. The projection operators $\hat{P}_{\{r,l\}}(x)$ can, however, be applied at locations throughout the cochlea, not just at $x=0$. In particular, they enable us to locate the region of dominant scattering, even allowing us to look inside the scattering region to determine how the wave amplitudes vary with position.

Figure 13 shows the magnitude of the wave coefficient $C_l(x)$. $C_l(x)$ is defined so that $\bar{P}_l(x)=C_l(x)W_l(x)$, and its value can found from the solution $\bar{P}(x)$ using the equation (see footnote 4)

$$C_l(x)\equiv\frac{\hat{P}_l(x)\{\bar{P}(x)\}}{W_l(x)}, \tag{61}$$

where the projection operator is defined by Eq. (25). The coefficient $C_l(x)$ indicates how the amplitude of the reverse-traveling wave varies with position, and its detailed form depends on the particular distribution of perturbations employed. Here, we highlight general trends by averaging over multiple random realizations of the function $\epsilon(x)$; the irregularity characteristic of individual curves is therefore smoothed out in the mean. In both 1-D and 2-D models, the coefficient $C_l(x)$ rises rapidly from zero over a relatively short interval close to the characteristic place and quickly approaches an almost constant value at locations closer to the stapes. [The corresponding coefficient, $C_r(x)$, for the forward-traveling wave is essentially constant on the scale of the figure.] Since changes in $C_l(x)$ arise via scattering of the forward-traveling wave, the region of dominant scattering occurs where $C_l(x)$ changes rapidly. Scattering in both long- and short-wave models thus occurs principally near the peak of the traveling wave.

Spatial fluctuations in the amplitude of the net reverse-traveling wave due to the random distribution of perturbations produce the large variance in the magnitude of $C_l(x)$ seen within the scattering region. Note, however, that in the 2-D model $C_l(x)$ approaches its final, asymptotic value somewhat more slowly (and smoothly) than it does in the 1-D model. Measured in this way (i.e., in the scalae-averaged pressure), the effective scattering region thus extends somewhat more basally in the 2-D model than it does in 1-D. Because of the breakdown in approximation (41) for $\bar{G}_0(x|x')$ this "near-field" effect is not captured by Eq. (44) for $\bar{P}(x)$.

VII. DISCUSSION

The theory of coherent reflection filtering explains the empirical form for the cochlear reflectance by showing how it emerges from the coherent "backscattering" of forward-traveling waves by random impedance perturbations in the mechanics of the cochlear partition (Shera and Zweig, 1993b; Zweig and Shera, 1995; Talmadge *et al.*, 1998). The theory follows from the analysis of wave scattering in the one-dimensional cochlear model and indicates that at low stimulus intensities the creation of realistic reflection-source OAEs involves three basic principles: First, *the peak of the traveling wave is tall*. As a result, wavelets reflected near the peak have larger amplitudes than those reflected elsewhere, effectively localizing the reflection to the region about the peak. Second, the *peak of the traveling wave is broad relative to the distance between perturbations* (e.g., the width of a hair cell). Consequently, the peak region contains many scattering centers, whose irregular distribution comprises many different spatial frequencies. The many perturbations produce many scattered wavelets, each originating from a different location within the peak, and these wavelets combine and interfere with one another both constructively and destructively. Finally, *the wavelength of the traveling wave is approximately constant over the peak region*. Consequently, wavelets reflected by perturbations arrayed at a particular spatial period undergo a phase change due to scattering that precisely compensates for the phase change due to wave propagation forth and back to the point of reflection (an analog of Bragg's law). Such wavelets therefore combine constructively with one another, and their sum dominates the net reflected wave. The particular spatial period that produces maximal reflection is determined dynamically by the traveling wave. More precisely, coherent backscattering occurs from perturbations arrayed at a spatial period matching half the wavelength of the traveling wave at its peak ($\hat{\lambda}$). Wavelets scattered by spatial-frequency components whose peri-

ods are either considerably larger or smaller than $1/2\hat{\lambda}$ combine incoherently and largely cancel one another out.

Although it successfully accounts for a wide variety of otoacoustic phenomena, the theory of coherent reflection was derived using an assumption about cochlear hydrodynamics (the long-wave assumption) that breaks down near the region of maximal scattering (see Fig. 1). Therefore, to understand how short-wave behavior near the peak of the traveling wave affects the properties of reflection-source OAEs, we have solved the problem of wave scattering by distributed mechanical perturbations in a two-dimensional cochlear model that supports both long and short waves and the transition between the two. Just as in the 1-D theory, we find that the cochlear reflectance can be expressed as an integral representing the summation of wavelets scattered by perturbations located throughout the cochlea. In response-matched models the integrand is identical to the 1-D case, with the exception of an additional factor of $\alpha(x)$ that encapsulates the 2-D hydrodynamics. The function $\alpha(x)$ is defined as the ratio of the difference pressure driving the cochlear partition to the pressure averaged over the scalae cross section [Eq. (18)]. Because $\alpha(x)$ peaks near the characteristic place but has a relatively slowly varying phase (see Fig. 5), it has quantitative but no significant qualitative effects on the analytic structure of the scattering integral. As a result, the physical mechanism of coherent reflection operates essentially unchanged.

Although both Zwislocki's proof and naive application of Siebert's uncoupled equations suggest that wave reflection does not occur in the short-wave regime, our results establish that reflection from the peak region is actually significantly enhanced ($|\alpha| \gg 1$) relative to the long-wave case (Figs. 10 and 11). In effect, the short-wave hydrodynamics act to magnify the apparent size of the perturbations located near the peak of the traveling wave, thereby increasing the amount of scattering. In addition to boosting emission amplitude, short-wave effects also modify the emission group delay (Fig. 12). The group delay sets the rate at which emission phase varies with frequency and is the major determinant of OAE fine-structure spacings (e.g., Talmadge *et al.*, 1998; Shera, 2003a). The short-wave analysis yields slightly longer group delays (τ) and improves the accuracy of the first-order approximation $\tau \cong 2\hat{\tau}_{\mathrm{BM}}$ used to estimate BM group delays from OAE measurements (e.g., Shera and Guinan, 2003; Shera *et al.*, 2002). To second order the analysis predicts $\tau \cong 2\hat{\tau}_{\mathrm{BM}} - \hat{\tau}_k < 2\hat{\tau}_{\mathrm{BM}}$, consistent with direct comparisons of otoacoustic and BM group delays in the basal turns of the cochlea (Cooper and Shera, 2004).

Despite these quantitative differences, the principal qualitative conclusions of the long-wave theory, including its explication of the mechanism of coherent reflection responsible for emission generation, survive intact. The fundamental reason for this is simple: The theory indicates that although the mechanisms of coherent scattering depend strongly on functional characteristics of the traveling-wave peak such as its height, width, and wavelength, they remain relatively insensitive to details of the biophysical processes that determine how that peak originates.

As a corollary, we note that although we have illustrated our findings and procedures with numerical simulations performed using a variant of the model obtained by solving the inverse problem in squirrel monkey (Zweig, 1991), our arguments and conclusions are considerably more general. Indeed, none of them depends on any particular biophysical detail of the model employed. Other models that produce realistic cochlear traveling waves—whether those models be largely phenomenological in character or deduced from first principles involving strings and branes—would serve just as well. As our analytic results make clear, the qualitative form of R depends primarily on the form of the BM velocity response [which determines the wave number, $k(x)$, via Eq. (50)] and not on unknown, model-dependent, or currently controversial micromechanical details concerning the biophysics of force generation within the organ of Corti.

A. The dimensional reduction

The arguments needed to justify the results summarized above require surmounting (or at least circumventing) a number of technical obstacles of interest in their own right. The foundation of the analysis is the observation that OAEs couple to the middle ear via pressures in the long-wave regime averaged across the surface of the stapes. This observation buttressed our early intuition (i.e., hope) that the potentially complicated details of the pressure distribution $P(x,y)$ within the scattering region would ultimately prove unimportant for predicting the value of the reflectance at the stapes. Duifhuis' (1988) averaging procedure then allowed us to reduce the general 2-D problem to an effective 1-D wave equation for the scalae-averaged pressure, $\bar{P}(x)$. This strategy of focusing on a useful level of detail proved successful, since we were then able to find a simple, approximate expression for the reduced traveling-wave Green's function that gives the far-field response to great precision.

The reduced traveling-wave Green's function is derived from a complex-valued (or frequency-domain) Green's function $G(x,y|x',y')$ that differs from the conventional real-valued Green's function often used to describe fluid coupling in the cochlea (e.g., Allen, 1977; Mammano and Nobili, 1993; Parthasarathi *et al.*, 2000; Shera *et al.*, 2004).[11] Although both Green's functions satisfy the equivalent of Eq. (26) and have vanishing normal derivatives at the walls, they differ in the boundary conditions satisfied at the BM. Whereas the conventional Green's function treats the BM as another hard wall (the BM dynamics enter at a later stage), the Green's function introduced here has a normal derivative determined by the smooth component of the BM impedance [see discussion after Eq. (26)]. Thus, unlike the conventional Green's function, our $G(x,y|x',y')$ builds in the collective, wavelike phenomena that emerge from interactions between the cochlear partition and the surrounding fluids. It is therefore well suited for solving linear (or quasilinear) perturbative problems, such as those involving the production of OAEs [for further discussion, see Shera *et al.* (2004)].

As a cautionary note, we point out that an integral equation with the same form as Eq. (29) can be derived by rewriting wave equation (19) for the scalae-averaged pressure in the equivalent inhomogeneous form

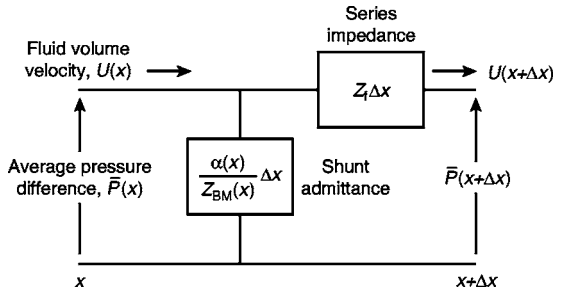

FIG. 14. Equivalent transmission-line analog for a section of the 2-D model of the cochlea of length Δx. The series impedance $Z_f\Delta x$ includes the inertia of the cochlear fluids oscillating in the longitudinal direction. The effective shunt admittance $Y(x)\Delta x$, where $Y(x)=\alpha(x)/Z_{BM}(x)$, characterizes the transverse response of the cochlear partition to the average pressure difference $\bar{P}(x)$. The "current" flowing in the transmission line is the longitudinal component of the fluid volume velocity, $U(x)$.

$$(\partial_x^2+k^2)\bar{P}=-\varrho\bar{P}, \tag{62}$$

so that the mechanical perturbations are isolated on the right-hand side of the equation. If this equation is now naively converted to an integral equation using the one-dimensional, long-wave Green's function $G(x|x')$ [see Eq. (37) and Appendix B], one obtains the (incorrect) relation

$$\bar{P}(x)\overset{\text{☹}}{=}\bar{P}_r(x)+\int_0^\infty G(x|x')\varrho(x')\bar{P}(x')dx', \tag{63}$$

a result identical to Eq. (29) except that the long-wave Green's function, $G(x|x')$, appears in place of the reduced traveling-wave Green's function, $\bar{G}_0(x|x')$. The error in this analysis is that although the pressure $\bar{P}(x)$ satisfies a one-dimensional wave equation, the "sources" $\varrho\bar{P}$ remain inherently two-dimensional—they are located at points *on* the BM rather than being distributed uniformly over y. As outlined in Sec. IV B, the correct procedure for deriving the integral representation for $\bar{P}(x)$ is to derive the integral representation for $P(x,y)$ *before* averaging over y.

B. The equivalent transmission line

The existence of a wave equation for $\bar{P}(x)$ means that the equivalent 1-D system can be represented as a transmission line, a section of which is illustrated in Fig. 14. The dynamical variables are the average pressure difference, $\bar{P}(x)$, and the longitudinal component of the volume velocity, $U(x)$. To find the series impedance and shunt admittance that characterize the line, we begin with Eq. (6),

$$\partial_x\bar{P}=-Z_fU, \tag{64}$$

an equation obtained by averaging the linearized Euler equation over the scalae. Differentiating this equation with respect to x and rewriting the result using Eqs. (19) and (20) yields the equation

$$\partial_xU=-Y\bar{P}, \tag{65}$$

where $Y(x)\equiv\alpha(x)/Z_{BM}(x)$. Equations (64) and (65) represent the pair of coupled first-order equations defining a one-dimensional transmission line with series impedance Z_f and shunt admittance Y, both per unit length (e.g., Slater, 1942). In the long-wave limit $\alpha\to1$ and $Y\to1/Z_{BM}$, so that the system shown in Fig. 14 reduces to the standard equations describing the one-dimensional transmission-line model (e.g., Wegel and Lane, 1924; Zwislocki-Mościcki, 1948; Peterson and Bogert, 1950; Zweig *et al.*, 1976).

Do short-wave effects modify the effective scalae area?

The equivalent transmission line illustrated in Fig. 14 associates the factor α with the BM impedance, using it to define an effective admittance, $Y\leftarrow\alpha/Z_{BM}$. But from the perspective of the definition $k^2=-\alpha Z_f/Z_{BM}$ [Eq. (20)] and the derivation preceding it, the factor α might just as well have been associated with the impedance Z_f and used to define an effective fluid impedance $Z_{eff}\leftarrow\alpha Z_f$. In this latter case, the factor α would act to modify the effective scalae area and hence the acoustic mass (mass density per cross-sectional area) associated with fluid movement in the duct. In this view, Eq. (8) for Z_f would naturally be rewritten to read

$$Z_{eff}(x)\equiv2i\omega\rho_0/S_{eff}(x), \tag{66}$$

where $S_{eff}(x)=bH_{eff}(x)$, with $H_{eff}(x)\equiv H/\alpha(x)$. Since $\alpha(x)$ is essentially real basal to $\hat{x}$ and increases with distance from the stapes, the effective height $H_{eff}(x)$ tapers down toward the characteristic place;[12] the effective acoustic mass $\rho_0/S_{eff}(x)$ therefore increases correspondingly. Although this formulation has considerable intuitive appeal, the notion that short-wave effects can be regarded as reducing the effective height or cross-sectional area of the scalae (e.g., Zwislocki, 1983, 2002; Hubbard and Mountain, 1996) cannot be used to find the equivalent one-dimensional wave equation. The derivation outlined above implies that Fig. 14, in which α modifies Z_{BM} rather than Z_f, uniquely specifies the equivalent transmission line.

Although mistakenly associating the factor α with the impedance of the fluid rather than with the impedance of the BM has no effect on the wave number, it does modify the apparent characteristic impedance of the system.[13] In particular, the characteristic impedance becomes $Z_0=\sqrt{\alpha}Z_0^{lw}$ (where $Z_0^{lw}=\sqrt{Z_fZ_{BM}}$), which differs by a factor of $\alpha(x)$ from its actual value, $Z_0^{lw}/\sqrt{\alpha}$. Since $\alpha\cong\alpha_{WKBs}\to-H^2Z_f/Z_{BM}$ in the short-wave limit [see Eqs. (51) and (52)], the (incorrect) characteristic impedance approaches $Z_0\to-iHZ_f=2\omega\rho/b$, a value independent of Z_{BM}.[14]

Recall from the Introduction that Zwislocki (1983, 2002) applied this counter-intuitive and evidently erroneous result—namely, the apparent cancellation of all factors of Z_{BM} in the short-wave formula for Z_0—to deduce that wave reflection arising from spatial variations in the BM impedance cannot occur in the short-wave regime. The error in Zwislocki's argument is that no such cancellation occurs when the series impedance and shunt admittance of the equivalent transmission line are correctly identified.[15]

C. Need for the inverse procedure

Another crucial component of our argument follows from the recognition that meaningful comparisons between models of different heights or dimensionality require control-

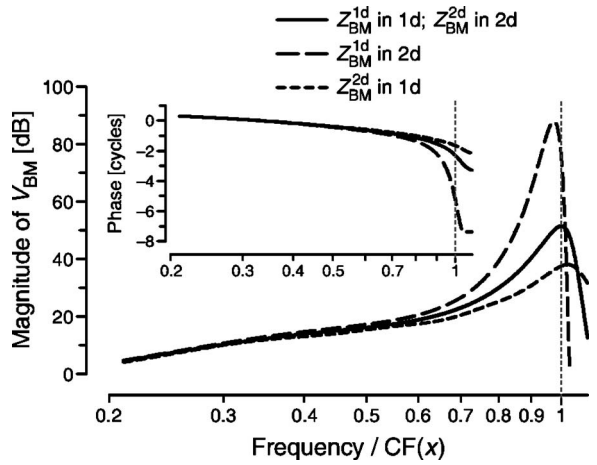

FIG. 15. Results of model cross-breeding. The panels show the BM velocity responses computed by crossing 1-D and 2-D models and their respective impedances, $Z_{BM}^{1d}(x)$ and $Z_{BM}^{2d}(x)$, taken from Fig. 9. All four possible combinations of model/impedance are shown. The solid lines show the normal, ''homozygous'' cases (i.e., 1-D/1-D and 2-D/2-D), reproduced from the top panel of Fig. 9. The two homozygous cases are indistinguishable on the scale of the graph. The long dashed lines show the heterozygous case 1-D/2-D, and the short dashed lines show the case 2-D/1-D. BM velocity magnitudes are shown in the main panel, phases in the inset. For reference, vertical dotted lines locate the peak of the target (i.e., homozygous) BM velocity response along the abscissae.

ling for variations in mechanical tuning that occur when the geometry of the model is varied with $Z_{BM}(x)$ held fixed. Although differences between $Z_{BM}^{1d}(x)$ and $Z_{BM}^{2d}(x)$ appear relatively minor in the context of Fig. 9, they nonetheless have striking functional consequences, as demonstrated in Fig. 15, which plots the ''mutant'' responses that result from model ''cross-breeding'' (e.g., computing V_{BM} in a 2-D model using the 1-D impedance and vice versa).[16] Corresponding to the sizable amplitude differences illustrated in the main panel are large differences in response phase (inset) that greatly affect the reflectance group delay. Unless controlled for using an inverse procedure such as that outlined here, these fundamental differences in the basic response properties of the model would hopelessly swamp the relatively small differences in OAE characteristics actually attributable to short- versus long-wave scattering.

In the one-dimensional model, Eq. (50)—or Zweig's (1991) WKB-based method for finding the wave number—provides a complete solution to the inverse problem because the BM impedance can be found from $k^2(x)$ using the equation $Z_{BM}^{1d}(x) = -Z_f/k^2(x)$, obtained from Eq. (51) with $\alpha = 1$. (The fluid impedance Z_f is set by the model geometry and is assumed known.) But the solution remains incomplete in 2-D because $\alpha(x)$, and the information it encodes about hydrodynamic contributions to the response, remains undetermined. For this reason, we need to supplement the wave number inversion with a procedure to determine $\alpha(x)$; the iterative method illustrated in Fig. 8 solves this problem.

Although applied here within the specific context of the 2-D scattering problem, the inversion procedure developed in Sec. V provides an alternative to existing inverse methods in the literature. The BM velocity response $V_{BM}(x)$ that serves as input to the procedure can be obtained experimentally either by direct spatial measurement (e.g., Ren, 2002) or by transforming frequency-domain measurements to the place domain with the aid of approximate symmetries such as scaling (e.g., Zweig, 1976). Although a number of technical issues complicate the inversion procedure when applied to experimental data sets (cf. Zweig, 1991; de Boer, 1995a,b; de Boer and Nuttall, 1999),[17] none of them compromises the conclusions of this paper.

D. Review of the assumptions

To derive the results reported here we employed a number of simplifying assumptions. For example, rather than labor under the added complexity of the full three-dimensional, coiled, asymmetric, tapered geometry of the actual cochlea, we deliberately adopted the simplest geometry that manifests both short- and long-wave behavior (i.e., the symmetric 2-D box model). Although these geometric restrictions can be relaxed [e.g., Duifhuis' (1988) dimensional reduction procedure was originally applied to a 3-D model; see also Talmadge *et al.* (2001)], we see no reason to expect that the effort will produce anything but minor quantitative changes to the results. We have shown elsewhere that the long-range (far-field) hydrodynamics of an uncoiled but otherwise realistic 3-D model (Mammano and Nobili, 1993) are captured by a simple, one-dimensional transmission line (Shera *et al.*, 2004, Appendix A). And in the short-wave regime near the peak of the traveling wave the pressure field decreases rapidly with distance from the cochlear partition (e.g., Olson, 2001), so that the precise geometry of the scalae walls becomes unimportant. These hand-waving physical arguments are corroborated by computations showing that mechanical perturbations introduced into a 3-D model for the purposes of simulating SOAEs produce results in accord with the theory of coherent reflection (de Boer *et al.*, 2004).

Since our goal has been to understand short- versus long-wave effects on the cochlear reflectance R, rather than provide a description of reflection-source OAEs as measured in the ear canal, we assumed for simplicity [e.g., in obtaining Eq. (44) from Eq. (43)] that the stapes presents a perfectly reflectionless boundary to reverse-traveling waves ($R_{stapes} = 0$). Since reflection from the stapes occurs in the long-wave regime, the effects of multiple internal reflection (e.g., the production of intracochlear standing waves, small systematic shifts in fine-structure spacings, etc.) carry over from previous analyses (e.g., Talmadge *et al.*, 1998; Dhar *et al.*, 2002; Shera, 2003a).

The model assumes that the mechanical properties of the cochlear partition vary irregularly (i.e., nonsmoothly) with position. This assumption is consistent with general arguments that locate the origin of reflection-source OAEs in preexisting (place-fixed) mechanical perturbations in the organ of Corti (Kemp and Brown, 1983; Shera and Guinan, 1999). In the ear, the precise nature of these perturbations remains unknown, although spatial variations in hair-cell number and geometry (Engström *et al.*, 1966; Bredberg, 1968; Wright, 1984; Lonsbury-Martin *et al.*, 1988)—and perturbations not so visible in the anatomy, such as variations in OHC forces due to random, cell-to-cell variations in the number of OHC motor proteins—all presumably contribute.

The perturbations used here were introduced by "jiggling" the poles of the BM admittance randomly with position (see Appendix D). However, none of our conclusions depend on the precise form of the perturbations; other schemes (such as jiggling the real or imaginary parts of the BM impedance, jiggling the "active" part of the impedance, jiggling particular model parameters, etc.) give similar results. Although the model assumes for simplicity that the BM impedance changes discontinuously (e.g., from hair cell to hair cell), equivalent results are obtained with much smoother patterns so long as the "roughness" contains spatial frequencies within the passband of the "spatial-frequency filter" that arises through the dynamical action of the traveling wave (see Zweig and Shera, 1995, Figs. 6 and 10).

Considerable evidence indicates that the production of low-level evoked and spontaneous OAEs involves the biophysical and hydromechanical mechanisms that serve to amplify the motion of the basilar membrane. We have therefore assumed that active forces exerted within the cochlear partition couple primarily into the transverse motion of the partition, and thereby into the classical traveling pressure wave that drives it. As a result, we have neglected the possibility that the accelerations of structures within the organ of Corti (e.g., the outer hair cells) also produce significant acoustic compressional waves that propagate through the cochlear fluids at the speed of sound uninfluenced by the basilar membrane (or other tuned mechanical structures, in the case of nonmammalian tetrapods such as frogs and lizards). In principle, back propagation via compressional waves provides an additional mechanism for energy to escape from the inner ear, and mounting albeit not unequivocal evidence suggests that the mechanism operates in the mammalian ear (e.g., Wilson, 1980; Ren, 2004; Ruggero, 2004). Emissions due to compressional waves presumably mix and interfere with those propagated via the transverse pressure difference wave, and their relative amplitudes must depend on factors not currently known with any certainty (e.g., the magnitude of the mechanical perturbations and the strength of any compressional sources). Despite differences in the mechanisms of back propagation, we nevertheless find that the principal physical mechanisms operating in the coherent reflection model (e.g., mechanical irregularity, phase-coherent summation, and dynamical spatial-frequency filtering) also play an important role in shaping the characteristics of any "compressional-wave" OAEs (Shera *et al.*, 2005).

Finally, since the model underlying our analysis is linear, its region of validity is strictly limited to the low-level linear regime near the threshold of hearing. Nevertheless, just as with the 1-D analysis, we expect that many of the more qualitative concepts of the theory will continue to apply, mutatis mutandis, at higher intensities. Furthermore, the 2-D scattering formalism developed here can easily be generalized—just as it was in 1-D (e.g., Talmadge *et al.*, 2000; Shera, 2003b)—to provide a framework for investigating perturbative nonlinear effects, such as "nonlinear roughness" and the generation of distortion products.

E. Effects of scalae height revisited

Our finding that short-wave hydrodynamics enhance the reflection of traveling waves subverts the introductory speculation that the scalae evolved their curiously large size in order to suppress unwanted reflections. If we assume that oversized scalae are conserved not as developmental spandrels (Gould and Lewontin, 1979) but via selective pressure from some direct adaptive advantage, then whatever detriments to cochlear signal processing follow from the increased reflection must be offset by other benefits that accrue to the organism. One obvious possibility is that large scalae confer homeostatic and protective benefits as buffers that help to dampen fluctuations in ionic concentrations.

But another possibility suggested by our analysis is that scalae size plays an important role in shaping the characteristics of cochlear tuning. The mutant BM velocity responses shown in Fig. 15 demonstrate that large changes in mechanical tuning can be produced even when the "active elements" in cochlear mechanics (the BM impedance functions) are held invariant. For example, when the impedance $Z_{\mathrm{BM}}^{1\mathrm{d}}(x)$ is used in the 2-D model the gain of the BM velocity response increases substantially. And vice versa—when $Z_{\mathrm{BM}}^{2\mathrm{d}}(x)$ is employed in a context where the hydrodynamics are effectively one-dimensional the BM velocity response decreases. The dimensions of the scalae in which the organ of Corti finds itself embedded therefore directly affect the sensitivity and bandwidth of mechanical tuning. These results illustrate the power of global hydrodynamic effects in cochlear mechanics. Since scalae sizes vary considerably across species (e.g., Thorne *et al.*, 1999), purely geometric and hydromechanical factors unrelated to active processes or micromechanics within the organ of Corti may make significant contributions to observed species differences in OAE amplitudes and cochlear tuning (e.g., Zurek, 1985; Probst *et al.*, 1991; Shera *et al.*, 2002; Oxenham and Shera, 2003).

ACKNOWLEDGMENTS

We thank Stephen Neely for generously sharing his finite-difference algorithms and thereby providing an independent check on our numerical solutions. We also thank Egbert de Boer, Paul Fahey, John Guinan, Robert Withnell, and the two anonymous reviewers for their helpful comments on the manuscript. This work was supported by Grant Nos. R01 DC003687 (CAS) and R01 DC003094 (CLT) from the NIDCD, National Institutes of Health.

APPENDIX A: FINDING THE BASIS WAVES

The basis waves $W_{\{r,l\}}(x)$ are defined as solutions to Eq. (23) and represent the two independent traveling-wave solutions in the smooth cochlea (Shera and Zweig, 1991; Talmadge *et al.*, 1998). Knowledge of the basis waves is necessary for finding the projection operators $\hat{P}_{\{r,l\}}$ [Eq. (25)], for determining R_{stapes} from a given load impedance at the oval and round windows, and for computing the traveling wave Green's function [Eq. (41) and Appendix B]. Determining the form of the basis waves is therefore central to any discussion of bi-directional wave propagation in the cochlea.

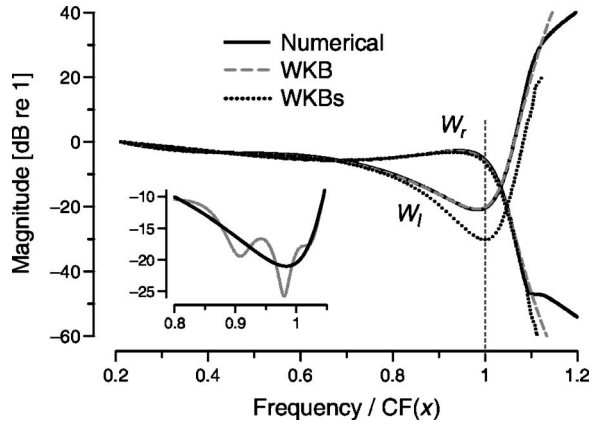

FIG. 16. The basis waves $W_{\{r,l\}}(x)$, numerically and approximately computed. The main panel shows the magnitudes $|W_{\{r,l\}}(x)|$ computed numerically (solid lines) using the procedures outlined in the text. The panel also shows two alternative forms of the WKB basis waves. The dashed gray line shows the functions $W^{\mathrm{WKB}}_{\{r,l\}}(x)$ derived here [Eq. (A3)]; the dotted line shows the functions $W^{\mathrm{WKBs}}_{\{r,l\}}(x)$ [Eq. (A4)] derived by integrating the "standard" WKB approximation for the 2-D model over the scalae height. For reference, a vertical dotted line locates the peak of the corresponding BM velocity response along the abscissa. Inset: The inset shows the numerical solution for $W_l(x)$ (gray line) obtained using the initial estimate for Δ [namely, $-2i\ \mathrm{Im}\{W_r'(0)\}\cong 0.843i\ \mathrm{mm}^{-1}$]. The numerical solution from the main panel, reproduced for comparison (black line), was obtained by varying Δ to minimize the integrated curvature of the solution [Eq. (A2)]. The minimum curvature occurs at $\Delta\cong -0.048+0.85i\ \mathrm{mm}^{-1}$; for comparison, $\Delta(W_r^{\mathrm{WKB}}, W_l^{\mathrm{WKB}})=2ik_0\cong -0.04+0.84i\ \mathrm{mm}^{-1}$.

1. Numerical computation of the basis waves

In a smooth cochlea, forward-traveling waves normally undergo negligible internal reflection (e.g., Shera and Zweig, 1991), so that the basis wave $W_r(x)$ can readily be obtained by solving the model equations with a stimulus applied at the stapes (see Fig. 16). Numerical computation of the reverse-traveling basis wave $W_l(x)$ can be substantially more difficult, however, because wave reflection at the stapes complicates the computation of a pure reverse-traveling solution (Shera and Zweig, 1991).

Perhaps the most straightforward approach to computing $W_l(x)$ numerically is to apply d'Alembert's reduction of order method (e.g., Ince, 1956), which allows a second independent solution to be determined if the first is known. When applied to the wave equation (23) the method yields the explicit formula

$$W_l(x;\Delta)=W_r(x)\left[1+\Delta\int_0^x\frac{dx'}{W_r^2(x')}\right], \tag{A1}$$

where the adjustable complex constant Δ sets the Wronskian determinant $\Delta(W_r,W_l)$ and the constant of integration has been chosen so that $W_l(0)=1$. Although the solution $W_l(x;\Delta)$ given by Eq. (A1) is linearly independent of $W_r(x)$, it does not necessarily represent a *pure* reverse-traveling wave. Unless Δ is chosen so that $W_l(x;\Delta)$ satisfies no-reflection boundary conditions at the stapes, the solution will be a mixture of forward- and reverse-traveling waves.[18]

To obtain a pure reverse-traveling wave we need to minimize boundary reflection by adjusting Δ so that $W_l(0)/W_l'(0)$ is proportional to the "wave impedance" of a reverse-traveling wave at the stapes (Shera and Zweig, 1991; Viergever and de Boer, 1987).[19] A reasonable first approximation is to set $W_l'(0)$ equal to the complex conjugate of $W_r'(0)$, yielding the estimate $\Delta\cong[W_r'(0)]^*-W_r'(0)=-2i\,\mathrm{Im}\{W_r'(0)\}$. The amplitude of any residual forward-traveling component can often be significantly reduced by varying the value of Δ in a neighborhood about this initial estimate. Note, for example, that contamination of the resulting solution for $W_l(x)$ by a reflected forward-traveling wave component produces standing-wave-like oscillations in the magnitude and phase of $W_l(x)$ (see Fig. 16, inset). Since any standing-wave component increases the total curvature of the solution, adjusting Δ to minimize the value of

$$\kappa^2(\Delta)\equiv\int|\partial_x^2[W_lW_r]|^2\,dx, \tag{A2}$$

where κ^2 measures the integrated squared curvature, often works well in practice (Fig. 16, inset). Note that before computing the second derivative we multiply W_l by W_r in order to maximize the standing-wave contribution to κ^2 by dividing out as much of the secular curvature in W_l as possible. Our choice of divisor is based on the expectation that to zeroth order $W_l\sim 1/W_r$. Alternatively, one could estimate $W_l(x)$ using the WKB approximation (see below) and then minimize the total curvature of the ratio W_l/W_l^{WKB}.

Figure 16 shows the basis waves $W_{\{r,l\}}(x)$ computed using the numerical procedures outlined above (solid lines). The amplitude notch/plateau visible in the cutoff region apical to the characteristic place betrays the influence of non-propagating modes in the pressure (e.g., de Boer and Viergever, 1982; Watts, 2000). The inset illustrates the substantial reduction in standing-wave amplitude [i.e., unwanted mixing of forward- and reverse-traveling waves in the solution $W_l(x)$] that can be achieved by minimizing the integrated curvature, $\kappa^2(\Delta)$.

2. Approximate WKB basis waves

Applying the first-order WKB approximation (e.g., Bender and Orszag, 1978; Fröman and Fröman, 1965) to Eq. (23) yields the basis waves

$$W^{\mathrm{WKB}}_{\{r,l\}}(x)=\sqrt{\frac{k_0}{k(x)}}\exp\left(\mp i\int_0^x k(x')dx'\right), \tag{A3}$$

where $k_0\equiv k(0)$. Note that these basis waves differ from those obtained by averaging the "standard" WKB expression for $P(x,y)$ (e.g., Steele and Taber, 1979; Viergever, 1980) over the duct cross-section, which yields

$$W^{\mathrm{WKBs}}_{\{r,l\}}(x)=\frac{A[k_{\mathrm{eik}}(x)H]}{A[k_{\mathrm{eik}}(0)H]}\exp\left(\mp i\int_0^x k_{\mathrm{eik}}(x')dx'\right), \tag{A4}$$

where the amplitude prefactor A has the form

$$A(\eta)\equiv\frac{\sinh(\eta)}{\eta\sqrt{2\eta+\sinh(2\eta)}}. \tag{A5}$$

Note that the wave numbers $k(x)$ and $k_{\mathrm{eik}}(x)$ appearing in Eqs. (A3) and (A4) are not identical. Whereas the wave number $k(x)$ is given by Eq. (20) with $\epsilon=0$, the wave num-

ber $k_{\mathrm{eik}}(x)$ is defined as the principal solution to the complex dispersion relation

$$k_{\mathrm{eik}}H\tanh(k_{\mathrm{eik}}H)=(k_{\mathrm{lw}}H)^2=-H^2Z_{\mathrm{f}}/Z_{\mathrm{BM}}. \tag{A6}$$

Sometimes referred to as the "eikonal equation," dispersion relation (A6) is equivalent to Eq. (20) evaluated under the additional assumption that $\alpha(x)=\alpha_{\mathrm{WKBs}}(x)$ [i.e., that approximation (52) is exact]. Although the transcendental equation has infinitely many solutions (due to the periodicity of the hyperbolic tangent along the imaginary axis), the principal solution is that which satisfies $k_{\mathrm{eik}}(x)\rightarrow k_{\mathrm{lw}}(x)$ in the basal, long-wave region of the cochlear response. Other solutions can become important in the cutoff-region apical to the traveling-wave peak (e.g., de Boer and Viergever, 1982; Watts, 2000). Using Eq. (20) to express $k_{\mathrm{lw}}(x)$ in terms of $k(x)$ shows that the two wave numbers are related via the equation

$$k_{\mathrm{eik}}H\tanh(k_{\mathrm{eik}}H)=(kH)^2/\alpha. \tag{A7}$$

Since $\alpha_{\mathrm{WKBs}}(x)$ is only approximately equal to $\alpha(x)$, the wave number $k_{\mathrm{eik}}(x)$ is only approximately equal to the wave number $k(x)$.

Figure 16 compares $W^{\mathrm{WKB}}_{\{r,l\}}(x)$ and $W^{\mathrm{WKBs}}_{\{r,l\}}(x)$ to the basis waves computed numerically. As illustrated in the figure, the WKB solutions $W^{\mathrm{WKB}}_{\{r,l\}}(x)$ provide excellent analytic approximations to both the forward- and reverse-traveling basis waves. The standard approximations $W^{\mathrm{WKBs}}_{\{r,l\}}(x)$, however, are less uniformly successful. Although $W^{\mathrm{WKBs}}_{r}(x)$ hugs the forward-traveling basis wave quite closely, the corresponding approximation for the reverse-traveling wave, $W^{\mathrm{WKBs}}_{l}(x)$, deviates from the numerical result quite significantly near the characteristic place.

The amplitude prefactor $A(k_{\mathrm{eik}}H)$ that multiplies the complex exponential in Eq. (A4) is most readily derived using energy-flow arguments (e.g., de Boer and Viergever, 1984; Watts, 1992). Since the derivation assumes an approximate form of the wave number [namely, $k_{\mathrm{eik}}(x)$], the functional form of the prefactor must necessarily be distorted to compensate for this approximation if the overall solution is to remain consistent with energy conservation. The comparison in Fig. 16 indicates that this compensatory distortion works well for forward-traveling waves but fails for waves traveling back toward the stapes. Evidently, the $W^{\mathrm{WKBs}}_{\{r,l\}}(x)$ are not optimal approximate solutions to Eq. (23).

Problems with the standard approximations $W^{\mathrm{WKBs}}_{\{r,l\}}(x)$ might have been anticipated by noting that unlike the waves $W^{\mathrm{WKB}}_{\{r,l\}}(x)$, the functions $W^{\mathrm{WKBs}}_{\{r,l\}}(x)$ have a nonconstant Wronskian determinant; thus, according to the Abel identity (e.g., Ince, 1956; Bender and Orszag, 1978), they cannot be exact solutions to *any* Helmholtz equation.

APPENDIX B: THE LONG-WAVE GREEN'S FUNCTION $G(x|x')$

The long-wave Green's function $G(x|x')$ is the symmetric solution to the equation

$$(\partial_x^2+k^2)G=-\delta(x-x'), \tag{B1}$$

subject to the boundary conditions imposed on the waves in the cochlea. To find $G(x|x')$ we note that the point source $\delta(x-x')$ splits the cochlea naturally into two regions: the basal region between the stapes and the source at x', and the apical region between x' and the helicotrema.[20] In each region the general solution consists of a superposition of basis waves $W_{\{r,l\}}(x)$ traveling in opposite directions. The Green's function is therefore given by an expression of the form

$$G(x|x')=\begin{cases} b_rW_r(x)+b_lW_l(x) & \text{for } x<x', \\ a_rW_r(x)+a_lW_l(x) & \text{for } x>x'. \end{cases} \tag{B2}$$

The constants $a_{\{r,l\}}$ and $b_{\{r,l\}}$ (named for "apical" and "basal," respectively) are chosen so that $G(x|x')$ satisfies matching conditions at x' and any boundary conditions at the ends of the cochlea.

To construct the Green's function we begin by rewriting Eq. (B2) in the simplified form

$$G(x|x')\propto\begin{cases} w_b(x) & \text{for } x<x', \\ w_a(x) & \text{for } x>x'. \end{cases} \tag{B3}$$

Here, the function $w_b(x)$ represents a linear combination of basis waves chosen to satisfy the basal boundary condition imposed at the cochlear boundary with the middle ear. For example, if reverse-traveling waves incident on the stapes are reflected with reflection coefficient R_{stapes} (Shera and Zweig, 1991; Talmadge *et al.*, 1998; Puria, 2003; Shera *et al.*, 2004), then $b_r=R_{\mathrm{stapes}}b_l$, so that $w_b(x)$ has the form $b_l[W_l(x)+R_{\mathrm{stapes}}W_r(x)]$. Likewise, the function $w_a(x)$ represents another linear combination chosen to satisfy the apical boundary condition at the helicotrema. The function $G(x|x')$ in Eq. (B3) thus satisfies the appropriate (although as yet unspecified) boundary conditions at both ends of the cochlea.

The matching conditions can be obtained by integrating Eq. (B1) for $G(x|x')$ over an interval containing x' and taking the limit as the interval shrinks to zero; at x' they require that $G(x|x')$ be continuous and that $\partial_xG(x|x')$ have a unit step discontinuity arising from the delta-function source (e.g., Friedman, 1956). After imposing the matching conditions one obtains

$$G(x|x')=w_b(x_<)w_a(x_>)/\Delta(w_a,w_b), \tag{B4}$$

where $x_<(x,x')\equiv\min(x,x')$ and $x_>(x,x')\equiv\max(x,x')$. The function $\Delta(w_a,w_b)$ is the Wronskian determinant of $w_a(x)$ and $w_b(x)$, defined by

$$\Delta(w_a,w_b;x)\equiv w_a(x)w_b'(x)-w_a'(x)w_b(x), \tag{B5}$$

where the primes denote derivatives. Since $w_a(x)$ and $w_b(x)$ are solutions of a 1-D wave equation [Eq. (19)], the Abel identity implies that $\Delta(w_a,w_b;x)$ is independent of x (e.g., Ince, 1956; Bender and Orszag, 1978); the Wronskian can therefore be evaluated at any convenient point.[21]

If the constants a_l and b_r in Eq. (B2) are both zero, the cochlea is effectively infinite in extent (i.e., waves incident upon its boundaries are not reflected). The long-wave Green's function then becomes

$$G_\infty(x|x')=\gamma W_l(x_<)W_r(x_>), \tag{B6}$$

where

$$1/\gamma \equiv \Delta(W_r, W_l). \tag{B7}$$

If reflections occur at the stapes ($b_r = R_{\text{stapes}} b_l$), the Green's function becomes

$$G(x|x') = G_\infty(x|x') + \gamma R_{\text{stapes}} W_r(x) W_r(x'). \tag{B8}$$

APPENDIX C: THE REDUCED GREEN'S FUNCTION $\bar{G}_0(x|x')$

To illustrate and justify the more heuristic discussion in the text we construct an analytic expression for the reduced traveling-wave Green's function $\bar{G}_0(x|x')$ in the simple case where the BM impedance is independent of position. Our construction generalizes to yield an approximate expression valid when the BM impedance varies sufficiently slowly with position.

We first consider the set of functions $Y_n(y)$ defined by

$$(\partial_y^2 - k_n^2) Y_n(y) = 0 \quad (n = 1,2,...) \tag{C1}$$

and subject to the standard boundary conditions at the top and bottom of the scala:

$$\partial_y Y_n|_{y=H} = 0 \tag{C2}$$

and

$$\partial_y \ln Y_n|_{y=0^+} = H Z_f / Z_{\text{BM}}. \tag{C3}$$

The wave numbers k_n are assumed constant (independent of x and y) with $\text{Re}\{k_n\} > 0$. The functions $Y_n(y)$ are given explicitly by

$$Y_n(y) = C_n \cosh[k_n(H-y)], \tag{C4}$$

with

$$k_n H \tanh[k_n H] = -H^2 Z_f / Z_{\text{BM}} \equiv (H k_{\text{lw}})^2. \tag{C5}$$

If the constants C_n are taken to be

$$C_n = [2/(H + \sinh(2k_n H)/2k_n)]^{1/2}, \tag{C6}$$

then

$$\int_0^H Y_n(y) Y_m(y) dy = \delta_{nm}, \tag{C7}$$

where δ_{nm} is the Kronecker delta; the $Y_n(y)$ therefore form a bi-orthogonal set (e.g., Morse and Feshbach, 1953, Part I, pp. 884–886). Passing over some delicate mathematical issues related to establishing the completeness of the $Y_n(y)$ on the interval $(0,H)$ (see, e.g., Dunford and Schwartz, 1971), we assume the closure relation

$$\sum_{n=1}^{\infty} Y_n(y) Y_n(y') = \delta(y - y'). \tag{C8}$$

A particular solution to Laplace's equation is given by

$$P(x,y) = X_n(x) Y_n(y), \tag{C9}$$

where the functions $X_n(x)$ satisfy the wave equation

$$(\partial_x^2 + k_n^2) X_n(x) = 0. \tag{C10}$$

By introducing the right- and left-moving wave solutions $X_{n;\{r,l\}}(x) \equiv e^{\mp i k_n x}$, we can construct a family of one-dimensional Green's functions, $g_n(x|x')$, defined by

$$(\partial_x^2 + k_n^2) g_n(x|x') = -\delta(x - x'), \tag{C11}$$

with $g_n(x|x') = g_n(x'|x)$. We assume no-reflection boundary conditions so that $g_n(x|x')$ takes the form of waves traveling *away* from the source at x': that is, $g_n(x|x') \sim X_{n;r}(x)$ for $x > x'$ and $g_n(x|x') \sim X_{n;l}(x)$ for $x < x'$. Constructing the Green's function using the procedure outlined in Appendix B yields

$$g_n(x|x') = \frac{1}{2ik_n} e^{-ik_n|x-x'|}. \tag{C12}$$

The 2-D hydrodynamic Green's function may now be represented as

$$G(x,y|x',y') = \sum_{n=1}^{\infty} g_n(x|x') q_n(y|y'), \tag{C13}$$

where $q_n(y|y') \equiv Y_n(y) Y_n(y')$. The procedure outlined in the text (Sec. IV B 2) can now be used to construct integral representations of $P(x,y)$ and $\bar{P}(x)$ with the same form as Eqs. (28) and (29). The reduced Green's function is given by Eq. (30); evaluating the integral yields

$$\bar{G}_0(x|x') = -iH \sum_{n=1}^{\infty} C_n^2 \frac{\sinh(2k_n H)}{2k_n H} e^{-ik_n|x-x'|}. \tag{C14}$$

To obtain an approximate expression for $\bar{G}_0(x|x')$ generalizable to the more realistic case of a nonconstant BM impedance we assume that any $n > 1$ modal contributions to $P(x,y)$ are negligible and approximate $G(x,y|x',y')$ using only the $n = 1$ term in Eq. (C13). Substituting into Eq. (30) then yields

$$\bar{G}_0(x|x') \cong g_1(x|x') Y_1(0^+;x') \int_0^H Y_1(y;x) dy, \tag{C15}$$

where we have included x or x' among the list of independent variables for Y_1 as a bookkeeping device. Note that in this approximation $\alpha(x) \cong Y_1(0^+;x)/\bar{Y}_1(;x)$, where $\bar{Y}_1(;x)$ is the scalae-averaged value of $Y_1(y;x)$. Equation (C15) therefore becomes

$$\bar{G}_0(x|x') \cong g_1(x|x') \alpha(x') \bar{Y}_1(;x') H \bar{Y}_1(;x). \tag{C16}$$

We define the scalae-averaged basis waves as

$$W_{\{r,l\}}(x) \equiv X_{1;r,l}(x) \bar{Y}_1(;x)/\bar{Y}_1(;0), \tag{C17}$$

where the factor $\bar{Y}_1(;x)/\bar{Y}_1(;0)$, everywhere equal to 1 when Z_{BM} is constant, is included to guide generalization to the more realistic case. Equation (C16) can then be written

$$\bar{G}_0(x|x') \cong H \bar{Y}_1^2(;0) \alpha(x') G_\infty(x|x'), \tag{C18}$$

where $G_\infty(x|x')$ is given by Eq. (B6) and the corresponding Wronskian determinant has been evaluated at $x = 0$ assuming that the basal region of the cochlea is long-wave. (When Z_{BM} is constant, $k_n H$ is constant throughout the cochlea.) The same assumption implies that $\bar{Y}_1^2(;0) \cong C_1^2 \cong 1/H$. Thus,

$$\bar{G}_0(x|x') \cong \alpha(x') G_\infty(x|x'). \tag{C19}$$

The reduced traveling-wave Green's function thus agrees with the approximation obtained heuristically in Eq. (41).

Although it is not generally possible to derive an analytic representation of the 2-D hydrodynamic Green's function for the case of an x-dependent BM impedance, an approximate representation can be obtained if we assume that $Z_{\mathrm{BM}}(x)$ varies sufficiently slowly with x. In this case, the $Y_n(y)$ defined by Eqs. (C1)–(C3) depend on x as well as y, and are written as $Y_n(y;x)$, where the x is now more than a bookkeeping device. If we then assume a particular solution of Laplace's equation of the form (C9) and neglect the x derivatives of $Y_n(y;x)$, we again obtain Eq. (C10), but now as an approximate relationship. Construction of the approximate Green's functions $G(x,y|x',y')$ and $\bar{G}_0(x|x')$ then proceeds essentially as before. We assume the validity of these generalized constructions in this paper and show that the results derived from them are in impressive agreement with those obtained from direct finite-difference solutions of the 2-D cochlear-model equations (e.g., Figs. 6 and 10).

APPENDIX D: MODELING DETAILS

1. Form and parameters of the wave number

We adopt a variant of the wave number obtained by solving the inverse problem in squirrel monkey (Zweig, 1991). In particular, the model k^2 has the form

$$k^2(x,\omega)=k^2[\beta(x,\omega)]=\frac{(4N/l)^2\beta^2}{1-\beta^2+i\delta\beta+\rho e^{-2\pi i\mu\beta}}. \tag{D1}$$

The scaling variable $\beta(x,\omega)$ is defined by $\beta(x,\omega)\equiv\omega/\omega_{\mathrm{r}}(x)$, where $\omega_{\mathrm{r}}(x)=2\pi f_{\mathrm{r}}(x)$. The frequency $f_{\mathrm{r}}(x)$ is the undamped, *in vacuo* resonant frequency of the partition [i.e., the resonant frequency in the limit when δ and ρ (see below) are both negligible] and is assumed to vary exponentially with position. Thus, $f_{\mathrm{r}}(x)=f_{\mathrm{r}}(0)e^{-x/l}$ with $l\cong 7$ mm, based on estimates of the human cochlear map (Greenwood, 1961, 1990). The dimensionless parameter N represents the approximate number of wavelengths of the traveling wave on the basilar membrane produced by sinusoidal stimulation (Zweig *et al.*, 1976; Zweig, 1991). The dimensionless parameter δ determines the net damping in the model, and the dimensionless parameters ρ and μ characterize, respectively, the strength and the time delay (in periods of the local resonant frequency) of the stabilizing feedback force.

For ease of analysis, the model variant used here has the same functional form as Zweig's original, but differs somewhat in its parameter values. In particular, we use the simpler "double-pole" form of the wave number (Zweig and Shera, 1995; Shera, 2001) in which the parameter values $\{\delta,\rho,\mu\}$ are determined by requiring that the two poles of the BM admittance principally responsible for the peak in the BM velocity response coincide at a given distance, α_*, from the real frequency axis. Formulas for $\{\delta,\rho,\mu\}$ are given in footnote 8 of Shera (2001). For the standard parameters used here we took $\alpha_*=0.06$, yielding $\{\delta,\rho,\mu\}\cong\{-0.063,0.095,1.74\}$. These parameters were chosen to yield $\hat{k}H\cong 6$ for $H\cong 0.7$ mm, in agreement with the estimates from Fig. 1 at 3 kHz. The standard model parameter values are listed in Table I.

TABLE I. Standard model parameter values used in the simulations. Parameter values were chosen to provide rough agreement with Fig. 1 (i.e., $\hat{k}H\cong 6$ at 3 kHz) but may not accurately reproduce other mechanical or otoacoustic responses of the human cochlea. The stimulus frequency (f) and scalae height (H) were sometimes systematically varied from the standard values listed here (e.g., Figs. 10 and 11).

Parameter	Values
f	3.0 kHz
H	0.7 mm
$f_{\mathrm{r}}(0)$	15.0 kHz
$f_{\mathrm{r}}(L)$	2.0 kHz
l	7.0 mm
ρ_0	1.0g/cm^3
b	1.0 mm
N	3.5
α_*	0.06
σ_*	0.005
δ	−0.063
ρ	0.095
μ	1.74
R_{stapes}	0.0
N_x	1500
N_y	100

Mechanical impedance perturbations were introduced by jiggling α_* irregularly with position using random numbers drawn from a Gaussian distribution (with standard a deviation σ_* roughly 1% of the mean). In order to ensure that the mechanical perturbations had no effect on the wave impedances at the ends of the cochlea, the roughness was confined to the central 90% of the cochlear length using a spatial taper.

2. Integrity of the numerical solutions

Simulating OAEs in active cochlear models requires special care. Active models propagate and amplify numerical errors much as they do actual responses to the stimulus. Once they appear, small errors can grow rapidly and thereafter masquerade as genuine otoacoustic responses. Since relative OAE amplitudes are often quite small—human TEOAEs and SFOAEs are typically 10–100 times smaller than the stimulus—computational procedures that suffice when solving solely for the primary response to the stimulus may fail completely when calculating OAEs.

Finite-difference algorithms necessarily discretize the spatial coordinates in the model, and employing too coarse a grid can lead to spurious results. Since the optimal grid spacing depends on both the numerical algorithms employed and the size of the acceptable error, there are no hard and fast rules for determining the number of required sections. In the context of modeling OAEs, an extreme lower bound on N_x might be the number (N_{min}) necessary to represent the spatial frequencies important for emission generation. The theory of coherent reflection filtering yields the estimate $N_{\mathrm{min}}\sim 8L/\hat{\lambda}$ sections, where L is the cochlear length and $\hat{\lambda}$ is the wavelength at the traveling-wave peak for the frequency of interest. The factor of 8 arises as the product 4×2, where the

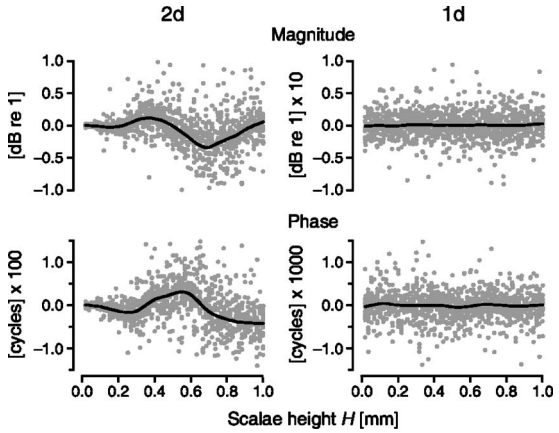

FIG. 17. Scatterplot of the ratio $R_{\mathrm{num}}/R_{\mathrm{Born}}$ in response-matched 1-D and 2-D cochlear models versus scalae height, H. Ratios computed from each of the 2400 simulations used in Fig. 11 are arrayed in four panels: The columns correspond to model dimensionality and the rows to magnitude and phase. The y axes for the 1-D model (column 2) span a range ten times smaller than for the 2-D model. Data points are shown as gray dots and loess trend lines are superposed to guide the eye (Cleveland, 1993). A small percentage of the data (<4%) falls outside the ranges shown.

factor of 4 is needed to encompass the range of spatial frequencies falling within the pass-band of the "spatial-frequency filter" (e.g., Zweig and Shera, 1995, Fig. 6) and the additional factor of 2 arises from Nyquist's sampling theorem. Using estimates of $\hat{\lambda}$ for the human cochlea obtained from measurements of SFOAEs (Shera and Guinan, 2003, Table II) yields $N_{\mathrm{min}}\sim 650$ sections for a model that matches human SFOAE group delays over the full range of human hearing.

Whether any particular grid spacing suffices in practice can only be determined by detailed numerical analysis. Decreasing the grid spacing until the solution no longer varies on scales relevant to the issues at hand often provides a useful empirical assay. Our experience modeling OAEs indicates that the necessary number of sections can sometimes be significantly greater than the lower bound estimated above. To obtain the results reported here we used a longitudinal grid spacing roughly five times finer than L/N_{min}. [To speed up the calculations we truncated our model ($L\cong 14$ mm) so that it did not represent the full range of CFs typical of a healthy human ear. The numbers of sections we employed in the horizontal and vertical directions (N_x and N_y) are given in Table I.] For the 2-D calculations we employed a vertical spacing (H/N_y) similar to that used in the longitudinal direction. In all cases we verified that the solution did not change—at least on the scales relevant here—when the grid spacing was decreased further.

In addition, we checked the accuracy of our numerical procedures by comparing with approximate analytical results (e.g., perturbative calculations of R, WKB approximations for $W_{\{r,l\}}$, etc.) whenever possible. For example, Fig. 17 shows a scatterplot of the ratio $R_{\mathrm{num}}/R_{\mathrm{Born}}$ for each of the 2×1200 simulations reported in Fig. 11. R_{num} is the reflectance computed numerically by solving Laplace's equation (in 2-D) or the Helmholtz equation (in 1-D) using finite-differences (e.g., Neely, 1981; Watts, 2000); R_{Born} is the first-order perturbative expression given by Eq. (45). Quantitative agreement between the methods is generally excellent, with mean ratios indistinguishable from 1 and interquartile ranges for the 2-D model less than 0.25 dB in magnitude and 0.005 cycles in phase (and at least an order of magnitude smaller for the 1-D model). Interestingly, the 2-D scatterplot reveals systematic oscillations with H that appear roughly 90° out of phase in the magnitude and phase plots. These deviations presumably result from small errors in approximation (41) for $\bar{G}_0(x'|x')$ and/or the influence of higher-order nonpropagating pressure modes in the finite-difference solution.

APPENDIX E: FREQUENTLY USED SYMBOLS

Independent variables

x, x', x''	longitudinal distance from stapes
y	vertical distance from BM
ω	$2\pi\times$stimulus frequency, f

Cochlear parameters and maps

H	scalae height
b	BM width
L	cochlear length
ρ_0	density of cochlear fluids
$\mathrm{CF}(x)$	characteristic frequency for location x
$\hat{x}(\omega)$	characteristic place for stimulus frequency ω

Cochlear impedances

$Z_{\mathrm{f}}(\omega)$	fluid acoustic impedance (per unit length) [Eq. (8)]
$\tilde{Z}_{\mathrm{BM}}(x,\omega)$	BM acoustic impedance (times unit length) with perturbations [Eq. (10)]
$Z_{\mathrm{BM}}(x,\omega)$	"smooth" BM impedance without perturbations [Eq. (12)]
$Z^{\mathrm{1d}}_{\mathrm{BM}}(x,\omega)$	BM impedance in response-matched 1-D model
$Z^{\mathrm{2d}}_{\mathrm{BM}}(x,\omega)$	BM impedance in response-matched 2-D model

Dynamical variables

$P(x,y,\omega)$	scalae difference pressure [Eq. (1)]
$U(x,\omega)$	longitudinal component of fluid volume velocity [Eq. (4)]
$U_{\mathrm{ow}}(\omega)$	volume velocity of oval window [Eq. (4)]
$V_{\mathrm{BM}}(x,\omega)$	BM velocity [Eq. (3)]

Wave numbers and wavelengths

$\tilde{k}_{\mathrm{lw}}(x,\omega)$	long-wave wave number with perturbations [Eq. (17)]
$\tilde{k}(x,\omega)$	wave number with perturbations [Eq. (20)]
$k(x,\omega)$	smooth wave number [Eq. (21)]
$\hat{\lambda}(\omega)$	wavelength at $\hat{x}$
$\hat{k}(\omega)$	wave number at $\hat{x}$

Mechanical perturbations

$\Delta Z_{\mathrm{BM}}(x,\omega)$	BM impedance perturbations [Eq. (12)]
$\epsilon(x,\omega)$	fractional wave number perturbations [Eq. (21)]
$\varrho(x,\omega)$	wave number perturbations ϵk^2 [Eq. (29)]

Derived variables

$\bar{P}(x,\omega)$	difference pressure $P(x,y)$ averaged over y [Eq. (7)]
$P_0(x,\omega)$	difference pressure $P(x,0^+)$ across BM [Eq. (16)]
$\alpha(x,\omega)$	pressure ratio $P_0(x)/\bar{P}(x)$ [Eq. (18)]
$\alpha_{\mathrm{WKBs}}(x,\omega)$	α from standard WKB approximation for $P(x,y)$ [Eq. (52)]
$T(x,\omega)$	BM velocity transfer function $V_{\mathrm{BM}}/V_{\mathrm{stapes}}$

Wave components

$W_{\{r,l\}}(x,\omega)$	forward- and reverse-traveling (right- and left-moving) basis waves [Eq. (23)]
$\hat{P}_{\{r,l\}}(x,\omega)$	wave projection operators [Eq. (24)]
$\bar{P}_{\{r,l\}}(x,\omega)$	forward- and reverse-traveling waves
$\bar{P}_0(\omega)$	amplitude of forward-traveling wave at stapes, $\bar{P}_r(0)$
$C_{\{r,l\}}(x,\omega)$	wave coefficients[4]

Green's functions

$G(x,y\|x',y';\omega)$	2D hydrodynamic Green's function [Eq. (26)]
$\bar{G}_0(x\|x';\omega)$	reduced traveling-wave Green's function [Eq. (30)]
$Q(y;x\|y';x',\omega)$	2D Green's function with traveling-wave dependence factored out [Eq. (36)]
$G(x\|x';\omega)$	long-wave traveling-wave Green's function [Eq. (37) and Appendix B]
$G_\infty(x\|x';\omega)$	long-wave traveling-wave Green's function for "infinite" cochlea [Eq. (42)]

Reflectances

$R(\omega)$	apical looking cochlear reflectance [Eq. (13)]
$R_{1\mathrm{d}}(\omega)$	cochlear reflectance in response-matched 1-D model
$R_{2\mathrm{d}}(\omega)$	cochlear reflectance in response-matched 2-D model
$R_{\mathrm{Born}}(\omega)$	first-order (Born) approximation for R [Eq. (45)]
$R_{\mathrm{stapes}}(\omega)$	stapes reflection coefficient

Group delays

$\tau_{\mathrm{BM}}(\omega)$	BM group delay, $-\partial_\omega T$
$\tau(\omega)$	reflectance group delay, $-\partial_\omega R$
$\tau_{1\mathrm{d}}(\omega)$	reflectance group delay in response-matched 1-D model
$\tau_{2\mathrm{d}}(\omega)$	reflectance group delay in response-matched 2-D model

Miscellaneous

$\delta(x)$	Dirac delta function [Eq. (26)]
$\Delta(f,g)$	Wronskian determinant of functions f and g [Eq. (B5)]
γ	reciprocal of Δ [Eq. (B7)]

[1]Informal discussions at the 2002 workshop on the Biophysics of the Cochlea: From Molecules to Models held in Titisee, Germany.

[2]Solutions to the inverse problem in sensitive preparations indicate that at low and moderate intensities the peak of the traveling wave occurs close to the point where traveling-wave amplification reverses sign and the accumulated power is dumped into the organ of Corti. At this point, $\mathrm{Im}\{k(x)\}$ goes through a negative-going zero-crossing (e.g., Zweig, 1991; de Boer, 1995b), and $\hat{k}$ is therefore essentially real.

[3]Our general argument is corroborated by the observation that the approximate analytic expression for $\alpha(x)$ obtained using the WKB approximation[7] applies equally to waves traveling in either direction.

[4]Behind the curtain, the projection operators work by finding the coefficient functions $C_{\{r,l\}}(x)$ needed to write $\bar{P}(x)$ in the form

$$\bar{P}(x)=\underbrace{C_r(x)W_r(x)}_{\bar{P}_r(x)}+\underbrace{C_l(x)W_l(x)}_{\bar{P}_l(x)},$$

where $\bar{P}(x)$ and its first derivative [proportional to U by Eq. (6)] are matched exactly at every point. In other words, the coefficient functions $C_{\{r,l\}}(x)$ are the solutions to the pair of simultaneous equations

$$\bar{P}(x)=C_r(x)W_r(x)+C_l(x)W_l(x),$$

$$\partial_x\bar{P}(x)=C_r(x)\partial_xW_r(x)+C_l(x)\partial_xW_l(x).$$

Solving these equations for the $C_{\{r,l\}}(x)$ and computing the products $\bar{P}_{\{r,l\}}(x)\equiv C_{\{r,l\}}(x)W_{\{r,l\}}(x)$ yields Eqs. (24) and (25). Because they enforce a certain continuous intimacy with the solution, the coefficient functions $C_{\{r,l\}}(x)$ are known as "osculating parameters" (e.g., Mathews and Walker, 1964; Shera and Zweig, 1991; Talmadge *et al.*, 1998).

[5]After Max Born, who derived an analogous expansion in the context of the quantum mechanical theory of collisions (e.g, Born, 1926; Born and Wolf, 1959).

[6]In previous derivations based on the 1-D model (e.g., Shera and Zweig, 1991; Zweig and Shera, 1995; Talmadge *et al.*, 1998, 2000) we solved the scattering problem using a method known as "variation of parameters" (e.g., Mathews and Walker, 1964). The 1-D results can also be derived using a mathematically equivalent procedure based on the long-wave Green's function.

[7]In the standard WKB approximation for the 2-D model (e.g., Steele and Taber, 1979; Viergever, 1980; de Boer and Viergever, 1982), the pressure $P(x,y)$ has the form

$$P_{\mathrm{WKBs}}(x,y)=P_0(x)\,\frac{\cosh[k(x)(H-y)]}{\cosh[k(x)H]}.$$

Calculating $\bar{P}_{\mathrm{WKBs}}(x)$ by averaging this expression over y yields Eq. (52) for $\alpha_{\mathrm{WKBs}}(x)$.

[8]A region of net negative BM resistance near the base of the cochlea is a feature of the Zweig model, which was derived by finding an analytic approximation to the wave number obtained using the inverse method. Note, however, that the uncertainty in the inverse solution is largest in the tail of the response, where the BM velocity response is relatively insensitive to the precise value of the BM resistance.

[9]For clarity we note that the responses of the 1-D model were obtained by solving the 1-D equations—derived by assuming that the pressure is nearly uniform over the scalae—using the specified values of H. Thus, both the 1-D and 2-D models used the same impedances Z_{f} and manifest identical values of $\hat{k}H$.

[10]More explicitly, if $\angle k=\mathrm{atan}(k_i/k_r)$, where k_r and k_i are the real and imaginary parts of k, then $\partial_x\angle k\cong(k_r/|k|^2)\partial_xk_i$, where we have assumed that $k_i\partial_xk_r\cong 0$ because of the zero-crossing in k_i near the peak at $\hat{x}$ (see footnote 2). Scaling implies that spatial derivatives at fixed frequency have the same sign as frequency derivatives at fixed position ($\partial_x/\partial_\omega>0$). Thus, if $k_r>0$ and $\partial_xk_i<0$ near the peak, then $\hat{\tau}_k=-\partial_\omega\angle k>0$.

[11]For an historical introduction to Green and his many functions, see the recent review by Challis and Sheard (2003).

[12]In the short-wave regime, $\alpha\cong kH$ so that the effective scalae height $H_{\mathrm{eff}}\equiv H/\alpha\to 1/k$. Thus $H_{\mathrm{eff}}\cong\hat{\lambda}/2\pi$ near the characteristic place.

[13]According to standard transmission-line theory (with the identification $Z\leftarrow Z_{\mathrm{f}}$), the wave number of the waves on the line is given by $k=\sqrt{-ZY}$ and the characteristic impedance by $Z_0=\sqrt{Z/Y}$ (e.g., Slater, 1942).

[14]In contrast, $Z_0 \rightarrow iZ_{\mathrm{BM}}/H$ when α modifies the shunt admittance.

[15]Zwislocki's (1983) proof is based on a wave equation for the difference pressure $P_0(x)$ obtained using an averaging procedure similar to that of Duifhuis (1988). Rather than average the pressure, Zwislocki (1953) integrates the x derivative of the longitudinal component of the fluid particle velocity over the scalae to obtain an effective cross-sectional area, $q(x)$, defined by the equation $q(x) \equiv S\partial_x \bar{u}/\partial_x u_0$, where $u_0(x) \equiv u(x,0)$ and $u(x,y)$ is the x-component of the fluid particle velocity. Zwislocki (1983) then deduces the transmission-line equations corresponding to the resulting wave equation by intuitively (but mistakenly) associating $q(x)$ with the series impedance characterizing the longitudinal inertia of the fluids. [By following Zwislocki and neglecting small derivatives one can show that $q(x) \cong S/\alpha(x)$.] However, the actual transmission-line equations corresponding to Zwislocki's wave equation are $\partial_x P_0 = -2i\omega\rho u_0$ and $\partial_x u_0 = -P_0/qZ_{\mathrm{BM}}$. In the correct equations, the effective cross-sectional area, proportional to $1/\alpha(x)$, is associated with the BM impedance, just as it is in Fig. 14.

[16]Our terminology derives from de Boer, who refers to the process of deriving the BM impedance with one model and resynthesizing the response with another as "cross-fertilization" (de Boer and Nuttall, 2000).

[17]The various practical complications include (1) transforming frequency-domain responses measured at fixed location $[V_{\mathrm{BM}}(x_0,\omega)]$ into spatial responses measured at fixed frequency $[V_{\mathrm{BM}}(x,\omega_0)]$, as required for use in Eq. (50); (2) minimizing and handling uncertainty due to measurement errors; (3) smoothing the measurements to reduce effects of noise and internal reflection; (4) interpolating and extrapolating to estimate values of V_{BM} at points where measurements are not available; and (5) enforcing known (or presumed) constraints on the functions V_{BM} and k^2 (e.g., causality, minimum-phase behavior, smoothness, asymptotic form at low and high frequencies and/or in extreme basal and apical regions of the cochlea).

[18]To illustrate the d'Alembert formula, consider the wave equation with constant wave number, k_0, and take $W_r(x)$ equal to the forward-traveling wave, e^{-ik_0x}. Equation (A1) for $W_l(x)$ with nonzero $\Delta = 2ik_0(1+\delta)$ then gives

$$W_l(x) = (1+\delta)e^{+ik_0x} - \delta e^{-ik_0x}.$$

When $\delta = 0$, the formula for $W_l(x)$ yields a pure reverse-traveling wave, e^{+ik_0x}; any other value ($\delta \neq -1$) yields a mixture of forward and reverse waves.

[19]Shera and Zweig (1991) show that using the characteristic impedance rather than the retrograde wave impedance can produce large reflections from the stapes (e.g., $|R_{\mathrm{stapes}}| > 0.5$ in Fig. 5 of the 1991 paper). Although terminating the system in its characteristic impedance would eliminate boundary reflection in a uniform transmission line, it does not do so in a nonuniform system where the characteristic impedance varies with position (e.g., a box model of the cochlea).

[20]The procedure for finding $G(x|x')$ outlined here is essentially the same as that used to find the response to a sinusoidal force applied to BM, as described in words in Shera *et al.* [2004, Eq. (1) and surrounding text].

[21]Note that

$$\Delta(w_a,w_b) \equiv \det\begin{pmatrix} w_a & w_b \\ w_a' & w_b' \end{pmatrix} = \det\left[\begin{pmatrix} W_r & W_l \\ W_r' & W_l' \end{pmatrix}\begin{pmatrix} a_r & b_r \\ a_l & b_l \end{pmatrix}\right] = (a_rb_l - a_lb_r)\Delta(W_r,W_l).$$

Evaluating $\Delta(W_r,W_l)$ using the approximate WKB forms $W_{\{r,l\}}^{\mathrm{WKB}}(x)$ given in Eq. (A3) yields $1/\gamma_{\mathrm{WKB}}(\omega) \equiv \Delta(W_r^{\mathrm{WKB}}, W_l^{\mathrm{WKB}}) = 2ik_0(\omega)$.

Allen, J. B. (**1977**). "Two-dimensional cochlear fluid model: New results," J. Acoust. Soc. Am. **61**, 110–119.

Bender, C. M., and Orszag, S. A. (**1978**). *Advanced Mathematical Methods for Scientists and Engineers* (McGraw-Hill, New York).

Beranek, L. L. (**1986**). *Acoustics* (American Institute of Physics, New York).

Born, M. (**1926**). "Quantenmechanik der Stossvorgänge (Quantum mechanics of impact processes)," Z. Phys. **38**, 803–827.

Born, M., and Wolf, E. (**1959**). *Principles of Optics: Electromagnetic Theory of Propagation, Interference and Diffraction of Light* (Pergamon, Oxford).

Bredberg, G. (**1968**). "Cellular patterns and nerve supply of the human organ of Corti," Acta Oto-Laryngol., Suppl. **236**, 1–135.

Carlin, H. J., and Giordano, A. B. (**1964**). *Newtork Theory: An Introduction to Reciprocal and Nonreciprocal Circuits* (Prentice Hall, Englewood Cliffs, NJ).

Challis, L., and Sheard, F. (**2003**). "The Green of Green functions," Phys. Today **56**, 41–46.

Cleveland, W. S. (**1993**). *Visualizing Data* (Summit Hobart, NJ).

Cooper, N. P., and Shera, C. A. (**2004**). "Backward traveling waves in the cochlea? Comparing basilar membrane vibrations and otoacoustic emissions from individual guinea-pig ears," Assoc. Res. Otolaryngol. Abs. **27**, 1008.

Courant, R. (**1988**). *Differential and Integral Calculus, Vol. II* (Wiley Interscience, New York).

Courant, R., and Hilbert, D. (**1953**). *Methods of Mathematical Physics* (Wiley Interscience, New York).

de Boer, E. (**1979**). "Short-wave world revisited: Resonance in a two-dimensional cochlear model," Hear. Res. **1**, 253–281.

de Boer, E. (**1983**). "Wave reflection in passive and active cochlea models," in *Mechanics of Hearing*, edited by E. de Boer and M. A. Viergever (Martinus Nijhoff, The Hague), pp. 135–142.

de Boer, E. (**1995a**). "The inverse problem solved for a three-dimensional model of the cochlea. I. Analysis," J. Acoust. Soc. Am. **98**, 896–903.

de Boer, E. (**1995b**). "The inverse problem solved for a three-dimensional model of the cochlea. II. Application to experimental data sets," J. Acoust. Soc. Am. **98**, 904–910.

de Boer, E. (**1996**). "Mechanics of the cochlea: Modeling efforts," in *The Cochlea*, edited by P. Dallos, A. N. Popper, and R. R. Fay (Springer-Verlag, New York), pp. 258–317.

de Boer, E. (**2001**). "The short-wave model and waves in two directions," J. Acoust. Soc. Am. **109**, 291–293.

de Boer, E., and Nuttall, A. L. (**1999**). "The inverse problem solved for a three-dimensional model of the cochlea. III. Brushing-up the solution method," J. Acoust. Soc. Am. **105**, 3410–3420.

de Boer, E., and Nuttall, A. L. (**2000**). "The mechanical waveform of the basilar membrane. II. From data to models—and back," J. Acoust. Soc. Am. **107**, 1487–1496.

de Boer, E., and Viergever, M. A. (**1982**). "Validity of the Liouville-Green (or WKB) method for cochlear mechanics," Hear. Res. **8**, 131–155.

de Boer, E., and Viergever, M. A. (**1984**). "Wave propagation and dispersion in the cochlea," Hear. Res. **13**, 101–112.

de Boer, E., Nuttall, A. L., and Grosh, K. (**2004**). "Elusive entrainment," Assoc. Res. Otolaryngol. Abs. **27**, 544.

Dhar, S., Talmadge, C. L., Long, G. R., and Tubis, A. (**2002**). "Multiple internal reflections in the cochlea and their effect on DPOAE fine structure," J. Acoust. Soc. Am. **112**, 2882–2897.

Duifhuis, H. (**1988**). "Cochlear macromechanics," in *Auditory Function: Neurological Bases for Hearing*, edited by G. M. Edelman, W. E. Gall, and W. M. Cowan (Wiley, New York), pp. 189–212.

Dunford, N., and Schwartz, J. T. (**1971**). *Linear Operators, Part III* (Wiley, New York).

Engström, H., Ades, H. W., and Andersson, A. (**1966**). *Structural Pattern of the Organ of Corti* (Williams and Wilkins, Baltimore).

Friedman, B. (**1956**). *Principles and Techniques of Applied Mathematics* (Wiley, New York).

Fröman, N., and Fröman, P. O. (**1965**). *JWKB Approximation: Contributions to the Theory* (North-Holland, Amsterdam).

Gould, S. J., and Lewontin, R. C. (**1979**). "The spandrels of San Marco and the Panglossian paradigm: a critique of the adaptationist programme," Proc. R. Soc. London, Ser. B **205**, 581–598.

Greenwood, D. D. (**1961**). "Critical bandwidth and the frequency coordinates of the basilar membrane," J. Acoust. Soc. Am. **33**, 1344–1356.

Greenwood, D. D. (**1990**). "A cochlear frequency-position function for several species—29 years later," J. Acoust. Soc. Am. **87**, 2592–2605.

Hubbard, A. E., and Mountain, D. C. (**1996**). "Analysis and synthesis of cochlear mechanical function using models," in *Auditory Computation*, edited by H. L. Hawkins, T. A. McMullen, A. N. Popper, and R. R. Fay (Springer-Verlag, New York), pp. 62–120.

Ince, E. L. (**1956**). *Ordinary Differential Equations* (Dover, New York).

Jay, R. (**2001**). *Jay's Journal of Anomalies: Conjurers, Cheats, Hustlers, Hoaxsters, Pranksters, Jokesters, Imposters, Pretenders, Side-Show Showmen, Armless Calligraphers, Mechanical Marvels, Popular Entertainments* (Farrar Straus & Giroux, New York).

Kemp, D. T., and Brown, A. M. (**1983**). "An integrated view of cochlear mechanical non-linearities observable from the ear canal," in *Mechanics*

of Hearing, edited by E. de Boer and M. A. Viergever (Martinus Nijhoff, The Hague), pp. 75–82.
Lighthill, J. (**1981**). "Energy flow in the cochlea," J. Fluid Mech. **106**, 149–213.
Lonsbury-Martin, B. L., Martin, G. K., Probst, R., and Coats, A. C. (**1988**). "Spontaneous otoacoustic emissions in the nonhuman primate. II. Cochlear anatomy," Hear. Res. **33**, 69–94.
Mammano, F., and Nobili, R. (**1993**). "Biophysics of the cochlea: Linear approximation," J. Acoust. Soc. Am. **93**, 3320–3332.
Mathews, J., and Walker, R. (**1964**). *Mathematical Methods of Physics* (Benjamin, New York).
Morse, P. M., and Feshbach, H. (**1953**). *Methods of Theoretical Physics, Parts I and II* (McGraw-Hill, New York).
Nedzelnitsky, V. (**1980**). "Sound pressures in the basal turn of the cat cochlea," J. Acoust. Soc. Am. **68**, 1676–1689.
Neely, S. T. (**1981**). "Finite difference solution of a two-dimensional mathematical model of the cochlea," J. Acoust. Soc. Am. **69**, 1386–1393.
Olson, E. S. (**2001**). "Intracochlear pressure measurements related to cochlear tuning," J. Acoust. Soc. Am. **110**, 349–367.
Oxenham, A. J., and Shera, C. A. (**2003**). "Estimates of human cochlear tuning at low levels using forward and simultaneous masking," J. Assoc. Res. Otolaryngol. **4**, 541–554.
Parthasarathi, A. A., Grosh, K., and Nuttall, A. L. (**2000**). "Three-dimensional numerical modeling for global cochlear dynamics," J. Acoust. Soc. Am. **107**, 474–485.
Peake, W. T., Rosowski, J. J., and Lynch, T. J. (**1992**). "Middle-ear transmission: Acoustic versus ossicular coupling in cat and human," Hear. Res. **57**, 245–268.
Peterson, L. C., and Bogert, B. P. (**1950**). "A dynamical theory of the cochlea," J. Acoust. Soc. Am. **22**, 369–381.
Probst, R., Lonsbury-Martin, B. L., and Martin, G. K. (**1991**). "A review of otoacoustic emissions," J. Acoust. Soc. Am. **89**, 2027–2067.
Puria, S. (**2003**). "Measurements of human middle ear forward and reverse acoustics: Implications for otoacoustic emissions," J. Acoust. Soc. Am. **113**, 2773–2789.
Ren, T. (**2002**). "Longitudinal pattern of basilar membrane vibration in the sensitive cochlea," Proc. Natl. Acad. Sci. U.S.A. **99**, 17101–17106.
Ren, T. (**2004**). "Reverse propagation of sound in the gerbil cochlea," Nat. Neurosci. **7**, 333–334.
Ruggero, M. A. (**2004**). "Comparison of group delays of $2f_1-f_2$ distortion product otoacoustic emissions and cochlear travel times," ARLO **5**, 143–147.
Schairer, K. S., Fitzpatrick, D., and Keefe, D. H. (**2003**). "Input-output functions for stimulus-frequency otoacoustic emissions in normal-hearing adult ears," J. Acoust. Soc. Am. **114**, 944–966.
Shera, C. A. (**2001**). "Intensity-invariance of fine time structure in basilar-membrane click responses: Implications for cochlear mechanics," J. Acoust. Soc. Am. **110**, 332–348.
Shera, C. A. (**2003a**). "Mammalian spontaneous otoacoustic emissions are amplitude-stabilized cochlear standing waves," J. Acoust. Soc. Am. **114**, 244–262.
Shera, C. A. (**2003b**). "Wave interference in the generation of reflection- and distortion-source emissions," in *Biophysics of the Cochlea: From Molecules to Models*, edited by A. W. Gummer (World Scientific, Singapore), pp. 439–453.
Shera, C. A., and Guinan, J. J. (**1999**). "Evoked otoacoustic emissions arise by two fundamentally different mechanisms: A taxonomy for mammalian OAEs," J. Acoust. Soc. Am. **105**, 782–798.
Shera, C. A., and Guinan, J. J. (**2003**). "Stimulus-frequency-emission group delay: A test of coherent reflection filtering and a window on cochlear tuning," J. Acoust. Soc. Am. **113**, 2762–2772.
Shera, C. A., and Zweig, G. (**1991**). "Reflection of retrograde waves within the cochlea and at the stapes," J. Acoust. Soc. Am. **89**, 1290–1305.
Shera, C. A., and Zweig, G. (**1992a**). "Analyzing reverse middle-ear transmission: Noninvasive Gedanken experiments," J. Acoust. Soc. Am. **92**, 1371–1381.
Shera, C. A., and Zweig, G. (**1992b**). "An empirical bound on the compressibility of the cochlea," J. Acoust. Soc. Am. **92**, 1382–1388.
Shera, C. A., and Zweig, G. (**1992c**). "Middle-ear phenomenology: The view from the three windows," J. Acoust. Soc. Am. **92**, 1356–1370.
Shera, C. A., and Zweig, G. (**1993a**). "Noninvasive measurement of the cochlear traveling-wave ratio," J. Acoust. Soc. Am. **93**, 3333–3352.
Shera, C. A., and Zweig, G. (**1993b**). "Order from chaos: Resolving the paradox of periodicity in evoked otoacoustic emission," in *Biophysics of Hair Cell Sensory Systems*, edited by H. Duifhuis, J. W. Horst, P. van Dijk, and S. M. van Netten (World Scientific, Singapore), pp. 54–63.
Shera, C. A., Guinan, J. J., and Oxenham, A. J. (**2002**). "Revised estimates of human cochlear tuning from otoacoustic and behavioral measurements," Proc. Natl. Acad. Sci. U.S.A. **99**, 3318–3323.
Shera, C. A., Talmadge, C. L., and Tubis, A. (**2000**). "Interrelations among distortion-product phase-gradient delays: Their connection to scaling symmetry and its breaking," J. Acoust. Soc. Am. **108**, 2933–2948.
Shera, C. A., Tubis, A., and Talmadge, C. L. (**2004**). "Are there forward and reverse traveling waves in the cochlea? Countering the critique of Nobili *et al.*," J. Assoc. Res. Otolaryngol. **5**, 349–359.
Shera, C. A., Tubis, A., and Talmadge, C. L. (**2005**). "Coherent-reflection models of reflection-source OAEs with and without slow transverse retrograde waves," Assoc. Res. Otolaryngol. Abs. **28**, 657.
Siebert, W. M. (**1974**). "Ranke revisited—a simple short-wave cochlear model," J. Acoust. Soc. Am. **56**, 594–600.
Slater, J. C. (**1942**). *Microwave Transmission* (McGraw-Hill, New York).
Steele, C. R., and Taber, L. A. (**1979**). "Comparison of WKB and finite difference calculations for a two-dimensional cochlear model," J. Acoust. Soc. Am. **65**, 1001–1006.
Talmadge, C. L., Tubis, A., and Tong, C. (**2001**). "Cochlear wave reflection due to roughness in 2-D and 3-D cochlear models," Assoc. Res. Otolaryngol. Abs. **24**, 44.
Talmadge, C. L., Tubis, A., Long, G. R., and Piskorski, P. (**1998**). "Modeling otoacoustic emission and hearing threshold fine structures," J. Acoust. Soc. Am. **104**, 1517–1543.
Talmadge, C. L., Tubis, A., Long, G. R., and Tong, C. (**2000**). "Modeling the combined effects of basilar membrane nonlinearity and roughness on stimulus frequency otoacoustic emission fine structure," J. Acoust. Soc. Am. **108**, 2911–2932.
Thorne, M., Salt, A. N., DeMott, J. E., Henson, M. M., Henson, O. W., and Gewalt, S. L. (**1999**). "Cochlear fluid space dimensions for six species derived from reconstructions of three-dimensional magnetic resonance images," Laryngoscope **109**, 1661–1668.
Viergever, M. A. (**1980**). *Mechanics of the Inner Ear: A Mathematical Approach* (Delft U.P., Delft).
Viergever, M. A., and de Boer, E. (**1987**). "Matching impedance of a non-uniform transmission line: Application to cochlear modeling," J. Acoust. Soc. Am. **81**, 184–186.
Voss, S. E., Rosowski, J. J., and Peake, W. T. (**1996**). "Is the pressure difference between the oval and round window the effective stimulus for the cochlea?" J. Acoust. Soc. Am. **100**, 1602–1616.
Watts, L. (**1992**). *Cochlear Mechanics: Analysis and Analog VLSI*, Ph.D. thesis, California Institute of Technology.
Watts, L. (**2000**). "The mode-coupling Liouville-Green approximation for a two-dimensional cochlear model," J. Acoust. Soc. Am. **108**, 2266–2271.
Wegel, R. L., and Lane, C. E. (**1924**). "The auditory masking of one pure tone by another and its probable relation to the dynamics of the inner ear," Phys. Rev. **23**, 266–285.
Wilson, J. P. (**1980**). "Model for cochlear echoes and tinnitus based on an observed electrical correlate," Hear. Res. **2**, 527–532.
Wright, A. A. (**1984**). "Dimensions of the cochlear stereocilia in man and in guinea pig," Hear. Res. **13**, 89–98.
Zurek, P. M. (**1985**). "Acoustic emissions from the ear: A summary of results from humans and animals," J. Acoust. Soc. Am. **78**, 340–344.
Zweig, G. (**1976**). "Basilar membrane motion," in *Cold Spring Harbor Symposia on Quantitative Biology, volume XL, 1975* (Cold Spring Harbor Laboratory, Cold Spring Harbor), pp. 619–633.
Zweig, G. (**1991**). "Finding the impedance of the organ of Corti," J. Acoust. Soc. Am. **89**, 1229–1254.
Zweig, G., and Shera, C. A. (**1995**). "The origin of periodicity in the spectrum of evoked otoacoustic emissions," J. Acoust. Soc. Am. **98**, 2018–2047.
Zweig, G., Lipes, R., and Pierce, J. R. (**1976**). "The cochlear compromise," J. Acoust. Soc. Am. **59**, 975–982.
Zwislocki, J. (**1953**). "Wave motion in the cochlea caused by bone conduction," J. Acoust. Soc. Am. **25**, 986–989.
Zwislocki, J. J. (**1983**). "Sharp vibration maximum in the cochlea without wave reflection," Hear. Res. **9**, 103–111.
Zwislocki, J. J. (**2002**). *Auditory Sound Transmission: An Autobiographical Perspective* (Erlbaum, Mahwah, NJ).
Zwislocki-Mośćicki, J. (**1948**). "Theorie der Schneckenmechanik: Qualitative und Quantitative Analysis," Acta Oto-Laryngol., Suppl. **72**, 1–112.

Auditory brainstem responses in the Eastern Screech Owl: An estimate of auditory thresholds

Elizabeth F. Brittan-Powell[a] and Bernard Lohr
Department of Psychology, University of Maryland, College Park, Maryland 20742

D. Caldwell Hahn
USGS Patuxent Wildlife Research Center, Laurel, Maryland 20708-4019

Robert J. Dooling
Department of Psychology, University of Maryland, College Park, Maryland 20742

(Received 9 December 2004; revised 14 April 2005; accepted 18 April 2005)

The auditory brainstem response (ABR), a measure of neural synchrony, was used to estimate auditory sensitivity in the eastern screech owl (*Megascops asio*). The typical screech owl ABR waveform showed two to three prominent peaks occurring within 5 ms of stimulus onset. As sound pressure levels increased, the ABR peak amplitude increased and latency decreased. With an increasing stimulus presentation rate, ABR peak amplitude decreased and latency increased. Generally, changes in the ABR waveform to stimulus intensity and repetition rate are consistent with the pattern found in several avian families. The ABR audiogram shows that screech owls hear best between 1.5 and 6.4 kHz with the most acute sensitivity between 4–5.7 kHz. The shape of the average screech owl ABR audiogram is similar to the shape of the behaviorally measured audiogram of the barn owl, except at the highest frequencies. Our data also show differences in overall auditory sensitivity between the color morphs of screech owls. © *2005 Acoustical Society of America.* [DOI: 10.1121/1.1928767]

PACS number(s): 43.64.Ri, 43.64.Tk [JAS] Pages: 314–321

I. INTRODUCTION

Owls (order Strigiformes) as a group have among the most sensitive hearing observed in birds. Most owls are crepuscular or nocturnal predators that must detect, localize, and capture prey under low light conditions. The hearing of owls appears to be adapted for these circumstances, and at least some species can capture prey in complete darkness using auditory cues alone (Konishi, 1973; Payne, 1971). Owls are known to be sensitive across a wide range of frequencies, with hearing being particularly acute at high frequencies compared with most other birds (Dooling *et al.*, 2000; Dyson *et al.*, 1998; Konishi, 1973; Van Dijk, 1973). High-frequency auditory limits in some owl species approach 14 kHz, noticeably higher than that for passerines and other nonpasserines, and is indicative of the importance of high frequencies to the nocturnal predatory behavior of these birds (Dyson *et al.*, 1998). In contrast, songbirds, and other species that use vocal signals for communication have hearing abilities that reflect the predominance of such signals for the social behavior of these species. Most auditory work to date with owls has focused on medium–large birds, in particular the barn owl (*Tyto alba*): Tytonidae, a sound localization specialist. Unlike many owls in the family Strigidae, barn owls are not overtly territorial, have fairly limited vocal repertoires, and communicate acoustically over relatively short distances (Marti, 1992). As a comparison with larger owls, auditory tests were performed here with a small, common, very vocal species, the eastern screech owl (*Megascops asio*).

During the last several decades, the auditory brainstem response (ABR) has been used to study the functionality of the auditory system in a wide variety of vertebrates (e.g., Burkard *et al.*, 1996a, 1996b; Donaldson and Rubel, 1990; Higgs *et al.*, 2002a; Higgs *et al.*, 2002b; Jewett, 1970; Jewett *et al.*, 1970; Kenyon *et al.*, 1998; Walsh *et al.*, 1992), and the responses to auditory stimuli are similar across most vertebrate classes (e.g., Corwin *et al.*, 1982; Walsh *et al.*, 1992). Studies with birds have recently shown the value of the ABR as a method for assessing peripheral auditory system function and estimating hearing thresholds. In general, though, these studies comprise only a few species, particularly small nonpasserines such as the budgerigar and a few songbirds (e.g., Aleksandrov and Dmitrieva, 1992; Brittan-Powell and Dooling, 2004; Brittan-Powell *et al.*, 2002; Dmitrieva and Gottlieb, 1992, 1994; Lucas *et al.*, 2002; Saunders *et al.*, 1973; Woolley *et al.*, 2001; Woolley and Rubel, 1999; Wright *et al.*, 2004). The present data on the screech owl represent an important addition to this database by providing the first complete ABR audiogram for a Strigiform bird (but see Köppl and Nickel, 2004; Moiseff *et al.*, 1996). Two experiments involving ABR responses to click and tone-burst stimuli in the eastern screech owl were conducted. The effects of stimulus intensity and frequency on the ABR were examined in experiment 1. The effects of stimulus presentation rate on wave latency and amplitude were examined in experiment 2.

[a]Corresponding author: Elizabeth Brittan-Powell. Electronic mail: bbrittanpowell@psyc.umd.edu

 0001-4966/2005/118(1)/314/8/$22.50

The purpose of our tests with eastern screech owls was to determine (1) whether screech owl ABR characteristics were like those of other birds; (2) whether the ABR could be used as an estimate of auditory sensitivity in this species; and (3) whether estimated auditory sensitivity paralleled the vocal ability of the screech owl.

II. METHODS

Thirteen screech owls (8 males, 3 females, 2 female juveniles between five–six months of age) served as subjects in these experiments. All but four individuals (1 male, 1 female, and the 2 juveniles) were of the gray plumage morph of this species, which is the most common phenotype in the local area and throughout the northern portions of its geographic range (Gehlbach, 1994; Gehlbach, 1995). The birds were housed in an avian vivarium at the USGS Patuxent Wildlife Research Center and tested at the University of Maryland. All birds were sedated with an intramuscular injection of ketamine (25–35 mg/kg) and diazepam (2 mg/kg) prior to electrode placement. Subjects remained relatively motionless for up to 75 min. After ABR data collection was completed, the bird was placed in a heated therapy unit and allowed to recover from sedation. The Animal Care and Use Committee at the University of Maryland and Patuxent Wildlife Research Center approved all animal use.

The procedure for recording ABRs has been described earlier (see Brittan-Powell and Dooling, 2004; Brittan-Powell *et al.*, 2002; Wright *et al.*, 2004). Briefly, the bird was positioned so that the speaker (KEF SP 3235, Model 60S, frequency range 100 Hz to 20 kHz, KEF Electronics of America, Inc., Holliston, MA) was 20 cm from the bird's right ear (45° azimuth relative to the bird's beak; 0° elevation relative to the bird's right ear). Standard platinum alloy, subdermal needle electrodes, (Grass F-E2; West Warwick, RI) were twisted together to reduce electrical noise and placed just under the skin at the vertex of the skull (active), behind the ipsilateral pinna (reference), and behind the pinna of the ear contralateral to stimulation (left ear; ground). The stimulus presentation, ABR acquisition, equipment control, and data management were coordinated using a Tucker-Davis Technologies (TDT; Gainesville, FL, USA) System 3 modular rack-mount system controlled by a FI5 Gigabit interface module cable-linked 2.66-GHz Pentium4 PC containing a TDT PI5 Gigabit interface PCI card and running TDT "BIOSIG" software. Sound stimuli were generated using TDT "SIGGEN" software and fed through a RP2.1, which can synthesize and process wideband signals in real time. The RP2.1 fed to a TDT programmable attenuator (PA5), which directly drove the speaker. Recording electrodes were connected to the low-impedance Medusa Digital Biological Amplifier System (RA4L Headstage and RA16PA PreAmp; RA16BA Medusa Base station), which added an additional 10× gain. All biological signals were notch filtered at 60 Hz and bandpass filtered below 30 Hz and above 3000 Hz after collection using the BIOSIG program.

Tone bursts and clicks were both used as stimuli to generate the screech owl ABR. Stimulus intensities were calibrated in the free field by placing the $\frac{1}{2}$ in. microphone of a sound level meter (System 824; Larson Davis, Inc. Provo, UT) at the approximate position of the bird's right ear. Long duration tone bursts (1000 ms) were generated and played using the TDT SIGGEN program. Frequencies above 500 Hz were measured using the fast-weighting A scale on the sound level meter (dB SPL). The $\frac{1}{3}$ octave band filter on the sound level meter was used to measure the sound pressure level at 500 Hz. The SPL required to match the amplitude of the click, as indicated on the sound level meter, was determined by adjusting the level of a 1000 Hz tone until the peak-to-peak voltage was identical to that for the click (peak equivalent SPL; dB pSPL).

III. EXPERIMENT 1: EFFECTS OF INTENSITY AND FREQUENCY ON THE ABR OF EASTERN SCREECH OWLS

A. Introduction

Experiment 1 measured changes in the ABR waveform as a function of stimulus intensity and frequency. ABR thresholds (i.e., the lowest intensity at which detectable responses were observed) were computed as an estimate of hearing sensitivity in the screech owl, and this estimate was then compared to audiograms of other species.

B. Stimuli

Thirteen eastern screech owls were presented with multiple-intensity stimulus trains (see Brittan-Powell and Dooling, 2004; Brittan-Powell *et al.*, 2002) that varied in frequency and intensity. Each train consisted of nine single clicks or single frequency tone bursts that increased in intensity. These trains were presented at a rate of 3/s. The rectangular-pulse broadband clicks were 0.1 ms in duration with an interstimulus interval (ISI) of 25 ms. Tone burst stimuli ranged from 0.5–12 kHz and were 5 ms in duration (1 ms $\cos^2$ rise/fall) with 20 ms ISI. Each ABR represents the response of 300 alternating phase stimulus presentations, sampled at 20 kHz for 235 ms following onset of the stimulus. Each intensity level was replicated.

C. Analysis

ABR waveforms produced in response to high intensities were examined visually. We chose a range of 1–10 ms to measure a response. Since test stimulus intensities in the region of threshold differed by 5 dB, ABR thresholds were defined as the intensity 2.5 dB (one-half step in intensity) below the lowest stimulus level at which a response could be visually detected on the trace, regardless of wave (see, for example, Brittan-Powell and Dooling, 2004; Brittan-Powell *et al.*, 2002). Thresholds were estimated for each replication, and the average of the two estimates was used in statistical tests.

D. Results

As the intensity of stimulation increased, ABR amplitudes increased and peak latencies decreased. Figure 1 shows typical ABR waveforms for an adult screech owl to a click and 3 frequencies (2.0, 4.0, and 6.4 kHz) as a function of

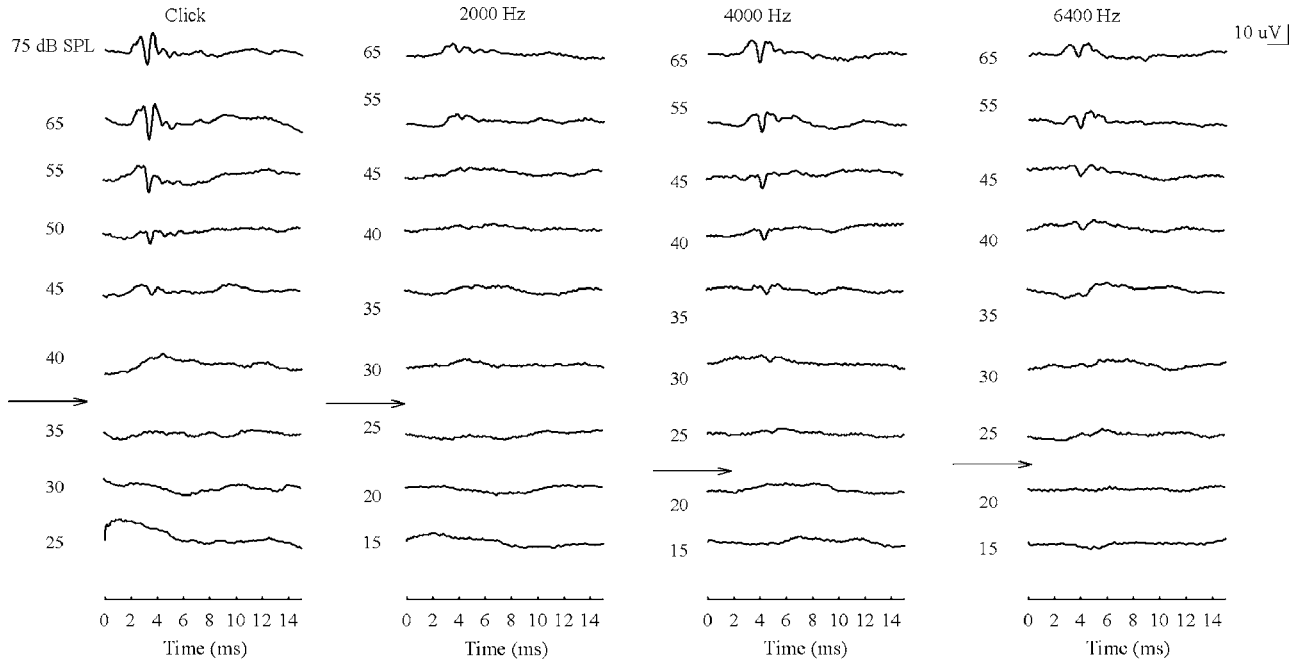

FIG. 1. ABR waveforms for a single owl for the click stimulus and 2000, 4000, and 6400 Hz tones as a function of SPL. Amplitude decreased and latency increased with decreasing SPL. Arrow along side of graph denotes the threshold estimates for this bird.

intensity. Visual examination of the waveforms showed 2–3 prominent peaks that occurred within the first 4–5 ms after sound reached the owl's external ear canal, with the trough of peak 1 showing the largest deflection, a pattern found in other birds (Brittan-Powell and Dooling, 2004; Brittan-Powell *et al.*, 2002; Lucas *et al.*, 2002; Moiseff *et al.*, 1996; Wright *et al.*, 2004). The average click threshold for all 13 owls was 32.69±1.46 dB pSPL (mean ± SE), with the click threshold being significantly lower for the rufous morph (27.50±2.04 dB pSPL) than for the gray morph (35.00±1.32 dB pSPL) [$t_{(11)}=3.13, p<0.05$]. Male and female owls showed no difference in their ABR thresholds across frequencies ($F_{1,107}=4.08, p=0.071$), so these data were combined. Figure 2(a) shows the average ABR thresholds for all owls tested. Figure 2(b) shows the average ABR thresholds for the nine eastern screech owls of the gray plumage morph and the four owls of the rufous plumage morph. Interestingly, the ABR thresholds for the rufous morph were 10–15 dB more sensitive than those for birds of the gray morph. A two-way repeated measures ANOVA showed significant differences between both morphs ($F_{1,107}=42.52, p<0.001$) and frequencies ($F_{1,107}=194.44, p<0.001$), as well as the interaction of morph *x* frequency ($F_{10,107}=3.52, p<0.001$).

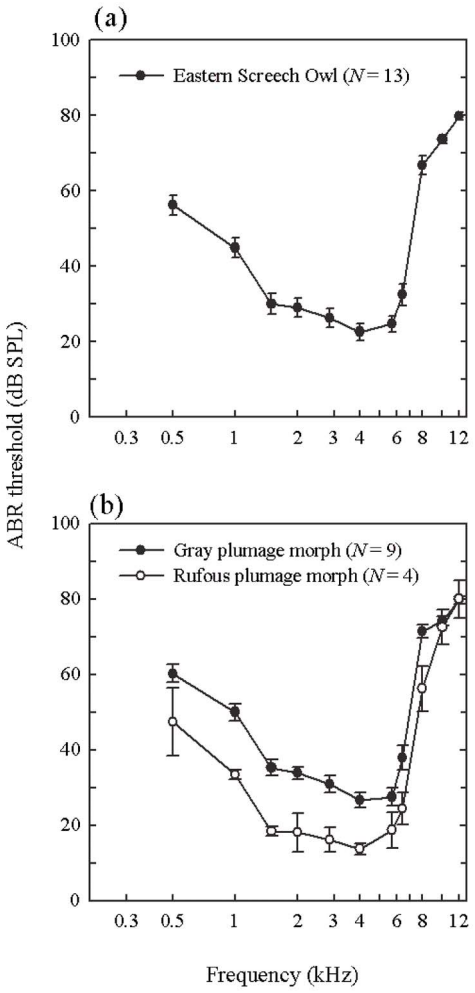

FIG. 2. (a) Average (+/− SE) ABR audiogram 13 eastern screech owls (*Megascops asio*). (b) Separate average ABR audiograms for birds of the gray plumage morph ($N=9$) and the rufous plumage morph ($N=4$).

IV. EXPERIMENT 2: EFFECTS OF CLICK REPETITION RATE ON THE ABR OF EASTERN SCREECH OWLS

A. Introduction

We investigated the effect of click repetition rate on ABR latency and amplitude. ABR changes to click repetition rate are often used to assess change in neural transmission (e.g., neural fatigue and adaptation; see the review in Hall, 1992) or for assessing brainstem neuropathology. Typically,

TABLE I. Average (+/− SE) latency and amplitude measures as a function of the repetition rate.

	5 Hz	10 Hz	30 Hz	60 Hz	90 Hz
LATENCY (ms)					
Wave 1	1.40 (0.06)	1.43 (0.05)	1.45 (0.05)	1.46 (0.06)	1.49 (0.05)
Wave 2	1.91 (0.01)	1.93 (0.02)	1.95 (0.02)	1.98 (0.01)	2.00 (0.02)
Wave 3	2.54 (0.04)	2.55 (0.06)	2.62 (0.08)	2.65 (0.08)	2.69 (0.08)
Wave 1–2 interval	0.50 (0.06)	0.50 (0.05)	0.50 (0.06)	0.52 (0.06)	0.51 (0.06)
Wave 1–3 interval	1.13 (0.10)	1.12 (0.11)	1.17 (0.13)	1.19 (0.13)	1.20 (0.13)
AMPLITUDE (μV)					
Wave 1	6.33 (0.56)	5.91 (0.55)	4.48 (0.43)	3.82 (0.48)	3.28 (0.49)
Wave 2	5.15 (0.56)	4.42 (0.66)	3.55 (0.63)	2.64 (0.43)	2.21 (0.31)
Wave 3	8.83 (1.83)	9.91 (1.98)	9.54 (1.70)	7.82 (0.98)	6.78 (0.73)
Ratio 1/2	1.29 (0.17)	1.53 (0.30)	1.47 (0.28)	1.61 (0.30)	1.58 (0.26)
Ratio 1/3	0.92 (0.23)	0.73 (0.16)	0.55 (0.11)	0.52 (0.08)	0.51 (0.08)

as click repetition rates increase, peak latencies of the ABR also increase and peak amplitudes of the ABR decrease, resulting in alterations of wave morphology (e.g., Burkard and Voigt, 1989; Donaldson and Rubel, 1990; Jewett and Romano, 1972). While such changes have been studied extensively in mammals, such as gerbils, cats, and rats, the only birds studied to date have been the white leghorn chick (Burkard *et al.*, 1994) and the budgerigar (Brittan-Powell and Dooling, 2004; Brittan-Powell *et al.*, 2002). The present results extend our knowledge of the effect of click repetition rate on ABR latency and amplitude by testing a Strigiform bird. Five of the birds (three males and two females) used in the previous experiment were tested in Experiment 2. All equipment and procedures have been previously described in detail (Brittan-Powell *et al.*, 2002) and are the same as in Experiment 1, except where noted below.

B. Stimuli

Short duration, broadband clicks (0.1 ms) were presented at 5 rates: 5, 10, 30, 60, and 90 per second (Hz). The click level was held constant at 100 dB pSPL. Each ABR represented the average response of 300 alternating stimulus presentations, sampled at 20 kHz for 10 ms following onset of the stimulus. Each presentation rate was replicated.

C. Analysis

The first three wave components (designated wave 1, wave 2, and wave 3) were described by their amplitude and latency characteristics. Positive evoked potential peaks were identified by cursors, and associated amplitudes and latencies were automatically saved. Latencies to the waves were corrected for conduction delays between the sound source and the entrance of the ear canal of the animal (0.58 ms). The latency of the interwave interval was calculated as the difference in latency from wave 1 peak to wave 2 peak (1–2 interval) and wave 1 peak to wave 3 peak (1–3 interval). ABR wave amplitudes were measured as peak to baseline (wave 1) and peak to preceding trough (wave 2 and 3). The average latency and amplitude data for wave 1, 2, and 3 were calculated based on all replications (e.g., average latency for 5 Hz based on 2 replications for each of 5 birds). The statistical tests were conducted on the average latency and amplitude of each bird's two replicates.

D. Results

Like mammals and other birds, screech owl ABR responses are dependent on the temporal properties of the stimulus. Increasing click repetition rate resulted in increases in latency and decreases in amplitude for all waves (Table I). The general shape of the waveform also changed, especially at rates higher than 10 Hz. Figure 3 shows ABR waveforms from a single bird in response to the click rates presented in this study. The latency of waves 1, 2, and 3 and the intervals 1–2 and 1–3 were evaluated with a two-way ANOVA; tables summarize the results. As the repetition rate increased, latency increased significantly for all three waves, but the interval between the waves remained fairly stable. Bonferroni-adjusted posthoc comparisons showed that the lowest repetition rates (5 and 10 Hz) resulted in significantly shorter latencies than higher repetition rates (90 Hz) across all three waves.

With an increased click repetition rate, the absolute amplitude decreased significantly for waves 1 and 2, as did the ratio of wave 1 to wave 3 (see summary Table II). Bonferroni-adjusted posthoc comparisons showed that amplitudes of waves 1 and 2 were significantly larger for lower repetition rates than for higher rates. The same trend was seen for wave 3 as well, but it was not significant. The mean wave 1 to wave 2 amplitude ratio was larger than 1.0 (i.e., the amplitude of wave 1 was larger than the amplitude of wave 2). However, the ratio of the two waves remained relatively constant across repetition rates suggesting that they were equally affected by increased presentation rate. The ratio of wave 1 to wave 3, however, decreased as a function of increased click repetition rate, suggesting that the generators of the two waves were differentially affected by increased presentation rate.

V. DISCUSSION

The goals of this study were to determine (1) whether the ABR characteristics (e.g., thresholds and effects of stimulus presentation rate on neural synchrony) in a small Strigi-

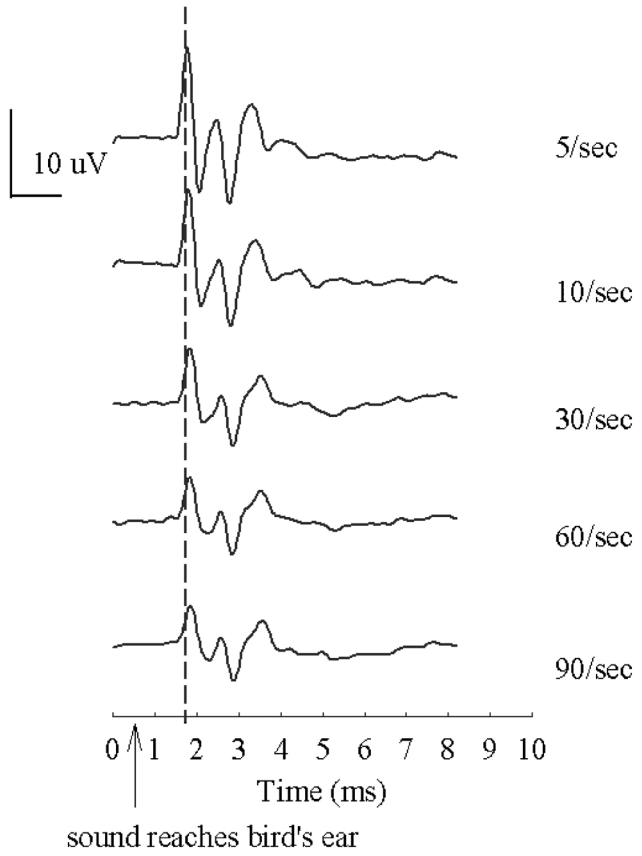

FIG. 3. Typical ABR waveform for an adult screech owl for each repetition rate. Increased rate caused increased latencies and decreased amplitudes, with the largest changes occurring at rates above 10 Hz. An arrow denotes the time at which the stimulus reached the outer ear.

form bird, the eastern screech owl, were comparable to those of other birds, (2) whether the ABR could be used to obtain an estimate of auditory sensitivity in this species, and (3) whether the ABR estimates of auditory sensitivity paralleled the owls' vocal abilities.

A. ABR morphology in screech owls

Eastern screech owl ABR waveforms showed 2–3 measurable peaks that occurred within the first 5 ms after stimulation. These results are typical of findings with several other

TABLE II. Results of ANOVA for latency and amplitude as a function of the repetition rate.

Dependent variable	*N*	F ratio	Probability
Wave 1 latency	5	7.54	$p<0.001$
Wave 2 latency	5	16.98	<0.001
Wave 3 latency	5	10.90	<0.001
Wave 1-2 interval	5	0.72	0.59
Wave 1-3 interval	5	2.71	0.068
Wave 1 amplitude	5	51.00	<0.001
Wave 2 amplitude	5	18.20	<0.001
Wave 3 amplitude	5	2.86	0.058
Ratio 1/2	5	1.58	0.229
Ratio 1/3	5	5.25	<0.05

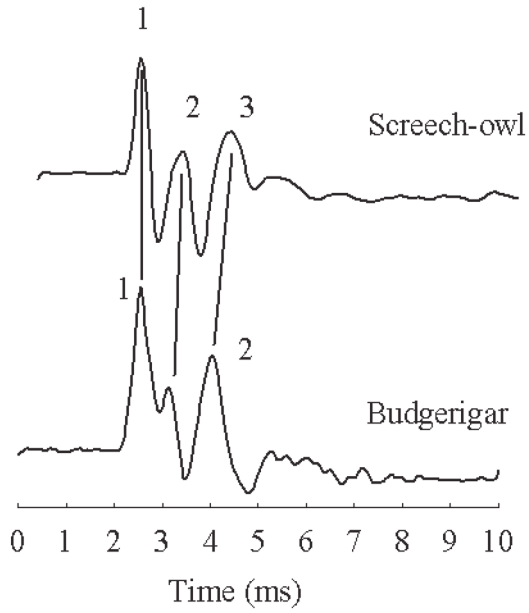

FIG. 4. A comparison of screech owl and budgerigar ABR waveforms in response to a 100 dB pSPL click stimulus. Budgerigar data is from Brittan-Powell *et al.* (2002).

bird species (Brittan-Powell and Dooling, 2004; Brittan-Powell *et al.*, 2002; Lucas *et al.*, 2002; Moiseff *et al.*, 1996; Umemoto *et al.*, 1993; Woolley *et al.*, 2001; Woolley and Rubel, 1999; Wright *et al.*, 2004). Figure 4 shows a comparison of ABR waveform responses to a 100 dB pSPL click in a screech owl (current study) and a budgerigar (from Brittan-Powell *et al.*, 2002). Wave 1 in most animals is consistently attributed to the auditory nerve. Given the similarity in time course and shape between the waveform of budgerigars and screech owls, it is likely that the auditory nerve is the neural generator for this first peak in the screech owl waveform as well.

While the ABR waveforms for budgerigars and screech owls are very similar in most respects (Fig. 4), the third peak in the owl waveform most likely corresponds to the second peak in the budgerigar waveform, given the timing and shape of the waveform (see the review in Brittan-Powell *et al.*, 2002). Likewise, the second peak for the owl closely corresponds to the shoulder seen in wave 1 for the budgerigar. Based on similarities in latency in budgerigars, chickens (Katayama, 1985), and cats (Burkard *et al.*, 1996a), Brittan-Powell *et al.* (2002) argued that wave 2 in budgerigars may be generated by nucleus laminaris in the auditory brainstem of the budgerigar. To extend this reasoning to the screech owl, if wave 3 corresponds to the budgerigar wave 2, we suggest that wave 3 is most likely generated by nucleus laminaris.

With increasing click repetition rate, mammalian and avian ABRs all show increases in peak latencies and decreases in peak amplitudes (Brittan-Powell *et al.*, 2002; Burkard *et al.*, 1994; Burkard *et al.*, 1996a, 1996b; Burkard and Voigt, 1989; Donaldson and Rubel, 1990; Lasky, 1997). The same effect was observed in screech owls (Table I). As the rate increased, there was a greater latency change for wave 3 than wave 2, which is similar to what has been found

in other vertebrates. Furthermore, while waves 1 and 2 seem to be equally affected by increasing rate, wave 3 shows a slower rate of amplitude decrease as compared to wave 1 (see Table I). Together these results suggest screech owls show a pattern of ABR peaks similar to that of other vertebrates tested.

B. ABR thresholds in screech owls

Avian ABR thresholds yield estimates of hearing that are about 30 dB higher than direct behavioral measures of hearing [see Fig. 5(a) and the discussion in Brittan-Powell *et al.*, 2002]. However, across vertebrates the ABR thresholds provide a good estimate of audiogram shape (e.g., Borg and Engström, 1983; Brittan-Powell *et al.*, 2002; Stapells and Oates, 1997; Wenstrup, 1984; Wolski *et al.*, 2003). The current study shows that screech owls have the typical U-shaped audiogram found in most bird species and hear fairly well over the range of 1.5–6.4 kHz. Figure 5(b) compares ABR thresholds for the screech owl in the current study and from a single barn owl (using the same procedures) with a behavioral audiogram for the barn owl (Dyson *et al.*, 1998; Fay, 1988; Konishi, 1973). In general, the owl ABR thresholds are remarkably similar to each other and similar in shape to the barn owl behavioral audiogram, with the exception that ABR thresholds are 35–40 dB higher than behavioral estimates of auditory sensitivity across most frequencies. These data also suggest that the screech owl may be less sensitive than the barn owl at some of the higher frequencies since there is a large difference between the ABR audiograms around 8 kHz.

In the screech owls we tested, there is a statistical difference in the ABR thresholds between the gray and rufous plumage morphs. The owls of the rufous morph are not only more sensitive but this sensitivity difference varies as a function of frequency [as is evident in Fig. 2(b)].

Color polymorphism occurs naturally in many groups of animals, but in birds it has evolved most often in raptors (Roulin and Wink, 2004). In most cases, plumage variation in raptors is thought to be genetically controlled, rather than the influence of environmental factors such as diet (Roulin and Wink, 2004), and the screech owls in this study were all fed the same diet. A recent study involving the molecular basis of plumage polymorphism in a songbird has shown that the presence of distinct color morphs can be the result of a single gene mutation (Theron *et al.*, 2001). Plumage polymorphism in screech owls is also likely to be genetically based (Gehlbach, 1994). Intermediates between the gray and rufous morphs (such as a "brown" phenotype) are common, suggesting the presence of more than two alleles or genes controlling plumage color in this species.

This result is intriguing, and we know of no other parallels. In some domesticated mammals, particularly certain breeds of dog, congenital sensorineural deafness is associated with certain phenotypic patterns of eye and coat color (Strain *et al.*, 1992). In these cases, the auditory deficits linked to color patterns are also known to have a genetic basis, though the precise associations and mechanisms remain elusive (Juraschko *et al.*, 2003).

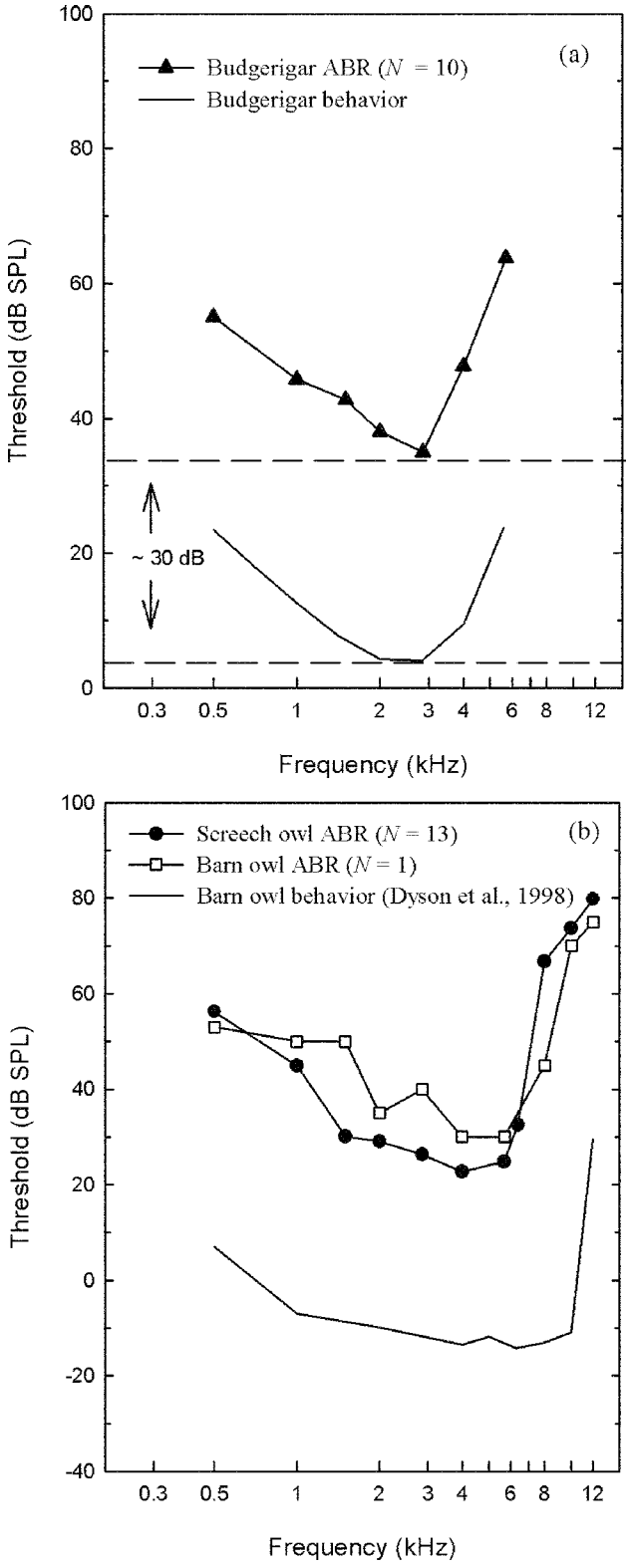

FIG. 5. (a) A comparison of ABR and behavioral audiograms for budgerigars (adapted from Brittan-Powell *et al.*, 2002). Dashed lines represent a typical offset of the ABR audiogram from behavior in birds (see Brittan-Powell *et al.*, 2002). (b) A comparison of screech owl (closed circle) and barn owl (open square) ABR audiograms and a barn owl behavioral audiogram (barn owl, solid line, Dyson *et al.*, 1998). The screech owl ABR audiogram is an average of *all* individuals tested.

It also is possible that differences in our ABR thresholds are not a result of differences in auditory sensitivities, *per se*,

but rather an indication of variation in some other feature. For instance, skull size and shape, or neuroanatomical differences, could also contribute to the differences in ABR thresholds measured here. Only a study using behavioral measurements can definitively determine that the rufous color morphs have greater hearing sensitivity. Testing additional birds, collected from other geographical areas, would also provide additional insight. It is possible that at least one gene controlling plumage color in screech owls could be linked to auditory effects. Future studies investigating the relationship between hearing ability and the range of color morphology in this species would help elucidate whether the underlying genetics played a role in the differences we find in ABR sensitivity in the color morphs of this species.

C. ABR thresholds and vocal ability in birds

Most birds hear best between 1 and 5 kHz with absolute sensitivity approaching 0–10 dB SPL at the frequency of best hearing, which is typically around 2–3 kHz (see a review in Dooling *et al.*, 2000). In non-Strigiform birds, peak sensitivity in the audiogram typically coincides with regions of peak energy in the bird's songs and calls (Dooling *et al.*, 2000), reflecting the likely coevolution of hearing and vocalizations. Among nocturnal predatory birds, hearing is thought to have evolved for detecting and localizing prey in the dark (Konishi, 1973; Payne, 1971). Barn owls are known to be highly specialized in this capacity, and they have both good absolute sensitivity and excellent high-frequency hearing compared with other birds (Konishi, 1973). Best auditory sensitivity is in the range of 4–8 kHz for this species, and behavioral auditory thresholds remain below 0 dB SPL up to 10 kHz (see Fig. 4, Dyson *et al.*, 1998; Konishi, 1973). This degree of specialization and sensitivity may not extend to other species of owls, such as the great horned owl (*Bubo virginianus*), which appears to exhibit a dramatic decline in hearing ability above 2–3 kHz (Trainer, 1946). Several species of European owls may be somewhat intermediate in their range of best hearing, with most species showing excellent auditory sensitivity to about 6–8 kHz, but exhibiting rapid declines in sensitivity above this range (Dyson *et al.*, 1998; Van Dijk, 1973).

Unlike the barn owl, some owls (such as screech owls) are extremely vocal during the breeding season and may use a variety of long-distance acoustic communication signals in the establishment and maintenance of territories. The screech owls (*Megascops* spp.) have some of the most extensive vocal repertoires among North American owls (Cannings and Angell, 2001; Gehlbach, 1995; Gehlbach and Gehlbach, 2000). The eastern screech owl is fairly typical of many small North American owls, producing long-distance calls with fundamental frequencies (and frequencies of maximum amplitude) between 500–1500 Hz (Cavanagh and Ritchison, 1987; Klatt and Ritchison, 1994). Unlike passerines, the lowest ABR thresholds in the screech owl are at higher frequencies than the peak spectral energy in its vocal signals. This is consistent with the pattern typical of other owls that use hearing for prey detection [see Fig. 4(b)]. Given that the ABR underestimates true hearing sensitivity in other birds by about 30–35 dB over the range of hearing (Brittan-Powell *et al.*, 2002), however, we might expect screech owls to show excellent hearing sensitivity across a range of frequencies that include the frequency regions in which its calls are produced.

VI. CONCLUSIONS

ABR waveforms in the eastern screech owl are similar in shape and temporal characteristics to those of other birds tested previously (Brittan-Powell and Dooling, 2004; Brittan-Powell *et al.*, 2002; Lucas *et al.*, 2002; Moiseff *et al.*, 1996; Woolley *et al.*, 2001; Woolley and Rubel, 1999; Wright *et al.*, 2004). Likewise, ABR thresholds are similar to those of other birds, but are most comparable to the thresholds of other owls. Like other owls, screech owls show lower thresholds at higher frequencies presumably used in prey detection and localization, despite having an elaborate vocal repertoire concentrated at lower frequencies. Also like other owls, their region of best hearing extends over a broad range of frequencies (Dyson *et al.*, 1998). This broad sensitivity serves for both the detection of prey species and effective vocal communication over long distances. The broad range of sensitivity in screech owls may be adaptive in that it can serve a dual function of facilitating both auditory communication abilities and nocturnal prey detection. Studies of auditory development in this species might also prove interesting in this regard (Hahn, 2004; Kozlowski, 2005).

ACKNOWLEDGMENTS

The authors would like to thank Amanda Lauer and Michael Osmanski for comments on earlier drafts. We would also like to thank Dr. Catherine Carr for the use of her barn owl (for the ABR audiogram) and Wayne Bauer for animal care and quarantine. This work was supported in part by Grant No. DC04664 from the National Institute of Deafness and Communicative Disorders (NIDCD) of the National Institutes of Health, NIDCD Grant No. DC04762 to BL; National Institutes of Health Grants No. DC00198 and No. DC001372 to RJD, and USGS-Patuxent Wildlife Research Center awards to DCH.

Aleksandrov, L. I., and Dmitrieva, L. P. (**1992**). "Development of auditory sensitivity of altricial birds: absolute thresholds of the generation of evoked potentials," Neurosci. Behav. Physiol. **22**, 132–137.

Borg, E., and Engström, B. (**1983**). "Hearing thresholds in the rabbit," Acta Oto-Laryngol. **95**, 19–26.

Brittan-Powell, E. F., and Dooling, R. J. (**2004**). "Development of auditory sensitivity in budgerigars (*Melopsittacus undulatus*)," J. Acoust. Soc. Am. **115**, 3092–3102.

Brittan-Powell, E. F., Dooling, R. J., and Gleich, O. (**2002**). "Auditory brainstem responses (ABR) in adult budgerigars (*Melopsittacus undulatus*)," J. Acoust. Soc. Am. **112**, 999–1008.

Burkard, R., and Voigt, H. F. (**1989**). "Stimulus dependencies of the gerbil brain-stem auditory-evoked response (BAER): I. Effects of click level, rate, and polarity," J. Acoust. Soc. Am. **85**, 2514–2525.

Burkard, R., Jones, S., and Jones, T. (**1994**). "Conventional and cross-correlation brain-stem auditory evoked responses in the white leghorn chick: Rate manipulations," J. Acoust. Soc. Am. **95**, 2136–2144.

Burkard, R., McGee, J., and Walsh, E. J. (**1996a**). "Effects of stimulus rate on feline brain-stem auditory evoked response during development. I. Peak latencies," J. Acoust. Soc. Am. **100**, 978–990.

Burkard, R., McGee, J., and Walsh, E. J. (**1996b**). "Effects of stimulus rate on feline brain-stem auditory evoked response during development. II.

Peak amplitudes," J. Acoust. Soc. Am. **100**, 991–1002.
Cannings, R. J., and Angell, T. (**2001**). "Western Screech-Owl (*Otus kennicottii*)," in *The Birds of North America, No. 597*, edited by A. Poole and F. Gill (The Birds of North America, Inc., Philadelphia, PA).
Cavanagh, P. M., and Ritchison, G. (**1987**). "Variation in the bounce and whinny songs of the Eastern Screech-Owl," Wilson Bull. **99**, 620–627.
Corwin, J. T., Bullock, T. H., and Schweitzer, J. (**1982**). "The auditory brain stem response in five vertebrate classes," Electroencephalogr. Clin. Neurophysiol. **54**, 629–641.
Dmitrieva, L. P., and Gottlieb, G. (**1992**). "Development of brainstem auditory pathway in mallard duck embryos and hatchlings," J. Comp. Physiol. **171**, 665–671.
Dmitrieva, L. P., and Gottlieb, G. (**1994**). "Influence of auditory experience on the development of brain stem auditory-evoked potentials in Mallard duck embryos and hatchlings," Behav. Neural Biol. **61**, 19–28.
Donaldson, G. S., and Rubel, E. W. (**1990**). "Effects of stimulus repetition rate on ABR threshold, amplitude and latency in neonatal and adult Mongolian gerbils," Electroencephalogr. Clin. Neurophysiol. **77**, 458–470.
Dooling, R. J., Lohr, B., and Dent, M. L. (**2000**). "Hearing in birds and reptiles," in *Comparative Hearing: Birds and Reptiles*, edited by R. J. Dooling, A. N. Popper, and R. R. Fay (Springer-Verlag, New York), pp. 308–359.
Dyson, M. L., Klump, G. M., and Gauger, B. (**1998**). "Absolute hearing thresholds and critical masking ratios in the European barn owl: a comparison with other owls," J. Comp. Physiol., A **182**, 695–702.
Fay, R. R. (**1988**). "Hearing in Vertebrates: A Psychophysics Databook" (Hill-Fay Associates, Winnetka, IL).
Gehlbach, F. R. (**1994**). "The Eastern Screech Owl: Life History, Ecology and Behavior in the suburbs and countryside," (University Press, College Station, TX).
Gehlbach, F. R. (**1995**). "Eastern Screech-Owl (*Otus asio*)," in *The Birds of North America*, edited by A. Poole and F. Gill (The Academy of Natural Sciences, Philadelphia, and The American Ornithologists' Union, Washington, DC), pp. 1–24.
Gehlbach, F. R., and Gehlbach, N. Y. (**2000**). "Whiskered Screech-Owl (*Otus trichposis*)," in *The Birds of North America, No. 507*, edited by A. Poole and F. Gill (The Birds of North America, Inc., Philadelphia, PA).
Hahn, D. C. (**2004**), "Effects of auditory stimulation on embryo development," Report to Patuxent Wildlife Research Center, October 2004.
Hall, J. (**1992**), "Handbook of Auditory Evoked Responses" (Allyn and Bacon, Boston, MA).
Higgs, D. M., Brittan-Powell, E. F., Soares, D., Souza, M. J., Carr, C. E., Dooling, R. J., and Popper, A. N. (**2002a**). "Amphibious auditory responses of the American alligator (*Alligator mississipiensis*)," J. Comp. Physiol., A **188**, 217–223.
Higgs, D. M., Souza, M. J., Wilkins, H. R., Presson, J. C., and Popper, A. N. (**2002b**). "Age- and size-related changes in the inner ear and hearing ability of the adult zebrafish (*Danio rerio*)," J. Assoc. Res. Otolaryngol. **3**, 174–184.
Jewett, D. (**1970**). "Volume-conducted potentials in response to auditory stimuli as detected by averaging in the cat," Electroencephalogr. Clin. Neurophysiol. **28**, 609–618.
Jewett, D., and Romano, M. (**1972**). "Neonatal development of the auditory system: Potentials averaged from the scalp of rat and cat," Brain Res. **36**, 101–115.
Jewett, D., Romano, M., and Williston, J. (**1970**). "Human auditory evoked potentials: possible brainstem components detected on the scalp," Science **167**, 1517–1518.
Juraschko, K., Meyer-Lindenberg, A., Nolte, I., and Distl, O. (**2003**). "A regressive model analysis of congenital sensorineural deafness in German Dalmatian dogs," Mamm Genome **14**, 547–554.
Katayama, A. (**1985**). "Postnatal development of auditory function in the chicken revealed by auditory brain-stem responses (ABRs)," Electroencephalogr. Clin. Neurophysiol. **62**, 388–398.
Kenyon, T. N., Ladich, F., and Yan, H. Y. (**1998**). "A comparative study of hearing ability in fishes: the auditory brainstem response approach," J. Comp. Physiol. **182**, 307–318.
Klatt, P. H., and Ritchison, G. (**1994**). "The effect of mate removal on the vocal behavior and movement patterns of male and female Eastern Screech-Owls," Condor **96**, 485–493.
Konishi, M. (**1973**). "How owl tracks its prey," Am. Sci. **61**, 414–424.
Köppl, C., and Nickel, R. (**2004**), "Prolonged maturation of cochlear function in the barn owl after hatching." (Association for Research in Otolaryngology, Daytona Beach, FL), pp. 55.
Kozlowski, C. P. (2005), "Embryonic vocalizations and parent-offspring communication in the eastern screech owl," MS Thesis, Cornell University.
Lasky, R. E. (**1997**). "Rate and adaptation effects on the auditory evoked brainstem response in human newborns and adults," Hear. Res. **111**, 165–176.
Lucas, J. R., Freeberg, T. M., Krishnan, A., and Long, G. R. (**2002**). "A comparative study of avian auditory brainstem responses: correlations with phylogeny and vocal complexity, and seasonal effects," J. Comp. Physiol., A **188**, 981–992.
Marti, C. D. (**1992**). "Barn Owl," in *The Birds of North America, No. 1*, edited by A. Poole, P. Stettenheim, and F. Gill (The Academy of Natural Sciences, Philadelphia, and The American Ornithologists' Union, Washington, DC).
Moiseff, A., Haresign, T., and Wang, J. (**1996**). "Sound localization from binaural cues by the barn owl auditory system," in *Neuroethological studies of cognitive and perceptual processes*, edited by C. F. Moss and S. J. Shettleworth (Westview Press, Colorado), pp. 305–323.
Payne, R. S. (**1971**). "Acoustic location of prey by barn owls," J. Exp. Biol. **54**, 533–573.
Roulin, A., and Wink, M. (**2004**). "Predator–prey polymorphism: relationships and the evolution of colour a comparative analysis in diurnal raptors," Biol. J. Linn. Soc. **81**, 565–578.
Saunders, J. C., Coles, R. B., and Gates, G. R. (**1973**). "The development of auditory evoked responses in the cochlea and cochlear nuclei of the chick," Brain Res. **63**, 59–74.
Stapells, D. R., and Oates, P. (**1997**). "Estimation of pure-tone audiogram by the auditory brainstem response: A review," Audiol. Neuro-Otol. **2**, 257–280.
Strain, G. M., Kearney, M. T., Gignac, I. J., Levesque, D. C., Nelson, H. J., Tedford, B. L., and Remsen, L. G. (**1992**). "Brainstem auditory-evoked potential assessment of congenital deafness in Dalmatians: associations with phenotypic markers," J. Vet. Intern Med. **6**, 175–182.
Theron, E., Hawkins, K., Bermingham, E., Ricklefs, R. E., and Mundy, N. I. (**2001**). "The molecular basis of an avian plumage polymorphism in the wild: A melanocortin-1-receptor point mutation is perfectly associated with the melanic plumage morph of the bananaquit, *Coereba flaveola*," Curr. Biol. **11**, 550–557.
Trainer, J. E. (**1946**). "The auditory acuity of certain birds. Doctoral dissertation. Cornell University," in *Hearing in vertebrates: a psychophysical databook*, edited by R. R. Fay (Hill-Fay Assoc., Winnetka, Illinois).
Umemoto, M., Sakagami, M., Ashida, K., Fukazawa, K., Matsunaga, T., Senda, T., and Fujita, H. (**1993**). "The ultrastructure of the basilar papilla of the budgerigar's inner ear," Acta Oto-Laryngol. **501**, 66–71.
Van Dijk, T. (**1973**). "A comparative study of hearing in owls of the family strigidae," Neth. J. Zool. **23**, 131–167.
Walsh, E. J., Gorga, M., and McGee, J. (**1992**). "Comparisons of the development of auditory brainstem response latencies between cats and humans," Hear. Res. **60**, 53–63.
Wenstrup, J. J. (**1984**). "Auditory sensitivity in the fish-catching bat, *Noctilio leporinus*," J. Comp. Physiol. **155**, 91–101.
Wolski, L. F., Anderson, R. C., Bowles, A. E., and Yochem, P. K. (**2003**). "Measuring hearing in the harbor seal (*Phoca vitulina*): comparison of behavioral and auditory brainstem response techniques," J. Acoust. Soc. Am. **113**, 629–637.
Woolley, S. M., Wissman, A. M., and Rubel, E. W. (**2001**). "Hair cell regeneration and recovery of auditory thresholds following aminoglycoside ototoxicity in Bengalese finches," Hear. Res. **153**, 181–195.
Woolley, S. M. N., and Rubel, E. (**1999**). "High-frequency auditory feedback is not required for adult song maintenance in Bengalese Finches," J. Neurosci. **19**, 358–371.
Wright, T., Brittan-Powell, E. F., Dooling, R. J., and Mundinger, P. (**2004**). "Sex-linkage of deafness and song frequency spectrum in the Waterslager strain of domestic canary," *Proceedings of the Royal Society B (Suppl). Biology Letters*, DOI: 10.1098/rsbl.2004.0204.

Effects of informational maskers within and across trials

Robert A. Lutfi[a] and Joshua M. Alexander
Department of Communicative Disorders, and Waisman Center, University of Wisconsin, Madison, Wisconsin 53705

(Received 11 June 2004; revised 18 March 2005; accepted 5 April 2005)

The across-trial effect of maskers in conditions of informational masking was evaluated from performance on occasional trials in which the signal was presented alone. For 6 of 12 listeners participating in the study, a significant number of errors were obtained on signal-alone trials; in some cases equivalent to that signal+masker trials. On immediately preceding trial blocks for which there were no intervening maskers, performance for these signals was perfect. The results indicate that informational maskers can have a significant effect on signal threshold, both within and across trials. © *2005 Acoustical Society of America.* [DOI: 10.1121/1.1923348]

PACS number(s): 43.66.Ba, 43.66.Fe [GDK] Pages: 322–324

I. INTRODUCTION

Informational masking is the term often used to describe elevations in signal threshold that cannot be accounted for by traditional energy detection or auditory filter models of masking. It is a term typically reserved for cases where the maskers are highly uncertain and are far removed from the signal in frequency and/or time (Neff and Green, 1987; Watson and Kelly, 1981). Accounts vary, but generally focus on the immediate effect of maskers within each observation interval or trial. The focus on within-trial effects is explicit, for example, in the component-relative-entropy (CoRE) model, a model that has been shown to accurately predict many of the results from studies of informational masking (Lutfi, 1993; Oh and Lutfi, 1998). It is also evident in perceptual accounts of the effects of signal-masker similarity (Arbogast, Mason, and Kidd, 2002; Kidd *et al.*, 2001; Kidd, Mason, and Arbogast, 2002; Kidd *et al.*, 1994; Neff, 1995), and in molecular analyses intended to reveal aspects of the decision process from trial to trial (Lutfi, 1992; Richards, Tang, and Kidd, 2002; Tang and Richards, 2002; Wright and Saberi, 1999). In each of these cases the signal and masker components on a given trial are assumed to combine or interact somehow so as to influence the listener's decision only on that trial.

Predominant attention to the within-trial effects of maskers is understandable given that such effects seem likely to have the greatest impact on listener performance. Yet, the signature of informational masking is that maskers need not be in close spectral or temporal proximity to the signal to exert a significant effect (Watson and Kelly, 1981). This raises the question as to whether informational masking can occur across trials. The CoRE model predicts that maskers can have an across-trial effect by establishing listener expectations in the presence and absence of the signal regarding the sum of levels at the output of independent auditory filters (a criterion effect). Maskers may also have an across-trial effect by interfering with memory for the signal over the course of many trials (cf. Neff, 1985; Neff and Jesteadt, 1983). There is evidence, for example, that such interference may cause listeners to "confuse" the signal for a component of the masker even in cases where the signal is previewed before each trial (Lutfi *et al.*, 2003).

The goal of the present study was to evaluate the across-trial effects of informational maskers by examining performance on occasional trials in which the signal is presented alone. Where the signal is presented alone there can be no immediate effect of maskers within the trial; hence, errors can only reflect the effect of maskers across trials.

II. METHODS

A. Listeners

Twelve (1 male, 11 females) paid listeners between the ages of 18 and 20 years were recruited from the U.W.-Madison campus. Each listener used his or her right ear for the experiments. All listeners had normal hearing based on standard audiometric measurements of pure-tone air conduction thresholds at the octave frequencies between 250 and 8000 Hz (ANSI, 1996). None of the listeners had any prior experience on psychoacoustic tasks.

B. Stimuli

The signal and maskers were coincident pure tones gated with 5 ms, $\cos^2$ onset/offset ramps for a total duration of 100 ms. The frequency of the signal was 2000 Hz. Masker frequencies were selected at random on each trial with replacement from a uniform distribution of frequencies separated by 5 Hz from 1500 to 2500 Hz, excluding a protected region from 1940 to 2060 Hz. The levels of the masker tones were selected from a uniform distribution from 22 to 62 dB SPL, independent of each other and of masker frequency. The signal and maskers were computer generated and were played over a 16 bit sound card (Sound Blaster™ 16 MultiCD™ audio card; Creative Technology, Ltd.) at a 20 kHz sampling rate before being passed through a programmable attenuator (Tucker-Davis Technologies, PA4). All stimuli were presented monaurally through a Sennheiser HD 520 (II) headphone. A TDH-50 earphone with known trans-

[a]Electronic mail: ralutfi@wisc.edu

 0001-4966/2005/118(1)/322/3/$22.50

fer function was used to calibrate the Sennheiser headphones using a binaural loudness balancing procedure at the signal frequency (ANSI, 1996).

C. Procedure

Thresholds in all experimental conditions were measured using an adaptive, two-down-one-up, single-interval, yes–no procedure with feedback (Levitt, 1971). The use of the single-interval procedure, which is subject to response bias, was dictated by the need to measure responses to the signal that could not in any way be influenced by maskers that occurred within the same trial. Response bias, analyzed as the sum of the z-scores for hits and false alarms (Macmillan and Creelman, 1991), showed listener S08 to have a significant negative bias on SMM tracks (see below) which was largely responsible for the lower than chance performance on SMM trials. For the remaining listeners the magnitude of the bias was never so great as to be identified as a significant factor contributing to the large amounts of informational masking obtained. Listeners were informed that the signal frequency would remain the same throughout the experiment and that it would be presented on about half of the trials at random. To familiarize listeners with the task at least one 40-trial block of each experimental condition was run prior to data collection. Starting levels for the signal on subsequent trial blocks were 10 dB above the running average of threshold estimated from all previous blocks, beginning with the practice block. Step size for the adaptive track was 3 dB. Threshold for a block was defined as the average level of the points making up each track, excluding the first 4 trials of each type. Mean threshold is reported as the average of 5 such estimates.

D. Experimental design

Our goal was to measure performance on signal-alone trials in conditions known to produce large amounts of informational masking from past studies (cf. Neff and Green, 1987). The challenge was to include enough signal-alone trials to obtain meaningful estimates of performance, but not so many as to change the fundamental nature of the task. The level of the signal was adjusted independently for three different pairings of signal and nonsignal trials, i.e., three types of tracks. For SQ tracks signal-alone trials were randomly mixed with trials of quiet, each type of trial having an equal probability of occurrence within the trial block. For SMM tracks signal-plus-masker trials were randomly mixed with masker-alone trials that always included a two-tone masker. Note, a two-tone masker was used so that the listener could not simply base judgments on qualitative differences associated with one (masker) and two (signal-plus-masker) tones. Finally, for SM tracks signal-alone trials were randomly mixed with masker-alone trials that always included a single-tone masker. SMM and SM tracks differed from SQ tracks in that they were interleaved within a single block of 80 trials, 40 trials each track. This was done to increase the similarity to conditions of past informational masking studies by increasing the number of possible masker and signal-plus-masker combinations and by decreasing the proportion of signal-alone trials. Before the start of each block, the listeners were informed of which type of block they would be listening to (SQ or SM+SMM blocks). For SM+SMM blocks, listeners were also informed of the exact nature of the two independent tracks. SQ blocks were alternated with the SM+SMM blocks for the purpose of aiding memory for the signal.

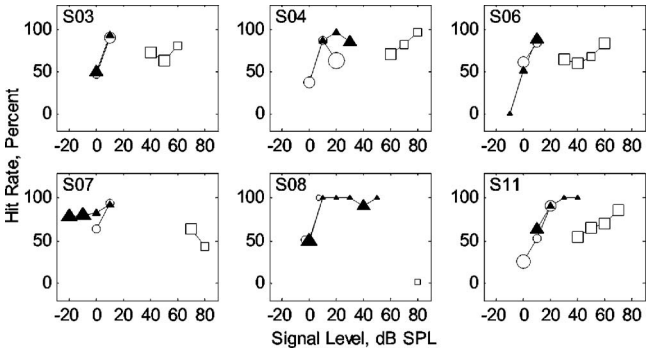

FIG. 1. Psychometric functions (hit rate) for SQ (open circles), SM (closed triangles), and SMM (open squares) trials. Vertical extent of each symbol is approximately equal to the square-root of the binomial variance associated with each point. Data are from six listeners whose results indicate little or no across-trial effect of maskers.

III. RESULTS

The focus of our analysis is on the comparison between signal-alone trials for SQ, SM tracks. Across-trial effects of maskers should be evidenced as substantial number of errors on SM trials for signal levels well above quiet threshold. In other words, the prediction is that data from SM and SQ trials belong to very different psychometric functions. Psychometric functions (hit rate versus signal level) for each type of trial for each listener are given in Figs. 1–3; SQ trials are denoted by open circles, SM trials by closed triangles, and SMM trials by open squares. Each point gives the hit rate based on at least 5 responses within ±5 dB of the signal level indicated; each function is based on a total of approximately 90 trials. Symbol size gives an indication of the reliability of each point; vertical extent being very nearly equal to the square-root of the binomial variance associated with each point.

In the three figures listeners are roughly grouped according to their overall pattern of results. Figure 1 gives the data from listeners whose results indicate no across-trial effects of maskers. For SM trials there is no evidence of errors beyond that of SQ trials. At signal levels for which the SM and SQ functions overlap the hit rate for these listeners is never measurably poorer on SM trials, and at higher signal levels hit

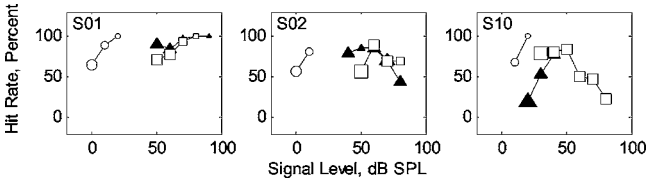

FIG. 2. Same as Fig. 1 except the data are from 3 listeners whose results indicate a significant across-trial effect of maskers.

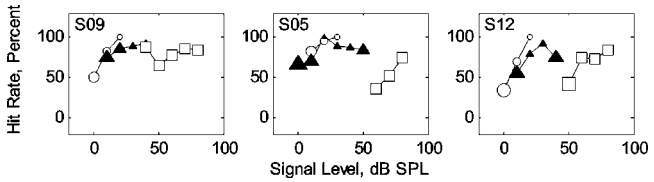

FIG. 3. Same as Fig. 2 except the data are from 3 listeners who showed intermediate results between the listeners of Figs. 1 and 2.

rate on SM trials is equal to or very nearly equal to 100%. All listeners in Fig. 1 also show a far rightward shift of the psychometric functions for SMM trials indicating substantial amounts of within-trial informational masking. These results stand in stark contrast to those of Fig. 2 where the three listeners show a clear across-trial effect of maskers. Here large numbers of errors are observed on SM trials of the same order of magnitude as on SMM trials.[1] There is also clear evidence of psychometric functions with negative slopes. Listener S02 shows a negative slope for SM trials while listener S10 shows a negative slope for SMM trials. The negative slopes appear to provide further evidence of confusion inasmuch as they occur in the region where the signal is likely to be clearly audible; that is where the signal level typically exceeds that of the masker. In this regard the functions are reminiscent of those of Brungart (2001) where plateaus attributed to confusion have been observed when the signal level roughly equals that of the masker. Finally, Fig. 3 gives the results of three listeners who show results intermediate between Figs. 1 and 2. These listeners show many fewer errors on SM trials than on SMM trials, but they nonetheless make large numbers of errors on SM trials at signal levels well above their quiet threshold.

IV. DISCUSSION

The results of this study make clear that informational maskers have the potential to exert significant across-trial effects on detection. To what extent these effects generalize to other studies remains an open question. In order to test for across-trial effects the conditions of this study needed to differ in fundamental ways from those of past informational masking studies. Moreover, the listeners of this study were not highly practiced. Practice is known to reduce the amount of informational masking and would likely have also reduced errors on signal-alone trials (Leek and Watson, 1984; Neff, 1995). Typically more practice has been given in past studies but the exact amount has varied greatly from one study to the next. Though it is unclear to what extent these results generalize to other studies, they at least suggest that greater consideration be given to the potential of informational maskers to exert effects that extend across trials.

ACKNOWLEDGMENTS

The research was supported by a grant from the NIDCD No. (R01 DC1262-10). The authors would like to thank Dr. Gerald Kidd, Dr. Nathaniel Durlach, and two anonymous reviewers for their comments on earlier versions of this manuscript.

[1]Note that because the range of signal levels visited on the SM+SMM tracks was generally greater than that for the SQ tracks, there is a degree of uncertainty regarding signal level on the SM+SMM tracks that was not present on SQ tracks. Such level uncertainty could be both a contributor to and product of the across-trial criterion effect predicted by the CoRE model. The model would predict no errors if the same levels had been visited at random on SQ tracks.

Arbogast, T. L., Mason, C. R., and Kidd, G. K., Jr. (**2002**). "The effect of spatial separation on informational and energetic masking of speech," J. Acoust. Soc. Am. **112**, 2086–2098.

Brungart, D. S. (**2001**). "Informational and energetic masking effects in the perception of two simultaneous talkers," J. Acoust. Soc. Am. **109**, 1101–1109.

Kidd, G., Jr., Arbogast, T. L., Mason, C. R., and Walsh, M. (**2001**). "Informational masking in listeners with sensorineural hearing loss," J. Assoc. Res. Otolaryngol. **3**, 107–119.

Kidd, G., Jr., Mason, C. R., and Arbogast, T. L. (**2002**). "Similarity, uncertainty, and masking in the identification of nonspeech auditory patterns," J. Acoust. Soc. Am. **111**, 1367–1376.

Kidd, G., Jr., Mason, C. R., Deliwala, P. S., Woods, W. S., and Colburn, S. H. (**1994**). "Reducing informational masking by sound segregation," J. Acoust. Soc. Am. **95**, 3475–3480.

Leek, M. R. and Watson, C. S. (**1984**). "Learning to detect auditory pattern components," J. Acoust. Soc. Am. **76**, 1037–1044.

Levitt, H. (**1971**). "Transformed up-down methods in psychoacoustics," J. Acoust. Soc. Am. **49**, 467–477.

Lutfi, R. A. (**1992**). "Informational processing of complex sound. III. Interference," J. Acoust. Soc. Am. **91**, 3391–3401.

Lutfi, R. A. (**1993**). "A model of auditory pattern analysis based on component-relative-entropy," J. Acoust. Soc. Am. **94**, 748–758.

Lutfi, R. A., Kistler, D. J., Callahan, M. R., and Wightman, F. L. (**2003**). "Psychometric functions for informational masking," J. Acoust. Soc. Am. **114**, 3273–3282.

Macmillan, N. A. and Creelman, D. C. (**1991**). *Detection Theory: A User's Guide* (Cambridge University Press, New York), pp. 271–274.

Neff, D. L. (**1985**). "Stimulus parameters governing confusion effects in forward masking," J. Acoust. Soc. Am. **78**, 1966–1976.

Neff, D. L. (**1995**). "Signal properties that reduce masking by simultaneous random-frequency masker," J. Acoust. Soc. Am. **98**, 1909–1920.

Neff, D. L. and Green, D. M. (**1987**). "Masking produced by spectral uncertainty with multicomponent maskers," Percept. Psychophys. **41**, 409–415.

Neff, D. L. and Jesteadt, W. (**1983**). "Additivity of forward masking," J. Acoust. Soc. Am. **74**, 1695–1701.

Oh, E. L. and Lutfi, R. A. (**1998**). "Nonmonotonicity of informational masking," J. Acoust. Soc. Am. **104**, 3489–3499.

Richards, V. M., Tang, Z., and Kidd, G., Jr. (**2002**). "Informational masking with small set sizes," J. Acoust. Soc. Am. **111**, 1359–1366.

Tang, Z. and Richards, V. M. (**2002**). "Internal noise invariance across two informational masking tasks," J. Acoust. Soc. Am. **111**, 2470.

Watson, C. S. and Kelly, W. J. (**1981**). "The role of stimulus uncertainty in the discrimination of auditory patterns," in *Auditory and Visual Pattern Recognition*, edited by D. J. Getty and J. H. Howard, Jr. (Erlbaum, Hillsdale, NJ).

Wright, B. A. and Saberi, K. (**1999**). "Strategies to detect auditory signals in small sets of random maskers," J. Acoust. Soc. Am. **105**, 1765–1775.

Effect of variability in level on forward masking and on increment detection[a)]

Walt Jesteadt,[b)] Kim S. Schairer, and Donna L. Neff
Center for Hearing Research, Boys Town National Research Hospital, 555 N. 30th St., Omaha, Nebraska 68131

(Received 28 February 2004; revised 25 March 2005; accepted 15 April 2005)

In the first of four experiments, all with the same four subjects, varying the level of a forward masker from interval to interval in a two-interval forced-choice (2IFC) adaptive procedure had little effect on threshold. In the second experiment, the signal level was fixed and performance was measured in units of d'. Varying the level of the forward masker again had little effect. Analyses of trial-by-trial data indicated that subjects did not vote for the interval with the higher-level masker, as would an energy detector. Performance was better on trials where the masker level in the interval with the signal was lower and was relatively independent of masker level in the nonsignal interval. In the third experiment, these results were replicated for a wider range of masker variability and with maskers lower in frequency than the signal. In the fourth experiment, the same range of variability from interval to interval was imposed on the level of the pedestal in an increment-detection task. Results were similar to those observed in forward masking. The results suggest that decision processes involved in both forward masking and increment detection are similar and that neither is based on energy detection. Template matching remains a viable alternative. [DOI: 10.1121/1.1928709]

PACS number(s): 43.66.Fe, 43.66.Dc, 43.66.Ba [NFV] Pages: 325–337

I. INTRODUCTION

In a series of papers, Oxenham and Plack (Oxenham and Plack, 1997, 2000; Plack and Oxenham, 1998) have demonstrated that the effects of forward masker level, masker frequency, and signal delay on masked thresholds can be accounted for in terms of basilar membrane nonlinearity. Their model, presented in greatest detail in Plack and Oxenham (1998), assumes a compressive nonlinearity as described by Yates *et al.* (1990), followed by a linear temporal window, and a decision process. In Schairer *et al.* (2003), we presented psychometric-function data that supported the basic assumptions of the model concerning the effects of compressive nonlinearity on forward masking. Here we present data concerning the decision process in forward masking and compare it to the decision process in increment detection.

Plack and Oxenham (1998) assume that in a typical two-interval forced-choice (2IFC) task, the subject compares the output levels of the temporal window for the two observation intervals and votes for the interval where the output level is greater. The threshold is described as a ratio, k, representing the level of the signal relative to the masker that is equivalent to $10\log(\Delta I/I)$ in internal units. The value of k is assumed to be constant across conditions, equivalent to a limitation on performance by multiplicative internal noise. A further limitation on performance at low levels is assumed to result from an additive internal noise. The amount of additive noise is estimated from the threshold for the signal in the absence of the masker (Oxenham and Moore, 1994). In this model, k is a measure of efficiency analogous to the efficiency parameter in models of the auditory filter (e.g., Patterson, 1976). A decision process of this kind, even when performance is not limited by variability in masker energy, can still be described as an energy detector (Patterson and Henning, 1977).

As an alternative to the decision process described in the formal model, Oxenham and Plack (2002) have suggested that decisions might be based on processes similar to those proposed for increment and decrement detection by Moore *et al.* (1999) and by Glasberg *et al.* (2001). In those models, the subject is assumed to detect the presence of a brief increment or decrement in the level of a longer duration tone by comparing the output of the temporal window in each interval to a template representing the output pattern over time that would be expected if the increment or decrement were present. The models assume that the template is obtained by averaging the output of the temporal window for several presentations at levels where the signal is clearly audible. Template matching is implemented in the models by computing the cross-correlation between the template and the waveform at the output of the temporal window for each stimulus presentation. The hypothetical observer then votes for the interval with the higher or highest correlation. Either the template or the sensory representation on each trial is assumed to be degraded by internal and/or external noise. The template matching process and its limitations are not well defined compared to the properties of energy detectors, which have been described in great detail (e.g., Green and Swets, 1966).

In the present studies, properties of the decision process in forward masking were explored by varying the level of the forward masker from one observation interval to the next. The same subjects were then tested in increment-detection conditions with variable pedestal levels to determine whether the effects of level variation were similar in the two tasks. If

[a)]A portion of this work was presented at the ARO 2002 and 2003 Midwinter Meetings.
[b)]Electronic mail: Jesteadt@boystown.org

decisions are based on the overall level of the output of the temporal window, varying the level of the forward masker or the level of the pedestal from interval to interval should interfere with detection of the signal. Because level variation will result in some trials where the signal is more audible and others where it is less audible, one might assume that these effects would cancel, leaving performance unchanged. Performance of an energy detector would decrease, however, because the level variation would increase the variance of the decision distributions, making any given difference at the output of the temporal window a less reliable cue for the presence of the signal. For intensity discrimination, where the task is to discriminate between two tones differing only in level, varying the level of the pedestal from interval to interval degrades performance in an orderly way, allowing an estimate of internal noise to be obtained (Jesteadt *et al.*, 2003). Similar effects should be observable for forward masking or increment detection if the decision process in these tasks can be correctly represented as an energy detector.

A precise prediction of the effect of masker level variation on forward masking requires an assumption concerning the effect of a given change in masker level, measured externally, on the internal signal-to-noise ratio. The effect of changing the masker level from interval to interval could be attenuated, for example, by the compressive nonlinearity or by nonlinear adaptation. Specific assumptions in the Plack and Oxenham (1998) model about the earlier stages of processing provide a framework in which the properties of the decision process can be tested. The model predicts that the effect of compressive nonlinearity can be avoided by using a forward masker that is well below the signal in frequency, a condition for which the growth of masking as a function of masker level has been shown to be linear (Oxenham and Plack, 2000). The model assumes that adaptation plays no role in forward masking and that the temporal window is linear. The windowing operation attenuates the effective level of the masker and the attenuation increases as a function of signal delay, but a 6 dB change in the level of the forward masker from interval to interval will still appear as a 6 dB change at the window output, if the masker is well below the signal in frequency. The change for an on-frequency masker would be significantly less. The model therefore predicts that the introduction of variability in the level of a lower-frequency forward masker with a standard deviation of x dB will result in variability at the output of the temporal window with a standard deviation of x dB for both the signal and nonsignal interval. This external variability is assumed to combine with internal noise in the decision process and the threshold increase or change in d' associated with a given amount of external variability can be used to obtain an estimate of the amount of internal noise (Jesteadt *et al.*, 2003). If internal noise, the parameter k in the Plack and Oxenham (1998) model, is 2.6 dB or less, masker level variation with an SD of 6 dB should result in a threshold increase of 3 dB or more for forward maskers well below the signal frequency.

If subjects in forward masking tasks make decisions based on template matching, as has been proposed for increment and decrement detection (Glasberg *et al.*, 2001; Moore *et al.*, 1999), random variation in the level of the forward masker from interval to interval might have little or no effect on threshold. There is no consensus regarding a specific model of template matching, but there is no reason to assume that it involves a comparison of the levels in the two observation intervals in the same sense that energy detection does. The cross-correlation process described above would be totally insensitive to changes in overall level that preserved the shift in the output of the temporal window resulting from presentation of the signal. The models described by Moore *et al.* (1999) and Glasberg *et al.* (2001) have been used (albeit with less than total success) to predict results in conditions where the pedestal level was fixed but the signal level varied adaptively. In the present study, the forward masker or pedestal level varied randomly from interval to interval, but the signal level was fixed. The two cases should be roughly equivalent.

We are not aware of studies of increment detection for tones where the pedestal level has been varied from interval to interval, but level variation has little or no effect on the detection of short increments in a longer duration noise (Formby *et al.*, 1994; Heinz and Formby, 1999). Likewise, randomization of the overall level from interval to interval has little effect on the detection of tones in noise (Formby *et al.*, 2002; Kidd *et al.*, 1989; Spiegel and Green, 1982). We would expect similar results for increment detection, and to the extent that decision processes in forward masking and increment detection are comparable, similar results for forward masking. Results suggesting that the decision process in forward masking was based on template matching or some other alternative to an energy detector would not present severe problems for the Plack and Oxenham (1998) model, because the decision process could be changed with no change in the earlier stages of the model.

In addition to observing the effects of level variability on performance, additional information about the decision process can be obtained through correlational analyses that test the relation between the relative level of the masker in the two observation intervals and subjects' decisions on individual trials (Berg, 1989, 2004a, b; Berg and Green, 1990; Lutfi, 1995; Richards and Zhu, 1994). These analyses can be done in the context of adaptive procedures, but have typically been done for fixed-level procedures. The present study used both types of procedures, but correlational analyses will be presented only for the fixed-level conditions, where the interpretation is more straightforward.

The first experiment described below examines the effects of variability in forward masker level on adaptive thresholds. The second experiment examines the effects of masker level variability when signal level is fixed and performance is measured in units of d'. The third and fourth experiments use greater variability than the first two experiments and directly compare the effects of level variability on forward masking and increment detection in conditions where signal level is fixed and performance is measured in units of d'.

II. GENERAL METHOD

The four experiments used the same subjects and equipment, with uniform stimulus parameters whenever possible. Common elements across experiments are described here.

A. Subjects

Four paid volunteers, ages 29, 25, 23, and 35, participated. All were college students with previous experience with the forward-masking task. All subjects had thresholds in quiet at 0.5, 2, and 4 kHz of $\leqslant$15 dB SPL for all test frequencies, bilaterally using a 2IFC adaptive procedure.

B. Stimuli and apparatus

In all conditions, the signal was a 4 kHz tone of 10 ms total duration, with 5 ms $\cos^2$ ramps. The off-frequency forward masker was a 70 dB SPL (mean), 2.4 kHz tone of 200 ms total duration, with 2 ms $\cos^2$ ramps. The on-frequency forward masker was identical, except that it was a 4 kHz tone. The pedestal in the increment detection experiment was also a 200 ms, 4 kHz tone with a mean level of 70 dB SPL. In all conditions where the masker (or pedestal) level varied from interval to interval, the signal level was either fixed or controlled by the adaptive procedure, independent of the masker level. Because the signal level did not rove with the masker (or pedestal) level, the variability in masker level resulted in signals that varied in detectability across trials.

All stimuli were generated digitally at a sampling rate of 50 kHz using an array processor (TDT AP2) and 16-bit digital-to-analog converters (TDT DD1). The forward masker was generated on one channel of the DD1, while the signal was generated on the other. The output of each channel was low-pass filtered at 20 kHz (TDT FT6) and attenuated (TDT PA4), then the outputs of the two channels were combined (TDT SM3) and presented to the listener through a headphone buffer (TDT HB6), a remote passive attenuator in the soundproof chamber, and a Sennheiser HD 250 Linear II headphone. All stimuli were presented to the left ear. Parallel use of multiple attenuators, summers, and headphone buffers made it possible to test up to four listeners simultaneously.

C. Procedure

In Experiment 1, an adaptive procedure controlled signal level, while in the other experiments, the signal level was fixed and performance was measured in units of d'. Trials were presented in blocks of 50 using a 2IFC procedure. In all but the final experiment, each trial consisted of a 500 ms warning interval, two 500 ms observation intervals separated by 500 ms, and a 300 ms feedback interval following the response of the final subject. There was a 500 ms pause before the beginning of the next trial. Subjects were given visual markers for the warning and observation intervals and correct-interval feedback in a message window on a keypad that they used to indicate their responses.

III. EXPERIMENT 1: EFFECT OF FORWARD MASKER VARIABILITY ON ADAPTIVE THRESHOLDS

For an initial test of the effects of masker variability, we used conditions taken from Oxenham and Plack (2000) and selected masker levels from distributions that were normally distributed in dB, centered on the nominal level of the forward masker. Plack and Oxenham (1998) assumed that the decision process is the same for on- and off-frequency maskers, but it could be argued that subjects adopt different detection strategies in conditions with off-frequency maskers that might minimize the effect of masker variability. Conditions with on-frequency maskers were therefore included for a comparison.

A. Stimuli and procedure

In separate conditions, the signal followed the masker with a delay of 0 or 30 ms, measured at the 0-voltage points. When the masker level varied from interval to interval, the levels were chosen at random from a distribution that was Gaussian in dB, but limited to a range of ±3 standard deviations (SDs). The SD was 2, 4, or 6 dB.

The signal level was controlled by an adaptive procedure with a decision rule that estimated 70.7% correct (Levitt, 1971). Step sizes were 4 dB until the fourth reversal and 2 dB thereafter. The subjects had been tested previously with these stimuli for the condition with no masker level variability (Schairer *et al.*, 2003). The current study began with conditions using a 2.4 kHz masker with SD=4 dB. Subjects completed four 50-trial blocks for the 0 ms signal delay, followed by eight blocks with the 30 ms delay, and an additional four with 0 ms delay. The entire sequence was then repeated, resulting in 16 replications (800 trials) at each signal delay. Conditions without masker-level variability were then tested, with eight blocks per signal delay in counterbalanced order. Finally, 16 blocks were completed for each signal delay for the 2 dB condition, followed by 16 blocks for the 6 dB condition. Eight additional blocks without masker level variability were interleaved with the data collection for the 2 dB and 6 dB conditions, so that 16 replications were available for all conditions.

After completion of data collection with 2.4 kHz maskers, thresholds were obtained with 4 kHz maskers. Four 50-trial blocks for the 0 ms signal delay were followed by eight blocks for the 30 ms delay, and an additional four blocks for 0 ms delay, for SDs of 4, 0, 2, and 6 dB. Thus, eight replications were available for all conditions. The Plack and Oxenham (1998) model assumes that the decision statistic is based on a nonlinear transform of power rather than of level and one could therefore argue that the variability in masker level should be Gaussian in power to achieve the clearest results. After data collection had been completed for forward maskers drawn at random from a distribution that was Gaussian in dB, additional data were therefore collected using 2.4 and 4 kHz maskers with the masker intensity drawn at random from a distribution that was Gaussian in power. The SD of the masker intensities was 1/3 the mean intensity. Only the 0 ms delay was used.

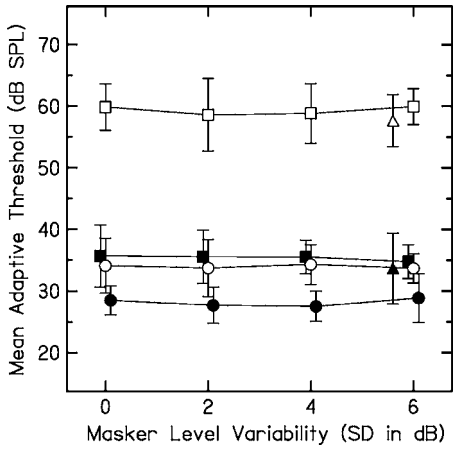

FIG. 1. Forward masked threshold as a function of the variability in the level of the forward masker in Experiment 1. Each data point represents the mean and standard deviation across four subjects. The open symbols are for a 4 kHz masker and signal. The filled symbols are for a 2.4 kHz masker and a 4 kHz signal. The filed symbols have been plotted slightly to the left and right of the open symbols to clarify the error bars. The squares show thresholds obtained with a 0 ms delay between the masker offset and the signal onset. The circles show thresholds obtained with a 30 ms delay. The triangles show data obtained with a 0 ms delay, but with masker level variability that was Gaussian in power rather than in dB.

B. Results

Figure 1 shows the mean forward-masked adaptive threshold across the four subjects at two signal delays (squares=0 ms; circles=30 ms) for on- and off-frequency maskers (open versus solid symbols, respectively) as a function of masker SD. As expected, thresholds are lower for off-frequency maskers than on-frequency maskers. They are lower in the 30 ms delay conditions than at the 0 ms delay, and this effect of signal delay is smaller for a forward masker at a frequency well below that of the signal, in agreement with Oxenham and Plack (2000). A repeated-treatments analysis of variance (ANOVA) indicated significant effects of masker frequency $[F(1,3)=191.6; p<0.05]$, signal delay $[F(1,3)=153.7; p<0.05]$ and the interaction of those two effects $[F(1,3)=287.7; p<0.05]$. The effect of masker variability was not significant, and there was no significant interaction of masker variability with the other factors. In addition, none of the individual subjects showed an effect of masker variability. Given a decision process based on energy detection, thresholds should have increased significantly in the off-frequency masker conditions.

The triangles in Fig. 1 show results obtained using on- and off-frequency forward maskers whose power varied from one presentation to the next, with samples drawn from a Gaussian distribution having a mean of 70 dB SPL, with SD equal to 1/3 of the mean power, and a range of ±3 SD. The triangles are plotted at 5.6 dB on the abscissa because individual samples taken from the Gaussian power distribution have that SD when converted to dB. There is clearly no difference between thresholds obtained in the absence of variability (SD=0) and those obtained with the maximum variability that can be achieved in a distribution that is Gaussian in power.

IV. EXPERIMENT 2: EFFECT OF FORWARD MASKER VARIABILITY ON DECISIONS WHEN SIGNAL LEVEL IS FIXED

The first experiment showed no effect of masker variability on forward-masked thresholds. One possible explanation for this result is that the masker variability interfered with the adaptive procedure. Increased variability should result in a decrease in performance, but this variability would also result in some trials where the signal was more detectable and others where it was less detectable, independent of the changes in signal level called for by the adaptive-procedure decision rule. This could result in greater variability or bias in the adaptive thresholds. The goal of Experiment 2, therefore, was to repeat the basic conditions in Experiment 1 using a more sensitive procedure in which signal level was fixed and performance was measured in units of d'. To facilitate comparisons to data obtained in increment detection and intensity discrimination, we used only on-frequency forward maskers.

A. Stimuli and procedure

The stimuli were a subset of those used in Experiment 1: the on-frequency 4 kHz forward masker and the 0 ms delay. Masker levels were chosen at random, from interval to interval, from a distribution that was Gaussian in dB with a mean of 70 dB SPL and SD=0, 2, 4, or 6 dB. The subjects had extensive experience with these stimuli in 2IFC adaptive procedures, including conditions where the signal level was fixed and masker level was adapted, but no experience in conditions where the level of difficulty was constant. Based on several blocks of practice trials, signal levels were selected that would result in performance in the range from 75% to 85% correct. To ensure that performance was in a measurable range in all conditions for all subjects, subjects were tested individually and a different signal level was selected for each subject. These signal levels, which ranged from 56 dB SPL to 63.5 dB SPL across the four subjects, were then used in all of the SD conditions. Eight 50-trial blocks were completed for each condition.

B. Results

The 50-trial blocks were always run in pairs with a brief break between blocks. A value of d' was therefore computed for each pair of blocks (i.e., 100 trials) and the four resulting values were averaged to arrive at a mean d' for each subject for each condition. The mean values of d' (which are plotted with data from Experiment 3 in Fig. 4, later) were 1.26, 1.17, 1.12, and 1.05 in conditions where the SDs were 0, 2, 4, and 6 dB, respectively. A one-way repeated treatments ANOVA showed no significant effect of masker SD $[F(3,12)=2.02; p>0.05]$. The use of different signal levels across subjects made performance more uniform, reducing the size of the standard deviations across subjects, and making the significance test more sensitive. As in Experiment 1, however, the increase in masker level variability had no significant effect on overall performance. Differences in masker level from interval to interval and from trial to trial did have an impact on the subjects' decisions on individual trials. We

TABLE I. Correlation analyses for Experiment 2. The first two columns of data show the correlation between the difference in the masker level across the two intervals and the subject's response, with trials where the signal was present in Interval 1 analyzed separately from those where the signal was present in Interval 2. The next two columns show the correlation between the masker level in the signal and nonsignal intervals and the correctness of the response. The final column shows the proportion of Interval 2 responses. Correlations significant at the 0.05 level are marked by a single asterisk, while those significant at the 0.01 level are marked by a double asterisk. For the first two columns, where $N=200$ trials, the coefficients significant at the 0.05 and 0.01 levels have absolute values ≥ 0.139 and 0.182, respectively. For the next two columns, where $N=400$ trials, the corresponding absolute values are ≥ 0.098 and ≥ 0.129.

		Point biserial correlation coefficient				
Subject	Standard dev.	M_2-M_1 vs $R\|S$ in Int 1	M_2-M_1 vs $R\|S$ in Int 2	M_s vs correctness	M_n vs correctness	$P(R_2)$
1	2	−0.187**	−0.166*	−0.243**	0.013	0.510
	4	−0.214**	−0.226**	−0.372**	−0.060	0.448
	6	−0.033	−0.316**	−0.261**	−0.131**	0.480
2	2	0.022	−0.098	−0.068	−0.010	0.495
	4	−0.099	0.177*	0.001	−0.062	0.483
	6	−0.010	−0.094	−0.220**	−0.154**	0.493
3	2	−0.061	−0.131	−0.181**	−0.061	0.550
	4	0.011	−0.151*	−0.128**	−0.043	0.518
	6	0.171*	−0.142*	−0.151**	−0.180**	0.528
4	2	−0.222**	−0.022	−0.129**	0.043	0.548
	4	−0.247**	−0.243**	−0.271**	0.039	0.570
	6	−0.313**	−0.175*	−0.336**	0.094	0.638

assessed those effects using correlational analyses and by computing values of d' for subsets of the data.

If subjects base their decisions on some transform of energy at the output of the temporal window, they should show a tendency to vote for the interval that contains the higher masker level. To determine the effect of differences in masker level on the decision process, point-biserial correlations were computed between the difference in masker level for the two intervals (Interval 2 − Interval 1) and the subject's binary response (1 or 2, for the signal present in Interval 1 or Interval 2) for the 400 trials for each condition. Subjects will, of course, vote for Interval 2 more often when the signal is presented in Interval 2. To remove the effect of signal position, we computed separate correlation coefficients for the 200 trials where the signal was presented in Interval 1 and the 200 trials where the signal was presented in Interval 2. Table I shows the correlation coefficients for individual subjects for conditions where the masker level varied with an SD of 2, 4, or 6 dB. If subjects were basing their decisions on the output of the temporal window, the correlation coefficients in both columns would be positive. All but one of the coefficients that are significantly different from zero are negative. That is, the subjects tended to vote for the interval with the lower masker level and, in terms of the Plack and Oxenham (1998) model, a smaller quantity at the output of the temporal window. Because correlation coefficients can be attenuated by a severe response bias (Richards and Zhu, 1994), the proportion of Interval 2 decisions is also given in the rightmost column of Table I. There is no relation between the proportion of Interval 2 decisions and the magnitude of the correlation coefficients.

Although these results indicate that variability in the forward masker level has no effect on overall performance, we would still expect more intense maskers to be more effective than less intense maskers. To determine the relation between masker level and performance, we computed the correlation of the correctness of the response on individual trials with masker level in the signal interval, M_s, and (separately) with the masker level in the nonsignal interval, M_n. The correlation coefficients for individual subjects for the three SD conditions are given in Table I. As expected, 10 of the 12 correlation coefficients for the relation between M_s and the correctness of the response were significant, indicating poorer performance when the level of the forward masker in the interval with the signal was higher. The two nonsignificant correlations were for the smaller SD conditions. Only three of the 12 correlation coefficients for the relation between M_n and the correctness of the response were significant, however, indicating little effect of the level of the forward masker in the nonsignal interval, except in the largest SD condition where the effect was again negative.

To determine the effect on d' of the forward masker level in the signal and nonsignal intervals, we rank ordered the 400 trials for each standard-deviation condition on the basis of masker level in the signal interval for one set of analyses and on the basis of masker level in the nonsignal interval for the other. We then divided the trials into quartiles of 100 trials each and computed a value of d' for each quartile for each of the four subjects, as well as a mean masker level for each quartile. Figure 2 shows mean values of d' across subjects for each masker-level quartile as a function of the mean masker level. The effect of masker level in the signal interval is shown in the left-hand panel while the effect of masker level in the nonsignal interval is shown in the right. Regression lines have been fitted to the data points in each panel. These results are consistent with the correlation analysis, showing a large effect of masker level in the signal interval, but a surprisingly small effect in the nonsignal interval.

If the decision process were based on energy detection, we would expect higher masker levels in the signal interval to result in higher levels of d', because subjects would vote

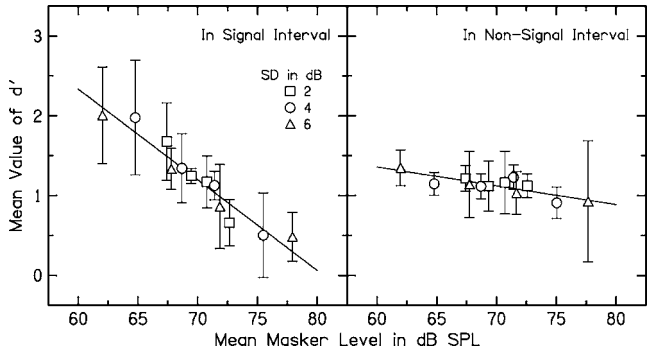

FIG. 2. Mean values of d' as a function of the forward masker level in the signal and nonsignal interval in Experiment 2. Each set of 400 trials was divided into quartiles based on the masker level. Each data point represents the mean for four subjects and error bars represent standard deviations in d' across subjects. Because subjects were tested individually, the mean masker levels also varied across subjects, but those standard deviations were generally smaller than the symbols. The lines show the linear regression of d' on the forward masker level.

for the interval with more energy and they would be credited with a correct response. Likewise, higher masker levels in the nonsignal interval should have an equal, but opposite, effect. To provide an example of the expected pattern of results, we carried out a similar analysis of data obtained in a study of intensity discrimination where the level of the pedestal varied randomly from interval to interval (Jesteadt *et al.*, 2003). The variability was Gaussian in dB with a maximum SD of 1.1 dB, small compared to the maximum SD's of 6 to 8 dB used here. Mean values of d' and level were computed for 100-trial quartiles for each of 7 SD values. Figure 3 shows the resulting means across seven subjects. The data show the pattern expected for an energy detector, in which the effect of masker level is equal (but opposite) in the signal and nonsignal intervals.

V. EXPERIMENT 3: FIXED SIGNAL LEVEL COMBINED WITH GREATER VARIABILITY IN THE LEVEL OF ON- AND OFF-FREQUENCY FORWARD MASKERS

The overall d' results from Experiment 2 showed an effect of masker SD that was in the predicted direction, but was not significant. Before carrying out the more detailed analyses summarized above, we reasoned that the subjects might be operating as energy detectors, but that internal noise at the output of the temporal window was still large with respect to the amount of external noise introduced by level variation from interval to interval. To test that hypothesis, we obtained a third set of data using forward masker levels selected at random from rectangular distributions rather than Gaussian distributions and using off-frequency forward maskers as well as on-frequency forward maskers. The use of rectangular distributions allowed us to achieve greater level variability without presenting maskers greater than 90 dB SPL. The use of off-frequency forward maskers avoided the compression of the range of masker levels predicted to occur for on-frequency forward maskers as a result of peripheral nonlinearity.

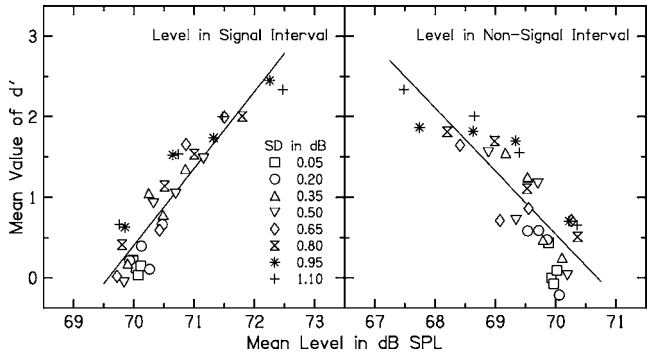

FIG. 3. Mean values of d' as a function of the level of a 2 kHz tone in the signal interval and in the nonsignal interval, for an intensity discrimination task (signal and pedestal 300 ms in duration) in which level variation was added independently to both observation intervals, from Jesteadt *et al.* (2003).

A. Stimuli and procedure

The stimuli were a subset of those used in Experiment 1, with both the on-frequency 4 kHz masker and the off-frequency 2.4 kHz masker, but only the 0 ms signal delay. When the masker level varied from interval to interval, the levels were chosen at random from a distribution that was rectangular in dB, with a total range of 7, 14, 21, or 28 dB in different conditions. Ranges were always centered on 70 dB SPL and were selected to create distributions with SDs of approximately 2, 4, 6, and 8 dB, given that the SD of a rectangular distribution is $1/\sqrt{12}$ times the range (Abramowitz and Stegun, 1970, p. 930).

As in Experiment 2, the signal was adjusted for each subject to a level that produced a score between 75% and 85% in the condition without variability in masker level. Average adaptive thresholds for the signal in the off- and on-frequency, fixed-level masker conditions were used as the starting point. Signal levels ranged from 34.8 to 45 dB SPL across the four subjects in the off-frequency conditions and from 58 to 65.5 dB SPL in the on-frequency conditions. The same signal levels were used for all ranges. The off-frequency masker conditions were run first, for masker level ranges of 0, 7, 14, and 21 dB, including the search for a fixed signal level. The on-frequency masker conditions were then run for the same ranges. Subjects were tested individually and eight 50-trial blocks were completed for each condition. After testing had been completed for the first four ranges for both off- and on-frequency maskers, we added the 28 dB range condition and obtained eight 50-trial blocks in the off-frequency condition, followed by the on-frequency condition.

B. Results

A value of d' was computed for each set of 100 trials (two consecutive 50-trial blocks) and the four values were averaged to arrive at a mean d' for each subject for each condition. Figure 4 shows mean values of d' across subjects for each condition, with error bars showing the standard deviations across subjects. Results for the on-frequency condition from Experiment 2, where the distribution of masker levels was Gaussian rather than rectangular, are also included in Fig. 4. The effect of variability in masker level in the new data is small, but significant $[F(4,12)=4.70; p<0.05]$. The

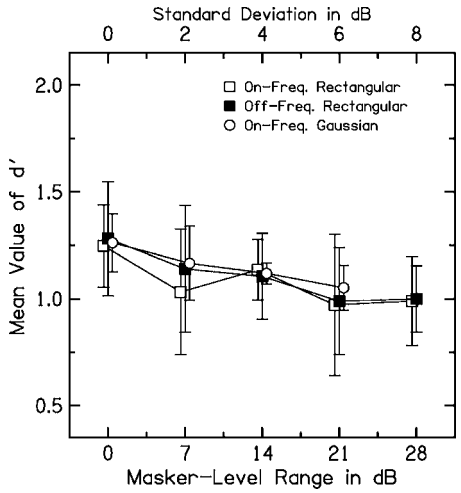

FIG. 4. Values of d' as a function of the variability in level of the forward masker for conditions where the distribution of masker levels was rectangular in dB. The scale at the bottom of the figure shows the total range of masker levels in dB while the scale at the top of the figure shows the corresponding standard deviations. Each data point represents the mean and standard deviation across four subjects. The open and filled squares represent data from Experiment 3 for 4 kHz and 2.4 kHz maskers, respectively, as in Fig. 1. The open circles represent data for the corresponding condition (4 kHz masker with a 0 ms signal delay) from Experiment 2, where the distribution of masker levels was Gaussian in dB with standard deviations referenced to the upper scale.

lack of an overall effect of masker frequency is meaningless because signal levels were adjusted to equate performance for the two masker frequencies. The lack of a significant interaction between masker frequency and variability in masker level $[F(4,12)=0.16; p>0.05]$ is noteworthy, however, because variability in the level of the off-frequency forward masker should have had a larger effect at the signal frequency than variability in the level of the on-frequency masker, as a result of compression in the on-frequency conditions. The comparison of results from Experiments 2 and 3 indicates that the shape of the distribution has no effect on performance. This is not surprising, given the small effect of variability in masker level in the two individual sets of data.

The correlation analyses developed in the course of analyzing the results of Experiment 2 were repeated for the larger set of conditions in Experiment 3. The results are presented in Table II. In the columns showing correlations between the difference in masker level for the two intervals and the response, 37 of the 64 coefficients are significantly different from zero. All but two of the significant correlations are negative, however, indicating a bias toward the interval with the forward masker that was lower in level. For correlations between the level of the forward masker in the interval with the signal and the correctness of the response, all but five of the 32 coefficients were significantly different from zero and all significant correlations were negative, as expected. For correlations between the level of the forward masker in the interval without the signal and the correctness of the response, only 15 out of the 32 coefficients were significantly different from 0 and 12 of those 15 were negative. There were no consistent differences between correlations for on-frequency and off-frequency conditions.

As in Experiment 2, we rank ordered the 400 trials for each range condition on the basis of masker level in the signal interval for one set of analyses and on the basis of masker level in the nonsignal interval for the other. We then divided the trials into quartiles of 100 trials each and computed a value of d' for each quartile for each of the four subjects, as well as a mean masker level for each quartile. Figure 5 shows mean values of d' across subjects for each masker-level quartile as a function of the mean masker level. The dashed reference lines in Fig. 5 are taken from the corresponding left- and right-hand panels of Fig. 2. In the upper two panels of Fig. 5 (on frequency), the agreement between the current data and the data from Experiment 2 (represented by the dashed lines) is excellent. In the lower two panels (off frequency), both sets of data show an effect of the forward masker level that is greater than the effect in the upper panels or in the Experiment 2 reference lines. A greater effect for the off-frequency forward masker is in agreement with the assumption that the effect of a change in the level of the on-frequency masker is attenuated by the peripheral nonlinearity.

VI. EXPERIMENT 4: EFFECT OF PEDESTAL-LEVEL VARIABILITY ON INCREMENT DETECTION WHEN SIGNAL LEVEL IS FIXED

The analysis of intensity-discrimination data collected by Jesteadt *et al.* (2003), shown in Fig. 3, provides strong evidence that decision processes in forward masking differ from those in intensity discrimination. The results of the first three experiments reported here demonstrate a resistance to the effects of variability in overall level from interval to interval that has also been found for the detection of increments in noise waveforms (Formby *et al.*, 1994; Heinz and Formby, 1999). Recent models of the decision process in the detection of increments and decrements in sinusoids (Glasberg *et al.*, 2001; Moore *et al.*, 1999) offer an alternative to the energy-detector model that could be applied to forward masking. To explore the relation between decision processes in forward masking and those in increment detection, we obtained data from the same group of subjects for an increment-detection task, using stimuli and procedures modeled on those used in Experiment 3.

A. Stimuli and procedure

The pedestal for the increment-detection conditions was a 4 kHz, 200 ms tone with a mean level of 70 dB, identical to the on-frequency forward masker in the earlier experiments. The increment, or signal, was a 10 ms, 4 kHz tone identical to the signal in the forward masking experiments, presented in cosine phase to the pedestal at the temporal center of the pedestal waveform. For conditions in which the pedestal level varied from interval to interval, the levels were chosen at random from a distribution that was rectangular in dB, with a total range of 7, 14, 21, or 28 dB. The pedestal and signal were presented on different channels, as in the forward masking experiments, and then summed. The warning interval was shortened to 300 ms, and the observation intervals were shortened to 200 ms, separated by 460 ms.

TABLE II. Correlation analyses for Experiment 3. The format is described in the heading for Table I. Correlations significant at the 0.05 level are marked by a single asterisk. Those significant at the 0.01 level are marked by a double asterisk.

			Point biserial correlation coefficient				
Subject	Masker	Range	M_2-M_1 vs $R\|S$ in Int 1	M_2-M_1 vs $R\|S$ in Int 2	M_s vs correctness	M_n vs correctness	$P(R_2)$
1	On freq	7	−0.185**	−0.144*	−0.243**	−0.001	0.470
		14	−0.129	−0.227**	−0.331**	−0.067	0.488
		21	0.008	−0.280**	−0.303**	−0.104*	0.440
		28	0.129	−0.236**	−0.304**	−0.224**	0.478
	Off freq	7	−0.227**	−0.043	−0.222**	0.000	0.585
		14	−0.036	−0.080	−0.304**	−0.220**	0.512
		21	0.096	−0.118	−0.310**	−0.304**	0.545
		28	0.126	0.150*	−0.199**	−0.381**	0.490
2	On freq	7	−0.220**	−0.145*	−0.178**	0.082	0.525
		14	−0.027	−0.046	−0.110*	−0.057	0.498
		21	0.053	−0.049	−0.194**	−0.193**	0.512
		28	0.034	−0.026	−0.120*	−0.122*	0.520
	Off freq	7	−0.311**	−0.336**	−0.476**	−0.041	0.552
		14	−0.472**	−0.512**	−0.627**	0.068	0.525
		21	−0.330**	−0.404**	−0.499**	0.009	0.565
		28	−0.164*	−0.293**	−0.414**	−0.090	0.498
3	On freq	7	−0.048	−0.077	−0.058	0.030	0.470
		14	0.191**	−0.055	−0.066	−0.166**	0.550
		21	−0.001	−0.297**	−0.279**	−0.079	0.498
		28	−0.051	−0.118	−0.218**	−0.107*	0.568
	Off freq	7	−0.049	−0.105	−0.080	0.032	0.495
		14	0.169*	−0.015	−0.064	−0.155**	0.515
		21	0.371**	−0.082	0.010	−0.214**	0.520
		28	0.155*	−0.005	−0.121*	−0.221**	0.490
4	On freq	7	−0.204**	−0.264**	−0.147**	0.149**	0.552
		14	−0.136	−0.299**	−0.290**	−0.006	0.548
		21	−0.422**	−0.401**	−0.405**	0.193**	0.498
		28	−0.179*	−0.273**	−0.292**	0.009	0.585
	Off freq	7	−0.343**	−0.399**	−0.482**	0.055	0.530
		14	−0.349**	−0.418**	−0.512**	0.033	0.512
		21	−0.516**	−0.520*	−0.551**	0.183**	0.528
		28	−0.300**	−0.400**	−0.478**	0.012	0.492

To select appropriate signal levels, the threshold for detection of the signal in the presence of the pedestal was estimated using a 2IFC adaptive procedure with a decision rule chosen to estimate the level required for 70.7% correct (Levitt, 1971). The initial step size of 4 dB was reduced to 2 dB after four reversals. The mean threshold across eight repetitions was used as a starting point to estimate the fixed-signal level that produced 75%–85% correct, which was determined individually for each subject. The same signal levels, which ranged from 66.25 to 70.25 across the four subjects, were then used in all conditions. Eight 50-trial blocks of data were collected for the condition with no variability in the pedestal level, followed by eight blocks for ranges of 14, 28, 7, and 21 dB, in that order.

B. Results

A value of d' was computed for each set of 100 trials (two consecutive 50-trial blocks) and the four values were averaged to arrive at a mean d' for each subject for each condition. Figure 6 shows mean values of d' across subjects for each increment-detection condition, with error bars showing the standard deviations across subjects. For comparison purposes, mean values of d' for the on-frequency forward-masking conditions in Experiment 3 have been included both in Fig. 6 and in the corresponding ANOVA. The average value of d' in the 0 dB range condition was somewhat lower for increment detection than for forward masking, but that is a result of the choice of signal levels. The ANOVA showed no significant effect of variability in level and no interaction of the effect of level variability and task (forward masking versus increment detection).

The results of the correlation analysis for Experiment 4, presented in Table III, are consistent with the analyses for the earlier experiments. In the columns showing correlations between the difference in pedestal level for the two intervals and the response, 25 of the 32 coefficients are significantly different from zero, all in the direction that indicates a bias towards the interval with the lower-level pedestal. For correlations between the level of the pedestal in the interval with the signal and the correctness of the response, all coefficients were highly significant and negative. For correlations be-

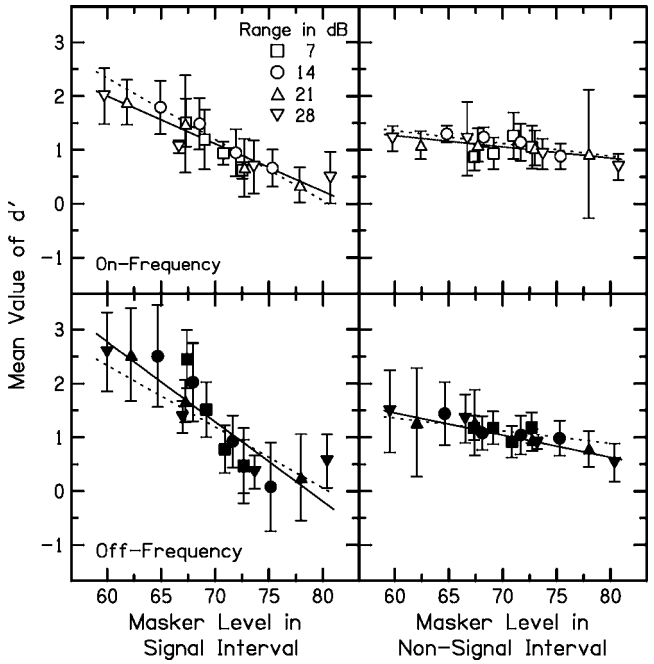

FIG. 5. Values of d' in Experiment 3 as a function of the masker level in the signal and nonsignal interval (colums), for conditions with on-frequency and off-frequency forward maskers (rows). Each data point represents the mean for four subjects and error bars represent standard deviations in d' across subjects. Different symbols represent the range of masker level variation in dB, as indicated in the legend. The solid lines show the linear regression of d' on the forward masker level. The dashed lines show the corresponding effect observed in Experiment 2.

tween the level of the pedestal in the interval without the signal and the correctness of the response, only 6 out of the 16 coefficients were significantly different from zero and four of those six were negative.

As for Experiments 2 and 3, we rank ordered the 400 trials for each range condition on the basis of pedestal level in the signal interval for one set of analyses and on the basis of pedestal level in the non-signal interval for the other. We then divided the trials into quartiles of 100 trials each and computed a value of d' for each segment for each of the four subjects, as well as a mean pedestal level for each segment.

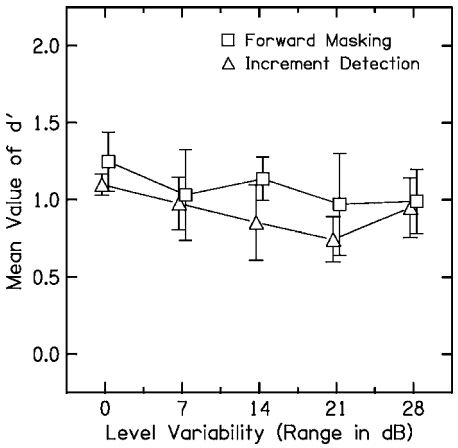

FIG. 6. Values of d' in Experiment 4 for increment detection (triangles) as a function of the variability in the level of the pedestal from interval to interval, with corresponding data for forward masking (squares) replotted from Fig. 4.

Figure 7 shows mean values of d' across subjects for each pedestal-level quartile as a function of the mean pedestal level. Different symbols represent data for the four ranges of variability. The dashed reference lines, taken from Fig. 2, show the effect observed in the forward masking conditions with on-frequency maskers. The solid lines are best fitting functions for the data in each panel. The pattern here is similar to that observed in Figs. 2 and 5, in that only the level of the pedestal in the interval with the signal has a strong effect on detectability. The effect of the pedestal level is stronger than the effect of the forward masker level in the interval with the signal and is totally absent in the nonsignal interval.

VII. DISCUSSION

A. Components and tests of the decision process

Green (1960) noted that "detection theory is a combination of two distinct theoretical structures: decision theory and the theory of ideal observers." Macmillan and Creelman (1991) examined alternative models of statistical decision theory that have been developed in the context of research on a wide range of topics and they explicitly excluded discussion of the ideal observer. Most of the recent discussions of decision processes in psychoacoustics, on the other hand, have assumed a standard decision-theory model based on overlapping equal-variance Gaussian distributions and have focused entirely on the properties of the stimuli that form the basis of the decision, the ideal-observer component in Green's classification scheme. In a typical detection or discrimination task, there are many stimulus properties that a subject could use and those properties are highly correlated. Richards (2001), for example, notes that adding a tone to a narrow band of noise results, on average, in an increase in intensity, a less modulated envelope, and a more regular fine structure. Because different subjects may use different strategies, it is difficult to determine or control the specific cues underlying decisions in different tasks or even in different conditions within a task. An interpretation of the data always depends, however, on assumptions concerning the specific stimulus properties governing performance.

Models of many auditory detection and discrimination tasks assume that decisions are based on a comparison of the energy or power, or some monotonic transform of one of those quantities, in a given frequency region at a given point in time. That assumption underlies discussions of critical bands and critical ratios (Fletcher, 1940), measures of the auditory filter (Patterson, 1976), and most theoretical discussions of temporal integration, intensity discrimination, or detection of tones in noise, as well as the model of forward masking described by Plack and Oxenham (1998). A standard test of such models, used extensively in the literature on profile analysis (Green, 1988), is to vary the overall level of the stimuli across observation intervals, eliminating any cues based on overall energy. Spiegel and Green (1982) and Kidd *et al.* (1989) used this approach to demonstrate that an overall difference in energy is not required for the detection of tones in noise. Richards and Nekrich (1993) reversed the approach, demonstrating that subjects could detect tones in noise when the energy was identical in the signal and non-

TABLE III. Correlation analyses for Experiment 4. The format is described in the heading for Table I. Correlations significant at the 0.05 level are marked by a single asterisk. Those significant at the 0.01 level are marked by a double asterisk.

		Point biserial correlation coefficient				
Subject	Range	M_2-M_1 vs $R\|S$ in Int 1	M_2-M_1 vs $R\|S$ in Int 2	M_s vs correctness	M_n vs correctness	$P(R_2)$
1	7	−0.168*	−0.194**	−0.270**	−0.014	0.478
	14	−0.199**	−0.295**	−0.380**	−0.017	0.485
	21	−0.091	−0.016	−0.275**	−0.194**	0.515
	28	−0.290**	−0.222**	−0.409**	−0.066	0.508
2	7	−0.413**	−0.109	−0.403**	−0.054	0.640
	14	−0.324**	−0.361**	−0.404**	0.078	0.475
	21	−0.360**	−0.490**	−0.554**	0.027	0.500
	28	−0.337**	−0.397**	−0.519**	−0.007	0.570
3	7	−0.291**	−0.190**	−0.384**	−0.031	0.568
	14	−0.078	−0.157*	−0.305**	−0.124*	0.478
	21	−0.040	−0.113	−0.317**	−0.213**	0.518
	28	−0.007	−0.256**	−0.360**	−0.141**	0.490
4	7	−0.357**	−0.229**	−0.347**	0.070	0.512
	14	−0.333**	−0.556**	−0.530**	0.097	0.522
	21	−0.489**	−0.496**	−0.516**	0.172**	0.488
	28	−0.633**	−0.668**	−0.655**	0.284**	0.512

signal intervals. Formby *et al.* (1994) and Heinz and Formby (1999) showed that level variability did not interfere with the detection of an increment in noise, unless the increment had both the same bandwidth and duration as the noise background. Most recently, Formby *et al.* (2002) have shown that temporal integration results do not depend on reliable energy differences.

Dau *et al.* (1996a, b) describe an alternative decision process based on the correlation between the temporal pattern generated on each stimulus presentation and a stored template derived from presentation of the masker with a clearly audible signal. This time-domain model of the decision process can generate predictions for forward and backward masking (Dau *et al.*, 1996b) and can be extended to generate predictions concerning the detection and discrimination of modulation (Dau *et al.*, 1997a, b). Moore *et al.* (1999) and Glasberg *et al.* (2001) have assumed a similar template-matching decision process, in combination with the peripheral signal processing stages used in their earlier models (e.g., Moore and Oxenham, 1998). The template-matching decision process is not sensitive to overall changes in level from one stimulus presentation to the next, unless those changes alter the shape of the internal temporal pattern.

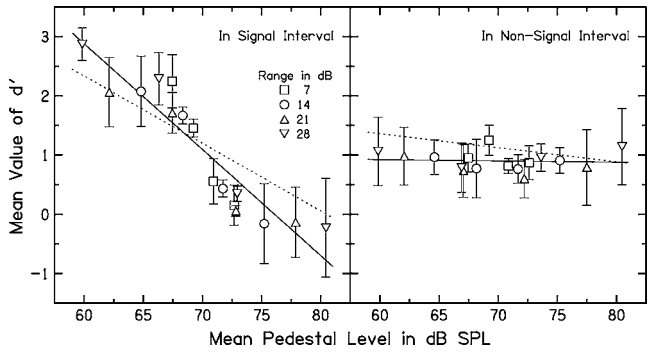

FIG. 7. Values of d' in Experiment 4 as a function of the pedestal level in the signal and nonsignal interval. Each data point represents the mean and standard deviation in d' across subjects. Different symbols represent the range of pedestal level variation in dB, as indicated in the legend. The solid lines show the linear regression of d' on pedestal level. The dashed lines show the effect observed in Experiment 2, which was very similar to the effect observed in Experiment 3.

B. Decision processes in forward masking and increment detection

The data presented here do not support the hypothesis that decisions in either forward masking or increment detection are based on a comparison of relative levels in the two observation intervals. Template matching, as described by Dau *et al.* (1996a), Moore *et al.* (1999), and Glasberg *et al.* (2001), remains a viable alternative. In using the current data to test models of template matching, it is important to note that only the level of the masker or pedestal varied from interval to interval. Unlike the roving-level conditions typically used in studies of profile analysis, the signal level did not vary with masker level. Thus, the shape of the internal temporal pattern associated with a presentation of the signal would have differed from trial to trial. These changes in the signal-to-noise ratio were greater in some conditions than others, but the amount of variability *per se* had little impact on performance. Varying the signal level with the masker level to maintain a constant temporal pattern might have resulted in an even smaller effect of masker variability, but would have required strong assumptions concerning the change in signal level required for a given change in the level of the forward masker. Because the signal level was constant in these conditions, the signal-to-noise ratio was markedly poorer on trials where the interval with the signal contained a masker or pedestal level randomly selected from the top of the available range. The solid and dashed lines in Fig. 7 provide a comparison of signal-to-noise ratio effects in

increment detection and forward masking. It is not surprising that the pedestal level in the signal interval in Experiment 4 had a greater effect on performance than the forward masker level in the signal interval in Experiments 2 and 3, given the difference in the slope of masking for the two tasks. The increase in increment level at threshold is almost 1 dB for every dB increase in the pedestal level, while the increase in signal level at threshold is rarely more than 0.5 dB for every dB increase in the level of on-frequency forward maskers (Jesteadt *et al.*, 1982). The most problematic aspect of the present data was that subjects tended to vote for the interval with the masker or pedestal that was lower in level. Even if the subjects were not basing decisions on a comparison of overall levels in the two observation intervals, it would be reasonable for them to assume that a higher-level masker or pedestal would make the signal more difficult to detect. In that case, given a trial on which the location of the signal was unclear, they would presumably vote for the interval with the higher-level masker. A clear demonstration that subjects do not pursue that strategy would require catch trials in which no signal was presented.

The data presented here suggest similar decision processes in forward masking and increment detection. The effects of variability in level on d' for these two tasks differ markedly from those for intensity discrimination, where no template matching strategy is available and variability in the pedestal level from interval to interval results in a predictable decrease in performance. The differences in decision processes in increment detection and intensity discrimination may underlie some of the differences in the results obtained with these two procedures (e.g., Green *et al.*, 1979).

C. Correlation coefficients and values of d' as measures of perceptual weight

Many studies have assessed the importance of specific stimulus features by estimating the correlation between a change in a given feature and a subject's response on individual trials (for a recent review, see Berg, 2004b). Of the 76 significant correlation coefficients in the first two columns of Tables I–III, all but seven are negative, a result inconsistent with an energy detector model of the decision process. Correlations between masker or pedestal level in the signal and nonsignal interval and the correctness of the response were also negative. The masker or pedestal level in the signal interval was a better predictor of performance than the masker or pedestal level in the nonsignal interval. Zhang (1995) reported similar analyses for detection of tones in noise, with similar results. Zhang found strong correlations only for features in the interval with the signal and, given a difference in masker level between the intervals, his subjects tended to vote for the interval with the lower-level masker.

Although discussions of correlational analyses and analyses conditioned on single stimuli (Berg, 1989) emphasize the goal of relating stimulus features to subjects' decisions, without regard to the correctness of the decisions (e.g., Berg, 2004a, b), the initial step of sorting trials based on the interval containing the signal makes it impossible to exclude correctness as a factor. The first column of Tables I–III, for example, describes results for trials where the signal was always presented in the first interval. The negative correlations in this case mean that subjects were more likely to vote for Interval 2 when the masker level or pedestal level was lower in Interval 2 than in Interval 1. These also tend to be trials where the level in Interval 1 was higher than average. Votes for Interval 2 on trials where the signal is in Interval 1 are incorrect responses and we therefore have a result indicating a higher percentage of incorrect responses on trials where the masker or pedestal level in the interval with the signal is higher than average. Similar logic can be applied to the correlations in the second column, where negative correlations represent a higher percentage of correct responses on trials where the signal is presented in the second interval and the masker or pedestal level is lower than average in that interval. The negative correlations can be interpreted as an assignment of negative weight to nonsignal portions of the stimulus (e.g., Berg, 2004a; Berg and Green, 1990), but given the simplicity of these stimuli, a more straightforward interpretation would be that higher-level maskers result in poorer performance.

The correlational analyses are consistent with the analyses of the change in d' associated with a change in the masker or pedestal level in the signal and nonsignal intervals. This is to be expected, given that the d' and correlational analyses work with the same information, but partition it differently. These issues have been addressed in greater detail by Buus *et al.* (1996), who derived perceptual weights directly from changes in d' as a function of the signal level.

D. Implications for the multi-stage model of forward masking

One of our goals in exploring the effect of variability in level on forward masking was to determine whether the decision process in forward masking was analogous to intensity discrimination at the output of the temporal window, as assumed by Plack and Oxenham (1998). Our conclusion that the decision process is instead analogous to increment detection at the output of the temporal window does not require any changes in the earlier stages of the model or invalidate any conclusions regarding the role of peripheral nonlinearity in accounting for the results observed in studies of forward masking. Because both energy detection and template matching are sensitive to the signal-to-noise ratio, there may be cases where a simple energy detection framework can be substituted for a more complicated template matching process at the output of a multistage model without changing the interpretation of the results. Both internal and external noise may have a different effect on template matching, however, than on energy detection.

Assumptions concerning the decision processes used by human subjects also have an impact on efforts to relate psychophysical results to physiological data obtained from animal models. Plack and Oxenham (1998), for example, assume that forward masking reflects persistence rather than peripheral adaptation. A recent paper by Nizami (2003) reaches the same conclusion. Oxenham (2001) was unable to distinguish between the two alternatives based on psychophysical data, but noted that physiological data favored per-

sistence over adaptation. Although there is extensive evidence of peripheral adaptation in the physiological literature (see Abbas, 1997 for a review), the physiological study using procedures most analogous to human psychophysics (Relkin and Turner, 1988) found that the adaptation produced by a forward masker often did not result in a change in threshold at the level of individual auditory nerve fibers. Relkin and Turner obtained their result by comparing the number of spikes in the signal and nonsignal intervals. Because adaptation reduced spontaneous rate, as well as the response to the signal, it tended to have little effect on the net difference in the number of neural responses. Nizami (2003) also assumed that decisions are based on a comparison of the number of spikes in the two intervals.

The decision process that Relkin and Turner (1988) and Nizami (2003) assumed is equivalent to an energy detector rather than a template matcher. Relkin and Turner, for example, would have found large effects of variable masker level on the forward masked threshold. The Relkin and Turner results, therefore, provide only indirect data concerning the relative importance of persistence and adaptation. Because the effects of peripheral adaptation could be avoided in most cases by a comparison of neural counts across observation intervals, the fact that subjects clearly do not use that strategy might suggest that peripheral adaptation is not the major source of forward masking. A better understanding of the decision processes in forward masking may lead to a better understanding of the underlying mechanisms.

VIII. CONCLUSIONS

(1) The small effect of variability in level from interval to interval on either forward masking or detection of an increment in a sinusoid indicates that subjects are not using a decision process based on energy detection in either task. Results are consistent with a decision process based on template matching.
(2) Analyses of trial-by-trial data indicate that the level of the forward masker or the pedestal in the observation interval in which the signal is presented has a stronger effect on performance than the level of the forward masker or pedestal in the nonsignal interval. These results are also consistent with a decision process based on template matching.
(3) Analyses of trial-by-trial data obtained by Jesteadt *et al.* (2003) for an intensity discrimination task in which levels varied from interval to interval show the pattern that would be expected for a decision process based on energy detection. This indicates that decision processes in increment detection and intensity discrimination are fundamentally different from one another.
(4) Relkin and Turner (1988) demonstrated that little forward masking would be predicted at the level of the auditory nerve if decisions were based on the difference in the number of spikes elicited by the forward masker alone and the forward masker plus the signal. Since human subjects do not base their decisions on a comparison of the magnitude of the responses in the two observation intervals, the implications of the Relkin and Turner result are unclear.

ACKNOWLEDGMENTS

This work was supported by Grants No. R01 DC00136, No. R01 DC006648, and No. T32 DC00013 from the National Institute on Deafness and Other Communication Disorders of the National Institutes of Health. This work benefited from discussions with Christopher Plack, Andrew Oxenham, Soren Buus, and Robert Lutfi. We appreciate the help of Barbara Olmedo and Hongyang Tan in the preparation of the manuscript and helpful comments by Lance Nizami on an earlier version.

Abbas, P. J. (**1997**). "Adaptation in the auditory system," in *Encyclopedia of Acoustics*, edited by M. J. Crocker (Wiley, New York), pp. 1535–1544.
Abramowitz, M., and Stegun, I. A. (Eds.) (**1970**). *Handbook of Mathematical Functions With Formulas, Graphs, and Mathematical Tables* (Dover, New York).
Berg, B. G. (**1989**). "Analysis of weights in multiple observation tasks," J. Acoust. Soc. Am. **86**, 1743–1746.
Berg, B. G. (**2004a**). "A molecular description of profile analysis: Decision weights and internal noise," J. Acoust. Soc. Am. **115**, 822–829.
Berg, B. G. (**2004b**). "A temporal model of level-invariant, tone-in-noise detection," Psychol. Rev. **111**, 914–930.
Berg, B. G., and Green, D. M. (**1990**). "Spectral weights in profile listening," J. Acoust. Soc. Am. **88**, 758–766.
Buus, S., Zhang, L., and Florentine, M. (**1996**). "Stimulus-driven, time-varying weights for comodulation masking release," J. Acoust. Soc. Am. **99**, 2288–2297.
Dau, T., Kollmeier, B., and Kohlrausch, A. (**1997a**). "Modeling auditory processing of amplitude modulation. I. Detection and masking with narrow-band carriers," J. Acoust. Soc. Am. **102**, 2892–2905.
Dau, T., Kollmeier, B., and Kohlrausch, A. (**1997b**). "Modeling auditory processing of amplitude modulation. II. Spectral and temporal integration," J. Acoust. Soc. Am. **102**, 2906–2919.
Dau, T., Puschel, D., and Kohlrausch, A. (**1996a**). "A quantitative model of the effective signal processing in the auditory system. I. Model structure," J. Acoust. Soc. Am. **99**, 3615–3622.
Dau, T., Puschel, D., and Kohlrausch, A. (**1996b**). "A quantitative model of the effective signal processing in the auditory system. II. Simulations and measurements," J. Acoust. Soc. Am. **99**, 3623–3631.
Fletcher, H. (**1940**). "Auditory patterns," Rev. Mod. Phys. **12**, 47–65.
Formby, C., Heinz, M. G., and Aleksandrovsky, I. V. (**2002**). "Temporal integration of sinusoidal increments in the absence of absolute energy cues," J. Speech Lang. Hear. Res. **45**, 1285–1296.
Formby, C., Heinz, M. G., Luna, C. E., and Shaheen, M. K. (**1994**). "Masked detection thresholds and temporal integration for noise band signals," J. Acoust. Soc. Am. **96**, 102–114.
Glasberg, B. R., Moore, B. C., and Peters, R. W. (**2001**). "The influence of external and internal noise on the detection of increments and decrements in the level of sinusoids," Hear. Res. **155**, 41–53.
Green, D. M. (**1960**). "Psychoacoustics and detection theory," J. Acoust. Soc. Am. **32**, 1189–1203.
Green, D. M. (**1988**). *Profile Analysis: Auditory Intensity Discrimination* (Oxford University Press, New York).
Green, D. M., Nachmias, J., Kearney, J. K., and Jeffress, L. A. (**1979**). "Intensity discrimination with gated and continuous sinusoids," J. Acoust. Soc. Am. **66**, 1051–1056.
Green, D. M., and Swets, J. A. (**1966**). *Signal Detection Theory and Psychophysics* (Krieger Publishing Company, New York).
Heinz, M. G., and Formby, C. (**1999**). "Detection of time- and bandlimited increments and decrements in a random-level noise," J. Acoust. Soc. Am. **106**, 313–326.
Jesteadt, W., Bacon, S. P., and Lehman, J. R. (**1982**). "Forward masking as a function of frequency, masker level, and signal delay," J. Acoust. Soc. Am. **71**, 950–962.
Jesteadt, W., Nizami, L., and Schairer, K. S. (**2003**). "A measure of internal

noise based on sample discrimination," J. Acoust. Soc. Am. **114**, 2147–2157.
Kidd, G. J., Mason, C. R., Brantley, M. A., and Owen, G. A. (**1989**). "Roving-level tone-in-noise detection," J. Acoust. Soc. Am. **86**, 1310–1317.
Levitt, H. (**1971**). "Transformed up-down methods in psychoacoustics," J. Acoust. Soc. Am. **49**, 467–477.
Lutfi, R. A. (**1995**). "Further comments on proportional duration and proportional variance as factors in auditory pattern discrimination," J. Acoust. Soc. Am. **97**, 1339–1340.
Macmillan, N. A., and Creelman, C. D. (**1991**). *Detection Theory: A User's Guide* (Cambridge University Press, New York).
Moore, B. C., and Oxenham, A. J. (**1998**). "Psychoacoustic consequences of compression in the peripheral auditory system," Psychol. Rev. **105**, 108–124.
Moore, B. C., Peters, R. W., and Glasberg, B. R. (**1999**). "Effects of frequency and duration on psychometric functions for detection of increments and decrements in sinusoids in noise," J. Acoust. Soc. Am. **106**, 3539–3552.
Nizami, L. (**2003**). "Afferent response parameters derived from postmasker probe-detection thresholds: 'the decay of sensation' revisited," Hear. Res. **175**, 14–35.
Oxenham, A. J. (**2001**). "Forward masking: Adaptation or integration?," J. Acoust. Soc. Am. **109**, 732–741.
Oxenham, A. J., and Moore, B. C. (**1994**). "Modeling the additivity of nonsimultaneous masking," Hear. Res. **80**, 105–118.
Oxenham, A. J., and Plack, C. J. (**1997**). "A behavioral measure of basilar-membrane nonlinearity in listeners with normal and impaired hearing," J. Acoust. Soc. Am. **101**, 3666–3675.
Oxenham, A. J., and Plack, C. J. (**2000**). "Effects of masker frequency and duration in forward masking: further evidence for the influence of peripheral nonlinearity," Hear. Res. **150**, 258–266.
Oxenham, A. J., and Plack, C. J. (**2002**). (private communication).
Patterson, R. D. (**1976**). "Auditory filter shapes derived with noise stimuli," J. Acoust. Soc. Am. **59**, 640–654.
Patterson, R. D., and Henning, G. B. (**1977**). "Stimulus variability and auditory filter shape," J. Acoust. Soc. Am. **62**, 649–664.
Plack, C. J., and Oxenham, A. J. (**1998**). "Basilar-membrane nonlinearity and the growth of forward masking," J. Acoust. Soc. Am. **103**, 1598–1608.
Relkin, E. M., and Turner, C. W. (**1988**). "A reexamination of forward masking in the auditory nerve," J. Acoust. Soc. Am. **84**, 584–591.
Richards, V. M. (**2001**). "Varying feedback to evaluate detection strategies: The detection of a tone added to noise," J. Assoc. Res. Otolaryngol. **3**, 209–221.
Richards, V. M., and Nekrich, R. D. (**1993**). "The incorporation of level and level-invariant cues for the detection of a tone added to noise," J. Acoust. Soc. Am. **94**, 2560–2574.
Richards, V. M., and Zhu, S. (**1994**). "Relative estimates of combination weights, decision criteria, and internal noise based on correlation coefficients," J. Acoust. Soc. Am. **95**, 423–434.
Schairer, K. S., Nizami, L., Reimer, J. F., and Jesteadt, W. (**2003**). "Effects of peripheral nonlinearity on psychometric functions for forward-masked tones," J. Acoust. Soc. Am. **113**, 1560–1573.
Spiegel, M. F., and Green, D. M. (**1982**). "Signal and masker uncertainty with noise maskers of varying duration, bandwidth, and center frequency," J. Acoust. Soc. Am. **71**, 1204–1210.
Yates, G. K., Winter, I. M., and Robertson, D. (**1990**). "Basilar membrane nonlinearity determines auditory nerve rate-intensity functions and cochlear dynamic range," Hear. Res. **45**, 203–219.
Zhang, L. (**1995**). "Detection mechanisms for hearing signals in noise," Doctoral dissertation, Northeastern University.

Pitch discrimination of patterned electric stimulation[a)]

Hongbin Chen,[b)] Yumi Christine Ishihara, and Fan-Gang Zeng[c)]
Hearing and Speech Research Laboratory, Departments of Anatomy and Neurobiology, Biomedical Engineering, Cognitive Sciences and Otolaryngology—Head and Neck Surgery, University of California, Irvine, California 92697

(Received 24 January 2005; revised 21 April 2005; accepted 26 April 2005)

One reason for the poor pitch performance in current cochlear-implant users may be the highly synchronized neural firing in electric hearing that lacks stochastic properties of neural firing in normal acoustic hearing. This study used three different electric stimulation patterns, jittered, probabilistic, and auditory-model-generated pulses, to mimic some aspects of the normal neural firing pattern in acoustic hearing. Pitch discrimination was measured at standard frequencies of 100, 250, 500, and 1000 Hz on three Nucleus-24 cochlear-implant users. To test the utility of the autocorrelation pitch perception model in electric hearing, one, two, and four electrodes were stimulated independently with the same patterned electric stimulation. Results showed no improvement in performance with any experimental pattern compared to the fixed-rate control. Pitch discrimination was actually worsened with the jittered pattern at low frequencies (125 and 250 Hz) than that of the control, suggesting that externally introduced stochastic properties do not improve pitch perception in electric stimulation. The multiple-electrode stimulation did not improve performance but did not degrade performance either. The present results suggest that both "the right time and the right place" may be needed to restore normal pitch perception in cochlear-implant users. [DOI: 10.1121/1.1937228]

PACS number(s): 43.66.Hg, 43.66.Fe, 43.66.Ts [BLM] Pages: 338–345

I. INTRODUCTION

Pitch perception has been studied for more than 150 years but its underlying mechanisms still remain elusive (Ohm, 1843; Helmholtz, 1863). Two theories have been proposed based on temporal neural firing patterns (Wever, 1948; Siebert, 1970; Goldstein and Srulovicz, 1977) and the place of excitation in the cochlea (Zwicker, 1956; Henning, 1967). In the temporal theory, the pitch of a stimulus is determined by the interval between two adjacent neural firings. Strictly speaking, a pure temporal model is independent of the place of excitation in the cochlea. In the place theory, the pitch is determined by the place of excitation in the cochlea, although the exact meaning of the "place" is still debatable with the sharp apical edge, rather than the excitation peak, in the excitation pattern being a more likely code for the place pitch (Chatterjee and Zwislocki, 1997).

To account for pitch of complex stimuli, such as residual pitch and periodicity pitch (Ritsma, 1962; Schouten *et al.*, 1962; Ritsma, 1963), an autocorrelation model has been proposed, in which pitch is interpreted as the peak in the autocorrelation function of the neuron response to the stimuli (Licklider, 1951). In a recently extended model (Meddis and Hewitt, 1991), complex tones were passed through a bank of gammatone filters followed by a hair-cell simulator which converted the mechanical motion of the basilar membrane into spike trains propagated along the auditory nerve fiber. An autocorrelation function on the function (ACF) relating probability of neural firing to time was generated for each auditory nerve fiber. A summary autocorrelation function was generated by summing up the autocorrelation functions from these individual fibers. Pitch was determined by the largest peak in the summary autocorrelation function. The computational model of Meddis *et al.* has successfully predicted several of the classical pitch phenomena, such as the missing fundamental, ambiguous pitch, and inharmonicity.

Variations of the temporal model also exist. For example, several researchers proposed the "first-order" theory (Srulovicz and Goldstein, 1983; Kaernbach and Demany, 1998), suggesting that the auditory system is sensitive only to the first-order intervals, i.e., the interval between two adjacent spikes, between successive spikes in the neural firing. In a stream of neural firing with different intervals, pitch is derived from the longest first-order interval. Carlyon *et al.* (2002) provided evidence for an even stronger first-order model, in which only the interspike intervals contribute to the temporal pitch percept, with the longest first-order intervals receiving more weights than the short first-order intervals.

Based on these temporal pitch theories, the pitch strength ought to be more salient in electric hearing than acoustic hearing, because the neurophysiological studies have found that neural spikes are highly synchronized to electric stimuli (Kiang and Moxon, 1972; Hartmann *et al.*, 1984; Dynes and Delgutte, 1992; Litvak *et al.*, 2001). However, behavioral pitch discrimination data in electric hearing do not support this prediction. Compared to the sharp pitch discrimination in normal-hearing listeners who can detect 1% or less difference for frequencies up to 4000 Hz (Harris, 1952; Moore, 1973; Wier *et al.*, 1977; Nelson *et al.*, 1983),

[a)]Portions of this work were presented at the 2004 American Auditory Society annual meeting, Scottsdale, AZ, 7–9 March 2004.
[b)]Electronic mail: hchen@uci.edu
[c)]Electronic mail: fzeng@uci.edu

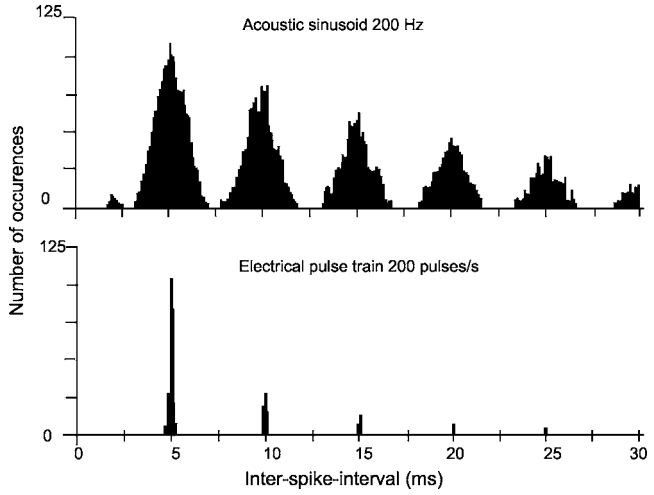

FIG. 1. The histogram of the interspike intervals for a single neuron fiber in response to a pure tone with frequency of 200 Hz (top panel) and a biphasic pulse train with stimulation rate of 200 pulses/s (reproduced from Javel).

cochlear-implant listeners can only detect 10%–25% differences for frequencies up to 500 Hz and typically cannot discriminate any pitch difference for frequencies higher than 500 Hz (Bilger, 1977; Eddington *et al.*, 1978; Shannon, 1983a; Carlyon *et al.*, 2002; Zeng, 2002; Chen and Zeng, 2004). The poor pitch discrimination is likely responsible for the cochlear-implant users' extreme difficulty in speech recognition in noise (Friesen *et al.*, 2001; Garnham *et al.*, 2002), music appreciation (Gfeller and Lansing, 1991; Gfeller *et al.*, 1997; Pijl, 1997; Kong *et al.*, 2004), and tonal language understanding (Wei *et al.*, 2004).

One apparent reason for poor pitch discrimination in cochlear implant users may be the lack of sharp frequency tuning in electric hearing. Neurophysiological data showed no tuning at all to electric stimulus frequency as long as the stimulus was delivered to the same pair of electrodes (Kiang and Moxon, 1972; Hartmann *et al.*, 1984). The place code can be only crudely reproduced or represented by a limited number of electrodes placed in different sites of the cochlea. More often than not, the number of independent electrodes is further reduced by electrical current filed interaction between electrodes (Shannon, 1983b; Fishman *et al.*, 1997).

The discrepancy between the temporal pitch model prediction and the behavioral data may be due to the significant difference in stochastic neural firing between acoustic and electric stimulation (Rose *et al.*, 1967; Javel *et al.*, 1987; van den Honert and Stypulkowski, 1987). Figure 1 shows the interspike-interval (ISI) histogram for neural responses to acoustic and electric stimuli. The top panel shows the ISI histogram for a single auditory nerve fiber in response to a pure tone at 200 Hz, while the bottom panel shows the ISI histogram in response to a biphasic pulse train at 200 pulses/s. There is clearly greater variability in neural firing in response to acoustic stimulation than electric stimulation. First, at the stimulus period (5 ms) and its multiples, the neural firing has much greater standard deviation in acoustic hearing than in electric hearing. Second, the neural firing occurs randomly at many more modes (the stimulus period and its multiples) in acoustic stimulation than electric stimulation.

Restoring similar stochastic responses in electric stimulation may enhance the pitch extraction process and signal detection at threshold level in cochlear implants (Morse and Evans, 1999; Rubinstein *et al.*, 1999; Zeng *et al.*, 2000). This has been investigated by using high-rate (>2000 Hz) stimulation and adding white noise to a fixed-rate stimulus, while another possible way to introduce stochastic resonance is to temporally modulate pulse trains by a stochastic function. As it is also shown in the auditory model, pitch extraction is an analysis not only "within-channel" but also "between-channel." In the model, if each channel is independent, ACF from different channels will have the same peaks at the period of the stimuli and small peaks at different delay because of the noise. In the summary ACF, the significance of common peaks is the same as that from one channel, but other peaks are smaller because of the process of averaging. Therefore, the model predicts better performance with multiple channels if each channel is independent but has a similar pulse pattern. It is unknown whether this temporal information from different channels could be utilized for high-level pitch extraction in electric hearing.

The main questions addressed in this study were: (1) To what extent do we have to reproduce the normal temporal discharge patterns in electric stimulation to improve cochlear implant pitch discrimination? (2) Can multiple-electrode stimulation improve the performance as predicted by the autocorrelation model? (3) Does the site of stimulation matter in electric pitch discrimination? To answer the first question, we designed three types of novel electric stimulus patterns, including jittered pulses, probabilistic pulses, and auditory-model-generated pulses, which mimic either one or several aspects of the ISI pattern in response to a sinusoid in acoustic stimulation. To answer the second question, we tested pitch discrimination using single- and multiple-electrode stimulation. To answer the third question, we used different spacing between stimulating electrodes in the multiple-electrode condition. To the best of our knowledge, none of the experimental conditions have been reported in the literature.

II. METHODS

A. Subjects

One male and two female adults (S1–S3) who were postlingually deafened and implanted with Nucleus-24 devices took part in this study. The subjects ranged in age from 70 to 79 years with a mean age of 73 years and were all native speakers of American English. All of the subjects had extensive psychophysical test experience and were compensated for their participation in the study. Local IRB approval and informed consent were obtained prior to the experiments. Table I lists the detailed information of the subjects. Vowel stimuli were taken from materials recorded by (Hillenbrand *et al.*, 1995) and consonant stimuli were taken from materials created by (Turner *et al.*, 1992). The stimuli were presented to cochlear implant listeners with custom software (Robert, 1997).

TABLE I. Subject information of the three Nucleus-24 cochlear-implant users who participated in this study.

Subject	Gender	Age (yr)	Cause of deafness	Duration of implant use (yr)	Vowel recognition	Consonant recognition
S1	F	71	Fever	4	51%	54%
S2	M	79	Unknown	2	38%	51%
S3	F	70	Virus	7	64%	70%

B. Stimuli

Three pulse trains with different temporal patterns were used in this study to mimic one or more aspects of the stochastic neural firing in acoustic stimulation. As an example with the 1000 Hz standard frequency, Fig. 2 shows the constructed ISI histograms and the first 20 ms of these three pulse trains.

1. Jittered pulses

In the jittered pulses, the interpulse interval followed a Gaussian distribution with a mean at the standard frequency and a standard deviation of d. In the present experiment, d was set at 0.0, 0.1, 0.2, or 0.3. When $d=0$, the jitters were removed to produce the traditional fixed-rate pulse train. We noted that Dobie and Dillier (1985) conducted jitter discrimination on two Ineraid cochlear-implant users and found a detection threshold of about 10% at the stimulation rate of 1000 Hz. No pitch discrimination of the jittered pulses has been reported. The standard deviation was set at 0.3 in Fig. 2. As can be seen from the ISI histogram in Fig. 2, the jittered pulses produced a random distribution at the first mode (i.e., the period) that was similar to the normally produced ISI pattern in acoustic stimulation (Fig. 1).

2. Probabilistic pulses

In the probabilistic pulses, the occurrence of a pulse in the pulse train was determined by a probability p. When $p=1$, the probabilistic pulses were equivalent to a fixed-rate pulse train. When p was less than 1, the total number of pulses in the probabilistic pulses equaled the number of pulses in the fixed-rate pulse train $\times p$. The interval between two consecutive pulses was multiples of the period in the fixed-rate train. In the present study, the value of p was set at 1, 0.8, 0.5, or 0.3 (the value of 0.3 was used in Fig. 2). The probabilistic pulses produced multiple modes but no jitters in the ISI histogram (middle panel in Fig. 2).

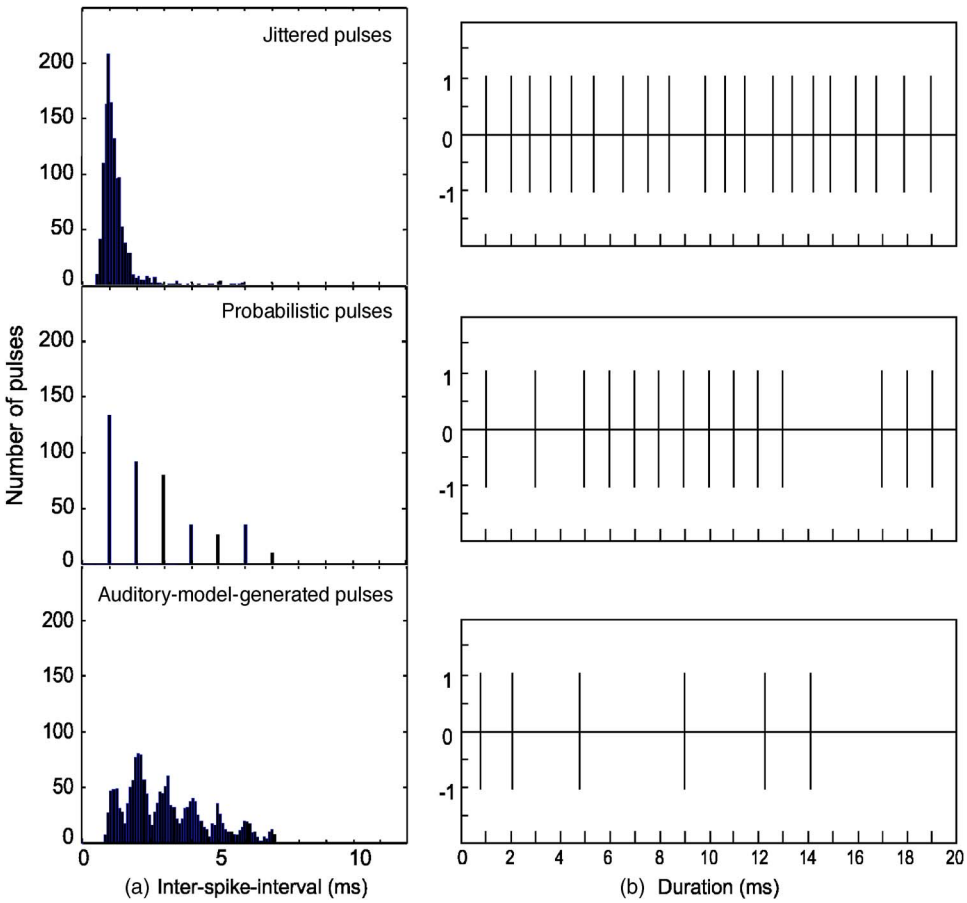

FIG. 2. (a) The interspike-interval histograms for three different types of stimuli: jittered pulses, probabilistic pulses, and auditory-model-generated pulses (from top to bottom). (b) The pulse trains for the three different types of stimuli. Only the first 20 ms of the pulse trains are shown here.

3. Auditory-model-generated pulses

The pulses were generated by Meddis's auditory model, which incorporated a basilar membrane model (DRNL) (Lopez-Poveda and Meddis, 2001), gammatone filters, an inner hair cell model (Meddis, 1986), and an auditory nerve model (Carney, 1993). A C++ implementation of the auditory model was provided by Meddis and his colleagues and implemented on a PC as DSAM libraries. Default values were used for all parameters in the model. Twenty auditory nerve fibers were selected to have characteristic frequencies (CF) ranging from 20 to 10000 Hz. The output of each fiber in response to a sinusoid of a standard frequency was used to define a pulse train in electric hearing. The bottom panel of Fig. 2 shows an auditory nerve fiber's (CF=1000 Hz) ISI response to a 1000 Hz sinusoid.

The present pitch discrimination test used standard frequencies of 100, 250, 500, and 1000 Hz. Stimuli were presented to one, two, or four active electrodes, respectively. When one electrode was presented, the selected electrode had a CF that was based on the Greenwood map (Greenwood, 1990) and was presumably equal to the stimulus's standard frequency. When multiple electrodes were presented, the most apical electrode was the same as in the single-electrode case, while the remaining electrodes were selected based on zero-, one-, or two-electrode separation. For example, the electrode pair selected for single electrode condition at the 1000 Hz standard frequency was [12,14]. In the two-electrode condition, the two electrode pairs were [12,14] and [13,15] with zero separation, [12,14] and [14,16] with one-electrode separation, and [12,14] and [15,17] with two-electrode separation.

Each pulse was converted into a biphasic pulse (negative pulse first followed by a short gap and a positive pulse) in electric stimulation with a total duration of 500 ms, a per-phase duration of 50 μs, and a phase separation of 5 μs. Bipolar (BP+1) configuration mode was always used, resulting in a 1.5 mm spacing between two intracochlear electrodes. In multiple-electrode stimulation, the biphasic pulses were interleaved between electrodes with a delay of 10 μs toward apex. The electric stimuli were delivered to the subject and controlled via a customized research interface[1] (Shannon *et al.*, 1990).

C. Procedures

The dynamic range for each selected electrode was measured individually using jittered pulses with $d=0.2$, probabilistic pulses with $p=0.8$, and auditory-model-generated pulses, respectively, at all standard frequencies. The threshold (THR) was the level that the stimuli were just perceptible for subjects. The most comfortable level (MCL), defined as 65%–70% of the maximum loudness level that subjects could tolerate, was employed as the stimulus level. For multiple-electrode stimulation, the dynamic range of each electrode was measured first and the MCL of the stimulation with all electrodes was obtained by proportionally increasing the amplitude of each electrode based on its dynamic range. For example, in the condition of two electrodes, the dynamic ranges for electrode 20 (THR=45 dB) and electrode 18 (THR=50 dB) were 10 and 5 dB, respectively. To measure the MCL of the stimulation with these two electrodes, subjects first received threshold stimulation on the both electrodes, 18 and 20. And then the amplitude of each electrode was increased by a certain percentage (10%) of the dynamic range (2 dB on electrode 20 and 1 dB on electrode 18) until the MCL was reached. A loudness balance procedure was used to balance all stimuli before the test. To further discourage the use of the loudness cue, the amplitude of each interval was roved by a value that was uniformly distributed between −1 and 0 dB (see Chen and Zeng, 2004) so that the levels of all three stimuli in each trial were randomized 1 dB lower than their MCLs. Finally, the stochastic nature of these pulses produced additional uncertainties in terms of the total number of the pulses and the interpulse duration, making the use of the loudness cue highly unlikely. The only exception was for the auditory-model-generated pulses, whose number would decrease when the signal frequency was increased to be greater than the electrode's CF. This was because the neural activities gradually shifted to the next adjacent channel in the model when signal frequency approached the center frequency of the next channel. If this were the case, subjects would recognize the signal by picking the relatively softer sound. However, because of the amplitude roving, the loudness might be a cue only if the frequency of the signal was much higher than the standard frequency and it would not necessarily affect the result of the experiment.

Pitch discrimination was measured using a three-interval, forced-choice, adaptive procedure. In each trial, a subject heard 3 sounds, including two sounds with the standard frequency and a signal with higher frequency. The order of presentation was randomized. The subject was asked to identify the interval with the highest pitch by pressing a button on the computer monitor. Graphical feedback was given after each trial. A two-down, one-up decision rule was employed to track the 70.7% correct point on the psychometric function. To complete each run, the subject had to incur either 13 reversals or 60 trials with at least 8 reversals. The step size was about 25% of the standard frequency for the first 4 reversals and reduced to 3%–5% after that. All subjects completed 3 successful runs with an average standard deviation of about 50% of the mean value.

III. RESULTS

A. Jittered pulses

Figure 3 shows the individual data (panels) in pitch discrimination of jittered pulses in terms of the difference limen (Hz) as a function of the standard deviation at four standard frequencies (100, 250, 500, and 1000 Hz). Each data point is the mean of three trials and the error bar represents the standard deviation of the mean. Had the jitters helped pitch discrimination performance, a negative-sloping curve would be expected in the data. Except for the 250 Hz condition in S3 where the difference limen decreased with the standard deviation, there was no evidence supporting the idea that adding jitters improved pitch discrimination. The jitter degraded the performance at the 100 Hz standard frequency while producing no effects on performance at high frequencies

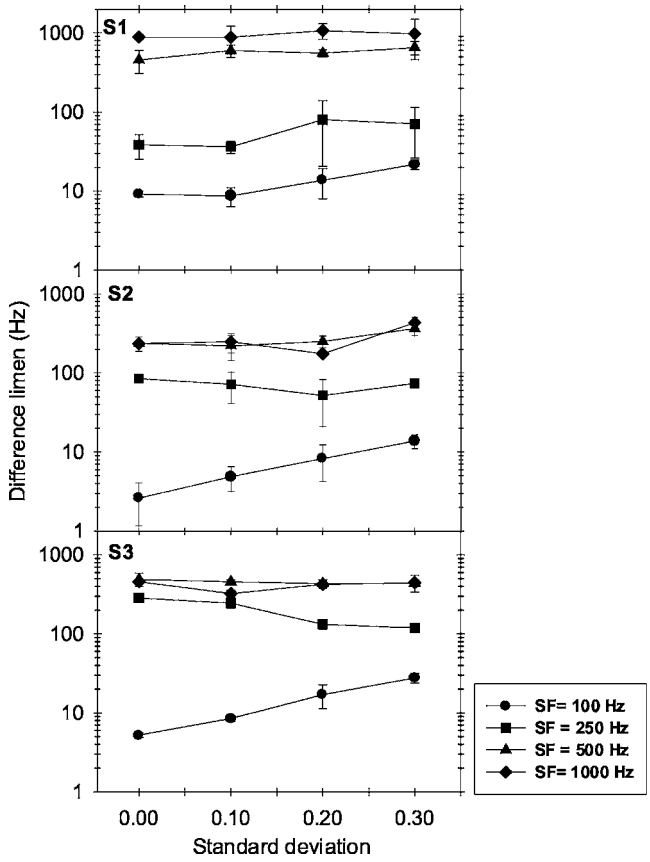

FIG. 3. Individual data (panels) in pitch discrimination of jittered pulses in terms of the difference limen (Hz) as a function of the standard deviation at four standard frequencies (100, 250, 500 and 1000 Hz). Each data point is the mean of three trials and the error bars show the standard deviation of these trials.

(>250 Hz). A within-subjects ANOVA supported these observations by revealing a significant effect of the standard frequency $[F(3,6)=5.9, p<0.05]$, with a significant effect of the standard deviation at only the 100 Hz standard frequency $[F(3,6)=5.9, p<0.05]$.

Figure 4 shows the average pitch discrimination data for jittered pulses as a function of the number of active electrodes at four standard frequencies (panels). Since the electrode spacing produced no significant effect in either the two-electrode condition $[F(2,4)=3.3, p>0.05]$ or the four-electrode condition $[F(1,2)=6.9, p>0.05]$, pitch discrimination data were averaged across the different electrode spacing conditions for presentation and analysis. Different symbols represent pitch discrimination with the standard deviation of 0.0, 0.1, 0.2, and 0.3, respectively. With a 0.0 standard deviation (open circles), the jittered pulses were the same as the traditionally used fixed-rate pulses. The one-electrode data were the same as plotted in Fig. 3. Three important points can be noted in this figure. First, there was no effect of the number of electrodes on pitch discrimination because the overall pattern of the data was essentially flat. Second, pitch discrimination in terms of the difference limen increased with standard frequencies, noting the ascending trend in difference limens from left to right panels. Third, consistent with the single-electrode data, jitters degraded the performance only at the 100 Hz frequency. A three-way (standard frequency $\times$ electrode number $\times$ standard deviation) repeated-measures ANOVA showed a significant effect of the standard frequency $[F(3,6)=167.1, p<0.01]$. Although the standard deviation was not a significant factor in the three-way ANOVA due to the overwhelmingly large variability caused by the standard frequency, a two-way ANOVA showed a significant effect of standard deviation only at the 100 Hz standard frequency $[F(3,6)=23.9, p<0.01]$.

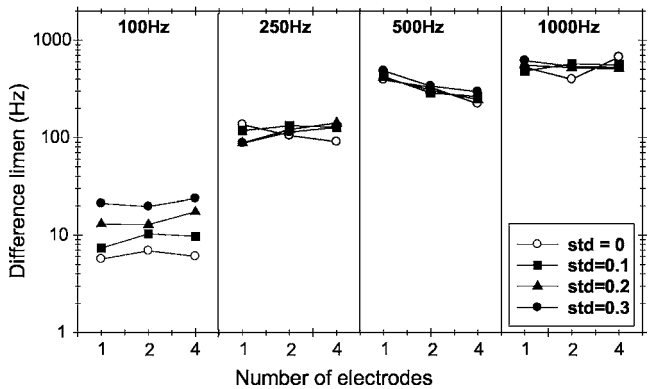

FIG. 4. The average pitch discrimination data for jittered pulses as a function of the number of active electrodes at four standard frequencies (panels). In each panel, different symbols represent pitch discrimination in difference limens with standard deviation of 0, 0.1, 0.2, and 0.3.

B. Probabilistic pulses

Figure 5 shows individual pitch discrimination data for probabilistic pulses as a function of pulse probability. Different symbols represent the data at standard frequencies of 100, 250, 500, and 1000 Hz. No improvement in pitch discrimination was observed in any of the three subjects. The general trend was similar to the data obtained with the fixed-rate stimuli. Difference limen increased with the standard frequency and was nearly independent of the probability except for the 100 Hz standard frequency. A within-subjects ANOVA revealed that the standard frequency produced a significant effect $[F(3,6)=12.0, p<0.01]$, and that the probabilistic pulses significantly increased the difference limen only at the 100 Hz standard frequency $[F(3,6)=12.5, p<0.01]$.

Figure 6 shows the average pitch discrimination data for probabilistic pulses as a function of the number of active electrodes at four standard frequencies (panels). Since the electrode spacing produced no significant effect in either the two-electrode condition $[F(2,4)=4.4, p>0.05]$ or the four-electrode condition $[F(1,2)=0.01, p>0.05]$, pitch discrimination data were averaged across the different electrode spacing conditions for presentation and analysis. Open circles denote the pitch discrimination for $p=1$, at which the probabilistic-pulse train was the same as the fixed-rate pulse train. Similar to the three trends in the jittered pulse experiment, the difference limen for the probabilistic pulses was independent of the number of electrodes $[F(2,4)=2.4, p>0.05]$, increased with the standard frequency $[F(3,6)=19.1, p<0.05]$, and decreased with the probability only at the 100 Hz standard frequency $[F(3,6)=32.8, p<0.01]$.

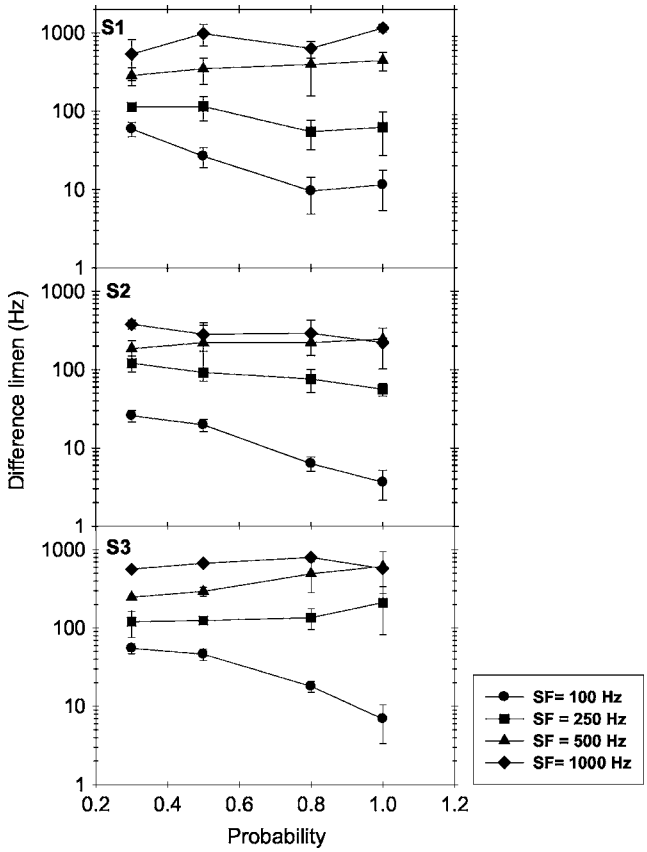

FIG. 5. Individual data (panels) in pitch discrimination of probabilistic pulses in terms of the difference limen (Hz) as a function of the pulse probability at four standard frequencies (100, 250, 500, and 1000 Hz). Each data point is the mean of three trials and the error bars show the standard deviation of these trials.

C. Auditory-model-generated pulses

Figure 7 shows the average pitch discrimination data for the auditory-model-generated pulses (closed symbols connected by the solid line) and the fixed-rate pulses (open circles connected by the dashed line) as a function of the number of active electrodes at four standard frequencies (panels). Since the electrode spacing produced no significant effect in either the two-electrode condition $[F(2,4)=0.001, p>0.05]$ or the four-electrode condition $[F(1,2)=11.3, p>0.05]$, pitch discrimination data were averaged across the different electrode spacing conditions for presentation and analysis. Similar to the trends in the jittered and probabilistic pulse experiments, the difference limen for the auditory-model-generated was independent of the number of electrodes $[F(2,4)=0.38, p>0.05]$ and increased with the standard frequency $[F(3,6)=18.5, p<0.01]$. In addition, the auditory-model-generated pulses produced significantly poorer performance than the fixed-rate pulses across the number of electrodes and standard frequencies $[F(1,2)=32.1, p<0.01]$.

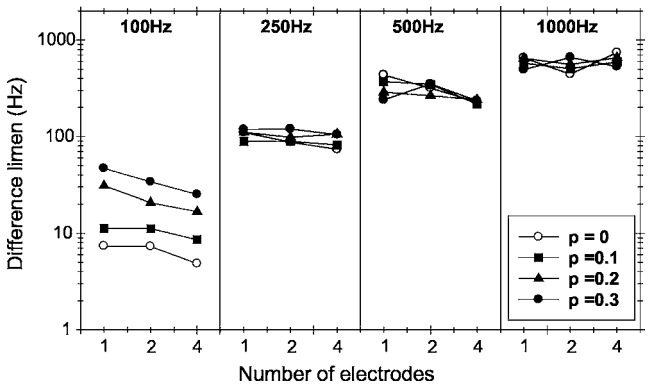

FIG. 6. The average pitch discrimination data for probabilistic pulses as a function of the number of active electrodes at four standard frequencies (panels). In each panel, different symbols represent pitch discrimination in difference limens with probability of 1, 0.8, 0.5, and 0.3.

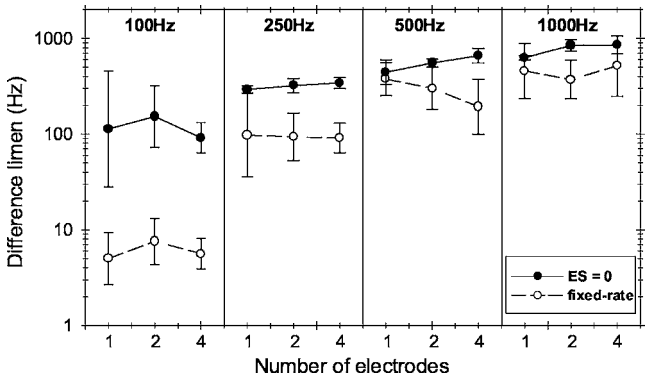

FIG. 7. The average pitch discrimination data auditory-model-generated pulses (closed symbols connected by the solid line) and the fixed-rate pulses (open circles connected by the dashed line) as a function of the number of active electrodes at four standard frequencies (panels). Data were averaged across three subjects and different electrode spacing. The error bars show the standard deviation of the three subjects.

IV. DISCUSSION

A. Temporal patterns

The most important finding in the present study was that none of the three types of stochastic pulses produced better performance in pitch discrimination than the traditional fixed-rate pulses. To the extent that the ISI histogram reflects the normal temporal firing properties, the auditory-model-generated pulses best represent the normal neural temporal response. However, the present result shows worst performance with the auditory-model-generated pulses, especially at low standard frequencies. As mentioned in Sec. II B, if loudness were an effective cue in the present experiment, we would expect better performance with the auditory-model-generated pulses. The present result was not consistent with the potential use of loudness cue in pitch discrimination.

It is difficult to explain why the auditory-model-general pulses produced the worst performance. In acoustic stimulation, not only is the spike activity stochastic in single auditory nerve fibers but also the activities across different fibers are stochastic and independent (Johnson and Kiang, 1976). The brain may need to compare statistically independent temporal firing patterns between fibers to produce optimal performance. These statistically independent across-fiber spike activities are difficult to achieve with current cochlear implant technology.

The randomness introduced by the present methods did not affect performance at high standard frequencies (>250 Hz) but significantly degraded performance at the

100 Hz standard frequency range. The present result indicates that an accurate temporal cue is essential for pitch discrimination at low frequencies in electric hearing with current cochlear implant technology. Disruption of this temporal cue by introducing randomness to either the period in jittered pulses or the first-order interval in probabilistic pulses will degrade pitch discrimination at low frequencies. At high frequencies, the neuronal membrane and central circuitry will likely produce stochastic response, thus adding randomness in the stimulus will less likely affect pitch discrimination at these high frequencies.

B. Autocorrelation models

According to the autocorrelation theory, pitch information extracted from multiple channels should be more salient than that from a single channel if each channel is independent but contains the same information. Furthermore, pitch perception for multiple channels should be robust in the presence of jitters, because these jitters would likely be averaged out in the process of the summarizing between channels. However, the present result showed that neither multiple-electrode stimulation nor electrode spacing produced any significant difference in pitch discrimination compared with single-electrode stimulation. This result was inconsistent with the autocorrelation theory's prediction.

There are three possible reasons that could explain the failure of improvement of pitch in cochlear implant users using auditory models. The first reason is that current cochlear implants do not provide the critical number of independent channels for this autocorrelation model to aggregate and then extract adequate pitch information. The second possible reason is that pitch requires that not only the proper temporal information be present in each channel, but also this temporal information come from the proper place (Miller and Sachs, 1984; Shamma, 1985b; Oxenham *et al.* 2004). While it is relatively difficult to differentiate these models in acoustic hearing because of the tightly coupled temporal-place information, modern cochlear implants provide ample opportunities to explore and test these working hypotheses. The third plausible class of explanation comes from the lack of consistent timing differences between channels, as proposed by Loeb *et al.* (1983) and by Shamma (1985a). For the simplicity of the implementation, the present study used 10 μs fixed delay between channels disregarding the electrode and electrode spacing. The future implementation of the model should take this into account and a variable time delay depending on the location of the stimulation could be used.

C. Practical considerations

Current speech strategies in most cochlear implants deliver electric stimulation by temporally amplitude-modulating a fixed-rate pulse train, disregarding the fine structure information. Pitch information, in these strategies, is coded by either the modulation frequency in the time domain or the location of the stimulation in the "place" domain. Unfortunately, neither delivers a salient pitch percept as evidenced by the poor pitch discrimination via stimulation rate only (Bilger, 1977; Eddington *et al.* 1978; Shannon, 1983a; Carlyon *et al.* 2002; Zeng *et al.* 2002; Chen and Zeng, 2004) or electrode position only, due to electrode interaction (Shannon, 1983b; Fishman *et al.* 1997) and frequency-to-electrode mismatch (Townshend *et al.*, 1987). In a normal auditory system, pitch information is encoded by both place and temporal cues. The failure to improve pitch perception by stochastic pulses suggests that to restore normal pitch perception in cochlear implants, future processing strategies may need to take both place and temporal cues into account.

V. CONCLUSIONS

Three stochastic temporal patterns were used to frequency modulate a fixed-rate pulse train in an attempt to improve pitch perception in cochlear-implant users. The three temporal patterns simulated one or several aspects of the stochastic temporal firing pattern observed in a normal auditory nerve fiber in response to a pure-tone stimulus in acoustic hearing. Perceptual results showed that, compared with the traditional fixed-rate pulse train stimulation, the three stochastic temporal patterns did not improve pitch discrimination in electric hearing but actually degraded performance at low frequencies ($<$250 Hz). Neither multiple-electrode stimulation nor electrode spacing significantly affected pitch discrimination in cochlear implants, suggesting that a strict version of the autocorrelation model for pitch perception needs to be required, and additionally, that the absolute place information may need to be taken into account to restore normal pitch perception in cochlear implant users.

ACKNOWLEDGMENTS

We thank our cochlear-implant subjects for their time and dedication. We also thank Dr. Ray Meddis and Dr. Lowel O'Mard for providing the code of DSAM and technical assistance during the implementation of the auditory-model in the HEINRI system. Thanks also to the associate editor Brenda Lonsbury-Martin for her very helpful comments on the manuscript. This work was partially supported by a NIH Grant No. 2R01DC02267.

[1]J. Wygonski and M. E. Robert, "HEI Nucleus research interface specification," House Ear Institute (2001).

Bilger, R. C. (**1977**). "Psychoacoustic evaluation of present prostheses," Ann. Otol. Rhinol. Laryngol. Suppl. **86**, 92–140.

Carlyon, R. P., van Wieringen, A., Long, C. J., Deeks, J. M., and Wouters, J. (**2002**). "Temporal pitch mechanisms in acoustic and electric hearing," J. Acoust. Soc. Am. **112**, 621–633.

Carney, L. H. (**1993**). "A model for the responses of low-frequency auditory-nerve fibers in cat," J. Acoust. Soc. Am. **93**, 401–417.

Chatterjee, M. and Zwislocki, J. J. (**1997**). "Cochlear mechanisms of frequency and intensity coding. I. The place code for pitch," Hear. Res. **111**, 65–75.

Chen, H. and Zeng, F.-G. (**2004**). "Frequency modulation detection in cochlear implant subjects," J. Acoust. Soc. Am. **116**, 2269–2277.

Dobie, R. A. and Dillier, N. (**1985**). "Some aspects of temporal coding for single-channel electrical stimulation of the cochlea," Hear. Res. **18**, 41–55.

Dynes, S. B. and Delgutte, B. (**1992**). "Phase-locking of auditory-nerve discharges to sinusoidal electric stimulation of the cochlea," Hear. Res. **58**, 79–90.

Eddington, D. K., Dobelle, W. H., Brackmann, D. E., Mladejovsky, M. G., and Parkin, J. L. (**1978**). "Auditory prostheses research with multiple channel intracochlear stimulation in man," Ann. Otol. Rhinol. Laryngol. **87**, 1–39.

Fishman, K. E., Shannon, R. V., and Slattery, W. H. (**1997**). "Speech recognition as a function of the number of electrodes used in the SPEAK cochlear implant speech processor," J. Speech Lang. Hear. Res. **40**, 1201–1215.

Friesen, L. M., Shannon, R. V., Baskent, D., and Wang, X. (**2001**). "Speech recognition in noise as a function of the number of spectral channels: Comparison of acoustic hearing and cochlear implants," J. Acoust. Soc. Am. **110**, 1150–1163.

Garnham, C., O'Driscoll, M., Ramsden R., and Saeed, S. (**2002**). "Speech understanding in noise with a Med-El COMBI 40+ cochlear implant using reduced channel sets," Ear Hear. **23**, 540–552.

Gfeller, K. and Lansing, C. R. (**1991**). "Melodic, rhythmic, and timbral perception of adult cochlear implant users," J. Speech Hear. Res. **34**, 916–920.

Gfeller, K., Woodworth, G., Robin, D. A., Witt, S., and Knutson, J. F. (**1997**). "Perception of rhythmic and sequential pitch patterns by normally hearing adults and adult cochlear implant users," Ear Hear. **18**, 252–260.

Goldstein, J. L. and Srulovicz, P. (**1977**). "Auditory-nerve spike intervals as an adequate basis for aural frequency measurement," in *Psychophysics and Physiology of Hearing*, edited by E. F. Evans and J. P. Wilson (Academic, London), pp. 337–347.

Greenwood, D. D. (**1990**). "A cochlear frequency-position function for several species—29 years later," J. Acoust. Soc. Am. **87**, 2592–2605.

Harris, J. D. (**1952**). "Pitch discrimination," J. Acoust. Soc. Am. **24**, 750–755.

Hartmann, R., Topp, G., and Klinke, R. (**1984**). "Discharge patterns of cat primary auditory fibers with electrical stimulation of the cochlea," Hear. Res. **13**, 47–62.

Helmholtz, H. L. F. (**1863**). "Die lehre von den tonempfindungen als physiologische grundlage fur die theorie der musik," in *On the Sensations of Tone as a Physiological Basis for the Theory of Music* (Dover, New York).

Henning, G. B. (**1967**). "A model for auditory discrimination and detection," J. Acoust. Soc. Am. **42**, 1325–1334.

Hillenbrand, J., Getty, L. A., Clark, M. J., and Wheeler, K. (**1995**). "Acoustic characteristics of American English vowels," J. Acoust. Soc. Am. **97**, 3099–3111.

Javel, E., Tong, Y. C., Shepherd, R. K., and Clark, G. M. (**1987**). "Responses of cat auditory nerve fibers to biphasic electrical current pulses," Ann. Otol. Rhinol. Laryngol. Suppl. **128**, 26–30.

Johnson, D. H. and Kiang, N. Y. (**1976**). "Analysis of discharges recorded simultaneously from pairs of auditory nerve fibers," Biophys. J. **16**, 719–734.

Kaernbach, C. and Demany, L. (**1998**). "Psychophysical evidence against the autocorrelation theory of auditory temporal processing," J. Acoust. Soc. Am. **104**, 2298–306.

Kiang, N. Y. and Moxon, E. C. (**1972**). "Physiological considerations in artificial stimulation of the inner ear," Ann. Otol. Rhinol. Laryngol. **81**, 714–730.

Kong, Y. Y., Cruz, R., Jones, J. A., and Zeng, F. G. (**2004**). "Music perception with temporal cues in acoustic and electric hearing," Ear Hear. **25**, 173–185.

Licklider, J. C. (**1951**). "A duplex theory of pitch perception," Experientia **7**, 128–134.

Litvak, L., Delgutte, B., and Eddington, D. (**2001**). "Auditory nerve fiber responses to electric stimulation: Modulated and unmodulated pulse trains," J. Acoust. Soc. Am. **110**, 368–379.

Loeb, G. E., White, M. W., and Jenkins, W. M. (**1983**). "Biophysical considerations in electrical stimulation of the auditory nervous system," Ann. N.Y. Acad. Sci. **405**, 123–136.

Lopez-Poveda, E. A. and Meddis, R. (**2001**). "A human nonlinear cochlear filterbank," J. Acoust. Soc. Am. **110**, 3107–3118.

Meddis, R. (**1986**). "Simulation of mechanical to neural transduction in the auditory receptor," J. Acoust. Soc. Am. **79**, 702–711.

Meddis, R. and Hewitt, M. (**1991**). "Virtual pitch and phase sensitivity studied using a computer model of the auditory periphery: Pitch identification," J. Acoust. Soc. Am. **89**, 2866–2882.

Miller, M. I. and Sachs, M. B. (**1984**). "Representation of voice pitch in discharge patterns of auditory-nerve fibers," Hear. Res. **14**, 257–279.

Moore, B. C. (**1973**). "Frequency difference limens for short-duration tones," J. Acoust. Soc. Am. **54**, 610–619.

Morse, R. P. and Evans, E. F. (**1999**). "Additive noise can enhance temporal coding in a computational model of analogue cochlear implant stimulation," Hear. Res. **133**, 107–119.

Nelson, D. A., Stanton, M. E., and Freyman, R. L. (**1983**). "A general equation describing frequency discrimination as a function of frequency and sensation level," J. Acoust. Soc. Am. **73**, 2117–2123.

Ohm, G. S. (**1843**). "Uber die definition des tones, nebst daran geknufter theorie der sirene and ahnlicher tonbildender vorichtungen," Ann. Phys. Chem. **59**, 513–565.

Oxenham, A. J., Bernstein, J. G. W., and Penagos, H. (**2004**). "Correct tonotopic representation is necessary for complex pitch perception," Proc. Natl. Acad. Sci. U.S.A. **101**, 1421–1425.

Pijl, S. (**1997**). "Labeling of musical interval size by cochlear implant patients and normally hearing subjects," Ear Hear. **18**, 364–372.

Ritsma, R. J. (**1962**). "Existence region of the tonal residue. I," J. Acoust. Soc. Am. **34**, 1224–1229.

Ritsma, R. J. (**1963**). "Existence region of the tonal residue. II," J. Acoust. Soc. Am. **35**, 1241–1245.

Robert, M. E. (**1997**). "AIPSS-ID—Phoneme identification software," House Ear Institute, Los Angeles.

Rose, J. E., Brugge, J. F., Anderson, D. J., and Hind, J. E. (**1967**). "Phase-locked response to low-frequency tones in single auditory nerve fibers of the squirrel monkey," J. Neurophysiol. **30**, 769–793.

Rubinstein, J. T., Wilson, B. S., Finley, C. C., and Abbas, P. J. (**1999**). "Pseudospontaneous activity: Stochastic independence of auditory nerve fibers with electrical stimulation," Hear. Res. **127**, 108–118.

Schouten, J. F., Ritsma, R. J., and Cardozo, B. L. (**1962**). "Pitch of the residue," J. Acoust. Soc. Am. **34**, 1418–1424.

Shamma, S. A. (**1985a**). "Speech processing in the auditory system. I. The representation of speech sounds in the responses of the auditory nerve," J. Acoust. Soc. Am. **78**, 1612–1621.

Shamma, S. A. (**1985b**). "Speech processing in the auditory system. II. Lateral inhibition and the central processing of speech evoked activity in the auditory nerve," J. Acoust. Soc. Am. **78**, 1622–1632.

Shannon, R. V. (**1983a**). "Multichannel electrical stimulation of the auditory nerve in man. I. Basic psychophysics," Hear. Res. **11**, 157–189.

Shannon, R. V. (**1983b**). "Multichannel electrical stimulation of the auditory nerve in man. II. Channel interaction," Hear. Res. **12**, 1–16.

Shannon, R. V., Adams, D. D., Ferrel, R. L., Palumbo, R. L., and Grandgenett, M. (**1990**). "A computer interface for psychophysical and speech research with the Nucleus cochlear implant," J. Acoust. Soc. Am. **87**, 905–907.

Siebert, W. M. (**1970**). "Frequency discrimination in the auditory system: Place or periodicity mechanisms," Proc. IEEE **58**, 723–730.

Srulovicz, P. and Goldstein, J. L. (**1983**). "A central spectrum model: A synthesis of auditory-nerve timing and place cues in monaural communication of frequency spectrum," J. Acoust. Soc. Am. **73**, 1266–1276.

Townshend, B., Cotter, N., Van Compernolle, D., and White, R. L. (**1987**). "Pitch perception by cochlear implant subjects," J. Acoust. Soc. Am. **82**, 106–115.

Turner, C. W., Fabry, D. A., Barrett, S., and Horwitz, A. R. (**1992**). "Detection and recognition of stop consonants by normal-hearing and hearing-impaired listeners," J. Speech Hear. Res. **35**, 942–949.

van den Honert, C. and Stypulkowski, P. H. (**1987**). "Temporal response patterns of single auditory nerve fibers elicited by periodic electrical stimuli," Hear. Res. **29**, 207–222.

Wei, C. G., Cao, K., and Zeng, F. G. (**2004**). "Mandarin tone recognition in cochlear-implant subjects," Hear. Res. **197**, 87–95.

Wever, E. G. (1948). "Theory of Hearing," in (Wiley, New York).

Wier, C. C., Jesteadt, W., and Green, D. M. (**1977**). "Frequency discrimination as a function of frequency and sensation level," J. Acoust. Soc. Am. **61**, 178–184.

Zeng, F.-G. (**2002**). "Temporal pitch in electric hearing," Hear. Res. **174**, 101–106.

Zeng, F.-G., Fu, Q. J., and Morse, R. (**2000**). "Human hearing enhanced by noise," Brain Res. **869**, 251–255.

Zeng, F.-G., Grant, G., Niparko, J., Galvin, J. J., Shannon, R. V., Opie, J., and Segel, P. (**2002**). "Speech dynamic range and its effects on cochlear implant performance," J. Acoust. Soc. Am. **111**, 377–386.

Zwicker, E. (**1956**). "Die elementaren grundlagen zur bestimmung der informationskapazitat des gehors," Acustica **6**, 356–381.

Discrimination of interaural phase differences in the envelopes of sinusoidally amplitude-modulated 4-kHz tones as a function of modulation depth

Mark A. Stellmack,[a] Neal F. Viemeister, and Andrew J. Byrne
Department of Psychology, University of Minnesota, Minneapolis, Minnesota 55455

(Received 29 December 2004; revised 6 April 2005; accepted 7 April 2005)

Psychometric functions were measured for the discrimination of the interaural phase difference (IPD) of the envelope of a sinusoidally amplitude-modulated (SAM) 4-kHz pure tone for modulation frequencies of 128 and 300 Hz and modulation depths (m) of 0.2, 0.6, 0.9, and 1.0. Contrary to recent modeling assumptions, it was found that a constant change in normalized interaural envelope correlation, with or without additional model stages to simulate peripheral auditory processing, did not produce a constant level of performance. Rather, in some cases, performance could range from chance to near perfect across modulation depths for a given change in normalized interaural envelope correlation. This was also true for the maximum change in normalized interaural envelope correlation computed across the cross-correlation functions for the stimuli to be discriminated. The change in the interaural time difference (ITD) computed from the IPD accounted for discriminability across modulation depths better than the change in normalized interaural envelope correlation, although ITD could not account for all the data, particularly those for lower values of m. © *2005 Acoustical Society of America.* [DOI: 10.1121/1.1923370]

PACS number(s): 43.66.Pn [AK] Pages: 346–352

I. INTRODUCTION

A. Correlation-based models of interaural envelope phase discrimination

Although human listeners are insensitive to interaural delays of high-frequency pure tones, listeners can lateralize an amplitude-modulated high-frequency tone on the basis of interaural delays of the envelope (e.g., Henning, 1974; Nuetzel and Hafter, 1976, 1981). Sensitivity to interaural delays is often modeled in terms of interaural-delay-based coincidence detection that presumably takes place at a level of auditory processing at which binaural interaction occurs (e.g., Jeffress, 1948; Stern and Colburn, 1978). When applied to lateralization of the envelope of a high-frequency carrier, these models presume that the auditory system extracts and encodes the relatively slow envelope fluctuations permitting binaural coincidence detection based on the stimulus envelope. The output of a bank of such coincidence detectors tuned to different values of interaural delay can be described by a cross-correlation function. In its simplest form, the cross-correlation function, $\rho(\tau)$, depicts a measure of the correlation between the left- and right-ear stimuli as a function of an internal delay (τ) of the stimulus at one ear relative to the stimulus at the other. Because the interaural correlation is computed following the application of this internal delay, the peak value of the cross-correlation function occurs at the value of τ corresponding to the interaural delay of the stimulus.

Several psychophysical models of interaural envelope discrimination performance are based upon changes in activity expressed in terms of interaural correlation computed at various locations along a bank of coincidence detectors. For example, it has been shown that the change in the normalized interaural correlation of the envelope of the physical stimulus (the value of the cross-correlation function computed at $\tau=0$) can account for thresholds in a variety of binaural detection and discrimination tasks at high frequencies (Bernstein and Trahiotis, 1996a; van de Par and Kohlrausch, 1998; Bernstein *et al.*, 1999). The normalized interaural correlation of the envelope is defined as

$$\rho = \frac{\int l(t)r(t)dt}{\sqrt{\int l(t)^2 dt}\sqrt{\int r(t)^2 dt}}, \tag{1}$$

where $l(t)$ and $r(t)$ are instantaneous amplitudes of the envelopes of the left- and right-ear stimuli, respectively. The normalized correlation is distinguished from the Pearson product-moment correlation in that the numerator contains the instantaneous envelope values rather than deviations about the mean values. It is this property that allows the normalized correlation to account for binaural masking level difference (MLD) data gathered for high-frequency signals in noise, as illustrated by Bernstein and Trahiotis (1996a). [The difference in normalized interaural correlation between two binaural stimuli computed with no internal delay applied to the stimuli, that is, the value of the cross-correlation function at $\tau=0$, will be abbreviated $\Delta\rho(0)$ in the present manuscript.]

Bernstein and Trahiotis (1996a) analyzed data showing threshold interaural time differences (ITDs) as a function of modulation depth for sinusoidally amplitude-modulated (SAM) pure tones that were previously reported by Nuetzel

[a]Electronic mail: stell006@umn.edu

 0001-4966/2005/118(1)/346/7/$22.50

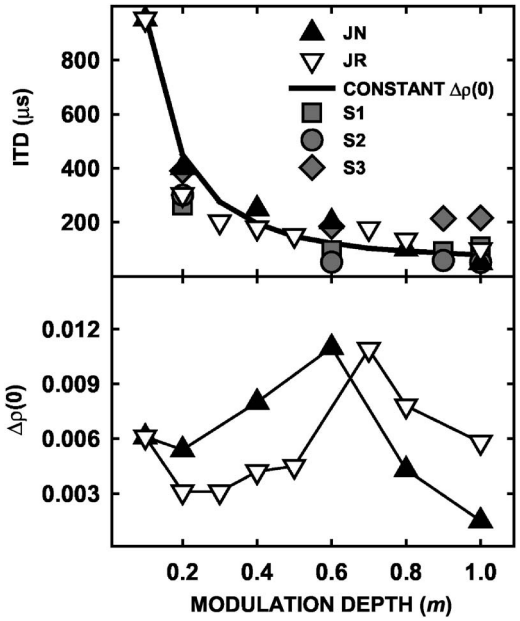

FIG. 1. In the upper panel, threshold ITD (in μs) is plotted as a function of modulation depth for a 4-kHz pure tone sinusoidally amplitude-modulated at 300 Hz. The different triangle symbols represent different listeners. These data were digitized from Fig. 5 of Bernstein and Trahiotis (1996a) who in turn extracted the data from Nuetzel and Hafter's (1981) Fig. 4. The solid line is a prediction based on the assumption that listeners require a constant normalized interaural envelope correlation at threshold for discrimination. The gray symbols are thresholds measured for a 4-kHz carrier amplitude-modulated at 300 Hz for the three listeners in the present study. In the lower panel, the threshold ITDs represented by the triangles from the upper panel are plotted as normalized interaural envelope correlations.

and Hafter (1981). In their Fig. 5 (reproduced in the top panel of Fig. 1), Bernstein and Trahiotis (1996a) presented data from Nuetzel and Hafter along with predictions of threshold change in ITD that were computed under the assumption that the ITD at threshold corresponds to a constant $\Delta\rho(0)$. As shown in the top panel of Fig. 1, the predicted function is similar in form to the data and visual inspection of this figure led Bernstein and Trahiotis (1996a) to conclude that $\Delta\rho(0)$ accounts for these data well. However, an alternative way of analyzing the Nuetzel and Hafter data is to convert the measured threshold ITDs to values of $\Delta\rho(0)$ as in the lower panel of Fig. 1. If the threshold change in ITD at each modulation depth reflects a constant $\Delta\rho(0)$, this value at threshold should be constant across modulation depth. It appears that this is not the case when the data are plotted as in the lower panel of Fig. 1 and that a different conclusion might be reached by visual inspection of those data. The important point is that without an estimate of variability for the original data points, there is no way to evaluate the significance of the differences illustrated in the two panels of Fig. 1. Although the transformation of $\Delta\rho(0)$ to ITD results in compressed values of ITD at high modulation depths, any estimate of variability that might have been provided would likewise be compressed and would serve as a metric of the goodness of fit of the constant-$\Delta\rho(0)$ prediction represented by the solid line. In the present paper, psychometric functions (PFs) for discrimination of interaural phase differences (IPDs) of the envelope of a SAM 4-kHz pure tone were measured. The PFs measured here serve the same purpose that estimates of variability on the data shown in Fig. 1 would have: they permit one to determine whether a given value of $\Delta\rho(0)$ corresponds to a constant level of discrimination performance across modulation depth.

While the predictions of Bernstein and Trahiotis (1996a), shown in the top panel of Fig. 1, are based upon a criterion value of $\Delta\rho(0)$ computed on the envelopes of the pressure waveforms (i.e., prior to any peripheral processing), more realistic predictions might take into account stages of auditory processing that occur prior to binaural comparisons. In subsequent modeling efforts, Bernstein and Trahiotis (1996b; 2002) included preprocessing stages prior to computation of $\Delta\rho(0)$. These preprocessing stages were designed to mimic aspects of peripheral auditory processing: bandpass filtering to simulate critical-band filtering that occurs in the cochlea, envelope compression to simulate basilar-membrane compression, half-wave, square-law rectification to simulate transduction by inner hair cells, and a combination of low-pass filters to simulate the loss of neural synchrony to the fine structure of high-frequency stimuli that occurs at the auditory periphery (Weiss and Rose, 1988) as well as the decreased temporal resolution to envelope fluctuations above about 130 Hz (Kohlrausch *et al.*, 2000). These additional stages of processing were applied to the stimulus waveforms prior to computing $\Delta\rho(0)$ in an attempt to account for threshold changes in the ITD of the envelopes of high-frequency carriers measured for various modulation frequencies (Bernstein and Trahiotis, 2002) as well as the detection of dichotic signals in diotic noise (Bernstein and Trahiotis, 1996b). In the present paper, the ability of this more elaborate model to account for IPD-discrimination performance across modulation depth is tested. It will be seen that $\Delta\rho(0)$ either with or without the additional stages of stimulus processing fails to account for the present results.

Another potential decision statistic is based on changes in interaural correlation across the entire range of the cross-correlation function. Colburn *et al.* (2005) showed that when responses of neural coincidence detectors are modeled on the basis of auditory nerve responses (inputs to the coincidence detectors) with consideration of the distribution of characteristic delays across the population of coincidence detectors, and further assuming an optimal combination of information across that population, a single coincidence detector provides the most information with respect to changes in IPD around IPDs other than that to which the coincidence detector is "tuned." In other words, while the change in interaural correlation discussed in the preceding paragraphs corresponds to the change in the response of a coincidence detector tuned to IPD=0 (for discrimination from a diotic standard), it may be more appropriate to consider the response of coincidence detectors that exhibit the maximum change in response (i.e., those tuned to IPDs other than that of the standard or comparison stimulus). In terms of modeling, this amounts to evaluating the change in interaural correlation between the cross-correlation functions of the stimuli to be discriminated for the value of τ that exhibits the maximum change (a statistic abbreviated as $\Delta\rho_{\max}$ in the present manuscript). In a study of binaural masking, van der Heijden and Trahiotis (1999) showed that $\Delta\rho(0)$ failed to account for their data

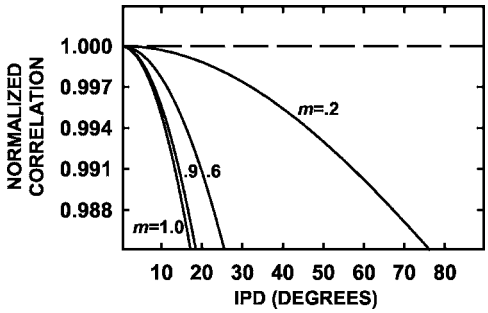

FIG. 2. Normalized interaural envelope correlation computed as a function of envelope IPD (in degrees) for SAM. Each curve represents a different modulation depth as indicated. The dashed line represents the normalized correlation of the diotic standard in the present experiment.

from conditions in which listeners detected an interaurally in-phase (S0) or out-of-phase ($S\pi$) 500-Hz pure tone in the presence of an interaurally delayed noise masker. Instead, it was necessary to consider the change in interaural correlation that would be carried by units tuned to interaural delays other than that of the masker. Furthermore, van der Heijden and Trahiotis (1999) found that their model suggested that coincidence detectors with characteristic delays of up to 3 ms were operative, with the assumption of increased internal noise with increasing characteristic delay. For the present task involving lateralization of the envelope of a 4-kHz carrier, PFs in terms of $\Delta\rho_{\max}$ also are evaluated. Because of the large values of threshold IPD in some conditions, it is necessary to assume the presence of coincidence detectors tuned to ITDs of up to several ms in order to evaluate the viability of $\Delta\rho_{\max}$ as a decision statistic. It will be seen that the $\Delta\rho_{\max}$ metric also fails to account for the present data.

B. Applying normalized interaural correlation as a decision statistic in lateralization tasks

The listening task of Nuetzel and Hafter (1981) was a "left–right" discrimination task in which listeners discriminated between stimuli carrying interaural envelope delays of the same magnitude leading to the left and right ears. The same value of normalized interaural correlation is computed for an envelope delay of a given magnitude regardless of the ear to which the envelope leads. In this way, the normalized interaural correlation is insensitive to direction and as a result, as Bernstein and Trahiotis (1996a) pointed out, it would be impossible for listeners to use this value alone as a decision statistic in performing such a discrimination task. According to Bernstein and Trahiotis (1996a), the listener "solves" the left–right discrimination task by discriminating between peaks of activity on an internal cross-correlation surface (e.g., Stern and Colburn, 1978). In this framework, the normalized interaural correlation merely serves as a predictor of the magnitude of threshold values of interaural envelope delay in a left–right discrimination task.

Figure 2 shows the relationship between normalized interaural correlation and IPD (or frequency-dependent ITD) for SAM tones of different modulation depths. From this figure, it is clear that if discriminability is determined by the IPD, which determines the location of the peak of activity on the cross-correlation surface for a given frequency, then it cannot also be determined by normalized interaural correlation, which varies with modulation depth. With respect to the PFs reported in the following, this means that if the PFs (measured across modulation depth) coincide when plotted in terms of IPD (or ITD) they cannot coincide when plotted in terms of normalized interaural correlation (and vice versa).

In the experimental conditions described here, discrimination d' was measured for the change in the envelope IPD of a SAM pure tone for a standard IPD of 0°. Because listeners discriminated a nonzero IPD from IPD=0° in the present conditions (a "left-center" task), the normalized interaural correlation differed between the stimuli to be discriminated. In the following, for brevity, the term "normalized correlation" refers specifically to the normalized interaural correlation of the envelope as defined in Eq. (1).

II. METHODS

Discriminability of the IPD of the envelope of a SAM 4-kHz pure-tone carrier (70 dB SPL) was measured in a single-cue, two-interval, two-alternative forced-choice procedure in which a stimulus carrying the standard IPD (0°) was presented in the cue interval followed by two listening intervals. A stimulus with the standard IPD (a diotic stimulus) was presented in one of the listening intervals while the remaining interval, the signal interval, contained a stimulus with a different IPD leading to the left ear (a dichotic stimulus). The signal interval was chosen randomly with equal probability from the two listening intervals on each trial. Psychometric functions (PFs) were constructed as described below for modulation frequencies of 128 and 300 Hz and modulation depths (m) of 0.2, 0.6, 0.9, and 1.0. (Nuetzel and Hafter gathered data for modulation frequencies of 150 and 300 Hz and ms ranging from 0.1 to 1.) All stimuli were presented against a continuous background of Gaussian noise low-pass filtered at 1 kHz (60-dB/octave roll-off) and a spectrum level of 40 dB SPL (measured at 1 kHz prior to filtering) which was designed to mask potential distortion products at the frequency of modulation of the 4-kHz carrier. The low-pass noise was intended to prevent listeners from performing the task on the basis of the lateralization of such distortion products (Nuetzel and Hafter, 1976). The continuous, low-pass noise was uncorrelated at the two ears.

Discrimination performance was measured in terms of d' for a range of signal IPDs. The signal IPD was varied adaptively based on the listener's responses in order to sample a useful range of IPDs (those producing neither chance nor perfect performance) within each block of trials. It was found that a useful range of signal IPDs could be sampled using a modified version of a 2-down-1-up adaptive procedure. In the present procedure, after every two trials the number of correct responses made by the listener in those two trials was assessed. If the listener made two correct responses, the signal IPD was reduced by a predetermined step size. If the listener made one or two incorrect responses, the signal IPD was increased by twice the step size. All IPDs led to the left ear. Responses were binned in terms of signal IPD on each trial such that d' could be computed for each signal

IPD and PFs could be constructed. Because an adaptive procedure was used, a variable number of trials was obtained at each signal IPD. Trials were run in blocks of 50 until at least 100 trials had been accumulated at 3-5 IPDs. In most cases, the largest number of trials for any point on a given psychometric function was between about 120 and 160. In the most extreme case, one point on a psychometric function was based on 204 trials.

Within each block of trials, the modulation frequency and m were fixed. The signal IPD at the start of a block of trials was selected and adjusted as blocks were completed so that the initial signal IPD was within the range of IPDs that were visited most frequently in prior completed blocks. The step size also was selected on the basis of trial and error in order to yield 3-5 IPDs that produced the desired range of d' values (between chance and perfect performance, centered approximately between $d'=1.0$ and 1.5). If the step size was changed between blocks of trials for a particular modulation frequency and m, the data for that PF were accumulated from scratch with the new step size. Thus a single step size was used to gather the data in each PF reported here although the step size varied between PFs.

Stimuli were generated within MATLAB (Math Works) on a PC and sent to a real-time digital signal processor (RP2.1, Tucker-Davis Technologies, TDT S3). The continuous, low-pass masker was generated by the signal processor using the accompanying software. Stimulus and masker were mixed within the RP2.1, then they were attenuated (TDT PA5), passed to a headphone buffer (TDT HB7), and presented via Sony MDR-V6 headphones to listeners seated in an IAC sound-attenuating chamber. The sampling rate was set to the 12.207-kHz rate available on the processor. The internal reconstruction filter of the RP2.1 removed any spectral components above the Nyquist frequency produced by digital-to-analog conversion.

The three listeners were the first and third authors (S2 and S1, respectively) and an undergraduate student (S3) from the University of Minnesota who was paid to participate in the study. All three listeners had extensive experience in various binaural listening tasks. All listeners had pure-tone thresholds of 15 dB HL or better at octave frequencies from 250 to 8000 Hz.

III. RESULTS AND DISCUSSION

PFs for modulation frequencies of 128 and 300 Hz are shown in Figs. 3 and 4, respectively, with data from the individual listeners plotted in separate rows. PFs showing d' as a function of change in IPD (relative to the standard IPD=0°) are plotted in the left-hand panels of each row. Within each panel, different symbols represent different values of m. Best-fitting straight lines determined by least-squares linear regression (with each data point weighted equally) are plotted through each set of data points. The shaded regions around some PFs represent estimates of error associated with each PF (based on the standard error associated with each data point).[1]

In order to compare thresholds to those reported by Nuetzel and Hafter (1981), threshold IPDs were estimated from the 300 Hz functions for $d'=1.0$ and converted to ITDs (compared to Nuetzel and Hafter's estimates of threshold as the 75%-correct point on the psychometric function). The gray symbols in the upper panel of Fig. 1 show threshold

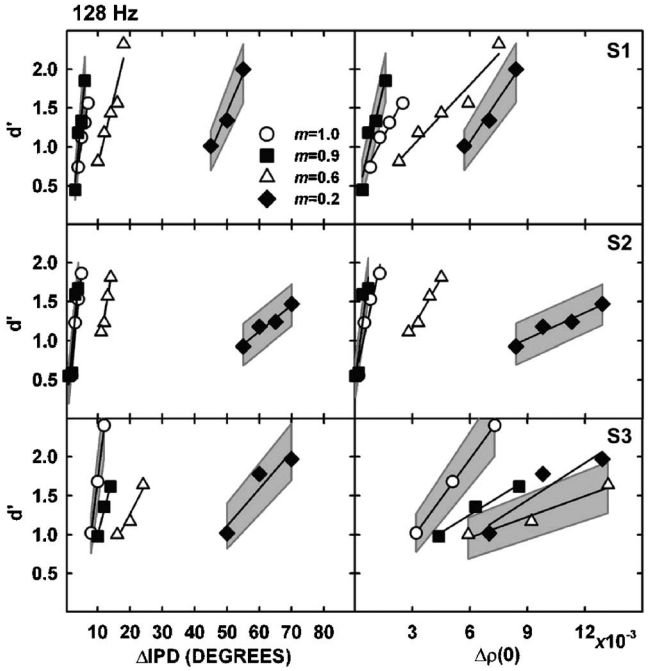

FIG. 3. Psychometric functions for discrimination of envelope IPD for 128-Hz SAM in terms of IPD of the signal (left-hand column) and difference in normalized correlation between standard and signal [$\Delta\rho(0)$, right-hand column]. Different symbols represent different modulation depths as shown. Straight lines were fit to each set of data points by least-squares linear regression. Each row shows data from a single listener. The shaded regions are estimates of error associated with each psychometric function, as described in footnote 1.

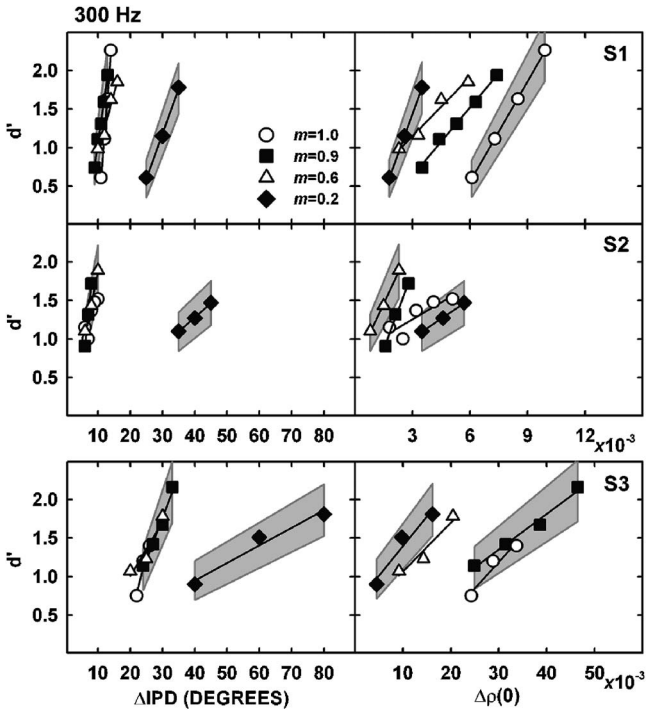

FIG. 4. Same as Fig. 3 for 300-Hz SAM. Note that the right-hand panel for S3 is scaled differently than for the other two listeners.

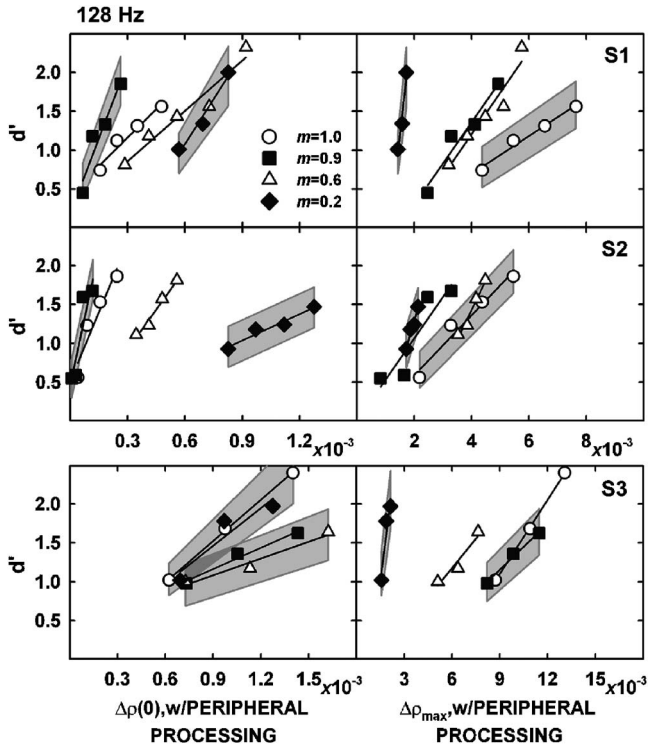

FIG. 5. The psychometric functions for 128-Hz SAM from Fig. 3 replotted in terms of $\Delta\rho(0)$ (left-hand column) and $\Delta\rho_{max}$ (right-hand column), both computed subsequent to processing designed to mimic peripheral auditory processing. Note that the panels for S3 are scaled differently than for the other two listeners. The shaded regions are estimates of error associated with each psychometric function, as described in Footnote 1.

ITDs for the three individual listeners as a function of m for the 300-Hz modulation frequency. Although the experimental task of Nuetzel and Hafter was a left–right task, their ITDs in Fig. 1 represent the total difference between ITDs in the two intervals of their task so this comparison is valid. Plotted in this way, the thresholds measured in the present experiment are comparable to those of the two listeners of Nuetzel and Hafter.

In the right-hand panel of each row of Figs. 3 and 4, the PFs from the left-hand panels are replotted in terms of change in normalized correlation [relative to the standard normalized correlation of 1.0, i.e., $\Delta\rho(0)$] computed on the envelopes of the unprocessed pressure waveforms. In order to conclude that a given stimulus parameter is a possible basis of discrimination across conditions, the PFs associated with that parameter for different modulation depths should coincide. Based on this criterion, it is clear from the right-hand panels of Figs. 3 and 4 that $\Delta\rho(0)$ cannot account for performance in this discrimination task. From the psychometric functions, discrimination d' cannot be predicted on the basis of $\Delta\rho(0)$. Consequently, for a given modulation frequency and a given $\Delta\rho(0)$, the discriminability measured in terms of d' varies with m. For example, for listener S1 at 300 Hz, a value of $\Delta\rho(0)$ of 0.006 yields d' around 1.5 for $m=0.9$ while the same $\Delta\rho(0)$ would produce d' around 0.5 for $m=1.0$ and essentially perfect performance (infinitely large d') for $m=0.2$.

In Figs. 5 and 6 (for modulation frequencies of 128 and 300 Hz, respectively), the PFs are expressed in terms of the other correlation-based metrics described in Sec. I. The left-hand panels of Figs. 5 and 6 express the PFs in terms of $\Delta\rho(0)$ and the right-hand panels show the PFs in terms of $\Delta\rho_{max}$, both following preprocessing designed to mimic the effects of peripheral auditory processing. The stages of preprocessing were those described by Bernstein *et al.* (1999): bandpass filtering by a Gammatone filter centered on the carrier frequency; compression of the waveform with an exponent of 0.23; half-wave, square-law rectification; low-pass filtering at 425 Hz using the parameters of Weiss and Rose (1988), and low-pass filtering at 150 Hz. As was the case for the normalized correlation computed on the envelopes of the unprocessed pressure waveforms, it can be seen in Figs. 5 and 6 that these additional stages of preprocessing and alternate decision metrics fail to align the PFs. The fact that the threshold values of $\Delta\rho(0)$ following preprocessing are orders of magnitude smaller than those reported elsewhere for low-frequency (e.g., Gabriel and Colburn, 1981) and high-frequency stimuli (e.g., Bernstein and Trahiotis, 1992; 1996a) provides additional, indirect evidence that $\Delta\rho(0)$ likely was not the decision metric that was used by listeners in the present conditions.

None of the above-considered correlation-based metrics lead to considerable alignment of the PFs. As an attempt to identify a metric that might lead to alignment of the PFs, it was observed that some of the PFs appear to be coincident when expressed in terms of IPD (left-hand panels of Figs. 3 and 4). For $m=0.6$, 0.9, and 1.0 at 300 Hz, the PFs are nearly coincident for all three listeners, as they are for the 128 Hz PFs for $m=0.9$ and 1.0. In Fig. 7, the data of the PFs that appear to coincide in terms of IPD (300 Hz, $m=0.6$, 0.9, and 1.0 and 128 Hz, $m=0.9$ and 1.0) are replotted in terms of ITD. Although these data represent only a selected subset of the available data, the PFs shown in Fig. 7 coincide reasonably well for the individual listeners (or at least to a greater extent than for any of the correlation-based metrics) indicating that discriminability at these modulation frequencies and depths is best described by an ITD-based measure. [Nuetzel and Hafter (1981) and Bernstein and Trahiotis (1994) also found nearly constant threshold ITDs across comparable rates and depths of SAM for high-frequency carriers.]

In terms of a bank of coincidence detectors tuned to ITD (e.g., Stern and Colburn, 1978), this predictor of performance (envelope ITD) corresponds to the change in location of the peak of activity on the cross-correlation surface, which is determined by the ITD. If discriminability is based on the location of the peak of activity on the cross-correlation surface, it might be expected that discriminability would diminish as the peaks of the envelope become broader in time and shallower and thus more difficult to resolve or encode with precision (as noted by Bernstein and Trahiotis, 1996a), which occurs as m and/or modulation frequency decreases. A trend consistent with such an effect is seen in the data in that psychometric functions plotted in terms of IPD are shifted progressively to the right for smaller values of m (Figs. 3 and 4). For the psychometric function plotted in terms of normalized correlation, there is no consistent trend across modulation depths. Thus, these data show that the psychometric

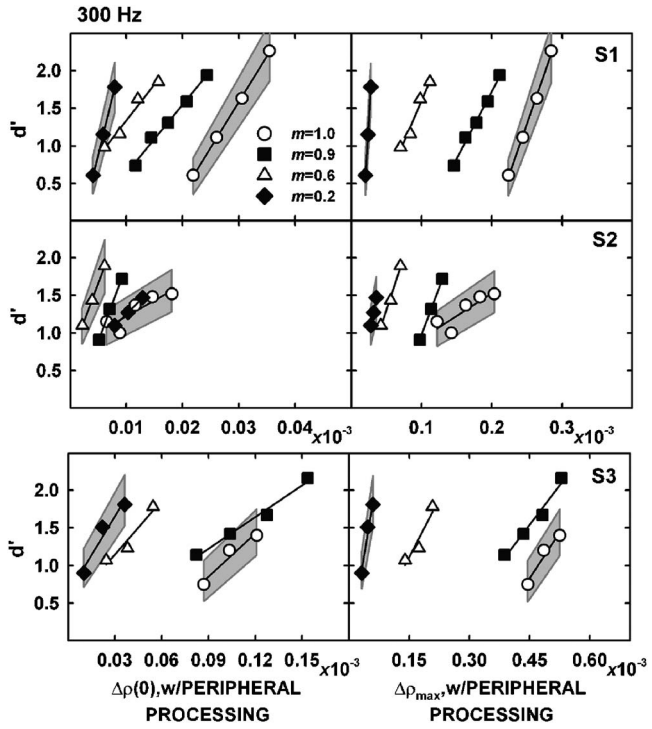

FIG. 6. Same as Fig. 5, but for the psychometric functions for 300-Hz SAM from Fig. 4. Note that the panels for S3 are scaled differently than for the other two listeners.

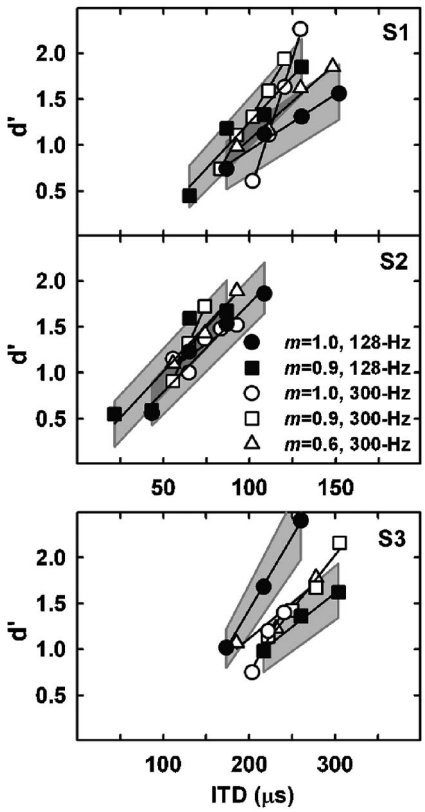

FIG. 7. The psychometric functions from Figs. 3 and 4 that overlapped in the IPD panels replotted in terms of ITD in μ_s. Each panel shows data from a different listener. Note that the panel for S3 is scaled differently than for the other two listeners.

functions plotted in terms of ITD qualitatively account for lateralization performance better than those plotted in terms of correlation-based metrics.

Note that the preprocessing stages that were applied prior to computation of the normalized correlation will not change the interaural delay of the stimulus (because those processing stages only change the effective modulation depth of the stimulus at the two ears) and, as a result, the delay at which the peak of the cross-correlation function occurs also will be unchanged. Therefore, the positions of the PFs expressed in terms of ITD and IPD remain unchanged whether or not the effects of peripheral processing are considered.

Although the PFs plotted in terms of ITD of the physical stimulus appear to coincide for only the larger modulation depths, perhaps a decision statistic based on envelope ITD following a physiologically realistic envelope-encoding scheme could bring the data into closer agreement across all modulation depths. Given the lack of orderly progression of the PFs across modulation depth and modulation frequency, it is not clear what additional processing must be implemented in order to generate correlation-based metrics that will account for these lateralization data. However, it should be noted that this conclusion does not appear to hold for IPD discrimination for low-frequency pure tones (below 1000 Hz) in that discrimination thresholds in those conditions are more nearly equal across frequency in terms of IPD (and thus $\Delta\rho$) rather than ITD (e.g. Klumpp and Eady, 1956).

As indicated in Sec. I, Bernstein and Trahiotis (2002) reported that $\Delta\rho(0)$ computed subsequent to simulated peripheral processing accounts for threshold ITDs across modulation frequency for SAM pure tones ($m=1$). Their conclusion was based in part on visual inspection of constant-$\Delta\rho(0)$ predictions plotted against threshold ITDs (as was the case for their analysis of threshold ITDs across modulation depth illustrated in the upper panel of Fig. 1). Although not the focus of the present paper, to evaluate that claim on the basis of the PFs for the two modulation frequencies examined here, the PFs in terms of $\Delta\rho(0)$ computed after peripheral processing (from the left-hand panels of Figs. 5 and 6) are replotted in Fig. 8 for $m=0.9$ and 1.0. It can be seen from the PFs that $\Delta\rho(0)$ fails to account for performance across the two modulation frequencies examined here. The same is true for $m=0.2$ and 0.6. The apparent goodness of fit of the constant-$\Delta\rho(0)$ predictions of Bernstein and Trahiotis (2002) appears to be in part a result of the compressive relationship between $\Delta\rho(0)$ and IPD (as illustrated in Fig. 2). The fact that a relatively large range of $\Delta\rho(0)$ corresponds to a relatively small range of IPDs for large modulation depths means that a prediction of threshold ITD across modulation frequency based on a constant-$\Delta\rho(0)$ criterion will appear to be reasonably accurate for a large range of criterion values.

To summarize the results presented here, the just-discriminable change in envelope IPD for a SAM 4-kHz pure tone with modulation frequencies of 128 or 300 Hz does not correspond to a constant change in the normalized interaural envelope correlation, whether or not the effects of peripheral auditory processing are taken into consideration. Nor does the just-discriminable change in envelope IPD in these conditions correspond to a constant change in the value of the

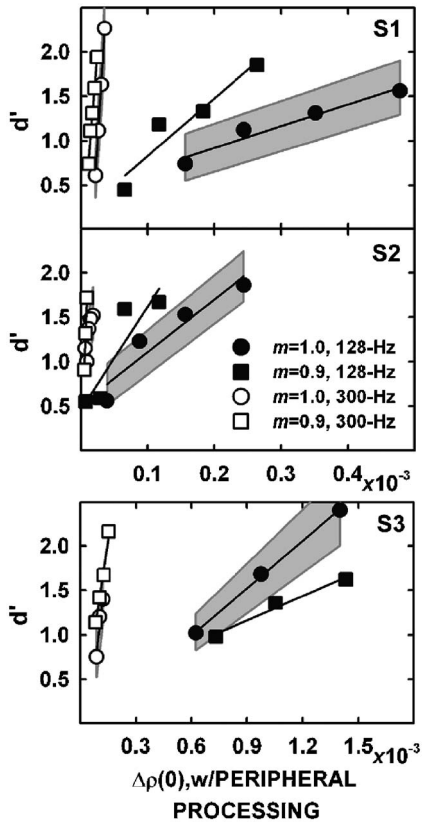

FIG. 8. Psychometric functions in terms of $\Delta\rho(0)$ computed subsequent to simulated peripheral processing for $m=0.9$ (squares) and 1.0 (circles) for 128 Hz (closed symbols) and 300 Hz (open symbols) replotted from the left-hand columns of Figs. 5 and 6. Each panel shows data from a single listener. Note that the panel for S3 is scaled differently than for the other two listeners.

cross-correlation function computed at the point of maximum change along the function when the effects of peripheral processing are included. The change in normalized correlation at threshold varies with modulation depth. At higher modulation depths, thresholds at these modulation frequencies more nearly correspond to a constant change in envelope ITD. Thresholds at lower modulation depths are qualitatively in agreement with this interpretation if one assumes that the precision with which envelopes are encoded decreases with decreasing modulation depth.

ACKNOWLEDGMENTS

The authors thank Dr. Armin Kohlrausch and two anonymous reviewers for their helpful comments. This work was supported by Research Grant No. R03 DC 05343-01 from the National Institute on Deafness and Communication Disorders, National Institutes of Health.

[1][For the data in Figs. 3–8, estimates of the error associated with each PF were computed. In order to do so, the standard error of each d' value was estimated as described by Macmillan and Creelman (2005). Vertically oriented error bars were constructed about each point spanning a range of ±1standard error. By way of a least-squares linear regression procedure, a straight line was then fit to the upper end points and, separately, to the lower end points of each error bar within a psychometric function, which yielded upper and lower bounds of the error estimate for each PF. For clarity, a shaded region between the upper and lower bounds of the error estimate is shown for only one leftward PF and one rightward PF (chosen arbitrarily) in each panel. It was felt that showing only the most extreme error regions within each panel was sufficient to allow one to determine whether the PFs within each panel could be considered to overlap. For PFs with very steep slopes, the shaded regions are very narrow and consequently may be difficult to discern.]

Bernstein, L. R. and Trahiotis, C. (**1992**). "Discrimination of interaural envelope correlation and its relation to binaural unmasking at high frequencies," J. Acoust. Soc. Am. **91**, 306–316.

Bernstein, L. R. and Trahiotis, C. (**1994**). "Detection of interaural delay in high-frequency sinusoidally amplitude-modulated tones, two-tone complexes, and bands of noise," J. Acoust. Soc. Am. **95**, 3561–3567.

Bernstein, L. R. and Trahiotis, C. (**1996a**). "On the use of the normalized correlation as an index of interaural envelope correlation," J. Acoust. Soc. Am. **100**, 1754–1763.

Bernstein, L. R. and Trahiotis, C. (**1996b**). "The normalized correlation: Accounting for binaural detection across center frequency," J. Acoust. Soc. Am. **100**, 3774–3784.

Bernstein, L. R. and Trahiotis, C. (**2002**). "Enhancing sensitivity to interaural delays at high frequencies by using 'transposed stimuli,' " J. Acoust. Soc. Am. **112**, 1026–1036.

Bernstein, L. R., van de Par, S., and Trahiotis, C. (**1999**). "The normalized interaural correlation: Accounting for NoSπ thresholds obtained with Gaussian and 'low-noise' masking noise," J. Acoust. Soc. Am. **106**, 870–876.

Colburn, H. S., Zhou, Y., and Dasika, V. (**2005**) "Inhibition in models of coincidence detection," in *Auditory Signal Processing: Physiology, Psychoacoustics, and Models*, edited by D. Pressnitzer, A. de Cheveigne, S. McAdams, and L. Collet (Springer, New York).

Gabriel, K. J. and Colburn, H. S. (**1981**). "Interaural correlation discrimination. I. Bandwidth and level dependence," J. Acoust. Soc. Am. **69**, 1394–1401.

Henning, G. B. (**1974**). "Detectability of interaural delay in high-frequency complex waveforms," J. Acoust. Soc. Am. **55**, 84–90.

Jeffress, L. A. (**1948**). "A place mechanism of sound localization," J. Comp. Physiol. Psychol. **41**, 35–39.

Klumpp, R. G. and Eady, H. R. (**1956**). "Some measurements of interaural time difference thresholds," J. Acoust. Soc. Am. **28**, 859–860.

Kohlrausch, A., Fassel, R., and Dau, T. (**2000**). "The influence of carrier level and frequency on modulation and beat-detection thresholds for sinusoidal carriers," J. Acoust. Soc. Am. **108**, 723–734.

Macmillan, N. A. and Creelman, C. D. (**2005**). *Detection Theory: A User's Guide*, 2nd ed. (Erlbaum, Mahwah, NJ).

Nuetzel, J. M. and Hafter, E. R. (**1976**). "Lateralization of complex waveforms: Effects of fine structure, amplitude, and duration," J. Acoust. Soc. Am. **60**, 1339–1346.

Nuetzel, J. M. and Hafter, E. R. (**1981**). "Discrimination of interaural delays in complex waveforms: Spectral effects," J. Acoust. Soc. Am. **69**, 1112–1118.

Stern, R. M. and Colburn, H. S. (**1978**). "Theory of binaural interaction based on auditory-nerve data. IV. A model of subjective lateral position," J. Acoust. Soc. Am. **64**, 127–140.

van der Heijden, M., and Trahiotis, C. (**1999**). "Masking with interaurally delayed stimuli: The use of 'internal' delays in binaural detection," J. Acoust. Soc. Am. **105**, 388–399.

van de Par, S. and Kohlrausch, A. (**1998**). "Diotic and dichotic detection using multiplied-noise maskers," J. Acoust. Soc. Am. **103**, 2100–2110.

Weiss, T. F. and Rose, C. (**1988**). "A comparison of synchronization filters in different auditory receptor organs," Hear. Res. **33**, 175–180.

The role of high frequencies in speech localization

Virginia Best[a] and Simon Carlile
Department of Physiology, University of Sydney, Sydney, NSW, 2006, Australia

Craig Jin and André van Schaik
School of Electrical and Information Engineering, University of Sydney, Sydney, NSW, 2006, Australia

(Received 25 January 2005; revised 14 April 2005; accepted 14 April 2005)

This study measured the accuracy with which human listeners can localize spoken words. A broadband (300 Hz–16 kHz) corpus of monosyllabic words was created and presented to listeners using a virtual auditory environment. Localization was examined for 76 locations on a sphere surrounding the listener. Experiment 1 showed that low-pass filtering the speech sounds at 8 kHz degraded performance, causing an increase in polar angle errors associated with the cone of confusion. In experiment 2 it was found that performance in fact varied systematically with the level of the signal above 8 kHz. Although the lower frequencies (below 8 kHz) are known to be sufficient for accurate speech recognition in most situations, these results demonstrate that natural speech contains information between 8 and 16 kHz that is essential for accurate localization. © *2005 Acoustical Society of America.* [DOI: 10.1121/1.1926107]

PACS number(s): 43.66.Qp [AJO] Pages: 353–363

I. INTRODUCTION

Human speech is a dynamic acoustic stimulus, varying in both frequency and intensity over time in a complex manner. A large body of research exists that is concerned with how speech recognition depends on the identification of these acoustic patterns, as well as how recognition is influenced by the presence of noise or other interfering sources. It is well known that the spatial layout of sources in a noisy environment has a large impact on how well they can be segregated, and differences in spatial location can aid in the focusing of selective attention on a talker of interest (see Zurek, 1993; Bronkhorst, 2000). However the spatial perception of human speech sounds in quiet has actually received little attention in the literature.

The ability of subjects to locate a sound in space is dependent on the integration of information from a number of acoustic cues (see Carlile, 1996; Blauert, 1997 for reviews). A sound source located away from the midline results in differences in the arrival time and the level of the sound at each ear. Thus for a sound source positioned around a listener, there will be a set of interaural cues that the auditory system can use to estimate the direction of the incoming source. However, as the ears are placed more or less symmetrically on the head, these interaural cues are ambiguous and result in the so-called "cone of confusion" where a single interaural difference corresponds to the surface of a cone centered on the interaural axis. The three-dimensional asymmetry of the outer ear results in a location-dependent spectral filtering of sounds which can provide spectral cues to resolve the ambiguities in the interaural cues. The dynamic nature of speech provides the spatial auditory system with particular challenges. In particular, it is likely that spectral fluctuations inherent in the source spectrum would hinder the extraction of the spectral cues introduced by the head and pinnae.

Speech is widely used as a stimulus in auditory research, especially in the important areas of hearing loss and communication in noisy environments. Importantly, it has become apparent that such studies have frequently used low-pass filtered (8 kHz or below) speech stimuli. The explanation for this is that most of the important sound components for speech recognition, such as formants, occur well below 8 kHz. However, naturally produced speech does contain significant amounts of energy above 8 kHz. Broadband segments can extend up to around 20 kHz [an example is shown in Fig. 1(b)]. It is also known that energy in this high-frequency region (above 8 kHz) is important for accurate auditory localization of nonspeech signals (Bronkhorst, 1995; King and Oldfield, 1997; Carlile and Delaney, 1999; van Schaik *et al.*, 1999). As the impact of these high-frequency cues on speech localization is unclear, the primary aim of the current experiment was to compare localization of broadband and low-pass filtered speech stimuli.

A few studies have examined speech localization in the horizontal plane using single words presented in virtual auditory space and found that although the lateral angle (the angle away from the median plane) was estimated as accurately as for nonspeech broadband stimuli, there was an increase in front–back confusions (Begault and Wenzel, 1993; Ricard and Meirs, 1994). Using a larger range of locations, Gilkey and Anderson (1995) compared the localization of click trains to recorded single words. They examined positions distributed randomly on a sphere (including elevations between −45° and 90°). They reported that performance was comparable in the left–right dimension, but poorer in the front–back dimension and in elevation for speech stimuli. The kinds of errors reported for speech stimuli are typical cone of confusion errors, arising commonly in situations where the spectral cues to sound source location are somehow compromised.

[a]Electronic mail: ginbest@cns.bu.edu

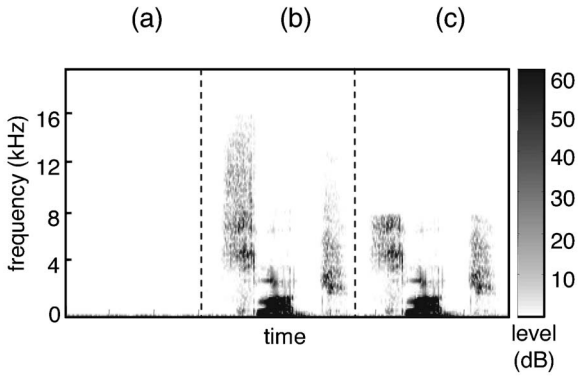

FIG. 1. Spectrograms of (a) a silent period, (b) the recorded word "sludge," and (c) the same word after low-pass filtering at 8 kHz. The spectrograms show that the recordings were made with high signal-to-noise ratio and that substantial energy exists above 8 kHz in the recorded speech.

While this previous work indicates that cone of confusion errors are increased for speech localization compared to localization of simple nonspeech stimuli, the present study explored directly the relationship between speech bandwidth and localization performance for a large range of spatial locations.

II. EXPERIMENTAL METHODS

A. Subjects and environment

Five subjects participated in the experiments (3 male, 2 female, aged 24–34) and all had previous experience in auditory localization experiments. Stimuli were delivered over headphones using virtual auditory space technology (see Sec. II B) at a level of approximately 75 dB SPL. Acoustical recordings for the generation of virtual stimuli as well as localization testing took place in an anechoic chamber situated at the University of Sydney (dimensions 4 m $\times$ 4 m $\times$ 4 m).

B. Generation of virtual auditory space

Virtual auditory space (VAS) is generated by recording the acoustic filter functions of the auditory periphery of individual listeners [the head-related transfer functions (HRTFs)] and convolving these filter functions with sounds subsequently presented over headphones to create a realistic, externalized percept. HRTFs were measured using a "blocked-ear" recording technique. This approach involves embedding a small recording microphone in an earplug secured flush with the distal end of the ear canal (Møller *et al.*, 1995). The recordings were performed in the anechoic chamber with the subject at the center. A loudspeaker, mounted on a robotic arm, delivered the stimuli from locations on an imaginary sphere of 1 m radius around the listener's head. The automated recording procedure recorded an HRTF for the right and left ear at 393 locations evenly distributed around the sphere. The position of the subject's head was stabilized using a chin rest and head orientation was monitored using an electromagnetic tracking system to ensure that it was fixed. Impulse responses were measured using Golay code pairs of length 1024 and a sampling rate of 80 kHz (Golay, 1961). The HRTFs are composed of a location-independent component (LIC) and a location-dependent component. The LIC for a given ear is estimated as the rms magnitude spectrum of the entire set of recordings for that ear. The LIC is then deconvolved from the recorded HRTFs to obtain the directional transfer functions (DTFs). The primary reason for performing such a manipulation is to remove measurement artifacts including speaker and microphone transfer functions and the detailed acoustic effects associated with the precise location of the microphone.

The desired acoustical stimulus is then convolved with the right and left ear DTFs appropriate for a particular sound location and presented via in-ear headphones (Etymotic ER-2). These headphones are designed to have a flat frequency response up to 10 kHz, and were considered appropriate for the purposes of this study on the basis of their ability to produce high-fidelity VAS (see Sec. II D). All stimuli were windowed by applying a raised cosine to the first and last 10 ms before convolution with DTFs.

C. Speech stimuli

As a publicly available broadband speech corpus (i.e., not filtered at 8 kHz or below) could not be found, the Harvard list (Egan, 1948) was recorded by a male actor with extensive vocal training from the National Institute of Dramatic Arts (Sydney). This corpus consists of 20 phonetically balanced word lists each containing 50 monosyllable words. These were recorded using a Brüel and Kjær 4165 microphone and a Brüel and Kjær 2610 amplifier. The speech was digitized at a sample rate of 80 kHz using an anti-aliasing filter with a 30 kHz cut-off. The first 5 of the 20 lists were used in the present experiment. The duration of the words in these lists ranged between 418 and 1005 ms with an average duration of 710 ms.

Because this experiment examines the influence of high-frequency spectral information on localization, it was very important that background noise be eliminated. This was accomplished by: (i) recording the speech stimuli in the anechoic chamber, (ii) seating the actor (in a quiet chair) close to the microphone; (iii) setting the amplifier so that signals were within and spanned the maximum range of the analog-to-digital converter; (iv) turning off unnecessary equipment. Figure 1 shows a spectrogram of a silent period and a recorded speech signal (the word "sludge") under two different filtering conditions (8 and 16 kHz low-pass). The spectrograms show that the recordings were made with high signal-to-noise ratio and that background noise was not a concern.

D. Localization testing

The localization testing paradigm in place in the laboratory (Carlile *et al.*, 1997) was used to validate the VAS

stimuli as well as to measure localization for the specific test stimuli under examination in this study.

Briefly, in the validation test, the ability of a subject to localize a burst of broadband noise in free-field anechoic space was compared with his/her localization performance for the same type of stimulus presented in VAS. The test required the subject to stand in darkness in the center of the anechoic chamber and indicate the perceived direction of a series of 150 ms broadband noise bursts presented from 76 random locations evenly distributed on an imaginary sphere surrounding his/her head. For the free-field component of the test, sound sources were presented from a loudspeaker that could be positioned at any location on this sphere. For the VAS component, stimuli were presented over headphones at the corresponding "virtual" locations on this sphere. To respond, the subject was required to turn and face the perceived location of the target and point his/her nose at the source. An electromagnetic tracking receiver mounted on the top of the head (Polhemus: IsoTrack) was used to measure the orientation of the head and thus provided an objective measure of the perceived direction. Five such tests were completed by each subject in the two conditions. If performance under the two stimulation conditions was accurate (spherical correlation coefficient of at least 0.85, see Sec. II E), the subject was considered a sufficiently accurate localizer and the VAS a valid simulation. This was the case for all subjects used in this study.

Localization performance under the test stimulus conditions for Experiments 1 and 2 was measured using the same paradigm as above. Each experiment consisted of three stimulus conditions and Experiment 1 was completed by each subject before the commencement of Experiment 2. Experiment 1 compared the ability of subjects to localize broadband noise, broadband speech, and 8 kHz low-pass filtered speech. In Experiment 2, subjects localized speech stimuli in which the *level* of the high-frequency information was systematically varied.

For each condition, five localization responses were obtained for each of the 76 stimulus locations. For each of the five replicates, the spoken word signals were chosen randomly from one of the five balanced lists. As there were 76 locations and only 50 words per list, 26 of the words were played twice per condition. For each condition, the same word stimuli were played from the same location on the sphere, thus keeping the stimulus set identical between conditions. Within each experiment, trials from the three conditions were interleaved and stimuli were presented in a randomized fashion. Each of the two experiments consisted of 1140 localization trials in total (3 conditions $\times$ 76 locations $\times$ 5 replicates), which were divided into 15 localization tests. Thus in total, each subject completed 30 tests (approximately 8 h of listening time) over a period of about two months.

Subjects understood that they did not have to identify the spoken words, only localize them. However, when questioned after testing, they did not report any difficulty in recognizing the relatively common words.

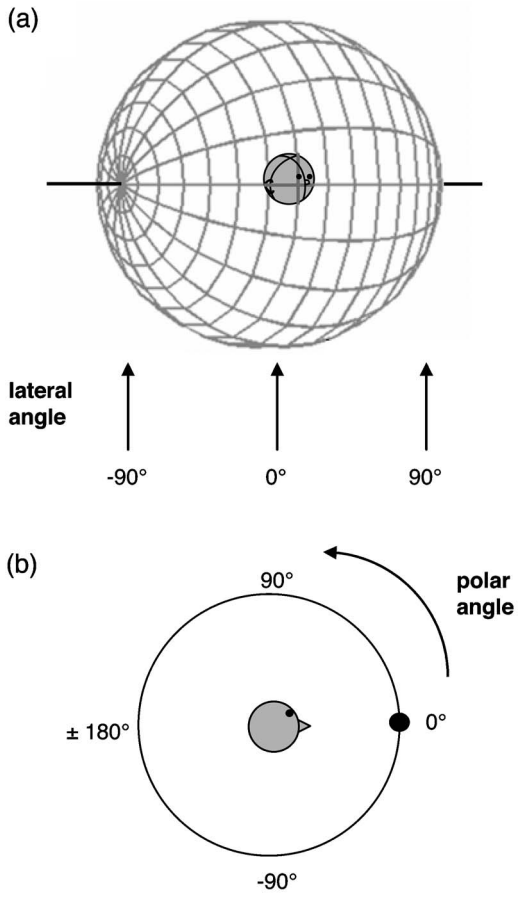

FIG. 2. The lateral/polar coordinate system consists of a single pole passing through the two ears. (a) The lateral angle is the horizontal angle away from the midline, with 0° defining the median sagittal plane and −90° and 90° defining the left- and right-most extremities of the sphere. (b) The polar angle describes the angle around the circle described by a particular lateral angle. A polar angle of 0° describes the front-most location on this circle, with polar angle increasing to 90° at the top and −90° at the bottom, with 180° and −180° coinciding at the back.

E. Data analysis

In order to gauge the overall performance of subjects in the different experimental conditions, the spherical correlation coefficient (SCC; Fisher *et al.*, 1987) was calculated. Its use with localization data is described in detail elsewhere (Leong and Carlile, 1998), but in brief, it describes the degree of correlation between target and response locations based on their directional cosines (1 = perfect correlation; 0 = no correlation).

To investigate the pattern of responses more closely, the localization data were analyzed in terms of lateral and polar angles (Fig. 2). Analysis of localization responses involved plotting actual target lateral (or polar) angle against perceived lateral (or polar) angle. Furthermore, lateral and polar angle errors were calculated for each trial and pooled in order to compare performance across stimulus conditions. Finally, in order to compare results to those of previous studies, it was useful to calculate the percentage of cone of confusion errors made by subjects in each condition. These were de-

TABLE I. Spherical correlation coefficients (SCCs) for each of the five subjects in Experiment 1 (and the mean). Each of the three rows contains values for the three stimulus conditions. Each SCC is calculated on the basis of five repetitions at each of 76 stimulus locations (i.e., 380 trials in total). See the text for details of this statistic.

	S1	S2	S3	S4	S5	Mean
BB noise	0.82	0.88	0.91	0.90	0.91	0.88
BB speech	0.75	0.87	0.87	0.88	0.87	0.85
LP speech	0.40	0.79	0.66	0.76	0.66	0.65

fined as large polar angle errors (>90° in magnitude) and as such included the commonly reported front–back and up–down confusions.

III. EXPERIMENT 1: SPEECH LOCALIZATION

A. Conditions

Experiment 1 consisted of three stimulus conditions. In condition A, which acted as a control, the stimulus was a 150 ms white noise burst that was windowed by applying a raised cosine to the first and last 10 ms. In condition B, stimuli were broadband speech signals. Both noise and speech signals were band-passed between 300 Hz and 16 kHz. Importantly, the duration of noise and speech stimuli were not matched. However, if this were to have an effect, it would be expected that the longer duration of the speech stimuli might confer an advantage for localization over the control broadband noise condition. Note also that as the stimuli were presented in virtual auditory space, any head movements made during stimulus presentation would not have provided any dynamic localization cues. However, subjects were instructed to keep their head still during the stimulus to ensure that the perceived position did not change in relation to the measurement apparatus. In condition C, stimuli were speech signals low-pass filtered at 8 kHz before DTF filtering. Low-pass filtering was performed in the time domain using brick-wall FIR filters (60 dB down in the stop band). The effect of the low-pass filtering is demonstrated in Fig. 1 where it can be seen that certain parts of speech signals contain substantial high-frequency information that is removed with the 8 kHz low-pass filtering.

B. Results

Table I shows the SCC calculated for each subject under the three stimulus conditions. The SCC was highest in the broadband noise condition, fell slightly in the broadband speech condition, and fell considerably in the low-pass speech condition.

The correspondence between target and response lateral angles is illustrated in Fig. 3. As all subjects showed a very similar pattern, their data were combined for plotting. It can be seen that response direction lateral angles correspond well to the target direction lateral angles in all conditions, as most of the data fall on or near the "perfect response" diagonal.

As the polar angle data showed patterns that were highly individualized, the polar angle analysis is presented for each of the five subjects separately. Figure 4 illustrates the correspondence between target and response polar angles.

It must be noted that these data are collapsed across lateral angle, and thus variations in the scale of polar angles are ignored. Referring to Fig. 2, it is clear that larger lateral angles (approaching ±90°) give rise to smaller polar angle circles on the coordinate sphere. This means that polar angle space becomes increasingly compressed at the sides, and thus small absolute errors can translate to extremely large polar angle errors. Thus in this kind of analysis one can expect to see many large polar angle errors overall, even in optimal listening conditions.

In the broadband noise control condition, all subjects estimated the polar angle relatively accurately. In the broadband speech condition, performance was also relatively good. However all subjects showed some increase in error, which appears to be predominantly due to front–back confusions.

Individualized polar angle response patterns were most evident in the low-pass speech condition. S1 and S5 were dramatically affected by the low-pass filtering, showing a strong tendency to localize stimuli presented in the lower hemisphere of space (polar angle range −180°–0°) to the upper hemisphere (polar angle range 0°–180°). S2 and S4's performance was the most robust to low-pass filtering, but showed a spread in responses and some back-to-front confusions. Finally, S3 demonstrated some large polar angle re-

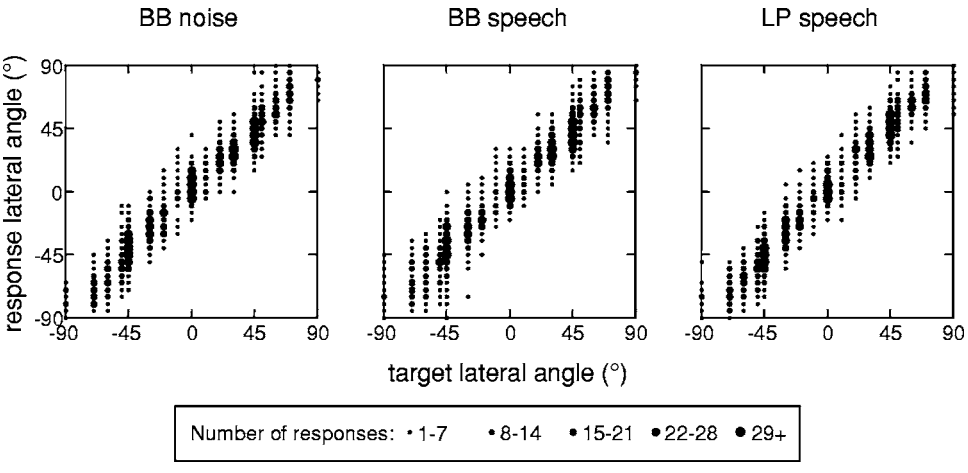

FIG. 3. Scatter plots showing lateral angle data (pooled across all subjects) for Experiment 1. The three panels contain data for the three stimulus conditions: broadband noise (left), broadband speech (middle), and low-pass filtered speech (right). Target lateral angle (abscissa) is plotted against response lateral angle (ordinate) and the size of the dots represents the number of responses clustered at a point.

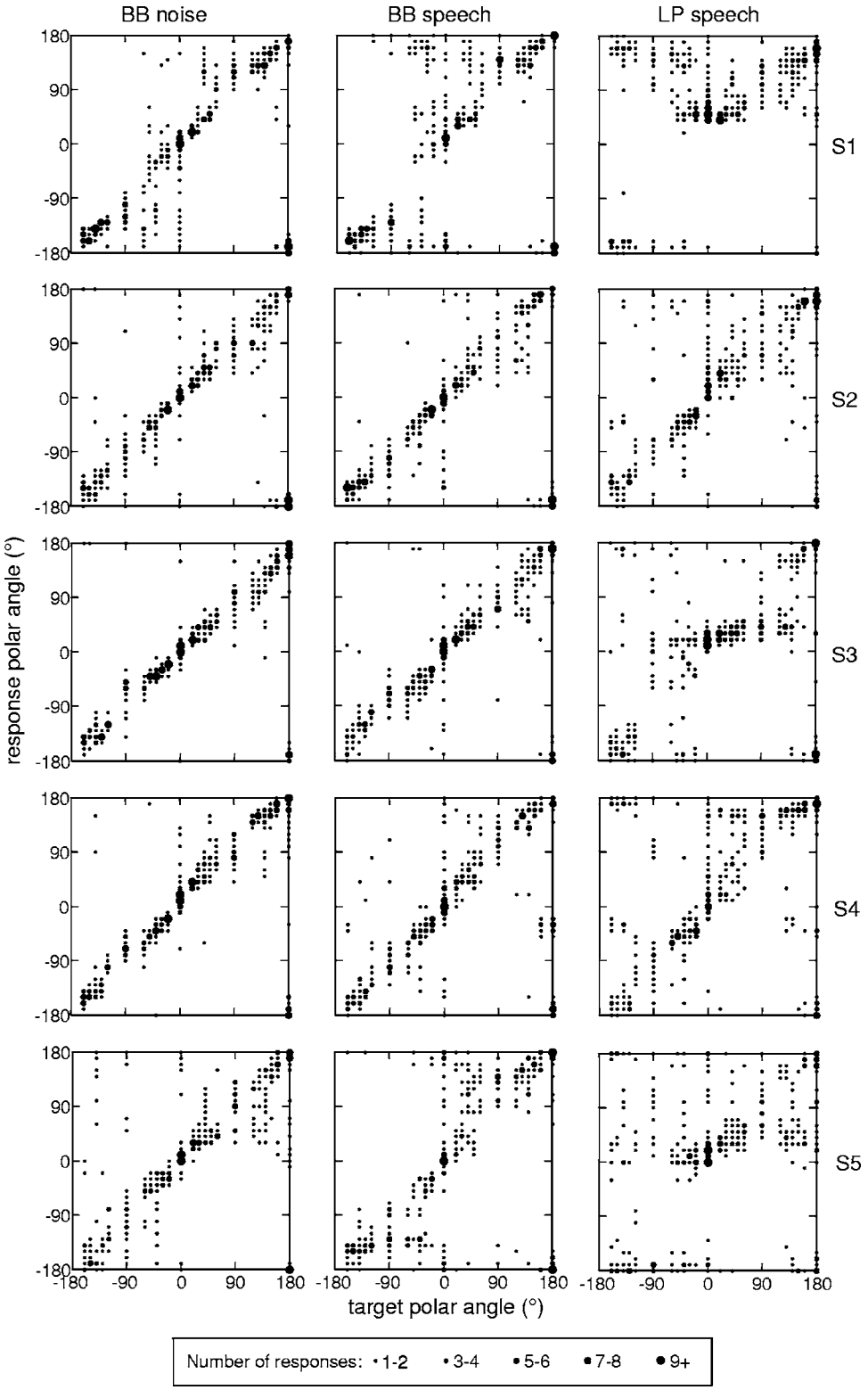

FIG. 4. Scatter plots showing polar angle data for Experiment 1. Each row shows data for a different subject as labeled. The three panels contain data for the three stimulus conditions: broadband noise (left), broadband speech (middle), and low-pass filtered speech (right). Target polar angle (abscissa) is plotted against response polar angle (ordinate) and the size of the dots represents the number of responses clustered at a point.

sponse errors, particularly for stimuli presented in the lower frontal regions (polar angle range $-90°-0°$).

In order to summarize the magnitude of the lateral and polar angle errors, the absolute value of the errors was calculated and the mean was obtained for each subject in each stimulus condition. Mean errors and standard errors of the means (SEMs) are shown in Fig. 5. Lateral angle errors [Fig. 5(a)] were small in general and did not appear to vary systematically across the three stimulus conditions (means of 8.3°, 8.9°, and 8.5°). A Kruskal–Wallis nonparametric ANOVA performed on the group data revealed no significant differences across conditions $[\chi^2(2,5697)=5.35, p=0.069]$. Mean polar angle errors [Fig. 5(b)], however, varied considerably between stimulus conditions. Overall, polar angle errors were consistently smallest in the broadband noise condition (mean 12.3°), higher in the broadband speech condition (mean 30.9°), and highest for low-passed speech (mean 46.4°). A Kruskal–Wallis nonparametric ANOVA per-

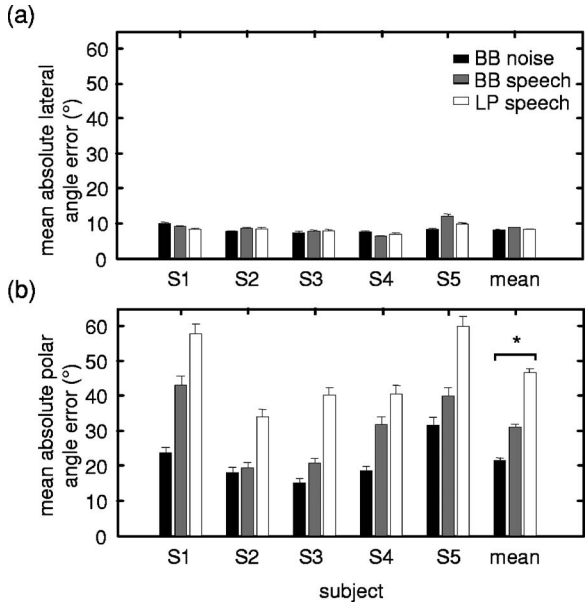

FIG. 5. (a) Mean absolute lateral angle errors from Experiment 1. The six clusters of bars show results for the five subjects as well as the mean across subjects. Mean errors are shown for broadband noise (black bars), broadband speech (gray bars), and low-pass filtered speech (white bars). Error bars show standard error of the mean. (b) Mean absolute polar angle errors from Experiment 1. All other details as for (a). The asterisk indicates that for the mean data all three conditions were significantly different from each other ($p<0.05$).

formed on the group data revealed a highly significant effect of condition [$\chi^2(2,5622)=401.94, p<0.001$], and post-hoc analysis (Tukey HSD, $p=0.05$) found significant differences between all three conditions.

Table II shows the calculated cone of confusion error rates. For different subjects, the number and distribution of cone of confusion errors across the sound conditions varied, although there were fewer errors on average for the broadband noise condition, an increase in the broadband speech condition, and a much larger number of errors for the low-pass speech condition.

C. Discussion

The findings of the current study were consistent with those of previous studies. Subjects accurately estimated the lateral angle of a source regardless of spectral content, as the available interaural differences provide a robust cue to lateral angle. This has been reported previously for both speech (Ricard and Meirs, 1994; Gilkey and Anderson, 1995) and nonspeech stimuli (Gilkey and Anderson, 1995; Carlile *et al.*, 1997). Performance in the control condition confirmed the well-supported notion that broadband flat-spectrum sounds are well localized in polar angle (Carlile *et al.*, 1997; King and Oldfield, 1997). In terms of the localization errors that arise when the monaural spectral cues are ambiguous, the present study confirmed and extended the findings of previous researchers. Our basic finding was that polar angle errors increased somewhat for sound stimuli with time-varying spectra (speech) but particularly when high-frequency content was removed (low-passed speech).

TABLE II. Percentage of cone of confusion (COC) errors made by each of the five subjects in Experiment 1 (and the mean). Each of the three rows contains values for the three stimulus conditions. Each value represents the percentage of trials (out of the total 380) in which a COC error was made. See the text for details of this statistic.

	S1	S2	S3	S4	S5	Mean
BB noise	5.8	2.9	1.8	2.9	1.8	3.0
BB speech	18.2	4.2	3.7	12.4	3.7	8.4
LP speech	22.6	11.6	15.5	16.6	15.5	16.4

It was interesting to find that subjects were relatively accurate at localizing broadband speech, despite some increase in confusions compared to broadband noise. Speech has a spectrum that is nonflat, and also varies over time, and yet listeners showed a reasonable capacity for distinguishing spectral cues to location from spectral features of the source spectrum. It may be that familiarity with the source spectrum plays an important role here, as suggested by Plenge and Brunschen (1971). These authors showed that familiar voices (with familiar spectra) are localized better in the median plane than unfamiliar voices, presumably because the spectrum due to directional filtering can be calculated. In the current experiment the same talker was used on every trial and thus his voice would have been familiar to listeners. Poorer polar angle estimates might be expected if the talker was varied randomly from trial to trial such that the source spectrum could not be predicted. However even for unfamiliar stimuli with nonflat spectra the spectral cue localization process shows some robustness. For example, subjects can accurately localize "scrambled spectrum" and "rippled spectrum" sounds as long as the spectral manipulations are moderate (Wightman and Kistler, 1989; Wightman and Kistler, 1997; Kulkarni and Colburn, 1998; Macpherson and Middlebrooks, 2003).

The low-pass filtered speech stimuli were included in this study because speech stimuli in the large majority of previous work have been low-pass filtered at 8 kHz or below. The results presented here indicate that low-pass filtered speech stimuli are localized much less accurately in the polar angle dimension than broadband speech stimuli. Out of the literature consulted, only two localization studies used a cut-off frequency higher than 8 kHz. One was the Gilkey and Anderson study (1995), where speech stimuli were band-pass filtered from 400 Hz to 11 kHz. Due to the differences in analyses, it is difficult to compare performance of subjects in that study to the current one. However, it appears, by inspection of their figures, that the number of errors in Gilkey and Anderson's data is larger than in our broadband speech (300 Hz–16 kHz) condition. This suggests that frequency bands as high as 11–16 kHz are useful for accurate sound localization of speech.

In another study, consonant–vowel (CV) localization was examined in the presence of diffuse background noise (Karlsen, 1999). In that study, CVs were recorded in an anechoic environment with a low-pass cut-off frequency of 10 kHz. Localization was tested in the horizontal plane. The author reported a relatively low percentage of front–back errors which, by inspection of the data, appears to be approximately 15% of the total trials. This is greater than the pro-

portion of cone of confusion errors calculated in the present study for broadband speech (8.4%). This may suggest that frequencies between 10 and 16 kHz can benefit speech localization, or it may be that CVs are more spectrally impoverished than monosyllabic words. In any case, comparisons must be made with caution, as the testing locations and criteria for defining cone of confusion errors differed between the present study and that of Karlsen.

D. Analysis of high frequency content of stimuli

An interesting analysis included in Karlsen's work (1999) looked at the differences in localization accuracy for different CVs. In other words, he was probing the specific components of human speech that are useful for localization. He reported that subjects were most sure of the location (fastest response time) if the CV contained the /s/ consonant. However, a surprising finding was that the strong consonants /s/ and /t/, containing high-frequency energy, resulted in a relatively large number of front–back errors.

It was of interest for the present experiment to take this approach and examine whether the specific frequency content of different words was related to the localization performance. Specifically, it was suspected that words with substantial energy above 8 kHz would be well localized and performance on these words would be *most* affected by the low-pass filtering. To examine this, a spectrogram of each of the 250 words used was calculated using a routine from the Auditory Toolbox for MATLAB (Slaney, version 2, 1998). The total energy above 8 kHz was summed and taken as a metric (in arbitrary units) of high frequency content. The words were ranked on this basis, and then divided into 10 bins each containing 25 words. For each bin, polar angle errors were calculated for all trials (across all subjects) in which its members were the stimulus. Mean absolute polar angle errors were calculated independently for the broadband and low-pass filtered conditions.

Figure 6 shows the mean errors for the 10 bins. Note that the bins represent words with increasing amounts of high-frequency energy, i.e., bin 1 has the least and bin 10 has the most. Three main points emerge from this simple analysis. First, it is clear that the curves do not change smoothly as a function of high-frequency energy. This may be because the energy below 8 kHz in these words (which varies independently of the high-frequency energy) has an influence on the amount of error. Second, for the broadband condition, there appears to be an overall decrease in the mean polar angle error with increasing high-frequency content, suggesting that words with more high frequency energy were better localized. The low-passed condition shows a nonsystematic variation, but since these sounds were presented without any of their high-frequency energy, no relationship is expected here between high-frequency content and performance. Third, for all bins, the mean errors are significantly lower in the broadband condition compared to the low-passed condition. Even for the first bin, i.e., the 25 words with the lowest amount of high-frequency energy, the improvement is substantial. Clearly these words have enough energy above 8 kHz to afford the auditory system a better estimate of the location.

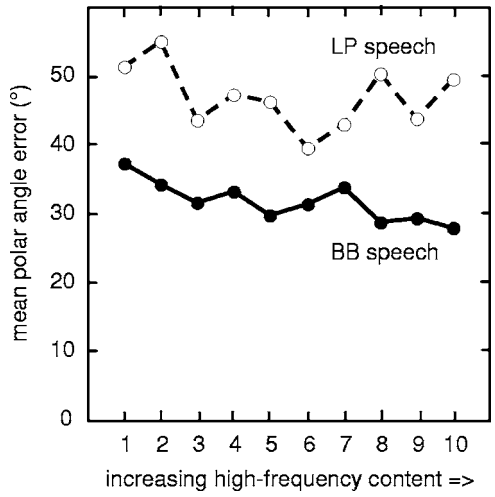

FIG. 6. Mean polar angle errors for different groups of words. The numbers 1 to 10 on the abscissa denote 10 groups of words of increasing high-frequency content (see the text for details). Mean errors are shown for broadband speech (closed symbols, solid line) and low-pass filtered speech (open symbols, dashed line). It can be seen that *all* words were localized more poorly after low-pass filtering.

This analysis showed that all of the 250 word stimuli used in this experiment contained high-frequency information (above 8 kHz) that was useful for polar angle localization. This emphasizes that naturally spoken speech is a broadband stimulus, a notion that is frequently overlooked in the literature. Experiment 2 was conducted to test the hypothesis that the preservation of this high-frequency energy, even at a very low level, can benefit the localization of natural speech. To examine whether accuracy is related to the level of this energy, or simply its presence, localization performance was measured with the high-frequency region systematically attenuated.

IV. EXPERIMENT 2: INFLUENCE OF HIGH-FREQUENCY LEVEL ON SPEECH LOCALIZATION

A. Conditions

Experiment 2 consisted of three stimulus conditions. Condition A acted as a control and stimuli were broadband speech signals (identical to those of Experiment 1 condition B). In conditions B and C, the level of the high-frequency information (above 8 kHz) was systematically varied. In condition B the high-frequency region was attenuated by 20 dB and in condition C it was attenuated by 40 dB. This was achieved by low-pass filtering the signals (as in Experiment 1 condition C) with varying attenuation in the stop band. Figure 7 shows the power spectral density plots of a typical word under the different conditions.

B. Results

Table III shows the SCC calculated for each subject under the three stimulus conditions of this experiment as well as the low-pass condition of Experiment 1. The SCC was

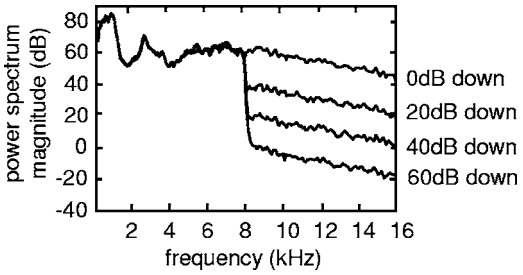

FIG. 7. An illustration of the stimulus conditions employed in Experiment 2. Shown are power spectral density plots of a speech stimulus after low-pass filtering with varying attenuation in the stopband (0, 20, 40, and 60 dB down). Note that 60 dB down was not retested, but is equivalent to the low-pass speech condition of Experiment 1 and is included for comparison.

highest in the broadband speech condition and in nearly all cases showed a gradual decline with increasing attenuation in the high-frequency region.

The correspondence between target and response lateral angles for the three speech conditions is illustrated in Fig. 8. As the performance data across all subjects showed a very similar pattern, their data were combined for plotting. It can be seen that target lateral angles correspond well with response lateral angles in all conditions, as most of the data fall on or near the "perfect response" diagonal.

As in Experiment 1, the polar angle data were highly individualized. Figure 9 illustrates the correspondence between target and response polar angles. In the broadband speech condition, polar angle estimates were accurate across all subjects, as was seen in Experiment 1. When the high-frequency level was lowered, S1 and S5 showed a dramatic increase in error for the 20 dB down condition, which was exacerbated in the 40 dB down condition. As was seen for low-passed speech in Experiment 1, these two subjects had strong tendency to localize stimuli presented in the lower hemisphere of space (polar angle range $-180°$–$0°$) to the upper hemisphere (polar angle range 0°–180°). The other subjects were less affected by the 20 dB drop in high-frequency level, with their response data showing just a small spread. For the 40 dB down condition, this spread in error was more severe and many large errors are evident.

Figure 10 summarizes the magnitude of the lateral and polar angle errors. Mean lateral and polar angle errors (with SEMs) are shown for each subject under the three conditions

TABLE III. SCCs for each of the five subjects in Experiment 2 (and the mean). The first three rows contain values for the three new stimulus conditions and the fourth row is a reiteration of the data from the low-pass condition of Experiment 1. Each SCC is calculated on the basis of five repetitions at each of 76 stimulus locations (i.e., 380 trials in total). See the text for details of this statistic.

	S1	S2	S3	S4	S5	Mean
BB speech	0.78	0.88	0.86	0.87	0.86	0.85
20 dB down	0.57	0.82	0.75	0.82	0.75	0.74
40 dB down	0.56	0.77	0.70	0.78	0.70	0.70
LP speech	0.40	0.79	0.66	0.76	0.66	0.65

of this experiment. Data from the low-pass condition of Experiment 1 are also included for comparison. Mean lateral angle errors [Fig. 10(a)] were again small and did not vary systematically across conditions (means of 9.4°, 9.7°, and 9.6° for 0, 20, and 40 dB down). A Kruskal–Wallis nonparametric ANOVA performed on the group data revealed no significant differences across conditions [$\chi^2(2,5697) = 1.68, p = 0.432$]. Mean polar angle errors [Fig. 10(b)], however, varied considerably across conditions. Values were consistently smallest in the control broadband speech condition (mean 26.6°) and increased with increasing attenuation in the high-frequency region (means of 38.0° and 42.3° for attenuations of 20 and 40 dB, respectively). A Kruskal–Wallis nonparametric ANOVA performed on the group data revealed a highly significant effect of condition [$\chi^2(2,5622) = 128$, $p < 0.001$], and post-hoc analysis (Tukey HSD, $p = 0.05$) found significant differences between all three conditions. Inspection of the low-pass data from Experiment 1 (60 dB down) suggests that this gradual trend continues with further decreases in high-frequency level.

Table IV shows the calculated cone of confusion error rates. On average, the error rate increased with increasing attenuation in the high-frequency region.

C. Discussion

These results showed that the polar angle localization of speech is related to both the *presence* and the *level* of high-frequency information in the stimulus. There are two possibilities to explain the gradual decline in performance with increasing attenuation in the region above 8 kHz. One option

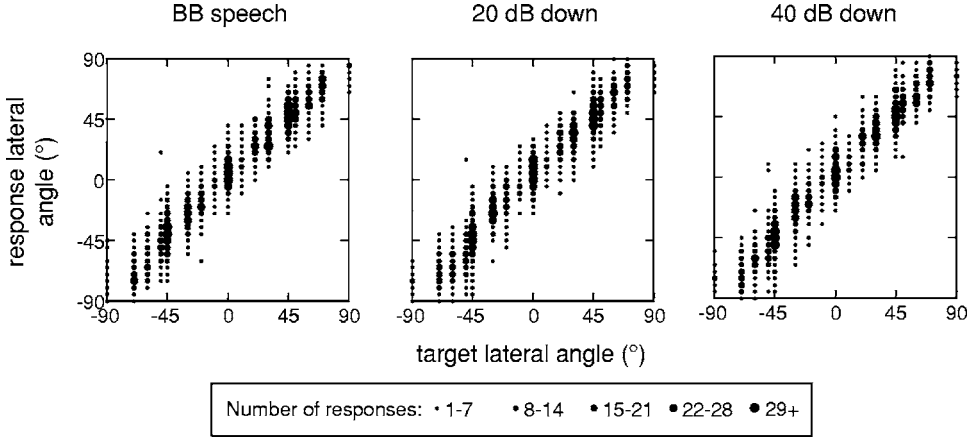

FIG. 8. Scatter plots showing lateral angle data (pooled across all subjects) for Experiment 2. The three panels contain data for the three stimulus conditions: broadband speech (left), 20 dB down low-pass speech (middle), and 40 dB down low-pass speech (right). Target lateral angle (abscissa) is plotted against response lateral angle (ordinate) and the size of the dots represents the number of responses clustered at a point.

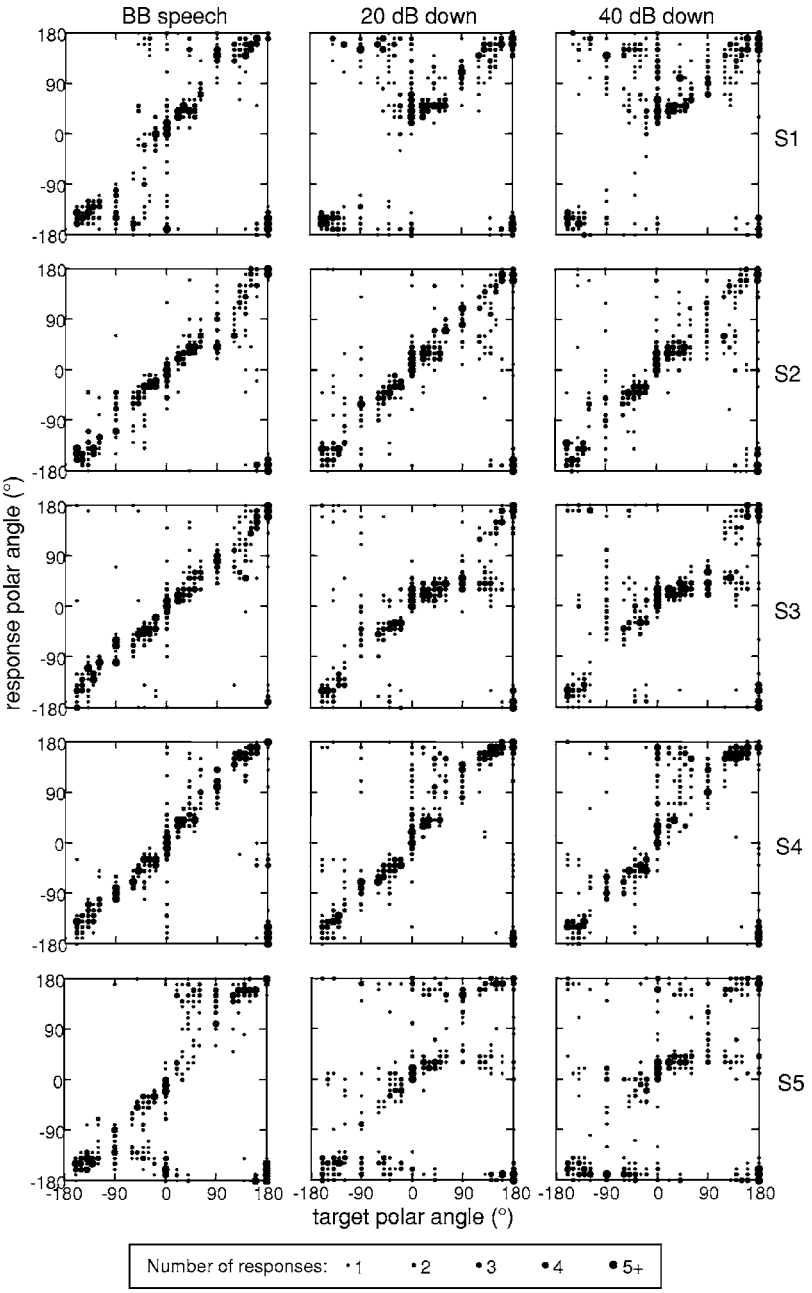

FIG. 9. Scatter plots showing polar angle data for Experiment 2. Each row shows data for a different subject as labeled. The three panels contain data for the three stimulus conditions: broadband speech (left), 20 dB down low-pass speech (middle), and 40 dB down low-pass speech (right). Target polar angle (abscissa) is plotted against response polar angle (ordinate) and the size of the dots represents the number of responses clustered at a point.

is that more and more words in the corpus have their high-frequency content attenuated to an inaudible level (depending on the original level) and thus the error rate may be related to the *number* of broadband words presented. The extreme case would be the low-pass speech (60 dB down) condition, where it is assumed that no words carry high-frequency information. A second possibility is that most words retain some high-frequency content in the 20 and 40 dB down conditions, and that the system has an ability to make use of this low-level energy. Indeed the analysis following Experiment 1 showed that words with very low high-frequency energy were localized better if this energy was preserved. If this is the case, then the gradual decline in performance with increasing attenuation must mean that localization is impaired at low levels.

It has been observed using nonspeech stimuli that localization accuracy is a function of stimulus level (Harris, 1998). Using broadband noise, it was reported that elevation perception worsened and front–back confusions increased if the stimuli were presented at low sound pressure levels (close to the audibility threshold). Furthermore, Abouchacra *et al.* (1998) presented speech phrases in diffuse noise, and reported that localization accuracy in the horizontal plane improved as signal-to-noise ratio increased (18%, 89%, and 95% accuracy at −18 dB, +12 dB, and in quiet, respectively). Although these level manipulations were not restricted to the high-frequency region, they demonstrate that the auditory localization system has an ability to utilize localization cues that appears to depend on the level of the signal. Further to this, Hofman and Van Opstal (2003) demonstrated that the spectral cues are binaurally weighted, with the perceived elevation of a source being more strongly influenced by the spectral cue at the near ear than that at the far. It is possible that this weighting is related to the relative

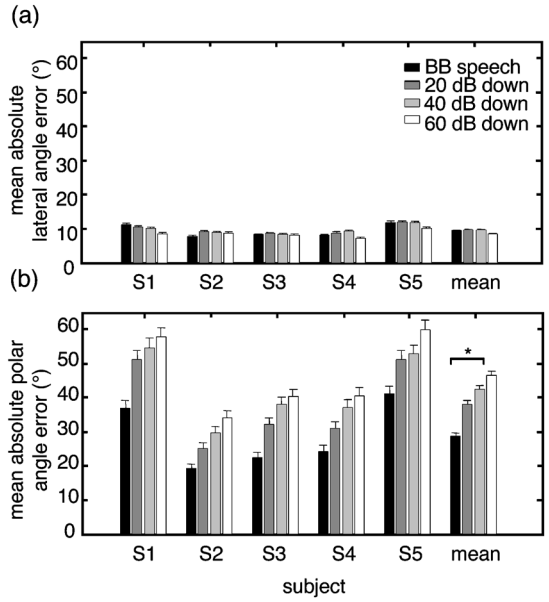

FIG. 10. (a) Mean absolute lateral angle errors from Experiment 2. The six clusters of bars show results for the five subjects as well as the mean across subjects. Mean errors are shown for broadband speech (black bars), 20 dB down low-pass speech (dark gray bars), and 40 dB down low-pass speech (light gray bars). Errors for low-pass filtered speech (60 dB down) from Experiment 1 are also shown for comparison (white bars). Error bars show standard error of the mean. (b) Mean absolute polar angle errors from Experiment 2. All other details as for (a). The asterisk indicates that for the mean data the three new conditions were significantly different from each other ($p < 0.05$).

level of the source at the two ears, consistent with the idea that the utilization of spectral cues is level-dependent.

V. GENERAL DISCUSSION

One of the striking features of the data collected in these experiments is the presence of strong individual differences. The subjects varied in their baseline localization accuracy, their vulnerability to low-pass filtering of the speech stimuli, and their error patterns. A likely explanation for the differences seen with low-pass filtering is that some subjects are more reliant on high-frequency spectral features for localization than others. As the high-frequency spectral cues derive from the physical features of the outer ears, subjects with smaller ears (conchae in particular) will produce spectral cues at higher frequencies than subjects with larger ears. This will mean that they are more affected by low-pass cut-offs in the higher frequency regions. Indeed the two subjects who were most affected by the 8 kHz low-pass filtering in these experiments (S1 and S5) were the only two females in the group and had smaller ears than the males.

TABLE IV. Percentage of COC errors made by each of the five subjects in Experiment 2 (and the mean). The first three rows contain values for the three new stimulus conditions and the fourth row is a reiteration of the data from the low-pass condition of Experiment 1. Each value represents the percentage of trials (out of the total 380) in which a COC error was made. See the text for details of this statistic.

	S1	S2	S3	S4	S5	Mean
BB speech	13.4	3.4	5.3	6.1	5.3	6.7
20 dB down	20.8	6.6	10.8	10.8	10.8	12.0
40 dB down	23.4	6.6	12.6	13.9	12.6	13.8
LP speech	22.6	11.6	15.5	16.6	15.5	16.4

One of the aims of this work, and the work of others, was to define the features important in optimizing the spatial perception of speech. It has been shown here that the inclusion of high frequencies, which are so often filtered out of speech in playback situations, can greatly improve the spatial perception. The reason this is thought to be important is because spatial perception plays an important role in competing source situations. However, there is also some evidence that the preservation of high-frequency speech information can be of benefit in nonspatial tasks. For example, it has been shown that children and adults require an upper cut-off frequency of 9 kHz to optimally identify fricatives in quiet (Stelmachowicz *et al.*, 2001). Furthermore, the intelligibility of vowel–consonant–vowel sounds presented monaurally (to listeners with mild high-frequency hearing loss) was shown to increase steadily with the low-pass cut-off of the speech and performance did not plateau by the maximum tested cut-off of 8 kHz (Vickers *et al.*, 2001).

VI. CONCLUSIONS

A broadband speech corpus (300 Hz–16 kHz) was used to investigate the ability of human listeners to localize monosyllabic words. Experiment 1 showed that low-pass filtering the stimuli at 8 kHz dramatically degraded performance in the polar angle dimension and increased errors associated with the cone of confusion. Experiment 2 showed that the preservation of information above 8 kHz, even at a low level, provided a benefit for polar angle localization. Although the lower frequencies (below 8 kHz) are known to be sufficient for accurate speech recognition in most situations, these results demonstrate that natural speech contains information above 8 kHz that is essential for accurate polar angle localization.

Abouchacra, K. S., Emanuel, D. C., Blood, I. M., and Letowski, T. R. (**1998**). "Spatial perception of speech in various signal to noise ratios," Ear Hear. **19**, 298–309.
Begault, D. R., and Wenzel, E. M. (**1993**). "Headphone localization of speech," Hum. Factors **35**, 361–376.
Blauert, J. (**1997**). *Spatial Hearing: The Psychophysics of Human Sound Localization* (MIT, Cambridge).
Bronkhorst, A. W. (**1995**). "Localization of real and virtual sound sources," J. Acoust. Soc. Am. **98**, 2542–2553.
Bronkhorst, A. W. (**2000**). "The cocktail party phenomenon: A review of research on speech intelligibility in multiple-talker conditions," Acust. Acta Acust. 86, 117–128.
Carlile, S. (**1996**). "The physical and psychophysical basis of sound localization," in *Virtual Auditory Space: Generation and Applications*, edited by S. Carlile (Landes, Austin), Chap. 2.
Carlile, S., and Delaney, S. (**1999**). "The localization of spectrally restricted sounds by human listeners," Hear. Res. **128**, 175–189.
Carlile, S., Leong, P., and Hyams, S. (**1997**). "The nature and distribution of errors in sound localization by human listeners," Hear. Res. **114**, 179–196.
Egan, J. P. (**1948**). "Articulation testing methods," Laryngoscope **58**, 955–991.
Fisher, N. I., Lewis, T., and Embleton, B. J. J. (**1987**). *Statistical Analysis of Spherical Data* (Cambridge University Press, Cambridge).
Gilkey, R. H., and Anderson, T. R. (**1995**). "The accuracy of absolute localization judgments for speech stimuli," J. Vestib. Res. **5**, 487–497.
Golay, M. J. E. (**1961**). "Complementary series," IRE Trans. Inf. Theory **7**, 82–87.

Harris, S. (1998). "The effect of sound level on sound localisation accuracy," Honours thesis, University of Sydney.
Hofman, P. M. and Van Opstal, A. J. (**2003**). "Binaural weighting of pinna cues in human sound localization," Exp. Brain Res. **148**, 458–470.
Karlsen, B. L. (1999). "Spatial localization of speech segments," Ph.D. thesis, Aalborg University.
King, R. B., and Oldfield, S. R. (**1997**). "The impact of signal bandwidth on auditory localization: Implications for the design of three-dimensional auditory displays," Hum. Factors **39**, 287–295.
Kulkarni, A., and Colburn, H. S. (**1998**). "Role of spectral detail in sound-source localization," Nature (London) **396**, 747–749.
Leong, P., and Carlile, S. (**1998**). "Methods for spherical data analysis and visualization," J. Neurosci. Methods **80**, 191–200.
Macpherson, E. A., and Middlebrooks, J. C. (**2003**). "Vertical-plane sound localization probed with ripple-spectrum noise," J. Acoust. Soc. Am. **114**, 430–445.
Møller, H., Sørensen, M. F., Hammershøi, D., and Jensen, C. B. (**1995**). "Head-related transfer functions of human subjects," J. Audio Eng. Soc. **43**, 300–321.
Plenge, G., and Brunschen, G. (**1971**). "*A priori* knowledge of the signal when determining the direction of speech in the median plane," Proceedings of the Seventh International Congress on Acoustics, Vol. **19**, p. H10.
Ricard, G. L., and Meirs, S. L. (**1994**). "Intelligibility and localization of speech from virtual directions," Hum. Factors **36**, 120–128.
Stelmachowicz, P. G., Pittman, A. L., Hoover, B. M., and Lewis, D. E. (**2001**). "Effect of stimulus bandwidth on the perception of /s/ in normal and hearing-impaired children and adults," J. Acoust. Soc. Am. **110**, 2183–2190.
van Schaik, A., Jin, C., and Carlile, S. (**1999**). "Human sound localization of band-pass filtered noise," Int. J. Neural Syst. **9**, 441–446.
Vickers, D. A., Moore, B. C. J., and Baer, T. (**2001**). "Effects of low-pass filtering on the intelligibility of speech in quiet for people with and without dead regions," J. Acoust. Soc. Am. **110**, 1164–1175.
Wightman, F. L., and Kistler, D. J. (**1989**). "Headphone simulation of free field listening. II. Psychophysical validation," J. Acoust. Soc. Am. **85**, 868–878.
Wightman, F. L., and Kistler, D. J. (**1997**). "Monaural sound localization revisited," J. Acoust. Soc. Am. **101**, 1050–1063.
Zurek, P. M. (**1993**). "Binaural advantages and directional effects in speech intelligibility," in *Acoustical Factors Affecting Hearing Aid Performance*, edited by G. A. Studebaker and I. Hochberg (Allyn and Bacon, Boston), pp. 255–276.

Extracting the frequencies of the pinna spectral notches in measured head related impulse responses

Vikas C. Raykar[a] and Ramani Duraiswami[b]
Perceptual Interfaces and Reality Laboratory, Institute for Advanced Computer Studies, Department of Computer Science, University of Maryland, College Park, Maryland 20742

B. Yegnanarayana[c]
Department of Computer Science and Engineering, Indian Institute of Technology, Madras, Chennai-600036, Tamilnadu, India

(Received 13 July 2004; revised 6 April 2005; accepted 6 April 2005)

The head related impulse response (HRIR) characterizes the auditory cues created by scattering of sound off a person's anatomy. The experimentally measured HRIR depends on several factors such as reflections from body parts (torso, shoulder, and knees), head diffraction, and reflection/diffraction effects due to the pinna. Structural models (Algazi *et al.*, 2002; Brown and Duda, 1998) seek to establish direct relationships between the features in the HRIR and the anatomy. While there is evidence that particular features in the HRIR can be explained by anthropometry, the creation of such models from experimental data is hampered by the fact that the extraction of the features in the HRIR is not automatic. One of the prominent features observed in the HRIR, and one that has been shown to be important for elevation perception, are the deep spectral notches attributed to the pinna. In this paper we propose a method to robustly extract the frequencies of the pinna spectral notches from the measured HRIR, distinguishing them from other confounding features. The method also extracts the resonances described by Shaw (1997). The techniques are applied to the publicly available CIPIC HRIR database (Algazi *et al.*, 2001c). The extracted notch frequencies are related to the physical dimensions and shape of the pinna. © *2005 Acoustical Society of America.* [DOI: 10.1121/1.1923368]

PACS number(s): 43.66.Qp, 43.64.Ha, 43.66.Pn [AK] Pages: 364–374

I. INTRODUCTION

Humans have an amazing ability to determine the elevation and azimuth of the sound source relative to them (Blauert, 1996; Middlebrooks and Green, 1991). The mechanisms responsible for the localization ability of the human hearing system have been fairly well understood though not completely. Interaural time and level differences (ITD and ILD) are known to provide primary cues for localization in the horizontal plane, i.e., azimuth of the sound source (Blauert, 1996; Kuhn, 1977; Strutt, 1907; Wightman and Kistler, 1997). However these differences do not account for the ability to locate sound for positions in the so-called *cone of confusion*, which have the same ITD cues, or the *torus of confusion* which have the same ILD cues (Shinn-Cunningham *et al.*, 2000). Additional cues are provided by the distinctive location specific features in the received sound arising due to interactions with the torso, head, and pinna. This filtering process can be described using a complex frequency response function called the head related transfer function (HRTF). For a particular sound source location, the HRTF is defined as the ratio of the complex sound pressure level (SPL) at the eardrum to the SPL at the location of the center of the head when the listener is absent. The corresponding impulse response is called the head related impulse response (HRIR).

The HRTF varies significantly between different individuals due to differences in the sizes and shapes of different anatomical parts like the pinna, head, and torso. Applications in the creation of virtual auditory displays require individual HRTFs for perceptual fidelity. A generic HRTF would not work satisfactorily since it has been shown that nonindividual HRTF results in poor elevation perception (Wenzel *et al.*, 1993). The usual customization method is the direct measurement of HRTFs, which is a time-consuming and laborious process. Other approaches that have met with varying success include numerical modeling (Kahana *et al.*, 1999), frequency scaling the nonindividual HRTF to best fit the listeners one (Middlebrooks, 1999), and database matching (Zotkin *et al.*, 2002).

A promising approach for HRTF customization is based on building structural models (Algazi *et al.*, 2002; Brown and Duda, 1998; Raykar *et al.*, 2003) for the HRTF. Different anatomical parts contribute to different temporal and spectral features in the HRIR and HRTF, respectively. Structural models aim to study the relationship between the features and anthropometry. While good geometrical models (Algazi *et al.*, 2002; Duda and Martens, 1998) exist for the effects of head, torso and shoulders, a simple model for the pinna that connects pinna anthropometry to the features in the HRIR does not exist.

The prominent features contributed by the pinna are the

[a]Electronic mail: vikas@umiacs.umd.edu
[b]Electronic mail: ramani@umiacs.umd.edu
[c]Electronic mail: yegna@cs.iitm.ernet.in. This work was performed when the author was visiting the University of Maryland, College Park.

 0001-4966/2005/118(1)/364/11/$22.50

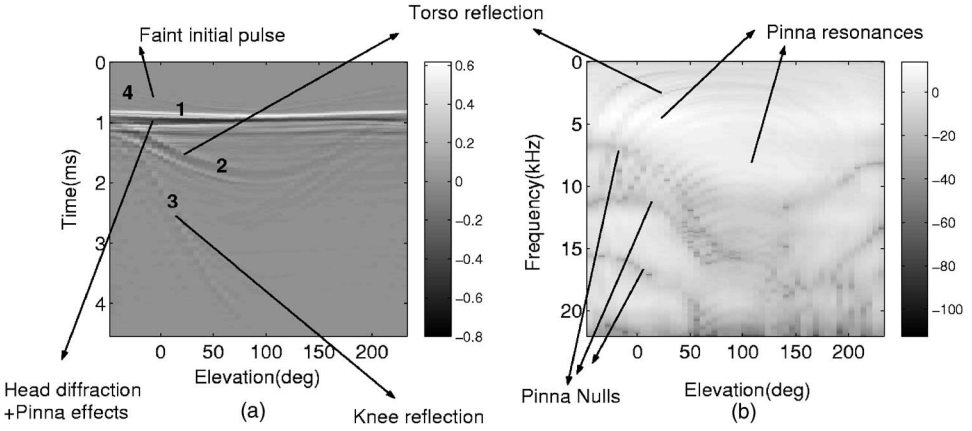

FIG. 1. (a) HRIR and (b) HRTF displayed as images for the right ear for subject 10 in the CIPIC database for azimuth angle $\theta=0°$ for all elevations varying from −45° to +230.625°. The different features are marked in both the HRIR and the HRTF plots. In (a) the gray scale value represents the amplitude of HRIR, and in (b) the gray scale value is the log magnitude of the HRTF in dB.

sharp notches in the spectrum, commonly called the *pinna spectral notches*. There is substantial psychoacoustical (Moore *et al.*, 1989; Wright *et al.*, 1974), behavioral (Gardner and Gardner, 1974; Hebrank and Wright, 1974a; Hofman *et al.*, 1998), and neurophysiological (Poon and Brugge, 1993a,b; Tollin and Yin, 2003) evidence to support the hypothesis that the pinna spectral notches are important cues for vertical localization, i.e., determining the elevation of the source.

One difficulty in developing structural models for the pinna is that it is difficult to automatically extract these frequencies from measured data. Once we have quantitative values for the frequencies of the spectral peaks and notches, a model could be built relating them to the shape and the anthropometry of the pinna. Based on these, new approaches for HRTF customization using these features could be developed, and the role of the pinna in spatial localization better understood. Various psychoacoustical and neurophysiological experiments which explore the significance of the pinna spectral notches can benefit from a procedure that automatically extracts the pinna spectral notches from the measured impulse responses.

The focus of the work presented in this paper is to automatically extract the frequencies corresponding to the spectral notches. A major difficulty is that the experimentally measured HRIR includes the combined effects of the head diffraction and shoulder, torso, and, as an artifact, the knee reflection. Robust signal processing techniques need to be developed to extract the frequencies of the spectral notches due to the pinna alone, in the presence of these confounding features. The methods proposed are based on the residual of a linear prediction model, windowed autocorrelation functions, group-delay function, and all-pole modeling, guided by our prior knowledge of the physics of the problem. Our method also extracts the normal modes first described by Shaw (1997).

Several studies were made to approximate HRTFs by pole-zero models (Asano *et al.*, 1990; Blommer and Wakefield, 1997; Durant and Wakefield, 2002; Haneda *et al.*, 1999; Kulkarni and Colburn, 2004). These studies fit a pole-zero model based on a suitable error measure. However since the spectral notches extracted by them are caused due to various phenomena it is not obvious which of the spectral notches extracted by the model are due to the pinna.

II. STRUCTURAL COMPOSITION OF THE HRIR

Following the work of Algazi *et al.* (2001b) we illustrate the potential of explaining and eventually synthesizing HRTFs from the anthropometry. To this end we will consider measured HRIRs from the CIPIC database (Algazi *et al.*, 2001c). This is a public domain database of high spatial resolution HRIR measurements along with the anthropometry for 45 different subjects. The azimuth is sampled from −80° to 80° and the elevation from −45° to +231° in a head-centered interaural polar coordinate system. For any given azimuth, we form a two-dimensional array, where each column is the HRIR or the HRTF for a given elevation, and the entire array is displayed as an image. This method of visualization helps to identify variation of different features with elevation (Algazi *et al.*, 2001a). Figure 1 shows the HRIR and HRTF images (for all elevations) corresponding to azimuth 0° for the right ear for subject 10 in the CIPIC database. In Fig. 1(a) the gray scale value represents amplitude of the HRIR, and in Fig. 1(b) it is the magnitude of the HRTF in dB. The different features corresponding to different structural components are also marked by hand. Figure 2 shows the HRIR as a mesh plot so that the features can be clearly seen.

Composition of the responses in terms of head diffraction, head and torso reflection, pinna effects and the knee reflection artifact can be seen both in the time domain and in the frequency domain. Most features marked in Fig. 1 were confirmed experimentally with the KEMAR mannequin, where the responses were measured by removing and adding different parts like the pinna, head and torso (Algazi *et al.*, 2001b).

Three distinct ridges, which are marked as 1, 2, and 3, can be seen in the HRIR image plot [Fig. 1(a) and Fig. 2]. The first distinct ridge is due to the direct sound wave that reaches the pinna. We see that immediately after the direct wave, activity is seen in the close vicinity (within 1.2 ms), which is due to diffraction of the sound around the head and the pinna. The corresponding diffraction pattern due to the head in the frequency domain can be explained by Lord Rayleigh's analytical solution for scattering from a sphere (Duda and Martens, 1998; Strutt, 1907).

The second valley shaped ridge between 1 and 2 ms is due to the reflected wave from the torso, reaching the pinna. The delay between the direct and the reflected sound from

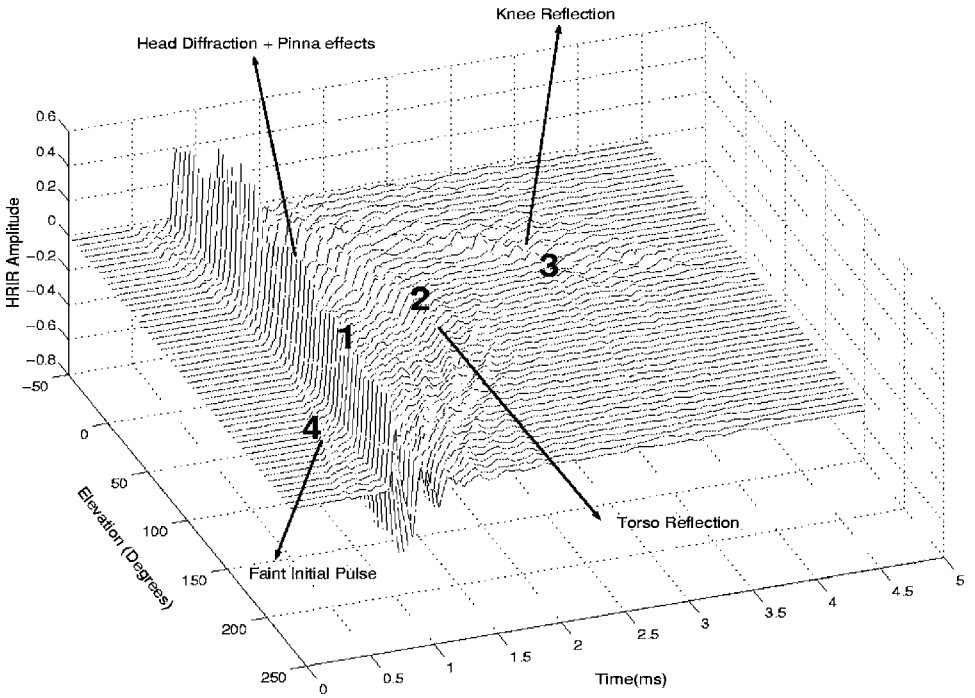

FIG. 2. The HRIR shown as a mesh plot for the right ear for subject 10 in the CIPIC database for azimuth angle $\theta=0°$ for all elevations varying from −45° to +230.625°. The faint initial pulse, the torso reflection, and the knee reflection can be clearly seen in this plot.

the torso is maximum above the head, and decreases on either side. This can be explained using simple ellipsoidal models for the head and torso (Algazi *et al.*, 2002). In the frequency domain the effect of this delay is the arch shaped comb-filter notches that can be seen throughout the spectrum [see Fig. 1(b)]. Some studies have shown that the notches of the comb-filter in the low frequency range (<3 kHz) could be used as a potential cue for vertical localization for low frequency sounds (Algazi *et al.*, 2001a).

The activity seen after 2 ms is due to knee reflections, since these measurements were done with the subjects seated (Algazi *et al.*, 2001c). This is confirmed by the observation that similar activity is not seen in the back ($\varphi>90°$) and absent in the KEMAR. The other artifact is the faint pulse [marked 4 in Figs. 1(a) and 2] seen arriving before the main pulse. This is probably due to the nature of the probe microphone used in the measurements (Algazi *et al.*, 2001c). The probe microphone has a 76 mm silicone probe tube which conducts the acoustic wave to the microphone. It is likely that the signal first hits the microphone outside before reaching the probe.

The other prominent features in the frequency domain, but difficult to see in the time domain, are the prominent notches above 5 kHz. Three prominent notches can be seen in Fig. 1(b) for elevations from −45° to 90°. As the elevation increases the frequency of these notches increases. Experiments with the KEMAR mannequin, in which the HRIRs were measured with and without the pinna (Algazi *et al.*, 2001b), confirm that these notches are caused due to the pinna. Also present in the response are the resonances due to the pinna [the bright patches in the HRTF image in Fig. 1(b)]. The resonances correspond to the six normal modes which were experimentally measured by Shaw (1997) and numerically verified by Kahana *et al.* (1999).

Batteau (1967) suggested that the structure of the pinna caused multiple reflections of sound, and the delay between the direct and the reflected sound varies with the direction of the sound source, providing a localization cue. These delays cause the notches in the spectrum. Hebrank and Wright (1974a,b) attributed the pinna spectral notches to the reflection of sound from the posterior concha wall. This idea was further refined by Lopez-Poveda and Meddis (1996) who incorporated diffraction in the model.

Previous studies done both on humans and animals that discuss the pinna features can be classified as: psychoacoustical (Langendijk and Bronkhorst, 2002; Moore *et al.*, 1989; Wright *et al.*, 1974), behavioral (Gardner and Gardner, 1974; Hebrank and Wright, 1974a; Hofman *et al.*, 1998) and neurophysiological (Poon and Brugge, 1993a,b; Tollin and Yin, 2003). Psychoacoustical experiments have demonstrated that high frequencies are necessary for localization in the vertical plane (Gardner and Gardner, 1974; Hebrank and Wright, 1974b; Musicant and Butler, 1984). By progressively occluding the pinna cavities, it was shown that localization ability decreases with increasing occlusion (Gardner and Gardner, 1974). Hofman *et al.* (1998) measured the localization ability of four subjects before and after the shapes of their ears were changed by inserting plastic moulds in the pinna cavity. Although localization of sound elevation was dramatically degraded immediately after the modification, accurate performance was steadily acquired again.

The spectral peaks and the notches are the dominant cues contributed by the pinna. Since the notch frequency varies smoothly with elevation, it is thought to be the main cue for perception of elevation. On the other hand, the spectral peaks do not show this smooth trend. However, it is likely that the presence or absence of the spectral peak could itself be a strong cue for the elevation. For example, the second normal mode identified by Shaw is excited strongly only for elevations around 90°. Wright *et al.* (1974) present experiments to determine whether delays caused due to pinna reflections are detectable by humans. The results show

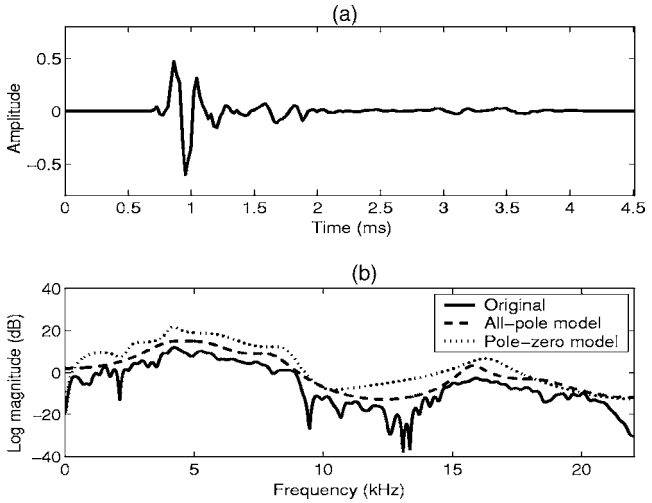

FIG. 3. (a) A typical HRIR for an elevation of 45° and an azimuth of 0°, (b) the log magnitude spectrum, a (12, 12)th order pole-zero model spectrum and a 12th order all-pole model spectrum. In the plots the all-pole spectrum and the pole-zero spectrum are displaced vertically by 5 and 10 dB, respectively, for clarity.

that delay times of 20 μs are easily recognizable when the level of the delayed signal is at least −3.5 dB with respect to the leading signal. Experiments by Moore *et al.* (1989) show that changes in the center frequency of the notches are detectable even for rather narrow notches. Experiments on cats suggest that single auditory nerve fibers are able to signal in their discharge rates the presence of a spectral notch embedded in bursts of noise or in continuous noise (Poon and Brugge, 1993a). A vertical illusion that was observed in cats by Tollin and Yin (2003) can be explained well by a model that attributes vertical localization to recognition of the spectral shape cues.

Thus many studies have clearly established the importance of the pinna spectral notches in the ability to localize sounds. However we must reiterate that these studies are not able to relate the location of the notch to the pinna anthropometry, something that may be of importance in applications that seek to create personalized HRTFs without the measurements.

While previous studies address the issue of how the HRTF is *composed*, there is no attempt to *decompose* the measured HRTF of a real subject into different components. Structural models aim to decompose the HRIR into different components and then build a model for each component.

III. EXTRACTING THE FREQUENCIES OF PINNA SPECTRAL NOTCHES

One obvious way to extract the spectral notches and peaks is through pole-zero modeling (Makhoul, 1975; Steiglitz and McBride, 1965). Several studies were made to approximate the HRTFs by pole-zero models (Asano *et al.*, 1990; Blommer and Wakefield, 1997; Durant and Wakefield, 2002; Haneda *et al.*, 1999; Kulkarni and Colburn, 2004). Figure 3 shows a typical HRIR (subject 10, right ear, elevation 45° and azimuth 0°) we consider for illustration throughout this section. The HRIR is 200 samples long at a sampling frequency of 44.1 kHz, corresponding to 4.54 ms. The log magnitude spectrum, a (12, 12)th order pole-zero model spectrum and a 12th order all-pole model spectrum are also shown in the figure. As can be seen from the plots, due to the combined effects of different phenomena, it is difficult to isolate the notches due to the pinna alone. Also, in order to approximate the spectrum envelope better, the model would typically need to be of high order (>30). Even with the increased order, it is not guaranteed that the relevant notches can be captured. Pole-zero or all-pole models merely approximate the spectrum envelope, as best as they can, depending on the order of the model and the criterion used for approximation. Both the order and the criteria are independent of the nature of the signal being analyzed, and also the features expected to be highlighted. Thus these modeling techniques are unlikely to bring out the specific features one is looking for in the HRIR signal. Our proposed methods do not rely on any models. We apply several signal processing techniques, including windowing, linear prediction residual analysis, group-delay function, and autocorrelation. We will motivate these in the following discussions and present the complete algorithm at the end.

In the measured HRIR there is a very faint pulse arriving before the main direct pulse, due to the nature of the measurement setup. This behavior is likely to cause problems in analysis and hence we consider the signal from the instant of the main pulse [around 0.8 ms in Fig. 3(a)]. This instant is found by taking the slope of the unwrapped phase spectrum or by locating the instant of the maximum amplitude in the signal and shifting back until there is an increase in the signal amplitude.

The spectral notches are caused due to multiple reflections from different parts like the head, torso, knees, and pinna cavities. In order to highlight the effects due to pinna alone, the HRIR signal is first windowed using a half Hann window (Oppenheim and Schafer, 1989). Windowing in the time domain helps isolate the direct component of the signal from the reflected components. A window of size 1.0 ms is used in order to eliminate the torso reflection [at around 1.6 ms in Fig. 3(a)] and the knee reflection [at around 3.2 ms in Fig. 3(a)]. Figure 4(b) shows the log magnitude spectrum of the windowed signal. We see that windowing the wave form reduces the effect of reflection significantly compared to the log magnitude spectrum in Fig. 3(b). We would like to point

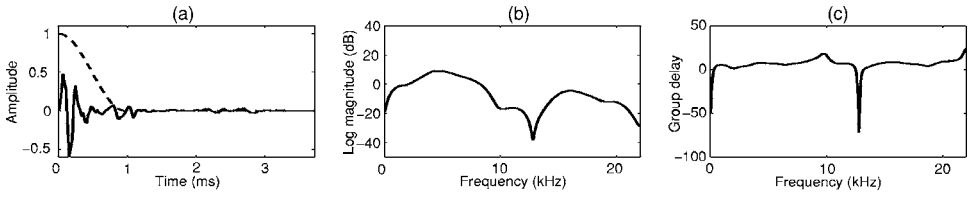

FIG. 4. Effect of windowing the HRIR. (a) HRIR (solid line) and half-Hann window (dotted line) of size 1.0 ms, (b) log magnitude spectra of the windowed signal, and (c) the corresponding group-delay function.

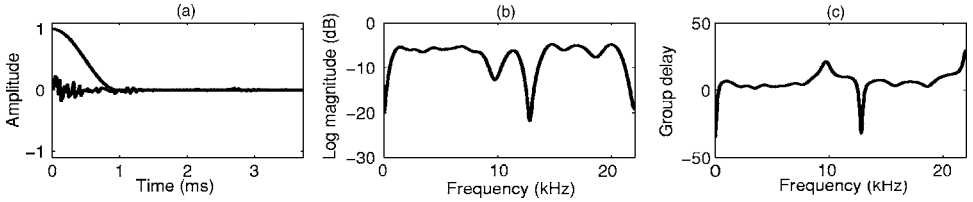

FIG. 5. Effect of windowing the LP residual of the HRIR. (a) The 12th order LP residual and half Hann window of size 1.0 ms, (b) the log magnitude spectra of the windowed LP residual signal, and (c) the corresponding group-delay function.

out that the exact size of the window is not crucial. A window size of 1.0 ms should be sufficient to suppress the reflections due to the torso and the knees.

We extract the spectral notches from the group-delay function rather than the magnitude spectrum. The additive nature of the phase spectra of systems in cascade and the high frequency resolution properties of the group-delay functions help in providing better resolution of peaks and valleys even for a short time segment of the data (Yegnanarayana, 1978; Yegnanarayana *et al.*, 1984). The group delay function is the negative of the derivative of the phase spectrum of a signal. If $X(\omega)$ is the complex frequency response of a signal $x(n)$, then the group-delay function $\tau(\omega)$ is given by

$$\tau(\omega) = -\frac{d\theta(\omega)}{d\omega} \tag{1}$$

where ω is the angular frequency, and $\theta(\omega)$ is the phase angle of $X(\omega)$. The group-delay function can be computed directly using the Fourier transform of $x(n)$ and $nx(n)$, as follows (Oppenheim and Schafer, 1989). Let $X(\omega)$ and $Y(\omega)$ be the Fourier transforms of $x(n)$ and $nx(n)$, respectively,

$$\begin{aligned} X(\omega) &= \sum_{n=0}^{N-1} x(n)e^{-j\omega n} = X_R(\omega) + jX_I(\omega), \\ Y(\omega) &= \sum_{n=0}^{N-1} nx(n)e^{-j\omega n} = Y_R(\omega) + jY_I(\omega). \end{aligned} \tag{2}$$

Since

$$\log X(\omega) = \log|X(\omega)| + j\theta(\omega), \tag{3}$$

the group-delay function can be written as

$$\begin{aligned} \tau(\omega) &= -\frac{d}{d\omega}[\theta(\omega)] = -\operatorname{Im}\left(\frac{d}{d\omega}[\log X(\omega)]\right) \\ &= \frac{X_R(\omega)Y_R(\omega) + X_I(\omega)Y_I(\omega)}{X_R^2(\omega) + X_I^2(\omega)}, \end{aligned} \tag{4}$$

where $\operatorname{Im}(z)$ corresponds to the imaginary part of z. Figure 4(c) shows the group-delay function of the windowed signal (window size 1.0 ms). Compared to the log magnitude spectrum in Fig. 4(b), the group-delay function shows a better resolution of the notches.

However, windowing reduces the frequency domain resolution and also introduces artifacts. The artifacts of windowing may also mask or alter the frequencies of the spectral notches due to the pinna. One way to reduce the artifacts due to windowing is to remove the interdependence among adjacent signal samples by using the linear prediction (LP) residual of the original HRIR and then windowing the residual. This corresponds to removing the resonances from the signal.

The residual signal is derived using a 12th order LP analysis (Makhoul, 1975). LP analysis basically fits an all-pole model to the given signal. In LP analysis the signal $x(n)$ is predicted approximately from a linearly weighted summation of the past p samples, i.e.,

$$\hat{x}(n) = -\sum_{k=1}^{p} a_k x(n-k). \tag{5}$$

The error in the prediction, i.e., the LP residual, is therefore given by

$$e(n) = x(n) - \hat{x}(n) = x(n) + \sum_{k=1}^{p} a_k x(n-k). \tag{6}$$

The total squared error is

$$E = \sum_n e(n)^2 = \sum_n \left[x(n) + \sum_{k=1}^{p} a_k x(n-k) \right]^2. \tag{7}$$

Minimization of the mean squared error with respect to the coefficients $\{a_k\}$ gives the following normal equations (Makhoul, 1975):

$$\sum_{k=1}^{p} a_k R(n-k) = -R(k), \quad k = 0,1,\ldots,p, \tag{8}$$

where $R(k) = \Sigma_n x(n)x(n-k)$ is called the autocorrelation function for a lag of k samples. Equation (8) can be solved to get the coefficients $\{a_k\}$. Substituting the solution of the normal equations Eq. (8) into the expression for the error in Eq. (6) gives the sequence corresponding to the minimum total error, the LP residual.

LP analysis can be interpreted as the removal of redundancy in the signal samples by removing the predictable part from the signal. The linearly weighted past samples are used to predict the sample at the current sampling instant. The LP residual looks like noise, as correlation among samples is significantly reduced compared to the original signal. The autocorrelation function of the LP residual looks like an impulse at the origin (zero delay) with very small amplitudes for other lags. Effect of direct windowing of the LP residual is shown in Fig. 5, where the spectral notches can be seen to appear more prominently compared to the plots in Fig. 4.

The autocorrelation function of the windowed LP residual helps to reduce the effects due to truncation and noise. The autocorrelation function $R(m)$ of a signal $x(n)$ of length N is given by

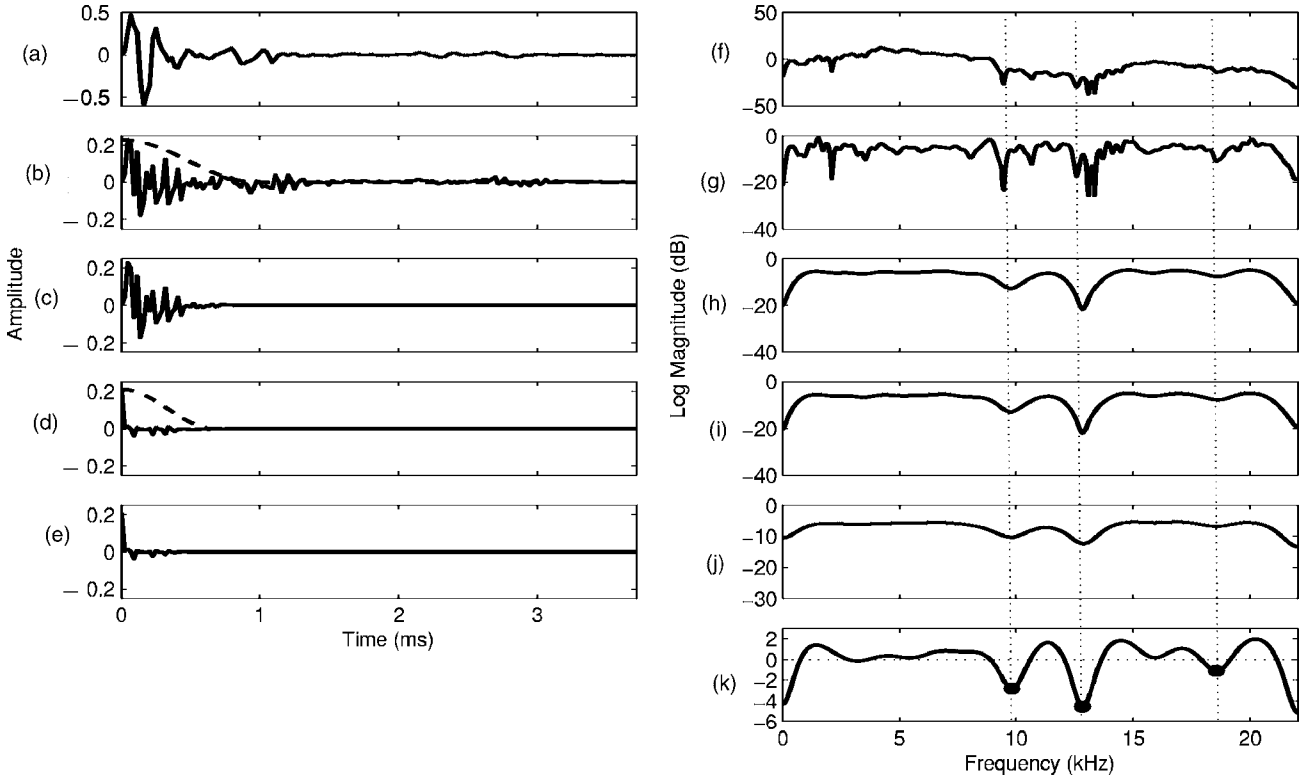

FIG. 6. Signal processing steps for extracting the pinna spectral notch frequencies. (a) Original HRIR signal, (b) 12th order LP residual, (c) windowed LP residual (1.0 ms half Hann window), (d) autocorrelation function of the windowed LP residual, and (e) windowed autocorrelation function (0.7 ms half Hann window). The plots (f), (g), (h), (i), and (j) show the log magnitude spectrum (in dB) corresponding to signals in (a), (b), (c), (d), and (e), respectively. The plot (k) shows the group-delay function of the windowed autocorrelation function. The local minima in the group-delay function (zero thresholded) are shown.

$$R(m) = \sum_{n=m}^{N-1} x(n)x(n-m). \tag{9}$$

The autocorrelation function of a signal produces decreasing amplitudes away from its peak, which helps in computing the group-delay function better, while at the same time preserving most of the details of the spectral envelope. The resolution of the spectral components is enhanced in the group-delay function of the autocorrelation function of the windowed LP residual. Using the zero threshold for the group delay function, all valleys below the zero value are marked as relevant notches and their frequencies are noted. In practice a slightly lower threshold of −1 was found to give better results and eliminated any spurious nulls caused due to windowing.

The sequence of signal processing operations is summarized in the following and the effect of each step on the HRIR and HRTF is shown in Fig. 6.

(1) Determine the initial onset of the HRIR and use the HRIR from that instant.
(2) Derive the pth ($p=10-12$) order LP residual from the given HRIR [Fig. 6(b)].
(3) Window the LP residual using a half Hann window of around 1.0 ms [Fig. 6(c)].
(4) Compute the autocorrelation function of the windowed LP residual [Fig. 6(d)].
(5) Window the autocorrelation function using a half Hann window of around 1.0 ms [Fig. 6(e)].
(6) Compute the group-delay function of the windowed autocorrelation function [Fig. 6(k)].
(7) Threshold the group-delay function and locate the local minima.

Since the spectra of the windowed LP residual is a smooth function with nulls, the spectrum can be inverted to obtain a spectrum with prominent peaks. An all-pole model can be fit to this spectrum by computing the autocorrelation function, and then applying the Levinson–Durbin method (Makhoul, 1975) for the first few (10) autocorrelation coefficients. The frequencies corresponding to the complex roots of the all-pole model correspond to the frequencies of the prominent nulls in the spectrum of the windowed HRIR. This method also helps to get the depth and the width of the spectral notches. However, in order to extract the frequencies of the spectral notches the method based on group-delay is preferred since we do not need to specify the model order.

IV. RESULTS

The developed algorithm is applied on the measured HRIRs of different subjects and for different elevations and azimuth angles in the CIPIC database. As an example, Figs. 7(a)–7(h) show the spectral notch frequencies for the right ear HRTF corresponding to subject 10 in the CIPIC database. The notch frequencies are plotted as a function of elevation for different azimuths. Note that negative azimuth angles correspond to the contralateral HRTF, with the pinna in the

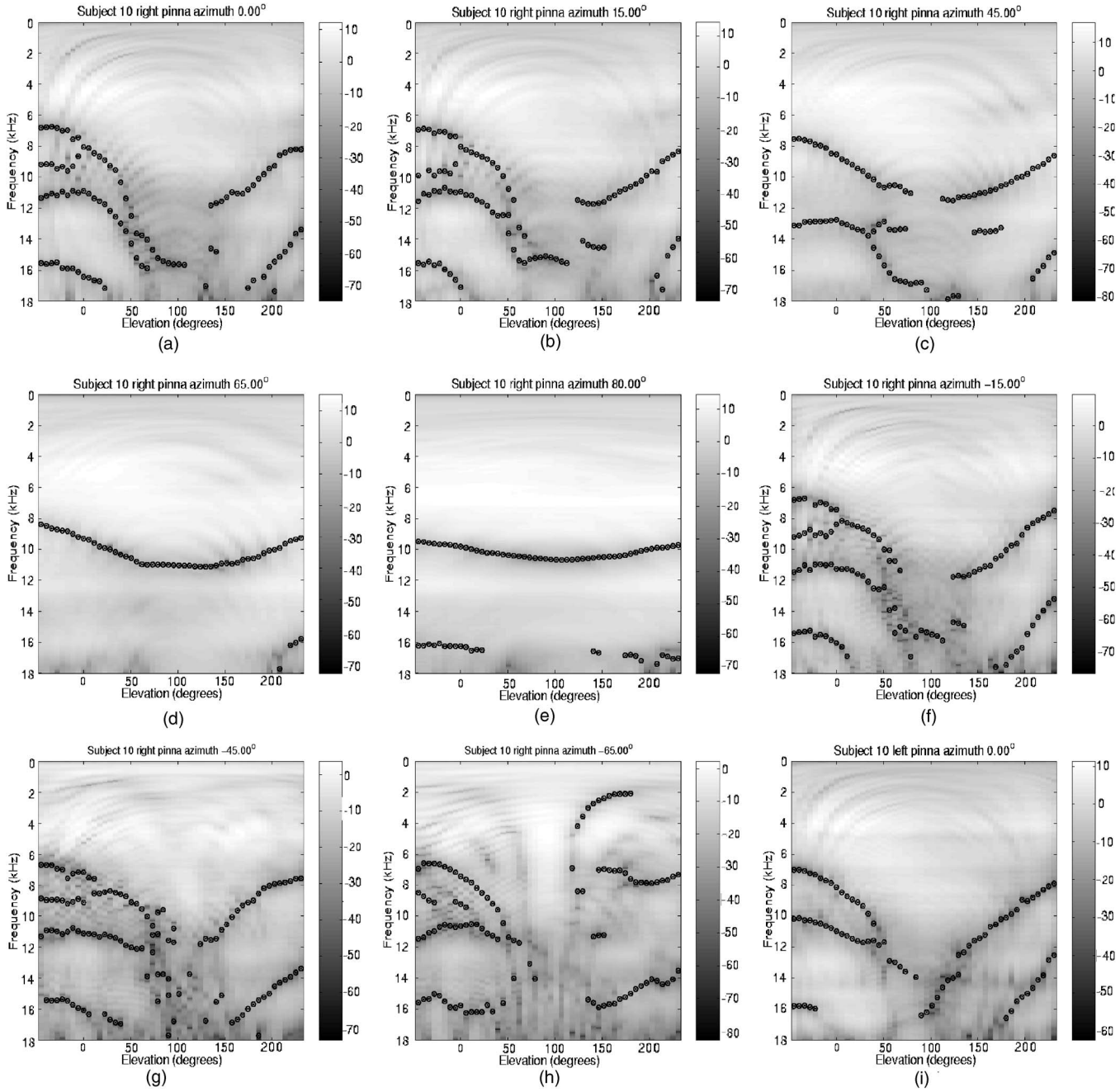

FIG. 7. The spectral notch frequencies extracted for subject 10 *right* pinna in the CIPIC database for azimuth angles (a)0°, (b)15°, (c)45°, (d)65°, (e)80°, (f) −15°, (g)−45°, and (h)−65°. (i) The spectral notch frequencies corresponding to the *left* pinna of subject 10 for azimuth 0°.

shadow region of the head and the diffraction effects prominent. However, some pinna notches are still dominant and we were able to extract them using the same algorithm. A few notches due to head diffraction effects also appear [see Fig. 7(h)].

The pinna notches in the contralateral side can be explained if we assume that the sound diffracts around the head entering the contralateral concha at approximately the same elevation angle as if the source were in the ipsilateral hemisphere (Lopez-Poveda and Meddis, 1996). However, since elevation perception is essentially thought to be monaural (Middlebrooks and Green, 1991) it is likely that humans use only the near ear (i.e., the ear closest to the source) for vertical localization. It is still possible that the pinna notches in the contralateral HRTF could provide extra cues for vertical localization. Figure 7(i) shows the notch frequencies for the left pinna for subject 10 and azimuth 0°. It was observed for most subjects that left and the right pinna do not have the same shape and dimensions (Algazi *et al.*, 2001c). The frequencies of the notches and their variation with elevation are different for the left and the right pinna. Figures 8 show the same results for nine different subjects and for azimuth 0°. Similar results are obtained when the analysis is applied to all the subjects in the database.

We note that LP analysis can also be used to extract spectral peaks in the spectrum. The poles extracted by LP analysis appear to correspond to the resonances of the pinna reported by Shaw (1997), who identified the normal modes

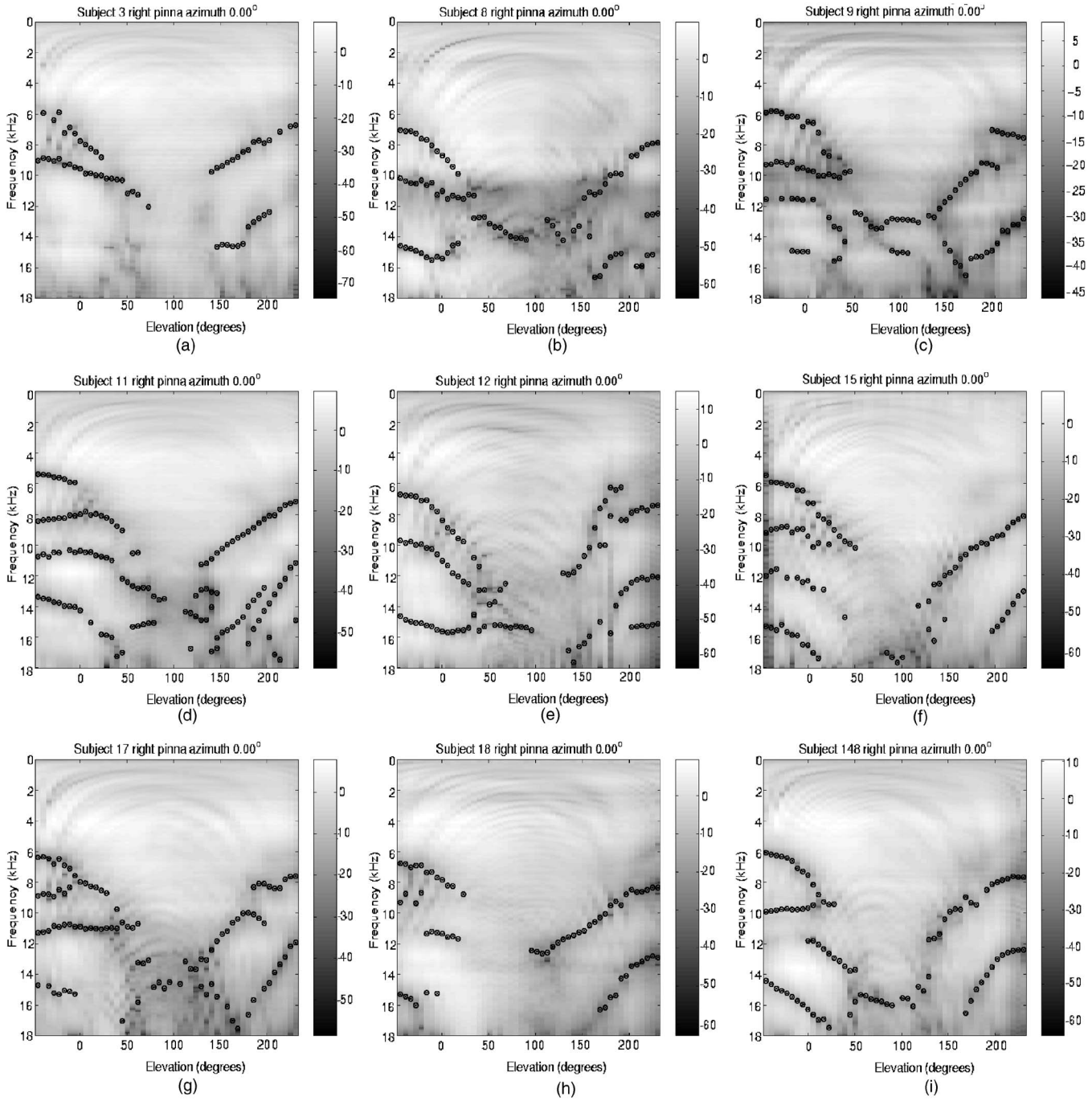

FIG. 8. The spectral notch frequencies for different elevations extracted for the right pinna for azimuth 0° for different subjects in the CIPIC database.

by searching for the response maxima as the sound frequency and the source position were varied. The first mode is a simple quarter-wavelength depth resonance with uniform sound pressure across the base of the concha. It is strongly excited from all directions. The other modes are essentially transverse and fall into two groups: a vertical pair (modes 2 and 3) and a horizontal triplet (modes 4, 5, and 6). The poles extracted by LP analysis correspond to the resonances of the pinna reported by Shaw. Figure 9 shows the frequency response of the 12th order all-pole model for the subject 10 for azimuth 0° as a function of different elevations as a mesh plot. These six modes are marked in the plot.

V. SPECTRAL NOTCHES AND PINNA SHAPE

The proposed procedure was successful in extracting the pinna spectral notches, visible to the human eye. We hope this would be a useful tool for researchers to study the significance of the pinna spectral notches to location perception and also to build structural models for the pinna. While perceptual tests are beyond the scope of this paper, we demonstrate a potential use of our procedure by showing that the pinna spectral notches are indeed related to the shape and anthropometry of the pinna.

The structure of the pinna is fairly complicated and difficult to characterize by simple models. To a first approxima-

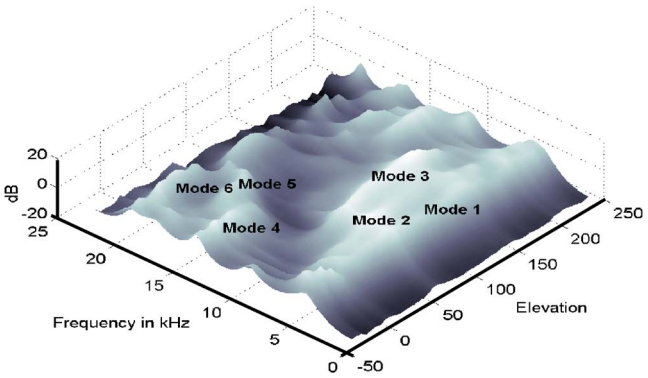

FIG. 9. Frequency response of the 12th order all-pole model for azimuth 0° as a function of different elevations. The six modes are approximately marked.

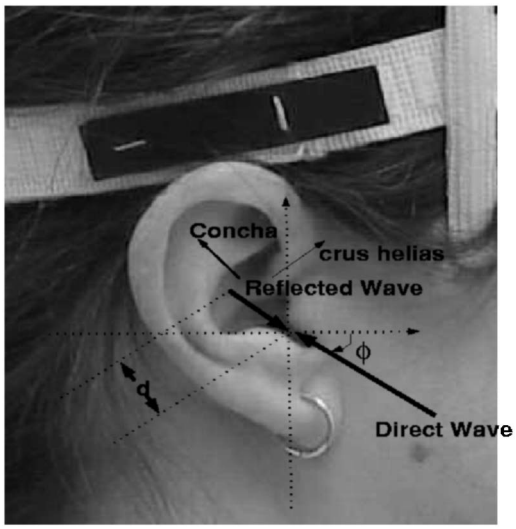

FIG. 10. A simple reflection model for the pinna spectral notches. The direct wave incident at an angle ϕ gets reflected from the concha. The time delay corresponds to a length of $2d$. The pinna image is taken from the CIPIC database.

tion the response can be characterized by peaks and notches observed in the spectrum. Figure 10 shows the simple reflection model. The direct wave incident at an angle φ is reflected from the concha wall. If $x(t)$ is the incident wave then the measured signal $y(t)$ is the sum of the direct and the reflected wave,

$$y(t) = x(t) + ax(t - t_d(\varphi)), \tag{10}$$

where a is the reflection coefficient and $t_d(\varphi)$ is the time delay given by

$$t_d(\varphi) = \frac{2d(\varphi)}{c}, \tag{11}$$

where $2d(\varphi)$ is the distance corresponding to the delay and c is the speed of the sound (approximately 343 m/s). The dis-

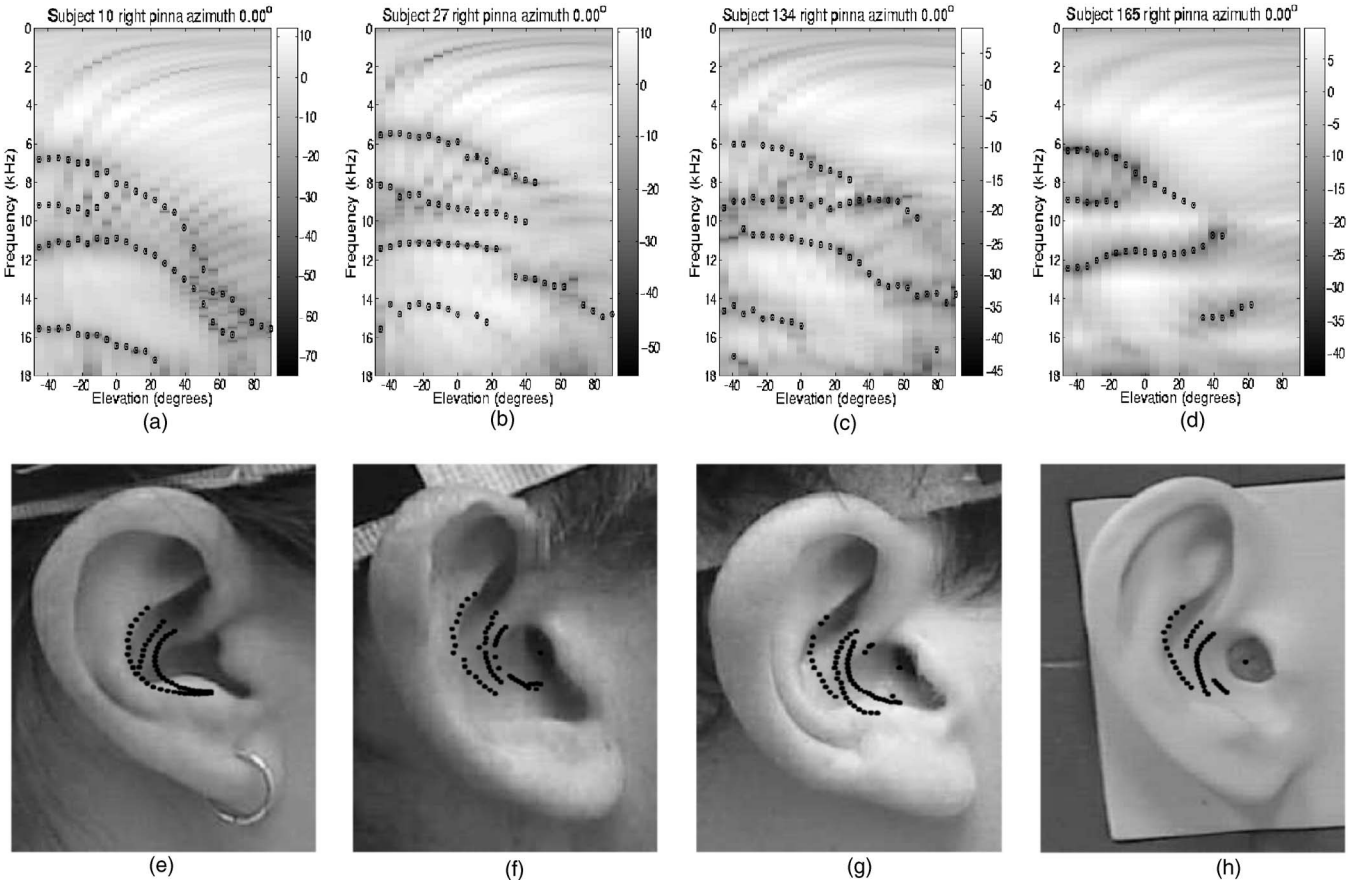

FIG. 11. The spectral notch frequencies for different elevations (from −45° to 90°) extracted for the right pinna for azimuth 0° (a) subject 10, (b) subject 27, (c) subject 134, and (d) subject 165 in the CIPIC database. The dimensions corresponding to the spectral notches marked on the pinna image for (e) subject 10, (f) subject 27, (g) subject 134, and, (h) subject 165, respectively. The pinna images are taken from the CIPIC database.

tance $d(\varphi)$ depends on the angle φ and shape of the pinna. The delay $t_d(\varphi)$ causes periodic notches in the spectrum, whose frequencies are given by

$$f_n(\varphi) = \frac{(2n+1)}{2t_d(\varphi)} = \frac{c(2n+1)}{4d(\varphi)}, \quad n = 0, 1, \ldots . \tag{12}$$

The frequency of the first spectral notch is given by

$$f_0(\varphi) = \frac{c}{4d(\varphi)}. \tag{13}$$

In practice there are multiple reflections occurring in the pinna. Each reflection gives rise to a series of periodic spectral notches. In the previous section we extracted the frequencies of the spectral notches. From Eq. (13) we can calculate the distance $d(\phi)$ corresponding to the notch frequency $f_0(\phi)$. As the angle ϕ is varied, the notch frequency varies depending on the the shape of the pinna. The variation of the notch frequency reflects the shape of the pinna. The pinna images as well as the ear anthropometry are available in CIPIC database. The distance can be marked on the pinna image approximately. Figure 11(a) shows the notch frequencies extracted for aximuth 0° and elevation varying from −45° to 90° (subject 10 right pinna). We consider only elevations in front of the head, since for elevations behind the ear the mechanism of the spectral notches is not clear. For each of the extracted notches the corresponding distance is plotted on the image of the pinna [Fig. 11(e)] and appears consistent with this argument. It is interesting to see that the shape and dimensions of the concha are clearly seen in the extracted frequencies of the spectral nulls. The first spectral null thus appears to be caused due to reflection from the concha. As the elevation is varied it traces out the shape of the concha. The third spectral null could be due to the inner cavity in the concha caused by the crus helias dividing the concha into two. Figure 11 shows the same results for three other subjects in the CIPIC database, and exhibit similar trends.

These results suggest that the shape of the different cavities in the pinna are as important as the gross dimensions. A model for the pinna should take this into consideration. Since measurement of the HRIR is a tedious process, a particularly appealing method for synthesizing the HRIR would be to take the image of a pinna and obtain the notch frequencies by analyzing the pinna anthropometry.

VI. SUMMARY

We proposed signal processing algorithms for extraction of the pinna spectral notch frequencies from experimentally measured HRIRs. The difficulties in the analysis of HRIR caused by the combined effects of several components are discussed, and windowing in the time domain was proposed to reduce the effects of the reflected components. The effectiveness of the methods in isolating and determining the frequencies of the spectral nulls due to pinna has been demonstrated using the CIPIC database. The extracted spectral notch frequencies are related to the shape of the pinna. The code is made available to the research community on the first author's website.

ACKNOWLEDGMENTS

The support of NSF Award No. ITR-0086075 is gratefully acknowledged. We would also like to thank associate editor and the two reviewers for their comments and suggestions which helped to improve the clarity and quality of the paper. The first author would like to thank Prof. Richard Duda for the discussions on the CIPIC database.

Algazi, V. R., Avendano, C., and Duda, R. O. (**2001a**). "Elevation localization and head-related transfer function analysis at low frequencies," J. Acoust. Soc. Am. **109**, 1110–1122.

Algazi, V. R., Duda, R. O., Duraiswami, R., Gumerov, N. A., and Tang, Z. (**2002**). "Approximating the head-related transfer function using simple geometric models of the head and torso," J. Acoust. Soc. Am. **112**, 2053–2064.

Algazi, V. R., Duda, R. O., Morrison, R. P., and Thompson, D. M. (**2001b**). "Structural Composition and Decomposition of HRTF's," in Proceedings of the 2001 IEEE Workshop on Applications of Signal Processing to Audio and Acoustics (Mohonk Mountain House, New Paltz, NY), pp. 103–106.

Algazi, V. R., Duda, R. O., Thompson, D. M., and Avendano, C. (**2001c**). "The CIPIC HRTF Database," in Proceedings of the 2001 IEEE Workshop on Applications of Signal Processing to Audio and Acoustics (Mohonk Mountain House, New Paltz, NY), pp. 99–102.

Asano, F., Suzuki, Y., and Sone, T. (**1990**). "Role of spectrum cues in median plane localization," J. Acoust. Soc. Am. **88**, 159–168.

Batteau, D. W. (**1967**). "The role of the pinna in human localization," Proc. R. Soc. London, Ser. B **168**, 158–180.

Blauert, J. (**1996**). *Spatial Hearing: The Psychophysics of Human Sound Localization* (MIT, Cambridge, MA).

Blommer, M. A. and Wakefield, G. H. (**1997**). "Pole-zero approximations for head-related transfer functions using a logarithmic error criterion," IEEE Trans. Speech Audio Process. **5**, 278–287.

Brown, C. P. and Duda, R. O. (**1998**). "A structural model for binaural sound synthesis," IEEE Trans. Speech Audio Process. **6**, 476–488.

Duda, R. O. and Martens, W. L. (**1998**). "Range dependence of the response of a spherical head model," J. Acoust. Soc. Am. **104**, 3048–3058.

Durant, E. A. and Wakefield, G. H. (**2002**). "Efficient model fitting using a genetic algorithm: Pole-zero approximations of HRTFs," IEEE Trans. Speech Audio Process. **10**, 18–27.

Gardner, M. B. and Gardner, R. S. (**1974**). "Problem of localization in the median plane: Effect of pinna cavity occlusion," J. Acoust. Soc. Am. **53**, 400–408.

Haneda, Y., Makino, S., Kaneda, Y., and Kitawaki, N. (**1999**). "Common-acoustical-pole and zero modeling of head-related transfer functions," IEEE Trans. Speech Audio Process. **7**, 188–196.

Hebrank, J. and Wright, D. (**1974a**). "Are two ears necessary for localization of sound sources on the median plane?," J. Acoust. Soc. Am. **56**, 935–938.

Hebrank, J. and Wright, D. (**1974b**). "Spectral cues used in the location of sound sources on the median plane," J. Acoust. Soc. Am. **56**, 1829–1834.

Hofman, P., Van Riswick, J., and Van Opstal, A. (**1998**). "Relearning sound localization with new ears," Nat. Neurosci. **1**, 417–421.

Kahana, Y., Nelson, P. A., Petyt, M., and Choi, S. (**1999**). "Numerical modelling of the transfer functions of a dummy-head and of the external ear," in Proceedings of the AES 16th International Conference on Spatial Sound Reproduction, Rovaneimi, pp. 330–345.

Kuhn, G. F. (**1977**). "Model for interaural time differences in the azimuthal plane," J. Acoust. Soc. Am. **62**, 157–167.

Kulkarni, A. and Colburn, H. S. (**2004**). "Infinite-impulse-response models of the head-related transfer function," J. Acoust. Soc. Am. **115**, 1714–1728.

Langendijk, E. H. A. and Bronkhorst, A. W. (**2002**). "Contribution of spectral cues to human sound localization," J. Acoust. Soc. Am. **112**, 1583–1596.

Lopez-Poveda, E. A. and Meddis, R. (**1996**). "A physical model of sound diffraction and reflections in the human concha," J. Acoust. Soc. Am. **100**, 3248–3259.

Makhoul, J. (**1975**). "Linear prediction: A tutorial review," Proc. IEEE **63**, 561–580.

Middlebrooks, J. C. (**1999**). "Virtual localization improved by scaling nonindividualized external-ear functions in frequency," J. Acoust. Soc. Am. **106**, 1493–1509.

Middlebrooks, J. C. and Green, D. M. (**1991**). "Sound localization by human listeners," Annu. Rev. Psychol. **42**, 135–159.
Moore, B. C. J., Oldfield, S. R., and Dooley, G. (**1989**). "Detection and discrimination of spectral peaks and notches at 1 and 8 kHz," J. Acoust. Soc. Am. **85**, 820–836.
Musicant, A. and Butler, R. (**1984**). "The influence of pinnae-based spectral cues on sound localization," J. Acoust. Soc. Am. **75**, 1195–1200.
Oppenheim, A. and Schafer, R. W. (**1989**). *Discrete-Time Signal Processing* (Prentice-Hall, Englewood Cliffs, NJ).
Poon, P. and Brugge, J. F. (**1993a**). "Sensitivity of auditory nerve fibers to spectral notches," J. Neurophysiol. **70**, 655–666.
Poon, P. and Brugge, J. F. (**1993b**). "Virtual-space receptive fields of single auditory nerve fibers," J. Neurophysiol. **70**, 667–676.
Raykar, V. C., Yegnanarayana, B., Duraiswami, R., and Davis, L. (**2003**). "Extracting significant features from the HRTF," in Proceedings of the 2003 International Conference on Auditory Display, pp. 115–118.
Shaw, E. A. G. (**1997**). "Acoustical features of the human ear," in *Binaural and Spatial Hearing in Real and Virtual Environments*, edited by R. H. Gilkey and A. T. B. (Erlbaum, Mahwah, NJ), pp. 25–47.
Shinn-Cunningham, B. G., Santarelli, S. G., and Kopco, N. (**2000**). "Tori of confusion: Binaural cues for sources within reach of a listener," J. Acoust. Soc. Am. **107**, 1627–1636.
Steiglitz, K. and McBride, L. E. (**1965**). "A technique for the identification of linear systems," IEEE Trans. Autom. Control **10**, 461–464.
Strutt, J. W. (**1907**). "On our perception of sound direction," Philos. Mag. **13**, 214–232.
Tollin, D. J. and Yin, T. C. T. (**2003**). "Spectral cues explain illusory elevation effects with stereo sounds in cats," J. Neurophysiol. **90**, 525–530.
Wenzel, E. M., Arruda, M., Kistler, D. J., and Wightman, F. L. (**1993**). "Localization using nonindividualized head-related transfer functions," J. Acoust. Soc. Am. **94**, 111–123.
Wightman, F. L. and Kistler, D. J. (**1997**). "Factors affecting the relative salience of sound localization cues," in *Binaural and Spatial Hearing in Real and Virtual Environments*, edited by R. H. Gilkey and T. B. Anderson (Erlbaum, Mahwah, NJ).
Wright, D., Hebrank, J. H., and Wilson, B. (**1974**). "Pinna reflections as cues for localization," J. Acoust. Soc. Am. **56**, 957–962.
Yegnanarayana, B. (**1978**). "Formant extraction from linear prediction phase spectra," J. Acoust. Soc. Am. **63**, 1638–1640.
Yegnanarayana, B., Saikia, D. K., and Krishnan, T. R. (**1984**). "Significance of group delay functions in signal reconstruction from spectral magnitude or phase," IEEE Trans. Acoust., Speech, Signal Process. **32**, 610–623.
Zotkin, D. N., Duraiswami, R., Davis, L., Mohan, A., and Raykar, V. C. (**2002**). "Virtual audio system customization using visual matching of ear parameters," in Proceedings of the 2002 International Conference on Pattern Recognition, pp. 1003–1006.

Enhancement of temporal periodicity cues in cochlear implants: Effects on prosodic perception and vowel identification

Tim Green,[a] Andrew Faulkner, Stuart Rosen, and Olivier Macherey
Department of Phonetics and Linguistics, University College London, Wolfson House, 4 Stephenson Way, London, NW1 2HE, United Kingdom

(Received 27 July 2004; revised 22 March 2005; accepted 8 April 2005)

Standard continuous interleaved sampling processing, and a modified processing strategy designed to enhance temporal cues to voice pitch, were compared on tests of intonation perception, and vowel perception, both in implant users and in acoustic simulations. In standard processing, 400 Hz low-pass envelopes modulated either pulse trains (implant users) or noise carriers (simulations). In the modified strategy, slow-rate envelope modulations, which convey dynamic spectral variation crucial for speech understanding, were extracted by low-pass filtering (32 Hz). In addition, during voiced speech, higher-rate temporal modulation in each channel was provided by 100% amplitude-modulation by a sawtooth-like wave form whose periodicity followed the fundamental frequency (*F*0) of the input. Channel levels were determined by the product of the lower- and higher-rate modulation components. Both in acoustic simulations and in implant users, the ability to use intonation information to identify sentences as question or statement was significantly better with modified processing. However, while there was no difference in vowel recognition in the acoustic simulation, implant users performed worse with modified processing both in vowel recognition and in formant frequency discrimination. It appears that, while enhancing pitch perception, modified processing harmed the transmission of spectral information. © *2005 Acoustical Society of America.* [DOI: 10.1121/1.1925827]

PACS number(s): 43.66.Ts, 43.71.Bp, 43.66.Hg [KWG] Pages: 375–385

I. INTRODUCTION

As cochlear implant systems have becoming increasingly successful at providing basic speech recognition abilities, consideration has begun to be given to their performance in aspects of speech perception that have previously received little attention. One such aspect is intonation, as conveyed by voice pitch variation. Intonation is, of course, crucial to the perception of tonal languages in which pitch information conveys lexical meaning, but also has important functions in all other languages. It is a major component of prosody, and is widely held to play an important role in early language development (e.g., Jusczyk, 1997), which is of particular significance in light of the increasing number of very young children receiving implants.

In normal hearing, the principal cues to voice pitch derive from the ability of the auditory periphery to divide the speech input into a large number of frequency channels. Lower speech harmonics are resolved, and the neural coding of resolved harmonics provides both place and temporal cues related to *F*0. In contrast, in most commonly used cochlear implant speech processing strategies, spectro-temporal information is conveyed in the form of fixed-rate pulse trains that are amplitude modulated by low-pass envelopes extracted from a relatively small number of frequency bands (Seligman and McDermott, 1995; Wilson *et al.*, 1991; Vandali *et al.*, 2000). As a consequence, speech harmonics are not resolved, the spectral ("place") cues used in normal hearing are not available, and pitch perception is thought to depend upon the derivation of temporal cues from modulation components of the amplitude envelope that are related to voice *F*0. Such cues are, in principle, available, as long as the cutoff frequency of the envelope smoothing filter is high enough to pass *F*0, and the pulse rate is at least four to five times the modulation frequency, allowing accurate representation of the modulating envelope (McKay, McDermott, and Clark, 1994; Wilson, 1997). However, the ability to perceptually encode temporal amplitude modulation is limited, particularly for frequencies at the higher end of the human voice pitch range, both in normally hearing listeners presented with amplitude modulated noise (Burns and Viemeister, 1976; Burns and Viemeister, 1981; Formby, 1985; Grant, Summers, and Leek, 1998; Hanna, 1992; Pollack, 1969) and in implant users detecting amplitude modulations in pulse trains (Busby, Tong, and Clark, 1993; Cazals *et al.*, 1994; Donaldson and Viemeister, 2002; Shannon, 1992).

Consistent with these constraints on the availability of pitch cues, the limited amount of research examining voice pitch perception in continuous interleaved sampling (CIS) or similarly processed speech has shown levels of intonation perception that are severely limited compared to normal hearing. This is true both for implant users (Au, 2003; Barry *et al.*, 2002; Ciocca *et al.*, 2002; Green, Faulkner, and Rosen, 2004; Lee *et al.*, 2002; Peng *et al.*, 2004; Wei *et al.*, 2000; Wei *et al.*, 2004), and for normally hearing subjects listening to noise-excited vocoder acoustic simulations (Fu *et al.*, 1998; Green, Faulkner, and Rosen, 2002; Green, Faulkner, and Rosen, 2004; Xu, Tsai, and Pfingst, 2002).

[a]Electronic mail: tim@phon.ucl.ac.uk

In some early speech processing strategies, the rate of pulsatile stimulation was controlled by *F*0 (e.g., Fourcin *et al.*, 1979; Tong *et al.*, 1980). Implant users are generally able to discriminate differences in pulse rate reasonably well for rates up to a few hundred hertz (McDermott and McKay, 1997; Pijl and Schwarz, 1995; Townshend *et al.*, 1987; Wilson *et al.*, 1997; Zeng, 2002) and such an approach may well be optimal for conveying voice pitch information. However, such strategies are typically worse on standard measures of speech perception than CIS-like strategies, presumably because of poorer transmission of spectral information (e.g., McKay and McDermott, 1993; McKay *et al.*, 1992; Skinner *et al.*, 1999). Consequently, this kind of strategy has largely been discarded, although there has recently been some interest in the possibility that, for implant users who speak tonal languages, the advantages in tone recognition afforded may outweigh the potential disadvantages (Lan *et al.*, 2004). In general, however, for the foreseeable future, the majority of implant users are likely to use CIS-like strategies, particularly since most recent developments in the design of implant systems have been motivated by the possibility that very high pulse rates may lead to patterns of neural responses that more closely resemble those found in normal hearing (e.g., Rubenstein *et al.*, 1999).

One recent approach to enhancing pitch cues in CIS-processed speech involved modifying the properties of the analysis filters that divide the input into frequency bands, to try to restore a form of place cue to pitch (Geurts and Wouters, 2004). The filters typically used in CIS processing have flat passbands and are relatively broad, particularly at lower frequencies. In contrast, Geurts and Wouters' modified processing strategy employed triangular filters, designed to have a sharply peaked frequency response, and, ideally, a maximum width of one octave. The aim was that the first harmonic would be resolved in two adjacent filters, and changes in its frequency would be closely reflected in the relative outputs of the two filters. McDermott and McKay (1994) found that when pulse trains were presented simultaneously to two adjacent electrodes, implant users perceived a single pitch which varied according to the relative difference in levels between the pulses on the two electrodes. On this basis it was expected that the modified filtering would result in an effective place cue to changes in voice pitch. This expectation was supported by the fact that the four users of the LAURA cochlear implant tested were generally better at discriminating differences in the *F*0 of synthesized monophthongs with the modified, rather than the typical, filtering. However, it remains unclear whether this approach will still be effective with more natural speech stimuli. Natural speech typically contains dynamic variations in spectral shape, resulting in changes in the distribution of energy in different channels which may conflict with and obscure the place cue to *F*0.

Other attempts to improve intonation perception in cochlear implant systems have focused on enhancing the temporal pitch cues derived from envelope modulations corresponding to *F*0. Geurts and Wouters (2001) implemented a modified version of CIS processing that featured a number of changes from standard strategies, including the subtraction of the output of a 50 Hz low-pass filter from that of the standard 400 Hz low-pass filter, resulting in a larger modulation depth for *F*0-related fluctuations. However, they did not find significant improvements in the ability of four users of the LAURA cochlear implant to discriminate changes in the *F*0 of synthesized monophthongs with the new strategy compared to standard CIS processing.

Green, Faulkner, and Rosen (2004) adopted a different approach to the enhancement of temporal pitch cues, based on the idea that *F*0 could be extracted from voiced segments of the speech input and reintroduced in a simplified form. In a modified processing strategy amplitude envelopes were effectively split into two separate components. One consisted of slow rate information ($<$32 Hz) conveying the dynamic changes in spectral shape that are crucial for speech; the second presented *F*0 information in the form of a simplified synthesized wave form, allowing complete control over the form in which *F*0-related information was presented. In addition to maximizing the depth of the *F*0 modulation and allowing the same wave form to be applied to each channel, a key feature of such an approach is that the shape of the modulation wave form can be optimized so as to maximize the salience of temporal pitch cues.

In the experiments conducted by Green, Faulkner, and Rosen (2004), *F*0-related modulation was presented in the form of a sawtooth wave form, on the assumption that such a "temporally sharpened" modulation envelope, with a rapid onset in each period, would lead to more consistent interpulse intervals in the neural firing pattern, and therefore to more salient temporal pitch cues. Implant users, and normally hearing subjects listening to noise-excited vocoder simulations, were required to label the direction of pitch movement of processed synthetic diphthong glides. In both cases there was a significant advantage for modified compared to standard CIS processing, indicating that the modified processing scheme was successful in enhancing the salience of temporal pitch cues. It also appeared that, at least in some cases, performance was better when the sawtooth modulation was subject to additional temporal sharpening, such that the fall from peak to zero occurred in the first half of each period, and the second half of each period remained at zero.

Conditions in which slow-rate spectral dynamics were eliminated, so that within-channel amplitude changes reflected only *F*0, showed that the effectiveness of temporal cues to pitch was hindered by the variations in spectral envelope caused by the changing formant structure of the diphthongal vowel glides. This finding emphasizes the fact that cues that may provide useful pitch information in the context of certain simplified stimuli may not be robust in the presence of natural speech. It is also possible that the *F*0 modulation patterns associated with synthetic speech stimuli are less temporally complex than those of natural speech, which might, for example, feature secondary peaks within modulation periods. If so the simplified modulation wave form provided by Green, Faulkner, and Rosen's (2004) modified strategy may have additional benefits relative to traditional CIS processing.

The current study carried out further comparisons of the modified strategy with standard CIS processing, which again were performed both in implant users and in acoustic simulations. In this study only the modified sawtooth wave form, the additional temporal sharpening of which appeared beneficial in the previous study, was used to convey *F*0-related modulation. Pitch perception abilities were assessed using natural speech stimuli in tests of the ability to distinguish between questions and statements, a task which reflects an everyday use of intonation information. As a first step toward ensuring that benefits in pitch perception are not achieved at the expense of other linguistic information, vowel recognition scores were obtained. In addition, implant users were tested on their ability to discriminate differences in formant frequencies, as there is evidence that this ability is a primary determinant of implant users' vowel perception (Harnsberger *et al.*, 2001).

II. ACOUSTIC SIMULATION EXPERIMENTS

A. Subjects

Five undergraduate students aged between 22 and 25 who were native speakers of British English took part in both acoustic simulation experiments. They were paid £5 per hour for their participation.

B. Speech processing

1. Standard CIS

Noise-excited vocoder processing was carried out as in Green, Faulkner, and Rosen (2004). Simulation of standard CIS processing comprised the following sequence of steps: analysis bandpass filtering (sixth-order Butterworth) to divide the spectrum into eight frequency bands; full-wave rectification and low-pass filtering (second-order Butterworth) with a cutoff frequency of 400 Hz to extract the amplitude envelope for each band; modulation of independent noise carriers by these envelopes; output filtering matching the initial analysis filtering; summation across channels. The cutoff frequencies of the analysis filters, which were based on the Clarion S-Series Pulsatile Table with extended low- and high-frequency settings (Clarion Device Fitting Manual, 2001), were 250, 500, 730, 1015, 1450, 2000, 2600, 3800, and 6800 Hz.

2. Enhanced *F*0 (Sawsharp)

Processing in the Sawsharp condition differed from standard CIS processing in two respects. First, the cutoff frequency of the low-pass filters used in envelope extraction was 32 Hz rather than 400 Hz, eliminating *F*0-related fluctuations but passing the low-rate envelope information essential for speech perception. Second, during voiced sections of the speech input, temporal pitch cues were introduced by modulating the noise carrier in each channel with a sharpened sawtooth wave form with periodicity matching that of the speech input. The detection of voicing and the periodicity of the voiced segments were determined from laryngograph recordings. The modulation depth of the sharpened sawtooth wave form was always 100%.

C. Stimuli and procedure

1. Question/Statement identification

Thirty sentences were used. They included eight sentences used by Lieberman and Michaels (1962) in their investigation of the role of pitch in conveying emotional content in speech; thirteen sentences from the Question/Statement subtest of the Minimal Auditory Capabilities Battery (Owens *et al.*, 1981); and nine other simple declarative sentences (e.g., "They're playing in the garden;" "She's reading a newspaper"). Simultaneous audio and laryngograph recordings were made in an anechoic room of each of the sentences being read three times as a statement (falling pitch contour), and three times as a question (rising pitch contour), by one male and one female native speaker of Southern British English. The range of *F*0 values was approximately 100–220 Hz for the male speaker, and 120–360 Hz for the female speaker. Example *F*0 contours are shown in Fig. 1.

Blocks of trials contained 10 of the 30 sentences spoken as both question and statement by both speakers. Both processing conditions were included within each block resulting in a total of 80 trials per block. A total of nine blocks were presented in random order, incorporating each of the three versions of each utterance from each speaker. Stimuli were presented diotically through Sennheiser HD 414 headphones at a comfortable listening level (peak of 85–90 dB SPL measured over an 80 ms window). On each trial subjects heard a single sentence and were required to identify it as either "question" or "statement." They responded via computer mouse; visual feedback was provided. Before each block of trials subjects were able to listen to a selection of the sentences to be presented in that block, visually labeled as "question" or "statement."

2. Vowel recognition

Stimuli were selected from recordings of monophthongs in a /bVd/ context spoken by one male and one female native speaker of Southern British English. Simultaneous audio and laryngograph recordings had again been made in an anechoic room, but the speakers were different from those who read the Question/Statement sentences. The selected stimuli comprised two recordings from each speaker of the words "bead," "bird," "board," "bard," "booed," "bid," "bed," "bad," "bud," "bared," "bode," and "beard."

Processing condition was varied across blocks of 48 trials (12 vowels $\times$ 2 speakers $\times$ 2 exemplars). Four blocks were completed for each processing condition with the first counted as practice. Stimuli were presented as in the Question/Statement task. Responses were made by clicking on the desired word on a computer screen showing all twelve possible answers. Feedback was provided by highlighting the correct word after each response. Before each block listeners could listen to as many examples of each word as they wished by clicking on that word on the screen.

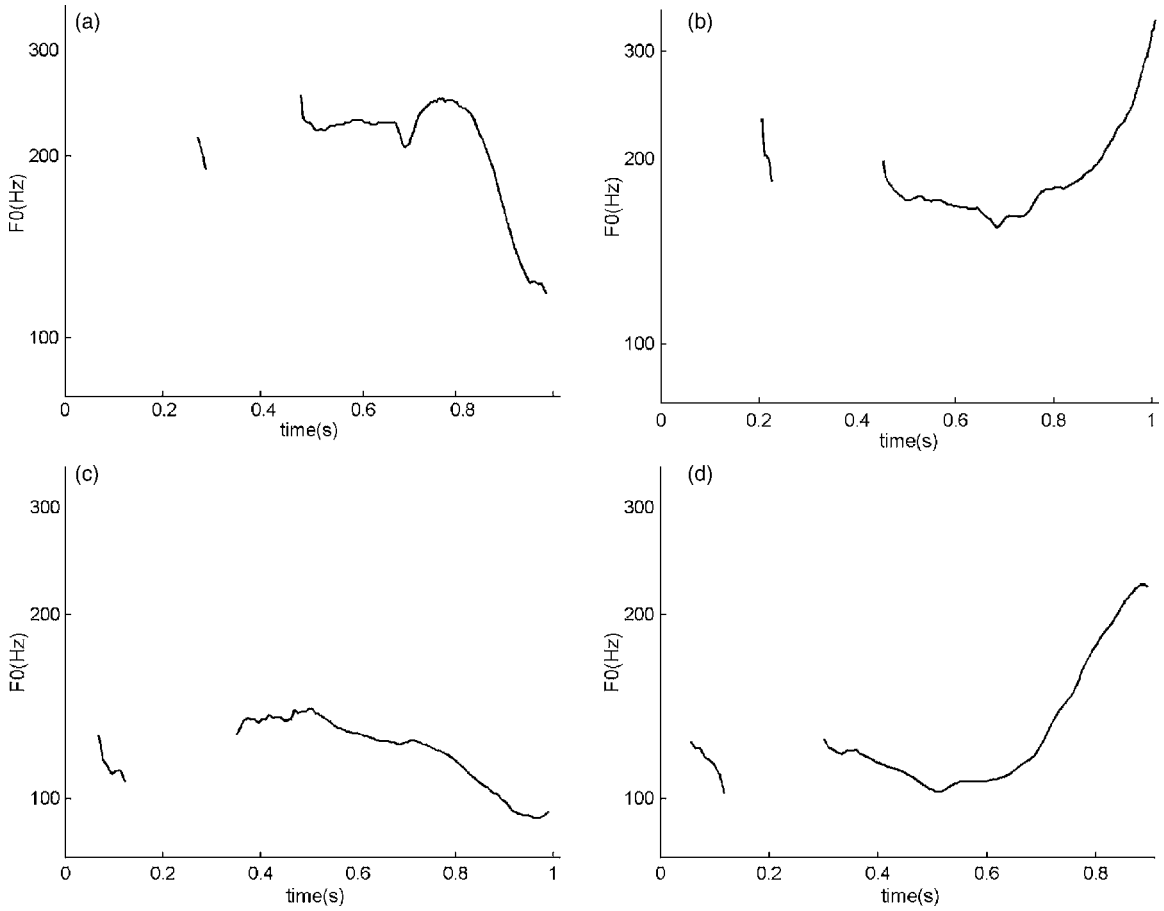

FIG. 1. Fundamental frequency contours for four different versions of the sentence "it's down there." (a) Female speaker, statement; (b) female speaker, question; (c) male speaker, statement; (d) male speaker, question.

D. Results and discussion

1. Question/Statement identification

In Fig. 2 Question/Statement identification performance with Sawsharp processing is plotted against performance with CIS processing, for each subject and speaker. Performance was consistently higher with Sawsharp than with CIS processing (all points are on or above the diagonal). With the exception of subject S5 with CIS processing, performance was better for the female than for the male speaker (open symbols are to the right of, and above, their closed counterparts). Mean performance with CIS processing was 78.2% with the male speaker and 81.8% with the female, while with Sawsharp processing the means were 81.8% with the male speaker and 87.3% with the female. A repeated measures ANOVA with factors of type of processing and speaker gender showed a significant effect of processing [$F(1,4)=20.85, p=0.010$], but neither the effect of speaker gender [$F(1,4)=1.85, p=0.245$], nor the interaction [$F(1,8)=0.43, p=0.547$] was significant. In order to assess possible biases in responding, signal detection theory techniques were used to calculate sensitivity (d') and response criterion (c) across speaker gender for each listener and type of processing. Values of d' showed the same pattern as percent correct. Values of c were almost exclusively positive, indicating a bias toward "statement" responses, but there was no clear change of response criterion according to processing condition.

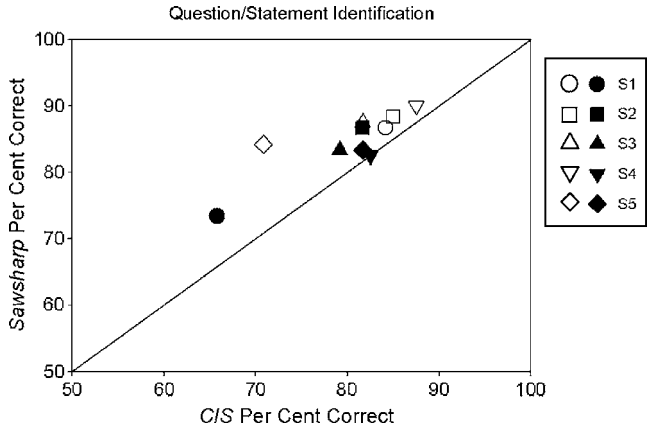

FIG. 2. Percent correct Question/Statement identification for each normally hearing listener for the male and female speakers (closed and open symbols, respectively). Performance in the Sawsharp condition is plotted against that in the CIS condition. The diagonal line represents equal performance in the two conditions.

The increased ability to identify sentences as questions or statements with the modified strategy compared to standard CIS processing presumably reflects the greater transmission of intonation information with modified processing. However, it should be acknowledged that other cues, such as differences in amplitude contour across questions and statements, may have been available. Such cues probably contrib-

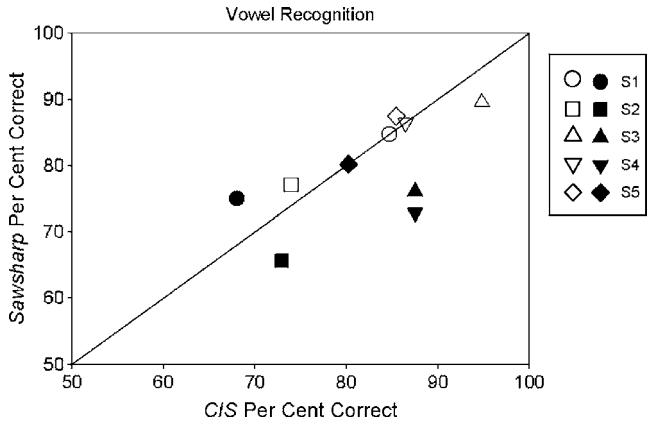

FIG. 3. Percent correct vowel recognition for each normally hearing listener for the male and female speakers (closed and open symbols, respectively). Performance in the Sawsharp condition is plotted against that in the CIS condition. The diagonal line represents equal performance in the two conditions.

uted to the relatively high scores obtained even in the standard CIS condition. It is noticeable that, despite the higher voice pitch of the female speaker, and the fact that temporal envelope cues to pitch decline in utility with increasing *F*0, performance is in fact slightly better for the female speaker than the male. One possible explanation is that amplitude contour differences may have been more pronounced for the female speaker. In addition, the *F*0 contours shown in Fig. 1 suggest that the female speaker displayed greater variation in *F*0, which would help to overcome the lesser utility of temporal envelope cues to pitch at higher *F*0s. Regardless of such issues, the significant advantage for modified processing strongly suggests that this strategy enhances the salience of temporal cues to voice pitch, as had been found previously with synthetic speech materials (Green, Faulkner, and Rosen, 2004).

2. Vowel recognition

Averaged across speakers, vowel recognition with the different types of processing was very similar. Performance was generally better with the female than with the male speaker (Fig. 3). Averaged across listeners, performance was identical across processing conditions for the female speaker (85.1%), but was slightly poorer with Sawsharp processing for the male speaker (74.0% compared to 79.2%). A repeated measures ANOVA showed a significant effect of speaker gender $[F(1,4)=35.08, p=0.004]$, but neither the effect of processing condition $[F(1,4)=1.33, p=0.314]$, nor the interaction $[F(1,4)=2.04, p=0.227]$ were significant. Thus, in acoustic simulations, the modified processing strategy delivers enhanced temporal pitch cues without harming the transmission of spectral information necessary for vowel recognition. The significant effect of speaker gender may result from the higher formant frequencies of the female speaker, which, in conjunction with the particular analysis filter cutoff frequencies used, may have produced distributions of energy across channels that were more different for similar vowels for the female than the male speaker.

III. IMPLANT USERS

A. Subjects and equipment

A total of nine post-lingually deafened adult users of the eight-channel Clarion 1.2 cochlear implant system participated. At least seven subjects took part in each test. Summary information is contained in Table I. Eight of the subjects had taken part in the vowel glide labeling experiments reported in Green, Faulkner, and Rosen (2004). As in that study, experiments were controlled by a PC connected to a Clarion Research Interface (CRI) system (Wygonski *et al.*, 1999), allowing direct control over the stimulus patterns presented to the electrode array. Stimulation consisted of con-

TABLE I. Demographic information.

Subject	Age	Gender	Cause of deafness	Age at onset	Age at implantation	Implant type	Strategy[a]	Mean threshold (clinical units)	Mean MCL (clinical units)
C1	73	M	Otosclerosis	69	70	Enhanced bipolar	SAS	93	329
C2	75	F	Unknown	69	71	Enhanced bipolar	MPS	97	397
C3	71	M	Unknown	40	68	Enhanced bipolar	MPS	60	633
C4	72	M	Skull fracture	64	69	Hifocus 1.2	SAS	49	228
C5	61	F	Unknown	51	59	Hifocus 1.2	MPS	40	138
C6	45	F	Unknown	30	41	Hifocus 1.2	MPS	26	499
C7	65	F	Unknown	45	62	Hifocus 1.2	MPS	85	174
C8	56	F	Sensorineural	42	51	Enhanced bipolar	CIS	100	614
C9	57	F	Sensorineural	14	55	Hifocus 1.2	SAS	21	133

[a]MPS is a variant of the CIS strategy in which pairs of channels are stimulated simultaneously.

tinuously interleaved, monopolar, biphasic pulses with a duration of 76.9 μs per phase. The carrier rate was 812.5 pulses per second per electrode (ppse) and electrodes were activated sequentially in apical-to-basal order.

B. Speech processing

A full description of the processing methods appears in Green, Faulkner, and Rosen (2004); only brief details are given here. Analysis filtering and envelope extraction were implemented as in the acoustic simulations for both modified and standard CIS processing. Envelopes were resampled to a rate of 6500 Hz, consistent with the overall pulse rate. In the CIS condition pulse levels were determined by logarithmic compression and mapping of a 50 dB range of envelope sample values onto the dynamic range of the particular subject and channel. In the Sawsharp condition the starting point of each successive period of *F*0 during voiced speech segments was determined from the laryngograph recording. During these segments, the carrier for each channel consisted of a pulse train 100% amplitude modulated by a sharpened sawtooth wave form; when voicing was absent the carriers were simply unmodulated pulse trains. The final stage of processing consisted of modulation of the pulse carriers by low-rate amplitude envelopes with compression and mapping carried out as in CIS processing.

C. Stimuli and procedure

Implant users carried out the same two tasks that were used in the acoustic simulations, with the exception that vowel recognition was tested using a smaller set of stimuli. This reflected the fact that the implant users' performance was substantially poorer than that of normally hearing listeners. Seven implant users were tested with nine, rather than twelve, vowels, with the words "bared," "bode," and "beard" omitted. The remaining two (C3 and C9) were tested with just five vowels: "bad," "bard," "bead," "bird," and "booed."

Implant users also performed a formant frequency discrimination task. Stimuli consisted of processed versions of a continuum of synthetic two-formant vowel sounds. These were created using an implementation of the KLSYN88 Klatt synthesizer in cascade mode with a 20 kHz sample rate and parameters specified every 5 ms. The first formant frequency was fixed at 500 Hz, while the second (*F*2) was varied between 1500 and 3000 Hz in 30 equal logarithmic steps. *F*0 declined logarithmically from 139 to 92 Hz over the 500 ms duration. A three-interval, 2AFC task with an adaptive two-down, one-up procedure was used. The first interval always had *F*2 at 1500 Hz. The second and third intervals contained, in random order, one stimulus with the same *F*2 and one with a higher *F*2. The time gap between intervals was 500 ms. The listener's task was to identify the interval containing the higher *F*2. In order to minimize overall loudness cues, the levels of stimuli within a trial were varied pseudo-randomly. Four different levels were employed, differing in 2 dB steps. The combination of levels of the three stimuli in a particular trial was selected at random from a subset of 8 of the total of 64 possible level combinations.

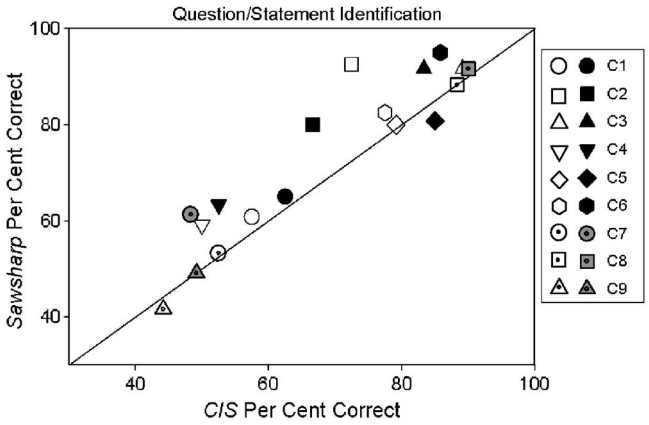

FIG. 4. Percent correct Question/Statement identification for each implant user for the male and female speakers (closed and open symbols, respectively). Performance in the Sawsharp condition is plotted against that in the CIS condition. The diagonal line represents equal performance in the two conditions.

In the first trial of each run the stimulus to be identified had *F*2 at 3000 Hz. Over the first three reversals the step size was gradually reduced from 5 (out of 30) steps to 1. A threshold was calculated for each run from the average of eight subsequent reversals. Reported threshold values for each processing condition are the average of either five or six runs.

D. Results and discussion

1. Question/Statement identification

For both speakers, mean performance was around 5% better with Sawsharp than with CIS processing (75.4% compared to 69.3% for the male speaker and 72.2% compared to 67.9% for the female). Four subjects (C1, C5, C8, and C9) showed little difference between the two processing conditions (Fig. 4). Ceiling effects may have occurred for C8, but not in the other cases. The other five subjects showed an advantage for Sawsharp processing of between approximately 5% and 15%. A repeated measures ANOVA showed a significant effect of type of processing $[F(1,8)=7.17, p=0.028]$, while neither the effect of speaker gender $[F(1,8)=1.50, p=0.256]$, nor the interaction $[F(1,8)=0.85, p=0.383]$ were significant.

Values of response criterion (c) also displayed considerable variability but were generally positive, reflecting a bias toward "statement" responses. In contrast to the acoustic simulation data, there was a consistent different between Sawsharp and CIS processing, with the former resulting in an increased proportion of "question" responses. However, a repeated measures t-test comparing d' values showed that the advantage for Sawsharp processing was not dependent upon this change in response bias $[t(8)=2.85, p=0.022]$.

Both the absence of an effect of speaker gender and the significant advantage for the modified processing over standard CIS are consistent with the data obtained in the noise-excited vocoder acoustic simulation. As was also the case in the glide labeling task used by Green, Faulkner, and Rosen (2004), mean performance by implant users was poorer than that of normally hearing listeners in acoustic simulations, but the better implant users achieved scores similar to those ob-

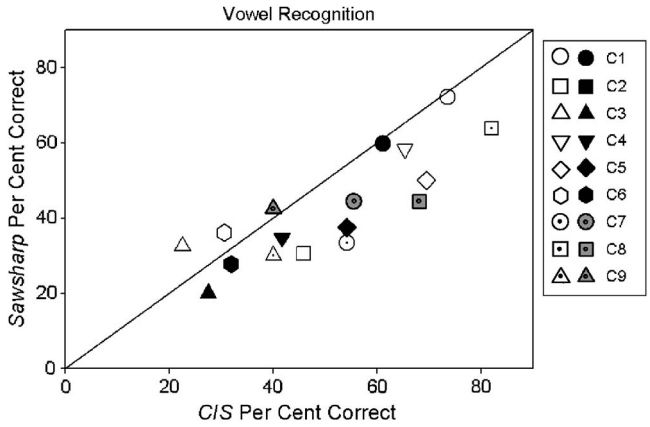

FIG. 5. Percent correct vowel recognition for each implant user for the male and female speakers (closed and open symbols, respectively). Performance in the Sawsharp condition is plotted against that in the CIS condition. The diagonal line represents equal performance in the two conditions.

tained in the simulations. This provides further evidence that the temporal cues to voice pitch available in noise-excited vocoder simulations are broadly similar to those available with CIS-like processing. Most important, these data, obtained with natural speech stimuli in a task reflecting an everyday use of intonation information, indicate that the modified processing scheme, by providing enhanced *F*0-related modulation, leads to better voice pitch perception.

2. Vowel recognition

In contrast to the acoustic simulation data, vowel recognition (Fig. 5) was substantially affected by processing condition. Averaged across listeners, performance for the male speaker was 47.3% with CIS processing compared to 38.0% with Sawsharp processing, while for the female speaker the respective means were 53.7% and 45.2%. Averaged across speakers, performance varied little across processing condition for four subjects (C1, C3, C6, and C9), but was substantially poorer with Sawsharp processing for the remaining five subjects. A repeated measures ANOVA showed a significant effect of processing condition $[F(1,8)=9.57, p=0.015]$, but neither the effect of speaker gender $[F(1,8)=3.85, p=0.085]$, nor the interaction $[F(1,8)=0.08, p=0.786]$ were significant.

To further investigate this deficit, sequential information analysis (SINFA, Wang and Bilger, 1973) was carried out. Only data from the seven subjects who were tested on all nine vowels were included in these analyses. The features on which vowels were classified were *duration, open*, and *front* (Table II). Assignment of vowels to different feature categories followed the standard IPA classification, with one exception. Although "bad" is typically classified as a short vowel, in the stimuli used here it was the longest vowel for the male speaker and the third longest for the female speaker, and was therefore classified as long. SINFA was performed for each combination of speaker and processing condition, both on individual implant users' confusion matrices and on pooled data (Fig. 6).[11]

The analysis of the pooled data (Table III) shows that, for both speakers, and for all three features, less information

TABLE II. Classification of the vowel features used in SINFA: o=open; om=open-mid; cm=closed-mid; c=closed; f=front; ce=central; b=back; l=long; s=short. Standard IPA classifications were used with one exception. Although "bad" is typically classified as a short vowel, in the stimuli used here it was the longest vowel for the male speaker and the third longest for the female speaker, and was thus classified as long.

	Bad æ	Bard ɑ	Bead i	Bed e	Bid ɪ	Bird ɜ	Board ɔ	Booed u	Bud ʌ
Open	o	o	c	om	c	cm	om	c	om
Front	f	b	f	f	f	ce	b	b	b
Duration	l	l	l	s	s	l	l	l	s

is transmitted with Sawsharp than with standard CIS processing. The results of the analysis of individual data (Fig. 7) are largely consistent with the pooled data, though there is much individual variability. The decrease in transmitted information for the *open* and *front* features with Sawsharp processing suggests that the modified processing strategy, while providing enhanced pitch information, also has a harmful effect on the perception of spectral information essential for speech understanding.

Surprisingly, the proportion of duration information transmitted also declined with the modified processing. One relevant factor may be that the male speaker's stimuli were consistently longer than those of the female (mean 0.69 s, compared to 0.53 s). Because stimuli from both speakers were presented in the same block of trials, it is plausible that the ability to identify the speaker's gender limits the extent to which it is possible to make full use of duration information. Notwithstanding the improved representation of *F*0 information with modified processing, it is likely that the primary cue distinguishing male and female voices is the different distribution of energy across frequency channels due to differences in formant frequencies. Thus, to the extent that the ability to make use of duration cues depended on being able to distinguish between the two speakers, a decline in the transmission of spectral information might result in a decline in the availability of duration information. An alternative possibility concerns the reduction in the cutoff frequency of

***CIS* Male Speaker**

	æ	ɑ	i	e	ɪ	ɜ	ɔ	u	ʌ
æ	25	19	0	0	0	10	1	1	0
ɑ	6	43	0	0	0	3	4	0	0
i	6	1	29	1	7	3	4	5	0
e	5	0	0	32	2	1	0	0	16
ɪ	5	1	1	32	11	1	2	0	3
ɜ	12	10	0	0	0	28	4	2	0
ɔ	4	17	0	0	0	5	28	2	0
u	2	15	0	0	0	5	13	21	0
ʌ	3	0	0	11	0	1	0	0	41

***CIS* Female speaker**

	æ	ɑ	i	e	ɪ	ɜ	ɔ	u	ʌ
æ	27	6	1	1	1	11	1	0	8
ɑ	8	30	0	0	0	11	7	0	0
i	3	0	26	8	4	6	4	5	0
e	1	0	0	26	13	0	0	0	16
ɪ	0	0	0	7	42	0	0	0	7
ɜ	3	5	0	8	1	32	1	3	3
ɔ	0	0	0	0	0	1	52	3	0
u	1	2	0	1	0	19	12	19	2
ʌ	0	0	0	3	4	0	0	0	49

***Sawsharp* Male Speaker**

	æ	ɑ	i	e	ɪ	ɜ	ɔ	u	ʌ
æ	14	22	0	0	0	16	2	2	0
ɑ	6	32	0	0	0	13	4	1	0
i	9	2	24	4	1	4	2	10	0
e	3	0	0	29	3	4	0	3	14
ɪ	5	1	1	27	8	4	0	3	7
ɜ	19	16	0	0	0	14	6	1	0
ɔ	4	15	1	0	0	9	24	2	1
u	4	12	1	0	0	7	15	17	0
ʌ	6	0	0	7	1	2	0	1	39

***Sawsharp* Female Speaker**

	æ	ɑ	i	e	ɪ	ɜ	ɔ	u	ʌ
æ	6	9	1	2	0	21	3	8	6
ɑ	4	21	0	0	0	6	12	10	3
i	1	0	25	3	1	4	7	13	2
e	2	0	3	21	9	1	0	4	16
ɪ	0	0	1	6	41	0	0	3	5
ɜ	6	1	0	1	1	24	10	10	3
ɔ	0	1	1	0	0	4	45	3	2
u	1	1	1	2	0	8	17	24	2
ʌ	1	0	0	2	9	0	0	3	41

FIG. 6. Confusion matrices for each combination of processing type and speaker gender, representing pooled data from the seven subjects who were tested on all nine vowels.

TABLE III. Proportion of information transmitted based on SINFA performed on pooled data from the seven implant users tested with all nine vowels.

	Duration	Open	Front
CIS M	0.663	0.221	0.241
CIS F	0.678	0.354	0.283
Sawsharp M	0.578	0.139	0.146
Sawsharp F	0.541	0.208	0.155

the envelope filter from 400 to 32 Hz in the modified processing condition. Although we would not have expected this reduction to have significantly affected access to vowel duration differences, it is perhaps conceivable that poorer definition of the attack and decay portions of the envelope with the lower cutoff frequency could have contributed to the decline in transmission of duration information.

In order to assess any possible relationship between decrements in vowel recognition and enhancements in pitch perception, a Pearson's correlation coefficient was calculated for the differences between the processing conditions in vowel recognition and Question/Statement performance (averaged across speakers). The results ($r=-0.02, p=0.96$) showed clearly that there was no such relationship. Thus, it is not the case that a greater benefit in pitch perception from modified processing was associated with a larger decrement in vowel recognition.

However, although there are not enough subjects to draw any strong conclusions, it does appear that the strategy normally used by the subjects influences the decrement in vowel recognition with modified processing. The decrement for the single CIS user was nearly 21%, while for the five users of the multiple pulsatile sampler (MPS) strategy the mean decrement was 9.5%, and for the three SAS users it was 4%. The MPS strategy is similar to CIS in that it presents interleaved stimulation, although in this case the interleaving is only partial, with two separate channels receiving pulses simultaneously. If, on this basis, users of MPS are considered to be more familiar with CIS processing than

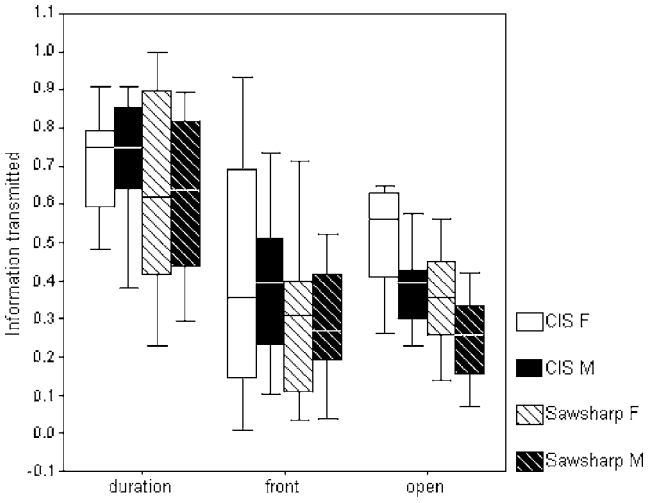

FIG. 7. Boxplot showing results of SINFA performed on confusion matrices from each of the seven implant users who were tested with all nine vowels.

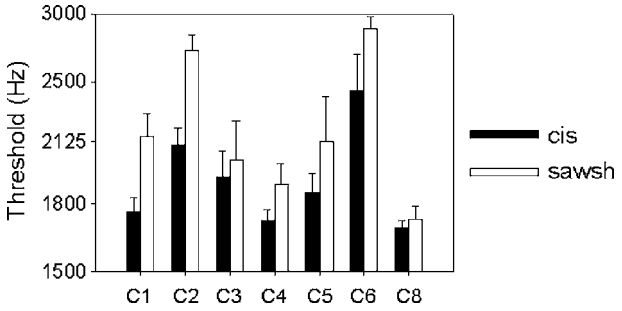

FIG. 8. Implant users' mean threshold $F2$ values for discrimination from a 1500 Hz standard. Error bars show one standard deviation.

SAS users, then it would appear that the greater the degree of familiarity with CIS processing then the larger the advantage in vowel recognition for CIS than for Sawsharp processing.

3. Formant discrimination

Thresholds for discriminating a difference in $F2$ were higher with Sawsharp than with CIS processing for all seven subjects, although the difference in thresholds for the two types of processing varied substantially (Fig. 8). A repeated measures t-test showed that the effect of type of processing was significant [$t(6)=3.77, p=0.009$]. This provides further evidence suggesting a detrimental impact of the modified processing strategy on the perception of spectral information necessary for speech understanding.

Pearson correlation coefficients were calculated in order to assess the relationship between formant discrimination performance (expressed logarithmically) and vowel recognition (averaged across speakers). With CIS processing, the correlation just missed significance ($r=-0.723, p=0.067$). With Sawsharp processing the relationship was not significant ($r=-0.505, p=0.248$). If the data from subject C3, whose vowel recognition was tested with only five vowels, are omitted then substantially larger correlations are obtained. The correlation was significant with CIS processing ($r=-0.901, p=0.014$) and close to significance with Sawsharp processing ($r=-0.724, p=0.104$). Omitting the data of one further outlier (C1) in the Sawsharp condition resulted in a highly significant correlation ($r=-0.983, p=0.003$). Clearly, considerably more subjects would be required to accurately determine the extent of the relationship between the two measures, though this limited sample does suggest a reasonably strong relationship.

However, there appears to be virtually no relationship between the effects of processing condition in the two different tasks. For example, subject C8 showed the largest decrement for Sawsharp processing in vowel recognition, but had the smallest difference in $F2$ discrimination thresholds. Conversely, for C1, $F2$ discrimination was much poorer with Sawsharp processing, but there was only a very small difference in vowel recognition. Consequently, the correlation coefficient for the percentage difference in vowel recognition and the difference in $F2$ discrimination threshold was minimal ($r=0.091, p=0.846$).

IV. GENERAL DISCUSSION

As was the case with synthetic stimuli in Green, Faulkner, and Rosen (2004), relatively small, but significant, benefits in voice pitch perception for modified processing of natural speech were observed both in implant users and in acoustic simulations. However, for implant users there was a significant deficit in vowel recognition with the modified strategy. It appears that the modified processing strategy resulted in poorer transmission of spectral information relative to standard CIS processing, although it is not easy to identify specific causes of the decrement in vowel recognition. Of course, it is possible that different factors may contribute to differences between processing conditions for different implant users.

One major element of the modified scheme is that it relies upon slow-rate ($<$32 Hz) modulations to convey the dynamic spectral variation essential for speech understanding. There is considerable evidence to suggest that speech perception, as assessed by standard speech tasks such as vowel and consonant recognition, depends only upon low frequency temporal envelope information (e.g., Drullman, Festen, and Plomp, 1994; Fu and Shannon, 2000; Shannon *et al.*, 1995; Van Tasell *et al.*, 1992). In conjunction with the absence of an effect of processing condition in the acoustic simulation data, this suggests that while the reduction of the envelope filter cutoff frequency from 400 to 32 Hz in the modified processing condition may have some impact, it is unlikely to be primarily responsible for the decrement in vowel recognition observed in implant users.

One possible explanation of the deficit could be a form of conflict between temporal and spectral information. There is evidence that spectral and temporal information interact in the determination of implant users' perception of pitch (Green, Faulkner, and Rosen, 2004; Zeng, 2002). This suggests the possibility that the enhanced temporal pitch information provided by the modified processing scheme may interfere with implant users' perceptual processing of the spectral information that is encoded in between-channel differences in level. However, the absence of any relationship between benefits in pitch perception and deficits in vowel recognition would appear to count against such an explanation.

It may be important that in the Sawsharp instantiation of the modified processing strategy implemented here, the level of the pulse carrier for voiced speech declines from its maximum value to threshold over the first half of each period, and remains at threshold for the second half of each period. Thus, with this modulation wave form shape, only a small part of the voicing cycle is carrying spectral information. We used the Sawsharp wave form here because in our previous study (Green, Faulkner, and Rosen, 2004), it appeared to be close to optimal for conveying temporal cues to voice pitch. It was hoped that it would also adequately convey spectral information. Although the present findings suggest that this is not the case, it is important to bear in mind that subjects had very little experience of the Sawsharp processing strategy prior to testing. Particularly in light of the apparent relationship between the extent of the decrement in vowel recognition and the implant user's normal processing strategy, it is conceivable that, given sufficient experience, implant users might adjust to the different way in which spectral information is presented with Sawsharp processing, thereby eliminating the deficit relative to standard CIS processing.

Even if extra experience with Sawsharp processing were not sufficient to restore optimal vowel recognition performance, there are a number of potential changes to the modified processing strategy that may improve matters. One possibility concerns the shape of the synthesized wave form carrying *F*0-related modulation. While Green, Faulkner, and Rosen (2004) found that performance in their glide labeling task was best in the Sawsharp condition, there was only a small advantage over a condition that used a standard sawtooth wave form, in which the decline from maximum to minimum level occurred over the whole period. If the decrement in vowel perception with Sawsharp processing is related to the small proportion of the voicing cycle that is available to convey spectral information, then using a standard sawtooth wave form may overcome this deficit.

The modulation depth of the simplified *F*0 wave form could also be manipulated. Fu (2002) showed that cochlear implant users' modulation detection thresholds decrease with increasing stimulation level, although the pattern of this decrease varies markedly across individuals. This suggests that an approach in which the depth of the *F*0-related modulation was varied according to stimulation level, with the pattern of the variation determined on an individual basis, may help to preserve the benefits to voice pitch perception provided by the modified processing strategy while minimizing the harmful impact on vowel perception.

Another possibility concerns the number of channels to which the clarified *F*0-related modulation is applied. Based on evidence of better discrimination of the modulation frequency of sinusoidally amplitude modulated pulse trains with three adjacent channels stimulated concurrently, compared to any one channel alone (Geurts and Wouters, 2001), the modified processing scheme was implemented with the simplified *F*0 wave form applied to all eight channels. However, it is conceivable that applying the clarified *F*0 modulation to a subset of channels might provide enhanced pitch cues, while affording better transmission of spectral information.

It should also be borne in mind that the present research has been carried out in users of implant systems that have a pulse rate of approximately 800 ppse. Newer implant systems are typically capable of much faster pulse rates (e.g., 5000 ppse) which may provide greater scope for using the kind of approach adopted here to provide enhanced temporal cues to voice pitch.

ACKNOWLEDGMENTS

The authors thank all participants and are grateful to the cochlear implant team at the Royal National Throat Nose and Ear Hospital for help in recruiting implant users. Ken Grant, Fan-Gang Zeng, and Monita Chatterjee made helpful com-

ments on an earlier version of this manuscript. This research was supported by the Royal National Institute for Deaf People (UK).

[1]Typically in SINFA, the feature for which the proportion of transmitted information is highest is held constant for subsequent iterations. In order to allow comparisons across different conditions, in the few cases where the order of analysis differed from the most common sequence (*duration, open, front*), analyses were repeated with this order and it is these results that are reported.

Au, D. K. K. (**2003**). "Effects of stimulation rates on Cantonese lexical tone perception by cochlear implant users in Hong Kong," Clin. Otolaryngol. **28**, 533–538.

Barry, J. G., Blamey, P. J., Martin, L. F. A., Lee, K. Y.-S., Tang, T., Ming, Y. Y., and Van Hasselt, C. A. (**2002**). "Tone discrimination in Cantonese-speaking children using a cochlear implant," Clin. Linguist. Phonet. **16**, 79–99.

Burns, E. M., and Viemeister, N. F. (**1976**). "Nonspectral pitch," J. Acoust. Soc. Am. **60**, 863–869.

Burns, E. M., and Viemeister, N. F. (**1981**). "Played-again SAM: Further observations on the pitch of amplitude-modulated noise," J. Acoust. Soc. Am. **70**, 1655–1660.

Busby, P. A., Tong, Y. C., and Clark, G. M. (**1993**). "The perception of temporal modulations by cochlear implant patients," J. Acoust. Soc. Am. **94**, 124–131.

Cazals, Y., Pelizzone, M., Saudan, O., and Boex, C. (**1994**). "Low-pass filtering in amplitude modulation detection associated with vowel and consonant identification in subjects with cochlear implants," J. Acoust. Soc. Am. **96**, 2048–2054.

Ciocca, V., Francis, A. L., Aisha, R., and Wong, L. (**2002**). "The perception of Cantonese lexical tones by early-deafened cochlear implantees," J. Acoust. Soc. Am. **111**, 2250–2256.

Donaldson, G., and Viemeister, N. (**2002**). "TMTFs in cochlear implant users: The role of loudness clues," Assoc. Res. Otolaryngol. Abstr. **25**, 121.

Drullman, R., Festen, J. M., and Plomp, R. (**1994**). "Effect of temporal envelope smearing on speech reception," J. Acoust. Soc. Am. **95**, 1053–1064.

Formby, C. (**1985**). "Differential sensitivity to tonal frequency and to the rate of amplitude modulation of broadband noise by normally hearing listeners," J. Acoust. Soc. Am. **78**, 70–77.

Fourcin, A. J., Rosen, S. M., Moore, B. C. J., Douek, E. E., Clarke, G. P., Dodson, H., and Bannister, L. H. (**1979**). "External electrical stimulation of the cochlea: Clinical, psychophysical, speech-perceptual and histological findings," Br. J. Audiol. **13**, 85–107.

Fu, Q.-J. (**2002**). "Temporal processing and speech recognition in cochlear implant users," NeuroReport **13**, 1635–1639.

Fu, Q.-J. and Shannon, R. V. (**2000**). "Effect of stimulation rate on phoneme recognition by Nucleus-22 cochlear implant listeners," J. Acoust. Soc. Am. **107**, 589–597.

Fu, Q.-J., Zeng, F.-G., Shannon, R. V., and Soli, S. D. (**1998**). "Importance of tonal envelope cues in Chinese speech recognition," J. Acoust. Soc. Am. **104**, 505–510.

Geurts, L., and Wouters, J. (**2001**). "Coding of the fundamental frequency in continuous interleaved sampling processors for cochlear implants," J. Acoust. Soc. Am. **109**, 713–726.

Geurts, L., and Wouters, J. (**2004**). "Better place-coding of fundamental frequency in cochlear implants," J. Acoust. Soc. Am. **115**, 844–852.

Grant, K., Summers, V., and Leek, M. (**1998**). "Modulation rate detection and discrimination by normal-hearing and hearing-impaired listeners," J. Acoust. Soc. Am. **104**, 1051–1060.

Green, T., Faulkner, A., and Rosen, S. (**2002**). "Spectral and temporal cues to pitch in noise-excited vocoder simulations of continuous-interleaved-sampling cochlear implants," J. Acoust. Soc. Am. **112**, 2155–2164.

Green, T., Faulkner, A., and Rosen, S. (**2004**). "Enhancing temporal cues to voice pitch in continuous interleaved sampling cochlear implants," J. Acoust. Soc. Am. **116**, 2298–2310.

Hanna, T. (**1992**). "Discrimination and identification of modulation rate using a noise carrier," J. Acoust. Soc. Am. **91**, 2122–2128.

Harnsberger, J. D., Svirsky, M. A., Kaiser, A. R., Pisoni, D. B., Wright, R., and Meyer, T. A. (**2001**). "Perceptual 'vowel spaces' of cochlear implant users: Implications for the study of auditory adaptation to spectral shift," J. Acoust. Soc. Am. **109**, 2135–2145.

Jusczyk, P. (**1997**). *The Discovery of Spoken Language* (MIT, Cambridge, MA).

Lan, N., Nie, K. B., Gao, S. K., and Zeng, F.-G. (**2004**). "A novel speech processing strategy incorporating tonal information for cochlear implants," IEEE Trans. Biomed. Eng. **51**, 752–760.

Lee, K. Y. S., van Hasselt, C. A., Chiu, S. N., and Cheung, D. M. C. (**2002**). "Cantonese tone perception ability of cochlear implant children in comparison with normal-hearing children," Int. J. Pediatr. Otorhinolaryngol. **63**, 137–147.

Lieberman, P., and Michaels, S. B. (**1962**). "Some aspects of fundamental frequency and envelope amplitude as related to the emotional content of speech," J. Acoust. Soc. Am. **34**, 922–927.

McDermott, H. J., and McKay, C. M. (**1994**). "Pitch ranking with non-simultaneous dual-electrode electrical stimulation of the cochlea," J. Acoust. Soc. Am. **96**, 155–162.

McDermott, H. J., and McKay, C. M. (**1997**). "Musical pitch perception with electrical stimulation of the cochlea," J. Acoust. Soc. Am. **101**, 1622–1631.

McKay, C. M., and McDermott, H. J. (**1993**). "Perceptual performance of subjects with cochlear implants using the Spectral Maxima Sound Processor (SMSP) and the Mini Speech Processor (MSP)," Ear Hear. **14**, 350–367.

McKay, C. M., McDermott, H. J., and Clark, G. M. (**1994**). "Pitch percepts associated with amplitude-modulated current pulse trains by cochlear implantees," J. Acoust. Soc. Am. **96**, 2664–2673.

McKay, C. M., McDermott, H. J., Vandali, A. E., and Clark, G. M. (**1992**). "A comparison of speech perception of cochlear implantees using the Spectral Maxima Sound Processor (SMSP) and the MSP (Multipeak) processor," Acta Oto-Laryngol. **112**, 752–761.

Owens, E., Kessler, D., Telleen, C. C., and Schubert, E. (**1981**). "The minimal auditory capabilities (MAC) battery," Hearing Aid J. **9**, 9–34.

Peng, S.-C., Tomblin, J. B., Cheung, H., Lin, Y.-S., and Wang, L.-S. (**2004**). "Perception and production of Mandarin tones in prelingually deaf children with cochlear implants," Ear Hear. **25**, 251–263.

Pijl, S., and Schwarz, D. W. F. (**1995**). "Melody recognition and musical interval perception by deaf subjects stimulated with electrical pulse trains through single cochlear implant electrodes," J. Acoust. Soc. Am. **98**, 886–895.

Pollack, I. (**1969**). "Periodicity pitch for white noise—fact or artefact," J. Acoust. Soc. Am. **45**, 237–238.

Rubinstein, J. T., Wilson, B. S., Finley, C. C., and Abbas, P. J. (**1999**). "Pseudospontaneous activity: Stochastic independence of auditory nerve fibers with electrical stimulation," Hear. Res. **127**, 108–118.

Seligman, P., and McDermott, H. (**1995**). "Architecture of the Spectra 22 speech processor," Ann. Otol. Rhinol. Laryngol. Suppl. **166**, 139–141.

Shannon, R. (**1992**). "Temporal modulation transfer functions in patients with cochlear implants," J. Acoust. Soc. Am. **91**, 2156–2164.

Shannon, R. V., Zeng, F.-G., Kamath, V., Wygonski, J., and Ekelid, M. (**1995**). "Speech recognition with primarily temporal cues," Science **270**, 303–304.

Skinner, M. W., Fourakis, M. S., Holden, T. A., Holden, L. K., and Demorest, M. E. (**1999**). "Identification of speech by cochlear implant recipients with the Multipeak (MPEAK) and Spectral Peak (SPEAK) speech coding strategies," Ear Hear. **20**, 443–460.

Tong, Y. C., Millar, J. B., Clark, G. M., Martin, L. F., Busby, P. A., and Patrick, J. F., (**1980**). "Psychophysical and speech perception studies on two multiple channel cochlear implant patients," J. Laryngol. Otol. **94**, 1241–1256.

Townshend, B., Cotter, N., Van Compernolle, D. V., and White, R. L. (**1987**). "Pitch perception by cochlear implant subjects," J. Acoust. Soc. Am. **82**, 106–115.

Vandali, A. E., Whitford, L. A., Plant, K. L., and Clark, G. M. (**2000**). "Speech perception as a function of electrical stimulation rate: Using the Nucleus 24 cochlear implant system," Ear Hear. **21**, 608–624.

Van Tasell, D. J., Greenfield, D. G., Logemann, J. J., and Nelson, D. A., (**1992**). "Temporal cues for consonant recognition: Training, talker generalization, and use in evaluation of cochlear implants," J. Acoust. Soc. Am. **92**, 1247–1257.

Wang, M. D. and Bilger, R. C. (**1973**). "Consonant confusions in noise: A study of perceptual features," J. Acoust. Soc. Am. **54**, 1248–1266.

Wei, C.-G., Cao, K., and Zeng, F.-G. (**2004**). "Mandarin tone recognition in Chinese cochlear-implant subjects," Hear. Res. **197**, 87–95.

Wei, W. I., Wong, R., Hui, Y., Au, D. K. K., Wong, B. Y. K., Ho, W. K., Tsang, A., Kung, P., and Chung, E. (**2000**). "Chinese tonal language rehabilitation following cochlear implantation in children," Acta Oto-Laryngol. **120**, 218–221.

Wilson, B. (**1997**). "The future of cochlear implants," Br. J. Audiol. **31**, 205–225.

Wilson, B., Finley, C., Lawson, D., Wolford, R., Eddington, D., and Rabinowitz, W. (**1991**). "Better speech recognition with cochlear implants," Nature (London) **352**, 236–238.

Wilson, B., Zerbi, M., Finley, C., Lawson, D., and van den Honert, C. (1997). Eighth Quarterly Progress Report, 1 May through 31 July 1997. NIH Project N01-DC-5-2103: Speech Processors for Auditory Prostheses: Research Triangle Institute.

Wygonski, J. J., Lee, J., Faltys, M., Shannon, R. V., and Robert, M. (**1999**). "Configurable speech strategy implementation using the Clarion research interface," 1999 Conference on Implantable Auditory Prostheses, Pacific Grove, CA.

Xu, L., Tsai, Y., and Pfingst, B. E. (**2002**). "Features of the stimulation affecting tonal-speech perception: Implications for cochlear prostheses," J. Acoust. Soc. Am. **112**, 247–258.

Zeng, F.-G. (**2002**). "Temporal pitch in electric hearing," Hear. Res. **174**, 101–106.

The effect of rate of stimulation on perception of spectral shape by cochlear implantees

Colette M. McKay[a)]
School of Life and Health Sciences, Aston University, Birmingham, B4 7ET, United Kingdom and Department of Otolaryngology, The University of Melbourne, Melbourne 3052, Australia

Katherine R. Henshall and Alicia E. Hull
Department of Otolaryngology, The University of Melbourne, Melbourne 3052, Australia

(Received 18 November 2004; revised 27 April 2005; accepted 27 April 2005)

The effect of rate of stimulation on spectral shape perception was measured in six users of the Nucleus CI24 cochlear implant. Three spectral shapes were created by using three profiles of current across seven electrode positions. Each current profile was replicated in three stimuli that interleaved stimulus pulses across the seven electrodes with cycle rates (rate per electrode) of 450, 900, and 1800 Hz. The stimulus space resulting from a multidimensional scaling experiment showed a clear dimension related to the rate of stimulation that was orthogonal to the dimension related to the spectral shapes. A second experiment was performed with the same subjects to investigate whether the perceptual dimension related to rate in Experiment 1 could be attributed to different perceptual flatness of the profiles at different rates. In Experiment 2, the rate of stimulation was fixed at 900 Hz and three profiles were created for each spectral shape that differed in flatness. This experiment did not, however, result in an independent perceptual dimension related to the flatness of the profile. In conclusion, rate of stimulation provided an independent perceptual dimension in the multiple-electrode stimuli, in spite of the rates being not discriminable or barely discriminable in single-electrode stimulation. [DOI: 10.1121/1.1937349]

PACS number(s): 43.66.Ts, 43.66.Jh, 43.66.Mk [AJO] Pages: 386–392

I. INTRODUCTION

Cochlear implants are now an accepted clinical device for the alleviation of severe to profound hearing loss, with a large proportion of implantees enjoying good speech understanding in quiet with their device. One of the stimulation parameters that can be individually adjusted when fitting a cochlear implant is the rate at which the signal is updated and the current pulses presented. However, the rate that optimizes speech perception varies across individuals. This paper investigates the changes in spectral shape perception that may result from using different high rates of stimulation.

The output of a speech processor usually consists of a train of biphasic current pulses that are interleaved across multiple electrode positions. Each electrode position is assigned to one of a set of bandpass filters in tonotopic fashion. In each stimulation cycle, at least six electrodes are activated (either selected from a larger number of available electrodes based upon the highest filter outputs, or all of a smaller set of fixed electrodes, depending on the processing strategy used). The pattern of current amplitudes across electrode positions conveys to the implantee the spectral shape of the acoustic signal, that is, the instantaneous pattern of intensity change across frequency, and hence the identity of the signal source. In order to improve the coding of temporal envelope and fine structure, there has been a trend in recent years for the rate at which the pulses are output to be increased. This increase in rate of stimulation has been made possible partly by improved techniques in transmitting the stimulation instructions between sound processor and implant. Although rate of stimulation in early devices that used transcutaneous information transfer was generally limited to about 250 Hz cycle rate (Skinner *et al.*, 1994), current devices are all capable of delivering cycle rates of at least 2400 Hz (Ziese *et al.*, 2000; Frijns *et al.*, 2002; Skinner *et al.*, 2002a).

Studies aimed at finding the optimal rate of stimulation for speech understanding have generally found that this rate is subject dependent (Brill *et al.*, 1997; Vandali *et al.*, 2000; Skinner *et al.*, 2002a, b). From a theoretical perspective, it is difficult to postulate why a very high rate should improve speech perception over a moderate rate (for example, 4000 Hz/channel compared to 1000 Hz/channel). Although some subjects appear to benefit from the use of very high rates (Brill *et al.*, 1997), this is not universally found. For example, Kiefer *et al.* (2000) found that, although average speech perception in a group of 13 implantees improved when rate was increased from 600 to about 1500 Hz, there was little effect of increasing the rate further to more than 3000 Hz. Furthermore, they found no significant effect of the low-pass smoothing filter cutoff, when changed from 400 to 200 Hz or to values greater than 400 Hz. Similarly, Fu and Shannon (2000) found that speech perception increased with rate of stimulation up to 150 Hz/channel but did not improve further between 150 and 500 Hz/channel. Furthermore, they found that the cut-off frequency of the low-pass smoothing filter did not affect speech perception above 20 Hz. These results are consistent with the proposal that temporal envelope information above 20 Hz does not

a)Electronic mail: c.m.mckay@aston.ac.uk

 0001-4966/2005/118(1)/386/7/$22.50

significantly contribute to speech perception, and that rates above 150 Hz are sufficiently high to sample temporal envelope changes. Certainly, even with low-pass filters up to 200 Hz, a 1000 Hz sampling rate would convey this information well. Again, Friesen *et al.* (2005) showed no effect of stimulation rate on speech recognition for rates above 200 Hz. The above-mentioned results suggest that the effect of rate of stimulation on speech perception is not necessarily due to improved perceptual transmission of amplitude envelope fluctuations.

Given that subjects generally cannot distinguish rates of stimulation above about 300 Hz (e.g., Zeng, 2002), and so presumably would not be able to perceive fine temporal structure that fluctuates faster than this, it is not obvious why a stimulation rate of 4000 Hz would be perceptually distinct from one of 1000 Hz. However, it is an everyday clinical experience that patients report large perceptual changes when the rate of stimulation of their sound processor is altered, even when the two rates are both higher than 300 Hz. Often the difference is reported as a pitch change. One possible explanation for this phenomenon is that the spatial excitation pattern produced by electrical stimulation may be altered when the rate is changed. This can come about first because the current level must be reduced for higher rates to obtain the same loudness, and second, because neurons may respond differentially in response to a higher rate, leading to a change in the excited neural population. A recent study by Landsberger and McKay (2005) confirmed that, for rates higher than 1200 Hz, single-electrode stimulation at two different (high) rates can often be distinguished by subjects, and they often label the difference as pitch.

In the experiments reported here, three spectral shapes were defined by different patterns of current across seven electrode positions. The seven electrodes were activated sequentially with cycle rates (rate per electrode) of 450, 900, or 1800 Hz. These stimuli represent typical patterns of excitation at the output of a speech processor for three sounds with different spectral shapes (i.e., different patterns of intensity across frequency). The experiments used a multidimensional scaling (MDS) technique to explore the perceptual effects on spectral shape perception of varying the rate of stimulation (Experiment 1). This method was used instead of a simple discrimination task in order to analyze the nature of perceptual changes that occur with rate. If, for example, the change of percept was due to a basal or apical shift in the excitation pattern with a change of rate, then the stimuli of different rates would be separated in the same perceptual dimension as the stimuli differing only in spectral shape. In addition, and as a control for the first experiment, the effect of varying the flatness of the spectral shape on spectral shape perception was tested (Experiment 2). To further facilitate interpretation of Experiment 1, the ability to discriminate 450 and 1800 Hz pulse trains from 900 Hz pulse trains in single-electrode stimuli was measured for each subject (Experiment 3).

II. METHODS

A. Subjects

Six subjects, all users of the CI24 Cochlear Ltd. cochlear implant, participated in this study. Four of the subjects used the CI24M "straight" electrode array, and two used the CI24R(CS) "contour" array. Subject details regarding cochlear implant use and etiology are listed in Table I.

TABLE I. Subject details.

Subject	Implant type	Years of deafness[a]	Aetiology	Experiment electrodes
S1	CI24R(CS)	12	Unknown	14–20
S2	CI24M	4	Unknown	15–21
S3	CI24R(CS)		Progressive, following noise injury	14–20
S4	CI24M	1	Trauma	13–19
S5	CI24M	2	Trauma and infections	14–20
S6	CI24M	2	Chronic infection	14–20

[a]Years of profound deafness prior to implantation.

B. Stimuli

For each subject, seven adjacent apical electrodes (generally 14–20) in the apical region (where vowel spectra are usually represented) were selected from their maps for use in the multiple electrode stimuli in Experiments 1 and 2. If possible, a region with uniform T and C levels was selected. [T level is the current that elicits a threshold loudness and C level is the current that elicits a comfortably loud sensation, for a pulse train on a particular electrode.] Thus the electrode set for subjects S2 and S4 were shifted one electrode apically or basally, respectively. The seven electrodes chosen for each subject are shown in Table I.

Each stimulus comprised a biphasic pulse train that activated each of the seven electrodes sequentially, beginning with the most apical electrode. The cycle of seven biphasic pulses on seven electrodes was repeated with cycle rates of 450, 900, or 1800 Hz in Experiment 1, and 900 Hz only in Experiment 2 for a total duration of 500 ms. Within each stimulation cycle, the seven pulses were equally spaced in time (resulting in overall rates of 3150, 6300, and 12 600 Hz). Monopolar mode (MP1+2) was used, and each pulse had a phase duration of 26 μs, and interphase gap of 8.4 μs.

Three "spectral profiles" were created by adjusting the currents of the pulses at each electrode position. The loudness balanced C levels from the subject's clinical map were used as a baseline and specified numbers of current steps (in clinical units) were subtracted from these to create the three profiles (see Table II). A clinical current unit for the CI24 implant is equal to a 0.1759 dB increment in current. In further level manipulations (adjusting for comfortable loudness and loudness balancing), all current step values across the seven electrodes were adjusted in equal numbers of current steps, so as to maintain the same profile.

In Experiment 1, nine stimuli were created for each subject using all combinations of the three profiles in Table II and the three rates of stimulation (450, 900, and 1800 Hz). These nine stimuli are labeled according to both their profile and rate; thus stimulus A450 had profile A and rate 450 Hz.

In Experiment 2, a second series of multiple-electrode stimuli were created, all with a rate of 900 Hz. The purpose of this second experiment was to measure the effect of per-

TABLE II. The three spectral profiles for Experiment 1. Under each electrode number, the number of current steps subtracted from the balanced comfortably loud levels (C levels) is given. Patterns A, B, and C have peaks of current at electrodes 15, 17, and 19, respectively.

	Electrodes[a]						
Profile	14	15	16	17	18	19	20
Pattern A	5	0	5	15	20	25	25
Pattern B	25	18	5	0	5	18	25
Pattern C	25	25	20	15	5	0	5

[a]Note that the particular electrodes used are different for two subjects (see Table I).

ceptual profile flatness to ascertain how this may affect the interpretation of the first experiment. In this case, each of the three previous spectral profiles were used, but with three degrees of flatness to make nine stimuli (see Table III). The stimuli labeled A2, B2, and C2 are the same as stimuli A900, B900, and C900 in Experiment 1, whereas A1 and A3 are flatter and steeper versions of A900, respectively (and similarly for B1, B3, C1, and C3). Stimuli A1 and A3 were created by considering the average change in dynamic range when going from 900 Hz to 1800 or 450 Hz, respectively, and setting the currents so as to create profile depths that were equivalent to those in Experiment 1 for A1800 and A450, when expressed as a proportion of the dynamic range. For example, average dynamic ranges over a large number of subjects and electrodes in our clinic are 44, 51, and 63 current steps for 450, 900, and 1800 Hz, respectively. Thus the A450 stimulus in Experiment 1 varied the current steps across a wider part of the (smaller) dynamic range than did A900. Stimulus A3 (using 900 Hz) mimics the spectral profile of A450 when expressed in proportion of dynamic range. Similarly, stimulus A1 mimics the profile of A1800 when expressed as a proportion of the dynamic range.

In Experiment 3, the stimuli were all single-electrode pulse trains with rates of 450, 900, and 1800 Hz. The selected electrode was the center one from the set of seven used in Experiments 1 and 2. The mode, phase duration, interphase gap duration, and stimulus duration were all the same as in Experiments 1 and 2.

C. Procedures

The nine stimuli in Experiments 1 and 2 and the three stimuli in Experiment 3 were first loudness balanced. The reference stimuli (B900 in Experiment 1, A2 in Experiment 2, and 900 Hz in Experiment 3) were first set to a comfortable level, and each of the remaining stimuli in each set were balanced to these references. The loudness balancing procedure was an adaptive two-alternative forced choice procedure, in which subjects were asked to choose the louder of the two stimuli. In the first run, the reference stimulus was fixed at the reference level, and the level of the second (variable) stimulus was decreased or increased, based on the response of the previous trial (whether or not the variable stimulus was rated the louder of the pair). The adaptive step size was four current levels until the second turning point, followed by two current levels, until a further six turning points had been obtained. The final four turning points were averaged. A second run was completed with the reference stimulus becoming the variable stimulus and vice versa. The entire procedure was then repeated (making four runs of the adaptive procedure in total) and the average difference in level between the two balanced stimuli was calculated to set the balanced level for the second stimulus.

For Experiments 1 and 2, each set of nine stimuli was presented to the subjects in a MDS task. The subjects were first familiarized with the stimuli. Subsequently all possible pairs of the nine stimuli (in each order) were presented in

TABLE III. The nine spectral profiles for Experiment 2. Under each electrode number, the number of current steps subtracted from the balanced C levels is given. Patterns A, B, and C have peaks at electrodes 15, 17, and 19, respectively.

	Electrode[a]						
Profile	14	15	16	17	18	19	20
A1	4	0	4	12	16	20	20
A2	5	0	5	15	20	25	25
A3	6	0	6	17	23	29	29
B1	20	12	4	0	4	12	20
B2	25	18	5	0	5	18	25
B3	29	17	6	0	6	17	29
C3	20	20	16	12	4	0	4
C2	25	25	20	15	5	0	5
C3	29	29	23	17	6	0	6

[a]The actual electrode numbers used for each subject are in Table I.

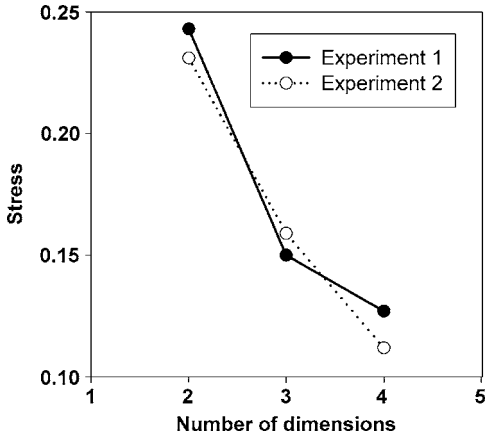

FIG. 1. The stress of the solutions for differing numbers of dimensions of the MDS analysis for Experiments 1 and 2.

random order (72 pairs in total). Subjects were instructed to judge the dissimilarity of the two stimuli in each pair, and to respond using a sliding bar on the test box. The sliding bar was unmarked except for the labels "exactly the same" and "the most different" at each end. The computer converted the response position to a number between 0 and 100. Subjects were encouraged to use the whole range of the scale. They were also encouraged to use any perceived difference in the stimuli in their rating of dissimilarity. Six or seven complete response matrices from each subject (depending on time constraints and subject fatigue) were recorded for analysis. These data matrices were combined, creating one matrix per subject per experiment. The matrices were then analyzed using nonparametric individual-differences MDS.

In Experiment 3, the ability to discriminate stimuli based on differences in rate was measured. The ability to discriminate 450 or 1800 Hz single-electrode stimuli (the test stimuli) from the 900 Hz stimulus (reference stimulus) was measured in a three-alternative forced-choice procedure, in which one of three intervals contained the test stimulus and the remaining two intervals contained the reference stimulus. To reduce the likelihood of use of cues due to residual loudness differences, a random level variation was applied to each interval of ±2 current steps. The percentage correct response over 50 trials was recorded for each comparison.

III. RESULTS

The dissimilarity matrices from the MDS experiments were first analyzed in different numbers of dimensions to assess the appropriate number of dimensions for interpretation. The stress (a measure of badness-of-fit of the stimulus space to the data) was plotted versus number of dimensions to look for a kneepoint in the function (Fig. 1). This kneepoint is theoretically where additional dimensions are fitting error in the data rather than real perceptual dimensions (Kruskal, 1964). For Experiment 1, there was a clear kneepoint at three dimensions. For Experiment 2, there was not a clear kneepoint in the function. However, the analysis was performed in three dimensions for both experiments so that the stimulus spaces could be easily compared to each other.

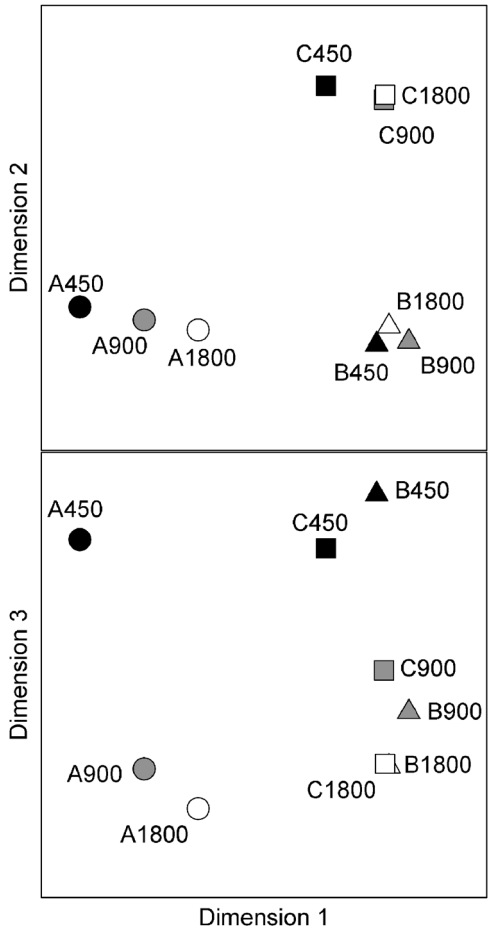

FIG. 2. The three-dimensional stimulus space resulting from Experiment 1. The three spectral profiles are denoted by different symbol shapes and the three rates by different symbol fillings.

The three-dimensional stimulus space resulting from Experiment 1 is shown in Fig. 2. It can be seen in the top panel of Fig. 2 (dimension 1 versus dimension 2), that the stimuli are grouped according to stimulus spectral profile. That is, the three stimuli with pattern A (and different rates) are considered very similar in these dimensions as are the three with pattern B and with pattern C. It might have been predicted that the A's, B's, and C's would be arranged linearly in this plane (implying a single dimension related to the position of the spectral peak in the patterns). However, previous experi-

TABLE IV. Individual weights for spectral profile and rate dimensions in Experiment 1.

	S1	S2	S3	S4	S5	S6	Average rms
Spectral profile	0.8795	0.9379	0.7053	0.7538	0.8717	0.7740	0.8244
Rate dimension	0.2445	0.0608	0.3875	0.4609	0.3232	0.4641	0.3526

ments using MDS and varying place-of-stimulation have always shown a better fit when the stimulus space was two dimensional, with the stimuli being arranged around a single curve in this dimension, the position around the curve being related to electrode position (Collins and Throckmorton, 2000; Henshall and McKay, 2001; McKay and McDermott, 1996). A curve is obtained rather than a straight line probably because stimuli that are very distinct cannot readily be ranked in perceptual difference (Collins and Throckmorton, 2000). For example, in Fig. 2 (top panel) the distance between patterns A and C is very similar to the distance between A and B, or between B and C, resulting in a triangular pattern in these two dimensions. Looking at the bottom panel in Fig. 2 (dimension one versus dimension three), it can be seen that dimension three is clearly related to the rate of stimulation. The 450, 900, and 1800 Hz stimuli are arranged in vertical order along dimension three, although there is more distance between 450 and 900 Hz than there is between 900 and 1800 Hz.

Table IV shows the dimension weights for each subject. The squared weights are the proportion of data variance accounted for by the particular dimension. Weights that are equal in all dimensions imply that the subject weighted the importance of the dimensions equally (as depicted in the group stimulus space of Fig. 2), whereas a weight near zero implies that the subject did not use that dimension when ranking differences. The weights from dimensions one and two have been combined (square root of the sum of squares) to represent a single weight for the spectral profile dimension, and the weight for dimension three is considered to be the weight for the rate dimension. It can be seen that only one subject (S2) had a negligible weight for the rate dimension, although generally, the weight for the rate dimension (rms average 0.3526) was about half that for the spectral profile dimension (rms average 0.8244).

The stimulus space resulting from Experiment 2 is shown in Fig. 3. As with Experiment 1, the plane defined by dimensions one and two depicts the perceptual dimension related spectral profile shape (that is, the electrode position related to the peak in the profile). In this plane, the three profiles with pattern A are grouped together, as are the three with patterns B and C, respectively. In dimension three (bottom panel, vertical direction) the stimuli are not ordered in any systematic way. Although the three A patterns with differing spectral flatness are separated in this dimension, the B and the C patterns do not show the same ordering or separation.

The individual subject weights for the spectral profile dimension (a combination of dimensions one and two) and the third dimension are shown in Table V. Subject S2, who was the only subject with a negligible weight for the rate dimension in Experiment 1, was the subject who placed the most weight on dimension three in Experiment 2. In general the weights attached by the subjects to the third dimension (rms average 0.1991) were less than a quarter of the weight attached to the spectral profile dimensions (rms average 0.8958). The small weight attached to the third dimension, and the lack of kneepoint in the stress function at three dimensions (Fig. 1), together with the difficulty interpreting the dimension in relation to stimulus parameters, lends support to the proposition that subjects did not rate the flatness of the spectrum as an independent perceptual dimension in the stimulus set of Experiment 2. In fact, the third dimension in Experiment 2 might be merely fitting experimental noise.

The results of Experiment 3 are shown in Table VI. It can be seen that four of the subjects could significantly dis-

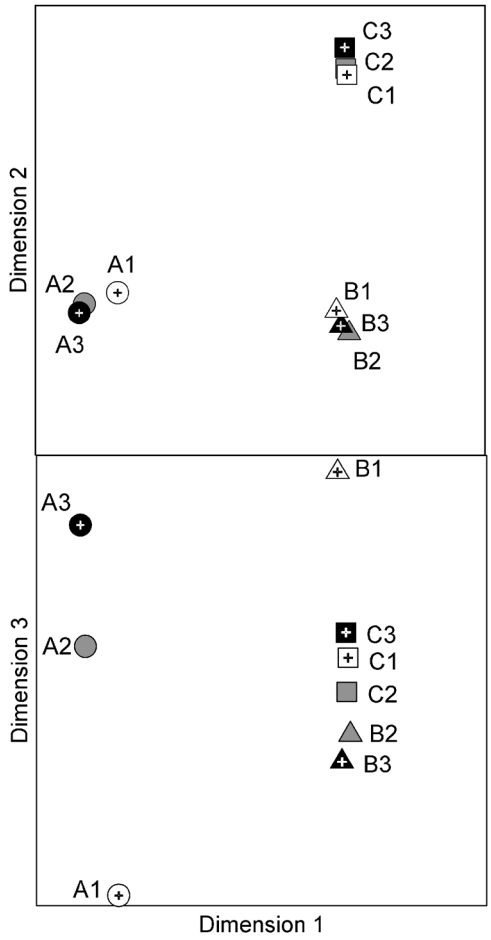

FIG. 3. The three-dimensional stimulus space resulting from Experiment 2. Stimuli A2, B2, and C2 correspond to A900, B900, and C900 from Experiment 1. As in Experiment 1, different spectral profiles are denoted by different symbol shapes, and in this experiment, different profile flatness is denoted by different symbol fillings.

TABLE V. Individual weights for spectral profile and dimension three in Experiment 2.

	S1	S2	S3	S4	S5	S6	Average (rms)
Spectral profile	0.9819	0.6968	0.9897	0.9176	0.8190	0.9344	0.8958
Dimension three	0.1247	0.3188	0.0763	0.1933	0.2380	0.1447	0.1991

TABLE VI. The percentage of correct responses from 50 trials for the rate discrimination (3IFC) test. Individual scores of 46% or more (in bold) are significant at the 0.05 level (without a correction for multiple comparisons). The chance level is 33%.

	S1	S2	S3	S4	S5	S6	Average
450 vs 900 Hz	**80**	34	**46**	**54**	42	42	49.6
900 vs 1800 Hz	**46**	32	26	30	36	**58**	38.0

criminate at least one of the rate pairs. However, only one comparison in one subject (S1, 450 vs 900) elicited a score (80%) that would exceed the common definition of a difference limen (usually 70%–75% correct).

IV. DISCUSSION

The result of Experiment 1 showed that five of the six subjects perceived an independent dimension related to the rate of stimulation when listening to multiple-electrode stimuli, even though the rates of stimulation were barely or not distinguishable when presented in a discrimination task on a single electrode (Experiment 3). The result of Experiment 2 showed that the rate dimension in Experiment 1 was very unlikely to have been a by-product of the change in dynamic range due to changes in rate. If that were the case, then changing the flatness of the profiles (as in Experiment 2), without changing the rates, should have produced a similar stimulus space to that of Experiment 1.

It was postulated in the introduction that changes of high rates may cause changes in the excitation pattern shape because lower currents are used for higher rates and neurons may respond differentially to high rates. If this were the case, it would be expected that the stimuli with different rates and same profile in Experiment 1 would have been shifted relative to each other within the dimension related to spectral profile. For example, the A450, A900, and A1800 stimuli would be separated in the plane of dimensions one and two in Fig. 2. If A1800 resulted in an apical shift in the excitation pattern compared to A450, for example, it would be expected to shift toward B450 in the stimulus space. However, such shifts are not evident in Fig. 2. It appears that all the same-profile stimuli in Experiment 1 remained extremely similar in the perceptual dimensions related to spectral profile (top panel).

The dimension that separated the different rates (dimension three) was orthogonal to the spectral profile dimension. This orthogonality is what would be expected if the rate dimension was related to the perception of temporal features in the stimuli. Temporal and spatial aspects of electrical stimulation have previously been shown to be orthogonal dimensions (Tong *et al.*, 1983; McKay *et al.*, 2000). Thus it is tempting to propose that the subjects in Experiment 1 were perceiving the rate of stimulation, even though the rates used were barely discriminable in single-electrode stimuli. The subject (S2) who had a negligible weight in the rate dimension (Table IV) also showed chance scores on the rate discrimination task (Table VI). However, the second subject with only chance scores for both rate comparisons (S5) had a weight for the rate dimension close to the average for all subjects, and the subject with the best rate discrimination (S1) had the second lowest weight for the rate dimension. If the subjects were indeed rating perceptual differences between the multiple-electrode stimuli on the basis of rate of stimulation, the results perhaps indicate that rates are easier to distinguish when multiple electrodes are carrying the rate information. It should be noted, however, that in the multiple electrode stimuli, the pulses on different electrodes were temporally shifted relative to each other, which would have smeared the rate information for neurons activated by more than one electrode. Whether or not subjects were perceiving the rate *per se*, or some other unknown perceptual attribute related to rate of stimulation, it is clear that some feature of the stimulus perception changed with rate, and that it was perceptually independent to the spectral profile perception.

The results of this experiment do not throw any light on the issue of why some subjects perceive speech better with higher rates and some do not. In contrast, the results suggest that changes in rate do not in general affect spectral profile perception. The perceptual distances between A450, B450, and C450, were very similar to those between A1800, B1800, and C1800. The results are, however, consistent with the reports from clinicians that changes in high rates are noticeable by patients. Further experiments may elucidate the source of the perceptual change with rate.

V. CONCLUSIONS

These experiments showed that changing the rate in multiple electrode stimuli does not alter the perception of spectral shape, but does lead to a perceptual dimension that is orthogonal to that of spectral profile perception. This is true even though the rates are difficult or impossible to discriminate in single-electrode stimuli.

ACKNOWLEDGMENTS

This work was supported by the Australian National Health and Medical Research Council, through a fellowship to C.M.M. We thank the subjects who gave generously of their time for these experiments.

Brill, S. M., Gstottner, W., Helms, J., von Ilberg, C., Baumgartner, W., Muller, J., and Kiefer, J. (**1997**). "Optimization of channel number and stimulation rate for the fast continuous interleaved sampling strategy in the COMBI 40+," Am. J. Otol. **18**, S104–106.

Collins, L. M., and Throckmorton, C. S. (**2000**). "Investigating perceptual features of electrode stimulation via a multidimensional scaling paradigm," J. Acoust. Soc. Am. **108**, 2353–2365.

Friesen, L. M., Shannon, R. V., and Cruz, R. J. (**2005**). "Effects of stimulation rate on speech recognition with cochlear implants," Audiol. Neuro-Otol. **10**, 169–184.

Frijns, J. H., Briaire, J. J., de Laat, J. A., and Grote, J. J. (**2002**). "Initial

evaluation of the Clarion CII cochlear implant. Speech perception and neural response imaging," Ear Hear. **23**, 184–197.
Fu, Q. J., and Shannon, R. V. (**2000**). "Effect of stimulation rate on phoneme recognition by nucleus-22 cochlear implant listeners," J. Acoust. Soc. Am. **107**, 589–597.
Henshall, K. R., and McKay, C. M. (**2001**). "Optimizing electrode and filter selection in cochlear implant speech processor maps," J. Am. Acad. Audiol **12**, 47–489.
Kiefer, J., von Ilberg, C., Rupprecht, V., Hubner-Egner, J., and Knecht, R. (**2000**). "Optimized speech understanding with the continuous interleaved sampling speech coding strategy in patients with cochlear implants: Effect of variations in stimulation rate and number of channels," Ann. Otol. Rhinol. Laryngol. **109**, 1009–1020.
Kruskal, J. B. (**1964**). "Multidimensional scaling by optimizing goodness of fit to a nonmetric hypothesis," Psychometrika **29**, 115–129.
Landsberger, D. M., and McKay, C. M. (2005). "Perceptual differences between low and high rates of stimulation on single electrodes for cochlear implantees," J. Acoust. Soc. Am. (in press).
McKay, C., McDermott, H., and Carlyon, R. (**2000**). "Place and temporal cues in pitch perception: Are they truly independent?," Acoustic Res. Lett. Online **1**, 25–30.
McKay, C. M., and McDermott, H. J. (**1996**). "The perception of temporal patterns for electrical stimulation presented at one or two intracochlear sites," J. Acoust. Soc. Am. **100**, 1081–1092.
Skinner, M. W., Arndt, P. L., and Staller, S. J. (**2002a**). "Nucleus 24 advanced encoder conversion study: Performance versus preference," Ear Hear. **23**, 2S–17S.
Skinner, M. W., Clark, G. M., Whitford, L. A., Seligman, P. M., Staller, S. J., Shipp, D. B., Shallop, J. K., Everingham, C., Menapace, C. M., Arndt, P. L., Antogenelli, T., Brimacombe, J. A., Pijl, S., Daniels, P., George, C. R., McDermott, H. J., and Beiter, A. L. (**1994**). "Evaluation of a new spectral peak coding strategy for the Nucleus 22 Channel Cochlear Implant System," Am. J. Otol. **15**, 15–27.
Skinner, M. W., Holden, L. K., Whitford, L. A., Plant, K. L., Psarros, C., and Holden, T. A. (**2002b**). "Speech recognition with the nucleus 24 SPEAK, ACE, and CIS speech coding strategies in newly implanted adults," Ear Hear. **23**, 207–223.
Tong, Y. C., Blamey, P. J., Dowell, R. C., and Clark, G. M. (**1983**). "Psychophysical studies evaluating the feasibility of a speech processing strategy for a multiple-channel cochlear implant," J. Acoust. Soc. Am. **74**, 73–80.
Vandali, A. E., Whitford, L. A., Plant, K. L., and Clark, G. M. (**2000**). "Speech perception as a function of electrical stimulation rate: Using the nucleus 24 cochlear implant system," Ear Hear. **21**, 608–624.
Zeng F. G. (**2002**). "Temporal pitch in electric hearing," Hear. Res. **174**, 101–106.
Ziese, M., Stutzel, A., von Specht, H., Begall, K., Freigang, B., Sroka, S., and Nopp, P. (**2000**). "Speech understanding with the CIS and the n-of-m strategy in the MED-EL COMBI 40+ system," ORL **62**, 321–329.

Classification and identification of recorded and synthesized impact sounds by practiced listeners, musicians, and nonmusicians

Robert A. Lutfi, Eunmi Oh,[a] Eileen Storm, and Joshua M. Alexander
Department of Communicative Disorders and Waisman Center, University of Wisconsin, Madison, Wisconsin 53706

(Received 21 May 2004; revised 13 April 2004; accepted 25 April 2005)

Three experiments were conducted to test the viability of a low-parameter modal model for synthesizing impact sounds to be used in commercial and psychoacoustic research. The model was constrained to have four physically based parameters dictating the amplitude, frequency, and decay of modes. The values of these parameters were selected by ear to roughly match the recordings of ten different resonant objects suspended by hand and struck with different mallets. In experiment 1, neither 35 professional musicians nor 187 college undergraduates could identify which of the two matched sounds was the real recording with better than chance accuracy, though significantly better than chance performance was obtained when modal parameters were selected without the previously imposed physical constraints. In experiment 2, the undergraduates identified the source corresponding to the recorded and synthesized sounds with the same level of accuracy and largely the same pattern of errors. Finally, experiment 3 showed highly practiced listeners to be largely insensitive to changes in the acoustic waveform resulting from an increase in the number of free parameters used in the modal model beyond 3. The results suggest that low-parameter, modal models might be exploited meaningfully in many commercial and research applications involving human perception of impact sounds.
[DOI: 10.1121/1.1931867]

PACS number(s): 43.66.Yw, 43.66.Fe [AK] Pages: 393–404

I. INTRODUCTION

Impact sounds, the sounds produced by objects coming in brief contact with one another, are abundant in nature and in music. They constitute an important class of sounds in the fields of physical and musical acoustics (Morse and Ingard, 1968; Rossing and Fletcher, 1999), and they play a significant role in ongoing efforts to automate sound animation for computer gaming applications and interactive virtual environments (Durlach and Mavor, 1995). This paper is concerned primarily with the use of impact sounds in psychoacoustic research, where they are the favored stimulus in studies of human sound source identification. The goal is to provide an initial evaluation of a low-parameter modal model for synthesizing impact sounds that could be practically applied in psychoacoustic studies of how listeners recover source attributes from sound.

In most past psychoacoustic studies using impact sounds the sounds have been generated "live" or have been recorded from live sources (cf. Carello *et al.*, 1998; Freed, 1990; Kunkler-Peck and Turvey, 2000; Lakatos *et al.*, 1997; Li *et al.*, 1991; Repp, 1987; Warren and Verbrugge, 1984). Such manner of presentation ensures that most, if not all, acoustic information about the source is preserved in the sound reaching the listener's ears, but there are drawbacks. Live sounds are difficult to control and replicate accurately without special apparati. The time and cost of constructing such apparati can be great and is likely the reason that few studies have attempted to replicate the results of other laboratories using live sound. Sound recordings have an advantage in that they can be reliably replicated and easily manipulated. However, sound recordings are impractical in research applications where the acoustic cues must be precisely related to the physical dynamics of the sound-producing source (Lutfi, 2001; Lutfi and Oh, 1994, 1997; Lutfi and Wang, 1999) or, as in gaming applications, where one requires real-time interactive or adaptive control over source parameters (cf. Cook, 1996, 1997; Durlach and Mavor, 1995; Van den Doel, 1998; Van den Doel and Pai, 1996, 1998; Van den Doel *et al.*, 2002).

As a reaction to these problems there has been recent growing interest in physically informed (PI) models for synthesizing impact sounds for use in both commercial and research applications (Gaver, 1993a, b; Giordano and Petrini, 2003; Lakatos *et al.*, 2000; Lutfi, 2001; Lutfi and Oh, 1997; Roussarie *et al.*, 1998, and Takala and Hahn, 1992). This work uses what is known regarding the physics of vibrating bodies to exert greater control over relevant acoustic parameters and their relations. Gaver (1993a) proposed an early working model of this type in which the vibrating object is represented as a bank of damped oscillators driven by an external force. Subsequent work has offered specific suggestions for how to select the parameters of this model based on the material and geometric properties of the object, the type of driving force, and the point at which the driving force is

[a]Present address: at Samsung AIT P.O. Box 111, Suwon, Korea 440-600; Electronic mail: ralutfi@wisc.edu

applied to the object (Cook, 1996, 1997; Lambourg *et al.*, 2001; Chaigne and Doutaut, 1997; Lutfi, 2001; Lutfi and Oh, 1994, 1997; Morrison and Adrien, 1993; Roussarie *et al.*, 1998; Van den Doel, 1998; Van den Doel and Pai, 1996, 1998; Van den Doel *et al.*, 2002). The product of these efforts in each case is a precise analytic representation of the stimulus that serves to specify the various sources of acoustic information for identification. The representation also affords the freedom in manipulating stimuli necessary to determine precisely how listeners make use of this information (e.g., Lutfi, 2001; Lutfi and Oh, 1994, 1997).

Though much work has already been undertaken using the physically informed approach, few studies have addressed the question as to how much detail is required in a PI model for it to be generally applicable in psychoacoustic research. Most published studies to date have been intended for applications in music and audio animation where the goal has been to reduce the computational load involved in the sound synthesis. These studies have mostly used similarity metrics to evaluate the degree to which listeners judge the synthesized sounds to "sound like" the real thing (Charbonneau, 1981; Grey, 1977; Grey and Moorer, 1977; Van den Doel *et al.*, 2002)—a different criterion than would be required for many applications in psychoacoustic research. Where just-noticeable differences have been measured using forced-choice methods the primary concern has been with the perceptible effects of data reduction schemes applied to the acoustic waveforms (Grey and Moorer, 1977; McAdams *et al.*, 1999; Sandell and Martens, 1995). Such results bear only indirectly on the problem of determining the minimal number of parameters required of a PI model to produce an acceptable psychophysical approximation to live sound.

The present study was undertaken to get some sense of the amount of detail required of a PI model for it to be of general use in psychophysical research. Our approach was to begin with a generic model having a small number of free parameters (a large number of physical constraints) and to add complexity until certain criteria for psychophysical validity were met. For practical reasons, described later, we chose not to pursue the strictest criterion, which would be to require that real and synthesized sounds be indistinguishable from one another. Instead, the following three criteria were chosen: First, in forced-choice comparisons between real-recorded and synthesized sounds, highly trained listeners (professional musicians) were required to identify the real sound with no greater than chance accuracy. Second, in a source identification task involving untrained listeners, real-recorded and synthesized sounds were required to produce no significant differences in performance or pattern of errors. Third, for a given number of free parameters satisfying the first two criteria, highly practiced listeners were required to be largely insensitive to the changes resulting from further increases in the number of parameters used to synthesize the sounds. As it turned out, the generic model with fewest parameters tested satisfied all three criteria. The results imply that in many cases low-parameter PI models can be applied with efficacy in psychoacoustic studies of human sound source identification using impact sounds.

II. SOUND RECORDING AND SYNTHESIS

The general PI model that we have adopted is fundamentally the one proposed by Gaver (1993a) and used in most current applications in psychophysical research referenced above. The sound-producing object is represented as a series of N coupled oscillators driven at some point x_c by an impulse and damped by both external and internal frictional forces. The parameters of this model are a vector of N modal frequencies, ν_n, with associated gain, $C_{n,x}$, and decay moduli, τ_n that depend on the geometric and material properties of the source (cf. Kinsler and Frey, 1962; Lutfi, 2001; Rossing and Fletcher, 1999). The gain values further depend on the location x where the radiated sound is measured and the point x_c where the impulse is applied. The sound-pressure waveform radiated at x is given by

$$y_x(t) = \sum_{n=1}^{N} C_{n,x,x_c} e^{-t/\tau_n} \sin(2\pi\nu_n t). \quad (1)$$

Allowing overall intensity to vary arbitrarily, the maximum number of free parameters of this model is $3N-1$. Our intent was to systematically vary the number of free parameters up to $3N-1$ to find the minimum number that would satisfy the three criteria for "psychophysical validity" previously stated. This turned out to be unnecessary as the model with fewest free parameters tested satisfied these criteria. We will refer to this as the physically least-informed (PLI) model.

The PLI model had four free parameters that were chosen to capture the gross acoustic effect of various physical properties of the object, how it was held, and how it was struck. Note that it is the physically informed constraints placed on parameter selection that distinguish the PLI model from a pure modal model in which parameters are selected without constraint to match those of the source signal. The first parameter specified the ratios ν_n/ν_1 of the modal frequencies as is associated with the gross geometric dimensions of the object; i.e., its class or type. This parameter could take on one of two values depending on whether the object to be simulated was judged to have acoustic properties more like that of a bar or more like that of a plate. For the bar the frequency ratios were 1.00, 6.26, and 17.54; for the plate they were 1.00, 2.80, 5.15, 5.98, 9.75, 14.09, 14.91, 20.66, and 26.99. These values appear in standard acoustics texts as theoretical values representing ideal homogenous bars clamped at one end and loosely suspended circular plates (e.g., Rossing and Fletcher, 1999). Higher frequency ratios given in these texts were not included as the frequencies would have been outside the audible range for the objects we selected for simulation. The second and third free parameters were the frequency, ν_1, and decay modulus, τ_1, of the first partial. The frequency ν_1 was used to largely capture the effects of object size and material, while decay modulus τ_1 was used to approximate the degree of damping of the source resulting from internal friction and/or the manner in which the source was suspended by hand and struck (Morse and Ingard, 1968). The decay modulus of the first partial further dictated the decay moduli of higher partials. For the bar these were constrained to vary in inverse proportion to the cube of frequency, $\tau_n = \tau_1(\nu_1/\nu_n)^3$ (cf. Morse and Ingard, 1968; Lutfi

TABLE I. Description of objects used to produce sound recordings including hammers used and approximately where the objects were held and struck.

Object	Description	Hammer	Grip	Point of contact
A	Small pipe, holes each end, $\sim 6 \times 1$ in.^{2}	All plastic, handle end	$\frac{1}{4}$ way down	bottom
B	Small ceramic plate, ~6-in. diameter	metal head- pointy end	$\frac{1}{4}$ way down	$\frac{3}{4}$ way down
C	Square hollow aluminum tube ~ 3 ft $\times 1.5$ in.	Plumb permabond plastic end	$\frac{1}{4}$ way down	middle
D	Rectangular wood slab, cedar, $\sim 18 \times 0.5 \times 6$ in.^{3}	metal head- pointy end	$\frac{1}{4}$ way down	$\frac{3}{4}$ way down
E	Small juice glass	metal head- pointy end	bottom	middle
F	Large hollow iron pipe, rusted ~ 1.5 ft $\times 4$ in.	Plumb permabond plastic end	top	$\frac{3}{4}$ way down
G	Small ceramic bowl, ~5-in. diameter	metal head- pointy end	$\frac{1}{4}$ way down	$\frac{3}{4}$ way down
H	Light metal rectangular strip with sides folded over, $\sim 12 \times 1$ in.^{2}	metal head- pointy end	top	$\frac{3}{4}$ way down
I	Small hollow metal chime, $\sim 5 \times 0.3$ in.^{2}	metal head- pointy end	$\frac{1}{4}$ way down	$\frac{3}{4}$ way down
J	Thin brass rod ~ 3 ft $\times \frac{1}{8}$ in.	All plastic, handle end	$\frac{1}{4}$ way down	$\frac{3}{4}$ way down

and Oh, 1997; Lutfi, 2001). For the plate they varied in inverse proportion to frequency (Rossing and Fletcher, 1999). The fourth and final parameter was spectral tilt, linear in dB/oct, which specified the relative gain values $C_{n,x}/C_{1,x}$ of the partials. The values of spectral tilt could be either positive or negative and were used to roughly approximate the effects of the point of impact, type of hammer used, and the manner in which the source was held. For example, a soft mallet produces an impulse that increases more gradually over time, resulting in a loss of high frequencies in the driving force and concomitant attenuation of higher frequency partials in the response (Fletcher and Rossing, 1991, pp. 547–548).

Altogether ten stimuli were synthesized using the PLI model. The parameters of the model in each case were selected by ear by a laboratory assistant so as to roughly match the sound recordings of ten everyday resonant objects suspended by hand and struck with different hammers. Details of the stimulus generation for the matching phase of the study were the same as those used in the experiments as described in Sec. III A. After one or more comparisons the assistant would adjust one or more of the free parameters of the modal model in an attempt to reconstruct a synthesized sound that was a closer match to the recording. There was no systemic procedure or order for selecting parameters; rather the selection was made simply by trial and error. Again, the intent was not to make sounds indiscriminable from one another, only to achieve a realistic qualitative match.

A description of the objects used in these experiments is given in Table I along with a description of the hammers used, and an indication of approximately where the objects were held and struck. These objects were selected because they made a variety of different sounds and because they could be readily found in our lab and machine shop. There were no other special criteria for selecting these objects. We chose the objects to be held by hand because we were interested in the sounds that occur naturally when a person picks up an object and strikes it to determine its physical properties from sound. Table II gives the values of the model parameters chosen for each of the ten objects used in the study. Recordings were made in a sound-treated room using a Shure SM81 directional microphone (all-pass setting) and a USBpre 16-bit analog-to-digital conversion system that sampled at a 44.1-kHz rate. The microphone was suspended on a boom and was pointed directly toward the sound source at approximately 2/3 m from the sound source. Both synthesized sounds and sound recordings were edited to be 1 s in duration from the beginning of the impact by applying a 10 -ms cosine-squared ramp at offset. In all but a few cases the sounds decayed to inaudibility within 1 s.

TABLE II. Parameter values of the modal model used in experiments I–III. See Table I for description of simulated objects and see text for description of acoustic parameters.

Object	ν_n/ν_1	ν_1 (Hz)	τ_1 (s)	C_n/C_1 (dB/oct)
A	Plate	5862	0.103	−6
B	Plate	1532	0.065	0
C	Plate	407	0.872	−6
D	Plate	808	0.037	−6
E	Plate	1827	0.194	−60
F	Plate	1591	0.397	0
G	Plate	1789	0.177	1
H	Plate	1460	0.069	0
I	Bar	2109	0.163	−12
J	Bar	3521	0.179	−6

III. EXPERIMENT 1. CLASSIFICATION OF IMPACT SOUNDS AS REAL OR SYNTHESIZED

The first experiment of the series addressed the first criterion for psychophysical validity. The ten real-recorded sounds were paired with their synthesized counterparts to create a sequence of ten, two-interval, forced-choice identification trials. Thirty-four members of the Madison Symphony Orchestra (MS listeners) and 187 undergraduate students from the University of Wisconsin—Madison (UW listeners) were asked to identify on each trial which of the two sounds corresponded to the real-recorded sound. We wished to determine whether either group would be able to identify the real-recorded sound with greater than chance accuracy. Note that the classification task differs from the task in which a listener is asked to give a subjective judgment regarding the perceived "realism" of a sound. The former has correct response, whereas the latter does not.

As a control a different group of UW listeners was asked to identify the real-recorded sounds when paired with synthesized sounds for which the frequencies and decay moduli were selected at random over roughly the same range of values used in the first experiment.

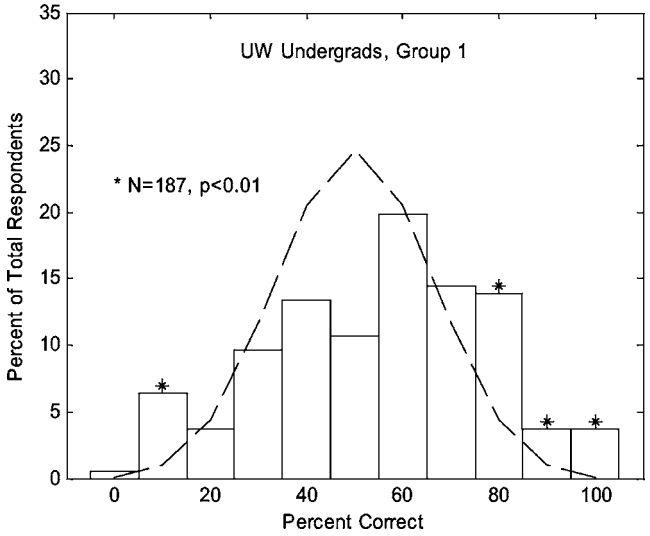

FIG. 1. The percentage of UW listeners that obtained each of the possible percent correct scores in the real versus synthesized classification task (experiment 1) is shown along with the predicted percentages given that true performance for all listeners was chance (dashed line). Where asterisks are shown the obtained percentages are significantly greater than would be predicted assuming that true performance for all listeners was at chance.

A. Procedure

The details of the procedure were slightly different for the MS and UW listeners. For the UW listeners the sounds were played in a large 16.8-m-wide by 17.5-m-long, two-story high, octagon-shaped, lecture hall over a modern, built-in, four-speaker, PA system (TOA Model F-605W). The frequency response of the speakers was flat (±5 dB) from 0.1 to 15.0 kHz. The walls of the lecture were largely covered by curtains offering little in the way of hard-reflecting surfaces. Listeners sat at different points in the room but were never less than 3 m away from the closet wall and never less than 4 m away from the closest speaker. For the MS listeners the sounds were played on the stage of a large orchestra concert hall (where the MS listeners were seated) over a pair of small Acoustic Research speakers with built-in amplifiers. Curtains surrounded the back of the stage and the listeners closest to the speakers were seated about 4 m away. The frequency response of the speakers was flat (±5 dB) from 0.2 to 15.0 kHz. For both groups of listeners the sounds were played at the 44.1-kHz rate with 16-bit resolution using a DELL notebook with an on-board Sound-Blaster Card. Sound level was adjusted to be at a comfortable listening level (roughly 65–70 dB SPL) near the center of each listening environment. The two sounds played on each trial were separated by 0.5 s with trials separated by approximately 8 s. Listeners were instructed that on each trial they would hear a pair of sounds corresponding to a common everyday object struck by a mallet. They were told that one of the sounds was a recording of the real object while the other was created artificially on a computer using mathematical equations—their task was to indicate which of the two sounds corresponded to the recording of the real object. Listeners marked their answers in pencil on a standard bubble sheet for later scoring by the UW grading center. No feedback was given on each trial as to which response was correct. UW listeners were also asked to rate their own musical ability on a 5-point scale from "can't carry a tune" to "highly-trained professional musician." For their participation the UW listeners received extra credit for a class in communicative disorders; the MS listeners received candy. The ten trials can be heard at http://www.aip.org/pubservs/epaps.html, the correct responses are respectively, 1st, 1st, 2nd, 1st, 2nd, 2nd, 2nd, 1st, 1st, 1st.

B. Results and discussion

Figure 1 shows the proportion of UW listeners that obtained each of the possible percent correct scores. The dashed line represents the predicted proportions, based on binomial probabilities, given that true performance was at chance; asterisks denote the obtained proportions that are significantly greater than would be predicted assuming true performance was at chance ($N=187$, $p<0.01$). Overall, the mean score of the UW listeners was 55.2% correct, not much better than chance. However, Fig. 1 shows that the mean score is not exactly representative of the "typical" listener since a disproportionate number of listeners scored both well above and well below chance. The results suggest that many listeners were able to identify some general quality that distinguished the two classes of sounds, but that they were about equally likely to identify this quality with the real as with the synthesized sounds.

The pattern of results was much the same for the MS listeners, as is shown in Fig. 2. The mean score for MS listeners was 49.1% correct, slightly less than the UW listeners, with a larger proportion of MS listeners scoring well below chance. A correlational analysis of the musical ability ratings of the UW listeners also failed to indicate a relation between musical ability and performance. Interestingly, the mean performance of UW listeners who rated themselves as "highly-trained musicians" ($N=30$) was, like the MS listen-

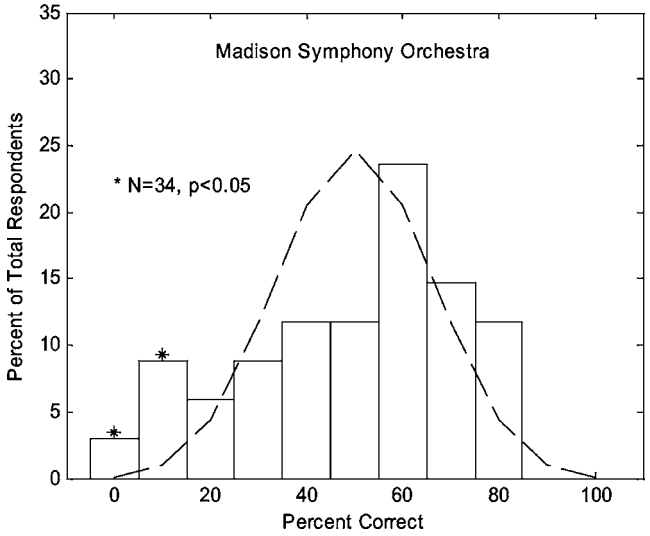

FIG. 2. Same as Fig. 1 except percentages are for MS listeners.

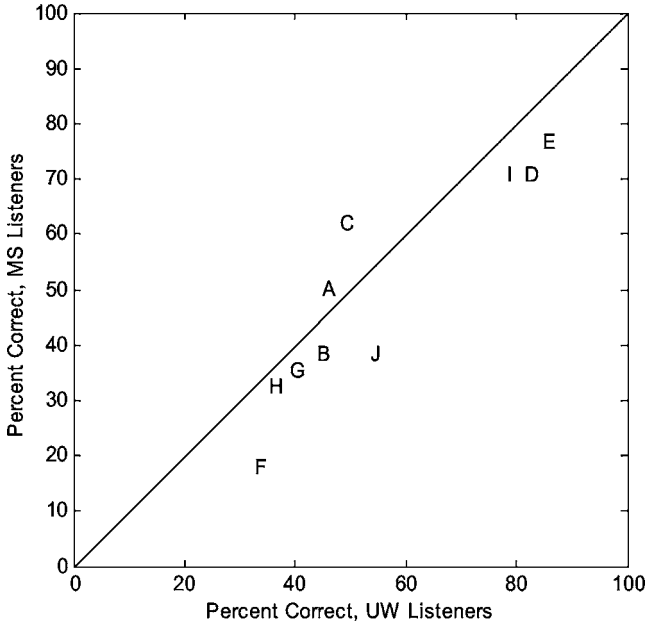

FIG. 3. Comparison of percent correct performance for UW and MS listeners in the real versus synthesized classification task (experiment 1) broken down by stimulus item. Letter symbols denote the different stimulus items as listed in Table I. Diagonal represents equal scores for the two groups.

ers, below chance. The failure to obtain an effect of musical training is, perhaps, not surprising given that past studies have obtained mixed results regarding the effect of musical training. Spiegel and Watson (1984) report that musicians generally perform better on frequency discrimination tasks than nonmusicians. Burns and Houtsma (1999) report that musicians are better at detecting harmonicity. Closer to the present study, however, Eagleson and Eagleson (1947) report that musicians are not much better at identifying musical instruments from isolated notes than college students and that neither group is very good.

We might speculate as to the reason for the extreme scores above and below chance. The difference was subtle, but, to our ears the synthesized sounds had what might be described as a "pure" or "musical" quality that distinguished them from the real-recorded sounds. Acoustically, we suspect this was due to the broader bandwidth of the partials in the real-recorded sounds, the presence of additional modes, and the interaction ("beating") among modes. The synthesized sounds also differed in having uniform attack properties; note that no attempt was made to model the interaction between the hammer and the vibrating object in this synthesis. Figure 3 gives a breakdown of percent correct performance for each item (symbol number) for each group of listeners. The figure shows clear differences in performance across items with good agreement between groups. It also shows that a few items in each case were responsible for the extreme scores: the large rusty pipe, ceramic bowl, and metal strip yielding scores below chance; the chime, wood slab, and juice glass yielding scores above chance ($N=2210$, $p<0.001$). We had hoped that such differences would provide further insights into the reason for the extreme scores; however, the particular grouping of items offers no obvious clues. Lakatos *et al.* (1997) report a similar result in which listeners more often than chance misidentified the shape of struck bars from their impact sounds. Though their study involved a very different type of judgment it is in keeping with the present results in showing consistent confusions for certain items.

Finally, to ensure that chance performance did not result from a simple failure of listeners to understand the task or to perform their best, we ran a control experiment. A second group of 158 UW listeners was given an easier task in which the synthesized sounds were created by selecting a random number of tones (from one to nine) with random frequencies uniformly distributed between 100 and 10000 Hz, and random decay moduli uniformly distributed from 0 to 0.8 s. All other aspects of the experiment were the same as before. The results are shown in Fig. 4. Mean performance in this case was 81.5% correct, well above chance ($N=1580$; $p<0.001$).

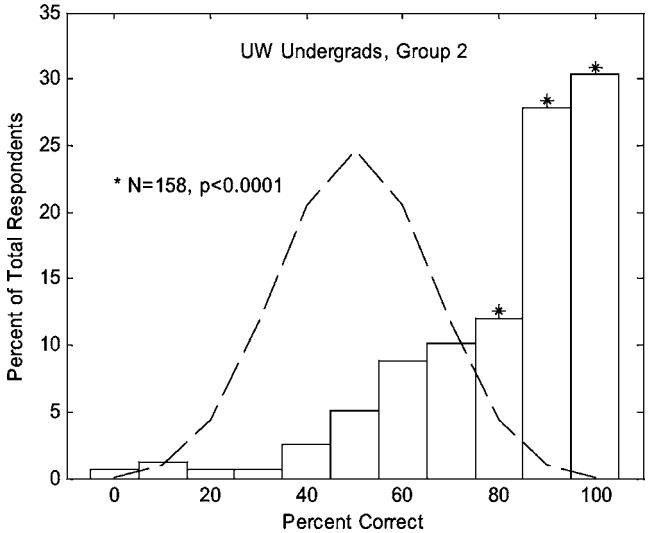

FIG. 4. Same as Fig. 1 except percentages are for a separate group of UW listeners who participated in a control experiment in which the synthesized sounds were created by selecting a random number of tones with random frequencies and decay moduli (see text for further details).

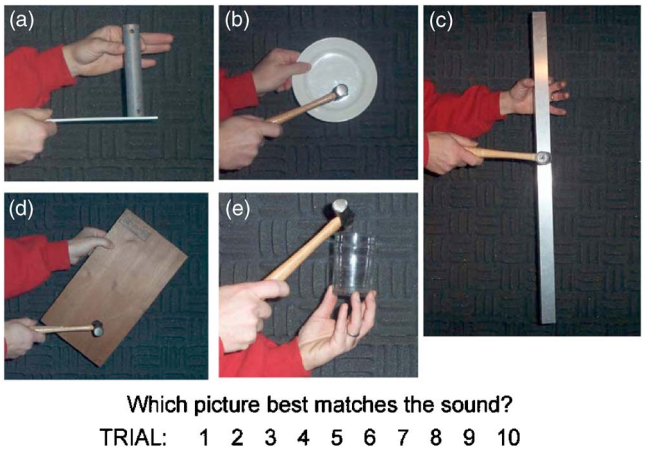

FIG. 5. Visual display used in experiment 2 for sound source identification.

The results fail to support a significant contribution of motivational or other extraneous factors to the chance performance obtained in the first experiment.

IV. EXPERIMENT 2. SOURCE IDENTIFICATION BASED ON REAL AND SYNTHETIC IMPACT SOUNDS

Despite the apparent ability of some listeners to detect a difference in quality between the real-recorded and synthesized sounds, the general failure of both UW and MS listeners to reliably identify the real-recorded sound satisfies our first criterion for psychophysical validity. This result does not, however, preclude the possibility that overall performance and/or the pattern of errors would be very different for the two types of sounds if listeners were asked to identify the sound source. It is entirely possible, for example, that the synthesized version of the juice glass sounded nothing like a juice glass to our listeners, even though it sounded quite real. One obvious way to test this possibility would be to obtain perceived similarity ratings from listeners. The problem with this approach is that it tells us little about the effect of the synthesis on identification—our primary goal. Different juice glasses, afterall, make different sounds. Hence, synthesized and real versions may be perceived as dissimilar but both may still equally likely be identified as a juice glass. The next experiment was undertaken to test the second criterion for psychophysical validity. The goal was to determine whether there would be any significant differences in source identification performance for the real-recorded and synthesized sounds.

A. Procedure

Five matched stimulus pairs were selected for this experiment from the ten used in experiment 1. We used only a subset of all pairs as we did not wish to tax the demands of memory and attention by providing too large a number of response alternatives. The particular sources selected were items A–E (see Table I). These sources were selected because their gross material and geometric properties were largely evident from photographed images and because they were easy to describe to listeners. Figure 5 shows these images exactly as they were seen by listeners throughout the experimental trials. A brief description of each object and the hammer used (per Table I) was given to listeners prior to experimental trials. The ten stimuli corresponding to the five matched pairs were used to construct ten single-interval, five-alternative, identification trials. One of the stimuli (either real-recorded or synthesized) was selected at random without replacement and played on each trial. Listeners were instructed on each trial to "pick the picture that best matches the sound." As in experiment I, listeners marked their answers in pencil on a standard bubble sheet for later scoring by the UW grading center; no feedback was given on each trial. The experiment was conducted approximately one month after experiment 1 on the same class of UW undergraduates (190 listeners altogether, mostly the same as those participating in experiment 1). All other aspects of the experiment were identical to experiment 1.

B. Results and discussion

Figure 6 shows the confusion matrices resulting from separate analyses of the responses to the real-recorded and synthesized impact sounds (left and middle panels, respectively). The relative proportion of responses is indicated by number and by grayscale with darker regions representing fewer responses. Correct responses are represented by cells that fall on the positive diagonal. The figure makes clear at a

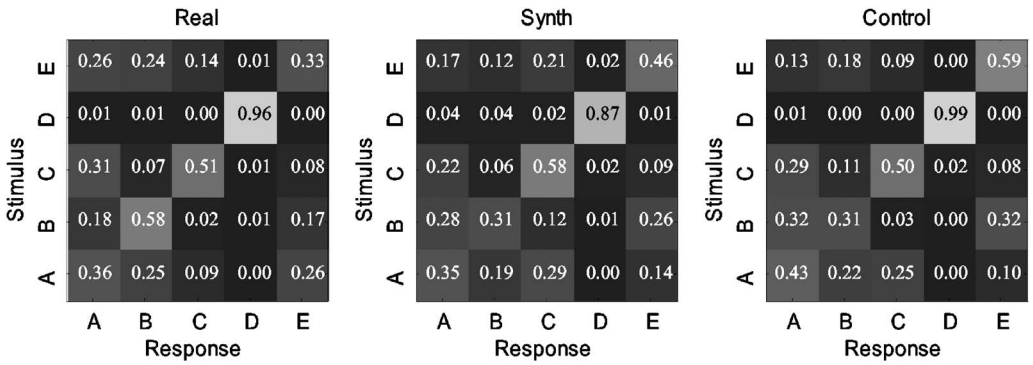

FIG. 6. Confusion matrices from source-identification experiment (experiment 2). The relative proportion of responses is indicated in grayscale with darker regions representing fewer responses. Entries are the actual proportions of responses. Responses of the first group of UW listeners to the real-recorded and synthesized impact sounds are analyzed separately in the left and right panels, respectively. Responses of the second group of listeners to the real-recorded sounds at the same positions in the sequence as the synthetic sounds are shown in the right panel (see text for further details).

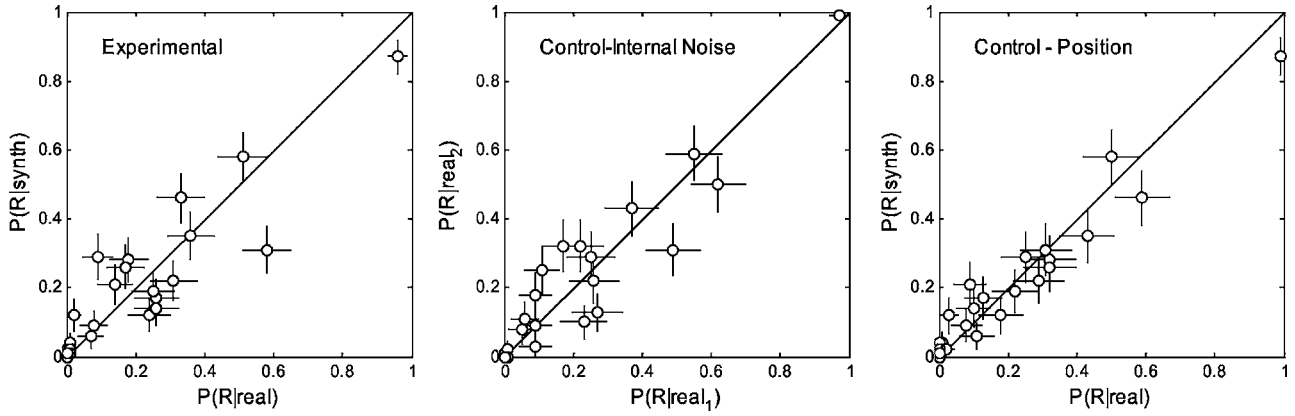

FIG. 7. Left panel: The probability of each response associated with each item (grayscale values in the first two panels of Fig. 6) is given for both the real-recorded and synthesized sounds from the first group of listeners. Error bars represent 95% confidence intervals. Middle panel: Shows agreement in responses to the first and second presentations of the real-recorded sounds for the second group of listeners. Right panel: Shows agreement in responses to the real-recorded sounds of the second group of listeners and the synthesized sounds for the first group of listeners, where the synthesized sounds occurred in the same positions in the trial sequence (see text for details).

glance the degree of agreement between the two confusion matrices. In both cases, for example, the item most often correctly identified is the rectangular wood slab (item D). And, with the exception of the synthesized ceramic plate (item B), the items least often identified correctly are the small pipe (item A) and the small juice glass (item E) in both cases. There are also some differences in the confusion matrices. For example, the synthetic sound corresponding to the small pipe (item A) is often identified as belonging to the square hollow rod (item C), but for the real-recorded version this is rarely true. The left panel of Fig. 7 better shows the extent of the differences. Plotted is the probability of each response associated with each item for both the real-recorded and synthesized sounds (i.e., the values indicated by grayscale in Fig. 6). Error bars give the 95% confidence intervals for each value assuming binomial error ($N=190$). Perfect agreement between the two confusion matrices would result in all points falling on the positive diagonal. It is clear from the figure that many values deviate significantly from the diagonal.

There are at least two factors, other than perceived differences between the real-recorded and synthesized sounds, which could contribute to the discrepancies between these confusion matrices. The first is internal inconsistencies in judgments—the tendency of listeners to make a different judgment in response to a repeated presentation of the same stimulus. The second is order effects—the influence that prior judgments can have on subsequent judgments. A control experiment was conducted to evaluate the relative contributions of these factors. The identification experiment was repeated on a new group of UW undergraduates ($N=150$) with the synthesized sounds simply replaced by their real-recorded counterparts at their same positions in the sequence of trials. Listeners in this experiment, thus, had two "looks" at the real-recorded sounds.

The middle panel of Fig. 7 shows the agreement in the responses for the first and second "looks," denoted real_1 and real_2, respectively. The deviations from the diagonal in this case reflect the combined contribution of internal inconsistencies and order effects; they are on the same order of magnitude as those of the left panel of Fig. 7, which shows the agreement in responses for the real and synthesized sounds obtained from the first group of listeners (data shown in the first two panels of Fig. 6). The good agreement suggests that internal inconsistencies and/or order effects, not perceived differences between real and synthesized sounds, are responsible for the discrepancies in responses. The right panel shows the agreement in responses for the real-recorded sounds of this experiment and the synthesized sounds from the first group of listeners. This comparison controls for order effects inasmuch as the two sets of sounds occurred in the same positions in the trial sequence. Here, the agreement in responses is quite good, indicating that much of the variability in judgments was due to order effects and not perceived differences between the real and synthesized sounds. Reinforcing this conclusion is the confusion matrix for the real-recorded sounds of this experiment, given in the right panel of Fig. 6. Here too the agreement between responses is quite good. Overall these results demonstrate excellent agreement between the identification responses given to the real-recorded and synthesized sounds once the effects of order in the sequence are partialled out.

V. EXPERIMENT 3. COMPARISON OF HEADPHONE AND SPEAKER PRESENTATION

To obtain reliable estimates of the distributional properties of listener responses in experiments 1 and 2 it was necessary to recruit a large number of participants. The most practical way of doing this was to present stimuli once and at the same time to a large group of listeners over speakers. This approach, of course, is problematic in that the acoustics of any setting in which sounds are delivered over speakers can potentially have an adverse effect on the quality of the sound reaching the listener's ear. Moreover, in many research applications in psychoacoustics involving the identification of sound sources, the sounds are likely to be delivered over headphones, not over speakers. Two observations suggest that room acoustics was not a significant factor contributing to the results of experiments 1 and 2: the good performance

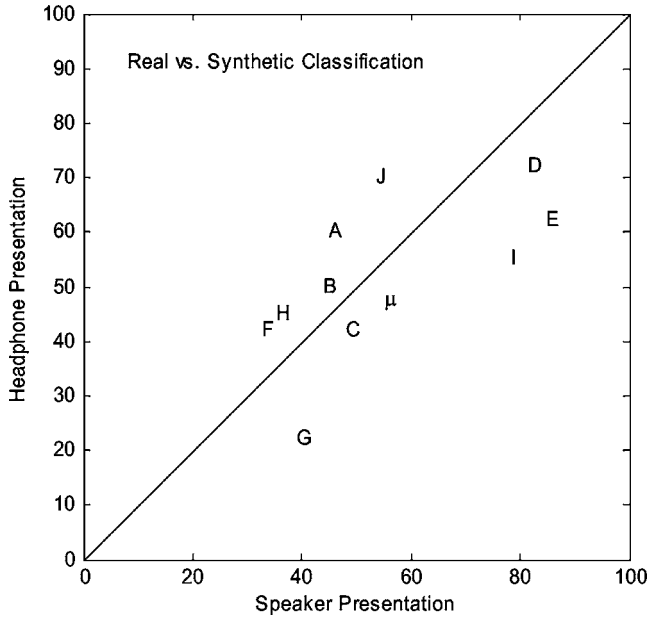

FIG. 8. Percent correct performance in the real-recorded versus synthesized classification task for UW listeners, headphone versus speaker presentation, broken down for each stimulus item. Letter symbols denote the different stimulus items as listed in Table I. Mu gives mean performance across items. Diagonal represents equal scores for the two listener groups.

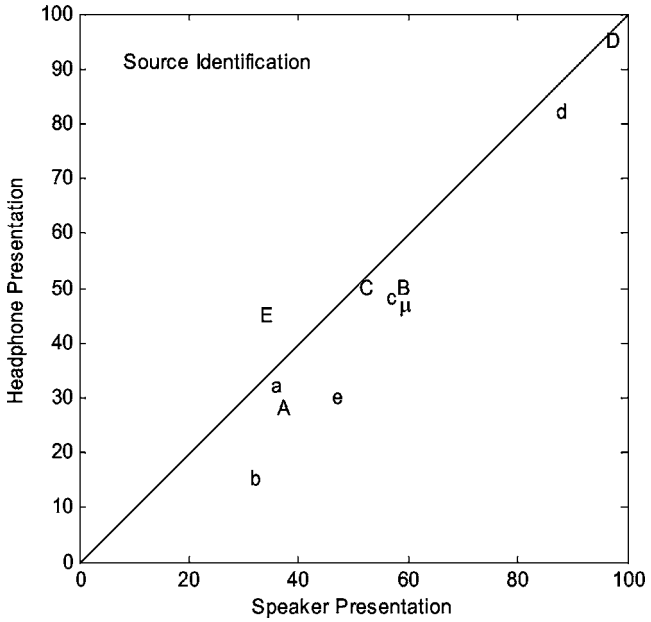

FIG. 9. Same as Fig. 8 except for the source identification task. Upper-case letters indicate real-recorded items, lower-case letters indicate synthesized counterparts.

of UW listeners in the control experiment to experiment 1, and the fact that sounds were delivered to MS listeners in a concert hall designed to reduce reverberation. To be confident, however, that room acoustics was not a factor we replicated experiments 1 and 2 using a smaller group of listeners with sounds delivered over headphones.

A. Procedure

All details regarding stimulus generation and procedure were identical to those of experiments 1 and 2 except that the sounds were presented diotically over circumaural headphones (Beyerdynamic DT990) to individual listeners seated in a sound-isolated room. Also, for experiment 2 the visual display (Fig. 5) was viewed on a computer monitor rather than on a large projection screen. A total of 40 UW undergraduates were recruited for these experiments. None had participated in the previous experiments. We did not want previous exposure to the stimulus items to confound the comparison between headphone and speaker presentation. As before the students received extra credit in an introductory class in communication disorders for their participation.

B. Results and discussion

Figure 8 compares percent correct performance using speaker and headphone presentation in the real-recorded versus synthesized classification task which tested our first criterion for psychophysical validity. The data for speaker presentation are taken from the 187 UW listeners of experiment 1. Performance is broken down by stimulus item with letter symbols denoting each item as listed in Table I. The diagonal represents equal scores for the two presentation modes. We expect some variability about the diagonal given the differences in the two groups of listeners used for the two presentation modes. Importantly, however, there is no evidence of an advantage of headphone presentation. Indeed, average performance for headphone presentation (indicated by the Greek letter mu) is slightly worse (48.3% correct) than average performance for speaker presentation (55.2% correct). A similar outcome is obtained for the headphone replication of the source-identification experiment (experiment 2). Figure 9 gives performance broken down by stimulus item in the same manner as Fig. 8. The upper-case letters denote the real-recorded items while the lower-case letters denote their synthesized counterparts. The figure shows generally good agreement between the headphone and speaker presentation modes with headphone presentation, once again yielding slightly worse performance overall (47.5% correct) than speaker presentation (58.2% correct). We conclude based on these results that room acoustics had little to do with the poor performance of listeners in experiments 1 and 2.

VI. EXPERIMENT 4. DISTINGUISHING SYNTHESIZED IMPACT SOUNDS WITH DIFFERENT NUMBERS OF FREE PARAMETERS

The results of experiments 1–3 suggest that the PLI model might justifiably be applied to source identification tasks in which the response categories are rather broad; e.g., wood slab vs. metal pipe vs. ceramic plate, etc. What, however, of more subtle distinctions within these categories? Consider, for example, the task of distinguishing from sound a metal bar that is bent from one that is true. Here, differences in the frequency ratio and/or relative decay moduli of modes are likely to be potential cues. But, because the PLI model constrains these to be constant, it would not be applicable in this case. Recognizing that no single model is likely to be suitable for all identification tasks, we would like to have some measure of the perceptual consequences associated with particular model constraints. The approach we take

in the next experiment is to measure the listener's ability to detect changes in the acoustic waveform that result when these constraints are relaxed; that is, when a greater number of free parameters are allowed. We argue that a PI model should have a broader potential for application to the extent that highly practiced listeners are insensitive to such changes.

A. Procedure

Unlike the previous experiments, our goal here is simply to determine whether listeners can detect the acoustic effect of relaxing constraints of the PLI model. We chose, therefore, to simulate a single sound source so that listeners would not potentially confuse a change in source with a change in model constraints. Two sets of sounds, 100 samples each set, were constructed according to the PLI model as described in Sec. II. For both sets the nominal values of parameters were chosen to simulate the sound of a common tuning fork (a homogeneous bar clamped at one end and struck at the other): ν_1=461 Hz, τ_1=0.55 s, and C_n/C_1=6 dB/oct. This source had been used in the previously referenced studies by Lutfi (2001) and Lutfi and Oh (1994, 1997) (real-recorded and synthesized versions can be heard at http://www.aip.org/pubservs/epaps.html). Different samples within each set of 100 sounds were obtained by jittering the frequencies of the partials at random about their nominal values. The jitter was a multiplier of these values and was normally distributed with mean 1.0 and standard deviation in different conditions of 0.1, 0.2, and 0.3. The nominal values of the decay moduli varied accordingly, in inverse proportion to the cube of frequency. For the first set of sounds the frequencies of partials covaried; the value selected for ν_1 dictated the values of ν_2 and ν_3 according to the ideal ratios given in Sec. II. In effect, these sounds had one free parameter. For the second set of sounds the frequencies of the three partials varied independently, thus relaxing one of the constraints of the PLI model. These sounds, in effect, had three free parameters (one for each partial). A second condition was also run in which both the frequencies and the decay moduli of partials in the second set varied independently (six free parameters); although, once again the values of frequency and decay were identically distributed. On each trial one sample from both sets was drawn at random and played over headphones (Sennheiser HD520) to the right ear of listeners seated in a double-wall, IAC sound-attenuation booth. All sounds were generated at a 40-kHz rate using a Tucker-Davis 16-bit D/A conversion system with 20-kHz low-pass antialias filter.

In the standard two-interval, forced-choice procedure, the listener's task was to choose the sound drawn from the one-free-parameter set (most constrained model). In physical terms the task was principally like that of identifying which of two metal bars is true, as in the example described above. For an ideal homogenous bar (without bend) the frequency ratios of modes are given by the one-free-parameter set; these are the ideal ratios given for the struck clamped bar. For a bent bar the frequency (and decay) ratios would deviate from ideal as for the three- and six-free parameter sets. Also, note that because the frequencies and decay moduli of the partials were identically distributed for the two sets of sounds the listener could not perform above chance by basing decisions on simple differences in frequency or decay. Listeners were given feedback after each trial and they were instructed to use the feedback during training to identify the quality difference between the two types of sounds. Five UW-Madison students ranging in age from 20 to 26 years were paid at an hourly rate for their participation in the experiment. They were highly practiced in the task, each receiving 1000 or more trials of training before data collection began.

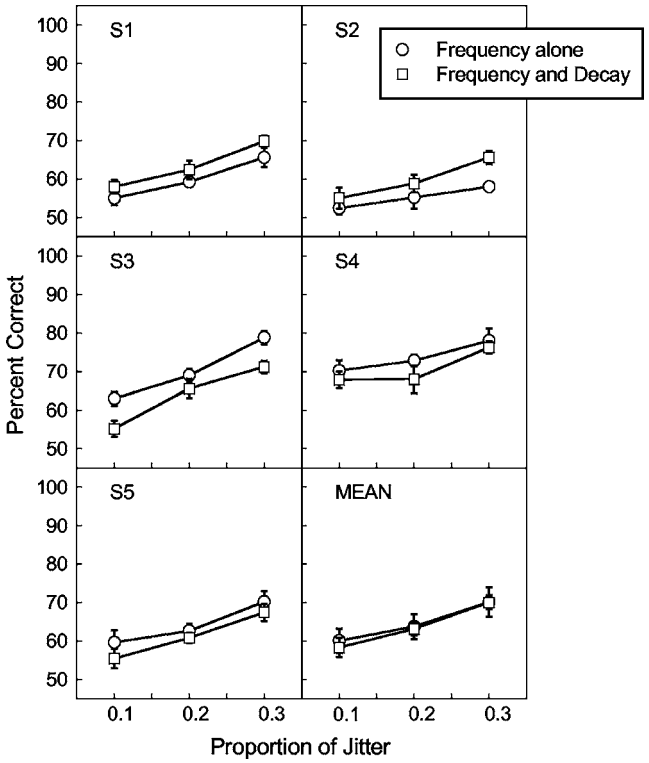

FIG. 10. Percent correct performance of the five listeners (panels) in both conditions (different symbols) of experiment III is plotted as a function of the standard deviation of the frequency jitter of partials (see text for details). Circular symbols denote the condition for which frequency alone was jittered and squares denote the condition for which both frequency and decay was jittered independently. Each symbol with error bar represents the mean and standard error of five estimates obtained on different days, 100 trials each estimate.

B. Results and discussion

Figure 10 shows the percent correct performance of the five listeners (panels) in both conditions (different symbols) as a function of the standard deviation of the frequency jitter. As the standard deviation of the jitter is increased we expect performance to improve since the frequency ratios of the three- and six-free parameter set will deviate more from the ideal values of the one-free parameter set. Circular symbols give the data for the three-free parameter set in which frequency alone was jittered; squares give the data for the six-free parameter set in which both frequency and decay were jittered independently. Each symbol with error bar represents the mean and standard error of five estimates obtained on different days, 100 trials each estimate. The mean and stan-

dard error of the estimates across listeners is given in the lower right panel. The pattern of results is quite similar for the five listeners and for the two conditions. Percent correct performance improves from near chance for 10% standard deviation in jitter to near 70% correct for 30% standard deviation in jitter.

The results of this experiment show that highly practiced listeners are, indeed, capable of discriminating the difference between sounds synthesized with different numbers of free parameters. However, for the difference to be reliably detected the amount of jitter in the free parameters must be exceedingly large, 30% or greater. Note by comparison that the difference limen for a change in decay, for durations greater than 10 ms, is less than 20% (Jarvelainen and Tolonen, 2001; Schlauch *et al.*, 2001); the difference limen for a change in frequency it is but a fraction of a percent (Wier *et al.*, 1977). Increasing the number of free parameters from three to six did little to improve performance. This is noteworthy because six parameters is the largest number of parameters that may freely vary in this case while holding the relative levels of partials constant. While it is possible that sounds with a greater number of partials (hence, a greater possible number of free parameters) might have yielded a different result, the failure to obtain even a small improvement in performance indicates that listeners are rather insensitive to the acoustic effect of increasing the number of free parameters beyond three.

The present experiment was conducted using a single simulated source under a restricted set of conditions, so it is by no means clear that the same result would be obtained when simulating other sources under other conditions. Still, the principle design of the experiment is such that it provides, at least, a basis for estimating the minimum number of free parameters that are likely to be needed for a given application. For the tuning fork simulated here, there is a diminishing return of including more than the first three free parameters inasmuch as the effect on the acoustic waveform of including additional free parameters goes largely unnoticed by trained listeners given feedback in the two-interval, forced-choice task. In this one case, at least, the results are in keeping with those of experiments 1–3, and largely satisfy our third criterion for psychophysical validity.

VII. GENERAL DISCUSSION

Understanding how we use sound to identify objects and events in the world is one of the most significant challenges for contemporary research on hearing (cf. Bregman, 1990; Gibson, 1966). Yet, because of the multifarious nature of the stimulus progress has been limited. Ideally, one would like to have a precise representation of the stimulus that would allow predictions for performance and the types of errors expected based on the different available cues for identification and the manner in which they covary. Such a representation is difficult to achieve in the case of real or recorded sounds. It can be achieved through the analytic expressions of PI models, but only to the extent that these models faithfully represent the acoustic properties of the resonant sources they simulate.

The present study was undertaken to provide some measure of the detail required of a PI model for it to have meaningful application in studies of human sound source identification from impact sounds. Since each application places different demands on a model, one can only go so far in generalizing beyond the present results. We have investigated but a few exemplars of a class of resonant objects that is indeterminately large; hence, there are likely to be many types of classifications for which these results do not apply. (A notable example pertains to the manner of impact, since little effort was made to model this feature of the sound event.) Neither do these experiments permit us to determine the basis for classification—the wood slab, for example, could have easily been classified based on its material properties alone from the decay of a single partial (cf. Lutfi and Oh, 1994, 1997; Wildes and Richards, 1988). Notwithstanding these qualifications, the results do, at least, suggest that a modal model with as few as three to four free parameters may be adequate for many applications in psychoacoustic research involving impact sounds produced by relatively simple resonant sources. This model produced sounds that professional musicians and college undergraduates alike could not recognize as synthesized versus real with better than chance accuracy. And, it produced sounds that yielded the same level of identification accuracy and largely the same pattern of errors when listeners where asked to identify the source. While these are not the only or even the strictest criteria for psychophysical validity, they are two meaningful criteria that go some way in encouraging a physically informed approach.

Other studies have used different criteria for evaluating psychophysical validity, but with an eye towards achieving different goals. Grey and Moorer (1977) and McAdams *et al.* (1999), for example, adopted a strict criterion by challenging highly trained musicians to detect any difference between real-recorded and synthesized sounds. These studies were undertaken with the goal of reducing the computational load required to produce a transparent synthesis of notes played by musical instruments. The various algorithms used to reduce data (e.g., smoothing of the spectral and temporal envelope, forced harmonicity, and the like) did not and were not intended to have a specific representation in the parameters of a PI model. Also, because the goal was to synthesize a very specific and small set of musical instrument sounds, a strict "no-differences-detected" approach was both meaningful and feasible. The same cannot be said for the present study where a small number of resonant objects are sampled to model an indefinitely large class of naturally occurring impact sounds. Similar differences in goals are noted in the studies of Charbonneau (1981), Sandell and Martens (1995), and Grey (1977) where somewhat different techniques were used to synthesize musical instrument tones.

A study whose goal was much closer to that of the present study was conducted by Van den Doel *et al.* (2002). These authors had listeners rate the perceived dissimilarity between recorded and synthesized versions of the impact sounds produced by a ceramic bowl and metal vase. A 10 point scale was used with a rating of 1 corresponding to "no perceived difference." The synthesized sounds were con-

structed according to the modal model given by Eq. (1); a phase-unwrapping algorithm was used to estimate the modal parameters from the recordings. The independent variable of interest was the number of audible (unmasked) modes used in the synthesis. Perceived dissimilarity generally decreased as the number of modes increased, however there was a precipitous drop to "no perceived difference" at about six modes. While it is not possible to draw direct comparisons to the present study, the results nonetheless suggest that a realistic synthesis for simple resonant sources, like those used in the present study, can be achieved with relatively few modal parameters. This is consistent with our finding that highly practiced listeners are largely insensitive to an increase in free parameters such that would be required to model more specific differences between these sound sources (experiment 4).

The question of specificity is a larger problem that clearly requires further study. Several authors have offered analytic treatments of the acoustic relations that would uniquely identify specific source attributes, such as size, shape, and material, despite variation in other attributes (Jenison, 1997; Kunkler-Peck and Turvey, 2000; Lutfi, 2001; Wildes and Richards, 1988). Few studies, however, have tested whether listeners are, in fact, sensitive to such relations. Two studies by Lutfi (2000, 2001) are particularly relevant in this regard. In both, simulations were conducted in which the effect of sensory noise was estimated by introducing small perturbations in the acoustic parameters of the modal model. The magnitude of the perturbations for each parameter was estimated to be consistent with psychoacoustic data describing listener sensitivity to differences in the frequency, amplitude, and decay of single tones (cf. Jesteadt *et al.*, 1977; Schlauch *et al.*, 2001; Wier *et al.*, 1977). The results show that quite small perturbations, as would be associated with sensory noise, can significantly obscure relevant acoustic relations, even when variation in the acoustic signal is largely dominated by physical variation in the source. The results suggest that the acoustic relations relevant to particular identification tasks may, to a much greater extent than previously anticipated, be vulnerable to information loss in the auditory system. Such a conclusion would go some way in explaining the present failure to find significant differences in the listeners' response to real-recorded and synthesized impact sounds. Though the results of this study do not bring us much closer to understanding how listeners identify simple sound sources, they do at least support the use of simple PI models as a means of approaching the problem.

ACKNOWLEDGMENTS

This research was supported by a grant from the NIDCD (R01 CD01262-10). The authors wish to thank Robert Kim Todd and Gregory Minx for their technical support, Michi Adelmund and Karen Malott for assistance in data collection, and Dr. Armin Kohlrausch, Dr. Douglas Keefe, and three anonymous reviewers for helpful comments on an earlier version of this manuscript.

Bregman, A. S. (**1990**). "Auditory Scene Analysis" (M.I.T. Press, Cambridge, Massachusetts).

Burns, E. M. and Houtsma, A. J. M. (**1999**). "The influence of musical training on the perception of sequentially presented mistuned harmonics," J. Acoust. Soc. Am. **106**, 3564–3570.

Carello, C., Anderson, K. A., and Kunkler-Peck, A. J. (**1998**). "Perception of object length by sound," Psychol. Sci. **9**, 211–214.

Chaigne, A., and Doutaut, V. (**1997**). "Numerical simulations of xylophones. I. Time-domain modeling of the vibrating bars," J. Acoust. Soc. Am. **101**, 539–557.

Charbonneau, G. R. (**1981**). "Timbre and the perceptual effects of three types of data reduction," Comput. Music J. **5**(2, 10–19.

Cook, P. R. (**1996**). "Physically informed sonic modeling (PhISM): Percussive synthesis," in Proceedings of the International Computer Music Conference, Hong Kong, pp. 228–231.

Cook, P. R. (**1997**). "Physically inspired sonic modeling (PhISM): Synthesis of percussive sounds," Comput. Music J. **21**, 38–49.

Durlach, N. I. and Mavor, A. S. (eds.) (**1995**). *Virtual Reality, Scientific and Technological Challenges* (National Academic Press, Washington, DC).

Eagleson, H. V., and Eagleson, O. W. (**1947**). "Identification of musical instruments when heard directly and over a public-address system," J. Acoust. Soc. Am. **19**, 338–342.

Fletcher, N. H., and Rossing, T. D. (**1991**), "The Physics of Musical Instruments" (Springer-Verlag, New York).

Freed, D. J. (**1990**). "Auditory correlates of perceived mallet hardness for a set of recorded percussive sound events," J. Acoust. Soc. Am. **87**, 311–322.

Gaver, W. W. (**1993a**). "Synthesizing auditory icons," in Proceedings of the ACM INTERCHI'93, pp. 228–235.

Gaver, W. W. (**1993b**). "What in the world do we hear?: An ecological approach to auditory event perception," Ecological Psychol. 5(1), 1–29.

Gibson, J. J. (**1966**). *The Senses Considered as Perceptual Systems* (Houghton-Mifflin, Boston).

Giordano, B. L., and Petrini, K. (**2003**). "Hardness recognition in synthetic sounds," in Proceedings of the Stockholm Music Acoustics Conference, Stockholm, Sweden.

Grey, J. M. (**1977**). "Multidimensional scaling of musical timbres," J. Acoust. Soc. Am. **61**, 1270–1277.

Grey, J. M., and Moorer, J. A. (**1977**). "Perceptual evaluations of synthesized musical instrument tones," J. Acoust. Soc. Am. **62**, 454–462.

Jarvelainen, H., and Tolonen, T. (**2001**). "Perceptual tolerances for the decaying parameters in plucked string synthesis," J. Audio Eng. Soc. **49**(11), 1049–1059.

Jenison, R. L. (**1997**). "On acoustic information for motion," Ecological Psychol. 9, 131–151.

Jesteadt, W., Wier, C. C., and Green, D. M. (**1977**). "Intensity discrimination as a function of frequency and sensation level," J. Acoust. Soc. Am. **61**, 169–177.

Kinsler, L. E., and Frey, A. R. (**1962**). *Fundamentals of Acoustics* (Wiley, New York), pp. 55–78.

Kunkler-Peck, A. J., and Turvey, M. T. (**2000**). "Hearing shape," J. Exp. Psychol. **26**, 279–294.

Lakatos, S., Cook, P. C., and Scavone, G. P. (**2000**). "Selective attention to the parameters of a physically-informed sonic model," ARLO **107**(5). L31–L36.

Lakatos, S., McAdams, S., and Causse, R. (**1997**). "The representation of auditory source characteristics: Simple geometric form," Percept. Psychophys. **59**, 1180–1190.

Lambourg, C., Chaigne, A., and Matignon, D. (**2001**). "Time-domain simulation of damped impacted plates: II. Numerical model and results," J. Acoust. Soc. Am. **109**, 1433–1447.

Li, X., Logan, R. J., and Pastore, R. E. (**1991**). "Perception of acoustic source characteristics: Walking sounds," J. Acoust. Soc. Am. **90**, 3036–3049.

Lutfi, R. A. (**2000**). "Source uncertainty, decision weights, and internal noise as factors in auditory identification of a simple resonant source," Abstr. Assoc. Res. Otolaryngol. **23**, 171.

Lutfi, R. A. (**2001**). "Auditory detection of hollowness," J. Acoust. Soc. Am. **110**, 1010–1019.

Lutfi, R. A., and Oh, E. (**1994**). "Auditory discrimination based on the physical dynamics of a tuning fork," J. Acoust. Soc. Am. **95**, 2967.

Lutfi, R. A., and Oh, E. (**1997**). "Auditory discrimination of material changes in a struck-clamped bar," J. Acoust. Soc. Am. **102**, 3647–3656.

Lutfi, R. A., and Wang, W. (**1999**). "Corrlelational analysis of acoustics cues

for auditory motion," J. Acoust. Soc. Am. **106**, 919–928.
McAdams, S., Beauchamp, J. W., and Meneguzzi, S. (**1999**). "Discrimination of musical instrument sounds resynthesized with simplified spectrotemporal parameters," J. Acoust. Soc. Am. **105**, 882–897.
Morrison, J. D., and Adrien, J.-M. (**1993**). "Mosaic: A framework for modal synthesis," Comput. Music J. **17**(1), 45–56.
Morse, P. M., and Ingard, K. U. (**1968**). *Theoretical Acoustics* (Princeton U.P., Princeton, NJ), pp. 175–191.
Repp, B. H. (**1987**). "The sound of two hands clapping: An exploratory study," J. Acoust. Soc. Am. **81**, 1100–1109.
Rossing, T. D., and Fletcher, N. H. (**1999**). *Principles of Vibration and Sound* (Springer, New York).
Roussarie, V., McAdams, S., and Chaigne, A. (**1998**). "Perceptual analysis of vibrating bars synthesized with a physical model," 16th International Congress on Acoustics, Seattle, pp. 2227–2228.
Sandell, G. J., and Martens, W. L. (**1995**). "Perceptual evaluation of principal-component-based synthesis of musical timbres," J. Audio Eng. Soc. **43**, 1013–1028.
Schlauch, R. S., Ries, D. T., and DiGiovanni, J. J. (**2001**). "Duration discrimination and subjective duration for ramped and damped sounds," J. Acoust. Soc. Am. **109**, 2880–2887.
Spiegel, M. F., and Watson, C. S. (**1984**). "Performance on frequency discrimination tasks by musicians and nonmusicians," J. Acoust. Soc. Am. **76**, 1690–1695.
Takala, T., and Hahn, J. (**1992**). "Sound rendering," Proc. SIGGRAPH 92, ACM Computer Graphics **26**(2) 211–220.
Van den Doel, K. (**1998**). "Sound Synthesis for Virtual Reality and Computer Games," Ph.D. thesis, University of British Columbia.
Van den Doel, K., and Pai, D. K. (**1996**). "Synthesis of shape dependent sounds with physical modeling," in Proceedings of the International Conference on Auditory Displays, Palo Alto.
Van den Doel, K., and Pai, D. K. (**1998**). "The sounds of physical shapes," Presence **7**(4), 382–395.
Van den Doel, K., Pai, D. K., Adam, T., Kortchmar, L., and Pichora-Fuller, K. (**2002**). "Measurements of the perceptual quality of contact sound models," Proceedings of the International Conference on Auditory Display, Kyoto, Japan.
Warren, W. H., and Verbrugge, R. R. (**1984**). "Auditory perception of breaking and bouncing events: A case study in ecological acoustics," J. Exp. Psychol. **10**, 704–712.
Wier, C. C., Jesteadt, W., and Green, D. M. (**1977**). "Frequency discrimination as a function of frequency and sensation level," J. Acoust. Soc. Am. **61**, 178–184.
Wildes, R., and Richards, W. (**1988**). "Recovering material properties from sound," in *Natural Computation*, edited by W. Richards (MIT, Cambridge, MA), pp. 356–363.
See EPAPS Document No. E-JASMAN-118-036507 for (.wav) stimulus files. This document can be reached via a direct link in the online article's HTML reference section or via the EPAPS homepage (http://www.aip.org/pubservs/epaps.html).

Empirical modeling of human face kinematics during speech using motion clustering

Jorge C. Lucero[a] and Susanne T. R. Maciel[b]
Department of Mathematics, University of Brasilia, Brasilia DF 70910-900, Brazil

Derek A. Johns[c] and Kevin G. Munhall[d]
Departments of Psychology and Otolaryngology, Queen's University, Kingston ON, K7L 3N6, Canada

(Received 23 November 2004; revised 19 April 2005; accepted 19 April 2005)

In this paper we present an algorithm for building an empirical model of facial biomechanics from a set of displacement records of markers located on the face of a subject producing speech. Markers are grouped into clusters, which have a unique primary marker and a number of secondary markers with an associated weight. Motion of the secondary markers is computed as the weighted sum of the primary markers of the clusters to which they belong. This model may be used to produce facial animations, by driving the primary markers with measured kinematic signals. © *2005 Acoustical Society of America.* [DOI: 10.1121/1.1928807]

PACS number(s): 43.70.Aj, 43.70.Bk, 43.70.Jt [RLD] Pages: 405–409

I. INTRODUCTION

The purpose of this work is to develop a model of human face biomechanics that may be used as a tool for speech production and perception studies. This model must be capable of producing computer-generated animations of speech production, with an acceptable level of realism. Further, it must allow systematic manipulation of the facial movements (cf. Cohen and Massaro, 1990). It has been claimed that experimental control of visual stimuli has been lacking in audiovisual speech research and a system that permitted the direct manipulation of facial movement parameters would be a significant advance (Munhall and Vatikiotis-Bateson, 1998). Answering this claim, several efforts have been undertaken to develop data-driven animation systems (e.g., Badin *et al.*, 2002; Beskow, 2004; Bevacqua and Pelachaud, 2004; Kuratate *et al.*, 1998; Lucero and Munhall, 1999; Ouni *et al.*, 2005; Pitermann and Munhall, 2001; Zhang *et al.*, 2004).

In a previous work (Lucero and Munhall, 1999), we described a three-dimensional (3-D) model based on the physiological structure of the human face. The model followed the muscle-based approach of Terzopoulos and Waters (1990), and consisted of a multilayered deformable mesh that was deformed by the action of forces, generated by modeled muscles of facial expression. Animations of speech production were produced by controlling the time history of the levels of activity of the muscles, using recorded perioral electromyographic (EMG) records. In general, the animations compared well with the actual facial kinematics, and showed good levels of visual realism.

However, some difficulties were detected that prevented practical applications of the model. First, the intramuscular EMG recording required by the model is an invasive technique with a complex experimental setup. Further, the collected signals are still not a good representation of the true muscle activation patterns (Pitermann and Munhall, 2001), due to interdigitation of different muscle fibers, nonlinear transfer functions between EMG and generated force, among other problems. A second problem is the difficulty of producing a good representation of the facial muscle structure and skin biomechanics that could be adapted to individual speakers.

A solution to the first problem proposed by Pitermann and Munhall (2001) is using an inverse dynamic approach. This approach uses kinematic data of facial movements, collected from a subject producing speech. A dynamical inversion algorithm based on the Lucero and Munhall (1999) model was used to infer muscle activity signals for the modeled muscles. Those signals, in turn, were used to animate the facial model. In this way, realistic animations could be produced driving the model from kinematics data, which is much easier to collect than the intramuscular EMG. The kinematic control signals may be manipulated at will, to produce all variations of visual stimuli for perceptual experiments. Other attempts at physically based facial animation have been reported recently, with a similar degree of success as the above (see, e.g., Zhang *et al.*, 2004), and sharing a similar problem for our intended application to speech perception research.

Here we propose an empirical modeling approach to represent facial biomechanics. Essentially, we try to infer the biomechanical structure of facial muscle and tissues from a set of facial movement records. In its data-driven aspect, this approach is similar to the statistical modeling technique by Kuratate *et al.* (1998). In that technique, an empirical model of the face is built by adapting a deformable mesh to a number of static scans from a laser range finder. In each scan, the subject adopts one of a set of predetermined facial postures that sample the range of possible deformations. Principal component analysis is next used to express an arbitrary facial

[a]Electronic mail: lucero@mat.unb.br
[b]Research student of CNPq (Brazil). Electronic mail: susanne@mat.unb.br
[c]Electronic mail: derek.johns@mail.mcgill.ca
[d]Electronic mail: munhallk@post.queensu.ca

shape in terms of a set of shape eigenvectors derived from the static scan data. Finally, the 3-D positions of a set of facial markers during speech production are recorded, and used to produce time-varying coefficients for the basis of facial shape eigenvectors. Here, we propose to base the model on facial movement data instead of static shapes, in order to capture the full dynamic behavior of the face. Further, in spite of being a data-driven empirical model, we still want to relate it to underlying biomechanical principles. Our assumption is that the activation of individual muscles will produce regional patterns of deformation on the facial surface (cf. Ekman *et al.*, 2002). Identification of these kinematic regions will thus allow us to isolate biomechanical "units" determined by the lumped action of muscle and skin biophysical characteristics.

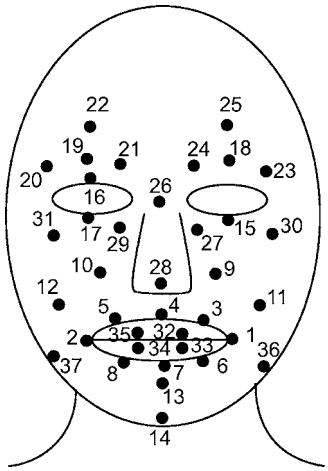

FIG. 1. Approximate location of facial markers.

II. DATA

The data consist of the 3-D position of 38 markers distributed on a subject's face, recorded with Vicon equipment (Vicon Motion Systems Inc., Lake Forest, CA) at a 120 Hz sampling frequency. The recorded position of an additional six markers located on a headband were used to compute the origin and orientation of a head coordinate system, and the positions of the facial 38 markers were expressed in head coordinates. The origin of this system was defined at the position of a marker between the eyes at the nose bridge, with the x axis in the horizontal direction from right to left, the y axis in the vertical direction to the top, and the z axis in the protrusion direction to the front. The approximate location of the markers is shown in Fig. 1.

The data were recorded while the subject was producing five repetitions of ten Central Institute for the Deaf Everyday sentences (Davis and Silverman, 1970), shown in Table I. Sentences 1 to 5 and 7 to 10 were used to build the facial clusters, and sentence 6 was used for testing the results. This sentence was selected for having an average-sized duration, compared to the sentence set, and a variation of mouth opening and lip protrusion movements.

In the recording session, the subject was asked to adopt a consistent rest position at the beginning of each sentence. The recorded initial positions of the markers were taken as representative of a rest (neutral) configuration. The records of the marker at the top of the left eyelid contained several missing data values, and was therefore discarded.

III. COMPUTATION OF CLUSTERS

A cluster is defined as a group of markers in a connected region that may move in the same direction during some interval of time. Each cluster has one primary marker, which defines and drives the movement of all the other secondary markers. Let the column vector $\mathbf{x}_i(t)=(x_i(t),y_i(t),z_i(t))^T$ denote the displacement of marker i from its rest position. Then marker i (secondary) belongs to the cluster controlled by marker k (primary) if $\mathbf{x}_i(t)=a_{ik}\mathbf{x}_k(t)$, where a_{ik} is a constant (weight) in the interval (0, 1). Condition $a_{ik}>0$ implies that the markers move in the same direction, and $a_{ik}<1$ implies that the primary marker has the largest displacement magnitude, on the cluster motion. A secondary marker may belong to more than one cluster, in which case its motion is expressed as a linear combination of the primary markers of those clusters. A primary marker may only belong to the cluster it drives.

Our algorithm works by expressing the displacement of each marker as a linear combination of the displacement of the neighboring markers. Therefore, the neighborhood of each marker must be initially defined, as the set of all markers that surround it. We adopt the mesh structure shown in Fig. 2. The markers are shown in their actual initial positions, obtained from the measured data. The mesh was built simply by linking each marker to its nearest neighbors forming triangular polygons, and avoiding links across the mouth, nostrils, and eyes.

The algorithm works as follows. In the first step, all of the 37 markers are defined as primary markers of their own clusters. The displacement of each marker is next expressed as a linear combination of the displacements of its neighboring markers, using a least squares approach. As an example, consider marker 17, which has markers 10, 26, 29, 31 as neighbors. Then, the algorithm seeks the values of weights $a_{17,10}, a_{17,26}, a_{17,29}, a_{17,31}$ to the approximation of marker 17's displacement,

$$\hat{\mathbf{x}}_{17} = a_{17,10}\mathbf{x}_{10} + a_{17,26}\mathbf{x}_{26} + a_{17,29}\mathbf{x}_{29} + a_{17,31}\mathbf{x}_{31}, \qquad (1)$$

such that the error measure,

TABLE I. CID sentences.

Number	Sentence	Number of frames
1	Walking's my favorite exercise	2035
2	Here's a nice quiet place to rest	2334
3	Our janitor sweeps the floors every night	2216
4	It would be much easier if everyone would help	1800
5	Good morning	1728
6	Open your window before you go to bed	1758
7	Do you think that she should stay out so late?	2033
8	How do you feel about changing the time when we begin work?	2311
9	Here we go	1592
10	Move out of the way	1223

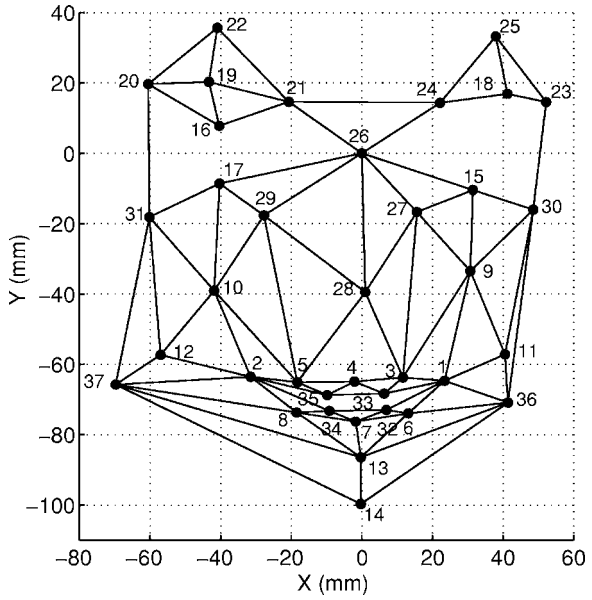

FIG. 2. Geometrical structure of facial mesh.

$$E_{17} = \frac{\|\mathbf{x}_{17} - \hat{\mathbf{x}}_{17}\|}{\|[\mathbf{x}_{10}, \mathbf{x}_{17}, \mathbf{x}_{26}, \mathbf{x}_{29}, \mathbf{x}_{31}]\|}, \tag{2}$$

is minimum, where the norms are computed in the Frobenius sense (Kincaid and Cheney, 2002).

This process is repeated for all markers. Finally, the marker that produces the smallest error is eliminated from the list of primary markers, and its recorded displacement is replaced by the displacement computed from its neighbors, as above. The rationale is that this marker carries a small amount of motion information (which is independent of its neighbors), and so it may be included in a cluster with a small error (small information loss). Note that Eq. (2) uses a measure of error relative to the size of the measured displacement of the considered marker and its neighbors. Using an absolute measure would yield small errors for markers with small displacements, and so we would just eliminate those markers that are far from the mouth. Also, using a measure relative to the size of the considered marker alone (without its neighbors) might produce large error measures for markers that almost do not move. These markers would then remain as primary markers, even though their motions are not relevant for speech. The above measure was adopted as a middle ground alternative.

In successive steps, a similar process is repeated for the remaining primary markers, and the list of primary markers is reduced one by one, always keeping the total relative error to a minimum. At the same time, markers eliminated from the set of primary markers are added to the set of secondary markers, and their motion expressed as linear combination of the remaining primary markers, as shown above. The process is stopped when the intended final number of primary markers (equal to the predetermined number of clusters) is reached.

IV. RESULTS

A. Clusters

We show results for a dataset when grouping the markers into 15 clusters, using the above algorithm on CID sentences 1–5 and 7–10. The 15 clusters were chosen for this example because it amounted to a more than 50% reduction in the dimensionality of the marker data and it is also consistent with the number of dimensions in muscle models used for facial animation (e.g., Lucero and Munhall, 1999; Pitermann and Munhall, 2001). Our intention here is just to illustrate the results that the algorithm can produce; the appropriate number of clusters is a subject for further study.

The clusters are shown in Table II and Fig. 3. In this figure, the primary marker of each cluster is indicated with a filled circle, and the secondary markers with unfilled circles. Each secondary marker is linked to the primary markers of the clusters to which it belongs. The position of clusters follows the muscle structure of the face adopted in previous works (e.g., Fidaleo and Neumann, 2002; Lucero and Munhall, 1999; Zhang *et al.*, 2004). Roughly, clusters 1, 2, 3, 4, and 15, around the mouth, reflect action of the orbicularis oris muscles, combined with the levator labii superioris (clusters 1 and 3), zygomatic major and levator anguli oris (clusters 5 and 6), depressor labii inferioris and mentalis (clusters 4 and 15). Cluster 7 incorporates motion of the jaw, and clusters 8 and 10 reflect an action component by the levator labii superioris combined with the orbicularis oculi. At the upper part of the face, cluster 9 incorporates the blinking action of the orbicularis oculi. Clusters 12 and 14 reflect action by the frontalis and corrugator, respectively, on the left side. On the right side, due to the absence of a marker in the eyelid, the clusters have a different configuration. In this case, cluster 11 incorporates the effect of blinking and the action of the outer frontalis, and cluster 13 includes action of the inner frontalis and corrugator.

We also observe some asymmetry of the clusters between the two sides of the face. This is a result of asymmetries in the position of the markers, but is also due to asymmetries of facial motion during speech.

B. Animations

The 15 clusters generated in the previous section were used to reproduce the facial movements for CID sentence 6 (see Table I). The primary markers were driven by the measured data, and the trajectories of the secondary markers were computed as explained above.

Figure 4 shows a portion of the computed trajectories for marker 7 (center of lower lip), comprising the first two repetitions of sentence 6. There is a good match between computed (full line) and measured (broken line) trajectories. In the case of the z component (protrusion), there seems to be a reduction in the amplitude of the movement, relative to the initial position. However, the general pattern of the trajectory is preserved. The absolute rms error in the displacement of this marker (along the total sequence of 5 repetitions of the sentence) is 0.65 mm, and the error relative to the rms of its measured displacement is 15.18%. Other markers produced similar results, with absolute errors from 0.08 mm (marker

TABLE II. Computed clusters, for a total number of 15.

Cluster	Main	Second.	Weight	Cluster	Main	Second.	Weight
1	3	1	0.749	8	15	9	0.499
		32	0.670			27	0.218
		29	0.174	9	16	20	0.024
		28	0.086			21	0.019
		27	0.038			19	0.003
2	4	35	0.351	10	17	10	0.551
		32	0.336			29	0.382
3	5	2	0.694			31	0.261
		35	0.629	11	18	25	0.239
		8	0.156			23	0.135
		10	0.110			30	0.062
		29	0.091	12	22	20	0.657
		32	0.017			19	0.613
4	6	33	0.731			21	0.347
		7	0.403	13	24	25	0.349
		1	0.198			23	0.345
		13	0.085			19	0.086
5	11	36	0.710			21	0.069
		9	0.253	14	26	28	0.761
		30	0.225			27	0.591
		1	0.168			21	0.302
		32	0.041			9	0.270
6	12	37	0.971			29	0.202
		2	0.541			10	0.089
		10	0.359			19	0.077
		31	0.249	15	34	8	0.771
		8	0.142			7	0.639
		29	0.023			33	0.325
7	14	13	0.938				
		8	0.128				
		36	0.018				

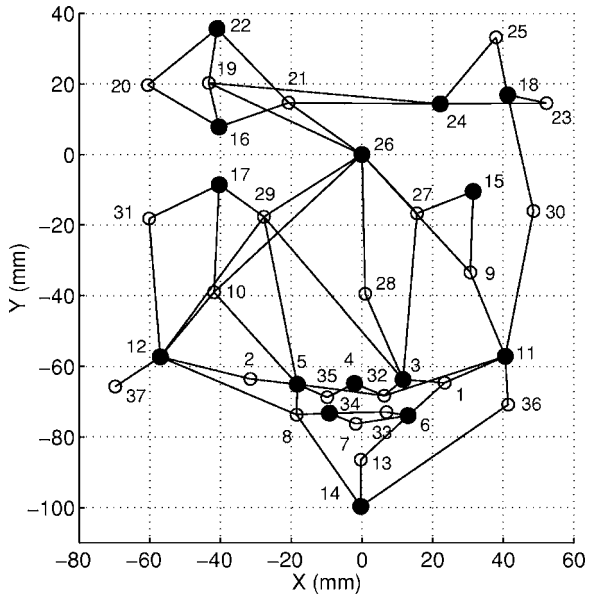

FIG. 3. Computed clusters, for a total number of 15 clusters. The primary marker of each cluster is shown as a filled circle, linked to the associated secondary markers in unfilled circles.

25) to 1.64 mm (marker 2), and relative errors from 6.57% (marker 13) to 111.47% (marker 28). The large relative error of marker 28, at the nose tip, is an artifact resulting from its small displacement amplitude. Marker 13, on the other hand, is the secondary marker closest to jaw, and its large movement amplitude results in the low relative error. The mean errors across all markers are 0.34 mm and 33.19%, respectively.

For visual assessment of the animations using this technique, we created movies showing motion of the markers, for a number of clusters ranging from 37 (all markers are primary markers) to 9, which is the minimum number that the algorithm can detect in the dataset. They are available in the URL http://www.mat.unb.br/~lucero/facial/cluster_e.html, in AVI format. It may be seen that animations using a low number of clusters provide a good match to the measured motion pattern. For example, there is hardly any visible difference between the animation with 15 clusters and the one using the full measured dataset.

V. CONCLUSIONS

In this paper we have presented a technique for building a mathematical model of the human face biomechanics based

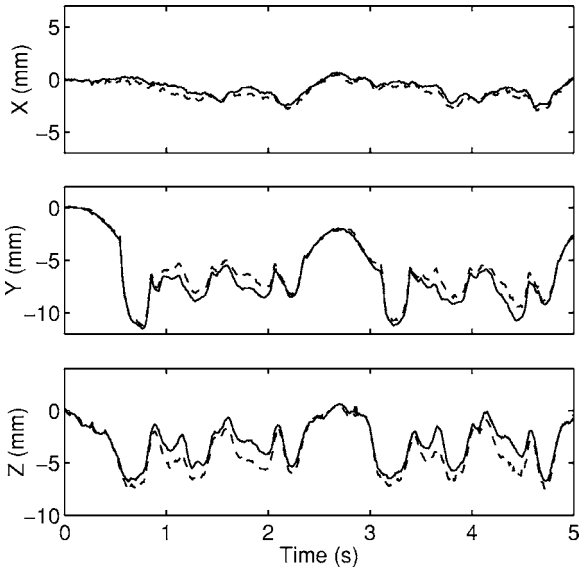

FIG. 4. Trajectories for marker 7. Full line: computed trajectory, dashed line: measured data.

on identifying facial regions (clusters) with a common motion pattern. The model consists of the cluster structure given by Table II and the associated marker spacial configuration. It is an empirical model, derived from kinematic data, rather than a theoretical one built from considerations of the physiological structure of the face (as in the case of Lucero and Munhall, 1999). However, it still reflects the underlying biomechanical structure of the face. We assume that the deformation patterns we are modeling represent the degrees of freedom of the system and the tissue biomechanics. Our modeling includes the dimensions of the deformation (distances and magnitudes) and the surface propagation of the deformations. This is influenced by the viscoelasticity of the tissue and the geometrical pattern of the muscles' connection to the skin tissue.

After the model has been set up, it may be used to produce facial animations, by driving the clusters with recorded kinematic data.

This technique might serve the purpose of a visual aid for speech perception studies, because its data-driven characteristic allows the construction of individualized models for different subjects. Further, animations of the model are driven with kinematic signals, which are relatively easy to collect and to manipulate. The technique provides a methodology for structuring animation systems that reflect the motion patterns across the face. In doing so, the motion patterns are modeled in a way that provides an efficient representation of the independent movement components.

Our results are still preliminary in nature, but indicate that good animations might be obtained from this technique. Here we have used this technique with speech movements, but it may be used also with movements of general facial expression.

Further analyses are still required to investigate the potential of this technique. For example, its capability for producing complete face animations must be assessed using better facial models, with meshes of higher resolution, texture maps for the skin, and other detailed effects of facial motion. Further, the appropriate number of clusters, the robustness of the results when using various configurations of the facial marker mesh, sets of signals for various speech utterances, and also different subjects and speaking rates must be explored. The spatial resolution of the facial markers must be also improved to obtain a better definition of the clusters. These and related issues are currently being considered as our next research steps.

ACKNOWLEDGMENTS

This research was supported by CT-Info/MCT/CNPq (Brazil), the National Institute on Deafness and Other Communication Disorders (Grant No. DC-05774), and the Communication Dynamics Project, ATR Human Information Science Laboratories (Kyoto, Japan).

Badin, P., Bailly, G., and Revéret, L. (**2002**). "Three-dimensional linear articulatory modeling of tongue, lips, and face, based on MRI and video images," J. Phonetics **30**, 533–553.

Beskow, J. (**2004**). "Trainable articulatory control models for visual speech synthesis," International Journal of Speech Technology **7**, 335–349.

Bevacqua E., and Pelachaud C. (**2004**). "Expressive audio-visual speech," Computer Animation and Virtual Worlds **15**, 297–304.

Cohen, M. M., and Massaro, D. W. (**1990**). "Synthesis of visible speech," Behav. Res. Methods Instrum. Comput. **22**, 260–263.

Davis, H., and Silverman, S. R. (Eds.) (**1970**). *Hearing and Deafness*, 3rd ed. (Holt, Rinehart and Winston, New York).

Ekman, P., Friesen, W. V., and Hager, J. C. (**2002**). *The Facial Action Coding System*, 2nd ed. (Research Nexus eBook, Salt Lake City).

Fidaleo, D., and Neumann, U. (**2002**). "CoArt: Co-articulation region analysis for control of 2D characters," Proceedings of Computer Animation 2002, pp. 17–24

Kincaid, D., and Cheney, W. (**2002**). *Numerical Analysis: Mathematics of Scientific Computing* (Brooks/Cole, Pacific Grove, CA).

Kuratate, T., Yehia, H., and Vatikiotis-Bateson, E. (**1998**). "Kinematics-based synthesis of realistic talking faces," in *International Conference on Auditory-Visual Speech Processing (AVSP'98)*, edited by D. Burnham, J. Robert-Ribes, and E. Vatikiotis-Bateson (Causal Productions, Terrigal-Sydney, Australia), pp. 185–190.

Lucero, J. C., and Munhall, K. G. (**1999**). "A model of facial biomechanics for speech production," J. Acoust. Soc. Am. **106**, 2834–2842.

Munhall, K. G., and Vatikiotis-Bateson, E. (**1998**). "The moving face during speech communication," in *Hearing By Eye, Part 2: The Psychology of Speechreading and Audiovisual Speech*, edited by R. Campbell, B. Dodd, and D. Burnham (Taylor & Francis Psychology, London).

Ouni, S., Cohen, D. M., and Massaro, D. W. (**2005**). "Training Baldi to be multilingual: A case study for an Arabic Badr," Speech Commun. **45**, 115–137.

Pitermann, M., and Munhall, K. G. (**2001**). "An inverse dynamics approach to face animation," J. Acoust. Soc. Am. **110**, 1570–1580.

Terzopoulos, D., and Waters, K. (**1990**). "Physically-based facial modeling, analysis, and animation," Journal of Visualization and Computer Animation **1**, 73–80.

Zhang, Y., Prakash, E. C., and Sung, E. (**2004**). "A new physical model with mutilayer architecture for facial expression animation using dynamic adaptive mesh," IEEE Trans. Vis. Comput. Graph. **10**, 339–352.

Aeroacoustic production of low-frequency unvoiced speech sounds

Michael H. Krane[a)]
CAIP Center, Rutgers University, Piscataway, New Jersey 08854-8088

(Received 4 October 1999; revised 28 April 2003; accepted 5 November 2004)

A theoretical approach to describing unvoiced speech sound production is outlined using the essentials of aerodynamics and aeroacoustics. The focus is on the character and role of nonacoustic air motion in the vocal tract. An idealized picture of speech sound production is presented showing that speech sound production involves the dynamics of a jet flow, characterized by vorticity. A formal expression is developed for the sound production by unsteady airflow in terms of jet vorticity and vocal-tract shape, and a scaling law for the aeroacoustic source power is derived. The generic features of internal jet flows such as those exhibited in speech sound production are discussed, particularly in terms of the vorticity field, and the relevant scales of motion are identified. An approximate description of a jet as a train of vortex rings, useful for sound-field prediction, is described using the scales both of motion and of vocal-tract geometry. It is shown that the aeroacoustic source may be expressed as the convolution of (1) the acoustic source time series due to a single vortex ring with (2) a function describing the arrival of vortex rings in the source region. It is shown that, in general, the characteristics of the aeroacoustic source are determined not only by the strength, spatial distribution, and convection speed of the jet vorticity field, but also the shape of the vocal tract through which the jet flow passes. For turbulent jets, such as those which occur in unvoiced sound production, however, vocal-tract shape is the dominant factor in determining the spectral content of the source. [DOI: 10.1121/1.1862251]

PACS numbers: 43.70.Aj, 43.70.Bk, 43.28.Py, 43.28.Ra [AL] Pages: 410–427

LIST OF SYMBOLS

A	vocal tract cross-sectional area
$A_{\min}$	vocal tract cross-sectional area at axial location of maximum constriction
A_v	cross-sectional area of vortex core$=\pi\delta_v^2/4$
B	total enthalpy
B'	total enthalpy fluctuation
c	speed of sound
D_j	vocal-tract diameter at jet formation point
$\mathbf{e}_\theta$	unit vector in the direction of vorticity in vortex ring, points in θ direction
$F(t)$	aerodynamic force on vocal tract walls
f_{arr}	frequency of vortex ring arrival in source region
f_n	nth resonance frequency of vocal-tract acoustic pressure
f_{us}	shear layer instability frequency
f_z	frequency of zero of vocal-tract acoustic pressure
G	Green's function$=G(x,t;y,\tau)$, the acoustic transfer function between source location y and receiver position x
H	axial length of constriction
$H(t)$	Heaviside function
$I(t)$	vortex ring arrival function, weighted by vortex ring circulation
L_h	transverse distance between jet formation point and wall downstream of jet formation point
L_f	axial length of front cavity, between jet formation point and lip termination
L_r	axial length of recirculation zone downstream of jet formation
L_s	axial distance between jet origin and source location
ℓ	length scale of airflow
M	Mach number v/c
$R_{\min}$	radius of minimum vocal-tract constriction
R_p	radius of duct away from constriction
R_v	vortex ring radius
Re	Reynolds number $U\ell/\nu$
$S(t)$	aeroacoustic source strength
St	Strouhal number, $f\ell/U$
T_{arr}	mean period for vortex rings arrival in source region
U	particle velocity of air in regions far from constriction
U^*	velocity disturbance to unit incident flow, caused by change in vocal-tract shape
U_c	convection speed of vortex ring in jet
U_j	jet speed
u'	acoustic particle velocity
v	air particle velocity
$W(t)$	source strength function for vortex ring of unit strength
x	observer position
y	source position
α	angle between $\mathbf{U}^*$ and $\mathbf{v}$ for vortex ring in source region
Γ	vortex circulation, $\omega(\pi\delta_v^2)$
γ	reflection coefficient of vocal tract terminations
Δt	time interval between vortex arrivals in source region$=T_{\text{arr}}+\Phi$
$\delta(t)$	Dirac delta function

a)Electronic mail: mkrane@caip.rutgers.edu

δ_i spacing between coherent structures in jet
δ_v vortex ring core diameter
δ_b boundary layer thickness
θ azimuthal coordinate, tangent to vortex ring
ν air kinematic velocity
ρ air density
ρ^{∞} air density in jet
ρ' acoustic density fluctuation
σ_Φ variance of random process describing vortex arrival in source region
τ source time
Φ vortex arrival phase jitter
ϕ^* velocity potential of $\mathbf{U}^*$, $\mathbf{U}^*=\nabla\phi^*$
ω vorticity, $=\nabla\times\mathbf{v}$

I. INTRODUCTION

This article presents a theoretical framework for describing the physics of sound production by vocal-tract airflow, which has long been known to be not only the primary mechanism of unvoiced consonant sound production, but also a secondary source of sound in voicing. While the discussion touches on issues related to flow-induced vibration of the vocal folds (phonation), it deals primarily with unvoiced sound production. This problem has been addressed in speech science only indirectly. The primary reason for this is that the physics of sound production and propagation in speech science has until recently focused on lumped-element models of primarily acoustic motion of the air in the vocal system. This approach has enabled a great deal of progress in understanding the mechanism of flow-induced vibration of the vocal folds and its attendant sound production, but not of purely aerodynamically produced speech sounds. Two elements have been largely missing in the speech science literature: first, a proper distinction between what constitutes ''flow'' and what constitutes ''sound,'' and second, aeroacoustic theory, which describes how airflows produce sound. The lack of a distinction between flow and acoustic modes of motion was, for example, a central failing in the work of Teager (1980, 1981), Teager and Teager (1983, 1990), and Kaiser (1983).

Consideration of these two points leads to a focus on vorticity, the flow quantity essential in understanding not only the dynamics of turbulent airflow motion, but also how that airflow produces sound. Even studies in speech sound production using more sophisticated flow models (Liljencrants, 1989; Alipour *et al.*, 1996) have not focused on the role of vorticity or its central role in aeroacoustic theory. While McGowan (1988) was the first to incorporate concepts from aeroacoustics in discussing the production of speech sounds, he limited his discussion to voiced sounds. While the later, more comprehensive, contributions by Hirschberg and collaborators (Hirschberg, 1992; Pelorson *et al.*, 1994; 1997; Hofmans, 2003; Lous *et al.*, 1998) have successfully incorporated many of these ideas, they also focused largely on voiced sound production, and did not emphasize the distinction between the flow and sound modes of motion. Davies *et al.* (1993) addressed the effect of bulk air displacement from lungs through the vocal tract on sound propagation in the vocal tract by applying the acoustics of moving media to speech, but did not discuss directly the production of sound by airflow. Davies (1996) and Barney *et al.* (1997) used the aeroacoustic approach of Davies *et al.* (1993), but again were primarily interested in voiced sound production, and using the theory as a framework for data reduction. More recently, Zhang *et al.* (2002b) applied the aeroacoustic formalism of Ffowcs-Williams and Hawkings (1969) to voiced sound production, but did not consider unvoiced sound production. Zhang *et al.* (2002a) reported experimentally derived aeroacoustic source spectra of jets in a pipe, but these measured the direct radiation from the jet, not the interaction of the jet with changes in pipe shape, which, as described below, is the primary mechansim for unvoiced speech sound production.

A qualitative physical picture of unvoiced speech sound production has developed over a long time. Early contributions to speech science (e.g., Fant, 1960) noted the necessity of ''turbulent'' airflow for producing unvoiced sounds, but other than noting the random, broadband character of the source, they provided few details of the mechanism involved. Stevens (1971) incorporated many ideas from the aeroacoustics literature, notably the form of the acoustic spectrum from a turbulent jet and the notion that airflow produces the noise most efficiently in the presence of a ''spoiler'' or ''obstacle,'' so that the sound is produced not where the turbulent flow is formed, but instead where that turbulent flow interacts with an obstacle such as the teeth. In other words, the majority of sound radiation does not come directly from the turbulent jet itself, but from the interaction of the jet with its environment. Shadle (1985) confirmed the latter idea in a series of *in vitro* model experiments, but was unable to clarify the sound production mechanism when a distinct obstacle was not present. Later work by Shadle (1991) strongly suggested that the sound produced by airflow in the vocal tract is sensitive to the three-dimensional details of vocal-tract geometry, so that a simple axial area distribution may not be enough to characterize the vocal tract for the purposes of predicting unvoiced speech sounds. None of the above work directly addressed, or conclusively resolved, questions concerning the turbulent flow acoustic source characteristics (level, spectrum, spatial distribution) from first principles of air motion. These questions cannot be answered in terms of the traditional speech science approach to air motion in the vocal tract: either that (1) the flow is irrotational, quasisteady, and that the Bernoulli equation is sufficient to describe the relationship between pressure and particle velocity, or that (2) the acoustic excitation due to the flow is simply described by bandlimited white noise. The aerodynamics and its acoustic effect are far more complex, particularly when unvoiced sounds are produced.

From the very complexity of airflow dynamics arises the need for approximations, in order to make the problem tractable (even a numerical simulation is an approximation). Aeroacoustic theory provides a means for introducing reasonable approximations by providing formal expressions in which the nonacoustic motion is cast in the form of an acoustic source. The formal expression for sound pressure arising from aeroacoustic theory in fact represents a filtering of in-

formation concerning the airflow; an exact representation of the airflow is unnecessary and the form of the source term provides essential guidance concerning how to make valid approximations concerning the airflow.

This paper presents the essential ideas concerning fluid dynamics and aeroacoustics which are necessary not only for a fundamental understanding of the process of unvoiced speech sound production, but also for prediction of sound levels and spectral characteristics. First, an idealized picture of fluid motion in the vocal tract is presented. From this picture we see that, no matter what sort of sound is being produced, we have essentially two modes of motion involved, namely flow and sound. A qualitative discussion of the properties of these two modes is presented. The flow mode is seen to have a jet structure whose dynamics is dominated by *vorticity*, or air particle rotational motion. *It is argued that characterizing aerodynamically generated speech sound production can be carried out in two steps: (1) a description of the production and evolution of jet vorticity, and (2) a description of how this motion produces sound.*

The latter of these two issues is addressed first. Section II presents the integral expression for the aeroacoustic source at low frequencies. Note that the role of high-frequency, nonplanar acoustic modes in this context is not covered here but will be the subject of a subsequent paper. The implications of the formal expression concerning speech sound production are discussed. Then, a scaling law is derived for the sound-pressure fluctuation due to a vortex ring in an infinite tube. It is shown how the aeroacoustic source expression requires only limited information regarding the vorticity field. Guided by these considerations, Sec. III briefly discusses jet structure in order to define the relevant scales of motion from which order of magnitude estimates can be derived. Then, in Sec. IV the aeroacoustic source characteristics for an idealized vocal-tract flow are presented formally in terms of a model for the jet, resulting in an estimate for the shape of the aeroacoustic source spectrum. This theoretical treatment provides a framework for conclusively resolving the heretofore unanswered issues regarding unvoiced speech sound production—in particular, aeroacoustic source strength, spatial distribution, frequency content, and source impedance.

II. AEROACOUSTIC EXCITATION OF THE VOCAL TRACT

A. Nature of air motion in speech sound production

In examining the motion of air involved in speech sound production, it can be seen that at least two modes of motion are involved. For the moment, these can loosely be defined as being a flow mode and a sound mode. The flow mode essentially consists of the air being displaced from the lungs through the vocal tract and out of the mouth. Along the way, the kinetic energy of this motion can be harnessed to drive flow-induced vibration of soft tissues and/or an unsteady jet, both of which can acoustically excite the vocal resonator. Thus, the flow mode, which includes these jet- and flow-induced vibratory motions, can be seen as an intermediate mode of motion between the physiological inputs and the sound mode we perceive as speech.

Although this qualitative physical picture has implicitly existed since the beginnings of speech science, two questions have not been sufficiently addressed: (1) what is the nature of the flow mode and how can its behavior be predicted, or at least characterized, quantitatively, and (2) even if the flow mode motion is known perfectly, how does that mode convert some of its energy into sound? These questions have been answered, albeit in a greatly approximated way, for flow-induced vocal-fold vibration and its attendant sound production. In this description, the effects of the flow mode, especially the formation, convection, and dissipation of vorticity, which can have pronounced effects not only on the flow-induced vibration of the vocal folds (Pelorson *et al.*, 1994; Lous *et al.*, 1998; Hofmans, 2003), but also on aspirative and unvoiced sound production (Stevens, 1971; Shadle, 1985, 1991). Using a quasisteady Bernoulli model of the flow mode, where the effects of flow separation are incorporated as a lumped-element loss, as first done by Ishizaka and Flanagan (1972), seems to work well for simple models of vocal-fold vibration, but does not include a description of the vorticity dynamics relevant for unvoiced or aspirative sound production. Going beyond this simple description, or developing quantitative or predictive models of unvoiced speech sounds, means going beyond these simple quasisteady Bernoulli-equation descriptions of the flow mode.

A first step in this direction is a consideration of the properties of the modes of motion just described. First, we note that perhaps more precise, descriptive names for the modes are ''convective'' (or ''incompressible'') and ''propagative'' (or ''irrotational''). The propagative mode will be considered first because it is more familiar to speech researchers. Motion of air particles in the sound mode is characterized by *propagative* transfer of energy and momentum. In other words, these quantities are transmitted *through* air particles by the propagation of waves of compression/expansion. A fluid particle experiences no net displacement from its initial position during the passage of a sound wave. The only forces active in a sound field are pressure forces, which act uniformly on a fluid particle, producing no rotation upon it. A mathematical description of the sound mode must have these properties: (1) it must support volume fluctuations, and (2) it must be irrotational. The convective mode is by contrast characterized by transfer of energy and momentum through the actual displacement and rotation of air particles, which as a result end up far away from their initial location, as when air is displaced from the lungs and expelled out of the body. At air speeds observed in speech, which might locally approach 40 m/s (M = Mach number $= 0.12$), these motions proceed without appreciable volume fluctuations, i.e., they are essentially *incompressible*. Therefore, a mathematical description of this mode in speech type air flows must (1) support air particle rotation, and (2) be incompressible.

Figure 1 shows a sketch representing a vocal-tract airflow in which speech sounds are produced. This geometry has the generic features of all speech sounds, no matter their origin. First, a high-pressure reservoir (the lungs) to the left pushes air through the passage. Upon being accelerated through the leftmost constriction, the airstream decelerates

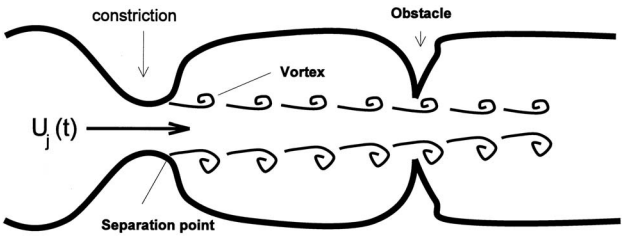

FIG. 1. Schematic of air motions in speech sound production. Air flowing from the lungs from left to right is forced through constriction at the right, at velocity $U_j(t)$. The airstream separates at some point downstream of the location of maximum constriction, forming a jet. The jet boundaries consist of vortical flow, which quickly breaks down into coherent vortical structures. These structures convect from left to right at the local flow speed, a fraction of U_j. As the vortices convect through the vocal tract, they induce unsteady forces on the vocal-tract walls. These forces produce sound. For wall features such as the "obstacle" shown here, where the shape changes rapidly, these forces, and hence the sound produced, are particularly intense.

and the flow becomes *separated* from the wall, forming a *jet*. This jet consists of a focused high-momentum region in the center, surrounded by stagnant air. These two regions are bounded by *shear layers* in which air particles undergo not only translation, but also rotation. *Vorticity* (in some sense, a measure of rotational motion) in the shear layer tends to coalesce into *coherent structures* (Cantwell, 1981; Hussain, 1986), which may or may not be "turbulent," and which convect from left to right. The shear layer diffuses, through the action of viscous forces enhanced by coherent structure mixing, in the direction perpendicular to the flow, causing the jet to spread in the transverse direction. This process mixes the jet core flow and the stagnant region air, so that the momentum of the jet is ultimately spread out over the whole vocal-tract cross section. The presence of vorticity in the jet is a consequence of *boundary layer separation* (see Sec. II B 1) which injects into the bulk flow rotational motion formed in the thin viscous layer near the wall. Note that until the point of separation, the vorticity is confined to the boundary layers. Because vorticity corresponds to a definite amount of momentum [see, e.g., Batchelor (1968), or Saffman (1992)], it will persist even if the flow producing the jet is shut off. If, as is shown in Fig. 1, the jet encounters a change in duct area, the vortical structures in the jet will produce unsteady forces on the walls of the obstacle as they pass by it. These forces will excite (transfer energy) to the irrotational (acoustic) mode in the vocal tract.

Contrast this picture with those which have propagated in the speech community, as seen in the work of Flanagan and Cherry (1969), Flanagan and Ishizaka (1976), or Stevens (1971) and Shadle (1985). In the first two, turbulent flow is treated as occurring only in those regions where the particle velocity of the airflow/sound field rises above a critical Reynolds number, above which a steady duct flow is usually turbulent. The source strength is prescribed as proportional to the square of the local particle velocity, and the spectral content is modeled as bandlimited white noise. Shadle (1985), following Stevens (1971), suggested modeling the aerodynamic source as a dipole in the vicinity of the obstacle, but was not able to resolve further questions regarding the spatial distribution of the source, particularly when no clear obstacle-type geometric feature was involved. Sondhi and Schroeter (1987) used a similar approach, but the same questions concerning the fundamental nature of the source were left largely unanswered. Furthermore, the notion that the jet has any definite structure, despite the "random" character of turbulent flow, and that this structure has any consequence for sound production, is largely missing from the speech literature. While Stevens (1971) and Shadle (1985) recognized that jets do have spatially distributed structure, they did not translate that realization into a concrete connection between that structure and sound production. Teager (1980, 1981), Teager and Teager (1983, 1990), and Kaiser (1983) also argued for the importance of jet structure in voiced sound production, but failed to provide a clear theoretical connection between jet structure and sound production. The spatio-temporal structure of internal flow jets is discussed in more detail in Sec. III.

The types of speech sound which are represented in Fig. 1 may be classified according to the behavior of both the constriction and the jet flow through that constriction. If the flow and the constriction are involved in flow-induced oscillation, then the sketch represents phonation, a trill, or a guttural sound. In the case of phonation, the sound produced at the obstacle is the source of aspirative noise, the "breathy" part of the voice. If the constriction is first closed and then suddenly opened, releasing a transient puff of air, then the sketch represents a plosive. On the other hand, if both the constriction geometry and the airflow through it are steady, then an unvoiced fricative is represented, while a voiced fricative is modeled by a steady constriction geometry and an unsteady periodic air flow due to the resonances of the voicing.

Speech sounds may be thought of as being produced by three mechanisms: (1) volume displacement due to vocal-tract wall motion, and (2) unsteady forces on the obstacle and the constriction walls (or, more generally, a change in duct geometry) induced by the unsteady motion of jet vorticity structures, and (3) direct radiation due to unsteady motion of the jet structures [see, e.g., the appendix of Zhang *et al.* (2002b)]. The second mechanism is the focus of this paper. Once the sound is produced, because the ends of the vocal tract do not perfectly absorb or allow perfect transmission of sound waves, some acoustic energy is reflected back into the tract, so that acoustic energy accumulates there in the form of standing waves. The standing wave structure at the open (mouth) end of the vocal tract is particularly important, since it transmits the oscillations inside the resonator to the outside world.

At this point in the discussion, it is possible to make more precise the sequence of events between diaphragm contraction and unvoiced sound production, as described in brief at the beginning of this section. First, the flow mode, which consists not only of the air displaced from the lungs, but also the unsteady jet motion formed at a constriction. Both of these motions, being essentially incompressible, are distinct from the sound field, and give up only a small fraction of their kinetic energy in generating it. Most of the kinetic energy of this convective mode of air motion is in fact either

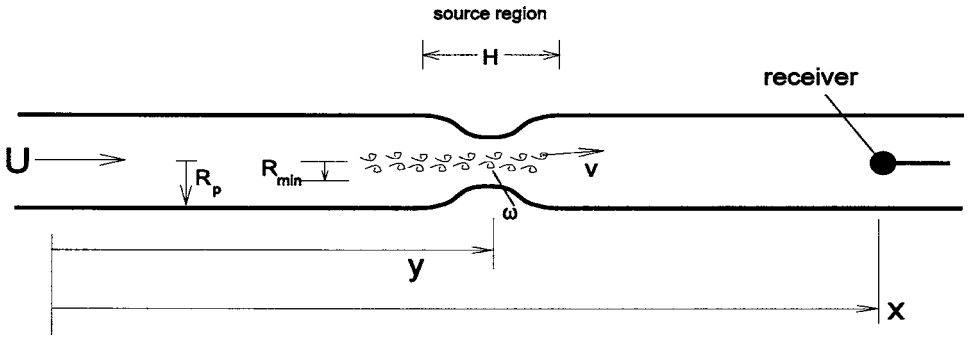

FIG. 2. Schematic of aeroacoustics problem: find the sound pressure at observer location, x, in an infinitely long duct of uniform cross section (radius R_p) containing a narrow constriction (radius $R_{\min}$) of axial length H. The air in the pipe far away from the constriction is a combination of steady motion (velocity U) and the sound produced by an unsteady aerodynamic force on the constriction walls at source coordinate y. Forces are due to vorticity ω convected at local velocity $\mathbf{v}$ through the constriction.

dissipated by viscosity with the aid of turbulence, or convected out the mouth by the airstream. The rotational (vortical) motions of the jet shear layers, which are shown below to be directly involved in sound production, are formed using energy taken from the airstream. Thus, the problem of unvoiced sound production may be seen more precisely to involve (a) how jet vorticity is formed and how it evolves, and (b) how this motion produces sound.

B. Acoustic pressure due to aerodynamic sources

To gain insight into the production of sound by vortical flow in the vocal tract, let us first look at the problem of sound production by vorticity convecting past an obstacle in an otherwise uniform cross-section pipe. Using this idealization of the vocal tract, an integral expression for the sound pressure can be derived. The integral expression is desirable because, in general, obtaining a high-fidelity description of the vorticity field is prohibitively expensive [see, e.g., Hardin and Pope, 1992; Hulshoff *et al.* (2001) for an example relating to duct aeroacoustics], if not impossible, motivating the use of an approximate description. The integral form works well in this context because it is relatively insensitive to errors involved in approximating the flow field. In addition, as will be shown, not all information regarding the vorticity field is relevant, so the formal result is informative in discriminating the aeroacoustically relevant information. The integral expression will then be used to demonstrate how the aeroacoustic source excitation of the vocal-tract pipe due to a single vortex ring may be determined.

1. Formal solution for sound pressure due to an aeroacoustic source

The problem under initial consideration is shown in Fig. 2. The air in an infinitely long pipe is in steady motion at speed U. The pipe has uniform cross section area A, except for a short section which contains a constriction. The steady airflow convects vortical disturbances through the constriction, a process which produces unsteady forces on the constriction walls, producing acoustic disturbances which radiate away from the constriction. If the duct shape, U, and the vortical disturbances are known, an expression is sought to describe the sound-pressure field at an observer location $\mathbf{x}$ due to the source processes at location $\mathbf{y}$. The solution to problems of this type is the domain of aeroacoustics. Several texts on this subject are available for a more complete study (Goldstein, 1976; Dowling and Ffowcs-Williams, 1983; Blake, 1986; Lighthill, 1978; Howe, 1998).

For computing the sound field due to nonuniform flow in a duct, Howe (1975, 1998) has shown that a concise formulation may be derived using the acoustic total enthalpy $B' \approx p'/\rho_\infty + \mathbf{U}\cdot\mathbf{u}'$ as the acoustic variable, where $\mathbf{U}$ is the steady flow speed and $\mathbf{u}'$ is the particle velocity of acoustic disturbances. Here, and throughout the text, ρ_∞ is the ambient undisturbed air density. In speech-like geometries, the constrictions are rather severe, so that the steady flow speed in the unconstricted portion of the flow is extremely small. Thus, far from the region where the sound is produced, U is small, so $B' \approx p'/\rho_\infty$. Howe also showed that for low Mach number flows such as those seen in speech sound production, the convected wave equation for the low-frequency acoustic field variable B' is given by

$$\frac{D^2B'}{Dt^2} - c^2\frac{\partial^2 B'}{\partial x^2} = \frac{\partial}{\partial x}(\boldsymbol{\omega}\times\mathbf{v})_x, \tag{1}$$

where c is the speed of sound and DB'/Dt is the convective or material derivative of B', *following a fluid particle as it moves through space*

$$\frac{DB'}{Dt} = \frac{\partial B'}{\partial t} + U\frac{\partial B'}{\partial x}, \tag{2}$$

where the first term represents the time rate of accumulation of total enthalpy *at a fixed location in space* and the second term represents the time rate of change of total enthalpy *at a fixed location* due to convection of total enthalpy fluctuations past that fixed point. Note that the effect of the latter term in the wave operator describes the convection of sound waves by motion of the medium.

The wave equation states that, if the right-hand side is zero, an acoustic disturbance will propagate such that its energy is conserved. In the quasi-one-dimensional propagation described here, energy of the disturbance will be conserved. If the right-hand side is nonzero, the disturbance will either gain or lose energy. If no disturbance exists (the "disturbance" has zero energy), then one will be generated. Because the terms on the right-hand side of Eq. (1) do work on the acoustic field, they are referred to as "sources" [although

they may also act as "sinks" in an ambient sound field—see Howe (1980, 1998), Bechert (1980), Hirschberg (1992)].

The physical mechanism responsible for modifying the acoustic disturbance field is the axial component of the vector $\boldsymbol{\omega}\times\mathbf{v}$, the acceleration due to the motion of vorticity in the vocal-tract airflow. This term is central to the understanding of turbulent flow dynamics (see, e.g., Tennekes and Lumley, 1972), and relates not only to the direct radiation of sound from the jet (see Powell, 1964; Howe, 1998), but also to the aerodynamic forces induced on the vocal-tract walls by the jet (see Howe, 1998). Formulating the aeroacoustic problem in this manner has several advantages over the more commonly used one due to Curle (1955) [a development of Lighthill (1952, 1978)]. A discussion of these advantages is delayed until the solution for the sound field has been obtained, when they are more clear.

The solution of Eq. (1) for the sound-pressure fluctuation arising from the interaction of the jet and the constriction is found by convolving a tailored Green's function with the source term $\partial(\boldsymbol{\omega}\times\mathbf{v})_x/\partial x$ (see the Appendix for details)

$$p'(x,t)=-\rho_\infty\frac{\mathrm{sgn}(x-y)}{2A(1+M)}\int_A\int_y[\boldsymbol{\omega}\times\mathbf{v}\cdot\mathbf{U}^*]dA\,dy, \quad (3)$$

where $\mathrm{sgn}(x-y)$ is the signum function

$$\mathrm{sgn}(x-y)=\begin{cases}1 & \text{for } x-y>0\\ -1 & \text{for } x-y<0,\end{cases}$$

so that the acoustic pressure changes sign across the source, consistent with a dipole source. Here, A and M refer to the cross-sectional area and the steady flow Mach number, respectively, at the receiver location x where the sound pressure. Note that the integrand is written inside square brackets to denote that it is a function of source position $\mathbf{y}$ and retarded time $t-|\mathbf{x}-\mathbf{y}|/(c(1+M))$ it takes the signal to reach the observer at $\mathbf{x}$ from the source at $\mathbf{y}$. This expression can also be written (Howe, 1998) as

$$p'(x,t)=-\frac{\mathrm{sgn}(x-y)}{A(1+M)}\int_A\int_y[F(y)]dA\,dy, \quad (4)$$

where F is the axial component of the aerodynamic force on the constriction, which in Eq. (2) has been expressed in terms of the scalar product of jet flow vorticity acceleration $\boldsymbol{\omega}\times\mathbf{v}$ and the quantity $\mathbf{U}^*$. Strictly speaking, $\mathbf{U}^*$ is the ideal flow velocity field that would exist if the duct contained a unit speed steady airflow. It should be recognized that $\mathbf{U}^*$ is not a flow which actually occurs—it arises in the expression from the correction to the retarded time in the Green's function (see the Appendix), and so reflects the effect of source motion and diffraction around the change in vocal-tract shape. It should then be thought of as a property of the vocal-tract shape (Howe, 1975, 1998).

The integral solution of the convected wave equation shows that the force on the constriction (and hence sound production) occurs when vorticity moves across the streamlines of $\mathbf{U}^*$, or when $\mathbf{v}$ is not parallel to $\mathbf{U}^*$. The constriction drag force, and hence sound generation, is maximum for $\mathbf{v}$ oriented perpendicular to $\mathbf{U}^*$, and minimum (zero) when $\mathbf{v}$ and $\mathbf{U}^*$ are parallel. (Streamlines are simply lines of tangency to the velocity field.) It should be stressed that, due to the contribution of vorticity, the streamlines of the flow $\mathbf{v}$ which is actually realized will have a very different geometry than that of an ideal flow such as $\mathbf{U}^*$ (see, e.g., Saffman, 1992).

A few comments are in order regarding the relationship between Eq. (2) and the more commonly used expression [Eq. (3)] derived by Curle (1955) [see, e.g., Shadle (1985), Verge (1994), Hofmans (2003)], referred to hereafter as the Lighthill/Curle formulation. First, both express the dipole source in terms of the net force on a compact body, or, in this case, the vocal-tract walls. The difference is that the Lighthill/Curle formulation casts the force directly in terms of the net axial wall pressure force [see, e.g., Lighthill (1978)], while Howe (1975) writes the force in terms of the motion of separated flow vorticity and the duct shape. For the purposes of predicting unvoiced speech sound production, the advantage of the Howe formulation over that of Lighthill/Curle is due to three factors. First, the Lighthill/Curle result expresses the sound field in terms of integrals over the airflow Reynolds stresses and the pressure fluctuations on the vocal-tract walls. The Reynolds stresses occupy a much more extensive volume than the vorticity which may be thought of as "driving" this part of the flow. The vorticity occupies only a tiny fraction of the total volume of the vocal tract. Because the Howe formulation is given explicitly in terms of the vorticity, it requires integration over a much smaller volume than the Lighthill/Curle formulation (see also Powell, 1964). Second, Howe's approach results in an expression for the sound pressure in terms of the separated flow vorticity *away from the walls*. In other words, the contribution of the vorticity in the wall boundary layers does not contribute to the sound field. (There will be no aerodynamic drag on the constriction, aside from a small skin friction drag, unless the flow separates, or unless it is placed in a separated flow.) These two factors result in a greatly reduced amount of flow information required to predict the sound field. Third, the integral in Eq. (2) depends not only on the jet flow, but also is an explicit function of the shape of the vocal tract, as reflected in $\mathbf{U}^*$. The shape of the vocal tract, and hence $\mathbf{U}^*$, may be specified with a good deal more precision than the vorticity acceleration $\boldsymbol{\omega}\times\mathbf{v}$ (because of the expense in specifying $\boldsymbol{\omega}$ to any level of precision). However, a simplified description of the vorticity field can still yield an accurate estimate of the acoustic source characteristics. This may be seen by inspection of Eq. (2): the dot product between $\boldsymbol{\omega}\times\mathbf{v}$ and $\mathbf{U}^*$ effectively reduces the amount of vorticity field information required because only those components of vorticity normal to the streamlines of $\mathbf{U}^*$ will contribute to sound production. In this way, the sound production process may be thought to "filter" the vorticity field, the filter shape being determined by the shape of the vocal tract.

2. Relevance of formal result for unvoiced speech sound production

To proceed further in obtaining the acoustic pressure field due to the interaction of the nonuniform vocal tract with a full jet flow, it is necessary to determine at least approxi-

mate behavior for $\boldsymbol{\omega}$, $\mathbf{v}$, and the angle between $\boldsymbol{\omega}\times\mathbf{v}$ and $\mathbf{U}^*$. The reasoning used to choose scales for these quantities is explained in Secs. III and IV. However, even without that information several important points can be made at this stage. These relate (1) to the necessity of flow separation (jet formation) for unvoiced speech sounds to be produced at all; (2) to the extent to which a distinct obstacle is necessary for sound generation; and (3) to the suitability of the traditional speech science approximation of quasi-one-dimensional air motion for description of unvoiced speech sound production.

From the comments outlined above concerning Eq. (2), it is clear that, expressing the aerodynamic sound source in terms of the motion of free vorticity, the flow must separate somewhere in the vocal tract for sound to be produced. Since the vocal-tract wall lies on a streamline of $\mathbf{U}^*$, vorticity in boundary layers will not contribute to sound generation. This is equivalent to saying that the unsteady axial (drag) force resulting from the sum of the axial pressure force contributions on the vocal-tract walls is zero unless flow separation occurs [D'Alembert's paradox—see the remarks of Teager (1980, 1981)].

In addition, from the conceptual picture given above, it is clear that it is not necessary for the jet to actually "impact" or "strike" the obstacle, as has been stated by Stevens (1971) and Shadle (1985). Indeed, a definite "obstacle" shape is not even necessary for sound to be produced by the jet. Shadle (1985) shows results for "no-obstacle" cases, where the jet flow passes through a change in the duct shape itself, including the open end of the tube. From inspection of Eq. (2), it is clear the crossing of $\mathbf{U}^*$ streamlines by vorticity necessary for sound generation will occur for any change in duct shape, not just in the case of a definite obstacle. A clear theoretical example of this effect is given in Howe (1975), where Eq. (2) is derived for a simple reduction in cross-sectional area. [The same case was studied numerically, by Hulshoff *et al.* (2001)]. Here, there is no obstacle *per se*, only a change in duct area. A similar example can be seen in the whistler nozzle (Hirschberg *et al.*, 1989), in which flow through two sudden changes in duct area can, under the proper conditions, lead to intense sound production *without a direct impact of a jet on the pipe walls*. Thus, it can be seen that the distinction Shadle (1985) made between the obstacle- and no-obstacle cases is in some sense an artificial one, at least in terms of the fundamental mechanism by which the sound is produced. In all cases, the aeroacoustic source is located wherever vorticity in a separated flow passes through a nonuniform duct.

It is also evident from the theoretical model of Howe (1975) that, because both the jet behavior and the streamlines of $\mathbf{U}^*$ are determined by details of vocal-tract geometry, the traditional axisymmetric, quasi-one-dimensional representation of the vocal tract is likely not sufficient for prediction and study of unvoiced speech sound production. This point supports the observations of Shadle (1991), who noted the marked sensitivity of the sound produced by airflow through vocal-tract-like models to model geometry. The modeling efforts of Krane *et al.* (2005) and Sinder (1999) also demonstrate clearly that if the geometry of the flow passage is known precisely, Howe's theory predicts the sound produced very well, whereas if a highly three-dimensional flow passage (such as the vocal tract) is approximated by an axisymmetric duct, the resulting prediction of sound is not entirely correct. It should be emphasized that this sensitivity to geometry impacts only the description of the aeroacoustic source, not the propagation of the sound field once generated. Thus, while the computation of aeroacoustic source characteristics does require a more detailed geometric description, the computation of the sound field by the traditional approach acoustic is quite sufficient, at least for low frequencies at which only plane waves propagate. At higher frequencies, nonplanar modes will propagate and will likely dominate the acoustic field. A treatment of the aeroacoustics of nonplanar mode generation in speech will be given in a subsequent paper.

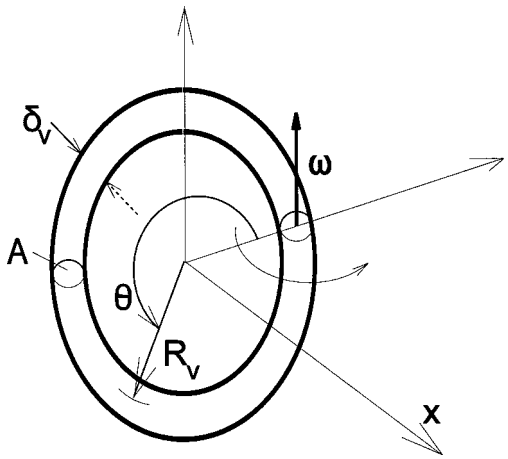

FIG. 3. Structure of a vortex ring, showing the definitions of the vorticity vector and the coordinates used in Eqs. (4) and (5). The vorticity vector points in a direction tangent to the ring, as shown. The ring radius is R_v, the core radius δ_v, the cross-sectional area of the core $A_v=\pi\delta_v{}^2$, and θ is the azimuthal coordinate along the ring.

3. Sound produced by single vortex ring passing an obstacle in an infinite tube

As an example of the process of unvoiced sound production, the sound produced by the convection of a single vortex ring through an axisymmetric constriction in an infinite pipe of otherwise uniform circular cross section will be discussed. The structure of a vortex ring is shown in Fig. 3. The ring consists of a circular tube of vorticity, such that the vorticity vector points in the azimuthal (θ) direction, the tube cross section has diameter δ_v, and the ring has radius R_v. The ring moves from left to right in motion induced by the vorticity in the ring itself (and its images in the duct walls), as well as the irrotational steady flow $\mathbf{U}$. For more on how vorticity is convected, please see Saffman (1992). Using the definition of circulation, Γ, the volume integral of the vorticity is given by

$$2\pi R_v\Gamma=\int_0^{2\pi}\int_{A_v}\boldsymbol{\omega}\cdot d\mathbf{A}\,d\theta \tag{5}$$

(where $A_v=\pi\delta_v^2$ is the area of the vortex ring normal to ω and θ is the coordinate tangent to the vorticity vector, i.e., tangent to the ring). The integral expression for the pressure

fluctuation $p' \approx \rho_\infty B'$ far from the source region then becomes

$$p' = -\frac{\rho_\infty \pi \, \mathrm{sgn}(x-y) R_v}{A(1+M)} [\Gamma(\mathbf{e}_\theta \times \mathbf{v}) \cdot \mathbf{U}^*], \tag{6}$$

where $\mathbf{e}_\theta$ is the unit vector in the vorticity direction. Note that the triple product in this expression is nonzero only where $\omega \neq \mathbf{0}$, and the square brackets have the same meaning as in Eq. (2). If we assume the vortex takes an essentially axial path, then $\boldsymbol{\omega} \times \mathbf{v}$ always points radially outward, and the vortex will generate sound if the radial component of $\mathbf{U}^*$ is nonzero. As the vortex ring convects through the constriction, the radial component of $\mathbf{U}^*$ points initially radially inward upstream of the point of maximum constriction, then radially outward downstream of this point. This behavior is shown in Fig. 4(a) as the vortex ring convects through the constriction, and the source strength takes the appearance of a single period of a sinusoid wave, as shown in Fig. 4(b). The sign change occurs when the vortex passes over the centerline of the obstacle.

Because of the signum function in Eq. (6), the temporal pressure signature is a time-delayed image of the source signal for $x > y$, and an inverted, time-delayed image of the source for $x < y$. This behavior is consistent with dipole source behavior. The duration of the disturbance is roughly ℓ / U_c, where U_c is the convection speed of the vortex through the constriction, and ℓ is estimated by either H, the axial length of the constriction, or δ_v, the radius of the vortex core. The choice of H or δ_v as the length scale depends on which determines the duration of the interaction between the vortex and the change in vocal-tract shape. For cases where the vortex core is much smaller than the obstacle ($\delta_v / H \ll 1$), then H is the proper choice. This corresponds, for example, to the case of the glottal jet produced in /h/ interacting with the bend in the vocal tract or anatomical features such as the epiglottis. In the opposite case, where the obstacle is "sharp" relative to the vortex core size (as in perhaps /s/ or /ʃ/) then δ_v is the proper length scale. [In Fig. 4(a), the case $\delta_v / H \ll 1$ is shown.) The aeroacoustic source spectrum, shown in Fig. 4(c), is a broad peak centered on $f = U_c / \ell$, where ℓ is either H or δ_v, as described above, with width approximately U_c / ℓ. Note that the breadth of the peak is due to the relatively short duration of the source. It is clear from this result that the frequency of the sound will increase as the axial extent of the vocal-tract shape change decreases or as the convection speed increases.

The amplitude of the peaks in the acoustic pressure signal may be estimated from the scales of motion. These are the axial length and height of the constriction, the vortex core radius and ring radius, the vortex circulation, and the vortex convection speed. Writing out the scalar product in Eq. (5), and using $U^* = U(x)/U = A/A(x)$ (Howe, 1975), we obtain

$$p' \approx \rho_\infty \frac{\pi}{A} R_v \Gamma v \, \frac{A}{A(x)} \sin \alpha(t), \tag{7}$$

where α is the angle between the pipe axis (the direction of $\mathbf{v}$, by assumption) and $\mathbf{U}^*$. Now, since $\omega \sim U_c / \delta_v$, then $\Gamma \sim \omega \delta_v^2 \sim U_c \delta_v$. Furthermore, $A(x)$ may be estimated by its minimum, $A_{\min} = \pi R_{\min}^2$, and $\sin \alpha$ may be estimated by $(R_p - R_{\min}) / (H^2 + (R_p - R_{\min})^2)^{1/2}$, where R_p is the radius of the pipe away from the constriction, and $R_{\min}$ is the minimum radius in the constriction. Using these scales in Eq. (6), the acoustic pressure peak has amplitude proportional to

$$p' \sim \rho_\infty \frac{R_v \delta_v}{R_{\min}^2} U_c^2 \frac{R_p - R_{\min}}{((R_p - R_{\min})^2 + H^2)^{1/2}}. \tag{8}$$

From this expression it is clear that the sound pressure increases linearly with both R_v and δ_v, quadratically with U_c, and inversely with the square of $R_{\min}$. In other words, sound production is greater for larger vortex rings (in terms of either its core size or its ring radius), faster convection speeds

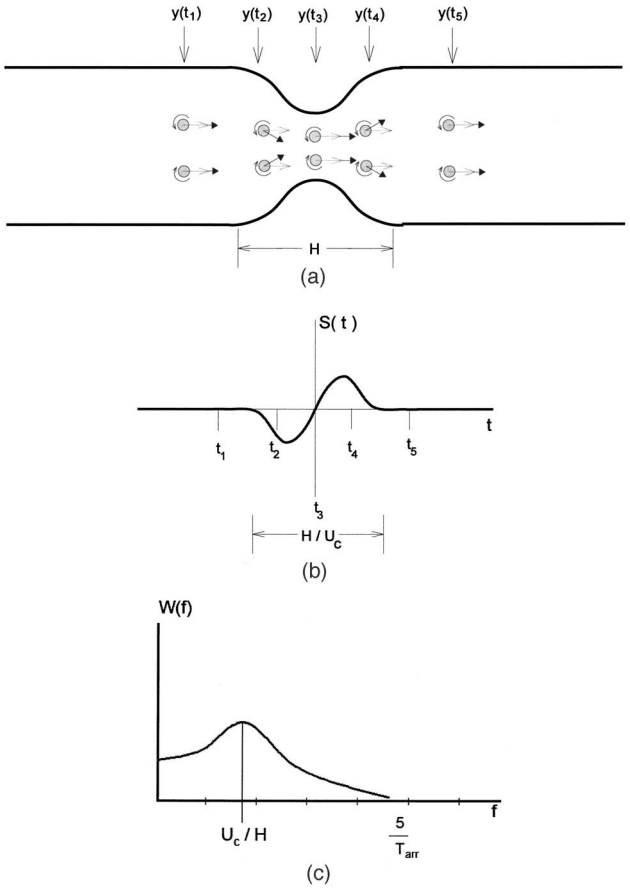

FIG. 4. Aeroacoustic source behavior due to convection of single vortex ring through a constriction in an infinite pipe. Airflow is from left to right, vortex ring diameter is R_v, vortex core diameter is δ_v, and the axial length of the constriction is H. (a) Location $y(t)$ of vortex ring, shown in cross section, at five instants t_1, t_2, t_3, t_4, and t_5 during vortex passage. Orientation of vectors $\boldsymbol{\omega}$, $\mathbf{v}$, and $\mathbf{U}^*$ are shown, $\boldsymbol{\omega}$ in terms of its rotation sense in the plane of the page, $\mathbf{v}$ by lined arrowheads, and $\mathbf{U}^*$ by solid arrowheads. Equation (2) states that the aerodynamic force on the constriction will be maximum when $\mathbf{v}$ is perpendicular to $\mathbf{U}^*$, and zero when they are parallel. (b) Waveform of aeroacoustic source strength due to vortex ring passage through constriction, with times indicated corresponding to vortex ring positions in Fig. 4(a). Duration of source is the time H/U_c that the vortex ring takes to convect through the constriction. Note that $S(t) = 0$ when $t = t_1$, t_3 and t_5, because $\mathbf{v}$ and $\mathbf{U}^*$ are parallel. The aerodynamic force changes sign as the vortex passes through the maximum constriction. (c) Spectrum of sound pressure due to the passage of a single vortex ring through the constriction. Peak occurs at U_c/H, the reciprocal of the time the source is "on." Peak width is related to temporal extent of source signal, and becomes broader as U_c/H becomes smaller.

(i.e., the quicker it moves through the constriction, and the higher the frequency of sound generated), and larger radial changes of vocal-tract shape. These trends explain why the teeth, being the geometric feature in the mouth with by far the sharpest change in shape, are the primary geometric feature in the production of fricatives such as /s/, /ʃ/, or /z/, when the entire mouth is quite nonuniform in shape. It also explains why the vocal-tract walls near the constriction where the jet is formed are not typically as important in unvoiced sound generation—the shape does not change as drastically in that region.

A scaling law for the acoustic source energy as a function of vortex ring convection speed follows:

$$\frac{p'^2}{\rho_\infty c^2} \sim \rho_\infty U_c^2 M^2, \tag{9}$$

which shows that the sound power is proportional to the second power of the ring convection speed times the square of Mach number based on that speed. It is important to note that this particular scaling law (valid for the infinite pipe only) is given here for illustrative purposes; its form will change considerably in a finite-length pipe depending on source location and the local acoustic impedance of vocal-tract terminations.

Note that the velocity dependence for the dipole source energy (U_c^4 or $U_c^2 M^2$) seen in Eq. (8) differs from that of the classical free-field aeroacoustic dipole source (U_c^6) (Curle, 1955; Howe, 1975, 1998). This behavior is true in general for aeroacoustic sources which generate one-dimensional plane waves, compared to the same compact source in free space. This is due entirely to the difference between the manner in which one-dimensional plane waves and three-dimensional spherical waves propagate, reflected in the difference in Green's function for these two cases [see Howe (1975, 1998) for the equivalent Green's function for three-dimensional wave propagation]. For a one-dimensional plane wave, the amplitude is independent of distance from the source, whereas it is inversely proportional to distance from the source for a spherical wave. In addition, the acoustic impedance for a one-dimensional plane wave is frequency independent, whereas the curvature of the spherical wave causes a frequency-dependent impedance, where the impedance becomes larger as frequency decreases. Thus, the source impedance is higher at low frequencies in a situation where spherical waves can propagate. This frequency dependence of the source impedance in free-field geometries is responsible for the higher value of velocity exponent in the scaling law for acoustic source power. This discussion emphasizes how the solution for the sound field given by Eq. (2) incorporates the source impedance.

Note also that the U_c^4 scaling for the aeroacoustic source strength appears to agree with that developed by Flanagan and Cherry (1969). Flanagan and Cherry used the correlation developed by Meyer-Eppler (1953), who measured the sound levels produced by flow through constricted pipes. Their scaling, while in principle correct, did not result from consideration of the physics of sound production by airflow, which the present theoretical development does. Note also that predictive models for unvoiced sound generation based upon Meyer-Eppler's scaling found it necessary to develop a model for the source impedance, which the theoretical development does implicitly by inverting the wave equation with the Green's function.

The efficiency of conversion of flow kinetic energy into sound-field energy may be seen from the ratio of the sound-field energy per unit volume, given in Eq. (8), and the flow kinetic energy per unit volume $\rho_\infty U_c^2/2$. The ratio is proportional to M^2, which means that, since the Mach number of speech flows never exceeds 0.15, the aeroacoustic source is not a particularly efficient means of transforming flow energy into acoustic energy. This crucial realization was missing from the work of Teager (1980, 1981), Teager and Teager (1983, 1990), and Kaiser (1983). They based their arguments on Teager's claims to have measured high-energy (relative to the sound field radiated from the mouth) jet-like air motion in the vocal tract, as opposed to the acoustic plane waves they claimed the traditional view predicted. Questions about Teager's experimental method aside (see the commentary in Kaiser, 1983), he was in fact measuring the velocity distribution of the jet-like flow just above the glottis. As can be seen from the above discussion, this motion is to be distinguished from the sound field. However, lacking the theoretical underpinning for the distinction between convective and propagative motion, they argued for discarding the traditional plane-wave description of acoustic propagation in the vocal system. Here, it is argued that the traditional acoustic description is sufficient, with modifications due to the motion of the air (see, e.g., Davies, 1980; Davies *et al.*, 1993). Furthermore, an intermediate mode of air motion is involved in sound production, namely the convective mode, and the specific manner in which this mode of motion is manifested in speech and how it produces sound needs to be clarified.

4. Effect of finite-length vocal tract

For a finite pipe such as the vocal tract, reflections at the pipe terminations must be incorporated into the analysis. For most unvoiced speech sounds, the constriction at which the jet is formed divides the vocal tract into a ''front'' and ''back'' cavity. Because the acoustic impedance of this narrow constriction is high, the front cavity is often treated as acoustically decoupled from the back cavity. This approximation works well for fricatives and plosives, but perhaps not as well for voiced fricatives. In our approximation of the acoustically relevant part of the vocal tract as a closed–open tube, the ''closed'' end can be thought to be located at the constriction where the jet is formed, while the ''open'' end may be thought to be located at the lips. In addition, the source is in general not located at the closed end of the front cavity, but somewhere inside it. Using the method of images (see Morse and Feschbach, 1953), the Green's function may be constructed for a finite-length closed–open pipe, which represents the end reflections as virtual sources located outside the pipe itself (Pierce, 1989), as shown in Fig. 5

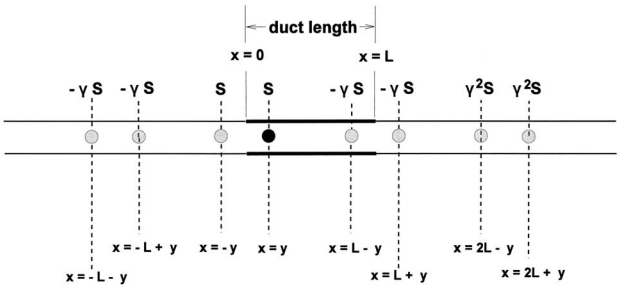

FIG. 5. Treatment of acoustic effect of vocal-tract terminations as the superposition of image sources. Sound field in pipe of length L is equivalent to that due to the real source S, located at $x=y$, and its images, placed in an infinite pipe as shown. Note that the image sources shown are only the first few of the infinite series given in Eq. (9).

$$G(x,t|y,\tau)=\rho_\infty\frac{c}{2A}\sum_{n=-\infty}^{\infty}\gamma^n H\left(t-\tau-\frac{x\pm 2nL_f}{c(1+M)}+\frac{\phi^*(y)}{c(1+M)}\right), \tag{10}$$

where γ is the open-end pressure reflection coefficient, which takes a value between 0 and -1, and $H(\xi)$ is the Heaviside function, which is equal to 1 for $\xi>0$ and 0 for $\xi<0$. The resulting expression for the sound at the open end is given by

$$p'(x,t)=-\frac{\rho_\infty}{2A(1+M)}\sum_{n=-\infty}^{\infty}\gamma^n \times\int_{-\infty}^{\infty}\int_{A}[\boldsymbol{\omega}\times\mathbf{v}\cdot\mathbf{U}^*]_n dA\,dy, \tag{11}$$

where the expression in square brackets is now evaluated at location $x=x\pm 2nL_f$ and retarded time $t-(x\pm 2nL_f)/(c(1+M))$. Note that while the integral over source space, y, is from $-\infty$ to $+\infty$, observer space, x, is defined only over the interval $0<x<L$. Thus, it can be seen that the effect of the open and closed ends of the tube is equivalent to the placement of time-synchronous virtual sources outside the vocal-tract domain. The net effect of these additional sources is the accumulation of sound at the resonance frequencies $f_n=c(2n+1)/4L_f$, where $n=0,1,2,...$, and L_f is the axial length of the front cavity. When the source is not located either at the inlet or outlet of the cavity, then a zero appears in the spectrum at approximately $f_z=nc/(2L_s)$ $(n=0,1,2,...)$, where L_s is the distance between the jet origin and the source location. The width of the resonance peaks depends on the value of γ: the higher γ is, the more acoustic energy radiates out the open end per round trip; the wider the resonance peaks, the lower the resonant levels become.

To this point, the open-end pressure reflection coefficient has been assumed frequency independent for clarity. In a more physically correct description, the reflection coefficient is frequency dependent, because the radiation efficiency of the open end of the tube increases with frequency. In this case, the product of the Heaviside function with the reflection coefficient is generalized to a convolution of the reflection coefficient time series with the Heaviside function. The net effect of the frequency-dependent reflection coefficient is that the amplitude of the resonance peaks at the tube exit decreases with the square of frequency. Thus, the acoustic spectrum in the tube due to an aeroacoustic source is the product of the Green's function spectrum, which consists of resonance peaks with an inverse-frequency squared decay envelope, and the spectrum of the source. The form of the source spectrum is discussed in Section IV.

III. SOME PARTICULARS OF INTERNAL JET FLOWS

While the necessity of turbulent jets in unvoiced sound production has been acknowledged for some time, the relation between jet structure and sound radiation has never been made clear in a speech context. The results in Sec. II clearly show that the convection of vorticity through a nonuniform vocal tract will produce sound. Because the vocal tract is essentially nonuniform everywhere, it is necessary to determine where and how vorticity enters into the flow *in a manner relevant to sound production*. This last qualification is important, because vorticity is always present, at least on the vocal-tract walls where it is formed when the air is in motion. But vorticity will not be relevant for speech sound production unless it is injected into the flow away from the wall, as explained above in Sec. II B. Thus the issue may be summarized in three questions: (1) when and where do jets appear in speech-like flows; (2) for how much time and for what distance from the formation point does a jet persist, and (3) what range of length and time scales characterizes the jet motion. To answer these questions it is necessary to discuss some essentials of jet physics.

A particular point of emphasis in this discussion is that the jet, even when turbulent, is not simply random, but rather possesses a definite spatio-temporal structure. While this point has been recognized to some extent in the speech literature, it has yet to be fully integrated into models of speech sound generation. The variation of jet structure with flow speed, cross-sectional area, and other parameters has a definite pattern. Thus, while the physics of jet flows is rather subtle and complex, the features of jet-flow behavior relevant for production of sound by interaction between the jet and the vocal tract walls may be summed up in a few simple scaling laws.

A. Global jet structure

As described above in the Introduction, the generic flow pattern that arises in speech sound generation involves the formation and evolution of a jet, which may or may not be turbulent. A jet is quite simply a focused region of high-momentum air surrounded by stagnant air. The transition region in between the high-momentum and stagnant regions is the *shear layer*. This shear layer is characterized by a high transverse gradient in particle velocity, representing the change from the velocity found in the core flow of the jet and that in the surrounding stagnant region. It is also the region in which vorticity is present in the flow. Once formed, a jet does not persist for a great length downstream of its formation point. Instead, the jet spreads transversely with distance from its formation location. This occurs for two related rea-

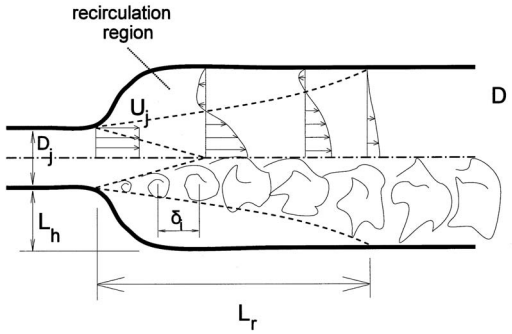

FIG. 6. Schematic of global structure of a jet formed at a sudden expansion in a duct. The top half of the figure shows the distribution of particle velocity (and local momentum) as a function of distance from the centerline, at four axial locations. The bottom half shows the growth in size of the coherent structures through diffusion, as well as the breakdown of coherent structures. Note that the outer edge of the jet is curved due to the recirculatory flow caused by entrainment of stagnant region air by friction with the jet. D_j is the diameter of the duct at the jet formation location, U_j is the particle velocity at that location, L_h is the "step height," L_r is the recirculation length, and δ_i is the spacing between shear layer coherent structures. Note that $\delta_i = U_c / f_{us}$, where U_c is the convection speed of the vortical structure and f_{us} is the jet instability frequency. The relationship between L_s and L_r depends upon the Reynolds number $U_j D_j / \nu$.

sons: diffusion (both "laminar" and "turbulent") of the shear layer, and the setup of a recirculation in the stagnant region. This structure is shown in Fig. 6.

The first mechanism of jet spreading is the transverse spatial growth of the shear layer width with distance from the jet formation point. This spreading is governed by the rate of transverse diffusion of momentum. In other words, through diffusion the jet gives up its momentum to the stagnant region, so that the total momentum of the jet decreases (which is why flow separation acts as a dissipator of flow energy). Thus the jet is said to entrain the surrounding stagnant fluid. The rate of diffusion (or entrainment) depends on the local shear layer thickness—it is highest where the shear layer is thinnest, i.e., at the point of jet formation. In addition, the entrainment rate depends critically on whether the shear layer is laminar, turbulent, or something in between. For a laminar shear layer, the width δ_s grows as $\delta_s \sim x^{1/2}$. A turbulent shear layer tends to grow as $\delta_s \sim x$. Thus a turbulent shear layer diffuses much faster than a laminar one, due to mixing by the unsteady interaction of *coherent structures*, or regions over which vorticity is highly correlated (Hussain, 1986). A transitional shear layer is initially laminar, but becomes turbulent somewhere downstream of the formation point. The spreading rate is thus spatially dependent, i.e., the laminar and turbulent regions each have different rates of diffusion.

The second mechanism of jet spreading is a direct result of the entrainment of stagnant air mass in the confined stagnant region into the jet, an effect which is strongest near the jet origin. Note that the mechanism for entrainment is the one just described, in which fluid particles originally not in the jet have jet momentum transferred to them by diffusion. The entrained air moves with the jet along the jet boundary, producing a weak countercirculation near the walls to replace the stagnant air mass lost to entrainment. In this way a weak recirculatory flow is set up in the "stagnant" region. Further downstream, near the end of the recirculation zone, the countercirculation tends to spread the jet at an even faster rate than that arising from diffusion alone. Note that the spreading of the jet due to recirculation is not independent of the spreading by diffusion. Instead, jet spreading due to recirculation affects the rate of entrainment which drives the recirculation. This recursive relationship between recirculation and diffusion is typical of the nonlinear problems which arise in fluid dynamics.

If for any reason the recirculation is stronger on one side of the jet, then the jet to will tend to be pulled more strongly in that direction, so that the jet does not flow down the middle of the flow passage, but instead will cling to the wall on the side with stronger recirculation. This effect is typically observed in asymmetrical flow passages, such as those seen in the vocal tract. This phenomenon, the Coanda effect, is widely observed in nature and technology and has been proposed as an essential element in glottal flow behavior (Teager, 1980 and 1981; Teager and Teager, 1983 and 1990; Kaiser, 1983; Liljencrants, 1989), although recent experiments (Hofmans, 2003) seem to discount this notion, because the time for this flow pattern to manifest itself is much longer than a glottal pitch period. In unvoiced speech sound production, however, the time scale of the flow (the time the sound is being produced, during which the jet exists) is at least as long as the formation time for a Coanda flow pattern, so it is likely to be important for this class of sounds, particularly for fricatives.

Both mechanisms of jet spreading result in a recirculating region whose length L_r depends on the Reynolds number $\mathrm{Re} = U_j D_j / \nu$ (U_j=jet velocity, D_j=diameter of vocal tract at jet formation location) and the change in radius L_H at the location at which the jet is formed, as shown in Fig. 6. For $\mathrm{Re} < 200$, L_r / L_H increases uniformly with Re. In the range $200 < \mathrm{Re} < 2000$, L_r / L_H is sensitive to the jet velocity profile shape and the level of flow disturbances. Above $\mathrm{Re} = 2000$, $6 < L_r / L_H < 12$ (Blevins, 1984). These results for steady jet flows provide an estimate of the axial vocal-tract length a jet will persist. The spreading rate thus determines the recirculation zone length, the axial extent of the jet flow. This distance is the spatial extent over which vorticity has been injected into the flow and is able to participate in sound generation. If a change in duct area occurs downstream of the recirculation zone, then the jet vorticity will have largely reattached to the wall and will thus contribute little to sound production, as explained above.

B. Shear layer behavior

Because the acoustically relevant parts of the flow involve the vorticity concentrated in the separated shear layers, it is necessary to look more closely at free-shear layer dynamics. In general, the shear layer undergoes unsteady motion involving the coalescence of vorticity into concentrated coherent structures. While this motion is in some sense random in appearance, it has a definite temporal and spatial structure which may be described by scaling laws. This spatiotemporal structure varies with flow speed and duct area in a systematic way, allowing the scales of motion to be parametrized.

1. Shear layer formation—flow separation

Jet shear layers are simply the boundary layers which have been lifted off the wall. This process of *flow separation* is determined by the upstream development of the boundary layer and the shape of the wall (White, 1998; Panton, 1994; Batchelor, 1968; Bejan, 1984).

The pressure gradient force (a strong function of duct shape) and the velocity distribution of the boundary layer both determine whether the boundary layer will separate. Upstream of the constriction where a jet is formed, the vocal tract has a convergent shape, so that the flow accelerates as the minimum constriction area is approached. From the Bernoulli equation, it is clear that the static pressure decreases as the constriction is approached. The resulting pressure gradient force acts in the flow direction, augmenting the momentum in the boundary layer. Downstream of the minimum constriction area location, however, the flow begins to decelerate as the area widens, resulting in an increase in pressure with distance from the constriction, so that now the pressure gradient force progressively degrades the boundary layer momentum uniformly across the height of the boundary layer.

Although the deceleration associated with the adverse pressure gradient acts uniformly across the boundary layer, fluid particles in the outer stream have more kinetic energy to lose than those near the wall. In fact, the fluid particles near the wall are prevented from reversing course by being pulled along by the outer stream via the viscous drag in the boundary layer. If, however, the time scale of deceleration of the main flow, $-(\rho U_\infty)/(\partial p/\partial x)$, is faster than the time for the deceleration to diffuse through the boundary layer, δ_s^2/ν (for a laminar boundary layer), then the fluid particles near the wall will reverse course, separating the boundary layer from the wall. In a steady flow, this process takes place over a finite length, so that separation occurs downstream of the location of minimum constriction. Because the process depends on the rate that momentum diffuses through the boundary layer, a turbulent boundary layer will take a longer length to separate, as the changes in the outer stream will be communicated to the flow near the wall much faster than in a laminar boundary layer. In practice, predicting the location of boundary layer separation and the manner in which the separated shear layer moves away from the wall is a difficult problem which must be solved numerically, even for highly idealized geometries.

2. Shear layer dynamics—coherent structures

How the shear layer behaves once it separates from the wall is a complex interrelationship between diffusion and the dynamics of the vorticity, which is often described in terms of the stability of the steady flow solution to perturbations in the flow (see, e.g., Drazin and Reid, 1982). Because the shear layer is highly unstable, shear layer vorticity quickly coalesces into concentrated, coherent regions of vorticity (Cantwell, 1981; Hussain, 1986). This process occurs over a range of frequencies centering on the *most unstable frequency* of the shear layer. In a shear layer, velocity fluctuations at a fixed point are typically caused by the passage of vortical coherent structures which convect at U_c, a fraction of the jet speed U_j, and have a length scale δ_i commensurate with the shear layer thickness δ_s. In this instance, then, the frequency of a velocity fluctuation measured at a fixed point is proportional to $U_c/\delta_i \sim U_c/\delta_s$. Fluctuations with the highest amplitude will occur at the most unstable frequency of the shear layer.

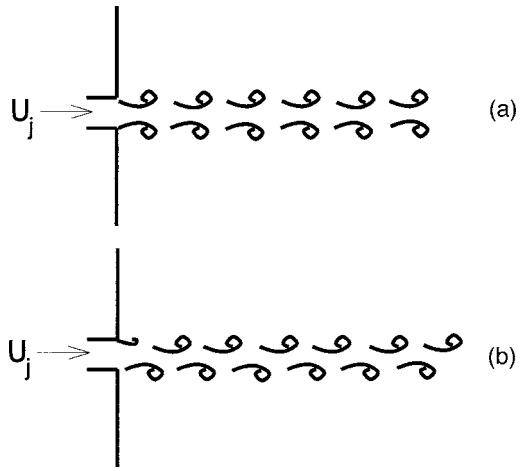

FIG. 7. Jet instability modes. (a) Varicose (symmetric) mode, in which shear layer vorticity coalesces into vortex ring-like structures. (b) Sinuous (antisymmetric) mode, in which the shear layer vorticity coalesces into inclined vortex pair-like structures.

Several instability modes are possible, and spatial structure of the jet is determined by the dominant mode exhibited. One of two modes in particular will be predominant. These are the symmetric (''varicose'') and antisymmetric (''sinuous'') modes, shown in Fig. 7. The symmetric mode occurs when the cross-sectional shape of the vocal tract at the constriction where the jet is formed is near circular. Examples of this geometry occur for production of /s/ or /ʃ/, and for whistling by blowing through rounded lips. The antisymmetric mode occurs when the constriction cross section is much wider than it is high, especially when shear layer thickness is close to the constriction radius (i.e., when the unseparated flow is fully developed) (see Bejan, 1984). A prime example of this geometric configuration occurring in speech is the glottal jet, which is also used in producing /h/. This case is probably the most extreme, since the jet used in /h/ is formed at the vocal folds; most constrictions at which jets are formed to produce unvoiced speech sound have an essentially elliptical shape.

The ''coherent structures'' may be approximated as discrete vortex rings whose motion may be predicted from the vorticity distribution in the flow and the wall geometry (see Saffman, 1992). Typically, these structures convect at a fraction of the jet speed. If we consider an axisymmetric jet, the rings will be circular in shape. Otherwise, the rings will be roughly elliptical.

The vortex rings in a jet will interact with one another. For example, a ring may pass through the ring just downstream, and the two rings may pass through each other several times before merging. On the other hand, the rings themselves may instead develop azimuthally wavy structures that increase in amplitude through self-induction. These struc-

tures may then develop disturbances on yet smaller scales, until the smaller structures diffuse their kinetic energy to heat under the action of viscosity. Through this process of *turbulent diffusion*, what begins as a more or less coherent vortex ring becomes quite diffuse and disorganized. The degree to which turbulent diffusion dominates the dynamics of the jet depends on the Reynolds number of the flow, $U_j D/\nu$, where U_j is the jet speed, D the diameter of the flow passage at the jet formation point, and ν the kinematic viscosity. The Reynolds number is a measure of the relative magnitudes of flow inertia to molecular dissipative (i.e., friction) forces. The higher the Reynolds number, the more inertia will dominate the dynamics, and the larger a range of spatial and temporal scales will develop (i.e., the spectrum of a flow quantity will be more broadband). Also, the higher the Reynolds number, the shorter the coherent structure lifetime, since turbulent diffusion will cause the coherent structures to lose their coherence more rapidly. At lower Reynolds number, however, the coherent structures may not even undergo the formation of smaller wavy structures, and will thus decay slowly through the action of viscosity. Thus, the coherent structures, while they will eventually lose their identity, may persist for a long time indeed, so that their effect on the flow is always felt.

When the jet is not axisymmetric, the tendency of the ring to deform rapidly from its initial coherent state is enhanced greatly (see, e.g., Saffman, 1992). In this case, the breakdown of coherent structures does not occur initially through small disturbances on the ring, but instead by the rapid deformation of the large structure of the ring itself. This greatly enhances the rate of turbulent diffusion, and hence jet spreading. For more on turbulent diffusion, and turbulent motion in general, see the discussions in Lugt (1983).

3. Scales of motion relevant for sound production

No matter how the turbulent diffusion process takes place, the process is (1) three-dimensional; (2) highly dissipative; and (3) involves vorticity dynamics. To abstract these motions into a simple model for sound generation is a formidable task unless certain simplifications can be made. First, a rationale for these simplifications comes from the aeroacoustic source expression [Eq. (2)]. First, note that no matter how three-dimensional the vorticity field, only vorticity which is oriented normal to the streamlines of $\mathbf{U}^*$ will be involved in producing sound. In the axisymmetric vocal-tract approximation used in this paper, only the azimuthal component of the vorticity field is involved. Second, however the coherent structures evolve after forming, the initial coalescence of vorticity is preserved in some sense even while the structure is undergoing diffusion. Thus the initial spacing of coherent structures will determine the spacing of concentrations of vorticity throughout the jet. Furthermore, the coherent structures, while not truly axisymmetric, may be treated as such. *Thus a jet may be modeled, for purposes of developing an aeroacoustic source model, as a train of vortex rings (axisymmetric jet) or as a train of inclined vortex pairs (planar jet).*

At the Reynolds numbers and jet geometries seen in the production of unvoiced speech sounds, the jets are asymmetric and initially laminar. They will develop some coherence with length scale δ_i, which is proportional to the thickness of the jet (Bejan, 1984). Because vorticity is the curl of the velocity field, its magnitude is roughly the change in velocity through the shear layer divided by the shear layer thickness, U_j/δ_s. The circulation of a coherent structure is then roughly [see Eq. (4)] the vorticity times the area δ_s^2 over which the structure is concentrated, so that

$$\Gamma \sim \frac{U_j}{\delta_s}\delta_s^2 \sim U_j \delta_s . \tag{12}$$

Coherent structures convect at a fraction of the jet speed, depending on the geometry, so that $U_c \sim U_j$. The time spacing between arrival of vortices at a fixed location has order of magnitude δ_s/U_j. Thus, the frequency, f_{arr}, of vortex arrival at a fixed point in space is roughly the same as the instability frequency. For a jet in which the axisymmetric mode dominates, this may be given as

$$f_{us} \sim \frac{U_j}{D_j}, \tag{13}$$

since $\delta_s \sim \delta_i \sim D$ (Hussain, 1986), while for a jet in which the antisymmetric mode dominates, the result is given by

$$f_{us} \sim 0.03\frac{U_j}{D_j} \tag{14}$$

[Sato (1960), Bjørnø and Larson (1984), Verge (1994)]. This can also be written as a rule in terms of the Strouhal number $\text{St}=f_{us}D_j/U_j \sim O(1)$ or $O(10^{-2})$, respectively. From these results, it is clear that for a jet in which the symmetric mode dominates, the most unstable frequency will be higher than for a jet of similar size and speed, but for which the antisymmetric mode dominates.

IV. UNVOICED SPEECH SOUND SOURCE CHARACTERISTICS

The aerodynamic source of unvoiced speech sounds arises from the convection of fluid particles possessing vorticity through the nonuniform potential flow associated with a nonuniform vocal-tract shape. The sharper the shape change, the more noise is produced, and the higher the frequency at which the sound is radiated. This much information is available using the approximate analysis presented above. It is possible to say more at this point about the shape of the source spectrum, using the same level of approximation in the previous sections.

In order to study the generic properties of the source spectrum, let us use the idealized flow pattern used in Sec. II B 4. The jet flow occurs in a tube of uniform cross section (radius R_p), with the exception of an obstacle of axial extent H and minimum radius $R_{\min}$. The jet flow vortices convect in straight paths past the obstacle. The form of the source spectrum is simplified greatly if we further assume that the acoustic excitation may be concentrated in a point location. With this restriction, the expression for sound radiated in an infinite length tube becomes

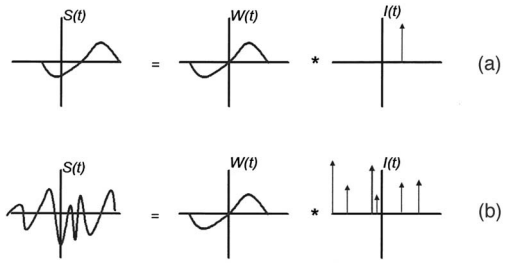

FIG. 8. Aeroacoustic source expressed as a convolution of $W(t)$ and $I(t)$. $W(t)$ is the spectrum of a unit-circulation vortex ring passing through the constriction at speed U_j, reflecting the shape of the duct and the path of the vortex. $I(t)$ is a circulation-weighted function indicating the arrival in the source region of a vortex ring. (a) Single vortex ring. (b) Many vortex rings. The broadband behavior of $S(t)$ arises due to the random phase of the time of arrival of each successive vortex ring into the source region.

$$p'(x,t) = \frac{-\rho_\infty \operatorname{sgn}(x-y)}{2A(1+M)} \int_{-\infty}^{+\infty} \int_A [(\boldsymbol{\omega}\times\mathbf{v})\cdot\mathbf{U}^*(y)]dA\,dy$$

$$= \frac{\operatorname{sgn}(x-y)}{A} S\left(y, t - \frac{|x-y|}{c(1-M)}\right), \tag{15}$$

where S is the source strength located at $x=y$, the source location. The square brackets denote that the integrand is evaluated at the retarded time $t-y/(c(1-M))$. For a single vortex pair or ring passing through the source region, S has the form shown in Fig. 4(b), as described in Sec. II B 4. In the finite-length vocal tube case, the lip sound pressure will be the convolution of $S(t)$ with the transfer function of the tube between the source location and the lips.

A. Relation between source expression for a jet to that for a single vortex

To describe the source function for the convection of a *train* of vortices of arbitrary arrival to the source region, the source function may be written as the convolution of the waveform $W(t)$ for a single vortex, scaled by the source amplitude corresponding to each vortex, with an arrival function $I(t)$, which is a series of delta functions whose phase is adjusted to the arrival time of the vortex

$$S(y,t) = W(t) * I(t) = \int_{-\infty}^{\infty} W(\tau) I(t-\tau) d\tau. \tag{16}$$

This behavior is shown in Fig. 8(a) for a single vortex ring and in Fig. 8(b) for a train of vortex rings which arrive at different times. In Eq. (15), $W(t)$ is a normalized version of $S(t)$ shown in Fig. 4(b), since it represents the contribution of a single vortex ring of unit circulation passing through the constriction at speed $U_c \sim U_j/2$. As explained above, the characteristic time scale of this waveform is either H/U_c or δ_v/U_c, the time during which a given jet vortex induces a force on the obstacle. This waveform also contains the information regarding both the shape of the obstacle and the vortex ring path, as explained in Sec. II. Thus, $W(t)$ depends on both the vortex path and the shape of the vocal tract

$$W(t) = \rho_\infty R_v \frac{\pi A}{A(x)} \frac{U_j}{2} \sin\alpha(t).$$

$I(t)$ for a train of N vortex rings is given by

$$I(t) = \rho_\infty \sum_{n=0}^{N} \delta(t - nT_{\text{arr}} + \theta_n) \frac{(U_j)_n^2}{2} (T_{\text{arr}} + \Phi_n). \tag{17}$$

Here, $\delta(t)$ is the Dirac delta function, T_{arr} the mean period of vortex ring arrival in the source region, and Φ the vortex arrival phase jitter. Note that $T_{\text{arr}} = 1/f_{\text{arr}} \approx 1/f_{us}$, or the reciporcal of the jet instability frequency. Note also that the circulation of the nth vortex $\Gamma_n = (U_j)_n^2 \Delta t_n/2$ is included in this function because it is proportional to the time $\Delta t_n = (T_{\text{arr}} + \Phi_n)$ since the last vortex arrived in the source region, and because the jet velocity may have changed since the vortex was injected into the flow at the jet formation point (which happens in voiced fricatives and plosives, as well as aspirative sounds in voicing). The vortex arrival phase jitter, Φ, may be considered as a random process of zero mean and a variance σ_Φ which depends on the jet Reynolds number and distance from the jet formation point. The larger σ_Φ becomes, the shorter the coherence time scale of the $I(t)$ time series. Note that for the low-frequency sound production discussed in this paper, this model applies equally to the antisymmetric and axisymmetric jet modes discussed in Sec. III. Any differences in the distribution of vorticity between the two instability modes are manifested in the form of $W(t)$.

B. Form of source spectrum for unvoiced speech sounds

Having expressed the aeroacoustic source time series as the convolution of a time series describing the passage of a single vortex ring and the statistics of arrival of a train of vortex rings, the aeroacoustic source spectrum due to a jet modeled as in Sec. III may now be studied. The spectral shape of W has been shown in Fig. 4(c). $W(f)$ has a single peak centered at roughly U_c/ℓ, with a bandwidth of roughly that amount, as discussed in Sec. II B 3, where ℓ is either the constriction length H or the vortex core radius δ_i, as appropriate. (Note that here, the radius δ_v of the vortex ring used to model the coherent structure of the jet has core size which is proportional to the coherent structure spacing $\delta_i \sim \delta_s$.) In other words, the faster the vortex passes through the source region (either because of either high convection speed or narrow obstacle), the broader the peak.

The spectral behavior of I is shown in Fig. 9. The spectral shape of $I(f)$ depends critically on the statistics of σ_Φ, demonstrated by the following limiting cases. Figure 9(a) shows the case for $\sigma_\Phi = 0$, where $I(t)$ is periodic, and its spectrum is a series of sharp peaks occurring at harmonics of the vortex arrival frequency $f_{\text{arr}} = 1/T_{\text{arr}} = f_{us}$. As σ_Φ increases, these peaks become broader, and the amplitude of the harmonics decays with frequency, until the spectrum becomes broadband with a peak at the mean vortex passage frequency, as shown in Fig. 9(b).

Because the source function $S(t)$ is the convolution of W and I, the spectrum of S is the product in frequency space of $W(f)$ and $I(f)$

$$S(f) = W(f) I(f); \tag{18}$$

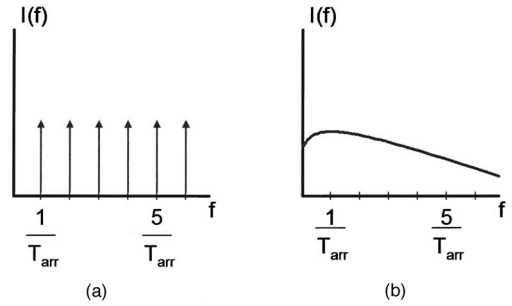

FIG. 9. Frequency-behavior the arrival indicator function I, showing dependence on the variance of the random process describing the arrival phase Φ. (a) $I(f)$ for $\sigma_\Phi \ll 1$ (highly periodic flow), as found in whistling, where the sound field becomes phase-locked to vortex shedding at the separation point, resulting in a spectrum composed of a fundamental (the jet instability frequency, $1/T_{arr}$) and its harmonics. (b) $I(f)$ for $\sigma_\Phi \gg 1$ (highly turbulent flow), as usual in unvoiced speech sounds, where the peak occurs at the jet instability frequency, but which exhibits no tonal quality.

the vortex arrival spectrum could be said to filter the contribution due to a single vortex ring. The character of $S(f)$ depends on which of $W(f)$ and $I(f)$ has narrower peaks, as shown in Fig. 10. If $I(f)$ is more or less periodic, then $I(f)$ will consist of narrow harmonic peaks and will dominate the spectral content of $S(f)$. This behavior is illustrated in Fig. 10(a). On the other hand, if $I(f)$ is broadband, and is wider than $W(f)$, then $W(f)$ dominates the spectral content of $S(f)$. This behavior corresponds to the situation shown in Fig. 10(b). In practice, unvoiced speech sounds such as fricatives and plosives correspond more closely to the latter case. The former case is more akin to the occurrence of a strong flow–acoustic interaction such as whistling, where vortex shedding and the resonant sound field become phase locked (see Blake, 1986; Hirschberg *et al.*, 1989), producing

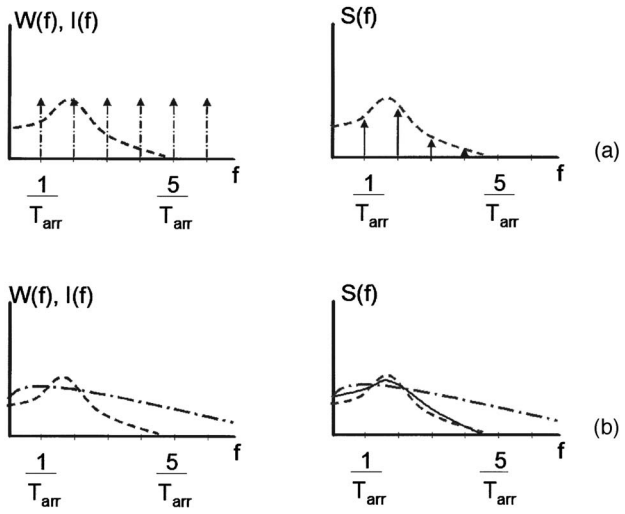

FIG. 10. Aeroacustic source spectrum $S(f)$ as a function of σ_Φ. Because $S(f)$ is the spectrum of a single vortex filtered by the arrival function spectrum $I(f)$, the statistics of the vortex ring arrival determine the character of the source spectrum. $S(f)$ ———; $I(f)$ –·–·–, $W(f)$ ---. (a) For $\sigma_\Phi \ll 1$, the jet is periodic, and $I(f)$ exhibits tonal behavior, with tone levels modulated by shape of ($W(f)$, reflecting both vortex path and wall shape. (b) For $\sigma_\Phi \gg 1$, $I(f)$ is broad enough (flow is highly turbulent) that the shape of $W(f)$ limits the shape of the source spectrum. In this case, the wall shape and vortex path dominate behavior of $S(f)$.

a highly periodic jet vortex structure. Other speech sounds which are likely to display this type of behavior are aspiration noise in voicing and voiced fricatives, although in these cases the sounds still maintain a broadband character because of two effects: first, the time scale of modulation of the jet velocity is much longer than the vortex shedding period; second, the amplitude of the jet modulation is small compared to the jet speed. The first effect applies to both voiced fricatives and aspirative noise because the modulation of the jet by the resonant sound field occurs at frequencies on the order of the voice frequency (~100 Hz), while the jet instability is on the order of 1–10 kHz. In aspirative noise, however, the modulation of the glottal jet is complete (the jet shuts off either completely or close to completely once every pitch period), so the second effect applies only to voiced fricatives.

V. SUMMARY

This paper presents an outline of the theoretical groundwork necessary for understanding and predicting the characteristics of aerodynamically generated speech sounds, using as much as possible the fundamental principles of air motion embodied in the fields of aerodynamics and aeroacoustics. The presentation focused initially on a generic picture of speech sound production, emphasizing that all speech sounds involve the unsteady flow through a constriction in the vocal tract, where a jet is produced. This jet interacts with the vocal-tract geometry downstream of its formation, inducing forces on the vocal-tract walls. These forces then produce sound. An expression for the sound field in terms of jet vorticity and the vocal-tract shape was then presented. The sound field was seen to be determined uniquely by the interaction of jet vorticity and the shape of the vocal tract, as reflected in both vorticity trajectories and the steady flow streamline shape. Thus, the aeroacoustic source characteristics depend on the shape of the duct, and are particularly powerful near ''sharp'' or discontinuous changes in areas such as those seen at the teeth. A definite ''obstacle'' is not necessary for sound generation, only the flow of jet vorticity through a change in vocal-tract area.

Jet motion relevant for sound production was shown to be characterized by the jet velocity and diameter, and by the temporal spacing of concentrations of vorticity (vortices). Using scales of motion characteristic of internal jet flows, a scaling law for aerodynamically generated speech sounds was derived by convolving the vortical source term of the wave equation with the Green's function for plane-wave propagation in a duct.

An expression for the aeroacoustic source spectrum was developed as the convolution two waveforms. The first is a ''shape'' function, the sound source waveform due to the passage of a single, unit circulation vortex ring through the source region, which depends on the wall shape and vortex path. The second is an ''arrival'' function, a series of pulses, each of which indicates the phase of arrival of each vortex in the source region. Each pulse in this function is scaled by the aeroacoustic source strength of each vortex. The vortex arrival statistics determines whether the source spectrum is dominated by the vorticity field arrival statistics or the wall

shape. If the vortex arrival time series is highly coherent and periodic, then it will dominate character of the source spectrum, which will consist of discrete peaks filtered by the shape function. On the other hand, if the vortex arrival time series is broadband, the wall shape will dominate the character of the source spectrum.

The results presented here represent a formal development of aeroacoustic source spectral characteristics for unvoiced speech sounds at low frequencies. For an application of these ideas to pipe flow noise prediction and to speech synthesis, see Krane *et al.* (2005), and Sinder (1999).

ACKNOWLEDGMENTS

The author would like to thank the following for their contributions to this work: Dan Sinder for many fruitful discussions and his careful evaluation of this presentation; Mico Hirschberg for a particularly enlightening talk and helpful comments on this manuscript; Rich McGowan and the reviewers for their careful consideration of this work and their helpful comments on how to improve the presentation. The author also greatefully acknowledges partial support from the National Science Foundation Grant NSF-9800999 and the national Institutes of Health (NIDCD) Grant 1R01DC054642-01.

APPENDIX: GREEN'S FUNCTION SOLUTION TO CONVECTED WAVE EQUATION

The convected wave equation [Eq. (1)] may be solved using a Green's function, which is defined by the following equation:

$$\frac{1}{c^2}\frac{D^2G}{Dt^2}-\frac{\partial^2 G}{\partial x^2}=\delta(\mathbf{x}-\mathbf{y})\,\delta(t-\tau), \tag{A1}$$

and the appropriate boundary conditions. Here, $G(x,t|y,\tau)$ is the Green's function, $\mathbf{x}$ is the location of the observer, t is the time when the observer feels the effect of the source, $\mathbf{y}$ is the location of the impulsive source, and τ is the time during which it is active. From this equation, it is clear that the Green's function is the response of the wave equation to a spatially localized impulsive source, i.e., it is a spatially dependent impulse response function. In general, the solution to the boundary value problem has the form (Haberman, 1997)

$$\begin{aligned}B'(x,t)=&\int_{-\infty}^{t}\int_{A}\int_{0}^{L}G(x,t|y,\tau)\nabla\cdot(\boldsymbol{\omega}\times\mathbf{v})\,d\tau\,dA\,dy\\&+\int_{A}\int_{0}^{L}\Big[\frac{\partial B'}{\partial\tau}(y,\tau=0)G(x,t|y,\tau=0)\\&-B'(y,\tau=0)\frac{\partial G'}{\partial\tau}(x,t|y,\tau=0)\Big]dA\,dy\\&-c^2\int_{-\infty}^{t}\Big[B'(y=0,\tau)\frac{\partial G'}{\partial y}(x,t|y=0,\tau)\\&-\frac{\partial B'}{\partial y}(y=0,\tau)G(x,t|y=0,\tau)\Big]d\tau.\end{aligned} \tag{A2}$$

Note that the first integral gives the contribution due to the aeroacoustic source, and must be taken not only over the vorticity in the flow, but vorticity in the vocal tract wall boundary layers. The second and third integrals contain terms which are determined by the initial and boundary conditions for both G and the acoustic variable B'. It should be noted that the Green's function is not unique in that there is considerable freedom in choosing what boundary conditions G satisfies. In particular it is sometimes possible to define a *tailored* Green's function which simplifies greatly the form of Eq. (6). For more on solving boundary value problems using Greens's functions, see Crighton *et al.* (1992), or Morse and Feschbach (1953).

All but the first term in Eq. (6) give the effect of boundary conditions for the finite-length vocal tract. For simplicity, let us first consider an infinite length tube. This tube is identical to that shown in Fig. 1, except that there are no lungs and no mouth opening. The solution for the finite-length vocal tract will then be constructed from the infinite tube solution using the method of images. A tailored Green's function for the problem has been derived by Howe (1975), given by

$$G(x,t|y,\tau)=\frac{c}{2A}H\left(t-\tau-\frac{x}{c(1+M)}+\frac{\phi^*(y)}{c(1+M)}\right), \tag{A3}$$

where H is the Heaviside function

$$H(f)=\begin{cases}1, & f>1\\ 0, & f<1,\end{cases}$$

ϕ^* is the velocity potential of a unit steady irrotational flow velocity field $\mathbf{U}/U_1=\nabla\phi^*=\mathbf{U}^*$, and A is the cross-sectional area of the pipe everywhere except in the region of the obstacle. This Green's function describes low-frequency acoustic wave propagation in a nonuniform duct with a steady flow. Note that it differs from the free-space Green's function for planar waves only in the correction factor $\phi^*/(c(1+M))$, which is a correction to account for both the diffraction through the potential flow disturbance due to the change in duct shape and the motion of vortical sources through this disturbance (Howe, 1975). Again, the convenience of using this tailored Green's function is that the first term need only consider the vorticity that has been injected into the flow, away from the walls. In other words, the acoustic effect of incompressible wall pressure fluctuations (which sum to a net unsteady force on the vocal-tract walls) due to vorticity convection are lumped into the first integral containing only terms relating to the vorticity dynamics in the flow itself. Note that this Green's function only accounts for the dipole source caused by aerodynamically generated forces on the walls, not for the direct radiation from the jet vorticity itself. The direct radiation is less efficient, by a factor of Mach number squared (Howe, 1975), so it is not considered here.

The solution for B' is then found by convolving the Green's function with the source term $\nabla\cdot(\boldsymbol{\omega}\times\mathbf{v})$

$$B'(x,t) = -\frac{\mathrm{sgn}(x-y)}{2A(1+M)}\int_A [\boldsymbol{\omega}\times\mathbf{v}\cdot\mathbf{U}^*]dA\,dy, \qquad \text{(A4)}$$

where $\mathrm{sgn}(x-y)$ is the signum function

$$\mathrm{sgn}(x-y) = \begin{cases} 1 & \text{for } x-y>0 \\ -1 & \text{for } x-y<0 \end{cases},$$

so that the acoustic total enthalpy (and thus the pressure) changes sign across the source. In arriving at this form of the integral, use has been made of the property of convolution integrals

$$f^*\mathcal{L}\{g\} = \mathcal{L}\{f\}^*g,$$

and because $\nabla H(f) = \delta(f)\nabla f$, $g(f')^*\delta(f-f') = g(f)$, where $\mathcal{L}$ is any linear operator (such as ∇, in this case), and * denotes a convolution relationship $[f^*g = \int f(t)g(t-\tau)d\tau]$, and $\delta(f)$ is the Dirac delta function.

Using the definition of total enthalpy, the solution may be rewritten in terms of sound pressure

$$p'(x,t) \approx \rho_\infty B'(x,t) = -\rho_\infty\frac{\mathrm{sgn}(x-y)}{2A(1+M)}\int_A\int [\boldsymbol{\omega}\times\mathbf{v}\cdot\mathbf{U}^*]dA\,dy. \qquad \text{(A5)}$$

Alipour, F., Fan, C., and Scherer, R. C. (**1996**). "A numerical simulation of laryngeal flow in a forced-oscillation glottal model," Comput. Speech Lang. **10**, 75–93.

Barney, A., Davies, P. O. A. L., and Shadle, C. H. (**1999**). "Fluid flow in a dynamic mechanical model of the vocal folds and tract. I. measurements and theory," J. Acoust. Soc. Am. **105**(1), 444–455.

Batchelor, G. K. (**1968**). *An Introduction to Fluid Dynamics* (Cambridge University Press, Cambridge, 1968).

Bechert, D. W. (**1980**). "Sound absorption caused by vorticity shedding, demonstrated with a jet flow," J. Sound Vib. **70**, 389–405.

Bejan, A. (**1984**). *Convection Heat Transfer* (Wiley, New York).

Bjørnø, L., and Larsen, P. (**1984**). "Noise of air jets from rectangular slits," Acustica **54**, 247–256.

Blake, W. K. (**1986**). *Mechanics of Flow-Induced Sound and Vibration*. Vol. 1: General Concepts and Elementary Sources (Academic, New York).

Blevins, R. D. (**1984**). *Applied Fluid Dynamics Handbook* (Van Nostrand Reinhold, New York).

Cantwell, B. J. (**1981**). "Organized motion in turbulent flow," Annu. Rev. Fluid Mech. **13**, 457–515.

Crighton, D. G., Dowling, A. P., Ffowcs-Williams, J. E., Heckl, M., and Leppington, F. G. (**1992**). *Modern Methods in Analytical Acoustics* (Springer, London, 1992).

Curle, N. (**1995**). "The influence of solid boundaries upon aerodynamic sound," Proc. R. Soc. London, Ser. A **231**(1887), 505–514.

Davies, P. O. A. L. (**1980**).

Davies, P. O. A. L. (**1996**). "Aeroacoustics of time varying systems," J. Sound Vib. **190**(3), 345–362.

Davies, P. O. A. L., McGowan, R., and Shadle, C. (**1993**). "Practical flow duct acoustics applied to the vocal tract," in *Vocal Fold Physiology: Frontiers in Basic Science* (Singular, San Diego, 1993), pp. 93–134.

Dowling, A. P., and Ffowcs-Williams, J. E. (**1983**). *Sound and Sources of Sound*. Ellis Horwood Series in Engineering Science (Halsted, New York).

Drazin, P. G., and Reid, W. H. (**1982**). *Hydrodynamic Stability* (Cambridge University Press, Cambridge, 1982).

Fant, G. (**1960**). *Acoustic Theory of Speech Production* (Mouton, the Hague).

Ffowcs-Williams, J., and Hawkings, D. (**1969**). "Sound generated by turbulence and surfaces in arbitrary motion," Philos. Trans. R. Soc. London, Ser. A **264**(1151), 321–342.

Flanagan, J. L., and Cherry, L. (**1969**). "Excitation of vocal-tract synthesizers," J. Acoust. Soc. Am. **45**(3), 764–769.

Flanagan, J. L., and Ishizaka, K. (**1976**). "Automatic generation of voiceless excitation in a vocal cord-vocal tract speech synthesizer," IEEE Trans. Acoust., Speech, Signal Process. **24**(2), 163–170.

Goldstein, M. E. (**1976**). *Aeroacoustics* (McGraw-Hill, New York).

Haberman, R. (**1997**). *Applied Partial Differential Equations With Fourier Series and Boundary Value Problems* (Prentice-Hall, New York).

Hardin, J. C., and Pope, D. S. (**1992**). "Sound generation by a stenosis in a pipe," AIAA J. **30**(2), 312–317.

Hirschberg, A. (**1992**). "Some fluid dynamic aspects of speech," Bull. Commun. Parlee **2**, 7–30.

Hirschberg, A., Bruggeman, J. C., Wijnands, A. P. J., and Smits, N. (**1989**). "The whistler nozzle and horn as aeroacoustic sources in pipe systems," Acustica **68**, 157–160.

Hofmans, G., Groot, G., Rancci, M., Graziani, G., and Hirschberg, A. (**2003**). "Unsteady flow through in-vitro models of the glottis," J. Acoust. Soc. Am. **113**(3), 1658–1675.

Howe, M. S. (**1975**). "Contributions to the theory of aerodynamic sound, with application to excess jet noise and the theory of the flute," J. Fluid Mech. **71**(4), 625–673.

Howe, M. S. (**1980**). "The dissipation of sound at an edge," J. Sound Vib. **70**, 625–673.

Howe, M. S. (**1998**). *Acoustics of Fluid–Structure Interactions*. Cambridge Monographs on Mechanics (Cambridge University Press, New York, 1998).

Hulshoff, S., Hirschberg, A., and Hofmans, C. (**2001**). "Sound production of vortex–nozzle interactions," J. Fluid Mech. **439**, 335–352.

Hussain, A. K. M. F. (**1986**). "Coherent structures and turbulence," J. Fluid Mech. **173**, 303–356.

Ishizaka, K., and Flanagan, J. L. (**1972**). "Synthesis of voiced sounds from a two-mass model of the vocal cords," Bell Syst. Tech. J. **51**(6), 1233–1268.

Kaiser, J. F. (**1983**). "Some observations on vocal tract operation from a fluid flow point of view," in *Vocal Fold Physiology: Biomechanics, Acoustics, and Phonatory Control*, edited by I. R. Titze and R. C. Scherer (The Denver Center for the Performing Arts, Denver, CO), pp. 358–386.

Krane, M. H., Sinder, D. J., and Flanagan, J. L. (**2005**). "A reduced complexity prediction method for pipe flow noise," J. Sound Vib. (in press).

Lighthill, M. J. (**1952**). "On sound generated aerodynamically. I. General theory," Proc. R. Soc. London, Ser. A **211**, 564–587.

Lighthill, M. J. (**1978**). *Waves in Fluids* (Cambridge University Press, New York).

Liljencrants, J. (**1989**). "Numerical simulation of glottal flow," in *Vocal Fold Physiology: Acoustics, Perception and Physiological Aspects of Voice Mechanisms*, edited by J. Gauffin and B. Hammarberg (Singular, San Diego), pp. 99–104.

Lous, N. J. C., Hofmans, G. C. J., Veldhuis, R. N. J., and Hirschberg, A. (**1998**). "A symmetrical two-mass vocal-fold model coupled to a vocal tract and trachea, with application to prosthesis design," Acta Acust. (Beijing) **84**(4), 1135–1150.

Lugt, H. J. (**1983**). *Vortex Flow in Nature and Technology* (Wiley, New York).

McGowan, R. S. (**1988**). "An aeroacoustic approach to phonation," J. Acoust. Soc. Am. **83**(2), 696–704.

Meyer-Eppler, W. (**1953**). "Zum erzeugungsmechanismus der Geräuschlate," Z. Phone, Sprachwissenschaft llgemeine Kommunicationsforschung **7**, 196–212.

Morse, P., and Feschbach, H. (**1953**). *Methods of Theoretical Physics* (McGraw-Hill, New York), Vols. I and II.

Panton, R. L. (**1994**). *Incompressible Flow* (Wiley, New York).

Pelorson, X., Hofmans, G. C. J., Ranucci, M., and Bosch, R. C. M. (**1997**). "On the fluid mechanics of bilabial plosives," Speech Commun. **22**, 55–172.

Pelorson, X., Hirschberg, A., van Hassel, R. R., Wijnands, A. P. J., and Auregan, Y. (**1994**). "Theoretical and experimental study of quasisteady-flow separation within the glottis during phonation—application to a modified two-mass model," J. Acoust. Soc. Am. **96**(6), 3416–3431.

Pierce, A. D. (**1989**). *Acoustics: An Introduction to Its Physical Principles and Applications* (McGraw-Hill, New York).

Powell, A. (**1964**). ''Theory of vortex sound,'' J. Acoust. Soc. Am. **36**(1), 177–195.
Saffman, P. G. (**1992**). *Vortex Dynamics* (Cambridge University Press, Cambridge).
Sato, H. (**1960**). ''The stability and transition of a two-dimensional jet,'' J. Fluid Mech. **7**, 53–80.
Shadle, C. H. (**1985**). ''The Acoustics of Fricative Consonants,'' Ph.D. thesis, Massachusetts Institute of Technology.
Shadle, C. H. (**1991**). ''The effect of geometry on source mechanisms of fricative consonants,'' J. Phonetics **19**, 409–424.
Sinder, D. J. (**1999**). ''Synthesis of unvoiced speech sounds using an aeroacoustic source model,'' Ph.D. thesis, Rutgers University.
Sondhi, M. M., and Schroeter, J. (**1987**). ''A hybrid time-frequency domain articulatory speech synthesizer,'' IEEE Trans. Acoust., Speech, Signal Process. **ASSP-35**(7), 955–967.
Stevens, K. N. (**1971**). ''Airflow and turbulence noise for fricative and stop consonants: Static considerations,'' J. Acoust. Soc. Am. **50**, 1180–1192.
Teager, H. M. (**1980**). ''Some observations on oral air flow during phonation,'' IEEE Trans. Acoust., Speech, Signal Process. **ASSP-28**(5), 599–601.
Teager, H. M. (**1981**). ''The effect of separated air flow on vocalization,'' in *Proceedings of the Conference on Vocal Fold Physiology* (College Hill Press, Madison, WI, San Diego, CA).
Teager, H. M., and Teager, S. (**1983**). ''Active fluid dynamic voice production models, or there is a unicorn in the garden,'' in *Vocal Fold Physiology: Biomechanics, Acoustics, and Phonatory Control*, edited by I. R. Titze and R. C. Scherer (Denver Center for the Performing Arts).
Teager, H. M., and Teager, S. M. (**1990**). ''Evidence for nonlinear production mechanisms in the vocal tract,'' in *Speech Production and Speech Modeling*, edited by W. J. Hardcastle and A. Marchal (Kluwer Academic, Dordrecht, The Netherlands).
Tennekes, H., and Lumley, J. (**1972**). *A First Course in Turbulence* (MIT Press, Cambridge).
Verge, M.-P. (**1994**). ''Aeroacoustics of confined jets,'' Ph.D. thesis, Technical University of Eindhoven.
White, F. M. (**1998**). *Fluid Mechanics* (McGraw-Hill, New York).
Zhang, Z., Mongeau, L., and Frankel, S. (**2002a**). ''Broadband sound generation by confined turbulent jets,'' J. Acoust. Soc. Am. **112**(2), 677–689.
Zhang, Z., Mongeau, L., and Frankel, S. (**2002b**). ''Experimental verfication of the quasisteady approximation for aerodynamic sound generation by pulsating jets in tubes,'' J. Acoust. Soc. Am. **112**(4), 1652–1663.

Three-dimensional electromagnetic articulography: A measurement principle

Tokihiko Kaburagi and Kohei Wakamiya
Department of Acoustic Design, Faculty of Design, Kyushu University, 4-9-1 Shiobaru, Minami-ku, Fukuoka, 815-8540 Japan, and CREST, Japan Science and Technology Corporation, 4-1-8 Honmachi, Kawaguchi, Saitama 332-0012 Japan

Masaaki Honda
Department of Sport Science, Waseda University, 2-579-15 Mitsugashima, Tokorozawa, Saitama, 359-1192 Japan, and CREST, Japan Science and Technology Corporation, 4-1-8 Honmachi, Kawaguchi, Saitama 332-0012 Japan

(Received 23 June 2004; revised 14 April 2005; accepted 14 April 2005)

A measurement principle of the three-dimensional electromagnetic articulographic device is presented. The state of the miniature receiver coil is described by five variables representing the position in the three-dimensional coordinate system and the rotation angles relative to it. When the receiver coil is placed in the magnetic field produced from the distributed transmitter coils, its state can be optimally estimated by minimizing the difference between the measured strength of the received signal and the predicted one using the known spatial pattern of the magnetic field. Therefore, the design and calibration of the field function inherently determine the accuracy in estimating the state of the receiver coil. The field function in our method is expressed in the form of a multivariate B spline as a function of position in the three-dimensional space. Because of the piecewise property of the basis function and the freedom in the selection of the rank and the number of basis functions, the spline field function has a superior ability to flexibly and accurately represent the actual magnetic field. Given a set of calibration data, the spline function is designed to form a smooth curved surface interpolating all of these data samples. Then, an iterative procedure is employed to solve the nonlinear estimation problem of the receiver state variables. Because the spline basis function is a polynomial, it is also shown that the calculation of the Jacobian or Hessian required to obtain updated quantities for the state variables can be efficiently performed. Finally, experimental results reveal that the measurement accuracy is about 0.2 mm for a preliminary condition, indicating that the method can achieve the degree of precision required for observing articulatory movements in a three-dimensional space. It is also experimentally shown that the Marquardt method is a better nonlinear programming technique than the Gauss–Newton or Newton–Raphson method for solving the receiver state problem. [DOI: 10.1121/1.1928707]

PACS number(s): 43.70.Aj, 43.70.Jt [AL] Pages: 428–443

I. INTRODUCTION

A. Observation of articulatory movements

Movements of the articulatory organs can be seen as internal variables that control the production of speech. The estimation of the articulatory states from speech presents various problems due to, for example, the one-to-many relationship between the acoustic and articulatory variables (Atal *et al.*, 1978; Sondhi, 1979; Maeda, 1990), the nonstationary characteristics of stop consonants, and the difficulty of obtaining sufficient morphological information about the vocal tract. Therefore, observation techniques applied to the articulatory organs are still quite important for exposing the articulatory states and understanding the underlying mechanisms engaged in the production of speech.

Such techniques may be roughly classified into imaging and position tracking techniques. Imaging techniques, such as the x-ray (Chiba and Kajiyama, 1941; Perkell, 1969; Harshman *et al.*, 1977) or MRI (Rokkaku *et al.*, 1986; Baer *et al.*, 1991), have the ability to visualize the entire vocal tract usually for sustained utterances. Real-time MRI (Narayanan *et al.*, 2004) or ultrasonic techniques (Morrish *et al.*, 1984; Shawker *et al.*, 1985; Stone *et al.*, 1988; Stone, 1990; Kaburagi and Honda, 1994a; Stone and Lundberg, 1996) have also been studied, but their framing rate is still restricted and an increase of the framing rate entails degradation of the image quality or reduction of the visible area.

On the other hand, position tracking techniques, such as the x-ray microbeam system (Fujimura *et al.*, 1973; Kiritani *et al.*, 1975), have a sufficiently high temporal resolution and are capable of observing dynamic articulatory behavior. Much less invasive methods have been investigated using alternating and static magnetic fields (Hixon, 1971; Sonoda, 1974), and further developments based on the principle of magnetic induction have been accomplished by Schönle *et al.* (1987, 1989) and Perkell *et al.* (1992), establishing two different methods of multiple point tracking. Besides studies of speech motor control, these magnetic devices were used to construct dynamic models of articulatory movements (Kaburagi and Honda, 2001), articulatory-based speech syn-

 0001-4966/2005/118(1)/428/16/$22.50

thesis (Kaburagi and Honda, 1998), and acoustic-to-articulatory inversion problems (Suzuki *et al.*, 1998).

B. Electromagnetic articulograph

A widely used device called the electromagnetic articulograph (EMA) was developed by Schönle *et al.* (1987). It measures the electromagnetically induced currents in the receiver coil and detects the position and orientation in the midsagittal measurement plane. To obtain the spatial information, they used a voltage-to-distance function (VDF) in which the received signal is approximated to be inversely proportional to the transmitter-receiver distance cubed. In addition, the signal is reduced by a factor of $\cos\theta$, where θ expresses the tilt angle. The position of the receiver coil is then determined as the crossing point of three circles, the center and radius of each given by the transmitter position and corresponding transmitter–receiver distance estimated using the VDF from the received signal.

By evaluating the magnetic field devices (Tuller *et al.*, 1990; Perkell *et al.*, 1992; Kaburagi and Honda, 1994b, 1997, 2002), it has been shown that the measurement error is still small even when the receiver coil is rotated relative to the magnetic flux if it is located in the midsagittal measurement plane. On the other hand, the error rapidly increases as the receiver coil deviates from the measurement plane in a lateral direction. For example, Kaburagi and Honda (2002) reported that, although the error is less than 0.1 mm when the coil is exactly on the measurement plane, it reaches about 3 mm when the rotation angles with respect to the x and y axes are both 20° and the lateral displacement is 6 mm.

To resolve this problem, the measurement principle and architectural design of a three-dimensional position tracking device have been extensively investigated by Andreas Zierdt. Beginning with his article that first showed the spatial alignment of six transmitter coils (Zierdt, 1993), and followed by Zierdt *et al.* (1999) and related articles (Zierdt *et al.*, 2000) Zierdt proposed a method for estimating the unknown state of a receiver coil, which has five degrees of freedom in a three-dimensional space. In principle, the lateral and rotational movements of the receiver coil have no influence on the accuracy of the position estimation. Therefore, the device is capable of monitoring movements even when a coil is attached to the tip of the tongue or soft palate, where the tissue is quite flexible and rotational movements easily take place. For these reasons, the three-dimensional EMA device has a much greater potential ability to provide observations of articulatory motions with a satisfactory accuracy and to give more reliable information than a two-dimensional device.

C. Magnetic field representation

The position and orientation of the receiver coil are determined in EMA devices by minimizing the difference between the measured and predicted receiver signals. A prediction of the receiver signal is possible if one knows the spatial pattern of the magnetic field. The measurement accuracy of the EMA device consequently depends on the methods used to represent the magnetic field, e.g., the VDF of the two-dimensional device, and calibrate unknown parameters included in the field function.

To accurately represent the magnetic field in a two-dimensional device, Perkell *et al.* (1992) expressed the exponent part of the VDF as a polynomial function of the transmitter–receiver distance. They also described a method for calibrating the VDF parameters in the local region in which the receiver coil would be located during the experiment. It has been recognized that the parameter calibration is of importance as well as the field representation problem (Gracco and Nye, 1993; Hoole, 1993). Kaburagi and Honda (1997) extended the idea of the local calibration to propose an adaptive calibration method. Then, more recently, they represented the magnetic field with a multivariate spline function (Kaburagi and Honda, 2002), which results in the same measurement accuracy as the adaptive method while the computational cost of position detection is reduced.

The effectiveness of these methods indicates that the global pattern of the actual magnetic field deviates from the theoretical one derived from the assumption that a transmitter coil functions as a dipole source, and hence that a VDF with fixed parameters only holds for a restricted region. A possible source of this pattern deviation is interference among the transmitting channels of the EMA device. For example, the transmitter coils could be mutually inductive. Then, for any given transmitter coil, currents would be induced by the neighboring transmitters so that the resulting reproduction of magnetic fields attenuates the surrounding fields at corresponding frequencies.

In this paper, a measurement principle for a three-dimensional EMA device is discussed based on the adoption of a novel nonparametric field function. In contrast to the ordinal dipole-source assumption (Zierdt *et al.*, 1999; Raab *et al.*, 1979), the spatial pattern of the magnetic field is represented by a multivariate B-spline function. The spline function generally has a superior ability to depict a smooth curved surface as a linear combination of piecewise basis functions, because each basis function is defined locally, and the rank and the number of basis functions can be freely selected. These flexibilities allow the spline function to accurately approximate the actual pattern of the field by interpolating given samples of the calibration data. In addition, the magnetic field is expressed directly as a function of position in the coordinate system. Therefore, the proposed method explicitly accommodates the field function to the actual magnetic field, even when the transmitting channels interfere and the field has location-dependent fluctuations.

The design of the hardware system used in the present study is attributed to Zierdt (1993) and Zierdt *et al.* (1999): the receiver coil has a single axis and six transmitter coils produce the magnetic fields. Given the spline field function, it is possible to predict the received signal as a function of the state variables and define an error criterion between the measured and predicted signals. The values of the state variables are then determined so that the error criterion is minimized. Here, the problem to be solved becomes nonlinear, since the magnetic field is represented by piecewise polynomial functions, so the solution is then found by an iterative

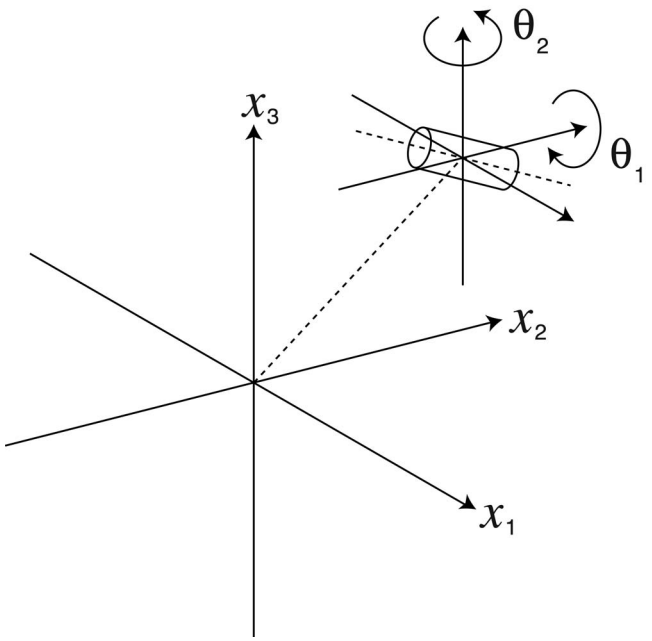

FIG. 1. An illustration of the variables specifying the state of the receiver coil. The position is represented in a three-dimensional Cartesian space by variables x_1, x_2, and x_3. The orientation is expressed as the relative angle between the axis of the receiver coil and the coordinate system and defined by a variable θ_1, the rotation angle with respect to the x_2 axis, and θ_2, that to the x_3 axis.

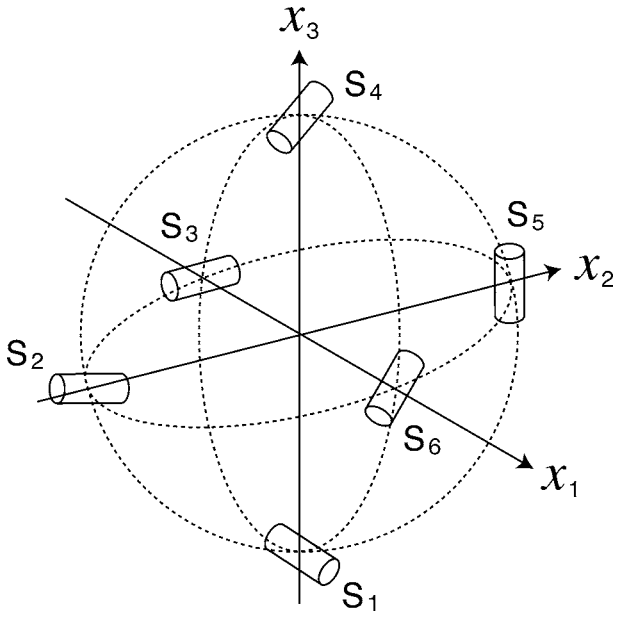

FIG. 2. Spatial alignment of six transmitter coils proposed by Zierdt (1993). In his method, they are positioned along the axes of the coordinate system. The axis of the transmitter coil is parallel with x_1, x_2, and x_3 for S_1, S_3, and S_5, respectively. For S_2, S_4, and S_6, on the other hand, the axis is, respectively, parallel with lines S_2S_6, S_4S_2, and S_6S_1. Following Zierdt, the number of the transmitting coils is assumed to be six in this study. It should be noted that their spatial alignments are independent parameters in the proposed position estimation method.

optimization procedure. The accuracy of the proposed position estimate depends on the type of optimization method used, its theoretical motivations, and convergence properties. Therefore, we quantitatively compare three methods in terms of their rate of convergence and determine the optimal one for the current problem. In addition, the basic accuracy of the proposed position estimation method is experimentally shown.

To present the three-dimensional measurement principle, this paper is organized as follows. In Sec. II we describe the definition of variables expressing the state of the receiver coil and outline the method for determining the values of these unknown variables. Methods for representing the magnetic field and estimating the receiver position are, respectively, described in Sec. III and IV. Results of preliminary experiments are shown in Sec. V to quantitatively evaluate the accuracy of the proposed method. Finally, in Sec. VI we summarize this work and give the conclusions.

II. PRINCIPLE FOR DETERMINING STATES OF THE RECEIVER COIL

In this section we define the variables that represent the state of the receiver coil and outline the basic measurement principle. As shown in Fig. 1, the receiver coil is assumed to be a miniature single-axis solenoid. Its state can be described by variables

$$\mathbf{x} = (x_1, x_2, x_3) \tag{1}$$

and

$$\theta = (\theta_1, \theta_2), \tag{2}$$

respectively, representing its position in a three-dimensional orthogonal coordinate system (measurement coordinate system) and its rotational angles with respect to the axes x_2 and x_3. The exact mathematical representation of these rotations will be given in Sec. IV.

The values of these unknown variables are determined by using alternating magnetic fields. Following Zierdt (1993), the number of transmitter coils is assumed to be six in this study. In his method, each coil is positioned along an axis of the coordinate system, as shown in Fig. 2. They are driven at different carrier frequencies to generate alternating magnetic fields. To obtain the component corresponding to each transmitting channel, induced signals in the receiver coil are separated in the frequency domain. The measured strength of the received signal is then denoted as

$$\mathbf{z} = (z_1, z_2, z_3, z_4, z_5, z_6)^T, \tag{3}$$

where z_l is the component corresponding to the lth transmitting channel. T denotes the transposition.

On the other hand, the received signal is predicted as a function of the state variables, and they are denoted again in a vector form as

$$\hat{\mathbf{z}}(\mathbf{x}, \theta) = (\hat{z}_1(\mathbf{x}, \theta), \hat{z}_2(\mathbf{x}, \theta), \hat{z}_3(\mathbf{x}, \theta), \hat{z}_4(\mathbf{x}, \theta), \hat{z}_5(\mathbf{x}, \theta), \hat{z}_6(\mathbf{x}, \theta))^T. \tag{4}$$

Then the values of the state variables are determined so that the difference between the measured and predicted signals is minimized. The error criterion used to predict the received signal is defined as

$$S(\mathbf{x},\theta) = |\mathbf{z} - \hat{\mathbf{z}}(\mathbf{x},\theta)|^2, \tag{5}$$

where the predicted signal is expressed as

$$\hat{z}_l(\mathbf{x},\theta) = |\mathbf{y}_l(\mathbf{x})|\cos\psi_l(\mathbf{x},\theta), \tag{6}$$

for the lth transmitting channel. $\mathbf{y}_l$ represents the spatial pattern of the magnetic field as a function of position in the measurement coordinate system. This field function can be written as a three-dimensional vector,

$$\mathbf{y}_l(\mathbf{x}) = (y_1(\mathbf{x}), y_2(\mathbf{x}), y_3(\mathbf{x}))^T, \tag{7}$$

where y_i is the field component in the direction of the x_i axis ($i=1, 2, 3$). $|\mathbf{y}_l|$ means the norm of the vector representing the magnitude of the magnetic field. ψ_l is the angle between the axis of the receiver coil and the direction of the magnetic flux. The received signal is then reduced by a factor of $\cos\psi_l$. The method for predicting the received signal is explained in more detail in Sec. IV A.

It might be noted that the position and orientation of the transmitter coils are implicit variables in the proposed position estimation method. This is because the spatial pattern of the magnetic field is directly represented as a function of the axes of the coordinate system in the form of a multivariate spline function, as will be described in the next section. However, the transmitter alignments have a significant influence on the estimation accuracy, and should be carefully selected so that the sensitivity of the received signals over any change of the state variables is preserved. The positions of the transmitter coils shown in Fig. 2 are symmetrical with respect to the origin. The axes of the coils S1, S3, and S5 are in parallel to x_1, x_2, and x_3 axes, respectively, and hence they are orthogonal with each other. The axes of S2, S4, and S6 are respectively located on the x_1-x_2, x_2-x_3, and x_3-x_1 planes, and directed toward the positions of S6, S2, and S1.

III. MAGNETIC FIELD REPRESENTATION

In this section we describe the nonparametric method of representing the magnetic field using a multivariate B-spline function. The B-spline function can be formally defined as a linear combination of piecewise basis functions. These basis functions are uniquely constructed from the spatial alignment of the internal nodes that also control the smoothness of the resulting spline function. The values of weighting coefficients used when summing constructed basis functions are determined so that the spline function interpolates given samples of the calibration data. The overall configuration of the magnetic field is then represented as a function of position in the measurement coordinate system.

There can exist several ways to represent the pattern of a three-dimensional magnetic field using a spline. One way is based on a two-dimensional spline representation in a transmitter-specific coordinate system. When a plane that includes the axis of a specific transmitter coil is considered, the field pattern in that plane has two orthogonal components. Each of these components can be represented using a two-variate spline as a function of position in the plane. Then the three-dimensional field pattern can be obtained by rotating this two-dimensional pattern with respect to the axis of the transmitter coil. By transforming it in reference to the position and orientation of the transmitter coil, the field pattern can be expressed in the measurement coordinate system.

In the present study, a much more simple and straightforward approach is employed: the pattern of the three-dimensional vector field is directly expressed in the measurement space using three splines representing each of the three orthogonal field components. Using this method, calibration data can be sampled at equal spatial intervals in the measurement space, as will be discussed later. Because the spline function is formed so that it interpolates these data samples, this method can attain a uniform representation accuracy in the measurement area. In addition, it is capable of fitting the field function to the actual magnetic field even when there is interference between the transmitting channels and the field has location-dependent fluctuations, since each spline is directly defined as a function of the three axes of the coordinate system. The explanations of the spline function given in this section are based on Schumaker (1981) and Dierckx (1993).

A. Spline-based field function

The magnetic field produced by each transmitter coil can be viewed as a three-dimensional vector field. It is expressed using a multivariate B-spline function as

$$y_i(x_1,x_2,x_3) = \sum_{p=1}^{P}\sum_{q=1}^{Q}\sum_{r=1}^{R} c_{pqr}N_p(x_1)N_q(x_2)N_r(x_3), \tag{8}$$

where y_i is the field component in the direction of the x_i axis ($i=1, 2, 3$). N_p, N_q, and N_r are piecewise polynomial functions, i.e., B-spline basis functions, with respect to the x_1, x_2, and x_3 axes, respectively. The rank of these basis functions is assumed to be m. P, Q, and R indicate the number of basis functions used to represent the entire field pattern. c_{pqr} is the weight in summing combinations of basis functions in the tensor product form.

The field function given in Eq. (8) can depict a smooth curved surface over the three-dimensional space so that it interpolates given samples of calibration data, each of which consists of a pair of data respectively representing the position of measurement point and the strength of the magnetic field. Therefore, the field pattern is represented, regardless of the transmitter position or orientation, directly as a function of position in the measurement space. By virtue of the piecewise property of its basis functions, the spline function generally provides a good result when used for interpolating a set of data samples and approximating the overall shape of a curved surface. In addition, the smoothness of the surface can be controlled by the parameter m, which determines the polynomial order of the basis functions.

The number of unknown coefficients is much larger in the proposed nonparametric representation than in the ordinal field functions defined by a dipole source assumption. Therefore, a large set of calibration data should be measured covering the entire measurement region. If the intervals between the data sampling points are equal, then it is to be expected that the resulting spline field function will have almost the same approximation accuracy everywhere in the region. Obviously, a dense spatial sampling of the calibration

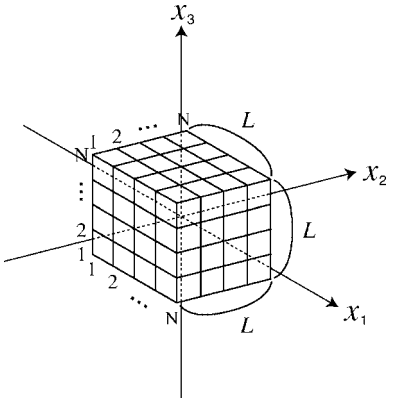

FIG. 3. An illustration of a cubic measurement region with the sides of length L assumed to be sufficient for articulatory observation. The internal nodes in the spline field representation are placed at the crossing points of the grid drawn to cover the entire measurement region. Calibration data samples usable for determining the weights of the spline function can be gathered by placing the receiver coil at these crossing points and measuring the induced signals. The number of data samples for each side of the cubic region is denoted as N.

data would result in a higher approximation accuracy. In that case, a better approximation might be obtained by applying a spline smoothing technique that can cancel random noise components included in the calibration data (Kaburagi and Honda, 2002). However, the number of samples increases at a cubic rate in the three-dimensional case, and only the spline interpolation method is considered in this paper.

B. Constructing the B-spline basis functions

Basis functions of the spline representation can be uniquely determined by setting the internal nodes irrespective of the data samples to be interpolated. As shown in Fig. 3, a simple node alignment method is used here in which each node is located at a grid point of a cubic measurement region with the side of length L. The center of the region is supposed to coincide with the origin of the coordinate system, and the grid lines are drawn at equal intervals. When we define $a=-L/2$ and $b=L/2$, the position of internal nodes $\xi_{i,p}$ along ith axis can be, respectively, written for $i=1$, 2, and 3 as follows:

$$a=\xi_{1,1-m}=\cdots=\xi_{1,-1}=\xi_{1,0}<\xi_{1,1}<\cdots<\xi_{1,p}<\cdots<\xi_{1,P-m+1}=\xi_{1,P-m+2}=\cdots=\xi_{1,P-1}=\xi_{1,P}=b,$$

$$a=\xi_{2,1-m}=\cdots=\xi_{2,-1}=\xi_{2,0}<\xi_{2,1}<\cdots<\xi_{2,q}<\cdots<\xi_{2,Q-m+1}=\xi_{2,Q-m+2}=\cdots=\xi_{2,Q-1}=\xi_{2,Q}=b,$$

and

$$a=\xi_{3,1-m}=\cdots=\xi_{3,-1}=\xi_{3,0}<\xi_{3,1}<\cdots<\xi_{3,r}<\cdots<\xi_{3,R-m+1}=\xi_{3,R-m+2}=\cdots=\xi_{3,R-1}=\xi_{3,R}=b.$$

It should be noted that m nodes overlap on both sides of each axis, and P $(=Q=R)$ represents the number of basis functions as defined in Eq. (8). The total number of internal nodes in each axis is $P+m$ $(=Q+m=R+m)$, and the number of nonoverlapping nodes equals $P-m$ $(=Q-m=R-m)$.

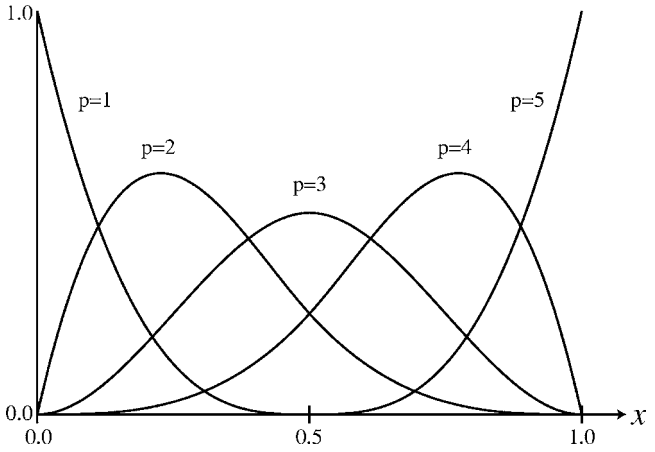

FIG. 4. An illustration of B-spline basis functions with the rank of four constructed by assigning nine internal nodes along the axis. Four nodes are overlapped on both sides at $x=0.0$ and 1.0, and the nonoverlapping node is located at $x=0.5$. The values of each basis function were computed at 256 axis positions within the interval from zero to one, by using de Boor's algorithm (de Boor, 1972) instead of directly evaluating divided differences of truncated power functions. The traces were then drawn for each basis function by linearly interpolating the obtained values. The evaluation method of the basis function is described in Appendix B.

Basis functions of the spline representation are defined from the position of successive $m+1$ nodes as

$$N_p(x_1)=(\xi_{1,p}-\xi_{1,p-m})M_p(x_1;\xi_{1,p-m},\ldots,\xi_{1,p}),$$

$$N_q(x_2)=(\xi_{2,q}-\xi_{2,q-m})M_q(x_2;\xi_{2,q-m},\ldots,\xi_{2,q}),$$

and

$$N_r(x_3)=(\xi_{3,r}-\xi_{3,r-m})M_r(x_3;\xi_{3,r-m},\ldots,\xi_{3,r}),$$

for $1\leqslant p\leqslant P$, $1\leqslant q\leqslant Q$, and $1\leqslant r\leqslant R$. Here, M_p, M_q, and M_r are defined using the divided difference of the truncated power function $M(x;z)=(x-z)_+^{m-1}$ with respect to $z=\xi_{p-m},\ldots,\xi_p$ for $x=x_1$, $z=\xi_{q-m},\ldots,\xi_q$ for $x=x_2$, and $z=\xi_{r-m},\ldots,\xi_r$ for $x=x_3$, respectively. These basis functions have the following piecewise properties:

$$N_p(x_1)\begin{cases}>0, & \xi_{1,p-m}<x_1<\xi_{1,p},\\ =0, & \text{otherwise;}\end{cases} \tag{9}$$

$$N_q(x_2)\begin{cases}>0, & \xi_{2,q-m}<x_2<\xi_{2,q},\\ =0, & \text{otherwise;}\end{cases} \tag{10}$$

and

$$N_r(x_3)\begin{cases}>0, & \xi_{3,r-m}<x_3<\xi_{3,r},\\ =0, & \text{otherwise,}\end{cases} \tag{11}$$

indicating that each basis function takes a nonzero value only for a limited interval along the axis. The values of these basis functions can be effectively calculated using de Boor's algorithm (de Boor, 1972), instead of directly evaluating the divided difference of the truncated power function. Figure 4 illustrates the shape of the basis function $N_p(x)$, where the rank is set at four and the internal nodes are placed at 0.0, 0.5, and 1.0 on the x axis. Four nodes overlap on both sides at 0.0 and 1.0. It is clear from the figure that each basis function is locally supported.

C. Determining the weighting coefficients

The weighting coefficients of the spline field function are determined so that it forms a curved surface interpolating a given set of calibration data samples. The field strength in a given location is obtained by positioning a receiver coil and measuring the induced signal. Since the field function [Eq. (8)] expresses an orthogonal component of the vector field, the direction of the receiver coil should be set in parallel with that vector component. The data sampling points are selected at the grid points shown in Fig. 3. Then every datum stores the measured field strength $v_{p'q'r'}$ sampled at the position $\mathbf{x}_{p'q'r'}=(x_{1,p'},x_{2,q'},x_{3,r'})$ for $1\leqslant p'\leqslant N, 1\leqslant q'\leqslant N$, and $1\leqslant r'\leqslant N$, where N gives the number of data samples along each axis. N must satisfy the condition $N=P=Q=R$ so that the number of data samples is coincident with that of unknown weighting coefficients.

By setting the positions of the internal nodes and data sampling points as described above, it is clear that each data sample is supported by at least one basis function of the spline representation. Then the Schoenberg–Whitney condition,

$$x_{1,p'} < \xi_{1,p'} < x_{1,p'+m},$$

$$x_{2,q'} < \xi_{2,q'} < x_{2,q'+m},$$

and

$$x_{3,r'} < \xi_{3,r'} < x_{3,r'+m}$$

are satisfied for p', q', $r'=1,2,\ldots,N-m$. By substituting each data sample into Eq. (8), the equation

$$v_{p'q'r'}=\sum_{p=1}^{P}\sum_{q=1}^{Q}\sum_{r=1}^{R} c_{pqr}N_p(x_{1,p'})N_q(x_{2,q'})N_r(x_{3,r'}) \qquad (12)$$

is derived for every combination of p', q', $r'=1,2,\ldots,N$. These constitute $N\times N\times N$ simultaneous linear equations with respect to c_{pqr} (see Appendix A). This set of equations can be solved, for example, by using the Gauss elimination method to determine the value of the weighting coefficients.

IV. ESTIMATION OF THE RECEIVER STATE

In this section we describe how the position and orientation of the receiver coil are estimated using the spline-based representation of the magnetic field. This problem can be regarded as the determination of five unknown variables ($\mathbf{x}$ and θ) from the induced signal in the receiver coil ($\mathbf{z}$), and an iterative procedure is used here to solve this nonlinear problem. In addition, we examine three types of the nonlinear optimization algorithm, i.e., Gauss–Newton, Marquardt, and Newton–Raphson methods, for deriving updating quantities of the state variables by an iterative procedure. It is known that they have different theoretical backgrounds and convergence properties (Dennis and Schnabel, 1983) and their performance generally depends on the type of problem to be solved.

The Marquardt method has a free parameter that can adjust the convergence property between that of the Gauss–Newton method and that of the steepest descent method. Therefore, it is possible to expect a rapid convergence if the free parameter is adequately selected, depending on the distance between the value of the state variables and the optimal solution in each iterative step. On the other hand, the Newton–Raphson method has a quadratic convergence while it is the first order in the other two methods.[1] This quadratic property indicates that the iterative procedure converges very quickly if the initial estimation of the state variables is properly given in the vicinity of the optimal solution. In the next section, these three methods are applied to the empirical data for the quantitative evaluation. Then it will lead us to the optimal selection of the estimation algorithm.

A. Prediction of the received signal

When the set of spline field functions is determined as described in the previous section, the induced signal in the receiver coil can be predicted as a function of the state variables in the form given in Eq. (6). The strength of the magnetic field, $|\mathbf{y}_l(\mathbf{x})|$, is represented as the norm of the vector given by three field functions $y_1(\mathbf{x})$, $y_2(\mathbf{x})$, and $y_3(\mathbf{x})$. The tilt angle, $\psi_l(\mathbf{x},\theta)$, is defined as the relative angle between the axis of the receiver coil and the direction of the vector field.

Equation (6) can be rewritten as

$$\hat{z}_l(\mathbf{x},\theta)=\mathbf{y}_l(\mathbf{x})\cdot\mathbf{e},$$

using a unit length vector $\mathbf{e}$ expressing the direction of the axis of the receiver coil. The notation $\cdot$ indicates the inner product of two vectors. The rotations of the receiver coil with respect to the x_2 and x_3 axes are shown in Fig. 1, and they can be respectively represented using the following transformation matrices:

$$U_1=\begin{pmatrix}\cos\theta_1 & 0 & \sin\theta_1\\ 0 & 1 & 0\\ -\sin\theta_1 & 0 & \cos\theta_1\end{pmatrix}$$

and

$$U_2=\begin{pmatrix}\cos\theta_2 & -\sin\theta_2 & 0\\ \sin\theta_2 & \cos\theta_2 & 0\\ 0 & 0 & 1\end{pmatrix}.$$

Then the vector $\mathbf{e}$ can be expressed as

$$\mathbf{e}=U_2U_1\mathbf{e}_1,$$

where $\mathbf{e}_1$ is a unit length vector in the direction of the x_1 axis. Finally, the received signal can be predicted as

$$\hat{z}_l(\mathbf{x},\theta)=y_1(\mathbf{x})\cos\theta_1\cos\theta_2+y_2(\mathbf{x})\cos\theta_1\sin\theta_2 - y_3(\mathbf{x})\sin\theta_1, \qquad (13)$$

where y_i $(i=1,2,3)$ is the ith component of the vector field given by the spline representation in Eq. (8) for the lth transmitting channel.

B. Estimation procedure

The state of the receiver coil can be estimated by minimizing the error criterion in Eq. (5) given as the difference between the measured and predicted receiver signals. This

optimization problem is nonlinear because the magnetic field is represented by piecewise polynomial functions and the signal representation in Eq. (13) is also a nonlinear function of the state variables. Therefore, a nonlinear optimization procedure is employed in which the values of the state variables are iteratively updated. The estimated position and orientation of the receiver coil is the solution to this nonlinear problem.

The procedure for obtaining the optimal solution can be written as follows. Given the measured signal ($\mathbf{z}$) and initial values of the state variables ($\mathbf{x}^0$ and θ^0), an index of the iterations (k) is set at zero. Then the prediction of the received signal ($\hat{\mathbf{z}}$) and calculation of the Jacobian and Hessian, required in obtaining the updating quantity of the state variables, are performed for $\mathbf{x}^k$ and θ^k. Here, the updating vector is defined as

$$\Delta\mathbf{x} = (\Delta x_1, \Delta x_2, \Delta x_3, \Delta\theta_1, \Delta\theta_2)^T, \tag{14}$$

where the first three components correspond to the positional variables and the other two to the rotational ones. The updating vector is determined by solving a normal equation by the Gauss–Newton, Marquardt, or Newton–Raphson method, explained later. Then the values of the state variables are revised such as

$$\begin{aligned} x_1^{k+1} &= x_1^k + \alpha\,\Delta x_1^k, \\ x_2^{k+1} &= x_2^k + \alpha\,\Delta x_2^k, \\ x_3^{k+1} &= x_3^k + \alpha\,\Delta x_3^k, \\ \theta_1^{k+1} &= \theta_1^k + \alpha\,\Delta\theta_1^k, \\ \theta_2^{k+1} &= \theta_2^k + \alpha\,\Delta\theta_2^k, \end{aligned} \tag{15}$$

where α is a reduction parameter that scales the updating vector and enables it to determine a better updating quantity by using the one-dimensional search in the state space. If a set of scalar values usable as the reduction parameter is defined as $\{\alpha_j; j=1,2,\ldots,J\}$ $(0<\alpha_j\leqslant 1)$, each value is applied to update the state variables, predict the receiver signal, and calculate the signal prediction error. The optimal value of the reduction parameter is then selected for which the signal prediction error is a minimum. When convergence with respect to the prediction error is obtained, the process is terminated and the optimal values of the state variables are determined, otherwise, the counter is set as $k=k+1$ and the procedure is repeated.

The total number of spline field functions given in the form of Eq. (8) is the number of transmitting channels (six in the present study) multiplied by the dimensionality of the vector field (three). For simplicity, the rank of the basis functions, the number of nonoverlapping nodes, and hence the number of basis functions are assumed to be identical among the transmitting channels, although they can be set independently. Under these conditions, the basis functions $N_p(x_1)$, $N_q(x_2)$, and $N_r(x_3)$ are also identical for 18 spline field functions because they are constructed from the same set of internal nodes. As a result, the weighting coefficients are the only different constituents of the spline field functions, and they are determined independently from the calibration data.

Let $c_{pqr}^{(il)}$ represent the weighting coefficient of the ith field component with respect to the lth transmitting channel $(i=1,2,3;\ l=1,2,\ldots,6)$. In the kth iteration of the optimization procedure, the received signal is predicted as

$$\begin{aligned} \hat{z}_l(\mathbf{x}^k, \theta^k) = {} & y_1(\mathbf{x}^k)\cos\theta_1^k\cos\theta_2^k + y_2(\mathbf{x}^k)\cos\theta_1^k\sin\theta_2^k \\ & - y_3(\mathbf{x}^k)\sin\theta_1^k, \end{aligned}$$

where the field components are calculated as

$$y_i(\mathbf{x}^k) = \sum_{p=1}^{P}\sum_{q=1}^{Q}\sum_{r=1}^{R} c_{pqr}^{(il)} N_p(x_1^k) N_q(x_2^k) N_r(x_3^k).$$

On the other hand, components of the Jacobian can be obtained by calculating

$$\partial\hat{z}_l(\mathbf{x},\theta)/\partial x_i \quad (i=1,2,3),$$

$$\partial\hat{z}_l(\mathbf{x},\theta)/\partial\theta_i \quad (i=1,2),$$

and substituting $\mathbf{x}=\mathbf{x}^k$ and $\theta=\theta^k$. As briefly described in Appendix B, the evaluation of the basis functions and their partial derivatives for specific values of the state variables can be effectively performed by utilizing de Boor's incremental algorithm (de Boor, 1972).

In the remaining part of the section, we explain about the Gauss–Newton, Marquardt, and Newton–Raphson methods used to determine the updating vector in the iteration procedure (Dennis and Schnabel, 1983). These three methods are compared using the empirical data in the succeeding section.

C. Gauss–Newton method

In the Gauss–Newton method, the updating vector $\Delta\mathbf{x}$ is determined by solving the following normal equation:

$$A^T A\,\Delta\mathbf{x} = A^T[\mathbf{z} - \hat{\mathbf{z}}(\mathbf{x},\theta)], \tag{16}$$

where A is the Jacobian,

$$A = \begin{pmatrix} \partial\hat{z}_1/\partial x_1 & \partial\hat{z}_1/\partial x_2 & \partial\hat{z}_1/\partial x_3 & \partial\hat{z}_1/\partial\theta_1 & \partial\hat{z}_1/\partial\theta_2 \\ \partial\hat{z}_2/\partial x_1 & \partial\hat{z}_2/\partial x_2 & \partial\hat{z}_2/\partial x_3 & \partial\hat{z}_2/\partial\theta_1 & \partial\hat{z}_2/\partial\theta_2 \\ \partial\hat{z}_3/\partial x_1 & \partial\hat{z}_3/\partial x_2 & \partial\hat{z}_3/\partial x_3 & \partial\hat{z}_3/\partial\theta_1 & \partial\hat{z}_3/\partial\theta_2 \\ \partial\hat{z}_4/\partial x_1 & \partial\hat{z}_4/\partial x_2 & \partial\hat{z}_4/\partial x_3 & \partial\hat{z}_4/\partial\theta_1 & \partial\hat{z}_4/\partial\theta_2 \\ \partial\hat{z}_5/\partial x_1 & \partial\hat{z}_5/\partial x_2 & \partial\hat{z}_5/\partial x_3 & \partial\hat{z}_5/\partial\theta_1 & \partial\hat{z}_5/\partial\theta_2 \\ \partial\hat{z}_6/\partial x_1 & \partial\hat{z}_6/\partial x_2 & \partial\hat{z}_6/\partial x_3 & \partial\hat{z}_6/\partial\theta_1 & \partial\hat{z}_6/\partial\theta_2 \end{pmatrix},$$

representing the sensitivity of the unknown variables over the predicted signals. These components can be efficiently computed as well as the signal prediction error $(\mathbf{z}-\hat{\mathbf{z}})$, by using de Boor's algorithm, as described previously.

D. Marquardt method

The normal equation in the Marquardt method (Marquardt, 1963) can be written as

$$(A^TA + \lambda I)\Delta\mathbf{x} = A^T[\mathbf{z} - \hat{\mathbf{z}}(\mathbf{x}, \theta)], \tag{17}$$

where λ ($\lambda \geqslant 0$) and I represent the weighting parameter and identity matrix, respectively. When $\lambda = 0$, the above equation is obviously identical to that in the Gauss–Newton method. It has also been proved that it approaches the steepest descent method when $\lambda > \|A^TA\|$; here $\|\cdot\|$ denotes the matrix norm. Therefore, the Marquardt method can generalize these two methods by treating λ as a free parameter. It should be noted that when the Marquardt method is used, the reduction parameter in the iterative procedure is fixed at $\alpha = 1$ and an optimal value of λ is searched in each iteration.

In early iterations where the signal error $S(\mathbf{x}, \theta)$ is relatively large and the nonlinearity of the optimization process may be high, the updating vector can take the steepest-descent direction by selecting a large value of the free parameter. When the error is decreased after a number of iterations, it is expected that the value of the state variables is close to a solution and the optimization process is less nonlinear. Then the Gauss–Newton updating vector is effective and the value of the free parameter should be reduced. The actual value of the free parameter and convergence property are controlled on the basis of the signal error.

E. Newton–Raphson method

The updating vector is determined by solving the following equation:

$$H\,\Delta\mathbf{x} = -\,\mathbf{d}, \tag{18}$$

where H is the Hessian matrix with respect to the error criterion,

$$H = \begin{pmatrix} \partial^2 S/\partial x_1\,\partial x_1 & \partial^2 S/\partial x_1\,\partial x_2 & \partial^2 S/\partial x_1\,\partial x_3 & \partial^2 S/\partial x_1\,\partial \theta_1 & \partial^2 S/\partial x_1\,\partial \theta_2 \\ \partial^2 S/\partial x_2\,\partial x_1 & \partial^2 S/\partial x_2\,\partial x_2 & \partial^2 S/\partial x_2\,\partial x_3 & \partial^2 S/\partial x_2\,\partial \theta_1 & \partial^2 S/\partial x_2\,\partial \theta_2 \\ \partial^2 S/\partial x_3\,\partial x_1 & \partial^2 S/\partial x_3\,\partial x_2 & \partial^2 S/\partial x_3\,\partial x_3 & \partial^2 S/\partial x_3\,\partial \theta_1 & \partial^2 S/\partial x_3\,\partial \theta_2 \\ \partial^2 S/\partial \theta_1\,\partial x_1 & \partial^2 S/\partial \theta_1\,\partial x_2 & \partial^2 S/\partial \theta_1\,\partial x_3 & \partial^2 S/\partial \theta_1\,\partial \theta_1 & \partial^2 S/\partial \theta_1\,\partial \theta_2 \\ \partial^2 S/\partial \theta_2\,\partial x_1 & \partial^2 S/\partial \theta_2\,\partial x_2 & \partial^2 S/\partial \theta_2\,\partial x_3 & \partial^2 S/\partial \theta_2\,\partial \theta_1 & \partial^2 S/\partial \theta_2\,\partial \theta_2 \end{pmatrix},$$

and $\mathbf{d}$ is the vector,

$$\mathbf{d}^T = \left(\frac{\partial S}{\partial x_1} \frac{\partial S}{\partial x_2} \frac{\partial S}{\partial x_3} \frac{\partial S}{\partial \theta_1} \frac{\partial S}{\partial \theta_2} \right).$$

From the definition of the error ($S(\mathbf{x}, \theta)$), each component of this matrix and vector can be determined, for example, such that

$$\frac{\partial S}{\partial x_i} = -2 \sum_{l=1}^{6} \frac{\partial \hat{z}_l}{\partial x_i} (z_l - \hat{z}_l)$$

or

$$\frac{\partial S}{\partial x_i\,\partial x_j} = 2 \sum_{l=1}^{6} \left\{ \frac{\partial \hat{z}_l}{\partial x_i} \frac{\partial \hat{z}_l}{\partial x_j} - \frac{\partial^2 \hat{z}_l}{\partial x_i\,\partial x_j} (z_l - \hat{z}_l) \right\}.$$

The term $\partial^2 \hat{z}_l / \partial x_i \partial x_j$ is the quadratic partial derivative of the predicted receiver signal ($\hat{z}_l$) and is usually difficult to evaluate when it is a nonlinear function of x_i. Using our method, however, it can be computed conveniently by slightly modifying the procedure presented in Appendix B.

V. EXPERIMENT

A. Experimental conditions

An experiment was performed to investigate the accuracy of the proposed position estimation method. The hardware we used was the AG500 electromagnetic articulographic system and an automatic position calibrator both constructed by Carstens Medizinelektronik GmbH (Germany). The experimental procedure was as follows. Calibration and test datasets were first gathered by controlling the position of the receiver coil, using the automatic calibrator, and measuring the receiver signal. A sample of these signal data was collected as the received signal strength by digitally recording the received signals, separating them into six frequency components according to the frequencies of the transmitting signals, and then by taking the mean of 50 samples. During calibration, the axis of the receiver coil was set in parallel to each of the x_1, x_2, and x_3 axes in turn to obtain the orthogonal components of the three-dimensional magnetic field for every transmitter coil. These calibration data were interpolated by spline functions as described in Sec. III to construct the field function. The test data were then used to evaluate the accuracy of the proposed method in (1) representing the magnetic field based on the spline interpolation and (2) estimating the position of the receiver coil.

In the experiment, we used a cubic region, as shown in Fig. 3, with 8-cm and 6-cm side lengths for the calibration and test datasets, respectively. The number of sampling points along each side (N) was five for the calibration and three for the test. Consequently, the sampling positions of the test samples were coincident with those of the calibration data samples only at the origin of the coordinate system. In the spline interpolation of the calibration data, the rank of the basis function was set at four ($m=4$), and the number of nonoverlapping nodes at one. As a result, internal nodes were positioned at three points along each axis at $x_i = -40$, 0, 40 (mm) for $i = 1$, 2, 3.

Three types of evaluations were conducted using the gathered magnetic data. First, the accuracy of the spline rep-

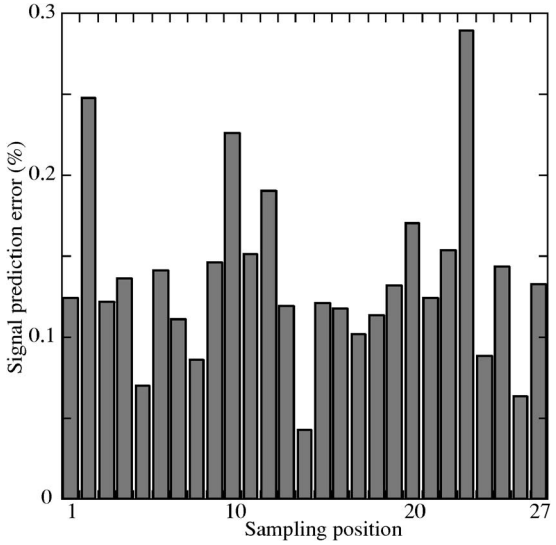

FIG. 5. The error in predicting the receiver signal based on the spline interpolation of the calibration data. The axis of the receiver coil is in parallel with the x_1 axis. The error plotted along the ordinate is normalized by the receiver signal at the origin of the coordinate system. The abscissa indicates the sampling position of each test sample.

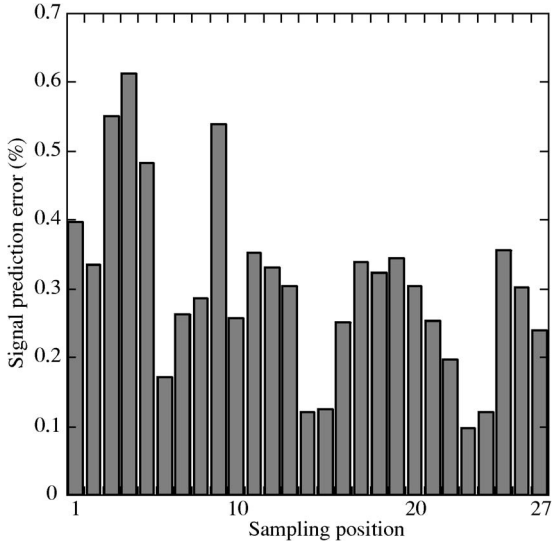

FIG. 6. The error in predicting the receiver signal based on the spline interpolation of the calibration data. The axis of the receiver coil is in parallel with the x_2 axis.

resentation was tested. Here, the state of the receiver coil was given and the error in predicting the receiver signal was calculated. Second, the receiver position was estimated using the Gauss–Newton method. In the iterative optimization procedure, initial values of the positional variables were set at zero, i.e., the origin of the coordinate system. On the other hand, since the angular variables are more sensitive to the prediction of the receiver signal, they were set so that the axis of the receiver coil was in $\pm x_1$, $\pm x_2$, and $\pm x_3$ directions. Before the iteration, the signal error $S(\mathbf{x},\theta)$ in Eq. (5) was calculated for each of these angular conditions, and the optimal one for which the error was minimized was selected as the actual initial value of the iterative procedure. Third, three optimization methods are compared in terms of the rate and degree of convergence of the iterative procedure. Fourth, the candidate initial values of the positional variables were also varied, to examine their influence on the rate of convergence.

The reduction parameter in the Gauss–Newton and Newton–Raphson methods was set as $\alpha=10^{-5}$, 10^{-4}, 0.0005, 0.001, 0.005, 0.01, 0.05, 0.1, 0.5, 1.0 in the present study. The free parameter in the Marquardt method was set to $\lambda=0$, 10^k, where $k=-6,-5,-4,\ldots,2$. The iterative procedure was terminated when one of the following conditions was satisfied: (a) the error ($S(\mathbf{x},\theta)$) was smaller than a fixed value (10^{-12}), (b) the iteration number was greater than a fixed number (100), or (c) the error was greater than that calculated in the previous iteration.

B. Experimental results on the measurement accuracy

Figures 5–7 show the error in predicting the receiver signal, i.e., the absolute difference $\sqrt{S(\mathbf{x},\theta)}$ between the measured signal at a given position and the signal predicted from the spline field function at the same sampling position. The direction of the axis of the receiver coil in the test samples was respectively set in parallel with the x_1, x_2, or x_3 axis in each figure. In the vertical axis, the signal error was normalized by the signal strength of the receiver coil positioned at the origin without rotation ($\theta_1=\theta_2=0$), multiplied by a hundred, and averaged for five trials. The horizontal axis indicates the sampling position of the test sample. When the sampling position is written as $(x_{1i},x_{2j},x_{3k})=(30(i-2),30(j-2),30(k-2))$ (mm) where $i,j,k=1, 2, 3$, the numerical value along the horizontal axis is related to the sampling position as $i+3(j-1)+9(k-1)$.

It should be noted, due to the direction of the receiver coil, that the received signal of the test samples shown in Fig. 5 only reflected the y_1 component of the magnetic field [see Eq. (7)]. Therefore, irrespective of the angle ψ_l between the magnetic flux and the axis of the coil, the error $\sqrt{S(\mathbf{x},\theta)}$ represents the difference between the measured field strength

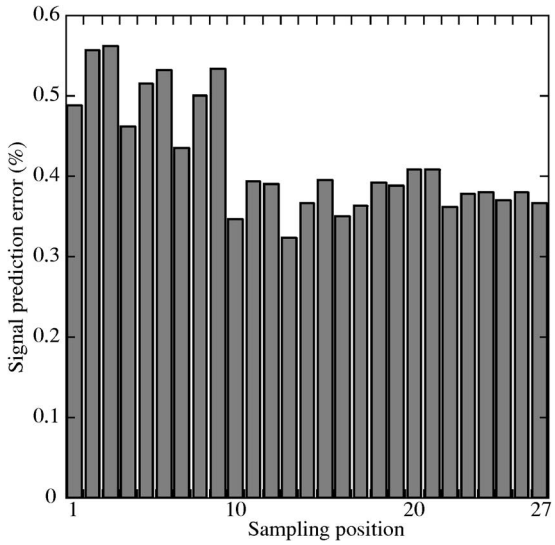

FIG. 7. The error in predicting the receiver signal based on the spline interpolation of the calibration data. The axis of the receiver coil is in parallel with the x_3 axis.

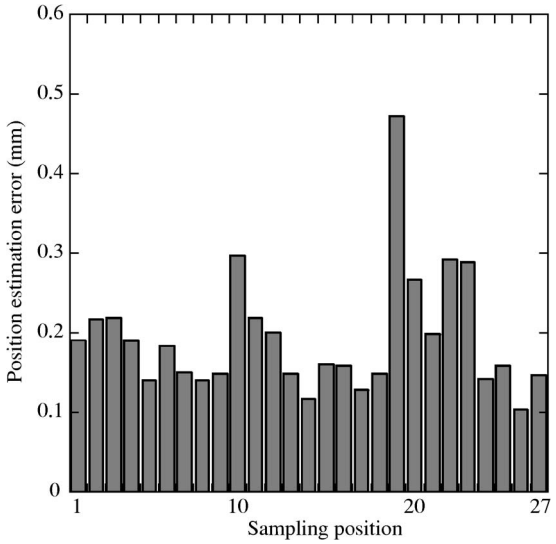

FIG. 8. The error in estimating the position of the receiver coil. The axis of the receiver coil is in parallel with the x_1 axis. The error plotted along the ordinate represents the Euclidean distance between the estimated and actual positions. The abscissa indicates the sampling position of each test sample.

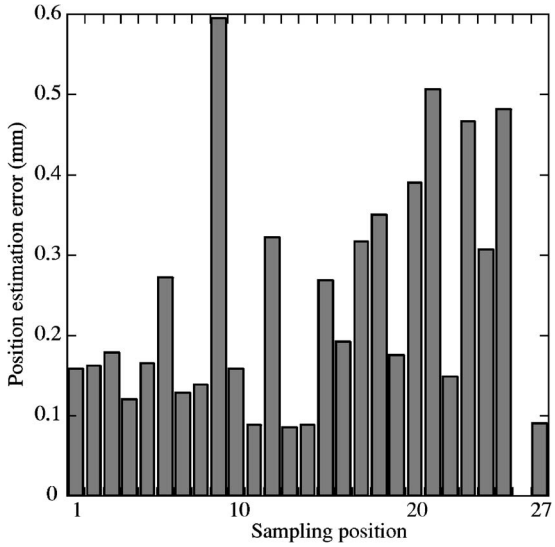

FIG. 10. The error in estimating the position of the receiver coil. The axis of the receiver coil is in parallel with the x_3 axis.

and the field strength predicted from the spline field function in the direction of the x_1 axis accumulated for six transmitter channels. Consequently, the error can be interpreted as a measurement of the accuracy of the spline field function y_1 given by Eq. (8) determined by the calibration data. Similarly, Figs. 6 and 7 indicate the accuracy of the spline function for the y_2 and y_3 field components, respectively. It is clear from the results that the signal prediction error is less than 0.50% for most of the test samples. A mean error of about 0.28% indicates that the spline field function in general agrees well with the actual field pattern, and that an interpolation of the calibration data is an effective field representation.

Next, the error in estimating the receiver position is shown in Figs. 8–10. The orientation of the receiver coil was set in the same manner as in Figs. 5–7: it was, respectively,

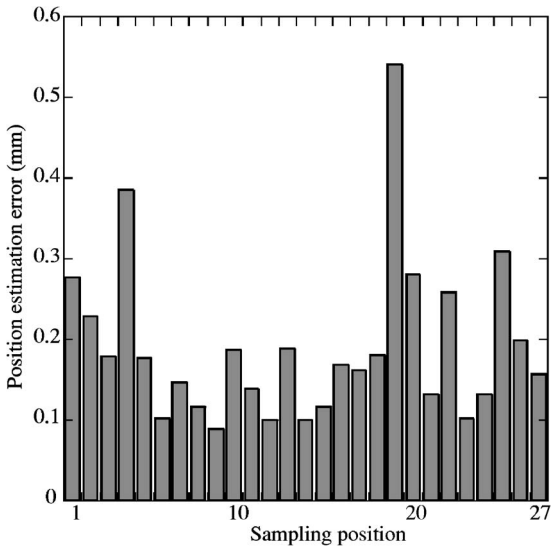

FIG. 9. The error in estimating the position of the receiver coil. The axis of the receiver coil is in parallel with the x_2 axis.

in parallel with the x_1, x_2, or x_3 axis. The coil position was determined using the received signal in the test sample and the calibrated field function, and the result was then compared with the actual position stored in each test sample. The positional error was calculated as the Euclidean distance between them and plotted in the vertical axis as the mean of five trials. In the horizontal axis, the sampling position of each test sample is indicated. In Fig. 10, the error for the 26th point was huge (about 1.92 mm), and it is not shown. A consideration of this peculiar test point will be discussed later. The mean error is 0.19, 0.19, and 0.24 mm in each figure, and the total mean error is 0.21 mm when the 26th point in Fig. 10 is excluded. When included, the total mean error is about 0.23 mm. The maximum error is, respectively, 0.47 mm (the 19th point in Fig. 8), 0.53 mm (the 19th point in Fig. 9), and 0.59 mm (the 9th point in Fig. 10 when the 26th point is excluded). In addition, the mean error of 0.23 mm is smaller than that of about 0.46 mm obtained using a dipole model as the representation of the magnetic field.[2] It can be concluded from these results that the estimated receiver position agreed well with the actual one for most of the test samples, indicating that the proposed position estimation method is quite effective as a three-dimensional articulatory observation technique used with the AG500 hardware system.

The error in the spline field representation (Figs. 5–7) is one of several possible error sources in the position estimation. However, it is difficult to find a clear correlation between them. When the results shown in Figs. 5 and 8 are compared, for example, the position estimation error of the 19th point is much greater than that of the 23rd point. On the contrary, the signal prediction error is obviously larger at the 23rd point than at the 19th. Similarly, the largest error at the 19th point of Fig. 9 cannot be attributed to the signal error plotted in Fig. 6. In the case of the 26th point of Fig. 10, the positional error was about 2 mm, even though the signal error was relatively small when compared with other test points shown in Fig. 7. It should also be mentioned that the

positional error at this test point was relatively constant in the five trials (2.29, 1.84, 1.74, 1.85, and 1.90 mm), indicating the reliability of the data acquisition process and the results.

As a possible cause of this large error, it might be suspected that multiple local minima existed in the error metric ($S(\mathbf{x},\theta)$) used for position estimation, and that the convergence point of the iterative procedure fell into one of them resulting in an improper solution. Usually, a nonquadratic error metric such as $S(\mathbf{x},\theta)$ has multiple local minima, and the convergence point depends on the initial value of the iterative procedure. In the case of the 26th point, on the other hand, the position estimation error was independent of the initial condition: it was the same even when the initial values of the positional and rotational variables were set to the true position. This finding suggests that the dependence of the solution on initial conditions was not the source of error in this instance. Here, it should be pointed out that, due to error included in the calibrated spline field function, the error criterion defined in Eq. (5) becomes greater than zero if the position estimate is correct. For the 26th test point, the signal error criterion was smaller at the estimated position, even though that position was 2 mm away from the true position. These results might suggest the existence of improper local minima at which the signal error $S(\mathbf{x},\theta)$ could take a small value, and the convergence point of the optimization procedure fell into one of them due to the error included in the field function or some other noise components in the received signal.

In addition, based on the idea that a reduction of the sampling interval of the calibration data will result in a better estimate of the magnetic field, we remeasured the data in the vicinity of the 26th test point at 1 cm intervals instead of at a 2 cm spacing. As a result, the position estimation error decreased from 1.92 mm to 0.44 mm. This suggests the possibility of using nonuniform sampling of the calibration data to obtain a relatively constant measurement accuracy over the entire measurement region: calibration data can be sampled at a relatively sparse interval in regions where the position estimation error is small and sampled densely when the error is large. At this point, it is a simple task to fit the spline function to nonuniformly sampled calibration data and produce a better representation of the magnetic field for the purpose of three-dimensional position estimation.

Next, the influence of the rotation of the coil axis was examined with respect to the angular variable θ_1, and the results are plotted in Fig. 11. The abscissa indicates the actual angle of the axis of the receiver coil relative to the x_1 axis. The coil was first directed in parallel to the x_1 axis ($\theta_1=0$) in the vicinity of the origin, and then it was rotated to the direction of the x_3 axis ($\theta_1=\pi/2$) with the interval of five degrees. In the ordinate of the figure, the error in estimating the position and orientation of the receiver coil was shown as the mean of three trials.

The positional error was 0.13 and 0.20 mm when the coil axis was in parallel to the x_1 and x_3 axes, respectively, and it increased for other orientations except the 75° condition. The mean error of these 19 orientations (0.35 mm) was slightly larger than the error obtained in the previous experiment (0.23 mm) shown in Figs. 8–10. We suspect that this increase of error might come from the difficulty in setting the direction of the coil axis precisely in parallel to each of the x_1, x_2, and x_3 axes during the collection of the calibration data. This problem is related to the method by which the orientation of the coil axis was determined in our experiments.[3] On the other hand, the angular error shown is the absolute difference between the actual and estimated angles of the coil axis, including the effect of both angular variables (θ_2 was supposed to be zero in the actual orientation). The results indicate that the estimation of the coil orientation was quite accurately performed: the error was less than 1° and the mean error was only 0.38°.

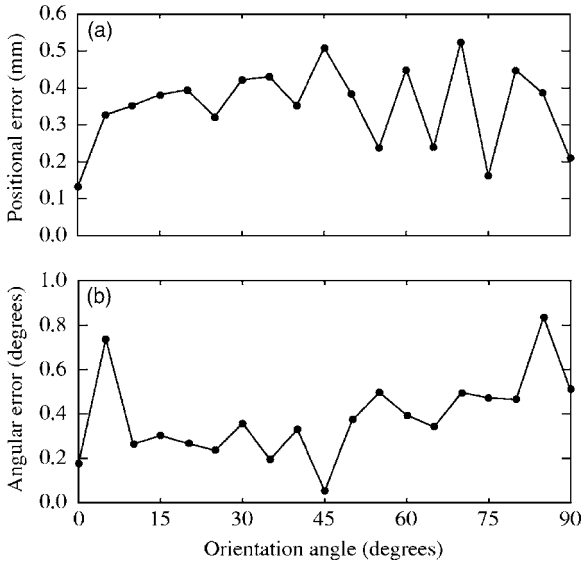

FIG. 11. Estimation accuracy of the receiver state when the coil was rotated with respect to the angular variable θ_1. The ordinate represents the error in estimating (a) the receiver position and (b) the rotational angle. The abscissa is the actual direction of the receiver coil relative to the x_1 axis.

C. Comparison of the optimization methods

Finally, three optimization methods (Gauss–Newton, Marquardt, and Newton–Raphson methods) are compared in Figs. 12–14 in terms of their convergence over a number of iterative steps. The vertical axis in each figure shows the signal prediction error [Eq. (5)] averaged over 27 points of six test datasets in which the orientation of the receiver coil was set in the direction of the x_1, x_2, and x_3 axes. The error is plotted in a logarithmic scale.

In these iterative procedures, the initial values of the unknown state variables need to be given. The actual initial value was selected from multiple candidates by choosing the candidate with a minimum signal error. For the positional variables, only the origin of the coordinate system was used in Fig. 12 as the candidate while eight positions $x_i=\pm 20$ mm, $i=1,2,3$) and 27 positions ($x_i=0,\pm 26.67$ mm, $i=1,2,3$) were respectively used as the candidates in Figs. 13 and 14. On the other hand, the orientation of the axis of the receiver coil was set in the direction of $\pm x_1$, $\pm x_2$, and $\pm x_3$ and the signal error was compared among them for each candidate of the positional variables. Consequently, the total number of candidates was six in Fig. 12, 48 in Fig. 13, and

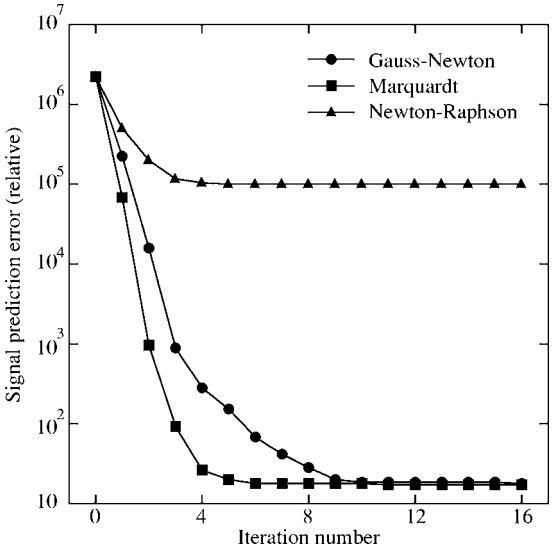

FIG. 12. The convergence speed of three optimization methods is compared. The signal prediction error is used as a measure of the convergence, and it is plotted as a function of the number of iterations. The number of candidates for the initial value of the iterative procedure was set at one for the positional variables and three for the rotational variables. See the text for a detailed description.

162 in Fig. 14. In the figures, the signal error at the zeroth iterative number indicates the difference between the observed receiver signal and the calculated one for the selected initial value of the state variables. As expected, this error decreased as the number of candidates increased.

It is clear from the figures that the convergence pattern depends both on the optimization method and the number of preserved initial values. Among the optimization methods, the signal error decreased most quickly in the Marquardt method. It can be seen from Fig. 14 that it only required, on average, three or four repetitions to converge. The error in the Gauss–Newton method also fell to the same level as it

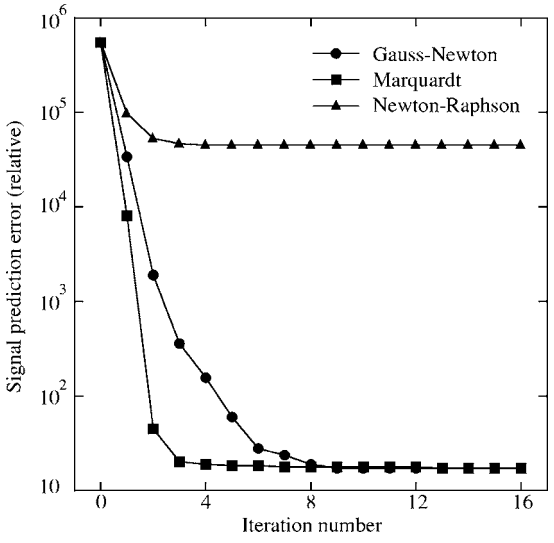

FIG. 13. The convergence speed of three optimization methods is compared. The number of the initial candidates was eight for the positional variables and three for the rotational variables.

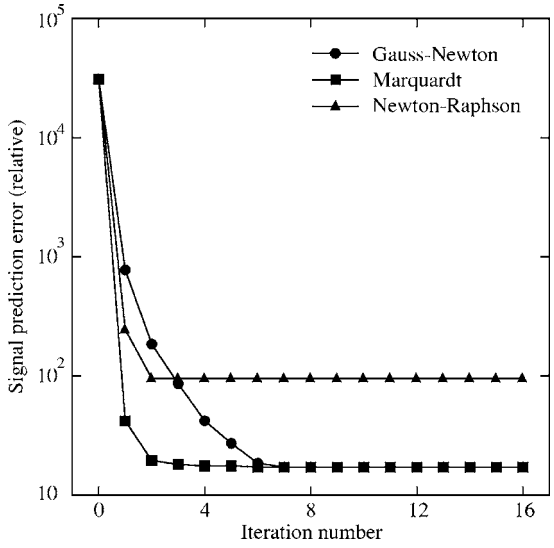

FIG. 14. The convergence speed of three optimization methods is compared. The number of the initial candidates was 27 for the positional variables and three for the rotational variables.

did when using the Marquardt method, but the convergence speed was slower: about four or five additional iterations were required to converge.

The Newton–Raphson method, on the other hand, did not substantially decrease the signal error for about 6% (Fig. 13) to 7% (Fig. 12) of the test samples. For two or more iterations in Fig. 14, the signal error was about six times larger than that in the Gauss-Newton or Marquardt methods for about 33% of the test samples. As a result, a large signal error was observed in each figure after two iterations. It is speculated that these large errors could be due to the relatively small convergence region of the Newton–Raphson method.

VI. SUMMARY AND CONCLUSIONS

A measurement method for the three-dimensional electromagnetic articulographic device is presented. The state of the receiver coil is defined by five positional and rotational variables and their values are estimated using alternating magnetic fields. Instead of assuming that each transmission coil behaves like an electromagnetic dipole (Raab *et al.*, 1979; Schönle *et al.*, 1987; Perkell *et al.*, 1992; Zierdt, 1993), the spatial pattern of the magnetic field is expressed in a nonparametric form using the multivariate spline. Given a set of calibration data collected from the measurement region, the spline function can provide a closed form representation of the entire field by smoothly interpolating the data samples. By assuming that the calibration data preserve information about the actual pattern of the magnetic field, the proposed method can explicitly fit the field function to the actual field, even when it has location-dependent fluctuations caused by interference between the transmitting channels.

The measurement method presented in this paper is, in principle, different from that proposed by Zierdt in the way in which it represents the magnetic field. The ordinal dipole-based method has the advantage that the number of unknown parameters is much smaller than that required by the non-

parametric method: the dipole model usually includes only a few parameters to be calibrated, while the proposed method requires that a large amount of calibration data be collected to determine the unknown weighting coefficients. On the other hand, a dipole model can be applied on the assumption that the distance between the transmitter and the receiver coils is sufficiently large. But, if the size of the transmitter coil is not negligible, or if interference among the transmitting channels occurs, an appropriate correction of the dipole model is necessary. Our nonparametric approach is an alternative to the dipole-based model, and it is characterized by a superior representation of the actual field pattern.

As well as the field representation method, in this paper we described how the state variables of the receiver coil can be related to the receiver signals in a different way from the previous studies (Raab *et al.*, 1979; Zierdt *et al.*, 1999). Based on this signal prediction model, the values of the state variables are estimated so that the difference between the observed and predicted receiver signals is minimized. Since the problem is nonlinear, it is quite important to select a good optimization method, and so we compared three different methods of deriving the updating vector in an iterative optimization procedure. It is also shown that the spline field function is convenient for calculating the Jacobian or Hessian in these optimization methods.

Finally, experiments were conducted to investigate the effectiveness of the proposed field function and position estimation method. The three optimization methods were also compared in terms of their speed and degree of convergence. The main experimental results and related considerations are as follows.

(1) The accuracy of the spline function was quantitatively investigated as a representation of the spatial pattern of the magnetic field produced by the transmitter coils. The error was calculated as the difference between the measured receiver signal and the predicted one using the calibrated spline function, and normalized by the received signal at the origin of the coordinate system as the reference. This relative error was shown to be about 0.28%, on average, when the size of the test region was $6\times6\times6$ (cm^3).
(2) The accuracy in estimating the position of the receiver coil was investigated for the same test region. As a result, a mean error of 0.23 mm was obtained, indicating the potential that the proposed method holds for capturing the three-dimensional movements of articulatory organs. In addition, this error is smaller than that obtained using a dipole model as the representation of the magnetic field.
(3) A peculiar test point was found at which the estimation error was quite huge (1.92 mm) when compared with other test points. This error might be caused by the presence of an improper local minimum in the signal estimation error, and it was shown that the error could be reduced by sampling the calibration data with a smaller interval. If this test point was excluded, the maximum error was 0.47, 0.53, and 0.59 mm when the orientation of the receiver coil was set in the direction of the x_1, x_2, and x_3 axis, respectively.
(4) The error in estimating the receiver position increased slightly (about 0.1 mm) when the coil was rotated with respect to one of the angular variables. On the other hand, estimation of the coil orientation was quite accurately performed with an error of 0.38°.
(5) As a means of solving the nonlinear problem, it was shown that the Marquardt method is able to achieve rapid convergence of the signal prediction error by adequately selecting the free parameter value that controls the convergence property. Also, the Gauss–Newton method can achieve the same level of convergence at a slower rate, but the performance of the Newton-Raphson method is inadequate for the present problem.
(6) In the Gauss–Newton or Marquardt method, the initial value of each of the positional variables can be fixed at the origin of the coordinate system. On the other hand, the values of the rotational variables are more sensitive in predicting the receiver signal, and consequently their initial values should be carefully selected. In our experiment, the initial value was selected from six orientation patterns of the receiver coil so that the signal error was minimized. Then, the results showed an adequate convergence and position estimation accuracy.

From these experimental results, it is concluded that our methods for representing the magnetic field and estimating the receiver position are useful when used with the hardware system of the three-dimensional electromagnetic articulographic device. The information about the convergence of several optimization methods and the setting of the initial value in the iterative procedure has a practical importance since a complicated nonlinear problem must be solved. On the other hand, the time required to compute each iteration of the optimization methods was about 1.5, 1.6, and 3.1 ms for the Gauss–Newton, Marquardt, and Newton–Raphson methods, respectively, with a personal computer having a 2 GHz CPU. It indicates that the Gauss-Newton and Marquardt methods have the same computational complexity, and that the computational time for ten receiver coils is about 64 ms when the iteration number of the Marquardt method is four.

To further determine the capability of the device for articulatory research on human subjects, the side length of the measurement region should be doubled to include the movement range of the jaw, lips, tongue, and soft palate, as well as several maxillary references. Experimental studies will be performed for that extended region to discover the amount of calibration data needed to accurately represent the magnetic field and estimate the receiver state.

ACKNOWLEDGMENTS

The authors wish to thank Mr. A. Zierdt and Dr. P. Hoole for their valuable discussions. We also thank Mr. T. Mochida for his support given to record the magnetic data at NTT Communication Science Laboratories. This research was partly supported by the Grant-in-Aid for Scientific Research from the JSPS (Grant No. 14101001).

APPENDIX A: MATRIX REPRESENTATION OF THE SPLINE INTERPOLATION CONDITION

The spline interpolation condition given in Eq. (12) constructs a set of simultaneous linear equations. It can be written in a matrix form as

$$A\mathbf{c} = \mathbf{v}, \tag{A1}$$

where $\mathbf{c}$ and $\mathbf{v}$ are vectors, respectively, representing the weighting coefficients and field strength data,

$$\mathbf{c} = (c_{111}, c_{211}, \ldots, c_{P11}, c_{121}, c_{221}, \ldots, c_{P21}, \ldots, c_{pqr}, \ldots, c_{1QR}, c_{2QR}, \ldots, c_{PQR})^T \tag{A2}$$

and

$$\mathbf{v} = (v_{111}, v_{211}, \ldots, v_{N11}, v_{121}, v_{221}, \ldots, v_{N21}, \ldots, v_{p'q'r'}, \ldots, v_{1NN}, v_{2NN}, \ldots, v_{NNN})^T. \tag{A3}$$

P, Q, and R are the number of basis functions in the x_1, x_2, and x_3 axes and N is the number of data samples for each axis where $N=P=Q=R$ holds. A is an $N^3 \times N^3$ matrix and can be separated into $N^2 \times N^2$ matrix $B_{r',r}$ and $N \times N$ matrix $C_{q',q}$ such as

$$A = \begin{pmatrix} B_{1,1} & B_{1,2} & \cdots & B_{1,R-1} & B_{1,R} \\ \vdots & \ddots & & & \vdots \\ \vdots & & B_{r',r} & & \vdots \\ \vdots & & & \ddots & \vdots \\ B_{N,1} & B_{N,2} & \cdots & B_{N,R-1} & B_{N,R} \end{pmatrix}, \tag{A4}$$

$$B_{r',r} = \begin{pmatrix} C_{1,1} & C_{1,2} & \cdots & C_{1,Q-1} & C_{1,Q} \\ \vdots & \ddots & & & \vdots \\ \vdots & & C_{q',q} & & \vdots \\ \vdots & & & \ddots & \vdots \\ C_{N,1} & C_{N,2} & \cdots & C_{N,Q-1} & C_{N,Q} \end{pmatrix}, \tag{A5}$$

and

$$C_{q',q} = \begin{pmatrix} a_{1,1} & a_{1,2} & \cdots & a_{1,P-1} & a_{1,P} \\ \vdots & \ddots & & & \vdots \\ \vdots & & a_{p',p} & & \vdots \\ \vdots & & & \ddots & \vdots \\ a_{N,1} & a_{N,2} & \cdots & a_{N,P-1} & a_{N,P} \end{pmatrix}. \tag{A6}$$

Each component in Eq. (A6) is a function of indices p, p', q, q', r, and r'. They are calculated by substituting the data sampling position $\mathbf{x}_{p'q'r'} = (x_{1,p'}, x_{2,q'}, x_{3,r'})$ to the basis functions as

$$a_{p',p} = N_p(x_{1,p'}) N_q(x_{2,q'}) N_r(x_{3,r'}), \tag{A7}$$

where $1 \leqslant p \leqslant P$, $1 \leqslant q \leqslant Q$, $1 \leqslant r \leqslant R$, and $1 \leqslant p', q', r' \leqslant N$.

Suppose that a data sampling point is located at $x_{1,p'}$ along the x_1 axis between two internal nodes $\xi_{1,k}$ and $\xi_{1,k+1}$ such that $\xi_{1,k} < x_{1,p'} < \xi_{1,k+1}$. Because of the piecewise property represented in Eq. (9), only m basis functions N_p for $p = k+1, k+2, \ldots, k+m$ take nonzero values, where m is the rank of the basis function. N_q and N_r have the similar piecewise property making the matrices in Eqs. (A4)–(A6) band-limited.

For example, when the rank is set at four, the number of nonoverlapping nodes is one, and $P(=Q=R=N)$ equals 5, the internal nodes and data sampling points may, respectively, locate at $\xi_{1,p}, \xi_{2,q}, \xi_{3,r} = 0,0,0,0,0.5,1,1,1,1 (-3 \leqslant p,q,r \leqslant 5)$ and $x_{1,p'}, x_{2,q'}, x_{3,r'} = 0, 0.25, 0.5, 0.75, 1$ $(1 \leqslant p', q', r' \leqslant 5)$ along each axis of a $(0,1) \times (0,1) \times (0,1)$ cubic region. The basis functions constructed from these settings are illustrated in Fig. 4. Then the matrix A can be written as

$$A = \begin{pmatrix} B_{1,1} & O & O & O & O \\ B_{2,1} & B_{2,2} & B_{2,3} & B_{2,4} & O \\ O & B_{3,2} & B_{3,3} & B_{3,4} & O \\ O & B_{4,2} & B_{4,3} & B_{4,4} & B_{4,5} \\ O & O & O & O & B_{5,5} \end{pmatrix}, \tag{A8}$$

where

$$B_{r',r} = \begin{pmatrix} C_{1,1} & O & O & O & O \\ C_{2,1} & C_{2,2} & C_{2,3} & C_{2,4} & O \\ O & C_{3,2} & C_{3,3} & C_{3,4} & O \\ O & C_{4,2} & C_{4,3} & C_{4,4} & C_{4,5} \\ O & O & O & O & C_{5,5} \end{pmatrix} \tag{A9}$$

and

$$C_{q',q} = \begin{pmatrix} a_{1,1} & 0 & 0 & 0 & 0 \\ a_{2,1} & a_{2,2} & a_{2,3} & a_{2,4} & 0 \\ 0 & a_{3,2} & a_{3,3} & a_{3,4} & 0 \\ 0 & a_{4,2} & a_{4,3} & a_{4,4} & a_{4,5} \\ 0 & 0 & 0 & 0 & a_{5,5} \end{pmatrix}. \tag{A10}$$

APPENDIX B: EVALUATION OF B-SPLINE BASIS FUNCTION AND ITS DERIVATIVE

Let ξ_p $(1-m' \leqslant p \leqslant P)$ represent a set of internal nodes and $N_p(x)$ $(1 \leqslant p \leqslant P)$ B-spline basis functions with the rank of m', where P denotes the number of basis functions $(P = n+m')$ and n is that of nonoverlapping nodes (see Sec. III). Assume that x is a specific axis value between two successive nodes as $\xi_{p'-1} \leqslant x < \xi_{p'}$. From the piecewise property, only m' basis functions take nonzero values for x. If we consider a single-variate spline function $S(x)$, it can be written from this piecewise property as

$$S(x) = \sum_{p=1}^{P} c_p N_p(x) = c_{p'} N_{p'}(x) + c_{p'+1} N_{p'+1}(x) + \cdots + c_{p'+m'-1} N_{p'+m'-1}(x).$$

When the values of the weights c_p are determined from the interpolation condition, it is clear that one can evaluate $S(x)$ and its derivative $dS(x)/dx$ by calculating $N_p(x)$ and $dN_p(x)/dx$ for $p = p', p'+1, \ldots, p'+m'-1$.

$N_p(x)$ and $dN_p(x)/dx$ are defined as

$$N_p(x) = (\xi_p - \xi_{p-m'})M_p^{(m')}(x) \tag{B1}$$

and

$$\frac{dN_p(x)}{dx} = (\xi_p - \xi_{p-m'})\frac{dM_p^{(m')}(x)}{dx}, \tag{B2}$$

where $M_p^{(m')}(x)$ represents the divided difference of the truncated power function of rank m', as described in Sec. III. By utilizing de Boor's algorithm (de Boor, 1972), $M_p^{(m')}(x)$ and $dM_p^{(m')}(x)/dx$ can be simultaneously computed for $x(\xi_{p'-1} \leqslant x < \xi_{p'})$ in a recurring formula with respect to p and m as

$$M_p^{(m)}(x) = \frac{(x - \xi_{p-m})M_{p-1}^{(m-1)}(x) + (\xi_p - x)M_p^{(m-1)}(x)}{\xi_p - \xi_{p-m}} \tag{B3}$$

and

$$\frac{dM_p^{(m)}(x)}{dx} = \frac{d}{dx}\frac{(x - \xi_{p-m})M_{p-1}^{(m-1)}(x) + (\xi_p - x)M_p^{(m-1)}(x)}{\xi_p - \xi_{p-m}}, \tag{B4}$$

where $m=2,3,\ldots,m'$ and $p=p',p'+1,p'+2,\ldots,p'+m-1$. The initial conditions are given as

$$M_{p'}^{(1)}(x) = \frac{1}{\xi_p - \xi_{p-1}} \tag{B5}$$

and

$$\frac{dM_{p'}^{(1)}(x)}{dx} = 0. \tag{B6}$$

In addition, the terms $M_{p'-1}^{(m)}(x)$, $M_{p'+m}^{(m)}(x)$, $dM_{p'-1}^{(m)}(x)/dx$, and $dM_{p'+m}^{(m)}(x)/dx$ are all set at zero in the recursion.

With these conditions, the recursion formula (B3) and (B4) first calculates $M_p^{(2)}(x)$ and $dM_p^{(2)}(x)/dx$ for $p=p'$ and $p'+1$, where $M_{p'-1}^{(1)}(x)=M_{p'+1}^{(1)}(x)=0$ and $dM_{p'-1}^{(1)}(x)/dx = dM_{p'+1}^{(1)}(x)/dx=0$. Then, it proceeds to the next step where m is set at 3 and p at p', $p'+1$, and $p'+2$ with conditions $M_{p'-1}^{(2)}(x)=M_{p'+2}^{(2)}(x)=0$ and $dM_{p'-1}^{(2)}(x)/dx=dM_{p'+2}^{(2)}(x)/dx=0$. The procedure is repeated until m reaches m'. Finally, $N_p(x)$ and $dN_p(x)/dx$ can be calculated from $M_p^{(m')}(x)$ and $dM_p^{(m')}(x)/dx$ for $p=p',p'+1,\ldots,p'+m'-1$. The above procedure can be applied to the three-variate spline as well by computing $N_p(x_1)$,$N_q(x_2)$, and $N_r(x_3)$ independently.

[1]It was proved in the following literature that the Marquardt method has a quadratic convergence under a specific condition. Dan, H., Yamashita, N., and Fukushima, M. (**2002**). "Convergence properties of the inexact Levenberg–Marquardt method under local error bound," Optimization Methods and Software **17**, 605–626.

[2]The measurement accuracy of the dipole model was investigated using a software TAPADCon.exe (version 2.20) downloaded from the following homepage: *http://www.phonetik.uni-muenchen.de/~andi/EMAPage/*. Calibration and test data were measured using the AG500 system and the automatic position calibrator, where the size of these regions was the same as that used for the spline field model. We used a software Calview.exe (Carstens Medizinelektronik GmbH) to calibrate the gain parameter of the dipole field model, and TAPADCon.exe to estimate the receiver position. It should be noted that the direction of the axis of the receiver coil in the test set was the same as that in the calibration set, and it was set in parallel to the x_1 and x_2 axes to measure the mean error.

[3]In the experiment, the direction of the axis of the receiver coil was manually adjusted by using the received signal strength as the reference. At the origin, the direction of the magnetic flux is orthogonal with each other for transmitting coils S1, S3, and S5 (see Fig. 2). Therefore, the axis of the receiver coil can be set, for example, in parallel to the x_1 axis by maximizing the received signal from S1 and jointly by minimizing the signals from S3 and S5. The orientation of the receiver coil is also determined relative to the x_1 axis by adjusting the received signal from S1 as $A\cos\theta$, where θ is the rotational angle and A is the maximum signal amplitude. This adjustment method is possibly the best way, but not perfect, to determine the coil direction for gathering a set of calibration data. Even when the coil is perpendicular to the magnetic flux, the received signal from that magnetic field does not become zero because of some noisy offset component. In addition, it is rather difficult to simultaneously minimize the signals coming from two transmitting coils. If the coil direction is not perfectly adjusted, the measured calibration data cannot represent each orthogonal component of the actual magnetic field precisely and it will lead to an increase of the measurement error.

Atal, B. S., Chang, J. J., Mathews, M. V., and Tukey, J. W. (**1978**). "Inversion of articulatory-to-acoustic transformation in the vocal tract by a computer-sorting technique," J. Acoust. Soc. Am. **63**, 1535–1555.

Baer, T., Gore, J. C., Gracco, L. C., and Nye, P. W. (**1991**). "Analysis of vocal tract shape and dimensions using magnetic resonance imaging: Vowels," J. Acoust. Soc. Am. **90**, 799–828.

Chiba, T., and Kajiyama, M. (**1941**). *The Vowel, Its Nature and Structure* (Tokyo Kaisenkan, Tokyo).

de Boor, C. (**1972**). "On calculating with B-splines," J. Approx. Theory **6**, 50–62.

Dennis, J. E., and Schnabel, R. B. (**1983**). *Numerical Methods For Unconstrained Optimization and Nonlinear Equations* (Prentice–Hall, Englewood Cliffs, NJ).

Dierckx, P. (**1993**). *Curve and Surface Fitting With Splines* (Oxford University Press, Oxford).

Fujimura, O., Ishida, Y., and Kiritani, S. (**1973**). "Computer-controlled radiography for observation of movements of articulatory and other human organs," Comput. Biol. Med. **3**, 371–384.

Gracco, V. L., and Nye, P. W. (**1993**). "Magnetometry in speech articulation research: Some misadventures on the road to enlightenment," *Proceedings of the ACCOR Workshop on Electromagnetic Articulography in Phonetic Research*, FIPKM 31, der Universität München, pp. 91–104.

Harshman, R., Ladefoged, P., and Goldstein, L. (**1977**). "Factor analysis of tongue shapes," J. Acoust. Soc. Am. **62**, 693–707.

Hixon, T. J. (**1971**). "An electromagnetic method for transducing jaw movements during speech," J. Acoust. Soc. Am. **49**, 603–606.

Hoole, P. (**1993**). "Methodological considerations in the use of electromagnetic articulography in phonetic research," *Proceedings of the ACCOR Workshop on Electromagnetic Articulography in Phonetic Research*, FIPKM 31, der Universität München, pp. 143–64.

Kaburagi, T., and Honda, M. (**1994a**). "An ultrasonic method for monitoring tongue shape and the position of a fixed point on the tongue surface," J. Acoust. Soc. Am. **95**, 2268–2270.

Kaburagi, T., and Honda, M. (**1994b**). "Determination of sagittal tongue shape from the positions of points on the tongue surface," J. Acoust. Soc. Am. **96**, 1356–1366.

Kaburagi, T., and Honda, M. (**1997**). "Calibration methods of voltage-to-distance function for an electro-magnetic articulometer (EMA) system," J. Acoust. Soc. Am. **101**, 2391–2394.

Kaburagi, T., and Honda, M. (**1998**). "Determination of the vocal tract spectrum from the articulatory movements based on the search of an articulatory-acoustic database," *Proceedings of the International Conference on Spoken Language Processing* (ICSLP98), pp. 433–436.

Kaburagi, T., and Honda, M. (**2001**). "Dynamic articulatory model based on multidimensional invariant-feature task representation," J. Acoust. Soc. Am. **110**, pp. 441–452.

Kaburagi, T., and Honda, M. (**2002**). "Electromagnetic articulograph based on a nonparametric representation of the magnetic field," J. Acoust. Soc. Am. **111**, 1414–1421.

Kiritani, S., Itoh, K., and Fujimura, O. (**1975**). "Tongue-pellet tracking by a computer-controlled x-ray microbeam system," J. Acoust. Soc. Am. **57**, 1516–1520.

Maeda, S. (**1990**). "Compensatory articulation during speech: Evidence

from the analysis and synthesis of vocal-tract shapes using an articulatory model," in *Speech Production and Speech Modeling*, edited by W. J. Hardcastle and A. Marchal (Kluwer, Dordrecht), pp. 131–150.
Marquardt, D. W. (**1963**). "An algorithm for least squares estimation of nonlinear parameters," J. Soc. Ind. Appl. Math. **11**, 431–441.
Morrish, K., Stone, M., Sonies, B., Kurtz, D., and Shawker, T. (**1984**). "Characterization of tongue shape," Ultrason. Imaging **6**, 37–47.
Narayanan, S., Nayak, K., Lee, S., Sethy, A., and Byrd, D. (**2004**). "An approach to real-time magnetic resonance imaging for speech production," J. Acoust. Soc. Am. **115**, 1771–1776.
Perkell, J. S. (**1969**). *Physiology of Speech Production: Results and Implications of a Quantitative Cineradiographic Study*, Research Monograph No. 53 (MIT Press, Cambridge).
Perkell, J. S., Cohen, M. H., Svirsky, M. A., Matthies, M. L., Garabieta, I., and Jackson, M. T. T. (**1992**). "Electromagnetic midsagittal articulometer (EMMA) systems for transducing speech articulatory movements," J. Acoust. Soc. Am. **92**, 3078–3096.
Raab, F. H., Blood, E. B., Steiner, T. O., and Jones, H. R. (**1979**). "Magnetic position and orientation tracking system," IEEE Trans. Aerosp. Electron. Syst., **AES-15**, 709–717.
Rokkaku, M., Hashimoto, K., Imaizumi, S., Niimi, S., and Kiritani, S. (**1986**). "Measurements of the three-dimensional shape of the vocal tract based on the magnetic resonance imaging technique," Ann. Bull. RILP **20**, 47–54.
Schönle, P. W., Gräbe, K., Wenig, P., Höhne, J., Schrader, J., and Conrad, B. (**1987**). "Electromagnetic articulography: use of alternating magnetic fields for tracking movements of multiple points inside and outside the vocal tract," Brain Lang **31**, 26–35.
Schönle, P. W., Müller, C., and Wenig, P. (**1989**). "Echtzeitanalyse von orofacialen Bewegungen mit Hilfe der elektromagnetischen Artikulographie," Biomed. Tech. **34**, 126–130.
Schumaker, L. L. (**1981**). *Spline Functions: Basic Theory*. (Wiley-Interscience, New York).
Shawker, T. H., Stone, M., and Sonies, B. C. (**1985**). "Tongue pellet tracking by ultrasound: Development of a reverberation pellet," J. Phonetics **13**, 135–146.
Sondhi, M. M. (**1979**). "Estimation of vocal-tract areas: The need for acoustical measurements," IEEE Trans. Acoust., Speech, Signal Process. **ASSP–27**, pp. 268–273.
Sonoda, Y. (**1974**). "Observation of tongue movement employing magnetometer sensor," IEEE Trans. Magn.. **MAG-10**, 954–957.
Stone, M. (**1990**). "A three-dimensional model of tongue movement based on ultrasound and x-ray microbeam data," J. Acoust. Soc. Am. **87**, 2207–2217.
Stone, M., and Lundberg, A. (**1996**). "Three-dimensional tongue surface shapes of English consonants and vowels," J. Acoust. Soc. Am. **99**, 3728–3737.
Stone, M., Shawker, T. H., Talbot, T. L., and Rich, A. H. (**1988**). "Cross-sectional tongue shape during the production of vowels," J. Acoust. Soc. Am. **83**, 1586–1596.
Suzuki, S., Okadome, T., and Honda, M. (**1998**). "Determination of articulatory positions from speech acoustics by applying dynamic articulatory constraints," *Proceedings of the International Conference on Spoken Language Processing* (ICSLP98), pp. 2251–2254.
Tuller, B., Shao, S., and Kelso, J. A. S. (**1990**). "An evaluation of an alternating magnetic field device for monitoring tongue movements," J. Acoust. Soc. Am. **88**, 674–679.
Zierdt, A. (**1993**). "Problems of electromagnetic position transduction for a three-dimensional articulographic measurement system," *Proceedings of the Accor Workshop on Electromagnetic Articulography in Phonetic Research*, FIPKM 31, der Universität München, pp. 137–142.
Zierdt, A., Hoole, P., and Tillmann, H. G. (**1999**). "Development of a system for three-dimensional fleshpoint measurement of speech movements," *Proceedings of the International Congress on Phonetic Sciences* (ICPhS99), pp. 73–76.
Zierdt, A., Hoole, P., Honda, M., Kaburagi, T., and Tillmann, H. G. (**2000**). "Extracting tongues from moving heads," *Proceedings of the 5th Seminar on Speech Production*, pp. 313–316.

Modeling the articulatory space using a hypercube codebook for acoustic-to-articulatory inversion

Slim Ouni[a)]
Perceptual Science Laboratory, University of California—Santa Cruz, Santa Cruz, California 95064

Yves Laprie[b)]
LORIA, UMR 7503, BP 239, 54506 Vandœuvre-lès-Nancy Cedex, France

(Received 30 August 2003; revised 14 February 2005; accepted 1 April 2005)

Acoustic-to-articulatory inversion is a difficult problem mainly because of the nonlinearity between the articulatory and acoustic spaces and the nonuniqueness of this relationship. To resolve this problem, we have developed an inversion method that provides a complete description of the possible solutions without excessive constraints and retrieves realistic temporal dynamics of the vocal tract shapes. We present an adaptive sampling algorithm to ensure that the acoustical resolution is almost independent of the region in the articulatory space under consideration. This leads to a codebook that is organized in the form of a hierarchy of hypercubes, and ensures that, within each hypercube, the articulatory-to-acoustic mapping can be approximated by means of a linear transform. The inversion procedure retrieves articulatory vectors corresponding to acoustic entries from the hypercube codebook. A nonlinear smoothing algorithm together with a regularization technique is then used to recover the best articulatory trajectory. The inversion ensures that inverse articulatory parameters generate original formant trajectories with high precision and a realistic sequence of the vocal tract shapes.
[DOI: 10.1121/1.1921448]

PACS numbers: 43.70.−h, 43.70.Bk, 43.70.Aj [DOS] Pages: 444–460

I. INTRODUCTION

Estimating vocal tract shape from speech signal has received considerable attention because it offers new perspectives for speech processing. Indeed, recovering the vocal tract shape would enable knowing how a speech signal has been articulated. This potential knowledge could give rise to a number of breakthroughs in automatic speech processing. For speech coding, this would allow spectral parameters to be replaced by a small number of articulatory parameters[1] that vary slowly with time. In the case of automatic speech recognition the location of critical articulators could be exploited[2] to discard some acoustic hypotheses. For language acquisition and second language learning this could offer articulatory feedbacks. Lastly, in the domain of phonetics, inversion would enable knowing how sounds were articulated without requiring medical imaging or other measurement techniques.

Most of the acoustic-to-articulatory methods rest on an analysis-by-synthesis approach. Indeed, among the variety of acoustic signals the ear is exposed to, speech is one of the few for which a sufficiently good numerical simulation (including the deformations of the vocal tract geometry together with the resolution of the acoustical equations) is available. One of the essential issues is to evaluate the precision required by this numerical model to guarantee that sufficiently accurate and relevant information is recovered so that it can be interpreted from a phonetic point of view. The precision issue concerns both the geometric measures giving the vocal tract shape and the dynamic commands that control the vocal tract shape over time.

An inversion method as neutral as possible with respect to the articulatory behavior of the vocal tract should be devised. That is to say the inversion method should not provide particular solutions and omit other solutions. We will then study how modeling errors and with external constraints provided by either phonetic, physiological knowledge, x-ray data or the tracking of visible articulators influence results.

Using an analysis-by-synthesis approach means that the articulatory-to-acoustic mapping is used directly or indirectly in the inversion. Generally, the mapping is used indirectly, either explicitly, in the form of a table giving acoustic parameters (in general formants frequencies) for well chosen articulatory points (see Larar *et al.*[3] for instance), or implicitly, in the form of neural networks.[4] An articulatory synthesizer built on an articulatory model is generally used to generate a table (also called codebook) or to provide the training data for the neural network. The quality of the table construction strongly influences inverse solutions recovered since these trajectories use vectors of articulatory parameters of the table.

In our work, we want to develop an inversion method that easily enables the evaluation of constraints that can be added to reduce the underdetermination of the problem, independently of the inversion algorithm itself. The evaluation comprises both the acoustical distance between resynthesized and measured acoustic parameters together with the realism of the temporal dynamics of the recovered vocal tract shapes. Thus, this requires that a complete description of the possible inverse solutions is potentially easily available. For these reasons, we have developed an adaptive sampling al-

[a)]Electronic mail: slim@fuzzy.ucsc.edu
[b)]Electronic mail: laprie@loria.fr

gorithm to ensure that the acoustic resolution is almost independent of the region under consideration in the articulatory space. The adaptive sampling leads to a codebook that is organized in the form of a hierarchy of hypercubes, and ensures that, within each hypercube, the articulatory-to-acoustic mapping can be approximated by means of a linear transform. During the inversion, all the articulatory points that produce measured formants have to be found. Then, the best articulatory trajectories need to be constructed. This amounts to finding the best paths given the articulatory points recovered at the first step.

In this paper, we present the difficulties of the inversion and how the problems are usually resolved. Then, we present our inversion method in detail: we start by presenting the hypercube codebook generation method, the inversion using this codebook and the variational method to retrieve the temporal dynamics of the vocal tract shapes along time.

II. THE INVERSION PROBLEM

The articulatory-to-acoustic mapping can be defined as

$$A(\mathbf{x}) = \mathbf{b} \tag{1}$$

where $\mathbf{x}$ is an articulatory vector which gives the vocal tract shape and $\mathbf{b}$ is an acoustic vector, here the first three formants. A: $X \mapsto B$ is a nonlinear and many-to-one mapping from X, the articulatory domain, into B the acoustic domain. The inverse mapping consists of retrieving $\mathbf{x}$ from $\mathbf{b}$. $\mathbf{b}$ is evaluated from the speech signal, and therefore is only an approximation of the real formants. Indeed, formants are obtained by a formant tracking algorithm (see Laprie and Berger,[5] for instance) that searches for the best interpretation of the spectral peaks in terms of formants.

In addition, the articulatory synthesizer represented by A is based on a two-dimensional (2D) articulatory model, which is an approximation of the mid-sagittal section of the vocal tract, and the reconstruction of the three-dimensional (3D) vocal tract is made by an approximate transformation.[6–8] It should be also noted that the articulatory model does not fit exactly the geometry of the particular speaker to be analyzed. Existing adaptation methods are based either on the determination of factor scales applied to the global length of the vocal tract or to mouth and pharynx sizes.[9,10] More precise adaptation methods (for instance in Mathieu and Laprie[11] that adjusts the motionless contour of the vocal tract) can be applied only when images of the vocal tract are available. This means that it is nearly impossible to obtain an articulatory model that exactly represents speaker's vocal tract since this kind of adaptation only concerns the static and not the dynamic characteristics of the articulatory model.

Moreover, the measurement space, i.e., frequencies of the first three formants, is fairly under-dimensioned compared to the object space since the number of articulatory parameters is greater than that of acoustic parameters. Therefore, there is an infinite number of solutions for one 3-tuple of formant frequencies as shown by Atal *et al.*[12]

These reasons explain why there does not exist any direct inversion method and why optimization methods are often used to tackle this problem as they enable the exploration of the solution space. The optimization based methods act on articulatory parameters or area functions to minimize an acoustic or spectral distance between generated and measured acoustic parameters. Generally, one considers that a solution, or at least a local optimum, is found when the gradient of the cost function vanishes. Usually, optimization methods rely on some iterative scheme that requires the knowledge of initial solutions. In the case of acoustic-to-articulatory inversion, the initial solutions are obtained by searching a codebook, or by means of an artificial neural network trained on selected articulatory and acoustic data.

As the solution space is potentially vast and solutions possibly not realistic from a phonetic point of view, constraints can be incorporated to focus the exploration in articulatory regions of interest. Schoentgen and Ciocea[13] introduced a local constraint based on either kinematic or potential energy to select one solution at each step of the inversion. More generally, a common solution used to address ill-posed problems is to add a regularizing term. Sorokin *et al.*[14] chose a regularizing term that prevents inverse solutions to deviate too much from the neutral position of articulators. They particularly studied how to set-up the compromise between the discrepancy term, i.e., the acoustical distance with respect to original formants, and the regularizing term according to the error on measured formants and the articulatory model. Despite its interest with respect to the reduction of underdetermination this regularizing term may prevent correct vocal tract shapes to be retrieved simply because they present high values for some articulatory parameters. Shapes close to those expected for /i/, /y/, /a/ or /u/ could thus be penalized. We therefore advocate for a dynamic regularizing term (see Sec. VII A) that involves the temporal evolution of articulatory parameters. The expected advantage is that this gives rise to more natural and efficient constraints imposed on the regularity of articulatory parameters, and not directly on the values of these parameters. Furthermore, it provides an efficient manner to jointly improve the acoustical proximity to original acoustical data and the regularity of articulatory trajectories.

Neural network methods have also become very popular to address the inverse problem[15–20] because they propose an efficient way of exploring the solution space. However, it should be noted that these methods rely on an implicit sampling of the articulatory space for the training stage. Therefore, their main advantage lies instead in their ability to represent articulatory knowledge in a compact form rather than in their coverage of the articulatory space. The closer the training examples are to the solution the more accurate the result. For all the inverse methods, and particularly for neural based methods, because the sampling is implicit, the corpus of data used for training should be representative of the nonlinearities of the articulatory-to-acoustic mapping. For these reasons, special attention must be paid to generating codebooks, or more generally, sampling of the articulatory space.

Once allowable inverse solutions have been found at every time of the utterance some minimum path algorithm must be applied to recover trajectories for every articulatory parameter. This search can be carried out by using dynamic programming[21,1] or neural networks[22] that were trained to

identify dynamic patterns of the articulators. In many cases, the trajectories found can be optimized after choosing the startup solutions by means of genetic algorithms combined with a dynamic articulatory model[23] or more generally a gradient method.[24]

III. WHICH ARTICULATORY MODEL FOR INVERSION?

The choice of the vocal tract representation is crucial since it determines the number of parameters to recover. As the acoustic data are generally the frequencies of the first three formants, an as-concise-as-possible description must be adopted to reduce the indeterminacy of the problem. However, the phonetic exploitation of articulatory models goes against models that describe the vocal tract with a very small number of parameters, e.g., some area function models, even if they enable an excellent frequency precision as that used by Schoentgen and Ciocea.[13]

For this reason we accepted Maeda's model that approximates the sagittal slice of the vocal tract instead of an area function model[25–29] whose faithfulness with respect to the human vocal tract cannot be guaranteed. This model, as others, relies on the processing of vocal tract images (either x-ray images for Maeda[30] and Gabioud[31] or MRI for Badin[32] and Engwall[33]). Unlike purely geometric models, articulatory parameters correspond to deformations of the vocal tract produced by human speakers. Consequently, these models cover the domain of vocal tract shapes that a human speaker can produce well with a relatively small number of parameters—between 7 and 9. Note that the third dimension (section areas) must be approximated from the knowledge of the sagittal slice which is only 2D information. This would not be the case with true 3D models such as those of Badin and Engwall[32,33] for instance. However, we accepted Maeda's model because it is derived from a sufficiently large number of sagittal slices, and consequently provides a good coverage of possible articulatory configurations, which is not the case for true 3D models that exploit only a small number of MRI images. Another strong point of Maeda's model is the possibility to adapt it to a new speaker easily by modifying pharynx and mouth sizes.

Maeda's model was constructed by applying a factor analysis method derived from principal component analysis to vocal tract contours.[30,34] These contours were extracted by hand from x-ray images of vowels and projected onto a semipolar coordinate system that enables a one-dimensional parametrization of contours. These measures were then centered and normalized before deformation modes were extracted by the factor analysis in the form of linear components. Each of the seven parameters of Maeda's articulatory model is allowed to vary over a range of $\pm 3\sigma$ (where σ is the standard deviation of that parameter). For convenience each parameter is normalized by dividing it by its standard deviation. Thus the normalized parameters all vary between -3 and 3. Seven factors (see Fig. 1) are used to describe vocal tract deformations because they cover more than 98% of the total variance.

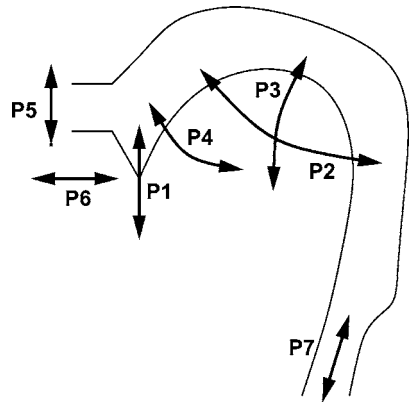

FIG. 1. Parameters of Maeda's articulatory model: P1 (jaw position, vertical movement), P2 (tongue dorsum position that can move roughly horizontally from the front to the back of the mouth cavity), P3 (tongue dorsum shape, i.e., rounded or unrounded), P4 (apex position; this parameter only deforms the apex part of the tongue by moving it up or down), P5 (lip height), P6 (lip protrusion), P7 (larynx height).

IV. METHODS FOR GENERATING ARTICULATORY CODEBOOKS

A codebook is a collection of a vast number of vocal tract shapes given by articulatory or area function parameters indexed by their acoustic parameters. The acoustic parameters, generally the first three formants, are obtained by using an articulatory synthesizer. The articulatory space should be spanned so that the codebook represents all of the possible geometric configurations of the vocal tract.

We experimented with three existing methods to generate a codebook. The first method is random sampling.[35,3] In this method, the codebook is generated by sampling articulatory parameters randomly. The inconvenience is that it does not respect the nonlinearities of the articulatory-to-acoustic mapping. Therefore, the codebook does not reliably represent the actual density of the articulatory space. The second method for generating codebooks is the root-shape interpolation.[3] This method consists of sampling the articulatory space in a nonuniform manner by sampling the most probable regions, i.e., those corresponding to the most often observed vocal tract shapes. To do this, two root-shapes are chosen among predefined shapes corresponding to vowels. The intermediate shapes produced by moving from one root shape to another linearly in the articulatory space are then added to the codebook. Sorokin and Trushkin[24] used this approach that allowed them to drastically reduce the size of the codebook to only 1900 nodes in the one-dimensional space of minimal cross-sectional area although their articulatory model comprises 17 parameters. The expected advantage of this method is that only realistic vocal tract shapes are taken into account. Preliminary experiments carried out by using a similar approach applied to Maeda's model have shown that this method suffers from two important weaknesses. The first is that there exists a possibly vast number of root shapes for each vowel or consonant. This results from the compensatory properties of the vocal tract geometry that probably are essential in the speech production process. In fact, in most, if not all cases, there is not a one-to-one relationship between an uttered sound and a particular vocal tract

configuration. Therefore, it is difficult to guarantee that root shapes accepted to derive the articulatory sampling are the most appropriate ones. It means that realistic vocal tract shapes may be "missed" by this sampling method. A second inconvenience is that moving from one shape to another by varying articulatory parameters linearly does not give rise to linear transitions of formant frequencies. This explains why parts of the acoustic space are sparsely covered. In Fig. 2, the acoustic space (F1-F2, F1-F3, and F2-F3 planes) is plotted for random sampling and root-shape codebooks. It appears clearly that the acoustic space produced with the root-shape method does not cover the whole possible acoustic space.

The third method for generating a codebook is the regular sampling of the articulatory space. The obvious weakness lies in the huge number of shapes generated even when the discretization is relatively rough. For instance, let us consider Maeda's model[30] that describes the vocal tract with seven parameters between -3σ and 3σ (σ is the standard deviation of the articulatory parameters). Using only ten steps to describe each articulatory parameter leads to about 8 000 000 shapes after unrealistic shapes have been eliminated. And to obtain a fine regular sampling of the seven parameters with a relatively rough sampling step equal to $1/3\sigma$ would lead to $19^7 \approx 900$ million vocal tract shapes, which becomes unrealistic from the point of view of both construction time and the codebook size required. Linear or polynomial interpolation could be used to reduce the size of a regularly sampling method.[36,37] However, this would require further processing to evaluate the precision of this interpolation.

The examination of the acoustic spreading of these three codebooks (see Fig. 2) together with preliminary inversion experiments have shown that they do not present accurate coverage of both the articulatory space and the acoustic space.

V. HYPERCUBE CODEBOOK

A. Introduction

The difficulty of generating codebooks lies in the fact that the relations between articulator positions and acoustics are non-linear.[38–41] In fact, there are articulatory regions where a small variation in articulatory parameters produces a large variation of acoustic parameters. And conversely, there are some regions where a large variation in articulatory parameters does not produce any significant acoustic changes.

Our approach aims at densely discretizing the articulatory space only in the regions where the mapping is highly nonlinear. For this purpose we use a hypercube structure to organize the codebook. In the next paragraphs, we describe how the codebook is generated.

B. Articulatory hypercubes

A hypercube of order N (N-hypercube) is a generalization in the N-dimensional space of a square in two-dimensional space and cube in the three-dimensional space. An N-hypercube is an N-dimensional convex polytope (N-polytope). An N-hypercube H_c is defined by its origin vertex $\mathbf{U}_0 \in IR^N$ (i.e., the vertex with the lowest coordinates) and the length $\ell \in IR$ of one edge. We denote this hypercube by $H_c(\mathbf{U}_0, \ell)$:

$$H_c(\mathbf{U}_0, \ell) = \prod_{j=1}^{N} [u_0^j, \ell], \tag{2}$$

where Π is the Cartesian product, ℓ the hypercube edge length, and $u_0^j \in IR$ is the jth component of $\mathbf{U}_0$. We represent a hypercube by its vertices. Let $\mathbf{V}_i$ be one of these vertices. The jth component v_i^j of $\mathbf{V}_i$ is calculated as follows:

$$v_i^j = u_0^j + \varphi_{ij}\ell, \tag{3}$$

where φ_{ij} is the jth digit of the number i written in binary form including leading zeroes (see Fig. 3). As we can note in Eq. (3), the hypercube is defined simply in terms of the origin coordinates and the edge length.

C. The hypercube generation method

Regardless of the articulatory or area function model used, the parameters vary within a limited range. As mentioned earlier, the articulatory parameters of Maeda's model vary between -3 and 3. Therefore the codebook is inscribed within a root hypercube denoted by $H_c^1(\mathbf{U}_0, \ell)$. Sampling the articulatory space amounts to finding reference points that limit linear regions. However, as the articulatory-to-acoustic mapping is not represented in a closed form some heuristic exploration and linearity evaluation have to be designed. Charpentier faced the same problem to sample parameters of the area function proposed by Ishizaka *et al.*[28] and proposed choosing these points by calculating the curvature of formant trajectories along articulatory trajectories obtained by varying one parameter at a time.[38] Reference points were chosen at regularly spaced intervals along the curvature. This solution cannot be used in the case of Maeda's model because there are more parameters and, above all, articulatory parameters do not control almost independent regions of the vocal tract as in the case of an area function model. The four jaw and tongue parameters, for instance, control the same region in the vocal tract and there are two levels of potential nonlinearities (from articulatory parameters to the area function, and from the area function to the acoustic parameters).

Therefore we devised a heuristic linearity test and evaluate its figure of merit by measuring the deviation between formants obtained by synthesis and those obtained by interpolation from codebook points (see Sec. V D). One of the issues is the choice of articulatory points where the deviation has to be calculated. Points can be chosen in each hypercube randomly, regularly with respect to each of the articulatory parameters or distributed according to another geometric strategy. This choice is important because most of the time spent for the codebook construction will be dedicated to evaluating linearity. Indeed, using only three, respectively, four, steps to sample each articulatory parameter gives, respectively, $3^7 = 2187$ and 16 384 tests. As the later solution would have led to an excessive construction time we accepted three regularly spaced samples for each articulatory parameter. This corresponds to middle points of segments formed by any two vertices (Fig. 3). For each segment the

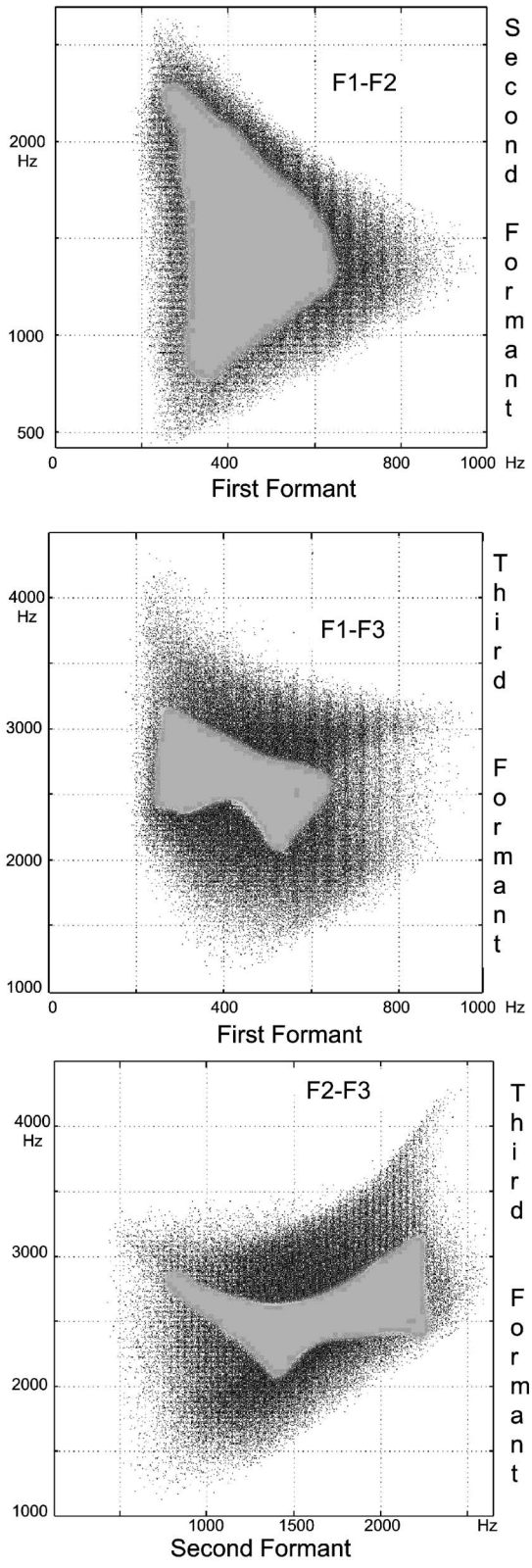

FIG. 2. Comparison of the first three formants of the root-shape and the random codebooks. We do not present the regular sampling codebook as it has almost the same covering space as the random codebook. The regions in light gray (respectively, dark gray) represent the acoustic space of the root-shape (respectively, random sampling) codebook. The random sampling codebook covers a space larger than that covered by the root-shape codebook.

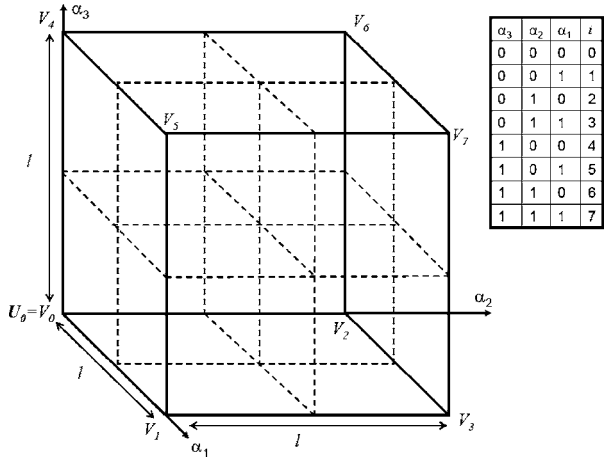

α_3	α_2	α_1	i
0	0	0	0
0	0	1	1
0	1	0	2
0	1	1	3
1	0	0	4
1	0	1	5
1	1	0	6
1	1	1	7

FIG. 3. For sake of clarity we represent a 3D hypercube. Note that the edge length is ℓ and U_0 is the origin of the hypercube. V_i $(i=0-7)$ are the vertices of the hypercubes. The linearity test is performed on the segments $[V_i, V_j]$ where $i \neq j$. If the test fails the hypercube is split into eight subhypercubes (eight is the number of the vertices in 3D). These subhypercubes are represented with dashed lines. The upper table gives the values of the parameter φ_{ij} for the eight vertices indexed from 0 to 7.

middle point interpolation takes into account only the two vertices and no other vertex of the hypercube. This means the linearity was assessed more than once for the midpoints, depending on how the two vertices are placed with respect to each other: one time for two contiguous vertices and 2^6 times for two vertices on the main diagonal, which correspond to the hypercube center. In all this gives $2^7 \times (2^7 - 1) = 8128$ linearity tests.

The test for linearity is carried out as follows: acoustic values, i.e., the first three formant frequencies, are linearly interpolated at the middle point between two vertices from the acoustic values calculated at these vertices and the result is compared against that directly given by the articulatory synthesizer, i.e.,

$$\text{abs}\left(\frac{F_a^i + F_b^i}{2} - f\left(\frac{p_a + p_b}{2}\right)\right) \leqslant \Delta\epsilon^i, \quad 1 \leqslant i \leqslant 3,$$

where i is the formant number, p_a, p_b are the two vertices, f represents the articulatory-to-acoustic mapping (the synthesizer), $\mathbf{F_a}$ and $\mathbf{F_b}$ the vector of the first three formants at the articulatory points p_a and p_b $[f(p_a) = \mathbf{F_a}$ and $f(p_b) = \mathbf{F_b}]$, and $\Delta\epsilon^i$ the predefined linearity threshold for formant i. The test succeeds if the three inequalities hold, and then, the articulatory-to-acoustic mapping is considered to be linear in the hypercube. Otherwise this hypercube is split into 2^7 equal subhypercubes and the linearity test is repeated for every new hypercube. This procedure is repeated recursively until the hypercube edge becomes smaller than a predefined value or no nonlinearity higher than the predefined threshold exists anymore. $\Delta\epsilon^i$ can be set experimentally for the first three formants. An articulatory region represented by a hypercube is considered linear (i.e., the articulatory-to-acoustic mapping is linear), if the 8128 tests succeed, otherwise, this region is considered nonlinear. As the allowable articulatory space, i.e., the space where articulatory parameters yield an open vocal tract, does not fit exactly in the hypercube, there are vertices for which acoustic parameters cannot be calcu-

lated because they correspond to a vocal tract shape with a complete constriction. These vertices thus belong to forbidden regions (the term used by Atal *et al.*[12]). When forbidden vertices are found in a hypercube, the hypercube is decomposed in order to obtain hypercubes where all the vertices are allowable. Boundaries of forbidden regions are thus well defined (Fig. 4). Nevertheless, there is a risk in creating a large number of small hypercubes to get a very precise boundary whereas this articulatory region is probably of little interest in practice. Therefore, a small hypercube with lowest edge size below which the decomposition stops is not accepted.

The result of these successive recursive decompositions is a hierarchical structure composed of hypercubes of different sizes; the bigger the hypercube, the more linear the articulatory-to-acoustic mapping within this articulatory region. Only the origin of the hypercube (in the articulatory space), the length of one edge and the acoustic values of the vertices are saved in the codebook. The advantage of the hierarchical structure is to accelerate the search procedure in the codebook.

D. Experimental evaluation of the hypercube codebook

We generated a first hypercube codebook (CB1), using the linearity test with threshold values as follows: $\Delta\epsilon=50$ Hz for F1, 75 Hz for F2, and 100 Hz for F3. This hypercube hierarchy is composed of 390 000 hypercubes. Then, we generated another codebook (CB2) using the linearity test threshold $\Delta\epsilon=0.3$ bark. The number of the hypercubes is 128 000. The average time spent for each linearity test, i.e., the calculation and comparison of 8128 middle points, thus represents a non-negligible time. It turns out that large size hypercubes at initial stages of the hypercube construction are eliminated because several vertices are outside the allowable articulatory space.

To evaluate the quality of sampling we used the codebook to calculate acoustic values by interpolating them from codebook entries. The interpolation was applied with respect to the hypercube center $\mathbf{P}_0$:

$$\mathbf{F_x}=\mathbf{F}_0+\mathbf{J_F}(\mathbf{P}_0)\cdot(\mathbf{P_x}-\mathbf{P_0}), \tag{4}$$

where $\mathbf{P_x}$ is the articulatory vector we calculate its acoustic image $\mathbf{F_x}$ for and $\mathbf{J_F}(\mathbf{P}_0)$ is the Jacobian matrix of $\mathbf{F}$ calculated at $\mathbf{P_0}$ by taking first differences. $\mathbf{P_0}$ can be chosen as the center or the nearest vertex of the hypercube $\mathbf{P_x}$ belongs to. We randomly chose 4000 articulatory vectors, 1850 of them representing valid area functions, then used the codebook CB1 to interpolate the acoustic values corresponding to the valid articulatory vectors. The mean error, i.e., the difference between formant frequencies calculated by the articulatory synthesizer and those interpolated from the codebook, does not exceed 10 Hz for F1 and F2, and 20 Hz for F3. Compared to the margin of error accepted for the codebook test linearity (50 Hz for F1, 75 Hz for F2, and 100 Hz for F3), it is clear that we have a good acoustic precision. For the second codebook CB2, that we used in the inversion experiments reported in Sec. VIII, we evaluated the acoustic precision on a much larger number of articulatory points. We randomly chose 1 000 000 articulatory vectors, 641 846 of them representing valid area functions. As shown in Table I the accuracy is very good since the overall mean error is less than 8 Hz. The precision obtained is better than that imposed during the codebook construction because, unlike the interpolation using the Jacobian matrix, the linearity test involves two vertices only to predict the unknown formant values. As can be noticed there is no significant precision difference between formants despite the bark scale that was used for linearity tests and should lead to a lower precision for F2 and F3. This is probably due to a certain redundancy between the linearity test applied to the three formants with different precisions. The most rigorous test is that for F1. Since the magnitude of formant frequency variations is roughly the same for the three formants the precision imposed on F1 gives the overall precision.

TABLE I. Acoustic precision of the interpolation (the precision is measured by comparing formant values interpolated from codebook points with those calculated by the articulatory synthesizer directly).

	Mean error (Hz)	Standard deviation (Hz)
F1	6.47	6.93
F2	7.90	9.96
F3	6.92	9.43

The above-reported tests confirm the expected properties of our codebook. Its main characteristic is that it offers a quasiuniform acoustic resolution because of the adaptive sampling. Therefore, the complete acoustic behavior of the articulatory model is accurately represented by this codebook.

VI. THE INVERSION METHOD EXPLORING THE SOLUTION SPACE

Our inversion method exploits the codebook by recovering the possible articulatory vectors for each acoustic entry of the signal to be inverted, i.e., the first three formants extracted at each time frame of the utterance by automatic formant tracking.[5] The second stage, i.e., the recovery of articulatory trajectories, is described in Sec. VII. For each acoustic entry, all the hypercubes whose acoustic image contains the acoustic entry are considered. The acoustic image is overestimated as the rectangular parallelepiped defined by minimal and maximal values of F1, F2, and F3. As the inclusion into hypercube is checked for each inverse solution (see Sec. VI B) this weaker assumption does not introduce any solution outside the hypercube.

A. The inversion method

The hypercube codebook is used to retrieve the articulatory parameters corresponding to the acoustic entry. All the hypercubes whose acoustic image contains the acoustic entry are examined. From now on, we only consider one hypercube to describe the inversion process. Let $\mathbf{F}$ be the acoustic vector (represented by the first three formants) to be inverted. Let H_c be the hypercube that contains articulatory vectors giving the acoustic vector $\mathbf{F}$. Let $\mathbf{P}$ be an articulatory vector (represented by the seven parameters of Maeda's articulatory

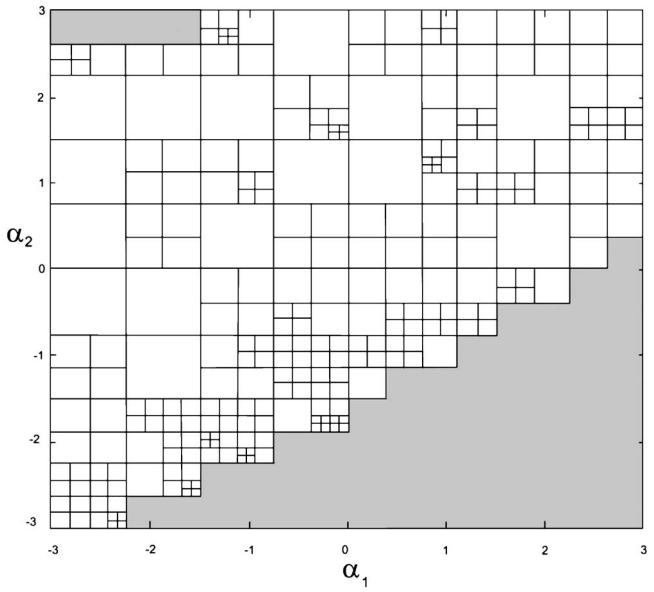

FIG. 4. A 2D partial representation of the hypercube codebook. For sake of clarity, we only present jaw and tongue (α_1, α_2). We clearly see that there are different regions more or less linear (i.e., the corresponding hypercubes are more or less big). Shaded regions are the forbidden.

model) that we are looking for. Using the Jacobian calculated at a particular point $\mathbf{P}_0$ in the hypercube (the center for instance) we approximate $\mathbf{F}$ by

$$\mathbf{F}=\mathbf{F_0}+\mathbf{J_F}(\mathbf{P_0})\cdot(\mathbf{P}-\mathbf{P_0}), \tag{5}$$

where $\mathbf{J_F}(\mathbf{P_0})$ is the Jacobian matrix of $\mathbf{F}$ calculated at $\mathbf{P_0}$ and $\mathbf{F_0}$ is the acoustic vector corresponding to $\mathbf{P_0}$.

Thus, to perform the inversion, we have to solve

$$\mathbf{F}-\mathbf{F_0}=\mathbf{J_F}(\mathbf{P_0})\cdot(\mathbf{P}-\mathbf{P_0}). \tag{6}$$

The matrix form is:

$$\begin{bmatrix} F^1-F_0^1 \\ F^2-F_0^2 \\ F^3-F_0^3 \end{bmatrix} = \begin{bmatrix} \frac{\partial F^1}{\partial \alpha_1} & \frac{\partial F^1}{\partial \alpha_2} & \cdots & \frac{\partial F^1}{\partial \alpha_7} \\ \frac{\partial F^2}{\partial \alpha_1} & \frac{\partial F^2}{\partial \alpha_2} & \cdots & \frac{\partial F^2}{\partial \alpha_7} \\ \frac{\partial F^3}{\partial \alpha_1} & \frac{\partial F^3}{\partial \alpha_2} & \cdots & \frac{\partial F^3}{\partial \alpha_7} \end{bmatrix} \begin{bmatrix} P^1-P_0^1 \\ P^2-P_0^2 \\ \vdots \\ P^7-P_0^7 \end{bmatrix}, \tag{7}$$

where F^i, F_0^i are the components of $\mathbf{F}$ and $\mathbf{F_0}$, i.e., the ith formant and P^i, P_0^i the components of $\mathbf{P}$ and $\mathbf{P_0}$. We chose the center of the hypercube as $\mathbf{P_0}$ because this guarantees that the underlying assumption of linearity is approximately correct everywhere in the hypercube with respect to this point. Equation (7) has the form

$$A\cdot\mathbf{x}=\mathbf{b}, \tag{8}$$

where A is the $(M\times N)$ Jacobian matrix, $\mathbf{b}$ and $\mathbf{x}$ are the acoustic and articulatory vectors. When M is less than N, A is singular and the $N-M$ dimensional space where vectors are transformed into zero is the null space. The general solution of Eq. (8) is given by a particular solution plus any vector from the null space. This means that adding a linear combination of the base vectors of the null space does not change formants. The SVD (*singular value decomposition*) method as described in Golub and Van Loan[42] gives one particular solution set, i.e., the one with the smallest norm $|x|^2$. Also, SVD constructs an orthonormal base of the null space. The particular solution together with the base of the null space completely describes the solution space. In our case, as $M=3$ (3 formants) and $N=7$ (7 articulatory parameters), the null space dimension is generally 4. To retrieve all the solutions for a given articulatory precision, the null space must be determined and sampled.

B. Sampling the null space

Let P_{SVD} be the particular solution given by the SVD method. A general solution is

$$\mathbf{P_s}=\mathbf{P_{SVD}}+\sum_{j=1}^{4}\beta_j\mathbf{v_j}, \tag{9}$$

where $\{\mathbf{v_j}\}_{j=1-4}$ is an orthonormal base of the null space and $\beta_{j=1-4}$ the coordinates in this space. Furthermore, this solution must belong to the hypercube where the linearity assumption holds. Therefore this solution is acceptable if

$$\mathbf{P_s}\in H_c\,. \tag{10}$$

Let α_{inf}^i and α_{sup}^i define the maximum and minimum values of the ith articulatory parameter in H_c (i.e., H_c is the Cartesian product $H_c=\Pi_{i=1}^{7}[\alpha_{\mathrm{inf}}^i,\alpha_{\mathrm{sup}}^i]$). Then we have

$$\alpha_{\mathrm{inf}}^i\leqslant P_{\mathrm{SVD}}^i+\sum_{j=1}^{4}\beta_j v_j^i\leqslant\alpha_{\mathrm{sup}}^i,\quad i=1-7, \tag{11}$$

where v_j^i is the projection of the jth basis vector of the null space onto the ith articulatory parameter. The matrix form of inequality (11) is

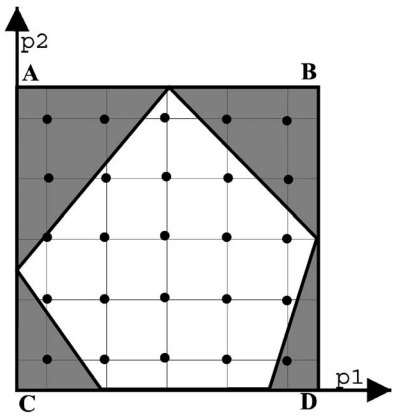

FIG. 5. The four-dimensional hypercube (for illustration, represented here by the square) is the smallest hypercube containing the 4-polytope (represented by the polygon). It is defined by the vertices A, B, C, D. The four-dimensional hypercube is discretized (the points represent the possible solutions) and the solutions that do not verify Eq. (10) are eliminated (the points lying outside the polygon).

$$\begin{bmatrix} \alpha_{\text{inf}}^1 \\ \alpha_{\text{inf}}^2 \\ \vdots \\ \alpha_{\text{inf}}^7 \end{bmatrix} \leqslant \begin{bmatrix} P_{\text{SVD}}^1 \\ P_{\text{SVD}}^2 \\ \vdots \\ P_{\text{SVD}}^7 \end{bmatrix} + \begin{bmatrix} v_1^1 & v_2^1 & v_3^1 & v_4^1 \\ v_1^2 & v_2^2 & v_3^2 & v_4^2 \\ \vdots & \vdots & \vdots & \vdots \\ v_1^7 & v_2^7 & v_3^7 & v_4^7 \end{bmatrix} \cdot \begin{bmatrix} \beta_1 \\ \beta_2 \\ \beta_3 \\ \beta_4 \end{bmatrix}$$

$$\leqslant \begin{bmatrix} \alpha_{\text{sup}}^1 \\ \alpha_{\text{sup}}^2 \\ \vdots \\ \alpha_{\text{sup}}^7 \end{bmatrix}. \tag{12}$$

This system defines a 4-polytope, i.e., a bounded intersection of four half-spaces. To completely define this 4-polytope, we need to find all the extreme points of this domain, since the polytope solution is the convex hull of these points and determine the space contained in the polytope. As far as we know, this problem, which is simple in dimension 2 (i.e., finding the intersection of a rectangle with a line), has not received any close form solution in the general case yet. This explains why we have developed this two-step algorithm to approximate the intersection. In the first step the smallest four-dimensional hypercube which contains the polytope is determined by linear programming. The second step consists in sampling this four-dimensional hypercube and keeping samples that belong to H_c. The four-dimensional hypercube is defined by its vertices which are given by the minimum and maximum values of β_i which satisfy inequalities of Eq. (12). The values of the β_i can be found by resolving the following eight linear programs:

(1) four linear programs defined by the inequalities of Eq. (12) to *maximize* β_i $(i=1-4)$, the objective function being the *maximization* of β_i.
(2) four linear programs defined by the inequalities of Eq. (12) to *minimize* β_i $(i=1-4)$, the objective function being the *minimization* of β_i.

By finding all the β_i, we can easily calculate the vertices of the 4-hypercube by replacing the β_i in Eq. (9). Then, this four-dimensional domain is sampled and solutions that do not belong to the hypercube H_c, i.e., Eq. (10), are eliminated (see Fig. 5).

For a given 3-tuple of formants and a hypercube whose image contains this 3-tuple of formants the number of inverse solutions directly depends on the sampling step of the null space. The smaller the sampling step, the smoother the trajectories recovered. We accepted three steps for each of the four dimensions of the null space which keeps the potential number of points at a reasonable value of $3^4=81$ while guaranteeing a sufficient smoothness of articulatory trajectories. Together with the hierarchical representation of the articulatory space, this null space exploration method provides a quasicomplete description of the inversion solution set.

We evaluated the acoustic precision of the inversion for 489 random 3-tuples of formants F1, F2, and F3 synthesized with the articulatory synthesizer. This yielded approximatively 4 million solutions. After resynthesis with the articulatory synthesizer, the acoustic values were compared with the original data. As shown in Table II, the accuracy is very good since the overall mean error is less than 11 Hz. It should be noted that this error is appreciably smaller than the frequency threshold of the linearity test used to decompose hypercubes. This indicates that even if the linearity test is potentially incomplete it is relatively strict. It is important to note that during the whole inversion process, as presented earlier, we did not use the articulatory synthesizer and all the inversion solutions were obtained by interpolation and sampling.

As shown earlier, this inversion method provides a quasiexhaustive description of all the possible vocal tract shapes that give a 3-tuple of formants, and with a very little error on formant frequencies. This method thus enables the investigation of articulatory constraints that can be added to guide inversion and to recover realistic articulatory trajectories. The key point is that this inversion method enables a

TABLE II. Acoustic precision of the inversion.

	ΔF1 (Hz)	ΔF2 (Hz)	ΔF3 (Hz)
Mean error	8.39	10.86	10.45
Standard deviation	10.03	12.11	12.53

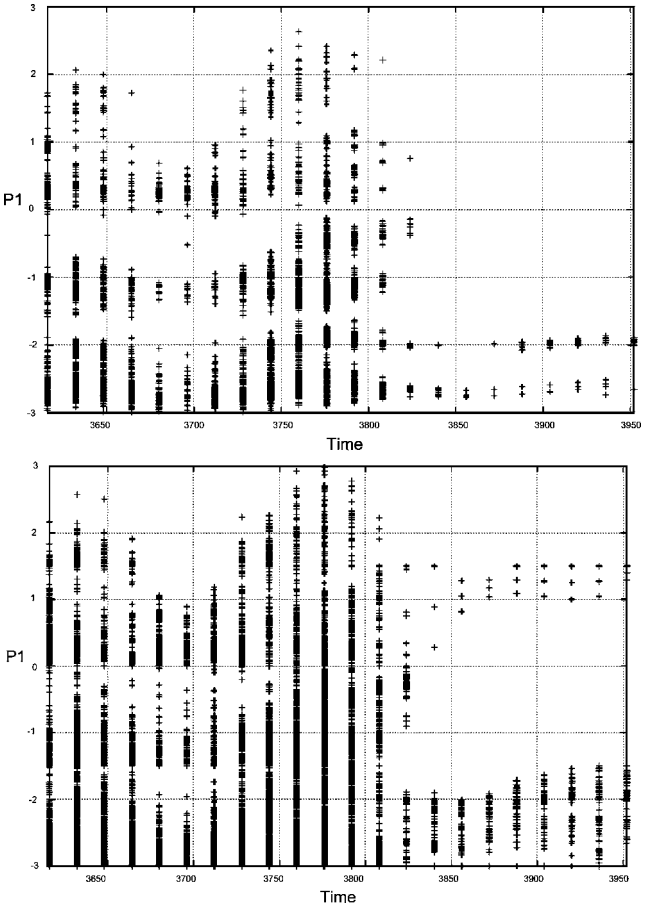

FIG. 6. Representation of the inversion solutions for the utterance [au] in the articulatory space (jaw parameter). The horizontal axis represents the time (in milliseconds) and the vertical axis represents the variation of one parameter expressed in standard deviations. The top graph presents all the solutions obtained by SVD without sampling the null space. The bottom graph presents solutions obtained by sampling the null space.

clear separation between the representation of the articulatory space and the incorporation of constraints or knowledge to guide inversion. Moreover, this inversion method provides potential tools to investigate articulatory variability of speech production and compensatory effects a speaker can exploit.

Figures 6 and 7 give inversion results of two speech sequences [au] and [ui] in the articulatory space for one articulatory parameter only (jaw parameter) for sake of clarity. For each sequence, the left graph presents the solution without sampling the null space, i.e., particular solutions given by the SVD method, and the right graph presents the solutions obtained by applying SVD and sampling the null space. Clearly, the solutions obtained after sampling the null space more finely cover the articulatory space.

VII. RECOVERING ARTICULATORY TRAJECTORIES

Recovering articulatory trajectories consists of choosing at each time an articulatory vector among those obtained by the above-presented inversion. This amounts to finding an ''articulatory path'' expressing the temporal sequence of the vocal tract shapes during the utterance to be inverted. The resulting articulatory trajectory should vary ''slowly'' (variations of articulatory parameters are small during an average pitch period, i.e., approximately 10 ms) and generates spectra as close as possible to those of the original speech. This corresponds to the satisfaction of two criteria: proximity to acoustic data and smoothness of articulatory trajectories. In this section, we present the overall inversion algorithm that combines these two criteria and works as follows:

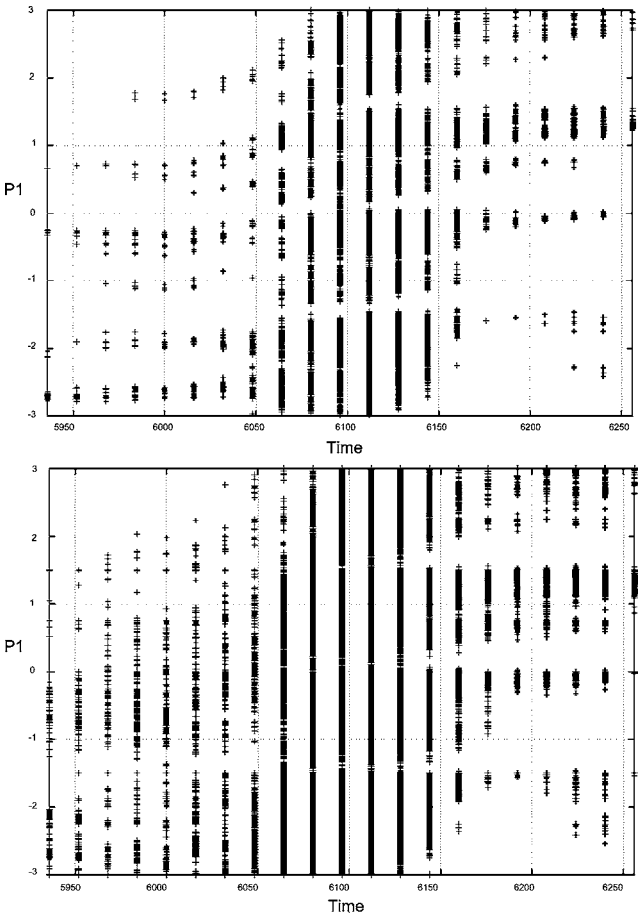

FIG. 7. Representation of the inversion solutions for the utterance [ui] in the articulatory space (jaw parameter). The horizontal axis represents the time (in milliseconds) and the vertical axis represents the variation of one parameter expressed in standard deviation. The first graph presents all the solutions obtained by SVD without sampling the null space. The second presents solutions obtained by sampling the null space.

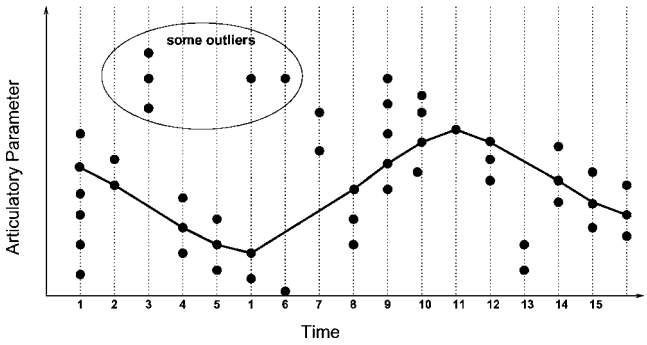

FIG. 8. Double selection achieved by the nonsmoothing algorithm: time frames and articulatory candidates. For clarity sake articulatory candidates are one-dimensional points. The articulatory candidates are given for each time frame (each vertical dotted line). The best trajectory is the solid line and contains some gaps (time frames 3, 6, 7, and 13) because the incorporation of outliers would decrease the quality of the whole trajectory.

(1) The first step of the inversion consists of recovering all of the inverse articulatory solutions at each point in time of the utterance to be processed by exploring the codebook.
(2) In the second step a nonlinear smoothing algorithm described in the following finds smooth articulatory trajectories from the knowledge of the sets of inverse points recovered at each point in time.
(3) The third step consists of regularizing the trajectories built by using the nonlinear smoothing algorithm. This regularization is achieved through a variational method.

The nonlinear smoothing algorithm used in the second step is derived from a nonlinear smoothing algorithm initially proposed by Ney[43] for postprocessing results of F0 determination. Let $s(i)$ be the set of inverse points retrieved at time frame i, and $S=(s(i)),\ 1\leqslant i\leqslant N$ the sequence of these sets over the utterance to be inverted. The construction of a trajectory gives rise to a double selection (see Fig. 8):

(i) the choice of time frames at which the trajectory is defined, i.e., the choice of a subsequence of S defined by a function j: $\bar{S}=(s(j(0))\ldots s(j(k))\ldots s(j(K)))$ where $K<N$ (N is the number of time frames) and j is a monotonic function: $0\leqslant j(k)<j(k+1)\leqslant N$.
(ii) the choice of one inverse point in each of the sets selected $s(j(0))\ldots s(j(k))\ldots s(j(K))$. The point chosen out of the set $s(j(k))$ is denoted $\alpha(j(k))$ ($\alpha(j(k))\in IR^7$) and the articulatory trajectory is therefore $\bar{A}=(\alpha(j(0))\ldots\alpha(j(k))\ldots\alpha(j(K)))$.

Let $f_j(t)$ be the jth formant frequency extracted from speech a time frame t, and $F_j(\alpha(j(k)))$ that computed by the acoustical simulation for the inverse point $\alpha(j(k))$. The cost of choosing $\alpha(j(k))$ after $\alpha(j(k-1))$ incorporates the acoustical distance together with the articulatory distance:

$$C(\alpha(j(k)),\alpha(j(k-1)))=\sum_{j=1}^{3}(f_j(t)-F_j(\alpha(j(k))))^2$$

$$+\lambda\sum_{i=1}^{7} m_i(\alpha_i(j(k))-\alpha_i(j(k-1)))^2, \quad (13)$$

where λ is the weight of the articulatory distance with respect to the acoustical distance. Based on this local cost, the overall cost function to be minimized is $D=\Sigma_{j=1}^{K}(C(\alpha(j(k)),\ \alpha(j(k-1)))-B)$ where B is a positive bonus (as proposed by Ney) that prevents the minimization of returning an empty trajectory. This bonus has been set to a constant value but it could render the probability that this inverse point can be articulated by the target subject. The minimization is solved by dynamic programming and returns the best articulatory trajectory.

The local smoothness depends on the quality of the inverse solutions, and particularly the step used to sample the null space. Furthermore, as mentioned earlier, trajectories may be incomplete. For these reasons, the best solution provided by the nonlinear smoothing algorithm is regularized through a variational method.

Variational regularization method. Any inversion method must lead to slowly changing parameters that generate spectra as close as possible to those of the original speech. This corresponds to satisfying two criteria: proximity to acoustic data and smoothness of articulatory trajectories. Generally, existing methods cannot allow for the two criteria at the same level, or at least must favor one criterion to the detriment of the other. Indeed, methods using dynamic programming often impose constraints upon the articulatory parameters dynamics. Then, a local optimization is used to improve the acoustic proximity with the input signal at each time of the utterance analyzed. In contrast, our regularizing method combines both local and global aspects. This method utilizes the well-known theory of variational calculus[44] which gives rise to an iterative process. This process starts with an initial solution (obtained by the nonlinear smoothing algorithm) and generates a sequence of articulatory trajectories which optimizes a cost function that combines acoustic distance and changing rate of articulatory parameters.

There are two major advantages of this method compared to many other existing methods. First, it involves the continuous nature of articulatory trajectories and the global acoustic and articulatory consistency without further optimization. Second, it incorporates the acoustic behavior of the articulatory model by means of sensitivity functions of formants, with respect to articulatory parameters.

The seven parameters of the articulatory model are time functions $\boldsymbol{\alpha}(t)=(\alpha_1(t)\ldots\alpha_i(t)\ldots\alpha_7(t)),\ \ t\in[t_i,t_f]$. Formant trajectories extracted from speech $f_j(t),\ 1\leqslant j\leqslant 3$ are the input data. Those generated by the acoustic simulation are $F_j(\boldsymbol{\alpha}(t))\ (1\leqslant j\leqslant 3)$. A cost function for evaluating acoustic-to-articulatory mapping incorporates two components:

(1) $\Sigma_{j=1}^{3}(f_j(t)-F_j(\boldsymbol{\alpha}(t)))^2$ which expresses the proximity between observed acoustic data, i.e., formants trajectories $f_j(t)$, and those generated by the articulatory model $F_j(\boldsymbol{\alpha}(t))$.

(2) $\Sigma_{i=1}^{7}m_i\alpha_i'(t)^2$ which expresses the changing rate of articulatory parameters. In order to penalize large articulatory efforts and prevent the vocal tract from reaching positions too far from equilibrium, a potential energy term $\Sigma_{i=1}^{7}k_i\alpha_i^2(t)$ is added.

The cost function to be minimized has the following form:

$$I=\int_{t_i}^{t_f}\sum_{j=1}^{3}(f_j(t)-F_j(\boldsymbol{\alpha}(t)))^2dt+\lambda\int_{t_i}^{t_f}\sum_{i=1}^{7}m_i\alpha_i'(t)^2dt$$

$$+\beta\int_{t_i}^{t_f}\sum_{i=1}^{7}k_i\alpha_i^2(t)dt, \quad (14)$$

where t_i and t_f define the time interval over which the inversion is carried out, λ and β express the compromise between the changing rate of articulatory parameters, their distance from equilibrium, and the acoustic distance. m_i is the pseudo-mass of the ith articulator, and k_i is its spring constant. Equation (14) can be written as

$$I=\int_{t_i}^{t_f}\Phi(\boldsymbol{\alpha}(t),\boldsymbol{\alpha}'(t),t)dt.$$

Variational calculus[44] can be used to minimize I. Euler–Lagrange equations express the vanishing of the derivative of I with respect to each of the α_i. These equations are a necessary condition to ensure a minimum of I and can be written

$$\frac{\partial\Phi}{\partial\alpha_1}-\frac{d}{dt}\frac{\partial\Phi}{\partial\alpha_1'}=0,$$

$$\cdots \quad (15)$$

$$\frac{\partial\Phi}{\partial\alpha_7}-\frac{d}{dt}\frac{\partial\Phi}{\partial\alpha_7'}=0.$$

Considering the definition of Φ, each of the Euler–Lagrange equations becomes

$$\sum_{j=1}^{3}(f_j(t)-F_j(\boldsymbol{\alpha}(t)))\frac{\partial F_j}{\partial\alpha_i}+\beta k_i\alpha_i(t)-\lambda m_i\alpha_i''(t)$$

$$=0,\quad i=1-7, \quad (16)$$

where $\alpha_i''(t)$ is the second time derivative of $\alpha_i(t)$. From now on we only consider one of the equations of the system (15) for sake of clarity. We can define an iterative process $\alpha_i^{\tau}(t)$ such that

$$\lim_{\tau\to\infty}\alpha_i^{\tau}(t)=\alpha_i(t)$$

[where $\alpha_i^{\tau=0}(t)$ is the startup solution] using the associated evolution equation

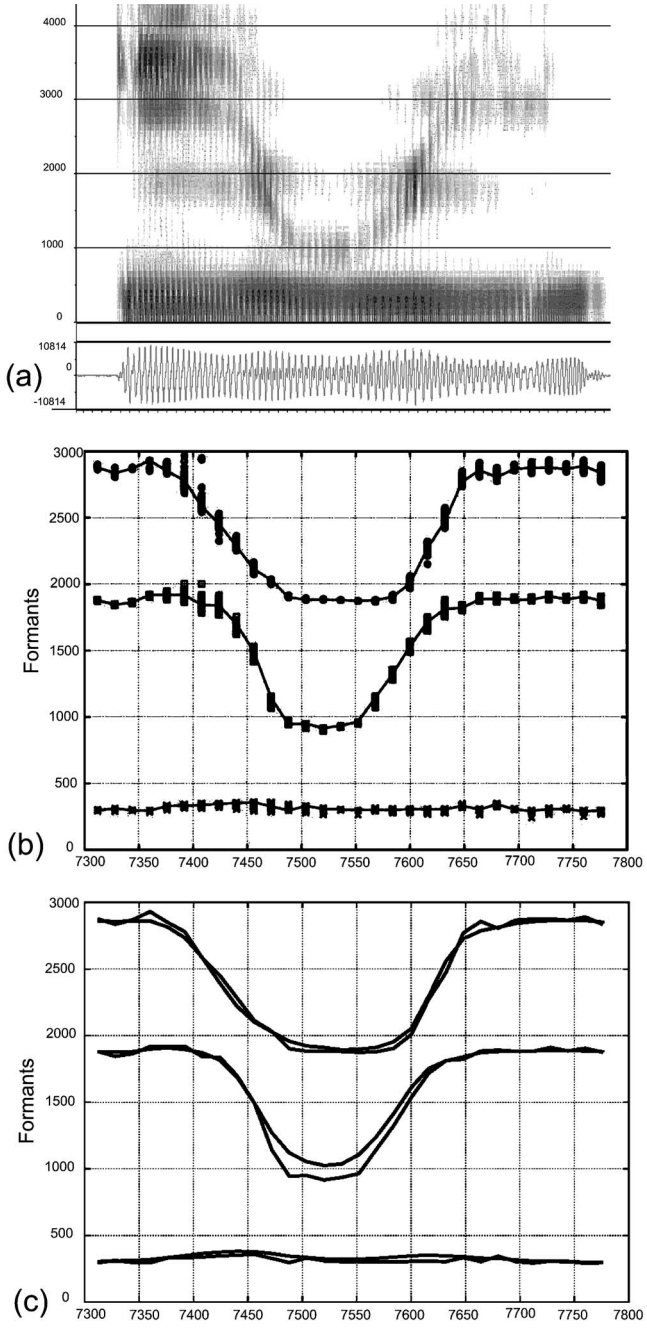

FIG. 9. Inversion result for the sequence [iui]. The horizontal axis represents the time (in milliseconds) and the vertical axis represents formants (in hertz). From top down: (a) spectrogram, (b) original formants trajectories and all the formants solutions resynthesized from articulatory points retrieved from the hypercube codebook, and finally, (c) formants trajectories resynthesized from results of the nonlinear smoothing before and after variational regularization (smooth trajectories).

$$\gamma\frac{\partial\alpha_i^\tau}{\partial\tau}+\beta k_i\alpha_i^\tau-\lambda m_i\alpha_i^{\tau\prime\prime}=-\sum_{j=1}^{3}(f_j(t)-F_j(\boldsymbol{\alpha}^\tau(t)))\frac{\partial F_j}{\partial\alpha_i^\tau},\tag{17}$$

where $\partial\alpha_i^\tau/\partial\tau$ represents the evolution of parameter α_i during the iteration process and γ a parameter for controlling the evolution rate. A solution to the static equation (16) is found when the term $\gamma(\partial\alpha_i^\tau/\partial\tau)$ vanishes. For sake of convenience we set m and k to 1. Let $\boldsymbol{\alpha}^\tau=(\alpha_{i,0}^\tau,\ldots\alpha_{i,k}^\tau,\ldots,\alpha_{i,N}^\tau)$ denote the discrete representation of $\alpha_i(t)$, $\alpha_{i,k}^\tau$ represents the value of α_i^τ at discrete time

$$t=t_i+k\frac{t_f-t_i}{N}$$

in the iteration τ. Since solving Eq. (17) for α_i is independent of other articulatory trajectories, $\alpha_{i,k}^\tau$ is denoted α_k^τ for sake of clarity. Let $(f_0,\ldots f_k,\ldots f_N)$ denote the observed formant trajectory and $(F_0,\ldots F_k,\ldots F_N)$ the formant trajectory generated by the acoustic simulation. Finite difference approximation of the derivative $\alpha''(t)$ leads to

$$\gamma(\alpha_k^\tau-\alpha_k^{\tau-1})+\beta\alpha_k^\tau-\lambda(\alpha_{k+1}^\tau-2\alpha_k^\tau+\alpha_{k-1}^\tau)=-\sum_{j=1}^{3}(f_{j,k}-F_{j,k})\left.\frac{\partial F_j}{\partial\alpha}\right|_{\alpha_{1,k}^\tau\ldots\alpha_{7,k}^\tau},\tag{18}$$

where τ represents the iteration under process and k the discrete time. The derivative term

$$\left.\frac{\partial F_j}{\partial\alpha}\right|_{\alpha_{1,k}^\tau\ldots\alpha_{7,k}^\tau}$$

is calculated for the parameter α_i at point $(\alpha_{1,k}^\tau\ldots\alpha_{7,k}^\tau)$ and incorporates the behavior of the acoustic modeling with respect to the evolution of articulatory parameters. Boundary conditions are needed to ensure that Eq. (18) has a unique solution. Since we do not impose any constraint on the positions of the extremities of $\alpha(t)$,

$$\alpha''(0)=\alpha''(N)=0$$

are the boundary conditions. Let B be an $(N+1)\times(N+1)$ matrix

$$B=\begin{bmatrix}\gamma+\beta+\lambda & -\lambda & 0 & \cdots & 0\\ -\lambda & \gamma+\beta+2\lambda & -\lambda & \cdots & 0\\ \vdots & \ddots & \ddots & \ddots & \vdots\\ 0 & \cdots & -\lambda & \gamma+\beta+2\lambda & -\lambda\\ 0 & \cdots & 0 & -\lambda & \gamma+\beta+\lambda\end{bmatrix},$$

$$\boldsymbol{\alpha}^\tau=(\alpha_0^\tau,\ldots\alpha_k^\tau,\ldots\alpha_N^\tau)^T,$$

$$\mathbf{c}^\tau=\begin{bmatrix}\gamma\alpha_0^{\tau-1}-\sum_{j=1}^{3}(f_{j,0}-F_{j,0})\frac{\partial F_j}{\partial\alpha}\\ \gamma\alpha_1^{\tau-1}-\sum_{j=1}^{3}(f_{j,1}-F_{j,1})\frac{\partial F_j}{\partial\alpha}\\ \cdots\\ \gamma\alpha_N^{\tau-1}-\sum_{j=1}^{3}(f_{j,N}-F_{j,N})\frac{\partial F_j}{\partial\alpha}\end{bmatrix}.$$

Equation (18) can be put in matrix form

$$B\boldsymbol{\alpha}^\tau=\mathbf{c}^\tau.$$

Solving Eq. (15) may be carried out as an iterative process. At each iteration $\boldsymbol{\alpha}^\tau$ is calculated for each of the seven articulatory parameters α_i. In order to ensure that a minimal

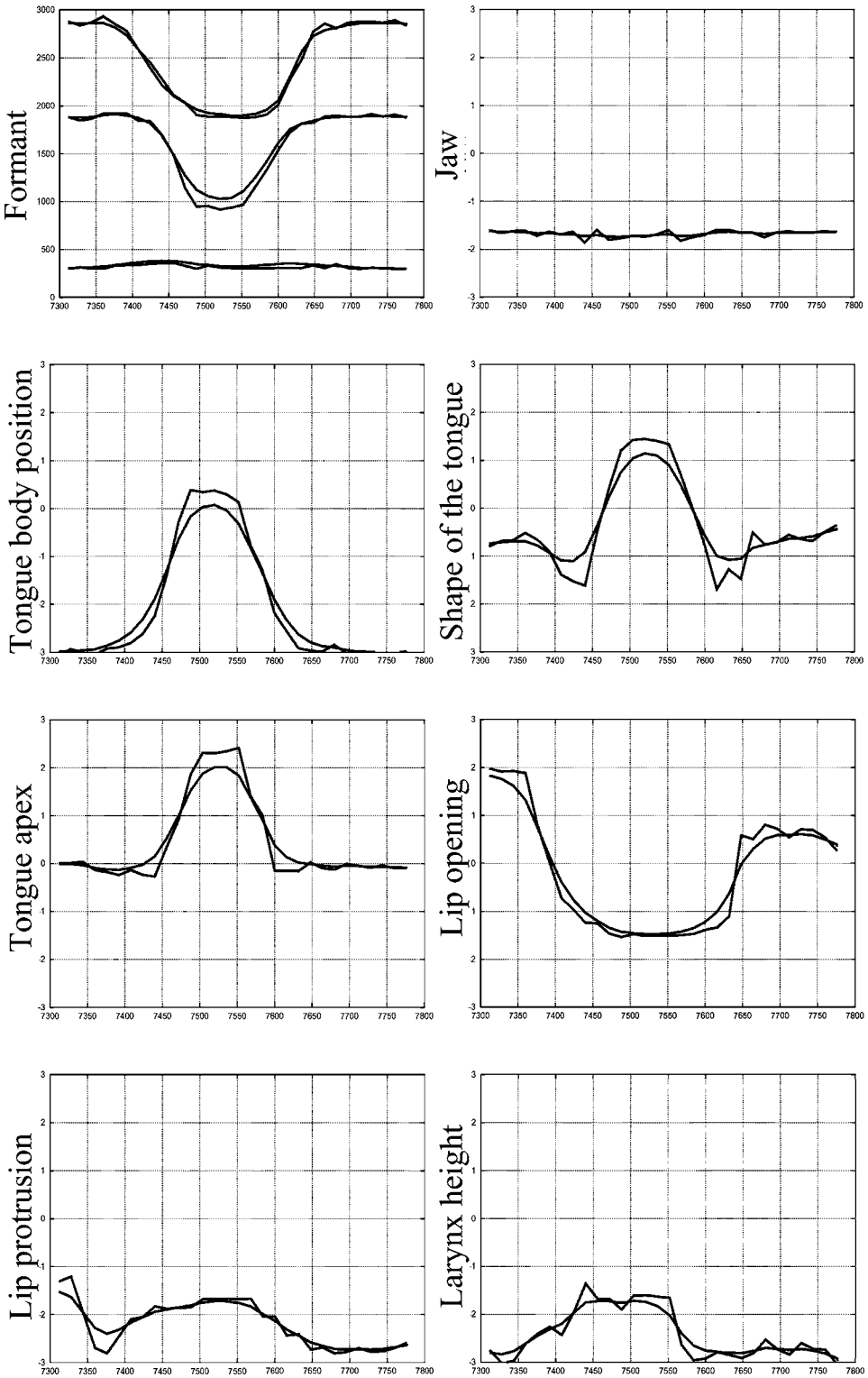

FIG. 10. Inversion results for the sequence [iui]. The first graph presents the formant trajectories and each of the other graphs shows the trajectory of one articulatory parameter. The horizontal axis represents the time (in milliseconds) and the vertical axis represents formants (in hertz). In each graph the trajectory obtained by nonlinear smoothing and that obtained by using the variational regularization method are plotted (the smoothest trajectories are those obtained by the variational regularization).

solution of Eq. (14) is reached, one needs to choose a good startup solution that provided by the nonlinear smoothing method. The startup solution is then iteratively transformed so that Eq. (14) is minimized.

VIII. EXPERIMENTS

Mouth and pharynx sizes of Maeda's model can be adjusted to take into account the morphology of the target speaker. We used the method proposed in Galván-Rdz[9] and also in Naito *et al.*[10] to adapt the articulatory model to our

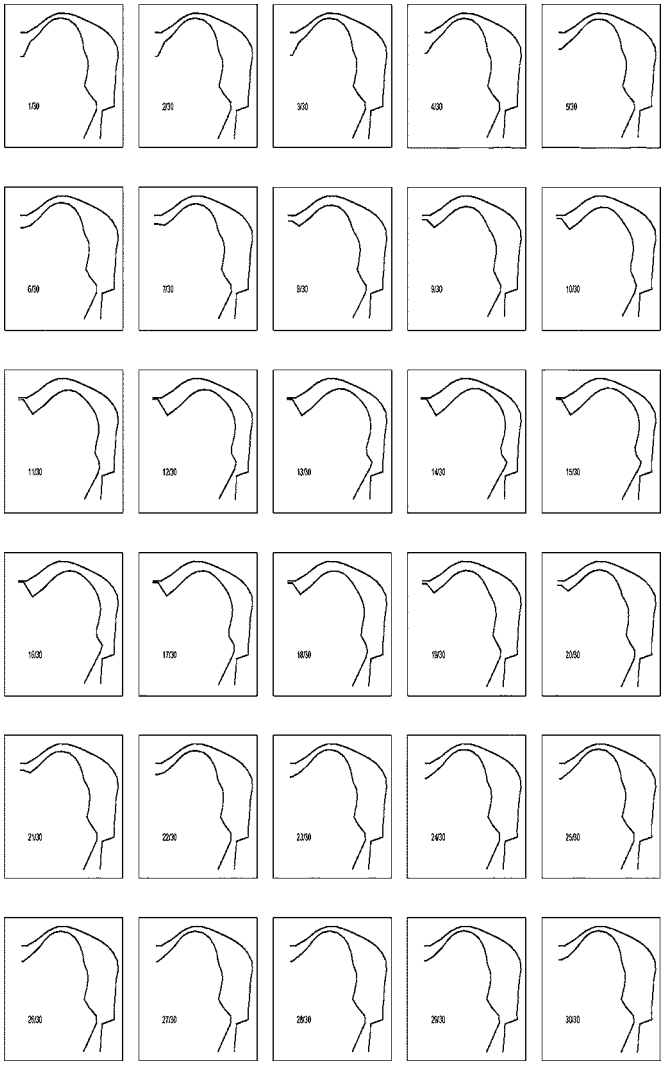

FIG. 11. Temporal dynamics of the vocal tract shapes for the sequence[iui].

subject. Two vocal tract scale factors were sampled in a reasonable domain to allow at most $\pm 20\%$ size variations. For each sample of this grid the first three formants of five extreme vowels /i e a o u/ were calculated from their reference articulatory parameters. The points given by the 5×3 formant frequencies build the surface of acoustical points that can be reached by deforming Maeda's model for these five extreme vowels. The point measured (three formant frequencies for the five vowels) for the target speaker from speech is thus projected orthogonally onto this surface. The orthogonal projection minimizes the distance between the surface and formants realized by the subject. The two scale factors corresponding to this point give the best adaptation of the articulatory model. The hypercube codebook was built for these scale factors. Therefore it cannot be used without further adaptation for another speaker.

The evaluation of an acoustic-to-articulatory inversion procedure comprises two aspects. The first is the acoustic accuracy, i.e., to ensure that inverted articulatory parameters are able to reproduce a speech signal as closely as possible to the original. Here the closeness is evaluated by measuring the distance between original and synthetic formants. It should be noted that the average distance is lower than 15 Hz and thus very accurate. The second aspect is that of the articulatory accuracy, which requires that the synthetic vocal tract shape, i.e., the output of the articulatory model using inverted articulatory parameters, is compared to vocal tract images of the speaker uttering the same speech segment. This is thus tightly connected to the avaibility of articulatory databases that associate the description of the vocal tract shape together with the speech signal. Despite their potential interest, there are almost no dynamic data available to perform this evaluation because either they do not provide the whole vocal tract (for instance cineradiographic databases recorded in the 1970s and recovered by Munhall *et al.*),[45] furthermore with a poor image and sound quality, or describe the vocal tract by a very small number of points in a limited region of the vocal tract (for instance the microbeam database).[46] Therefore, the evaluation consists of a qualitative analysis of results in terms of the evolution of the place of articulation and the main phonetic characteristics. These two characteristics enable the goodness of realism to be evaluated easily and, more important, independently of speaker's variablity.

To evaluate our inversion method, we inverted several vowel–vowel and vowel–vowel–vowel sequences. The evaluation criteria used in these experiments are the smoothness and slow variation in time of the articulatory trajectories. This is the general behavior of the vocal tract of a real speaker. We also examined the animation of the vocal tract frame by frame to see whether there is any unnatural movement of any articulator. More advanced evaluation technique might be consider as discussed in Sec. IX. The trajectories of the first three formants were extracted from spectrograms of the utterances produced by the subject. The first step of the inversion (i.e., the recovery of articulatory points that produce the 3-tuple of formants extracted from speech) gave between 500 and 8000 solutions for each 3-tuple depending on the number of the steps used to sample the null space. For these experiments, the number of steps was set to 3 for each of the four dimensions, and therefore the number of samples was less than $81=3^4$ (see Sec. VI B). The nonlinear smoothing algorithm was then applied to get regular and realistic articulatory trajectories. Finally, the variational regularization was applied to the best articulatory trajectories so that the trajectories are simultaneously smooth and produce formant trajectories close to those extracted from speech.

Figures 9 and 10 present inversion results for the sequence [iui]. In Fig. 9, the original spectrogram of the utterance together with original and resynthesized formants are presented. As we can clearly see, all the solutions present a good acoustic proximity to the original formants. In Fig. 10, we present the result in the articulatory space for each of the seven parameters of Maeda's model. Each graph shows the trajectory obtained by the nonlinear smoothing and the same trajectory optimized by applying the variational regularization (the smoothest trajectories are those obtained by the variational method). The obtained trajectories are smooth and vary slowly in time, which is the behavior of the vocal tract of a real speaker. In Fig. 11, we present for the same sequence [iui] the temporal dynamics of the vocal tract

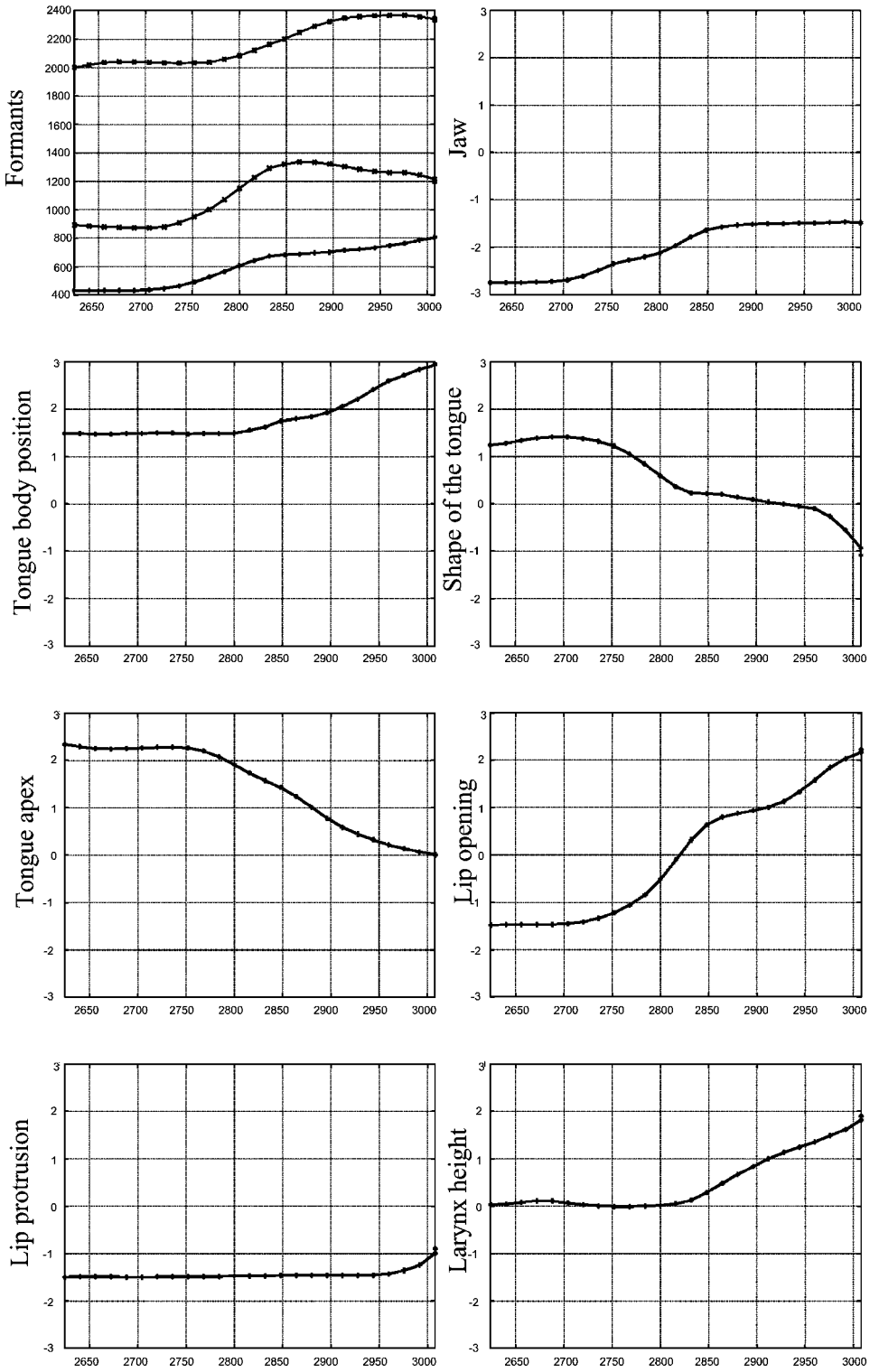

FIG. 12. Inversion results for the transition [ua]. The first graph presents the formant trajectories and each of the other graphs shows the trajectory of one articulatory parameter.

shapes (the mid-sagittal section), frame by frame. This ''animation'' clearly shows that the vocal tract goes from one shape to the other smoothly and does not present any unrealistic transition.

We carried out a large number of vowel–vowel and vowel–consonant–vowel inversion experiments.[47] The results are quite similar to those presented for the sequence [iui]. In Fig. 12, we present the inversion result of the transition [ua] (only final inversion results are displayed). Here again, all the articulatory parameters vary smoothly while guaranteeing a very good proximity to original data. Furthermore, inverse solutions recovered preserve main phonetic cues (main constriction position and vocal tract opening) as can be seen in Fig. 13.

As presented earlier the inversion method is the baseline system that we will use for further inversion studies. One

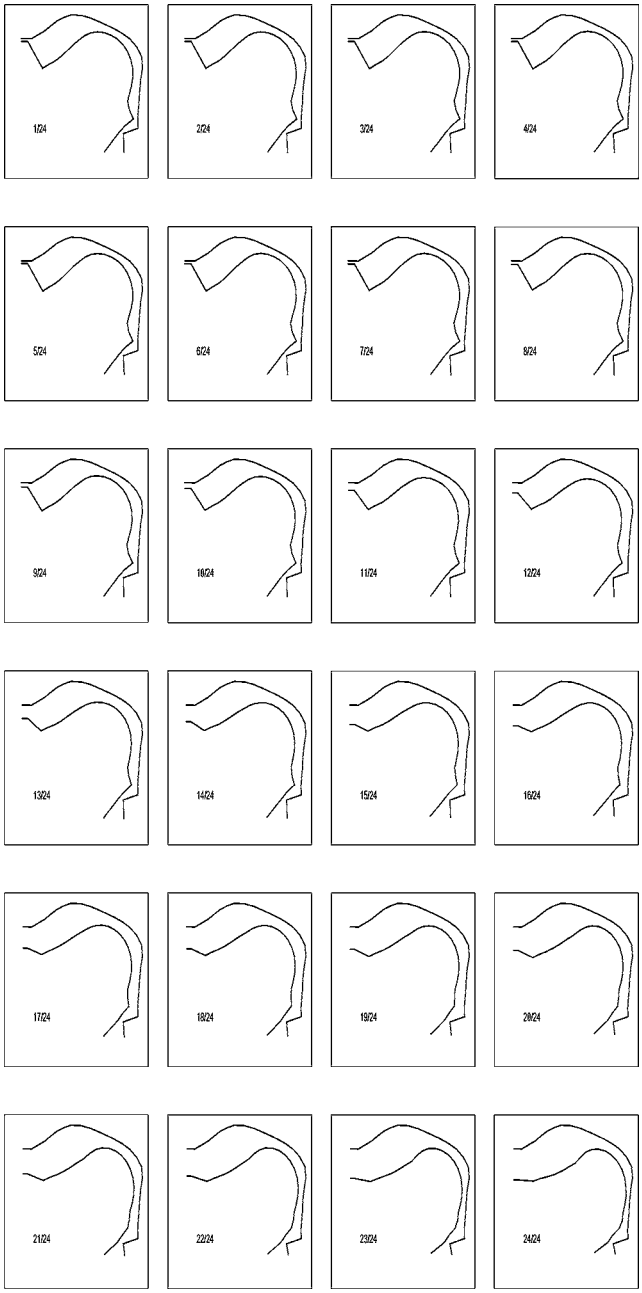

FIG. 13. Temporal dynamics of the vocal tract shapes for the transition [ua].

first stake will be the recovery of finer phonetic and articulatory cues which are very important for some phonemes. In Laprie and Ouni[48] we studied the solution space for the /yi/ transition because the main articulatory difference between /y/ and /i/ is the protrusion which is very strong for the French /y/. All the solutions recovered provide a very good fit between original and resynthesized formants and the main constriction and opening are correct. However, the best solution, in the sense of the criterion used for optimization in Ney's algorithm, does not present strong protrusion (see Fig. 14). In order to explore the solution space, we added a simple constraint on the lip protrusion (supplemented by a secondary constraint on jaw position). This constraint is implemented in the form of a strong bonus, attached to the first point of the inversion. Figure 15 shows that this simple constraint enables the recovery of a protrusion that is more

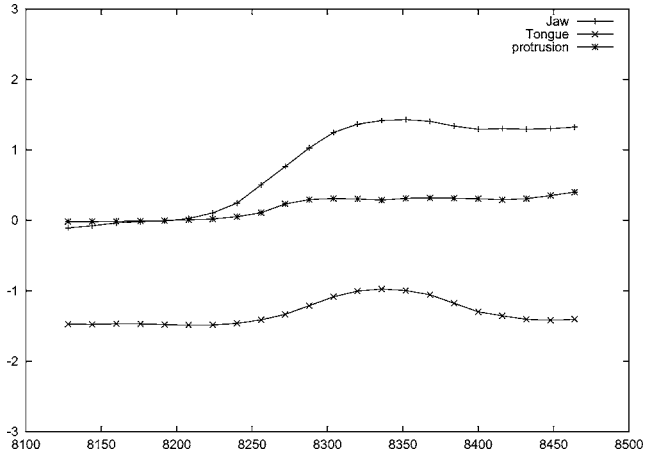

FIG. 14. Temporal evolution of three articulatory parameters (jaw, tongue position and protrusion) without any constraint imposed.

conform to phoentic knowledge. We thus will investigate how constraints can be derived from phonetic knowledge.

IX. CONCLUDING REMARKS

Most of the existing acoustic-to-articulatory inversion methods introduce biases in the solution obtained because they exploit codebooks that do not cover the whole articulatory space. Consequently, there exist articulatory trajectories not found by the inversion although they are quite relevant from an articulatory point of view. On the contrary, one of the advantages of our method is that it ensures that all the possible inversion solutions can be explored, given an articulatory model and the frequency precision set for the formants being recovered, and does not implicitly favor any particular articulatory solution. To the best of our knowledge, this is the only inversion method based on an articulatory model that may guarantee that all the trajectories allowed by the model are explored. Furthermore, the regularization applied to startup solutions allows a global optimization over whole trajectories to be applied and not an optimization that processes points independently from each other. Experiments carried out validate our approach in terms of acoustic precision with respect to original data and smoothness of trajectory recovered.

In some sense the main characteristic of our inversion method is its ''neutrality'' with respect to the articulatory trajectories recovered. However, early language acquisition leads human speakers to prefer some articulatory strategies. These preferences can be linked to a particular speaker, but the existence of phonetically invariant features argue for deeper reasons stemming from biomechanical and acoustic efficiency. The neutrality of our inversion method will enable us to evaluate several strategies for guiding the inversion process. The first strategy is the incorporation of constraints stemming either from phonetic knowledge (for instance, the fact that lips must be protruded for rounded vowels like /y/ and /u/ in French) or from facial information extracted by computer vision when a speaker's face is visible. The second strategy is to incorporate preferences into the articulatory codebook through a learning stage that can exploit EMG,

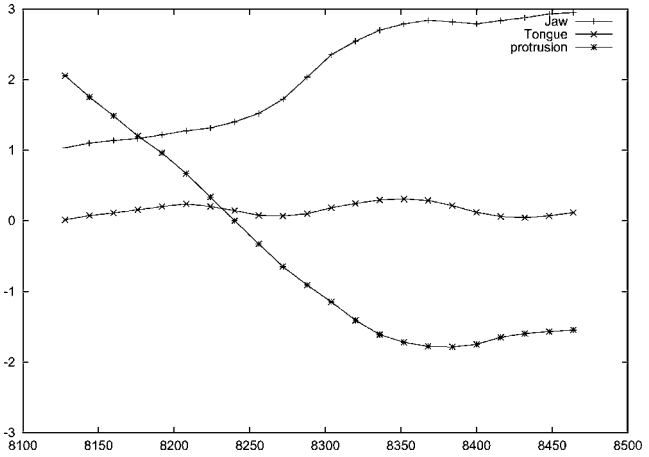

FIG. 15. Temporal evolution of three articulatory parameters (jaw, tongue position, and protrusion) when imposing the protrusion to be near to 2.7 and the jaw position to 1.5 for the first point.

x-ray, or MRI data, or, on the other hand, phonetic knowledge on articulatory features.

Other future work will concern the study of the precision required to adapt the articulatory model. Indeed, the acoustic space covered by the model depends on its geometric dimensions. Therefore, the model must be adapted before inversion. The adaptation, in our case that of Galván-Rdz,[9] often necessitates the knowledge of the articulatory configurations for several vowels. This prior knowledge is only approximate because of speaker variability and compensatory properties of the articulatory model. If the adaptation mismatch is too great there is a risk that the inversion may fail or, the inversion may improperly exploit compensatory properties of the model to compensate for the adaptation mismatch. Therefore, we will investigate the acoustic precision required to guarantee the relevancy of the articulatory information recovered from speech together with the precision required for the model adaptation.

[1] J. Schroeter and M. M. Sondhi, "Speech coding based on physiological models of speech production," in *Advances in Speech Signal Processing*, edited by S. Furui and M. M. Sondhi (Dekker, New York, 1992), pp. 231–267.

[2] R. C. Rose, J. Schroeter, and M. M. Sondhi, "An investigation of the potential role of speech production models in automatic speech recognition," in Proceedings of the International Conference on Spoken Language Processing, Yokohama, Japan, 1994, Vol. 2, pp. 575–578.

[3] J. N. Larar, J. Schroeter, and M. M. Sondhi, "Vector quantization of the articulatory space," IEEE Trans. Acoust., Speech, Signal Process. **ASSP-36**, 1812–1818 (1988).

[4] K. Shirai and T. Kobayashi, "Estimating articulatory motion from speech wave," Speech Commun. **5**, 159–170 (1986).

[5] Y. Laprie and M.-O. Berger, "Cooperation of regularization and speech heuristics to control automatic formant tracking," Speech Commun. **19**, 255–270 (1996).

[6] D. Beautemps, P. Badin, and R. Laboissière, "Deriving vocal tract area functions from midsagittal profiles and formant frequencies: A new model for vowels and fricative consonants based on experimental data," Speech Commun. **16**, 27–47 (1995).

[7] J. M. Heinz and K. N. Stevens, "On the relations between lateral cineradiographs, area functions and acoustic spectra of speech," in Proceedings of the Fifth International Congress on Acoustics, Liège, 1965, p. A44.

[8] P. Perrier, L.-J. Boë, and R. Sock, "Vocal tract area function estimation from midsagittal dimensions with ct scans and a vocal tract cast: Modeling the transition with two sets of coefficients," J. Speech Hear. Res. **35**, 53–67 (1992).

[9] A. Galván-Rdz, "Etudes dans le cadre de l'inversion acoustico-articulatoire: Amélioration d'un modèle articulatoire, normalisation du locuteur et récupération du lieu de constriction des plosives," Ph.D. thesis, Institut de la Communication Parlée, 1997.

[10] M. Naito, L. Deng, and Y. Sagisaka, "Model-based speaker normalization methods for speech recognition," in Proceedings of the Sixth European Conference on Speech Communication and Technology, Budapest, September, 1999, Eurospeech.

[11] B. Mathieu and Y. Laprie, "Adaptation of Maeda's model for acoustic to articulatory inversion," in Proceedings of the Fifth European Conference on Speech Communication and Technology, Rhodes, Greece, 1997, Eurospeech, Vol. 4, pp. 2015–2018.

[12] B. S. Atal, J. J. Chang, M. V. Mathews, and J. W. Tukey, "Inversion of articulatory-to-acoustic transformation in the vocal tract by a computer-sorting technique," J. Acoust. Soc. Am. **63**, 1535–1555 (1978).

[13] J. Schoentgen and S. Ciocea, "Kinematic formant-to-area mapping," Speech Commun. **21**, 227–244 (1997).

[14] V. N. Sorokin, A. S. Leonov, and A. V. Trushkin, "Estimation of stability and accuracy of inverse problem solution for the vocal tract," Speech Commun. **30**, 55–74 (2000).

[15] B. S. Atal and O. Rioul, "Neural networks for estimating articulatory positions from speech," J. Acoust. Soc. Am. **86**, 123–131 (1989).

[16] R. Laboissièrre and A. Galvàn, "Inferring the commands of an articulatory model from acoustical specifications of stop/vowel sequences," in Proceedings of the Fourth International Congress of Phonetic Sciences, Stockholm, August 1995, Vol. 1, pp. 358–361.

[17] G. Papcun, J. Hochberg, T. R. Thomas, F. Laroche, J. Zacks, and S. Levy, "Inferring articulation and recognizing gestures from acoustics with a neural network trained on x-ray microbeam data," J. Acoust. Soc. Am. **92**, 688–700 (1992).

[18] M. G. Rahim and C. C. Goodyear, "Estimation of vocal tract filter parameters using a neural net," Speech Commun. **9**, 49–55 (1990).

[19] K. Shirai and T. Kobayashi, "Estimating articulatory motion using neural networks," J. Phonetics **19**, 379–385 (1991).

[20] A. Soquet, M. Saerens, and P. Jospa, "Acoustic-articulatory inversion based on a neural controller of a vocal tract model: Further results," in *Artificial Neural Networks*, edited by O. Simula, T. Kohonen, K. Mokisara, and J. Kangas (North Holland, Elsevier, Amsterdam, 1991), pp. 371–376.

[21] H. B. Richards, J. S. Bridle, M. J. Hunt, and J. S. Mason, "Dynamic constraint weighting in the context of articulatory parameter estimation," in Proceedings of the Fifth European Conference on Speech Communication and Technology, Rhodes, Greece, 1997, Vol. 5, pp. 2535–2538, Eurospeech.

[22] M. G. Rahim, C. C. Goodyear, W. B. Kleijn, J. Schroeter, and M. M. Sondhi, "On the use of neural networks for in articulatory speech synthesis," J. Acoust. Soc. Am. **93**, 1109–1121 (1993).

[23] R. S. McGowan, "Recovering articulatory movement from formant frequency trajectories using task dynamics and a genetic algoritm: preliminary model tests," Speech Commun. **14**, 19–48 (1994).

[24] V. N. Sorokin and A. V. Trushkin, "Articulatory-to-acoustic mapping for inverse problem," Speech Commun. **19**, 105–118 (1996).

[25] R. Carré and M. Mrayati, "Articulatory-acoustic-phonetic relations and modeling, regions and modes," in *Speech Production and Speech Modelling*, edited by W. J. Hardcastle and A. Marchal (Kluwer Academic, Amsterdam, 1990), pp. 211–240.

[26] G. Fant, "Analytical constraints on the composition of speech spectra," in *Acoustic Theory of Speech Production*, 2nd Printing (Mouton, The Hague, 1970), pp. 48–62.

[27] G. Fant, "Swedish vowels and a new three-parameter model," Technical report No. TMH-QPSR 1, 2001.

[28] J. L. Flanagan, K. Ishizaka, and K. L. Shipley, "Signal models for low bit-rate coding of speech," J. Acoust. Soc. Am. **68**, 780–791 (1980).

[29] K. N. Stevens and A. S. House, "Development of a quantitative description of vowel articulation," J. Acoust. Soc. Am. **27**, 484–493 (1955).

[30] S. Maeda, "Un modèle articulatoire de la langue avec des composantes linéaires," in *Actes 10èmes Journées d'Etude sur la Parole*, Grenoble, May 1979, pp. 152–162.

[31] B. Gabioud, "Articulatory models in speech synthesis," in *Fundamentals of Speech Synthesis and Speech Recognition*, edited by E. Keller (Wiley, West Sussex, England, 1994), Chap. 10.

[32] P. Badin, L. Pouchoy, G. Bailly, M. Raybaudi, C. Segebarth, J. F. Lebas, M. Tiede, E. Vatikiotis-Bateson, and Y. Tohkura, "Un modèle articulatoire tridimensionnel du conduit vocal basé sur des données irm," in *Actes*

XXIImes Journées d'Etude sur la Parole (Martigny, Switzerland, 1998).
[33] O. Engwall, ''Modeling of the vocal tract in three dimensions,'' in *Eurospeech*, Budapest, 1999, pp. 113–116.
[34] S. Maeda, ''Compensatory articulation during speech: Evidence from the analysis and synthesis of vocal-tract shapes using an articulatory model,'' in *Speech Production and Speech Modelling*, edited by W. J. Hardcastle and A. Marchal (Kluwer Academic, Dordrecht, 1990), pp. 131–149.
[35] L.-J. Boë, P. Perrier, and G. Bailly, ''The geometric vocal tract variables controlled for vowel production: Proposals for constraining acoustic-to-articulatory inversion,'' J. Phonetics **20**, 27–38 (1992).
[36] G. Bailly, C. Abry, R. Laboissière, P. Perrier, and J.-L. Schwartz, ''Inversion and speech recognition,'' in *Signal Processing VI*, Theories and Applications Vol. 1, edited by J. Vandewalle, R. Boite, M. Mooner, and A. Osterlinck (Elsevier, Brussels, 1992), pp. 159–164.
[37] S. Dusan and L. Deng, ''Recovering vocal tract shapes from MFCC parameters,'' in Proceedings of the International Conference on Spoken Language Processing, Vol. 2, Sydney, Australia, December 1998.
[38] F. Charpentier, ''Determination of the vocal tract shape from the formants by analysis of the articulatory-to-acoustic non-linearities,'' Speech Commun. **3**, 291–308 (1984).
[39] G. Fant, *Acoustic Theory of Speech Production* (Mouton, The Hague, 1960).
[40] K. N. Stevens, *Human Communication: A Unified View* (McGraw Hill, New York, 1972), pp. 51–66.
[41] K. N. Stevens, ''On the quantal nature of speech,'' J. Phonetics **27**, 3–45 (1989).
[42] G. H. Golub and C. F. Van Loan, *Matrix Computations* (The John Hopkins University Press, Baltimore, 1989).
[43] H. Ney, ''A dynamic programmation algorithm for nonlinear smoothing,'' Signal Process. **5**, 163–173 (1983).
[44] R. S. Schechter, *The Variational Method in Engineering* (McGraw-Hill, New York, 1967).
[45] K. G. Munhall, E. Vatikiotis-Bateson, and Y. Tokhura, ''X-ray film database for speech research,'' J. Acoust. Soc. Am. **98**, 1222–1224 (1995).
[46] J. R. Westbury, ''X-ray microbeam speech production database user's handbook version 1.0,'' Technical report, Waisman Center on Mental Retardation & Human Development, University of Wisconsin, Madison, 1994.
[47] S. Ouni, ''Modélisation de l'espace articulatoire par un codebook hypercubique pour l'inversion acoustico-articualtoire,'' Ph.D. thesis, Université Henri Poincaré, 2001.
[48] Y. Laprie and S. Ouni, ''Introduction of constraints in an acoustic-to-articulatory inversion,'' in Seventh International Conference on Spoken Language Processing, Denver, CO, September 2002.

Gender and speaker identification as a function of the number of channels in spectrally reduced speech

Julio Gonzalez[a)]
Departmento de Psicologia Basica, Clinica y Psicobiologia, Universidad Jaume I, Castellon, 12071 - Castellon, Spain

Juan C. Oliver[b)]
Departmento de Psicologia Evolutiva, Educativa, Social y Metodologia, Universidad Jaume I, Castellon, 12071 - Castellon, Spain

(Received 8 August 2003; revised 26 January 2005; accepted 30 March 2005)

Considerable research on speech intelligibility for cochlear-implant users has been conducted using acoustic simulations with normal-hearing subjects. However, some relevant topics about perception through cochlear implants remain scantly explored. The present study examined the perception by normal-hearing subjects of gender and identity of a talker as a function of the number of channels in spectrally reduced speech. Two simulation strategies were compared. They were implemented by two different processors that presented signals as either the sum of sine waves at the center of the channels or as the sum of noise bands. In Experiment 1, 15 subjects determined the gender of 40 talkers (20 males + 20 females) from a natural utterance processed through 3, 4, 5, 6, 8, 10, 12, and 16 channels with both processors. In Experiment 2, 56 subjects matched a natural sentence uttered by 10 talkers with the corresponding simulation replicas processed through 3, 4, 8, and 16 channels for each processor. In Experiment 3, 72 subjects performed the same task but different sentences were used for natural and processed stimuli. A control Experiment 4 was conducted to equate the processing steps between the two simulation strategies. Results showed that gender and talker identification was better for the sine-wave processor, and that performance through the noise-band processor was more sensitive to the number of channels. Implications and possible explanations for the superiority of sine-wave simulations are discussed. [DOI: 10.1121/1.1928892]

PACS number(s): 43.71.Bp, 43.71.Ky, 43.72.Ar, 43.66.Ts [KWG] Pages: 461–470

I. INTRODUCTION

Speech is a robust signal that is resistant to many forms of information reduction. Speech recognition does not require all the fine spectral information present in the natural signal. This circumstance allows that deaf individuals fitted with cochlear implants can understand speech through a relatively small number of electrodes, or channels.

A useful approach in research is to test normal-hearing listeners with speech signals that have been processed in the manner of a cochlear-implant (CI) signal processor. In these types of experiments, two main signal processors have been used to create simulations of cochlear-implant signals. In the strategy of Shannon *et al.* (1995), the speech signal is bandpass filtered into *n* bands, or channels, and the envelope of each band is extracted, and used to modulate white noise, which is band limited with the same bandpass filter. This way, signals are presented as the sum of noise bands whose bandwidths were equal to the bandwidth of the original analysis channels. These authors showed that high levels of understanding of speech produced in quiet could be achieved using as few as four bands. Dorman *et al.* (1997) synthesized simulations as a sum of *n* sine waves at the center of the channels rather than noise bands. As in Shannon *et al.* (1995), high level of speech understanding could be achieved using only four channels. This strategy was based on the observation that CI users usually report after individual channel stimulation that the signals sound like beep tones and not like bands of noise. Comparison between both processors showed that the nature of the output signal, either noise bands or sine waves, made only a small difference in speech intelligibility (Dorman *et al.* 1997). Results also showed that the number of channels needed to approach asymptotic performance varied with the difficulty of the speech material. For the most difficult material (vowels) 8 channels were necessary, whereas for the least difficult material (high-context sentences) 5 channels were sufficient. On the other hand, comparison of speech recognition by CI users and by normal listeners in conditions simulating cochlear implants indicated that both processors work reasonably well as simulations of the CI signal (Dorman *et al.*, 1998; Fu *et al.*, 1998; Loizou *et al.*, 2000; Friesen *et al.*, 2001; Loizou and Poroy, 2001).

To date, most research work on the perception by CI users and simulation studies has been centered on the intelligibility of speech under a wide variety of conditions. Intelligibility is studied using different speech materials (consonants, vowels, words, and sentences) produced by a single or by multiple speakers as a function of the number of channels

[a)]Electronic mail: gonzalez@psb.uji.es
[b)]Electronic mail: oliverr@psi.uji.es

(Dorman *et al.*, 1997; Loizou *et al.*, 1999; Friesen *et al.*, 2001), location of the cutoff frequencies defining the bands (Shannon *et al.*, 1998), misalignments of spectral information (Shannon *et al.*, 1998; Spahr *et al.*, 2002), under different signal-to-noise ratios (Dorman *et al.*, 1998; Friesen *et al.*, 2001; Fu *et al.*, 1998), intensity resolutions (Loizou *et al.*, 1999; Loizou *et al.*, 2000), and other conditions.

However, in the last several years new questions have emerged about the perception through CI devices. For example, there is an increasing interest in sound-direction identification abilities by bilateral-CI users (Hoesel *et al.*, 2002; Hoesel and Tyler, 2003), pitch perception through CI for speech (Hiki and Fukuda, 2000; Qin and Oxeham, 2003) or for music (Gfeller *et al.*, 1997; McDermott and McKay, 1997; Fujita and Ito, 1999; Lobo *et al.*, 2002), timbre recognition (Gfeller *et al.*, 2002), and source identification for familiar environmental sounds (Shafiro *et al.*, 2003).

Perception of the gender and identity of a speaker via acoustic properties of speech is an important issue in natural communication. Many studies show that the acoustic cues for gender and speaker recognition are present in the coarse-grain structure of speech signals, such as the fundamental frequency, formant structure, or the average long-term spectrum (see review of Bricker and Pruzansky, 1976; Wu and Childers, 1991). In some cases, even radically reduced speech signals, such as sine-wave replicas of natural speech formed by two or three pure tones following the formant trajectories, can adequately convey information about the gender and identity of the speaker (Fellowes *et al.*, 1997; Remez *et al.*, 1997; Sheffert *et al.*, 2002). To date, little is known about whether the CI signal has the potential to allow gender and speaker identification. The exploratory work of Cleary and Pisoni (2002) tested discrimination abilities between pairs of female voices in 44 school-age deaf children who had used a CI for at least 4 years. Subjects were asked to answer "same voice" or "different voice." Two conditions were examined: (a) the sentence was held constant across the voices; (b) different sentences were used. In the first condition children performed 68% of correct responses, which although significantly different from chance (50%), suggests that the discrimination task was difficult for them. In the second condition, children were unable to discriminate between unfamiliar speaker's voices (only 57% of success). In some recent preliminary studies, Chinchilla and Fu (2003a, 2003b) provides data on voice gender discrimination from both CI patients and normal-hearing subjects with different simulation strategies and temporal/spectral resolution. Two additional studies provide data on cochlear implant user's ability to discriminate speaker identity (McDonald *et al.*, 2003) and the relative contributions of amplitude and frequency modulations to speaker identification (Kong *et al.*, 2003).

In the present study, the two processors most used in simulation studies were tested for comparative purposes. Normal-hearing adult subjects were tested to assess their ability to recognize the gender and identity of different speakers from acoustic simulations of cochlear-implant signals. We studied signals presented as either the sum of sine waves or as the sum of noise bands with a varying number of frequency channels. In a first experiment, subjects determined the gender of 40 unfamiliar speakers from a natural utterance processed through different numbers of channels with both processors. In the second experiment, listeners matched simulation replicas and natural recordings of a sentence uttered by 10 unfamiliar speakers. In the third experiment, different sentences were used for natural and processed stimuli. Finally, a control fourth experiment was done to equate the processing steps between the two simulation strategies.

II. EXPERIMENT 1: GENDER IDENTIFICATON

A. Method

1. Subjects

15 subjects (10 females and 5 males) with normal speech and audition participated in the experiment. They were students at the University Jaume I of Castellón in Spain with ages ranging from 21 to 30. Subjects participated voluntarily for course credit. None had participated in any other experiment that used CI simulations.

2. Test materials

A Spanish sentence (the question *¿Cuantos años tiene tu primo de Barcelona?* [How old is your cousin from Barcelona?]) was recorded from 40 native speakers of Spanish, 20 males and 20 females, from 25 to 40 years of age. The sentence was uttered at a comfortable level and recorded in a sound-attenuated booth with a Shure SM58 microphone at a distance of about 12 cm from the mouth, and a Sony-TCD D-8 digital audiotape (DAT) recorder with a sample frequency of 44.1 kHz. Then, the voice signal was digitally transferred to a PC computer and converted to 16 bit WAV files. Finally, the files were downsampled to 16 kHz and normalized for overall amplitude.

3. Signal processing

Each natural utterance was processed through a sine-wave and a noise-band processor. The sine-wave processor implementation followed procedures from Loizou *et al.* (1999) and Dorman *et al.* (1997)[11] in the following manner. The signal was first processed through a pre-emphasis filter (1200 Hz high-pass with −6 dB/octave slope) and then bandpassed afterwards into n frequency bands (n=3,4,5,6,8, 10,12,16) using sixth-order Butterworth filters. Following Loizou *et al.* (1999) logarithmic filter spacing was used for $n<8$ and semilogarithmic (mel) filter spacing was used for $n\geqslant 8$ (see the center frequencies and the 3 dB bandwidths of the filters in Tables I and II of Loizou *et al.*, 1999, respectively). The envelope of the signal was extracted by full-wave rectification, and low-pass filtering (second-order Butterworth) with 400 Hz cutoff frequency. Sinusoids were generated with amplitudes equal to the rms energy of the envelopes and with frequencies equal to the center frequencies of the bandpass filters. Finally, the sinusoids of each band were summed and the level was equated to the rms of original.

The noise-band processor was implemented in the following manner based on Shannon *et al.* (1995) and Dorman *et al.* (1997)[2,2]. The signal was first processed through a preemphasis filter (1200 Hz high-pass with −6 dB/octave slope) and was then band-passed into n frequency bands (n=3,4,5,6,8,10,12,16) with the same cut-off frequencies used for the sine-wave processor. Hann-bandpass filtering was performed with a smoothing factor of a tenth of the upper frequency of each band. The envelope of the signal was extracted by full-wave rectification, and by low-pass filtering with 160 Hz cutoff frequency, since Shannon *et al.* (1995) found no difference in performance for low-pass filters set at 160 Hz and above. The envelope of the signal served to modulate white noise, which was band limited with the same Hann-bandpass filter. Finally, each noise band was rescaled to have same power as the original and all the noise bands were summed.

4. Procedure

The experiment was based on a within-subject 2×8 (processors × number of channels) design. Each sentence was assigned to two channel conditions of each processor in a pseudorandom manner, assuring the same number of male and female speakers in each condition. This way, each channel condition for each processor was composed of a fixed set of 10 stimuli (5 male + 5 female speakers). The overall set of stimuli comprised 160 processed sentences derived from the 40 natural samples.

The experiment was performed individually on a Pentium PC equipped with a Creative Labs SoundBlaster 16 soundcard. Each listener completed two series of trials (one per processor) consisting of 80 trials (10 trials × 8 different numbers of channels) in each series. The order of presentation of both series was counterbalanced across the subjects.

Each trial consisted of the presentation of a processed sentence through headphones (AKG model HSC 200) at a comfortable sound level (65–70 dB SPL) and the subject was asked to decide whether the gender of the speaker was male or female. Each trial was auto-administered by the participant. The listeners were not familiar with the speakers whose speech samples were used.

Before each series, subjects were given a practice session with 16 examples of sentences processed through different numbers of channels by the same processor. None of the simulations used in the practice was used in the test. As in Loizou *et al.* (1999), each series followed the same sequential order, starting with the stimuli processed through the largest number of channels (n=16) and ending with stimuli processed by the smaller number of channels (n=3). This sequential design was chosen to give subjects time to adjust for listening to the altered speech signals.

B. Results and discussion

Subjects' decisions were scored as the proportion of correct responses. Results are shown in Fig. 1 (lines sine waves and noise bands). A two-way repeated measures analysis of variance (ANOVA) revealed a main effect of processor type [$F(1,14)=67.50, p<0.001$], with sine-wave processor producing higher scores (mean=0.96) than noise-band processor (mean=0.81). There was also a significant main effect of number of channels [$F(7,98)=23.29, p<0.001$], and a significant interaction between type of processor and number of channels [$F(7,98)=12.46, p<0.001$].

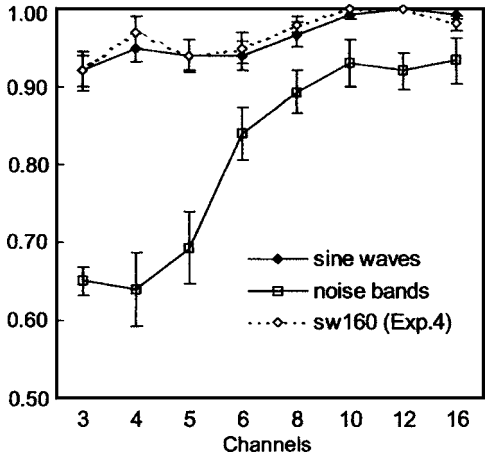

FIG. 1. Experiment 1. Gender identification (proportion correct) as a function of number of stimulation channels. The parameter is processor type: sine-wave output (closed diamonds) or noise-band output (squares). Error bars indicate ± 1 standard error of the mean. Results from Experiment 4 with sine-wave stimuli created with 160 Hz cutoff frequency are also included (sw-160, open diamonds).

The sine-wave processor yielded a high performance in all channel conditions, with a very narrow range of scores from 0.92 (3 channels) to 1 (12 channels). Planned comparisons between adjacent categories (difference contrasts) indicated no statistically significant differences in performance when the number of channels used for this processor was equal or fewer than 8.

Gender identification was worst through the noise-band processor and performance was more sensitive to the number of channels. Scores varied from 0.64 (4 channels) to 0.93 (10 and 16 channels). Planned comparisons between adjacent categories indicated no statistically significant differences in performance when the number of channels used for this processor was equal or fewer than 5. The largest differences were between 5 (0.69) and 6 channels (0.84), and between 6 (0.84) and 8 channels (0.89).

Results (see Fig. 1) showed that gender identification scores for the noise-band processor increased when the number of channels was increased from 4 to 10. However, the sine-wave processor was less sensitive to the number of channels, showing a high performance even at the fewest number of channels. According to the data of Dorman *et al.* (1997), the nature of the output signal, either noise bands or sine waves, makes only a small difference in speech intelligibility. Why did we find a significant difference between both processors in the gender recognition of a speaker? Chinchilla and Fu (2003b) recently studied gender discrimination and vowel recognition by CI and normal-hearing (NH) listeners using sine-wave and noise-band vocoders simulations. Results showed no effect of the simulation type on vowel recognition, but voice gender discrimination was significantly higher through sine-wave than through noise-band simulations.

Recognition of voice gender is dependent upon acoustic information related to the source and vocal tract properties. This information includes fundamental frequency, formant structure, and breathiness (Klatt and Klatt, 1990). Probably, a key factor to account for the superiority of the sine-wave simulations is that sine-wave carriers preserve better than noise carriers some information relevant to the identification of talker gender. This point will be discussed in detail in Sec. VI.

Beyond gender identification, the two following experiments tested the recognition of the identity of a speaker by means of a slightly more complex task.

III. EXPERIMENT 2: SPEAKER IDENTIFICATION—SAME SENTENCE

A. Method

1. Subjects

56 subjects (38 females and 18 males) with normal speech and hearing abilities participated in the experiment. They were students at the University Jaume I of Castellon (Spain), with ages ranging from 20 to 32. Subjects participated voluntarily for course credit. None had taken part in Experiment 1.

2. Test materials

A Spanish sentence (the question *¿Cuantos años tiene tu primo de Barcelona?* [How old is your cousin from Barcelona?]) was recorded from 10 native speakers of Spanish, 5 males and 5 females, with ages ranging from 25 to 39 years. The conditions of recording and creation of WAV files were the same as in Experiment 1.

3. Signal processing

Each natural sentence was treated both by a sine-wave processor and a noise-band processor. Signal processing was the same as in Experiment 1, with the exception that the number of channels used for each processor was $n=3,4,8,16$. The selection of these n followed procedures from the work of Fu *et al.* (1998). All 10 sentences were processed through all the different channel numbers.

4. Procedure

The experiment comprised 8 separate conditions (2 processors $\times$ 4 different numbers of channels). Each subject was randomly assigned to 1 of the 8 conditions (7 subjects per condition).

The experiment was performed in groups of 5 subjects or fewer on Pentium PCs equipped with a Creative Labs SoundBlaster 16 soundcard and the stimuli were individually administered through headphones (AKG model HSC 200) at a comfortable sound level (65–70 dB SPL). The procedure was the same as that used in Remez *et al.* (1997) studying speaker identification from sine-wave replicas. On every trial, a natural sentence was followed by two simulations. One of the pair of simulations was always derived from the natural sentence presented on that trial. The other simulation was derived from one of the other nine sentences (speakers). The subject was asked to report on an answer sheet which of the two simulations was based on the natural sentence presented on each trial.

With 10 different speakers, there were nine comparisons of each simulation with every other one, making 90 trials per condition. The order of the two simulations was counterbalanced along the trials. Because of that, the correct response for half of the trials was "first," and that for the other half was "second." A signal (beep) announced every trial 750 ms before its onset. On each trial, the three stimuli (the natural sentence and the two simulations) were separated by 750 ms of silence. Between each trial, there were 3 s of silence. In every experimental condition, the complete set of 90 trials was administered in blocks of five trials with a short break between blocks. The trials were presented in a pseudorandom order with a maximum of three consecutive similar trials sharing the same correct response.

Before the experimental test, subjects were given a practice session with ten trials of the same condition. None of the stimuli used in the practice were used in the test.

B. Results and discussion

Subjects' decisions were scored as the proportion of correct responses. Results are shown in Fig. 2 (upper panel). A two-way between-subject analysis of variance (ANOVA) revealed a main effect for type of processor [$F(1,48)=85.77, p<0.001$], with the sine-wave processor producing higher scores (mean=0.97) than the noise-band processor (mean=0.83). There was also a significant main effect of number of channels [$F(3,48)=10.56, p<0.001$], but the interaction between type of processor and number of channels did not reach statistical significance [$F(3,48)=1.66, p=0.188$]. However, a separate ANOVA for each processor revealed that the channel variable was not significant for the sine-wave processor [$F(3,24)=1.98, p=0.143$], though it was significant for the noise-band processor [$F(3,24)=10.21, p<0.001$]. Newman–Keuls' *post hoc* tests revealed that performance for the noise-band processor was significantly better with 16 channels than with 4 or 8 channels, which did not differ significantly between them. And performance with 4–8 channels was significantly better than with 3 channels.

The recognition of speaker identity was clearly better with the sine-wave processor. Speaker recognition from stimuli processed through the noise-band processor was more difficult and the number of channels affected performance.

For the purpose of examining the influence of gender on speaker identification, we separated responses to trials formed by stimuli from speakers of the same gender (40 trials per condition), from responses to trials whose stimuli corresponded to speakers of different gender (50 trials per condition). The proportions of correct responses are presented in the lower panel of Fig. 2. A Student t test found a significant effect of the same–different gender variable for the noise-band processor [$t(27)=4.31, p<0.001$], but not for the sine wave processor [$t(27)=0.91, p=0.370$]. As expected, performance in the noise-band processor was better

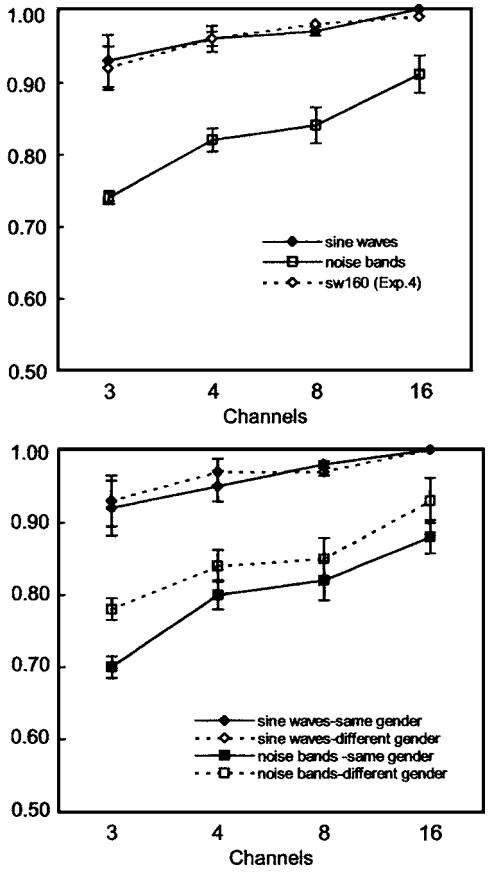

FIG. 2. Upper pannel: speaker identification (proportion correct) as a function of number of stimulation channels from Experiment 2 data (the same sentence was used for natural and processed stimuli). The parameter is processor type: sine-wave output (closed diamonds) or noise-band output (squares). Error bars indicate ± 1 standard error of the mean. Results from Experiment 4 with sine-wave stimuli created with 160 Hz cutoff frequency are also included (sw-160, open diamonds). The lower pannel shows responses to trials whose stimuli were from speakers of the same gender which have been separated from responses to trials whose stimuli were from speakers of different gender.

when the two stimuli to be compared pertained to speakers of different gender. This difference was not found in the sine-wave processor, probably as a result of a ceiling effect. The data from both processor conditions clearly indicated that speaker identification through CI simulations was possible beyond the recognition of gender.

Because sine-wave stimuli have a more regular fine structure, speaker identification could be based on a better modulation detection with the sine-wave carrier than with the noise carrier. In contrast, random level variations in the noise carrier serves to distort the speech envelope. It is probable that less information about speaker identity is available from the noise-band signal. In any case, the superiority of the sinewave simulation will be discussed in more detail in the final section.

On the other hand, it is conceivable that the perceptual judgments in this test may be based on stimulus duration. We reasoned that if the listeners chose between the two simulation alternatives on the basis of a duration strategy, the task would be easier when both simulations were more different in duration, i.e., a positive correlation would emerge across the trials between duration difference and performance. However, no Pearson correlation coefficient was found significant neither of the processor × channel conditions, nor in an average channel condition.

Results of this experiment allow for two alternative explanations. One explanation is that listeners based their performance on the acoustic characteristics of speech of each particular speaker, making an actual speaker identification task. However, given that the natural speech sample of each trial was the model from which the simulation was derived, a different explanation is that listeners based their perceptual judgment on a superficial comparison of the tokens. In this case, subjects would select the correct simulation attending to superficial auditory attributes of specific utterances that are irrelevant to the characteristics of particular speakers. To exclude this possibility we carried out another experiment with the same basic trial procedure using a different natural utterance produced by each talker. This way, listeners who chose the correct simulations would be those who were able to attend to the characteristic acoustic properties of each speaker, beyond the acoustic similarities of specific utterances. This is based on the same logic used by Remez and colleagues (Fellowes *et al.*, 1997; Remez *et al.*, 1997) studying speaker identification from sine wave replicas of speech.

IV. EXPERIMENT 3: SPEAKER IDENTIFICATION—DIFFERENT SENTENCES

A. Method

1. Subjects

A total of 72 subjects (49 females and 23 males) with normal speech and hearing abilities participated in the experiment. They were students at the University Jaume I of Castellon (Spain), with ages ranging from 20 to 32 years. Subjects took part voluntarily for course credit. Thirty-six of them had been participants in Experiment 2, which had been conducted from 3 to 5 months in advance.

2. Test materials

The natural stimuli used in this experiment differed from the utterances that were used as the models for the CI simulations. A new Spanish sentence (the question *¿Vienes mañana al estreno de la película?* [Will you come tomorrow to the opening of the film?]) was recorded from the same 10 speakers (5 males + 5 females) as in Experiment 2. The conditions of recording and creation of WAV files were the same as in Experiments 1 and 2.

The processed stimuli (simulations) were the same as in Experiment 2.

3. Procedure

The experiment comprised eight separate conditions (2 processors × 4 different numbers of channels). Conditions were the same as in Experiment 2: sine-wave processor versus noise-band processor, and number of channels (n=3,4, 8,16). Each subject was randomly assigned to one of the eight conditions (9 subjects per condition).

The experiment was performed in groups of 5 or fewer subjects on Pentium PCs equipped with a Creative Labs SoundBlaster 16 soundcard and the stimuli were individually

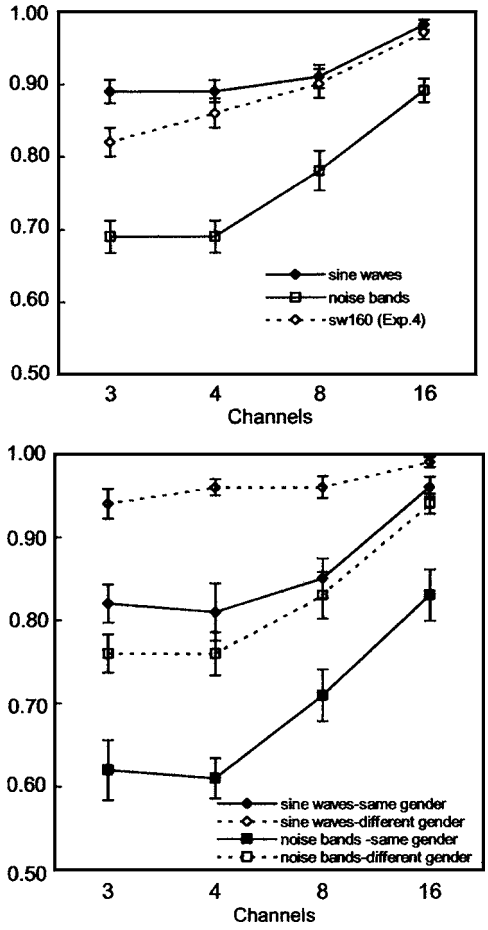

FIG. 3. Upper pannel: speaker identification (proportion correct) as a function of number of stimulation channels from Experiment 3 data (different sentences used for natural and processed stimuli). The parameter is processor type: sine-wave output (closed diamonds) or noise-band output (squares). Error bars indicate ± 1 standard error of the mean. Results from Experiment 4 with sine-wave stimuli created with 160 Hz cutoff frequency are also included (sw-160, open diamonds). The lower pannel shows responses to trials whose stimuli were from speakers of the same gender which have been separated from responses to trials whose stimuli were from speakers of different gender.

administered through headphones (AKG model HSC 200) at a comfortable level (65–70 dB SPL). The procedure was the same as that used in Remez *et al.* (1997). On every trial, a natural sentence (*¿Vienes mañana al estreno de la película?*) was followed by two simulations (both based on *¿Cuantos años tiene tu primo de Barcelona?*). One of the pairs of simulations was always derived from a natural utterance produced by the same speaker who had spoken the natural signal presented on that trial. The other simulation was derived from a natural utterance produced by one of the other nine speakers. The subject was asked to report on an answer sheet which of the two simulations was produced by the same speaker who spoke the natural utterance on each trial.

This experiment followed the same procedure as that in Experiment 2.

B. Results and discussion

The subjects' decisions were scored as the proportion of correct responses. The results are shown in Fig. 3 (upper panel: sine waves and noise bands). A two-way between-subject analysis of variance (ANOVA) revealed a main effect for type of processor $[F(1,64)=135.15, p<0.001]$, with sine-wave processor producing higher scores (mean=0.92) than noise-band processor (mean=0.76). There was also a significant main effect of the number of channels $[F(3,64)=25.26, p<0.001]$, and a significant interaction between type of processor and number of channels $[F(3,64)=3.84, p<0.05]$. Separate ANOVAs for each processor revealed that the channel variable was significant for the sine-wave processor $[F(3,32)=8.40, p<0.001]$, and for the noise-band processor $[F(3,32)=17.17, p<0.001]$. Newman–Keuls' *post hoc* tests identified only two statistically different conditions for the sine-wave processor: 3-4-8, and 16 channels. *Post hoc* tests identified three statistically different conditions for the noise-band processor: 3-4, 8, and 16 channels.

Pooling the data from Experiments 2 and 3, a main experiment effect was found $[F(1,112)=32.9, p<0.001]$, with better performance in Experiment 2 than in 3, as expected. However, no significant interaction was found between type of processor and experiment $[F(1,112)=0.941, p=0.334]$. In Experiment 3 we used stimuli selected to prevent subjects from performing a matching task by listening to acoustic similarities between a natural utterance and its derived processed stimulus. This was accomplished by using as the natural sample of the trials a different sentence from that used as a model to derive the CI simulations. This way, the matching task would be based on more abstract acoustic properties specific to each particular speaker rather than on an exact spectrotemporal match between specific tokens. Logically, performance from Experiment 3 is expected to be more difficult than that from Experiment 2, where in each trial the same token was used both as the natural sample and as the model to derive one of the simulations. Experiment 3 data show two findings:

(1) The sine-wave processor is clearly better than the noise-band processor allowing for speaker identification, showing a good performance (better than 90%) even with the fewest number of channels ($n=3$). The effect of number of channels in the sine-wave processor is only evident when n increases from 8 to 16 channels.
(2) Speaker identification from the noise-band simulations is more difficult but performance is better than chance (50%) in all the channel conditions. Noise-band processor is more sensitive to the number of channels and speaker identification increases from $n=4$ to $n=16$ (see Fig. 3).

As in the previous experiment, we separated in Experiment 3 responses to trials formed by stimuli from speakers of the same gender, from the responses to trials of different gender. The proportions of correct responses are presented in the lower panel of Fig. 3. A Student t test found a significant effect of the same-different gender variable for the sine-wave processor $[t(35)=7.17, p<0.001]$ and for the noise-band processor $[t(35)=8.43, p<0.001]$. As expected, performance in both processors was better when the two stimuli to be compared pertained to speakers of different gender. Never-

theless, data from both processor conditions indicated that speaker identification through CI simulations was possible beyond gender recognition.

V. EXPERIMENT 4: REPLICATION WITH SINE WAVES BASED ON 160 Hz LOW-PASS FILTERING

All the sine-wave stimuli of the present experiments were created using envelope information extracted from each band by low-pass filtering with a 400 Hz cutoff frequency. The rationale behind this cutoff frequency was based on two points. First, we wanted to be coherent with previous studies by using sine-wave processors that conformed to the characteristics of the Med El Corporation's cochlear-implant signal processor (Dorman *et al.*, 1997, 1998; Loizou *et al.*, 1999, 2000). Second, data obtained from intelligibility experiments had shown no difference in performance for low-pass filters set at 160 Hz and above (Shannon *et al.*, 1995). In fact, some experiments comparing speech intelligibility through sine-wave versus noise-band processors used 400 and 160 Hz cutoff frequencies, respectively (Dorman *et al.*, 1997).

Nevertheless, the clear and unexpected superiority of the sine-wave processor in the gender/speaker identification task raises the question whether this performance difference may be at least partially due to the use of a different envelope cutoff frequency for each simulation. To equate for cutoff frequency, we performed a control experiment replicating experiments 1–3 under sine-wave conditions only, using stimuli created with 160 Hz low-pass filtering.

A. Method

1. Subjects

A total of 92 subjects participated in this study. Sixteen subjects replicated Experiment 1 (gender identification). Thirty-six (9×4 channel conditions) replicated Experiment 2 (speaker identification with same sentence). And forty (10×4 channel conditions) replicated Experiment 3 (speaker identification with different sentences). Subjects were students at the University Jaume I of Castellon (Spain) and participated voluntarily for course credit. None of them had participated in any of the previous experiments.

2. Test materials

Only sine waves were used as processed stimuli. Sine-wave stimuli were created in the same way as in Experiments 1–3, except for the cutoff frequency used for low-pass filtering (160 instead of 400 Hz). The number of channels was also the same as in Experiments 1–3. The same natural stimuli from Experiments 2 and 3 were used here in the replication.

3. Procedure

The procedure was the same as in Experiments 1–3.

B. Results and discussion

The subjects' decisions were scored as the proportion of correct responses.

The pattern of results obtained with sine-wave stimuli created with a 160 Hz cutoff frequency (hereafter, sw-160) was the same as that obtained with sine-wave stimuli used in Experiments 1–3, and created with 400 Hz cutoff frequency (hereafter, sw-400), except for the most difficult condition, i.e., speaker identification across different sentences and through 3 channels.

Results are included in all figures adjacent to the findings from the replicated experiments. Gender recognition by means of sw-160 was the same as in the sw-400 condition (see Fig. 1). An analysis of variance (ANOVA) using cutoff frequency as a between-subject factor (sw-160 vs sw-400) showed no main effect $[F(1,29)=0.09, p=0.763]$. On the other hand, comparing performance from sw-160 and noise-band stimuli, gender identification was significantly higher in sw-160 (like sw-400). A between-subject ANOVA (sw-160 versus noise bands) revealed a main effect $[F(1,29)=47.0, p<0.001]$.

Speaker identification under Experiment 2 procedures (stimuli based on the same utterance) is not significantly different for sw-160 in comparison with sw-400 (see Fig. 2, upper panel). An ANOVA (sw-160 vs sw-400) revealed no main effect $[F(1,56)=0.01, p=0.994]$. At the same time, the sw-160 condition yielded higher performance than the noise-band condition: an ANOVA (sw-160 versus noise bands) showed a main effect $[F(1,56)=118.84, p<0.001]$.

It is in the speaker identification under Experiment 3 conditions (stimuli based on different utterances) where a significant difference emerges between results from sw-160 and sw-400 stimuli (see Fig. 3, upper panel). A two-way between-subject ANOVA (with cutoff-frequency and channel as factors) revealed a main effect for cutoff frequency $[F(1,68)=7.90, p<0.01]$, with sw-160 producing lower scores (mean=0.89) than sw-400 stimuli (mean=0.92). There was also a significant main effect of number of channels $[F(3,68)=21.95, p<0.001]$, but the cutoff frequency $\times$ number of channels interaction did not reach statistical significance $[F(3,68)=1.67, p=0.182]$. Comparing cutoff frequencies within each channel condition with a Student t test for independent samples, a significant difference was found between sw-16 and sw-400 only for 3 channels $[t(17)=2.50, p=0.023]$, but not for 4 channels $[t(17)=1.39, p=0.182]$, 8 channels $[t(17)=0.39, p=0.702]$, or 16 channels $[t(17)=1.32, p=0.204]$. A separate ANOVA revealed that the channel variable was significant for the sw-160 processor $[F(3,36)=15.03, p<0.001]$. Newman–Keuls' *post hoc* tests found that performance for sw-160 processor was significantly better with 16 channels than with 3, 4, or 8 channels; and performance with 8 or 4 channels (which did not differ significantly between them) was better than with 3 channels.

In sum, these results show that using the same smoothing filter (160 Hz) for both processors, performance of the sine-wave type remains clearly better that the one of the noise type. Nevertheless, a question remains open. Is it possible that had we used the 400 Hz smoothing filter for noise modulated stimuli the scores would have improved significantly? Noise conditions were more variable than sine-wave conditions. It may be that the 160 Hz filter may interact with

noise to make nearly impossible discerning the periodicity of the speech envelope. Whether performance might have been better under 400 Hz filter and noise carriers is a topic for further research.

VI. GENERAL DISCUSSION

The experiments in the present study assessed the ability of normal-hearing listeners to recognize the gender and identity of a speaker through simulations of cochlear-implant signals. We tested two processors used in simulation studies with a varying number of frequency channels. Previous studies focusing on speech intelligibility had shown that changes in the nature of the output signal from noise bands to sine waves only have a small effect in performance (Dorman *et al.*, 1997).

Nevertheless, when both processors were compared regarding the ability of listeners to recognize the gender and the identity of a speaker, a large and significant difference emerged in all the experiments. Our data showed a substantial superiority of the sine-wave processor in both tasks reaching a very high performance, even in condition with only 3 channels. Research on voice perception has shown that the fundamental frequency of phonation and the spectral properties of natural voice provide strong cues to recognize the gender and identity of a speaker (see review of Bricker and Pruzansky, 1976; Lass *et al.*, 1976, 1980; Klatt and Klatt, 1990; Wu and Childers, 1991; Mullennix *et al.*, 1995; Kreiman, 1997). Listeners take advantage of information provided by the sine-wave simulations that is not present in the noise-band simulations. Acoustic analysis of processed signals from both processors demonstrated that sine-wave simulations have a periodic structure in substantial portions of the signal that noise-band simulations do not have. An algorithm applied in acoustic periodicity detection on the basis of a noise-resistant autocorrelation method (Boersma, 1993) was capable of detecting consecutive pitch periods in an important proportion of the processed sine-wave signal. As expected, the same method failed to find pitch periods in the noise-band simulations. We hypothesize that one advantage of sine-wave versus noise carriers is in the time-amplitude envelope. Noise carriers have a rapidly fluctuating envelope whereas the sine wave has a fixed amplitude envelope. When the speech envelope is extracted and imposed on one of these carriers, random level variations in the noise carrier serves to distort the speech envelope. Noise-band simulations only provide information on the spectral distribution of energy. With this type of stimuli, listeners should base their perceptual judgments mainly on the rough spectral information carried by noise bands. In this case, the frequency resolution of the signal would increase as the processor implements more channels and this would explain why performance improved substantially with the number of channels.

A plausible interpretation for the observed results is in the modulation domain. Using a noise carrier, normal hearing subjects can detect typically 5%–10% amplitude modulation (Viemeister, 1979), whereas they can detect 1%–5% modulation when a sinusoidal carrier is used (Kohlrausch *et al.* 2000). This latter observation is more in line with the cochlear-implant user's ability to detect amplitude modulation (Shannon, 1992). The sine-wave carrier is a single frequency component, and when the speech envelope is imposed on this kind of carrier, side bands are generated reflecting the spectral content of the envelope. In the case of the noise carrier, these side bands are masked because they coincide with spectral components of the noise. The better result with the sine-wave simulations is likely due to (a) better modulation detection with the sine wave than with the noise carrier, and (b) the likely resolved side bands of amplitude modulation, particularly in the low-frequency bands. The modulation introduces spectral side bands, which may be detected as separate components if they are sufficiently far in frequency from the carrier frequency (Kohlrausch *et al.* 2000). In this sense, the better performance with sine-wave carriers would be due to a better representation of modulation as well as to the perception of the resolved side bands. From this point of view, the sine-wave stimuli could simulate the implant performance better than noise-band stimuli, supporting Zeng's assertion made by making quantitative comparisons between performance of normal and implant listeners (Zeng, 2004). On the other hand, one possibility is that some Fo information from the original signal remains in the sine-wave stimulus. The 160 Hz cutoff frequency with a second-order low-pass filter may still be too high to prevent leakage of Fo information into the envelope domain.

Roughly speaking, performance in gender and speaker identification increases as the number of channels increases, but this effect is more obvious in the noise band processor. Sine-wave stimuli attain a very high performance even at the fewest number of channels, giving rise to a ceiling effect that prevents a clear channel effect. Only in the most difficult task used for speaker recognition, i.e., across different utterances, the channel effect is significant for the sine-wave processor.

On the other hand, comparing results from Experiments 2 and 3 it is clear that speaker identification is easier across the same utterance than through different utterances. Linguistic and probably other idiosyncratic acoustic cues have contributed to the difference between both experiments. This is congruent with recent research by McDonald *et al.* (2003), where differences in talker discrimination by CI and normal-hearing listeners was studied under two linguistic conditions. In the first one, listeners heard pairs of stimuli (words or sentences) whose linguistic content was identical (e.g., cat–cat). In the second condition, the linguistic content of each pair was different (e.g., cat–dog). Discrimination accuracy was better in stimulus pairs where the linguistic content was held constant. In the same study it was found that talker discrimination was easier for male–female talker pairs than for within-gender stimulus pairs. Partial analysis of our data from Experiments 2 and 3 by separating trials between same-gender versus different-gender subsets yielded the same pattern of results. At the same time, our data clearly showed that speaker identification occurred beyond the recognition of gender, i.e., in the same-gender subset.

Replication of Experiments 1–3 using a 160 Hz cutoff frequency showed the same results as with the 400 Hz cutoff

frequency, except for the most difficult condition, in which there is less spectral information (3 channels) for speaker recognition. Results presented by Chinchilla and Fu (2003b) fit well with our data. These authors studied voice gender discrimination by CI and normal-hearing (NH) listeners using sine-wave and noise-band vocoders simulations, where number of channels (4 to 32) and the cutoff frequencies of the channel's envelope filters (from 20 to 320 Hz) were manipulated. Results for NH subjects with sine-wave stimuli showed that when only 4 spectral channels were available, gender discrimination improved as the envelope filter cutoff frequency was increased from 20 to 320 Hz. In other words, both spectral and temporal information contribute to gender and speaker identification, but the temporal information is especially important when there are few spectral cues for the identification task.

A last issue to be considered is which of the two processors is a better approximation to the actual performance of cochlear-implant users. When the focus of research is on speech intelligibility, the small differences found between both processors do not allow a clear conclusion on the matter. Empirical data about speech intelligibility seem to indicate that both processors work reasonably well as simulations of the CI signal (Dorman *et al.*, 1998; Fu *et al.*, 1998; Loizou *et al.*, 2000; Friesen *et al.*, 2001; Loizou and Poroy, 2001). However, results on gender and speaker recognition are very different depending on the nature of the output signal. To date, there are not enough data to support a conclusive statement. Chinchilla and Fu (2003b) found that gender discrimination scores were highly variable among CI listeners. However, the best-performing CI users scored similarly to normal-hearing (NH) subjects listening to the 4-channel sine-wave simulations. Based on this similarity, the authors suggested that sine-wave vocoder simulations may better approximate CI user's listening conditions than noise-band processors. Zeng (2004) considers that sine-wave stimuli can simulate CI performance better than noise-band stimuli because the CI listener's ability to detect amplitude modulation is more similar to the NH listener's ability when using a sinusoidal carrier than when a noise carrier is used. In any case, we think it is too soon for drawing firm conclusions. In speaker recognition there is a lack of data comparing CI's and NH's performance through sine-wave and noise-band processors. However, Chinchilla and Fu's data on voice gender discrimination show a good fit between the *best-performing* CI users and NH subjects listening sinewave stimuli processed through the *fewest* number of channels. In this respect, further studies on performance of non-best-performing CI users would be valuable, since they would perhaps show a good fit to the noise-band processor, which yields lower performance. Further research is needed to compare gender/speaker recognition performance between CI users and NH subjects listening to sine-wave and noise-band simulations.

ACKNOWLEDGMENTS

This study was partly supported by *Fundació Caixa Castelló-Bancaixa* and the Universitat Jaume I, Castellon (Project No. P1.1A2002-01) and the Ministry of Science and Technology of Spain (I+D+I, Project No. BSO2003-01002/PSCE). The authors would like to thank Philipos C. Loizou, who kindly provided by email his MATLAB routines to create the simulations based on the sine-wave processor. We would also like to thank Paul Boersma and David Weenink for their PRAAT software and Chris Darwin for his PRAAT script, since a modified version of it was used to create the simulations based on the noise-band processor. The authors would like to thank the Associate Editor, Dr. Kenneth W. Grant and Dr. Fan-Gang Zeng for helpful and valuable comments received on an earlier version of this paper. Most of the explanations for the superiority of the sine waves were suggested by Dr. Grant and Dr. Zeng.

[1]Signal processing with the sine-wave processor was implemented using the MATLAB routines (*Csim.m, Estfilt.m, Gethdr.m*, and *Mel.m*), kindly provided by Philipos C. Loizou (Department of Electrical Engineering, University of Texas at Dallas, Richardson, TX).

[2]Signal processing with the noise-band processor was implemented by means of the PRAAT software (Boersma and Weenink, 2001) using a modified version of a script provided by Chris Darwin (Laboratory of Experimental Psychology, University of Sussex, Brighton, UK) at the web address: http://www.biols.susx.ac.uk/home/Chris_Darwin/Praatscripts/Shannon.

Boersma, P. (**1993**). "Accurate short-term analysis of the fundamental frequency and the harmonics-to-noise ratio of a sampled sound," Proc. Institute of Phonetic Sciences **17**, 97–110.

Boersma, P., and Weenink, D. (2001). *Praat 4.0: A system for doing phonetics by computer* (computer software) (University of Amsterdam, Amsterdam, The Netherlands). Available online: http://www.praat.org

Bricker, P. D., and Pruzansky, S. (**1976**). "Speaker recognition," in *Contemporary Issues in Experimental Phonetics*, edited by N. J. Lass (Academic, New York), pp. 295–326.

Chinchilla, S. S., and Fu, Q. J. (2003a). "Discrimination and vowel recognition in normal-hearing and cochlear implant users," in Abstracts of the 26th Midwinter Research Meeting of the Association for Research in Otolaryngology.

Chinchilla, S. S., and Fu, Q. J. (2003b). "Voice gender discrimination and vowel recognition in normal-hearing and cochlear implant users," in Abstracts of the Conference on Implantable Auditory Prostheses, Asilomar, CA.

Cleary, M., and Pisoni, D. (**2002**). "Talker discrimination by prelingually deaf children with cochlear implants: Preliminary results," Ann. Otol. Rhinol. Laryngol. Suppl. **189**, 113–118.

Dorman, M., Loizou, P., Fitzke, J., and Tu, Z. (**1998**). "The recognition of sentences in noise by normal-hearing listeners using simulations of cochlear-implant signal processors with 6-20 channels," J. Acoust. Soc. Am. **104**, 3583–3585.

Dorman, M., Loizou, P., and Rainey, D. (**1997**). "Speech intelligibility as a function of the number of channels of stimulation for signal processors using sine-wave and noise-band outputs," J. Acoust. Soc. Am. **102**, 2403–2411.

Fellowes, J., Remez, R., and Rubin, P. (**1997**). "Perceiving the sex and identity of a talker without natural vocal timbre," Percept. Psychophys. **59**, 839–849.

Friesen, L., Shannon, R. V., Baskent, D., and Wang, X. (**2001**). "Speech recognition in noise as a function of the number of spectral channels: Comparison of acoustic hearing and cochlear implants," J. Acoust. Soc. Am. **110**, 1150–1163.

Fu, Q-J., Shannon, R., and Wang, X. (**1998**). "Effects of noise and spectral resolution on vowel and consonant recognition: Acoustic and electric hearing," J. Acoust. Soc. Am. **104**, 3586–3596.

Fujita, S., and Ito, J. (**1999**). "Ability of nucleus cochlear implantees to recognize music," Ann. Otol. Rhinol. Laryngol. **108**, 634–640.

Gfeller, K., Witt, S., Woodworth, G., Mehr, M. A., and Knutson, J. (**2002**). "Effects of frequency, instrumental family, and cochlear implant type on

timbre recognition and appraisal," Ann. Otol. Rhinol. Laryngol. **111**, 349–356.
Gfeller, K., Woodworth, G., Robin, D. A., Witt, S. G., and Knutson J. (**1997**). "Perception of rhythmic and sequential pitch patterns by normally hearing adults and cochlear implant users," Ear Hear. **18**, 252–260.
Hiki, S., and Fukuda, Y. (**2000**). "Pitch perception through the cochlear implant for speech and music," Adv. Oto-Rhino-Laryngol. **57**, 12–24.
Hoesel, R. J. M., Ramsden, R., and Odriscoll, M. (**2002**). "Sound-direction identification, interaural time delay discrimination, and speech intelligibility advantages in noise for a bilateral cochlear implant user," J. Acoust. Soc. Am. **23**, 137–149.
Hoesel, R. J. M., and Tyler, R. S. (**2003**). "Speech perception, localization, and lateralization with bilateral cochlear implants," J. Acoust. Soc. Am. **113**, 1617–1630.
Klatt, D. H., and Klatt, L. C. (**1990**). "Analysis, synthesis, and perception of voice quality variations among female and male talkers," J. Acoust. Soc. Am. **87**, 820–857.
Kohlrausch, A., Fassel, R., and Dau, T. (**2000**). "The influence of carrier level and frequency on modulation and beat-detection thresholds for sinusoidal carriers," J. Acoust. Soc. Am. **108**, 723–734.
Kong, Y.-Y., Vongphoe, M., and Zeng, F.-G. (2003). "Independent contributions of amplitude and frequency modulations to auditory perception. II. Melody, tone, and speaker identification," in Abstracts of the 26th Midwinter Research Meeting of the Association for Research in Otolaryngology.
Kreiman, J. (**1997**). "Listening to voices: Theory and practice in voice perception research," in *Talker Variability in Speech Processing*, edited by K. Johnson and J. W. Mullennix (Academic, San Diego, CA), pp. 85–108.
Lass N. J., Almerino, C. A., Jordan, L. F., and Wals, J. M. (**1980**). "The effect of filtered speech on speaker race and sex identification," J. Phonetics **8**, 101–112.
Lass, N. J., Hughes, K. R., Bowyer, M. D., Waters, L. T., and Bourne, V. T. (**1976**). "Speaker sex identification from voiced, whispered and filtered isolated vowels," J. Acoust. Soc. Am. **59**, 675–678.
Lobo, A. P., Toledos, F., Loizou, P., and Dorman, M. F. (**2002**). "Effect of envelope lowpass filtering on consonant melody recognition," J. Acoust. Soc. Am. **112**, 2245.
Loizou, P., Dorman, M., Poroy, O., and Spahr, T. (**2000**). "Speech recognition by normal-hearing and cochlear implant listeners as a function of intensity resolution," J. Acoust. Soc. Am. **108**, 2377–2387.
Loizou, P., Dorman, M., and Tu, Z. (**1999**). "On the number of channels needed to understand speech," J. Acoust. Soc. Am. **106**, 2097–2103.
Loizou, P., and Poroy, O. (**2001**). "Minimal spectral contrast needed for vowel identification by normal hearing and cochlear implant listeners," J. Acoust. Soc. Am. **110**, 1619–1627.
McDermott, H. J., and McKay, C. M. (**1997**). "Musical pitch perception with electrical stimulation of the cochlea," J. Acoust. Soc. Am. **101**, 1622–1631.
McDonald, C. J., Kirk, K. I., Krueger, T., and Houston, D. (2003). "Talker discrimination by adults with cochlear implants," in Abstracts of the 26th Midwinter Research Meeting of the Association for Research in Otolaryngology.
Mullennix, J. W., Johnson, K. A., Topcu-Durgun, M., and Farnsworth, L. M. (**1995**). "The perceptual representation of voice gender," J. Acoust. Soc. Am. **98**, 3080–3095.
Qin, M., and Oxeham, A. (**2003**). "The effects of simulated cochlear-implant processing on F0 discrimination," J. Acoust. Soc. Am. **113**, 2224.
Remez, R., Fellowes, J., and Rubin, P. (**1997**). "Talker identification based on phonetic information," J. Exp. Psychol. Hum. Percept. Perform. **23**, 651–666.
Shafiro, V., Jenkins, J., and Strange, W. (**2003**). "Identifying the sources of environmental sound with a varying number of spectral channels," J. Acoust. Soc. Am. **113**, 2326.
Shannon, R., Zeng, F.-G., Kamath, V., Wygonski, J., and Ekelid, M. (**1995**). "Speech recognition with primarily temporal cues," Science **270**, 303–304.
Shannon, R., Zeng, F.-G., and Wygonski, J. (**1998**). "Speech recognition with altered spectral distribution of envelope cues," J. Acoust. Soc. Am. **104**, 2467–2476.
Shannon, R. V. (**1992**). "Temporal modulation transfer functions in patients with cochlear implants," J. Acoust. Soc. Am. **91**, 2156–2164.
Sheffert, S. M., Pisoni, D. B., Fellowes, J. M. and Remez, R. E. (**2002**). "Learning to recognize talkers from natural, sinewave, and reversed speech samples," J. Exp. Psychol. Hum. Percept. Perform. **28**, 1447–1469.
Spahr, A., Dorman, M., and Loizou, P. (**2002**). "Effects on performance of partial misalignments of spectral information in acoustic simulations of cochlear implants," J. Acoust. Soc. Am. **112**, 2356.
Viemeister, N. F. (**1979**). "Temporal modulation transfer function based on modulation thresholds," J. Acoust. Soc. Am. **66**, 1364–1380.
Wu, K., and Childers, D. G. (**1991**). "Gender recognition from speech. I. Coarse analysis," J. Acoust. Soc. Am. **112**, 1828–1848.
Zeng, F. G. (**2004**). "Compression and cochlear implants," in *Springer Handbook of Auditory Research; Compression: From Cochlea to Cochlear Implants*, edited by S. P. Bacon, R. R. Fay, and A. N. Popper (Springer, New York), pp. 184–220.

Acoustic correlates of timbre space dimensions: A confirmatory study using synthetic tones[a)]

Anne Caclin,[b)] Stephen McAdams,[c)] Bennett K. Smith, and Suzanne Winsberg
Institut de Recherche et Coordination Acoustique/Musique (STMS-IRCAM-CNRS), 1 place Igor Stravinsky, F-75004 Paris, France

(Received 13 September 2004; revised 18 April 2005; accepted 18 April 2005)

Timbre spaces represent the organization of perceptual distances, as measured with dissimilarity ratings, among tones equated for pitch, loudness, and perceived duration. A number of potential acoustic correlates of timbre-space dimensions have been proposed in the psychoacoustic literature, including attack time, spectral centroid, spectral flux, and spectrum fine structure. The experiments reported here were designed as direct tests of the perceptual relevance of these acoustical parameters for timbre dissimilarity judgments. Listeners presented with carefully controlled synthetic tones use attack time, spectral centroid, and spectrum fine structure in dissimilarity rating experiments. These parameters thus appear as major determinants of timbre. However, spectral flux appears as a less salient timbre parameter, its salience depending on the number of other dimensions varying concurrently in the stimulus set. Dissimilarity ratings were analyzed with two different multidimensional scaling models (CLASCAL and CONSCAL), the latter providing psychophysical functions constrained by the physical parameters. Their complementarity is discussed. © *2005 Acoustical Society of America.* [DOI: 10.1121/1.1929229]

PACS number(s): 43.75.Cd, 43.66.Jh [NHF] Pages: 471–482

I. INTRODUCTION

Human abilities to recognize sound sources (the sound of a door slamming, footsteps, musical instruments, voices, etc.) are essential to our everyday behavior. Their sophistication allows for complex tasks such as recognizing the emotions embedded in speech or enjoying music. Such abilities are presumed to rely largely on a capacity to perceive and process timbre differences, making timbre analysis a fundamental task of the auditory system (see McAdams, 1993; Handel, 1995).

By definition, timbre is the *perceptual* attribute that distinguishes two tones of equal pitch, loudness, and duration (ANSI, 1973). Typically musical timbre is what distinguishes perceptually a piano from a clarinet playing the same note (e.g., A4), with the same intensity (e.g., mezzo forte), and for the same duration. This example highlights the relationship between timbre and sound source identification. Instrument identification on the basis of timbre has been investigated after various modifications of the original acoustic signals (Berger, 1964; Saldanha and Corso, 1964; Hajda, 1999). Hajda (1999) has shown that for brief tones (from impulsive instruments), the integrity of the temporal structure is crucial for identifying the instrument. However for long tones, the sustained part (played forward or backward) is sufficient to allow recognition. It implies that instrument recognition relies upon temporal and spectral or spectrotemporal information, suggesting that different perceptible acoustical parameters might be grouped under the term timbre.

Timbre is indeed usually described as a *multidimensional* perceptual attribute of complex tones. It has been hypothesized that contrary to pitch, which relies primarily on the tone's fundamental period, and loudness, which depends on tone intensity, timbre relies on several parameters (acoustical dimensions) of the sound. The holy grail of timbre studies has been to uncover the number and nature of these dimensions. Two major strategies have been used: ratings on verbal scales (see Kendall and Carterette, 1993, for a review) and most often, multidimensional scaling (MDS) of (dis)similarity ratings (see McAdams, 1993; Hajda *et al.*, 1997, for reviews).

First applied to musical timbre by Plomp (1970), MDS offers the advantage that it does not make any assumptions regarding the underlying acoustical dimensions. In such a study, listeners rate the dissimilarity between the two stimuli of all possible pairs of sounds from a set of stimuli. The resulting dissimilarity matrices are subjected to multidimensional scaling. MDS is a procedure in which dissimilarity data arising from N subjects ($N \geqslant 1$) are modeled to fit distances in some type of space, usually Euclidean of low dimensionality R. Several MDS models and techniques have been developed, such as INDSCAL (Carroll and Chang, 1970) or CLASCAL (Winsberg and De Soete, 1993). Some MDS models (e.g., Torgerson, 1958; Kruskal, 1964a, b) produce rotationally invariant solutions. Weighted Euclidean models in which the salience of each dimension is different for each subject (INDSCAL) or for each latent class of subjects (CLASCAL) produce solutions with axes oriented in a psychologically meaningful way. In the latent class approach, each of the N subjects is assumed to belong to one and only one of

[a)]Portions of this work were presented in "A confirmatory analysis of four acoustic correlates of timbre space," Acoustical Society of America, Cancun, Mexico, 2002.

[b)]Electronic mail: anne.caclin@chups.jussieu.fr. Present address: LENA-CNRS UPR 640, Hôpital Pitié-Salpétrière, 47 bd de l'Hôpital, 75013 Paris, France.

[c)]Electronic mail: smc@music.mcgill.ca. Present address: CIRMMT, Faculty of Music, McGill University, 555 rue Sherbrooke ouest, Montréal, Québec H3A IE3, Canada.

a small number T ($T \ll N$) of latent classes, and all the subjects in the same class are assumed to weight all dimensions identically. It is not known in advance to which latent class a particular subject belongs. This latent class approach, incorporated in CLASCAL, drastically reduces the number of parameters of the INDSCAL model. An extension of the Euclidean or weighted Euclidean model proposed by Winsberg and Carroll (1989) postulates that stimuli differ not only with respect to common dimensions, but also with respect to specific or unique dimensions possessed by each stimulus (these specificities could of course be zero). In the CLASCAL model, the distance between two objects i and j for class t is given by

$$d_{ijt} = \left[\sum_{r=1}^{R} w_{tr}(x_{ir} - x_{jr})^2 + v_t(s_i + s_j) \right]^{1/2}, \quad (1)$$

where R is the number of dimensions of the model, x_{ir} the coordinate of the ith stimulus on the rth dimension, s_i the square of the specificity value for object i, w_{tr} the weight assigned to the rth dimension by class t, and v_t the weight assigned to the whole set of specificity values by class t.

CONSCAL (Constrained Scaling) is a more recent development in MDS modeling (Winsberg and De Soete, 1997). The CONSCAL models are useful in situations in which a small number of known physical parameters may be used to describe the stimuli, and it is likely that these are the very attributes upon which the subjects make their dissimilarity ratings. The CONSCAL models constrain the axes of the distance model to be monotone transformations of these physical attributes. Two CONSCAL models have been proposed by Winsberg and De Soete (1997), where the distances between object i and object j are given by

$$d_{ij} = [(\mathbf{f}_i - \mathbf{f}_j)^t \mathbf{I} (\mathbf{f}_i - \mathbf{f}_j)]^{1/2}, \quad (2)$$

$$d_{ij} = [(\mathbf{f}_i - \mathbf{f}_j)^t \mathbf{A} (\mathbf{f}_i - \mathbf{f}_j)]^{1/2}, \quad (3)$$

where there are R physical dimensions, $\mathbf{f}_i$ is the vector of monotone transformations for the ith object, its rth component being $f^{(r)}(x_i^{(r)})$, $x_i^{(r)}$ is the coordinate for the ith object on the rth dimension, and $f^{(r)}$ is the monotone transformation for the rth dimension. $\mathbf{A}$ is an $R \times R$ symmetric matrix with ones on the diagonal and $\mathbf{I}$ is an $R \times R$ identity matrix. In the first model [Eq. (2)] the axes are assumed to be orthogonal, but in the second model [Eq. (3)] they are not.

The monotone transformation $f^{(r)}$ for the rth dimension is represented by a monotone spline function. Splines are piecewise polynomials of a given degree joined at a number of interior knots. Splines have the advantage of great flexibility, ease of computation, and local support. Note that in the CONSCAL models, instead of estimating a coordinate for each stimulus for each dimension, a function is estimated for each dimension. In the latent class extension of CONSCAL, a different function is estimated for each dimension for each latent class of subjects. Thus, the CONSCAL models have the advantage for psychophysical research of producing psychophysical functions, and the shapes of those functions are informative (see McAdams and Winsberg, 2000).

When applied to timbre dissimilarity ratings, MDS yields a perceptual space commonly known as a *timbre space*. This space is only derived from listeners' dissimilarity ratings, except when using a model like CONSCAL. In all cases, the distances between timbres in the space are perceptual distances. In using general (as opposed to constrained) MDS models the last step of such a timbre space study is to propose an interpretation for each of the perceptual dimensions, usually in terms of an underlying acoustical dimension.

Depending on the set of stimuli and the group of subjects, two- to four-dimensional timbre spaces have been reported in MDS studies using natural sounds from musical instruments or synthetic tones, generally made to imitate instruments of the orchestra. When acoustical correlates are proposed, most of the studies so far (e.g., Grey, 1977; McAdams *et al.*, 1995; Marozeau *et al.*, 2003) have emphasized the role of spectral center of gravity [(SCG), amplitude-weighted mean frequency of the energy spectrum] and attack time, the latter separating impulsive from sustained tones. Other parameters have been less systematically reported, e.g., spectral flux, a measure of the fluctuation of the spectrum over time (McAdams *et al.*, 1995), spectral spread (Marozeau *et al.*, 2003), spectral irregularity (Krimphoff, McAdams, and Winsberg, 1994), harmonic onset asynchrony (Grey, 1977). Along with these shared dimensions, a number of instruments are characterized by rather high specificity values (Krumhansl, 1989). It has not always been possible to propose an interpretation for these specificity values (McAdams *et al.*, 1995), although for some instruments there are good candidates (e.g., return of the hopper for the harpsichord).

From a psychophysical point of view, dissimilarity rating methods are known to be sensitive to judgment bias, in the sense that listeners usually pay attention to only a limited number of parameters, which is interpreted as reflecting the perceptual salience of the parameters (Miller and Carterette, 1975). MDS studies are thus presumed to highlight the most perceptually salient timbre parameters that are likely to be of importance in a variety of situations (voice recognition, music listening). Nevertheless they have a common drawback: given the multiplicity of acoustical parameters that could be proposed to explain perceptual dimensions, one can never be sure that the selected parameters do not merely covary with the true underlying parameters. This is especially true for three-dimensional (3D) or four-dimensional spaces, where for some dimensions only weak correlations between perceptual and acoustical dimensions are found. It turns out to be difficult in this case to select the appropriate acoustical parameter(s), particularly if the proposed parameters are correlated among themselves to some extent within the stimulus set. There are also concerns regarding whether or not it is valid to use MDS when some of the dimensions might be categorical in nature, which is the case when the stimulus set includes impulsive and sustained instruments. Therefore two questions remain open: (1) is a continuous space a good model of the perceptual relationships among timbres? and (2) if such a model is appropriate, are the proposed underlying acoustical dimensions correct?

The experiments reported here intend to deal with these issues, according to the following approach: we start with the

construction of spaces of synthetic sounds varying along continuous acoustical dimensions that have been chosen on the basis of previous MDS studies of timbre. We then use stimuli sampling these acoustical spaces in classical dissimilarity rating experiments. If the timbre space model is correct, there should be a good match between the physical space and the resulting perceptual space. We believe that this confirmatory approach is relevant both in the context of musical acoustics and for auditory perception studies in general, considering timbre perception as a model of complex sound perception. A similar approach has already been used (Miller and Carterette, 1975; Samson, Zatorre, and Ramsay, 1997). Miller and Carterette (1975) have shown that subjects can use fundamental frequency, amplitude envelope, and the number of harmonics when making dissimilarity ratings, but not harmonic structure or the pattern of harmonic onsets. A few points warrant mention here: First, no attempt was made *a priori* to equalize the perceptual ranges of variation of the different parameters in their study. Therefore, because fundamental frequency variations were very salient, they could have prevented subjects from using harmonic structure in their ratings. Second, their approach was to explore possible musical spaces, and they did not model explicitly the timbre dimensions arising from dissimilarity rating studies of natural instrument sounds. Samson, Zatorre, and Ramsay (1997) confirmed that attack time and spectral center of gravity values are used in timbre dissimilarity ratings. Note that in these two studies only a limited number of values (3) along each dimension were used, so the results could be explained in terms of categorical perception, and not as reflecting the perception of attributes varying along continuous axes. Further it is impossible to characterize adequately the corresponding psychophysical functions.

For the present study, the parameters varying between the sounds were selected on the basis of previous timbre dissimilarity studies (in particular Grey, 1977; Krimphoff *et al.*, 1994; McAdams *et al.*, 1995). Along each acoustical dimension, there were 16 different values to avoid creating unwanted categories. In the first experiment, we tested a space where attack time, spectral centroid, and spectral flux varied between the timbres. Based on the results of this first experiment, further testing was conducted to investigate contextual effects on the salience of spectral flux (Experiment 2). Finally a 3D space where attack time, spectral centroid, and spectral irregularity varied was tested (Experiment 3). Analyses were conducted both with CLASCAL and CONSCAL models. CLASCAL analyses aim to select freely the model best fitting the data, to uncover the most salient acoustical parameters. CONSCAL analyses allow for more refined interpretation, with an estimation of the shape of psychophysical functions for the different axes. CONSCAL has been used only once in the context of timbre studies (McAdams and Winsberg, 2000). The data sets of the present study offered a valuable opportunity to test the relative adequacy of the CLASCAL and CONSCAL models.

II. EXPERIMENT 1: ATTACK TIME, SPECTRAL CENTROID, AND SPECTRAL FLUX

A. Method

1. Participants

Thirty listeners (aged 19–51 years, 14 female) participated in Experiment 1. None of them reported any hearing loss, and 18 of them had received musical training. Musicians had been practicing music for 12 years on average (ranging from 4 to 27 years). Listeners were naive as to the purpose of the experiment and were paid for their participation.

2. Stimuli

Sixteen tones having 20 harmonics were created by additive synthesis, using MAX/ISPW (Lindemann *et al.*, 1991) on a NeXT workstation (sampling rate=44 100 Hz, resolution =16 bits). The fundamental frequency was 311 Hz (E♭4). Three parameters varied among the stimuli (Fig. 1): attack time, SCG, and fluctuation of the spectral envelope over the first 100 ms (spectral flux). The amplitude envelope was always composed of a linear rise (attack time), followed by a plateau and an exponential decay [Fig. 1(a)]. The spectrum was harmonic, and at any time point, the amplitude spectrum was a power function of harmonic rank n [Fig. 1(b)]:

$$A_n = k \times 1/n^{\alpha} \tag{4}$$

with A_n the amplitude of the nth harmonic. The exponent of this power function completely determined the value of the instantaneous spectral center of gravity.

A preliminary adjustment experiment run with eight listeners (who did not participate in the main experiment) allowed us to uncover formulas to keep perceived duration constant when changing attack time and loudness constant when changing SCG. The reference tone (T_0) had 15 ms attack, 400 ms plateau, and 200 ms decay, with a SCG of 933 Hz, and no spectral flux. Its level was approximately 80 dB SPL (A-weighted). Listeners had to adjust the plateau duration for a test tone with a 200 ms attack, so that it appeared as long as the reference tone. Listeners were also asked to adjust the SCG and spectral flux of test tones so that they would appear as different perceptually from the reference tone (T_0) as was the 200 ms attack tone. When SCG was adjusted, attack time was fixed at 15 ms and spectral flux at 0 Hz, and when spectral flux was adjusted, attack time was fixed at 15 ms and SCG at the third harmonic (933 Hz). The ranges of variation of the three parameters for the main experiment were chosen accordingly. Finally participants of this preliminary experiment had to adjust the levels of the test tones to match the loudness of the reference.

In the main experiment, attack time ($t1$) varied between 15 and 200 ms, in logarithmic steps, as it has often been proposed that the logarithm of attack time explains the corresponding timbre dimension better than the attack time itself (cf. Krimphoff *et al.*, 1994; McAdams *et al.*, 1995). The duration of the plateau ($t2$) was fixed at 400 ms when the attack lasted 15 ms, and was adjusted to keep perceived

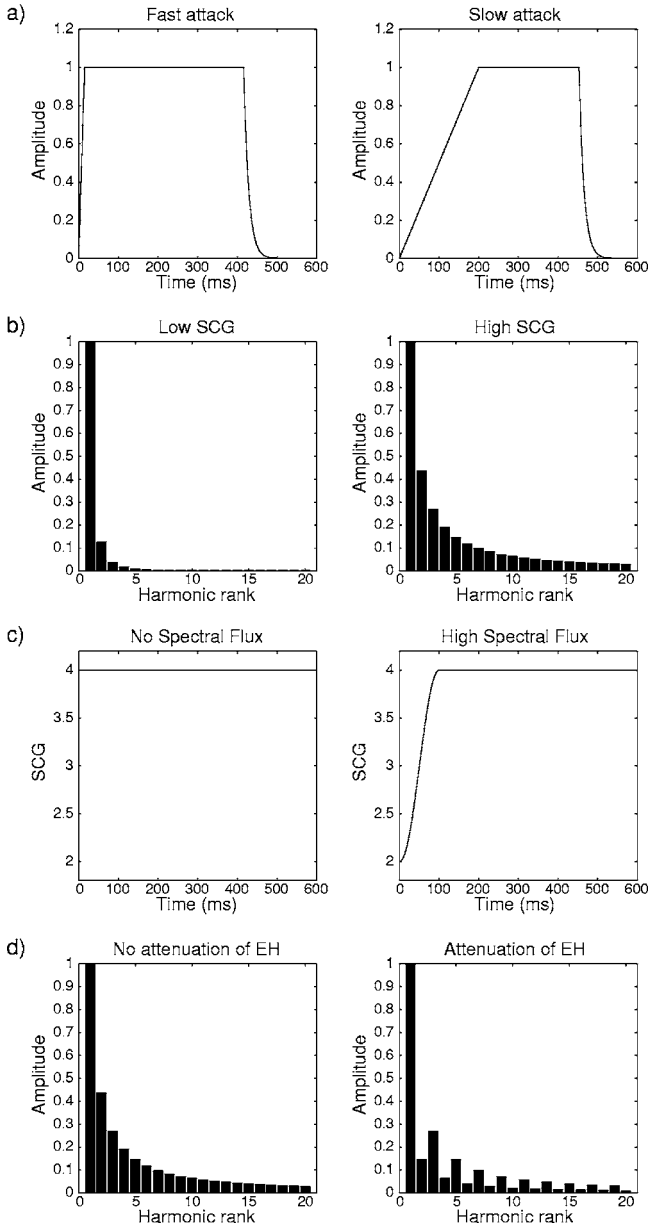

FIG. 1. Stimulus construction. (a) Attack time (Experiments 1, 2A, 3). (b) Spectral center of gravity (SCG, Experiments 1, 2B, 3). (c) Spectral flux with SCG plotted in units of harmonic rank (Experiments 1, 2A, 2B, 2C). (d) Even harmonic (EH) attenuation (Experiment 3). Amplitudes are given on arbitrary linear scales.

sound duration constant using a formula derived from the preliminary adjustment experiment: $t2=412-0.8\times t1$ ($t1$ and $t2$ in ms).

The spectral center of gravity was computed as follows:

$$\mathrm{SCG}=\frac{\sum_n n\times A_n}{\sum_n A_n}. \tag{5}$$

SCG was varied by changing the value of the exponent α in Eq. (4). SCG varied in linear steps between 933 and 1400 Hz (i.e., from 3 to 4.5 in harmonic rank units). After equalization of rms levels of T_i and T_0, the loudness of tone T_i was adjusted according to

$$20\log\frac{A(T_i)}{A(T_0)}=-1.9\times(\mathrm{SCG}(T_i)-\mathrm{SCG}(T_0)). \tag{6}$$

Spectral flux consisted of a half-cycle sinusoidal variation of SCG in the first 100 ms. It models the progressive expansion of the spectrum toward the higher harmonics that exists in some instruments, such as the trumpet. This variation of instantaneous SCG is equivalent to an asynchrony in the rise of the harmonics, the higher ones appearing later. Grey (1977) has proposed it as a correlate of one dimension of timbre. More generally, this model was chosen because it represents a variation of the spectrum over time that is not perceived as vibrato (see Hajda, 1999, for a detailed analysis of vibrato perception) and corresponds roughly to the kind of spectral envelope variation found in the attack portions of some musical instruments, although its evolution is necessarily independent of attack time in our stimuli. The parameter that varied between sounds was the difference between the SCG value in the steady portion of the tone and the initial value of the SCG. This difference ranged from 0 to 560 Hz (i.e., 0–1.8 harmonic ranks) with equally spaced steps.

The coordinates of the points sampling the physical space were chosen among a set of computer-generated random spaces complying with the following rules: each of the three parameters took 16 different values as described earlier, and each value was used only once, thus leading to a total of 16 different sounds. The retained distribution of stimuli in the 3D space was chosen as a compromise between two constraints: first, any two stimuli should not be too close to each other; second, the stimuli should be homogeneously distributed, avoiding "empty" regions in the space. In this way we obtained a good sampling of the physical space with no two sounds sharing a value on any of the three dimensions of interest [see Fig. 2(a) and Table I].

3. Procedure

All experimental routines were programmed using PSIEXP (Smith, 1995) on a NeXT workstation. The experiment took place in a soundproof booth, and the sounds were played to the subject via Sennheiser HD 520 II headphones after digital-to-analog conversion and amplification (Yamaha P2075 power amplifier). Participants were first asked to listen to the 16 sounds of the experiment to become familiarized with the range of variation. After ten randomly chosen practice trials, they were to rate the dissimilarity for all possible pairs of the 16 sounds (136 pairs). Dissimilarity ratings were made with the mouse on a scale presented on the computer screen with end points labeled "same" and "different" (in French). Scale values were digitized on a 0 to 1 scale. Listeners were allowed to listen to the pairs as many times as they wanted prior to making their ratings, and they were requested to keep their rating strategy as constant as possible.

4. Statistical analyses

First, correlations were computed among subjects' dissimilarity ratings for pairs of nonidentical sounds ($N=120$). Hierarchical clustering (average linkage algorithm) was per-

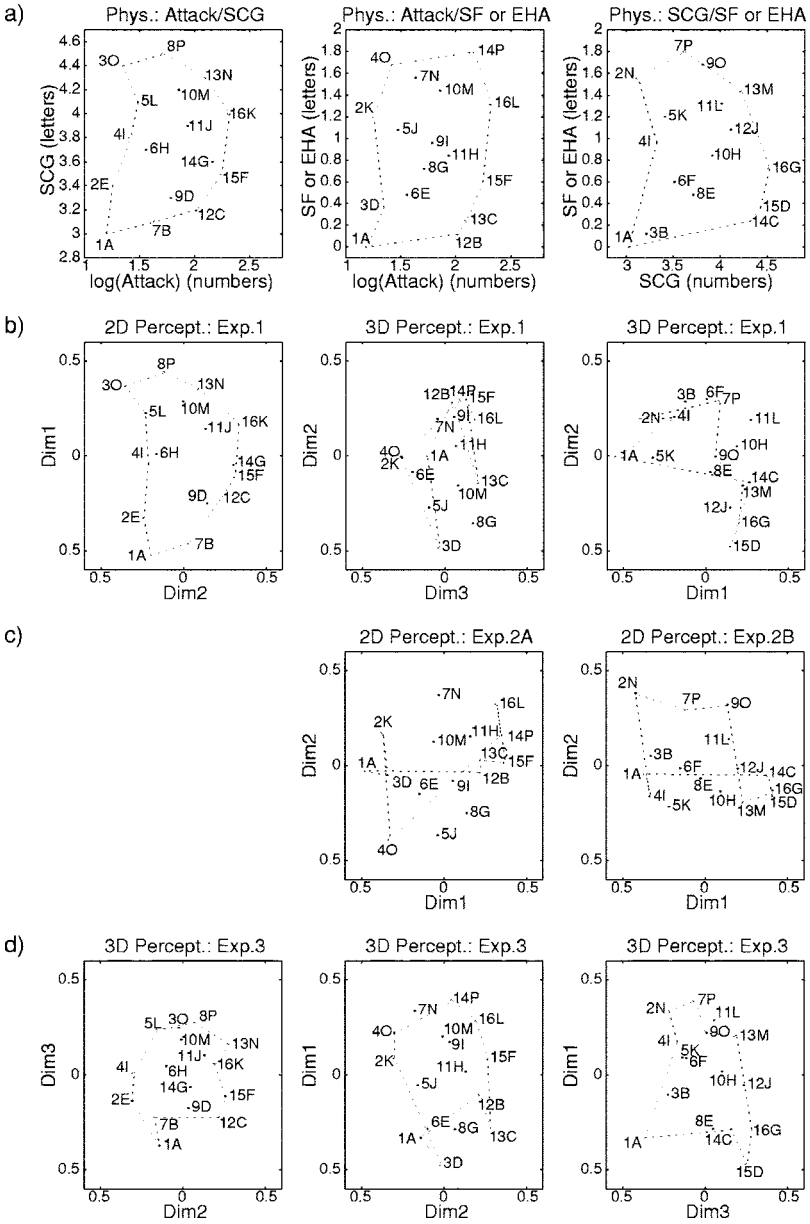

FIG. 2. Physical and perceptual spaces. (a) Physical space. (b) CLASCAL spaces for Experiment 1, left panel =2D space, middle and right panels=3D space. (c) 2D CLASCAL spaces for Experiment 2A (middle panel) and 2B (right panel). (d) 3D CLASCAL space for Experiment 3. In the top row, for each panel, the numbers refer to values for the physical dimension along the abscissa, and the letters to values for the physical dimension along the ordinate. The same labels are used in the other rows (per column). Note that any number–letter pairing only refers to the same sound within a column. Dotted lines connect the outer stimuli in the physical space to help appreciate visually the structural relations between physical and perceptual spaces.

formed on the correlation matrix in order to detect the subjects whose ratings systematically differed from the others. More precisely the values that were entered in the analysis were one minus the correlation coefficient (r), in order to transform the correlations into distances. Data from outlying subjects were discarded from subsequent analyses. The interest of this preliminary step in the analysis is practical: removing the subject(s) that is (are) the most different from all the others allows us to obtain more stable MDS solutions, making model selection an easier task.

Dissimilarity ratings from the remaining subjects were analyzed using CLASCAL (Winsberg and De Soete, 1993) and CONSCAL models (Winsberg and De Soete, 1997). The coordinates of the stimuli on the three physical dimensions tested (logarithm of attack time, SCG, and spectral flux values) were entered into the CONSCAL models. In both CLASCAL and CONSCAL analyses, model selection involves choosing the appropriate number of latent classes and the appropriate number of dimensions. Analyses were made in three steps as outlined in detail in Winsberg and De Soete (1993). A first choice is made for the number of latent classes (from one to five) using Hope's (1968) Monte Carlo test (using 100 repetitions) on the null model, i.e., a model with no spatial structure whatsoever. Bayesian Information Criterion (BIC statistic, see Winsberg and De Soete, 1993, for example), which reflects the fit of the model with a penalty for models with increasing number of parameters, is then used to select candidates for the best spatial model: for CLASCAL the number of dimensions with or without specificities; for CONSCAL the number of dimensions and the classes of spline functions (see the following for more details on spatial model selection). Finally, the appropriate number of latent classes is chosen using Hope's procedure on the spatial model. If the number of classes selected in the last step is not equal to that chosen on the null model, the last two steps (selection of spatial model and of number of classes) are repeated until they converge. After selection of the best CLASCAL model

TABLE I. Physical and CLASCAL perceptual coordinates for Experiment 1. Attack time is given in ms; SCG and spectral flux (SFl) are given in harmonic rank. Perceptual coordinates are given on an arbitrary scale. The superscripts indicate the perceptual dimensions significantly correlated ($p < 0.05$) with Attack (+) and SCG (●).

Physical space			2D perceptual space		3D perceptual space		
Attack^{+}	SCG$^{●}$	SFl	Dim 1$^{●}$	Dim 2^{+}	Dim 1$^{●}$	Dim 2^{+}	Dim 3^{+}
15	3.00	0.00	−0.53	0.21	−0.55	0.01	0.11
42	3.10	1.56	−0.46	−0.03	−0.41	−0.19	0.04
100	3.20	0.12	−0.23	−0.22	−0.13	−0.28	−0.04
59	3.30	0.96	−0.25	−0.14	−0.19	−0.21	−0.06
17	3.40	1.20	−0.33	0.25	−0.32	0.01	0.26
168	3.50	0.60	−0.11	−0.31	0.01	−0.30	−0.13
141	3.60	1.80	−0.05	−0.30	0.08	−0.29	−0.09
35	3.70	0.48	0.01	0.16	0.03	0.09	0.19
25	3.80	1.68	−0.04	0.22	0.06	0.00	0.26
84	3.90	0.84	0.14	−0.13	0.19	−0.05	−0.07
199	4.00	1.32	0.17	−0.33	0.27	−0.19	−0.18
29	4.10	1.08	0.23	0.23	0.15	0.27	0.10
70	4.20	1.44	0.29	0.00	0.22	0.16	−0.08
119	4.30	0.24	0.36	−0.08	0.26	0.14	−0.20
21	4.40	0.36	0.37	0.36	0.14	0.48	0.04
50	4.50	0.72	0.44	0.12	0.19	0.36	−0.17

and the best CONSCAL model, a parametric bootstrap procedure is used to compare them.

a. CLASCAL spatial model selection. For a given number of latent classes, the three models that best fit the data were determined on the basis of the BIC statistic. Two- to five-dimensional models, with or without specificity values, were considered. The best model among those three was selected according to the results of three Hope's tests. The CLASCAL algorithm also produces *a posteriori* probabilities for the belongingness of each subject to each of the latent classes. A subject was assigned to a particular class when any of these probabilities was greater than 0.9. Correlations between the perceptual dimensions and the original acoustical dimensions were computed and their significance was tested using Fisher's *r*-to-*z* test.

b. CONSCAL spatial model selection. For a given number of latent classes, we estimated several models, with spline orders (the degree of the piecewise polynomial plus 1) from two to four, and one to three interior knots (the number of polynomial pieces minus 1 in this case). We started modeling with the same kind of spline for all the dimensions, using the CONSCAL model assuming orthogonal dimensions. The best two models among these nine models were chosen according to the BIC statistics. We then looked at models with combinations of the two types of splines selected and models with lower-order splines or splines with less interior knots on one dimension. We selected the model with the smallest BIC. Finally, with Hope's test we compared the retained model with the model having the same types of splines as the selected one, but allowing dimensions to be nonorthogonal.

c. Comparison of CLASCAL and CONSCAL models. Monte Carlo samples were generated using the best CONSCAL model plus normal error. The log likelihood ratio for the real data obtained for the two models (the best CONSCAL model and the best CLASCAL model) was then compared to the distribution of log likelihood ratios obtained for the Monte Carlo samples. The null hypothesis was rejected when the log likelihood ratio for the real data exceeded the 0.95 level for the bootstrapped distribution under the null model (the best CONSCAL model in this case).

B. Results

The data from two subjects were removed after the hierarchical clustering analysis. The mean coefficient of determination between these two subjects and other subjects' ratings were $r^2(118)=0.14$ and $r^2(118)=0.15$, respectively. After removing those subjects, the mean coefficient of determination between subjects' dissimilarity ratings was $r^2(118)=0.23$ (SD=0.04).

1. CLASCAL space

MDS with CLASCAL on the data from the 28 remaining subjects yielded a two-dimensional (2D) perceptual space without specificity values and two latent classes of subjects [Fig. 2(b), left panel, Table I]. These two dimensions were correlated with SCG [$r^2(14)=0.96, p<0.0001$] and attack time [$r^2(14)=0.81, p<0.0001$], respectively (note that r^2 is the percentage of variance explained). For the second dimension, the correlation was even better using the logarithm of the attack time [$r^2(14)=0.87, p<0.0001$]. Neither of these two dimensions was correlated with spectral flux ($p>0.5$ in both cases). Even when considering the 3D solution [again with two latent classes of subjects and no specificity values, Fig. 2(b), middle and right panel, Table I], the additional dimension did not correlate significantly with spectral flux values [$r^2(14)=0.06, p=0.38$]. Adding a dimension actually tended to disorganize the attack-time dimension [Fig. 2(b), middle panel]. When considering the 2D solution with specificity values, sounds with high spectral flux values did not have greater specificity values than the rest of the sounds.

The subjects were classified *a posteriori* into two classes of 11 and 17 subjects. Subjects in the second class weighted more heavily the two dimensions (weights for dimensions 1 and 2: 1.20 and 1.36) than those in class 1 (weights: 0.80 and 0.65), suggesting that they used a larger range of the available dissimilarity scale. It is important to note that the ratios between the weights for the two dimensions are different for the two classes, with the first class weighting more on the first dimension (corresponding to SCG) and the second weighting more on the second dimension (corresponding to attack time). This means the dimensions do not have the same relative salience for each class. Both classes contained musically trained subjects (3 out of 11 in class 1 and 7 out of 17 in class 2).

2. CONSCAL space

MDS with CONSCAL selected a model with one class of subjects and orthogonal dimensions. A cubic spline with one interior knot best modeled the attack-time dimension and

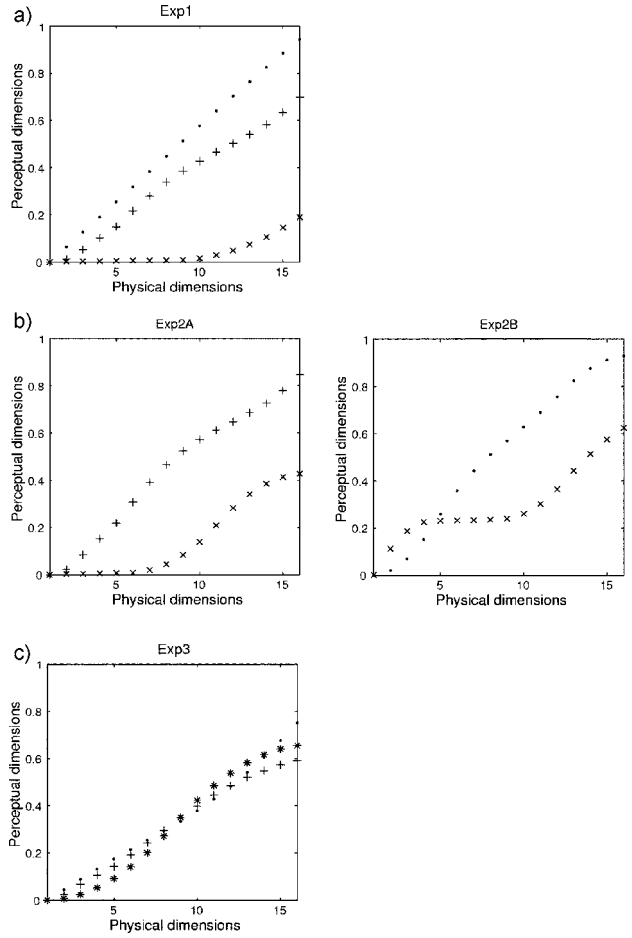

FIG. 3. Psychophysical functions as determined with CONSCAL. (+) Log(attack), (●) SCG, (×) spectral flux, and (*) even-harmonic attenuation. (a) 3D space for Experiment 1. (b) 2D spaces for Experiment 2A (left panel) and Experiment 2B (right panel). (c) 3D space for Experiment 3. The numbers on the abscissa are for the rank of the parameter value (from 1 to 16) in the stimulus set. Log(attack), SCG, spectral flux, and attenuation of even harmonics increase from left to right.

quadratic splines with one interior knot were sufficient for the other two dimensions (note that the monotone splines we are using are integrated B-splines as described in Winsberg and De Soete, 1997, and that the degrees reported here are those of the monotone splines, which correspond to the degrees of the B-splines plus 1). Given that CLASCAL analyses selected a 2D model with two dimensions correlated with the logarithm of attack time and SCG, we also compared the 3D CONSCAL model with the 2D CONSCAL model obtained when eliminating the axis corresponding to spectral flux. The 3D model was retained (Hope's test with 100 Monte Carlo simulations, $p<0.01$ for rejection of the 2D model). The 3D one-class CONSCAL model was finally compared to the 2D two-class CLASCAL model, and the CONSCAL model was not rejected ($0.09<p<0.10$ for rejecting CONSCAL). The CONSCAL spaces for all three experiments are represented in Fig. 3 using psychophysical functions. To help compare CLASCAL and CONSCAL models, an example of two such spaces represented in the same way (scatterplots) is provided in Fig. 4 (data from Experiment 2A).

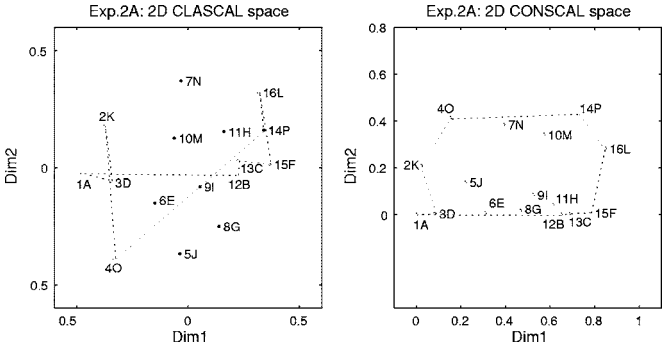

FIG. 4. Experiment 2A: 2D CLASCAL and CONSCAL spaces for comparison. Numbers refer to attack time, letters to spectral flux, as in the middle column of Fig. 2.

C. Discussion

These data confirm the perceptual significance of attack time as well as SCG, as revealed by dissimilarity ratings. It is also clear that listeners use a continuous range of attack times to perform their dissimilarity ratings. At the same time spectral flux is *not* used by listeners to perform their dissimilarity ratings according to the CLASCAL analysis. The CONSCAL analysis suggests that they might actually use spectral flux to some extent to perform their dissimilarity ratings, but this concerns only the sounds with the highest spectral flux values, and their contribution to the dissimilarity ratings is much smaller than for attack time and SCG [see the rightmost part of the psychophysical curves, Fig. 3(a)]. These MDS results are consistent with participants' subjective reports. Indeed they reported using attack-time information and "sound-color" information in their ratings but did not report using any *variation* of "sound-color."

The data from this first experiment contradict the idea that listeners take spectro-temporal variations into account in their dissimilarity ratings of timbre pairs. There are several possible explanations: either our model of spectral flux is not perceptually relevant, or it is a less salient parameter than the other two. Two facts must be mentioned here: First, participants of the preliminary adjustment experiment did not report any difficulty in adjusting the spectral flux value of the test tone, highlighting the fact that this parameter is salient when it is the only physical dimension to vary. Second, the values of the three physical parameters were chosen to correspond approximately to an equal range of perceived dissimilarity in unidimensional contexts. We therefore hypothesized that spectral flux salience might be sensitive to contextual effects, and particularly to the number of other dimensions varying concurrently. We investigated this hypothesis in the second experiment using physical spaces with only one or two parameters varying among the sounds.

III. EXPERIMENT 2: ONE- AND TWO-DIMENSIONAL SPACES WITH SPECTRAL FLUX

A. Method

1. Participants

Thirty-one listeners (aged 17–48 years, 22 females) were recruited to participate in this experiment. None of

them had participated in Experiment 1. None of them reported any hearing loss, and 15 of them had received musical training. Musicians had practiced music for 13 years on average (2–25 years). Listeners were naive as to the purpose of the experiment and were paid for their participation. They were randomly assigned to three groups (condition A: 11 subjects, conditions B and C: 10 subjects each).

2. Stimuli

Three different sets (A, B, and C) of 16 stimuli were constructed as in Experiment 1, except that for condition A SCG was kept constant (933 Hz, i.e., at the third harmonic), for condition B attack time was kept constant (15 ms), and for condition C both SCG and attack time were kept constant (933 Hz and 15 ms, respectively). Thus the stimulus set for condition A was the projection of the 3D space of Experiment 1 onto the SCG=3 plane, for condition B its projection onto the t1=15 ms plane, and for condition C its projection onto the spectral flux axis.

3. Procedure

Each of the three groups of subjects performed dissimilarity ratings on only one of the three sets of stimuli. The experimental procedure and statistical analyses were identical to those in Experiment 1 for conditions A and B, except for the number of latent classes in the MDS analyses, which was only allowed to vary between one and three given the smaller number of subjects in each condition. For the CONSCAL analyses, only the two physical variables used to create the sounds were entered in the analyses. For condition C, the experimental procedure was as in Experiment 1, but the analyses were different, since one may not perform unidimensional analyses with CLASCAL and CONSCAL. We simply looked at the correlation between dissimilarity measures and the distances predicted by the single physical axis.

B. Results

In each of the three conditions, the data from one subject were discarded after hierarchical clustering of the correlation matrix. The mean coefficients of determination with other subjects' ratings were $r^2(118)=0.13$, $r^2(118)=0.18$, and $r^2(118)=0.16$, for conditions A, B, and C, respectively. After removing these data, the mean coefficients of determination between subjects ratings were $r^2(118)=0.17$ (SD=0.03), $r^2(118)=0.23$ (SD=0.04), and $r^2(118)=0.20$ (SD=0.01), for conditions A, B, and C, respectively. In conditions A and B, CLASCAL analyses yielded 2D perceptual spaces, with two latent classes of subjects and no specificities. One-class CONSCAL models were retained in both cases. CLASCAL and CONSCAL spaces are represented in Figs. 2(c) and 3(b), and CLASCAL perceptual coordinates are reported in Table II.

1. Condition A: 2D attack and spectral flux

a. CLASCAL space. Dimension one of the perceptual space was correlated with attack time $[r^2(14)=0.75, p<0.0001]$, and again, the correlation was even better with its logarithm $[r^2(14)=0.91, p<0.0001]$. The second dimension was not significantly correlated with spectral flux values $[r^2(14)=0.05, p=0.4]$. A more detailed analysis revealed that the second dimension separated sounds with low spectral flux (data points collapsed in the center of the axis) from sounds with higher spectral flux, but within these two groups the sounds are not ordered according to spectral flux.

TABLE II. Physical and CLASCAL perceptual coordinates for Experiment 2. Units are as in Table I and the superscripts indicate the perceptual dimensions significantly correlated ($p<0.05$) with Attack (+), SCG (●), and SFI (×).

Experiment 2A (SCG=third harmonic)				Experiment 2B (Attack=15 ms)			
Physical space		Perceptual space		Physical space		Perceptual space	
Attack$^+$	SFl	Dim 1$^+$	Dim 2	SCG$^●$	SFl$^×$	Dim 1$^●$	Dim 2$^×$
15	0.00	−0.48	−0.03	3.00	0.00	−0.37	0.04
42	1.56	−0.03	0.37	3.10	1.56	−0.42	−0.38
100	0.12	0.22	−0.03	3.20	0.12	−0.33	−0.05
59	0.96	0.05	−0.08	3.30	0.96	−0.33	0.16
17	1.20	−0.38	0.18	3.40	1.20	−0.22	0.22
168	0.60	0.37	0.02	3.50	0.60	−0.15	0.01
141	1.80	0.34	0.16	3.60	1.80	−0.12	−0.29
35	0.48	−0.15	−0.15	3.70	0.48	−0.03	0.07
25	1.68	−0.33	−0.39	3.80	1.68	0.14	−0.32
84	0.84	0.16	0.15	3.90	0.84	0.09	0.14
199	1.32	0.31	0.32	4.00	1.32	0.14	−0.14
29	1.08	−0.04	−0.37	4.10	1.08	0.20	0.02
70	1.44	−0.06	0.13	4.20	1.44	0.22	0.19
119	0.24	0.22	0.03	4.30	0.24	0.38	0.05
21	0.36	−0.35	−0.06	4.40	0.36	0.40	0.16
50	0.72	0.14	−0.25	4.50	0.72	0.41	0.13

The two classes of subjects were composed of five subjects each. The first class weighted more heavily the first dimension corresponding to attack time than the second dimension (weights: 0.42 and 0.30), and the reverse was true for the second class (weights: 1.58 and 1.70). Both classes contained musically trained subjects (three out of five in class 1, two out of five in class 2).

b. CONSCAL space. The one-class model with orthogonal dimensions and having a cubic spline with one interiot knot for the attack-time dimension and a quadratic spline with two interior knots for the spectral-flux dimension was selected. This model was compared with the two-class 2D CLASCAL model. At the 5% and 1% levels, CLASCAL was selected ($p<0.01$ for rejecting CONSCAL).

2. Condition B: 2D SCG and spectral flux

a. CLASCAL space. Dimension one of the perceptual space was correlated with SCG $[r^2(14)=0.98, p<0.0001]$. Dimension two was weakly correlated with spectral flux values $[r^2(14)=0.26, p=0.04]$. Dimension two was more strongly correlated with the exponential of the spectral flux values $[r^2(14)=0.40, p=0.007]$.

The two classes of subjects were composed of three and six subjects. The second class weighted more heavily the first dimension corresponding to SCG than the second dimension (weights: 1.51 and 1.04), and the reverse was true for the first class (weights: 0.49 and 0.96). The first class was composed of three musically untrained subjects. Four out of six subjects in class 2 were musically trained.

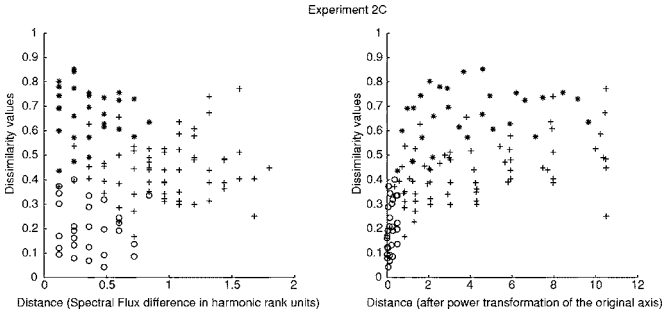

FIG. 5. Mean dissimilarities versus physical distances for Experiment 2C. Left panel: original physical distances along the abscissa in units of harmonic rank; right panel: physical distances computed after power transformation of the original physical axis. Dissimilarities along the ordinate are on an arbitrary scale [0-1]. (○) pairs of sounds with low spectral-flux values; (+) pairs of sounds with one having little spectral flux and one having a high spectral flux; (∗) pairs of sounds with high spectral flux values.

b. CONSCAL space. The one-class model with nonorthogonal dimensions having quadratic splines with three interior knots on both dimensions was selected ($0.01<p<0.02$ for rejecting the model with orthogonal dimensions). The off-diagonal coefficient in the 2×2 transformation matrix **A** [see Eq. (3)] was equal to −0.341. This means that in this model, the physical axes (SCG and spectral flux) are at an angle of 110° instead of being orthogonal (90°), suggesting that the perceptual effect of a high spectral flux is larger when the SCG in the steady portion of the tone is high (or conversely that the perceptual effect of a high SCG is larger when the spectral flux value is high). This one-class CONSCAL model was compared with the two-class 2D CLASCAL model, and CONSCAL was not rejected ($0.08<p<0.09$ for rejecting CONSCAL).

3. Condition C: One-dimensional spectral flux

As can been see in Fig. 5, dissimilarities were not well predicted by the distances along the spectral flux axis [$r^2(118)=0.0008, p=0.76$]. At first glance only a disappearance of very low dissimilarity ratings for the largest differences in spectral flux can be observed (compare the left and right halves of Fig. 5). A closer look at the results shows that even if dissimilarities and physical distances are not significantly correlated, there is some structure in the data. Because in Experiments 2A and 2B there was a trend for sounds with high spectral flux values to be separated from those with little or no spectral flux in subjects' ratings, we separated the 16 sounds into two groups of eight, according to spectral flux values (see Fig. 5). When the two sounds in a pair have little spectral flux (28 pairs), the perceived dissimilarity is small: 0.20 on average (SD=0.10), whereas it is bigger when one of the sounds has little spectral flux and the other a high spectral flux value: 0.44 on average (SD=0.12, 64 pairs). The average dissimilarity rating is even higher between two sounds with high spectral flux values: 0.67 (SD=0.11, 28 pairs). This confirms that sounds with high spectral flux values are separated from those with little spectral flux in dissimilarity ratings, and further that sounds with high spectral flux values are distinguished from one another.

Because CONSCAL analyses in Experiments 1, 2A, and 2B suggested that the psychophysical functions for the spectral flux axis were very compressive for low spectral flux values and expansive for high spectral flux values, we considered power transformations of the original physical scale. Instead of taking as explanatory physical distances the differences between spectral flux values (i.e., SF_j-SF_i as the distance between sounds i and j), we took the differences between power transformations of those values ($SF_j^a-SF_j^a$). In order to choose the most appropriate value for a, we computed the correlation coefficients between these transformed physical distances and dissimilarity ratings for increasing values of a. There was a sharp elbow in the correlation coefficient versus a curve for $a=4$, so we retained this value. The dissimilarity ratings were better predicted by these transformed physical distances than by the original ones [$r^2(118)=0.28, p<0.0001$]. For comparison, CONSCAL models explained more than 70% of the variance in dissimilarity ratings for the other experiments. So even if subjects used spectral flux in their dissimilarity ratings in this unidimensional context, spectral flux only explained part of the variance in the data, suggesting that there is a fair amount of uncertainty in listeners' ratings as far as this parameter is concerned. It may also be that the power transformation of the physical axis is not the best estimate of the psychophysical function for spectral flux.

C. Discussion

The perceptual significance of attack time and SCG was confirmed as in Experiment 1. The results of Experiment 2 shed new light on the relevance of spectral flux for timbre dissimilarity ratings. First, both in uni- and bi-dimensional contexts, listeners used spectral flux in their dissimilarity ratings, as shown in conditions A and B with the CONSCAL results, and in condition C by the correlation between transformed physical distances and dissimilarity ratings. In bi-dimensional contexts, as in Experiment 1, the range of dissimilarities accounted for by spectral flux is much smaller than that accounted for by either attack time or SCG. As compared with the first experiment (see Fig. 3), spectral flux information was used to a larger extent when variation only occurred along one concurrent dimension instead of two, and was more strongly inhibited by attack time than by SCG. This confirmed our hypothesis about the relationship between spectral flux salience and the number of concurrent variable acoustical dimensions.

These results raise a number of issues. First, it might be difficult to use a dynamic parameter when making dissimilarity ratings, especially in our spectral flux case, which values may not easily be ordered on a perceptual scale (see Experiment 2C). Second, there might exist interactions in the processing of spectral flux and other timbre dimensions. In particular, the preliminary adjustment data used to set the range of variation of spectral flux in the set of stimuli were collected with constant attack time (15 ms) and SCG (933 Hz), but the perceptual effect of a given spectral flux value might depend on attack time or SCG. The nonorthogonality of the dimensions of the CONSCAL space in Experiment 2B favors the existence of interactions of this type between

SCG and spectral flux. Finally, the spectral flux model chosen might have a limited perceptual salience. It is possible that modeling spectral flux by a fluctuation of the spectrum during the plateau of the sound might be more salient. The perceptual effects of such fluctuations have been studied by Hajda (1999), who was able to relate them to vibrato perception. We propose that subjects might be more sensitive to spectral variations when they are pseudoperiodic and when several cycles of variations are present in the sound.

The question remains open concerning whether or not it is possible to find a third dimension of timbre that is salient enough to be used in dissimilarity ratings when both attack time and SCG vary. In Experiment 3 we tested an additional dimension to address this issue.

IV. EXPERIMENT 3: ATTACK TIME, SPECTRAL CENTROID, AND SPECTRAL IRREGULARITY

A. Method

1. Participants

Thirty listeners (aged 19–45 years, 18 female) participated in this experiment. None of them participated in either of the previous experiments. None of them reported any hearing loss, and 15 of them had received musical training. Musicians had practiced music for 11 years on average (3–38 years). Listeners were naive as to the purpose of the experiment and were paid for their participation.

2. Stimuli

Sixteen sounds were created as in Experiment 1, except that the spectral flux dimension was replaced by a selective attenuation of even harmonics relative to odd harmonics. A preliminary adjustment experiment (with six listeners not included in the main experiment) was performed, as in Experiment 1, in order to choose a range of variation of this parameter that was perceptually equivalent to that for the other two parameters. In the main experiment, attenuation of even harmonics ranged from 0 to 8 dB, and could take 16 different values separated by equal steps (in dB, see Table III). In the preliminary experiment, subjects were also requested to adjust the level of a tone with attenuated even harmonics to match the loudness of a reference tone without attenuated even harmonics. We found that it was not necessary to adjust the level of the attenuated-even-harmonic tones.

3. Procedure

The experimental procedure and statistical analyses were as in Experiment 1.

B. Results

On the basis of hierarchical clustering of the correlation matrix, the data from two subjects were discarded from subsequent analyses. The mean coefficient of determination between these two subjects' and other subjects' ratings were $r^2(118)=0.08$ and $r^2(118)=0.10$, respectively. After removing those subjects, the mean coefficient of determination between subjects' dissimilarity ratings was $r^2(118)=0.23$ (SD $=0.04$).

TABLE III. Physical and CLASCAL perceptual coordinates for Experiment 3. Units are as in Table I and the superscripts indicate the perceptual dimensions significantly correlated ($p<0.05$) with Attack (+), SCG (●), and EHA (∗). Even harmonic attenuation (EHA) is given in dB relative to odd harmonics.

Physical space			Perceptual space		
Attack^{+}	SCG$^{\bullet}$	EHA*	Dim 1*	Dim 2^{+}	Dim 3$^{\bullet}$
15	3.00	0.00	−0.33	0.14	−0.37
42	3.10	6.93	0.34	0.18	−0.23
100	3.20	0.53	−0.10	−0.21	−0.23
59	3.30	4.27	0.17	−0.03	−0.17
17	3.40	5.33	0.09	0.31	−0.14
168	3.50	2.67	0.09	−0.26	−0.11
141	3.60	8.00	0.39	−0.05	−0.07
35	3.70	2.13	−0.28	0.10	0.05
25	3.80	7.47	0.22	0.30	0.01
84	3.90	3.73	0.02	−0.13	0.10
199	4.00	5.87	0.29	−0.19	0.05
29	4.10	4.80	−0.05	0.16	0.24
70	4.20	6.40	0.20	0.01	0.19
119	4.30	1.07	−0.28	−0.28	0.16
21	4.40	1.60	−0.47	0.02	0.25
50	4.50	3.20	−0.29	−0.07	0.28

1. CLASCAL space

MDS analysis showed that a 3D model without specificity values and two latent classes of subjects best fit the data. The three perceptual dimensions correlated with the three physical dimensions that were included in the synthetic space [Fig. 2(d) and Table III]. Dimension one was correlated with the degree of attenuation of even harmonics [$r^2(14)=0.74, p<0.0001$]. Dimension two was correlated with attack time [$r^2(14)=0.63, p=0.0001$], and with its logarithm [$r^2(14)=0.72, p<0.0001$]. Finally dimension three was correlated with SCG [$r^2(14)=0.95, p<0.0001$].

The two classes of subjects were composed of 8 and 19 subjects, respectively. One subject could not be assigned with certainty to either of the classes. The first class weighted more heavily the first dimension corresponding to even-harmonic attenuation (weights: 0.84, 0.67, and 0.60), and the second class weighted more heavily the third dimension corresponding to SCG (weights: 1.16, 1.13, and 1.40), suggesting that subjects in the different classes may favor one of the spectral dimensions over the other. Both classes contained musically trained subjects (5 out of 8 in class 1 and 9 out of 19 in class 2).

2. CONSCAL space

The one-class model with orthogonal dimensions having quadratic splines with one interior knot on all three dimensions was retained. When compared with the two-class 3D CLASCAL model, CLASCAL was selected at the 5% level ($0.04<p<0.05$ for rejecting CONSCAL), but at the 1% level, CONSCAL would not have been rejected. It is interesting to note that here [see Fig. 3(c)], the ranges of dissimilarities accounted for by the different dimensions are about equal, which contrasts with the results of Experiments 1 and 2.

C. Discussion

As in the two previous experiments, attack time and SCG appeared as two major determinants of timbre. Spectral irregularity (modeled with an attenuation of even-harmonic amplitudes) was also confirmed as a salient parameter of timbre. All three dimensions appear to have the same perceptual status: they contribute along a continuous scale to the dissimilarity ratings. Notice in Fig. 3 that the psychophysical functions are slightly S-shaped for the three parameters, but that there is no gross distorsion of the physical scale. This confirms that the perceptually relevant parameters are the logarithm of attack time, SCG on a linear frequency scale, and attenuation of even harmonics relative to odd ones on a linear dB scale. It is likely that with larger ranges of variation of these physical parameters saturation may occur.

V. GENERAL DISCUSSION

A. Timbre space dimensions

The experiments reported here were designed as direct tests of timbre space models. Synthetic timbre spaces were constructed using acoustical dimensions derived from natural and simulated instrument studies, and their perception was characterized using multidimensional scaling of dissimilarity ratings. We sought to confirm whether the structure of the perceptual spaces would closely parallel that of the acoustical spaces.

The present study intended in particular to confirm that attack time, spectral centroid, spectral flux, and attenuation of even harmonics explained timbre space dimensions, using fully controlled synthetic timbres. Overall it appeared to be the case, with one important restriction: spectral flux was hardly used in dissimilarity ratings when attack time and SCG varied concurrently in the stimulus set. Its contribution to timbre dissimilarity ratings was only evident when a single other attribute varied in the stimulus set. Hence, the salience of spectro-temporal parameters such as spectral flux might be more context-dependent than that of other parameters, because it decreases when the number of other parameters that vary in the stimulus set increases.

All the experiments reported here confirm that attack time and spectral centroid are salient timbre parameters, and can be used in a continuous fashion for dissimilarity ratings. As suggested earlier (e.g., McAdams *et al.*, 1995), it appears that the logarithm of attack time and not linear attack time is used in dissimilarity ratings. Spectral centroid seems to be ordered perceptually on a linear frequency scale. Attenuation of even harmonics was also confirmed as a salient timbre dimension. Attenuation in dB of even harmonics was used linearly in listeners' dissimilarity ratings. We propose that this dimension of timbre can be more generally interpreted as a model of the degree of spectral irregularity or spectrum fine structure. It is worth mentioning that people were able to use two different types of spectral information simultaneously in their ratings, one related to the global shape of the spectrum, modeled by SCG, and one related to the local shape of the spectrum, modeled by even-harmonic attenuation.

All together the present study fits well with the commonly accepted idea that attack time and spectral centroid are major determinants of timbre (Grey, 1977; Krimphoff, McAdams, and Winsberg, 1994; McAdams *et al.*, 1995; Marozeau *et al.*, 2003). The experiments reported here shed new light on possible third dimensions of timbre spaces. As stated in Sec. I, there is no established consensus on that topic. Proposed third dimensions mostly fall into two categories: spectro-temporal parameters (e.g., spectral flux) or spectral parameters (e.g., spectrum fine structure, spectral spread) related to the shape of the spectrum. Progressive expansion of the spectrum toward higher harmonics, a possible source of spectral flux, was not very influential in dissimilarity ratings when attack time and SCG also varied in the stimulus set (Experiment 1). Conversely, participants were able to use attenuation of even harmonics in dissimilarity ratings when attack time and SCG varied (Experiment 3). Therefore among all the previously proposed acoustic correlates of timbre dimensions, some might be more adequate than others. In particular, the type of spectro-temporal information that listeners can use in dissimilarity ratings remains unclear and warrants further testing.

The contrast between the respective contribution of spectral flux (Experiment 1) and attenuation of even harmonics (Experiment 3) to timbre dissimilarity ratings raises a number of questions related to dimension salience. In the current study, we have taken the contribution of a given parameter to dissimilarity ratings as an index of its perceptual salience, as in Miller and Carterette (1975). One might ask whether this index would predict performances in other tasks, such as timbre analogy judgments (see McAdams and Cunibile, 1992, for example), or speeded classification tasks (see Krumhansl and Iverson, 1992, for example). Furthermore, the relationship between dimension salience as defined here and sound source recognition remains to be explored.

B. Comparison of CLASCAL and CONSCAL models

We were able to directly compare CLASCAL and CONSCAL models in this study. Overall both of them appear adequate to model dissimilarity ratings. Out of four cases, CONSCAL was selected twice (Experiments 1 and 2B), CLASCAL once (Experiment 2A), and in one case (Experiment 3) it was not possible to decide with certainty. CONSCAL offers the theoretical advantage of requiring a much smaller number of parameters to be estimated than CLASCAL, and the psychophysical functions produced by CONSCAL analyses can provide additional information concerning the mapping of signal properties in the auditory system. Furthermore, the contribution to dissimilarity ratings of less salient dimensions such as spectral flux was better captured using CONSCAL than was the case with CLASCAL. Nevertheless, it is not possible to use such a parcimonious model without *a priori* knowledge about the underlying acoustical dimensions. Interestingly, when in all four cases CLASCAL analyses yielded two latent classes of subjects, only one class was necessary for CONSCAL models. This suggests that the shapes of psychophysical functions are rather similar across subjects.

C. Inter-individual differences

The present data suggest that inter-individual differences exist when making timbre dissimilarity ratings. Indeed, in all experiments, subjects were classified by CLASCAL into different classes of subjects that weighted timbre space dimensions differently. Several conclusions emerge from Experiments 1 and 3, where there are sufficient numbers of subjects to draw conclusions about inter-individual differences. First, the difference between subject classes depends partly upon the range of the rating scale used effectively. Another important difference in the classes concerns the different relative saliences of the axes for each class. In the first experiment, some subjects favored temporal information (attack time) over spectral information (SCG), and for other subjects the reverse was true. In the third experiment, the two classes of subjects favored a different type of spectral information. Whether these different weights reflect differences at a perceptual level or at a decisional level remains an open question. Finally, these inter-individual differences do not seem to be related to musical training. All together these results are consistent with previous findings (e.g., McAdams *et al.*, 1995), although it might be that the differences between the weights on the different dimensions are smaller in the present case. For example, in the McAdams *et al.* (1995) study the ratios between the weights on two axes could be as big as 3, whereas they never exceed 2 in our case. This could result from the greater homogeneity of synthetic timbre spaces as opposed to spaces of simulated natural instruments. In the latter case, it is likely that subjects select a limited number of acoustical parameters among all possibilities to make their ratings. Such a selection step is not necessary in the present context of low-dimensional synthetic timbre spaces.

D. Complex sound perception

Timbre space studies raise general questions about complex sound perception. In particular, one might hypothesize that the salient parameters found in these studies correspond to parameters that are extracted along the auditory pathway. There could either be pathways dedicated to the processing of each of these parameters or a more global mechanism might be involved. The present experiments were not designed to answer such a question, but using calibrated perceptual spaces such as those described here will prove to be a powerful tool for answering questions about the processing of complex sound dimensions.

ANSI (**1973**). *American National Standard—Psychoacoustical Terminology* (American National Standards Institute, New York).

Berger, K. W. (**1964**). "Some factors in the recognition of timbre," J. Acoust. Soc. Am. **36**, 1888–1891.

Carroll, J. D., and Chang, J. J. (**1970**). "Analysis of individual differences in multidimensional scaling via an *n*-way generalization of Eckart-Young decomposition," Psychometrika **35**, 283–319.

Grey, J. M. (**1977**). "Multidimensional perceptual scaling of musical timbres," J. Acoust. Soc. Am. **61**, 1270–1277.

Hajda, J. M. (1999). "The effect of time-variant acoustical properties on orchestral instrument timbres," Ph.D. thesis, University of California, Los Angeles.

Hajda, J. M., Kendall, R. A., Carterette, E. C., and Harschberger, M. L. (**1997**). "Methodological issues in timbre research," in *Perception and Cognition of Music*, edited by I. Deliège and J. Sloboda (Psychology, Hover), pp. 253–307.

Handel, S. (**1995**). "Timbre perception and auditory object identification," in *Hearing*, edited by B. C. J. Moore (Academic, San Diego), pp. 425–461.

Hope, A. C. (**1968**). "A simplified Monte Carlo significance test procedure," J. R. Stat. Soc. Ser. B. Methodol. **30**, 582–598.

Kendall, R. A., and Carterette, E. C. (**1993**). "Verbal attributes of simultaneous wind instruments timbres. I. von Bismarck's adjectives," Music Percept. **10**, 445–468.

Krimphoff, J., McAdams, S., and Winsberg, S. (**1994**). "Caractérisation du timbre des sons complexes. II. Analyses acoustiques et quantification psychophysique [Characterization of the timbre of complex sounds. II. Acoustical analyses and psychophysical quantification]," J. Phys. (Paris) **C5**, 625–628.

Krumhansl, C. L. (**1989**). "Why is musical timbre so hard to understand?," in *Structure and Perception of Electroacoustic Sound and Music*, edited by S. Nielsen and O. Olsson (Elsevier, Amsterdam), pp. 43–53.

Krumhansl, C. L., and Iverson, P. (**1992**). "Perceptual interactions between musical pitch and timbre," J. Exp. Psychol. Hum. Percept. Perform. **18**, 739–751.

Kruskal, J. B. (**1964a**). "Multidimensional scaling by optimizing goodness of fit to a nonmetric hypothesis," Psychometrika **29**, 1–27.

Kruskal, J. B. (**1964b**). "Nonmetric multidimensional scaling: A numerical method," Psychometrika **29**, 115–129.

Lindemann, E., Puckette, M., Viara, E., De Cecco, M., and Dechelle, F. (**1991**). "The architecture of the IRCAM musical workstation," Comput. Music J. **15**, 41–49.

Marozeau, J., de Cheveigné, A., McAdams, S., and Winsberg, S. (**2003**). "The dependency of timbre on fundamental frequency," J. Acoust. Soc. Am. **114**, 2946–2957.

McAdams, S. (**1993**). "Recognition of sound sources and events," in *Thinking in Sound: The Cognitive Psychology of Human Audition*, edited by S. McAdams and E. Bigand (Oxford University Press, Oxford), pp. 146–198.

McAdams, S., and Cunibile, J. C. (**1992**). "Perception of timbral analogies," Philos. Trans. R. Soc. London, Ser. B **336**, 383–389.

McAdams, S., and Winsberg, S. (**2000**). "Psychophysical quantification of individual differences in timbre perception," in *Contributions to Psychological Acoustics 8*, edited by A. Schick, M. Meis, and C. Reckhardt (BIS, Oldenburg), pp. 165–181.

McAdams, S., Winsberg, S., Donnadieu, S., De Soete, G., and Krimphoff, J. (**1995**). "Perceptual scaling of synthesized musical timbres: Common dimensions, specificities and latent subject classes," Psychol. Res. **58**, 177–192.

Miller, J. R., and Carterette, E. C. (**1975**). "Perceptual space for musical structures," J. Acoust. Soc. Am. **58**, 711–720.

Plomp, R. (**1970**). "Timbre as a multidimensional attribute of complex tones," in *Frequency Analysis and Periodicity Detection in Hearing*, edited by R. Plomp and G. F. Smoorenburg (Sijthoff, Leiden), pp. 397–414.

Saldanha, E. L., and Corso, J. F. (**1964**). "Timbre cues and the identification of musical instruments," J. Acoust. Soc. Am. **36**, 2021–2026.

Samson, S., Zatorre, R. J., and Ramsay, J. O. (**1997**). "Multidimensional scaling of synthetic musical timbre: Perception of spectral and temporal characteristics," Can. J. Exp. Psychol. **51**, 307–315.

Smith, B. (**1995**). "PsiExp: An environment for psychoacoustic experimentation using the IRCAM musical workstation," in *Society for Music Perception and Cognition*, edited by D. Wessel (University of California Press, Berkeley).

Torgerson, W. S. (**1958**). *Theory and Methods of Scaling* (Wiley, New York).

Winsberg, S., and Carroll, J. D. (**1989**). "A quasi-nonmetric method for multidimensional scaling via an extended Euclidean model," Psychometrika **54**, 217–229.

Winsberg, S. and De Soete, G. (**1993**). "A latent-class approach to fitting the weighted Euclidean model, CLASCAL," Psychometrika **58**, 315–330.

Winsberg, S., and De Soete, G. (**1997**). "Multidimensional scaling with constrained dimensions: CONSCAL," Br. J. Math. Stat. Psychol. **50**, 55–72.

Real-time synthesis of clarinet-like instruments using digital impedance models

Philippe Guillemain,[a] Jean Kergomard, and Thierry Voinier
CNRS-Laboratoire de Mécanique et d'Acoustique, 31 Chemin Joseph Aiguier, 13402 Marseille Cedex 20, France

(Received 21 April 2003; revised 28 September 2004; accepted 2 March 2005)

A real-time synthesis model of wind instruments sounds, based upon a classical physical model, is presented. The physical model describes the nonlinear coupling between the resonator and the excitor through the Bernoulli equation. While most synthesis methods use wave variables and their sampled equivalent in order to describe the resonator of the instrument, the synthesis model presented here uses sampled versions of the physical variables all along the synthesis process, and hence constitutes a straightforward digital transposition of each part of the physical model. Moreover, the resolution scheme of the problem (i.e., the synthesis algorithm) is explicit and all the parameters of the algorithm are expressed analytically as functions of the physical and the control parameters. © *2005 Acoustical Society of America.* [DOI: 10.1121/1.1937507]

PACS number(s): 43.75.Ef, 43.75.Pq [NHF] Pages: 483–494

I. INTRODUCTION

The calculation of the self-sustained oscillations of single-reed instruments such as the clarinet was proposed for the first time by Schumacher,[1] using a time domain discretization of the equations. This work, which does not attempt a real-time implementation, has later been widely developed (see, e.g., Gazengel *et al.*[2] or Ducasse[3]). Numerical methods, such as the harmonic balance, have been developed by Gilbert[4] in order to study the periodic solutions. In addition, in order to perform the calculations in real-time, several methods yielding a time domain formulation of the waves in the resonator have been developed. We can mention the well-known digital waveguide method (see, e.g., Smith[5] or Välimäki[6]) and wave digital modeling used by van Walstijn,[7] which consider the incoming and outgoing waves within each section of a bore and their scattering at the junctions between bores of different sections. We can also mention the calculation of the reflection function from impedance measurements using inverse Fourier transform, which has been used for the synthesis of the trumpet by Vergez.[8] Like the Schumacher method, since these methods consider the incoming and outgoing waves, the problem then lays in the formulation of the nonlinearity which, whatever the model, can only be expressed physically in terms of acoustic pressure and flow at the mouthpiece of the instrument.

In this paper, a real-time synthesis model using only physical variables is proposed. It first consists in directly expressing the impedance relationship at the mouthpiece between flow and pressure, which become the input and output of the linear part of the model characterizing the bore. The nonlinear coupling (based on the steady Bernoulli flow model) between the bore and the reed (described classically as a single mass-spring damped oscillator) is then modeled in a physical way. In the case of sampled signals, thanks to a suitable discretization scheme of the reed displacement, this coupling is solved explicitly whatever the shape of the bore without iterative or table-lookup schemes such as the **K**-Method described by Borin.[9]

The paper is organized as follows. Section II presents the classical physical model in the case of a cylindrical bore (see, e.g., Kergomard *et al.*[10]) allowing the construction of the main elements of the synthesis model. Section III presents a preliminary step toward the synthesis algorithm in the case of a cylindrical bore, extends it to the case of a truncated conical bore, and builds the complete synthesis model. A more complete formalism for bores of other geometries and different reed models is described in Guillemain *et al.*[11] Section IV deals with sampled variables, and presents an explicit time-domain scheme which solves the coupled system constituting the sampled physical model, its digital implementation, and its real-time control. Section V is devoted to conclusions and perspectives of this work.

II. SIMPLIFIED PHYSICAL MODEL

We first briefly describe the three components of the classical physical model. They are made of a linear impedance relationship between acoustic pressure and flow at the mouthpiece, a pressure driven linear oscillator modeling the first mode of vibrations of the reed, and a nonlinear characteristics coupling the flow to the pressure and the reed displacement at the mouthpiece.

A. Wave equation in a cylindrical lossy bore

1. Wave number expression

The first linear part of the physical model corresponds to the resonator of the instrument. We here consider a cylindrical bore. For such a geometry, if one assumes that the radius of the bore is large in front of the boundary layer thicknesses, the classical Kirchhoff's theory (see, e.g., Pierce[12]) leads, in the frequency domain, to the value of the complex wave number $k(\omega)$ for a plane wave:

[a]Electronic mail: guillem@lma.cnrs-mrs.fr

$$k(\omega)^2 = \frac{\omega^2}{c^2}(1 - i^{3/2}\alpha c^2 \omega^{-1/2}),$$

where

$$\alpha = 2/(Rc^{3/2})\left(\sqrt{l_v} + \left(\frac{c_p}{c_v} - 1\right)\sqrt{l_t}\right).$$

R is the radius of the bore: $R=7\cdot10^{-3}$ in the clarinet case. Typical values of the physical constants, in mK s units, are: $c=340$, $l_v=4\cdot10^{-8}$, $l_t=5.6\cdot10^{-8}$, $C_p/C_v=1.4$.

For the acoustic pressure, this corresponds to the time domain differential equation (see, e.g., Polack[13]):

$$\frac{\partial^2 p(x,t)}{\partial x^2} - \frac{1}{c^2}\frac{\partial^2 p(x,t)}{\partial t^2} - \alpha\frac{\partial^{3/2} p(x,t)}{\partial t^{3/2}} = 0. \quad (1)$$

To the same order of approximation, the classical expression of $k(\omega)$, that we shall use in the following is

$$k(\omega) = \frac{\omega}{c} - \frac{i^{3/2}}{2}\alpha c \omega^{1/2}. \quad (2)$$

2. Expression of the losses

Let us consider a bore of infinite length, excited in $x=0$ at $t=0$ by a Dirac impulse $\delta(x)\delta(t)$. At any point $x>0$, the acoustic pressure propagating from this source in the ($x>0$) direction can be written as a continuous sum of all the waves that can propagate in the bore:

$$p(x,t) = \int \exp(-ik(\omega)x)\exp(i\omega t)d\omega,$$

which is the inverse Fourier transform of $\exp(-ik(\omega)x)$. The filtering of a pressure wave propagating in the ($x>0$) direction between $x=0$ and $x=L$, including propagation delay, dispersion, and dissipation is then given by

$$F(\omega) = \exp(-ik(\omega)L) = \exp\left(-\frac{1}{2}\alpha c\sqrt{\frac{\omega}{2}}L\right) \times \exp\left(-i\left(\frac{\omega}{c}L + \frac{1}{2}\alpha c\sqrt{\frac{\omega}{2}}L\right)\right). \quad (3)$$

Dissipation, present in the modulus of $F(\omega)$, and dispersion, present in the nonlinear part of the phase of $F(\omega)$ are functions of frequency, and depend both on the radius and the length of the bore.

Figure 1 shows the behavior of the modulus of $F(\omega)$ as function of frequency. This filter expresses the modifications encountered by a pressure wave when it travels from one end of the bore to the other end.

3. Input impedance of a cylindrical bore (frequency domain)

For a cylindrical resonator, according to the transmission line theory, the Fourier transforms $[P_e(\omega), U_e(\omega)$ and $P_s(\omega), U_s(\omega)]$ of the dimensionless acoustic pressure and flow at the input $[p_e(t), u_e(t)]$ and at the open end $[p_s(t), u_s(t)]$ of the resonator are linked by

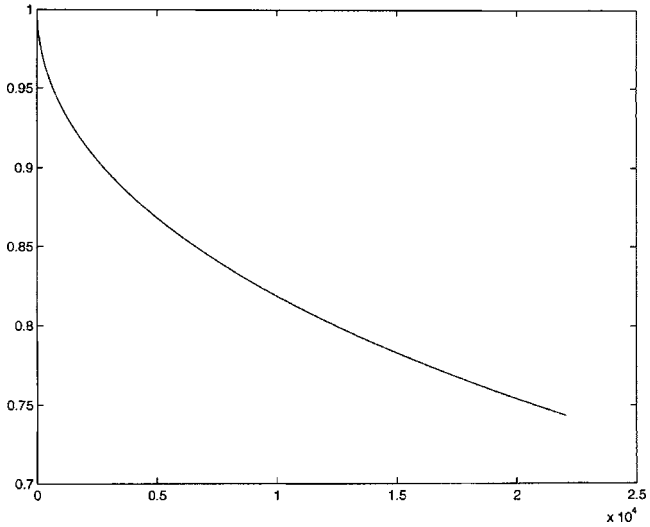

FIG. 1. Modulus of $F(\omega)$ as function of the frequency (in hertz). $L=0.5$ m, $R=7$ mm.

$$P_e(\omega) = \cos(k(\omega)L)P_s(\omega) + i\sin(k(\omega)L)U_s(\omega),$$

$$U_e(\omega) = i\sin(k(\omega)L)P_s(\omega) + \cos(k(\omega)L)U_s(\omega).$$

In these equations, the acoustic pressure $p_{e,s}$ and flow $u_{e,s}$ are normalized with respect to the physical variables $\tilde{p}_{e,s}$ and $\tilde{u}_{e,s}$ in the following way: $p_{e,s}=\tilde{p}_{e,s}/p_M$ and $u_{e,s}=Z_c/p_M\tilde{u}_{e,s}$, where $Z_c=\rho c/(\pi R^2)$ is the characteristic impedance of the resonator. The pressure p_M is the static beating-reed pressure, depending on the characteristics of the reed and defined in the Sec. II B.

As a first approximation, we assume that the radius of the bore is small compared to the wavelength. In this case, the radiation losses are negligible and the radiation effect is a length correction, taken into account in L. Under this classical hypothesis, the output impedance $P_s(\omega)/U_s(\omega)$ vanishes and only the internal losses contained in $k(\omega)$ are taken into account. This simplification let us express the relationship between acoustic pressure and flow at the input of the resonator in the following way:

$$P_e(\omega) = i\tan(k(\omega)L)U_e(\omega) = Z_e(\omega)U_e(\omega), \quad (4)$$

where $Z_e(\omega)=i\tan(k(\omega)L)$ is the dimensionless input impedance of the resonator.

B. Simple reed model

We here consider a reed model based upon a classical single mode model. This model describes in a simple way the dimensionless displacement $x(t)$ of the reed with respect to its equilibrium point $x=0$ when it is submitted to a dimensionless acoustic pressure $p_e(t)$:

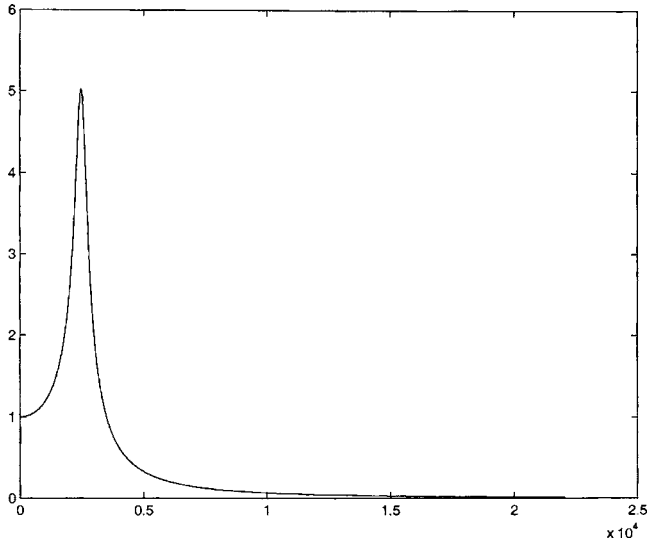

FIG. 2. Transfer function of the reed model (horizontal axis in hertz) (f_r =2500, q_r=0.2).

$$\frac{1}{\omega_r^2}\frac{d^2x(t)}{dt^2} + \frac{q_r}{\omega_r}\frac{dx(t)}{dt} + x(t) = p_e(t), \tag{5}$$

where $\omega_r = 2\pi f_r$ and q_r are, respectively, the circular frequency and the quality factor of the reed. Typical values for these parameters are: f_r=2500 Hz and q_r=0.2 in the clarinet case.

The dimensionless displacement x of the reed is defined from the physical reed displacement $\tilde{y}$ by: $x = \tilde{y}/H + p_m/p_M$, where H is the height of the opening between the reed and the mouthpiece and p_m is the static (slowly varying) pressure within the mouth. The static beating-reed pressure is expressed by: $p_M = \mu_r H \omega_r^2$, where μ_r is the mass per unit surface of the reed.

Assuming that the initial conditions of the reed movement correspond to a displacement and a velocity equal to zero, the Fourier domain equivalent of this equation gives the transfer function of the reed:

$$\frac{X(\omega)}{P_e(\omega)} = \frac{\omega_r^2}{\omega_r^2 - \omega^2 + i\omega q_r \omega_r}. \tag{6}$$

The reed displacement due to an impulse pressure $p_e(t) = \delta(t)$ is then given by

$$x(t) = \frac{2\omega_r}{\sqrt{4 - qr^2}} \exp\left(-\frac{1}{2}\omega_r q_r t\right) \sin\left(\frac{1}{2}\sqrt{4 - qr^2}\,\omega_r t\right). \tag{7}$$

Equation (7) shows that the response of the reed to an impulse can be considered noninstantaneous, since $x(0)=0$. Since the relation between $x(t)$ and $p_e(t)$ is a convolution, this property will be true for any excitation $p_e(t)$, and we will take advantage of this in the following.

Figures 2 and 3 show, respectively, the transfer function and the impulse response of this reed model.

C. Nonlinear characteristics

The dimensionless acoustic pressure $p_e(t)$, the dimensionless acoustic flow $u_e(t)$, and the dimensionless reed displacement $x(t)$ are linked in a nonlinear way at the input of the resonator through the stationary Bernoulli equation:

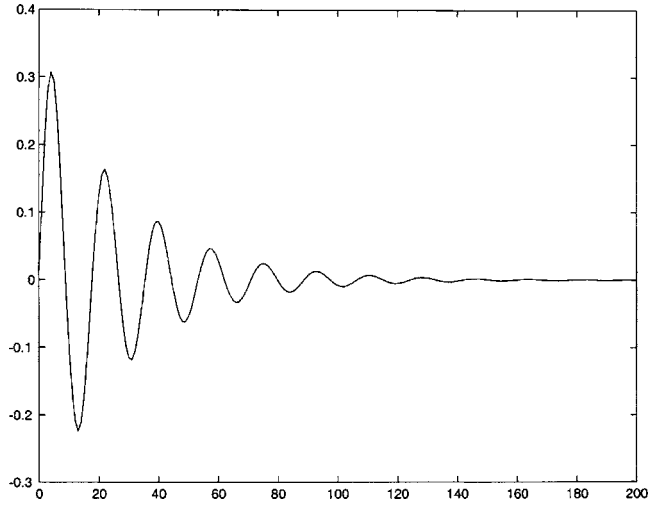

FIG. 3. Impulse response of the reed model (in samples, f_e=44 100).

$$u_e(t) = \Theta(1 - \gamma + x(t))\zeta(1 - \gamma + x(t)) \times \mathrm{sign}(\gamma - p_e(t))\sqrt{|\gamma - p_e(t)|}, \tag{8}$$

where Θ is the Heaviside function, the role of which is to keep the opening of the reed positive.

This simplified nonlinear characteristics is obtained through classical hypothesis (see, e.g., Hirschberg[14] and Kergomard[15]). The opening of the reed channel is proportional to the reed displacement. The acoustic flow generated by the reed (proportional to the reed velocity) and the unsteady term in the Bernoulli equation (proportional to the time derivative of the acoustic velocity) are ignored.

The parameter ζ is characteristic of the whole embouchure and is related to the maximum flow entering the instrument. It is defined by Kergomard,[15] after Wilson and Beavers,[16] and depends on the ratio between the reed opening and the tube cross-section area and on the reed stiffness: $\zeta = Z_c w H \sqrt{2/(\rho p_M)}$, where w is the width of the reed. Common values lay between 0.2 and 0.6 in the clarinet case. The parameter γ is the ratio between the pressure inside the mouth of the player and the static beating-reed pressure: $\gamma = p_m/p_M$. For a lossless bore and a massless reed, it evolves from 1/3, which is the oscillation threshold, to 1/2, which corresponds to the threshold of beating-reed. The parameters ζ and γ constitute two important performance parameters since they, respectively, represent the way the player holds the reed and its blowing pressure inside the instrument. Though, for clarity in the notations, the t variable is omitted, the playing parameters γ and ζ are functions of time, but slowly varying compared to the other time-dependent variables.

Figure 4 represents the nonlinear characteristics of the reed for the limit case $\omega_r = \infty$. In this case, the displacement $x(t)$ of the reed reduces to the acoustic pressure $p_e(t)$ itself and the reed behaves as a single spring.

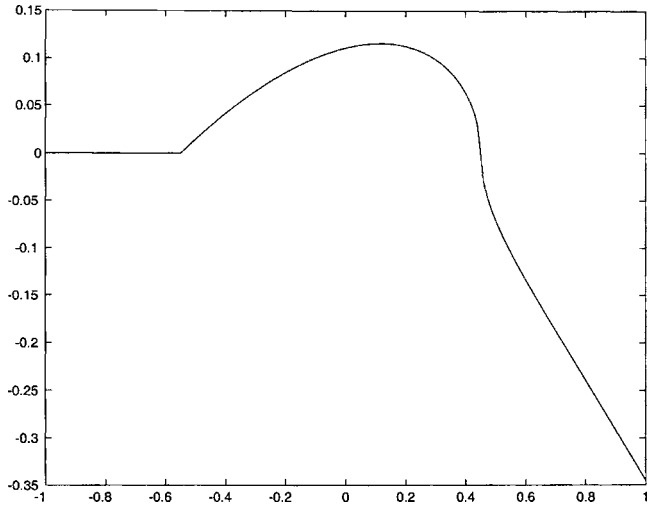

FIG. 4. Nonlinear characteristics of the reed (u as a function of p, ζ=0.3, γ=0.45).

D. Coupling of the reed and the cylindrical resonator

Combining the reed displacement equation, the impedance relation, and the nonlinear characteristics, the acoustic pressure at the mouthpiece level can finally be found by solving the following set of coupled equations:

$$\frac{1}{\omega_r^2}\frac{d^2x(t)}{dt^2} + \frac{q_r}{\omega_r}\frac{dx(t)}{dt} + x(t) = p_e(t), \tag{9}$$

$$P_e(\omega) = Z_e(\omega)U_e(\omega), \tag{10}$$

$$u_e(t) = \Theta(1-\gamma+x(t))\zeta(1-\gamma+x(t)) \times \mathrm{sign}(\gamma - p_e(t))\sqrt{|\gamma - p_e(t)|}. \tag{11}$$

The following sections will present a way of solving these equations in the time domain for sampled variables.

III. CONSTRUCTION OF THE SYNTHESIS MODEL FROM THE PHYSICAL MODEL

In order to solve this system of three equations, we first propose a different formulation of the impedance relation, compatible with a time-domain implementation. We first consider the case of a cylindrical bore, and further extend it to the case of a conical bore.

A. Expression of the input impedance of the resonator

1. Cylindrical bore

The input impedance, denoted $\mathcal{C}(\omega)$, of a cylindrical resonator is first described as a combination of looped filters. For that purpose, the impedance $Z_e(\omega)$ is written as

$$\mathcal{C}(\omega) = Z_e(\omega) = i\tan(k(\omega)L) = i\frac{\sin(k(\omega)L)}{\cos(k(\omega)L)} = \frac{\exp(ik(\omega)L) - \exp(-ik(\omega)L)}{\exp(ik(\omega)L) + \exp(-ik(\omega)L)}.$$

This last expression can be written as follows:

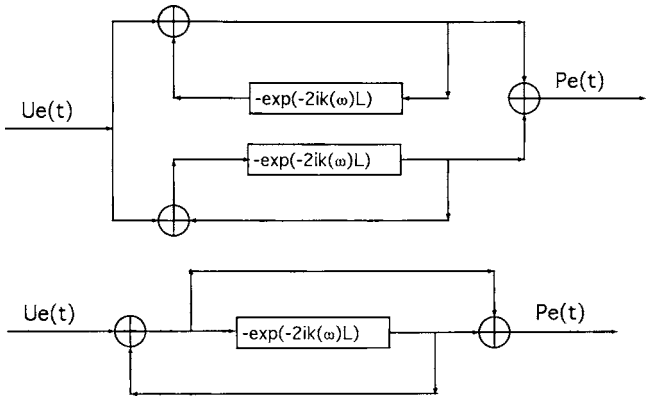

FIG. 5. Top panel: (a) Model representing the input impedance of a cylindrical resonator. Bottom panel: (b) Same model using a modified Schroeder representation.

$$\mathcal{C}(\omega) = \frac{1-\exp(-2ik(\omega)L)}{1+\exp(-2ik(\omega)L)} = \frac{1}{1+\exp(-2ik(\omega)L)} - \frac{\exp(-2ik(\omega)L)}{1+\exp(-2ik(\omega)L)}. \tag{12}$$

Figure 5(a) shows the interpretation of Eq. (12) in terms of looped filters. The transfer function of this model is directly the dimensionless input impedance of a cylindrical resonator. It is made of a sum of two elementary blocks. The upper block corresponds to the first term of the second equality in Eq. (12) and the lower block corresponds to the second term.

Figure 5(b) shows that the impedance $\mathcal{C}(\omega)$ of the cylindrical bore can be related to a Schroeder[17] all-pass filter, used for reverberation effects, by replacing the loop delay of the form $\exp(-i\omega D)$ by $-\exp(-2ik(\omega)L)$ and removing the gains and their signs. This interpretation will make the digital implementation of such filters similar up to the losses contained in $\exp(-2ik(\omega)L)$.

Figure 6 shows (top panel) the input impedance of the resonator with respect to frequency and (bottom panel) its

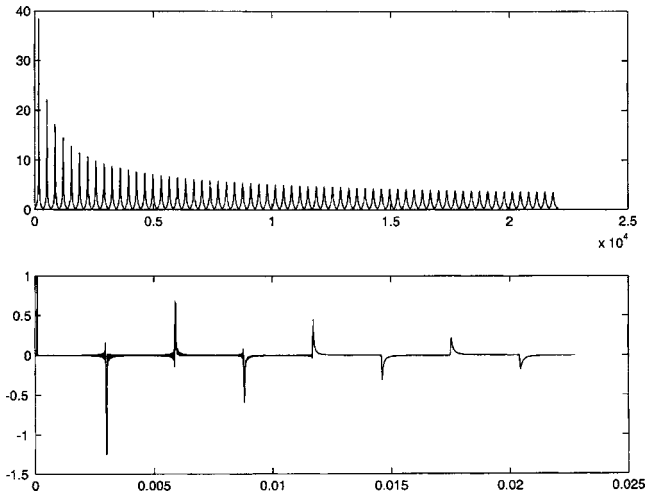

FIG. 6. Top panel: Input impedance of a cylindrical resonator (f in hertz). Bottom panel: Impulse response of a cylindrical resonator (t in seconds).

impulse response computed through an inverse Fourier transform. Bore length: $L=0.5$ m, radius $R=7$ mm.

Similarly, we denote by $\mathcal{C}^{-1}(\omega)$ the admittance of a cylindrical bore:

$$\mathcal{C}^{-1}(\omega)=\frac{1+\exp(-2ik(\omega)L)}{1-\exp(-2ik(\omega)L)}.$$

It is worth noticing that in the case of a perfectly cylindrical bore, Eq. (12) is not the most efficient way to describe the resonator. Indeed, in this case, the description based on wave variables and used, e.g., in the digital waveguides models is more efficient.

If we decompose the acoustic pressure and flow into wave variables: $P_e(\omega)=P_+(\omega)+P_-(\omega)$ and $U_e(\omega)=P_+(\omega)-P_-(\omega)$, we obtain $P_+(\omega)=(P_e(\omega)+U_e(\omega))/2$ and $P_-(\omega)=(P_e(\omega)-U_e(\omega))/2$. By denoting $\mathcal{R}(\omega)$ the reflection function satisfying $P_-(\omega)=\mathcal{R}(\omega)P_+(\omega)$, it becomes

$$\mathcal{R}(\omega)=\frac{Z_e(\omega)-1}{Z_e(\omega)+1}=-F(\omega)^2=-\exp(-2ik(\omega)L).$$

This last equation shows that the reflection function $\mathcal{R}(\omega)$ models the back and forth propagation of the pressure waves themselves, while Eq. (12) directly models the consequence of the propagation through the introduction of the reflection function inside two loops. This constitutes a difference between the method described here and wave variables methods, though both of them are physically equivalent since they consider the bore as an acoustic waveguide.

2. Conical bore

In the case of a conical bore, by assuming again that the radiation impedance can be ignored and by considering the propagation of spherical waves, the input impedance, denoted $\mathcal{S}(\omega)$, is written classically as a parallel combination of a cylindrical bore and an "air" bore:

$$\mathcal{S}(\omega)=\frac{1}{\dfrac{1}{i\omega\dfrac{x_e}{c}}+\dfrac{1}{\mathcal{C}(\omega)}},$$

where x_e is the distance between the apex and the input, expressed in terms of the angle θ of the cone and the input radius R as $x_e=R/\sin(\theta/2)$.

Noting $\mathcal{D}$ the differentiation operator: $\mathcal{D}(\omega)=i\omega$, the input impedance of a conical bore can be written in the form

$$\mathcal{S}(\omega)=\frac{\dfrac{x_e}{c}\mathcal{D}(\omega)}{1+\dfrac{x_e}{c}\mathcal{D}(\omega)\mathcal{C}^{-1}(\omega)},$$

yielding the equivalent scheme in Fig. 7.

As was the case for the cylindrical bore, this scheme shows that the wave variables and the reflection function are embedded in the model and that only the consequence of the propagation is considered.

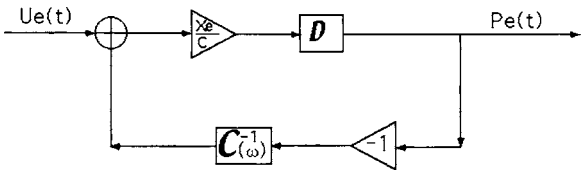

FIG. 7. Impedance model of a conical bore.

Moreover, as opposed to the case of a cylindrical bore, the use of wave variables in the case of a conical bore does not lead to a more compact description of the resonator since the reflection function $\mathcal{R}(\omega)$ is given by

$$\mathcal{R}(\omega)=-\frac{2\dfrac{x_e}{c}i\omega\exp(-2ik(\omega)L)+1-\exp(-2ik(\omega)L)}{2\dfrac{x_e}{c}i\omega+1-\exp(-2ik(\omega)L)}.$$

Here, $\mathcal{R}(\omega)$ does not reduce to a simple delay+filter and exhibits an instantaneous response proportional to $\Theta(t)\exp(-ct/(2x_e))$ for $t\leqslant 2L/c$. This is due to the presence of the "air" bore, which is a lumped element. These facts have been largely studied (see, e.g., Ref. 18).

B. Coupling of the resonator with the reed and the nonlinear characteristics

The system of two coupled equations (9) and (11), combined with any impedance model corresponding to Eq. (10), leads to the introduction of the reed and the nonlinearity as a nonlinear loop linking the output p_e to the input u_e of the resonator, as shown in Fig. 8 in the case of a cylindrical bore. The output of the model is made of the three coupled variables p_e, u_e, and x.

The model is piloted by the length L of the bore, the opening of the reed channel represented by the parameter $\zeta(t)$, and the blowing pressure represented by the parameter $\gamma(t)$.

C. External pressure

When a real instrument is simulated, the acoustic pressure in the mouthpiece is not the most perceptively relevant variable and the calculation of the external pressure is necessary. For a cylindrical bore, if we assume that the diameter is small compared to the wavelength of the frequencies

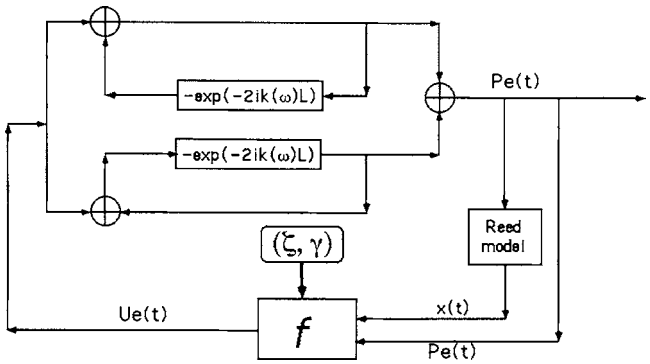

FIG. 8. Synthesis model in the case of a cylindrical bore.

propagating within the bore, the radiation is monopolar and the external pressure is expressed classically as the time derivative of the output flow: $p_{\text{ext}}(t)=du_s(t)/dt$. Let us express the output flow as a function of the dimensionless variables $p_e(t)$ and $u_e(t)$. Assuming again that the radiation impedance is negligible $[P_s(\omega)/U_s(\omega)=0]$, the following expression is obtained from the transmission line theory:

$$P_e(\omega) = i \sin(k(\omega)L)U_s(\omega),$$

$$U_e(\omega) = \cos(k(\omega)L)U_s(\omega),$$

which yields

$$U_s(\omega) = \exp(-ik(\omega)L)(P_e(\omega) + U_e(\omega)).$$

From a perceptive point of view, the quantity $\exp(-ik(\omega)L)$ can be ignored, since it represents the delay and the losses encountered by the acoustic pressure during a simple travel between the embouchure and the open end (see Fig. 1). This simplification leads to the following expression of the external pressure:

$$p_{\text{ext}}(t) = \frac{d}{dt}(p_e(t) + u_e(t)). \tag{13}$$

This approximation overestimates the high frequencies, but we point out that a deeper physical description of the radiation impedance and radiation losses is beyond the scope of this paper. For a deeper discussion, we refer the reader, e.g., to Ref. 19 for acoustic modeling or Ref. 20 for signal modeling.

IV. DISCRETE-TIME FORMULATION OF THE CONTINUOUS SYSTEM

In order to draw up the synthesis model, it is necessary to use a discrete formulation in the time domain for the impedance and the reed displacement models.

A. Approximation of the loop filter

The construction of a discrete version of the impedance relationship first requires an expression of the losses contained in $F(\omega)^2=\exp(-2ik(\omega)L)$ through a digital filter. In order to be modified easily according to the geometry of the resonator, the coefficients of the filter should make an explicit use of the geometrical variables such as the length of the bore and its radius. This requirement led us to express analytically the coefficients of the digital filter as functions of the geometrical parameters, rather than use numerical approximations and minimization techniques to compute the values of these coefficients. For that purpose, we use a classical one pole filter (see, e.g., Ref. 6), written in the following form:

$$\tilde{F}(\tilde{\omega}) = \frac{b_0 \exp(-i\tilde{\omega}D)}{1 - a_1 \exp(-i\tilde{\omega})}, \tag{14}$$

where f_e is the sampling frequency, $\tilde{\omega}=\omega/f_e$, and $D=2f_eL/c$ is the pure delay corresponding to the linear part of $k(\omega)$.

Let us express the parameters b_0 and a_1 as functions of the physical parameters, so that $|F(\omega)^2|^2=|\tilde{F}(\tilde{\omega})|^2$ for two given values ω_1 and ω_2 of ω. These two values will be different in the case of a cylindrical bore and in the case of a conical bore and will in both cases correspond to the frequencies of the two first impedance peaks, in order to ensure their exact heights. It is important to preserve this feature for a faithful simulation of the continuous dynamical system, since the linear impedance is coupled with the nonlinear characteristics. It will allow the decay times of the first two modes of the approximated impulse response of the impedance to match those of the exact impulse response, which is important for the transients induced by quick changes of $\gamma(t)$ and $\zeta(t)$. A detailed discussion on the role of the height of the first impedance peaks for the functioning of the clarinet, in particular for the oscillation threshold, can be found, e.g., in Ref. 10.

By ignoring the (small) dispersion introduced by the nonlinear part of the phase of $F(\omega)$ in the cylindrical case, the frequencies of the resonance peaks are given by $\omega_n=c\pi(n-1/2)/L$, n being an integer.

In the conical case, the frequencies of the impedance peaks are solutions of the following equation: $\sin(\omega L/c+\pi)=\omega x_e/c\cos(\omega L/c)$. In order to express the coefficients of the filter as functions of the physical parameters analytically, we use an approximation of the resonance frequencies, rather than a numerical method to solve this equation. The method consists in finding a first approximation of the solution and use a polynomial expansion around this approximation to find the final approximation. This first approximation is taken as the solution of the equation: $\sin(\omega L/c+\pi)=\cos(\omega L/c)$ and is given by $\omega_n=n\pi c/L-\pi c/(4L)$. Using a first-order limited expansion of $\sin(\omega L/c+\pi)$ and $\omega x_e/c\cos(\omega L/c)$ around $\omega=\omega_n+\epsilon_n$ and identifying the powers of ϵ_n gives directly $\epsilon_n=-c((4n-1)x_e\pi-4nL)/(L(4L+(4n-1)x_e\pi+4x_e))$. This lets us express the first two frequencies ω_1 and ω_2:

$$\omega_1 = \frac{c(12\pi L + 9\pi^2 x_e + 16L)}{4L(4L + 3\pi x_e + 4x_e)},$$

$$\omega_2 = \frac{c(28\pi L + 49\pi^2 x_e + 16L)}{4L(4L + 7\pi x_e + 4x_e)}.$$

Moreover, for the computation of $|F(\omega)^2|^2$ at frequencies ω_1 and ω_2, the radius R is replaced by an equivalent radius r_p defined by $r_p=R(1+5L/(12x_e))$. This value was determined empirically by comparing the impedance of a conical bore obtained by considering the propagation of spherical waves with an impedance of the same conical bore obtained with a concatenation of small elementary cylinders with different diameters (stepped cone), using the transmission line theory.

The system of equations to solve is then given by

$$|F(\omega_1)^2|^2(1 + a_1^2 - 2a_1\cos(\tilde{\omega}_1)) = b_0^2,$$

$$|F(\omega_2)^2|^2(1 + a_1^2 - 2a_1\cos(\tilde{\omega}_2)) = b_0^2,$$

where $|F(\omega)^2|^2=\exp(-2\alpha c\sqrt{\omega/2L})$.

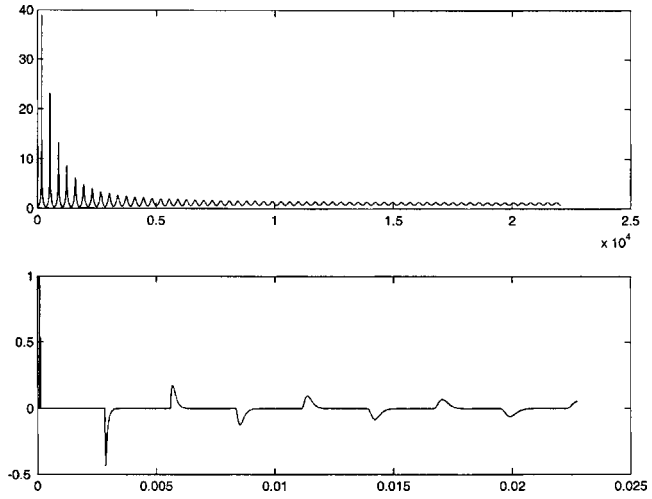

FIG. 9. Top panel: Approximated input impedance (f in hertz). Bottom panel: Approximated impulse response of the resonator (t in seconds).

By denoting $c_1=\cos(\tilde{\omega}_1)$, $c_2=\cos(\tilde{\omega}_2)$, $F_1=|F(\omega_1)^2|^2$, $F_2=|F(\omega_2)^2|^2$, $A_1=F_1c_1$, $A_2=F_2c_2$, $A_{12}=A_1-A_2$, $F_{12}=F_1-F_2$, the coefficients a_1 and b_0 are given by

$$a_1=\frac{A_{12}-\sqrt{A_{12}^2-F_{12}^2}}{F_{12}}, \tag{15}$$

$$b_0=\frac{\sqrt{2F_1F_2(c_1-c_2)(A_{12}-\sqrt{A_{12}^2-F_{12}^2})}}{F_{12}}. \tag{16}$$

B. Expression of the impedance

1. Cylindrical bore

From the expression of the input impedance of the cylindrical resonator [Eq. (12)], by denoting $z=\exp(i\tilde{\omega})$ it becomes directly:

$$\mathcal{C}(z)=\frac{1}{1+\left(\frac{b_0}{1-a_1z^{-1}}\right)z^{-D}}-\frac{\left(\frac{b_0}{1-a_1z^{-1}}\right)z^{-D}}{1+\left(\frac{b_0}{1-a_1z^{-1}}\right)z^{-D}}$$
$$=\frac{1-a_1z^{-1}-b_0z^{-D}}{1-a_1z^{-1}+b_0z^{-D}}$$

yielding the difference equation:

$$p_e(n)=u_e(n)-a_1u_e(n-1)-b_0u_e(n-D)+a_1p_e(n-1)$$
$$-b_0p_e(n-D). \tag{17}$$

Figure 9 shows the approximated input impedance as function of frequency and the impulse response of the resonator computed by the use of the difference equation. The length of the bore is $L=0.5$ m and its radius is $R=7$ mm. Comparisons with Fig. 6 show that the heights of the two first impedance peaks are equal, but that the heights of the higher order peaks are smaller. As a consequence, higher order modes decrease faster, yielding an apparently faster decay of the impulse response. Nevertheless, the decays of the first two resonance frequencies are exact. Though this phenomenon might appear as an inconvenience to the use of a first-order low pass filter to model the losses at high frequency, one can also consider it as an advantage. Indeed, it constitutes a way to take into account additional losses in the bore (coming, e.g., from a bell or tone holes radiation) that are not taken into account in the physical model, since they can be ignored at low frequencies but may play a role at higher frequencies.

2. Conical bore

In the case of a conical bore, we use the bilinear transformation: $\mathcal{D}(z)=2f_e(z-1)/(z+1)$ to approximate the differentiation operator $\mathcal{D}(\omega)$. The cylindrical bore admittance $C^{-1}(z)$ is given by $C^{-1}(z)=(1-a_1z^{-1}+b_0z^{-D})/(1-a_1z^{-1}-b_0z^{-D})$, and the digital transfer function of the conical bore is

$$\mathcal{S}(z)=\frac{1}{\frac{z+1}{2f_e\frac{x_e}{c}(z-1)}+\frac{1-a_1z^{-1}+b_0z^{-D}}{1-a_1z^{-1}-b_0z^{-D}}}.$$

By denoting $G_p=1+c/(2f_ex_e)$ and $G_m=1-c/(2f_ex_e)$, the transfer function reduces to

$$\mathcal{S}(z)=\frac{1-(a_1+1)z^{-1}+a_1z^{-2}-b_0z^{-D}+b_0z^{-D-1}}{G_p-(a_1G_p+G_m)z^{-1}+a_1G_mz^{-2}+b_0G_mz^{-D}-b_0G_pz^{-D-1}}$$

yielding the difference equation:

$$p_e(n)=b_{c0}u_e(n)+b_{c1}u_e(n-1)+b_{c2}u_e(n-2)$$
$$+b_{cD}u_e(n-D)+b_{cD1}u_e(n-D-1)$$
$$+a_{c1}p_e(n-1)+a_{c2}p_e(n-2)+a_{cD}p_e(n-D)$$
$$+a_{cD1}p_e(n-D-1), \tag{18}$$

where the coefficients b_{c0}, b_{c1}, b_{c2}, b_{cD}, and b_{cD1} are defined by

$$b_{c0}=\frac{1}{G_p},\quad b_{c1}=-\frac{a_1+1}{G_p},\quad b_{c2}=\frac{a_1}{G_p},$$

$$b_{cD}=-\frac{b_0}{G_p},\quad b_{cD1}=\frac{b_0}{G_p}$$

and the coefficients a_{c1}, a_{c2}, a_{cD}, and a_{cD1} are defined by

$$a_{c1}=\frac{a_1G_p+G_m}{G_p},\quad a_{c2}=-\frac{a_1G_m}{G_p},$$

$$a_{cD}=-\frac{b_0G_m}{G_p},\quad a_{cD1}=b_0.$$

Figure 10 shows the exact and approximated impedance of a conical bore. The characteristics of the bore are: $R=4\cdot10^{-3}$, $L=0.67$, $\theta=2°$. One can notice that the values of the exact and approximated impedances correspond for the frequencies of the first two peaks.

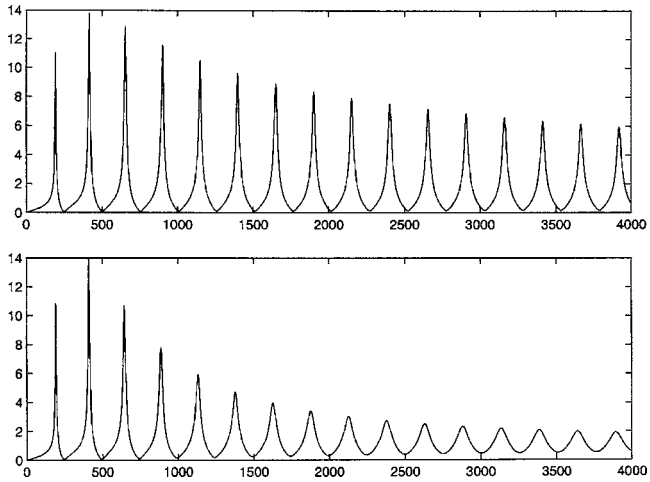

FIG. 10. Top panel: Exact impedance of a conical bore. Bottom panel: Approximated impedance of a conical bore (horizontal axis in hertz).

Figure 11 shows, for the same bore, the impulse response of the exact impedance computed through an inverse Fourier transform, and the impulse response of the approximated impedance computed through the difference equation.

As in the case of the cylindrical bore, the digital approximation of the losses leads to an underestimation of the height of high frequency impedance peaks and a faster decay of the impulse response. Nevertheless, it is worth noticing that the functioning of the whole system (e.g., its oscillation threshold) is mainly driven by the heights and frequencies of the first impedance peaks (see, e.g., Ref. 21 for a justification) and that mainly the nonlinear coupling of the impedance with the exciter, rather than the impedance itself, is responsible of the production of high frequency harmonics.

C. Approximation of the reed displacement

Similar to the propagation filter, the relationship between the acoustic pressure and the reed displacement is discretized in the time domain. Since the continuous impulse response of the reed is an exponentially damped sine function satisfying $x(0)=0$, it is natural to build a digital filter in which the displacement of the reed at time $t_n=n/f_e$ is not a function of the acoustic pressure at time t_n but at least at time $t_{n-1}=(n-1)/f_e$. It is important to point out that this is not an artificial shift of one sample that may introduce numerical instabilities in the whole scheme, as mentioned, e.g., in Ref. 22, but that it will let us keep the property $x(0)=0$ of the continuous system when the reed is submitted to a Dirac excitation. In order to satisfy this requirement, rather than using the bilinear transformation or other discretization schemes such as those studied in Ref. 22 to approximate the terms $i\omega$ and $-\omega^2$ appearing in the continuous transfer function of the reed, we use $i\omega \simeq f_e/2(z-z^{-1})$ and $-\omega^2 \simeq f_e^2(z-2+z^{-1})$. These two formulas correspond to classical centered numerical differentiation schemes that are both exact for second-order polynomials. Under these approximations, the digital transfer function of the reed is given by

$$\frac{X(z)}{P_e(z)} = \frac{\omega_r^2}{\omega_r^2 + f_e^2(z-2+z^{-1}) + \frac{f_e}{2}(z-z^{-1})q_r\omega_r}$$

$$= \frac{z^{-1}}{\frac{f_e^2}{\omega_r^2} + \frac{f_e q_r}{2\omega_r} - z^{-1}\left(\frac{2f_e^2}{\omega_r^2} - 1\right) - z^{-2}\left(\frac{f_e q_r}{2\omega_r} - \frac{f_e^2}{\omega_r^2}\right)}$$

yielding the difference equation:

$$x(n) = 0 \times p_e(n) + b_{1_a} p_e(n-1) + a_{1_a} x(n-1) + a_{2_a} x(n-2), \tag{19}$$

where the coefficients b_{1_a}, a_{1_a}, and a_{2_a} are defined by

$$a_{0_a} = \frac{f_e^2}{\omega_r^2} + \frac{f_e q_r}{2\omega_r}, \quad b_{1_a} = \frac{1}{a_{0_a}}, \quad a_{1_a} = \frac{\frac{2f_e^2}{\omega_r^2} - 1}{a_{0_a}},$$

$$a_{2_a} = \frac{\frac{f_e q_r}{2\omega_r} - \frac{f_e^2}{\omega_r^2}}{a_{0_a}}.$$

Figures 12 and 13 show, respectively, the transfer function and the impulse response of this approximated reed model ($f_r=2500$ Hz, $q_r=0.2$). Comparisons with Figs. 2 and 3 show the relevance of the approximation we used.

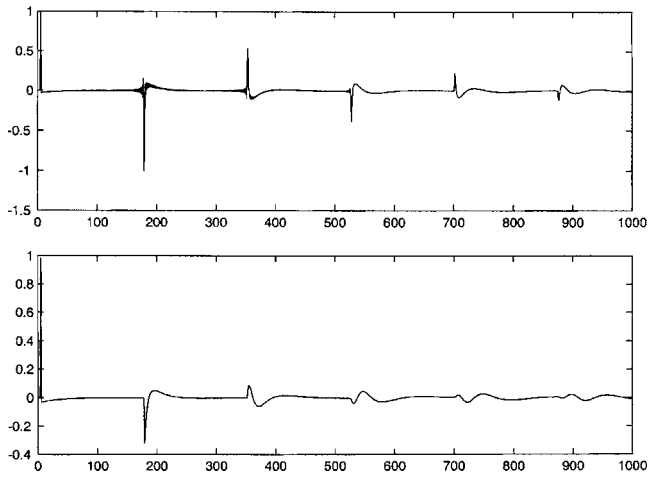

FIG. 11. Top panel: Exact impulse response of a conical bore. Bottom panel: Approximated impulse response of a conical bore (horizontal axis in samples, $f_e=44\,100$).

D. Explicit solution of the nonlinear coupled system

Either in the case of a cylindrical or a conical bore, the difference equation expressing the pressure $p_e(n)$ as function of the flow $u_e(n)$ can be written in the general form:

$$p_e(n) = b_{c0} u_e(n) + V$$

where $V=V(p_e(n-k), u_e(n-k))$, $k \geqslant 1$, contains all the terms in Eq. (17) or (18) that are known and do not depend on the time sample n. In the case of a cylindrical bore, the value of b_{c0} is set to $b_{c0}=1$, according to Eq. (17). Such a notation will let us propose a single resolution scheme valid for any bore geometry.

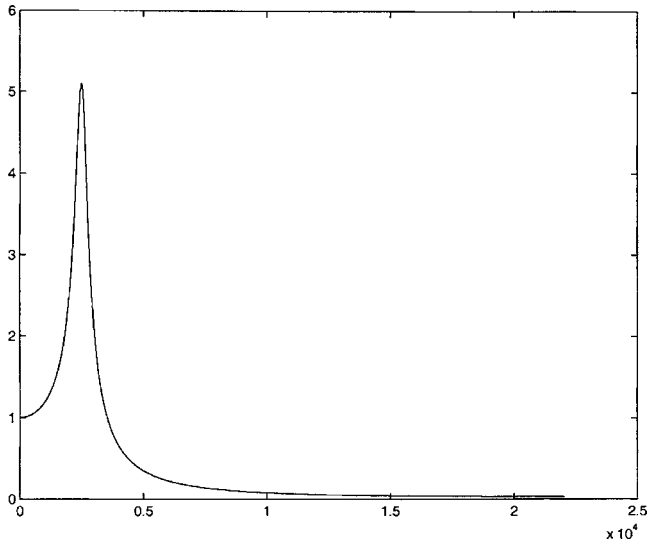

FIG. 12. Transfer function of the approximated reed model (in hertz).

The sampled formulations of the impulse responses of the reed displacement and of the impedance let us write the sampled version of the system of Eqs. (9)–(11):

$$x(n) = b_{1_a} p_e(n-1) + a_{1_a} x(n-1) + a_{2_a} x(n-2), \tag{20}$$

$$p_e(n) = b_{c0} u_e(n) + V, \tag{21}$$

$$u_e(n) = \Theta(1-\gamma+x(n))\zeta(1-\gamma+x(n)) \times \mathrm{sign}(\gamma - p_e(n))\sqrt{|\gamma - p_e(n)|}. \tag{22}$$

This system of equations is not explicit, but implicit, since the computation of $p_e(n)$ with the impedance equation (21) requires the knowledge of $u_e(n)$. In a similar way, $u_e(n)$ is obtained from the nonlinear equation (22) and requires $p_e(n)$.

Such a "delay-free loop" problem could be solved using, e.g., the **K**-method[9] for constant values of ζ and γ, but thanks to the discretization scheme of the reed displacement, the computation of $x(n)$ with Eq. (20) does not require the knowledge of $p_e(n)$ [but this of $p_e(n-1)$ which is known at time n]. This makes it possible to solve simply and exactly the coupled system in the case of time-varying values of ζ and γ.

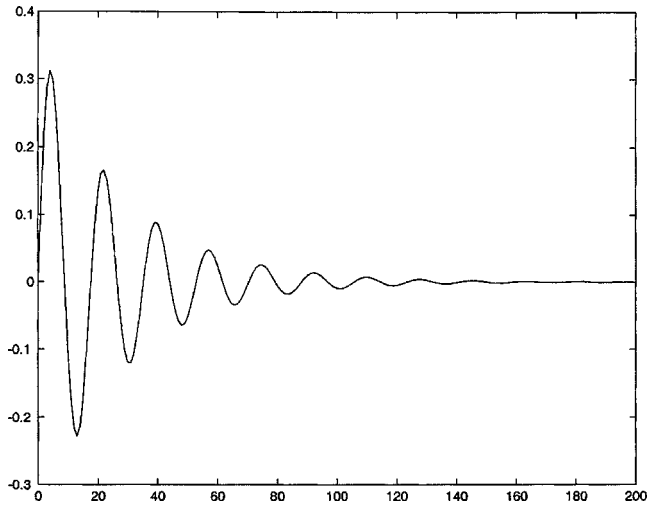

FIG. 13. Impulse response of the approximated reed model (in samples, f_e=44 100).

For that purpose, we use W [$W=W(p_e(n-k)), k \geqslant 1$] to denote all the terms in Eq. (22) that are known at time sample n:

$$W = \Theta(1-\gamma+x(n))\zeta(1-\gamma+x(n)). \tag{23}$$

With this notation, the two equations (21) and (22) can be written as

$$p_e(n) = b_{c0} u_e(n) + V, \tag{24}$$

$$u_e(n) = W\,\mathrm{sign}(\gamma - p_e(n))\sqrt{|\gamma - p_e(n)|}. \tag{25}$$

Since the role of the term $\Theta(1-\gamma+x(n))$ is to cancel W when $(1-\gamma+x(n))$ is negative, W always remain positive. We successively consider the two cases: $\gamma - p_e(n) \geqslant 0$ and $\gamma - p_e(n) < 0$ corresponding, respectively, to the cases $u_e(n) \geqslant 0$ and $u_e(n) < 0$.

When $u_e(n) \geqslant 0$, substituting the expression of $p_e(n)$ [Eq. (24)] into the equation giving $u_e(n)$ [Eq. (25)] gives

$$u_e(n) = W\sqrt{\gamma - (b_{c0} u_e(n) + V)}.$$

By taking the square of $u_e(n)$ and solving a second-order polynomial in $u_e(n)$, this expression yields

$$u_e(n) = \frac{1}{2}(-b_{c0}W^2 \pm W\sqrt{(b_{c0}W)^2 + 4(\gamma - V)}).$$

In this case, the (+) solution is the only solution for which $u_e(n)$ is real and positive [$\gamma - V \geqslant 0$ since $\gamma - p_e(n) \geqslant 0$ and $b_{c0}u_e(n) \geqslant 0$].

Similarly, when $u_e(n)$ is negative, one obtains

$$u_e(n) = -W\sqrt{(b_{c0}u_e(n) + V) - \gamma},$$

yielding

$$u_e(n) = \frac{1}{2}(b_{c0}W^2 \pm W\sqrt{(b_{c0}W)^2 - 4(\gamma - V)})$$

and the $(-)$ solution is the only solution for which $u_e(n)$ is real and negative [$\gamma - V < 0$ since $\gamma - p_e(n) < 0$ and $b_{c0}u_e(n) < 0$].

From these two solutions, one finally obtains

$$u_e(n) = \frac{1}{2}\mathrm{sign}(\gamma - V)(-b_{c0}W^2 + W\sqrt{(b_{c0}W)^2 + 4|\gamma - V|}).$$

This solution is unique since the function $\mathrm{sign}(\gamma - p_e(n))\sqrt{|\gamma - p_e(n)|}$ is a decreasing monotonous function of p_e.

The computation of the acoustic pressure and flow in the mouthpiece at time sample n is finally obtained by the sequential use of

$$x(n) = b_{1_a} p_e(n-1) + a_{1_a} x(n-1) + a_{2_a} x(n-2), \tag{26}$$

$$V = V(p_e(n-k), u_e(n-k))\ k \geqslant 1, \tag{27}$$

$$W = \Theta(1-\gamma+x(n))\zeta(1-\gamma+x(n)), \tag{28}$$

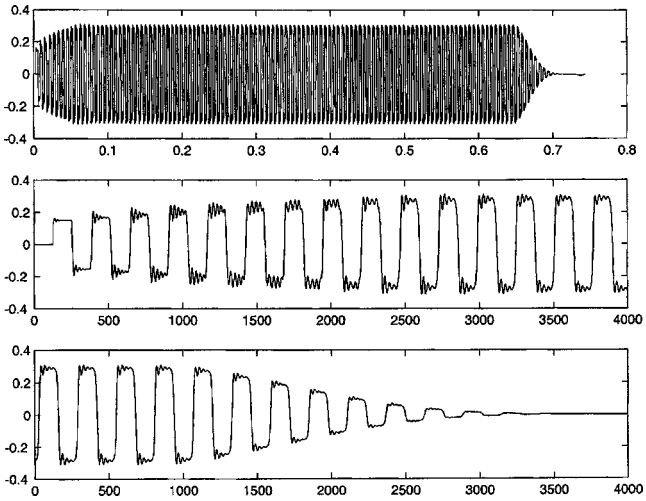

FIG. 14. Top panel: Internal acoustic pressure (in seconds). Middle panel: Blow-up of the attack transient (in samples, f_e=44 100). Bottom panel: Blow-up of the decay transient (in samples, f_e=44 100).

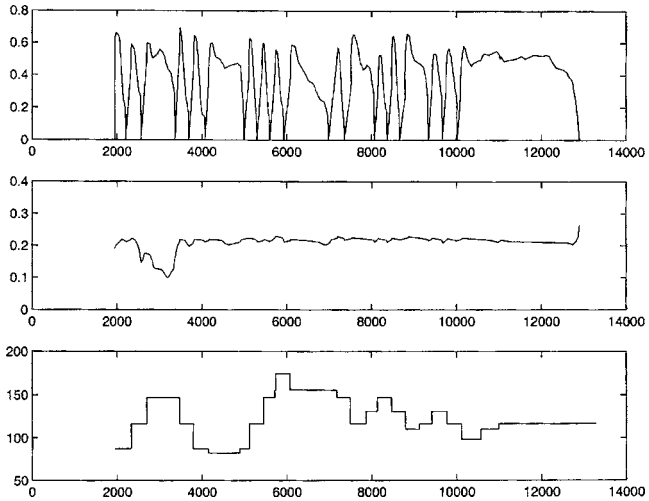

FIG. 15. Top panel: Control parameter $\gamma(t)$. Middle panel: Control parameter $\zeta(t)$. Bottom panel: Frequency of the note (in hertz) (horizontal axis in ms).

$$u_e(n) = \frac{1}{2}\text{sign}(\gamma - V)(-b_{c0}W^2 + W\sqrt{(b_{c0}W)^2 + 4|\gamma - V|}), \tag{29}$$

$$p_e(n) = b_{c0}u_e(n) + V. \tag{30}$$

The calculation of the sampled external pressure $p_{\text{ext}}(n)$ is performed by the use of a difference between the sum of internal pressure and flow at sample n and at sample $n-1$, corresponding to the simplest and classical approximation of the derivative of $p_{\text{ext}}(t)$. This approximation has the advantage of providing a light low-pass filtering compared to the perfect derivation, which "simulates" the radiation losses effects.

It is worth noting that this simple and explicit solution of the discrete nonlinear coupled problem is obtained thanks to the specific discretization scheme of the reed model, which allows a reduction of the complexity of the problem to the solution of a second-order polynomial equation rather than a third-order equation. Though there exist analytic solutions of such an equation, their use is probably not well adapted to a real-time implementation. In the same way, a traveling wave formulation of the whole problem would lead to a similar explicit resolution scheme, provided that the nonlinear characteristics and reed displacement are expressed first with wave variables. In the case of a cylindrical bore, this increase in complexity would be compensated by the simplified formulation of the resonator and the noninstantaneous response of its reflection function, but this gain would no longer remain in the case of a conical bore.

E. Results of simulation

Figure 14 shows the internal acoustic pressure in the mouthpiece for a cylindrical bore of length L=0.5 and radius $R=7\cdot10^{-3}$. The values of the parameters are: γ=0.4, ζ=0.4, f_r=2205, q_r=0.3. Three phases in the signal are visible: The attack transient corresponding to an abrupt increase of γ, the steady state oscillations during which γ is constant, the decay during which γ and ζ slowly and linearly decrease toward zero.

F. Real-time synthesis implementation

The synthesis model has been implemented in real-time in the C language as an external *Max-MSP* object, piloted from MIDI commands given by a *Yamaha WX5* controller. This controller measures, as a function of time, the lip pressure controlling the parameter $\zeta(t)$, and the blowing pressure controlling the parameter $\gamma(t)$. This information is received in MIDI format (between 0 and 127) and is scaled so that it corresponds to the range of the physical parameters. The tuning of the model is performed by the use of the MIDI Pitch information coming from the fingering that controls the length L of the bore by the relation $L=c/(4f_p)$ in the cylindrical case, where f_p is the playing frequency. The delay D is implemented through a circular delay line. Like in a real single-reed instrument, since the pitch changes with respect to physical parameters such as γ, ζ, ω_r, and q_r and since the real instrument is not perfectly tuned for all the fingerings, it seemed unnecessary, at least in a first step, to implement a fractional delay line. The transitions between two notes are handled through a cross-fade in the time domain between the difference equations corresponding to the two different resonator lengths.

In the example to follow, the real-time synthesis model has been used to play the first beats of the "cat" theme of *Pierre et le loup* by Serge Prokofiev. The sound file can be downloaded at: http://www.lma.cnrs-mrs.fr/~guillemain/jasa.mp3. The duration of the sequence is 11 s. The reed resonance frequency $\omega_r/2\pi$ and damping factor q_r have been set in order to facilitate the raising of squeaks, respectively, 1850 Hz and 0.2. During the performance, the external pressure p_{ext}, together with the three playing parameters made of $\zeta(t)$, $\gamma(t)$, and the midi pitch were recorded.

Figure 15 represents, with respect to time (in ms), from

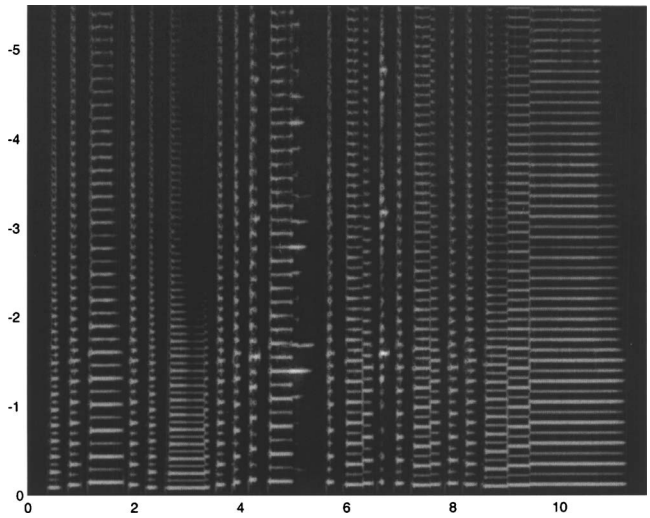

FIG. 16. Spectrogram of the sound sequence (vertical axis in kilohertz, horizontal axis in seconds).

top to bottom, the parameter γ, the parameter ζ, and the frequency of the midi pitch (in hertz).

Figure 16 shows the spectrogram (between 0 and 5500 Hz) of the sound sequence (vertical axis in kilohertz, horizontal axis in seconds).

One can notice that on long sustained notes, the blowing pressure is higher during the attack and decreases when the steady state of the self-oscillations is established. Reed squeaks in the sequence can be seen on the spectrogram around $t=5$ s and $t=6.5$ s. In this situation, the reed vibrates at a fundamental frequency located around the impedance peak the frequency of which is close to the reed resonance frequency, producing a treble sound with harmonic content.

Sound examples simulating various wind instruments are available from http://www.lma.cnrs-mrs.fr/~guillemain/index.html

V. CONCLUSION

The real-time synthesis model described in this paper has been obtained through a straightforward transposition of the simplified equations of the physical behavior of a single-reed instrument. In particular, the formulation of the input impedance of the bore, avoiding the classical P^+/P^- decompositions allows the addition of a nonlinear loop modeling the interaction between pressure, reed displacement, and flow to the linear parts of the model, as it is expressed physically. An explicit resolution scheme of the discretized version in time of the coupled system has been proposed. The structure of this scheme makes it possible to extend the model by replacing the linear parts of the system by equations obtained from more complex geometries of the bore and different reed models. Although there are strong connections between this method and other approaches based on wave variables (since the bore is also considered as an acoustic waveguide), working all along the synthesis process with physical variables makes it easy to use refined physical models of the nonlinear characteristics for real-time synthesis applications. Among such refinements, one can mention the additional flow generated by the reed displacement and unsteady terms in the Bernoulli model.

The advantage of this model is its ability to control all the synthesis parameters of the instrument in real-time. Indeed, all the coefficients of the digital filters and the control parameters are explicitly expressed in terms of physical parameters.

Future works using the same approach will present the modeling of other instruments such as saxophones and brasses and the piloting of the synthesis. The vocal tract, for example, could also be modeled through this approach, as has been done, e.g., by Kelly *et al.*[23] and Cook[24] using digital waveguides.

Similarily, mechanical impedance can be modeled using the same formalism. Current works are dealing with the simulation of hammer–string interaction using the nonlinear model described by Hunt *et al.*[25]

ACKNOWLEDGMENTS

The authors would like to thank the reviewers for their helpful remarks on the paper, as well as Cécile Le Cocq (presently at ETS, Montréal, Canada).

[1] R. T. Schumacher, "Ab initio calculations of the oscillation of a clarinet," Acustica **48**, 71–85 (1981).
[2] B. Gazengel, J. Gilbert, and N. Amir, "Time domain simulation of single reed wind instruments. From the measured input impedance to the synthesis signal. Where are the traps?," Acta Acust. **3**, 445–472 (1995).
[3] E. Ducasse, "Modélisation et simulation dans le domaine temporel d'instruments à vent à anche simple en situation de jeu: Méthodes et modèles" (Modeling and simulation in the time domain of single-reed wind instruments in performance situation: Methods and models), Ph.D. thesis, Université du Maine, Le Mans, France, 2001.
[4] J. Gilbert, J. Kergomard, and E. Ngoya, "Calculation of the steady-state oscillations of a clarinet using the harmonic balance technique," J. Acoust. Soc. Am. **86**, 35–41 (1989).
[5] J. O. Smith III, "Principles of digital waveguide models of musical instruments," in *Applications of DSP to Audio and Acoustics*, edited by M. Kahrs and K. Brandenburg (Kluwer, Dordrecht, 1998), pp. 417–466.
[6] V. Välimäki, "Discrete-time modeling of acoustic tubes using fractional delay filters," Ph.D. Thesis, Helsinki University of Technology, Finland, 1995.
[7] M. van Walstijn and M. Campbell, "Discrete-time modelling of woodwind instrument bores using wave variables," J. Acoust. Soc. Am. **113**, 575–585 (2003).
[8] C. Vergez, "Trompette et trompettiste: Un système dynamique non linéaire analysé modélisé et simulé dans un contexte musical" (Trumpet and trumpet player: A nonlinear dynamical system analyzed, modelled and simulated in a musical context), Ph.D. thesis, Université Paris 6, France, 2000.
[9] G. Borin, G. De Poli, and D. Rochesso, "Elimination of delay-free loops in discrete-time models of nonlinear acoustic systems," IEEE Trans. Speech Audio Process. **8**, 597–606 (2000).
[10] J. Kergomard, S. Ollivier, and J. Gilbert, "Calculation of the spectrum of self-sustained oscillators using a variable truncation method: Application to cylindrical reed instruments," Acust. Acta Acust. 86, 685–703 (2000).
[11] Ph. Guillemain, J. Kergomard, and Th. Voinier, "Procédé de simulation et de synthèse numérique d'un phénomène oscillant" (Process of simulation and digital synthesis of an oscillating phenomenon), French Patent No. FR2846768, Oct 2002, full text available online from http://www.inpi.fr
[12] A. D. Pierce, *Acoustics* (McGraw–Hill, New York, 1981), presently available from Acoustical Society of America, New York (1990).
[13] J. D. Polack, "Time domain solution of Kirchhoff's equation for sound propagation in viscothermal gases: A diffusion process," J. Acoust. **4**, 47–67 (1991).
[14] A. Hirschberg, "Aero-acoustics of wind instruments," in *Mechanics of Musical Instruments*, edited by A. Hirschberg *et al.*, Lectures Notes CISM (Springer, New York, 1995).

[15]J. Kergomard, "Elementary considerations on reed-instruments oscillations," in Ref. 14.
[16]T. A. Wilson and G. S. Beavers, "Operating modes of the clarinet," J. Acoust. Soc. Am. **56**, 653–658 (1974).
[17]M. R. Schroeder, "Natural sounding artificial reverberation," J. Audio Eng. Soc. **10**, 219–233 (1962).
[18]G. Scavone, "An acoustic analysis of single-reed woodwind instruments with an emphasis on design and performance issues and digital waveguide modeling techniques," Ph.D. thesis, Music Department, Stanford University, 1997.
[19]H. Levine and J. Schwinger, "On the radiation of sound from an unflanged circular pipe," Phys. Rev. **73**, 383–406 (1948).
[20]G. Scavone, "Modeling wind instrument sound radiation using digital waveguides," Proceedings of the 1999 International Computer Music Conference, Beijing, China, pp. 355–358.
[21]A. H. Benade, *Fundamentals of Musical Acoustics* (Oxford University Press, London, 1976).
[22]F. Avanzini, "Computational issues in physically-based sound models," Ph.D. thesis, University of Padova, Italy, 2001.
[23]L. Kelly Jr. and C. C. Lochbaum, "Speech synthesis," in Proceedings of the Fourth International Congress on Acoustics, Paper G42, Copenhagen, 1962, pp. 1–4.
[24]P. R. Cook, "Identification of control parameters in an articulatory vocal tract model, with applications to the synthesis of singing," Ph.D. thesis, Electrical Engineering Department, Stanford University, 1991.
[25]K. H. Hunt and F. R. E. Crossley, "Coefficient of restitution interpreted as damping in vibroimpact," ASME J. Appl. Mech. **97**, 440–445 (1975).

Parameter fitting for piano sound synthesis by physical modeling

Julien Bensa,[a] Olivier Gipouloux,[b] and Richard Kronland-Martinet
Laboratoire de Mécanique et d'Acoustique, 31 Chemin Joseph Aiguier, 13402 Marseille, France

(Received 23 December 2004; revised 19 April 2005; accepted 19 April 2005)

A difficult issue in the synthesis of piano tones by physical models is to choose the values of the parameters governing the hammer–string model. In fact, these parameters are hard to estimate from static measurements, causing the synthesis sounds to be unrealistic. An original approach that estimates the parameters of a piano model, from the measurement of the string vibration, by minimizing a perceptual criterion is proposed. The minimization process that was used is a combination of a gradient method and a simulated annealing algorithm, in order to avoid convergence problems in case of multiple local minima. The criterion, based on the tristimulus concept, takes into account the spectral energy density in three bands, each allowing particular parameters to be estimated. The optimization process has been run on signals measured on an experimental setup. The parameters thus estimated provided a better sound quality than the one obtained using a global energetic criterion. Both the sound's attack and its brightness were better preserved. This quality gain was obtained for parameter values very close to the initial ones, showing that only slight deviations are necessary to make synthetic sounds closer to the real ones. [DOI: 10.1121/1.1929230]

PACS number(s): 43.75.Mn, 43.75.Wx [NHF] Pages: 495–504

I. SCOPE OF THE PROBLEM

Even though the synthesis of piano tones by physical modeling has been widely addressed, musicians call for further improvements. Actually, the specificity and the complexity of the instrument lead to a unique timbre dynamically linked to the playing. As a consequence, listeners have developed cognitive knowledge of piano tones that allows them to evaluate sound quality by taking into account various aspects and subtleties of the sound.[1] Among numerous perceptually important contributions to piano tones, one can cite for example the inharmonicity of the partials, the frequency-dependent damping, the beating due to the coupling of several strings (possibly attached to different notes), and the relations between the hammer velocity and the sound brightness. All these "sound ingredients" are linked to the physics of the instrument, making a physical approach more adapted to the synthesis if the physical parameters are precisely known. However, the perceptual influence of these ingredients is far from obvious, making it even more difficult to adjust these parameters when one seeks to minimize the perceptual difference between a synthesis sound and an original piano sound. In this paper, we estimate the parameters of a physical model that describes the phenomenon occurring during and after the hammer–string interaction. This estimation is based on the minimization of a perceptual criterion measuring the difference between a recorded vibration of the string and a synthesized one. This approach allows one to use a single signal to estimate the parameters governing the hammer–string interaction, which are usually measured in static.[2] As already mentioned, an accurate estimation of those particular parameters is extremely useful (and difficult under dynamic conditions) since the hammer–string interaction determines a perceptually important part of the piano sound (especially the dynamic of the sound). Hence, this study constitutes a crucial step toward the design of realistic synthetic sounds. The estimation method is schematized in Fig. 1 and is an improved version of the method presented in Ref. 3. Starting from initial parameters, the optimization process computes a new set of parameters through the model algorithm and the perceptual criterion. This criterion measures perceptual differences between the synthetic signal given by the model and the original signal recorded on an experimental setup. The "optimized" parameters obtained provide a synthetic signal perceptually closer to the original.

In Sec. II, we describe the physical model, exhibiting the parameters that have to be estimated. A model was chosen that takes into account the hammer–string interaction and the string vibration. It does not constitute a full piano model since there is no soundboard and coupling between strings, for instance. However, a piano model taking into account all the elements in the sound production would be extremely complex and would exhibit many parameters to be taken into account in the optimization process. Our estimation method is presented for a simple case, which may be, in the future, applied to models that are more complex. In Sec. III, we address the direct problem, which consists in the study of the string behavior with respect to the model parameters. This aspect is mainly based on a numerical calculus of the solutions provided by the model. Some critical aspects of the physical behavior are also described, such as the hammer force behavior and the felt compression's influence. Section IV is devoted to the inverse problem consisting in estimating the parameters of the mechanical model by using reference

[a]Electronic mail: bensa@lma.cnrs-mrs.fr
[b]Also at: Modélisation et Calcul Scientifique, Université Lyon 1, Bâtiment ISTIL, 15 Boulevard Latarjet 69622 Villeurbanne Cedex, France.

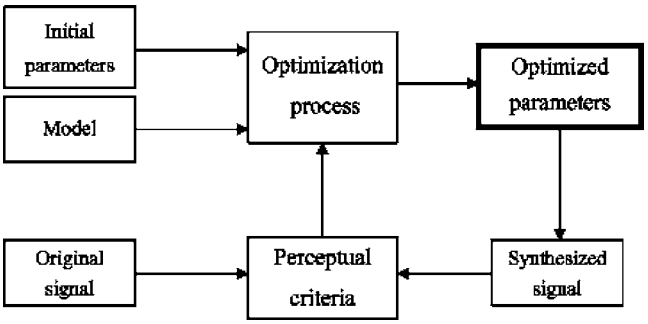

FIG. 1. Principal stages of the calibration process.

signals recorded on the experimental setup. This setup measures vibrations from one isolated string struck by a piano hammer, and of the corresponding hammer velocities. The setup is suitable for our model since there is no soundboard and string coupling. The use of real piano sounds would require using another model, since the damping and the frequencies of the partials may be modified by the finite impedance at the bridge and by the coupling between several strings. The collected data are further computed using an optimization technique that combines gradient and simulated annealing methods minimizing perceptual criteria. These criteria are based on the spectral energy in three frequency bands, analogous to the so-called perceptual tristimulus decomposition.[4] In Sec. V, the estimated parameters are used to validate the method through sound synthesis.

II. STRING AND HAMMER MODEL

Several models of piano–string and hammer–string interaction have been proposed. They generally consist of a set of PDEs governing the string motion[5–7] and the hammer displacement that are coupled by a power law describing the compression and losses of the felt as a function of the hammer and string displacement.[2,8–10] The model of wave propagation on the string we used was proposed in Ref. 7 and is given by

$$\frac{\partial^2 y_s}{\partial t^2} = c^2 \frac{\partial^2 y_s}{\partial x^2} - \kappa^2 \frac{\partial^4 y_s}{\partial x^4} - 2b_1 \frac{\partial y_s}{\partial t} + 2b_2 \frac{\partial^3 y_s}{\partial x^2 \partial t} \tag{1}$$

with y_s the string displacement, c the wave speed, κ the stiffness coefficient, b_1 and b_2 the loss coefficients (a symbols table may be found in Table I). The first term on the right-hand side gives rise to wave-like motion with speed c. The second term introduces dispersion, and the last two terms introduce frequency-dependent loss via mixed time–space derivative terms. This model differs from that of Hiller and Ruiz[5,11] only by the replacement of the term $2b_3(\partial^3 y/\partial t^3)$ in Ruiz's equation by $2b_2(\partial^3 y/\partial x^2 \partial t)$. This replacement avoids a nonphysical third unstable solution (which can lead to difficulties both analytically and numerically, see Ref. 7 for more details).

To take into account the modification of the tone with the dynamic, we use a nonlinear hammer model. Ghosh[8] was one of the first to propose a nonlinear spring model of the hammer felt,[2] obeying the power law:

TABLE I. Symbols used.

Symbol	Definition
y_s	String displacement
y_{s0}	Initial string displacement
v_s	String velocity
v_{s0}	Initial string velocity
c	Wave speed
κ	String stiffness coefficient
L	String length
b_1	String loss parameter 1
b_2	String loss parameter 2
yH	Hammer displacement
v_H	Hammer velocity
v_{H0}	Initial hammer velocity
F_H	String force acting on the hammer
f_H	Hammer force acting on the string
K_H	Felt stiffness coefficient
p	Stiffness exponent
μ	Felt loss coefficient
g	Window function
x_0	Contact location on the string

$$f_H(x) = K_H x^p, \tag{2}$$

where x refers to the compression of the felt, K_H is the stiffness coefficient, and p the stiffness exponent. Using Ghosh's model and Ruiz's string wave equation, Chaigne and Askenfelt[6,12] have produced realistic simulation of the hammer–string interaction. For a more realistic model, some papers suggest a hysteretic law for the hammer felt. The felt is actually compressed and extended several times during the contact and, because the relaxation is not instantaneous, the hardness of the felt increases. Boutillon[9] modeled this phenomena using several values of p for the increasing and decreasing part of the spring stiffness characteristic. But with this model the felt deformation tends to zero with the unloading of the force although measurements[13] show that the felt is still deformed after the force is removed. Stulov[2] proposed a mathematical model to account for the hysteretic feature of the felt, starting from a simple model of material with memory (obtained by replacing constant elastic parameters by time-dependent operators). Giordano and Millis[14] have shown that this model reproduces well the force exerted by a hammer on a sensor, in the static case. They have also mounted a very small accelerometer on the string, opposite to the hammer–string contact, and shown that this model is not well adapted for simulating the force characteristic in "dynamic" conditions.

The model we used was originally developed by Hunt and Crossley[10] to describe the interaction between two colliding objects (and adapted by Rochesso and Avanzini in Ref. 15 to model the hammer–string contact hysteresis). The losses are introduced by adding a first time derivative to Ghosh's model. Rochesso and Avanzini show that the force–compression diagrams are close to the ones of a real hammer. The force depends on the felt compression x and of the compression speed $\partial x/\partial t$,

$$f_H(x) = K_H x^p \left(1 + \mu \frac{\partial x}{\partial t}\right), \tag{3}$$

where μ is the felt loss coefficient ($\mu > 0$). The system of PDEs describing the hammer–string contact is then

$$\frac{\partial^2 y_s}{\partial t^2} = c^2 \frac{\partial^2 y_s}{\partial x^2} - \kappa^2 \frac{\partial^4 y_s}{\partial x^4} - 2b_1 \frac{\partial y_s}{\partial t} + 2b_2 \frac{\partial^3 y_s}{\partial x^2 \partial t} + g(x,x_0) f_H(y_s - y_H), \tag{4}$$

$$M_H \frac{d^2 y_H}{dt^2} = -F_H(y_s - y_H) \tag{5}$$

with the boundary and initial conditions:

$$y_s(x,0) = y_{s0}(x), \quad \frac{\partial y_s}{\partial t}(x,0) = v_{s0}, \quad y_0(0,t) = y_s(L,t) = 0, \quad \frac{\partial^2 y_s}{\partial x^2}(0,t) = \frac{\partial^2 y_s}{\partial x^2}(L,t) = 0, \tag{6}$$

$$y_H(0) = y_s(x_0,0), \quad \frac{\partial y_H}{\partial t}(0) = v_{H0} \tag{7}$$

where

$$F_H(u) = \begin{cases} K_H u^p \left(1 + \mu \dfrac{\partial u}{\partial t}\right) & \text{if } u > 0, \\ 0 & \text{if } u \leqslant 0 \end{cases}$$
$$f_H(u) = F_H(u) \left\{ M_S / L \int_L g(x,x_0) dx \right\}^{-1} \tag{8}$$

with y_H the hammer displacement. y_{s0} and v_{s0} are the initial string displacement and velocity, v_{H0} is the initial hammer velocity, and x_0 is the contact location. Finally, M_S (respectively, M_H) denote the string (respectively, hammer) mass; L is the length of the string, and g describes the area of the string in contact with the hammer during the interaction. [Please refer to Ref. 6 for more details about the definition of system (8).]

This nonlinear system does not admit any analytical solution. We show in Sec. III that the numerical solution of this system reproduces well the main phenomena in the hammer–string interaction, namely the nonlinear behavior with respect to the hammer velocity and the hysteresis of the hammer force.

III. DIRECT PROBLEM: NUMERICAL SOLUTION

There is no explicit solution of the system (4)–(7). To compute the solution, we chose finite differences method in the space and time variables (one may use finite volume or finite elements methods, but in the case of one-dimensional space variables, these approaches are very similar). At first we reduce from two to one the order of the time derivative in the system (4) and (5) by introducing two new variables: the string velocity $v_s = \partial y_s / \partial t$ and the hammer velocity $v_H = \partial y_H / \partial t$. This change of variable allows one to work with the displacements and velocities of the string and the hammer. Thereby, the initial conditions may be applied exactly on each of the unknowns. Also, the order of the time derivative is reduced, simplifying the discretization.

Using these variables, one may write system (4)–(7) as a system of first-order derivatives in time:

$$\frac{\partial y_s}{\partial t} = v_s, \tag{9}$$

$$\frac{\partial v_s}{\partial t} = c^2 \frac{\partial^2 y_s}{\partial x^2} - \kappa^2 \frac{\partial^4 y_s}{\partial x^4} - 2b_1 v_s + 2b_2 \frac{\partial^2 v_s}{\partial x^2} + g(x,x_0) f_H(y_s - y_H, v_s - v_H), \tag{10}$$

$$\frac{\partial y_H}{\partial t} = v_H, \tag{11}$$

$$\frac{\partial v_H}{dt} = -\frac{1}{M_H} F_H(y_s - y_H, v_s - v_H) \tag{12}$$

and the initial and boundary conditions are rewritten as

$$y_s(x,0) = y_{s0}(x), \quad v_s(x,0) = v_{s0}, \quad y_s(0,t) = y_s(L,t) = 0, \quad \frac{\partial^2 y_s}{\partial x^2}(0,t) = \frac{\partial^2 y_s}{\partial x^2}(L,t) = 0, \tag{13}$$

$$y_H(0) = y_s(x_0,0), \quad v_H(0) = v_{H0}. \tag{14}$$

Then, F_H and f_H are now defined by

$$F_H(u,v) = \begin{cases} K_H u^p (1 + \mu v) & \text{if } u > 0 \\ 0 & \text{if } u \leqslant 0, \end{cases}$$
$$f_H(u,v) = F_H(u,v) \left\{ M_S / L \int_L g(x,x_0) dx \right\}^{-1}.$$

It should be noted that F_H and f_H are now linear with respect to the velocity variable v, simplifying the numerical problem.

A. Time discretization and initial conditions

The system above (9)–(12) may be written

$$\frac{\partial X}{\partial t} = \mathcal{A}(X), \tag{15}$$

where $X = {}^t(y_s, v_s, y_H, v_H)$ [${}^t(M)$ denotes the transposed matrix of M] and $\mathcal{A}$ contain both the spatial differential operator and the nonlinear function corresponding to the right-hand side of Eqs. (9)–(12). Equation (15) is discretized in time by a Crank Nicholson scheme:[16]

$$\frac{X^{n+1} - X^n}{\delta t} = \frac{1}{2}(\mathcal{A}(X^{n+1}) + \mathcal{A}(X^n)). \tag{16}$$

This scheme is used because it has good stability properties (unconditionally stable). Here, X^n denotes the discrete value of $X(t)$ at the time $t = n\,\delta t$, where δt is the time step.

We need to compute initial conditions on both the velocity and the displacement of the hammer and the string. When a classical formulation is used (only in displacement variable),[6] one needs to discretize the velocity in terms of displacement and to use a pseudo-iteration time at $t = 0 - \delta t$ to adjust the initial velocity value. Using our formulation, one may directly apply the initial values on the velocity unknowns.

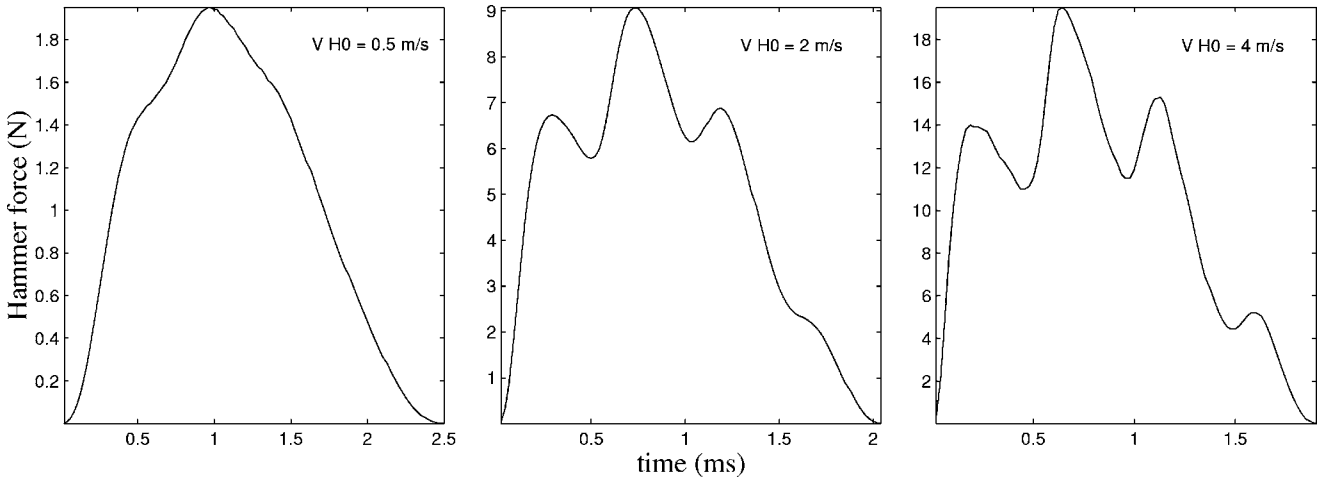

FIG. 2. Hammer force curves as a function of time, for a note C4 and three hammer velocities. The hammer parameters and the striking positions are as in Ref. 12.

B. Space discretization and boundary conditions

The discretization of the space derivatives in the operator $\mathcal{A}$ is done using a classical centered finite differences scheme. Consider the string $]0,L[$ discretized by $N+2$ points $\{x_i=ih\}_{i=0,\ldots,N+1}$ where $h=L/(N+1)$. Then one may approximate the space derivatives:

$$\frac{\partial^2 X}{\partial x^2}(x_i) \simeq h^{-2}(X_{i-1} - 2X_i + X_{i+1}), \tag{17}$$

$$\frac{\partial^4 X}{\partial x^4}(x_i) \simeq h^{-4}(X_{i-2} - 4X_{i-1} + 6X_i - 4X_{i+1} + X_{i+2}), \tag{18}$$

where X_i denotes $X(x_i)$.

We take into account the boundary conditions coming from Eqs. (13) and (14) to apply the discretization equations (17) and (18) on the displacement at the extremities $x=0$ and $x=L$. Actually, to apply those equations at $x=h$ (respectively, $x=L-h$), the value of the displacement needs to be introduced at "virtual" nodes ($x=0, x=-h$) (respectively, $x=L, x=L+h$). Consider the case at $x=0$. The boundary condition $y_s(x=0)=0$ gives $y_{s,i=0}=0$. The boundary condition on the string curvature $\partial^2 y_s/\partial x^2=0$ may be discretized at $x=0$ by $y_{s,i=-1}-2y_{s,i=0}+y_{s,i=1}=0$, which allows $y_{s,i=-1}$ to be eliminated using $y_{s,i=-1}=-y_{s,i=1}$.

C. Numerical results

The discretization in both the time and the space domains using Eqs. (16)–(18) leads to a system that is numerically solved at each time iteration. During the hammer–string contact, this system is nonlinear: a Newton–Raphson algorithm and a Choleski matrix decomposition algorithm are then used. After the contact, the system is linear: a Choleski decomposition is performed one time for all, and each time iteration needs only two triangular system resolutions.

As shown in Figs. 2–4, the system behaves in accordance with what is foreseen by the theory. The hammer–string contact lasts about 3 ms and decreases with the increase in the initial hammer velocity. Moreover, the reflections of the waves propagating between the hammer and the agraffe can be seen on the hammer force shape (especially for 2 and 4 m s^{-1}). Figure 3 shows the force as a function of the compression of the felt. We clearly see a

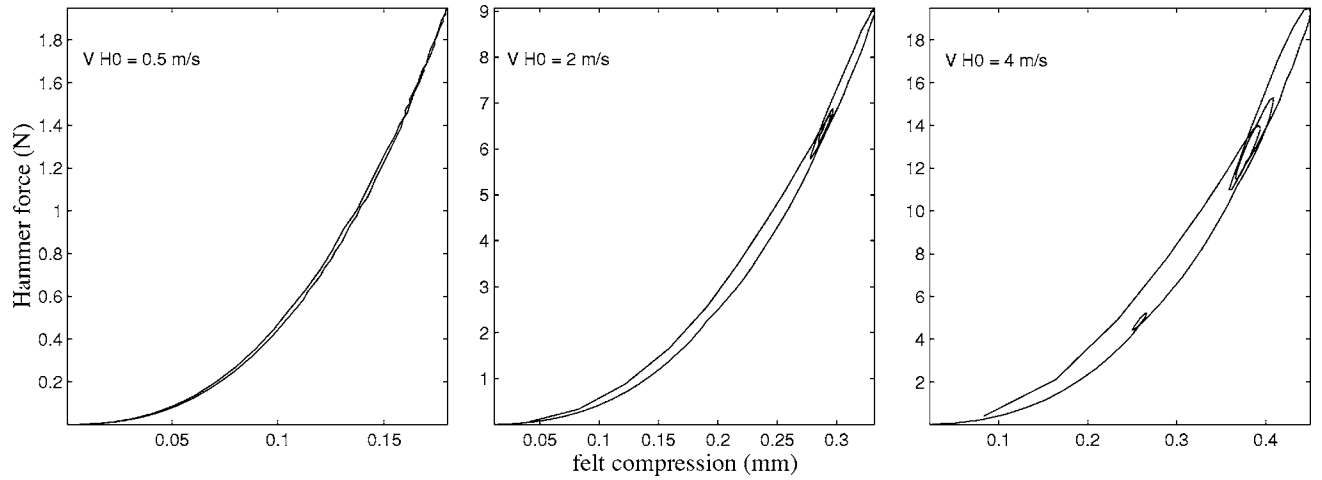

FIG. 3. Hammer force curve as a function of the felt compression, for a note C4 and a hammer velocity of 4 m s^{-1}. The hammer parameters and the striking positions are $\mu=0.1$.

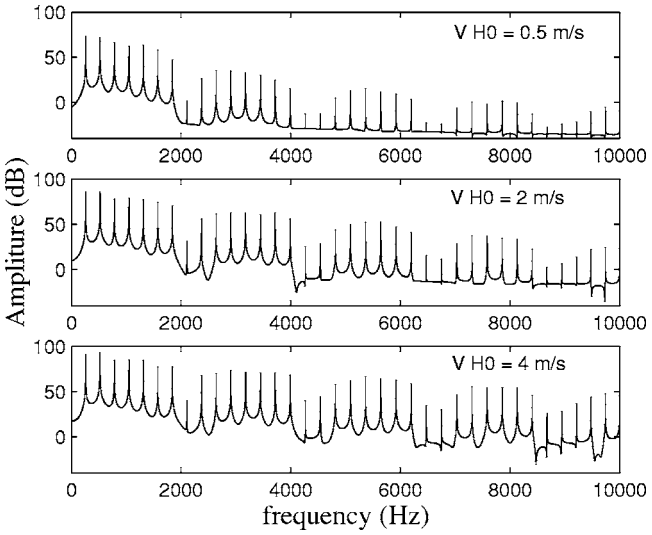

FIG. 4. The spectra of velocity signal for three hammer velocities for a note C4.

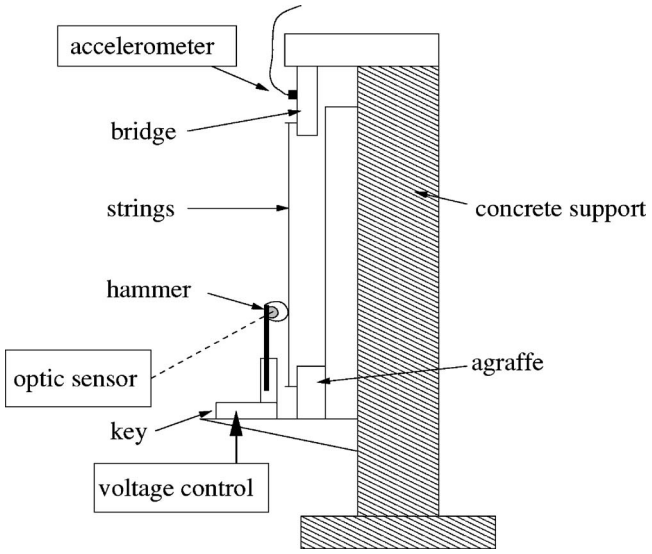

FIG. 5. Experimental setup.

hysteretic behavior [due to the term $K_H\mu(v_s-v_H)$ of the nonlinear force law] reflecting losses in the felt. In Fig. 4 the spectral modulus of the velocity signal is plotted for different initial hammer velocities v_{H0}. We see a modification of the spectral shape, namely increased amplitude of the high frequency partials with the hammer velocity (corresponding to increased brightness of the sound). Similar results may be found namely in Refs. 12 and 17–19.

IV. INVERSE PROBLEM: FITTING THE PARAMETERS OF THE MODEL WITH EXPERIMENTAL DATA

We deal here with the problem of identifying the parameters of the model so that the solution is perceptually close to the measured signal. To do so, we consider the solutions (y_s,v_s,y_H,v_H) of the system (9)–(14) as a function of all the physical parameters characterizing the vibration $(c,\kappa,b_1,b_2,K_H,\mu,M_H,p,v_{H0})$. We do not, however, consider the parameters x_0 and M_S in this identification process. x_0 is supposed to be known accurately and since only the ratio M_S/M_H plays a role in Eqs. (9)–(14), we consider only M_H.

Some of the parameters of the PDE model described in Sec. II can be accurately measured experimentally (the initial hammer velocity v_{H0}, the wave speed c, etc.). In contrast, parameters like the hammer stiffness K_H and the felt loss coefficient μ are very difficult to measure, especially under dynamic conditions. To get a realistic and perceptively accurate estimation of those parameters, we propose to look for the set of model parameters allowing a "good" match between the synthetic and original signal. Since the dependency of the computed signal as a function of the physical parameters is not explicit, we used nonlinear optimization techniques to find this set of parameters. First, Sec. IV A describes the experimental setup. Section IV B deals with the selection of the optimization criterion accounting for the perceptual feature of the sound. Finally, Sec. IV C describes the optimization method and its numerical implementation.

A. Experimental setup

We have designed an experimental setup (see Fig. 5) to measure the vibration of a string struck by a hammer at different velocities. This setup has been described in Ref. 20. It consists of a massive concrete support with, on the extremities, a piece of a bridge and an agraffe taken from a real piano. The string is then tightened between the bridge and the agraffe and tuned manually. The string length is 1 m. It is clear that the string is not totally uncoupled from its support, but this experiment was satisfactory for recording signals of struck strings in order to validate our calibration method. The string is struck with a hammer linked to an electronically piloted key. By imposing different voltages on the system, the hammer velocity can be controlled in a reproducible way. The precise velocity is measured immediately after escapement through an *optic sensor* (MTI 2000, probe module 2125H) pointing at the side of the head of the hammer. The vibration on the string (velocity signal) is measured by a *laser vibrometer* (Polytec OFV 050). The signals are directly recorded on Digital Audio Tape. We collected signals corresponding to hammer velocities between 0.8 and 2.3 m s^{-1}.

B. Choice of a perceptual criterion

The optimization criterion has to be chosen with care to take into account perceptual phenomena. For that, one has to be aware that the model is a simplified representation of reality. It does not take into account some physical phenomena leading to small perceptual contributions. This is for example the case for the beats due to the coupling between the two polarizations of the string[21,22] and for the finite impedance caused by the bridge.[23] Nevertheless, we expect the synthetic sound to be perceptually close to the original one, even though the wave forms corresponding to the signals may not be exactly identical. This latter notion implies that an error criterion based on the temporal signal behavior of the real and synthetic sounds is not appropriate for the optimization process.

On the other hand, the spectral repartition of the energy plays an important role, ensuring for example the inharmonicity of the partials and the frequency dependent damping. Since slight phase modifications in the frequency domain do not alter the perception of the sound, we based our optimization criterion on the power spectral energy density. Actually, even though the phase contains relevant information about the physical parameters, this information is also included in the spectral energy density. For example, the parameter κ related to the dispersion of waves acts on the group delay (which corresponds to the derivative of the phase of the Fourier transform), but also on the frequencies of the spectrum's partials (since the wave dispersion is responsible for the inharmonicity). One may notice that, even though we are interested in the behavior of a nonstationary signal, it is not necessary to base our optimization process upon a time-frequency representation. The energy in the system is entirely determined by the initial condition, given by the hammer–string contact. After the first milliseconds, the system behaves linearly and the energy decreases in the same way until extinction. The way the energy decreases is then fully determined by the shape of the frequency components of the signal spectrum.

The optimization process consists in minimizing the quadratic error $\mathcal{C}$ between the energy of the Fourier transform Y_S^c of the string velocity v_S obtained by Eqs. (4)–(7) and the energy of the Fourier transform S^m of the measured signal s:

$$\mathcal{C} = \frac{1}{2} \int (|Y_S^c|^2 - |S^m|^2)^2 d\omega. \tag{19}$$

Nevertheless, the direct use of such a criterion does not sufficiently take into account the hearing processes. Actually, when we first used it in the optimization process, we obtained a synthetic sound for which the attack was too smooth compared to the attack of the original sound. Moreover, the brightness of the sound was reduced. This reduction can be explained by the fact that the most important part of the energy is localized in the low frequency range of the spectrum. Consequently, this "global" criterion privileges low frequency components at the expense of high frequency ones, which are essential for the brightness and the sharpness of the attack.

To overcome this high frequency loss, we adapted the criterion to take perceptual features into account, by-following the so-called tristimulus concept.[4] This approach consists in separating the spectral range into three spectral bands. The first band $\boldsymbol{B}_1$ is centered around the fundamental frequency of the signal, whereas the second $\boldsymbol{B}_2$ and the third band $\boldsymbol{B}_3$ in our approach, respectively, contain the partials two to eight and all the components above the eighth partial. This approach has been successfully used for estimation of sound synthesis models by Ystad *et al.*[24] This spectral split has several advantages.

$\boldsymbol{B}_1$. Tracking of the fundamental ensures good estimation of the geometric and static parameters. This fundamental component is of importance for the sound since it is highly correlated to the pitch. We used it to estimate the wave speed c and the loss coefficient b_1.

$\boldsymbol{B}_2$. Components two to eight contain a large part of the energy. These components bring most of the perceptual information related to the damping behavior of the sound, and their frequencies are responsible for the sensation of inharmonicity.[25] Hence, this frequency band is used to estimate the loss coefficient b_2 as well as the string stiffness coefficient κ.

$\boldsymbol{B}_3$. High frequency components are also of great importance since they can dramatically change the timbre of the sound, even though their energy is low. These components are mainly correlated to the velocity and the stiffness of the hammer felt. They are characteristic of the dynamics of the playing. We used this frequency band to estimate the remaining coefficients $(K_H, \mu, M_H, p, v_{H0})$ governing the hammer behavior.

Such a decomposition of the "global" spectral power density criterion into three criteria acting on three frequency bands accounts for the limitations of the model and for the characteristics of our perception of sounds. As we discuss later, the decomposition permitted us to estimate parameters providing better synthetic sounds than the ones obtained using classical criteria.

C. The optimization process

We describe here the optimization applied to our problem. Two kinds of optimization algorithms were used. For the bands $\boldsymbol{B}_1$ and $\boldsymbol{B}_2$, we used a simple gradient method since only one minimum was usually found and the criterion was regular enough to be minimized by such a method. But the optimization problem in the last band $\boldsymbol{B}_3$ (concerning the hammer parameters) is more complex. Numerical experiments show the existence of local minima, and a classical gradient method does not permit convergence to the global minimum. We then considered an adapted simulated annealing method [(ASA), see Ref. 26], an algorithm known to give good results in such a situation.

For both methods, the gradient of the solution needs to be computed in regard to the physical parameters (see in the Appendix how to compute this gradient). The problem may be stated as the following. Let us denote:

$$(z_j)_{j=1,\ldots,9} = (c, \kappa, b_1, b_2, K_H, \mu, M_H, p, v_{H0}). \tag{20}$$

A set of physical parameters $(z_j)_{j=1,\ldots,9}$ is selected so that the system (9)–(14) gives a solution that sounds as close as possible to the experimental signal. More precisely, considering for each band the quadratic criterion $\mathcal{C}$ as defined in Eq. (19), one denotes $\tilde{\mathcal{C}}(z_1, \ldots, z_9)$ the value of $\mathcal{C}$ computed from the solution of the problem (9)–(14) using $(z_1, \ldots, z_9)$ as physical parameters. Then the general optimization problem is

$$\text{Find } (z_j)_{j=1,\ldots,9} \text{ such that } \tilde{\mathcal{C}}(z_1, \ldots, z_9) \text{ is minimum.} \tag{21}$$

By using the tristimuli formalism explained in Sec. IV B, we obtain the three-step process: Consider $(z_1^0, \ldots, z_9^0)$ (the superscript denotes the internal loop index needed to solve the nonlinear equation) given by the measured parameters on the experimental setup.

(1) Find (z_1^1, z_3^1) such that $\tilde{\mathcal{C}}(z_1^1, z_2^0, z_3^1, z_4^0, z_5^0, z_6^0, z_7^0, z_8^0, z_9^0)$ is minimum on the band $\boldsymbol{B}_1$.
(2) Find (z_2^1, z_4^1) such that $\tilde{\mathcal{C}}(z_1^1, z_2^1, z_3^1, z_4^1, z_5^0, z_6^0, z_7^0, z_8^0, z_9^0)$ is minimum on the band $\boldsymbol{B}_2$.
(3) Find $(z_5^1, z_6^1, z_7^1, z_8^1, z_9^1)$ such that $\tilde{\mathcal{C}}(z_1^1, \ldots, z_9^1)$ is minimum on the band $\boldsymbol{B}_3$.

To solve each of those problems, we then used the two optimization algorithms described below.

1. Gradient algorithm

Concerning the minimization of the criterion in the bands $\boldsymbol{B}_1$ and $\boldsymbol{B}_2$, the situation is regular enough (unique minimum) to use a classical gradient algorithm. Starting from the expression of the criterion (19), one can derive with respect to $(z_j^0)_{j=1,\ldots,9}$:

$$\nabla_z \tilde{\mathcal{C}} = 2 \int (|Y_S^c|^2 - |S^m|^2) |Y_S^c| \nabla_z Y_S^c d\omega.$$

∇_z denotes the gradient with respect to the physical parameters. Because the Fourier transform is linear, one can deduce $\nabla_z Y_S^c$ from $\nabla_z v_s$ (see the Appendix for how to compute the gradient $\nabla_z v_s$). To converge to the local minimum we then constructed the following algorithm:

ϵ given; $(z)_{i=1,n} = (z^0)_{i=1,n}$ given
while $\tilde{\mathcal{C}} > \epsilon$ *do*
  Compute (y_s, v_s, y_H, v_H) solution of (9)–(14) with parameter set $(z)_{i=1,n}$
  for $j = 1, n$ *do*
    Compute $(y_s^{(j)}, v_s^{(j)}, y_H^{(j)}, v_H^{(j)})$ as explained in the Appendix
    Compute $\tilde{\mathcal{C}}^{(j)}$ using $(y_s^{(j)}, v_s^{(j)}, y_H^{(j)}, v_H^{(j)})$ $\{\tilde{\mathcal{C}}^{(j)}, j^{th}$ component of $\nabla_z \tilde{\mathcal{C}}\}$
  end for
  chose h such that $\tilde{\mathcal{C}} + \nabla_c \tilde{\mathcal{C}} \cdot h \leqslant \tilde{\mathcal{C}}$
  for $j = 1, n$ *do*
    $z_j \Leftarrow z_j + h_j$
  end for
end while

This algorithm was successfully used to find the minimum of the criterion $\mathcal{C}$ in bands $\boldsymbol{B}_1$ and $\boldsymbol{B}_2$.

2. Simulated annealing algorithm

For the last frequency band $\boldsymbol{B}_3$, one needs an algorithm that is able to escape local minima in order to find the global minimum. Let us then consider an optimization method more adapted to this situation ASA. We give here only the basic principles of this method. A detailed description can be found in Ref. 26. As its name implies, the simulated annealing exploits an analogy between the way in which a metal cools and freezes into a minimum energy crystalline structure (the annealing process) and the search for a minimum in a more general system. As cooling proceeds, the system becomes more ordered and approaches a "frozen" ground state at "Temperature" $T=0$. Hence the process can be thought of as an adiabatic approach to the lowest energy state. If the initial temperature of the system is too low or cooling is done insufficiently slowly the system may become quenched forming defects or freezing out in metastable states (i.e., trapped in a local minimum energy state). Applied to our situation, this algorithm may be summarized as the following: considering an initial point $(z^0)_{i=1,n}$, a new point $(z)_{i=1,n}$ is generated using a given probability distribution function $g(z)$ and the criterion $\tilde{\mathcal{C}}$, evaluated at this point. The new point is accepted or refused, following an acceptance function $h(z^0, z)$ that depends both on the parameter called Temperature, and on the difference between values of the criterion $\tilde{\mathcal{C}}$ on the two points (z^0, z). If the new point is accepted, it becomes the old one, the Temperature is decreased, and the process is iterated.

TABLE II. Estimated and optimized physical coefficients for the string.

	String parameters			
	c	κ	b_1	$b2$
Initial	310.6		0.500	1.004$E-10$
Final	304.101	1.737	0.568	1.628$E-06$

V. RESULTS

We applied the optimization process on the sounds recorded by the experimental setup. As initial parameters, measured and published values were used. For the string, the parameters were extracted from measurements on the experimental setup. The parameters corresponding to the hammer characterization were collected in the literature.[12] Our results showed that the optimization process leads to a new set of physical parameters. The string parameters obtained are given in Table II. Table III shows the hammer parameters. This set of "optimized" values is the result of the optimization process and depends on the choice of the convergence criterion. The three-band criterion we used made it possible to estimate new parameters ensuring a better synthesis from a perceptual point of view. It is not sure, however, that they correspond to the actual physical values. Nevertheless, as shown in Tables II and III, these values are physically consistent and do not deviate too much from the starting point. Moreover, those optimized parameters were very similar from one measurement to another (for the same hammer velocity). The wave speed c was reduced, meaning that the string tension was weaker than expected. The loss coefficients, b_1 and b_2 were greater than those estimated on the experimental setup. For the hammer, note that the felt loss coefficient increased, as did the initial hammer velocity. For the stiffness exponent p, the value was almost unchanged.

This set of new parameters was then used to compute a synthetic signal [using Eqs. (4)–(7)]. In Fig. 6 are plotted the spectral modulus of the original and the synthesized signals

TABLE III. Estimated and optimized physical coefficients for the hammer.

	Hammer parameters				
	K_H	μ	p	M_H	v_0
Initial	1.516 47$E+09$	0.1000	2.55	0.006 790	0.740 78
Final	1.099 49$E+10$	0.1998	2.56	0.005 687	0.799 93

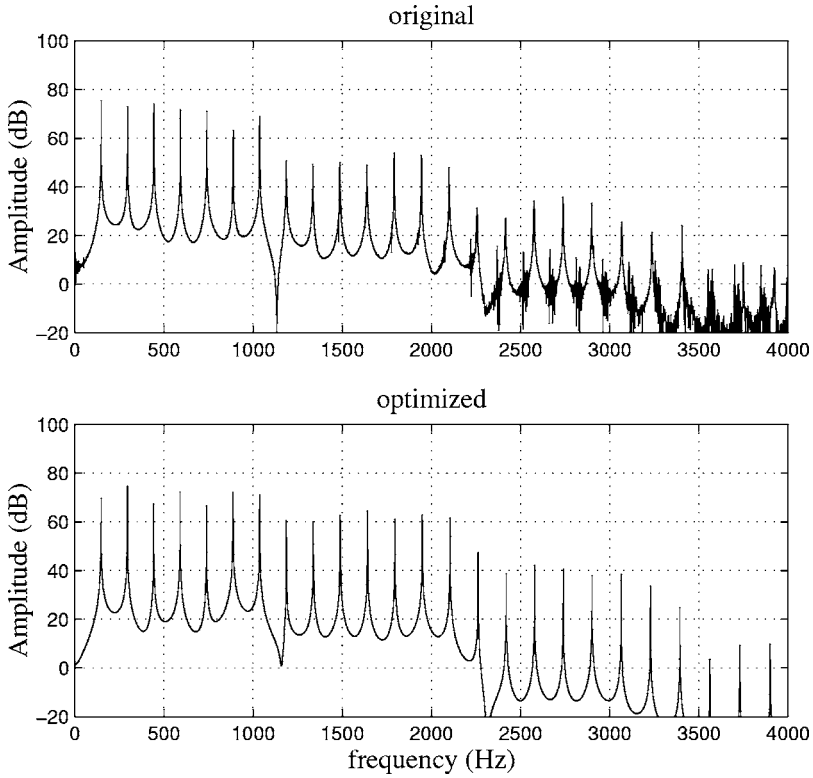

FIG. 6. Spectrum modulus (velocity signal) for a hammer velocity of 0.84 m s^{-1}. Top: original measured signal, bottom: synthesized optimized signal.

with optimized parameters. Even though they are not identical, they look very similar. The amplitudes of the partials are in good agreement for the first seven components, but differ for higher frequencies. Figure 7 represents the wave shape of the real and the synthesized sounds, before and after the optimization. The similarity between the signals has been clearly improved by the optimization of the parameters. Nevertheless, the synthesized signal contains slightly more energy in the high frequency range. As discussed in Sec. IV B, the tristimuli criterion, rather than the "global" criterion, was chosen for its better ability to take into account the energy of high frequency components. We believe here that the main part of the differences is due not only to the optimization method but also to the model approximation. Obviously, the optimization method is constrained by the model limitation;

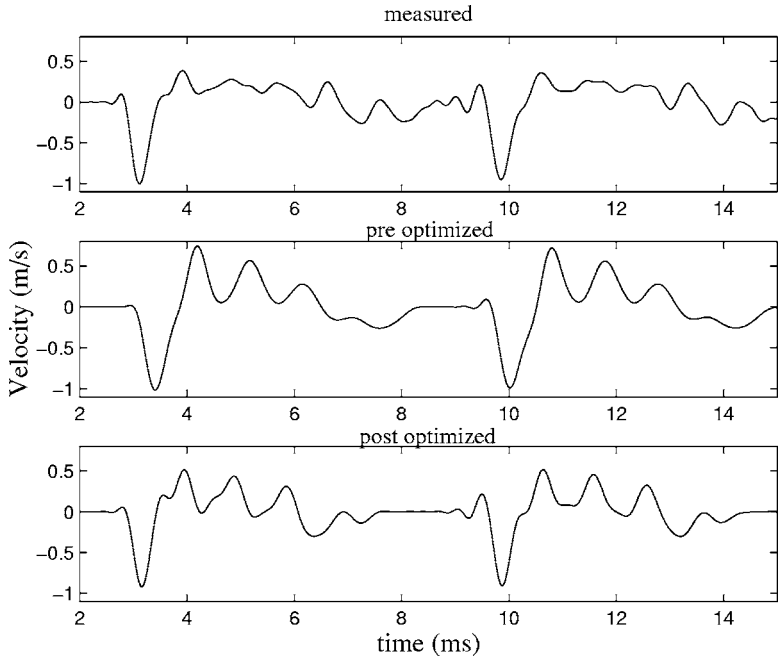

FIG. 7. Comparison of the measured and computed velocities of the string, for a hammer velocity of 1.1 m s^{-1}. Dashed line: measured signal, dash-dotted line: synthesis before optimization, plain synthesis after optimization.

better results would probably be obtained if first the model itself were reconsidered. This aspect is not in the scope of this article.

Another important point validating our approach is that with the optimized parameters the model still behaves as the measurements with the dynamic. This means that, if we compute the model for another hammer velocity, the signal obtained is still close to the signal measured for the same hammer velocity.

Informal listening test has shown that the quality of the resulting sounds increases using the optimized parameters (sound examples can be found at Ref. 27). The attack is more realistic and the decay closer to the original even though the tone still lacks realism. We believe that the explanation for this lack resides in the simplicity of the hammer model, which is not able to accurately simulate the nonlinear behavior of the hammer–string interaction. Actually, previous synthesis works have proved the accuracy of the string model itself.[7]

VI. CONCLUSION

One of the main issues when using physical modeling for synthesis purposes is the fitting of the model's parameters. These parameters can sometimes be extracted from data obtained by experiments, but in some cases the dynamic behavior of the models reduces the accuracy of static measurements. This is the case for piano sound models, in which it is difficult to estimate parameters like the stiffness coefficient and exponent characterizing the hammer.

We have addressed here the problem of parameter fitting for piano modeling, aiming at estimating the optimal parameters for synthesis purposes. This means that rather than focusing on the precision of the physical parameters, we wanted the synthetic sound to be as close as possible to the real one. This led us to a technique associating optimization processes and perceptual concepts. To take into account our perception of sounds, a minimization criterion (three-band criterion) was designed following the tristimulus concept. The frequency range was separated into three bands, respectively, containing the fundamental, partial 2 to 8, and the remaining high frequency components. Having in mind that real sounds are much more complex than the ones generated by the physical model, we compared signal characteristics that are as little as possible sensitive to small variations. This eliminated an estimation based on the time signal to the benefit of its spectral energy density. This choice does not minimize the influence of the phase information, and consequently the time behavior of the signal, since most of it is also contained in the frequency distribution of the energy. We showed how each band can be used to estimate the model's parameters thanks to an optimization process that combines a gradient method and a simulated annealing algorithm aimed at avoiding convergence problems in case of multiple local minima. The model's parameters make it possible to generate piano tones that are perceptually better than those obtained using a "global" criterion. Fine piano characteristics that are generally poorly synthesized are thus reproduced. This is the case for the attack time and the brightness. Nevertheless, slight differences between the real and the synthetic sounds can still be heard. We believe these differences are mainly due to the weakness of the model, especially for the string–hammer interaction. Also note that even though the parameters obtained by our technique are optimized for synthesis purposes, their values correspond to what is expected from a physical point of view. The generality of the method proposed in this paper makes it easy to be applied to other models of music instruments and sound generators.

APPENDIX: COMPUTATION OF THE PHYSICAL PARAMETERS DERIVATIVES

Here we explain how to get the gradient of the solution of system [Eqs. (9)–(14)] with respect to the physical parameters $(c,\kappa,b_1,b_2,K_H,\mu,M_H,p,v_{H0})$. We do not mention y_{s0}, v_{s0}, x_0, since we will not calculate the derivatives for those parameters. We suppose that $y_{s0}=0$, $v_{s0}=0$ and that x_0 can be precisely measured on the experimental setup. We will consider the first derivative with respect to one of those parameters: the celerity c. One may easily generalize this calculation for all the other parameters and for higher order derivatives.

We first write that $(y_s(c),v_s(c),y_H(c),v_H(c))$ are solutions of the system (9)–(14) for a value c of the celerity and that $(y_s(c+h),v_s(c+h),y_H(c+h),v_H(c+h))$ are solutions of the system (9)–(14) for a value $c+h$ of the celerity. By calculating term by term the difference between the two corresponding systems, dividing by h, and passing to the limit when h tends to zero, we obtain a linear system of equations, governing the derivatives $(y_s^{(1)},v_s^{(1)},y_H^{(1)},v_H^{(1)})$ of (y_s,v_s,y_H,v_H) in regard of c:

$$\frac{\partial y_s^{(1)}}{\partial t}=v_s^{(1)}, \tag{A1}$$

$$\begin{aligned}\frac{\partial v_s^{(1)}}{\partial t}&=c^2\frac{\partial^2 y_s^{(1)}}{\partial x^2}+2c\frac{\partial^2 y_s}{\partial x^2}-\kappa^2\frac{\partial^4 y_s^{(1)}}{\partial x^4}\\&\quad-2b_1v_s^{(1)}+2b_2\frac{\partial^2 v_s^{(1)}}{\partial x^2}+g(x,x_0)\\&\quad\times\nabla f_H(y_s-y_H,v_s-v_H)\cdot{}^t(y_s^{(1)},v_s^{(1)},y_H^{(1)},v_H^{(1)}),\end{aligned} \tag{A2}$$

$$\frac{\partial y_H^{(1)}}{\partial t}=v_H^{(1)}, \tag{A3}$$

$$\frac{dv_H^{(1)}}{dt}=-\frac{1}{M_H}\nabla F_H(y_s-y_H,v_s-v_H)\cdot{}^t(y_s^{(1)},v_s^{(1)},y_H^{(1)},v_H^{(1)}) \tag{A4}$$

and the initial and boundary conditions are given by

$$\begin{aligned}&y_s^{(1)}(x,0)=0,\quad v_s^{(1)}(x,0)=0,\quad y_s^{(1)}(0,t)=y_s^{(1)}(L,t)=0,\\&\frac{\partial^2 y_s^{(1)}}{\partial x^2}(0,t)=\frac{\partial^2 y_s^{(1)}}{\partial x^2}(L,t)=0,\end{aligned} \tag{A5}$$

$$y_H^{(1)}(0) = y_s^{(1)}(x_0,0), \quad v_H^{(1)}(0) = 0, \tag{A6}$$

where $\nabla f(y_s - y_H, v_s - v_H)$ denote the gradient of $f(y_s - y_H, v_s - v_H)$ in regard to (y_s, v_s, y_H, v_H) computed at the point (y_s, v_s, y_H, v_H). The derivatives $(y_s^{(j)}, v_s^{(j)}, y_H^{(j)}, v_H^{(j)})_{j=1,\ldots,9}$ in regard to the physical parameters are computed following the same scheme (16)–(18) as for the string and hammer displacements and velocities. More precisely, at each time iteration, once the values $(y_s^n, v_s^n, y_H^n, v_H^n)$ computed, the values $(y_s^{(j),n}, v_s^{(j),n}, y_H^{(j),n}, v_H^{(j),n})$ are obtained just by the solution of one linear system,

$$\frac{\partial y_s^{(j)}}{\partial t} = v_s^{(j)}, \tag{A7}$$

$$\begin{aligned}\frac{\partial v_s^{(j)}}{\partial t} &= c^2 \frac{\partial^2 y_s^{(j)}}{\partial x^2} - \kappa^2 \frac{\partial^4 y_s^{(j)}}{\partial x^4} - 2b_1 v_s^{(j)} + 2b_2 \frac{\partial^2 v_s^{(j)}}{\partial x^2} \\ &\quad + (c^2)^{(j)} \frac{\partial^2 y_s}{\partial x^2} - (\kappa^2)^{(j)} \frac{\partial^4 y_s}{\partial x^4} \\ &\quad - 2(b_1)^{(j)} v_s + 2(b^2)^{(j)} \frac{\partial^2 v_s}{\partial x^2} + g(x,x_0) \\ &\quad \times \nabla f_H(y_s - y_H, v_s - v_H) \cdot {}^t(y_s^{(j)}, v_s^{(j)}, y_H^{(j)}, v_H^{(j)}) \\ &\quad + g(x,x_0) f_H^{(j)}(y_s - y_H, v_s - v_H),\end{aligned} \tag{A8}$$

$$\frac{\partial y_H^{(j)}}{\partial t} = v_H^{(j)}, \tag{A9}$$

$$\begin{aligned}\frac{\partial v_H^{(j)}}{dt} &= -\frac{1}{M_H} \nabla F_H(y_s - y_H, v_s - v_H) \cdot {}^t(y_s^{(j)}, v_s^{(j)}, y_H^{(j)}, v_H^{(j)}) \\ &\quad - \left(\frac{1}{M_H}\right)^{(j)} F_H(y_s - y_H, v_s - v_H) \\ &\quad - \frac{1}{M_H} F_H^{(j)}(y_s - y_H, v_s - v_H)\end{aligned} \tag{A10}$$

and the initial and boundary conditions are given by

$$y_s^{(j)}(x,0) = y_{s0}^{(j)}, \quad v_s^{(j)}(x,0) = v_{s0}^{(j)}, \tag{A11}$$

$$y_s^{(j)}(0,t) = y_s^{(j)}(L,t) = 0, \quad \frac{\partial^2 y_s^{(j)}}{\partial x^2}(0,t) = \frac{\partial^2 y_s^{(j)}}{\partial x^2}(L,t) = 0, \tag{A12}$$

$$y_H^{(j)}(0) = y_s^{(j)}(x_0,0), \quad v_H^{(j)}(0) = v_{H0}^{(j)}. \tag{A13}$$

[1] J. Bensa, D. Dubois, R. Kronland-Martinet, and S. Ystad, in *Perceptive and Cognitive Evaluation of a Piano Synthesis Model*, LNCS 3310 of *CMMR 2004*, *Lecture Note in Computer Science Series* Vol. **1**, edited by U. Will (Springer, Berlin, 2004), pp. 232–245.

[2] A. Stulov, "Hysteretic model of the grand piano hammer felt," J. Acoust. Soc. Am. **97**, 2577–2585 (1995).

[3] J. Bensa, O. Gipouloux, and R. Kronland-Martinet, "Understanding the influence of physical parameters on piano sound by the use of an optimization method," in Proceedings of the International Symposium of Musical Acoustics (ISMA2001), The Musical and Architectural Acoustics Laboratory Perugia, Italy, 2001.

[4] H. Pollard and E. Jansson, "A tristimulus method for the specification of musical timbre," Acustica **51**, 162–171 (1982).

[5] P. M. Ruiz, "A technique for simulating the vibrations of strings with a digital computer," Ph.D. thesis, University of Illinois, 1970.

[6] A. Chaigne and A. Askenfelt, "Numerical simulation of piano strings. I. a physical model for a struck string using finite difference methods," J. Acoust. Soc. Am. **95**, 1112–1118 (1994).

[7] J. Bensa, S. Bilbao, R. Kronland-Martinet, and J. O. Smith III, "The simulation of piano string vibration: From physical model to finite difference schemes and digital waveguides," J. Acoust. Soc. Am. **114**, 1095–1107 (2003).

[8] M. Gosh, Indian J. Phys. **7**, 365–382 (1932).

[9] X. Boutillon, "Model for piano hammers: Experimental determination and digital simulation," J. Acoust. Soc. Am. **83**, 746–754 (1988).

[10] K. Hunt and F. Crossley, "Coefficient of restitution interpreted as damping in vibroimpact," ASME J. Appl. Mech. **42**, 440–445 (1975).

[11] L. Hiller and P. Ruiz, "Synthesizing musical sounds by solving the wave equation for vibrating objects," J. Audio Eng. Soc. **19**, 462–72 (1971); **19**, 542–51 (1971).

[12] A. Chaigne and A. Askenfelt, "Numerical simulation of piano strings. II. Comparisons with measurements and systematic exploration of some hammer-string parameters," J. Acoust. Soc. Am. **95**, 1631–1640 (1994).

[13] T. Yanagisana and K. Nakanura, "Dynamic compression characteristics of piano felt," J. Acoust. Soc. Jpn. **40**, 725–729 (1984).

[14] N. Giordano and J. P. Millis, "Hysteretic behavior of piano hammers," in Proceedings of the International Symposium of Musical Acoustics, The Musical and Architectural Acoustics Laboratory, Perugia, Italy, 2001, pp. 237–40.

[15] F. Avanzini and D. Rochesso, "Non linear contact force," in Proceedings of the COST G6 Conference on Digital Audio Effects, Department of Computer Science and Information Systems, University of Limerick, Limerick, Ireland, 2001.

[16] J. C. Strikwerda, *Finite Difference Schemes and Partial Differential Equations* (Wadsworth and Brooks, Pacific Grove, CA, 1989).

[17] D. E. Hall, "Piano string excitation. VI. Nonlinear modeling," J. Acoust. Soc. Am. **92**, 95–105 (1992).

[18] D. E. Hall and A. Askenfelt, "Piano string excitation. V. Spectra for real hammers and strings," J. Acoust. Soc. Am. **83**, 1627–1638 (1988).

[19] F. Avanzini, B. Bank, G. Borin, G. De Poli, and D. Rocchesso, "Musical instrument modeling: The case of the piano," in Proceedings of the Workshop on Current Research Directions in Computer Music, MOSART Research training network, Barcelona, 2001, pp. 124–125.

[20] J. Bensa, K. Jensen, and R. Kronland-Martinet, "A hybrid resynthesis model for hammer-strings interaction of piano tones," EURASIP Journal on Applied Signal Processing **2004**, 1021–1035 (2004).

[21] G. Weinreich, "Coupled piano strings," J. Acoust. Soc. Am. **62**, 1474–84 (1977), also contained in Ref. 28. See also Sci. Am. **240**, 94 (1979).

[22] M. Aramaki, J. Bensa, L. Daudet, P. Guillemain, and R. Kronland-Martinet, "Resynthesis of coupled piano string vibrations based on physical modeling," J. New Music Res. **30**, 213–226 (2002).

[23] N. Giordano, "Mechanical impedance of a piano soundboard," J. Acoust. Soc. Am. **103**, 2128–2133 (1998).

[24] S. Ystad, "Sound modeling applied to flute sounds," J. Audio Eng. Soc. **48**, 810–825 (2000).

[25] H. Järvelainen, V. Välimäki, and M. Karjalainen, "Audibility of inharmonicity in strings instruments sounds, and implications to digital sound synthesis," in Proceedings of the International Computer Music Conference, Computer Music Association, Beijing, 1999, pp. 359–362.

[26] L. Ingber, Adaptive Simulated Annealing, http://www.ingber.com/#ASA.

[27] http://www.lma.cnrs-mrs.fr/~kronland/JASA/sounds.html.

[28] *Five Lectures on the Acoustics of the Piano*, edited by A. Askenfelt (Royal Swedish Academy of Music, Stockholm, 1990), lectures by H. A. Conklin, A. Askenfelt, E. Jansson, D. E. Hall, G. Weinreich, and K. Wogram. Sound example CD included. Publication No. 64. Available online at http://www.speech.kth.se/music/5_lectures/.

Measurements of the anisotropy of ultrasonic velocity in freshly excised and formalin-fixed myocardial tissue

Steven L. Baldwin, Min Yang, Karen R. Marutyan, Kirk D. Wallace, Mark R. Holland, and James G. Miller[a)]
Department of Physics, Washington University, One Brookings Drive, Campus Box 1105, St. Louis, Missouri 63130

(Received 23 December 2004; revised 8 April 2005; accepted 13 April 2005)

The objective of this study was to quantify the anisotropy of ultrasonic velocity in freshly excised myocardial tissue and to examine the effects of formalin-fixation. Through-transmission radio-frequency-based measurements were performed on ovine and bovine myocardial specimens from 24 different hearts. A total of 81 specimens were obtained from specific locations within each heart to investigate the possibility of regional differences in anisotropy of velocity in the left ventricular wall and septum. No regional differences were observed for either lamb or cow myocardial specimens. In addition, no specific species-dependent differences were observed between ovine and bovine myocardium. Average values of velocity at room temperature for perpendicular and parallel insonification were 1556.9 ± 0.6 and 1565.2 ± 0.7 m/s (mean $\pm$standard error), respectively, for bovine myocardium ($N=45$) and 1556.3 ± 0.6 and 1564.7 ± 0.7 m/s for ovine myocardium ($N=36$). Immediately after measurements of freshly excised myocardium, ovine specimens were fixed in formalin for at least one month and then measurements were repeated. Formalin-fixation appears to increase the overall velocity at all angles of insonification and to increase the magnitude of anisotropy of velocity. [DOI: 10.1121/1.1925947]

PACS number(s): 43.80.Cs, 43.80.Ev [FD] Pages: 505–513

I. INTRODUCTION

The objective of this study was to quantify the anisotropy of ultrasonic velocity in freshly excised myocardial tissue and to examine the effects of formalin-fixation on velocity in myocardium. While some studies have examined insonification perpendicular or parallel to the predominant direction of the myofibers (Akashi *et al.*, 1995; Fei *et al.*, 1987; Goss *et al.*, 1980; Mol and Breddels, 1982; Saijo *et al.*, 1997; Shung and Reid, 1977; Shung and Reid, 1978), direct studies have not been performed on the anisotropy of velocity over a complete range of angles of insonification in freshly excised normal myocardial tissue. The speed of sound is usually taken to be 1540 m/s in medical ultrasonic imaging devices. With the growing number of approaches to ultrasonic tissue characterization, knowledge of the anisotropy of ultrasonic velocity in freshly excised myocardium may be helpful in determining the extent to which angle of insonification relative to direction of the myofibers may or may not influence results. Our approach was to perform broadband, through-transmission radio-frequency measurements in freshly excised ovine and bovine myocardial specimens at frequencies typical of those used in clinical echocardiography.

Previous studies have examined the influence of formalin-fixation on ultrasonic measurements in biological tissues other than myocardium (Bamber and Hill, 1979; Bamber *et al.*, 1979; Sasaki *et al.*, 2003). This study permits a direct examination of changes in the measured anisotropy of velocity resulting from formalin-fixation by quantifying the anisotropy of velocity in freshly excised myocardium and then comparing these results with measurements of the same myocardial specimens after formalin-fixation. We investigated the effects of fixation at a full range of angles of insonification relative to the predominant direction of the myofibers.

II. METHODS

A. Preparation of specimens

A total of 36 tissue specimens from 12 freshly excised lamb hearts and 45 tissue specimens from 12 freshly excised cow hearts were investigated in this study. The hearts were obtained within 30 min of slaughter from a local commercial slaughterhouse and immersed in 0.9% saline solution prior to specimen coring. From each ovine heart, three cylindrical plugs were cored, two from the left ventricular free wall and one from the septum using a 14.5-mm-i.d. coring tool. Specimens were cored from endocardium to epicardium such that the axis of symmetry of the cylindrical specimens was oriented orthogonal to the epicardial surface of the heart. The two left ventricular free wall specimens were cored in approximately the same plane perpendicular to the apex-to-base axis of the heart and superior to the anterior and posterior papillary muscles. The septal specimens were cored roughly halfway between the plane of the left ventricular specimens and the apex. Immediately following measure-

[a)]Electronic mail: jgm@wuphys.wustl.edu

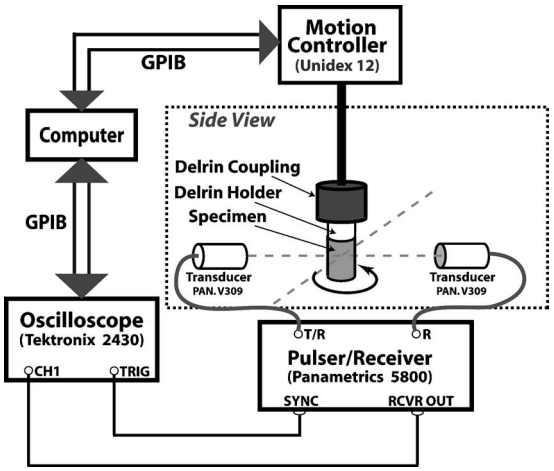

FIG. 1. Experimental setup for performing measurements of the anisotropic properties of ultrasonic velocity in myocardium.

ments of freshly excised myocardium, ovine specimens were fixed in formalin for at least one month prior to repeated measurements.

Because of their larger size, a total of four cylindrical plugs were cored from bovine hearts. Three were prepared in an identical manner to that for ovine specimens, and an additional left ventricular specimen was obtained in the same plane as the other left ventricular specimens, in the region between the anterior and posterior papillary muscles. This method of coring provided for a regional comparison of the anisotropy of the myocardial specimens. Epicardial surfaces were trimmed of excessive fat, if deemed necessary, prior to being glued to a plastic (Delrin®) mount of equivalent diameter for data acquisition.

B. Acquisition of ultrasonic quasilongitudinal velocity data

Each myocardial specimen was cored from an intact left ventricle at room temperature that had been stored in the saline solution to reduce the potential for osmotic effects. Immediately after coring, the specimen was mounted and then immersed in a water bath (also at room temperature) approximately 5–10 min prior to measurements. The total time from death of the animal to completion of all measurements on that particular heart was approximately 3–5 h. Temperature changes during any one data acquisition were no more than 0.1 °C. Figure 1 shows the equipment set up for measurements. The through-transmission radio-frequency data were acquired using a matched pair of 5 MHz focused piezoelectric transducers (Panametrics V309, 1/2 in. diameter, 2 in. focal length; Panametrics, Waltham, MA). The tissue specimens were positioned at the focus of both transducers and the ultrasonic beam was centered on the midmyocardial region of each specimen. Calculations of the beam diameter in the focal zone suggest that the −6 dB beamwidths were between 1 and 2 mm for the frequencies used in this study.

An ultrasonic pulse was generated with a Panametrics 5800 Pulser/Receiver operating in pitch/catch mode and sent to the transmit transducer. The through-transmitted signal was received by the receive transducer, amplified by the Panametrics 5800, and digitized with a Tektronix 2430A (Tektronix, Beaverton, OR) oscilloscope. The pulser/receiver settings were optimized to provide sufficient dynamic range over the usable bandwidth of the measurement system for all angles of insonification relative to the predominant fiber orientation.

For data acquisition, the Delrin mount of each myocardial specimen was friction fit into a cylindrical Delrin coupling that was, in turn, attached to the metal shaft of the rotational axis. A Unidex 12 motion controller (Aerotech, Pittsburgh, PA) was utilized to allow the measurement assembly to have x, y, and z translational movements as well as rotational freedom. The assembly was adjusted to minimize precession of the specimen upon rotation. A computer (Apple Computer, Cupertino, CA) served as a data acquisition system controller and off-line storage device for digitized data. Each myocardial specimen was rotated in 5° increments under computer control. Substitution through-transmission data were obtained by averaging 32 radio-frequency traces at each incremented angle over a complete rotation. In addition, immediately after through-transmission data acquisition, pulse-echo data were acquired for specimen thickness measurements at each incremented angle. Corresponding water path reference data were obtained to within ±0.1 °C of the corresponding specimen data.

C. Description of data analysis for measuring ultrasonic velocity

The determination of velocity was accomplished by separate measurements of specimen thickness and the difference in time-of-flight of an ultrasonic pulse traveling a specific distance through the host medium of known sound speed (in this case water) compared to that of a pulse traveling the same distance in the host medium with the myocardial specimen inserted in the path of insonification. These measurements were performed at each angle of rotation of the myocardial specimens in order to determine the anisotropy of velocity.

The velocity of sound in the specimen (V_{specimen}) at angle, θ, is obtained by

$$V_{\text{specimen}}(\theta) = \frac{V_{\text{water}}}{1 - \dfrac{V_{\text{water}} \cdot \Delta t(\theta)}{L_{\text{specimen}}(\theta)}}, \tag{1}$$

where V_{water} is the speed of sound in water, $L_{\text{specimen}}(\theta)$ is the thickness of the myocardial specimen through which the ultrasonic pulse propagates at an angle of rotation, θ, and $\Delta t(\theta)$ is the difference in arrival times between the specimen and water reference through-transmitted radio-frequency traces at angle of rotation, θ. The speed of sound in water was obtained by measurement of the temperature of the water bath and making a calculation based on a fifth-order polynomial expression for the speed as a function of temperature (Del Grosso and Mader, 1972).

D. Ultrasonic measurement of myocardial specimen thickness

In freshly excised myocardium cored with a cylindrical coring tool, specimens often have elliptical rather than perfectly circular cross sections (in the plane perpendicular to the axis of rotation for data acquisition). Ultrasonic measurements of thickness were performed at each angle of rotation for each myocardial specimen. These ultrasonically measured values of thickness showed reasonably good agreement with independent assessments carried out with vernier calipers.

Myocardial specimen thickness can be measured by first determining the distance between the transducers using the known speed of sound in water and the measured time-of-flight of an ultrasonic pulse transmitted through water (without the myocardial specimen). Then with the myocardial specimen inserted, for each angle of rotation, the part of the total path length occupied by water is determined by making time-of-flight measurements of the reflected ultrasound from the transmitting transducer to the front wall and separately from the receiving transducer to the back wall of the tissue. This approach overcomes a difficulty described in previous studies from this laboratory in making time-of-flight measurements of the back wall from pulse/echo through the attenuating specimen in which "attenuation of the signal caused a weakened back wall echo to be returned, thereby making it difficult to distinguish the specular echo surface phenomenon from the backscatter in bulk" (Verdonk *et al.*, 1992). By subtracting the part of the total path length occupied by water from the distance between the two transducers, the thickness of the specimen could then be determined at each angle of rotation. As described, this technique would require separate pulse/echo measurements at each angle of rotation for both the front wall and the back wall of the myocardial specimen. Because measurements can be time-sensitive, the following technique was used, in practice, to eliminate the need for two sets of pulse/echo measurements: Timing mark measurements for front and back wall echoes were made relative to a reference (the cylindrical plastic coupling of known thickness into which the plastic mount of the myocardial specimen was fit). The thickness of the specimen at angle θ then equals the thickness of the reference minus the difference between the front walls of the reference and the specimen at angle θ, minus the difference between the front walls of the reference and specimen at angle $\theta+180°$. By this relative approach, any slight precession in the measurement assembly would be intrinsically compensated because it would presumably act on both the plastic coupling and the myocardial specimen.

For calculations of the thickness of myocardial specimens using this technique, we used a 31-mm-diam plastic (Delrin) coupling as a reference as shown in Fig. 1. The difference in arrival times between the signal reflected back from the plastic coupling reference and that reflected back from the tissue specimen, $[\Delta t_{\text{front wall}}(\theta)]$, was calculated for each angle of rotation for the front wall. Measurements of the time differences were repeated upon rotation by 180° which corresponds to measurements of the time differences for the back wall at angle $[\Delta t_{\text{back wall}}(\theta)]$. Myocardial specimen thickness as a function of angle of rotation, $L_{\text{specimen}}(\theta)$, was then calculated by

$$L_{\text{specimen}}(\theta) = L_{\text{reference}}(\theta) - \frac{V_{\text{water}}}{2} \cdot (\Delta t_{\text{front wall}}(\theta) + \Delta t_{\text{back wall}}(\theta)) \quad (2)$$

in which V_{water} is the speed of sound in water, and $L_{\text{reference}}(\theta)$ is the known thickness of the plastic coupling reference which was measured ultrasonically.

Specific timing measurements were made on the envelope of the radio-frequency signal obtained by computing the magnitude of the analytic signal. Our criterion for making timing measurements was based on searching from baseline electronic noise toward the front wall echo for the first sample point with a voltage level that was equal to 15 times the standard deviation of the baseline noise (the value of 15 was chosen empirically). After timing marks were determined for each specimen, curves of timing mark as a function of angle of rotation were generated and smoothed with a four-point binomial filter for use in the calculation of thickness using Eq. (2).

E. Through-transmission timing measurements

For calculation of the velocity, Eq. (1) requires measurement of the difference in arrival times between the specimen and water reference through-transmitted radio-frequency traces at angle of rotation, θ. This was accomplished by cross correlation of the specimen and water reference through-transmitted radio-frequency signals. Unique maxima were determined by shifting data that had been sampled at 4 ns/point. In the Appendix, we address some important considerations for making time-of-flight measurements in attenuating media arising from changes in radio-frequency pulse shape resulting from the effects of varying attenuation.

III. RESULTS

The measured average ultrasonic velocities for freshly excised ovine and bovine myocardial specimens are shown in Fig. 2. Average values of velocity for perpendicular and parallel insonification were 1556.9 ± 0.6 and 1565.2 ± 0.7 m/s (mean±standard error), respectively, for bovine myocardium ($N=45$) and 1556.3 ± 0.6 and 1564.7 ± 0.7 m/s for ovine myocardium ($N=36$). No significant regional differences were observed for either lamb or cow myocardial specimens between specimens cored from the left ventricle compared to the septum. In addition, no significant regional differences between myocardial specimens cored from the left ventricles were observed for either lamb (specimens cored superior to the anterior and posterior papillary muscles) or for cow (same as lamb, but with an additional specimen cored from the left ventricle between the specimens cored from above the anterior and posterior papillary muscles).

Average measured values of velocity for perpendicular and parallel insonification in formalin-fixed ovine myocardium ($N=36$) were 1568.4 ± 0.4 and 1580.7 ± 0.7 m/s

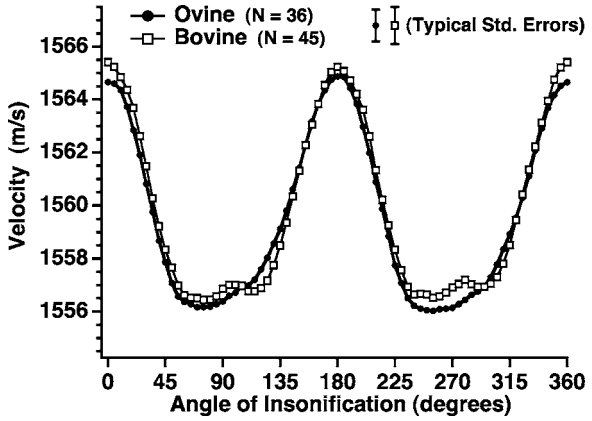

FIG. 2. Comparison of ultrasonic velocities vs angle of insonification relative to the predominant direction of the myofibers for freshly excised ovine (N=36 cylindrical specimens obtained from 12 ovine hearts) and freshly excised bovine (N=45 cylindrical specimens obtained from 12 bovine hearts) myocardial tissue. Representative standard errors are shown.

(mean±standard error), respectively. Values of average ultrasonic velocity in freshly excised and formalin-fixed ovine myocardial tissue are compared in Fig. 3 (upper panel). A more direct comparison of changes in the angular dependence of velocity resulting from formalin-fixation is seen in Fig. 3 (lower panel), which shows the corresponding velocities with the mean values subtracted. Formalin-fixation appears to increase the overall velocity at all angles of insonification (Fig. 3 upper panel) and to also increase the magnitude of anisotropy of velocity (Fig. 3 lower panel). The average magnitude of anisotropy is 8.4±0.9 m/s for freshly excised myocardium compared to 12.3±0.8 m/s for formalin-fixed myocardium. Again, no significant regional differences were observed in formalin-fixed ovine myocardial tissue (either between septum and left ventricle or among left ventricular specimens).

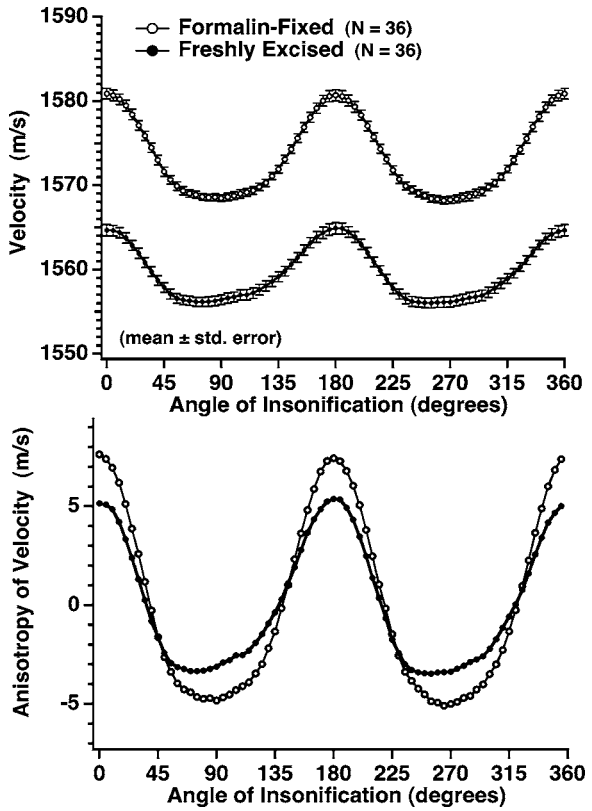

FIG. 3. Effects of formalin-fixation on measurements of ultrasonic velocity in ovine myocardial tissue (N=36 cylindrical specimens obtained from 12 ovine hearts). The top panel represents absolute measurements of ultrasonic velocity and the bottom panel shows the relative anisotropy with mean values subtracted. Formalin-fixation appears to result in an overall increase in ultrasonic velocity at all angles of insonification as well as a greater magnitude of anisotropy of ultrasonic velocity.

For 38 out of 45 freshly excised bovine specimens measured, the temperature was maintained between 19.3 and 20.4 °C. For the remaining 7 bovine specimens, temperature extremes were 16.2–18.8 °C. Mean results excluding these specimens were not significantly different (approximately 0.2 m/s larger and approximately constant with angle of insonification). For 27 out of 36 freshly excised ovine specimens measured, the temperature was maintained between 19.1 and 20.1 °C. For the remaining 9 ovine specimens, temperature extremes were 17.6–19.1 °C. Mean results excluding these specimens showed only a very modest increase of 0.7 m/s (approximately constant with angle of insonification). In the case of formalin-fixed ovine myocardium, all 36 specimens were measured over a temperature range of 19.0–20.1 °C.

IV. DISCUSSION

A. Anisotropy of velocity in freshly excised myocardial tissue

Previous measurements of the ultrasonic quasilongitudinal velocity of freshly excised myocardium have involved insonification strictly perpendicular and parallel to the predominant direction of the myofibers (Akashi *et al.*, 1995; Fei *et al.*, 1987; Mol and Breddels, 1982; Shung and Reid, 1977). A comparison of results from this study with previous results is shown in Table I (all values are reported as mean±one standard deviation). With the potential for differences in temperature of myocardial specimens upon data acquisition, current results appear to show reasonable agreement with previous results from other laboratories.

Measurements of ultrasonic velocity in freshly excised bovine heart muscle were performed by Akashi *et al.* using an ultrasonic transmission comparison method in the frequency range of 20 MHz to 40 MHz (Akashi *et al.*, 1995). They report measured velocities over a temperature range of 22–24 °C of 1565–1570 m/s, but it is unclear at what angle relative to the predominant direction of the myofibers these measurements were made. Our bovine myocardial measurements were performed at temperatures ranging from 18 to 20 °C and at lower frequencies (approximately 3–7 MHz). If the ultrasonic velocity of myocardial tissue were to experience a similar temperature dependence as that of water (3 m/s per °C), then these values would still fall within the range of values measured in the current study, as seen upon comparison of values in Table I. In addition, it should be noted that myocardium may be expected to exhibit velocity dispersion that increases modestly with increasing frequency. Previous studies in this laboratory have predicted a 2.5 m/s difference for phase velocities at 1 and 9 MHz for

TABLE I. Comparison of measured ultrasonic myocardial velocities of the current study with previous measurements from other laboratories (mean±one standard deviation).

	Velocity parallel to myofibers (m/s)	Velocity perpendicular to myofibers (m/s)	Magnitude of anisotropy of velocity (m/s)	Ratio of parallel to perpendicular
Results of current study				
Freshly excised bovine myocardium	1565±5	1557±4	8±3	0.51%
Freshly excised ovine myocardium	1565±4	1556±4	9±2	0.58%
Formalin-fixed ovine myocardium	1581±4	1568±3	12±3	0.83%
Results of previous studies				
Freshly excised bovine 23±1 °C, 20–40 MHz (Akashi *et al.*, 1995)	1565–1570[a]		···	···
Freshly excised calf 22±1 °C, 5 MHz (Shung and Reid, 1977, 1978)	···	1546±4	···	···
Freshly excised bovine 23±0.5 °C, 5 MHz (Fei, Shung, and Wilson, 1987)	···	1558±4	···	···
Freshly excised canine 20±2 °C, 5 MHz (Mol and Breddels, 1982)	1558±6	1550±6	7±3	0.52%
Formalin-fixed calf 22±1 °C, 5 MHz (Shung and Reid, 1977)	···	1559±7	···	···
Formalin-fixed human 18.1±1.2 °C, 5 MHz (Verdonk, Wickline, and Miller, 1992)	1550±5	1530±3	20±6 (reported[b]) 12 (reanalyzed using rf correlation[b])	···

[a]Angle of insonification relative to predominant direction of myofibers not specified.
[b]See the Appendix.

perpendicular insonification in freshly excised canine myocardium (O'Donnell *et al.*, 1981; Waters *et al.*, 2003; Waters *et al.*, 2000). Measurements on a limited number of hearts for perpendicular insonification (at 5 MHz and 22±1 °C) as reported by Shung and Reid showed a lower average value of ultrasonic velocity of 1546±4 m/s (Shung and Reid, 1977; Shung and Reid, 1978). However, these measurements were reported for calf myocardium. In our experience, calf myocardium appears to be qualitatively much less stiff than cow myocardium, as was measured in this current study. For this reason, measurements in young bovine myocardial specimens might exhibit lower (more water-like) values of ultrasonic velocity. In addition, specimens studied by Shung and Reid were excised randomly from both the ventricles and the atria. In our current study, measurements were performed only on the left ventricle and septum. Subsequent work at 5 MHz center frequency at 23±0.5 °C reported by Fei, Shung, and Wilson on bovine myocardium shows an average velocity at perpendicular insonification of 1558±4 m/s (Fei and Shung, 1985; Fei *et al.*, 1987).

Measurements of ultrasonic velocity in freshly excised canine myocardium for perpendicular and parallel insonification were reported by Mol and Breddels at 5 MHz at temperatures between 18 and 22 °C and were scaled to 20 °C assuming a temperature coefficient of 3 m/s per °C (Mol and Breddels, 1982). That study (which employed a zero crossing method of timing mark detection) showed an average of 1550±6 and 1558±6 m/s for perpendicular and parallel insonification, respectively. These averages are slightly lower than the averages for lamb and cow myocardium reported in our study. However, the magnitude of anisotropy of ultrasonic velocity in canine myocardium, 7±3 m/s, is in agreement with that of lamb and cow myocardium in our study (9±2 and 8±3 m/s, respectively).

Our results extend previous studies by measuring the anisotropy of ultrasonic quasilongitudinal velocity as a function of angle of insonification over a 360° rotation relative to the predominant direction of the myofibers in freshly excised myocardial tissue (Fig. 2). The ultrasonic velocity shows maxima for angles of insonification parallel to the predominant direction of the myofibers and minima for perpendicular insonification. Results show good agreement between freshly excised ovine and bovine myocardial tissue with ratios of the difference in measured ultrasonic velocities for parallel to perpendicular insonification of 0.58% and 0.51%, respectively. Maxima appear more sharply peaked compared to minima (as can perhaps more clearly be seen by viewing Fig. 2 upside down). This indicates greater sensitivity of mea-

sured ultrasonic velocity for slight angular deviations from insonification parallel to the myofibers than for slight angular deviations from perpendicular insonification.

B. Comparison of changes in the anisotropy of ultrasonic velocity from freshly excised to formalin-fixed myocardial tissue

The work by Shung and Reid reported an increase upon formalin-fixation of 13 m/s in the measured ultrasonic velocity compared to values in freshly excised calf myocardial tissue for insonification perpendicular to the predominant direction of the myofibers (Shung and Reid, 1977). As can be seen from Table I, this is very nearly equal to the increase in average measured ultrasonic velocity for formalin-fixed compared to freshly excised lamb myocardial tissue in the current study, which was observed to be 12 m/s for perpendicular insonification.

Previous measurements from this laboratory on formalin-fixed human myocardial tissue (at 5 MHz and 18.1 ± 1.2 °C) demonstrated a clear anisotropy of ultrasonic velocity with maxima for insonification parallel to the predominant direction of myofibers and minima for perpendicular insonification (Verdonk *et al.*, 1992). As described in the Appendix, when the data were reanalyzed using the approach of the current study in order to minimize the error in measurement introduced by specimen attenuation on timing mark determination, identical magnitudes of the anisotropy of velocity were determined between the formalin-fixed human myocardium of that study and the formalin-fixed ovine myocardium of the present study. Overall values of ultrasonic velocity for that study were lower than results for the current study and other studies as seen in Table I. We have observed a decrease in the measured speed of sound in formalin-fixed myocardial tissue as a function of time in the water bath before measurements are made. This decrease appears to be on the order of 10 m/s after approximately 3 h and 20 m/s after approximately 15 h. Measurements in the current study were made within 5–10 min of immersion in the water bath. However, if specimens were left in the water for long amounts of time prior to measurement, this may partially explain the lower overall values of velocity in the previous study. In addition, it should be noted that the formalin-fixed human myocardial measurements were performed on seven tissue specimens from six explanted human hearts obtained from patients who had undergone heart transplantation for ischemic cardiomyopathy. "Grossly normal myocardial segments, distant from regions of infarction, were selected for investigation" (Verdonk *et al.*, 1992). A detailed comparison of the results obtained from the seriously compromised hearts of that study with the results of the present study may not be appropriate.

Results of the current study allow a direct comparison of measured ultrasonic velocities for freshly excised and formalin-fixed ovine myocardial tissue as shown in Fig. 3. Formalin-fixation appears to result in an overall increase in ultrasonic velocity at all angles of insonification as well as in a small increase in the magnitude of anisotropy of ultrasonic velocity. (This corresponds to a 1.0% increase in velocity for parallel insonification and a 0.8% increase in velocity for perpendicular insonification.) Results show a ratio of measured ultrasonic velocities for parallel to perpendicular insonification for formalin-fixed ovine myocardial tissue of 0.83% (compared to 0.58% for freshly excised myocardium prior to fixation). Inspection of Fig. 3 reveals that the maxima for near parallel angles of insonification appear more peaked (reflected in the larger magnitude of anisotropy of ultrasonic velocity). This effect may result from a greater stiffening and corresponding increase in ultrasonic velocity along myofibers than between them as a result of the action of formalin-fixation.

C. Observations regarding measurements of ultrasonic velocity across species

In addition to the very good agreement between results for lamb and cow myocardial tissue reported in the current study, there is also good agreement between current measurements of velocity and the magnitude of anisotropy for freshly excised lamb and cow myocardium and the results for freshly excised canine myocardium reported by Mol and Breddels (1982) as seen in Table I. In formalin-fixed tissue, measurements of the magnitude of anisotropy in lamb myocardium (12 ± 3 m/s) were also in agreement with human myocardium (12 m/s). It has been observed that the ultrasonic velocity of biological tissues is determined by the ultrasonic properties of their constituent protein contents and that relatively small changes in collagen content can have a measurable effect (Goss *et al.*, 1980). The agreement in anisotropy of velocity for lamb, cow, dog, and human myocardial tissue may reflect the similarities in cardiac anatomy for various species of mammals.

D. Observations regarding the nature of uncertainties in measurements

It is also interesting to note the behavior of uncertainties in measurements of the average overall velocity compared to uncertainties in the average *anisotropy* of velocity. This was examined by comparing standard deviations for the average velocity with those calculated from individual myocardial results whose mean values had been subtracted prior to averaging. By subtracting the mean values from individual myocardial specimens, any contributions to uncertainty that resulted from constant offsets among specimens would be eliminated. Only differences in the relative shapes of curves of velocity as a function of angle of insonification would be reflected in subsequent standard deviations. In the results from freshly excised tissue, when constant offsets are subtracted prior to averaging, average standard deviations fall by roughly a factor of 3 for both ovine myocardial specimens (from 3.6 to 1.1 m/s) and for bovine myocardial specimens (from 4.5 to 1.6 m/s). This suggests that a substantial part of the uncertainty does result from constant offsets rather than from differences in shape between velocity curves as a function of angle of insonification (i.e., the anisotropy of velocity). Such offsets may result from such factors as small differences in temperature at the time of data acquisition, small differences in the time that the myocardial specimens were suspended in the water reference prior to the onset of mea-

surements (potential osmotic effects), or normal biological variation. This same effect was observed for formalin-fixed ovine myocardium, but to a slightly smaller degree, where average standard deviations decreased by a factor of 2 (from 3.1 to 1.5 m/s) for formalin-fixed ovine myocardial specimens. These results might hint at the possibility that formalin-fixed myocardium is less sensitive to factors that cause constant offsets in freshly excised myocardial tissue. This same effect was also observed in the fresh canine myocardial study of Mol and Breddels, as seen in Table I, where reported standard deviations in velocities parallel and perpendicular to the myofibers were ±6 m/s, but the standard deviations for the magnitude of anisotropy dropped to ±3 m/s.

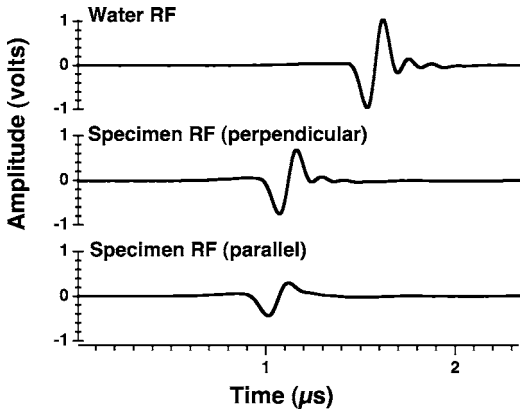

FIG. 4. Radio-frequency traces for water reference (top panel) and a representative myocardial specimen at perpendicular insonification (minimum attenuation) (middle panel) and at parallel insonification (maximum attenuation) (bottom panel).

V. SUMMARY

This study has quantified the anisotropy of ultrasonic velocity in freshly excised and formalin-fixed myocardium as a function of angle of insonification relative to the predominant direction of the myofibers. Maximum velocities were observed at parallel insonification and minima at perpendicular insonification. Formalin-fixation results in an increase in measured ultrasonic velocity as well as in an increase in the magnitude of the anisotropy of velocity.

ACKNOWLEDGMENTS

This work was supported, in part, by NIH R37 HL40302. The authors gratefully acknowledge Star Packing Company, St. Louis, MO for providing ovine and bovine myocardial tissues. These investigations benefited substantially from the very careful studies conducted by Edward Verdonk when he was a member of this Laboratory.

APPENDIX: IMPLICATIONS OF METHOD USED TO ESTIMATE TIME-OF-FLIGHT ON MEASUREMENTS OF VELOCITY IN SPECIMENS WITH ATTENUATION THAT DIFFERS SIGNIFICANTLY FROM THAT OF THE REFERENCE MEDIA

Previous work from this laboratory has employed a timing mark detection algorithm which searched for a fixed percentage (15%) of the baseline-to-peak voltage levels of the magnitude of the analytic signal of the radio-frequency trace (Verdonk *et al.*, 1992). With measurements using this technique in formalin-fixed human myocardium, the authors reported that "Complications introduced by the anisotropy of attenuation were a potential source of systematic error in our measurements of the anisotropy of velocity. The low-pass filtering effect exhibited by soft tissues can confound timing measurements by changing the pulse shape as the wideband ultrasonic signal propagates through the sample" (Verdonk *et al.*, 1992). While that work reported a clear anisotropy of velocity in myocardial tissue with maximal velocity along the myofibers, they suggested that potential errors in the measured values of velocity introduced by the anisotropy of attenuation (with that technique) would require future consideration (Verdonk *et al.*, 1992). This Appendix explores these potential errors and suggests a method for minimizing the effects of attenuation on measurements of velocity in soft tissues (in this case myocardium).

Figure 4 depicts three representative through-transmitted radio-frequency traces. The water reference trace (top panel) occurs later in time than either of the myocardial specimen traces, indicating the slower speed of sound in water compared to that in myocardial tissue. The earliest myocardial specimen trace in time corresponds to parallel insonification (bottom panel) and the later one corresponds to perpendicular insonification (middle panel). The effects of attenuation (weaker pulse amplitude and changed pulse shape compared to the water reference trace) are most apparent for parallel insonification. While clearly still experiencing attenuation, the trace corresponding to perpendicular insonification appears more "water-like" in shape. Previous work by Wear has examined the effects of frequency-dependent attenuation and dispersion on measurements of velocity in which a specific timing marker (e.g., a zero-crossing, maximum, or minimum) is designated for the specimen and the reference wave forms (Wear, 2000). In the case of sufficiently weakly dispersive media, like myocardium, the effect of dispersion on the received signal is not significant. (Previous studies in this laboratory have predicted a 2.5 m/s difference for phase velocities at 1 and 9 MHz for perpendicular insonification in freshly excised canine myocardium (O'Donnell *et al.*, 1981; Waters *et al.*, 2003; Waters *et al.*, 2000.) The study by Wear showed that for media that exhibit a frequency-dependent attenuation, the pulse spreads over time and the magnitude of the estimate of the difference in arrival times between the specimen and the reference depends on the point in the wave form that is analyzed (Wear, 2000). Similarly, the calculated time difference (and resulting calculated velocity) depends on the choice of percentage of magnitude of the analytic signal when using that technique for timing mark detection. Furthermore, when comparing results in which the attenuation varies (here as a consequence of changing angle of insonification relative to the predominant direction of the myofibers), the measured *anisotropy* of velocity also depends on that choice. Table II shows results of calculation of the anisotropy of velocity for specific percentages of the magnitude

TABLE II. Comparison of calculated velocities using different methods of timing mark detection in a representative specimen.

Method of timing mark determination	Measured apparent anisotropy of velocity (m/s)
rf Correlation	8.9
Zero crossing	8.8
Percentage magnitude analytic signal	
15%	21.5
30%	15.7
45%	14.5
60%	13.6
75%	13.1
90%	12.1
100% (peak)	11.7

of analytic signal for a representative specimen. The measured anisotropy of velocity is seen to increase with decreasing choice of percentage. This effect on measured velocity indicates that this method of velocity determination is biased because of changing pulse shape resulting from the frequency-dependent effects of attenuation. Similar to what was shown by Wear for timing mark detection using a particular marker on the radio-frequency wave form (Wear, 2000), a timing mark detection algorithm based on percentage of analytic signal appears to be more strongly affected by certain frequency components of the specimen trace because it only takes into account a certain point on the corresponding analytic signal which has been shown to depend on the attenuation of the specimen.

In order to facilitate an objective measure of timing differences that would reflect all present frequency components and, as a consequence, be less dependent on the effects of changing pulse shape resulting from attenuation in the specimen, we determined differences in signal arrival times by cross correlation of the specimen and water reference through-transmitted radio-frequency signals. Use of the radio-frequency trace (rather than the analytic signal) includes all measured information for use in determining timing marks. The work by Wear observed that when using a zero crossing method of timing mark detection, errors in group velocity estimates are minimized when the zero crossing marker is chosen near the center of the wave form (Wear, 2000). Furthermore, that study demonstrated that in media such as myocardium that have a faster speed of sound than in water, the effects of attenuation caused calculated velocities to be increasingly too high as timing marks were chosen nearer the leading edge of the wave forms and they were, correspondingly, increasingly too low as timing marks were chosen nearer the trailing edge of the wave forms (Wear, 2000). Because the effects of pulse spreading due to attenuation appear to have an approximately symmetric effect on velocity estimates for points nearer the leading edge of the wave form compared to points nearer the trailing edge of the wave form (Wear, 2000), this suggests that determining timing differences from radio-frequency trace correlation, which uses all points of the wave form in determining timing differences, may yield results closer to those obtained from timing mark choices nearer the center of the wave form and thus with minimized errors as a result of the effects of attenuation. Table II shows results of calculated anisotropy of velocity using radio-frequency trace correlation for comparison to results of specific choices of percentage of magnitude analytic signal for the representative specimen. In addition, results from radio-frequency trace correlation are seen to agree with results using a zero crossing method of timing mark detection as employed in the Mol and Breddels work (Mol and Breddels, 1982).

In order to compare current measurements of velocity made with the radio-frequency cross-correlation method for timing mark detection with previous measurements from this laboratory (Verdonk *et al.*, 1992) that employed 15% of the magnitude of analytic signal for timing mark detection, we analyzed our current data on formalin-fixed lamb myocardial specimens and also reanalyzed the historical data on formalin-fixed human myocardial specimens using both methods. Measured mean values of the anisotropy were in good agreement between the two data sets (22 m/s for the current lamb myocardial data compared to 19 m/s for the previous human myocardial data using 15% analytic signal for timing mark detection, and 12 m/s for current lamb myocardial data compared to 12 m/s for previous human myocardial data using cross correlation of the radio-frequency traces for timing mark detection). The larger measured anisotropy of velocity observed when using a percentage analytic signal method for timing mark detection would be expected because of the larger attenuation for parallel compared to perpendicular insonification and corresponding dependence of this method on pulse shape which is affected by changing attenuation in the rotating specimens. For these reasons, timing mark detection based on cross correlation of the radio-frequency traces may be a preferable choice for measurements of velocity in weakly dispersive specimens that exhibit attenuation different from the reference medium and for specimens that exhibit an anisotropy of velocity. In addition, the cross correlation of radio-frequency traces method of timing mark detection is more straightforward and less arbitrary than that based on a percentage of the magnitude of analytic signal.

Akashi, N., Kushibiki, J., Chubachi, N., and Dunn, F. (**1995**). "Acoustic properties of selected bovine tissues in the frequency range 20–200 MHz," J. Acoust. Soc. Am. **98**, 3035–3039.

Bamber, J. C., and Hill, C. R. (**1979**). "Ultrasonic attenuation and propagation speed in mammalian tissues as a function of temperature," Ultrasound Med. Biol. **5**, 149–157.

Bamber, J. C., Hill, C. R., King, J. A., and Dunn, F. (**1979**). "Ultrasonic propagation through fixed and unfixed tissues," Ultrasound Med. Biol. **5**, 159–165.

Del Grosso, V. A., and Mader, C. W. (**1972**). "Speed of sound in pure water," J. Acoust. Soc. Am. **52**, 1442–1446.

Fei, D. Y., and Shung, K. K. (**1985**). "Ultrasonic backscatter from mammalian tissues," J. Acoust. Soc. Am. **78**, 871–876.

Fei, D. Y., Shung, K. K., and Wilson, T. M. (**1987**). "Ultrasonic backscatter from bovine tissues: Variation with pathology," J. Acoust. Soc. Am. **81**, 166–172.

Goss, S. A., Frizzell, L. A., Dunn, F. and Dines, K. A. (**1980**). "Dependence of the ultrasonic properties of biological tissue on constituent proteins," J. Acoust. Soc. Am. **67**, 1041–1044.

Mol, C. R., and Breddels, P. A. (**1982**). "Ultrasound velocity in muscle,"

J. Acoust. Soc. Am. **71**, 455–461.
O'Donnell, M., Jaynes, E. T., and Miller, J. G. (**1981**). "Kramers-Kronig relationship between ultrasonic attenuation and phase velocity," J. Acoust. Soc. Am. **69**, 696–701.
Saijo, Y., Tanaka, M., Okawai, H., Sasaki, H., Nitta, S. I., and Dunn, F. (**1997**). "Ultrasonic tissue characterization of infarcted myocardium by scanning acoustic microscopy," Ultrasound Med. Biol. **23**, 77–85.
Sasaki, H., Saijo, Y., Tanaka, M., and Nitta, S. (**2003**). "Influence of tissue preparation on the acoustic properties of tissue sections at high frequencies," Ultrasound Med. Biol. **29**, 1367–1372.
Shung, K. K., and Reid, J. M. (**1977**). "Ultrasonic scattering from tissues," Ultrason. Symp. Proc. **77** CH 1264-1SU, 230–233.
Shung, K. K., and Reid, J. M. (**1978**). "Ultrasound velocity in major bovine blood vessel walls," J. Acoust. Soc. Am. **64**, 692–694.
Verdonk, E. D., Wickline, S. A., and Miller, J. G. (**1992**). "Anistropy of ultrasonic velocity and elastic properties in normal human myocardium," J. Acoust. Soc. Am. **92**, 3039–3050.
Waters, K. R., Hughes, M., Mobley, J. and Miller, J. G., (**2003**). "Differential forms of the Kramers-Kronig dispersion relations," IEEE Trans. Ultrason. Ferroelectr. Freq. Control **50**, 68–76.
Waters, K. R., Hughes, M. S., Mobley, J., Brandenburger, G. H., and Miller, J. G., (**2000**). "On the applicability of Kramers-Kronig relations for ultrasonic attenuation obeying a frequency power law," J. Acoust. Soc. Am. **108**, 556–563.
Wear, K. A. (**2000**). "The effects of frequency-dependent attenuation and dispersion on sound speed measurements: Applications in human trabecular bone," IEEE Trans. Ultrason. Ferroelectr. Freq. Control **47**, 265–273.

Characterizing noise in nonhuman vocalizations: Acoustic analysis and human perception of barks by coyotes and dogs

Tobias Riede[a)]
Institute for Theoretical Biology, Humboldt University of Berlin, D-10115 Berlin, Germany

Brian R. Mitchell[b)]
Department of Environmental Science, Policy and Management, University of California, Berkeley, Berkeley, California 94720

Isao Tokuda[c)]
Institute for Theoretical Biology, Humboldt University of Berlin, D-10115 Berlin, Germany

Michael J. Owren[d)]
Department of Psychology, Cornell University, Ithaca, New York 14853

(Received 16 December 2004; revised 5 April 2005; accepted 18 April 2005)

Measuring noise as a component of mammalian vocalizations is of interest because of its potential relevance to the communicative function. However, methods for characterizing and quantifying noise are less well established than methods applicable to harmonically structured aspects of signals. Using barks of coyotes and domestic dogs, we compared six acoustic measures and studied how they are related to human perception of noisiness. Measures of harmonic-to-noise-ratio (HNR), percent voicing, and shimmer were found to be the best predictors of perceptual rating by human listeners. Both acoustics and perception indicated that noisiness was similar across coyote and dog barks, but within each species there was significant variation among the individual vocalizers. The advantages and disadvantages of the various measures are discussed. © *2005 Acoustical Society of America.* [DOI: 10.1121/1.1928748]

PACS number(s): 43.80.Ka [JAS] Pages: 514–522

I. INTRODUCTION

Effective measurement and quantification of characteristics of nonhuman vocalizations is critical to understanding the functional significance of these signals, and great strides have been made in this area as bioacoustic analysis techniques have become more sophisticated (e.g., Hopp *et al.*, 1998). However, not all aspects of vocal signals are equally amenable to analysis. Harmonic components are more easily measured than nonharmonic aspects. In this paper, the latter will be referred to as "noise" or "noisiness," limiting that term specifically to irregular energy that is part of the vocalization itself rather than occurring in the background or as an artifact of the recording process. Our purpose is to compare the performance of a number of measures that can be used to characterize noisiness when applied to a representative mammalian vocalization, namely barks produced by coyotes and dogs. Outcomes from these measures are then examined in light of human ratings of noisiness in the sounds.

In mammalian vocal production, noise is most commonly produced either by irregularity in the oscillating tissue of the sound source (usually the vocal folds) or by turbulence created by constrictions or obstacles that impede airflow in the vocal tract (also known as "additive noise"). These noise components are potentially distinguishable both quantitatively (Tokuda *et al.*, 2002) and perceptually (Schneider, 2004), but they nonetheless present significant challenges in analysis. The greatest difficulty lies in characterizing the complexity of the time-series waveform of a signal and frequency-spectral properties created by noisiness, particularly from irregular vocal-fold vibration (illustrated in Fig. 1). Here, spectrograms of three coyote and three dog barks provide examples of vocalizations that are almost purely harmonic, almost purely noisy, and some combination of the two. This kind of variety and complexity has recently been explained as the expected workings of a nonlinear dynamic system, in this case with mammalian vocal folds acting as coupled oscillators whose behavior can best be modeled using the principles of chaos theory (e.g., Strogatz, 2001).

Research on vocal-fold biomechanics in several mammalian species has demonstrated that harmonically structured utterances reflect quasiperiodic, synchronized vibration of the vocal folds (domestic dogs: Solomon *et al.*, 1994; monkeys: West and Larson, 1999; Jürgens, 1994; Brown *et al.*, 2003). However, the many different kinds of irregularities that also occur reveal the classic workings of nonlin-

[a)]Present address and address correspondence to Tobias Riede, Indiana University, Medical Science Program, 315 Jordan Hall, Bloomington, Indiana 47405. Fax: +1 812 855 4436; electronic mail: tobiasriede@web.de
[b)]Present address: University of Vermont, Rubenstein School of Environment and Natural Resources, 81 Carrigan Drive, Burlington, Vermont 05405-0088. Electronic mail: Brian.Mitchell@uvm.edu
[c)]Present address: Department of Computer Science & Systems Engineering, Muroran Institute of Technology, Muroran, Hokkaido 050-8585, Japan. Electronic mail: i.tokuda@biologie.hu-berlin.de
[d)]Present address: Department of Psychology, Georgia State University, P.O. Box 5010, Atlanta, Georgia 30302-5010. Electronic mail: michaeljowren@gmail.com

 0001-4966/2005/118(1)/514/9/$22.50

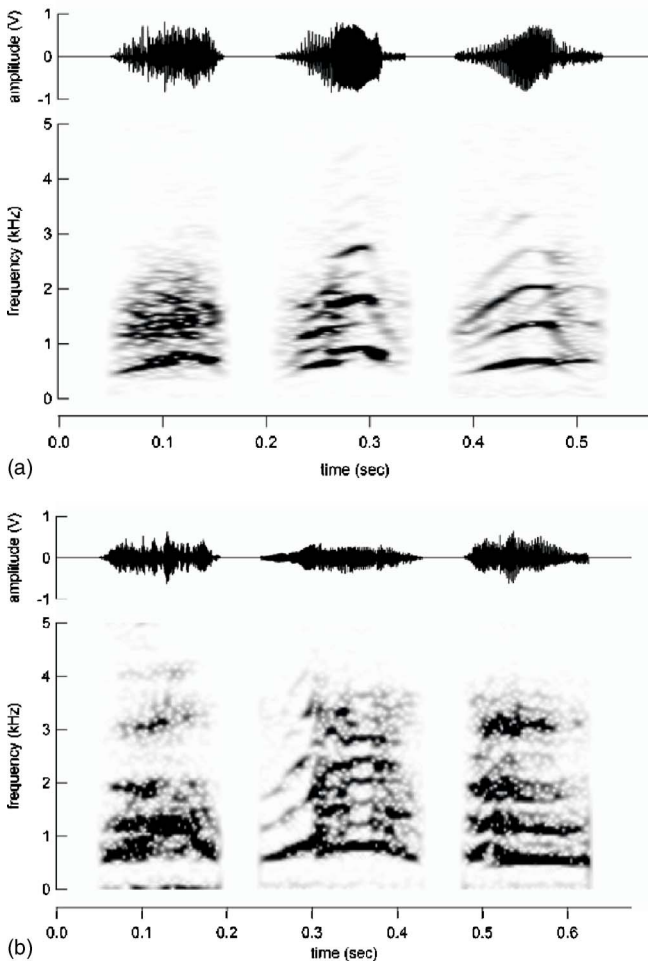

FIG. 1. Time series and spectrograms of (a) three coyote barks and (b) three dog barks. All vocalizations came from different individuals. Sounds were sampled at 22.05 kHz and spectrograms were produced using a 512-point FFT analysis window.

ear dynamic systems (Wilden *et al.*, 1998; Riede *et al.*, 2000, 2004; Fitch *et al.*, 2002; Brown, *et al.* 2003). These irregularities are now often referred to as "nonlinear phenomena," although all vocal-fold vibratory behaviors are technically nonlinear, including those that give rise to harmonically structured sounds.

Noisy mammalian sounds should therefore not be analyzed based solely on traditional methods, which include measuring the basic rate of vocal-fold vibration (known as fundamental frequency, or F_0), and the filtering effects of resonances of the vocal tract above the larynx (the formants). Here, F_0 is interesting only as a means of testing for the presence of deviations from periodicity, and formant analyses may play little, if any, role when measuring noisiness. If there are identifiable F_0 or harmonic components, one can apply algorithms designed to quantify the relative contribution of periodicity and noise, and to characterize cycle-to-cycle variation or "perturbation" in the waveform. However, some noisy vocalizations may not be truly periodic at all, instead reflecting deterministic chaos (Wilden *et al.*, 1998). An additional approach would involve measuring the degree of nonlinearity in the underlying vibrations. Each of these three approaches, namely periodicity versus noise, perturbation, and relative nonlinearity, are compared in this paper.

Periodicity and noise are typically compared using "harmonic-to-noise ratio" (HNR) algorithms, also known as "signal-to-noise ratio," "harmonicity," and the like. A number of such algorithms have been developed in speech science (see Baken and Orlikoff, 1999), where the typical approach is based on first identifying F_0-related cyclicity present in a waveform (a process referred to as "pitch extraction;" although see Klingholz, 1987). The amount of energy attributable to this periodic component is then used as the basis for inferring how much noise is present, essentially by subtracting periodic energy from total energy. The Praat acoustic analysis system (Boersma and Weeninck 1996, available as freeware from www.praat.org), includes a particularly robust version of this kind of algorithm, which we will refer to as Praat-HNR (Boersma, 1993).

HNR measurement has not been used much in the study of nonhuman vocalizations, although a number of researchers have suggested doing so (e.g., Owren and Linker, 1995; Schrader and Hammerschmidt, 1997; Riede *et al.*, 2001; Darden *et al.*, 2002). One practical impediment has been that pitch-extraction algorithms do not necessarily work well for nonhuman vocalizations, especially when there is only a weak periodic component. Riede *et al.* (2001) therefore developed an alternative that we will refer to as Spectral-HNR. This is a simpler method that operates solely in the frequency domain and is therefore not dependent on pitch extraction. Instead, the approach is to compute a Fourier spectrum of the sound segment of interest, smooth away the harmonic peaks in the spectrum, and estimate HNR as the difference between harmonic peaks in the original spectrum and the average amplitude of the smoothed spectrum. As a result, there are parameter settings for the spectrum computation and the amount of smoothing. The particular settings chosen can have a significant impact on the final outcomes (e.g., Beecher, 1988).

Measuring vocal perturbation, a second technique for quantifying noisiness, has also been more widely used in speech science than in bioacoustics (although see Owren and Linker, 1995). In speech, much of the interest has derived from the fact that irregularity in otherwise synchronized vocal-fold vibration can be a clinical marker of dysfunction (e.g., Kent and Ball, 1999). As a result, measuring irregularity can be an important diagnostic tool in identifying and treating vocal-fold pathologies affecting speech production. "Jitter" is the most widely used perturbation measure, and is defined as cycle-to-cycle F_0 variability. The irregularity in question is variability in the period (or frequency) of successive opening and closings of the vocal folds (referred to as glottal pulses). "Shimmer" is similar, referring to cycle-to-cycle variability in the peak waveform amplitude. This measure is also well known and routinely implemented in quantifying perturbation (e.g., Jiang *et al.*, 2000; Dejonckere *et al.*, 2001).

Nonlinearity has not routinely been measured in either human or nonhuman vocal work, although it is becoming increasingly clear that vocal-fold vibration is best modeled as a nonlinear dynamic process (Sciamarella and

d'Alessandro, 2004). Tokuda, *et al.* (2002) have therefore recently developed a technique referred to as the "nonlinear measure" (NLM), which is designed to provide an overall estimate of the strength of nonlinearity in a signal. It does so by comparing the residual errors produced when modeling the signal waveform using deterministic nonlinear versus stochastic linear methods. The rationale is that if signal noise reflects low-dimensional chaos as produced through nonlinear processes, deterministic-nonlinear modeling will produce a relatively small error component. A stochastic linear model, on the other hand, will produce a relatively large error component when applied to such signals. The converse is expected if the noisiness primarily reflects a stochastic process. While thus technically not a measure of noisiness *per se*, we included NLM because high-energy noise in mammalian vocalizations is likely to reflect chaotic vocal-fold vibration. Using the NLM does not require the presence of periodicity, but it can nonetheless be applied to such sounds. As a result, it potentially has a broad applicability to nonhuman vocalizations.

In testing these measures, we first focused on coyote barks as an arguably representative example of a noisy, natural vocalization produced by a wild mammal (illustrated in Fig. 1). We then secondarily selected dachshund dog barks as sounds that are similar to the coyote vocalizations and are familiar to human listeners. The latter consideration was potentially important to comparing acoustic measurement outcomes to human perceptual ratings of noisiness. Investigations of human responses to domestic animal vocalizations has suggested that listeners reliably perceive relatively small differences in vocal noisiness (Feddersen-Petersen, 2000; Nicastro and Owren, 2003; Yin, 2002; Yin and McCowan, 2004).

II. METHODS

A. Study animals

The vocalization sample included barks from five coyotes (*Canis latrans*) and five dachshunds (*Canis familiaris*), with each species represented by three males and two females. Coyotes were recorded at the United States Department of Agriculture's National Wildlife Research Center (NWRC) field station in Logan, Utah, between July 8 and July 27, 1998. These animals were housed in outdoor 0.1-ha pens, and were between 2 and 5 years old. Their weights ranged from 8.4 to 15.0 kg. A Tascam DA-P1 digital tape recorder (DAT) was used with a Sennheiser MKH-70 shotgun microphone at a recording height of 1.0 m. The recording distance varied between 5 and 20 m. The dachshunds were dogs that had been brought to the Small Animal Veterinary Clinic of the Free University of Berlin, Germany for routine examination and were subsequently recorded at their owners' homes. All had been found to be free of disease and any clinical peculiarities, and ranged in age from 9 months to 11 years and in weight from 6.8 to 10.0 kg. These recordings were made with a Marantz PMD 222 tape recorder and a Sennheiser microphone (ME80 head with K3U power module) on BASF ChromeSuper II tapes. The distance between dog and microphone varied between 0.5 and 1.5 m.

B. Acoustic analysis

We analyzed ten barks from each of the ten animals. Coyote barks were selected as those having the least extraneous background noise among all the recordings available for a particular individual. For the dachshunds, we used the first ten barks recorded in that individual's session, while avoiding those contaminated by extraneous sounds or distorted through clipping during audio recording. Coyote vocalizations were originally recorded digitally at 48.0 kHz and downsampled to 25.0 kHz, while dog barks were recorded on analog tape and then digitized at 44.1 kHz. All recordings were downsampled to 22.05 kHz for use in the present investigation.

All barks were analyzed using two HNR methods (Spectral-HNR and Praat-HNR), the percentage of voiced frames identified through pitch extraction (%VF), Koike's (1973) "relative average perturbation" method of computing jitter (Jitter), shimmer computed from adjacent cycles (Shimmer), and the NLM measure. Measures were computed using Praat software (www.praat.org), with the exception of Spectral-HNR and NLM. Spectral-HNR was computed as described by Riede *et al.* (2001), using a routine written and implemented in Signal 4.0 (Engineering Design, www.engdes.com). Briefly, we computed an FFT transform from the middle of each bark and estimated noise level by passing a moving-average filter across the spectrum. The Spectral-HNR value was then set as the maximum amplitude difference between the original spectrum and the moving average spectrum, in dB. The computation involved 3 adjustable parameters: duration of the vocalization segment (segment duration, extracted from the middle of the vocalization), width of the Fourier window (FFT size), and number of points in the moving average (smoothing factor). We evaluated 27 parameter combinations by systematically varying segment duration (25 ms, 50 ms, or 75 ms), FFT size (256, 512, or 1024 points), and smoothing factor (5, 10, or 15 points). However, because a 1024-point FFT is longer than 25 ms for 22.05 kHz sounds, the 3 smoothing widths were not evaluated for the 25 ms segment and 1024-point FFT. NLM was computed using the method described by Tokuda *et al.* (2002), using a custom-written program, which is available at http://itb.biologie.hu-berlin.de/~tokuda/NLM/, implemented on a Linux workstation (Red Hat Linux 7.3, Kernel 2.4.18-3 on an i686, gcc version 2.96).

C. Perceptual rating

Perceptual testing was conducted in a room with five booths equipped with Beyerdynamic DT 831 headphones and Tucker-Davis Technologies (TDT) response boxes. The booths were operated from an adjacent room using TDT modules, a computer, and custom software (B. Tice & T. Carrell, http://hush.unl.edu/LabResources.html). Stimuli were prepared with Praat.

Participants were 21 female and 21 male Cornell University undergraduates, who rated either all the coyote or all

TABLE I. Variables and perceptual ratings for coyotes and dogs (mean of 10 barks per individual ± SD). ANOVA comparisons were made within species based on 10 bark vocalizations from each of 5 individuals, with two-sample *t* tests used for between-species comparisons based on mean values computed separately by an individual. Outcomes for two settings of the Spectral-HNR (segment duration—FFT size—smoothing factor) are given. Significant values are marked with an asterisk ($p < 0.01$).

	Sex/age	Mean perceptual rating	Spectral-HNR 75-256-10	Spectral-HNR 75-512-10	Praat-HNR	%VF	Jitter	Shimmer	NLM
Coyote 1	M/adult	2.53±0.33	8.7±2.1	9.4±1.5	17±10.7	29±21	0.07±0.2	0.32±0.08	0.11±0.07
Coyote 2	M/adult	3.47±0.33	16.6±3.3	13.7±2.9	26±6.9	75±16	0.1±0.2	0.19±0.1	0.11±0.08
Coyote 3	M/adult	4.07±0.33	15.1±3.4	13.5±2.9	23±6.9	73±17	0.03±0.1	0.15±0.09	0.28±0.26
Coyote 4	F/adult	4.33±0.33	18.5±5.2	17.1±4.9	21±6.7	82±16	0.04±0.003	0.13±0.08	0.33±0.2
Coyote 5	F/adult	4.21±0.33	19.9±2.1	15.5±3.5	24±7.5	85±12	0.07±0.1	0.15±0.05	0.27±0.11
All coyotes		3.6±0.9	15.7±5.1	13.8±4.1	7.0±3.9	69.1±25	0.05±0.1	0.18±0.1	0.22±0.18
F values		12.5*	16.3*	7.4*	20.9*	18.5*	0.6	7.1*	3.7
Dog 1	M/9 mo	3.31±0.4	12.4±2.4	10.1±1.0	26±9.9	53±19	0.1±0.2	0.29±0.06	0.06±0.04
Dog 2	M/11 yr	3.6±0.4	15.3±1.3	13.6±2.6	26±6.6	63±16	0.06±0.1	0.17±0.07	0.05±0.02
Dog 3	M/3 yr	3.86±0.4	17.0±3.8	20.0±4.3	27±6.9	88±10	0.15±0.1	0.2±0.07	0.29±0.38
Dog 4	F/5 yr	3.97±0.4	15.8±2.8	16.6±4.7	27±6.9	84±11	0.008±0.003	0.21±0.06	0.19±0.17
Dog 5	F/9 yr	3.08±0.4	16.9±3.5	15.4±4.4	22±9.8	95±10	0.001±0.0004	0.22±0.04	0.05±0.05
All dogs		3.7±0.5	15.4±3.3	15.1±4.8	5.8±1.9	77±21	0.07±0.1	0.22±0.07	0.13±0.2
F values		5.3*	4.1*	9.9*	4.8*	16.4*	2.6	4.2*	3.2
Btwn spp *t* values		0.43	0.13	−0.62	−1.9	−0.59	−0.06	−0.75	1.4

the dog barks. The coyote barks were rated by 12 female and 9 male students, while the dachshund barks were rated by 9 female and 12 male students. Participants provided informed consent, were rewarded with course credit, and reported themselves to be free of speech or hearing impairments. Their instructions included the information that the stimuli being presented had been recorded from either coyotes or dogs, and that they should rate the relative noisiness versus tonality of each sound using a seven-point scale. That scale was defined through labels on the response box. Buttons were arrayed in a line on the box, with the first, third, fifth, and seventh buttons labeled "very noisy," "noisy," "tonal," or "very tonal," respectively. We counterbalanced for label position by reversing the order of this scale on alternate days, and later rescored the scaled responses using 1 for most noisy and 7 for most tonal.

III. RESULTS

A. Acoustic measures

Species- and individual-level comparisons. None of the acoustic measures revealed significant differences between species (Table I). In contrast, only Jitter and NLM failed to reveal significant differences among individuals within species.

1. Spectral-HNR

For simplicity, Tables I, III, and IV present only two representative outcomes for Spectral-HNR, drawn from the 27 total combinations of parameter settings that were tested. Parameter settings did in fact have a major impact on mean measurement values, as illustrated both in Table II and Fig. 2. The smoothing factor had the largest effect. With a smoothing factor of 5, for example, the overall means were 9.3 and 10.3 dB for coyotes and dogs, respectively. In contrast, a smoothing factor of 15 points produced means of 21.3 and 21.1 dB (differences of 12.0 and 10.8 dB). The segment duration had a smaller effect, the 75 ms segment produced overall Spectral-HNR means of 13.9 and 15.1 dB for coyotes and dogs, while 25 ms duration yielded corresponding means of 18.3 and 18.7 dB (differences of only 4.4 and 3.6 dB). Finally, the FFT size showed the least influence; a setting of 1024 points produced mean Spectral-HNR values

TABLE II. Mean Spectral-HNR values for coyotes and dogs. ANOVA results are shown for comparisons among individuals within species and between species (for each of 9 parameter combinations). In each case, the target setting is paired with medium values for the two other parameters (i.e., segment duration=50 ms, FFT size=512, Smoothing Factor=10). Significant *F* values are marked with an asterisk ($p < 0.05$).

		Spectral-HNR coyotes	*F* values among coyotes	Spectral-HNR dogs	*F* values among dogs	*F* values between spp
Segment duration	25	18.3±5.3	4.6*	18.7±5.3	6.0*	0.1
	50	16.3±6.4	8.3*	16.8±5.1	9.1*	0.2
	75	13.9±4.1	7.4*	15.1±4.8	9.8*	1.7
FET size	256	17.3±5.0	12.2*	16.2±3.3	4.8*	1.7
	512	16.2±5.3	8.3*	16.7±5.1	9.1*	0.2
	1024	15.7±3.4	3.3*	16.8±2.8	5.1*	3.2
Smoothing factor	5	9.3±2.1	5.1*	10.3±1.6	3.3*	8.3*
	10	16.3±5.3	8.3*	16.8±5.1	9.2*	0.2
	15	21.3±5.7	12.5*	21.1±5.6	12.4*	0.7

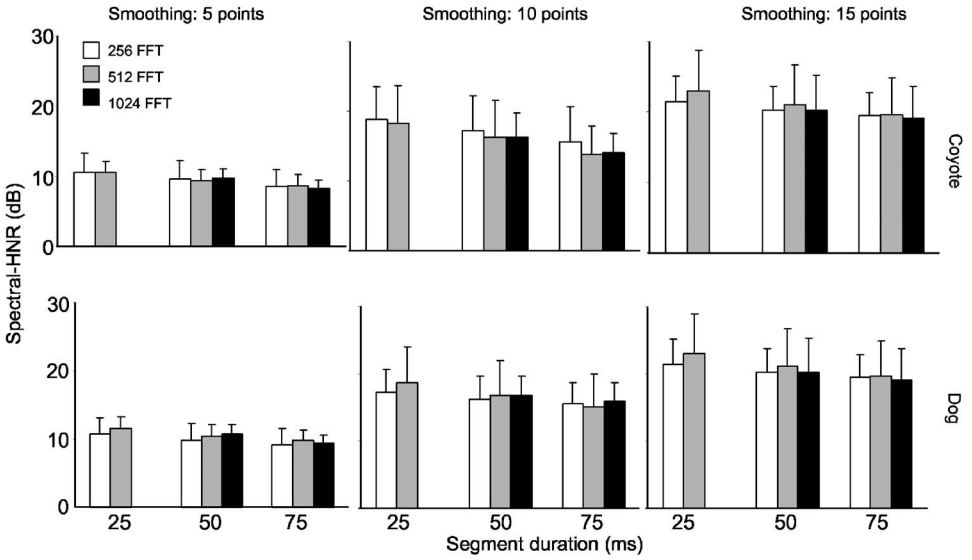

FIG. 2. Means and standard deviations of the Spectral-HNR measurements for different settings of segment duration, FFT size, and smoothing factor.

of 15.7 dB and 16.8 dB for coyotes and dogs, respectively. At 256 points, those values became 17.3 and 16.2 dB (differences of 1.6 and 0.6 dB).

Despite the effects of parameter settings on the absolute value of the Spectral-HNR measurements, ANOVA comparisons confirmed that differences among individuals in both species were significant across a subset of nine combinations of Spectral-HNR settings (Table II). In contrast, differences between species were significant for only one of the nine combinations. Spectral-HNR values obtained using different parameter settings were routinely significantly correlated (Spearman r values, $p<0.01$), although four combinations of parameter settings often failed to correlate with other settings.

In both species, these included combinations of 50-1024-5 (Segment duration-FFT size-smoothing factor) and 75-1024-5. In addition, combination 75-1024-10 produced nonsignificant correlations among coyote barks, while 75-512-5 yielded nonsignificant correlations among dog barks. For comparison to other measures, we chose to specifically focus on Spectral-HNR values obtained from two parameter combinations: 75-256-10 and 75-512-10.

2. Praat-HNR

Praat-HNR also requires parameter selection related to pitch extraction, specifically setting an analysis window length and an expected range of F_0 values. These settings are chosen based on the particular kind of signal being analyzed, and it is straightforward to make the necessary adjustments. It is therefore less interesting to examine Praat-HNR across a range of its potential settings. We set the values at levels that produced the most reliable pitch extraction, with resulting HNR means and standard deviations shown in Table I. The values were significantly correlated with outcomes derived using Spectral-HNR (Table III).

3. %VF, jitter, shimmer, and NLM

Mean and standard deviations for percent-voiced frames, vocal perturbation, and nonlinearity are also summarized in Table I. Of these four measures, jitter clearly stood out as being uncorrelated with other acoustic measures (Table III). In contrast, although %VF results varied dramatically among the barks of individual vocalizers, its overall values were significantly correlated with those of other measures. Vocal perturbation measured as shimmer was less variable, and was also strongly correlated with other outcomes. Finally, NLM showed intermediate variability and strong correlations.

B. Perceptual ratings of noisiness

1. Species- and individual-level comparisons

The overall noisiness of barks was rated as 3.6±0.7 by the 42 participants tested. This outcome was modestly, but

TABLE III. Matrix of Pearson correlations among acoustic outcomes. Values for coyote barks ($n=50$) are on the left, while values for dog barks ($n=50$) are on the right. Significant correlations ($p<0.05$) are marked with an asterisk.

	Spectral-HNR (75-256-10)	Spectral-HNR (75-512-10)	Praat-HNR	%VF	Jitter	Shimmer
Spectral-HNR (75-512-10)	0.79*/0.74*					
Praat-HNR	0.85*/0.49*	0.71*/0.70*				
%VF	0.65*/0.41*	0.42*/0.50*	0.80*/0.43*			
Jitter	−0.12/0.03	0.06/−0.13	−0.14/0.02	−0.18/−0.13		
Shimmer	−0.64*/−0.43*	−0.65*/−0.60*	−0.69*/−0.55*	−0.48*/−0.07	0.05/0.14	
NLM	0.35*/0.44*	0.47*/0.60*	0.52*/0.54*	0.32*/0.22	−0.19/−0.08	−0.54*/−0.33*

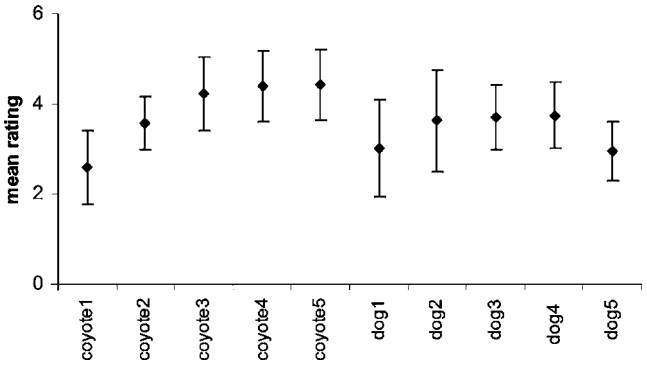

FIG. 3. Mean perceptual ratings (and standard deviations) for ten barks from each of five dogs and five coyotes. Two groups of 21 listeners rated the barks from each species using a 7-point scale that ranged from "very noisy" to "very tonal."

significantly, different from neutral, which in this scoring system would have been 4.0 ($t=-4.7, p<0.05$). Mean ratings of coyote and dog barks were 3.6±0.9 and 3.7±0.5, respectively, which was not different across species (see Table I and Fig. 3). However, ratings did differ significantly among individuals within each species, as was the case for most of the acoustic measures (Table I and Fig. 4). While the coyote sample yielded a broader range of mean ratings, mean coefficients of variation within individuals were higher in dogs (9.46% and 11.37% in coyotes and dogs, respectively).

2. HNR measures

Mean perceptual ratings were significantly correlated with Spectral-HNR (Table IV). For coyotes, the highest correlation ($r_c=0.69$) occurred using the smallest FFT size, the longest segment duration, and the intermediate smoothing factor (Fig. 4). For dogs, the highest correlation ($r_d=0.63$) occurred with intermediate FFT size, the longest segment duration, and intermediate smoothing factor (Fig. 4). However, as shown in the figure, the strength of the correlation was quite variable. Praat-HNR was also significantly correlated with perceptual ratings in both species, at levels approaching the best outcomes for Spectral-HNR ($r_c=0.63$, $r_d=0.52$).

3. %VF, jitter, shimmer, and NLM

Outcomes for the other noisiness measures generally paralleled those reported above. Shimmer and NLM showed significant correlations with human perceptual responses, and %VF did so for coyote barks, but not for dogs (Table IV). Jitter was the exception, failing to show a correlation for either species.

IV. DISCUSSION

A. Acoustic measures

1. Spectral-HNR

Spectral-HNR measures the difference between the amplitude of the harmonic peaks and the noise floor in the spectrum. We found that it performed best using a relatively long segment duration (75 ms), an intermediate smoothing factor (10 points), and a medium-to-short FFT size (coyotes: 256 points; dogs: 512 points). This outcome is reasonable based on understanding barks as a combination of harmonics and noise, where the harmonic frequencies in particular are likely to be nonstationary (meaning that they change through the course of the call). As a result, using longer segment durations for these sounds tends to produce a spectrum whose

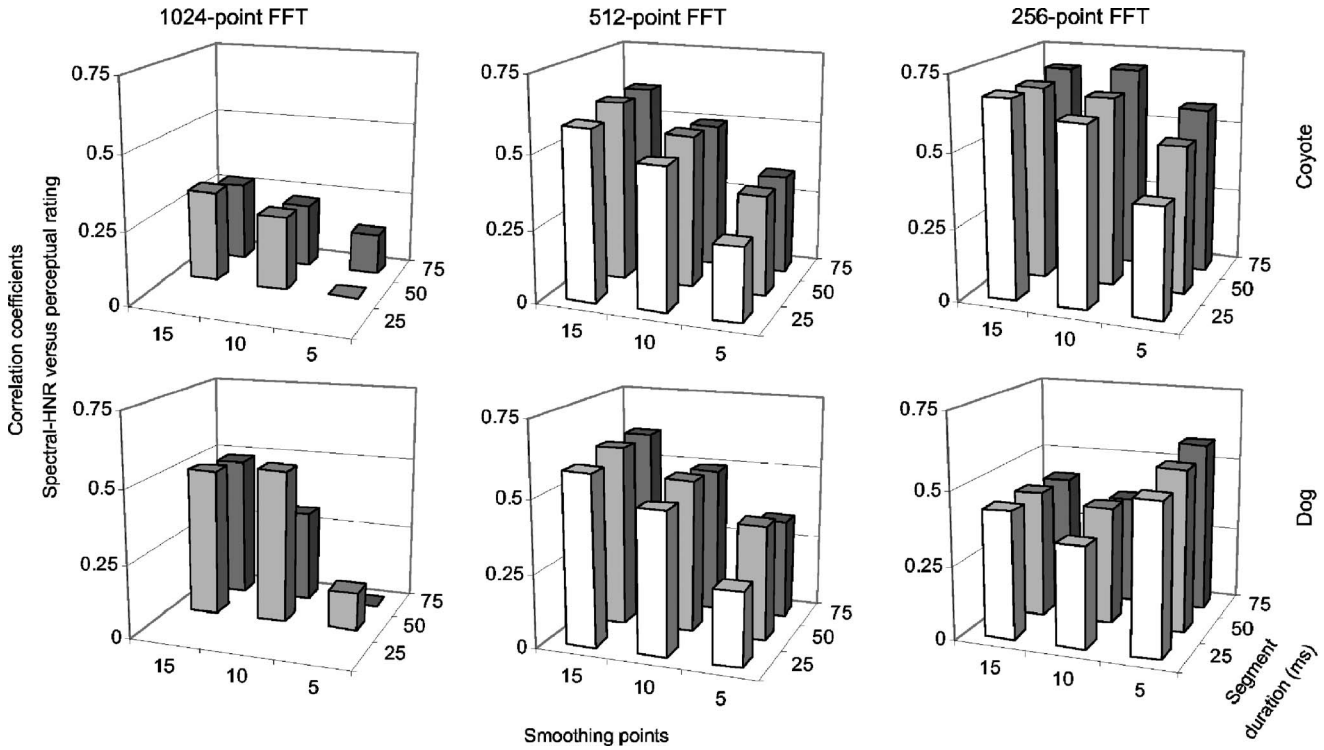

FIG. 4. Correlations between Spectral-HNR and human perceptual ratings, broken down by species and parameter settings.

TABLE IV. Regression analyses of perceptual ratings (dependent variable) against the various acoustic measures (independent variables). Significant outcomes are marked with an asterisk ($p<0.01$).

Independent variable	r^2		Slope		F value	
	Coyotes	Dogs	Coyotes	Dogs	Coyotes	Dogs
Spectral-HNR (75-256-10)	0.47	0.14	0.12	0.06	42.8*	7.9*
Spectral-HNR (75-512-10)	0.25	0.39	0.11	0.06	16.2*	31.4*
Praat-HNR	0.63	0.52	0.18	0.18	82.8*	53.5*
%VF	0.44	0.006	0.02	0.002	37.8*	0.27
Jitter	0.03	0.02	−1.13	−0.45	1.6	1.0
Shimmer	0.39	0.34	−5.39	−3.93	29.8*	25.6*
NLM	0.41	0.37	3.17	1.46	33.8*	28.4*

harmonic frequencies have been smeared through averaging. The net effect is to broaden the bandwidth of each harmonic, thereby also lowering peak amplitudes. Using longer segment durations thus tended to lower Spectral-HNR values, as illustrated in Table II. In contrast, the smoothing factor had its largest effect on the estimated noise level. In this case, higher values produced smoother and hence lower-amplitude spectra, which increased the differentiation from harmonic peaks. Data in Table II show that higher smoothing factors did, in fact, produce higher Spectral-HNR values.

We suggest that when using Spectral-HNR, the best approach is to choose intermediate values for segment duration and the smoothing factor, and to mainly focus on the FFT size. This parameter has the most complex effects, with optimal FFT size being heavily dependent on signal characteristics. For example, because lower F_0 values are associated with more closely spaced harmonics, FFTs should probably be longer in order to achieve higher-frequency resolution (Beecher, 1988). On the other hand, if the harmonics are nonstationary, the positive effects of increasing frequency resolution can be offset by inaccuracy due to averaging effects. The upshot is therefore that some preliminary work be done in order to optimize analysis parameters. We suggest selecting fixed values for both the segment duration and the smoothing factor, but conducting the analyses with two or more different values for FFT size. Resulting outcomes may be somewhat different, and potentially more revealing at one setting than another.

2. Comparing the HNR measures

The HNR measure implemented in Praat works by extracting pitch periods from short segments of the waveform through cross-correlation, then using the peak amplitude of the resulting cross-correlation function to estimate harmonicity (Boersma, 1993). When pitch extraction is reliable, Praat-HNR appears to provide a robust and straightforward measure of noisiness. Our evidence suggests that it performed well even when applied to these noisy and variable barks, producing values that correlated strongly with human noisiness ratings. These outcomes were better than those associated with many of the results for Spectral-HNR, but were not quite equal to the best performance of that algorithm. Praat-HNR is likely to perform well as a measure of noisiness for a variety of signals, but will work best for sounds with a clear harmonic structure. Spectral-HNR can be applied to any signal, regardless of the relative prominence of its harmonic peaks, but it requires more careful parameter tuning for best performance.

3. %VF, jitter, shimmer, and NLM

Quantifying the percentage of voiced frames through pitch extraction is a simple way of gauging signal noisiness, and one we found to be highly successful. This confirms findings from earlier studies on the vervet monkey (*Cercopithecus aethiops*) vocalization (Seyfarth and Cheney, 1984; Owren and Bernacki, 1988). %VF was positively correlated with perceptual rating and results from both HNR methods, and negatively correlated with shimmer. Each of these outcomes was appropriate for a measure of noisiness. In contrast, we did not find jitter to be useful. This is not necessarily surprising, as jitter is not meant to measure noisiness *per se*, but rather to characterize perturbation in largely periodic signals (Lieberman, 1963). Shimmer is also designed to quantify vocal perturbation, but may also have value as a measure of noisiness. This metric has, for instance, been applied to diagnosing pathological roughness in human voices (Baken and Orlikoff, 1999). We found shimmer to show strong negative correlations with perceptual rating values, both HNR measures, and %VF.

NLM results were positively correlated with perceptual ratings and HNR measurements, and negatively correlated with shimmer values—in other words, the opposite of what would be expected for a noisiness measure. However, such outcomes are understandable in that the NLM responds to all nonlinear phenomena, including not only the broadband noise of deterministic chaos, but also harmonic structures that reflect limit-cycle attractors (Tokuda *et al.*, 2002). In the current work, the pattern of correlations thus strongly suggests an influence of harmonic sound elements. The NLM is also not responsive to either high-dimensional or stochastic noise, with the latter here meaning any noisiness resulting from airflow turbulence. As a result, we suggest that NLM is likely to be most useful when specifically testing for the presence of low-dimensional chaos in noisy sounds, but less so when quantifying the overall degree of signal noisiness.

B. Perceptual ratings and species versus individual effects

Rating tests revealed that Spectral-HNR, Praat-HNR, %VF, shimmer, and NLM were all significantly correlated with the human perception of noisiness in coyote and dog barks, which provides general confirmation that humans are sensitive to such noise. In addition, both acoustic and perceptual findings suggest comparable noise levels in coyote and dog barks, although we may have biased the outcome by selecting a breed roughly matched to coyotes in overall size. There is nonetheless little reason to believe that size plays a critical role in vocal noise, or that dachshunds are more like coyotes in other physical features than are other dog breeds. Listeners were also found to be sensitive to differences among individual vocalizers within each species, and produced a larger range of differences for the coyotes than for the more inbred domestic dogs. We therefore suggest that these data provide preliminary evidence of general similarities among canid bark vocalizations, at least as far as noisiness is concerned.

The results are also indicative of individual variation in the noisiness of barks, with the caveat that the sample included both males and females within each species. Both objective acoustic measurement and subjective perceptual evaluation showed significant, vocalizer-specific variation in noisiness levels. As there was not a perfect correspondence in measurement outcomes and perceptual ratings when tabulated on a vocalizer-by-vocalizer basis, we cannot conclude that the particular acoustic measures tested here are optimal for capturing all perceptually salient nuances of noisiness, either in these barks or in other vocalizations. However, the overall similarity in outcomes is of interest nonetheless, particularly in light of experiments like those of Yin and McCowan (2004). They reported that human participants were able to discriminate among barks produced by dogs that were experiencing differentiated social/behavioral contexts. Our results suggest that noisiness in particular is likely to be playing a role in dog–human communication.

C. Conclusions

We believe that jitter is not suited to measuring noisiness in vocalizations, while remaining a useful measure of vocal perturbation. NLM outcomes were also of limited value, at least as far as characterizing the amount of noise is concerned. This outcome is understandable, as NLM is by design specifically responsive to all nonlinear phenomena that can occur in a vocalization, whether or not those events create perceptual noisiness. At this point, the best use of NLM appears to be in distinguishing chaos from turbulence as a contributing factor in noise generation.

Measures of HNR, %VF, and shimmer can all be valuable metrics for estimating noisiness in bark vocalizations. The two HNR approaches tested were the most successful, and have the advantage of providing a graded value for any given point in a signal. HNR can therefore be used not only for an overall characterization of the sound, but also to map noisiness throughout the course of the vocalization. %VF can also be useful, and is certainly simple in requiring only that pitch extraction can be performed. On the other hand, using successful pitch extraction as the criterion of noisiness means that each segment of the sound can only be scored in a one–zero fashion, resulting in a rating that applies only to the sound as a whole rather than any particular point within it. In contrast, both HNR measures can be used to return detailed information about any given point in a sound, and can therefore be used to map relative noisiness along its entire length. Shimmer also proved to be of value, in this case beyond its origins as a vocal perturbation measure. Like HNR, it quantifies noisiness in a continuous fashion over short segments of sound, and can be used to trace changes across a signal.

Significant correlations among these measures indicate that they were capturing overlapping attributes of the noise in the barks we tested. However, these correlations ranged from as low as 0.35 to as high as 0.85, which we take to be indicative of the additive value in accounting for noise-related variance. Our best advice at this point is therefore to make use of each technique, screening out any measurements that prove to be redundant after the fact. If one were to select only one approach, HNR appears to be the best single measure, taking into account the tradeoffs between a pitch-extraction-based and a spectrally based method. However, if pitch extraction can be performed, there appears to be little reason not to include %VF and shimmer in the characterization.

ACKNOWLEDGMENTS

BRM was supported by the United States Department of Agriculture's National Wildlife Research Center through a cooperative agreement with the University of California, Berkeley (12-03-7405-0235 CA). IT was supported by a research fellowship from the Alexander-von-Humboldt Foundation. MJO received support from NIMH award 1 R01 MH65317-01A2 Subcontract 8402-15235-X. TR thanks Hanspeter Herzel (Berlin) for support.

Baken, R. J., and Orlikoff, R. F. (**1999**). *Clinical Measurement of Speech and Voice*, 2nd ed. (Singular Publishing, San Diego).

Beecher, M. D. (**1988**). "Spectrographic analysis of animal vocalization: Implications of the uncertainty principle," Bioacoustics 1, 187–208.

Boersma, P. (**1993**). "Accurate short-term analysis of the fundamental frequency and the harmonics-to-noise ratio of a sampled sound," Proc. Inst. Phonetic Sci. of the University of Amsterdam **17**, 97–110.

Boersma, P., and Weenink, D. (**1996**). "Praat: A system for doing phonetics by computer," Technical Report 132, Institute of Phonetic Sciences of the University of Amsterdam.

Brown, C., Alipour, F., Berry, D. A., and Montequin, D. (**2003**). "Laryngeal biomechanics and vocal communication in the squirrel monkey (*Saimiri boliviensis*)," J. Acoust. Soc. Am. **113**, 2114–2126.

Darden, S. K., Pedersen, S. B., and Dabelsteen, T. (**2002**). "Methods of frequency analysis of a complex mammalian vocalization," Bioacoustics 13, 247–263.

Dejonckere, P. H., Bradley, P., Clemente, P., Cornut, G., Crevier-Buchman, L., Friedrich, G., Van De Heyning, P., Remacle, M., and Woisard, V. (**2001**). "A basic protocol for functional assessment of voice pathology, especially for investigating the efficacy of (phonosurgical) treatments and evaluating new assessment techniques: Guideline elaborated by the Committee on Phoniatrics of the European Laryngological Society (ELS)," Eur. Arch. Otorhinolaryngol. **258**, 77–82.

Feddersen-Petersen, D. (**2000**). "Vocalization of European wolves (*Canis lupus lupus L.*) and various dog breeds (*Canis lupus f. fam.*)," Arch. Anim. Breed **43**, 387–397.

Fitch, W. T., Neubauer, J., and Herzel, H. (**2002**). "Calls out of chaos: The

adaptive significance of nonlinear phenomena in mammalian vocal communication," Anim. Behav. **63**, 407–418.
Hopp, S. L., Owren, M. J., and Evans, C. (**1998**). *Animal Acoustic Research: Sound Analysis and Research Methods* (Springer-Verlag, Heidelberg).
Jiang, J., Lin, E., Wu, J., Gener, C., and Hanson, D. G. (**2000**). "Effects of simulated source of tremor on acoustic and airflow voice measures," J. Voice **14**, 47–57.
Jürgens, U. (**1994**). "The role of the periaqueductal grey in vocal behavior," Behav. Brain Res. **62**, 107–117.
Kent, R. D., and Ball, M. J. (**1999**). *Voice Quality Measurement* (Singular Publishing, San Diego).
Klingholz, F. (**1987**). "The measurement of signal-to-noise ratio (SNR) in continuous speech," Speech Commun. **6**, 15–26.
Koike, Y. (**1973**). "Application of some acoustic measures for evaluation of laryngeal dysfunction," J. Acoust. Soc. Am. **45**, 839–844.
Lieberman, P. (**1963**). "Some acoustic measures of the fundamental periodicity of normal and pathologic larynges," J. Acoust. Soc. Am. **35**, 344–353.
Nicastro, N., and Owren, M. J. (**2003**). "Classification of domestic cat (*Felis catus*) vocalizations by naive and experienced human listeners," J. Comp. Psychol. **117**, 44–52.
Owren, M. J., and Bernacki, R. H. (**1988**). "The acoustic features of vervet monkey alarm calls," J. Acoust. Soc. Am. **83**, 1927–1935.
Owren, M. J., and Linker, C. (**1995**). "Some analysis methods that may be useful to acoustic primatologists," in *Current Topics in Primate Vocal Communication*, edited by E. Zimmermann, J. D. Newman, and U. Jürgens (Plenum Press, New York), pp. 1–27.
Riede, T., Arcadi, A. C., and Owren, M. J. (**2004**). "Nonlinear acoustics in the pant hoot vocalizations of common chimpanzees (*Pan troglodytes*): Frequency jumps, subharmonics, biphonation, and deterministic chaos," Am. J. Primatol **64**, 277–291.
Riede, T., Herzel, H., Hammerschmidt, K., Brunnberg, L., and Tembrock, G. (**2001**). "The harmonic-to-noise-ratio applied to dog barks," J. Acoust. Soc. Am. **110**, 2191–2197.
Riede, T., Herzel, H., Mehwald, D., Seidner, W., Trumler, E., Böhme, G., and Tembrock, G. (**2000**). "Nonlinear phenomena in the natural howling of a dog-wolf mix," J. Acoust. Soc. Am. **108**, 1435–1442.
Schneider, G. T. (2004). "Magnitude estimation of chaotic and white noises: Listener evaluations of loudness and annoyingness," unpublished Baccalaureate thesis, Cornell University.
Schrader, L., and Hammerschmidt, and K. (**1997**). "Computer-aided analysis of acoustic parameters in animal vocalizations: a multiparametric approach," Bioacoustics 7, 247–265.
Sciamarella, D., and d'Alessandro, C. (**2004**). "On the acoustic sensitivity of a symmetrical two-mass model of the vocal folds to the variation of control parameters," Acta. Acust. Acust. **90**, 746–761.
Seyfarth, R. M., and Cheney, D. L. (**1984**). "The acoustic features of vervet monkey grunts," J. Acoust. Soc. Am. **75**, 1623–1628.
Solomon, N. P., Luschei, E., and Kang, L. (**1994**). "Fundamental frequency and tracheal pressure during three types of vocalizations elicited from anaesthetized dogs," J. Voice **9**, 403–412.
Strogatz, S. H. (**2001**). *Nonlinear Dynamics and Chaos* (Perseus Books, Reading, MA).
Tokuda, I., Riede, T., Neubauer, J., Owren, M. J., and Herzel, H. (**2002**). "Nonlinear analysis of irregular animal vocalizations," J. Acoust. Soc. Am. **111**, 2908–2919.
West, R., and Larson, C. R. (**1999**). "Laryngeal and respiratory activity during vocalization in macaque monkeys," J. Voice **7**, 54–68.
Wilden, I., Herzel, H., Peters, G., and Tembrock, G. (**1998**). "Subharmonics, biphonation, and deterministic chaos in mammal vocalization," Bioacoustics 9, 171–196.
Yin, S. (**2002**). "A new perspective on barking in dogs (*Canis familiaris*)," J. Comp. Psychol. **116**, 189–193.
Yin, S., and McCowan, B. (**2004**). "Barking in domestic dogs: Context specificity and individual identification," Anim. Behav. **68**, 343–355.

Click rates and silences of sperm whales at Kaikoura, New Zealand

Lesley A. Douglas and Stephen M. Dawson[a)]
Department of Marine Science, University of Otago, P.O. Box 56, Dunedin, New Zealand

Nathalie Jaquet
Texas A&M University, 5007 Avenue U, Galveston, Texas 77551

(Received 4 September 2004; revised 18 April 2005; accepted 27 April 2005)

Analysis of the usual click rates of sperm whales (*Physeter macrocephalus*) at Kaikoura, New Zealand, confirms the potential for assessing abundance via "click counting." Usual click rates over three dive cycles each of three photographically identified whales showed that 5 min averages of usual click rate did not differ significantly within dives, among dives of the same whale or among whales. Over the nine dives ($n=13\,728$ clicks) mean usual click rate was 1.272 clicks s^{-1} (95% CI=0.151). On average, individual sperm whales at Kaikoura spent 60% of their time usual clicking in winter and in summer. There was no evidence that whale identity or stage of the dive recorded affects significantly the percentage of time spent usual clicking. Differences in vocal behavior among sperm whale populations worldwide indicate that estimates of abundance that are based on click rates need to based on data from the population of interest, rather than from another population or some global average. © *2005 Acoustical Society of America.* [DOI: 10.1121/1.1937283]

PACS number(s): 43.80.Ka [WA] Pages: 523–529

I. INTRODUCTION

Assessing abundance of the deep diving cetaceans via sighting surveys is problematic because of the small proportion of time they spend at the water surface (Barlow, 1999). In some populations, sperm whales spend about 80% of their time underwater (Papastavrou *et al.*, 1989; Jaquet *et al.*, 2001; Amano and Yoshioka, 2003), during which they click almost continuously. The most common click type—the "usual click"—is a loud (up to 236 dB *re* 1 μPa), directional vocalization that when recorded on-axis is practically monopulsed and lasts 100 μs (Møhl *et al.*, 2003). Usual clicks are generally produced at a slow and metronomic rate of 1–2 per s, though click rate can change markedly (e.g., Goold and Jones, 1995). These features have prompted several authors to explore ways of using sperm whale vocalizations to assess whale density (e.g., Watkins and Moore, 1982; Whitehead and Weilgart, 1990; Barlow and Taylor, in press).

Information on sperm whale density can be gained from analyses of bearings to vocalizing whales gained via directional hydrophones (e.g., Leaper *et al.*, 1992) or hydrophone arrays (e.g., Barlow and Taylor, in press). Alternatively, if whales click at a characteristic rate, whale density could be estimated from counts of the number of clicks received in a given period by an omnidirectional hydrophone (Whitehead and Gordon, 1986). These approaches are not mutually exclusive; for example, information on click rate could be a useful adjunct in a study using a towed array, perhaps to aid in estimation of group size or to aid interpretation of acoustic detections made at night. In order to provide absolute rather than relative abundance estimates, all the above-mentioned approaches require an estimate of the proportion of time whales are *silent*. (Click counting methods use only usual clicks, so in this context *silence* means any vocal behavior other than usual clicking. At Kaikoura this includes creaking, slow clicking, and actual silence.)

The vocal behavior of sperm whales at Kaikoura. The typical foraging dive cycle of a subadult male sperm whale at Kaikoura can be divided into four phases based on the whales' vocal activity. These phases are:

1. Directly after fluke-up, until the first usual click.
2. During the dive itself, from the first usual click until the last usual click.
3. Near the end of the dive, from the last usual click until surfacing.
4. While at the surface before diving again.

Jaquet *et al.* (2001) showed that sperm whales at Kaikoura are silent during phases 1 and 3, and that these silences last on average 25 s and 3.6 min, respectively. While at the water surface, sperm whales are almost always silent (Jaquet *et al.*, 2001). During phase 2—which we assume is the foraging part of the dive—sperm whales produce usual clicks almost continuously (Jaquet *et al.*, 2001).

Published studies of the mean click rate of sperm whales have generally analyzed one dive each of several individuals (e.g., Mullins *et al.*, 1988; Goold and Jones, 1995), or have been calculated from many short recordings (Whitehead and Weilgart, 1990). These studies lack replication at the level of an individual's dives. Our intention here is to present data quantifying variation in usual click rates within dives, among dives of the same individual, and among individuals. Usual click rates are computed from three complete (or near complete) dive cycles from each of three photographically iden-

[a)]Electronic mail: steve.dawson@stonebow.otago.ac.nz

tified individuals. The proportion of time *silent* is calculated from eight of the nine dive cycles analyzed for usual click rate and from 30 randomly selected sections of dives of photographically identified individuals. Proportion of time silent is thus calculated from recordings taken from 16 different individuals.

II. METHODS

A. Study site and equipment

Data were collected within a 20×10 nautical mile study area south of the Kaikoura Peninsula (42°25′S 173°42′E) on the east coast of the South Island of New Zealand, from a 6.6 m rigid-hulled inflatable boat. Each year from 1990 to 1998 we visited Kaikoura for 3–9 weeks in summer and in winter. Sperm whales were located and tracked using a hand-held, custom-built, directional hydrophone. When a whale was sighted, surface time and sighting data were recorded using a GPS-linked palm-top computer. On fluke-up, the dive time was recorded and a photograph of the flukes taken for identification purposes (Arnbom, 1987). For more detail on general methods, and map of study location see Childerhouse *et al.* (1996).

If the whale was alone (no other whales heard vocalizing in the vicinity), we attempted to make an acoustic recording of the entire dive, from fluke-up to surfacing. Such recordings were terminated if: (1) signal-to-noise ratio declined so that the target whale could not be heard clearly; (2) vocalizations of other whales made it difficult for us to tell which clicks were from the target whale; or (3) noise from whale-watching or fishing vessels obscured clicks from the target whale. To ensure that we did not "switch" whales during the dive cycle, we tracked the whale with the directional hydrophone during the recording, and analyzed only those recordings for which we had high-quality photo-ID pictures from the start of the dive cycle, and from the next fluke-up.

Recordings were made by lowering an omnidirectional hydrophone into the water to a depth of about 20 m. Two sets of recording equipment were used. From May 1991 to January 1995 we used an analog UHER 4200 stereo tape recorder (at either 1 7/8 or 3 3/4 ips depending on the recording time needed), an amplifier with a high-pass filter at 500 Hz, and a Sippican hydrophone element. Since June 1996 recordings have been made using a Sony TCD-D10PROII Digital Audio tape-recorder (DAT), fixed gain amplifier, and Sonatech 8185 or 8178 hydrophones.

The frequency response of the Sonatech/Sony system far exceeds that of the Sippican/UHER system, but both were more than adequate for studies of click rate. The Sippican hydrophone varied by 20 dB from 200 Hz to 30 kHz. The UHER recorder had (±3 dB) responses of 25 Hz–13 kHz or 20 Hz–16 kHz at the tape speeds we used. The Sonatech hydrophones are relatively flat (±4 dB) from 100 Hz to 30 kHz, the fixed-gain amplifier had a flat response (dc–45 kHz), and the DAT recorder is flat (±1 dB) from 20 Hz to 22 kHz.

Recordings were transcribed, and then filtered using a Kemo VBF/8 48 dB/octave high- and low-pass filter set to 1 and 14.2 kHz, respectively. Recordings were sampled at 31.25 kHz, digitized (16 bit), and analyzed using a Macintosh Quadra 840AV with a Spectral Innovations analog/digital and digital signal processing board (MacDSP 256KNI).

TABLE I. Details of the nine sperm whale dive cycle recordings analyzed for usual click rate.

Whale ID	Dive cycle No.	Date	Season	Duration of recording (min:s)[a]
HR110	1	27/06/96	Winter	36:32
HR110	2	02/12/96	Summer	29:19
HR110	3	20/12/96	Summer	18:22[b]
NN80	1	14/11/96	Summer	40:52
NN80	2	12/12/96	Summer	44:09
NN80	3	16/12/96	Summer	30:39
NN160	1	11/06/97	Winter	41:20
NN160	2	11/06/97	Winter	40:50
NN160	3	14/06/97	Winter	36:01

[a]Times are taken from when each whale dived (or when recording started after the whale dived) until it resurfaced.
[b]Did not see whale surface.

B. Usual click rate

To enable sampling and analysis of long sections of sperm whale recordings for click counting, Jäke (1996) wrote MOBY CLICK v1.0ß software. MOBY CLICK calculates the root mean square of a signal and uses a set of parameter rules to detect and count pulses that rise at least six decibels above the noise. Five parameter rules are available (of which the first two are mandatory); minimum pulse width, maximum interpulse interval, minimum interclick interval, amplitude of pulse one, and number of pulses per click. The value assigned to each of these rules is user-defined and any combination of rules may be used. Recordings are scrolled through manually, and each usual click of the target sperm whale is saved while any other signal is rejected as background whale vocalization or noise. Usual clicks were sometimes aurally obvious but not loud enough to analyze using MOBY CLICK. In this case, the segment of the recording was labeled "whale too faint" and not analyzed.

Result files from MOBY CLICK contain information on interclick intervals (ICIs)—the time between successive usual clicks. Usual click rate was calculated by taking the reciprocal of each ICI. Three dive cycle recordings from each of three photographically identified whales were chosen for click rate analysis (Table I). The effect of dive section, whale identity, and season on these data was investigated via ANOVA.

C. Proportion of time spent *silent*

Due to the difficulty of gaining full dive cycle recordings of consistently high quality and with only one whale present, the number available for analysis is limited. By dividing dives into three sections (first 25%, middle 50%, and last 25%—based on time from fluke-up to surfacing) many more recordings are available to assess the proportion of time spent *silent*. We randomly chose ten high-quality re-

cordings for each of these three dive sections, and measured the time the target whale spent creaking, slow clicking, and/or truly silent in each. In a few cases the recording was incomplete. To avoid bias due to this, total time silent in each record was extrapolated from the proportion of silence in the recorded period, and a weighted average (and SE) computed using recording lengths as weights. Hence a complete recording would have a weight of unity and a recording that was 89% complete would have a weight of 0.89. Weighted averages of time spent silent, and standard errors were calculated as

$$\bar{x} = \frac{\sum w_i x_i}{\sum w_i}, \tag{1}$$

where $x_i = i$th value, $w_i =$ weight of ith value,

$$\mathrm{SE} = \sqrt{\frac{\sum [(x_i - \bar{x})^2 w_i]}{n(n-1)}}. \tag{2}$$

We then combined the mean silent periods in each of these dive sections (first 25%, middle 50%, last 25%) to arrive at an overall estimate of the time spent silent (and its CV, calculated as SE/mean). This, divided by mean dive time, gave a proportion of the dive for which the whales were silent. The CV of this proportion was calculated as

$$\mathrm{CV}_{(x/m)} = \sqrt{\mathrm{CV}_x^2 + \mathrm{CV}_m^2}. \tag{3}$$

Estimating the proportion of time spent silent in the eight full dive cycles discussed earlier was much simpler, involving the addition of the number of silent seconds in each dive phase, and then averaging over the eight dives. To gain an overall estimate of time spent silent, we combined the estimate from the 30 randomly chosen recordings and the eight dive cycles used in the usual click rate analysis. [Only eight dives could be analyzed because the surface time of HR110 #3 was not known (Table I), thus the length of the dive could not be calculated.] The resulting average was weighted by the dive time that each type of sample represented.

Since Jaquet *et al.* (2000) found that sperm whales at Kaikoura spent significantly longer periods diving and at the surface in summer than in winter, we calculated the average percentage of time sperm whales were *silent* during dive cycles (from fluke-up to fluke-up) separately for these seasons.

III. RESULTS

A. Usual click rate

Usual click rates were generally between 1 and 1.5 clicks s^{-1}, although this varied within and among dive cycles [Figs. 1(a)–1(c)]. To determine whether individuals have characteristic patterns of usual click rate, we computed means for 5 min sections then averaged them for the three dives for each individual. This was done for three reasons. First, to allow visualization of click rates over whole dive cycles (Fig. 2), second, to reduce statistical dependence, third, some research groups routinely make 5 min recordings (e.g., Whitehead and Weilgart, 1990), so 5 min means have some intrinsic comparative value. Subsequent interclick intervals are clearly not statistically independent. Computing 5 min means, and comparing those means reduces this problem. A mean could not be calculated for HR110 at 30–35 and 35–40 min segments as only one of the three dives was this long. No clear trends in usual click rate are evident (Fig. 2). There are no statistically significant differences within an individual over the duration of the dive, or among individuals.

Mean usual click rate was calculated for each entire dive (Table II). There was no evidence of a significant difference among the three whales (1 factor ANOVA, $p=0.28$, $df=8$). The overall mean usual click rate, calculated from the nine dive cycle means, was 1.272 clicks s^{-1} (95% CI=0.151).

B. Proportion of time spent *silent*

The percentage of time sperm whales creaked and slow-clicked during the 30 randomly selected recordings varied significantly with both dive section (i.e., first 25%, middle 50% end 25% of phase 2). (two factor ANOVA $p=0.0002$ and $\leqslant 0.0001$, $df=29$, respectively) and whale identity (two factor ANOVA $p=0.0094$ and $\leqslant 0.0001$, $df=29$, respectively). There was no evidence, however, that these two factors significantly affected the percentage of time sperm whales creaked during the eight click rate recordings (two factor ANOVA $p=0.607$ and 0.383, $df=23$, respectively). Slow clicks were present in too few of the dive cycle recordings to enable statistical analysis.

Estimates of the proportion of time whales spent silent during dives were virtually identical between the seasons and the two data sets (dive cycle recordings, summer mean =0.259, CV=0.138; winter=0.250, CV=0.141; randomly selected recordings, summer mean=0.261, CV=0.143; winter =0.251, CV=0.141). Taking surface interval into account, sperm whales were *silent* for 39% of entire dive cycles in summer (CV=3.8%) and winter (CV=5.5%; Table III).

IV. DISCUSSION

As would be expected if the primary function of sperm whale clicks is echolocation (see Jaquet *et al.*, 2001, Madsen *et al.*, 2002a, b; Møhl *et al.*, 2003, Miller *et al.*, 2004) instantaneous click rate varies considerably, from around 1 every 2 s, to over 200 per s (Gordon, 1987; Goold and Jones, 1995). Mean usual click rates, however, when averaged over 5 min sections, or over an entire dive, are surprisingly consistent. Surprising consistency in usual click rates is also evident in whales recorded elsewhere (see Fig. 1 in Teloni *et al.*, 2000; Fig. 4 in Madsen *et al.*, 2002a). Although 5 min means within a dive are not strictly independent in a statistical sense, they did not differ significantly, and were not significantly different among the different individuals for which we have data. This result suggests that it would be reasonable to apply a click-counting approach to assess abundance of sperm whales at Kaikoura, using an overall mean usual click rate of 1.272 clicks s^{-1} (±0.151 95% CI) per whale.

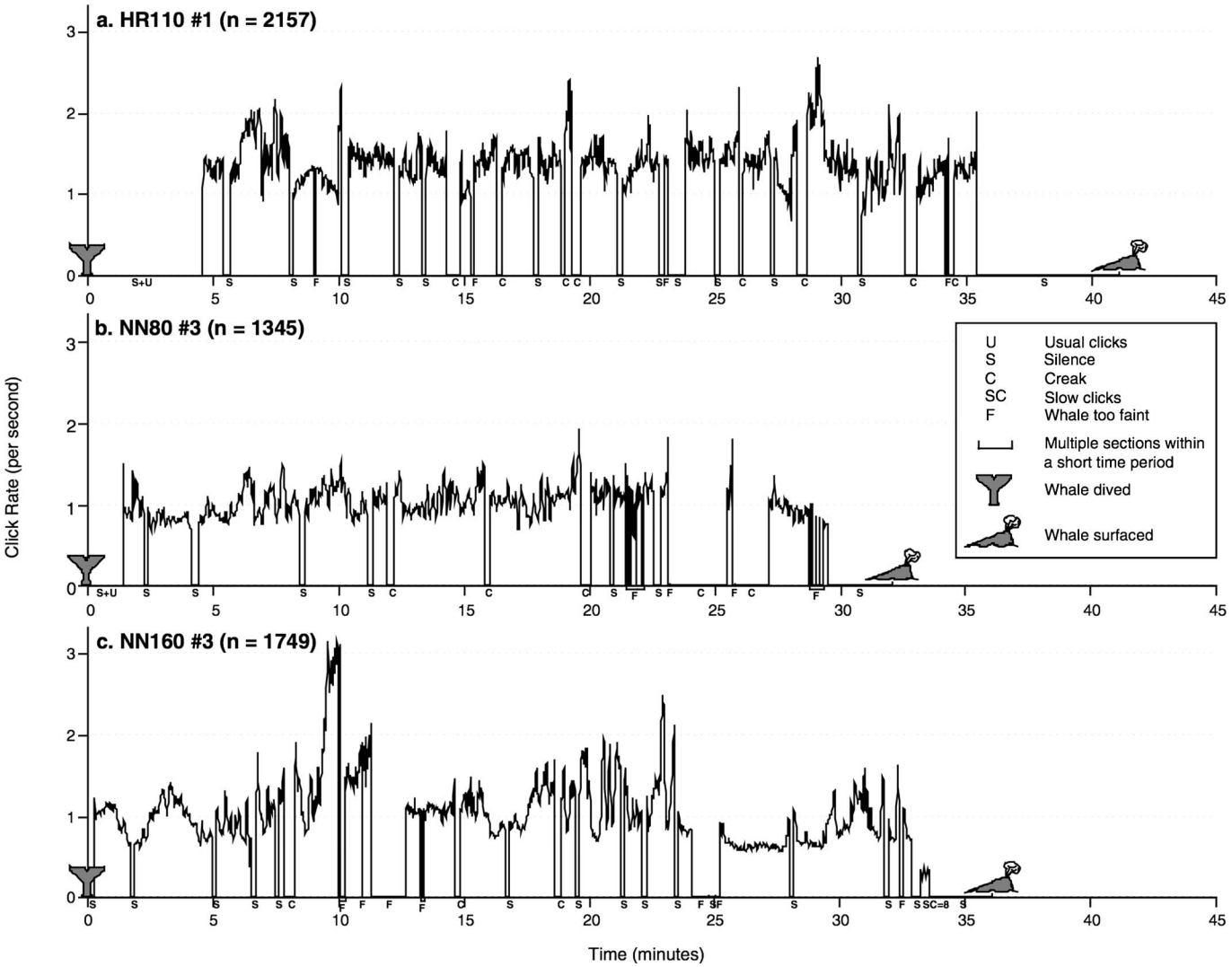

FIG. 1. Usual click rate during three of the nine dives analyzed: (a) dive 1 of HR110; (b) dive 3 of NN80; (c) dive 3 of NN160.

Mean usual click rates from different studies are different from each other and female sperm whales generally have a higher mean usual click rate than males (Table IV). Differences in mean usual click rates of whales from different regions, age groups, and of different sexes show that it would be inappropriate to apply one "standard" click rate in acoustic surveys of sperm whales. Additionally, factors such as

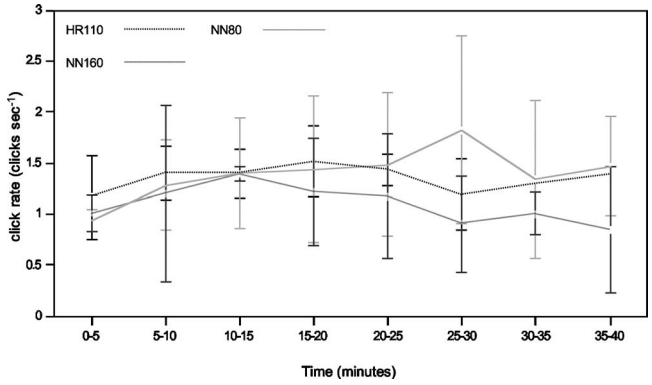

FIG. 2. Mean usual click rate (95% CI) calculated from 5 min segments of the three dives of each whale.

TABLE II. Summary statistics for mean usual click rate (s^{-1}); computed from the reciprocal of interclick intervals, over the duration of the dive for each of the nine dive cycle recordings analyzed. CV=SE/mean.

Whale ID	Mean click rate (s^{-1})	CV	Min click rate (s^{-1})	Max click rate (s^{-1})	Sample size (n)
HR110 #1	1.450	0.4%	0.672	2.681	2157
HR110 #2	1.412	0.6%	0.605	3.460	1498
HR110 #3	1.268	0.9%	0.193	2.625	992
Mean click rate for HR110=1.377 clicks s^{-1} (95% CI=0.238)[a]					
NN80 #1	1.603	0.7%	0.554	7.194	2172
NN80 #2	1.290	1.0%	0.450	2.571	757
NN80 #3	1.063	0.5%	0.588	1.931	1345
Mean click rate for NN80=1.319 clicks s^{-1} (95% CI=0.674)[a]					
NN160 #1	0.967	0.7%	0.541	2.392	1275
NN160 #2	1.172	0.9%	0.607	4.098	1790
NN160 #3	1.223	1.0%	0.368	3.155	1742
Mean click rate for NN160=1.121 clicks s^{-1} (95% CI=0.337)[a]					
Total n=13 728					

[a]Calculated from the three dive means of each individual.

TABLE III. The mean length and percentage of time sperm whales at Kaikoura were *silent* during the four phases of a dive cycle and over a complete dive cycle. CV=SE/mean. Note:(SE, *n*) or (SE). To increase sample size, data for phase 2 are augmented with data from Jaquet *et al.* (2001) which were gathered in the same area over the same period.

	Mean length of time spent *Silent* (s)		*Silence* as a percentage of entire dive cycle (fluke-up to fluke-up)	
Dive "phase"	Summer	Winter	Summer	Winter
1 (after diving—until first usual click)	17 (3.5, 5)	17 (1.4, 7)	0.53% (0.1)	0.56% (0.05)
2 (while diving)	439 (19.1, 24)	316 (20.2, 14)	13.60% (0.6)	10.35% (0.7)
3 (after last usual click—until surfacing)	237 (32.7, 12)	337 (51.8, 7)	7.35% (1.0)	11.03% (1.7)
4 (time at surface)	584 (20.7, 24)	530 (29.3, 14)	18.10% (0.9)	17.34% (1.1)
Length of dive (1 to 3)	2644 (98.8, 24)	2526 (108.1, 14)		
Length of dive Cycle (fluke-up to fluke-up)	3228 (108.7,24)	3055 (103.0, 14)		
Total % of time *silent* during a dive cycle			39.58% (CV=3.8%)	39.28% (CV=5.5%)

group size and behavioral state (Whitehead and Weilgart, 1990), and time of day (Weilgart, 1990) affect click rates in nursery groups. Mullins *et al.* (1988) and Whitehead and Weilgart (1990) have proposed that differences in prey may also affect acoustic behavior, while Madsen *et al.* (2002a) indicate that click rate increases with increasing dive depth. Hence click rate is probably influenced by ecological and oceanographic factors. We have too few data to test these ideas, but we note that sperm whales at Kaikoura occur in a relatively confined area, and, as they are almost constantly long-diving, they behave more consistently than sperm whales found elsewhere.

Sperm whales at Kaikoura start usual clicking on average 17 s after diving (Table III). This is similar to a male sperm whale recorded off Northern Norway (20 s; Wahlberg, 2002) and an unsexed 10 m adult off Papua New Guinea (15 s; Madsen *et al.*, 2002a) but much sooner than nursery groups off Sri Lanka (2–5 min; Gordon, 1987) and females

TABLE IV. Mean usual click rates from this and other studies of sperm whales.

Number/sex of whales analyzed	Sample size	Mean usual click rate s^{-1} (95%CI)	Author(s)/location
9 subadult males	13 728 clicks (9 dive cycles)	1.272 (0.029) range 0.193–7.194	This study Kaikoura, New Zealand
1 10 m individual	1804 clicks (1 dive cycle)	~1–4 (range)	Madsen *et al.* (2002a) Papua New Guinea
1 adult male	(1 dive cycle)	0.58–3.33 (range)	Wahlberg (2002) Northern Norway
5 males 4 females	4586 clicks 3954 clicks	Males 1.171 (0.009) Females 1.946 (0.015)	Goold and Jones (1995) Azores
9 females or young	1322 sessions	1.22 (0.36)	Whitehead and Weilgart (1990) Galápagos Islands
2 males presumed subadult	18 clicks 20 clicks	1.042 (0.069) 1.450 (0.083)	Mullins *et al.* (1988) Scotian Shelf, Nova Scotia
9 females or young	1397 clicks (9 sessions)	1.961 (median)	Weilgart and Whitehead (1988) Galápagos Islands
? groups of females/young	?	1–3 (range)	Watkins *et al.* (1985) SE Caribbean
?	?	2–5 (range)	Worthington and Schevill (1957) North Carolina Coast

and mature males off the Azores (2–3 min; Goold and Jones, 1995). Though the whales at Kaikoura spend significantly more time underwater in summer than winter (Jaquet *et al.*, 2000), there is no evidence that they spend proportionally more time usual clicking.

On average, sperm whales off Kaikoura stopped usual clicking 3.95 min before surfacing in summer and 5.62 min in winter. These results are similar to the mean of 5.5 min calculated for sperm whales at Kaikoura by Gordon *et al.* (1992), and to the sperm whale tagged by Madsen *et al.* (2002a), and substantially more than the 0–2 min determined for two subadult males off Nova Scotia by Mullins *et al.* (1988).

Sperm whales from different parts of the world seem to spend a similar amount of time at the surface between foraging dives (~6–11 min; Papastavrou *et al.*, 1989; Whitehead *et al.*, 1992; Watkins *et al.*, 1999; Jaquet *et al.*, 2000). Lack of vocal activity at the water surface is commonly reported (Watkins, 1980; Watkins *et al.*, 1985; Mullins *et al.*, 1988; Whitehead and Weilgart, 1990; Jaquet *et al.*, 2000).

At Kaikoura, there was no evidence that dive section or whale identity had an effect on the percentage of time sperm whales spent *silent* while in the foraging phase of a dive. This, and the fact that the mean actual silence is very short (16 s, SE=1.297, n=251; Douglas, 2000) suggests that whales are not likely to be missed during an acoustic survey because they are in a particular section of phase 2, nor are some whales more likely to be heard (and counted) than others.

Foraging sperm whales at Kaikoura produced usual clicks during 60% of entire dive cycles in summer and in winter. Mullins *et al.* (1988) produced the same estimate from two subadult males off the Scotian Shelf. Nursery groups nursery groups off the Galápagos Islands appear to be more vocal, usual clicking 70% of the time (Whitehead and Weilgart, 1990).

Though hard data are scant, it is highly likely that the percentage of time whales spend *silent* differs among populations. This is primarily due to some populations spending almost all of the time foraging (for example, at Kaikoura, Gordon *et al.*, 1992; Jaquet *et al.*, 2000), while others rest and/or socialize at the surface for extended periods (up to 25% of the day, Whitehead and Weilgart, 1990; Watkins *et al.*, 2002). Watkins (1977), and Watkins *et al.* (1985) reported that sperm whales in nursery groups were silent for extended periods during dives, and in some cases, silent for entire dives. Watkins (1980) also suggested that when out of acoustic contact with other whales, sperm whales seldom produced any audible sounds. This does not match our experience at Kaikoura, where sperm whales are almost always found alone (Gordon *et al.*, 1992; Childerhouse *et al.*, 1995; Jaquet *et al.*, 2000) and commonly vocalize throughout dive cycles in the absence of other audible whales (Jaquet *et al.*, 2001).

Of all cetaceans, sperm whales seem particularly suited to acoustic censusing (Gordon, 1996). Since populations differ in usual click rate (Table IV) and/or proportion of time *silent*, however, applicability of results from one population to another cannot be assumed.

ACKNOWLEDGMENTS

Our work on sperm whales was supported by New Zealand Lottery Board, World Wide Fund for Nature (NZ) together with Telecom NZ Ltd., and the University of Otago. Reckitt and Colman (NZ) Ltd., Hewlet Packard (NZ) Ltd., Ocean Electronics, and Hutchwilco also helped by providing equipment. L.D. was supported by a University of Otago Postgraduate Scholarship. Olaf Jäke wrote the click counting software used in this paper, and our GPS-linked sighting program. Our co-workers Dan Cairney, Carron Chessum, Simon Childerhouse, Olaf Jäke, Chris Richter, Liz Slooten, and several volunteers helped with data collection. We thank Chris Richter and anonymous reviewers for helpful comments on the manuscript.

Amano, M., and Yoshioka, M. (**2003**). "Sperm whale diving behaviour monitored using a suction-cup-attached TDR Tag," Mar. Ecol.: Prog. Ser. **258**, 291–295.

Arnbom, T. (**1987**). "Individual identification of sperm whales," Rep. Int. Whal. Commn **37**, 201–204.

Barlow, J. (**1999**). "Trackline detection probability for long-diving whales," in *Marine Mammal Survey and Assessment Methods*, edited by G. W. Garner, S. C. Amstrup, J. L. Laake, B. J. F. Manly, L. L. McDonald, and D. G. Robertson (Balkema, Rotterdam), pp. 209–221.

Barlow, J., and Taylor, B. L. (2005). "Estimates of sperm whale abundance in the northeastern temperate Pacific from a combined visual and acoustic survey," Marine Mammal Sci. (in press).

Childerhouse, S. J., Dawson, S. M., and Slooten, E. (**1995**). "Abundance and seasonal residence of sperm whales at Kaikoura, New Zealand," Can. J. Zool. **73**(4), 723–731.

Childerhouse, S. J., Dawson, S. M., and Slooten, E. (**1996**). "Stability of fluke marks used in individual photo-identification of male sperm whales at Kaikoura, New Zealand," Marine Mammal Sci. **12**, 447–451.

Douglas, L. A. (2000). "Click Counting: An acoustic censusing method for estimating sperm whale abundance," M.Sc. thesis, University of Otago, Dunedin, New Zealand (unpublished).

Goold, J. C., and Jones, S. E. (**1995**). "Time and frequency domain characteristics of sperm whale clicks," J. Acoust. Soc. Am. **98**, 1279–1291.

Gordon, J. (1996). "Acoustic surveys for cetaceans: Possibility and practice," Paper CAAW/02 submitted to the Cetacean Acoustic Assessment Workshop, Hobart, Tasmania.

Gordon, J., Leaper, R., Hartley, F. G., and Chappell, O. (1992). "Effects of whale-watching vessels on the surface and underwater acoustic behaviour of sperm whales off Kaikoura, New Zealand," Scientific and Research Series No. 52, Department of Conservation, Wellington, New Zealand, 64 pp.

Gordon, J. C. D. (1987). "The behaviour and ecology of sperm whales off Sri Lanka," Ph.D. thesis, University of Cambridge, Cambridge, UK (unpublished).

Jäke, O. (1996). "Acoustic censusing of sperm whales at Kaikoura, New Zealand: An inexpensive method to count clicks and whales automatically," M.Sc. thesis, University of Otago, Dunedin, New Zealand (unpublished).

Jaquet, N., Dawson, S. M., and Douglas, L. A. (**2001**). "Vocal behaviour of male sperm whales: Why do they click?" J. Acoust. Soc. Am. **109**, 2254–2259.

Jaquet, N., Dawson, S. M., and Slooten, E. (**2000**). "Seasonal distribution and diving behaviour of male sperm whales off Kaikoura: Foraging implications," Can. J. Zool. **78**(3), 407–419.

Leaper, R., Chappell, O., and Gordon, J. (**1992**). "The development of practical techniques for surveying sperm whale populations acoustically," Rep. Int. Whal. Commn **42**, 549–560.

Madsen, P. T., Payne, R., Kristiansen, N. U., Wahlberg, M., Kerr, I., and Møhl, B. (**2002a**). "Sperm whale sound production studied with ultrasound time/depth-recording tags," J. Exp. Biol. **205**, 1899–1906.

Madsen, P. T., Wahlberg, M., and Møhl, B. (**2002b**). "Male sperm whale (Physeter marcocephalus) acoustics in a high-latitude habitat: Implications for echolocation and communication," Behav. Ecol. Sociobiol. **53**, 31–41.

Miller, P. J. O., Johnson, M. P., and Tyack, P. L. (**2004**). "Sperm whale behaviour indicates the use of echolocation click buzzes 'creaks' in prey

capture," Proc. R. Soc. London, Ser. B **271**, 2239–2247.
Møhl, B., Wahlberg, M., Madsen, P. T., Heerfordt, A., and Lund, A. (**2003**). "The monopulsed nature of sperm whale clicks," J. Acoust. Soc. Am. **114**, 1143–1154.
Mullins, J., Whitehead, H., and Weilgart, L. S. (**1988**). "Behaviour and vocalisations of two single sperm whales, *Physeter macrocephalus*, off Nova Scotia," Can. J. Fish. Aquat. Sci. **45**, 1736–1743.
Papastavrou, V., Smith, S. C., and Whitehead, H. (**1989**). "Diving behaviour of the sperm whale, *Physeter macrocephalus*, off the Galápagos Islands," Can. J. Zool. **67**(4), 839–846.
Teloni, V., Zimmer, W. M. X., Fossati, C., Manghi, M., Pavan, G., and Priano, M. (**2000**). "Variability of temporal and spectral click characteristics of sperm whales (*Physeter macrocephalus*)," Proc. ECS (Cork, Ireland) **14**, 91–95.
Wahlberg, M. (**2002**). "The acoustic behaviour of diving sperm whales observed with a hydrophone array," J. Exp. Mar. Biol. Ecol. **281**, 53–62.
Watkins, W. A. (**1977**). "Acoustic behaviour of sperm whales," Oceanus **20**, 50–58.
Watkins, W. A. (**1980**). "Acoustics and the behaviour of sperm whales," in *Animal Sonar Systems*, edited by R. G. Busnel and J. F. Fish (Plenum, New York), pp. 283–290.
Watkins, W. A., Daher, M. A., DiMarzio, N. A., Samuels, A., Wartzok, D., Fistrup, K. M., Gannon, D. P., Howey, P. W., and Maiefski, R. R. (**1999**). "Sperm whale surface activity from tracking by radio and satellite tags," Marine Mammal Sci. **15**, 1158–1180.
Watkins, W. A., Daher, M. A., DiMarzio, N. A., Samuels, A., Wartzok, D., Fistrup, K. M., Howey, P. W., and Maiefski, R. R. (**2002**). "Sperm whale dives tracked by radio tag telemetry," Marine Mammal Sci. **18**, 56–68.
Watkins, W. A., and Moore, K. E. (**1982**). "An underwater acoustic survey for sperm whales (*Physeter catodon*) and other cetaceans in the southeast Caribbean," Cetology **46**, 1–7.
Watkins, W. A., Moore, K. E., and Tyack, P. (**1985**). "Sperm whale acoustic behaviours in the south east Caribbean," Cetology **49**, 1–15.
Weilgart, L. S., and Whitehead, H. (**1988**). "Distinctive vocalizations from mature male sperm whales (Physeter macrocephalus)," Can. J. Zool. **66**(9), 1931–1937.
Weilgart, L. S. (1990). "Vocalisations of the sperm whale (*Physeter macrocephalus*) off the Galápagos Islands as related to behavioural and circumstantial variables," Ph.D. thesis, Dalhousie University, Halifax, Nova Scotia, Canada (unpublished).
Whitehead, H., Brennan, S., and Grover, D. (**1992**). "Distribution and behaviour of male sperm whales on the Scotian Shelf, Canada," Can. J. Zool. **70**, 912–918.
Whitehead, H., and Gordon, J. (**1986**). "Methods of obtaining data for assessing and modelling sperm whale populations which do not depend on catches," Rep. Int. Whal. Commn **8**, 149–165.
Whitehead, H., and Weilgart, L. (**1990**). "Click rates from sperm whales," J. Acoust. Soc. Am. **87**, 1798–1806.
Whitehead, H., and Weilgart, L. (**1991**). "Patterns of visually observable behaviour and vocalisations in groups of female sperm whales," Behaviour **118**, 275–296.
Worthington, L. V., and Schevill, W. E. (**1957**). "Underwater sounds heard from sperm whales," Nature **10**, 291.

Sound radiation around a flying fly

Jérôme Sueur,[a] Elizabeth J. Tuck, and Daniel Robert
School of Biological Sciences, University of Bristol, Woodland Road, Bristol BS8 1UG, United Kingdom

(Received 3 November 2004; revised 19 April 2005; accepted 25 April 2005)

Many insects produce sounds during flight. These acoustic emissions result from the oscillation of the wings in air. To date, most studies have measured the frequency characteristics of flight sounds, leaving other acoustic characteristics—and their possible biological functions—unexplored. Here, using close-range acoustic recording, we describe both the directional radiation pattern and the detailed frequency composition of the sound produced by a tethered flying (*Lucilia sericata*). The flapping wings produce a sound wave consisting of a series of harmonics, the first harmonic occurring around 190 Hz. In the horizontal plane of the fly, the first harmonic shows a dipolelike amplitude distribution whereas the second harmonic shows a monopolelike radiation pattern. The first frequency component is dominant in front of the fly while the second harmonic is dominant at the sides. Sound with a broad frequency content, typical of that produced by wind, is also recorded at the back of the fly. This sound qualifies as pseudo-sound and results from the vortices generated during wing kinematics. Frequency and amplitude features may be used by flies in different behavioral contexts such as sexual communication, competitive communication, or navigation within the environment. © *2005 Acoustical Society of America.* [DOI: 10.1121/1.1932227]

PACS number(s): 43.80.Ka, 43.80.Ev, 43.80.Gx [JAS] Pages: 530–538

I. INTRODUCTION

Higher flies (Diptera, Brachycera) can emit sound in two different ways: incidentally from the wingbeat during flight, or actively through controlled wing vibrations when resting or walking (Ewing, 1989; Bailey, 1991; Greenfield, 2002). Controlled wing vibrations have been reported in numerous fly families (Sarcophagidae: Thomas, 1950; Chloropidae: Chvála *et al.*, 1974; Muscidae: Ewing, 1977; Tephritidae: Sivinski, 1988; Pscychodidae: Oliveira *et al.*, 2001) and have been studied extensively in *Drosophila* fruit flies (Drosophilidae) where they play a role in courtship behavior (Hall, 1994). In contrast, although the aerodynamics of insect flight have been extensively researched (for a review see Sane, 2003), the sound produced during flight has received less attention. Sotavalta (1947) listed the flight tones of numerous higher fly species, however, his study relied upon his "absolute ear (…) endowed by Nature" making it unrepeatable. Recordings of the tethered flight of *Drosophila melanogaster* made by Bennet-Clark and Ewing (1968), for comparison with the courtship song, were highly replicable but limited to a single position behind the animal.

Higher fly sounds may be of greater interest following a recent biomechanical study that found the antennae of several higher fly representatives responded to sound in a way physically similar to *D. melanogaster* (Robert and Göpfert, 2002). In *D. melanogaster* the male courtship wing vibrations cause air particle displacements that are received by the antennae. The *Drosophila* antenna works as a rotating simple harmonic oscillator, which activates a complex mechanosensory organ, the Johnston's organ (Göpfert and Robert, 2001, 2002). Widespread antennal hearing systems amongst the Brachycera imply the use of sound by more species, and in more contexts, than previously supposed. Robert and Göpfert (2002) suggested that flight sounds could be used by higher flies for flight control and, putatively, close-range echolocation. In some species, such sound could also assist territory defense (e.g., hoverflies—Syrphidae), relative positioning, and mating in swarms (e.g., dance flies—Empididae).

To investigate the possible function of flight sound in higher flies, more information about the radiation pattern and frequency content is needed, particularly in front of the fly where the auditory receivers lie. In insects, sound that is intended for a particular receiver is often directional (Bennet-Clark, 1971; Forrest, 1991; Heller and Krahe, 1994; Michelsen and Elsner, 1999; Michelsen and Fonseca, 2000). Is the sound produced by a flying fly concentrated in a particular direction?

Sotavalta (1947) discusses the reliability of the acoustic method for studying the wingbeat frequency, particularly as many previous authors were apparently confusing the first and the subsequent harmonics. He theorized that the discrepancies were simply due to disagreements in musical notation. Interestingly, Bennet-Clark and Ewing (1968) anecdotally noted that different sounds could be recorded around tethered flying *D. melanogaster*. Their observation presents the possibility of the dominant frequency varying around the fly. This would offer an alternative explanation to Sotavalta's, but has never been confirmed.

Here we analyze in detail the amplitude and frequency composition of the sound field during flight using a typical higher fly, the blowfly *Lucilia sericata* (Calliphoridae). In anechoic and dark conditions, we made high resolution, close-range recordings with miniature pressure-difference microphones revolving around tethered flying individuals. The plane of revolution of the microphones was chosen to

[a]Present address for correspondence: NAMC-CNRS UMR 8620, Université Paris Sud, 91405 Orsay, France. Electronic mail: jerome.sueur@ibaic.u-psud.fr

 0001-4966/2005/118(1)/530/9/$22.50

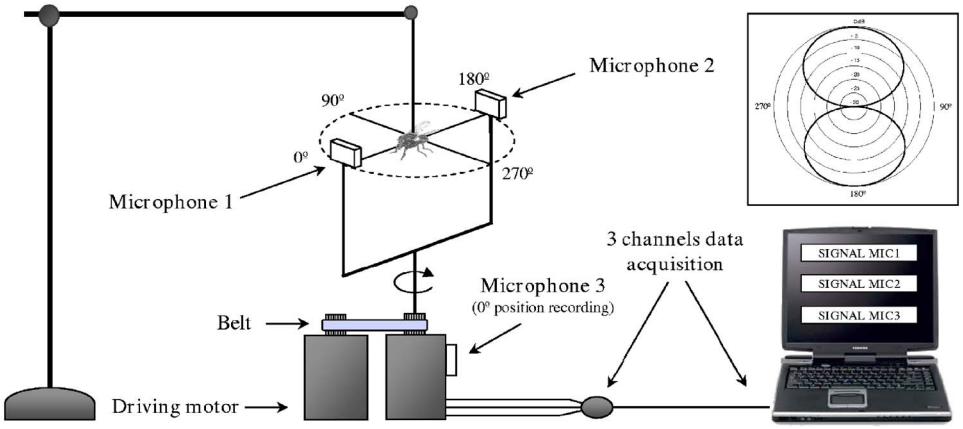

FIG. 1. Diagram of the recording setup and data acquisition system. The two microphones were 4 cm apart and revolved around a tethered fly. The motor was controlled with a second laptop (not shown). The microphone stand was isolated from the vibrations of the motor using a belt. The upper-right box shows the directivity pattern of the microphones (from Knowles™ specifications).

correspond to that of the antennal receiver. We describe both amplitude and frequency variations around the fly and show that the first two frequency bands of the wingbeat do not have the same radiation pattern. In effect the first harmonic dominates in front of the fly whereas the second harmonic is dominant on the sides. Moreover, noise due to vortex formation scrambles the wingbeat sound behind the fly. Such properties may be important for potential auto- or allo-communication.

II. MATERIAL AND METHODS

A. Animals

Male and female blowflies (Diptera, Brachycera, Calliphoridae, *Lucilia sericata*) were taken from laboratory cultures (Insect Ecology and Veterinary Parasitology Laboratory, University of Bristol). Prior to use, animals were maintained in plastic cages ($0.53\times0.22\times0.22$ m^3) and fed with sugar and water. Flies were anaesthetized with CO_2 and tethered with small piece of rigid card (surface $\approx$20 mm^2) fixed dorsally to the thorax with wax; the flies were then allowed at least 2 h to recover. Eight males and eight females whose free-flight behavior in the cage was unaffected by the tether and that flew consistently for more than a minute were selected.

B. Recording procedure

All recordings were carried out in the center of a soundproof room where the ambient temperature was kept at 25 °C and the relative humidity at 30%. To avoid any visual stimuli that could have modified the flight pattern, experiments were carried out in the dark, with the computer displays being screened by black fabric. The ambient noise level in the center of the setup was 31.3 dB SPL (*re* 20 μPa).

The recording setup consisted of a fly holder positioned between two miniature pressure-difference microphones, Knowles NR-3158 (Knowles Electronics Co, West Sussex, UK), that work as particle velocity receptors (Göpfert and Robert, 2002). The microphones were mounted on a rotating fork-shaped stand (Fig. 1). The vertical axle of this stand was belt driven, by a PC laptop controlled motor (Bipolar Stepper Motor, Milford Instruments, Leeds, UK). The belt mechanically isolated the stand and the acoustic recordings from the motors vibrations. The two microphones recorded the sound field from opposite sides of the fly to verify and double the data per sample. The microphones used were highly directional with a typical figure-of-eight directivity pattern (maximal input for a sound source angle at 0° or 180° and minimal input at 90° or 270°) (Fig. 1 inset) and they were therefore made to face the fly throughout each rotation. The microphone dimensions were $4.00\times5.59\times2.28$ mm^3 and their frequency response was flat between 0.1 and 2 kHz.

The revolution of the stand had a period 1.194 ± 0.012 s (n=200) indicating an error of 1%. A brief sound marking one complete rotation (duration=0.1 s, frequency=2.5 kHz) was triggered when the rotary stand crossed the zero degree position, i.e., just in front of the fly's head. The 2.5-kHz frequency was chosen as it would not interfere with the fly's flight sound. The reference sound was recorded using a Vivanco EM-216 microphone (Ahrensburg, Germany). To reduce the effect of irregular flight sound emissions during acquisition, each individual was recorded for ten revolutions of the stand, generating 320 sound files (16 individuals $\times$10 revolutions $\times$2 microphones).

The three microphones were connected to a second PC laptop through custom-made amplifiers and a four-channel Maya 44 USB audio interface (Audiotrak, San Jose, USA). Sounds were digitized at a sampling rate of 44.1 kHz and at 16-bit resolution using the multi-channel recording software Sonar 2.2 (http://www.cakewalk.com). They were stored as .wav files without data compression.

The distance between microphones was 4 cm and the fly was positioned directly in between. As the distance between the fly and the microphones was much smaller than the flight sound wavelength ($r/\lambda \ll 1$, with r=distance from the source, λ=wavelength), the microphones were in the acoustic near field. Any reflection and diffraction by surrounding setup is considered negligible since the width of the stand (0.01 m) was much smaller than the wavelength of the sound recorded (between 3.47 and 0.69 m for sounds between 100 and 500 Hz). No other object capable of interfering with the recordings was present in the surrounding sound field.

C. Amplitude analysis

Initial spectrographic analysis using the software package SYNTANA (Aubin, 1994) showed that the continuous wingbeat sound consisted of a harmonic series. The first ($F1$;

around 200 Hz) and second harmonic ($F2$; around 400 Hz) alternately contributed the most energy. To study the amplitude variations of the first and second harmonics two bandpass filters were independently applied. The filters were calculated by means of a fast Fourier transform (FFT) with a window of 4096 points enabling a frequency precision of 1.22 Hz. The first filter kept frequencies between 100 and 300 Hz and the second filter kept frequencies between 300 and 500 Hz.

In order to compensate for the 1% error in the revolution period and to obtain files with an identical number of points (5970) despite different durations, signals were undersampled at different frequencies (5000 ± 48 Hz, $n=200$) using the digital audio editor software Goldwave 5.6 (http://www.goldwave.com). This process did not affect the large amplitude modulations that we wanted to analyze.

Large amplitude modulations around the fly were estimated from the signal envelope. Envelopes were generated using the Hilbert transform (Mbu-Myamsi *et al.*, 1994). We normalized the envelopes to obtain values between 0 and 1. Ten first harmonic $F1$ and ten second harmonic $F2$ envelopes were calculated from both microphones and averaged for each individual. This resulted in four averaged envelopes per individual. To facilitate visual comparison, normalized envelopes were converted to an intensity decibel (dB) scale $[a_i(\mathrm{dB}) = 10 \log a_i]$.

D. Frequency analysis

To determine the dominant frequency around the fly, sound files were undersampled to the same sampling frequency (5000 Hz) and subjected to successive Fourier transforms (FTs) using a Hanning window of 1024 points (=0.2 s). This frame length led to a frequency resolution of 4 Hz. Ninety overlapping FTs were calculated per rotation enabling a spatial resolution of 4°.

Since the harmonics could be considered as discrete variables, we calculated the median instead of the mean of the ten frequency modulations obtained for each individual and calculated the male and female average frequency from this.

E. Control

The accuracy of the recording setup was estimated using a small unbaffled loudspeaker (Wharfedale AKI-1200, diameter 1.5 cm, impedance 32 Ω, 20–20 000 Hz) firmly clamped in place of the fly. The loudspeaker was successively fed with continuous sinusoidal signals of 200 and 400 Hz generated by SYNTANA. At these frequencies, an opened loudspeaker acts as a dipole sound source, i.e., radiating sound with a maxima along the 0° and 180° directions, and minima along the 90° and 270° directions (Russell *et al.*, 1999). Amplitude and frequency modulations of the 200- and 400-Hz signals were then estimated using the same process as described for the flies' acoustic emissions above.

F. Wing morphometry

Thoracic width measurements were made between the left and right wing articulations for eight male and eight female *L. sericata* using a binocular dissecting Wild M5 Microscope and an eyepiece graticule. The wings were cut and scanned at 800 dpi resolution and wing length and area were then measured using the software tpsDIG32 version 1.40 (Rohlf, 2004).

G. Statistical analysis

Sound data from the two microphones were aligned to 0° and the envelopes and dominant frequency values were compared using Spearman's rank correlation coefficient and Mann-Whitney test. The envelopes were considered as vectors, with vector length (modulus) corresponding to amplitude and vector angle (argument) corresponding to the microphones position around the fly. Amplitude directivity was estimated from the mean vector (L, θ) and circular standard deviation (ν) as (Fischer, 1995):

$$L = \frac{\sqrt{\left(\left(\sum_{i=1}^{i=n} a_i \cos \alpha_i\right)^2 + \left(\sum_{i=1}^{i=n} a_i \sin \alpha_i\right)^2\right)}}{n}, \text{ with } 0 < L < 1,$$

$$\theta = \begin{cases} \tan^{-1}\left(\dfrac{\sum_{i=1}^{i=n} \sin \alpha_i}{\sum_{i=1}^{i=n} \cos \alpha_i}\right) \text{ if } \sum_{i=1}^{i=n} \sin \alpha_i > 0, \sum_{i=1}^{i=n} \cos \alpha_i > 0, \\ 180 + \tan^{-1}\left(\dfrac{\sum_{i=1}^{i=n} \sin \alpha_i}{\sum_{i=1}^{i=n} \cos \alpha_i}\right) \text{ if } \sum_{i=1}^{i=n} \cos \alpha_i < 0, \\ 360 + \tan^{-1}\left(\dfrac{\sum_{i=1}^{i=n} \sin \alpha_i}{\sum_{i=1}^{i=n} \cos \alpha_i}\right) \text{ if } \sum_{i=1}^{i=n} \sin \alpha_i < 0, \sum_{i=1}^{i=n} \cos \alpha_i > 0, \end{cases}$$

$$\nu = \frac{180}{\pi}\sqrt{2(1-L)}, \quad \text{with } 0 < \nu < 81.03°.$$

Since the loudspeaker showed a centrally symmetrical amplitude distribution (i.e., bimodal), the vector of the resulting mean would be around zero and no mean angle could be determined. Following Fischer (1995), the mean vector and angle were calculated applying the following correction $\alpha_i \rightarrow 2\alpha_i$ when $2\alpha_i < 360°$ and $\alpha_i \rightarrow 2\alpha_i - 360°$ when $2\alpha_i \geqslant 360°$.

Wing morphometric data were compared using the Mann-Whitney test. Statistics tests followed Sokal and Rohlf (1995) and were computed with SPSS 11.0 software (SPSS Inc., Chicago, IL).

III. RESULTS

A. Control

Control recordings and analyses were done with a small unbaffled loudspeaker and the amplitude envelopes for both sine waves (200 and 400 Hz) showed a typical figure-eight pattern. With the minimum amplitude levels at 90° and 270° and an amplitude difference of about 2 dB between the back and the front of the loudspeaker, the mean direction was 0° (Fig. 2). Such a polar amplitude profile is typical of unbaffled loudspeakers. Small variations revealed that recordings at 200 Hz were noisier than at 400 Hz but these were not sufficient to affect the large amplitude modulations. The amplitude envelopes did not differ between the two micro-

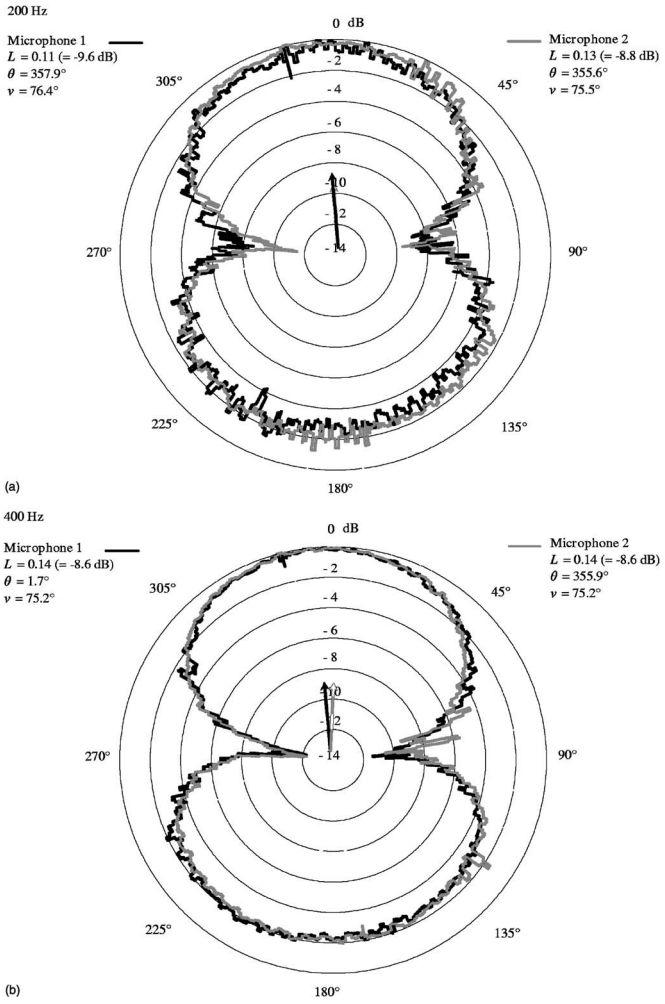

FIG. 2. Control of amplitude analysis: amplitude variations around a small unbaffled loudspeaker emitting successively a 200-Hz (a) and a 400-Hz (b) sine wave. The loudspeaker faced the 0° position. For each microphone, the amplitude directivity is characterized by mean vector length (L), mean vector direction (θ), and circular standard deviation (ν).

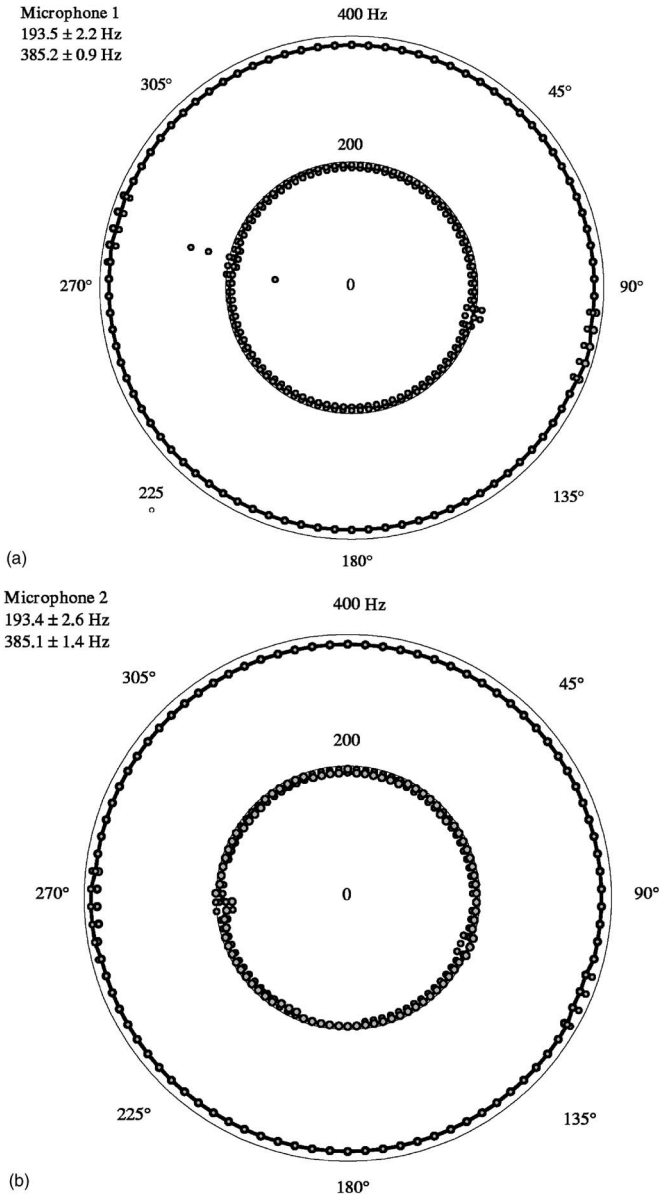

FIG. 3. Control of frequency analysis for the two microphones (a, b): measuring with 4° precision the frequency of 200- and 400-Hz sine waves. The points represent the dominant frequency every 4° during one revolution around the loudspeaker. Ten revolutions were analyzed. Low variability in the results led to point superposition. Black lines correspond to the median of the points.

phones ($P<0.0001$ in all cases, Spearman correlation). The average amplitude difference between the two microphones was 0.14 dB at 200 Hz and 0.04 dB at 400 Hz. Analysis of the dominant frequency indicated a slight frequency shift; 193.5±2.2 and 385.2±0.9 Hz for microphone 1, 193.4±2.6 and 385.1±1.4 Hz for microphone 2 (Fig. 3). The loudspeakers were forcibly very small (diameter=1.5 cm) to permit the microphone movement. The frequency error occurred due to the high impedance (32 Ω) of the small loudspeaker, which therefore required high broadcasting levels to obtain an acceptable signal. Two larger loudspeakers with static microphones confirmed that this was the case. Frequency analysis did not show any significant differences between the two microphones (absolute difference between microphones 1 and 2: 2.58 Hz at 200 Hz, 0.58 Hz at 400 Hz, $P>0.5$ in both cases, Mann-Whitney test). Microphones specifications could be then considered as similar.

B. Amplitude analysis

The spectrogram depicted in Fig. 4 illustrates a typical sound recorded around a flying *L. sericata*. The amplitude of the signal is modulated around the fly, with the maximum occurring around 180°. Amplitude modulations for the first ($F1$) and second harmonic ($F2$) obtained by signal envelope computation are shown in Fig. 5. In all cases, the mean vector modulus (L) was very small (<0.15), indicating a high level of dispersion. This was confirmed by the high values of angular dispersion (ν) around 80° for a scale ranging from 0° to 81°. Mean vector arguments were concentrated behind the flies ($201°<\theta<297°$), except for $F1$ produced by males where values were around 300°. Low L and ν values, such as those calculated for the male $F1$, however, indicate the mean vector argument is not very accurate.

The radiation pattern of $F1$ was a figure-eight, with the lowest amplitude values at 100° and 260° and the highest at 0° and 180°. Males and females produced similar overall

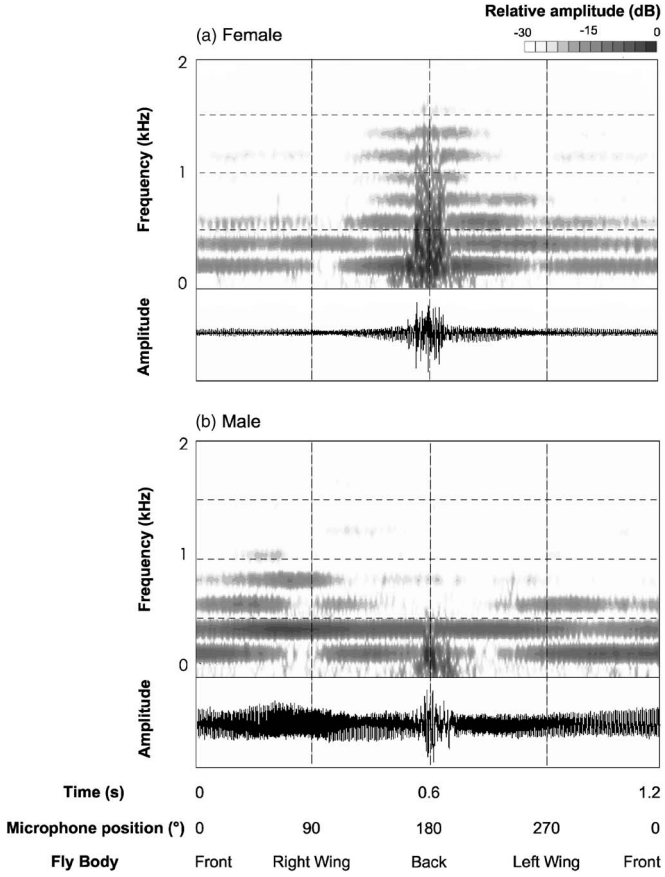

FIG. 4. Spectrogram of a typical sound recorded around *Lucilia sericata* female (a) and male (b). Fast Fourier transform window length=1024 points, frequency resolution=4.9 Hz, overlap=98%, Hanning window. 1 gray scale=2.5 dB.

patterns although the correlation between them for $F1$ was lower ($0.69, 0.71, P<0.0001$) than between the two microphones ($0.95, 0.97, P<0.0001$), indicating some differences between the two sexes. Indeed males produced louder $F1$ values than females (difference male-female: microphone 1 =3.0 dB, microphone 2=2.9 dB) and this difference was greater in the front (difference male-female between 270° and 90°: microphone 1=4.1 dB, microphone 2=4.2 dB) than the back (difference male-female between 90° and 270°: microphone 1=1.9 dB, microphone 2=1.6 dB).

The radiation of $F2$ exhibited a more circular pattern, with points of higher amplitude at approximately 100° and 260° (Fig. 5). The radiation differences of $F1$ and $F2$ are confirmed by the low correlation coefficient for females ($0.61, 0.77, P<0.0001$) and even negative correlation for males ($-0.55, -0.50, P<0.0001$). The correlation coefficients for $F2$ between the males and females were all significant ($0.62, 0.55, P<0.0001$) but lower than that of the two microphones ($0.93, 0.97, P<0.0001$). Again, the males were louder (microphone 1=1.3 dB, microphone 2=1.8 dB) with the greatest difference being in the front (microphone 1 =2.15 dB, microphone 2=2.5 dB) compared to the back (microphone 1=0.5 dB, microphone 2=1.1 dB).

C. Frequency analysis

When flying, *L. sericata* produced a series of harmonics the first of which ($F1$) was around 200 Hz and the second one ($F2$) also being consistently intense enough for recording. Male $F1$ and $F2$ values were respectively 192±30 and 390±24 Hz for the microphone 1 and 189±22 and 391±16 Hz for microphone 2. Female $F1$ and $F2$ values were respectively 193±18 and 377±8 Hz for the microphone 1 and 190±14 Hz and 377±7 Hz for microphone 2. $F1$ and $F2$ values were not different between microphones 1 and 2 ($P>0.5$ in all cases, Mann-Whitney test). $F1$ values were not significantly different between males and females ($U=3152.5$, $P>0.05$, microphone 1; $U=29295.5$, $P>0.05$, microphone 2; Mann-Whitney test) but there was a significant difference of about 13 Hz between males and females for $F2$ values ($U=1605$, $P<0.0001$, microphone 1; $U=1841$, $P<0.0001$, microphone 2; Mann-Whitney test).

Spectrograms of a typical recording around a flying individual clearly show that the relative energies of $F1$ and $F2$ were modulated around the fly (Fig. 2). $F1$ was of highest energy (i.e., dominant) at around 0°, but disappeared almost entirely between 100° and 260° where $F2$ increased to become dominant instead. In addition, an intense broadband noise partly covered both $F1$ and $F2$ at 180°.

To confirm these observations, we determined the dominant frequency at different positions around the fly (Fig. 6). The results from both microphones were similar ($r=0.892$ for male, $r=0.878$ for female, $P<0.0001$ in both cases, Spearman correlation) and the male and female frequency patterns were not significantly different ($r=0.889$ for microphone 1, $r=0.891$ for microphone 2, $P<0.0001$ in both cases, Spearman correlation). $F1$ was most frequently dominant in the front ([305°–45°]) and in the back ([125°–225°]) whereas $F2$ was dominant on both sides ([45°–125°], [225°–305°]). A single Fourier transform at 0°, 90°, 180°, and 270° for one individual further illustrates this phenomenon (Fig. 7). At the rear of the fly, the harmonic series is partly covered by airflow noise, generated by the fly, ranging from 0 to around 800 Hz.

D. Wing morphometry

Thorax width between left and right wing articulations was 3.0±0.2 mm for eight males and 3.0±0.1 mm for eight females. There were no differences between the male and female inter-wing distance ($U=27$, $P>0.05$, Mann-Whitney test). Male wing area was 13.58±1.70 mm^2 (left) and 13.35±1.38 mm^2 (right). Female wing area was 16.73±0.97 mm^2 (left) and 16.25±0.91 mm^2 (right). There were no differences between left and right wings ($U=28$, $P>0.5$ for males; $U=21$, $P>0.5$ for females; Mann-Whitney test). Male wings were smaller than female wings (left wing: $U=2$, $P<0.005$; right wing: $U=0$, $P<0.001$; Mann-Whitney test).

IV. DISCUSSION

A. Sound and flight

The flight sound of *L. sericata* is ineffectually directed and is characterized by a series of harmonics with a noise recorded behind the fly. Typically, the first harmonic was dominant in front and the second harmonic was dominant at the sides. The first harmonic showed a dipolelike pattern,

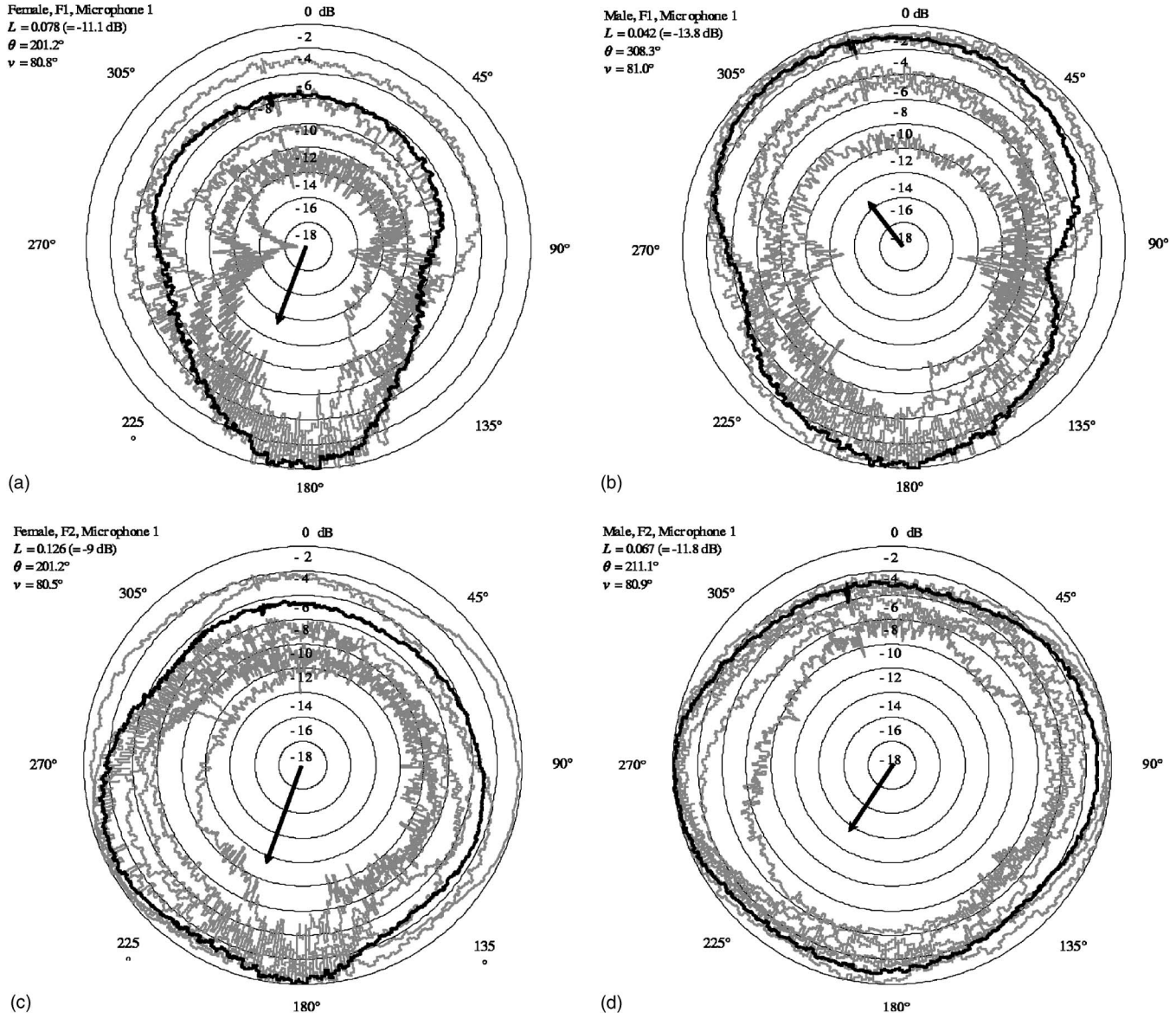

FIG. 5. Amplitude variations of first ($F1$) and second harmonic ($F2$) bands around flying tethered females (a, c) and males (b, d). Gray lines: mean of ten revolution around single individuals. Black lines: mean of the gray lines. Descriptive parameters as in Fig. 2. Data is shown for one microphone only but was typical of both.

whereas the second harmonic exhibits a more rounded envelope like a monopole.

Our finding that the dominant frequency switches between the first and second harmonic frequency at different positions around the fly could explain why earlier observers could not agree upon the flight tone of certain insect species (Sotavalta, 1947). This phenomenon may occur because the wing motion is not a simple vertical oscillation but includes velocity variations, wing deformations, and rotations (Ellington, 1984; Ennos, 1989; Lehmann and Dickinson, 1998; Dudley, 2000). Indeed, Fletcher (1992) points out that modeling the wing as a simple vibrating disc (dipole) is only moderately satisfactory. Bennet-Clark and Ewing (1968), however, showed that the flight sound waveform of *D. melanogaster* follows a similar time course to the wing-tip velocity. If we consider that the observed angle, motion, and velocity of the wing tips are dependent upon the viewer's position around the fly, this could explain how the dominant frequency also varies.

In the rear of the fly the harmonics were masked by a loud sound that had a broad unstructured frequency content and was analogous to recordings of airflows. This nonperiodic waveform may have been caused by vortices, which, having been formed and shed by the wings, trail behind a flying insect (Grodnitsky and Morozov, 1993; Brodsky, 1994; Dickinson and Götz, 1996; Ellington *et al.*, 1996; Dudley, 2000). Since this "sound" results from fluctuating movements of the airflow rather than periodic air vibrations, it should be more accurately described as "pseudo-sound" (Lighthill, 1962). Our recordings suggest that females produced more pseudo-sound than males. These differences were unlikely to be caused by body-size differences since thorax length measurements were similar in both sexes. Male flies had smaller wings however (wing area around 13 mm^2

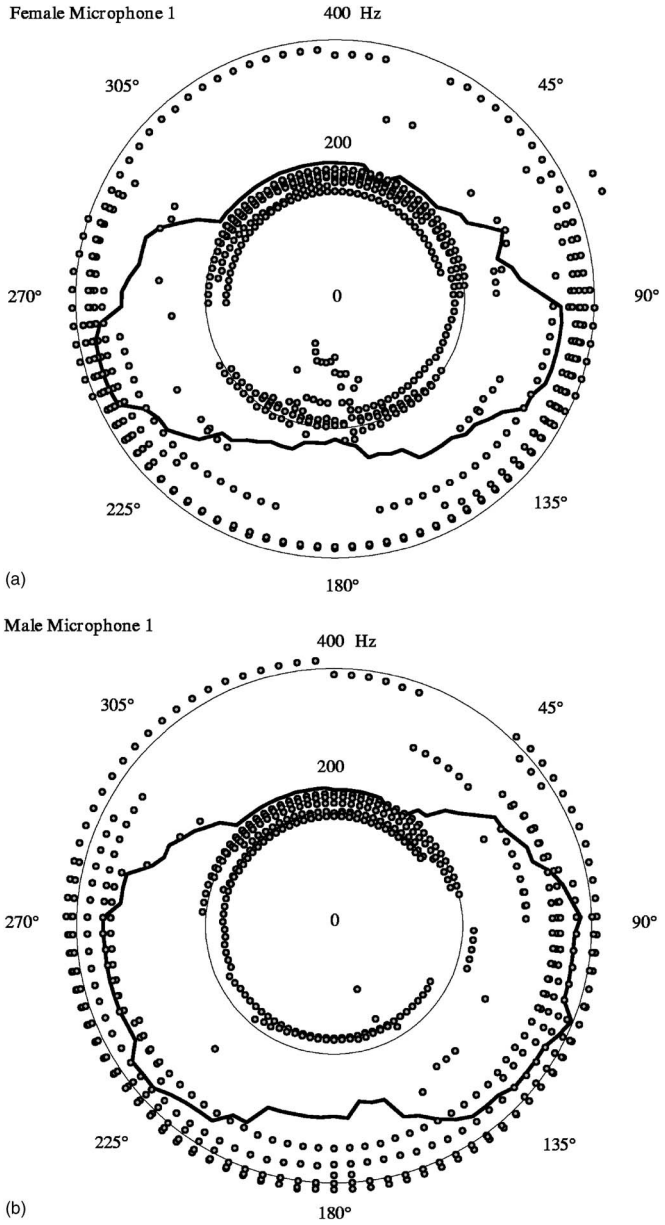

FIG. 6. Measuring with 4° precision of the dominant frequency band in female (a) and male (b). Each point represents the median of ten measures corresponding to ten revolutions around a single individual. Lines correspond to the mean of the points. Data is shown for one microphone only but was typical of both.

for males and 16 mm^2 for females), which might displace less air and therefore generate less intense wake vortices than females. One would expect any differences in the amplitude of the wingstroke to have a similar effect.

Interestingly Bennet-Clark and Ewing (1968) did not detect any such pseudo-sound when recording from behind a flying *D. melanogaster*. This may reflect differences in the wake dynamics of two distinct fly species and in the relative distances of recording. The work of Lighthill (1962) suggests that flight sound and pseudo-sound will dissipate differently. In the far field, sound pressure and sound velocity decrease inversely with the distance from the source $(1/r)$ whereas pseudo-sound amplitude decreases with at least the inverse square $(1/r^2)$ (Lighthill, 1962). In the near field pseudo-sound attenuation is unknown but sound pressure and sound velocity are thought to decrease by $1/r$ and $1/r^2$ respectively for a monopole, and by $1/r^2$ and $1/r^3$ respectively for a dipole (Bennet-Clark, 1998). In principle, then, further from the fly the harmonic series will outlast the pseudo-sound and should therefore be recorded instead.

The harmonic series and/or the pseudo-sound could potentially encode information relevant to a fly. Our results suggest, however, that the flight sounds of a fly are not radiated very efficiently. For efficient sound production, the source size must be higher than $\frac{1}{6}$ (monopole) or $\frac{1}{4}$ (dipole) of the wavelength (Bennet-Clark, 1998). Hence the size (or the mass) of the emitter is often inversely proportional to the frequency of the sound produced (Bennet-Clark, 1998; Fletcher, 2004). In this case, the wings of *L. sericata* are much smaller than the wavelength of the sound they produce (around 1.8 m).

Some insects solve the frequency-scale problem using external secondary structures, such as a baffle, which may also help direct the signal (e.g., tree-crickets: Forrest, 1991). A flying fly lacks any obvious external baffle and three of the mean vector analyses indicate that the flight sound of *L. sericata* is only weakly directed to around 200°. Unlike the envelopes and mean vectors computed for the fly, however, the control does not demonstrate this sagittal asymmetry. This suggests that an asymmetry in the animal preparation or in the experimental environment may have influenced the fly's flight. The rearward concentration of sound energy was probably due to the pseudo-sound at the back. The lesser pseudo-sound recorded behind male flies could explain why the energy of the males' first harmonic is weakly directed to around 300°. This would suggest that in the absence of pseudo-sound the energy of the first harmonic is concentrated forwards whereas the energy of the second harmonic remains angled backwards.

B. Flight sounds and hearing

Robert and Göpfert (2002) suggest that antennal sound reception might be possible in several families of higher flies. The use of flight sounds for communication by members of the Brachycera, however, has never been reported. In static *D. melanogaster* the resonant frequency range of the antenna peaks at around 420 Hz (Robert and Göpfert, 2002). Courtship song detection is usually used to explain this antennal tuning which interestingly also coincides with the acoustic wingbeat frequency (Bennet-Clark and Ewing, 1968). Potentially acoustic sensitivity to the wingbeat could present a sensory problem during flight. Indeed, animals that produce loud and continuous sounds risk deafening themselves by overworking their acoustic sensory organs. "Ear" protection can be achieved by actively modifying the properties of the hearing organ as an Australian cicada does by folding its tympanic membrane while calling (Henning *et al.*, 1990). Göpfert and Robert (2002) showed that in *D. melanogaster* as the sound intensity increases, the resonant frequency of the antenna shifts, so that its acoustic sensitivity decreases. Our results allude to a passive protective system. The antennae of *L. sericata* are in a position where the acoustic energy of the sound field is concentrated on the first

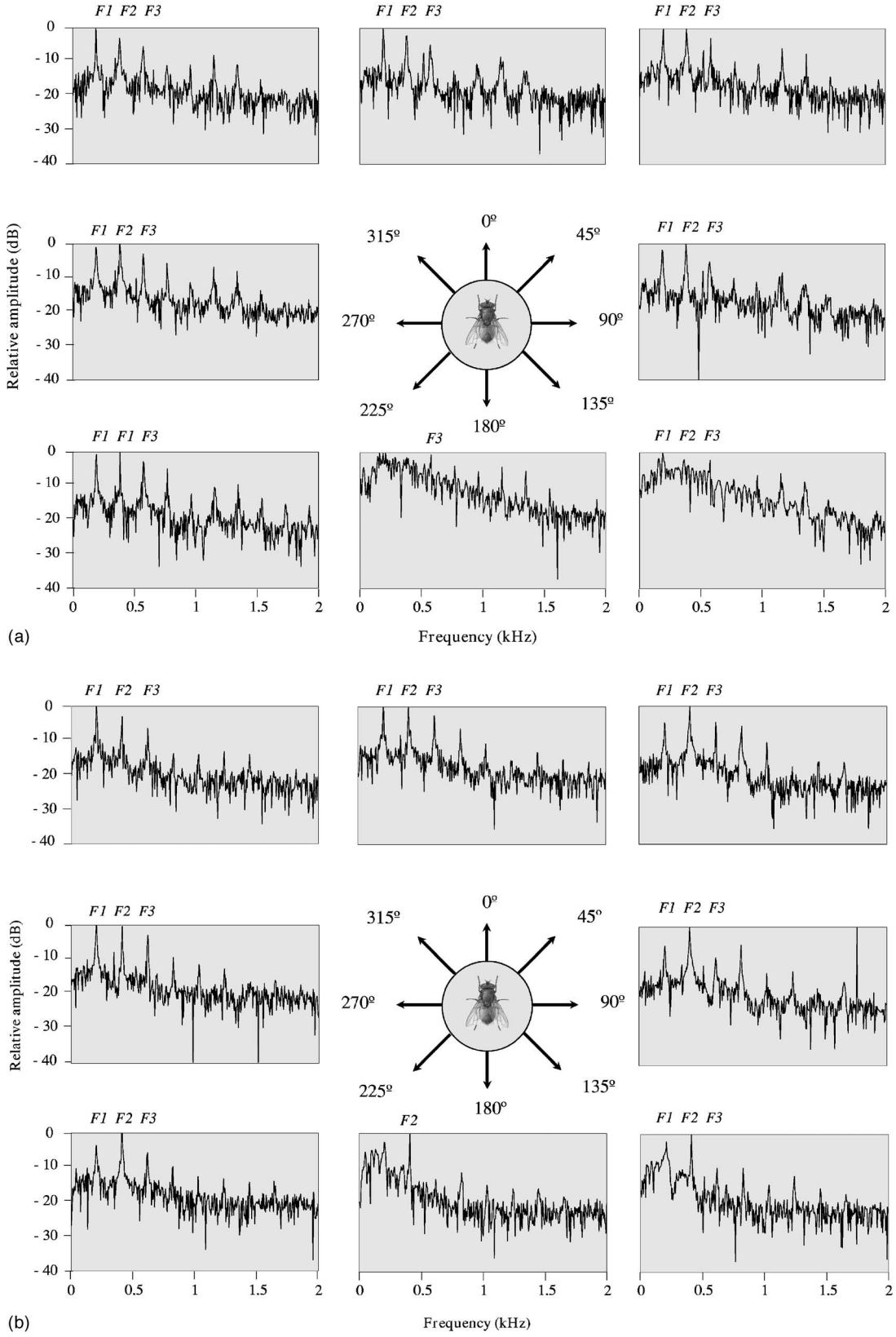

FIG. 7. Frequency spectrum of a recording around *Lucilia sericata* female (a) and male (b) at 45° positions. *F*1, *F*2, and *F*3 localize, respectively, the first harmonic, second, and third harmonic bands. Characters in bold indicate the dominant frequency. Fourier transform window length=1024 points, frequency resolution=4.9 Hz, Hanning window. Data is shown for one microphone only but was typical of both.

harmonic, around 200 Hz. If tuned to the second harmonic rather than to the first frequency band, *L. sericata* would be partially protected against its own sound, but would still be able to detect the sound produced on the sides by congeners.

If *L. sericata* can receive sound during flight without damage, it could exploit self-generated and conspecific flight sounds for auto- and allo-communication, respectively. As explained previously, the flight sounds of *L. sericata* are not radiated very efficiently and therefore are more likely to function in short-range communication. In the plane we studied, there was no evidence that the sound field was directed towards a particular receiver. The position of the receiver may still be important however, as the frequency content is variable around the fly.

In order to fully estimate how sound might be used during flight, the results we obtained would have to be completed by an analysis in three dimensions and analysis of the antennal reception mechanism. Behavioral experiments testing the potential role of such particular sound emissions should also be undertaken.

ACKNOWLEDGMENTS

We would especially like to thank Richard Wall for allowing us to use sheep blowfly cultures maintained in his laboratory (Insect Ecology and Veterinary Parasitology Laboratory, University of Bristol). We are indebted to Gareth Jones for technical support in sound analysis. We thank also James F. C. Windmill and Joseph C. Jackson for their support at many stages of this study. SYNTANA software was used with the kind authorization of Thierry Aubin. We gratefully acknowledge Knowles™ Company for providing miniature microphones. We greatly thank James Simmons and an anonymous reviewer for helpful comments on the manuscript. The study was supported by the Royal Society (U.K.). J.S. was funded by the Foundation Fyssen (France) and E.J.T. by the BBSRC (U.K.).

Aubin, T. (**1994**). "Syntana: a software for the synthesis and analysis of animal sounds," Bioacoustics **6**, 80–81.

Bailey, W. J. (**1991**). *Acoustic Behaviour of Insects: An Evolutionary Perspective* (Chapman and Hall, London).

Bennet-Clark, H. C. (**1971**). "Acoustics of insect song," Nature (London) **234**, 255–259.

Bennet-Clark, H. C. (**1998**). "Size and scale effects as constraints in insect sound communication," Philos. Trans. R. Soc. London **353**, 407–419.

Bennet-Clark, H. C., and Ewing, A. (**1968**). "The wing mechanism involved in the courtship of *Drosophila*," J. Exp. Biol. **49**, 117–128.

Brodsky, A. K. (**1994**). *The Evolution of Insect Flight* (Oxford U. P., Oxford).

Chvála, M., Doskćil, J., Mook, J. H., and Pokorný, V. (**1974**). "The genus *Lipara* Meigen (Diptera, Chloropidae), systematics, morphology, behaviour and ecology," Tijd Schr. Entomol. **117**, 1–25.

Dickinson, M. H., and Götz, K. G. (**1996**). "The wake dynamics and flight forces of the fruit fly *Drosophila melanogaster*," J. Exp. Biol. **199**, 2085–2104.

Dudley, R. (**2000**). *The Biomechanics of Insect Flight* (Princeton U. P., Princeton, NJ).

Ellington, C. P. (**1984**). "The aerodynamics of hovering insect flight. III. Kynematics," Philos. Trans. R. Soc. London, Ser. B **305**, 115–144.

Ellington, C. P., van den Berg, C., Willmott, A. P., and Thomas, A. L. R. (**1996**). "Leading-edge vortices in insect flight," Nature (London) **384**, 626–630.

Ennos, A. R. (**1989**). "The kinematics and aerodynamics of the free flight of some diptera," J. Exp. Biol. **142**, 49–85.

Ewing, A. W. (**1977**). "Communication in Diptera," in *How Animals Communicate*, edited by T. E. Sebeok (Indiana U. P., Bloomington), pp. 403–417.

Ewing, A. W. (**1989**). *Arthropod Bioacoustics: Neurobiology and Behaviour* (Univ. Press Edinburgh, Edinburgh).

Fisher, N. I. (**1995**). *Statistical Analysis of Circular Data* (Cambridge U.P., Cambridge).

Fletcher, N. H. (**1992**). *Acoustic Systems in Biology* (Oxford Univ. Press, Oxford).

Fletcher, N. H. (**2004**). "A simple frequency-scaling rule for animal communication," J. Acoust. Soc. Am. **115**, 2334–2338.

Forrest, T. G. (**1991**). "Power output and efficiency of sound production by crickets," Behav. Ecol. **2**, 327–338.

Göpfert, M. C. and Robert, D. (**2001**). "Turning the key on *Drosophila* audition," Nature (London) **411**, 908.

Göpfert, M. C., and Robert, D. (**2002**). "The mechanical basis of *Drosophila* audition," J. Exp. Biol. **205**, 1199–1208.

Greenfield, M. D. (**2002**). *Signalers and Receivers: Mechanisms and Evolution of Arthropod Communication* (Oxford U. P., Oxford).

Grodnitsky, D. L., and Morozov, P. P. (**1993**). "Vortex formation during tethered flight of functionally and morphologically two-winged insects, including evolutionary considerations in insect flight," J. Exp. Biol. **182**, 11–40.

Hall, J. C. (**1994**). "Mating of a fly," Science **264**, 1702–1714.

Heller, K.-G., and Krahe, R. (**1994**). "Sound production and hearing in the pyralid moth *Symmoracma minoralis*," J. Exp. Biol. **187**, 101–111.

Hennig, R. M., Weber, T., Huber, F., Kleindienst, H.-U., Moore, T. E., and Popov, A. V. (**1990**). "Auditory threshold change in singing cicadas," J. Exp. Biol. **187**, 45–55.

Lehmann, F. O., and Dickinson, M. H. (**1998**). "The control of wing kinematics and flight forces in fruit flies (*Drosophila* spp.)," J. Exp. Biol. **201**, 385–401.

Lighthill, M. J. (**1962**). "Sound generated aerodynamically," Proc. R. Soc. London, Ser. A **267**, 147–182.

Mbu Nyamsi, R. G., Aubin, T., and Brémond, J. C. (**1994**). "On the extraction of some time dependent parameters of an acoustic signal by means of the analytic signal concept. Its application to animal sound study," Bioacoustics **5**, 187–203.

Michelsen, A., and Elsner, N. (**1999**). "Sound emission and the acoustic far field of a singing acridid grasshopper (*Omocestus viridulus* L.)," J. Exp. Biol. **202**, 1571–1577.

Michelsen, A., and Fonseca, P. (**2000**). "Spherical sound radiation patterns of singing grass cicadas," J. Comp. Physiol., A **186**, 163–168.

Oliveira, S. G., Bottecchia, M., Bauzer, L. G. S. R., Souza, N. A., Ward, R. D., Kyriacou, C. P., and Peixoto, A. A. (**2001**). "Courtship song genes and speciation in sand flies," Mem. Inst. Oswaldo Cruz **96**, 403–405.

Robert, D., and Göpfert, M. C. (**2002**). "Acoustic sensitivity of fly antennae," J. Insect Physiol. **48**, 189–196.

Rohlf, F. J. (**2004**). "Tpsdig32," Department of Ecology and Evolution, State University New York, Stony Brook, NY.

Russell, D. A., Titlow, J. P., and Bemmen, Y.-J. (**1999**). "Acoustic monopoles, dipoles, and quadrupoles: an experiment revisited," Am. J. Phys. **67**, 660–664.

Sane, S. P. (**2003**). "The aerodynamics of insect flight," J. Exp. Biol. **206**, 4191–4208.

Sivinski, J. (**1988**). "What do fruit fly songs mean?," Fl. Ent. **71**, 462–426.

Sokal, R. R., and Rohlf, F. J. (**1995**). *Biometry* (Freeman and Company, New York).

Sotavalta, O. (**1947**). "The flight-tone (wing-stroke frequency) of insects," Act. ent. Fenn. **4**, 1–117.

Thomas, H. T. (**1950**). "Field notes on the mating habits of *Sarcophaga* Meigen (Diptera)," Proc. R. Ent. Soc. London A **25**, 93–98.

Characterization of ultrasound contrast microbubbles using *in vitro* experiments and viscous and viscoelastic interface models for encapsulation

Kausik Sarkar[a)]
Department of Mechanical Engineering, University of Delaware, Newark, Delaware 19716

William T. Shi
Department of Radiology, Thomas Jefferson University, Philadelphia, Pennsylvania 19107 and Philips Research, Briarcliff Manor, New York 10510

Dhiman Chatterjee
Department of Mechanical Engineering, University of Delaware, Newark, Delaware 19716 and Department of Mechanical Engineering, IIT Madras, Chennai 600036, India

Flemming Forsberg
Department of Radiology, Thomas Jefferson University, Philadelphia, Pennsylvania 19107

(Received 20 August 2004; revised 30 March 2005; accepted 6 April 2005)

Zero-thickness interface models are developed to describe the encapsulation of microbubble contrast agents. Two different rheological models of the interface, Newtonian (viscous) and viscoelastic, with rheological parameters such as surface tension, surface dilatational viscosity, and surface dilatational elasticity are presented to characterize the encapsulation. The models are applied to characterize a widely used microbubble based ultrasound contrast agent. Attenuation of ultrasound passing through a solution of contrast agent is measured. The model parameters for the contrast agent are determined by matching the linearized model dynamics with measured attenuation data. The models are investigated for its ability to match with other experiments. Specifically, model predictions are compared with scattered fundamental and subharmonic responses. Experiments and model prediction results are discussed along with those obtained using an existing model [Church, J. Acoust. Soc. Am. **97**, 1510 (1995) and Hoff *et al.*, J. Acoust. Soc. Am. **107**, 2272 (2000)] of contrast agents. © *2005 Acoustical Society of America.* [DOI: 10.1121/1.1923367]

PACS number(s): 43.80.Qf, 43.80.Ev, 43.25.Yw, 43.35.Wa [CCC] Pages: 539–550

I. INTRODUCTION

Microbubble based contrast enhancing agents can achieve significant improvement of ultrasound images of blood flow (Goldberg *et al.*, 2001; Frinking *et al.*, 2000). These bubbles are encapsulated by a layer of surface active materials such as lipids or proteins to stabilize them against premature dissolution in the blood stream (Goldberg *et al.*, 2001; Frinking *et al.*, 2000). The performance of these contrast agents *in vivo* depends on their interaction with the incident acoustic pressure. The encapsulation plays a significant role in this interaction. Accurate characterization of contrast agent behavior therefore critically relies on a good model of the encapsulation. *In vitro* attenuation and scattering experiments have been performed on various contrast agents (e.g., Albunex®, Molecular Biosystems Inc., San Diego, CA; Optison® GE Healthcare, Princeton, NJ; Sonazoid® GE Healthcare, Oslo, Norway; Definity® of Bristol-Myers Squibb Medical Imaging, N. Billerica, MA) to understand and characterize their properties (see, for example, Hoff *et al.*, 2000; de Jong *et al.*, 1992; de Jong and Hoff, 1993; Frinking and de Jong, 1998; Shi *et al.*, 1999; Morgan *et al.*, 2000). Recently, nonlinear contrast behaviors, both second- and sub-harmonic responses, have been studied by many researchers (Shi *et al.*, 1999; Simpson *et al.*, 1999; Chang *et al.*, 1996; de Jong *et al.*, 1994; Shankar *et al.*, 1998; Shi and Forsberg, 2000). Contrast agents exhibit stronger nonlinear response than the surrounding tissue. The enhanced nonlinear response is harnessed to improve contrast-to-tissue signal in various nonlinear imaging modalities such as harmonic, subharmonic, pulse inversion, or power Doppler imaging.

A number of models for contrast agents have been developed modifying the free bubble dynamics equation [see, e.g., Leighton (1994), p. 303] for the presence of encapsulation. de Jong and co-workers (de Jong *et al.*, 1992; de Jong and Hoff, 1993; Frinking and de Jong, 1998) initiated systematic contrast agent modeling with one of the first clinically approved agents, Albunex. They assumed the encapsulating shell to be made of a viscoelastic solid, and used lumped parameters in the free bubble equation to model its effects. Church (1995) provided a detailed theoretical model of contrast agents by treating the encapsulating shell as a nanometer thick layer of an incompressible rubbery medium with shear elasticity and viscosity. He demonstrated the sig-

[a)]Electronic mail: sarkar@me.udel.edu

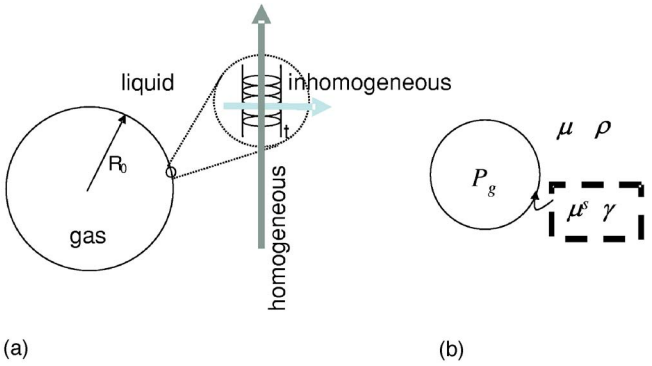

FIG. 1. (a) Schematic of a typical encapsulated bubble; R_0 is the initial bubble radius and t, the thickness of encapsulation. $t \ll R_0$. Due to the presence of molecules, the layer is inhomogeneous in the thickness direction unlike the in-plane directions. (b) The interface model with surface rheology. The gas is modeled as a bulk medium with a uniform gas pressure P_g. The outside liquid is also modeled as a bulk medium with density ρ and viscosity μ. The interface is taken to be a sharp interface of zero thickness, and endowed with intrinsic rheological properties surface viscosity (μ^s) and surface tension (γ).

nificance of the shell parameters by varying them over a wide range, and obtained fundamental and second-harmonic response by a perturbation method, but did not try to experimentally relate the model parameters to any specific contrast agent. Introducing slight compressibility and viscoelasticity of the surrounding liquid in the same model, Khismatullin and Nadim (2002) performed a theoretical analysis to conclude that these effects are less important than that of the encapsulation. Morgan *et al.* (2000) used a modified Herring equation with a similar model for the encapsulation to compare with optical observations obtained by high-speed digital camera.

Biochemical analysis with freeze-etching and SEM observations provides the detail structure of microbubble encapsulation (Christiansen *et al.*, 1994; Myrset *et al.*, 1996; May *et al.*, 2002; El-Sherif and Wheatley, 2003). It consists of a few nanometer thick layer of one or few molecules [Fig. 1(a)], and is therefore neither homogeneous in the thickness direction, nor is it isotropic. The finite thickness model of the microbubble encapsulation proposed by various authors (Church, 1995; Morgan *et al.*, 2000; Khismatullin and Nadim, 2002) containing incompressible materials with homogeneous and isotropic bulk material property therefore might not be appropriate (Evans and Skalak, 1980; Edwards *et al.*, 1991). On the other hand, a molecular model is prohibitively expensive and is not really necessary for describing the acoustic behavior. Chatterjee and Sarkar (2003) have adopted a new interface model [Fig. 1(b)] for the encapsulation that retains continuum character only in the in-plane direction. The model interface is of zero thickness, and assumed to have rheological properties such as *interfacial* tension and surface viscosity (in contrast to *bulk* viscosity and elasticity for the material of existing finite-thickness encapsulation models). The zero thickness assumption is justified in view of the thinness ($\sim$nm) of the encapsulation compared to the bubble radius ($\sim \mu$m). It avoids making any assumptions about the structure along the thickness direction of encapsulation, but the interface rheology captures its essential effects. Such an approach has been used for fluid interfaces with adsorbed surfactants and proteins (Graham and Phillips, 1980), a case very similar to the present one. The validity of any model has to be established by successful comparison with independent experimental observations. To date a comparative investigation into predictive capabilities of different models has not been performed.

Applying a Newtonian viscous rheology for the interface, Chatterjee and Sarkar (2003) have obtained interfacial properties (surface tension $\gamma = 0.9$ N/m, surface dilatational viscosity $\kappa^s = 0.08$ msP) of Optison (GE Healthcare, Princeton, NJ) from attenuation experiments. The model correctly predicted experimentally observed subharmonic emission from Optison measured by Shi *et al.* (1999). However, while one would expect the surface tension value to decrease due to adsorption of surface active materials, $\gamma = 0.9$ N/m determined by matching with experiment is much higher than that (~ 0.07 N/m) of a pure gas–water interface. They ascribed the large surface tension to the inadequacy of the Newtonian model for the encapsulation rheology. In the absence of an explicit surface elasticity term, all elastic effects were lumped in the surface tension term. The observation warrants introduction of a non-Newtonian viscoelastic interfacial rheology for the encapsulation.

In this paper, we develop such a viscoelastic interface model for the encapsulation of a thin-shelled contrast microbubble. We perform an *in vitro* acoustic investigation of contrast agent Sonazoid (GE Healthcare, Oslo, Norway), and apply both Newtonian (viscous) and viscoelastic models to it. Sonazoid (also known as NC100100) consists of fluorocarbon gas microbubbles with a flexible surfactant membrane. The bubble size distribution is relatively narrow with a median diameter of 3.2 μm (Sontum *et al.*, 1999). Sonazoid is a widely studied contrast agent. Recently, possibility of inertial cavitation following Sonazoid bubble destruction was investigated by Shi *et al.* (2000). Moran *et al.* (2002) investigated this agent at an intravascular imaging frequency of 30 MHz. Here, we perform attenuation at different dilutions of Sonazoid. Independently, we measure scattering at various frequencies and amplitudes. We develop interface models for the microbubble encapsulation using two rheologies, and obtain corresponding Rayleigh–Plesset type of equations for bubble radius. We determine the surface parameters using the experimental attenuation data. For comparison, we also compute similar results for the Church's shell model using a formulation appropriate for a thin shell as presented by Hoff *et al.* (2000) [Eq. 6 in their paper; this model hereafter is referred to as Church–Hoff's model]. Using the model parameters, we solve the Rayleigh–Plesset equation to determine the scattered response of the models. Measured fundamental and sub-harmonic scatterings are compared with the numerical model predictions. A detailed comparative study of the various model behaviors and their ability to predict experimental measurement is presented.

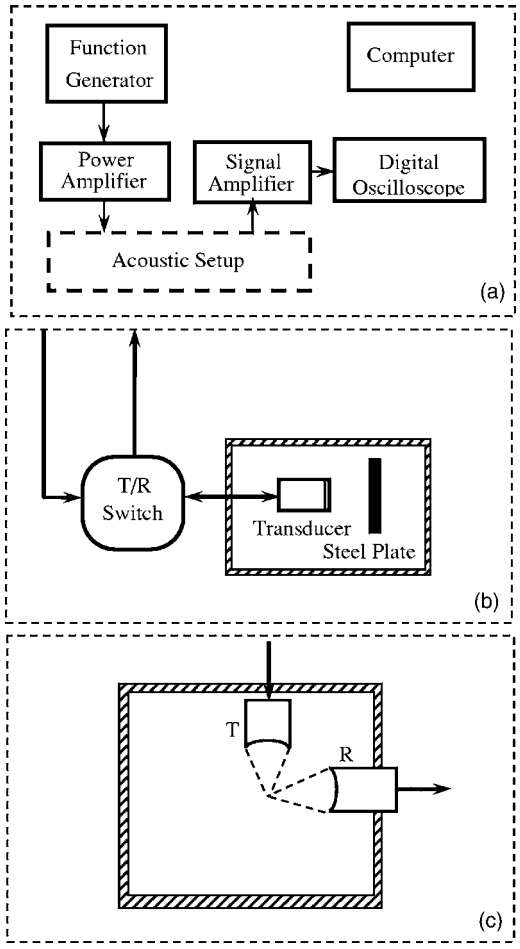

FIG. 2. Experimental setup for measuring attenuation and scattering.

II. EXPERIMENTAL SETUP AND METHOD

A. Experimental setup for measuring attenuation

A pulse-echo system was employed for measuring attenuation of ultrasound in a solution of contrast agent. The block diagrams of its electronic and acoustic arrangements are shown in Figs. 2(a) and 2(b), respectively. A programmable function generator (model 8116A; Hewlett Packard, Santa Clara, CA) produced short pulses at a pulse repetition frequency (PRF) of 10 Hz for transmission. The transmit signals were first amplified in a broadband 50 dB rf power amplifier (model 325LA; ENI, Rochester, NY) [Fig. 2(a)] and then supplied to a single-element broadband flat transducer (Etalon, Lebanon, IN) through an electronic Transmit/Receive switch (model RDX-6; Ritec, Warwick, RI) with a double-mixer range gate [see Fig. 2(b)]. The transducer had a diameter of 12.2 mm, a center frequency of 3.6 MHz, and a bandwidth (6 dB down from maximum) of 98%. A flat stainless steel plate was placed in front of the transducer as an acoustic reflector [Fig. 2(b)]. Reflected ultrasound pulses were received by the same transducer, and the received signals were amplified with a low noise rf amplifier (model 5052 PR; Panametrics, Waltham, MA). The amplified signals were acquired at a sampling frequency of 50 MHz using a digital oscilloscope equipped with mathematical functions (model 9350AM; LeCroy, Chestnut Ridge, NY). For each measurement, 64 sequences of 20 μs scattered signals were taken at the PRF of 10 Hz. An average spectrum of these 64 data sequences was then obtained using a FFT function in the oscilloscope. The average power spectrum was transferred via an IEEE-488 interface to a PowerPC for further analysis. The communication with the function generator and the data transfer from the digital oscilloscope were controlled by LABVIEW® (National Instruments, Austin, TX). The acoustic attenuation of diluted Sonazoid, as a function of frequency, was determined by subtracting the average spectrum prior to injection of the agent from the spectrum obtained after injection. Each attenuation measurement took less than 10 s. Similar attenuation measurement was performed by other investigators (see, e.g., Hoff *et al.*, 2000).

B. Experimental setup for measuring scattering

As shown in Fig. 2(c), an acoustic arrangement with two transducers (transmitter and receiver) was employed. All transducers were single element spherically focused transducers with a diameter of 12.2 mm and a focal length of 2.5 cm. One transducer (R1-4025; Etalon) with a bandwidth of 86% and a center frequency of 3.6 MHz was used as the transmitter [T in Fig. 2(c)] for insonation at frequencies of 2.0, 3.0, 4.4, and 6.0 MHz. The second transducer (C1-4035; Etalon) with a bandwidth of 120% and a center frequency of 6.2 MHz was used as the receiver [R in Fig. 2(c)]. The transmit transducer was positioned confocally at right angle to the receiving transducer. Since contrast microbubbles are much smaller than the acoustic wavelength and undergo volume pulsation in an ultrasound field, scattered signals received at 90° should be very similar to the backscattered echoes (Shi *et al.*, 2000). The advantage of this measurement system is its high spatial resolution. This is because scattered signals only come from the microbubbles in the small overlapping confocal region of the transmitting and receiving transducers.

For each measurement, ultrasound sine-wave tonebursts with 64 cycles were transmitted at a PRF of 10 Hz. A sequence of 64 scattered signals, each of 50 μs duration, was acquired using the LeCroy digital oscilloscope with a sampling frequency of 50 MHz. Acquired data were transferred via an IEEE-488 interface to a PC (Dell, Austin, TX) and processed using a FFT spectrum analyzer with Hamming window in LABVIEW. All spectra of scattered signals were averaged over 64 data sequences. The transient effects are limited only to the initial cycles, and the computed subharmonic response is independent of the pulse length (Shi *et al.*, 1999).

All measurements were carried out at room temperature (around 25 °C). Isoton® II (Coulter, Miami, FL) was utilized as the buffer for the contrast agent solution. It was kept in circulation by a magnetic stirrer. The acoustic output of the transmit transducer was calibrated in water using a 0.5 mm broadband acoustic needle hydrophone (Precision Acoustics, Dorchester, UK).

III. MATHEMATICAL FORMULATION

A. Interfacial rheology models for encapsulation and encapsulated bubble dynamics

The encapsulation of a contrast agent is made of a few layers (often a monolayer) of molecules (Fig. 1). As mentioned in Sec. I, such a layer is not homogeneous in the thickness direction and therefore neither is it isotropic. However, the encapsulation can be considered a macroscopic homogeneous continuum in the other two directions (Evans and Skalak, 1980; Edwards *et al.*, 1991). Due to its much smaller thickness compared to the bubble radius, we assume it to be an interface of infinitesimal thickness. It is endowed with intrinsic interface properties "that represents the effects integrated over the composite molecular structure in the thickness direction" (Evans and Skalak, 1980, p. 2). Biological membranes and fluid interfaces with adsorbed surfactants and proteins (Evans and Skalak, 1980; Edwards *et al.*, 1991; Graham and Phillips, 1980) have been modeled with such an interface. The interface gives rise to interfacial stresses that are to be modeled by interface rheology. The rationale for using zero-thickness interface models is stronger in case of thin-shelled contrast microbubbles. The thickness of the encapsulation is 4 nm for Sonazoid microbubble, whereas its mean diameter is 3.2 μm (Sontum *et al.*, 1999).

A micron size bubble in an acoustic pressure field of 1 MHz (the radius to wavelength ratio is $\sim 10^{-3}$) can be assumed to retain its spherical shape as the pressure varies little over the bubble surface. Substantial shape deformation, e.g., in case of microbubble breakup, is not considered in this model. Assuming spherical symmetry, the mass and momentum conservation equations in the surrounding liquid are

$$\frac{1}{r^2}\frac{\partial}{\partial r}(r^2 v_r) = 0, \tag{1}$$

$$\rho\left(\frac{\partial v_r}{\partial t} + v_r\frac{\partial v_r}{\partial r}\right) = -\frac{\partial p}{\partial r} + \mu\left[\frac{1}{r^2}\frac{\partial}{\partial r}\left(r^2\frac{\partial v_r}{\partial r}\right) - \frac{2v_r}{r^2}\right], \tag{2}$$

where v_r is the radial component of velocity, ρ the liquid density, p the pressure, and μ is the liquid viscosity. Note that incompressibility is assumed for the surrounding liquid. Effects of liquid compressibility and viscoelasticity have been investigated by Khismtullin and Nadim (2002) by a matched asymptotic technique and found to be small. We also examined the effects of compressibility on the characterization (see Sec. IV). From mass conservation (1), the radial velocity in the liquid is readily obtained as that due to a potential source:

$$v_r = \dot{R}R^2/r^2, \tag{3}$$

where R is the radius of the bubble. Note that the velocity being irrotational, the viscous terms vanish identically. Using Eq. (3), Eq. (2) can be integrated to give at $r=R$,

$$\rho\left(R\ddot{R} + \frac{3}{2}\dot{R}^2\right) = p_{r=R} - p_\infty, \tag{4}$$

where $p_{r=R}$ is the pressure in the liquid immediately outside the bubble, and p_∞ is the liquid pressure far away:

$$p_\infty = P_0 - p_A(t), \tag{5}$$

P_0 is the liquid hydrostatic pressure and $p_A(t)$ is the excitation pressure. The dynamic boundary condition at the bubble interface relates the pressure $p_{r=R}$ to the bubble dynamics.

1. Newtonian interfacial rheological model

The dynamic condition at the interface $r=R$ can be obtained by considering the force balance in a thin lamina containing the segment of the interface. Similar to the flow in the bulk, one can model the stresses at an interface by a constitutive equation. For a Newtonian interfacial rheology, the surface extra stress and the jump in the bulk viscous stress across the interface arising from the force balance are (Edwards *et al.*, 1991, p. 109)

$$\begin{aligned} &\tau_s = \gamma I_s + (\kappa^s - \mu^s)(I_s{:}D_s)I_s + 2\mu^s D_s, \\ &[\tau\cdot\mathbf{n}]_{\text{surface}} = \nabla_s\cdot\tau_s, \end{aligned} \tag{6}$$

where γ is the surface tension, κ^s and μ^s are interfacial dilatational and shear viscosities, I_s and D_s are the surface identity and surface strain rate tensors (Edwards *et al.*, 1991). The center dot represents a scalar product between two second-order tensors. The motion inside the bubble is neglected, and a spatially uniform interior pressure $P_G(t)$ is assumed. One can use the radial part of the jump condition (6) to obtain (see Edwards *et al.*, 1991, p. 114)

$$\begin{aligned} \left(-p + 2\mu\frac{\partial v_r}{\partial r}\right)_{r=R} + P_G &\equiv -p_{r=R} - 4\mu\frac{\dot{R}}{R} + P_G \\ &= \frac{2\gamma}{R} + \frac{4\kappa^s\dot{R}}{R^2}. \end{aligned} \tag{7}$$

For a free bubble, dilatational viscosity κ^s, which arises due to the encapsulation, is zero, and γ is at its clean surface value. The surface shear viscosity does not appear due to the spherical symmetry of the dynamics. The (dilatational) viscous term can be explained by noting that the bubble undergoes area dilation at a rate $A^{-1}dA/dt = 2\dot{R}/R, (A = 4\pi R^2)$. It results in a uniform tension of magnitude $2\kappa^s\dot{R}/R$ in Eq. (7), in addition to the surface tension γ. In an undisturbed condition (zero motion), using $p_{r=R} = P_0$ [see Eqs. (4) and (5), from Eq. (7) we obtain the initial gas pressure inside the bubble:

$$P_{G0} \equiv P_G(t=0) = P_0 + \frac{2\gamma}{R_0}, \tag{8}$$

where R_0 is the initial radius. Note that P_{G0} is not in equilibrium with the outside pressure P_0. In fact for a micron radius, the inside bubble pressure could be significantly higher depending on surface tension, leading to quick dissolution due to gas diffusion (Epstein and Plesset, 1950; Kabalnov et al., 1998; Chen et al., 2002). For this model the stability of the microbubble has to depend on the low solubility of the gas in the surrounding liquid, and more importantly on the low permeability of the encapsulation, making it an effective barrier to gas diffusion.

With the Newtonian rheology, the encapsulation is purely viscous characterized by γ and κ^s. As we saw in the case of Optison (Chatterjee and Sarkar, 2003), and also will see in the following, such a model for the encapsulation results in an unusually high value for surface tension. Adsorption of small amount of surface active materials leads normally to a reduction in surface tension from its value at a clean interface. At low surface concentrations, the adsorbed molecules behave like a perfect gas; their random motion leads to an osmotic pressure acting against the surface tension. The surface tension reduction can be modeled by Gibb's adsorption isotherm that is identical to the perfect gas law (Edwards *et al.*, 1991, p.25). However, in an encapsulation the molecules are at a high concentration and closely packed, with a strong attractive interaction between them, making the "ideal gas" law invalid. Due to the attractive interaction, any change in area will lead to an elastic force, a phenomenon commonly known as Gibb's elasticity [see Evans and Skalak (1980), pp. 80 and 86 and Edwards *et al.* (1991), pp. 118 and 172]. A Newtonian constitutive equation assumes that the deviatoric part of stress is entirely of viscous origin and has only an isotropic surface pressure term, namely the surface tension (Kralchevsky and Nagayama, 2001, p. 158). While fitting the experimental observation, all elastic effects get lumped into it, generating the high value. The resulting mechanical surface tension is significantly different from its thermodynamic value, and can alternately be interpreted as an effective parameter to represent all "elastic" effects (usual thermodynamic tension in the surface as well as dilatational elasticity arising from fractional increase in area over unstressed configuration) of the shell.

2. Viscoelastic interfacial rheological model

The above observation indicates the need for a viscoelastic rheology with explicit surface elasticities. Edwards *et al.* (1991, p.118) has shown that dilatational surface elasticity or Gibb's elasticity can also be treated as effects arising from surface tension gradients. Accordingly, the dilatational elasticity E^s is introduced as

$$E^s = \left(\frac{\partial \gamma}{\partial \alpha}\right)_{\beta=0}, \quad \gamma = \gamma_0 + E^s \beta, \tag{9}$$

where $\beta = \delta A/A = [(R/R_E)^2 - 1]$ is the fractional change in area from *equilibrium* that represents an unstrained equilibrium condition (denoted by unstrained radius R_E). γ_0 is the reference surface tension at zero area change. Note that in our Newtonian (purely viscous) approach the dynamics does not have such a reference unstrained state. A note of caution is warranted for the terminology. Edwards et al. (1991, p.118) states that because dilatational elasticity can be treated as a surface tension gradient effect, "such elastic behavior does not necessarily violate Newtonian model of interfacial rheological behavior." However, for clarity, we call the model with dilatational elasticity non-Newtonian or viscoelastic, and the one without explicit elasticity Newtonian. Evans and Skalak (1980, p.80) offered a similar model for membrane surface elasticity (they called E^s the area compressibility modulus). With the modification to surface tension γ, the dynamic boundary condition (7) at $r=R$ becomes

$$p_{r=R} = P_G - 4\mu\frac{\dot{R}}{R} - \frac{4\kappa^s \dot{R}}{R^2} - \frac{2\gamma_0}{R} - \frac{2E^s}{R}\left[\left(\frac{R}{R_E}\right)^2 - 1\right]. \tag{10}$$

At the initial zero motion state, the inside pressure satisfies

$$P_{G0} = P_0 + \frac{2\gamma_0}{R_0} + \frac{2E^s}{R_0}\left[\left(\frac{R_0}{R_E}\right)^2 - 1\right]. \tag{11}$$

In contrast to the Newtonian rheology [see Eq. (8)], we assume an *equilibrium of pressure* inside and outside the bubble $P_{G0}=P_0$, that ensures stability of microbubbles, even if the encapsulation is permeable to the gas. Imposing pressure equilibrium, we obtain the equilibrium radius

$$R_E = R_0\left(1 - \frac{\gamma_0}{E^s}\right)^{-1/2}.$$

Note that the initial radius is strained (smaller than R_E). The resulting compressive stress balances the stress due to surface tension giving rise to the pressure equilibrium.

3. Encapsulated bubble dynamics

The gas pressure inside the bubble is assumed to vary with bubble volume polytropically with k as the polytropic exponent as follows (Leighton, 1994, p.11):

$$P_G R^{3k} = P_{G0} R_0^{3k}. \tag{12}$$

P_{G0} is the gas pressure and R_0 is the initial radius. We have chosen $k=1$, corresponding to an isothermal gas behavior inside the bubble; the bubble size is too small compared to the thermal diffusion length in the time scale ($\sim 10^{-6}$ s) of oscillation (Hilgenfeldt et al., 1998). Models of heat transfer inside bubbles due to Devin (1959) and Eller (1970) indicate k to be close to unity [$\sim$1.006; see Hoff et al. (2000), their Eq. (21a)]. For the liquid–gas system, using Eqs. (5) and (10) in Eq. (4) we obtain the modified Rayleigh–Plesset equation

$$\rho\left(R\ddot{R} + \frac{3}{2}\dot{R}^2\right) = P_{G0}\left(\frac{R_0}{R}\right)^{3k} - 4\mu\frac{\dot{R}}{R} - \frac{4\kappa^s\dot{R}}{R^2} - \frac{2\gamma_0}{R} - \frac{2E^s}{R}\left[\left(\frac{R}{R_E}\right)^2 - 1\right] - P_0 + p_A(t) \tag{13}$$

for the viscoelastic interfacial rheology. Replacing Eq. (10) by Eq. (7), we obtain a similar equation for the Newtonian rheology:

$$\rho\left(R\ddot{R} + \frac{3}{2}\dot{R}^2\right) = P_{G0}\left(\frac{R_0}{R}\right)^{3k} - 4\mu\frac{\dot{R}}{R} - \frac{4\kappa^s\dot{R}}{R^2} - \frac{2\gamma}{R} - P_0 + p_A(t), \tag{14}$$

where the dilatational elasticity term is absent ($E^s=0$), and the surface tension term involves γ instead of γ_0. Equation (13) or (14) together with the initial conditions $R(t=0)=R_0$,

and $\dot{R}(t=0)=0$ describes the bubble dynamics. We conclude that (γ, κ^s) characterize a Newtonian rheology and $(\gamma_0, E^s, \kappa^s)$ a viscoelastic rheology for the encapsulation. The second order differential equation (13) or (14) is solved using a stiff solver routine of MATLAB® (Mathwork Inc, Natick, MA).

The acoustic pressure $P_s(t)$ scattered by a bubble is (Brennen 1995, p. 83) with the assumption of incompressibility for the surrounding liquid:

$$P_s(r,t) = \rho \frac{R}{r}(2\dot{R}^2 + R\ddot{R}). \tag{15}$$

The corresponding scattering cross section is given by

$$\sigma_s(t) = \frac{\langle r^2 P_s(t)^2 \rangle}{P_A^2}, \tag{16}$$

where the angular brackets indicate an average over a time period. Different frequency components, e.g., harmonic or subharmonic, of the scattered signal are determined by transforming the expression into frequency domain.

B. Determination of interfacial rheological parameters

The encapsulation models have unknown parameters, such as interfacial tension γ (or γ_0), dilatational viscosity κ^s, or dilatational elasticity E^s, as evident from bubble dynamics equations (13) or (14). Interfacial tension differs from its value for a pure gas–liquid interface by the presence of surfactants. The model parameters are phenomenological in nature, and must be determined experimentally. A linearized equation of motion is applied for determination purposes, by restricting the attenuation experiments to small amplitude oscillations (i.e., low excitation). The measured attenuation and scattering are integrated effects of a bubble distribution, and are difficult choices for obtaining individual bubble characteristics. Such inverse processes of parameter estimation are notorious for their ill-posed nature. We found that the linearization provides an easy and robust algorithm for the parameter determination. We also assume that the material parameters in a proper physical model are independent of the type of experiments, i.e., attenuation or scattering, and remain constant over a range of excitation frequency and amplitudes. The medical imaging is restricted to a range of frequency (~1–10 MHz), and one is justified in assuming reasonably constant properties in this frequency range. However, interface properties could vary significantly with excitation amplitudes (see Sec IV).

We assume a harmonic excitation $p_A(t)=P_A \sin(\omega t)$, where $\omega=2\pi f$ with f being the driving frequency, and P_A the acoustic pressure amplitude. For small oscillation $R=R_0+X$, one can linearize Eq. (13) or (14) in X to obtain a damped simple harmonic oscillator:

$$\ddot{X} + \frac{\dot{X}}{\rho R_0^2}\left(4\mu + \frac{4\kappa^s}{R_0}\right) + \frac{X}{\rho R_0^2}\left(3kP_0 - \frac{4\gamma_0}{R_0} + \frac{4E^s}{R_0}\right) = \frac{P_A}{\rho R_0}\sin \omega t, \tag{17}$$

or

$$\ddot{X} + \frac{\dot{X}}{\rho R_0^2}\left(4\mu + \frac{4\kappa^s}{R_0}\right) + \frac{X}{\rho R_0^2}\left[3kP_0 + \frac{2\gamma}{R_0}(3k-1)\right] = \frac{P_A}{\rho R_0}\sin \omega t, \tag{18}$$

respectively, for viscoelastic and Newtonian models. The corresponding resonance frequencies are

$$\omega_0^2 = \frac{1}{\rho R_0^2}\left(3kP_0 - \frac{4\gamma_0}{R_0} + \frac{4E^s}{R_0}\right),$$
$$\omega_0^2 = \frac{1}{\rho R_0^2}\left[3kP_0 + \frac{2\gamma}{R_0}(3k-1)\right]. \tag{19}$$

Note that the expression for resonance frequency in case of Newtonian rheology is the same as that of a free bubble (see Leighton, 1994, p. 183). The damping term is the same for both models and has an additional interface term compared to the free bubble case (Hoff *et al.*, 2000; Medwin, 1977):

$$\delta_{\text{total}} = \delta_{\text{liquid}} + \delta_{\text{interface}} + \delta_{\text{radiation}}, \quad \delta_{\text{liquid}} = \frac{4\mu}{\rho\omega_0 R_0^2},$$
$$\delta_{\text{interface}} = \frac{4\kappa^s}{\rho\omega_0 R_0^3}, \quad \delta_{\text{radiation}} = \frac{\omega^2 R_0}{\omega_0 c}. \tag{20}$$

Note that we have assumed the surrounding liquid to be incompressible, and thereby do not obtain the radiation damping terms in Eq. (17) or (18). However, including it by the standard prescription (20) does not change the parameter values significantly. The extinction cross section $\sigma_e^{(l)}$ for the linearized dynamics is

$$\sigma_e^{(l)} = 4\pi R_0^2 \frac{c\,\delta_{\text{total}}}{\omega_0 R_0} \frac{\Omega^2}{[(1-\Omega^2)^2 + \Omega^2 \delta_{\text{total}}^2]}, \tag{21}$$

where $\Omega=\omega/\omega_0$ and c is the sound speed in surrounding liquid [see, e.g., Sarkar and Prosperetti (1994)].

The power absorbed and scattered by microbubbles in frequency domain leads to attenuation $\alpha(\omega)$ in dB/distance

$$\alpha(\omega) = 10 \log_{10} e \int_{a_{\min}}^{a_{\max}} \sigma_e(a;\omega) n(a) da, \tag{22}$$

where e is the base of natural logarithm, $n(a)da$ is the number of bubbles per unit volume with radius in $(a, a+da)$, and $a_{\max(\min)}$ is the maximum (minimum) value of the range of bubble radii. For the case of N bubbles per unit volume of a uniform size the integral simplifies to $N\sigma_e$. Sonazoid has a relatively narrow size distribution with an average diameter of 3.2 μm and number concentration of 0.78×10^9/ml [Sontum et al. (1999), see also Hoff (2000)]. Notice that $\alpha(\omega)$ is a function of the unknown bubble parameters (γ, κ^s) or $(\gamma_0, E^s, \kappa^s)$. The experimental measurement of attenuation over a range of frequencies $\alpha^{\text{meas}}(\omega)$ is used to define an error $\text{Er}(\gamma, \kappa^s)$ or $\text{Er}(\gamma_0, E^s, \kappa^s)$:

$$\mathrm{Er}(\gamma, \kappa^s, \ldots) = \sum_i [\alpha(\omega_i) - \alpha^{\mathrm{meas}}(\omega_i)]^2. \quad (23)$$

The error is minimized to obtain the bubble parameters. MATLAB was used to execute the error minimization. The uncertainty in the estimated parameters is determined by finding the range for which the error residual reaches its minimum value. Similar method is used by previous authors for obtaining model parameters (e.g., Chatterjee and Sarkar, 2003; Hoff *et al.*, 2000).

C. Liquid compressibility and bubble breakup

We have neglected liquid compressibility in our model as did several other research groups (Church, 1995; de Jong *et al.*, 1992; de Jong and Hoff, 1993). To investigate the compressibility effect, we implemented a Keller–Herring type model to find that the model parameters do not vary substantially (see Sec. IV). For brevity, we omitted here a detailed description of the compressible model. Khismatullin and Nadim (2002) have also found that the compressibility and viscoelasticity of the surrounding liquid do not play significant role in the bubble dynamics. Prosperetti (1984) has discussed the suitability of different models of bubble dynamics in case of free bubbles. He has shown that for low Mach Numbers (based on bubble wall velocity) all models with and without compressibility work equally well. Contrast microbubbles are much stiffer compared to a free bubble of the same size, thereby significantly restricting bubble wall motion except at violent collapse. Sboros *et al.* (2002) have observed that at higher amplitudes of excitation incompressible Rayleigh–Plesset model does not perform well (see Sec IV). After determining the properties of Sonazoid, our numerical computation shows that the highest Mach number attained is less than 0.3, except for rare extreme cases, further justifying the assumption of incompressibility. The encapsulation of a contrast microbubble may rupture at high acoustic pressure amplitude, an effect not accounted for in our model.

IV. RESULTS AND DISCUSSION

A. Attenuation measurement and characterization

As was mentioned before, we take Sonazoid as a test case of available ultrasound contrast agent. Attenuation measurement for varying concentration of Sonazoid is shown in Fig. 3(a). The peak attenuation plotted against concentration in Fig. 3(b) displays a linear increase indicating that individual contributions of bubbles are additive, and interactions between them negligible [the void fraction of microbubbles is $\sim 10^{-6}$, which is too small for interaction, Commander and Prosperetti (1989)]. The method outlined in Sec. III B was used to determine interfacial properties for Sonazoid based on the experimental data (for the highest attenuation) of Fig. 3.

Figure 4 shows the Newtonian and viscoelastic models fitted to the experimentally measured attenuation. In the same figure, we also present the curve fit for the Church–Hoff model [Hoff *et al.* (2000); Eq. (6) in their paper] that assumes a 4-nm-thick layer of rubbery incompressible material. The encapsulation material in this model is characterized by a bulk shear modulus G_s, and a shear viscosity μ_s. The parameters determined for each model are presented in Table I. For the viscoelastic model, uncertainty range in γ_0 is not provided, because its variation leads to little change in the residual. Introducing compressibility in the Newtonian

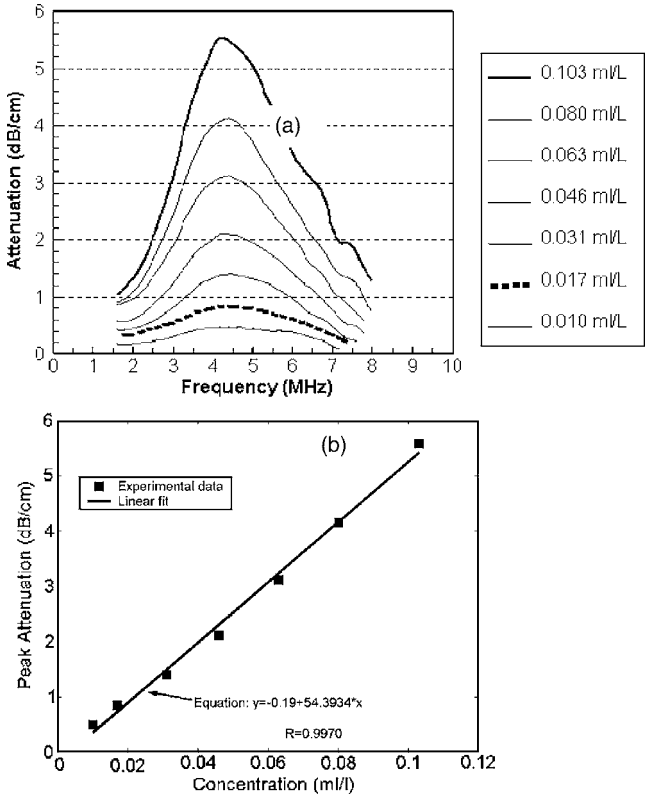

FIG. 3. (a) Attenuation at different concentrations of Sonazoid with one-cycle 5 MHz insonation. The experiments were conducted around 2 min after injections of 0.103, 0.080, 0.063, 0.046, 0.031, 0.017, 0.010 ml/l of Sonazoid in Isoton II (from top to bottom). (b) Variation of peak attenuation with concentration showing the linearity of attenuation with concentration.

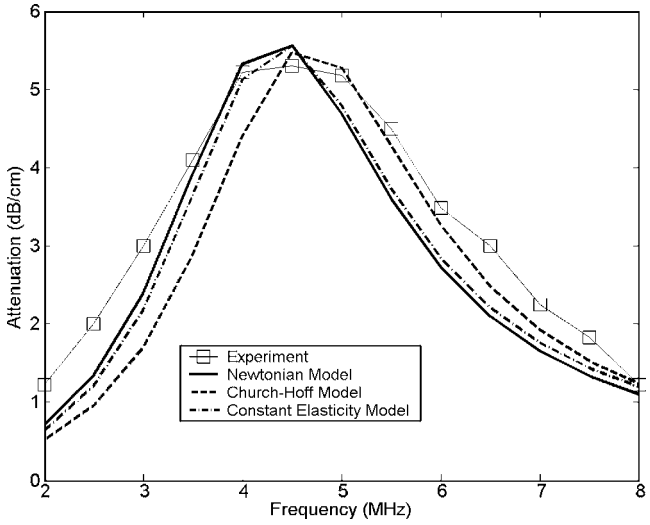

FIG. 4. Determination of the interface (Newtonian and viscoelastic models) and shell (in case of Church–Hoff's model) parameters corresponding to Sonazoid bubbles. Data correspond to a concentration of 0.103 ml/l of Sonazoid in Isoton-II.

TABLE I. Values of parameters estimated for Sonazoid using three different models.

	Newtonian model		Church–Hoff model		Constant elasticity model		
	$\kappa^s(msP=10^{-6}$ Ns/m)	γ(N/m)	G_s(MPa)	μ_s(Pa s)	$\kappa^s(msP=10^{-6}$ Ns/m)	γ_0(N/m)	E^s(N/m)
Mean	0.01	0.6	52	0.99	0.01	0.019	0.51
Range (about mean)	±0.0038	±0.14	±10	±0.3	±0.0038	…	±0.11

model resulted in $\kappa^s=0.012$ msP and $\gamma=0.54$ N/m, not substantially different from their incompressible counterparts. It may be noted that the values obtained for Church–Hoff model are close to those obtained by Hoff (2000).

The values of κ^s are similar to those obtained for other surfactant-laden interfaces [see e.g., Edwards *et al.* (1991), p. 241]. However, γ for the Newtonian model is an order of magnitude higher than that at the gas–water interface (at an air–water interface $\gamma=0.072$ N/m), a result very similar to what we obtained for contrast agent Optison (Chatterjee and Sarkar, 2003). As explained in Sec. III, the high value is a result of the Newtonian model with no explicit elastic term. The elastic contributions are all lumped into the surface tension. The interfacial parameters obtained with the viscoelastic interfacial rheology (containing an explicit dilatational elasticity term) substantiates this explanation. With this model we get $\gamma_0=0.019$ N/m, a value lower than that at the air–water interface. Note that the surface dilatational viscosity κ^s remains the same in these two interface models, as it should if the property represents a physical nature of the encapsulation and not just a mathematical fitting constant. Also surface tension γ in the Newtonian model is indeed a combination of surface tension and dilatational elasticity of the viscoelastic model—$\gamma_{\text{viscous}} \simeq (\gamma_0+E^s)_{\text{viscoelastic}}$. Parameters for three different models are obtained by fitting their linearized versions with the experimentally observed attenuation. In the following, we provide a detailed comparative study of these model behaviors and their ability to predict measurements from a different experiment, viz. scattering.

B. Experimental measurements of scattered fundamental and subharmonic emissions

We measure scattering of ultrasound through solution of Sonazoid at different driving frequencies and pressure amplitudes, and investigate fundamental [Fig. 5(a)] and subharmonic [Fig. 5(b)] scattered responses. The fundamental response increases linearly with exciting acoustic pressure for lower pressures, but saturates at higher pressures (e.g., above 0.6 MPa for 2 MHz insonation). Furthermore, it decreases with increasing excitation frequency. The saturation in fundamental response is due to the nonlinear energy transfer into other frequencies at higher excitations, as well as possible breakup.

Figure 5(b) shows that a subharmonic response roughly has three different regimes with increasing pressure amplitudes—initial slow increase, rapid growth, and saturation. It may be pointed out that similar trends were also observed in the case of Optison (Shi *et al.*, 1999). During initiation, the subharmonic component is insignificant (near the noise level, e.g., for pressures less than 0.3 MPa at 6 MHz insonation). During growth, the subharmonic response increases rapidly with the acoustic pressure, and usually has amplitudes much above the background noise. As the acoustic pressure increases further (e.g., 0.8 MPa for 6 MHz insonation), the growth of the subharmonic component saturates. At this stage, the variation in the data is substantially high possibly indicating chaotic response due to inertial cavitation (Shi *et al.*, 1999; also see Prosperetti, 1975; Apfel and Holland, 1991) Note that the first two regimes roughly coincide with the linear growth of the fundamental response in Fig. 5(a). For higher frequencies, the initiation of growth is

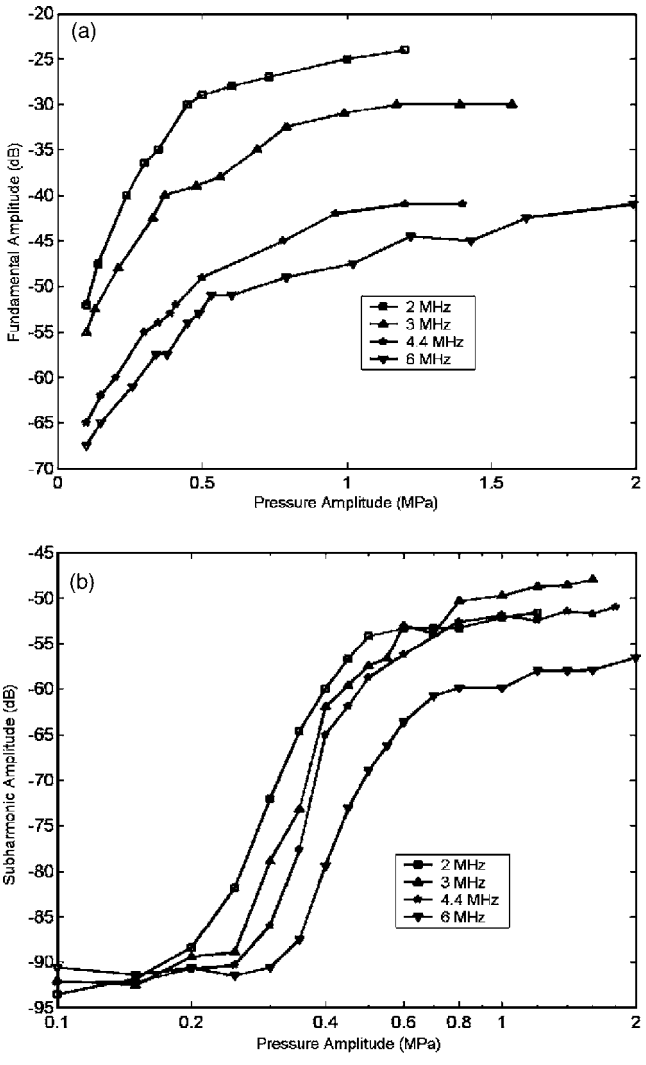

FIG. 5. Scattered fundamental (a) and subharmonic (b) response of Sonazoid vs transmitted acoustic pressure amplitudes at different insonication frequencies. Averaged values of four data sets were used for 2.0 MHz insonication and averaged values of eight data sets were used for 3.0, 4.4, and 6.0 MHz insonication.

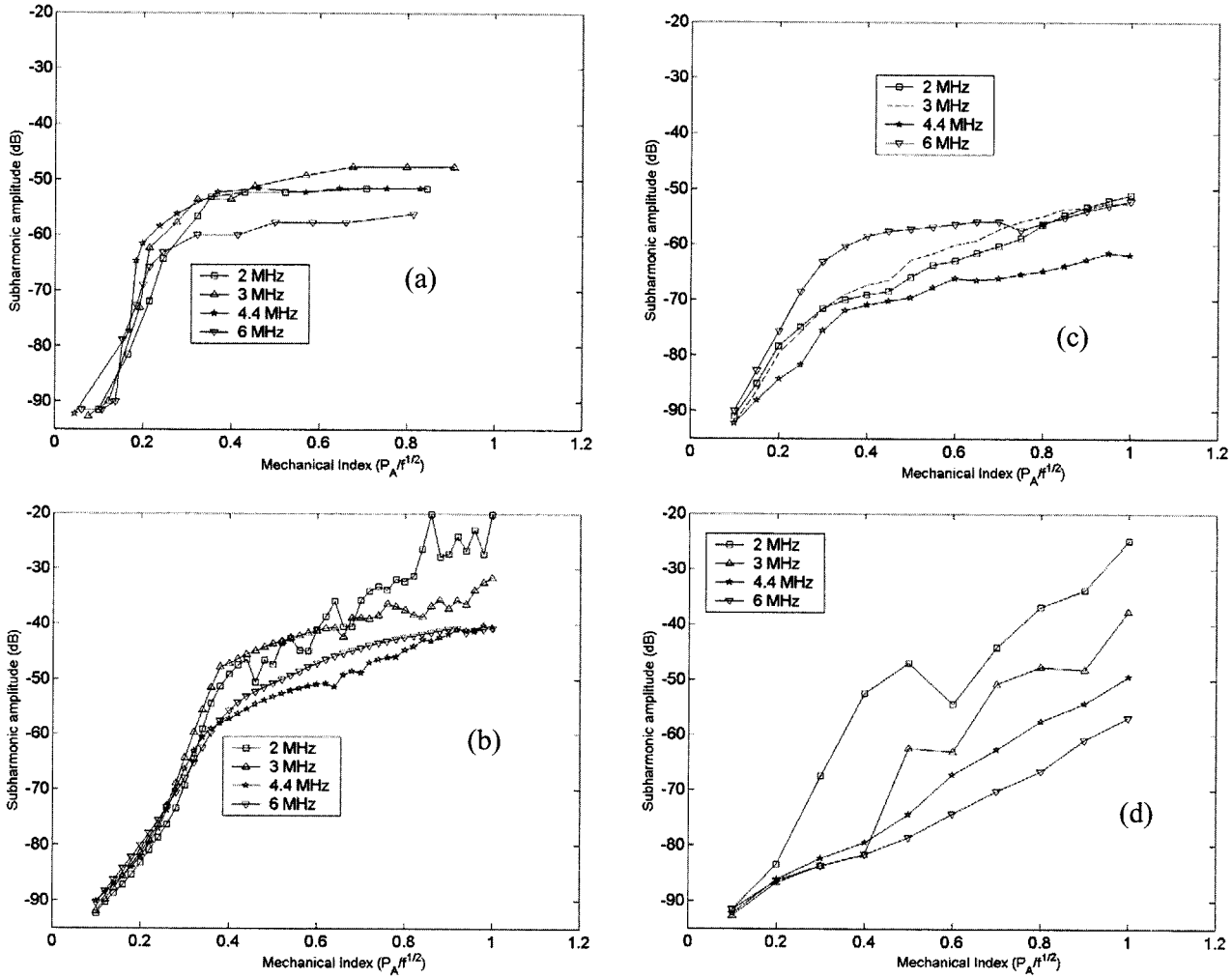

FIG. 6. (a) Subharmonic response against MI. (a) Experimental data [as presented in Fig. 5(b)], (b) simulation with Newtonian viscous model, (c) with Church–Hoff model, and (d) with viscoelastic model.

progressively delayed, and the subharmonic response is decreased. In case of a free bubble, a similar sharp initiation is observed for subharmonic response in contrast to superharmonic responses, which show continuous and gradual increase with pressure amplitudes (Eller and Flynn, 1969). Mechanical index MI=$P_A/f^{1/2}$ [P_A, the pressure amplitude measured in MPa and frequency (f) in MHz] is often used as a criterion for cavitation (Apfel and Holland, 1991). On the other hand detectable subharmonic response has been suggested as an experimental signature of cavitation (Prosperetti, 1975). Note that MI is a rough estimate of the energy of the excitation as well. One would therefore expect the subharmonic response to correlate with MI. In Fig. 6(a), we plot the subharmonic response for different frequencies as a function of MI. Such a rescaling of pressure with $f^{1/2}$ shows a collapse of the data for different frequencies at least in the rapid growth region [Fig. 6(a)]. However, the scaling is poor in the saturation region.

C. Model predictions and comparison of fundamental and subharmonic scattering

We use Rayleigh–Plesset equation (13) or (14) with model parameters determined by the procedure described in Sec. III B to simulate microbubble dynamics. The far-field scattering is computed from the time evolution of bubble radius using Eq. (16) followed by extraction of fundamental and subharmonic responses using FFT. They are compared to experimental observations. The simulation is scaled to match the experimental data for the lowest pressure level. Note that the model parameters were determined using attenuation with a linearized equation valid only for small oscillations. The underlying assumption is that the determined material properties retain their validity for different types of experiments (scattering or attenuation), and also remain constant in a range of magnitude of oscillation (they may change for large oscillation leading to, e.g., shear rate dependent interface viscosity/elasticity and interfacial tension).

In Figs. 6(b), 6(c), and 6(d) we plot the scattered subharmonic response with MI predicted by the Newtonian, Church–Hoff, and viscoelastic models. We find that the Newtonian model performs the best among three in capturing the observed collapse in Fig. 6(a) of subharmonic response for different frequencies. Next we perform a detailed comparison between observed scatterings at different frequencies and corresponding predictions of the three models—Fig. 7 for fundamental and Fig. 8 for subharmonic emissions. All mod-

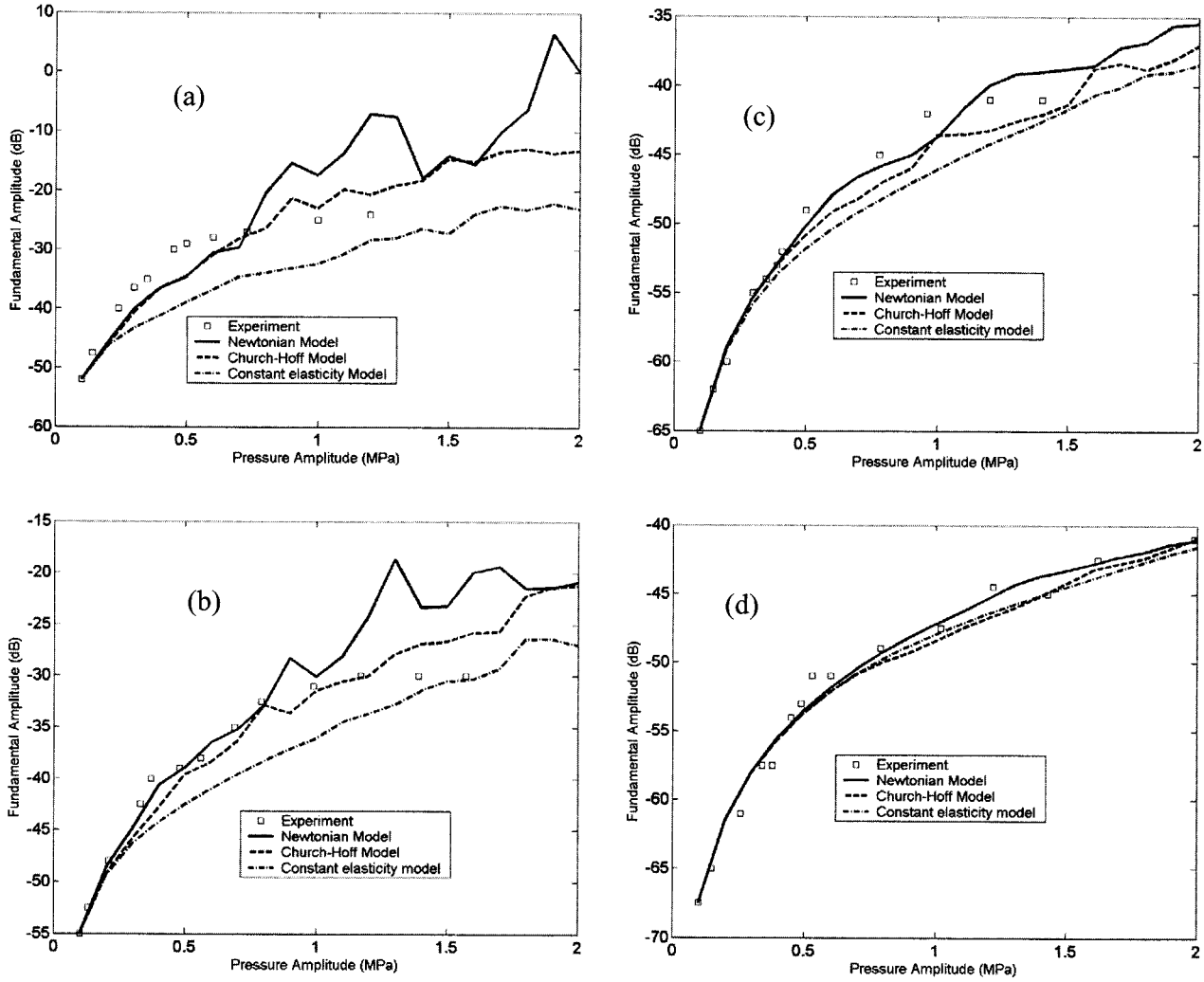

FIG. 7. Predicted and measured first harmonic response for Sonazoid at various insonation frequencies: (a) 2 MHz, (b) 3 MHz, (c) 4.4 MHz, and (d) 6 MHz.

els show fundamental response increasing with the acoustic pressure in keeping with the experiment. The Newtonian and the Church–Hoff models perform marginally better than the viscoelastic one. For the subharmonic data (Fig. 8), the Newtonian model provides the best match with experiment except at the highest frequency, 6 MHz, where Church–Hoff model predicts better than the other two. For all frequencies, the viscoelastic model predicts much less scattering than has been observed. Note that all models are fitted with a linear analysis and with a low amplitude attenuation data. The relative failure of the viscoelastic model at higher excitation might result from a very stiff encapsulation with a large surface dilatational elasticity. However, at higher excitations when bubble experiences larger excursion of the bubble surface, the encapsulation might "soften" with a far lower value of surface dilatational elasticity, not included in the model. One could incorporate a softening in the elasticity (by assuming, e.g., a nonlinear dilatational elasticity) to account for that. Note that the Newtonian model even with a high surface tension term (dilatational elasticity and interfacial tension lumped into one) predicts subharmonic response very well. The bubble dynamics with Newtonian (14) and viscoelastic (13) rheologies are remarkably similar, except for the elastic terms (surface tension and surface dilatational elasticity); they are matched and thereby produce the same results at small excitations. However, at higher excitations the Newtonian model (14) is far less stiff than the other one. Figures 6–8 show that all models display fine structures for some frequency values in their predictions especially for stronger excitations absent in their experimental counterparts. The structures are signatures of "near-chaotic" response in the bubble dynamics equations. Note that for strong excitations, the bubbles experience nonspherical oscillations, inertial cavitation, and possible breakup not included in any of the models considered here.

V. SUMMARY

We have presented a procedure to characterize encapsulated microbubble based ultrasound contrast agent through controlled *in vitro* attenuation and scattering experiments and analytical models. We applied it to contrast agent Sonazoid (GE Healthcare; Oslo, Norway) using three models for the bubble encapsulation. We have developed zero-thickness interface models with their intrinsic interfacial rheology. Here we presented two different rheological models-(1) *Newton-*

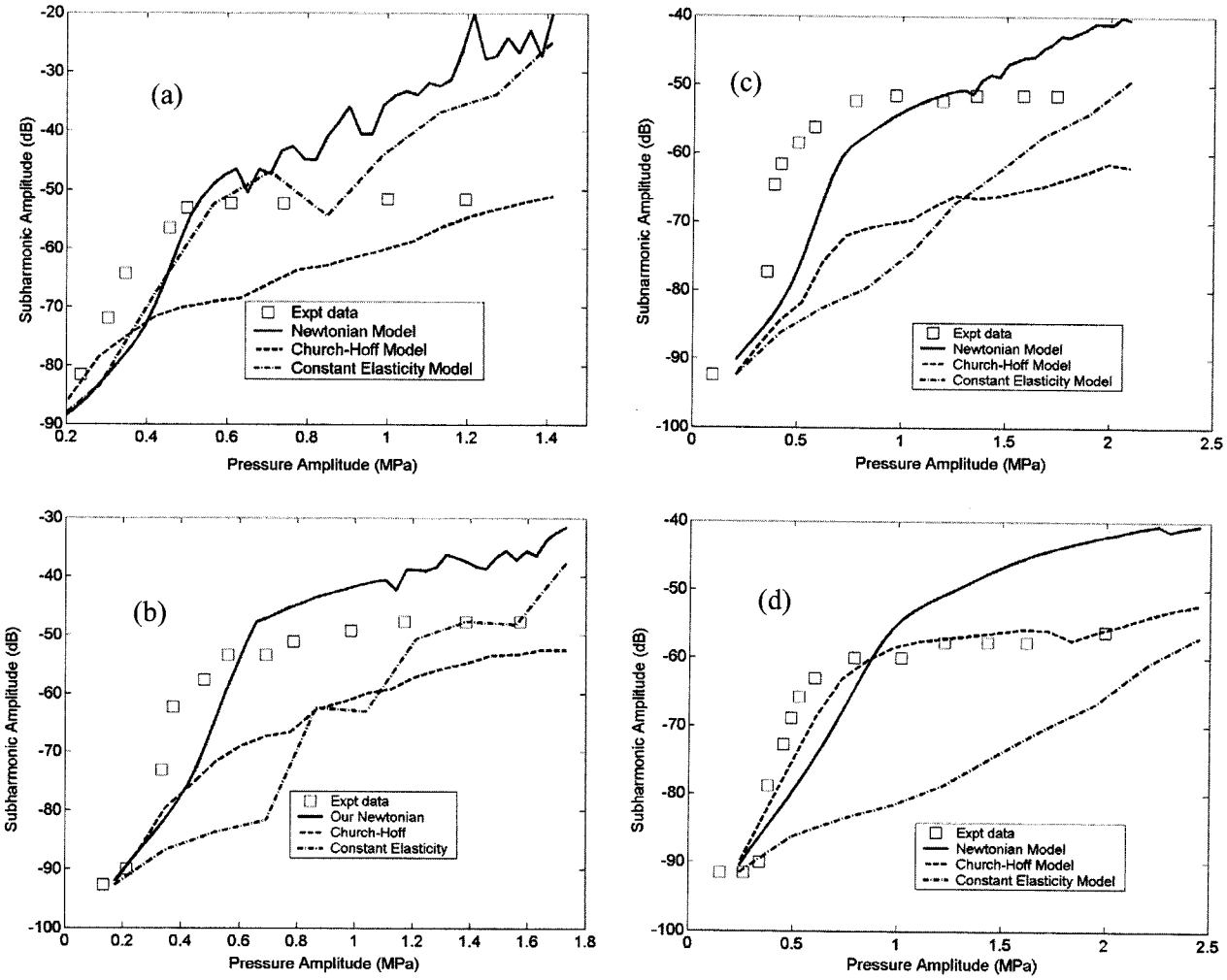

FIG. 8. Predicted and measured subharmonic response for Sonazoid at various insonation frequencies: (a) 2 MHz, (b) 3 MHz, (c) 4.4 MHz, and (d) 6 MHz.

ian (surface tension γ, dilatational surface viscosity κ^s) and (2) *viscoelastic* (surface tension γ_0, surface dilatational viscosity κ^s, and surface dilatational elasticity E^s). The rheological properties for the models were determined by comparing predictions of a linearized dynamics with attenuation measured at small excitations. The characteristic rheological properties for Sonazoid were $\gamma=0.6$ N/m, $\kappa^s=0.01$ msP($=10^{-6}$ Ns/m) for the Newtonian model. The abnormally high value of the interfacial tension motivated our viscoelastic model. The viscoelastic model results in $\kappa^s=0.01$ msP, $\gamma_0=0.0190$ N/m, a value indeed much lower than that (~ 0.07 N/m) at the air–water interface, and $E^s=0.51$ N/m. The value of dilatational viscosity remains the same for both models. For comparison, we also implemented a model due to Church (Church, 1995; Hoff *et al.*, 2000) that assumes a layer of finite thickness (4 nm) containing rubbery incompressible material for the encapsulation. It is characterized by bulk material properties (shear modulus G_s, and shear viscosity μ_s). For Sonazoid properties are $G_s=52$ MPa and $\mu_s=0.99$ Pa s.

We measured scattered fundamental and subharmonic responses from a Sonazoid solution at different frequencies and amplitudes of excitation, and compared them with predictions of the three models considered. For all frequencies, the fundamental response grows linearly for small values of excitations before slowing down at higher values, a feature matched well by all three models. The measured subharmonic emission displayed rapid growth beyond a critical pressure amplitude. The growth region of subharmonic emission scales with $P_A/f^{1/2}$, i.e., the mechanical index (MI). The resulting collapse of subharmonic response with MI for various frequencies is captured well only by the Newtonian model. The performance of the Newtonian model is better than the other two in matching the subharmonic response for most frequencies. The viscoelastic model consistently underpredicted the subharmonic response at all frequencies. We surmise that the high value of surface dilatational elasticity determined using the linear analysis of the low amplitude attenuation data has made a stiff encapsulation resulting in a lower response at higher excitation. A "softening" of the encapsulation by assuming a surface dilatational elasticity constant that decreases with fractional area increase can be a possible remedy. The comparative investigation delineates predictive capability of the three models for experimental responses that are different from those used to obtain the parameters. Further model development and their applications to other contrast agents will be the subject of future work.

ACKNOWLEDGMENTS

The authors acknowledge support from DOD Contract No. DAMD17-03-1-0119. K.S. acknowledges University of Delaware Research Foundation and NSF Contract No. CTS-0352829. K.S. also acknowledges editorial help from Pankaj Jain.

Apfel, R. E. and Holland, C. K. (**1991**). "Gauging the likelihood of cavitation from short-pulse low-duty cycle of diagnostic ultrasound," Ultrasound Med. Biol. **17**, 179–185.

Brennen, C. E. (**1995**). *Cavitation and Bubble Dynamics* (Oxford University Press, New York).

Chang, P. H., Shung, K. K., and Levene, H. B. (**1996**). "Quantitative measurements of second harmonic Doppler using ultrasound contrast agents," Ultrasound Med. Biol. **22**, 1205–1214.

Chatterjee, D. and Sarkar, K. (**2003**). "A Newtoninan rheological model for the interface of microbubble contrast agents," Ultrasound Med. Biol. **29**, 1749–1757.

Chen, W. S., Matula, T. J., Brayman, A. A., and Crum, L. A. (**2003**). "A comparison of the fragmentation thresholds and inertial cavitation doses of different ultrasound contrast agents," J. Acoust. Soc. Am. **113**, 643–651.

Christiansen, C., Kryvi, H., Sontum, P. C., and Skotland, T. (**1994**). "Physical and biochemical characterization of Albunex™, a new ultrasound contrast agent consisting of air-filled albumin microspheres suspended in a solution of human albumin," Biotechnol. Appl. Biochem. **19**, 307–320.

Church, C. C. (**1995**). "The effects of an elastic solid surface layer on the radial pulsations of gas bubbles," J. Acoust. Soc. Am. **97**, 1510–1521.

Commander, K. W. and Prosperetti, A. (**1989**). "Linear pressure waves in bubbly liquids-comparison between theory and experiments," J. Acoust. Soc. Am. **85**, 732–746.

de Jong, N., Cornet, R., and Lancèe, C. T. (**1994**). "Higher harmonics of vibrating gas-filled microspheres. Part two: Measurements," Ultrasonics **32**, 455–459.

de Jong, N. and Hoff, L. (**1993**). "Ultrasound scattering properties of Albunex microspheres," Ultrasonics **31**, 175–181.

de Jong, N., Hoff, L., Skotland, T., and Bom, N. (**1992**). "Absorption and scatter of encapsulated gas filled microspheres: Theoretical consideration and some measurements," Ultrasonics **30**, 95–103.

Devin, C. (**1959**). "Survey of thermal, radiation and viscous damping of pulsating air bubbles in water," J. Acoust. Soc. Am. **31**, 1654–1667.

Edwards, D. A., Brenner, H., and Wasan, D. T. (**1991**). *Interfacial Transport Processes and Rheology* (Butterworth-Heinemann).

Eller, A. I. (**1970**). "Damping constants of pulsating bubbles," J. Acoust. Soc. Am. **47**, 1469–1470.

Eller, A. and Flynn, H. G. (**1969**). "Generation of subharmonic of order one-half by bubbles in a sound field," J. Acoust. Soc. Am. **46**, 722–727.

El-Sherif, D. M. and Wheatley, M. A. (**2003**), "Development of a novel method for synthesis of a polymeric ultrasound contrast agent,"J. Biomed. Mater. Res. **66A**, 347–355.

Epstein, P. S. and Plesset, M. S. (**1950**). "On the stability of gas bubbles in liquid-gas solutions," J. Chem. Phys. **18**, 1505–1509.

Evans, E. A. and Skalak, R. (**1980**). *Mechanics and Thermodynamics of Biomembranes*(CRC Press, Boca Raton, FL).

Frinking, P. J. A., Boukaz, A., Kirkhorn, J., Ten Cate, F. J., and de Jong, N. (**2000**). "Ultrasound contrast imaging: Current and new potential methods," Ultrasound Med. Biol. **26**, 965–975.

Frinking, P. J. A. and de Jong, N. (**1998**). "Acoustic modeling of shell-encapsulated gas bubbles," Ultrasound Med. Biol. **24**, 523–533.

Goldberg, B. B., Raichlen, J. S., and Forsberg, F. (**2001**). *Ultrasound Contrast Agents: Basic Principles and Clinical Applications*, 2nd ed. (Martin Dunitz, London).

Graham, D. E. and Phillips, M. C. (**1980**). Proteins at liquid interfaces. IV. Dilatational properties," J. Colloid Interface Sci. **70**, 227–239; "Proteins at liquid interfaces. V. Shear properties," J. Colloid Interface Sci. **70**, 239–250.

Hilgenfeldt, S., Lohse, D., and Zomack, M. (**1998**). "Response of bubbles to diagnostic ultrasound: A unifying theoretical approach," Eur. Phys. J. B **4**, 247–255.

Hoff, L. (2000). "Acoustic characterization of contrast agents for medical ultrasound imaging," Ph.D. thesis, Norwegian University of Science and Technology.

Hoff, L., Sontum, P. C., and Hovem, J. M. (**2000**). "Oscillations of polymeric microbubbles: Effect of the encapsulating shell," J. Acoust. Soc. Am. **107**, 2272–2280.

Kabalnov, A., Klein, D., Pelura, T., Schutt, E., and Weers, J. (**1998**). "Dissolution of multicomponent microbubbles in the bloodstream. 1. Theory," Ultrasound Med. Biol. **24**, 739–749.

Khismatullin, D. B. and Nadim, A. (**2002**). "Radial oscillations of encapsulated microbubbles in viscoelastic liquids," Phys. Fluids **14**, 3534–3557.

Kralchevsky, P. A. and Nagayama, K. (**2001**). *Particles at Fluids Interfaces and Membranes*, Studies in Interface Science Vol. **10** (Elsevier, Amsterdam, The Netherlands).

Leighton, T. G. (**1994**). *The Acoustic Bubble* (Academic, San Diego).

May, D. J., Allen, J. S., and Ferrara, K. W. (**2002**). "Dynamics and fragmentation of thick-shelled microbubbles," IEEE Trans. Ultrason. Ferroelectr. Freq. Control **49**, 1400–1410.

Medwin, H. (**1977**). "Counting bubbles acoustically: A review," Ultrasonics **15**, 7–13.

Moran, C. M., Watson, R. J., Fox, K. A. A., and McDicken, W. N. (**2002**). "In vitro acoustic characterization of four intravenous ultrasonic contrast agents at 30 MHz," Ultrasound Med. Biol. **28**, 785–791.

Morgan, K. E., Allen, J. S., Dayton, P. A., Chomas, J. E., Klibanov, A. L. and Ferrara, K. W. (**2000**). "Experimental and theoretical evaluation of microbubble behavior: Effect of transmitted phase and bubble size," IEEE Trans. Ultrason. Ferroelectr. Freq. Control **47**, 1494–1509.

Myrset, A. H., Nicolaysen, H., Toft, K., Christiansen, C., and Skotland, T. (**1996**). "Structure and organization of albumin molecules forming the shell of air-filled microspheres: Evidence for a monolayer of albumin molecules of multiple orientations stabilizing the enclosed air," Biotechnol. Appl. Biochem. **24**, 145–153.

Prosperetti, A. (**1975**). "Nonlinear oscillation of gas bubbles in liquids: Transient solutions and the connection between subharmonic signal and cavitation," J. Acoust. Soc. Am. **57**, 810–821.

Prosperetti, A. (**1984**). "Bubble phenomena in sound fields. Part one," Ultrasonics **22**, 69–78.

Sarkar, K. and Prosperetti, A. (**1994**). "Coherent and incoherent scattering by oceanic bubbles," J. Acoust. Soc. Am. **96**, 332–341.

Sboros, V., MacDonald, C. A., Pye, S. D., Moran, C. M., Gomatam, J., and McDicken, W. N. (**2002**). "The dependence of ultrasound contrast agents backscatter on acoustic pressure: Theory versus experiment," Ultrasonics **40**, 579–583.

Shankar, P. M., Krishna, P. D., and Newhouse, V. L. (**1998**). "Advantages of subharmonic over second harmonic backscatter for contrast-to-tissue echo enhancement," Ultrasound Med. Biol. **24**, 395–399.

Shi, W. T. and Forsberg, F. (**2000**). "Ultrasonic characterization of the nonlinear properties of contrast microbubbles," Ultrasound Med. Biol. **26**, 93–104.

Shi, W. T., Forsberg, F., Hall, A. L., Chiao, R. Y., Liu, J., Miller, S., Thomenius, K. E., Wheatley, M. A., and Goldberg, B. B. (**1999**). "Subharmonic imaging with microbubble contrast agents: Initial results," Ultrason. Imaging **21**, 79–94.

Shi, W. T., Forsberg, F., Tornes, A., Ostensen, J., and Goldberg, B. B. (**2000**). "Destruction of contrast microbubbles and the association with inertial cavitation," Ultrasound Med. Biol. **26**, 1009–1019.

Simpson, D. H., Chin, C. T. and Burns, P. N. (**1999**), "Pulse inversion Doppler: a new method for detecting nonlinear echoes from microbubble contrast agents", IEEE Trans. Ultrason. Ferroelectr. Freq. Control **46**, 372–382.

Sontum, P. C., Østensen, J., Dyrstad, K., and Hoff, L. (**1999**). "Acoustic properties of NC100100 and their relation with the microbubble size distribution," Invest. Radiol. **34**, 268–275.

Erratum: Acoustic radiation force on a compressible cylinder in a standing wave [J. Acoust. Soc. Am. 116, 201–208 (2004)]

Wei Wei, David B. Thiessen, and Philip L. Marston[a)]
Department of Physics and Astronomy, Washington State University, Pullman, Washington 99164-2814

(Received 7 April 2005; accepted 8 April 2005)

[DOI: 10.1121/1.1925848]

PACS number(s): 43.25.Qp, 43.35.Ty [MFH]

Transcription errors appear in Eq. (28). Replace Eq. (28) by $f_2 = 2(1-\rho_o/\rho_i)/D$. For a slightly elliptical liquid column of fixed area in air, this yields the approximation noted at the end of Sec. IV for the dipole coefficient: $f_2 \approx 2[1+(\varepsilon/2)]$, where $\varepsilon = [(b/a)-1]$ is small and b/a is the axis ratio of the ellipse. Since the long-wavelength monopole term for the liquid cylinder in air is $f_1 \approx 1$, the radiation force is proportional to $f_1 + f_2 \approx 3[1+(\varepsilon/3)]$ in this approximation.

[a)]Electronic mail: marston@wsu.edu

 0001-4966/2005/118(1)/551/1/$22.50

Erratum: The role head-induced interaural time and level differences in the speech reception threshold for multiple interfering sound sources [J. Acoust. Soc. Am. 116, 1057 (2004)]

John F. Culling[a)]
School of Psychology, Cardiff University, PO Box 901, Cardiff, CF 10 3YG, United Kingdom

Monica L. Hawley[b)] and Ruth Y. Litovsky[c)]
Department of Biomedical Engineering, Boston University, 44 Cummington Street, Boston, Massachusetts 02215

(Received 12 April 2005; accepted 13 April 2005)

[DOI: 10.1121/1.1925967]

PACS number(s): 43.66.Ba, 43.66.Dc, 43.66.Pn, 43.10.Vx [PFA]

Equation (2) is incorrect, and can be substantially simplified. It should read

$$BMLD = 10 \log_{10} \left[\frac{k - \cos(\phi_s - \phi_m)}{k - \rho} \right],$$

where $k = (1 + \sigma_\varepsilon^2)\exp(\omega_0^2 \sigma_\delta^2)$.

Equation (3) is not needed. The predictions are not materially affected.

[a)]Electronic mail: cullingj@cf.ac.uk
[b)]Current address: Department of Otolaryngology, University of Maryland Medical School, 16 S. Eutaw St., Suite 500, Baltimore, MD 21201.
[c)]Current address: University of Wisconsin Waisman Center, 1500 Highland Avenue, Madison, WI 53705.

 0001-4966/2005/118(1)/552/1/$22.50